CONNECTING MOUNTAIN HYDROCLIMATE THROUGH THE AMERICAN CORDILLERAS

EDITED BY: Alfonso Fernandez, Michel Baraer and Bryan G. Mark
PUBLISHED IN: Frontiers in Earth Science



frontiers Research Topics



frontiers

Frontiers eBook Copyright Statement

The copyright in the text of individual articles in this eBook is the property of their respective authors or their respective institutions or funders. The copyright in graphics and images within each article may be subject to copyright of other parties. In both cases this is subject to a license granted to Frontiers.

The compilation of articles constituting this eBook is the property of Frontiers.

Each article within this eBook, and the eBook itself, are published under the most recent version of the Creative Commons CC-BY licence. The version current at the date of publication of this eBook is CC-BY 4.0. If the CC-BY licence is updated, the licence granted by Frontiers is automatically updated to the new version.

When exercising any right under the CC-BY licence, Frontiers must be attributed as the original publisher of the article or eBook, as applicable.

Authors have the responsibility of ensuring that any graphics or other materials which are the property of others may be included in the CC-BY licence, but this should be checked before relying on the CC-BY licence to reproduce those materials. Any copyright notices relating to those materials must be complied with.

Copyright and source acknowledgement notices may not be removed and must be displayed in any copy, derivative work or partial copy which includes the elements in question.

All copyright, and all rights therein, are protected by national and international copyright laws. The above represents a summary only. For further information please read Frontiers' Conditions for Website Use and Copyright Statement, and the applicable CC-BY licence.

ISSN 1664-8714
ISBN 978-2-88966-774-1
DOI 10.3389/978-2-88966-774-1

About Frontiers

Frontiers is more than just an open-access publisher of scholarly articles: it is a pioneering approach to the world of academia, radically improving the way scholarly research is managed. The grand vision of Frontiers is a world where all people have an equal opportunity to seek, share and generate knowledge. Frontiers provides immediate and permanent online open access to all its publications, but this alone is not enough to realize our grand goals.

Frontiers Journal Series

The Frontiers Journal Series is a multi-tier and interdisciplinary set of open-access, online journals, promising a paradigm shift from the current review, selection and dissemination processes in academic publishing. All Frontiers journals are driven by researchers for researchers; therefore, they constitute a service to the scholarly community. At the same time, the Frontiers Journal Series operates on a revolutionary invention, the tiered publishing system, initially addressing specific communities of scholars, and gradually climbing up to broader public understanding, thus serving the interests of the lay society, too.

Dedication to Quality

Each Frontiers article is a landmark of the highest quality, thanks to genuinely collaborative interactions between authors and review editors, who include some of the world's best academicians. Research must be certified by peers before entering a stream of knowledge that may eventually reach the public - and shape society; therefore, Frontiers only applies the most rigorous and unbiased reviews.
Frontiers revolutionizes research publishing by freely delivering the most outstanding research, evaluated with no bias from both the academic and social point of view. By applying the most advanced information technologies, Frontiers is catapulting scholarly publishing into a new generation.

What are Frontiers Research Topics?

Frontiers Research Topics are very popular trademarks of the Frontiers Journals Series: they are collections of at least ten articles, all centered on a particular subject. With their unique mix of varied contributions from Original Research to Review Articles, Frontiers Research Topics unify the most influential researchers, the latest key findings and historical advances in a hot research area! Find out more on how to host your own Frontiers Research Topic or contribute to one as an author by contacting the Frontiers Editorial Office: frontiersin.org/about/contact

CONNECTING MOUNTAIN HYDROCLIMATE THROUGH THE AMERICAN CORDILLERAS

Topic Editors:
Alfonso Fernandez, University of Concepcion, Chile
Michel Baraer, École de technologie supérieure (ÉTS), Canada
Bryan G. Mark, The Ohio State University, United States

Citation: Fernandez, A., Baraer, M., Mark, B. G., eds. (2021). Connecting Mountain Hydroclimate Through the American Cordilleras. Lausanne: Frontiers Media SA. doi: 10.3389/978-2-88966-774-1

Table of Contents

05 ***Editorial: Connecting Mountain Hydroclimate Through the American Cordilleras***
Alfonso Fernández, Bryan G. Mark and Michel Baraer

08 ***A Socio-Hydrological Perspective on Recent and Future Precipitation Changes Over Tropical Montane Cloud Forests in the Andes***
Fausto O. Sarmiento and Gabriel J. Kooperman

14 ***Projected Changes to Extreme Runoff and Precipitation Events From a Downscaled Simulation Over the Western United States***
Melissa L. Wrzesien and Tamlin M. Pavelsky

31 ***High Resolution Mapping of Ice Mass Loss in the Gulf of Alaska From Constrained Forward Modeling of GRACE Data***
Cheick Doumbia, Pascal Castellazzi, Alain N. Rousseau and Macarena Amaya

45 ***Corrigendum: High Resolution Mapping of Ice Mass Loss in the Gulf of Alaska From Constrained Forward Modeling of GRACE Data***
Cheick Doumbia, Pascal Castellazzi, Alain N. Rousseau and Macarena Amaya

47 ***Mass Balance and Climate History of a High-Altitude Glacier, Desert Andes of Chile***
Christophe Kinnard, Patrick Ginot, Arzhan Surazakov, Shelley MacDonell, Lindsey Nicholson, Nicolas Patris, Antoine Rabatel, Andres Rivera and Francisco A. Squeo

67 ***Future Meteorological Droughts in Ecuador: Decreasing Trends and Associated Spatio-Temporal Features Derived From CMIP5 Models***
Lenin Campozano, Daniela Ballari, Martin Montenegro and Alex Avilés

84 ***Observed and Projected Hydroclimate Changes in the Andes***
José Daniel Pabón-Caicedo, Paola A. Arias, Andrea F. Carril, Jhan Carlo Espinoza, Lluís Fita Borrel, Katerina Goubanova, Waldo Lavado-Casimiro, Mariano Masiokas, Silvina Solman and Ricardo Villalba

113 ***Hydroclimate of the Andes Part I: Main Climatic Features***
Jhan Carlo Espinoza, René Garreaud, Germán Poveda, Paola A. Arias, Jorge Molina-Carpio, Mariano Masiokas, Maximiliano Viale and Lucia Scaff

133 ***Climatological and Hydrological Observations for the South American Andes:* In situ *Stations, Satellite, and Reanalysis Data Sets***
Thomas Condom, Rodney Martínez, José Daniel Pabón, Felipe Costa, Luis Pineda, Juan Jose Nieto, Freddy López and Marcos Villacis

153 ***Detecting the Effects of Sustained Glacier Wastage on Streamflow in Variably Glacierized Catchments***
R. D. Moore, Ben Pelto, Brian Menounos and David Hutchinson

165 ***High Impact Weather Events in the Andes***
Germán Poveda, Jhan Carlo Espinoza, Manuel D. Zuluaga, Silvina A. Solman, René Garreaud and Peter J. van Oevelen

197 ***A Review of the Current State and Recent Changes of the Andean Cryosphere***

M. H. Masiokas, A. Rabatel, A. Rivera, L. Ruiz, P. Pitte, J. L. Ceballos, G. Barcaza, A. Soruco, F. Bown, E. Berthier, I. Dussaillant and S. MacDonell

224 ***Mountain Temperature Changes From Embedded Sensors Spanning 2000 m in Great Basin National Park, 2006–2018***

Emily N. Sambuco, Bryan G. Mark, Nathan Patrick, James Q. DeGrand, David F. Porinchu, Scott A. Reinemann, Gretchen M. Baker and Jason E. Box

242 ***Atmospheric Rivers Contribution to the Snow Accumulation Over the Southern Andes (26.5° S–37.5° S)***

Felipe Saavedra, Gonzalo Cortés, Maximiliano Viale, Steven Margulis and James McPhee

253 ***WRF High Resolution Dynamical Downscaling of Precipitation for the Central Andes of Chile and Argentina***

Vanucia Schumacher, Alfonso Fernández, Flavio Justino and Alcimoni Comin

272 ***High-Resolution Precipitation Gridded Dataset on the South-Central Zone (34°S–41°S) of Chile***

Francisco-J. Alvial Vásquez, Rodrigo Abarca-del-Río and Andrés I. Ávila

292 ***Development and Validation of a Model to Evaluate the Water Resources of a Natural Protected Area as a Provider of Ecosystem Services in a Mountain Basin in Southern Chile***

Sandra Fernández-Alberti, Rodrigo Abarca-del-Río, Cristian Bornhardt and Andres Ávila

310 ***Hydroclimate of the Andes Part II: Hydroclimate Variability and Sub-Continental Patterns***

Paola A. Arias, René Garreaud, Germán Poveda, Jhan Carlo Espinoza, Jorge Molina-Carpio, Mariano Masiokas, Maximiliano Viale, Lucia Scaff and Peter J. van Oevelen

frontiers in Earth Science

EDITORIAL
published: 23 March 2021
doi: 10.3389/feart.2021.667264

Editorial: Connecting Mountain Hydroclimate Through the American Cordilleras

Alfonso Fernández[1]*, *Bryan G. Mark*[2] *and Michel Baraer*[3]

[1]Department of Geography, Mountain Geoscience Group, Universidad de Concepción, Concepción, Chile, [2]Department of Geography, The Ohio State University, Columbus, OH, United States, [3]Hydrology, Climate and Climate Change Laboratory, École de Technologie Supérieure, Montréal, QC, Canada

Keywords: hydroclimate, mountain environments, climate change, cryosphere, hydrology, climate modeling, meteorological observations and measurements

Editorial on the Research Topic

Connecting Mountain Hydroclimate Through the American Cordilleras

Mountains are key hydroclimatic features that couple large-scale atmospheric processes with the earth surface, influencing the development of diverse waterscapes. Decades of transformative research have highlighted how mountains are valuable for society, revealing that changes in these landscapes exert significant impacts on downstream hydrological regimes that support lives and livelihoods of millions (Viviroli et al., 2020). Yet despite sharing common features of verticality and orographic uplift, the complexity of mountain environments is an inherent feature that inevitably leads to geographic particularities, and challenges maintaining consistent observations. Nowadays, many of these mountain waterscapes are undergoing significant alterations in the context of ongoing climate and environmental changes (Immerzeel et al., 2020). The vast latitudinal expanse of the Cordilleras that span from Patagonia to Alaska provides abundant examples of mountain hydroclimatic dynamics as they traverse entire atmospheric systems and delimit diverse climatic regions. Along this interhemispheric transect are similarities and contrasts in both biophysical and human components, whereby intercomparisons may broaden understanding. How similar and how distinct is the research emerging in this context? Can we, as a community of researchers, leverage our geographic diversity to gain new insights that so far have not been described in a frame facilitating cross comparisons along the American Cordilleras? The present collection of research papers aims to move us forward to questioning our perspectives and advance coordinated efforts, with studies highlighting different aspects of the hydroclimate along the American mountains. Our intention with this special edition is to show diverse research—distinct in methodology, scale, and topic—that is linked to a common mountain hydroclimatic theme. The context of rapid climate and environmental change raises the value and urgency of mountain research that allows for comparative views along the American Cordilleras, and we anticipate that such efforts might elucidate constructive perspectives into changes taking place at unprecedented rates, and ideally may support future strategies to tackle these emergent challenges.

Instrumental and satellite observations are vital tools for accurate hydroclimatic characterization. For mountain areas, acquiring, curating and organizing data remain challenging and thus systematization efforts need to be encouraged. Condom et al. have likely produced one of the most exhaustive analysis of available hydroclimatic datasets from the Andes. The study shows that in almost all countries actual instrumental records comprise a small percentage of national networks. They suggest that satellite data may become a crucial source for hydroclimatic analysis given the increasing coverage over the region, albeit with diverse spatiotemporal resolutions that necessitate

OPEN ACCESS

Edited and reviewed by:
Nick Van De Giesen,
Delft University of Technology,
Netherlands

***Correspondence:**
Alfonso Fernández
alfernandez@udec.cl

Specialty section:
This article was submitted to Biophysics, a section of the journal Frontiers in Earth Science

Received: *12 February 2021*
Accepted: *18 February 2021*
Published: *23 March 2021*

Citation:
Fernández A, Mark BG and Baraer M (2021) Editorial: Connecting Mountain Hydroclimate Through the American Cordilleras. Front. Earth Sci. 9:667264. doi: 10.3389/feart.2021.667264

further evaluations of these data. Sambuco et al. demonstrate that a relatively dense network of well-distributed embedded sensors recording continuous observations of a few variables in the Great Basin National Park, United States, reveal spatiotemporal patterns that may provide effective alternatives to more expensive single stations. They may allow for more accurate evaluation of water resources on mountains since they span over 2 km vertical range to record seasonal changes in lapse rates, document significant temperature changes in diverse microenvironments, and thus capture the influence of site characteristics on sensor's records. Under the scenario of notorious gaps of observations along the American Cordilleras, numerical modeling offers a viable alternative to develop process-based understanding of atmosphere-hydrosphere linkages within high elevation environments. Sarmiento and Kooperman provide a much-needed transdisciplinary perspective on the impacts of expected precipitation increases along the Tropical Andes derived from the Coupled Model Intercomparison Model Project phase five (CMIP5). In Ecuador, Campozano et al. combined instrumental observations, CMIP5 model output and dynamical downscaling to assess future scenarios of drought. They demonstrate that present day conditions are well reproduced by models within high elevation regions in this country, while projections point to lower probability of droughts.

Since global climate models are too coarse in resolution to adequately represent detailed processes within American mountain regions given their narrow zonal extension, limited area models and dynamical downscaling methods become relevant tools. By providing continuous climate fields/grids at finer-scales, such modeling studies may improve interpretations derived from observational networks and provide targeted projections for hydroclimatic planning. Wrzesien and Pavelsky used the Weather Research and Forecasting model (WRF) to downscale CMIP5 output, studying precipitation and runoff changes in the Western United States. They project that, in several mountainous catchments draining mountain areas, the timing of peak discharge changes and extreme runoff increases in the future. Along the same lines, Schumacher et al. downscaled the ERA-Interim reanalysis at different cell sizes over a ~500 km Andean strip between 32° and 38°S, and analyzed the performance of the WRF model to reproduce precipitation observational datasets, detecting that the modeling captured seasonal and interannual variability. They suggest that a better resolved topography improves model performance according to elevation. Over the same Andean region, Alvial Vásquez et al. developed a gridded precipitation dataset for hydroclimatic studies using a combination of WRF downscaling at 4 km and a multilinear regression model based on topography and locational descriptors. They deliver a final product at about 800 m grid cell resolution that describes the conditions in the study area well.

Complex interactions between topography and atmospheric systems determine features that need to be considered in the interpretation of changes in mountain hydroclimate. The tandem contributions of Arias et al. and Espinoza et al. deliver detailed characterizations of the climate and hydrology of the Andes from the tropics to Patagonia. This description was made by focusing on large-scale atmospheric dynamics and continental water balance, and in the process they propose open research questions. Pabón-Caicedo et al.'s review changes in Andean runoff, precipitation, and temperature, providing the most up-to-date synthesis of trends emerging within the region while featuring some of the latest scenario projections based upon climatic downscaling. These large-scale analyses are often used for developing case-studies that better support decision-making on mountain water resources. Fernández-Alberti et al. use hydrological modeling to assess water resources within mountain basins featuring diverse land uses, such as in the Andes of southern Chile, by computing a water balance and carefully considering supplies and demands. Two papers focus on characterization of particular atmospheric interactions: Poveda et al. provide a detailed overview of the consequences of extreme weather events along the Andes, highlighting the distinct mesoscale atmospheric systems that produce damaging events such as flash floods and cold waves. Saavedra et al. reveal that atmospheric rivers in the Andes between 26.5° and 36.5°S and the different phases of El Niño Southern Oscillation impact the number and intensity of snowfall events.

One of the most definitive features of the American Cordilleras running along the west edge of the continent is the glacier and perennial snow coverage. Thus, monitoring the cryosphere in this region is a fundamental requisite for hydroclimatic understanding. The different papers that focus on glaciers in this Frontiers' topic picture a generalized shrinking punctuated by short periods of slowing down of the general trends. Masiokas et al. review the latest literature on the Andean cryosphere, highlighting unprecedented advances in remotely sensed glacier monitoring during the last two decades afforded by the availability of imagery while stressing the need for continuous *in-situ* monitoring and further research on glacier-melt contribution to runoff. Kinnard et al. present a study over a cold-glacier in the Chilean Andes, analyzing a rich pool of data on volumetric fluctuations, glacier geochemistry, and climate, which facilitate a much needed process-based understanding and mass balance reconstruction for this particular region. In the Northern Hemisphere, Doumbia et al. quantified ice loss over the Gulf of Alaska by downscaling data from the Gravity Recovery And Climate Experiment (GRACE), providing a new estimate for this region as well as a downscaling method that may be applied in other regions with large glacier coverage. Finally, Moore et al. point to the increasingly concerning issue of hydrological thresholds in glacierized catchments, in this case exemplified in a section of the Columbia river basin where they find that late summer streamflow reveals the consequences of glacier shrinkage over the last four decades.

We assert that this collection of papers provides a compendium exemplifying current research underway all along the American Cordillera that documents the hydroclimatic diversity and vulnerability within mountain environments. We think that the variety of studies and

reviews presented attest to a healthy scientific community that is progressing in novel directions that could be incorporated to support more coordinated efforts and better management decisions under future hydroclimatic scenarios.

AUTHOR CONTRIBUTIONS

AF wrote the first draft of the manuscript. All authors contributed to manuscript revision, read, and approved the submitted version.

REFERENCES

Immerzeel, W. W., Lutz, A. F., Andrade, M., Bahl, A., Biemans, H., Bolch, T., et al. (2020). Importance and vulnerability of the world's water towers. *Nature* 577, 364–369. doi:10.1038/s41586-019-1822-y

Viviroli, D., Kummu, M., Meybeck, M., Kallio, M., and Wada, Y. (2020). Increasing dependence of lowland populations on mountain water resources. *Nat. Sustain.* 3, 917. doi:10.1038/s41893-020-0559-9

FUNDING

AF is funded by the Chilean Science Council (ANID) FONDECYT 1201429. MB is funded by the Natural Science and Engineering Research Council (NSERC) of Canada - RGPNS-2020-05612.

ACKNOWLEDGMENTS

BM acknowledges funding from the Western National Parks Association and the Department of Geography at The Ohio State University.

Conflict of Interest: The authors declare that the research was conducted in the absence of any commercial or financial relationships that could be construed as a potential conflict of interest.

Copyright © 2021 Fernández, Mark and Baraer. This is an open-access article distributed under the terms of the Creative Commons Attribution License (CC BY). The use, distribution or reproduction in other forums is permitted, provided the original author(s) and the copyright owner(s) are credited and that the original publication in this journal is cited, in accordance with accepted academic practice. No use, distribution or reproduction is permitted which does not comply with these terms.

frontiers in Earth Science

OPINION
published: 10 December 2019
doi: 10.3389/feart.2019.00324

A Socio-Hydrological Perspective on Recent and Future Precipitation Changes Over Tropical Montane Cloud Forests in the Andes

Fausto O. Sarmiento and Gabriel J. Kooperman*

Neotropical Montology Collaboratory and Climate, Clouds and Land Modeling Group, Department of Geography, University of Georgia, Athens, GA, United States

Keywords: tropical montane cloud forests, precipitation change, socio-hydrology, Tropandean landscapes, earth system models, climate change

Tropical montane cloud forests (TMCFs) in the Andes, with mild temperatures and plenty of water, boast prodigious biocultural diversity. Runoff from these slopes supports local communities by supplying drinking water and irrigation to growing lowland cities. However, precipitation in the region is sensitive to human environmental impacts and effective conservation planning requires assessing past and future climate changes in local cultural, historical, and political contexts. In particular, Earth System Models (ESMs) suggest a reduction in precipitation over most tropical land, including TMCFs in the Andes during the twentieth century, has been driven largely by increases in aerosol emissions (Wang, 2015). With the exception of the Amazon rainforest, this trend reverses in the twenty first century, with increases in precipitation over Asia, Central Africa, and the tropical Andes, as greenhouse gas-driven changes become the dominant response (Stocker et al., 2013; Kooperman et al., 2018a). Although multi-model mean changes are large, many ESMs show opposing trends on regional scales, and historical observations are limited, leading to uncertainties for past and future changes.

Focusing on TMCFs in the Andes, we survey how this reversal of precipitation change in the twenty first century, and its associated uncertainties, may impact the complex interplay of cultural ecosystem services (CES) that TMCFs provide. We seek to highlight the need for transdisciplinary perspectives to understand how recent and future precipitation changes interact with the socioecological systems of Tropandean mountainscapes. We present results from widely-used climate models, which have contributed to the Coupled Model Intercomparison Project Phase Five (CMIP5, Taylor et al., 2012), to highlight the large but uncertain changes in this region. We then assess single forcing experiments, provided by the Community Earth System Model (CESM1) Large Ensemble project (Hurrell et al., 2013; Kay et al., 2015), to identify the anthropogenic drivers of precipitation change over the Andes. These results serve to illustrate a global modeling perspective and communicate the need to consider local CES in the development of effective adaptation measures. We argue that understanding societal implications of climate change on TMCF hydroclimates should include past and future considerations of the socio-hydrological dimension as well as the physical climate.

In this opinion, we discuss the historic role of fire in cultural practices, the influence of present-day biomass burning aerosol on precipitation, future drivers of precipitation change and local water resource use, to highlight the need for new research at the intersection of these areas.

OPEN ACCESS

Edited by:
Alfonso Fernandez, Universidad de Concepción, Chile

Reviewed by:
Vernon Scarborough, University of Cincinnati, United States
Jeff La Frenierre, Gustavus Adolphus College, United States

****Correspondence:***
Fausto O. Sarmiento
fsarmien@uga.edu

Specialty section:
This article was submitted to Atmospheric Science, a section of the journal Frontiers in Earth Science

Received: *09 September 2019*
Accepted: *21 November 2019*
Published: *10 December 2019*

Citation:
Sarmiento FO and Kooperman GJ (2019) A Socio-Hydrological Perspective on Recent and Future Precipitation Changes Over Tropical Montane Cloud Forests in the Andes. Front. Earth Sci. 7:324. doi: 10.3389/feart.2019.00324

TROPANDEAN ECOREGION

Neotropical landscapes harbor globally important hotspots of biodiversity (Myers, 2003; Lovejoy and Hanna, 2019) and bolster ancestral cultures that have developed a manufactured landscape

(White, 2013; Scarborough et al., 2019) depending on rain water for irrigation and dry-slope agriculture. To illustrate the complexity of socio-hydrological coupling and change in mountainous areas with humans dating back thousands of years, we selected the Tropandean region of Central America and Northern South America. The equatorial mountains of the Andean crescent (*Chinchaysuyu*), reportedly the wettest part of the planet (Bush, 2002), exhibit the largest number of species per unit area in any terrestrial ecosystem, with predominant taxa including birds, reptiles, amphibians, and insects. This is also the place where most bryophytes are found, along with the largest diversity of broad-leaf species, mainly Lauracea and Areacacea families. In recent history, the landscape has been transformed by the pressures of modernity (e.g., monoculture, urbanization, invasive species, and biodiversity loss) and exhibits significant climate changes in historic and future ESM simulations (Stocker et al., 2013). But the influence of humans on the local mountainscape dates back much further—indigenous cultures have domesticated cloud forests and opened highland terrains of this region for hunting, gathering, planting, livestock rearing, and other more consumptive activities such as mining and handcrafting metals and fibers. Many of these activities involve the use of fire, the most important tool for Andean treeline ecotone region (ATER) transformation (Sarmiento and Frolich, 2002), which has reshaped local mountainscapes over centuries.

The long history of fire use in TMCFs is evident in records of charcoal cairns and in the generalized management to maintain and expand grasslands in the mountains (Luteyn and Balslev, 1992). This explains the mythology associated with burning and its connection with rain—in the Andean pantheon, fire has been used to placate the gods' wrath with their dry spell, and to bring back the rains to restore mountain harmony (*Urku kawsay*) (Steele and Allen, 2004). Inka mythology identifies the supreme deity *Wirakucha* who brought winds and rains to the mountains (Urton, 1999). Andean cultures follow practices of respect and reciprocity (*Ayni*) to promote a balanced subsistence for people, animals, plants, and mountains (*Sumak kawsay*). Thus, culturally appropriate to the Andean philosophy, burning of highland grasslands (or paramo) and TCMFs are daily occurrences in ATERs (Carrillo-Rojas et al., 2019; Knapp, 2019) producing heavy loads of atmospheric black carbon in the soils. At the same time, aerosol emissions from biomass burning can be pernicious sources of air pollution, with significant impacts on human health (Reddington et al., 2015). These emissions can be transported over long distances (Bourgeois et al., 2015) and impact remote ecosystems (Boy et al., 2008). Aerosol also influences the climate by modifying the atmospheric thermodynamic state and circulation patterns (Thornhill et al., 2018), as well as cloud microphysical properties, all of which can modulate precipitation patterns (Tao et al., 2012).

Precipitation is critical to the maintenance of CES and the overall availability of freshwater, which incorporate the intangibles to mountainscape (*Urkumanta*) conservation (Sarmiento, 2016). However, regional precipitation changes are driven by not only local pyroecology influences on the environment, but also non-local influences, such as biomass burning aerosol from the Amazon and global-scale climate change (Stocker et al., 2013). Additionally, it is challenging for conservation planning to bring ESM scale projections into the context of local cultural, historical, and political perspectives. Particularly in the tropical Andes, where large future changes in precipitation are projected (**Figure 1B**), but with significant uncertainty, in part because the fine-scale topographic features of the region are not resolved in global-scale models. Progress toward understanding regional climate changes and impacts thus requires ecological modeling across global to local scales, including paleoecological parameters in hindcasting and forecasting extreme scenarios of change (Cheddadi et al., 2019), and taking into account historical socioecological perspectives.

Below we separately present *global modeling* and *political ecological* perspectives in order to emphasize the need for research that connects across these disparate scales and disciplines.

GLOBAL MODELING PERSPECTIVE

Over the last decade, global climate models have evolved into fully capable representations of the Earth system, including interactive treatments of the atmosphere, ocean, land, and sea-ice. The atmospheric component of many ESMs includes aerosol particles that are advected from source regions and can influence cloud droplet number, radiative properties of the atmosphere and precipitation (Neale et al., 2010). The land component includes a variety of plant types with physiological properties that depend on temperature, moisture and CO_2 concentration (Lawrence et al., 2011). All of these processes are critical for capturing the complex coupled responses that govern changes in precipitation over the Andes, which undoubtedly will affect the distribution, community composition and structure of TMCFs in the Andean crescent.

The CMIP5 multi-model mean precipitation change over the twentieth century, from a subset of advanced models in which aerosol concentrations directly affect cloud droplet formation (i.e., CanESM2, von Salzen et al., 2013; CESM1-CAM5, Hurrell et al., 2013; CSIRO-Mk3-6-0, Rotstayn et al., 2012; GFDL-CM3, Donner et al., 2011; HadGEM2-ES, Martin et al., 2011; MIROC-ESM-CHEM, Watanabe et al., 2011; MIROC-ESM, Watanabe et al., 2011; MRI-CGCM3, Yukimoto et al., 2012; NorESM1-M, Iversen et al., 2013; FGOALS-g2, Li et al., 2013), shows drying across the tropics, particularly over Asia, northern South America, and Central America (**Figure 1A**). This pattern emerges even in simulations without changes in greenhouse gases and is linked instead to anthropogenic aerosol emissions (Wang, 2015). In a set of single forcing experiments, which isolate the contribution from different anthropogenic forcing agents (e.g., greenhouse gases, aerosol from industry and transportation, aerosol from biomass burning, and land-cover change), we find the historical drying pattern in CESM1 over the equatorial Andes (and Indonesia) results primarily from biomass burning aerosol emissions (**Figures 1C–G**).

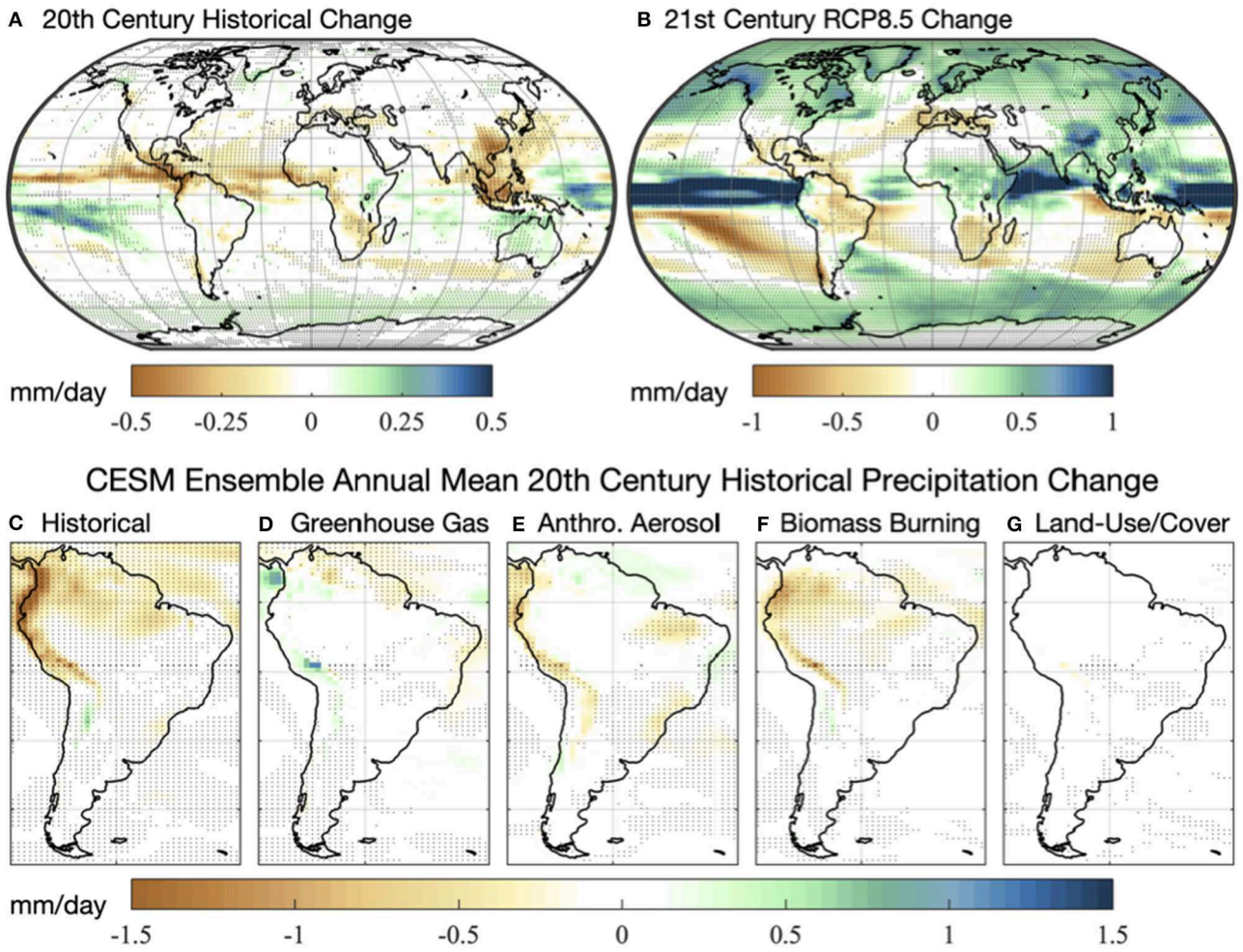


FIGURE 1 | Annual mean precipitation changes from **(A)** CMIP5 historical simulations (1971–2000 to 1871–1900), **(B)** CMIP5 RCP8.5 simulations (2071–2100 to 1971–2000), **(C)** CESM ensemble mean historical simulations (1971–2000 to 1850), and **(D–G)** contributions from single forcings as described in the text. Stippling in **(A,B)** indicates where 8 of 10 models have the same sign of change. Stippling in **(C)** indicates where changes are statistically significant at 95% confidence across 35 ensemble members. Stippling in **(D–G)** indicates where a single forcing contributes to at least 50% of the full historical change.

In the twenty first century, under the Representative Concentration Pathway 8.5 scenario, the same set of CMIP5 models show that this signal reverses over most tropical land, leading to increases over Asia, Central Africa, and the Andes (**Figure 1B**). Future changes over South America include a decrease over the Amazon and an increase over the Andes, which has been associated with both an atmospheric-radiative response to higher greenhouse gases and a plant-physiological response to higher CO_2 concentrations (i.e., reduced stomatal conductance and transpiration) (**Figure 1** from Kooperman et al., 2018a). The plant-physiological response leads to suppressed convection over the Amazon forest and circulation pathways that enhance moisture flow up the eastern slopes of the Andes (Langenbrunner et al., 2019). Reductions in transpiration due to plant responses to higher CO_2 also leave more moisture in the soil column, which can contribute to increases runoff and flooding in the Andes (Kooperman et al., 2018b).

These ESM results reveal a reversing trend in precipitation changes over the equatorial Andes from the twentieth to twenty first centuries. Historical simulations, and indigenous knowledge, suggest that fires have played an important role in the climate of Andes over the last hundred and thousands of years, respectively. As Amazon fires continue in the present-day, the long ranging impacts of their emissions are likely to remain a strong influence on the near-term climate of the Andes. But as the concentrations of greenhouse gases rise, global-scale warming and circulation changes may drive an opposing response that increases precipitation. However, despite the large magnitude of change in the multi-model mean, many individual models can disagree on the sign of

the change (i.e., lack of stippling in **Figures 1A,B**). These competing drivers of environmental change and uncertainty across model simulations in the region, in combination with local socio-cultural pressures, present a major challenge for conservation efforts.

POLITICAL ECOLOGICAL PERSPECTIVE

As dynamic constructs, press and pulse disturbances drive change in the socio-ecological landscapes of the Tropical Andes, which continues to ignite scholarly debate on whether forests or grasslands (Appenzeller, 2019). Amidst ancestral customary law and ritualized practices in relation to mountain fires, political decisions on resource use and nature conservation have overlooked the anthropogenic proxy for climate and land-use transformation (Chepstow-Lusty et al., 1996; Varela, 2008; Sarmiento, 2012). Historical accounts and other geocritical literature have been used to develop a critical discourse analysis of water-fire interactions (Garreaud, 2007; Sarmiento et al., 2019), but difficulties remain in bringing together multimethod approaches for the study of deforestation (Delabre et al., 2019). Of special note is the extensive impact of colonial timber use for construction and heating in growing Andean cities. Much of the regional deforestation has been driven by procuring cheap fuelwood and charcoal. In fact, charcoal production and commercialization became the most important activity of a growing domestic energy source (Wunder, 1996) often associated with impoverished populations (Garofalo, 2019).

Old approaches, favoring exotic plantations, increasing the agricultural frontier and establishing payments for ecosystem services, are beginning to shift toward new considerations of CES. These include reforestation with native species, agroecological practices, community-based conservation, and nature benefits to people, with value of spirituality, myths, traditions, and landscape memory of decolonial thinking of the sacred transition (Sarmiento et al., 2017; Oslender, 2019). This is a transitional phase where the multiple values of nature approach incorporates factors of local cosmological views as well as the intangibles (i.e., heirloom flavors, textile designs, rituals) and incommensurables (i.e., national identity, rootedness, spirituality) of CES (Alimonda, 2016). Most conservation programs from either governments or NGOs are required to include social science into the fabric of research for climate effects and sustainability, as Rousseau's (2017) manifesto claiming for transdisciplinary understanding of Earth systems. The political ecology of ice and water in the Andes remains an academic concern to secure climate adaptation measures (Nüsser, 2017; Hock et al., 2019) and adequate representation of mountain development priorities (Sarmiento, 2016).

Because of the shifting paradigm of decolonial histories, a new transdisciplinary effort is needed to fully grasp the water-climate conundrum (Fonstead, 2017). We must understand not only the changes to the physical climate system (e.g., observing and simulating river flow and discharge, horizontal precipitation, glacial mass, and snow pack), but develop a holistic portrait of environmental-societal interactions and impacts (Sarmiento, 2008) for a more comprehensive view of future adaptations to climate change in the ATER.

CONCLUSION

We emphasize that epistemes of climate changes in TMCFs of the Tropandean landscapes may only be reached by bridging the gap across the scales of ESM to the socio-hydrological tenants of a local community's perceptions. In the short-term climate, the ATER may continue to be strongly influenced by remote biomass burning emissions and forest fires at the fringes. In the long-term climate, a trend of increasing precipitation over the twenty first century due to rising CO_2 and global warming, may affect people of Andean communities with future impacts on water management and overflow control, landslide and rockslide (*Wayku*) management, and flooding. Coupled modeling of the past and future co-dependency of physical and human geographies in the mountainscape is needed to reduce uncertainty in the application of adaptation measures toward resilient, sustainable futures.

AUTHOR CONTRIBUTIONS

FS and GK both contributed to writing and editing the manuscript. FS contributed specifically to the political ecological section. GK contributed to the global modeling section.

ACKNOWLEDGMENTS

We acknowledge the World Climate Research Programme's Working Group on Coupled Modeling for CMIP5, and the climate modeling groups referenced in the manuscript for producing and making available their model output. For CMIP5 the U.S. Department of Energy's Program for Climate Model Diagnosis and Intercomparison provides coordinating support and led development of software infrastructure in partnership with the Global Organization for Earth System Science Portals. CESM development is led by the National Center for Atmospheric Research (NCAR) with support from the U.S. National Science Foundation and U.S. Department of Energy. Computing resources for the CESM Large Ensemble Community Project were provided on Yellowstone by NCAR Computational Information Systems Laboratory. GK acknowledges support from the U.S. Department of Energy Regional and Global Model Analysis (RGMA) Program (DE-SC0019459) as well as the University of Georgia's Office of Research, Junior Faculty Seed Grant Program and President's Interdisciplinary Seed Grant Program. FS acknowledges support from the U.S. National Science Foundation (NSF) counterpart funding to the Belmont Forum for Mountains (BF) on Vulnerability of Populations Under Extreme Scenarios (VULPES) grant (ANR-15-MASC-0003) as well as the UGA's Office of Research/Office of International Education Global Collaborative Research Program. We also thank the editors of this Special Issue and two reviewers who enhanced the manuscript.

REFERENCES

Alimonda, H. (2016). Notas sobre la ecología política latinoamericana: arraigo, herencias, diálogos. *Ecol. Polít.* 51, 36–42.

Appenzeller, T. (2019). Fire on the mountain. *Science* 365, 1094–1097. doi: 10.1126/science.365.6458.1094

Bourgeois, Q., Ekman, A. M. L., and Krejci, R. (2015). Aerosol transport over the Andes from the Amazon Basin to the remote Pacific Ocean: a multiyear CALIOP assessment. *J. Geophys. Res. Atmos.* 120, 8411–8425. doi: 10.1002/2015JD023254

Boy, J., Rollenbeck, R., Valarezo, C., and Wilcke, W. (2008). Amazonian biomass burning-derived acid and nutrient deposition in the north Andean montane forest of Ecuador. *Global Biogeochem. Cy.* 22:GB4011. doi: 10.1029/2007GB003158

Bush, M. B. (2002). Distributional change and conservation on the Andean flank: a palaeoecological perspective. *Glob. Ecol. Biogeogr.* 11, 463–473. doi: 10.1046/j.1466-822X.2002.00305.x

Carrillo-Rojas, G., Silva, B., Rollenbeck, R., Célleri, R., and Bendix, J. (2019). The breathing of the Andean highlands: net ecosystem exchange and evapotranspiration over the páramo of southern Ecuador. *Agri. Forest Meteorol.* 265, 30–47. doi: 10.1016/j.agrformet.2018.11.006

Cheddadi, R., Mahammdi, M., and Sarmiento, F. O. (2019). Past plant diversity changes and mountain tree species conservation. *Past Global Change. Mag.* 27:36. doi: 10.22498/pages.27.1.36

Chepstow-Lusty, A. J., Bennett, K. D., Switsur, V. R., and Kendall, A. (1996). 4000 years of human impact and vegetation change in the Central Peruvian Andes—with events parallelling the Maya record? *Antiquity* 70, 824–833. doi: 10.1017/S0003598X0008409X

Delabre, I., Alexander, A., Rowhani, P., and Antonarakis, A. (2019). "Politics and power in managing data on zero deforestation: lessons and challenges for integrating multi-disciplinary natural and social science methods," in *American Association of Geographers Annual Meeting* (Washington, DC).

Donner, L. J., Wymana, B. L., Hemlera, R. S., Horowitza, L. W., Minga, Y., Zhao, M., et al. (2011). The dynamical core, physical parameterizations, and basic simulation characteristics of the atmospheric component AM3 of the GFDL Global Coupled Model CM3. *J. Clim.* 24, 3484–3519. doi: 10.1175/2011JCLI3955.1

Fonstead, M. (2017). *Mountains: Physical, Human-Environmental and Socio-Cultural Dynamics*. New York, NY: Routledge.

Garofalo, L. (2019). "Black space production in Andean societies," in *Chapter 16: Transnational Perspectives on the Conquest and Colonization of Latin America*, eds J. Mander, D. Midgley, and C. Beaule (Abingdon: Routledge). doi: 10.4324/9780429330612-17

Garreaud, R. (2007). The Andes climate and weather. *Adv. Geosci.* 22, 3–11. doi: 10.5194/adgeo-22-3-2009

Hock, R. G., Rasul, C., Adler, B., Cáceres, S., Gruber, Y., Hirabayashi, M., et al. (2019). "Chapter 2: High mountain areas," in *IPCC SR Ocean and Cryosphere Report* (MRI Mountain Research Initiative).

Hurrell, J., Holland, M. M., and Gent, P. R. (2013). The community earth system model: a framework for collaborative research. *Bull. Am. Meteorol. Soc.* 94, 1339–1360. doi: 10.1175/BAMS-D-12-00121.1

Iversen, T., Bentsen, M., Bethke, I., Debernard, J. B., Kirkevåg, A.,Seland, O., et al. (2013). The Norwegian earth system model, NorESM1–M. Part 2: climate response and scenario projections. *Geosci. Model Dev.* 6, 1–27. doi: 10.5194/gmd-6-389-2013

Kay, J. E., Deser, C., Phillips, A., Mai, A., Hannay, C., Strand, G., et al. (2015). The Community Earth System Model (CESM) large ensemble project: a community resource for studying climate change in the presence of internal climate variability. *Bull. Amer. Meteor. Soc.* 96, 1333–1349. doi: 10.1175/BAMS-D-13-00255.1

Knapp, G. (2019). *Andean Ecology: Adaptive Dynamics in Ecuador*. Nashville, TN: Routledge. doi: 10.4324/9780429046186

Kooperman, G. J., Chen, Y., Hoffman, F. M., Koven, C. D., Lindsay, K., Pritchard, M. S., et al. (2018a). Forest response to rising CO_2 drives zonally asymmetric rainfall change over tropical land. *Nat. Clim. Change* 8, 434–440. doi: 10.1038/s41558-018-0144-7

Kooperman, G. J., Fowler, M. D., Hoffman, F. M., Koven, C. D., Lindsay, K., Pritchard, M. S., et al. (2018b). Plant physiological responses to rising CO_2 modify simulated daily runoff intensity with implications for global-scale flood risk assessment. *Geophys. Res. Lett.* 45, 12457–12466. doi: 10.1029/2018GL079901

Langenbrunner, B., Pritchard, M. S., Kooperman, G. J., and Randerson, J. T. (2019). Why does Amazon precipitation decrease when tropical forests respond to increasing CO_2? *Earths Fut.* 7, 450–468. doi: 10.1029/2018EF001026

Lawrence, D. M., Oleson, K. W., Flanner, M. G., Thornton, P. E., Swenson, S. C., Lawrence, P. J., et al. (2011). Parameterization improvements and functional and structural advances in version 4 of the community land model. *J. Adv. Model. Earth Syst.* 3:M03001. doi: 10.1029/2011MS00045

Li, L., Wang, B., Dong, L., Liu, L.,Shen, S., Hu, N., et al. (2013). Evaluation of grid-point atmospheric model of IAP LASG version 2 (GAMIL2). *Adv. Atmos. Sci.* 30, 855–867. doi: 10.1007/s00376-013-2157-5

Lovejoy, J., and Hanna, L. (eds.). (2019). *Climate Change and Biodiversity*. New Haven, CT: Yale University Press.

Luteyn, J. L., and Balslev, H. (eds.). (1992). *Páramo: An Andean Ecosystem Under Human Influence*. London: Academic Press.

Martin, G. M., Bellouin, N., Collins, W. J., Culverwell, I. D., Halloran, P. R., Hardiman, S. C., et al. (2011), The HadGEM2 family of met office unified model climate configurations. *Geophys. Model Dev.* 4, 723–757. doi: 10.5194/gmd-4-723-2011

Myers, N. (2003). Biodiversity hotspots revisited. *BioScience* 53, 916–917. doi: 10.1641/0006-3568(2003)053[0916:BHR]2.0.CO;2

Neale, R. B., Gettelman, A., Park, S., Conley, A. J., Kinnison. D., Marsh. D., et al. (2010). *NCAR Technical Note: Description of the NCAR Community Atmosphere Model (CAM 5.0)*. National Center for Atmospheric Research, Boulder, CO, United States.

Nüsser, M. (2017). Socio-hydrology: a new perspective on mountain waterscapes at the nexus of natural and social processes. *Mt. Res. Dev.* 37, 518–520. doi: 10.1659/MRD-JOURNAL-D-17-00101.1

Oslender, U. (2019). Geographies of the pluriverse: decolonial thinking and ontological conflict on Colombia's Pacific Coast. *Ann. Am. Assoc. Geogr.* 109, 1691–1705. doi: 10.1080/24694452.2019.1572491

Reddington, C. L., Butt, E. W., Ridley, D. A., Artaxo, P., Morgan, W. T., Coe, H., et al. (2015). Air quality and human health improvements from reductions in deforestation-related fire in Brazil. *Nat. Geosci.* 8, 768–771. doi: 10.1038/ngeo2535

Rotstayn, L. D., Jeffrey, S. J., Collier, M. A., Dravitzki, S. M., Hirst, A. C., Syktus, J. I., et al. (2012). Aerosol- and greenhouse gas-induced changes in summer rainfall and circulation in the Australasian region: a study using single-forcing climate simulations. *Atmos. Chem. Phys.* 12, 6377–6404. doi: 10.5194/acp-12-6377-2012

Rousseau, D. (2017). "February. manifesto for General Systems Transdisciplinarity (GSTD)," in *Proceedings of the 59th Annual Meeting of the ISSS-2015* (Berlin).

Sarmiento, F. O. (2008). Andes mountains and human dimensions of global change: an overview. *Pirineos Rev. Ecol. Mont.* 163, 7–13. doi: 10.3989/pirineos.2008.v163.18

Sarmiento, F. O. (2012). *Contesting Páramo: Critical Biogeography of the Northern Andean Highlands.* Charlotte, NC: Kona Publishing. Higher Education Division.

Sarmiento, F. O. (2016). "Neotropical mountains beyond water supply: environmental services as a trifecta of sustainable mountain development," in *Mountain Ice and Water: Investigations of the Hydrologic Cycle in Alpine Environments,* eds G. Greenwood and J. Shroder (New York, NY: Elsevier), 309–324. doi: 10.1016/B978-0-444-63787-1.00008-1

Sarmiento, F. O., and Frolich, L. M. (2002). Andean cloud forest tree lines. *Mt. Res. Dev.* 22, 278–288. doi: 10.1659/0276-4741(2002)022[0278:ACFTL]2.0.CO;2

Sarmiento, F. O., González, J. A., Lavilla, E. O., Donoso-Correa, M. E., and Ibarra, J. T. (2019). Onomastic misnomers in the construction of faulty andeanity and weak andeaness: biocoultural refugia in the Andes. *Pirineos. Rev. Ecol. Mont.* 174, 1–16. doi: 10.3989/pirineos.2019.174009

Sarmiento, F. O., Ibarra, J. T., Barreau, A., Pizarro, J. C., Rozzi, R., González, J. A., et al. (2017). Applied montology using critical biogeography in the Andes. *Ann. Am. Assoc. Geogr.* 107, 416–428. doi: 10.1080/24694452.2016.1260438

Scarborough, V. L., Isendahl, C., and Fladd, S. (2019). "Environment and landscapes of Latin America's past," in *Global Perspectives on Long Term Community Resource Management*, eds L. Lozny, T.

McGovern, H. Thomas, and R. Ludomir (Berlin: Springer), 213–234. doi: 10.1007/978-3-030-15800-2_10

Steele, P. R., and Allen, C. J. (2004). *Handbook of Inca Mythology*. Santa Barbara, CA: abc-clio.

Stocker, T. F. D., Qin, G. K., Tignor, P. M., Allen, S. K., Boschung, J., Nauels, A., et al. (2013). *Climate Change 2013: The Physical Science Basis. Contribution of Working Group I to the Fifth Assessment Report of the Intergovernmental Panel on Climate Change*. Cambridge: Cambridge University Press.

Tao, W. K., Chen, J. P., Li, Z., Wang, C., and Zhang, C. (2012). Impact of aerosols on convective clouds and precipitation. *Rev. Geophys.* 50:RG2001. doi: 10.1029/2011RG000369

Taylor, K. E., Stouffer, R. J., and Meehl G. A. (2012). An overview of CMIP5 and the experiment design. *Bull. Amer. Meteor. Soc.* 93, 485–498. doi: 10.1175/BAMS-D-11-00094.1

Thornhill, G. D., Ryder, C. L., Highwood, E. J., Shaffrey, L. C., and Johnson, B. T. (2018). The effect of South American biomass burning aerosol emissions on the regional climate. *Atmos. Chem. Phys.* 18, 5321–5342. doi: 10.5194/acp-18-5321-2018

Urton, G. (1999). *Inca Myths*. Austin, TX: University of Texas Press.

Varela, L. (2008). La alta montaña del norte de los andes: el páramo, un ecosistema antropogénico. *Pirineos. Rev. Ecol. Mont.* 163, 85–95. doi: 10.3989/pirineos.2008.v163.24

von Salzen, K., Scinocca, J. F., McFarlane, N. A., Li, J., Cole, J. N. S., Plummer, D., et al. (2013). The Canadian fourth generation atmospheric global climate model (CanAM4). Part I: representation of physical processes. *Atmos. Ocean*. 51, 104–125. doi: 10.1080/07055900.2012.755610

Wang, C. (2015). Anthropogenic aerosols and the distribution of past large-scale precipitation change. *Geophys. Res. Lett.* 42, 10876–10884. doi: 10.1002/2015GL066416

Watanabe, M., Chikira, M., Imada, Y., and Kimoto, M. (2011). Convective control of ENSO simulated in MIROC. *J. Clim.* 24, 543–562. doi: 10.1175/2010JCLI3878.1

White, S. (2013). Grass páramo as hunter-gatherer landscape. *Holocene* 23, 898–915. doi: 10.1177/0959683612471987

Wunder, S. (1996). Deforestation and the uses of wood in the Ecuadorian Andes. *Mt. Res. Dev.* 16, 367–381. doi: 10.2307/3673987

Yukimoto, S., Adachi, Y., Hosaka, M., Sakami, T., Yoshimura, H., Hirabara, M., et al. (2012). A new global climate model of the Meteorological Research Institute: MRI-CGCM3–Model description and basic performance. *J. Meteorol. Soc. Jpn.* 90, 23–64. doi: 10.2151/jmsj.2012-A02

Conflict of Interest: The authors declare that the research was conducted in the absence of any commercial or financial relationships that could be construed as a potential conflict of interest.

Copyright © 2019 Sarmiento and Kooperman. This is an open-access article distributed under the terms of the Creative Commons Attribution License (CC BY). The use, distribution or reproduction in other forums is permitted, provided the original author(s) and the copyright owner(s) are credited and that the original publication in this journal is cited, in accordance with accepted academic practice. No use, distribution or reproduction is permitted which does not comply with these terms.

frontiers in Earth Science

ORIGINAL RESEARCH
published: 21 January 2020
doi: 10.3389/feart.2019.00355

Projected Changes to Extreme Runoff and Precipitation Events From a Downscaled Simulation Over the Western United States

Melissa L. Wrzesien and Tamlin M. Pavelsky*

Department of Geological Sciences, The University of North Carolina at Chapel Hill, Chapel Hill, NC, United States

Extreme precipitation and runoff events, which often impact natural and social systems more than mean changes, generally occur over regional scales. Future climate projections can be used to estimate how the hydrologic cycle may change, but the coarse resolution of global climate models (GCMs) (>1°) makes it difficult to evaluate regional changes, such as over a single watershed. To estimate changes in hydroclimatic variables at finer spatial resolutions, we dynamically downscale the Community Climate System Model version 4 (CCSM4) with the Weather Research and Forecasting (WRF) regional climate model over the western United States at 9 km spatial resolution. By running WRF at a higher spatial resolution, we estimate future climate conditions, including 99% event magnitude, over 17 watersheds: the Columbia, Lower Colorado, Upper Colorado, the Upper Missouri/Yellowstone, and 12 basins draining the western slope of the Sierra Nevada in California. Over each basin, we compare a historical period (1996–2005) with mid-century (2041–2050) and end-century (2091–2100). From the WRF/CCSM simulations, most basins are projected to have earlier peaks in springtime streamflow. The Columbia and the Lower Colorado watersheds are both expected to experience more extreme wet days, with the 99th percentile of daily precipitation estimated to increase by over 10%. For the Upper Colorado, however, the 99th percentile of daily runoff is projected to decrease by over 30%. Basins in the northern and central Sierra Nevada are projected to have substantial increases in extreme runoff, with doubling of high flow event magnitude possible for some basins. By end-century, the contribution of high-magnitude runoff (>90th percentile) to total runoff is projected to increase from 46 to 56%, when averaged across all 12 Sierra Nevada basins. Though only one realization from a single GCM, the downscaled simulation presented here shows interesting results regarding how extreme events may change; these results can be tested by downscaling other global models with WRF to create an ensemble of dynamically downscaled future projections.

Keywords: climate change, extreme events, precipitation, runoff, downscaling

OPEN ACCESS

Edited by:
Alfonso Fernandez, University of Concepción, Chile

Reviewed by:
Enrico Scoccimarro, Euro-Mediterranean Center on Climate Change, Ca' Foscari University of Venice, Italy
Thanh Ngo-Duc, University of Science and Technology of Hanoi, Vietnam

****Correspondence:***
Melissa L. Wrzesien
wrzesien@unc.edu

Specialty section:
This article was submitted to Hydrosphere, a section of the journal Frontiers in Earth Science

Received: *07 October 2019*
Accepted: *24 December 2019*
Published: *21 January 2020*

Citation:
Wrzesien ML and Pavelsky TM (2020) Projected Changes to Extreme Runoff and Precipitation Events From a Downscaled Simulation Over the Western United States. Front. Earth Sci. 7:355. doi: 10.3389/feart.2019.00355

INTRODUCTION

Though much work has been done to estimate how climate change will impact the environment and society, research often considers mean changes (e.g., Cayan et al., 2008; Mote and Salathe, 2010; Peacock, 2012), such as how average temperature or annual precipitation may change by the end of the 21st century. However, extreme events often affect natural and social systems more than mean changes, particularly on local-to-regional scales. For example, heavy precipitation on snow cover can cause dramatic snowmelt and substantial streamflow, often leading to extensive flooding; a recent example is the 2017 Oroville Dam crisis in California, which caused the evacuation of more than 180,000 people (Vahedifard et al., 2017; Hollins et al., 2018). Infrastructure must meet design standards to handle such extreme events. However, aspects of the water supply system, such as dams and reservoirs, are designed for present-day climate patterns and generally assume the probability of precipitation or runoff extremes are statistically stationary, an assumption that may not hold true under climate change (Rosenberg et al., 2010; Sterle et al., 2019). While such systems may be able to adapt to increased or decreased annual precipitation by the end of the century, they may not be able to adapt to changes in extreme events.

Global climate models (GCMs), such as those used in Intergovernmental Panel on Climate Change reports (IPCC), for example, are commonly used to project how hydroclimatic variables may change under a warming environment (Taylor et al., 2012; Knutson et al., 2013; Knutti and Sedlacek, 2013). While GCMs are a useful tool for predicting changes over large geographical regions, they are of limited use for regional studies due to coarse spatial resolution and, frequently, bias over individual regions (Maraun et al., 2010; Ehret et al., 2012). Regional climate models (RCMs), on the other hand, are becoming an increasingly useful tool for climate projection via GCM downscaling. Though a GCM can generate more data than an RCM, both temporally and spatially, it is also significantly coarser. In analysis of the resolution dependence of precipitation extremes, van der Wiel et al. (2016) found that magnitude and seasonality of precipitation extreme events dramatically improves when increasing from 200 km to 50 km to 25 km resolution; the largest biases were maintained over the Sierra Nevada, suggesting either further resolution enhancements are necessary or precipitation is poorly constrained over the region in observations. Here we use an RCM over the western United States to provide resolution enhancement in a region where a GCM would only have a few grid points. The tradeoff of using an RCM over a GCM is that fewer years can be integrated due to computational constraints, but this is offset by providing higher resolution information. Ever-increasing computational resources allow for multi-year RCM simulations, providing the ability to simulate historical and future decades for comparison (Liu et al., 2017; Walton et al., 2017). Future projections with RCMs require the use of GCMs for meteorological forcing data as boundary and initial conditions. Since GCMs are often biased on the regional scale, the use of raw GCM data as forcing data would pass the biases onto the RCM simulations.

Multiple methods have been developed for bias correcting GCMs. A commonly used technique is the pseudo global warming (PGW) method (Schar et al., 1996; Hara et al., 2008; Kawase et al., 2009; Rasmussen et al., 2011), which adds a climate change signal from GCMs to reanalysis data. This method allows for easy comparison to historical reanalysis estimates and has been shown to produce reasonable results as an RCM forcing dataset (Liu et al., 2017; Musselman et al., 2017; Gutmann et al., 2018; Letcher and Minder, 2018). However, the PGW method assumes climate variability to be stationary in time; recent work suggests that climate stationarity is not a valid assumption (Christensen et al., 2008; Vannitsem, 2011; Maraun, 2012). Here we use an alternative bias correction approach, described below in section "Bias Correction," that does not assume stationarity.

Here we estimate historical and future climate over the western United States using simulations from the Weather Research and Forecasting (WRF; Skamarock et al., 2019) RCM forced by a bias-corrected GCM. By simulating historical, mid-century, and end-century decades, we not only evaluate how hydroclimatic variables may change over the 21st century, but, with the multi-year simulations, we also consider extreme events. That is, we estimate how the wettest of wet days may change by the end century. Changing the magnitude of extreme events has implications for built infrastructure, particularly when considering flood control.

We first consider major river watersheds of the western United States – the Columbia, Upper Colorado, Lower Colorado, and Upper Missouri/Yellowstone system (**Figure 1A**). Evaluating changes over these large river basins will highlight potential regional-scale climate impacts for these heavily managed systems. We then evaluate changes to small basins with headwaters in the Sierra Nevada mountains of California (**Figure 1B**). Water managers in this region must balance conserving snowmelt-derived streamflow with flood prevention measures (Dettinger et al., 2011); therefore, understanding a possible regime shift for substantial precipitation and runoff events is crucial for local water districts. We end by discussing how potential changes to extreme events may affect water resources and operations in each study region.

MATERIALS AND METHODS

Model Domain and Setup

We run WRF version 4.01 (Skamarock et al., 2019) with the Noah land surface model with multi-parameterization options (Noah-MP; Niu et al., 2011). We use a two-way nested domain, where the outer domain has a spatial resolution of 27 km and the inner domain a resolution of 9 km. Previous work suggests a model grid cell resolution of <10 km is necessary for capturing realistic simulations of orographic precipitation (Ikeda et al., 2010; Pavelsky et al., 2011; Rasmussen et al., 2011; Minder et al., 2016; Wrzesien et al., 2017, 2018). The 27 km outer domain covers North America and the eastern Pacific, to capture the moisture source for west coast storms. The 9 km inner domain (**Figure 1A**) includes the west coast of the United States and Canada and extends as far east as the Colorado Front

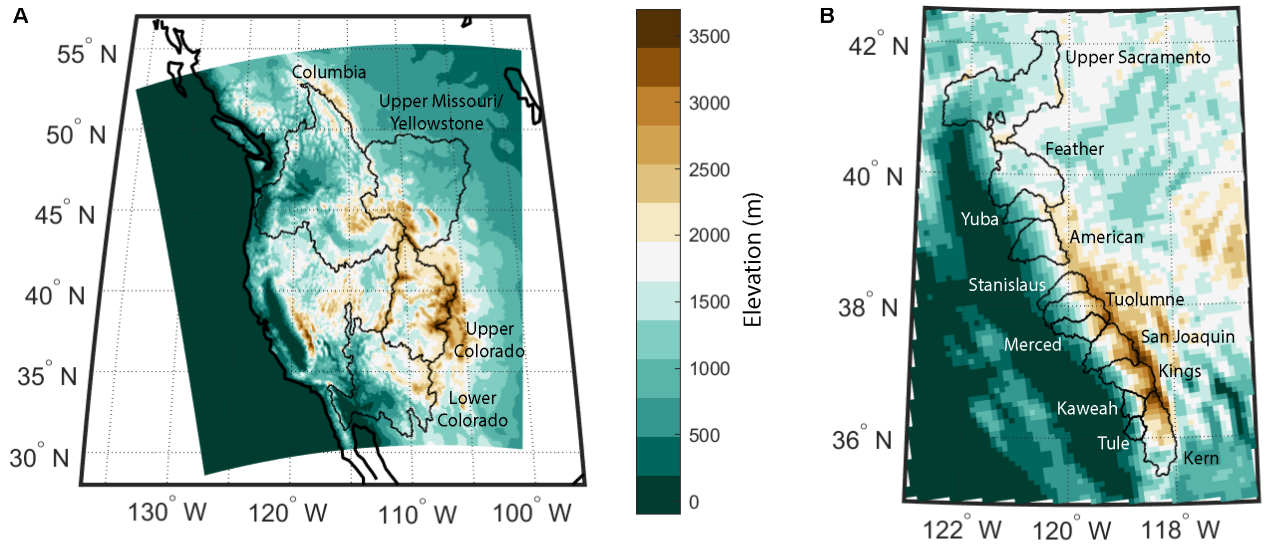


FIGURE 1 | (A) Elevation from 9 km WRF domain over the western United States and Canada. Boundaries of the four large western watersheds are shown in black. **(B)** Zoomed in elevation, with the same scale, over the Sierra Nevada mountains of California. Twelve basins of interest are outlined in black.

Range. Since two-way nesting allows for feedback between the nested and parent domain, the finer resolution inner domain simulation essentially overwrites the overlapping outer domain area; therefore, we only analyze the 9 km domain.

Previous work identified modifications to Noah-MP that improve representation of snow accumulation and summer low flows for basins with headwaters in the Sierra Nevada (Holtzman et al., submitted). We incorporate the same modifications here; the largest changes include allowing the microphysics scheme to partition the precipitation into rain and snow (opt_snf = 4 in the WRF namelist) and decreasing the depth of subsurface runoff generation from the deepest soil layer (depth of 1–2 m below surface) to the second-from-top soil layer (depth of 10–30 cm below surface). Holtzman et al. (submitted) also developed a statistical aquifer correction algorithm based on full natural flow (FNF) estimates, which improves simulated baseflow for Sierra Nevada basins. We apply the same correction to WRF streamflow here where daily FNF estimates are available.

Beyond the modifications to Noah-MP, we use the following physics options: the Thompson et al. (2008) cloud microphysics scheme, the Rapid Radiative Transfer Model longwave scheme (Mlawer et al., 1997), the Dudhia shortwave scheme (Dudhia, 1989), the Yonsei University planetary boundary layer scheme (Hong et al., 2006), and the modified Kain–Fritsch convective parameterization for the two outer domains (Kain and Fritsch, 1990, 1993; Kain, 2004). To constrain WRF simulations, particularly over the center of the model domain, two-way spectral nudging is applied to wind, geopotential height, temperature, and water vapor mixing ratio; nudging to temperature and moisture are only applied within the free troposphere, following recent literature on nudging for regional climate purposes (Spero et al., 2014, 2018).

Meteorological forcing data are provided by the Community Climate System Model version 4 (CCSM4; Gent et al., 2011) under a high emissions scenario (RCP 8.5), which was part of the Coupled Model Intercomparison Experiment phase 5 (CMIP5). Bias-corrected WRF intermediate files are available through the National Center for Atmospheric Research's Research Data Archive (NCAR RDA; dataset ds316.1; Monaghan et al., 2014). Selected variables are bias-corrected with values from ERA-Interim (Dee et al., 2011). The non-bias-corrected simulation is CCSM4 ensemble member 6 (b40.rcp8_5.1deg.007). Below in section "Bias Correction," we include more details about the bias correction process.

We simulate three decade-long periods: a historic period [water years (WYs) 1996–2005], a mid-century period (WYs 2041–2050), and an end-century period (WYs 2091–2100). Though bias-corrected CCSM4 data are available through NCAR RDA from 1951 to 2100, we only simulate individual decades to represent historical and future climate due to computational constraints of running WRF. We include an additional year in each decadal simulation for model spin-up (WYs 1995, 2040, and 2090), which provides time for the previous snow season to impact soil conditions and allows for land surface state equilibrium (Cosgrove et al., 2003; Barlage et al., 2015); the spin-up years are not included in the analysis presented here. CCSM4 does not include leap days, so each decade simulation covers 3650 days.

Bias Correction

The bias correction method applied here, developed by Bruyère et al. (2013), adjusts the CCSM4 mean toward the ERA-Interim mean, calculated from 1981 to 2005. Over the 1981–2005 reference period, CCSM4 6-hourly data are separated into a monthly mean and a deviation. To calculate the bias-corrected CCSM4, the monthly mean from ERA-Interim and the CCSM4 deviation are combined. Therefore, the

Bruyère et al. (2013) method corrects for mean errors in CCSM4 but incorporates the climate variability from CCSM4. The following equations are used in the bias correction:

$$\mathrm{ERAI_{ref}} = \overline{\mathrm{ERAI_{ref}}} + \mathrm{ERAI'}$$

$$\mathrm{CCSM} = \overline{\mathrm{CCSM_{ref}}} + \mathrm{CCSM'}$$

$$\mathrm{CCSM_{BC}} = \overline{\mathrm{ERAI_{ref}}} + \mathrm{CCSM'}$$

In the equations, subscript ref stands for the reference period over which the bias correction is calculated; in this case, the years 1981–2005 are used. On the right-hand side, the first term is the monthly mean, and the second term is the deviation from the mean. For future years, the 6-hourly deviations are applied to monthly means of the same historical reference period; therefore, deviations for CCSM4 predictions of 2006–2100 are applied to monthly means of ERA-Interim for the period 1981–2005.

Bias correction is applied to correct the mean bias in both 3-D fields and in surface fields. Corrected 3-D fields include geopotential height, wind, temperature, and humidity, while surface fields include surface pressure, sea level pressure, sea surface temperature, skin temperature, soil temperature, and soil moisture (Bruyère et al., 2013). This method retains the CCSM4 variability in the initial and lateral boundary conditions for WRF; other methods, such as PGW, retain variability from the reanalysis dataset. The Bruyère et al. (2013) method has been used in other studies to bias correct GCMs, including Wang and Kotamarthi (2015) and Pontoppidan et al. (2018).

Percentiles

To evaluate events with substantial precipitation and runoff, we calculate percentiles for each decade from the daily values. We are interested in the wettest days, so we consider the 99th percentile, which occur 37 times per decade. By calculating percentiles with daily values, we miss multi-day extreme events. However, consideration of daily magnitudes of precipitation and runoff demonstrates how the wettest single-day events may change by the middle and end of the 21st century.

Full Natural Flow

To evaluate the reasonableness of the WRF-downscaled streamflow for the historic period, we compare to estimated FNFs for eight Sierra Nevada basins (Huang, 2016). FNF estimates are downloaded from the California Data Exchange Center. By

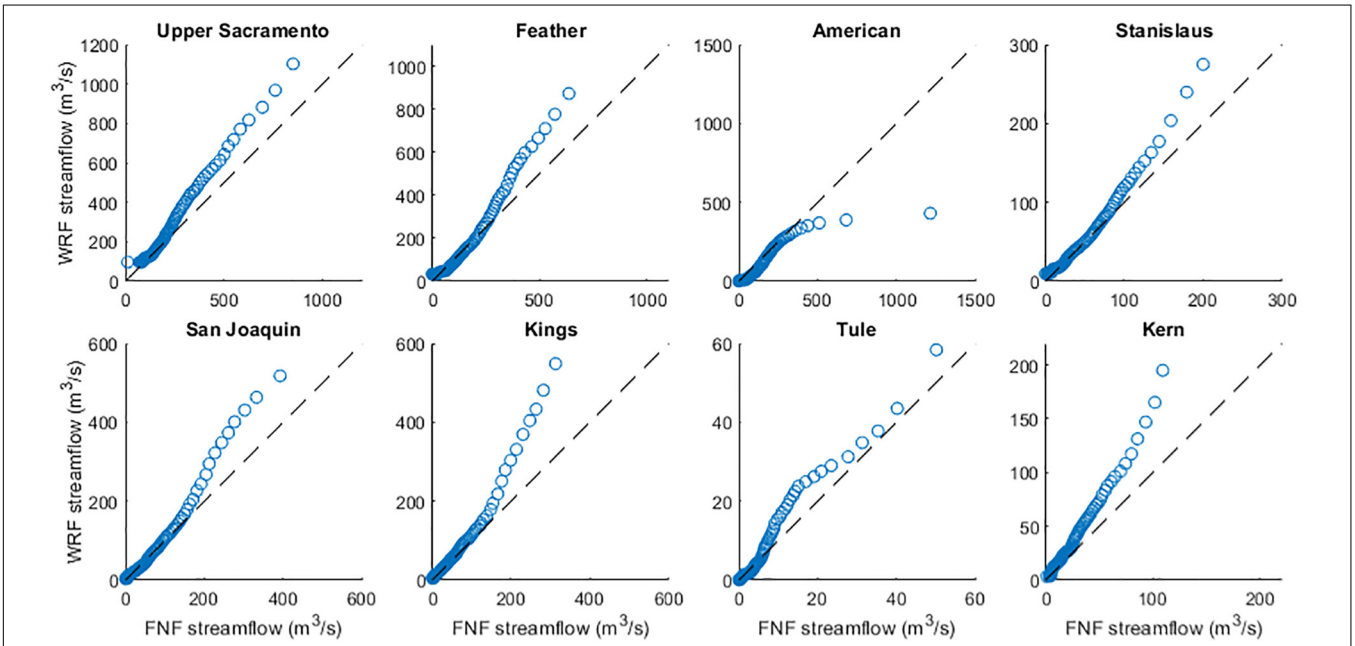


FIGURE 2 | Comparison of daily runoff from WRF and full natural flow for eight Sierra Nevada basins. Daily values are averaged over water years 1996 through 2005.

TABLE 1 | Change in volume of hydroclimate variables between end-century and historic average values for western watersheds.

Watershed	Precipitation difference (km^3)	Rainfall difference (km^3)	Snowfall difference (km^3)	Runoff difference (km^3)
Columbia	57.5 (10.1%)*	119.8 (31.7%)*	−62.3 (− 32.4%)*	25.2 (9.4%)
Lower Colorado	−17.4 (− 17.2%)	−10.0 (− 11.2%)	−7.4 (− 65.3%)*	−1.9 (− 32.2%)
Upper Colorado	−11.6 (− 11.6%)	1.6 (1.5%)	−13.1 (− 29.1%)*	−10.0 (− 31.7%)*
Upper Missouri/Yellowstone	8.5 (2.9%)	17.4 (8.0%)	−8.9 (− 12.7%)	−7.9 (− 11.4%)

Percent differences are shown in parenthesis. An asterisk denotes statistical significance at the 95% level.

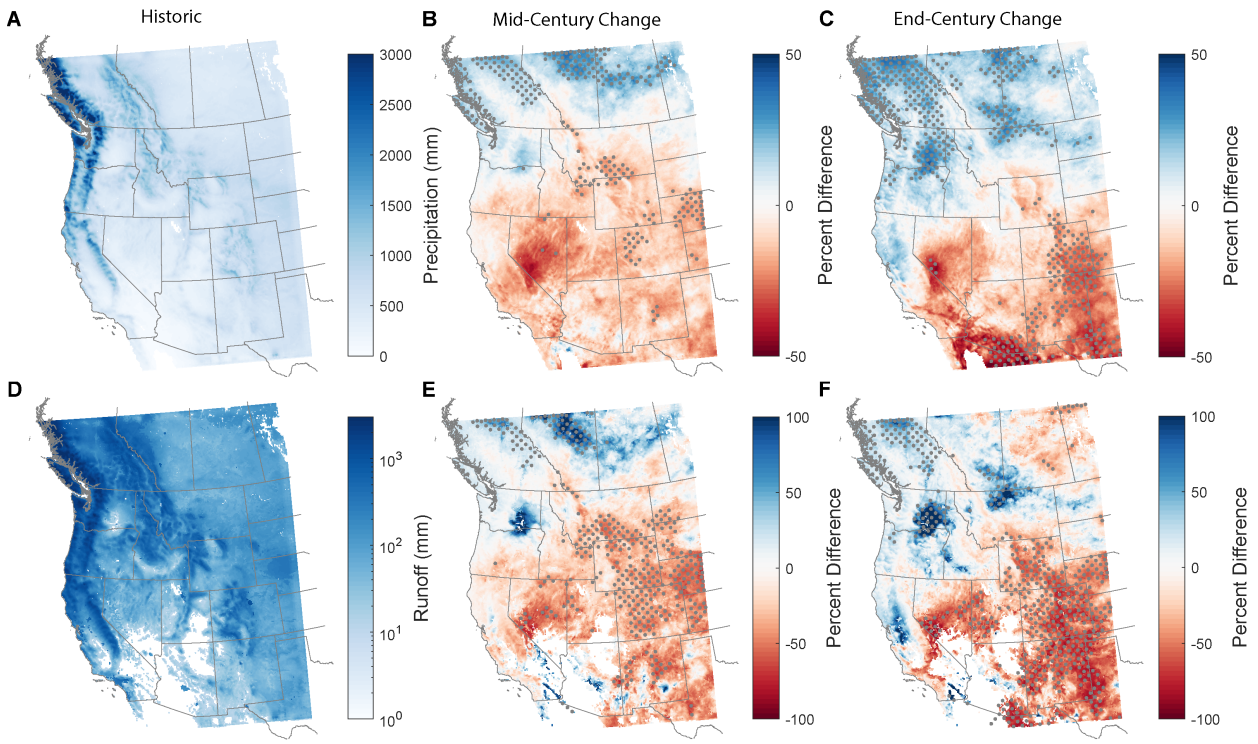


FIGURE 3 | (A) Average annual total precipitation from WRF/CCSM for the historical decade. **(B,C)** Percent difference in annual precipitation when comparing the mid-century **(B)** and end-century **(C)** decades to the historic. **(D)** Average annual total runoff from WRF/CCSM for the historical decade. **(E,F)** Percent difference in annual runoff when comparing the mid-century **(E)** and end-century **(F)** decades to the historic. Stippling indicates regions with a statistically significant change by mid- or end-century at the 95% confidence level.

calculating the decade-averaged streamflow from WRF and the FNF estimate, we can determine whether WRF simulations are reasonable. We also use the Sierra Nevada FNF estimates to calibrate the aquifer correction to simulated streamflow.

RESULTS

Prior to comparing future WRF simulations to the historic simulations, we first evaluate whether WRF streamflow estimates capture realistic conditions. By comparing WRF-simulated streamflow and FNF estimates at each percentile (from the 1st to 99th percentile), we see that at large streamflow magnitudes, WRF generally overestimates FNF (**Figure 2**). The notable exception is the American basin where FNF is larger for the highest percentiles (95th percentile and above). Streamflow magnitudes below the 80–90th percentile, depending on basin, are more comparable between the two datasets.

We next consider how decade-averaged precipitation and runoff is projected to change in the WRF simulations. To test whether there are statistically significant changes in annual precipitation and runoff between the historic decade and end century, we perform a two-sample *t*-test. We note that each decadal sample only has 10 values, potentially decreasing the statistical power of the *t*-test. Below and in **Table 1**, we report which decadal changes are statistically significant. When comparing average annual precipitation from the historical period to the end-century, we see a dipole pattern in the model domain (**Figure 3**). Precipitation is projected to increase in the northern half of the domain and along the west coast, matching with the spatial patterns of the 99th percentile values (**Figure 4**). Decreases are expected in the southern portion of the WRF domain. We can further split precipitation into snowfall and rainfall. As expected in a warming scenario, large decreases are projected for snowfall (**Figure 5**). In the Upper Colorado, changes to total precipitation are largely driven by decreases to snowfall: average annual total precipitation in the Upper Colorado is expected to decline by 11.6% by 2100 (**Table 1**), where snow is projected to decline by 29.1% (significant at the 95% confidence level), and rainfall is projected to increase by 1.5%. In the other three basins, projected changes to rainfall have larger magnitudes than snowfall changes.

Changes to annual runoff follow similar spatial patterns as precipitation, with increases along the Pacific coast and decreases in the eastern half of the domain (**Figure 3**). The desert southwest is projected to have less annual streamflow by the last decade of the 21st century, while the Pacific Northwest can expect increased streamflow. Of the four large watersheds, only the Columbia River basin is projected to increase annual total runoff (9.4%; not significant at the 95% confidence level), likely driven by the projected increase in annual precipitation (31.7%; significant at the 95% confidence

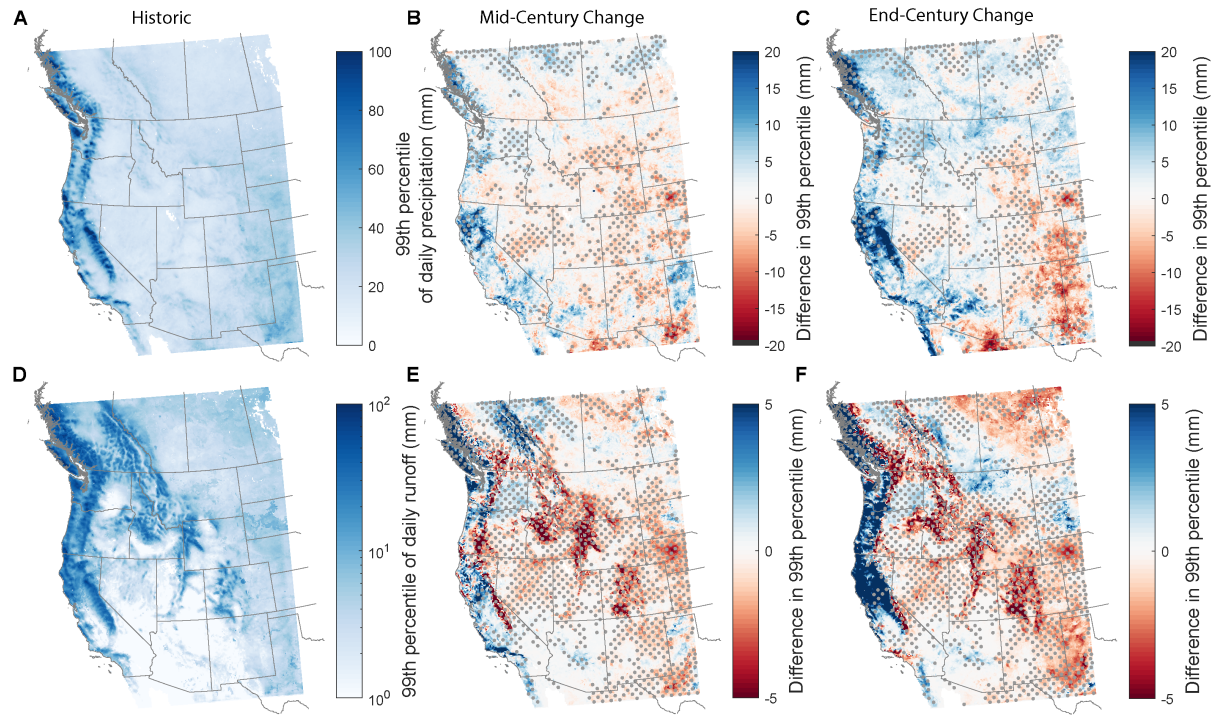


FIGURE 4 | (A) Grid cell values for the 99th percentile of daily precipitation for the WRF/CCSM historic decade. **(B,C)** Differences in magnitude of grid cell value of 99th percentile of daily precipitation when comparing the mid-century **(B)** and end-century **(C)** decades to the historic decade. **(D–F)** Same as **(A–C)** but for the 99th percentile of daily runoff. Stippling indicates regions with a statistically significant change by mid- or end-century at the 95% confidence level.

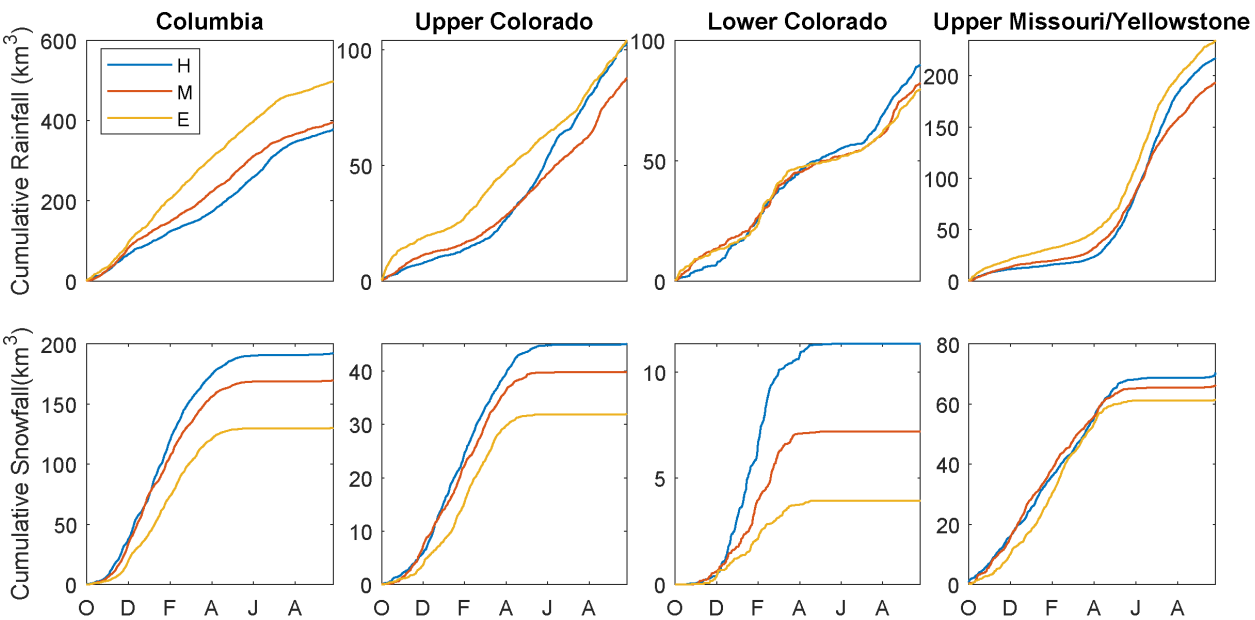


FIGURE 5 | Comparison of average annual cumulative rainfall **(top row)** and snowfall **(bottom row)** for the four western watersheds for the historic (blue), mid-century (orange), and end-century (yellow) decades.

level; **Table 1**). Of the other three basins, all are projected to have less annual streamflow, with the Upper Colorado (−31.7%) and Lower Colorado (−31.2%) having the largest declines; however, when comparing end-century changes to annual runoff, only the Upper Colorado has a statistically significant change.

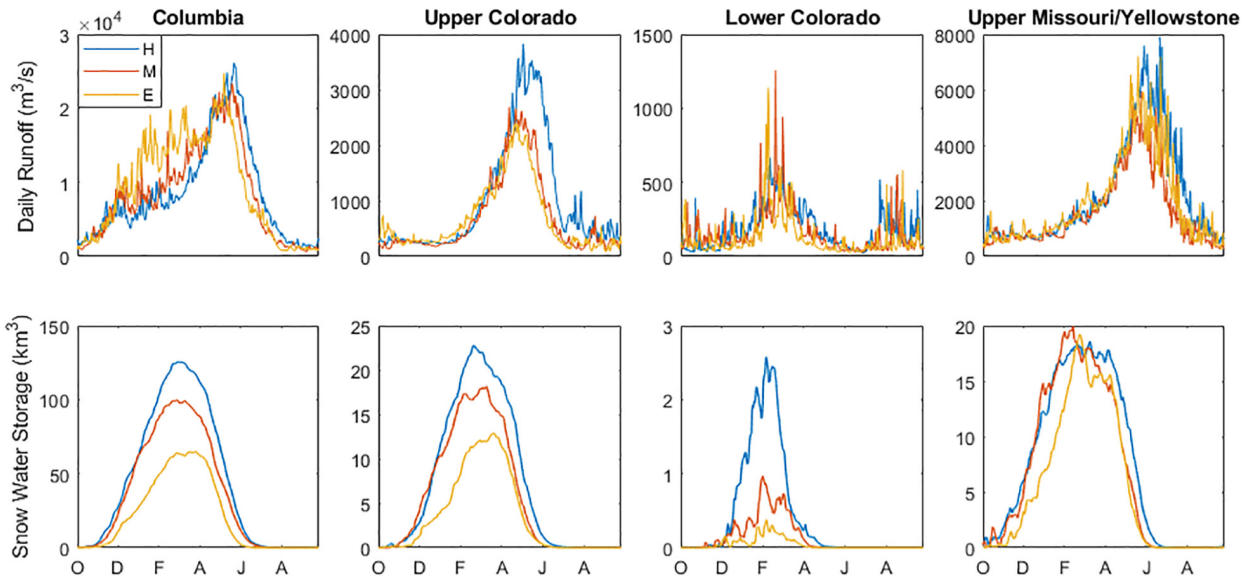


FIGURE 6 | Average daily runoff **(top row)**, and snow accumulation **(bottom row)** over each western watershed for the historic (blue), mid-century (orange), and end-century (yellow) periods.

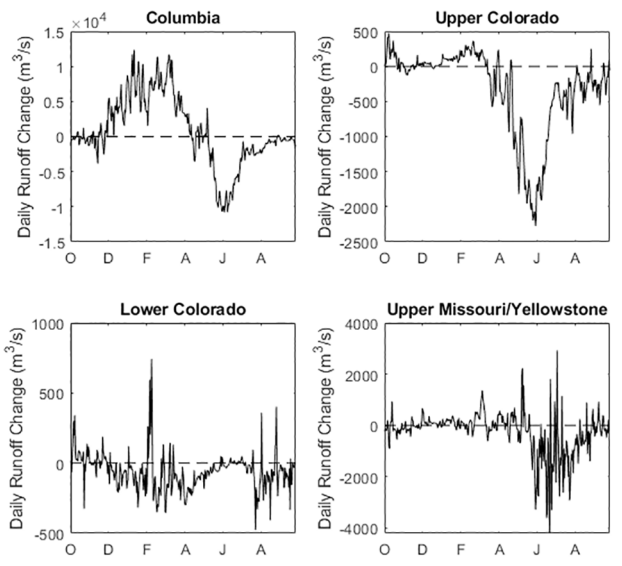


FIGURE 7 | Difference in decade-averaged annual hydrographs for western watersheds. Daily runoff change is calculated by subtracting historic values from end-century hydrograph.

In addition to differences in runoff amount, runoff timing is expected to change. Average hydrograph changes are clearest for the Columbia and Upper Colorado River Basins (**Figure 6**), two regions that receive significant amounts of snowfall in the historic simulation. In both watersheds, the end-century hydrograph peaks earlier and has a smaller magnitude than the historic hydrograph. Snowfall often has a delayed impact on streamflow since it can accumulate for several months until spring snowmelt, while rainfall generally impacts streamflow much more quickly. Earlier peaks in streamflow are consistent with a shift from snowfall to rainfall, as demonstrated in the Columbia and Upper Missouri/Yellowstone basins (**Figure 5**). In the Columbia, a larger fraction of runoff occurs in the winter months (December through March), suggesting that precipitation that fell as snowfall in the historic period may transition to rainfall by the end-of-century. In all basins except the Upper Missouri/Yellowstone, snow water storage is also expected to decrease (**Figure 6**). For the two watersheds with larger amounts of snow accumulation (Columbia and Upper Colorado), maximum SWS declines by over 40% by end-century. Interestingly, WRF results suggests day of peak SWS also shifts later.

All four watersheds are projected to have decreases in daily runoff by end-century for spring and summer months (**Figure 7**). Decreases in the Columbia and Upper Colorado are largest in May through July, which coincides with the snowmelt period. The Columbia watershed has positive values throughout the winter, which agrees with the higher streamflow values in the end-century hydrograph (**Figure 6A**). These larger winter/early spring streamflow values are driven by increased rainfall during the winter (**Figure 5A**). Throughout the 21st century, the snowfall in the Columbia watershed is projected to decrease and the rainfall is projected to increase. The Lower Colorado has the smallest changes by end-century, though it is the driest watershed of the four. Changes to daily runoff in the Upper Missouri/Yellowstone occur between June and September as the hydrograph maximum shifts earlier (**Figure 6**).

To examine extreme events, we first consider how the 99th percentile of precipitation and runoff change across the full model domain. We have chosen the 99th percentiles of the entire record to isolate the most extreme precipitation occurrences, which provides 37 samples. A two-sample Kolmogorov–Smirnov

test is used to determine statistical significance of the changes in extremes. This method has been previously applied to changes in hydrologic extreme distributions (e.g., Russo and Sterl, 2012; Donat et al., 2013; Harder et al., 2015; Erler and Peltier, 2016). Moreover, even with a GCM, previous research has used similar sample sizes to quantify hydrologic extremes and significance. For example, 100 and 20 samples were taken to characterize 1-year and 5-year United States precipitation extremes by van der Wiel et al. (2016). Rejection of the null hypothesis supports that the samples from the historical and future periods are from different distributions. **Tables 2**, **3** report statistical significance of each projected change; all projected changes to runoff are statistically significant. Since we perform significance tests on all extreme events (>99th percentile) together, calculating the percent change at an individual percentile may result in projected changes that do not appear significant. For example, for the San Joaquin basin, the magnitude of 99th percentile runoff events is projected to increase by 1% (**Table 3**), yet the full distribution of end-century extreme runoff events in the San Joaquin is significantly different from the historic distribution. Along the west coast, 99th percentile values of daily precipitation are increasing, signifying that wet days are getting wetter, particularly by the end-century

TABLE 2 | Percent change by end-century in daily precipitation and runoff percentiles for western watersheds.

Watershed	% change in 99th percentile of daily precipitation	% change in 99th percentile of daily runoff
Columbia	12.3*	−5.9*
Upper Colorado	2.5	−31.4*
Lower Colorado	8.5	2.7*
Upper Missouri/Yellowstone	4.8*	−4.9*

An asterisk denotes statistical significance at the 95% level.

TABLE 3 | Percent change by end-century in daily precipitation and runoff percentiles for Sierra Nevada basins.

Basin	% change in 99th percentile of daily precipitation	% change in 99th percentile of daily runoff
Upper Sacramento	27.1*	75.5*
Feather	29.5*	113.8*
Yuba	30.3*	142.0*
American	33.6*	124.3*
Stanislaus	32.6*	54.0*
Tuolumne	32.5*	54.2*
Merced	25.0*	36.7*
San Joaquin	24.2*	1.0*
Kings	19.3	−10.4*
Kaweah	19.3	29.7*
Tule	17.1	49.0*
Kern	6.7	−26.9*

Basins are sorted from north (Upper Sacramento) to south (Kern). An asterisk denotes statistical significance at the 95% level.

(**Figure 4**). For 2091–2100, increases are most prominent over the Sierra Nevada and southwest British Columbia. The four western watersheds – the Columbia, Upper Colorado, Lower Colorado, and Upper Missouri/Yellowstone – are projected to have increases in magnitude of percentiles (**Table 2**). The Columbia River basin has the largest increase, with the average amount of precipitation during an extreme event projected to increase by 12%. Runoff patterns are similar to those for precipitation: the wettest runoff days are expected to increase along the western coast of the United States and Canada, particularly along the windward side of the coastal mountain ranges (**Figures 4E,F**). By the end-century, decreases in extreme runoff are most notable in the Upper Colorado River basin, where basin-averaged daily runoff is estimated to decrease by 31 for the 99th percentile.

For a more local view, we also consider 12 basins with headwaters in the Sierra Nevada mountains. For all 12 basins, the streamflow hydrographs shift earlier in the season (**Figure 8**), consistent with decreasing snow accumulation (**Figure 9**). In the historical decade, streamflow decays to baseflow conditions in late July or early August; by the end century, streamflow decays to baseflow as early as June for some basins (e.g., American and Feather). From the decade-averaged hydrographs, it appears there are more flashy events in the winter and early spring, suggesting basins are either receiving increased rainfall or snowfall is melting shortly after deposition.

For extreme events, all basins are projected to have increases in the magnitude of the 99th percentile precipitation events (**Table 3**). Projected changes are statistically significant for 8 of the 12 basins; those that do not have statistically significant changes are in the southern Sierra Nevada. Wet days getting wetter may increase flood risks for regions downstream. For days with substantial runoff, the magnitude of the 99th percentile of daily streamflow is projected to increase for all basins other than the Kern and the Kings. The Yuba, American, and Feather basins are all projected to have 99th percentile magnitude increases greater than 100%. Projected changes to extreme runoff are statistically significant for all 12 basins (**Table 3**). Though extreme events are projected to have higher magnitudes by end-century, daily streamflow at other percentiles decreases for all basins (**Figure 10**). Streamflow magnitudes are similar for the mid-century and end-century decades. Declines at the 50th percentile between historical and end-of-century are particularly large for Kaweah, Kern, and Tuolumne basins.

We also consider how the contribution of extreme events to total precipitation and runoff may change throughout the 21st century. We first select all days with non-zero precipitation or runoff for each Sierra Nevada basin. By accumulating precipitation/runoff by percentile (i.e., summing all precipitation values in the 1st–10th percentile, 11th–20th percentile, etc.), we compare the amount of percentile-binned precipitation or runoff to the decadal total. Though an annual analysis would also be informative, it would not consider the most extreme events that occur only a handful of times per decade. Even on a decadal time scale, we see that the events in the highest percentile have the largest contribution to total precipitation

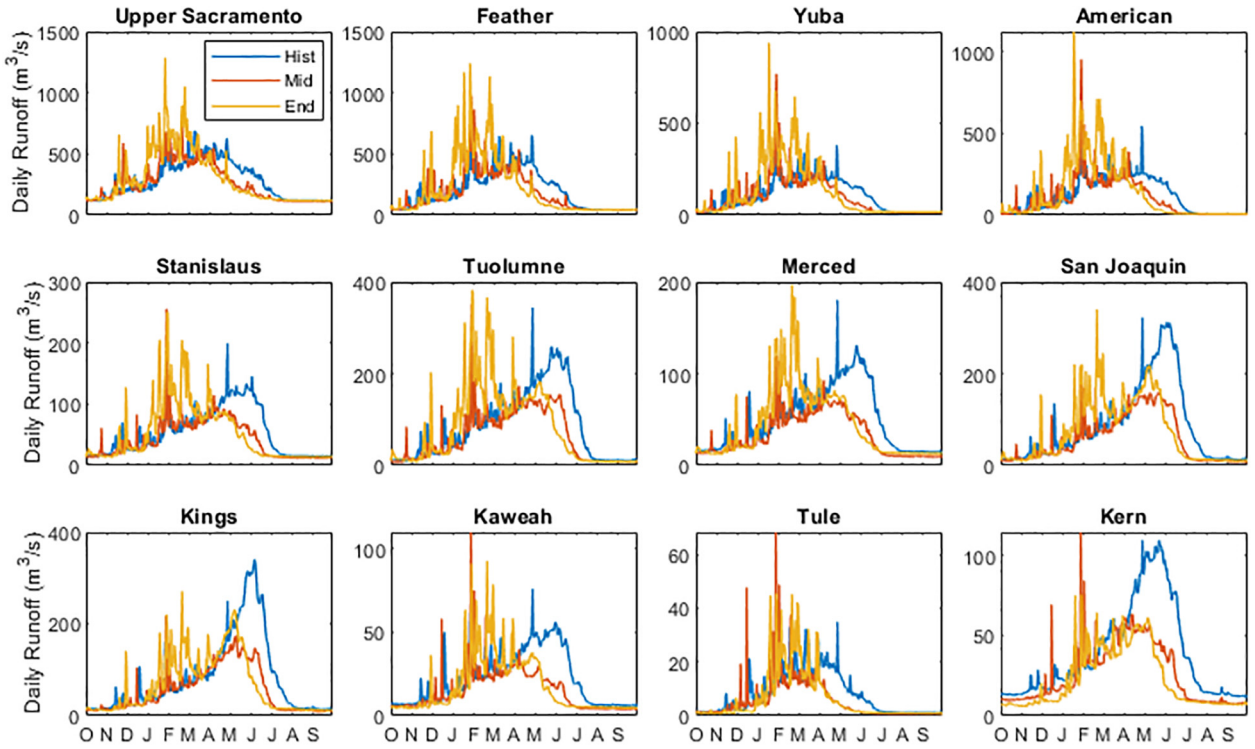


FIGURE 8 | Average hydrographs for basins with headwaters in the Sierra Nevada mountains for the historic (blue), mid-century (orange), and end-century (yellow) decades.

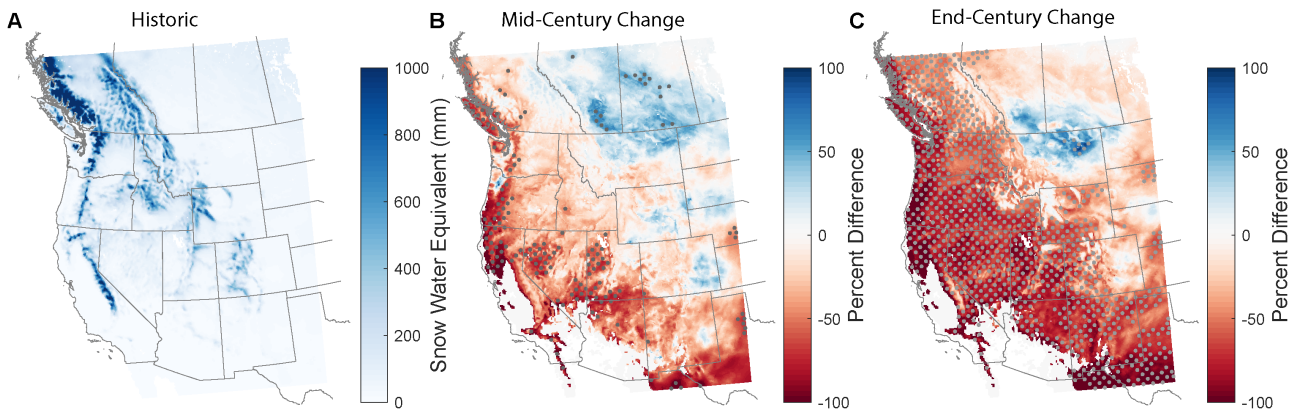


FIGURE 9 | (A) Average annual maximum snow water equivalent (SWE) from WRF/CCSM for the historical decade. **(B,C)** Percent difference in peak SWE when comparing the mid-century **(B)** and end-century **(C)** decades to the historic. Stippling indicates regions with a statistically significant change by mid- or end-century at the 95% confidence level.

(**Figure 11**) and runoff (**Figure 12**) for each basin. Though changes by end-century are small for precipitation, extreme runoff events by 2091–2100 will have a larger contribution to total runoff; for example, in the Yuba basin, the contribution of >90th percentile events is projected to increase from 41 to 58%. Increases to percent contribution are largest in the northern basins: the Upper Sacramento, Feather, Yuba, American, and Stanislaus are all projected to have increases larger than ten percentage points.

As all Sierra Nevada basins are projected to have statistically significant changes to extreme runoff, we can develop hypotheses regarding contributors to changes in high magnitude runoff events. Since precipitation and runoff are more coupled over small basins such as these, we consider the relationship between extreme runoff and extreme precipitation. By comparing all days with precipitation or runoff greater than the 99th percentile (37 days per decade), we see that for 8 of the 12 basins, at least one-third of the days with extreme runoff coincide with

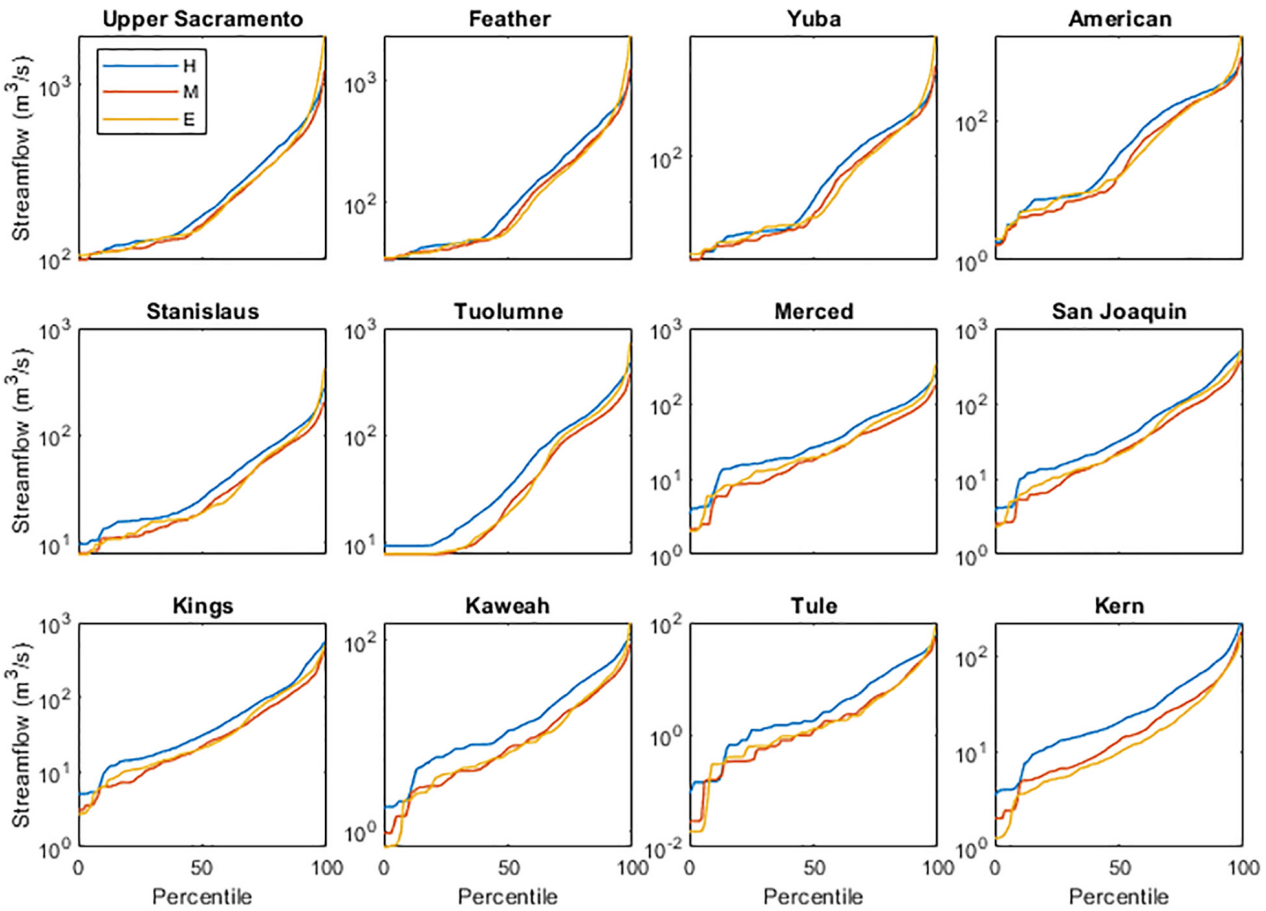


FIGURE 10 | Daily streamflow values at each percentile for 12 Sierra Nevada basins for the historic (blue), mid-century (orange), and end-century (yellow) periods.

an extreme precipitation days (**Table 4**), suggesting it is the intense precipitation driving the runoff in those cases. By end-century, most basins have at least one-half of extreme runoff days coinciding with days of extreme precipitation. To allow for a lag between precipitation and runoff, we consider whether days with extreme runoff occur within 5 days of an extreme precipitation event. For most basins, and particularly those in the northern Sierra Nevada, we see increases in the number of extreme runoff days that coincide with intense precipitation. Increases in time coincidence may be due to a shift from snowfall, which is not directly tied to same-day or same-week runoff, to rainfall, which is. To consider seasonality of extreme events, we compare timing of all 37 extreme runoff and precipitation events for each Sierra Nevada basin over the historic and end-century period (**Figure 13**). We also compare the average timing of the snowmelt season (colored bars in **Figure 13A**). In the southern basins, historic runoff events coincide with the melt season, suggesting that historic extreme streamflow is often due to snowmelt events. Alternatively, by end-century, many of the extreme runoff events occur prior to the snowmelt season, suggesting these high-magnitude events may be due to precipitation, likely as rain.

Despite the increase in time coincidence in extreme events when we account for a lag between precipitation and runoff, when we evaluate precipitation totals, we see less of a relationship between runoff magnitude and antecedent precipitation conditions. That is, we compare the correlation between extreme runoff and same-day precipitation versus the precipitation accumulated over 5 days prior to the day of extreme runoff (**Table 5**). In the historic period, all basins except the Kern have stronger correlations for same-day runoff and precipitation. In the Kern, antecedent precipitation amounts resulted in a larger R^2. In the end century, only runoff in the American basin has a stronger correlation with antecedent precipitation conditions. This result suggests that for most Sierra Nevada basins, large precipitation events lead to high magnitude runoff, often with little lag time. Projected end-century changes are not large, with increases to R^2 values only in the northern basins and the Kern to the south.

DISCUSSION AND CONCLUSION

We consider estimates of future hydroclimatic variability for the western United States and southwestern Canada and the effects of climate change on extreme events. That is, we compare how the 99th percentile of daily precipitation and runoff may change

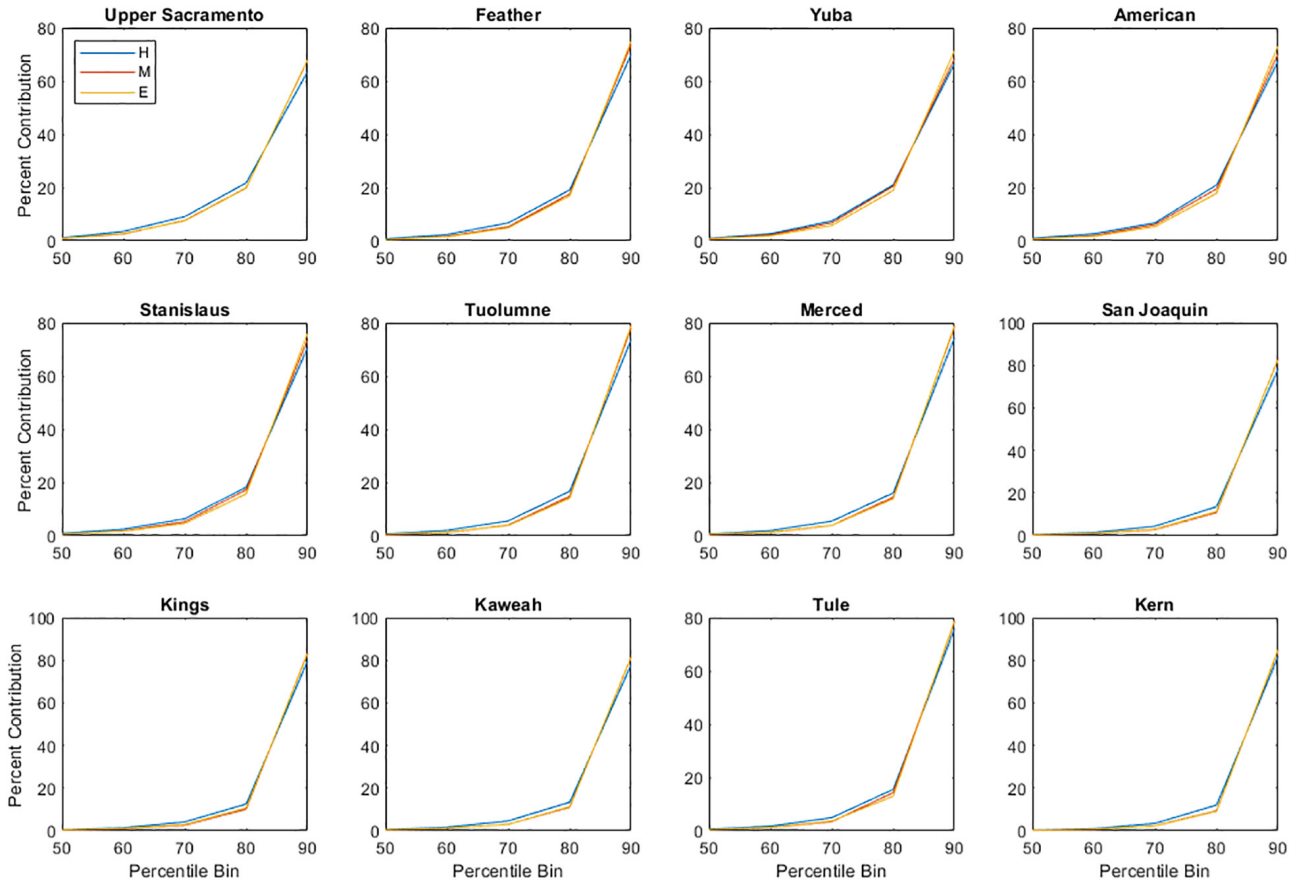


FIGURE 11 | Percent contribution of precipitation within each percentile bin to total precipitation, accumulated across each decade, for each Sierra Nevada basin. Percentile bins <50th are not shown due to their small contribution to total precipitation. Basins are sorted from north (Upper Sacramento) to south (Kern).

throughout the 21st century. Though we are most interested in changes from the historical decade to future decades, it is important to check whether WRF is performing as expected. Therefore, we first confirm whether WRF produces reasonable estimates of precipitation and streamflow. Much work has been done to compare WRF-simulated precipitation to both *in situ* and gridded datasets (Caldwell et al., 2009; Leung and Qian, 2009; Qian et al., 2010; Gutmann et al., 2012; Cardoso et al., 2013; Warrach-Sagi et al., 2013), and the consensus is that WRF estimates are reasonably skilled at capturing realistic precipitation patterns and magnitudes (Hughes et al., 2017). Recent work suggests that atmospheric models such as WRF provide better estimates of precipitation in mountainous regions than precipitation gauge networks (Lundquist et al., 2019); known errors in observational networks pose major challenges to validating climate simulations. Therefore, we do not aim to evaluate WRF-simulated precipitation in this work and instead focus on precipitation changes throughout the 21st century. For streamflow, though, less work has been done to evaluate whether WRF simulations are reasonable.

Here we evaluate the performance of WRF streamflow by comparing to estimates of FNF for basins in the Sierra Nevada (**Figure 2**). Since GCMs like CCSM4 are not constrained by observations, we do not expect CCSM4-forced WRF simulations to match FNF perfectly (Taylor et al., 2012). A below-average year in the historic record may not be a below-average year in CCSM4. However, by comparing streamflow magnitudes at each percentile (**Figure 2**), we can determine whether the distribution of streamflow values is similar between WRF and FNF. At the highest values of daily streamflow, WRF estimates are almost always larger than FNF. Only the American basin has larger values for FNF at the highest percentiles. Streamflow estimates for the Tule basin are similar between the two datasets. While it is apparent that WRF overestimates the largest flow days when compared to FNF, that does not preclude the use of WRF-downscaled streamflow when projecting future changes. We can assume that historic, mid-century, and end-century estimates of WRF streamflow are all likely biased high for the largest events. Since we are interested in changes between decades, the potential WRF bias does not affect our analysis. However, future work should aim to improve the performance of WRF for high flow events.

Across the full model domain, there is a dipole pattern in precipitation change (**Figure 3**), where annual precipitation is projected to increases in the Pacific Northwest, along the California coast, and in southwest Canada, while decreases

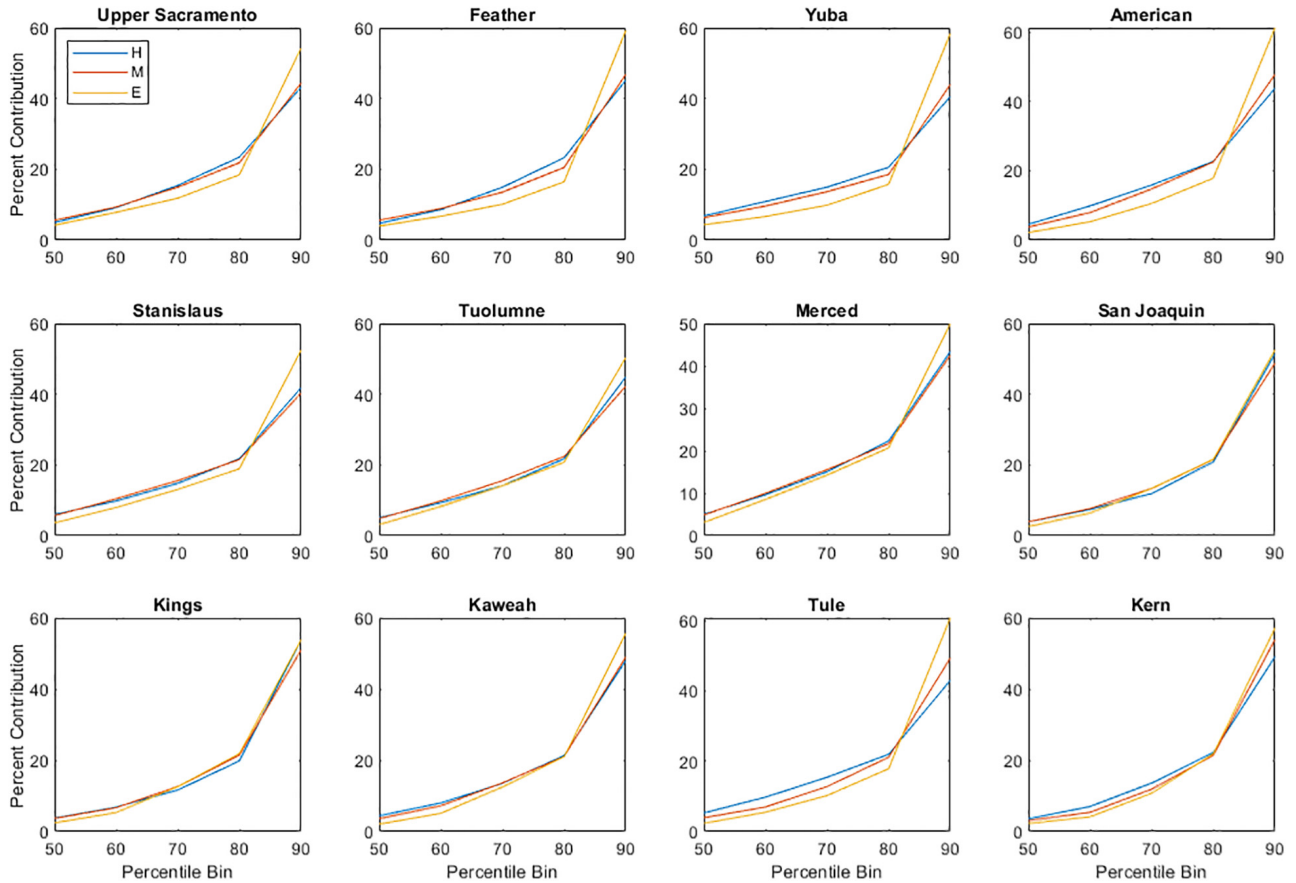


FIGURE 12 | Percent contribution of runoff within each percentile bin to total runoff, accumulated across each decade, for each Sierra Nevada basin. Percentile bins <50th are not shown due to their small contribution to total runoff. Basins are sorted from north (Upper Sacramento) to south (Kern).

are projected in the desert southwest and toward the Great Plains of the United States. The spatial pattern of precipitation changes is similar to that reported in other studies (Gutzler and Robbins, 2011; Kumar et al., 2013; Baker and Huang, 2014). Increased precipitation in the Pacific Northwest and decreased precipitation in the southwest United States is consistent with a projected poleward shift of midlatitude storm tracks (Yin, 2005; Salathé, 2006; Mbengue and Schneider, 2013). For annual precipitation, the Columbia and Upper Missouri/Yellowstone have end-century increases of 10.1 and 2.9%, respectively (**Table 1**). Both the Lower (−17.2%) and Upper Colorado (−11.6%) have decreased average annual precipitation in the end-century WRF simulations. By partitioning rainfall and snowfall, we can understand how the different phases of precipitation will change. As expected in a warming climate, all four watersheds will have decreased total snowfall; the Lower Colorado (−65.3%) has the largest decrease, though it is the watershed with the smallest amount of historical snowfall. In the historic period, the Columbia receives the most annual snowfall, and it is expected to decline by 32.4% by the last decade of the 21st century. Alternatively, all watersheds except the Lower Colorado are projected to have increases in rainfall. The Columbia has the largest increase at 31.7%; despite the large decrease in snowfall, the large increase in rainfall leads to a positive change in total precipitation. The decrease in Upper Colorado total precipitation is driven by the 29.1% decrease in snowfall.

Comparing end-century precipitation to historical simulations, all four western watersheds have projected increases in the magnitude of daily extreme events for the 99th percentile (**Table 2**). In the Columbia watershed, the 99th percentile of daily precipitation, or an event that occurs roughly three times a year, is projected to increase from 24.5 to 27.5 mm over the full domain (a volume increase of 2.0 km^3). Such events may increase the risk of flooding, depending on the timing of the rainfall. If soils are already saturated or if a rain-on-snow event occurs, likelihood of flooding increases. Other work projects increased flood risk by the end of the 21st century for the Columbia watershed (Rosenberg et al., 2010; Salathé et al., 2014; Tohver et al., 2014). While end-century changes aren't projected to be as large for the other three watersheds (**Table 2**), increases in heavy precipitation events could cause localized flooding.

While precipitation changes are mostly uniform for the four western watersheds, daily runoff changes have more variability. For the 99th percentile, streamflow magnitude is expected to decrease for all but the Lower Colorado basin (**Table 2**).

TABLE 4 | Number of extreme runoff events (at or above the 99th percentile; maximum of 37) that coincide with an extreme precipitation event for both same-day precipitation and a lag time of up to 5 days.

Basin	Same-day precipitation for historic period	5-day lag precipitation for historic period	Same-day precipitation for end-century period	5-day lag precipitation for end-century period
Upper Sacramento	12	20	22	30
Feather	18	30	21	31
Yuba	20	31	23	34
American	21	31	25	31
Stanislaus	12	15	21	32
Tuolumne	12	14	22	30
Merced	12	14	19	26
San Joaquin	6	7	19	29
Kings	4	4	19	25
Kaweah	11	16	26	34
Tule	16	29	22	32
Kern	3	3	14	20

Basins are sorted from north (Upper Sacramento) to south (Kern).

The Upper Colorado is projected to have the largest change, with decreases of 31.4% for the 99th percentile of daily runoff. Additionally, the annual total runoff volume for the Upper Colorado is estimated to decrease from 31.4 to 21.4 km^3, a decrease of nearly 32% (**Table 1**). Therefore, not only are extreme events expected to decrease in magnitude, likely decreasing the risk of flash flooding, annuals flows will decrease, following with previously published work on potential drying of the Colorado River (Christensen and Lettenmaier, 2006; Rajagopalan et al., 2009; Dawadi and Ahmad, 2012; Ficklin et al., 2013; Livneh et al., 2017; Udall and Overpeck, 2017); when decreased flows are coupled with decreased annual precipitation, the likelihood for drought or not meeting water demands increases.

In contrast, the Lower Colorado basin is projected to have an increase of 2.7% for the 99th percentile of daily runoff, though, annual runoff is expected to decrease by 32.2%. Increases in extreme event magnitude and decreases in annual total suggest that a large fraction of yearly streamflow may come from only a few events. For some years in the Colorado River basin, present-day flows are less than the allocated total (Christensen et al., 2004). Projected decreases in annual flow by end-century may strain an already-stressed system.

All Sierra Nevada basins examined here are projected to have decreased snowfall and snow accumulation (**Figure 9**) and decreased daily streamflow at most percentiles (**Figure 10**). As a warm maritime mountain range that receives most of its snow accumulation from a handful of storms (Margulis et al., 2016), it is not surprising that the majority of the basins are expected to have less snowfall and snow accumulation by end-century. With present-day conditions, annual spring snowmelt coincides with higher water demand. If streamflow begins to peak earlier in the spring, as reported in other studies (Dettinger et al., 2004; Stewart et al., 2004; Maurer et al., 2007; Schwartz et al., 2017) and as we suggest here (**Figure 8**), local management strategies will need to adapt (Sterle et al., 2019). Operational reservoir managers in the Sierra Nevada must balance capturing runoff for societal use with managing flood risk (Dettinger et al., 2011). Should the magnitude or timing of high flow events change, as we show for all 12 Sierra Nevada basins (**Figure 13**), reservoirs may need to be held at lower capacity or run the risk of mismanaging a potential flood event.

Unlike the larger western watersheds, which integrate increases and decreases to runoff and precipitation across very large drainage areas, projected changes to extreme precipitation and runoff are more closely coupled in the smaller Sierra Nevada basins (**Table 3**). All 12 basins are projected to have increases in magnitude of extreme precipitation (statistically significant for the northern half of the mountain range), and most Sierra Nevada basins have increased magnitude of extreme runoff events (all statistically significant). In the northern and central

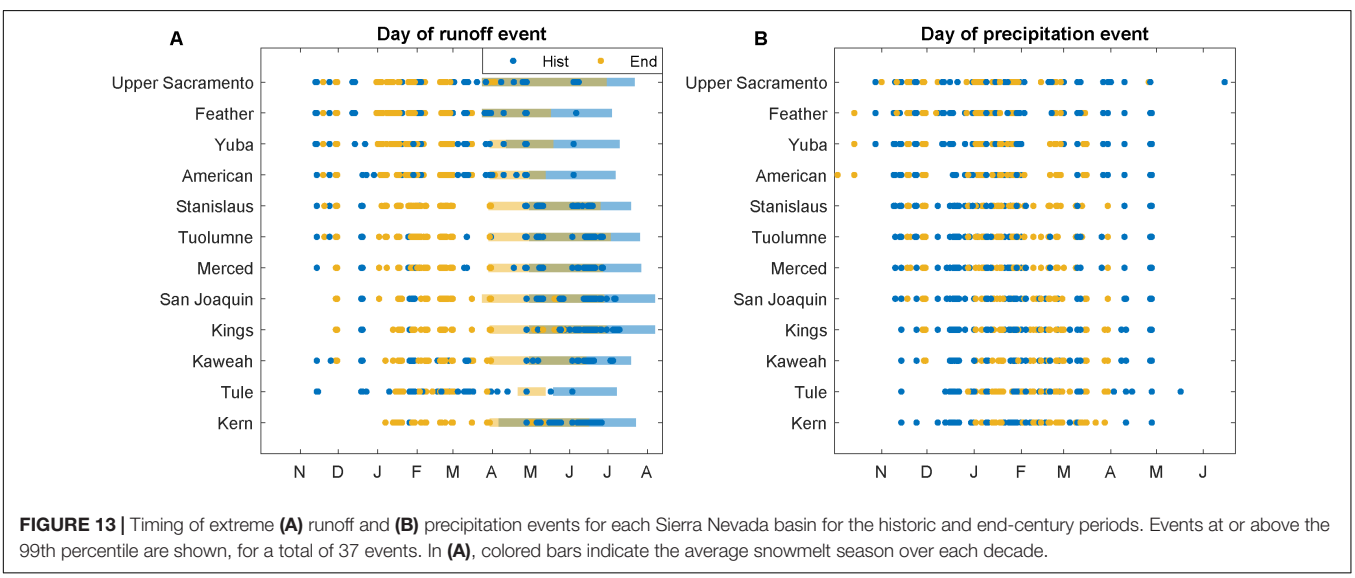


FIGURE 13 | Timing of extreme **(A)** runoff and **(B)** precipitation events for each Sierra Nevada basin for the historic and end-century periods. Events at or above the 99th percentile are shown, for a total of 37 events. In **(A)**, colored bars indicate the average snowmelt season over each decade.

TABLE 5 | Coefficient of determination for relationship between extreme runoff (at or above the 99th percentile) and precipitation, both for same-day precipitation and accumulated precipitation for 5 days prior to the extreme runoff event.

Basin	Historic same-day precipitation	Historic 5-day antecedent precipitation	End-century same-day precipitation	End-century 5-day antecedent precipitation
Upper Sacramento	0.22	0.17	0.42	0.17
Feather	0.20	0.08	0.50	0.07
Yuba	0.21	0.11	0.49	0.13
American	0.22	0.17	0.25	0.29
Stanislaus	0.36	0.12	0.25	0.14
Tuolumne	0.36	0.13	0.23	0.06
Merced	0.47	0.16	0.23	0.00
San Joaquin	0.67	0.13	0.33	0.04
Kings	0.69	0.25	0.52	0.16
Kaweah	0.60	0.26	0.47	0.00
Tule	0.49	0.07	0.48	0.00
Kern	0.09	0.24	0.37	0.18

Basins are sorted from north (Upper Sacramento) to south (Kern).

basins, projected increases to high flow events often exceed a 100% increase (**Table 3**). Southern basins, particularly the Kings and Kern, are projected to have smaller changes in extreme runoff or even decreases. Decreases to annual streamflow (**Figures 3F**, **11**) and increases in extreme runoff (**Table 3**) suggest that an increased proportion of Sierra Nevada streamflow will occur during extreme high flow events. We see this behavior when considering how the contribution of each runoff percentile to total runoff may change by end-century (**Figure 12**); for all Sierra Nevada basins, events at the >90th percentile will make up a larger proportion of total runoff. Similar results have been reported for an increased proportion of annual precipitation that occurs during heavy rainfall events (New et al., 2001; Groisman et al., 2005; Wuebbles et al., 2014). Though the most extreme events may only occur a few times a year, a doubling of streamflow, as projected for the American, Stanislaus, and Tuolumne basins with increases >100%, will require careful flood control management. The Feather basin, which includes the Oroville Dam, is projected to have increases of 114% for 99th percentile runoff events, which occur roughly three times a year; with increased high flows, flood crises such as the 2017 Oroville event may become more frequent by end-century.

For the Sierra Nevada basins, all are projected to have increases in the contribution of high magnitude precipitation to extreme runoff (**Table 4**). In the southern basins, increases are particularly large: where only 8 and 11% of extreme runoff events coincided with extreme precipitation in the historic simulations for the Kern and Kings basins, respectively, by the end century, 38 and 51% of the >99th percentile runoff events are projected to coincide with extreme precipitation. We suggest a shift from snowmelt to rainfall as the dominant cause of extreme runoff events, particularly in the southern Sierra Nevada where, by end-century, most high-magnitude runoff events occur prior to the spring snowmelt period (**Figure 13A**). If precipitation magnitude does increase for extreme events as a result of climate change, as recent literature suggests (Dominguez et al., 2012; Scoccimarro et al., 2013; Wuebbles et al., 2014), it follows that extreme runoff events and the risk of flooding will also increase.

A major limitation to this study is the short time periods available for comparing historical and future climate. Here we consider decadal snapshots of western United States climate throughout the 20th and 21st centuries; longer, perhaps 30+ years of simulations are necessary for assessing climate variability. However, due to the high computational cost of WRF, multi-decade, high-resolution simulations are not possible. Previous studies that use WRF to project climate change impacts are also limited by computational cost, with most simulations running for ∼10 years (Liu et al., 2017; Musselman et al., 2017; Schwartz et al., 2017; Musselman et al., 2018). Decade-scale simulations have also been used to evaluate changes to extreme events from WRF (Prein et al., 2017), and Gao et al. (2012) used a similar approach to ours in estimating changes between a historical and future period, though they compare over a 3 year period. Through advances in computational resources, WRF is an increasingly useful tool in climate projections, though limitations still exist. The computational cost of an RCM such as WRF is one of the tradeoffs between RCMs and GCMs; as described in the introduction, RCMs may not provide as much data as a GCM, but they allow for higher resolution information over regions that often have high biases in GCMs (van der Wiel et al., 2016).

Recent literature suggests a large ensemble approach is likely the best method for projecting future climate and changes to extreme events (Kay et al., 2015; van der Wiel et al., 2019). As computational resources continue to improve, a large ensemble of WRF simulations, similar to the Community Earth System Model Large Ensemble Project (Kay et al., 2015), may be possible. Until then, long-term, high-resolution climate projections are likely only possible through tools like the Intermediate Complexity Atmospheric Research Model (ICAR; Gutmann et al., 2016) or hybrid dynamical-statistical downscaling (Walton et al., 2015; Sun et al., 2016; Schwartz et al., 2017).

Results presented here are one representation of future hydroclimate conditions from a single downscaled GCM. Though the Bruyère et al. (2013) method only bias corrects a single GCM at a time, it does not make any assumptions about climate stationarity, like the PGW method. Future work, however, should prioritize the downscaling of multiple bias corrected GCMs to create an ensemble of possible scenarios, whether through dynamical downscaling or less computationally expensive tools like ICAR. Regardless of the method, downscaling GCMs to higher spatial resolution will improve understanding of not only mean hydroclimate changes but also of extreme events, whether heat waves, droughts, or, as we examine here, heavy precipitation and streamflow that can result in flooding. Since many river networks in western

United States and Canada are managed systems, regional-scale predictions of future hydroclimate are crucial for ensuring infrastructure is prepared for possible regime shifts in extreme event intensity.

DATA AVAILABILITY STATEMENT

The datasets generated for this study are available on request to the corresponding author.

AUTHOR CONTRIBUTIONS

MW and TP analyzed the data and wrote the manuscript. MW performed the model simulations.

FUNDING

This research was funded by NSF Innovations at the Nexus of Food, Energy and Water Systems (INFEWS) grant CNS-1639268 (PI G. Characklis, UNC).

ACKNOWLEDGMENTS

We thank Sarah B. Kapnick for helpful discussions that greatly improved the manuscript. We also acknowledge the two reviewers for critically reading the manuscript and suggesting improvements. WRF simulations used the Extreme Science and Engineering Discovery Environment (XSEDE) Stampede2 at the Texas Advanced Computing Center, The University of Texas at Austin, through allocation TG-ATM19008.

REFERENCES

Baker, N. C., and Huang, H. P. (2014). A comparative study of precipitation and evaporation between CMIP3 and CMIP5 climate model ensembles in semiarid regions. *J. Clim.* 27, 3731–3749. doi: 10.1175/jcli-d-13-00398.1

Barlage, M., Tewari, M., Chen, F., Miguez-Macho, G., Yang, Z. L., and Niu, G. Y. (2015). The effect of groundwater interaction in North American regional climate simulations with WRF/Noah-MP. *Clim. Change* 129, 485–498. doi: 10.1007/s10584-014-1308-8

Bruyère, C. L., Done, J. M., Holland, G. J., and Fredrick, S. (2013). Bias corrections of global models for regional climate simulations of high-impact weather. *Clim. Dyn.* 43, 1847–1856. doi: 10.1007/s00382-013-2011-6

Caldwell, P., Chin, H. N. S., Bader, D. C., and Bala, G. (2009). Evaluation of a WRF dynamical downscaling simulation over California. *Clim. Change* 95, 499–521. doi: 10.1007/s10584-009-9583-5

Cardoso, R. M., Soares, P. M. M., Miranda, P. M. A., and Belo-Pereira, M. (2013). WRF high resolution simulation of Iberian mean and extreme precipitation climate. *Int. J. Climatol.* 33, 2591–2608. doi: 10.1002/joc.3616

Cayan, D. R., Maurer, E. P., Dettinger, M. D., Tyree, M., and Hayhoe, K. (2008). Climate change scenarios for the California region. *Clim. Change* 87, S21–S42. doi: 10.1007/s10584-007-9377-6

Christensen, J. H., Boberg, F., Christensen, O. B., and Lucas-Picher, P. (2008). On the need for bias correction of regional climate change projections of temperature and precipitation. *Geophys. Res. Lett.* 35:L20709. doi: 10.1029/2008gl035694

Christensen, N., and Lettenmaier, D. P. (2006). A multimodel ensemble approach to assessment of climate change impacts on the hydrology and water resources of the Colorado River Basin. *Hydrol. Earth Syst. Sci. Discuss.* 3, 3727–3770. doi: 10.5194/hessd-3-3727-2006

Christensen, N. S., Wood, A. W., Voisin, N., Lettenmaier, D. P., and Palmer, R. N. (2004). The effects of climate change on the hydrology and water resources of the Colorado River basin. *Clim. Change* 62, 337–363. doi: 10.1023/B:CLIM.0000013684.13621.1f

Cosgrove, B. A., Lohmann, D., Mitchell, K. E., Houser, P. R., Wood, E. F., Schaake, J. C., et al. (2003). Land surface model spin-up behavior in the North American Land Data Assimilation System (NLDAS). *J. Geophys. Res. Atmos.* 108:8845. doi: 10.1029/2002JD003316

Dawadi, S., and Ahmad, S. (2012). Changing climatic conditions in the Colorado River Basin: implications for water resources management. *J. Hydrol.* 430, 127–141. doi: 10.1016/j.jhydrol.2012.02.010

Dee, D. P., Uppala, S. M., Simmons, A. J., Berrisford, P., Poli, P., Kobayashi, S., et al. (2011). The ERA-Interim reanalysis: configuration and performance of the data assimilation system. *Q. J. R. Meteorol. Soc.* 137, 553–597. doi: 10.1002/qj.828

Dettinger, M. D., Cayan, D. R., Meyer, M. K., and Jeton, A. E. (2004). Simulated hydrologic responses to climate variations and change in the Merced, Carson, and American River basins, Sierra Nevada, California, 1900–2099. *Clim. Change* 62, 283–317. doi: 10.1023/b:clim.0000013683.13346.4f

Dettinger, M. D., Ralph, F. M., Das, T., Neiman, P. J., and Cayan, D. R. (2011). Atmospheric rivers, floods and the water resources of California. *Water* 3, 445–478. doi: 10.3390/w3020445

Dominguez, F., Rivera, E., Lettenmaier, D. P., and Castro, C. L. (2012). Changes in winter precipitation extremes for the western United States under a warmer climate as simulated by regional climate models. *Geophys. Res. Lett.* 39:L05803.

Donat, M. G., Alexander, L. V., Yang, H., Durre, I., Vose, R., and Caesar, J. (2013). Global land-based datasets for monitoring climatic extremes. *Bull. Am. Meteorol. Soc.* 94, 997–1006. doi: 10.1175/bams-d-12-00109.1

Dudhia, J. (1989). Numerical study of convection observed during the winter monsoon experiment using a mesoscale two-dimensional model. *J. Atmos. Sci.* 46, 3077–3107. doi: 10.1175/1520-04691989046<3077:Nsocod<2.0.Co;2

Ehret, U., Zehe, E., Wulfmeyer, V., Warrach-Sagi, K., and Liebert, J. (2012). HESS opinions" Should we apply bias correction to global and regional climate model data?". *Hydrol. Earth Syst. Sci.* 16, 3391–3404. doi: 10.5194/hess-16-3391-2012

Erler, A. R., and Peltier, W. R. (2016). Projected changes in precipitation extremes for western Canada based on high-resolution regional climate simulations. *J. Clim.* 29, 8841–8863. doi: 10.1175/jcli-d-15-0530.1

Ficklin, D. L., Stewart, I. T., and Maurer, E. P. (2013). Climate change impacts on streamflow and subbasin-scale hydrology in the Upper Colorado River Basin. *PLoS One* 8:e71297. doi: 10.1371/journal.pone.0071297

Gao, Y., Fu, J. S., Drake, J. B., Liu, Y., and Lamarque, J. F. (2012). Projected changes of extreme weather events in the eastern United States based on a high resolution climate modeling system. *Environ. Res. Lett.* 7:044025. doi: 10.1088/1748-9326/7/4/044025

Gent, P. R., Danabasoglu, G., Donner, L. J., Holland, M. M., Hunke, E. C., Jayne, S. R., et al. (2011). The community climate system model version 4. *J. Clim.* 24, 4973–4991. doi: 10.1175/2011jcli4083.1

Groisman, P. Y., Knight, R. W., Easterling, D. R., Karl, T. R., Hegerl, G. C., and Razuvaev, V. N. (2005). Trends in intense precipitation in the climate record. *J. Clim.* 18, 1326–1350. doi: 10.1371/journal.pone.0123793

Gutmann, E., Barstad, I., Clark, M., Arnold, J., and Rasmussen, R. (2016). The intermediate complexity atmospheric research model (ICAR). *J. Hydrometeorol.* 17, 957–973. doi: 10.1175/JHM-D-15-0155.1

Gutmann, E. D., Rasmussen, R. M., Liu, C. H., Ikeda, K., Bruyere, C. L., Done, J. M., et al. (2018). Changes in hurricanes from a 13-Yr convection-permitting pseudo-global warming simulation. *J. Clim.* 31, 3643–3657. doi: 10.1175/Jcli-D-17-0391.1

Gutmann, E. D., Rasmussen, R. M., Liu, C. H., Ikeda, K., Gochis, D. J., Clark, M. P., et al. (2012). A comparison of statistical and dynamical downscaling of winter precipitation over complex terrain. *J. Clim.* 25, 262–281. doi: 10.1175/2011jcli4109.1

Gutzler, D. S., and Robbins, T. O. (2011). Climate variability and projected change in the western United States: regional downscaling and drought statistics. *Clim. Dyn.* 37, 835–849. doi: 10.1007/s00382-010-0838-7

Hara, M., Yoshikane, T., Kawase, H., and Kimura, F. (2008). Estimation of the impact of global warming on snow depth in Japan by the pseudo-global-warming method. *Hydrol. Res. Lett.* 2, 61–64. doi: 10.3178/hrl.2.61

Harder, P., Pomeroy, J. W., and Westbrook, C. J. (2015). Hydrological resilience of a Canadian Rockies headwaters basin subject to changing climate, extreme weather, and forest management. *Hydrol. Process.* 29, 3905–3924. doi: 10.1002/hyp.10596

Hollins, L., Eisenberg, D., and Seager, T. (2018). Risk and resilience at the Oroville Dam. *Infrastructures* 3:49. doi: 10.3390/infrastructures3040049

Hong, S. Y., Noh, Y., and Dudhia, J. (2006). A new vertical diffusion package with an explicit treatment of entrainment processes. *Monthly Weather Rev.* 134, 2318–2341. doi: 10.1175/Mwr3199.1

Huang, G. (2016). *Estimates of Natural and Unimpaired Flows for the Central Valley of California: Water Years 1922–2014*. Sacramento, CA: California Department of Water Resources.

Hughes, M., Lundquist, J. D., and Henn, B. (2017). Dynamical downscaling improves upon gridded precipitation products in the Sierra Nevada, California. *Clim. Dyn.* doi: 10.1007/s00382-017-3631-z

Ikeda, K., Rasmussen, R., Liu, C. H., Gochis, D., Yates, D., Chen, F., et al. (2010). Simulation of seasonal snowfall over Colorado. *Atmos. Res.* 97, 462–477. doi: 10.1016/j.atmosres.2010.04.010

Kain, J. S. (2004). The Kain-Fritsch convective parameterization: an update. *J. Appl. Meteorol.* 43, 170–181. doi: 10.1175/1520-04502004043<0170:Tkcpau<2.0.Co;2

Kain, J. S., and Fritsch, J. M. (1990). A one-dimensional entraining detraining plume model and its application in convective parameterization. *J. Atmos. Sci.* 47, 2784–2802. doi: 10.1175/1520-04691990047<2784:Aodepm<2.0.Co;2

Kain, J. S., and Fritsch, J. M. (1993). "Convective parameterization for mesoscale models: the Kain-Fritsch scheme," in *The Representation of Cumulus Convection in Numerical Models*, eds K. A. Emanuel, and D. J. Raymond, (Boston, MA: American Meteorological Society), 165–170. doi: 10.1007/978-1-935704-13-3_16

Kawase, H., Yoshikane, T., Hara, M., Kimura, F., Yasunari, T., Ailikun, B., et al. (2009). Intermodel variability of future changes in the Baiu rainband estimated by the pseudo global warming downscaling method. *J. Geophys. Res. Atmos.* 114:D241. doi: 10.1029/2009jd011803

Kay, J. E., Deser, C., Phillips, A., Mai, A., Hannay, C., Strand, G., et al. (2015). The Community Earth System Model (CESM) large ensemble project: a community resource for studying climate change in the presence of internal climate variability. *Bull. Am. Meteorol. Soc.* 96, 1333–1349. doi: 10.1175/bams-d-13-00255.1

Knutson, T. R., Zeng, F. R., and Wittenberg, A. T. (2013). Multimodel assessment of regional surface temperature trends: CMIP3 and CMIP5 twentieth-century simulations. *J. Clim.* 26, 8709–8743. doi: 10.1175/Jcli-D-12-00567.1

Knutti, R., and Sedlacek, J. (2013). Robustness and uncertainties in the new CMIP5 climate model projections. *Nat. Clim. Change* 3, 369–373. doi: 10.1038/Nclimate1716

Kumar, S., Merwade, V., Kinter, J. L. III, and Niyogi, D. (2013). Evaluation of temperature and precipitation trends and long-term persistence in CMIP5 twentieth-century climate simulations. *J. Clim.* 26, 4168–4185. doi: 10.1175/jcli-d-12-00259.1

Letcher, T. W., and Minder, J. R. (2018). The simulated impact of the snow albedo feedback on the large-scale mountain-plain circulation east of the Colorado rocky mountains. *J. Atmos. Sci.* 75, 755–774. doi: 10.1175/Jas-D-17-0166.1

Leung, L. R., and Qian, Y. (2009). Atmospheric rivers induced heavy precipitation and flooding in the western U.S. simulated by the WRF regional climate model. *Geophys. Res. Lett.* 36:L03820. doi: 10.1029/2008gl036445

Liu, C. H., Ikeda, K., Rasmussen, R., Barlage, M., Newman, A. J., Prein, A. F., et al. (2017). Continental-scale convection-permitting modeling of the current and future climate of North America. *Clim. Dyn.* 49, 71–95. doi: 10.1007/s00382-016-3327-9

Livneh, B., Badger, A. M., and Lukas, J. J. (2017). "Assessing the robustness of snow-based drought indicators in the Upper Colorado River basin under future climate change," *Paper Presented at the World Environmental and Water Resources Congress* 2017, Reston, VA.

Lundquist, J., Hughes, M., Gutmann, E., and Kapnick, S. (2019). Our skill in modeling mountain rain and snow is bypassing the skill of our observational networks. *Bull. Am. Meteorol. Soc.* doi: 10.1175/BAMS-D-19-0001.1

Maraun, D. (2012). Nonstationarities of regional climate model biases in European seasonal mean temperature and precipitation sums. *Geophys. Res. Lett.* 39:L06706. doi: 10.1029/2012gl051210

Maraun, D., Wetterhall, F., Ireson, A. M., Chandler, R. E., Kendon, E. J., Widmann, M., et al. (2010). Precipitation downscaling under climate change: recent developments to bridge the gap between dynamical models and the end user. *Rev. Geophys.* 48, 1–34. doi: 10.1029/2009rg000314

Margulis, S. A., Cortes, G., Girotto, M., and Durand, M. (2016). A landsat-era sierra nevada snow reanalysis (1985-2015). *J. Hydrometeorol.* 17, 1203–1221. doi: 10.1175/Jhm-D-15-0177.1

Maurer, E. P., Stewart, I., Bonfils, C., Duffy, P. B., and Cayan, D. (2007). Detection, attribution, and sensitivity of trends toward earlier streamflow in the Sierra Nevada. *J. Geophys. Res. Atmos.* 112:12.

Mbengue, C., and Schneider, T. (2013). Storm track shifts under climate change: what can be learned from large-scale dry dynamics. *J. Clim.* 26, 9923–9930. doi: 10.1175/jcli-d-13-00404.1

Minder, J. R., Letcher, T. W., and Skiles, S. M. (2016). An evaluation of high-resolution regional climate model simulations of snow cover and albedo over the Rocky Mountains, with implications for the simulated snow-albedo feedback. *J. Geophys. Res. Atmos.* 121, 9069–9088. doi: 10.1002/2016jd024995

Mlawer, E. J., Taubman, S. J., Brown, P. D., Iacono, M. J., and Clough, S. A. (1997). Radiative transfer for inhomogeneous atmospheres: RRTM, a validated correlated-k model for the longwave. *J. Geophys. Res. Atmos.* 102, 16663–16682. doi: 10.1029/97jd00237

Monaghan, A. J., Steinhoff, D. F., Bruyere, C. L., and Yates, D. (2014). *NCAR CESM Global Bias-Corrected CMIP5 Output to Support WRF/MPAS Research*. Boulder, CO: Research Data Archive at the National Center for Atmospheric Research, Computational and Information Systems Laboratory. doi: 10.5065/D6DJ5CN4

Mote, P. W., and Salathe, E. P. (2010). Future climate in the Pacific Northwest. *Clim. Change* 102, 29–50. doi: 10.1007/s10584-010-9848-z

Musselman, K. N., Clark, M. P., Liu, C. H., Ikeda, K., and Rasmussen, R. (2017). Slower snowmelt in a warmer world. *Nat. Clim. Change* 7, 214–219. doi: 10.1038/Nclimate3225

Musselman, K. N., Lehner, F., Ikeda, K., Clark, M. P., Prein, A. F., Liu, C., et al. (2018). Projected increases and shifts in rain-on-snow flood risk over western North America. *Nat. Clim. Change* 8, 808–812. doi: 10.1038/s41558-018-0236-4

New, M., Todd, M., Hulme, M., and Jones, P. (2001). Precipitation measurements and trends in the twentieth century. *Int. J. Climatol.* 21, 1889–1922. doi: 10.1002/joc.680

Niu, G. Y., Yang, Z. L., Mitchell, K. E., Chen, F., Ek, M. B., Barlage, M., et al. (2011). The community Noah land surface model with multiparameterization options (Noah-MP): 1. Model description and evaluation with local-scale measurements. *J. Geophys. Res. Atmos.* 116:D12109. doi: 10.1029/2010jd015139

Pavelsky, T. M., Kapnick, S., and Hall, A. (2011). Accumulation and melt dynamics of snowpack from a multiresolution regional climate model in the central Sierra Nevada, California. *J. Geophys. Res. Atmos.* 116, 15–32. doi: 10.1029/2010jd015479

Peacock, S. (2012). Projected twenty-first-century changes in temperature, precipitation, and snow cover over North America in CCSM4. *J. Clim.* 25, 4405–4429. doi: 10.1175/Jcli-D-11-00214.1

Pontoppidan, M., Kolstad, E. W., Sobolowski, S., and King, M. P. (2018). Improving the reliability and added value of dynamical downscaling via correction of large-scale errors: a norwegian perspective. *J. Geophys. Res. Atmos.* 123, 11875–11888. doi: 10.1029/2018jd028372

Prein, A. F., Rasmussen, R. M., Ikeda, K., Liu, C., Clark, M. P., and Holland, G. J. (2017). The future intensification of hourly precipitation extremes. *Nat. Clim. Change* 7, 48–52. doi: 10.1038/nclimate3168

Qian, Y., Ghan, S. J., and Leung, L. R. (2010). Downscaling hydroclimatic changes over the Western US based on CAM subgrid scheme and WRF regional climate simulations. *Int. J. Climatol.* 30, 675–693. doi: 10.1002/joc.1928

Rajagopalan, B., Nowak, K., Prairie, J., Hoerling, M., Harding, B., Barsugli, J., et al. (2009). Water supply risk on the Colorado River: can management mitigate? *Water Resour. Res.* 45:W08201. doi: 10.1029/2008WR007652

Rasmussen, R., Liu, C. H., Ikeda, K., Gochis, D., Yates, D., Chen, F., et al. (2011). High-resolution coupled climate runoff simulations of seasonal snowfall over colorado: a process study of current and warmer climate. *J. Clim.* 24, 3015–3048. doi: 10.1175/2010jcli3985.1

Rosenberg, E. A., Keys, P. W., Booth, D. B., Hartley, D., Burkey, J., Steinemann, A. C., et al. (2010). Precipitation extremes and the impacts of climate change on stormwater infrastructure in Washington State. *Clim. Change* 102, 319–349. doi: 10.1007/s10584-010-9847-0

Russo, S., and Sterl, A. (2012). Global changes in seasonal means and extremes of precipitation from daily climate model data. *J. Geophys. Res. Atmos.* 117:D01108. doi: 10.1029/2011JD016260

Salathé, E. P. Jr. (2006). Influences of a shift in North Pacific storm tracks on western North American precipitation under global warming. *Geophys. Res. Lett.* 33:L19820. doi: 10.1029/2006GL026882

Salathé, E. P., Hamlet, A. F., Mass, C. F., Lee, S.-Y., Stumbaugh, M., and Steed, R. (2014). Estimates of twenty-first-century flood risk in the pacific northwest based on regional climate model simulations. *J. Hydrometeorol.* 15, 1881–1899. doi: 10.1175/jhm-d-13-0137.1

Schar, C., Frei, C., Luthi, D., and Davies, H. C. (1996). Surrogate climate-change scenarios for regional climate models. *Geophys. Res. Lett.* 23, 669–672. doi: 10.1029/96gl00265

Schwartz, M., Hall, A., Sun, F. P., Walton, D., and Berg, N. (2017). Significant and inevitable end-of-twenty-first-century advances in surface runoff timing in California's Sierra Nevada. *J. Hydrometeorol.* 18, 3181–3197. doi: 10.1175/Jhm-D-16-0257.1

Scoccimarro, E., Gualdi, S., Bellucci, A., Zampieri, M., and Navarra, A. (2013). Heavy precipitation events in a warmer climate: results from CMIP5 models. *J. Clim.* 26, 7902–7911. doi: 10.1175/jcli-d-12-00850.1

Skamarock, W. C., Klemp, J. B., Dudhia, J., Gill, D. O., Liu, Z., Berner, J., et al. (2019). *A Description of the Advanced Research WRF Version 4. Technical Note 556*. Boulder, CO: National Center for Atmospheric Research.

Spero, T. L., Nolte, C. G., Mallard, M. S., and Bowden, J. H. (2018). A Maieutic exploration of nudging strategies for regional climate applications using the WRF model. *J. Appl. Meteorol. Climatol.* 57, 1883–1906. doi: 10.1175/Jamc-D-17-0360.1

Spero, T. L., Otte, M. J., Bowden, J. H., and Nolte, C. G. (2014). Improving the representation of clouds, radiation, and precipitation using spectral nudging in the Weather Research and Forecasting model. *J. Geophys. Res. Atmos.* 119, 11682–11694. doi: 10.1002/2014jd022173

Sterle, K., Hatchett, B. J., Singletary, L., and Pohll, G. (2019). Hydroclimate variability in snow-fed river systems: local water managers' perspectives on adapting to the new normal. *Bull. Am. Meteorol. Soc.* 100, 1029–1048. doi: 10.1175/Bams-D-18-0031.1

Stewart, I. T., Cayan, D. R., and Dettinger, M. D. (2004). Changes in snowmelt runoff timing in western North America under abusiness as usual'climate change scenario. *Clim. Change* 62, 217–232. doi: 10.1023/b:clim.0000013702.22656.e8

Sun, F. P., Hall, A., Schwartz, M., Walton, D. B., and Berg, N. (2016). Twenty-first-century snowfall and snowpack changes over the Southern California Mountains. *J. Clim.* 29, 91–110. doi: 10.1175/Jcli-D-15-0199.1

Taylor, K. E., Stouffer, R. J., and Meehl, G. A. (2012). An overview of CMIP5 and the experiment design. *Bull. Am. Meteorol. Soc.* 93, 485–498. doi: 10.1175/Bams-D-11-00094.1

Thompson, G., Field, P. R., Rasmussen, R. M., and Hall, W. D. (2008). Explicit forecasts of winter precipitation using an improved bulk microphysics scheme. Part II: implementation of a new snow parameterization. *Monthly Weather Rev.* 136, 5095–5115. doi: 10.1175/2008mwr2387.1

Tohver, I. M., Hamlet, A. F., and Lee, S. Y. (2014). Impacts of 21st-Century climate change on hydrologic extremes in the Pacific Northwest Region of North America. *J. Am. Water Resour. Assoc.* 50, 1461–1476. doi: 10.1111/jawr.12199

Udall, B., and Overpeck, J. (2017). The twenty-first century Colorado River hot drought and implications for the future. *Water Resour. Res.* 53, 2404–2418. doi: 10.1002/2016wr019638

Vahedifard, F., AghaKouchak, A., Ragno, E., Shahrokhabadi, S., and Mallakpour, I. (2017). Lessons from the Oroville dam. *Science* 355, 1139–1140. doi: 10.1126/science.aan0171

van der Wiel, K., Kapnick, S. B., Vecchi, G. A., Cooke, W. F., Delworth, T. L., Jia, L., et al. (2016). The resolution dependence of contiguous US precipitation extremes in response to CO2 forcing. *J. Clim.* 29, 7991–8012. doi: 10.1175/jcli-d-16-0307.1

van der Wiel, K., Wanders, N., Selten, F. M., and Bierkens, M. F. P. (2019). Added value of large ensemble simulations for assessing extreme river discharge in a 2°C warmer world. *Geophys. Res. Lett.* 46, 2093–2102. doi: 10.1029/2019gl081967

Vannitsem, S. (2011). Bias correction and post-processing under climate change. *Nonlinear Process. Geophys.* 18, 911–924. doi: 10.5194/npg-18-911-2011

Walton, D. B., Hall, A., Berg, N., Schwartz, M., and Sun, F. (2017). Incorporating snow albedo feedback into downscaled temperature and snow cover projections for California's Sierra Nevada. *J. Clim.* 30, 1417–1438. doi: 10.1175/jcli-d-16-0168.1

Walton, D. B., Sun, F. P., Hall, A., and Capps, S. (2015). A Hybrid dynamical-statistical downscaling technique. Part I: development and validation of the technique. *J. Clim.* 28, 4597–4617. doi: 10.1175/Jcli-D-14-00196.1

Wang, J. L., and Kotamarthi, V. R. (2015). High-resolution dynamically downscaled projections of precipitation in the mid and late 21st century over North America. *Earths Fut.* 3, 268–288. doi: 10.1002/2015ef000304

Warrach-Sagi, K., Schwitalla, T., Wulfmeyer, V., and Bauer, H. S. (2013). Evaluation of a climate simulation in Europe based on the WRF-NOAH model system: precipitation in Germany. *Clim. Dyn.* 41, 755–774. doi: 10.1007/s00382-013-1727-7

Wrzesien, M. L., Durand, M. T., Pavelsky, T. M., Howat, I. M., Margulis, S. A., and Huning, L. S. (2017). Comparison of methods to estimate snow water equivalent at the mountain range scale: a case study of the California Sierra Nevada. *J. Hydrometeorol.* 18, 1101–1119. doi: 10.1175/Jhm-D-16-0246.1

Wrzesien, M. L., Durand, M. T., Pavelsky, T. M., Kapnick, S. B., Zhang, Y., Guo, J. Y., et al. (2018). A new estimate of north american mountain snow accumulation from regional climate model simulations. *Geophys. Res. Lett.* 45, 1423–1432. doi: 10.1002/2017gl076664

Wuebbles, D., Meehl, G., Hayhoe, K., Karl, T. R., Kunkel, K., Santer, B., et al. (2014). CMIP5 climate model analyses: climate extremes in the United States. *Bull. Am. Meteorol. Soc.* 95, 571–583.

Yin, J. H. (2005). A consistent poleward shift of the storm tracks in simulations of 21st century climate. *Geophys. Res. Lett.* 32:L18701.

Conflict of Interest: The authors declare that the research was conducted in the absence of any commercial or financial relationships that could be construed as a potential conflict of interest.

Copyright © 2020 Wrzesien and Pavelsky. This is an open-access article distributed under the terms of the Creative Commons Attribution License (CC BY). The use, distribution or reproduction in other forums is permitted, provided the original author(s) and the copyright owner(s) are credited and that the original publication in this journal is cited, in accordance with accepted academic practice. No use, distribution or reproduction is permitted which does not comply with these terms.

frontiers in Earth Science

ORIGINAL RESEARCH
published: 23 January 2020
doi: 10.3389/feart.2019.00360

High Resolution Mapping of Ice Mass Loss in the Gulf of Alaska From Constrained Forward Modeling of GRACE Data

Cheick Doumbia[1], Pascal Castellazzi[2], Alain N. Rousseau[1] and Macarena Amaya[3]*

[1] Centre Eau Terre Environnement, Institut National de la Recherche Scientifique (INRS), Université du Québec, Québec City, QC, Canada, [2] Land and Water, Deep Earth Imaging FSP, Commonwealth Scientific and Industrial Research Organisation, Urrbrae, SA, Australia, [3] Facultad de Ciencias Astronómicas y Geofísicas, Universidad Nacional de La Plata, La Plata, Argentina

The resolution of Gravity Recovery And Climate Experiment (GRACE) Terrestrial Water Storage (TWS) change data is too low to discriminate mass variations at the scale of glaciers, small ensemble of glaciers, or icefields. In this paper, we apply an iterative constraint modeling strategy over the Gulf Of Alaska (GOA) to improve the resolution of ice loss estimates derived from GRACE. We assess the effect of the most influential parameters such as the type of GRACE solution and the degree of heterogeneity of the distribution map over which the GRACE data is focused. Three GRACE solutions from the most common processing strategies and three ice distribution maps of resolutions ranging from 55,000 to 20,000 km^2 are used. First, we present results from a series of simulations with synthetic data and a mix of synthetic/modeled data to validate the focusing strategy and we point out how inaccuracies arise while increasing the spatial resolution of GRACE data. Second, we present the recovery of the total GRACE-derived mass change anomaly at the scale of the GOA. At this scale, all solutions and distribution maps agree, showing ∼40 Gt/year of mean ice mass loss over the period 2002–2017. This result is similar to studies using GRACE solutions from the latest releases and time-series of more than 8 years. The first studies using GRACE data published during the 2005–2008 era generally overestimated the long-term ice mass loss. Third, we show results of the three resolutions tested to focus the mass anomaly. Using focusing units (mascon) of ∼30,000 km^2 or larger, the focusing procedure provides reliable results with errors below 15%. Below this threshold, errors of up to 56% are observed.

Keywords: glaciers, ice melt, GRACE, forward modeling, Gulf of Alaska

OPEN ACCESS

Edited by:
Alfonso Fernandez, University of Concepción, Chile

Reviewed by:
Robert McNabb, Ulster University, United Kingdom
Chris Harig, University of Arizona, United States

****Correspondence:***
Cheick Doumbia
Cheick.Doumbia@ete.inrs.ca

Specialty section:
This article was submitted to Cryospheric Sciences, a section of the journal Frontiers in Earth Science

Received: *27 July 2019*
Accepted: *30 December 2019*
Published: *23 January 2020*

Citation:
Doumbia C, Castellazzi P, Rousseau AN and Amaya M (2020) High Resolution Mapping of Ice Mass Loss in the Gulf of Alaska From Constrained Forward Modeling of GRACE Data. Front. Earth Sci. 7:360. doi: 10.3389/feart.2019.00360

INTRODUCTION

Glaciers represent 68.9% of fresh water resources worldwide. In many regions of the world, people rely on glacier meltwater for agriculture, hydropower, industries, and municipal water requirements (Chen and Ohmura, 1990; Blanchon and Boissière, 2009). However, over the last decades, the glacier mass losses have raised concerns in and beyond the research communities. Climate change leads to important reductions in glacial water storage. Glaciers have an important influence on sea level rise; hence, their melt threatens the living environment of costal dwellings.

Jin and Feng (2016) estimated the contribution of glacial melt to sea level change between 2003 and 2012 at 1.94 ± 0.29 mm/year. From 120,000 glaciers available in the World Glacier Inventory, Radić and Hock (2011) estimated that the total volume loss could be as much as 21 ± 6% by 2100, leading to a total sea level rise of 124 ± 37 mm.

Numerous studies focused on estimating the ice mass loss over specific continents, regions, or Mountain ranges. For example, Larsen et al. (2007) investigated glacier changes in southeast Alaska and northwest British Columbia over the period 1948–2000 and 1982/1987–2000, respectively. By combining the results from these periods, they estimated an average ice mass loss rate of 16.7 ± 4.4 Gt/year. In the Canadian Rocky Mountains, Castellazzi et al. (2019) estimated a total of 43 Gt of glacial mass loss over the period 2002–2015. Over the entire Gulf Of Alaska (GOA) area, Gardner et al. (2013) found 50 ± 17 Gt/year of glacier mass loss based on several published GRACE estimates over the period 2003–2009. Berthier et al. (2010) obtained 41.63 ± 8.6 Gt/year of glacier ice loss from Digital Elevation Models (DEM) for the period 1962–2006. Larsen et al. (2015) used airborne altimetry to estimate glacier mass loss rate over the period 1994–2013 and found 75 ± 11 Gt/year.

Gravity data provides direct information over ice mass changes, as the link between gravity and mass is direct and requires no calibration. *In situ* gravity measurements are labor-intensive, costly to acquire, and point-based; while satellite gravity data are limited in resolution due to the sensing distance. Since 2002, the United States (NASA) and the German (DLR) space agencies have led the Gravity Recovery And Climate Experiment (GRACE) mission. It aims at monitoring the variations of the Earth's gravity field with a temporal resolution of a few days to a month, with a spatial resolution of ± 400 km (Tapley et al., 2004; Ramillien et al., 2017). The variations in the Earth's mass distribution cause changes in the gravity field (Wahr et al., 1998). Thus, by mapping the variations of the gravitational field, GRACE monitors the Earth's mass distribution. The mass redistribution obtained from GRACE data contains changes in Terrestrial Water Storage (TWS), and oceanic mass (Wahr et al., 1998; Chen et al., 2006). Yirdaw et al. (2009) noted that the GRACE mission estimates could be used to monitor the rate of change of TWS over large spatial scales. Ramillien et al. (2017) further indicated that continental hydrology is one of the main applications of GRACE data. The variation of TWS aggregates changes in surface water, soil moisture, ground water, snow, and ice. Jin and Zou (2015) used GRACE data to estimate a high-precision glacier mass dynamics in Greenland. In the GOA region, GRACE data have already been used to estimate glacier mass loss (Tamisiea et al., 2005; Chen et al., 2006; Arendt et al., 2008, 2009, 2013; Luthcke et al., 2008; Baur et al., 2013; Beamer et al., 2016; Wahr et al., 2016; Jin et al., 2017).

Two main types of GRACE Level-3 solutions are used in hydrological applications. There are unconstrained solutions, relying on de-stripping and Spherical Harmonics (SH) truncation, and constrained solutions often relying on regularization or stabilization. Among the later, mascon solutions, obtained after inverting the GRACE signal into a mass change for each spatial unit ("mascon") of a predefined grid, have become particularly popular over the last years (e.g., Save et al., 2016). Meanwhile, the unconstrained GRACE Spherical Harmonics (SH) solutions present errors at high spatial frequencies (e.g., $N > 60$ or 300 km) and North-South stripes mainly due to gravitational model corrections, instrument errors, and gaps in data coverage. Destriping, truncation, and filtering are usually applied on these Level-2 solutions to reduce high frequency errors and to eliminate stripes. The challenge of using GRACE data to investigate hydrological fluxes, such as mass variations at the glacier scale, lies in the low spatial resolution (300/400 km) and the inability to discriminate close masses. Leakage effects are inherent to the GRACE sensing strategy, and are accentuated by the truncation and filtering used to "clean" the monthly gridded mass changes. This makes GRACE data prone to large errors when considering areas below 200,000 km^2 (e.g., Longuevergne et al., 2010). To overcome this problem, several authors combined GRACE data with other sources of information (e.g., Castellazzi et al., 2018, 2019).

Different strategies such as scaling approach, additive approach, multiplicative approach, and unconstrained or constrained forward modeling approaches permit to partially restore the signal loss (Long et al., 2016). A constrained inversion method can also be applied to improve the spatial resolution of GRACE data (Farinotti et al., 2015; Long et al., 2016; Castellazzi et al., 2018). Chen et al. (2015) used forward modeling to restore the GRACE signal amplitude of Antarctic ice and glacier loss due to the noise reduction. Long et al. (2016) showed that a constrained forward modeling can recover the distribution details of the GRACE signal. Farinotti et al. (2015) estimated the glacier mass loss in the Tien Shan (China) by subtracting the non-glacier contributions from the total mass change. They used an inversion method with *a priori* information about the glacier spatial distribution in area subdivisions (i.e., mascon and sub-mascon). By improving GRACE spatial resolution, their results are comparable to those derived from altimetry data and glacial melt modeling (e.g., the Cold Regions Hydrological Model—Pomeroy et al., 2007—and the Distributed Enhanced Temperature Index Model—Hock, 1999). Studying groundwater depletion in Central Mexico, Castellazzi et al. (2016, 2018) improved the GRACE spatial resolution using InSAR-derived ground-displacement maps to constrain the Forward Model (FM). They subtracted groundwater contributions from other components of TWS, built a distribution map of groundwater depletion using InSAR, and focused GRACE data over it. The potential of separating masses depends on the size, separation, and amplitude of the masses, as well as on the available constraining data and their efficiency in explaining the low resolution GRACE signal.

Although several authors have injected ancillary data into GRACE post-processing to improve the resolution, there is still a need to assess how constrained modeling improves the interpretation of GRACE data versus simplistic approaches such as spatial averaging (e.g., usually over watersheds or regions). While few studies already tested how constrained FM can help interpreting GRACE data, case studies are still lacking and more importantly, the limits of the procedure are still relatively unknown. In this study, we apply this procedure to build a high

resolution ice mass loss map from GRACE data over a large range of melting glaciers in the GOA. In that perspective, we use several GRACE solutions, apply a spatial constraint to focus the signal, and provide a high spatial resolution map of ice mass loss over the study area.

STUDY AREA

Our study area is delimited by zone 11 (**Figure 1**). The area was selected to cover the glaciers of the GOA and to include a stretch of ∼300 km of the surroundings to account for spatial leakages inherent to the GRACE signal. During the last decade, different studies used GRACE data to estimate glacier mass across the same region (**Figure 1**).

There are discrepancies in mass losses estimated over the GOA. Most authors obtain values ranging from −47 to −110 Gt/year of glacial mass change (**Figure 1** and **Table 1**). These studies consider different spatial extents and data time-periods. For example, the total surface coverage considered by Tamisiea et al. (2005) is 701,000 km^2, while Beamer et al. (2016) consider 420.300 km^2. The first three studies show higher values of mass loss (Tamisiea et al., 2005; Chen et al., 2006; Luthcke et al., 2008) than those more recent (Baur et al., 2013; Beamer et al., 2016; Wahr et al., 2016; Jin et al., 2017). It is potentially due to the relatively short GRACE time-series available at that time and the higher uncertainties in the earlier releases of GRACE data. In addition, variations in the GRACE data processing strategy, including levels of filtering and Spherical Harmonic (SH) truncation, might also contribute to discrepancies between studies. For example, some studies used unconstrained solutions (Tamisiea et al., 2005; Chen et al., 2006; Baur et al., 2013; Jin et al., 2017). Other authors used mascon solutions at different spatial and temporal resolutions (Arendt et al., 2008, 2009, 2013; Luthcke et al., 2008, 2013; Jacob et al., 2012; Beamer et al., 2016; Wahr et al., 2016). Tamisiea et al. (2005) used unconstrained solutions completed up to SH degree and order 70. Other authors used SH degree and order up to 60 (Chen et al., 2006; Baur et al., 2013; Jin et al., 2017). Jin et al. (2017) applied a Gaussian filter with a radius of 300 km while the aforementioned studies used a radius of 500 km. Using a scaling factor approach, Tamisiea et al. (2005) reduced the GRACE signal attenuation and leakage. A forward modeling approach was also used by several authors to restore signal leakages from coastal glaciers to the ocean (Baur et al., 2013; Jin et al., 2017).

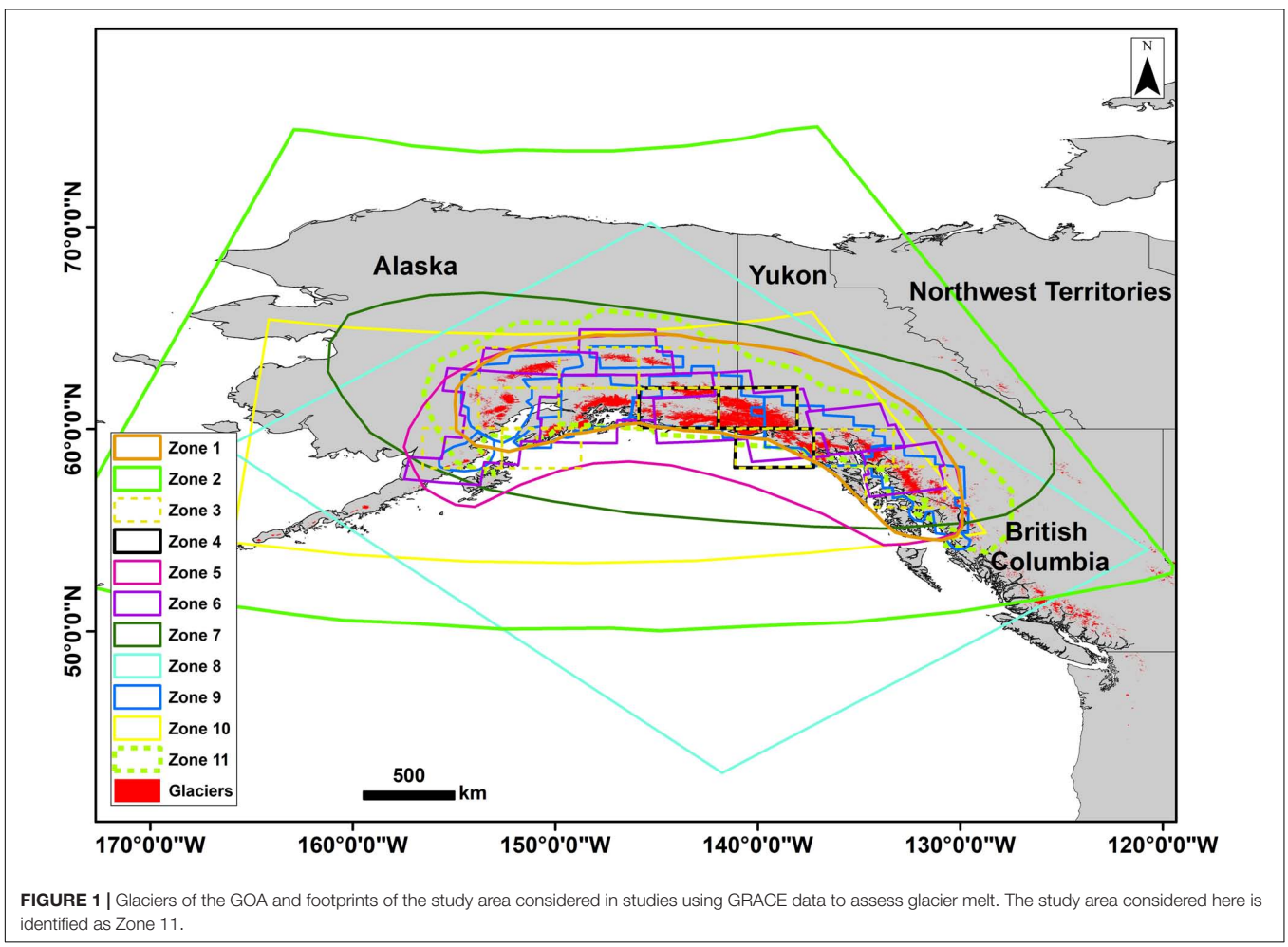


FIGURE 1 | Glaciers of the GOA and footprints of the study area considered in studies using GRACE data to assess glacier melt. The study area considered here is identified as Zone 11.

TABLE 1 | Estimates of glacier mass loss in the GOA according to different authors.

Study areas (Figure 1)	Authors (year)	Data time period	Estimated mass loss (Gt/year)	Data source	Glaciers area considered (km^2)
1	Tamisiea et al., 2005	2002–2004	110	GRACE	87,000
2	Chen et al., 2006	2002–2005	101	GRACE	~90,957
3	Luthcke et al., 2008	2003–2006	102	GRACE	~82,505
		2003–2007	84		
4	Arendt et al., 2008	2003–2007	20.6	GRACE	32,900
5	Jacob et al., 2012	2003–2010	46	GRACE	~90,000
6	Arendt et al., 2013	2003–2009	61	GRACE	82,505
		2003–2010	65		
		2004–2010	71		
7	Baur et al., 2013	(2002–2011)a	56	GRACE with geocenter correction	~80,000
		(2002–2011)b	47	GRACE without geocenter correction	
8	Beamer et al., 2016	2004–2013	60.1	GRACE	72,302
9	Wahr et al., 2016	2002–2014	52	GRACE and meteorological model	~72,600
10	Jin et al., 2017	2003–2009	57.5	ICESat altimetry and GRACE	86,715

Some authors also used auxiliary data to complement GRACE observations. Remote sensing of ice surface elevation (e.g., ICESat NASA, airborne laser altimetry) was combined with GRACE data (Arendt et al., 2008, 2013; Jin et al., 2017). Meteorological models also contributed to GRACE science (Arendt et al., 2009; Wahr et al., 2016). Some authors combined remote sensing and meteorological data to enrich and validate glacier mass loss estimates (Arendt et al., 2013; Luthcke et al., 2013). Beamer et al. (2016) developed hydrological models and compared their results with the airborne altimetry and GRACE data.

DATA AND METHODS

Glacier Data and Mascon Delineation

Glaciers are delimited using the GLIMS Glacier Database released on 27/10/2017 and available online[1] (GLIMS and NSIDC, 2005, updated in 2013). It is a continuation of the World Glacier Inventory (Raup et al., 2007) which compiles different sources: satellite imagery data, historical information from maps, and aerial photography. Recently, the GLIMS glacier Database was merged with the Randolph Glacier Inventory (RGI). According to Pfeffer et al. (2014), this combination was performed to support the fifth report of the Intergovernmental Panel on Climate Change. While the GLIMS database may contain errors, it is, at least for our study area, in good agreement with the glacier inventory of Alaska and northwest Canada proposed by Kienholz et al. (2015). According to GLIMS, the total glacier cover in the GOA area was around 90,000 km^2 in 2013 (**Figure 2**).

To ease data handling and make this dataset compatible with other GRACE grids used in this study, the glacier distribution was resampled to a 0.25° grid (~28 km by ~14 km pixels; **Figure 2**). The resampling is performed using the following steps: (1) creation of a global 0.25° raster; (2) overlay of the glacier footprint (taken as polygons) from the GLIMS data on the raster; and (3) creation of the distribution map. In the latter step, we consider that a pixel from step (1) contains glacial masses if its center is within a glacier polygon from GLIMS.

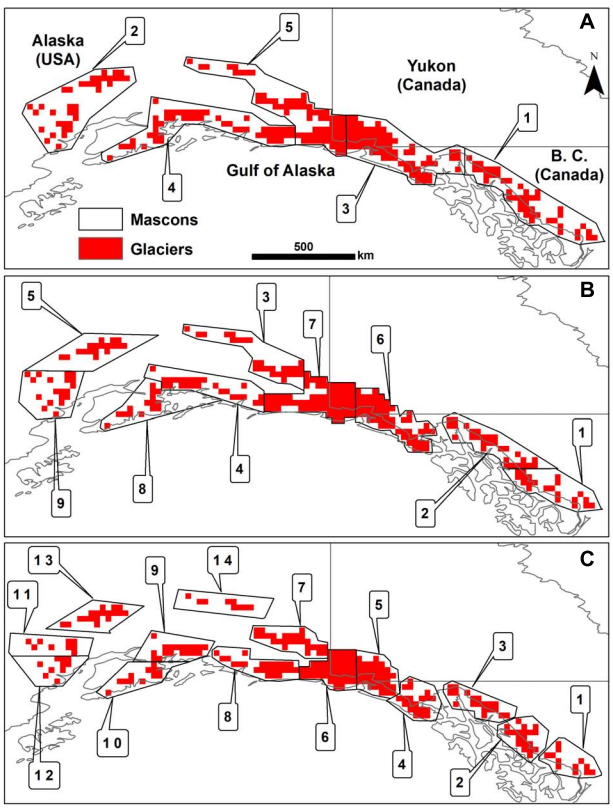


FIGURE 2 | Glacier distribution map used to focus GRACE trend maps. Three arbitrary mascon delineations are presented: **(A)** 5 mascons with an average area of ~55,000 km^2, **(B)** 9 mascons with an average area of ~30,000 km^2, and **(C)** 14 mascons with an average area of ~20,000 km^2.

Separating the contribution from a set of small masses to a low resolution signal (such as GRACE) can be challenging

[1]http://nsidc.org/glims/

and the success relies principally on the initial resolution, the final resolution, the size of the masses, the distance separating them, and the amplitude of the changes for each mass. Their spatial separation is important, close masses being harder to discriminate than those spatially distant. To test the separation of the signal into a set of contributing masses, we considered three different spatial distributions of mass at different resolutions (**Table 2**). Each area delimiting a mass is referred to as a mascon (mass concentration area).

The GOA glacial mass losses are spatially heterogeneous due to the difference in size of glaciers, local hypsometry, and climate (i.e., temperature and precipitation; Frans et al., 2018; Huss and Hock, 2018). For simplification, we assumed a uniform distribution of ice mass loss within each mascon and test this assumption through a synthetic test (section "Simulation With Synthetic Data"). This assumption has been used in other areas prone to ice mass loss by Chen et al. (2009) and in Farinotti et al. (2015).

GRACE TWS Data

Three versions of Level-3 GRACE data in Water Thickness Equivalent (WTE) are considered. The first solution is the stabilized solution from the Space Geodesy Research Group (GRGS RL04[2]) available up to SH degree and order 90. The second is an unconstrained solution from the Center for Space Research (CSR RL06) complete up to SH degree and order 96 and de-striped/filtered in a single step by applying the DDK8 filter (Kusche, 2007; Kusche et al., 2009). The third is the CSR RL05 regularized Mascon solution from Save et al. (2016). All solutions are truncated up to SH degree and order 90 to better perceive the differences in the data processing strategies without being influenced by the differences in resolution. The solutions are referred to as GRGS, T96DDK8, and CSR-MASC hereafter. These solutions follow different processing protocols and assumptions; hence, we consider that their discrepancy represents an estimation of the impact of the choice of the processing strategy. They comprise 150, 156, and 159 near-monthly measurements, respectively, extending from 2002 to 2017. For consistency, the land mask applied to produce the CSR-MASC solution (Save et al., 2016) is applied to all trend maps. All processing is performed over the same 0.25° grid.

2D trend maps are derived from the three near-monthly solutions. The trend is computed by subtracting an iteratively fitted sine curve of 1-year period. A 13-month moving average is then applied to smooth out the residual. These steps contribute to remove the seasonal variations and prevent contamination of trend estimates by seasonal signals. Finally, for each pixel, the slope of a fitted linear curve is interpreted as the mass change rate.

Glacial Isostatic Adjustment (GIA) influences over the TWS trend need to be removed. CSR-MASC, as available online, is already corrected for GIA effects using estimates from Geruo et al. (2013). We used the same model (ICE-5G) to correct the two other solutions (GRGS and T96DDK8). Apart from glacier, Chen et al. (2006) also considered other water storage components such as snow and soil moisture. In our case, we assume that the influence of the seasonal snow component over the total mass loss trend is removed by fitting and subtracting a stationary curve to the GRACE TWS data. We also consider that, by using more than 15 years of TWS data, the inter-annual variability of the snow cover does not affect our trend estimates significantly.

Inversion Procedure

An inversion procedure is applied to focus the low resolution mass trend map produced using the GRACE data. First, it uniformly allocates a synthetic mass to all glacier pixels within each mascon; resulting in a synthetic high resolution ice mass loss map. Second, a FM is built by truncating this map similarly to GRACE data, through the spherical harmonic domain. The FM is assessed by analyzing the difference with the actual GRACE TWS trend map. The mass allocation is iteratively modified until the FM converges to the closest possible value of the actual GRACE TWS signal. An Absolute Error (AE) approach applied over the spatial domain (the trend map in WTE) is used to quantify the degree of similarity between the FM and the actual GRACE trend map.

A Pattern search solver is used to iteratively change the mass allocated within each mascon until finding the optimal set of masses which, after truncation, is the closest to the actual GRACE-derived trend map. The Pattern search algorithm is a non-gradient-based optimization algorithm. It makes adjustments to each parameter value independently in order to iteratively converge toward a stable solution (Hooke and Jeeves, 1961; Kolda et al., 2003; Hingray et al., 2014). In order to prevent the solver to stop over local minimums, two sets of initial values are tested for each calculation. Both sets of initial values are uniform, the first is largely under the expected mass distribution, and the second largely above. This allows testing two extreme starting points and verifying that the results are not affected by the arbitrary assumption of the initial values.

We tested the three GRACE solutions with each mass distribution map. In GRACE processing, it is often assumed that the highest source of uncertainty arising in TWS estimation is related to the arbitrary choice of the processing strategy. Indeed, there are numerous methods to process GRACE data ("solutions"), and there is no obvious way to decide which one to use for any given application (see, e.g., Castellazzi et al., 2018). The shape of the GRACE trend anomaly is influenced by the highest spatial frequencies of the GRACE signal, which are the most sensitive to the processing strategy and parameterization. Hence, we assume that if different solutions are similar after focusing, the results are not affected by the processing strategy

[2]http://grgs.obs-mip.fr/grace

TABLE 2 | Description of the three mascon delineations.

Mascon number	Total surface (km^2)	Average (km^2)	Standard deviation (km^2)
5	272,400	54,480	1,214
9	282,970	31,441	1,657
14	278,760	19,911	690

and, consequently, are close to the true TWS signal. Conversely, when the focusing procedure is applied and the results are different for each GRACE solution, we consider that the trend maps are influenced by processing residues affecting the high resolution results.

Simulation With Synthetic Data

Synthetic tests are performed to assess the performance of the focusing procedure used to retrieve local or regional masses from low resolution GRACE data. In addition, as the GRACE signal is considered dominated by the ice mass change over the GOA, synthetic simulations are also used to verify if this assumption is true when considering masses at local or regional scales.

A synthetic map is created by allocating synthetic random values, close to the ice mass change rates expected across the GOA, to the distribution map (**Figure 2**). The mass change values are spread uniformly on glacier pixels within each mascon to reproduce a realistic high resolution glacier mass loss map. To account for spatially distributed signals, a diffuse mass trend map is derived by computing trends from monthly soil-moisture estimates (Noah model, GLDAS v2.1; Rodell et al., 2004) over the same time-period than the GRACE observations. The final map is a realistic model of cumulated signals from ice and distributed mass changes in realistic proportions. This map is truncated similarly to the three GRACE solutions, building a FM for GRACE trend map from known mass change rates.

First, the focusing procedure is applied using solely the mass distribution map presented in **Figure 2**. Finally, the high resolution mass loss values recovered through the procedure are compared with the values originally injected within each mascon. Second, the inversion procedure is performed after adding a background mascon covering the whole study area, with all pixel accounted for, except those corresponding to glaciers. The first test assesses the validity of the focusing procedure and the influence of diffuse masses over the local-scale mass retrieval. The second test verifies whether the local signal from glaciers is better recovered while accounting for surrounding low-frequency signals or not.

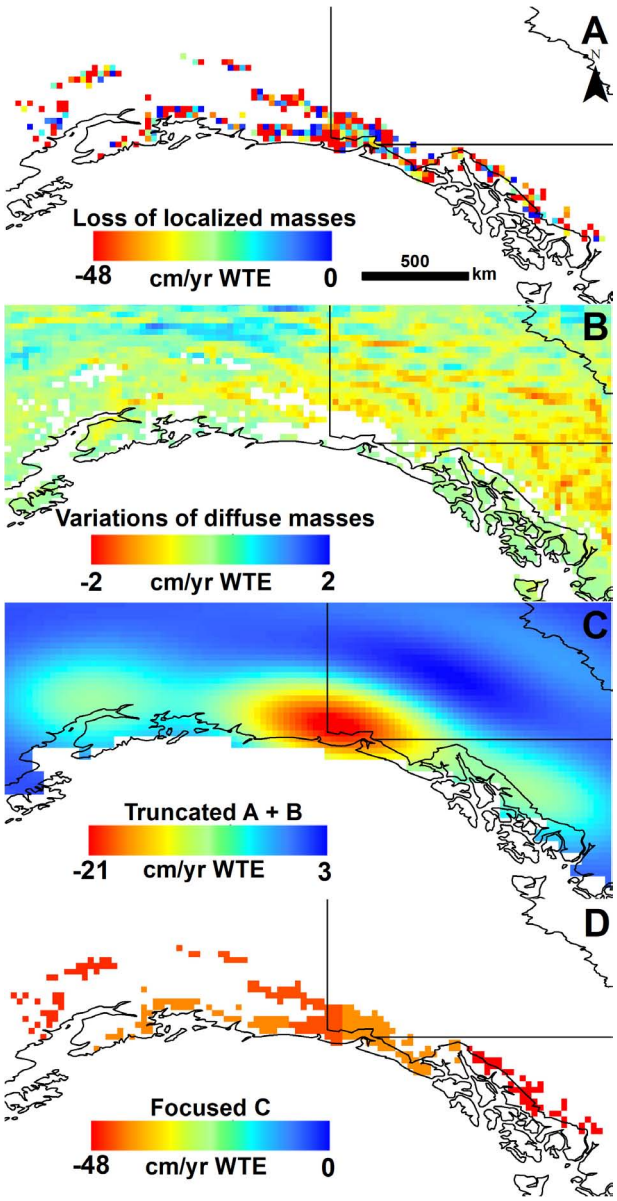


FIGURE 3 | (A) Synthetic mass randomly allocated to pixels corresponding to glaciers. **(B)** Soil moisture trend from GLDAS Noah Land Surface Model (LSM) v2.1. **(C)** Forward model (FM) of **A** overlaid on **B**, representing a realistic reproduction of the GRACE trend signal derived from known masses. It includes both concentrated and diffuse mass changes in realistic proportions. **(D)** Example of a high resolution glacier mass loss map retrieved by applying the inversion procedure over **C** and using the 5-mascon delineation shown in **Figure 2A**. This synthetic test allows to assess the inversion procedure and its ability to retrieve glacier mass losses at high resolution. Results are presented in **Supplementary Table S1**.

RESULTS AND DISCUSSION

Simulation With Synthetic Data

A synthetic map is created by allocating synthetic masses to the glacier distribution map (**Figure 3A**) over which a diffuse mass signal is added (**Figure 3B**). This map, after truncation, is a low resolution GRACE-like mass trend map (**Figure 3C**) built from a known high resolution map. The masses injected onto the distribution map are realistic; they are of a similar order of magnitude to the masses expected across the GOA (considering both individual mascon and the entire area. **Supplementary Table S1** shows the synthetic masses allocated to each mascon, and the mass recovered after applying the inversion procedure, considering or not the effect of a diffuse mass. The main observations from this synthetic test are compiled in **Table 3**. Such test, consisting in retrieving synthetic masses at different resolutions, allows to observe the limits of the focusing procedure and to better interpret the results obtained with real data presented in the subsequent sections.

We observe that the total mass is well recovered regardless of the number of mascons and of the consideration of a diffuse mass during the inversion (**Table 3**). The Mean Absolute Relative

Error (MARE) of the mass recovery at the mascon resolution ranges from ∼5 to ∼15%, and increases with the resolution of the mascon map. The maximum error goes up to ∼68% while recovering masses over small mascons (14-mascon delineation). We conclude that an acceptable accuracy is obtained while using mascon size up to ∼30,000 km^2.

The differences observed in the total mass recovery, considering or not a diffuse mass, are less than 3% for the three mascon delineations. The maximum additional error related to the inclusion of a diffuse mass is ∼2% for the 5 and 9-mascon delineations and reaches ∼12% for the 14-mascon delineation. This suggests that the inclusion of a supplementary mascon expected to account for diffuse masses (low-frequency signals) did not help to recover the glacial masses. This result, along with observations from the literature (e.g., Jin et al., 2017), and the apparently strong TWS trend (**Figure 3**), supports the common assumption that GRACE TWS signal is largely dominated by glacier ice mass changes in the GOA. It also suggests that the

TABLE 3 | Errors in recovering known synthetic masses allocated over the distribution map (**Figure 3**).

	Total mass recovery error (without diffuse mass)—%	Total mass recovery error (with diffuse mass)—%	Mean error per mascon (without diffuse mass)—%	Mean error per mascon (with diffuse mass)—%	Maximum error per mascon (without diffuse mass)—%	Maximum error per mascon (with diffuse mass)—%
5 Mascons 55,000 km^2-scale	2.514	5.071	2.435	5.141	8.406	9.937
9 Mascons 30,000 km^2-scale	2.683	5.207	9.544	10.347	15.508	17.472
14 Mascons 20,000 km^2-scale	3.244	4.761	13.568	14.600	55.994	68.195

Each test is performed with and without taking into account a diffuse mass, e.g., soil moisture storage changes.

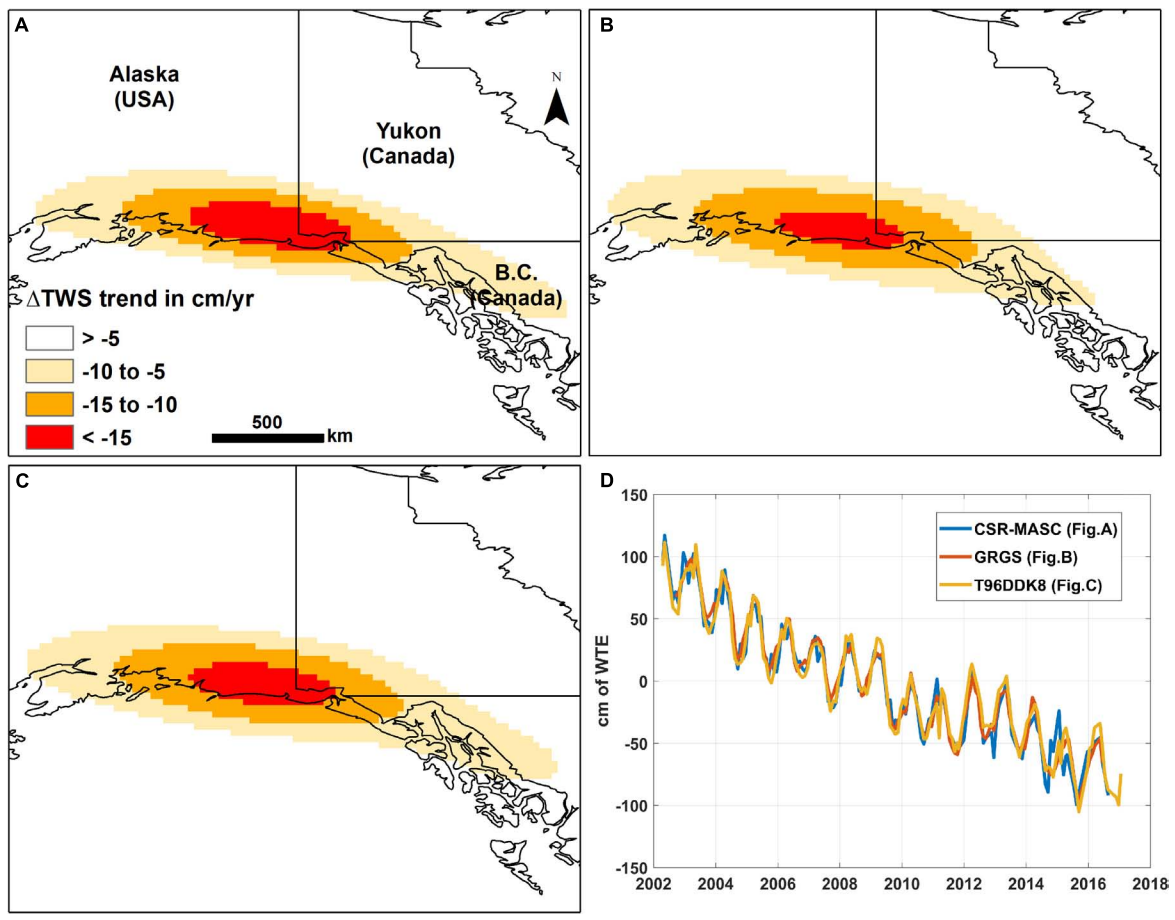


FIGURE 4 | TWS signal trend over the study area using the three GRACE solutions: **(A)** CSR-MASC, **(B)** GRGS, **(C)** T96DDK8, and **(D)** near-monthly time-series of TWS change in WTE for the period 2012–2017 observed at the center of the anomaly.

inversion performed with the actual GRACE TWS data does not need to consider a diffuse mass.

GOA-Scale Ice Mass Loss

GRACE TWS signal over the GOA shows a negative anomaly in all three solutions (**Figure 4**). They are all showing a very similar mass depletion across the GOA, in both amplitude and spatial extent (**Figures 4A–C**). The GRGS solution shows a slightly different spatial pattern at the eastern tip of the anomaly. Given that all solutions were corrected for GIA using the same model (Geruo et al., 2013) and that all solutions were at the same resolution (SH coefficients up to degree/order 90), the most likely reason for the perceptible differences is related to the de-striping strategy, which is different for all the three solutions considered.

The total mass loss rates were recovered by distributing mass loss values in each mascon until the FM reaches a minimum residual when subtracted from the GRACE TWS of each solution. Results are generally consistent regardless of the distribution considered (**Table 4**).

The test with synthetic data shows that the error in recovering the total mass is ∼5% regardless of the mascon resolution. On the one hand, using different solutions over the same distribution leads to a Coefficient Of Variation (COV) of ∼3.5% (**Table 4**). On the other hand, using different distributions with the same solution leads to a COV of ∼2.1%. The similarity between the solutions (**Figure 4D** and **Table 4**) proves a clear improvement in GRACE processing with the latest solutions from the 2016–2018 era such as CSR RL06. When considering an ample TWS anomaly like the GOA, solutions are usually leading to similar observations. However, it might not be the case when considering low amplitude signals which are closer to the noise level, and more sensitive to the processing strategy.

These results are compared with results from previous studies performed over the same area in **Table 1**. Jacob et al. (2012); Baur et al. (2013), and Wahr et al. (2016) found ice loss rates within the range 47–52 Gt/year, which is in good agreement with our results (**Figure 5**). Tamisiea et al. (2005); Chen et al. (2006), and Luthcke et al. (2008) found significantly higher ice loss rates. This can be related to the shorter TWS time-series and the larger uncertainties associated with the early releases of GRACE TWS data. Our results are close to the estimates from studies using

TABLE 4 | Total mass loss estimated using to the three GRACE TWS solutions and the three mascon delineations in Gt/year (**Figure 2**).

Number of mascons/scale	CSR-MASC	GRGS	T96DDK8	Mean (Stdev)	Coefficient Of Variation (COV) (%)
5/55,000 km^2	41.86	39.31	41.28	40.82 (1.34)	3.28
9/30,000 km^2	40.18	37.56	39.65	39.13 (1.39)	3.55
14/20,000 km^2	41.41	38.59	40.78	40.26 (1.48)	3.68
Mean (Stdev)	41.15 (0.87)	38.48 (0.88)	40.57 (0.84)		
Coefficient Of Variation (COV; stdev in % of the mean)	2.11	2.29	2.07		

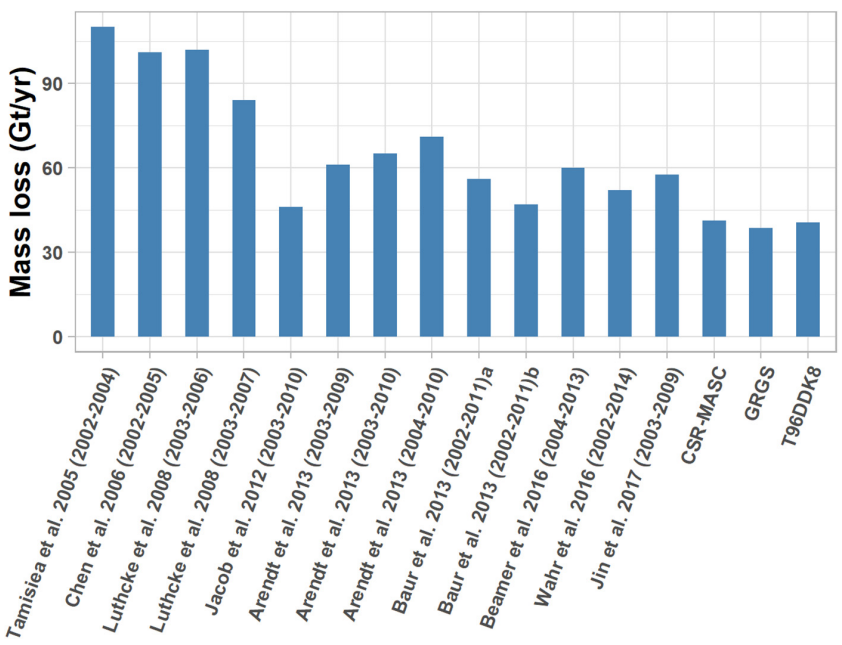


FIGURE 5 | Comparison between glacier mass loss estimates from this study with those of other studies listed in **Table 1**.

TABLE 5 | Mass losses measured in each mascon in Gt/year.

Mascon number (Figure 2)	1	2	3	4	5	6	7	8	9	10	11	12	13	14
5 Mascons, 55,000 km^2-scale														
CSR-MASC	6.74	3.23	9.35	14.31	8.23	–	–	–	–	–	–	–	–	–
GRGS	5.28	4.02	9.14	14.32	6.55	–	–	–	–	–	–	–	–	–
T96DDK8	6.5	4.02	9.29	14.13	7.34	–	–	–	–	–	–	–	–	–
9 Mascons, 30,000 km^2-scale														
CSR-MASC	2.68	4.84	3.22	8.88	1.06	7.03	8.74	1.27	2.47	–	–	–	–	–
GRGS	2.31	3.73	2.88	8.72	1.71	7.06	7.25	1.41	2.50	–	–	–	–	–
T96DDK8	2.85	4.43	3.39	8.39	1.65	7.21	7.58	1.50	2.64	–	–	–	–	–
14 Mascons, 20,000 km^2-scale														
CSR-MASC	2.50	1.3	4.47	0.85	6.69	2.97	2.43	8.28	4.93	1.55	0.38	1.77	1.61	1.68
GRGS	1.72	1.69	2.91	1.58	6.69	1.45	2.57	7.84	4.74	1.84	0.65	1.5	2.11	1.3
T96DDK8	2.29	1.76	3.82	1.09	7	1.7	2.62	8.09	4.60	1.87	0.75	1.55	2.05	1.59

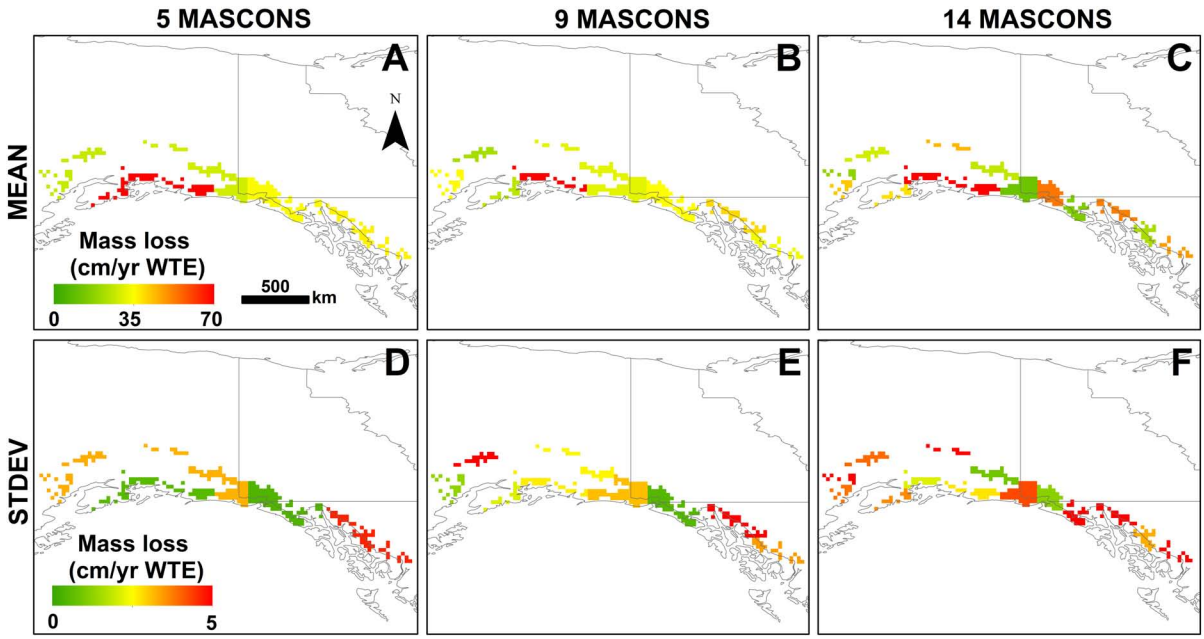


FIGURE 6 | High resolution mapping according to the three mass distribution scenarios (**Figure 2**): mean mass loss **(A–C)** and standard deviation **(D–F)**. Maps are presented in order of focusing resolution: **(A–D)** 5-, (**B–E)** 9-, and **(C–F)** 14-mascon delineations. Two different scales of the same color maps are used for **A**–**C** and **D**–**F**.

different methods (Berthier et al., 2010; Gardner et al., 2013; Larsen et al., 2015, values are listed in section "Introduction").

Differences in GRACE Level-3 data interpretation strategy can lead to discrepancies with estimates from other authors. The use of a constrained forward modeling strategy can lead to lower values, as it only recovers the signal spatially correlated to glaciers (see, e.g., Long et al., 2016, for an example related to groundwater depletion). The injection of a distribution constraint is known to reduce contributions from unwanted signals with contrasting spatial patterns. These signals cannot be focused onto the constraining distribution (Farinotti et al., 2015; Castellazzi et al., 2018). However, the distribution map is a simplification of the reality as it does not consider the intra-mascon heterogeneity of the ice loss signal. This might lead to uncertainties, depending on the level of unaccounted heterogeneity and its location on the distribution map.

Mascon-Scale Ice Mass Loss

In this section, we discuss the reliability of considering mass losses focused over mascon at different scales. For each inversion, the result corresponds to the best fit to reproduce the true GRACE TWS over the GOA. Total per-mascon masses are presented in **Table 5**, and the spatial patterns of the mean and standard deviation of glacier mass changes are shown in **Figure 6**. As discussed previously, we assume that the degree of similarity between the mass losses retrieved using the three solutions represents a good indicator of accuracy. The maximum value of variation within each mascon corresponds to ∼13, ∼25, and

TABLE 6 | Coefficient Of Variation (COV) of the focused masses.

Mascon number (Figure 2)														
1	2	3	4	5	6	7	8	9	10	11	12	13	14
For the 5-mascon delineation, 55,000 km^2 scale, in %													
13	12	1	1	11	–	–	–	–	–	–	–	–	–
For the 9-mascon delineation, 30,000 km^2 scale, in %													
10	13	8	3	25	1	10	9	4	–	–	–	–	–
For the 14-mascon delineation, 20,000 km^2 scale, in %													
19	16	21	32	3	40	4	3	3	10	32	9	14	13

It corresponds to the standard deviation of the results obtained from each GRACE solution expressed as a percentage of the mean.

∼40% of the mean mass allocated, for the 5-, 9-, and 14-mascon delineations, respectively. It is observed that this variation tends to increase over the East/West extremes of the study area (**Table 6** and **Figure 6**). This corresponds to differences observed by comparing the low resolution GRACE TWS trend maps (**Figure 4**) which propagates into the inversion results. These variations due to differences in processing strategies increase with the spatial resolution (**Table 6**); hence the estimates for the 14-mascon delineation have the highest level of uncertainty.

We evaluate the accuracy of our mass loss estimates by comparison with those from other studies. This comparison is based on the area with the largest mass losses, which are the Saint Elias Mountains and Glacier Bay, according to Luthcke et al. (2013). This was confirmed by Arendt et al. (2013), who showed that the Saint Elias Mountains, Glacier Bay, and Juneau icefield regions present the largest amount of glacier mass losses. Jin et al. (2017) indicated that the Malaspina and Bering glaciers, belonging to the Saint Elias Mountains, have the largest rates of ice mass losses. Glaciers of the Saint Elias Mountains correspond to mascons 6, 7, and 10 in Luthcke et al. (2008; see **Figure 7A**) and mascon 6 in Arendt et al. (2013; see **Figure 7B**). Our estimates agree with the aforementioned studies which indicate that glaciers of the Saint Elias Mountains have the largest mass loss rates in the region (see **Supplementary Tables S2**, **S3**).

Arendt et al. (2008) used the same delineation and GRACE TWS solution as Luthcke et al. (2008; see **Figure 7A**). By down-sampling the solution to the Saint Elias Mountains (cumulating rates from mascons 6, 7, and 10; **Figure 7A** in Luthcke et al., 2008), using the ratio of ice area in each mascon over the period 2003–2007, they obtained 20.6 ± 3.0 Gt/year of ice loss. Luthcke et al. (2008) calculated 36 ± 2.0 and 30 ± 2.0 Gt/year of ice mass loss by using GRACE data for 2003–2006 and 2003–2007, respectively. First, we compare the results from these two studies with our estimates over the period 2002–2017 (**Table 7**), and we create a temporal subset from our estimates to make our comparison insensitive to discordances in the time-period considered.

Comparing our results with two other studies (Arendt et al., 2008; Luthcke et al., 2008) after applying similar spatial

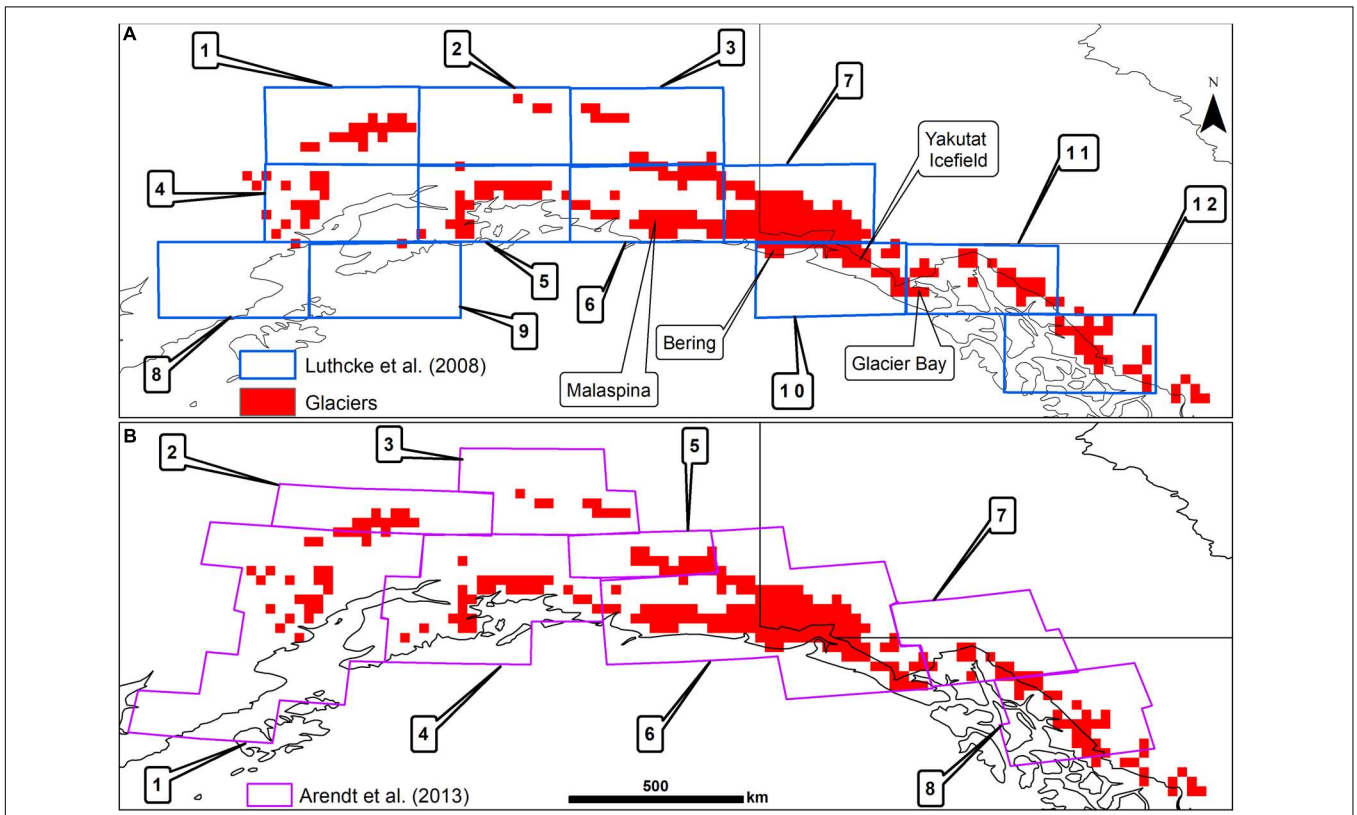


FIGURE 7 | Overlay of mascon delineations from other studies over the glacier distribution map used in this study: **(A)** delineation used by Luthcke et al. (2008) and **(B)** delineation used by Arendt et al. (2013), in which Glacier Bay is included in mascon 6, corresponding to the Saint Elias Mountains (**Supplementary Table S2**).

TABLE 7 | Mean mass losses in Gt/year considering three different time-periods over a spatial subset corresponding to mascons 6, 7, and 10 in Luthcke et al. (2008; see **Figure 7A**), which correspond to the Saint Elias Mountains.

Number of mascons	5	9	14
2002–2017	19.6 ± 0.8	18.8 ± 1.0	19.5 ± 1.4
2003–2007	23.7 ± 1.0	22.8 ± 1.2	23.7 ± 1.7
2003–2006	25.3 ± 1.0	24.2 ± 1.3	25.2 ± 1.8

constraints, we observe that the results from Arendt et al. (2008) are similar to our estimates regardless of the mascon delineation considered. Results from Luthcke et al. (2008) are generally larger than our estimates, as do most other studies using GRACE data from the 2003–2006 time-period. However, we note similarities for mascon numbers 5, 6, and 7, at the center of the GOA, where the mass change is the strongest (**Supplementary Table S3**). This observation coincides with our visual observation of the spatial patterns of mass losses (**Table 6**). It points out that the weaker signal at the extreme East-West side is sensitive to the processing strategy and its corresponding residual noise pattern.

Considering the ice loss rates over the same time-period allows us to understand the source of the differences observed between our results and these two studies. To do so, we calculated the ratios between the trend at the center of the Saint Elias Mountains derived from the full length of the GRACE time-series and the trend computed after selecting a temporal subset corresponding to the time scale of their study (**Supplementary Figure S2**). All the trends have been determined by using the method described in **Supplementary Figure S1**. We then reported the ratios obtained over the trend rates from our focused trend maps. The results from our study over these short periods (i.e., 2003–2006 and 2003–2007) are ∼20% larger than those over the period 2002–2017 (**Table 7**). We conclude that the use of a shorter time-series plays a significant role in the differences observed with results from other studies, and that these differences may not only be due to the choice of GRACE processing strategy. In other words, estimations built from a short GRACE times-series (3–4 years from 2003) have overestimated the long-term glacial mass loss by ∼20%. The inter-annual variability of the snow cover might strongly influence the TWS while considering short time-series.

We also compared our results over the Saint Elias Mountain with the mascon solution from NASA GSFC (v2.4; Luthcke et al., 2013; see **Supplementary Figure S3**), which considers GRACE data from 2003 to 2016. The mass loss rate obtained by using this dataset over the Saint Elias Mountains is 24.85 ± 2.1 Gt/year. Over the same area, we estimate the glacial mass loss at 22.01 ± 0.89, 21.57 ± 1.18, and 21.41 ± 1.64 Gt/year for our three

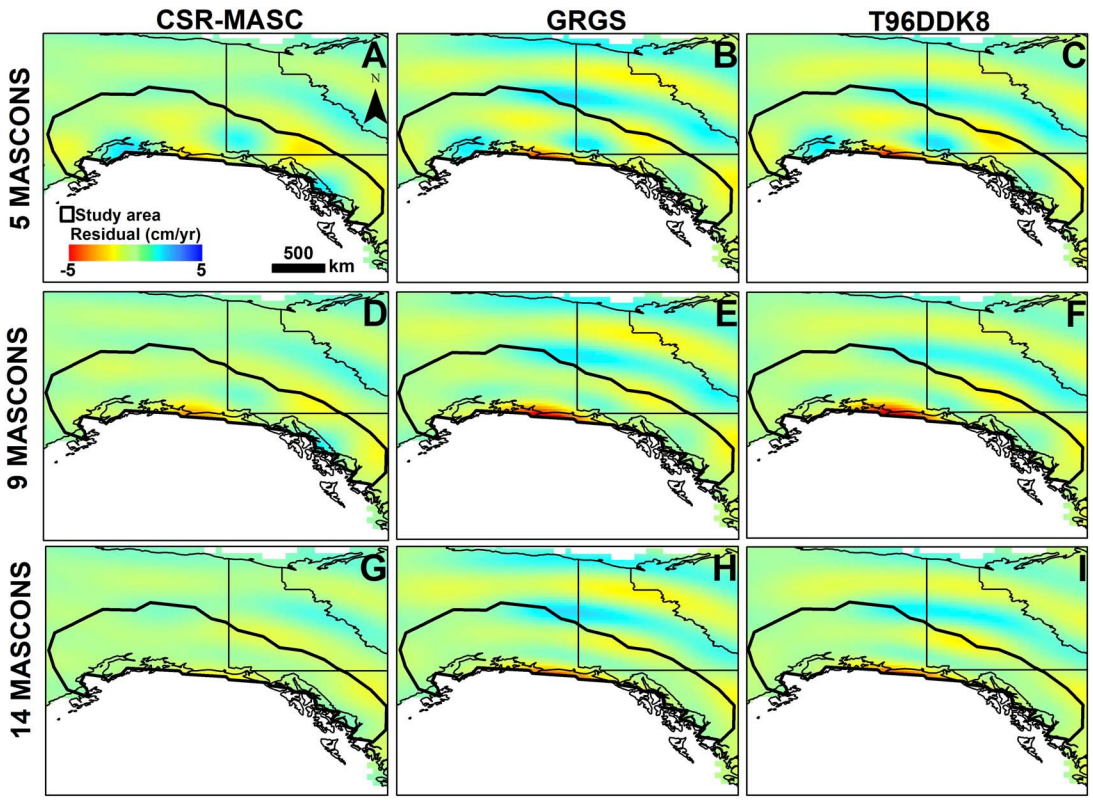


FIGURE 8 | Residual maps of the focusing procedure in WTE. These maps represent the signal remaining after subtracting the best forward model (FM) to the actual GRACE TWS signal. The labels showed in **(A)** correspond to all of the residuals **(A–I)**. According to these labels, the negative values of Mass loss, in cm/year, indicate that the estimates from GRACE solutions are higher than those from the forward model. The positive values show that the Mass loss from the forward model is higher.

mascon resolutions. Our results are very close to those from the NASA GSFC mascon data (v02.4), and the slight difference might be attributed to the difference in time-series length (2003–2016 versus 2002–2017).

Inversion Residuals

Residual maps are produced by subtracting the FM of the high resolution mass distribution maps from the actual GRACE TWS signal. The amplitude of the residual decreases with the mascon extent. This confirms the ability to retrieve the total mass when a large number of mascons are used. However, as previously discussed, it is at the cost of a lower accuracy at the mascon scale.

We note that the inversion residuals from the GRGS and T96DDK8 solutions have similar spatial patterns. It is negligible inland (values below $\pm$ 2 cm/year) and more important near the ocean (close to -5 cm/year). The high absolute residual value near the ocean could be due to coastal glaciers covered by the land mask, implying that a part of the signal from these glaciers is not recovered through the focusing procedure.

Following Wahr et al. (2006) and Ramillien et al. (2017), the GRACE TWS data contain noise patterns from measurements and processing errors. We compare the amplitude of the noise with the residuals of the inversion procedure to verify the performance of the inversion (**Figure 8**). We consider that the noise level can be approximated by observing the maximum amplitude of mass trends in the Pacific Ocean at similar latitudes than our study area. We found values of ∼1.4, 1.6, and 1.5 cm/year for the CSR-MASC, GRGS, and T96DDK8 solutions, respectively. These values are close to the residuals (values between [−2: +2] cm/year), which suggests that the remaining signal left after mass concentration might not be attributed to the glacial mass loss.

CONCLUSION

This study shows a downscaling approach of GRACE TWS data which can be used to retrieve a high resolution ice mass loss. We tested three GRACE solutions and three uniform focusing delineations, and applied an inversion method which relies on fitting iteratively a spatially constrained FM. We used the three solutions at the same truncation level (resolution) in order to isolate the effect of the processing strategy applied to the GRACE data from Level 1 to 3. From our study, we can draw three key findings.

First, synthetic simulations indicate that the forward modeling approach is efficient, with a mean error of ∼2.5% when considering the total mass loss over the GOA, and below 10% when considering masses at the mascon-scale and with mascons up to 30,000 km^2. It also shows that our inversion procedure is relatively insensitive to non-ice masses such as soil moisture.

Second, at the scale of the GOA, the resolution of the mass concentration units (referred to as mascon) and the choice of the GRACE solution strategy only account for an uncertainty of ∼2–4% in the total mass estimation. The three solutions provide approximatively the same total mass loss (∼40 Gt/year) over the era 2002–2017.

Third, at the scale of a mascon of 30,000 km^2 or larger, the focusing procedure recovers well the regional mass loss signal. At this scale, the mascon contain from 1 to 9 Gt/year of ice mass loss, the highest mass loss rates being at the center of the area, over the Saint Elias Mountains. Variations between solutions reach 40% of the mean signal when considering high resolution mascons of 20,000 km^2. Residuals are of the same order of magnitude as the noise level of GRACE TWS solutions. Thus, the glacier signals are well retrieved when using an inversion with a uniform constrained FM, and the distribution map is efficient at concentrating the mass loss observed by GRACE.

We compared our results with estimates reported in the literature and found a good agreement with studies using GRACE solutions from recent releases and time-series of more than 8 years. The first studies using GRACE data published during the 2005–2008 era generally overestimated the long-term ice mass loss at the GOA scale due to the data time-span, the interpretation strategy, and possibly the use of early release of GRACE data. Comparing our ice loss map at the highest resolution with those of Arendt et al. (2008) and the mascon solution from NASA GSFC over the Saint Elias Mountains, we obtained relatively similar ice loss rates. This area of comparison is at the center of the GOA, where our results are the most reliable, with mass losses and signal–noise ratio at the highest.

To our knowledge, this is the first study presenting a focused and spatially constrained ice loss map over the GOA. Comparison of our findings with results from other data sources (i.e., altimetry) could help further assessing the accuracy of our estimates. Constraining the focusing procedure using a heterogeneous mass loss map from other data sources would allow to cope with the heterogeneity of the losses, which is partially unaccounted for in this study. The findings of this study could help integrating an ice mass loss module into large-scale hydrological models; providing a framework to better understand the effect of climate change on the hydrological cycle of the main river basins of the GOA area.

DATA AVAILABILITY STATEMENT

We provided in the article/**Supplementary Material** the links and the references to access all datasets used for this study.

AUTHOR CONTRIBUTIONS

CD performed the data analysis and wrote the manuscript. PC trained the first author to process GRACE data, verified the results, and contributed to the writing of the manuscript. AR designed and led the project, supervised CD, and contributed to the writing of the manuscript. MA helped to build a comprehensive literature review on the topic.

FUNDING

The authors wish to gratefully acknowledge the financial support of the Natural Sciences and Engineering

Research Council of Canada (NSERC) and the Yukon Energy Corporation (YEC) for this research.

ACKNOWLEDGMENTS

The authors would like to thank Wei Feng (Chinese Academy of Sciences) for the development of GRAMAT (GRACE Matlab Toolbox) (MATLAB and Statistics Toolbox Release 2017a, The MathWorks, Inc., Natick, MA, United States) which was used to process GRACE data.

SUPPLEMENTARY MATERIAL

The Supplementary Material for this article can be found online at: https://www.frontiersin.org/articles/10.3389/feart.2019.00360/full#supplementary-material

REFERENCES

Arendt, A., Luthcke, S., Gardner, A., O'Neel, S., Hill, D., Moholdt, G., et al. (2013). Analysis of a GRACE global mascon solution for Gulf of Alaska glaciers. *J. Glacio.* 59, 913–924. doi: 10.3189/2013JoG12J197

Arendt, A. A., Luthcke, S. B., and Hock, R. (2009). Glacier changes in Alaska: can mass-balance models explain GRACE mascon trends? *Ann. Glaciol.* 50, 148–154. doi: 10.3189/172756409787769753

Arendt, A. A., Luthcke, S. B., Larsen, C. F., Abdalati, W., Krabill, W. B., and Beedle, M. J. (2008). Validation of high-resolution GRACE mascon estimates of glacier mass changes in the St Elias Mountains, Alaska, USA, using aircraft laser altimetry. *J. Glaciol.* 54, 778–787. doi: 10.3189/002214308787780067

Baur, O., Kuhn, M., and Featherstone, W. E. (2013). Continental mass change from GRACE over 2002–2011 and its impact on sea level. *J. Geodesy* 87, 117–125. doi: 10.1007/s00190-012-0583-2

Beamer, J. P., Hill, D. F., Arendt, A., and Liston, G. E. (2016). High-resolution modeling of coastal freshwater discharge and glacier mass balance in the Gulf of Alaska watershed: coastal fwd and gvl in goa watershed. *Water Resour. Res.* 52, 3888–3909. doi: 10.1002/2015WR018457

Berthier, E., Schiefer, E., Clarke, G. K. C., Menounos, B., and Rémy, F. (2010). Contribution of Alaskan glaciers to sea-level rise derived from satellite imagery. *Nat. Geosci.* 3, 92–95. doi: 10.1038/ngeo737

Blanchon, D., and Boissière, A. (2009). *Atlas Mondial de l'eau: De l'eau Pour Tous*. Paris: Autrement.

Castellazzi, P., Burgess, D., Rivera, A., Huang, J., Longuevergne, L., and Demuth, M. N. (2019). Glacial melt and potential impacts on water resources in the Canadian Rocky Mountains. *Water Resour. Res.* 55. doi: 10.1029/2018WR024295

Castellazzi, P., Longuevergne, L., Martel, R., Rivera, A., Brouard, C., and Chaussard, E. (2018). Quantitative mapping of groundwater depletion at the water management scale using a combined GRACE/InSAR approach. *Remote Sens. Environ.* 205, 408–418. doi: 10.1016/j.rse.2017.11.025

Castellazzi, P., Martel, R., Rivera, A., Huang, J., Pavlic, G., Calderhead, A. I., et al. (2016). Groundwater depletion in Central Mexico: use of GRACE and InSAR to support water resources management. *Water Resour. Res.* 52, 5985–6003. doi: 10.1002/2015WR018211

Chen, J., and Ohmura, A. (1990). "Estimation of Alpine glacier water resources and their change since the 1870s," in *Proceedings of the IAHS (Symopsium at Lausanne, 1990 – Hydrology in Mountainous Regions I)*, (Wallingford: IAHS), 127–135.

Chen, J. L., Tapley, B. D., and Wilson, C. R. (2006). Alaskan mountain glacial melting observed by satellite gravimetry. *Earth Planet. Sci. Lett.* 248, 368–378. doi: 10.1016/j.epsl.2006.05.039

Chen, J. L., Wilson, C. R., Blankenship, D., and Tapley, B. D. (2009). Accelerated Antarctic ice loss from satellite gravity measurements. *Nat. Geosci.* 2, 859–862. doi: 10.1038/ngeo694

Chen, J. L., Wilson, C. R., Li, J., and Zhang, Z. (2015). Reducing leakage error in GRACE-observed long-term ice mass change: a case study in West Antarctica. *J. Geodesy* 89, 925–940. doi: 10.1007/s00190-015-0824-2

Farinotti, D., Longuevergne, L., Moholdt, G., Duethmann, D., Mölg, T., Bolch, T., et al. (2015). Substantial glacier mass loss in the Tien Shan over the past 50 years. *Nat. Geosci.* 8, 716–722. doi: 10.1038/ngeo2513

Frans, C., Istanbulluoglu, E., Lettenmaier, D. P., Fountain, A. G., and Riedel, J. (2018). Glacier recession and the response of summer streamflow in the Pacific Northwest United States, 1960-2099. *Water Resour. Res.* 54, 6202–6225. doi: 10.1029/2017WR021764

Gardner, A. S., Moholdt, G., Cogley, J. G., Wouters, B., Arendt, A. A., Wahr, J., et al. (2013). A reconciled estimate of glacier contributions to sea level rise: 2003 to 2009. *Science* 340, 6134–6152. doi: 10.1126/science.1234532

Geruo, A., Wahr, J., and Zhong, S. (2013). Computations of the viscoelastic response of a 3-D compressible Earth to surface loading: an application to glacial isostatic adjustment in Antarctica and Canada. *Geophys. J. Int.* 192, 557–572. doi: 10.1093/gji/ggs030

GLIMS and NSIDC (2005, updated in 2013). *Global Land Ice Measurements from Space Glacier Database. Compiled and made available by the international GLIMS community and the National Snow and Ice Data Center*. Boulder, CO: National Snow and Ice Data Center.

Hingray, B., Picouet, C., and Musy, A. (2014). *Hydrologie 2 Une Science Pour l'ingénieur, 1ère édition*. Palawan: PPUR.

Hock, R. (1999). A distributed temperature index ice and snow melt model including potential direct solar radiation. *J. Glaciol.* 45, 101–111. doi: 10.3189/S0022143000003087

Hooke, R., and Jeeves, T. A. (1961). " Direct search" solution of numerical and statistical problems. *J. ACM* 8, 212–229. doi: 10.1145/321062.321069

Huss, M., and Hock, R. (2018). Global-scale hydrological response to future glacier mass loss. *Nat. Clim. Change* 8, 135–140. doi: 10.1038/s41558-017-0049-x

Jacob, T., Wahr, J., Pfeffer, W. T., and Swenson, S. (2012). Recent contributions of glaciers and ice caps to sea level rise. *Nature* 482, 514–518. doi: 10.1038/nature10847

Jin, S., and Feng, G. (2016). *Uncertainty of Grace-Estimated Land Water and Glaciers Contributions to Sea Level Change During 2003–2012* (Beijing: IEEE), 6189–6192. doi: 10.1109/IGARSS.2016.7730617

Jin, S., Zhang, T. Y., and Zou, F. (2017). Glacial density and GIA in Alaska estimated from ICESat, GPS and GRACE measurements: glacial density and GIA in Alaska. *J. Geophys. Res. Earth Surf.* 122, 76–90. doi: 10.1002/2016JF003926

Jin, S., and Zou, F. (2015). Re-estimation of glacier mass loss in Greenland from GRACE with correction of land–ocean leakage effects. *Glob. Planet. Change* 135, 170–178. doi: 10.1016/j.gloplacha.2015.11.002

Kienholz, C., Herreid, S., Rich, J. L., Arendt, A. A., Hock, R., and Burgess, E. W. (2015). Derivation and analysis of a complete modern-date glacier inventory for Alaska and northwest Canada. *J. Glaciol.* 61, 403–420. doi: 10.3189/2015JoG14J230

Kolda, T. G., Lewis, R. M., and Torczon, V. (2003). Optimization by direct search: new perspectives on some classical and modern methods. *SIAM Rev.* 45, 385–482. doi: 10.1137/S003614450242889

Kusche, J. (2007). Approximate decorrelation and non-isotropic smoothing of time-variable GRACE-type gravity field models. *J. Geodesy* 81, 733–749. doi: 10.1007/s00190-007-0143-3

Kusche, J., Schmidt, R., Petrovic, S., and Rietbroek, R. (2009). Decorrelated GRACE time-variable gravity solutions by GFZ, and their validation using a hydrological model. *J. Geodesy* 83, 903–913. doi: 10.1007/s00190-009-0308-3

Larsen, C. F., Burgess, A., Arendt, A., O'Neel, S., Johnson, A. J., and Kienholz, C. (2015). Surface melt dominates Alaskaglacier mass balance. *Geophys. Res. Lett.* 42, 5902–5908. doi: 10.1002/2015GL064349

Larsen, C. F., Motyka, R. J., Arendt, A. A., Echelmeyer, K. A., and Geissler, P. E. (2007). Glacier changes in southeast Alaska and northwest British Columbia and contribution to sea level rise. *J. Geophys. Res.* 112:F01007. doi: 10.1029/2006JF000586

Long, D., Chen, X., Scanlon, B. R., Wada, Y., Hong, Y., Singh, V. P., et al. (2016). Have GRACE satellites overestimated groundwater depletion in the Northwest India Aquifer? *Sci. Rep.* 6:24398. doi: 10.1038/srep24398

Longuevergne, L., Scanlon, B. R., and Wilson, C. R. (2010). GRACE hydrological estimates for small basins: evaluating processing approaches on the High Plains Aquifer, USA: grace hydrological estimates for small b. *Water Resour. Res.* 46:W11517. doi: 10.1029/2009WR008564

Luthcke, S. B., Arendt, A. A., Rowlands, D. D., McCarthy, J. J., and Larsen, C. F. (2008). Recent glacier mass changes in the Gulf of Alaska region from GRACE mascon solutions. *J. Glaciol.* 54, 767–777. doi: 10.3189/002214308787779933

Luthcke, S. B., Sabaka, T. J., Loomis, B. D., Arendt, A. A., McCarthy, J. J., and Camp, J. (2013). Antarctica, Greenland and Gulf of Alaska land-ice evolution from an iterated GRACE global mascon solution. *J. Glaciol.* 59, 613–631. doi: 10.3189/2013JoG12J147

Pfeffer, W. T., Arendt, A. A., Bliss, A., Bolch, T., Cogley, J. G., Gardner, A. S., et al. (2014). The Randolph Glacier Inventory: a globally complete inventory of glaciers. *J. Glaciol.* 60, 537–552. doi: 10.3189/2014JoG13J176

Pomeroy, J. W., Gray, D. M., Brown, T., Hedstrom, N. R., Quinton, W. R., Granger, R. J., et al. (2007). The cold regions hydrological model: a platform for basing process representation and model structure on physical evidence. *Hydrol. Process.* 21, 2650–2667. doi: 10.1002/hyp.6787

Radić, V., and Hock, R. (2011). Regionally differentiated contribution of mountain glaciers and ice caps to future sea-level rise. *Nat. Geosci.* 4, 91–94. doi: 10.1038/ngeo1052

Ramillien, G., Frappart, F., and Seoane, L. (2017). "La mission de gravimétrie spatiale GRACE: instruments et principe de fonctionnement," in *Observations Des Surfaces Continentales par Télédétection Micro-Onde: Techniques et Méthodes*, eds N. Baghdadi, and M. Zribi, (London: ISTE), 281–297.

Raup, B., Racoviteanu, A., Khalsa, S. J. S., Helm, C., Armstrong, R., and Arnaud, Y. (2007). The GLIMS geospatial glacier database: a new tool for studying glacier change. *Glob. Planet. Change* 56, 101–110. doi: 10.1016/j.gloplacha.2006.07.018

Rodell, M., Houser, P. R., Jambor, U., Gottschalck, J., Mitchell, K., Meng, C.-J., et al. (2004). The global land data assimilation system. *Bull. Am. Meteorol. Soc.* 85, 381–394. doi: 10.1175/BAMS-85-3-381

Save, H., Bettadpur, S., and Tapley, B. D. (2016). High-resolution CSR GRACE RL05 mascons: high-resolution CSR grace RL05 MASCONS. *J. Geophys. Res. Solid Earth* 121, 7547–7569. doi: 10.1002/2016JB013007

Tamisiea, M. E., Leuliette, E. W., Davis, J. L., and Mitrovica, J. X. (2005). Constraining hydrological and cryospheric mass flux in southeastern Alaska using space-based gravity measurements. *Geophys. Res. Lett.* 32:L20501. doi: 10.1029/2005GL023961

Tapley, B. D., Bettadpur, S., Watkins, M., and Reigber, C. (2004). The gravity recovery and climate experiment: mission overview and early results: grace mission overview and early results. *Geophys. Res. Lett.* 31:4. doi: 10.1029/2004GL019920

Wahr, J., Burgess, E., and Swenson, S. (2016). Using GRACE and climate model simulations to predict mass loss of Alaskan glaciers through 2100. *J. Glaciol.* 62, 623–639. doi: 10.1017/jog.2016.49

Wahr, J., Molenaar, M., and Bryan, F. (1998). Time variability of the Earth's gravity field: hydrological and oceanic effects and their possible detection using GRACE. *J. Geophys. Res. Solid Earth* 103, 30205–30229. doi: 10.1029/98JB02844

Wahr, J., Swenson, S., and Velicogna, I. (2006). Accuracy of GRACE mass estimates. *Geophys. Res. Lett.* 33:L06401. doi: 10.1029/2005GL025305

Yirdaw, S. Z., Snelgrove, K. R., Seglenieks, F. R., Agboma, C. O., and Soulis, E. D. (2009). Assessment of the WATCLASS hydrological model result of the Mackenzie River basin using the GRACE satellite total water storage measurement. *Hydrol. Process.* 23, 3391–3400. doi: 10.1002/hyp.7450

Conflict of Interest: The authors declare that the research was conducted in the absence of any commercial or financial relationships that could be construed as a potential conflict of interest.

Copyright © 2020 Doumbia, Castellazzi, Rousseau and Amaya. This is an open-access article distributed under the terms of the Creative Commons Attribution License (CC BY). The use, distribution or reproduction in other forums is permitted, provided the original author(s) and the copyright owner(s) are credited and that the original publication in this journal is cited, in accordance with accepted academic practice. No use, distribution or reproduction is permitted which does not comply with these terms.

frontiers in Earth Science

CORRECTION
published: 06 March 2020
doi: 10.3389/feart.2020.00057

Corrigendum: High Resolution Mapping of Ice Mass Loss in the Gulf of Alaska From Constrained Forward Modeling of GRACE Data

Cheick Doumbia[1]*, *Pascal Castellazzi*[2], *Alain N. Rousseau*[1] and *Macarena Amaya*[3]

[1] Centre Eau Terre Environnement, Institut National de la Recherche Scientifique (INRS), Université du Québec, Québec City, QC, Canada, [2] Land and Water, Deep Earth Imaging FSP, Commonwealth Scientific and Industrial Research Organisation, Urrbrae, SA, Australia, [3] Facultad de Ciencias Astronómicas y Geofísicas, Universidad Nacional de La Plata, La Plata, Argentina

Keywords: glaciers, ice melt, GRACE, forward modeling, Gulf of Alaska

A Corrigendum on

High Resolution Mapping of Ice Mass Loss in the Gulf of Alaska From Constrained Forward Modeling of GRACE Data

by Doumbia, C., Castellazzi, P., Rousseau, A. N, and Amaya, M. (2019). Front. Earth Sci. 7:360. doi: 10.3389/feart.2019.00360

OPEN ACCESS

Edited and reviewed by:
Alfonso Fernandez, University of Concepcion, Chile

***Correspondence:**
Cheick Doumbia
Cheick.Doumbia@ete.inrs.ca

Specialty section:
This article was submitted to Cryospheric Sciences, a section of the journal Frontiers in Earth Science

Received: *30 January 2020*
Accepted: *18 February 2020*
Published: *06 March 2020*

Citation:
Doumbia C, Castellazzi P, Rousseau AN and Amaya M (2020) Corrigendum: High Resolution Mapping of Ice Mass Loss in the Gulf of Alaska From Constrained Forward Modeling of GRACE Data. Front. Earth Sci. 8:57. doi: 10.3389/feart.2020.00057

In the original article there was an error in [the glacier mass loss rate from Larsen et al. (2007) and Berthier et al. (2010) and also in the method used by Gardner et al. (2013)]. The values in the article of Larsen et al. (2007) and Berthier et al. (2010) are in km^3/year water equivalent (w.e.). We converted them into Gt/year but that was not necessary because km^3/year (w.e.) is equivalent to Gt/yr. Also, Gardner et al. (2013) did not use spaceborne altimetry data (e.g., ICESat) over the entire Gulf Of Alaska (GOA) area to estimate glacier mass loss but they used several published GRACE estimates.

A correction has been made to the Introduction, paragraph 2:

"Numerous studies focused on estimating the ice mass loss over specific continents, regions, or Mountain ranges. For example, Larsen et al. (2007) investigated glacier changes in southeast Alaska and northwest British Columbia over the period 1948–2000 and 1982/1987–2000, respectively. By combining the results from these periods, they estimated an average ice mass loss rate of 16.7 ± 4.4 Gt/year. In the Canadian Rocky Mountains, Castellazzi et al. (2019) estimated a total of 43 Gt of glacial mass loss over the period 2002–2015. Over the entire Gulf Of Alaska (GOA) area, Gardner et al. (2013) found 50 ± 17 Gt/year of glacier mass loss based on several published GRACE estimates over the period 2003–2009. Berthier et al. (2010) obtained 41.63 ± 8.6 Gt/year of glacier ice loss from Digital Elevation Models (DEM) for the period 1962–2006. Larsen et al. (2015) used airborne altimetry to estimate glacier mass loss rate over the period 1994–2013 and found 75 ± 11 Gt/year."

The authors apologize for this error and state that this does not change the scientific conclusions of the article in any way. The original article has been updated.

REFERENCES

Berthier, E., Schiefer, E., Clarke, G. K. C., Menounos, B., and Rémy, F. (2010). Contribution of Alaskan glaciers to sea-level rise derived from satellite imagery. *Nat. Geosci.* 3, 92–95. doi: 10.1038/ngeo737

Castellazzi, P., Burgess, D., Rivera, A., Huang, J., Longuevergne, L., and Demuth, M. N. (2019). Glacial melt and potential impacts on water resources in the Canadian Rocky Mountains. *Water Resour. Res.* 55. doi: 10.1029/2018WR024295

Gardner, A. S., Moholdt, G., Cogley, J. G., Wouters, B., Arendt, A. A., Wahr, J., et al. (2013). A reconciled estimate of glacier contributions to sea level rise: 2003 to 2009. *Science* 340, 6134–6152. doi: 10.1126/science.1234532

Larsen, C. F., Burgess, A., Arendt, A., O'Neel, S., Johnson, A. J., and Kienholz, C. (2015). Surface melt dominates Alaskaglacier mass balance. *Geophys. Res. Lett.* 42, 5902–5908. doi: 10.1002/2015GL064349

Larsen, C. F., Motyka, R. J., Arendt, A. A., Echelmeyer, K. A., and Geissler, P. E. (2007). Glacier changes in southeast Alaska and northwest British Columbia and contribution to sea level rise. *J. Geophys. Res.* 112:F01007. doi: 10.1029/2006JF000586

Copyright © 2020 Doumbia, Castellazzi, Rousseau and Amaya. This is an open-access article distributed under the terms of the Creative Commons Attribution License (CC BY). The use, distribution or reproduction in other forums is permitted, provided the original author(s) and the copyright owner(s) are credited and that the original publication in this journal is cited, in accordance with accepted academic practice. No use, distribution or reproduction is permitted which does not comply with these terms.

frontiers in Earth Science

ORIGINAL RESEARCH
published: 25 February 2020
doi: 10.3389/feart.2020.00040

Mass Balance and Climate History of a High-Altitude Glacier, Desert Andes of Chile

Christophe Kinnard[1], Patrick Ginot[2], Arzhan Surazakov[3], Shelley MacDonell[3], Lindsey Nicholson[4], Nicolas Patris[5], Antoine Rabatel[2], Andres Rivera[6] and Francisco A. Squeo[3,7]*

[1] Département des Sciences de l'Environnement, Canada Research Chair in Cryosphere Hydrology, Université du Québec à Trois-Rivières, Trois-Rivières, QC, Canada, [2] Univ-Grenoble-Alpes, IRD, CNRS, Grenoble-INP, Institut des Géosciences de l'Environnement, Grenoble, France, [3] Centro de Estudios Avanzados en Zonas Áridas, La Serena, Chile, [4] Institute of Atmospheric and Cryospheric Sciences, Innsbruck, Austria, [5] HydroSciences Montpellier (HSM), IRD, CNRS, Université de Montpellier, Montpellier, France, [6] Departamento de Geografía, Universidad de Chile, Santiago, Chile, [7] Instituto de Ecología y Biodiversidad, Universidad de La Serena, La Serena, Chile

Glaciers in the dry Chilean Andes provide important ecological services, yet their mass balance response to past and ongoing climate change has been little studied. This study examines the recent (2002–2015), historical (1955–2005), and past (<1900) mass balance history of the high-altitude Guanaco Glacier (29.34°S, >5000 m), using a combination of glaciological, geodetic, and ice core observations. Mass balance has been predominantly negative since 2002. Analysis of mass balance and meteorological data since 2002 suggests that mass balance is currently mostly sensitive to precipitation variations, while low temperatures, aridity and high solar radiation and wind speeds cause large sublimation losses and limited melting. Mass balance reconstructed by geodetic methods shows that Guanaco Glacier has been losing mass since at least 1955, and that mass loss has increased over time until present. An ice core recovered from the deepest part of the glacier in 2008 revealed that the glacier is cold-based with a −5.5°C basal temperature and a warm reversal of the temperature profile above 60-m depth attributed to the recent atmospheric warming trend. Detailed stratigraphic and stable isotope analyses of the upper 20 m of the core revealed seasonal cycles in the $\delta^{18}O$ and $\delta^{2}H$ records with periods varying between 0.5 and 3 m. w.e. a^{-1}. Deuterium excess values larger than 10‰ suggest limited post-depositional sublimation, while the presence of numerous refrozen ice layers indicate significant summer melt. Tritium concentration in the upper 20 m of the core was very low, while ^{210}Pb was undetected, indicating that the glacier surface in 2008 was at least 100 years old. Taken together, these results suggest that Guanaco Glacier formed under drastically different climate conditions than today, with humid conditions causing high accumulation rates, reduced sublimation and increased melting. Reconstruction of mass balance based on correlations with precipitation and streamflow records show periods of sustained mass gain in the early 20th century and the 1980s, separated by periods of mass loss. The southern migration of the South Pacific Subtropical High over the course of the 20th and 21st centuries is proposed as the main mechanism explaining the progressive precipitation starvation of glaciers in this area.

Keywords: glacier mass balance, geodetic mass balance, ice core, dry Andes, climate change, stable isotopes, sublimation, drought

OPEN ACCESS

Edited by:
Bryan G. Mark, The Ohio State University, United States

Reviewed by:
Ninglian Wang, Chinese Academy of Sciences, China
Pascal Buri, University of Alaska Fairbanks, United States

****Correspondence:***
Christophe Kinnard
christophe.kinnard@uqtr.ca

Specialty section:
This article was submitted to Cryospheric Sciences, a section of the journal Frontiers in Earth Science

Received: *11 November 2019*
Accepted: *04 February 2020*
Published: *25 February 2020*

Citation:
Kinnard C, Ginot P, Surazakov A, MacDonell S, Nicholson L, Patris N, Rabatel A, Rivera A and Squeo FA (2020) Mass Balance and Climate History of a High-Altitude Glacier, Desert Andes of Chile. Front. Earth Sci. 8:40. doi: 10.3389/feart.2020.00040

INTRODUCTION

Glaciers are important freshwater sources and key regulators of the water cycle (Fountain and Tangborn, 1985; Jansson et al., 2003). This is especially true in arid and semi-arid climates where water availability is limited due to low precipitation rates. In addition, the bulk of surface runoff and groundwater recharge is generated in the high mountains, far from the coastal population centers and cultivated lowland valleys where the water is needed (e.g., Viviroli et al., 2007). As snow and ice melt play such an important role in the hydrology of arid zones, these regions are considered very sensitive to future temperature changes (Barnett et al., 2005). This situation is striking in the Norte-Chico region (26°S–32°S, **Figure 1**), which is the southernmost region of the Desert Andes of Chile (18–32°S, Barcaza et al., 2017). The semi-arid climate of Norte-Chico, combined with the marked climate variability arising from coupled atmosphere-ocean oscillations [El Niño Southern Oscillation (ENSO), Madden-Julian Oscillation (MJO)], induces a hydric stress on populations (Montecinos and Aceituno, 2003; Garreaud et al., 2009; Juliá et al., 2012). Nonetheless, and owing to efficient irrigation techniques, a productive agriculture sector exists and constitutes the economic pillar of the region. The existence and development of several mining projects near the headwaters of the main transverse valleys in the region also contribute to the reginal economy but raises environmental and resource equity disputes (Oyarzún and Oyarzún, 2011; Kronenberg, 2013). There is a strong concern that the observed (Falvey and Garreaud, 2009) and predicted (Cabré et al., 2016; Bozkurt et al., 2017) warming trend in the high Andes together with the apparent decreasing precipitation over recent decades (Fiebig-Wittmaack et al., 2012; Quintana and Aceituno, 2012; Schulz et al., 2012) could result in aggravated water stress in the Norte-Chico region. This in turn could exacerbate inter-sector conflicts about water usage and limit future development (Young et al., 2010; Valdés-Pineda et al., 2014).

Glaciers are sparsely distributed and relatively small in Norte Chico. Barcaza et al. (2017) inventoried 1334 glaciers and rock glaciers, covering a total area of 126.6 km^2. Nicholson et al. (2009) inventoried 112 glaciers covering 16.86 km^2 and 40 rock glaciers covering 6.30 km^2 in the upper Huasco River catchment. Despite their relatively small surface coverage, the hydrological contribution of an even limited glacier storage can become significant during drought periods and very dry summers (Bown et al., 2008; Gascoin et al., 2011; Huss, 2011; Rabatel et al., 2011). However, our understanding of recent glacier-climate interactions in the regions remains limited, hampering our ability to accurately predict future glacier contributions. The main limiting factor has been a dearth of glacier mass balance data. Within the Norte Chico, there is only one published study of glacier mass balance (Rabatel et al., 2011). Rabatel et al. (2011) presented 6 years of glaciological surface mass balance data from four ice bodies in the upper Huasco River catchments, as well as historical changes in surface area for 20 ice bodies, mapped form aerial photos and satellite images since 1955. They showed that the glacier cover decreased by ∼29% over the 1955–2007 period, and that glacier mass balance was negative over the 6-year monitoring period. Using these data combined with continuous streamflow measurements, Gascoin et al. (2011) evaluated the mean hydrological contribution of glacier melt in the upper Huasco River catchments which was found to vary between 3 and 24%.

Glaciological mass balance measurements records can be extended, or complemented, by calculating geodetic mass balance from historical satellite and aerial stereoscopic images (Cogley, 2009; Zemp et al., 2013), while longer mass balance reconstructions can be derived from ice core records (Ginot et al., 2006). While ice cores have greatly contributed to our knowledge of past hydroclimatic variability in the tropical Andes (Thompson, 2000; Vimeux et al., 2009), ice core records are almost non-existent in the subtropical region of South America. In arid zones, ice cores may represent the only source of high resolution (<decadal) paleoclimate information, as the scarcity of vegetation and lakes limits the use of tree-ring and lake sediment proxy records (Neukom and Gergis, 2012; Flantua et al., 2016). In addition, ice core records from high-altitude glaciers can also supply valuable climate information in otherwise data-scarce regions, as high-altitude weather stations are rare in the Desert Andes. To date, only one 'deep' (36 m, surface-to-bedrock) ice core paleoclimate record from the South American subtropics has been published, from the Cerro Tapado Glacier in the upper Elqui Valley of Norte-Chico (30°08′ S, 69°55′W, 5550 m a.s.l.) (Ginot et al., 2006). Additionally, preliminary analyses of a 104 m-long ice core form the Cerro Mercedario Glacier (31°58′ S, 70°07′W, 6100 m a.s.l.) are available (Bolius et al., 2006; Vimeux et al., 2009; Ciric et al., 2010). Given the recent persistent drought conditions observed in the region (Garreaud et al., 2017) and the anticipated aridification and warming trend (Boisier et al., 2018), there is a need for more information on the response of glaciers to climate change both under present and past climate conditions, in order to better assess the sensitivity of glaciers and related meltwater resources to climate change. The paleoclimate archive contained in high-altitude glaciers may also provide the best information source on past precipitation at high altitudes, which would give precious insights into natural climate variability and provide a comparative framework for the recent and ongoing drought experienced in the region.

This study presents a comprehensive assessment of the mass balance and climate history of a cold, high-altitude (>5000 m a.s.l.) glacier in the Desert Andes, using a combination of field, remote-sensing, and shallow ice core data. Our primary aims are (i) to provide an observation-based interpretation of glacier-climate relationships in the southern Desert Andes, (ii) to place recent glacier mass balance observations into a historical perspective, and (iii) to provide a first assessment of the paleoclimate information contained in such glaciers.

STUDY SITE

Guanaco Glacier is one of the largest glaciers (1.8 km^2) of the Huasco River basin (**Figure 1**). It drains predominantly into the Potrerillos River, a headwater tributary of the Huasco River basin (Atacama Region), but also contributes to the Argentinian

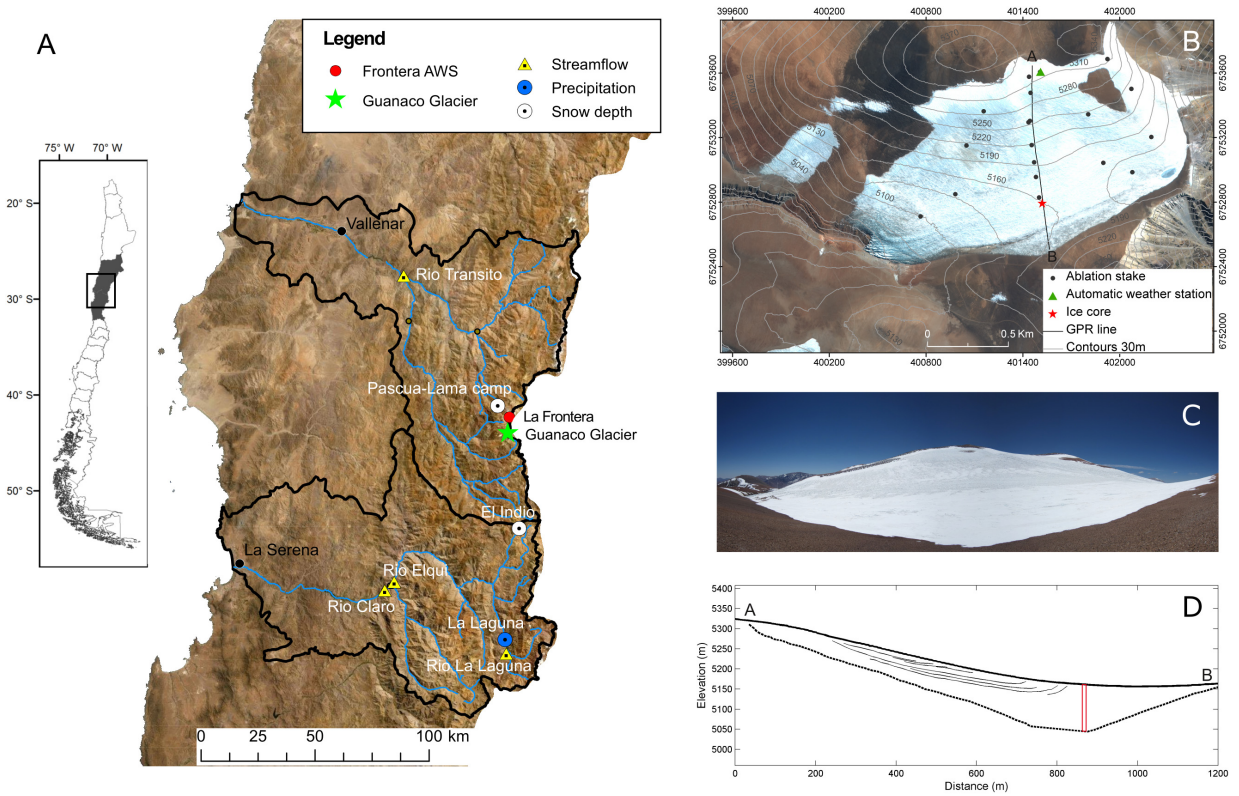


FIGURE 1 | Study area and sites. **(A)** region map showing the location of Guanaco Glacier and the hydroclimatic records used in this study. **(B)** Map of Guanaco Glacier showing mass balance stakes, automatic weather station and ice coring site; satellite image: Ikonos, March 26, 2007. **(C)** photograph of Guanaco Glacier taken from point B, looking North. **(D)** Surface and subglacial topography along GPR profile shown in **(C)** with mapped reflectors and ice core location shown in red.

de las Taguas River basin as it straddles the Chile-Argentina divide (29.34°S, 70.01°W, 4990–5350 m a.s.l). The climate in the area is semi-arid, with predominantly clear sky and strong solar radiation, and precipitation is almost exclusively snowfall from westerly circulation during the austral winter. Easterly convective precipitation events also occur episodically during the so-called Altiplano, or Bolivian winter, between December and February. While these events do not contribute much to annual totals, they can reduce glacier ablation by blanketing the surface with fresh snow and elevating the albedo (MacDonell et al., 2013; Abermann et al., 2014). The average snow precipitation measured at the Pascua-Lama mining camp at 3737 m a.s.l. was 240 mm w.e. a^{-1} for 2002–2015. In comparison, the long-term total annual precipitation was 173 mm w.e. a^{-1} for 1980–2004 at the El Indio Mine, 45 km south of the study area and at an altitude of 3869 m a.s.l., with 81% occurring in winter, between May and August.

Guanaco Glacier is located within the former Pascua-Lama bi-national mining project, which aimed to exploit an open-pit gold and silver mine straddling the Chile-Argentina Border. The project raised concerns regarding possible adverse impacts of mining activities, especially dust emissions, on nearby glaciers and glacierets (small glaciers with little or no sign of movement) (Fields, 2006; Brenning, 2008; Kronenberg, 2013; Arenson et al., 2015). These concerns led to the development and implementation of a vast program to monitor the state of the cryosphere in the vicinity of the project, which has been carried out by various private consulting companies as well as Chilean research institutes. This context explains the unique wealth of meteorological, hydrological and glaciological data in the area (Gascoin et al., 2011; Rabatel et al., 2011).

The glacier surface is smooth in its upper half and predominantly terraced at lower elevations. Ice penitents, which are vertical blades of ice up to ∼3 m high (e.g., Lhermitte et al., 2014) occur in the southwestern portion of the glacier, near the discharge outlet. An automatic weather station (AWS) was installed in 2008 on the uppermost part of the glacier (**Figure 1**). Air temperature varied between −25°C in winter to 5°C in summer (annual average = −9.3°C) over a 2.5 years period (November 2008 – April 2011) (MacDonell et al., 2013). Over the same period the relative humidity was low (mean ± standard deviation = 40 ± 26%) and wind speeds high (mean = 9.2 ± 4.2 m s^{-1}). The existence and surface mass balance of Guanaco Glacier is, at least partly, linked to snow redistribution by the wind as the glacier lies in the lee of a ridge (Gascoin et al., 2013). The current energy balance at the AWS shows that the net solar radiation is by far the dominant energy source, predominantly balanced by surface radiative cooling (negative longwave radiation) and strong negative latent heat (MacDonell et al., 2013). Hence ablation occurs mainly by sublimation there while melt is restricted to summer days with favorable conditions

(high incoming solar radiation and air temperature, low winds and high relative humidity). Reduced sublimation is thus one key condition for melting to occur on the upper glacier. Further down glacier, higher air temperature and the presence of penitents allow for more frequent melting there. Between 1955 and 2007 the glacier shrank by 0.334 km^2 or 15 ± 4% (Rabatel et al., 2011).

DATA AND METHODS

Mass Balance

Surface mass balance measurements using the glaciological method and the combined stratigraphic and floating-date system (Østrem and Brugman, 1991) have been initiated in 2002/2003 by Golder Associates S.A and continued by the Centro de Estudios Avanzados en Zonas Áridas (CEAZA) from 2007 to 2011 and by the Centro de Estudios Científicos (CECS) up to 2015 (WGMS, 2017). The winter mass balance is measured in late October/early November, using a combination of snowpits and probing to the previous summer surface. The summer balance is measured in late March/early April at a network of ablation stakes (**Figure 1**). The mean glacier mass balance (B) is calculated by averaging individual seasonal point mass balance values ($b_{w,s}$) weighted by their representative area. The (net) annual balance (B_a) is calculated by summing the winter (B_w) and summer balance (B_s). In 2009/10 and 2014/15 the glacier was inaccessible in winter so that only the annual balance was measured. The 2002/03 hydrological year was a wet year and glaciers were still snow-covered at the end of summer (Golder Associates, 2005). The snow thickness was measured in March 2003 at the stakes, supplemented by thickness estimates along a ground penetrating radar (GPR) survey (**Figure 1**), using the previous summer ice surface reflector as a stratigraphic reference (Golder Associates, 2005). Random mass balance errors arise for multiple causes and are notoriously difficult to quantify. Intrinsic errors may arise from imprecise stake readings, snow density determination, snow depth soundings, and from the sinking of stakes in firn and spatial sampling errors (Østrem and Haakensen, 1999). All stakes on Guanaco Glacier were drilled in ice so stake sinking is not considered to be an issue and averaging of nine snow probe measurements within a 2 m radius around stakes reduces the spatial sampling errors in local accumulation measurements. The mean annual error for the glacier-wide annual balance, B_a, is estimated to be ±0.09 m w.e and the error on the cumulative balance in 2014/15 is ±0.32 m w.e assuming independent errors between years (see **Supplementary Material**). However, unquantified systematic errors in glaciological mass balance can increase linearly over time (Thibert et al., 2008). The cumulative glaciological mass balance data was thus compared with independent geodetic balance estimates (c.f. section Geodetic Mass Balance), which allows detection of possible systematic errors (Østrem and Haakensen, 1999).

Meteorological Data

We make use of continuous meteorological measurements available since 1999 from a permanent automatic weather station at La Frontera (4927 m a.s.l.), 2 km north of Guanaco Glacier (**Figure 1**). Snow precipitation data is available since 1999 at the Pascua-Lama mining camp (3737 m a.s.l.), 10 km northwest of Guanaco Glacier (**Figure 1**). Snow thickness was measured manually by a meteorologist at a 3-h interval during snowfall events. The longest nearby high-altitude precipitation records are those from the former El Indio mining site (3869 m, 1980–2004) and La Laguna dam (3200 m, continuous since 1964), respectively located 45 km and 97 km south of the study area (**Figure 1**).

Geodetic Mass Balance

Historical elevation changes were estimated from digital elevation models (DEMs) of the glacier and surrounding areas. DEMs were constructed from stereo aerial photographs available in 1955 and 1978, and from two stereo pairs of Ikonos satellite images for 2005. The Ikonos images were acquired on March 1, 2005 as pan-sharpened multispectral products with 1 m resolution. The 2005 images were first triangulated using the Rational Polynomial Camera model supplied by the data provider. The exterior orientation solution was refined using a single ground control point (GCP) well visible near the center of the images. The two stereo pairs were triangulated in a single block solution, using 152 tie points representing ground features mutually visible between images in the stereo pairs. A set of three-dimensional (3D) points was extracted based on image correlation using the Automatic Terrain Extraction (ATE) module of the Leica Photogrammetric Suite Version 11 (Hexagon®) and manually edited to remove errors during the ATE procedure. The resulting sets of matched points from the two stereo pairs were merged and rasterized to a 5 m grid using bilinear interpolation.

In 1978 an aerial survey flight over Pascua-Lama area was performed by the Servicio Aerofotogramétrico de Chile using a Wild RC10 camera. The average scale of the photographs is about 1: 50,000. A stripe of four photographs with 60% end overlap was used in this study. The snow conditions on the photographs were favorable, showing good contrast and texture over most of the glacier surface. The original negatives were scanned at 16 μm resolution and provided with full camera calibration report. Prior to data processing, the photographs were radiometrically balanced to enhance brightness contrast. A Wallis adaptive filter was further applied to highlight local variation in brightness and enhance the accuracy of feature matching in the ATE procedure. Ten ground control points (GCPs) distributed over the whole Pascua-Lama area were collected from the 2005 Ikonos stereo pairs. The 10 GCPs were complemented with 45 tie points manually chosen on the overlapping parts of the images to strengthen the geometry of the image block. Image correlation was used to generate automatic tie points on the stereo image pairs. Aerial triangulation of all four images was performed in a single solution, so-called Bundle Block Adjustment. Image correlation on the 1978 aerial photographs resulted in much lower matching density than for the 2005 Ikonos imagery, despite the presence of visible features (crevasses, boundaries of snow facies, etc.). Mismatches also resulted in large clusters of erroneous points on the 1978 glacier surface. These errors were removed, and additional 3D points were manually digitized for the 1978 DEM. The two images were matched between each

other through parallax adjustment using a 3D digitizing cursor that "floats" in the vertical (Z) dimension. The 3D digitizing was performed in a quad buffered stereo environment facilitated by Nvidia 3D vision stereo glasses and a LG Flatron W2363D stereo.

Two aerial photographs from the Instituto Geográfico Militar (IGM) 1955 Hycon flight were acquired in a single flight line with approximately 60% end overlap. The overlap between photographs allowed triangulation of the images in a single bundle block adjustment. Photographs were scanned by the IGM at resolution of 1200 dpi (about 21-micron dot size) as 8-bit gray scale images. The overall quality of photographs is good, however the contrast over the glacier surface is rather poor. The same pre-processing, triangulation and terrain extraction procedures used for the 1978 photographs were applied to the 1955 pair. As the full calibration report was not available for the 1955 photographs, the internal frame coordinate system for each image was determined using the distances between the four center fiducials. Ten GCPs and 16 tie points were used for the bundle block adjustment.

The absolute vertical accuracy of the 2005 DEM was checked against 42 elevation points measured *in situ* at a reference geodetic network, yielding a bias of −0.42 m and standard deviation (std) of 1.19 m (**Supplementary Table 1**). Trend analysis of DEM residuals also did not reveal any spatial trends. Given the pixel size of Ikonos stereo imagery (1 m) the achieved vertical accuracy is considered as excellent. Changes in thickness, area and volume of Guanaco Glacier were estimated by comparing the 2005 DEM with those of 1978 and 1955. Elevation changes are typically calculated by differentiating glacier DEMs interpolated from 3D point clouds (e.g., Nuth and Kääb, 2011). This approach, however, assumes a comparable spatial density of the 3D point sets. Since the 1955 point cloud was sparser than in 1978, especially in the upper part of the glacier, this could lead to unrealistic surface change patterns. Therefore an approach was used that involves estimating elevation changes at locations of the 1978 point cloud (ΔZ) followed by the interpolation of a continuous ΔZ surface using the 1978 point cloud and the 1978 glacier boundary as zero change constraint (Surazakov and Aizen, 2006). The same approach was used for 1955. Systematic and random errors in glacier elevation changes were derived from elevation changes over stable surfaces surrounding the glacier, with slopes $< 25°$. Trend analysis of errors revealed a significant spatial trend in the east-west direction for both the 1955 and 1978 data. As the spatial error trend is practically linear, it is most probably related to vertical instability of the external orientation of the aerial stereo pairs (east-west "roll" of the stereo model relative to the reference coordinate system). The systematic spatial error trends were modeled with a first order polynomial surface and then removed (see **Supplementary Material**), and the remaining bias was subtracted from the DEMs. Uncertainties on mean elevation change were calculated from errors on stable ground, following Rolstad et al. (2009) (see **Supplementary Material**).

In October 2011 dual frequency Trimble 5700 GPS receivers were used to conduct kinematic surface profiling with a total length of 6 km on Guanaco Glacier. The base antenna was placed during the 6-h survey on a reference geodetic point 1.7 km north of Guanaco Glacier. Post-processing using the Automatic Precise Positioning Service (APPP) by JPL NASA resulted in a fixed solution with estimated errors of the coordinates of the base less than 3 cm (1 sigma). GPS kinematic data for Guanaco Glacier were post-processed to precision of less than 0.03 m and referenced to WGS84/EGM96 datum using the APPP solutions for the base station. Recent (2005–2011) surface elevation and volume changes for Guanaco Glacier were estimated by comparing the DGPS kinematic profiles with the 2005 DEM. To ensure the absence of systematic bias between DGPS data and the 2005 DEM, their elevation differences was estimated over stable terrain (off glacier) surveyed along 500 and 800 m profiles in proximity of the glacier. The results showed a very low random error (0.37 m) and a systematic error of −0.47 m. The bias was removed from the 2005 DEM before calculating elevation changes from DGPS values. The point estimations of glacier elevation changes were interpolated using Ordinary Kriging with a spherical function previously fitted to the empirical variogram. Cross-validation showed standardized RMS prediction error of 0.37 m. All elevation changes were converted to mass balance assuming a glacier wide average density of 900 kg m^{-3} and converted to volume changes using the mean glacier area over the considered time interval (Cogley, 2009).

Ice Core

During 9–20 November 2008 a 113 m-long, surface-to-bedrock ice core was retrieved from Guanaco Glacier (29.350°S, 70.014°W, 5161 m, **Figure 1**). The initial goal of the drilling was to confirm previous thickness estimates from GPR measurements and to check the possible accumulation of subglacial water and associated risk for catastrophic glacier collapse on nearby mining activities, a phenomenon documented in the region (Peña and Escobar, 1987; Iribarren Anacona et al., 2015). Other objectives included reconstructing the recent climate history of the area from ice core climate proxies. Hence the drilling location was chosen where the glacier is thickest (**Figure 1D**) and relatively planar – to ease drilling operations, and above the subglacial depression where subglacial lakes could potentially form. This implies that the ice core is located midway down a flowline running south from the glacier top to the drilling location, then deflecting southwest toward the Chilean outlet of the glacier (**Figure 1**). Analysis of previous GPR surveys (Golder Associates, 2005) shows that the main visible reflectors are tilted toward the surface near the drilling site in concordance with the sub-glacial bed, which occurs because glacier flow is constrained by the topographic depression. Drilling was done using the FELICS electro-mechanical drill specially designed for high-altitude drilling campaigns (Ginot et al., 2002). All recovered core segments were cut in 70 cm sections, placed in polyethylene tubes and stored in insulated boxes kept in a snow trench. Ice core boxes were delivered by refrigerated truck to Santiago Airport and shipped to the Laboratoire de Glaciologie et Géophysique de l'Environnement (LGGE) in Grenoble, France. Thermistors placed in the box revealed no melting during transport. A 15-thermistor chain with a ±0.1°C accuracy was installed in the borehole to monitor englacial temperatures and measured in November 2008, March 2010, April 2011, and

October 2011. Ice core processing and chemical analyses were conducted at LGGE, France. The ice core density was calculated by weighting individual core segments divided by the respective core volumes. Stratigraphic observations were conducted by placing each core segment on a backlit table, rotating the core to best see any visible features and related dip angle. The fraction of bubble-rich and bubble-poor ice, respectively representing glacier (compaction) and recongelation ice, was mapped from digital photographs of the backlit cores (Kinnard et al., 2008), and the dip angles of melt features was recorded. The core was then cut into separate longitudinal sections for analyses of stable water isotopes, radiogenic isotopes, major ion chemistry and insoluble particles and archives. Analyses of radiogenic isotopes were used to gain a first insight of the ice core age. Tritium (^{3}H) activity was measured for replicate samples of fresh surface snow as well the first 3 m of the ice core by U. Schotterer at the University of Bern, Switzerland, by direct liquid scintillation counting procedure (Schotterer et al., 1998). Cesium (^{137}Cs) and Lead 210 (^{210}Pb) activity was measured continuously along the first 20 m of the core at a 70 cm sampling interval at LGGE. Stable water isotope ratios (δ^{18}O and δ^2H) were analyzed continuously along the first 20 m of the core with a maximum sampling interval of 2 cm. Analyses were conducted at the LAMA laboratory (HSM, Montpellier, France) on an Elementar Isoprime mass spectrometer, coupled with an Aquaprep module using the classical water-CO_2 equilibration technique for δ^{18}O, and with a Eurovector PyrOH Elemental Analyzer in continuous-flow mode for δ^2H. Analytical errors were $\pm 0.8‰$ for δ^2H, and $\pm 0.10‰$ for δ^{18}O. Results from major ion chemistry analyses will be presented elsewhere.

Mass Balance Climate Interactions and Reconstructions

Glacier-climate interactions were investigated by correlating B_a with mean annual air temperature (Ta), wind speed (W) and vapor pressure deficit (VPD) recorded at the nearby La Frontera weather station and with winter (April to September) precipitation (P) recorded at La Laguna station. The annual and cumulative mass balance of Guanaco Glacier was reconstructed back to the mid-20th century based on linear regressions models between B_a and climate records and validated against geodetic estimates. Masiokas et al. (2016) also successfully reconstructed glacier mass balance from historical streamflow records in central Chile. Four long streamflow records are available for headwater catchments near Guanaco Glacier (**Figure 1A**), where discharge is strongly conditioned by snow accumulation, melt and sublimation (Favier et al., 2009). Mass balance was reconstructed back to the early 20th century by regressing B_a on a composite streamflow record, i.e., after averaging the four standardized streamflow series. 95% confidence uncertainty intervals on annually reconstructed B_a [$\varepsilon_{reco(t)}$] were taken as twice the cross-validated root-mean-squared error of predictions ($RMSE_{CV}$) (Wilks, 2011). Following Masiokas et al. (2016), the standard error on mean streamflow ($SE_{mean(t)}$) was also considered when estimating uncertainties for the reconstruction based on the composite streamflow record, using:

$$\varepsilon_{reco(t)} = \sqrt{RMSE_{cv}^2 + SE_{mean(t)}^2} \quad (1)$$

$$SE_{mean(t)} = \frac{\sigma}{\sqrt{n_{(t)}}} \quad (2)$$

where σ is the standard deviation of the composite record and n the number of records available at time t. $SE_{mean(t)} = 0$ for the climate-based reconstruction. Uncertainties on the reconstructed cumulative B_a series were derived by propagating (summing) the annual errors backward in time assuming independent errors between years, following Masiokas et al. (2016):

$$\varepsilon_{(T)} = \sqrt{\sum_{t=1}^{t=T} \epsilon_{reco(t)}^2} \quad (3)$$

RESULTS AND DISCUSSION

Recent Mass Balance

The mean mass balance of Guanaco Glacier was −0.85 m w.e. a^{-1} between hydrological years 2002/2003 and 2014/2015, with a maximum of 1.23 m w.e in 2002/2003 and a minimum of −1.13 m w.e. in 2014/15 (**Figure 2A**). Apart for the 2002/03 and 2005/06 years, the annual balance was negative, and the cumulative annual balance was −7.64 m w.e over the 2002–2015 period. The winter mass balance (**Figure 2B**) shows more pronounced variability (coefficient of variation = 1.2) than the summer balance (coefficient of variation = 0.3), in line with the other glaciers in the Pascua-Lama area (Rabatel et al., 2011). There is no direct relationship visible between the mass balance series and air temperature at the site (**Figure 2C**). Conversely, a positive relationship between winter and annual mass balance and precipitation measured at the two closest high-altitude weather stations is more striking. At first glance, interannual variability in glacier mass balance appears to be mostly controlled by interannual changes in precipitation, with changes in ablation playing a minor role.

In 2008 the stake network was expanded from 5 to 19 stakes, providing increased spatial coverage and enabling a more detailed analysis of the relationship between elevation and point mass balance at individual stakes (available up to 2013/14 only). The mass balance pattern of Guanaco Glacier is quite heterogeneous and shows only a weak relationship with elevation (**Figure 3**). From **Figure 3C** it is evident that winter mass balance, which is dominated by snow accumulation, is weakly but inversely related to elevation, opposite to common winter balance gradients which show positive increases with elevation due to orographic enhancement of precipitation and colder temperatures enhancing snowfall (e.g., Cuffey and Paterson, 2010). Strong spatial heterogeneity is also seen in summer mass balance, with positive, albeit weak, summer balance gradients (**Figure 3D**). Spatial correlations between seasonal mass balance components show that the pattern of annual mass balance is more influenced by summer conditions than by winter conditions

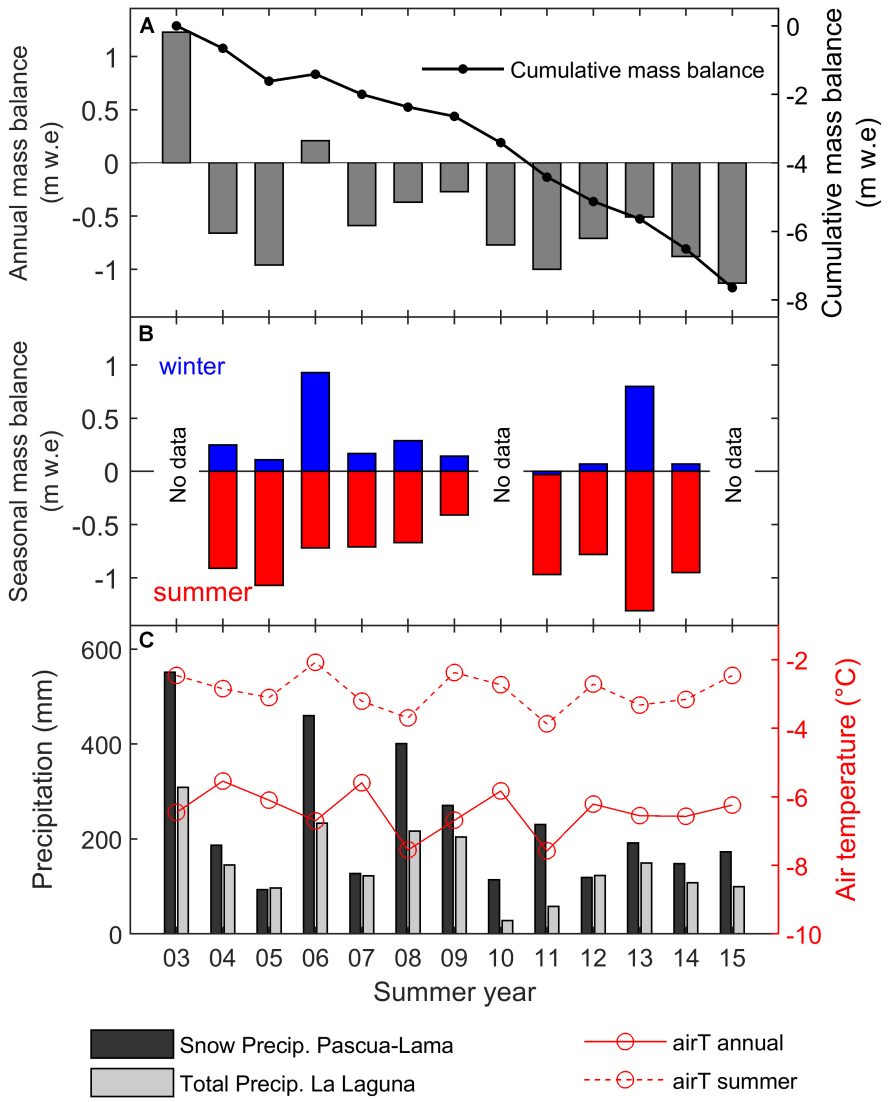


FIGURE 2 | Annual mass balance of Guanaco Glacier. **(A)** Annual (gray bars) and cumulative (black line) mass balance; **(B)** winter (blue) and summer (red) mass balance. Only the annual balance (B_a) was measured during the hydrological years 2002–2003, 2009–2010, and 2014–2015. **(C)** Annual precipitation (bars) at Pascua-Lama camp and La Laguna reference station and air temperature at La Frontera AWS (red lines).

(**Table 1A**). As a result, the annual mass balance gradient is weakly but positively related with elevation (**Figure 3A**).

The absence of any obvious mass balance gradients shows that there is no clear demarcation between accumulation and ablation zones on Guanaco Glacier, which was noted previously by Rabatel et al. (2011) for several glaciers in this catchment. This is in part caused by irregular snow accumulation patterns, which are strongly conditioned by blowing snow transport (Gascoin et al., 2013). The upper part of the glacier is exposed to strong winds, which redistributes snow to the lower glacier, and even sometimes causes a weak but noticeable downslope increase in winter mass balance (e.g., in 2010/2011). Interestingly, the higher than normal accumulation in 2012/2013 resulted in a positive and much better-defined (r^2 = 0.57) winter balance gradient. Given the small size and restricted altitudinal range of the glacier, this positive gradient may have been caused by a downslope increase in winter ablation rather than orographic enhancement of precipitation. The weak mass balance gradients are also consistent with the decreased sensitivity of mass balance to temperature in cold and dry climates (Kaser, 2001; Oerlemans, 2001; Cuffey and Paterson, 2010).

Results from the dynamic DGPS survey and the calculated elevation changes for 2005–2011 are presented in **Figure 4**. The mean geodetic mass balance calculated from elevation changes was −2.36 ± 0.33 m w.e. for 2005–2011. Considering that the DGPS survey was done in October 2011, i.e., at the end of winter, winter accumulation must be considered. The winter of 2011 was very dry, with a mean accumulation of only 0.07 m w.e. in October. Subtracting this value from the geodetic estimates yields a value of −2.43 ± 0.33 m w.e, which compares well

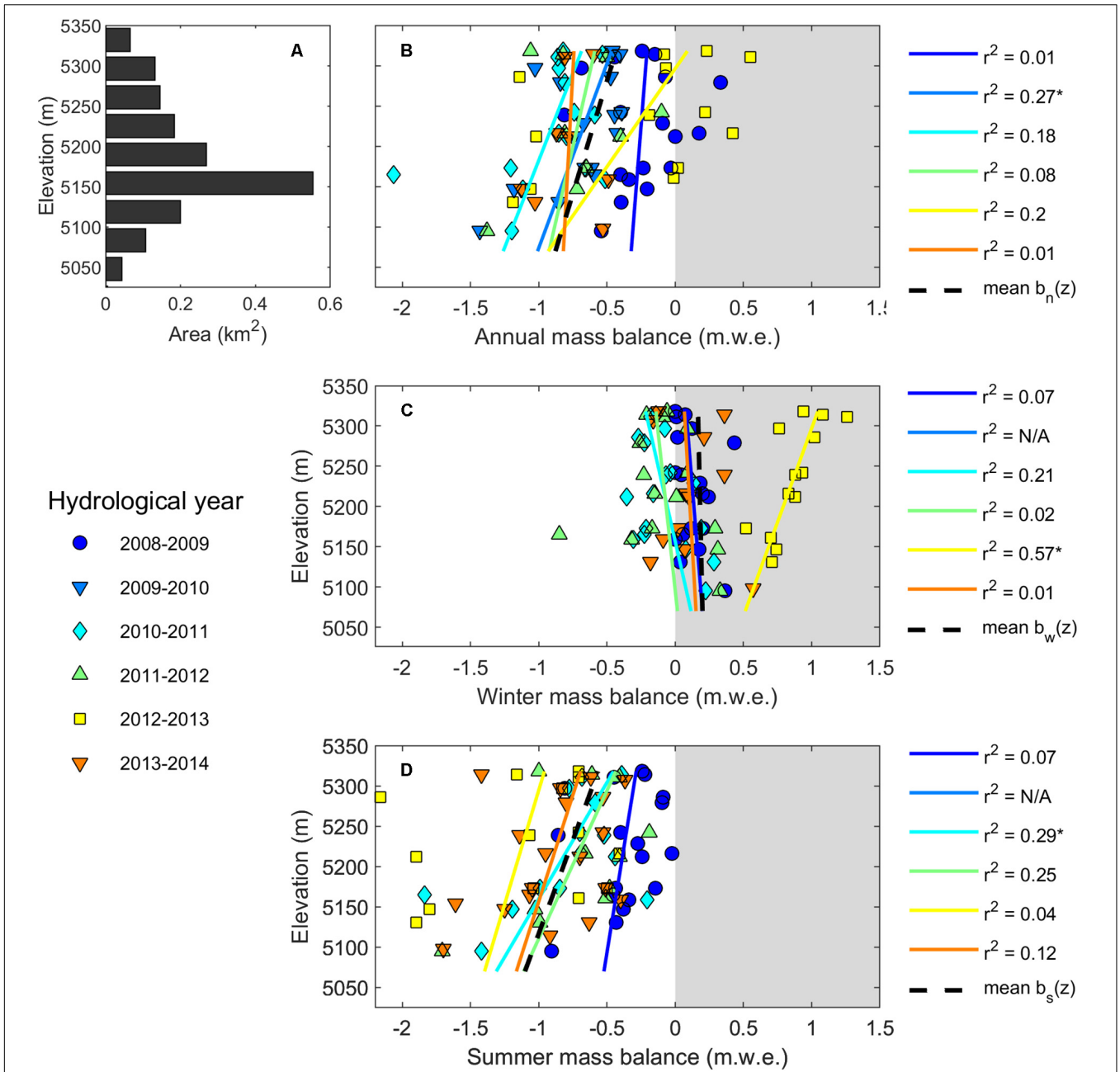


FIGURE 3 | Guanaco Glacier mass balance gradients. **(A)** Hypsometry; Mass balance – elevation relationships for **(B)** annual mass balance; **(C)** winter mass balance; **(D)** summer mass balance. The variance explained by each linear regression model (r^2) is shown in legend. Significant regression models are marked with an asterisk ($p < 0.05$). N/A: missing seasonal balance observations.

with the cumulative B_a measured by the glaciological method over the same period, −2.80 ± 0.22 m w.e. (**Table 2**). The precision of the geodetic estimate is especially good given the small changes involved. The good correspondence between the geodetic and glaciological estimates suggests that the glaciological mass balance surveys do not suffer from large systematic errors. The spatial pattern of elevation changes for 2005–2011 shows that almost the entire glacier surface has lowered since 2005 (**Figure 4B**). The contribution of ice flow to elevation changes is unknown, but surface horizontal velocities measured on Guanaco Glacier are low, in the order of 2 m a^{-1} (Golder Associates, 2005), which suggests small vertical velocity components. The lowest, southwest portion of the glacier shows the most pronounced surface lowering since 2005 with up to ca. 5 m ice loss since 2005 (**Figure 4B**).

Historical elevation changes (ΔZ) derived from aerial photographs show that the surface has lowered everywhere on the glacier since 1955, with an evident increase in ΔZ downslope

TABLE 1 | Pearson correlation coefficients between mass balance components.

(A) Spatial correlation

	b_w	b_s	b_a
b_w	1.00		
b_s	−0.23	1.00	
b_a	0.41*	0.68*	1.00

(B) Temporal correlation

	B_w	B_s	B_a
B_w	1.00		
B_s	−0.20	1.00	
B_a	0.75*	0.49	1.00

(A) Spatial correlation between point mass balances for hydrological years 2008/2009 to 2013/2014. The mean annual point balance was first removed from each year's b values so as to not introduce a variance bias in the padded series. (B) Temporal correlation between glacier-wide mass balance. w, winter balance; s, summer balance; a, annual balance. Significant correlations ($p < 0.05$) are marked by an asterisk.

(**Figure 5**). Maximum thinning of ca. −40 m is observed in the southwest end of the glacier since 1955. The pattern for 1978–2005 is similar, albeit of lesser magnitude given the shorter time period (28 years). Estimates of cumulative and mean annual geodetic mass balance are compared to recent mass balance measured since 2005 by both the glaciological and geodetic methods (**Table 2**). Mean annual B_a has been more negative in recent years than in the past, being -0.15 ± 0.13 m w.e. a^{-1} for 1955–1978, -0.10 ± 0.03 m w.e. a^{-1} for 1978–2005, and -0.64 ± 0.09 m w.e a^{-1} for 2005–2015 (glaciological B_a).

Ice Core Stratigraphy

The 113-m long ice core recovered from the lower Guanaco Glacier confirmed previous GPR thickness estimates and the absence of liquid water within, or at the base of the glacier. Temperature profiles measured in the borehole show that Guanaco Glacier is a cold glacier which had a basal temperature of ca. −5.5°C in 2008 (**Figure 6**). The profile is negative from the base up to a depth of 60 m, in accordance with typical borehole temperature profiles, which is related to the geothermal flux (Cuffey and Paterson, 2010). The 'warm reversal' above 60 m has been observed in other Andean glaciers and may be related to recent atmospheric warming (Vimeux et al., 2009). Seasonal temperature fluctuations are apparent down to ca. 20 m, where the average ice temperature is −6.3°C. However further interpretation of the temperature profile is complicated by the fact that the borehole intersects inclined isochrones (**Figure 1D**), so that the ice may have been deposited at different locations up-glacier and then advected down-glacier. The temperature profile thus likely contains flow-inherited temperature effects related to the varying elevation of snow deposition and melt-refreeze cycles.

The ice core stratigraphy for the uppermost 20 m is presented in **Figure 7**. The density varies between 0.86 at the surface to 0.89 at 20 m. Several melt features were observed throughout the top 20 m of the core. Interestingly, the dip angle of the best visible features varies significantly, between 40 and 73° (median = 61°). The fact that the range of dip angles is much larger than the maximum dip angles (20°) of the GPR isochrones near the drill site, which follow the bedrock topography (**Figure 1D**), and the significant scatter in dip angle values suggest that the angles are not depositional features. Instead, we interpret them to represent penitents developed at the glacier surface and succinctly buried. An example of these 'paleo penitents' is shown in **Figure 7D**. Penitents up to 50 cm-high are commonly found today around the drill site (**Figure 8**). Penitents form by differential ablation caused by the concentration of solar radiation in depressions, enhanced by the accumulation of debris, reduced wind and increased humidity between the penitent blades (Lliboutry, 1954; Bergeron et al., 2006; Lhermitte et al., 2014). Melting occurs in

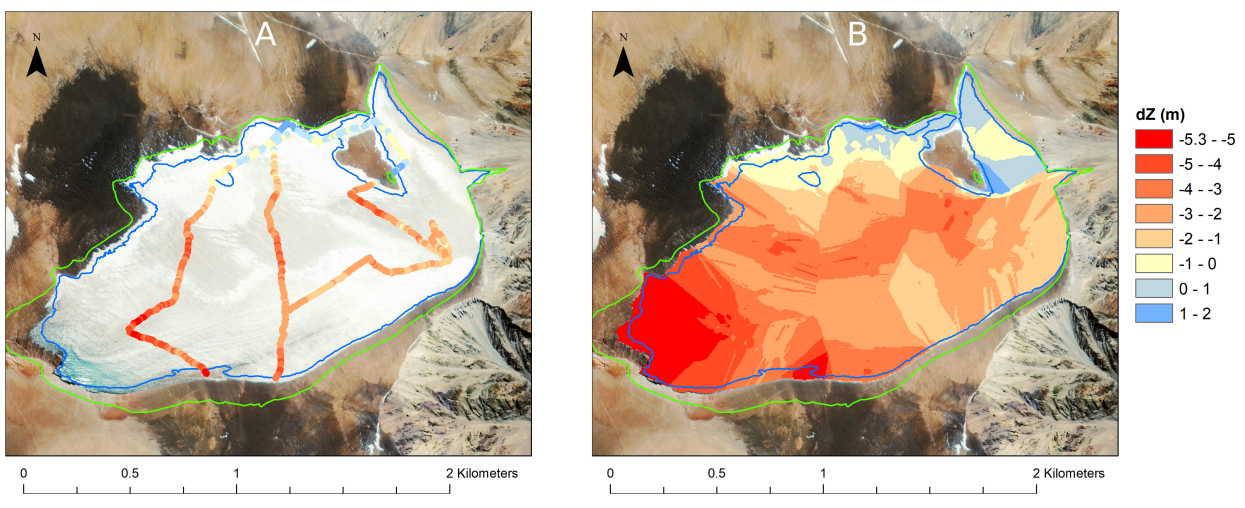


FIGURE 4 | Recent elevation changes on Guanaco Glacier, 2005–2011. **(A)** Satellite image of Guanaco Glacier (Ikonos, March 2005) showing DGPS tracks in October 2011 and measured elevation changes (dZ). Digitized glacier outlines in 1955 (green) and 2011 (blue) are shown. **(B)** Interpolated elevation changes using Ordinary Kriging.

TABLE 2 | Comparison between glaciological and geodetic mass balance estimates of Guanaco Glacier.

Period (calendar years)	Hydrological years	*B* (m w.e)	*B* error (±SE) (m w.e)	B_a (m w.e. a^{-1})	B_a error (±SE) (m w.e. a^{-1})
Glaciological method					
2002–2015	13	−6.4	0.32	−0.49	0.09
2005–2011	6	−2.8	0.22	−0.47	0.09
2011–2015	4	−3.2	0.18	−0.81	0.09
Geodetic method					
1955–1978	23	−3.6	3.2	−0.15	0.13
1978–2005	27	−2.9	0.9	−0.10	0.03
1955–2005	50	−6.5	3.1	−0.13	0.06
2005–2011	6	−2.4	0.3	−0.40	0.04

B, cumulative mass balance. B_a, mean annual mass balance. SE, standard error.

the penitent troughs, and we have observed that much of the meltwater refreezes there at the end of summer. Penitents are broadly aligned east-west and are inclined toward the sun at zenith. Naruse and Leiva (1997) measured slopes between 60 and 85° for the southern face of penitents on Piloto Glacier in Argentina. These values are consistent with the dip angles observed in the Guanaco ice core. The melt fraction is quite high (0–0.90, mean = 0.28), and variable (std = 0.29) and a broad increase in melt fraction with depth is noted. This trend parallels that seen in the density, but both variables are otherwise uncorrelated ($r = 0.16$ after applying a first-difference filter).

Ice Core Relative Dating

The average ^{3}H concentration measured in surface snow was 4.69 ± 0.38 TU, which is compatible with values for recent precipitation (Cauquoin et al., 2015). In contrast, ice samples all had near zero ^{3}H concentrations, which indicates that the ice formed before 1945 AD (see **Supplementary Table 3**). This conclusion is confirmed by the concentration of ^{137}Cs measured along the top 20 m of the core, which was found to be below the detection limit (0.011 Bq/kg), or undetected. Furthermore, ^{210}Pb was also undetected throughout the first 20 m of the core, despite the low detection limit (0.052 Bq/kg) used. These results indicate that the current glacier ice surface is more than 100 years old. This represents a minimum limit on the age of the upper ice core and more accurate absolute dating is not possible at this point.

Ice Core Stable Water Isotopes

The stable water isotopes ($\delta^{18}O$ and $\delta^{2}H$) profiles show well defined cycles (**Figure 9A**). The profiles are generally smooth, but a few sharp transitions occur, e.g., at a 13 m w.e. depth. The amplitude of the isotopic cycles (3–5‰ for $\delta^{18}O$; 20–40‰ for $\delta^{2}H$) is similar to that seen in surface snow on nearby Tapado Glacier (Sinclair and MacDonell, 2016) and is thus interpreted to correspond to an annual signal. The same periodicity is visible in the deuterium excess series (**Figure 9B**). Spectral analysis of the $\delta^{18}O$ profile based on the continuous wavelet transform (Torrence and Compo, 1998) confirms the presence of significant power along the 0.5–3 m w.e. spectral band which is significantly different from autocorrelated (red) noise (**Figures 9C,D**).

Stable isotopes of precipitation contain mixed information reflecting notably the temperature at the time of precipitation formation (condensation), the geographic location and meteorological conditions prevailing at the source of atmospheric humidity, and the amount of precipitation lost during air mass transport. When the moisture source, rainout rates and air mass pathway can be assumed constant, stable water isotopes are good proxies for the local air temperature, such as commonly used at high latitude sites (Dansgaard, 1964). However, this temperature control breaks down for low latitudes, where cloud systems are dominantly of convective character and the influence of surface or near-surface temperature on the formation of precipitation decreases. Hence variations in Andean ice core isotopic signals are generally thought to predominantly reflect atmospheric circulation (Hoffmann et al., 2003; Vimeux et al., 2009). On nearby Tapado Glacier, seasonal cycles in chemical and isotopic profiles were interpreted to arise from changing moisture sources: during the austral winter the westerly circulation brings cold air masses from the Pacific Ocean which carry most of the annual precipitation, while episodic convective storms in summer bring humid air masses from the Amazon Basin (Ginot et al., 2006). The same mechanism holds here. Post-depositional processes can also strongly modify the isotopic signal originally imprinted in snow. Sublimation in dry climates can induce a relative enrichment of the isotopic composition of surface snow. The deuterium excess, which characterizes the deviation from the global meteoric water line [d (‰) = $\delta^{2}H - 8 \times \delta^{18}O$], is an indicator of non-equilibrium phase changes characteristic of post-depositional processes. It is particularly sensitive to the relative humidity which governs these processes (Whillans and Grootes, 1985). Stichler et al. (2001) showed that sublimation on the summit of Tapado Glacier leads to a progressive enrichment of $\delta^{18}O$ and a decrease in d at the surface. However, the isotopic enrichment was limited to the first 5-10 cm of the snow and the enriched layers became preserved after being buried by the next snowfall. These disturbed layers showed as anomalous points on a $\delta^{2}H - \delta^{18}O$ scatter plot (Stichler et al., 2001, their Figure 6). Similar sublimation-induced enrichment of stable isotopes was observed at the surface of penitents at the beginning of the ablation season in the ablation zone of Tapado Glacier (Sinclair and MacDonell, 2016). Later in summer, melting tended to smooth the original isotopic profile. The linear relationship between $\delta^{2}H$ and $\delta^{18}O$ values for Guanaco is strong and without anomalous deviations (**Figure 10**), indicating that all precipitation events arose from well-defined and replicable meteorological processes. The high slope of the local meteoric line (8.49) and the relatively high d values (mean $d = +16.4 \pm 2.3$‰), as well as a positive correlation between $\delta^{18}O$ and d, indicate that precipitation can include a regular contribution of re-evaporated continental surface water on a seasonal basis (Putman et al., 2019). The fact that d is always larger than 10‰ (corresponding to the global meteoric water line) suggests that the profile along the first 20 m of the core was not significantly affected by post-depositional sublimation processes.

Melting, percolation and subsequent refreezing of meltwater tend to smooth and redistribute the isotopic signal, sometimes

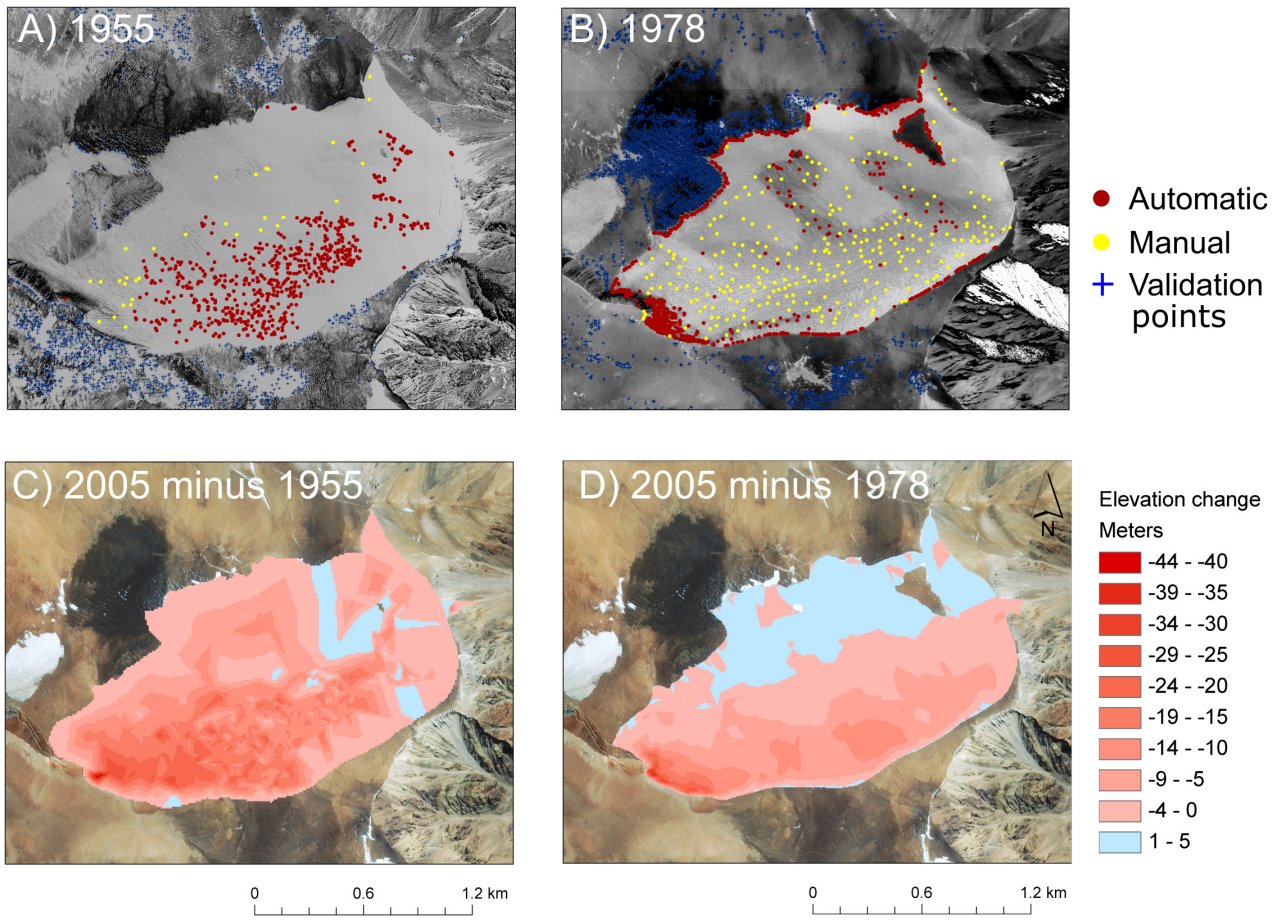


FIGURE 5 | Historical elevation changes on Guanaco Glacier for 1955-2005. **(A)** 1955 air photo showing elevation values extracted automatically (red dots) and manually (yellow dots), as well as validation points outside the glacier (blue crosses). **(B)** Same as **(A)** but for the 1978 aerial photo. **(C)** Elevation changes between 1955 and 2005. **(D)** Elevation changes between 1978 and 2005.

obliterating completely any seasonal signal originally present (Koerner, 1997; Schotterer et al., 2003). Several studies have looked at the effect of melting on isotopic and chemical signals of melt-affected ice cores. Grumet et al. (1998), Pohjola et al. (2002), Moore et al. (2005), and Kinnard et al. (2008) all found that although melting affects the isotopic and chemical record of ice cores, annual to biannual cycles are still detectable. As opposed to major ions, stable water isotopes are the least affected by melting and seasonal cycles are still observed provided that refreezing of meltwater occurs within the annual layer (Pohjola et al., 2002). Melting can be seen to have affected the integrity of the isotopic signal in **Figure 7**. The broad increase in melt fraction with depth is associated with sharper transitions in the stable isotope series and a blurring of the cyclicity (**Figure 9**). The significant spectral band in the $\delta^{18}O$ record, assumed to be of seasonal origin, is seen to spread toward larger periods between 12 and 16 m w.e. depths. We interpret this as an indication for possible percolation and refreezing beyond the depth of annual deposition, which smooths the annual cycle signal (Grumet et al., 1998). Despite this, melting does not seem to have completely obliterated the dominant cyclicity in the signal. Detailed analysis of the wavelet spectrum in **Figure 9** shows a first power band peak centered around 0.7 m w.e. and a second one around 1.7 m w.e., perhaps representing an annual/biannual signal. However, given the likelihood for melting to have displaced the original seasonal peaks, deriving a precise annual accumulation rate from seasonal cycles is not possible, and only a range (0.5–3 m w.e. a^{-1}) can be inferred.

Recent Glacier-Climate Relationships

While the spatial variability of annual mass balance (b_a) is mainly controlled by summer mass balance conditions, interannual variability in glacier-wide annual mass balance (B_a) was found to be predominantly driven by winter conditions (**Table 1**). This is also shown by correlations between B_a and climate variables (**Table 3**), which display the highest correlation with precipitation but no relationship with air temperature, contrary to most glaciers in temperate zones (Hock, 2005; Cuffey and Paterson, 2010). On the other hand B_a was found to be significantly correlated with the vapor pressure deficit and wind speed, which are two important drivers of sublimation (Kull et al., 2002; Stigter et al., 2018). Sublimation is currently the dominant

ablation process on Guanaco Glacier (MacDonell et al., 2013), a peculiarity of high-latitude glaciers and snow cover in the Arid Andes (Ayala et al., 2017; Réveillet et al., 2020). P and VPD were found to be the best combination of predictors of B_a variability on Guanaco Glacier (r^2_{adj} = 0.90, $p < 0.05$, **Table 3**). The positive influence of VPD on B_a suggests that increased sublimation during drier conditions limits mass loss by melting, due to the large quantity of latent heat consumed by sublimation. Conversely, wetter conditions will increase accumulation but also decrease sublimation, favoring more efficient mass loss by melting due to its much smaller latent heat consumption. As such, sublimation acts as a negative feedback on B_a because of its control on mass loss from melting.

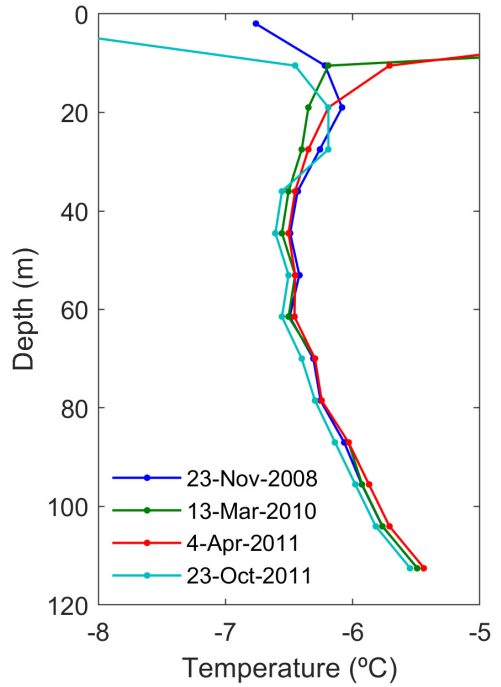


FIGURE 6 | Temperature profiles measured in the Guanaco Glacier borehole.

The little sensitivity of B_a to air temperature found in this study is consistent with the previously documented notion that the sensitivity of mass balance to temperature decreases in colder and drier climates (Kaser, 2001; Oerlemans, 2001; Cuffey and Paterson, 2010). As Guanaco Glacier lies above the 0°C isotherm, air temperature has little influence on the precipitation phase while sublimation limits the influence of temperature on melting. Rupper and Roe (2008) also showed that glaciers in central Asia with low precipitation and higher sublimation rates are less sensitive to temperature. In South America, Sagredo et al. (2014) showed that the glacier equilibrium line altitude (ELA) in the subtropical Andes is the least sensitive to temperature, and most sensitive to precipitation, consistent with the cold and dry climate conditions of that region (Sagredo and Lowell, 2012). More recently, Dussaillant et al. (2019) derived geodetic mass balance estimates for 2000–2018 for the whole Andes Cordillera based on ASTER stereoscopic imagery. They showed that the dry Andes had the smallest mass loss rates (-0.28 ± 0.18m w.e.a^{-1}), but that mass loss increased from slightly positive in 2000–2009 to a strongly negative mass balance in 2009–2018, a trend attributed to the recent prolonged drought conditions in North-Central Chile (Garreaud et al., 2019). These findings show again the

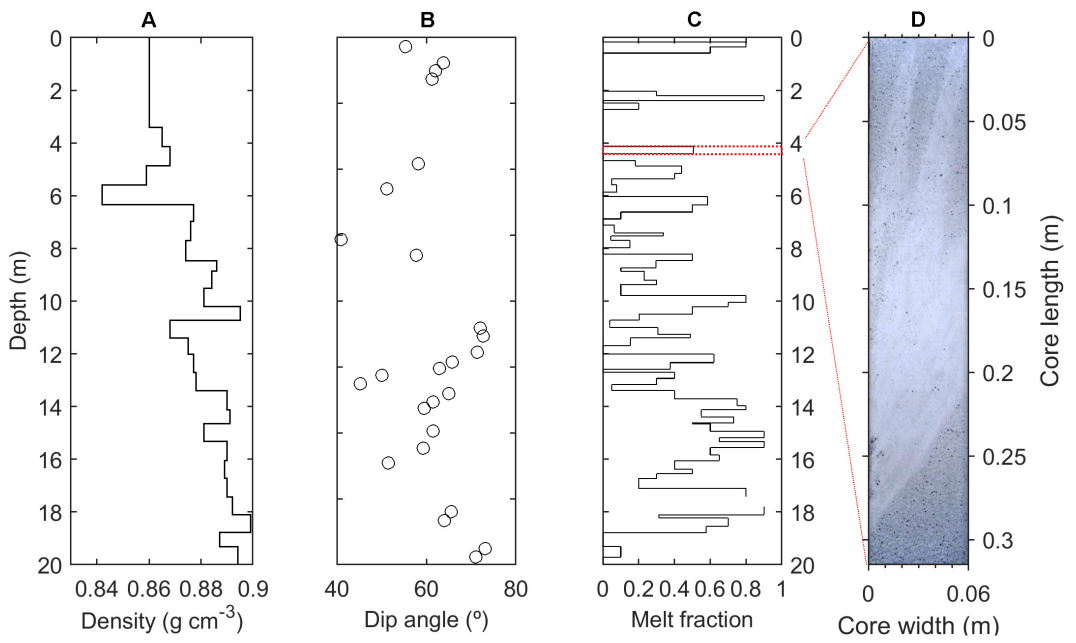


FIGURE 7 | Visual stratigraphy for the top 20 m of the ice core. **(A)** Density; **(B)** dip angles of melt features; **(C)** melt fraction; the red rectangle shows the location of the core shown in **(D)**; **(D)** example of melt feature reminiscent of penitent morphology.



FIGURE 8 | Photograph of Guanaco Glacier at the ice coring location, showing the presence of small penitents on the surface (March 12, 2010).

peculiarity of the cold and dry glaciers of the dry Andes where humidity, rather than air temperature plays a key role in the mass balance response to climate.

Historical Mass Balance and Climate Conditions: Observations

Glaciological and geodetic mass balance estimates show that Guanaco Glacier has been predominantly losing mass since at least 1955, and that mass loss has accelerated over time (**Table 2**). Mass loss rates during the most recent period (2005–2015: -0.64 ± 0.09 m w.e. a^{-1}) are five times higher than during the 1955–2005 period (-0.13 m $\pm$ 0.06 w.e. a^{-1}). Few long mass balance records exist in the region to compare with these results. The longest record comes from Echaurren Norte Glacier (33.58°S), in the central Andes where the climate becomes more Mediterranean. Its cumulative mass balance has been relatively stable since 1975, until 1993 when it started decreasing until today (Escobar et al., 1995; Masiokas et al., 2016). In the Argentinean Andes, the mass balance of Piloto East Glacier (32°S) broadly followed the same trend, with approximately neutral balance until 1993 followed by a negative balance (Leiva et al., 2007). Our results broadly agree with these trends, however with slightly negative mass balance during 1978–2005 (-0.10 ± 0.03 m w.e. a^{-1}) but increasing mass loss subsequently.

Ice core conditions on the other hand suggest drastically different mass balance conditions, with net accumulation rates of 0.5–3 m w.e. a^{-1} inferred from the stable isotope record (**Figure 9**), relatively high melting rates inferred from the significant proportion of refrozen ice in the core (**Figure 7**) and reduced sublimation inferred from small deuterium excess values (d) (**Figure 10**). Penitents occur on the present surface (**Figure 8**) and in the core (**Figure 7**). The formation of penitents is partly conditioned by microclimatic conditions: sublimation predominantly occurs on the wind-exposed tips while higher air humidity promotes melting and deepening of the sheltered troughs (Lliboutry, 1954). However the first-order process for the formation of penitents is not sublimation, but rather the focusing effect of solar radiation in depressions at high incidence angles (Cathles et al., 2014), a phenomenon favored at low latitudes and in clear atmospheric conditions such as in the Desert Andes. Hence penitents were also present under the more humid climate inferred from the ice core.

When did these humid climate conditions occur and when did the ice of the upper core form? Our radioactive isotopes measurements in the upper core show that the modern (2008) glacier surface is at least 100 years old. In addition, the ice core density profile (**Figure 7**) shows the presence of residual firn at the end of the compaction cycle, during which ice density increases slowly from the compression of air bubbles by creep of the surrounding ice (Ginot et al., 2006; Cuffey and Paterson, 2010). The absence of younger and more porous firn above suggest it has completely ablated. On nearby Tapado Glacier, ice has accumulated continuously until at least 2001, when a 36 m surface-to-bedrock was retrieved from the summit (5536 m a.s.l, 30.13°S, 69.92°W) (Ginot et al., 2006). The age at the bottom of the continuous accumulation sequence in the Tapado ice core was dated to 1920 AD, below which older, but undated ice was found separated by a hiatus. Annual accumulation since 1920 AD varied between 0.1 and 1.03 m w.e. a^{-1} with a mean of 0.32 m w.e. a^{-1}. The time span for the continuous accumulation of firn and its transformation to ice on Tapado Glacier (1920–2001: 81 years) is the closest analog for the time span of the missing firn on Guanaco Glacier. This figure is on the same order, but still smaller than the minimum age for the 2008 surface derived from radioactive isotopes (>100 years). Further South, a 104 m ice core was recovered in 2005 from La Ollada Glacier on Cerro Mercedario (31.97°S, 70.12°W, 6100 m a.s.l.), covering 92 years (1913–2004) of continuous accumulation varying between 0.3 and 1.8 m w.e. a^{-1} (mean = 0.91 m w.e. a^{-1}) (Ciric et al., 2010). Hence, climate conditions since the early 20th century have allowed continuous accumulation on Cerro Mercedario and Cerro Tapado, both located south and higher than Guanaco Glacier, but have resulted in mass loss on Guanaco Glacier.

Historical Mass Balance and Climate Conditions: Stochastic Reconstructions

In order to further our understanding of historical mass balance variability, the annual and cumulative mass balance of Guanaco Glacier was reconstructed back to the early 20th century using the statistical models developed in **Table 3** and the methods outlined in Section "Mass Balance Climate Interactions and Reconstructions" (see further details in **Supplementary Material**). The use of climate and streamflow records not located in the immediate vicinity of the glacier calls into question their representativity to reconstruct mass balance. The La Laguna winter precipitation record was found to be well correlated with the local snow record at Pascua-Lama ($r = 0.90$, $p < 0.01$, $n = 13$ years) as well as with the El Indio snow precipitation record ($r = 0.89$, $p < 0.01$, $n = 23$ years) (see **Figure 1** for locations), confirming the spatial coherence of winter precipitation in this region of the Desert Andes. On the other hand, streamflow records in the Norte Chico region are good proxies of net snow precipitation (precipitation minus sublimation) (Favier et al., 2009), which makes them ideal to

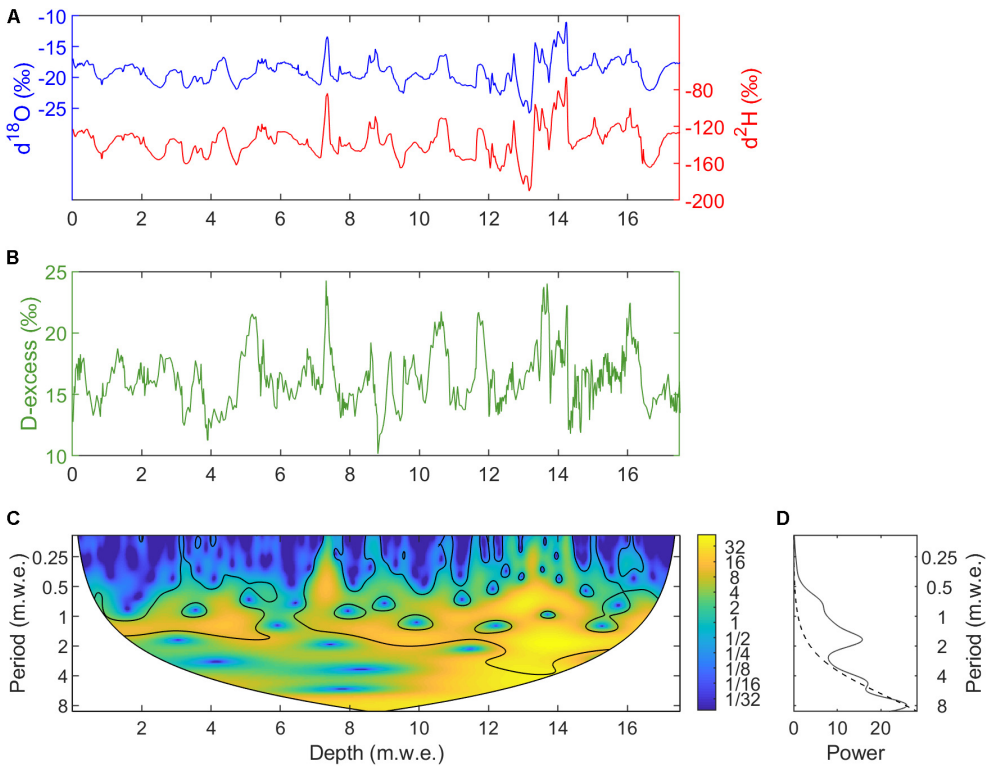


FIGURE 9 | Stable isotope profiles for the topmost 20 m of the Guanaco Glacier ice core. **(A)** $\delta^{18}O$ and $\delta^{2}H$; **(B)** Deuterium excess; **(C)** Wavelet power spectrum of the $\delta^{18}O$ series. Black contours delineate the 95% significance level against a red-noise (AR1) model with lag1 correlation $r = 0.9$; **(D)** mean wavelet power spectrum; stippled line shows the 95% significance level.

reconstruct the precipitation-sensitive glacier mass balance. B_a was found to be significantly and positively correlated (r^2_{adj} 0.65–0.80, $p < 0.01$) with the four long streamflow records in the upper Huasco and Elqui catchments (**Table 3**). The best correlation ($r^2_{adj} = 0.81$, $p < 0.01$) was obtained on a composite series of these four records (Q mean, **Table 3**). The composite record is itself well correlated with each individual record ($r = 0.93$–0.96, $p < 0.01$), confirming the presence of a strong, precipitation-based signal in headwater catchment outflows.

The model based on winter precipitation (P) and vapor pressure deficit (VPD) as predictors can only be forced using the VPD climatology, as La Frontera station is in operation since 1999, with reliable humidity data since 2002 only. Hence the model was forced with P measured at La Laguna since 1965 and the mean VPD ± one standard deviation (std) over the 2002–2015 period in order to check the sensitivity of the reconstructed B_a to VPD. Using the mean or low (mean − std) VPD yields a poor fit on geodetic balance estimates, while the fit improves when using the higher (mean + std) VPD estimate (lower blue curve on **Figure 11B**). This suggests that higher VPD prevailed prior to 2002 compared to more recent conditions (2002–2015). It also shows the feedback effect of air humidity on B_a at Guanaco Glacier: while higher precipitation increases B_a, a lower VPD during more humid years could favor mass loss by melting and as such decreases B_a.

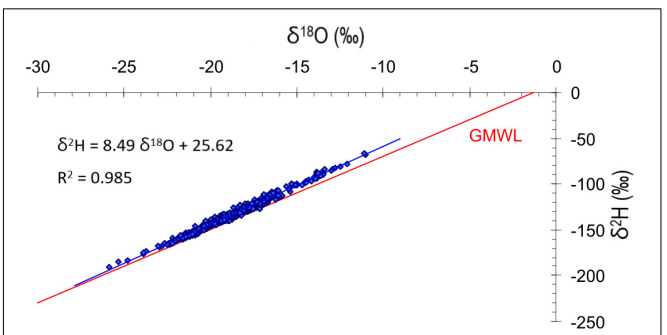


FIGURE 10 | Local (blue) and global (red) meteoric water line calculated from the Guanaco ice core.

The short VPD and P records do not allow extending B_a very far back in time. The composite streamflow record was thus used to reconstruct B_a back to 1915. The streamflow-based reconstruction agrees relatively well with the geodetic balance back to 1955, within error bounds (**Figure 11B**). The reconstructed B_a record shows a period with frequent positive mass balance conditions during the early part of the record (1915–1935), followed by a period with predominantly negative balance (1935–1975), a more neutral period with alternating negative and positive mass balance (1975–2005), and

TABLE 3 | Linear regression between climate variables (Ta, P, W, VPD), streamflow (Q) and annual mass balance (B_a).

Variable	Weights	*p*-value	r^2_{adj}	rmse (m w.e.)	$rmse_{CV}$ (m w.e.)	Normal	Indep
Ta	−0.06	0.75	−0.08	0.65	0.68	No	Yes
P	0.58	<0.01	0.83	0.26	0.34	Yes	Yes
W	−0.53	<0.01	0.68	0.36	0.55	Yes	Yes
VPD	0.44	<0.01	0.46	0.46	0.43	Yes	Yes
P, Ta	0.60, 0.09	0, 0.28	0.84	0.25	0.36	Yes	Yes
P, W	0.43, −0.19	0, 0.12	0.86	0.24	0.38	Yes	Yes
P, VPD	0.47, 0.19	0, 0.02	0.90	0.20	0.29	Yes	Yes
Q Transito	0.31	<0.01	0.79	0.29	0.32	Yes	Yes
Q Laguna	0.54	<0.01	0.65	0.38	0.48	Yes	Yes
Q Claro	0.20	<0.01	0.80	0.28	0.29	Yes	Yes
Q Elqui	0.09	<0.01	0.80	0.28	0.32	Yes	Yes
Q mean	0.56	<0.01	0.81	0.28	0.31	Yes	Yes

Regression weights are standardized to allow comparison of variable effects on B_a. r^2_{adj}, coefficient of determination adjusted for the number of parameters in the regression model; rmse, root-mean-square error of regression; $rmse_{CV}$, leave-one-out cross-validated rmse. Normal: Lilliefors normality test on residuals (yes = normally distributed residual, $p < 0.05$); Indep: Durbin-Watson test for independence of residuals (yes = independent residuals, $p < 0.05$).

sustained mass loss thereafter. This trend is similar overall to the reconstructed mass balance of Echaurren Norte Glacier in central Chile (Masiokas et al., 2016) (**Figure 11C**). Annually reconstructed B_a on Guanaco Glacier reached positive values up to 2 m w.e. during the 1975–2005 period, and even higher values in the early period (up to 4 m w.e.). Considering that ice was still accumulating on Guanaco Glacier from 1915 up to ∼1935 AD with a mean reconstructed net accumulation rate of 0.60 m w.e. a^{-1}, and that the reconstructed cumulative mass loss was 17.3 ± 6 m w.e. between 1935 and 2008, the age of the 2008 surface would be approximately equal to 1935 – (17.3 ± 6)/0.6 m w.e. = 1910 AD ± 10 years. This is a crude estimate, but which is in line with the radiometric minimum age of the 2008 glacier surface (<1908 AD). The mean (0.60 m w.e. a^{-1}) and maximum (4 m w.e. a^{-1}) accumulation rate during the early 1915–1935 period is also consistent with the range of values inferred from the stable isotope record (0.5–3 m w.e. a^{-1}). Based on this evidence, it is thus plausible that the ice sampled in the core dates back to the mid 19th to early 20th century period when precipitation in central Chile was higher than today (Garreaud et al., 2017) and several glacier advances were inferred from historical sources and dated moraines in the Dry Andes (Masiokas et al., 2009).

Link With Atmospheric Circulation

The sensitivity of mass balance to precipitation, and the recent sustained mass loss of Guanaco Glacier that occurred during a prolonged drought, calls into question the role of changing atmospheric circulation to explain the observed and reconstructed mass balance record. Precipitation in central Chile (30–37°S) is impacted by tropical sea surface temperature patterns, with precipitation increasing during El Niño Southern Oscillation (ENSO) events, although this association starts to decay North of 30°S (Houston, 2006; Garreaud et al., 2009; Boisier et al., 2018). Interdecadal variations in precipitation have also been ascribed to low-frequency variability in sea surface temperature, captured by the Pacific Decadal Oscillation (PDO) index (Garreaud et al., 2009). Extratropical circulation also conditions precipitation variability in subtropical Chile: the Southern Annular Mode (SAM), also known as the Antarctic Oscillation, is the leading pattern of tropospheric circulation variability south of 20°S and describes the north–south movement of the westerly wind belt that circles Antarctica. A positive correlation between the SAM index and precipitation exist at 30–45°S latitudes, but this correlation quickly decays north of 30°S (Garreaud et al., 2009; Boisier et al., 2018). The Bivariate ENSO index (Smith and Sardeshmukh, 2000) and the reconstructed (1905–2005) (Jones et al., 2009) and station-based (2006–2015), winter (JJA) SAM index were compared with the reconstructed B_a in **Figure 11**.The reconstructed B_a is positively correlated with the ENSO index ($r = 0.41$, $p < 0.01$) and high values of the index are often, but not always, associated with positive mass balance years. There is little correspondence between the reconstructed B_a and the SAM index ($r = 0.13$, $p = 0.13$). These results agree with those found for precipitation and the recent glaciological B_a record (see **Supplementary Material**).

Guanaco Glacier is located south of the so-called Arid Diagonal, a transitional zone separating the tropical circulation cell to the north and the extratropical westerly wind belt to the south. As such, Guanaco Glacier may be particularly sensitive to the displacement of these large-scale circulation features. Winter precipitation in the area are strongly conditioned by the intensity and position of the South Pacific Subtropical High (SPSH). This semi-permanent anticyclone is the surface manifestation of the subsiding branch of the Hadley cell, which in winter migrates north and allows the passage of frontal systems moving eastward from the Pacific (Garreaud, 2009). In recent decades a strengthening and expansion of the SPSH have been observed and attributed to global warming, leading to precipitation decreases from central to southern Chile (Falvey and Garreaud, 2009; Flores-Aqueveque et al., 2019). The

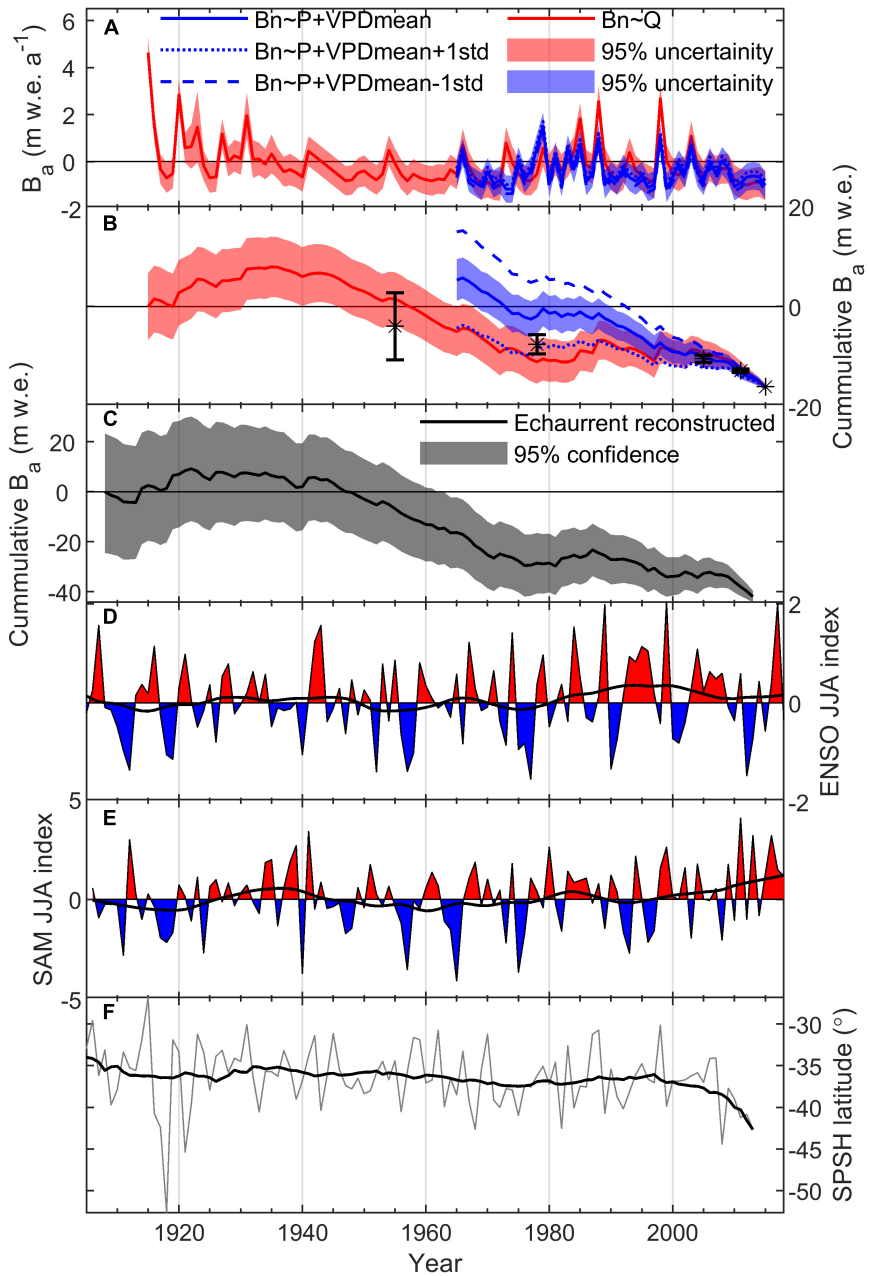


FIGURE 11 | Reconstructed mass balance of Guanaco Glacier. **(A)** Annual mass balance reconstructed from precipitation and vapor pressure deficit (VPD) (blue) and streamflow (red). Thick blue curve: model with mean VPD at La Frontera (1999–2015); upper dashed/lower dotted blue curves: models with mean ± one standard deviation from mean VPD. **(B)** Reconstructed cumulative mass balance of Guanaco Glacier based on precipitation and VPD ± std (blue) and composite streamflow (red). Cumulative geodetic (1955–2011) and glaciological (2011–2015) mass changes were computed backward from 2015 and shown as black asterisk with error bars. **(C)** Reconstructed mass balance of Echaurren Norte Glacier (33.58°S, 70.13°W) (Masiokas et al., 2016). **(D)** JJA Bivariate ENSO index with 21-year lowess curve (black trace); **(E)** Southern Annular Mode (SAM) index, with 21-year lowess curve (black); **(F)** Annual latitudinal position of the South Pacific Subtropical High (SPSH) 1020 isobar, with 21-year lowess curve (black).

decrease in precipitation and related mass loss on Guanaco Glacier may thus be closely associated with the intensity and position of the SPSH. **Figure 12** shows trends in winter (JJA) SLP for the period 1905–2012 computed from the Hadley Centre Sea Level Pressure dataset (HadSLP2) (Allan and Ansell, 2006). Decreasing SLP occur over the Bellingshausen Sea sector of Antarctica and increasing SLP south of the SPSH mean position. A similar pattern was previously highlighted for annual SLP trends by Falvey and Garreaud (2009) for the shorter 1979–2005 period based on reanalysis data. The trend pattern is also similar to the South Pacific dipole pressure pattern which has recently been associated with the so-called "Mega Drought" in

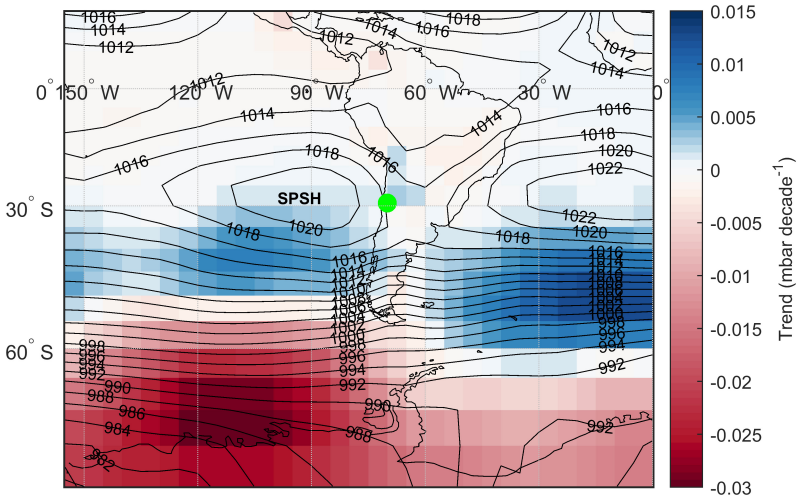


FIGURE 12 | Mean sea-level pressure (SLP) patterns during winter (JJA) over South America (black isobars), and linear trends in SLP (color scale) over the 1905–2012 period. SPSH, South Pacific Subtropical High; Green dot: Guanaco Glacier.

Chile (Garreaud et al., 2019). The increase in SLP south of the SPSH in **Figure 12** may be partly due to the expansion and/or southward migration of the SPSH. The latitudinal migration of the winter SPSH was investigated by tracking the southernmost latitude of the 1020 isobar over time (**Figure 11F**). The latitudinal position of the winter SPSH shows interannual variability as well as a broad negative trend over time, estimated at $-0.21 \pm 0.06°$ decade^{-1} ($p < 0.01$) from linear regression. The SPSH position is significantly correlated with the reconstructed B_a ($r = 0.39$, $p < 0.01$), consistent with the notion that an equatorward migration of the winter SPSH favors the advection of moist air masses and precipitation on the glacier. However, while ENSO and the position of the SPSH are both correlated with the reconstructed B_a, these two indices together can only explain 21% of the variability in the reconstructed B_a. Storms reaching the continent do not always reach the high Andes in winter, due to complicated orographic and synoptic atmospheric processes (Scaff et al., 2017; Viale and Nuñez, 2011) which limits our understanding of dynamical forcing of mass balance based on seasonal averages.

CONCLUSION

This study has brought together and analyzed a unique and diverse glacio-climate dataset comprising recent glaciological mass balance, geodetic and statistical mass balance reconstructions, and ice core measurements in order to investigate the evolution of Guanaco Glacier in the Dry Andes. This is a region where glacier-climate interactions are not yet well constrained, despite the fact that meltwater from snow and glaciers in spring and summer is vital to sustain populations and economic activities. This study showed that the measured mass balance on Guanaco Glacier has been predominantly negative since 2002, and that it is currently mostly sensitive to precipitation variations, while low temperatures, aridity and high solar radiation and wind speeds cause large sublimation losses and limited melting. As such, humidity plays a key role in glacier-climate interactions, with humid conditions favoring precipitation and snow accumulation but also increased ablation due to reduced sublimation and concurrent higher melting.

The reconstructed mass balance shows that the glacier gained mass during the early part of the record (1915–1935), followed by a period with predominantly negative balance (1935–1975), a more neutral period (1975–2005) and sustained mass loss thereafter. Ice core data suggest that high accumulation rates and higher melting prevailed before the early 20th century, matching the earliest period of glacier growth reconstructed from streamflow records. Understanding the causes of precipitation variability is key to understand and project future glacier and snow mass balance variability in the dry Andes. The reconstructed mass balance of Guanaco Glacier was shown to be positively correlated with the ENSO index as well as with the position of the South Pacific Subtropical High (SPSH). The apparent poleward migration of the SPSH observed in this study and elsewhere (Flores-Aqueveque et al., 2019) may have been driving a progressive starvation of precipitation over Guanaco Glacier, culminating in the sustained mass loss observed in the recent decade. Continued migration and/or expansion of the SPSH in the future, as predicted by general circulation models (Flores-Aqueveque et al., 2019), could continue to deplete accumulation on glaciers, exacerbating the ongoing hydrological drought and obliterating the paleoclimate potential of high-altitude glaciers in the Dry Andes.

DATA AVAILABILITY STATEMENT

The datasets generated for this study are available on request to the corresponding author.

AUTHOR CONTRIBUTIONS

CK designed the study, carried out the analyses, and wrote the manuscript. AS carried out geodetic mass balance calculations. PG, NP, LN, and ARa designed the ice coring study. PG and NP carried out glaciochemistry analyses and participated in the interpretation of the ice core data. CK, SM, LN, ARa, ARi, and FS participated in the Guanaco Glacier mass balance monitoring program. All authors reviewed the final manuscript.

FUNDING

Funding to CK was provided by the Natural Sciences and Engineering Research Council of Canada (grant number RGPIN-2015-03844) and the Canada Research Chair Program (grant number 231380). SM and FS were supported by CONICYT-Programa Regional R16A10003. The glacier monitoring program and ice core retrieval in Pascua-Lama was funded by Compañía Minera Nevada.

ACKNOWLEDGMENTS

CK thanks Mariano H. Masiokas for providing the reconstructed Echaurren Norte Glacier data, and the several members at CEAZA who participated in the glacier monitoring program. ARi thanks CECs and all the members of the glaciology laboratory that performed surveys at Guanaco Glacier for several years.

SUPPLEMENTARY MATERIAL

The Supplementary Material for this article can be found online at: https://www.frontiersin.org/articles/10.3389/feart.2020.00040/full#supplementary-material

REFERENCES

Abermann, J., Kinnard, C., and MacDonell, S. (2014). Albedo variations and the impact of clouds on glaciers in the Chilean semi-arid Andes. *J. Glaciol.* 60, 183–191. doi: 10.3189/2014jog13j094

Allan, R., and Ansell, T. (2006). A new globally complete monthly historical gridded mean sea level pressure dataset (HadSLP2): 1850–2004. *J. Clim.* 19, 5816–5842. doi: 10.1175/jcli3937.1

Arenson, L. U., Jakob, M., and Wainstein, P. (2015). "Effects of dust deposition on glacier ablation and runoff at the Pascua-Lama Mining Project, Chile and Argentina," in *Engineering Geology for Society and Territory-Volume 1*, G. Lollino, A. Manconi, J. Clague, W. Shan, and M. Chiarle, (Cham: Springer), 27–32. doi: 10.1007/978-3-319-09300-0_6

Ayala, A., Pellicciotti, F., MacDonell, S., Mcphee, J., and Burlando, P. (2017). Patterns of glacier ablation across North-Central Chile: identifying the limits of empirical melt models under sublimation-favorable conditions. *Water Resour. Res.* 53, 5601–5625. doi: 10.1002/2016wr020126

Barcaza, G., Nussbaumer, S. U., Tapia, G., Valdés, J., García, J.-L., Videla, Y., et al. (2017). Glacier inventory and recent glacier variations in the Andes of Chile, South America. *Ann. Glaciol.* 58, 166–180. doi: 10.1017/aog.2017.28

Barnett, T. P., Adam, J. C., and Lettenmaier, D. P. (2005). Potential impacts of a warming climate on water availability in snow-dominated regions. *Nature* 438, 303–309. doi: 10.1038/nature04141

Bergeron, V., Berger, C., and Betterton, M. (2006). Controlled irradiative formation of penitentes. *Phys. Rev. Lett.* 96:098502.

Boisier, J. P., Alvarez-Garretón, C., Cordero, R. R., Damiani, A., Gallardo, L., Garreaud, R. D., et al. (2018). Anthropogenic drying in central-southern Chile evidenced by long-term observations and climate model simulations. *Elem. Sci. Anth.* 6:74. doi: 10.1525/elementa.328

Bolius, D., Schwikowski, M., Jenk, T., Gäggeler, H. W., Casassa, G., and Rivera, A. (2006). A first shallow firn-core record from Glaciar La Ollada, Cerro Mercedario, central Argentine Andes. *Ann. Glaciol.* 43, 14–22. doi: 10.3189/172756406781812474

Bown, F., Rivera, A., and Acuna, C. (2008). Recent glacier variations at the Aconcagua basin, central Chilean Andes. *Ann. Glaciol.* 48, 43–48. doi: 10.3189/172756408784700572

Bozkurt, D., Rojas, M., Boisier, J. P., and Valdivieso, J. (2017). Climate change impacts on hydroclimatic regimes and extremes over Andean basins in central Chile. *Hydrol. Earth Syst. Sci. Discuss.* 2017, 1–29. doi: 10.5194/hess-2016-690

Brenning, A. (2008). "The impact of mining on rock glaciers and glaciers," in *Darkening Peaks: Glacier Retreat, Science, and Society*, eds B. S. Orlove, E. Wiegandt, and B. Luckman, (Oakland, CA: University of California Press).

Cabré, M. F., Solman, S., and Núñez, M. (2016). Regional climate change scenarios over southern South America for future climate (2080-2099) using the MM5 Model. Mean, interannual variability and uncertainties. *Atmósfera* 29, 35–60. doi: 10.20937/atm.2016.29.01.04

Cathles, L. M., Abbot, D. S., and Macayeal, D. R. (2014). Intra-surface radiative transfer limits the geographic extent of snow penitents on horizontal snowfields. *J. Glaciol.* 60, 147–154. doi: 10.3189/2014jog13j124

Cauquoin, A., Jean-Baptiste, P., Risi, C., Fourré, É, Stenni, B., and Landais, A. (2015). The global distribution of natural tritium in precipitation simulated with an Atmospheric General Circulation Model and comparison with observations. *Earth Planet. Sci. Lett.* 427, 160–170. doi: 10.1016/j.epsl.2015.06.043

Ciric, A., Gäggeler, H., and Schwikowski, M. (2010). "ENSO related accumulation variability on cerro Mercedario," in *Paul Scherrer Institut, Labor für Radio- und Umweltchemie, Annual Report 2009*, eds B. S. Orlove, E. Wiegandt, and B. Luckman, (Berkeley, CA: Lawrence Berkeley National Laboratory).

Cogley, J. G. (2009). Geodetic and direct mass balance measurements: comparison and joint analysis. *Ann. Glaciol.* 50, 96–100. doi: 10.3189/172756409787769744

Cuffey, K. M., and Paterson, W. S. B. (2010). *The Physics of Glaciers*, 4th Edn. Amsterdam: Academic Press.

Dansgaard, W. (1964). Stable isotopes in precipitation. *Tellus* 16, 436–468.

Dussaillant, I., Berthier, E., Brun, F., Masiokas, M., Hugonnet, R., Favier, V., et al. (2019). Two decades of glacier mass loss along the Andes. *Nat. Geosci.* 12, 802–808. doi: 10.1038/s41561-019-0432-5

Escobar, F., Pozo, V., Salazar, A., and Oyarzo, M. (1995). *"Balance de Masa en el Glaciar Echaurren Norte, 1975 a 1992" Publicación DGA, H. A. y G. 97/1, Dirección General de Aguas*. (Santiago: InteRNA Technologies B.V).

Falvey, M., and Garreaud, R. D. (2009). Regional cooling in a warming world: recent temperature trends in the southeast Pacific and along the west coast of subtropical South America (1979–2006). *J. Geophys. Res. Atmos.* 114:D04102. doi: 10.1029/2008JD010519

Favier, V., Falvey, M., Rabatel, A., Praderio, E., and López, D. (2009). Interpreting discrepancies between discharge and precipitation in high-altitude area of Chile's Norte Chico region (26–32(S). *Water Resour. Res.* 45:W02424.

Fiebig-Wittmaack, M., Astudillo, O., Wheaton, E., Wittrock, V., Perez, C., and Ibacache, A. (2012). Climatic trends and impact of climate change on agriculture in an arid Andean valley. *Clim. Change* 111, 819–833. doi: 10.1007/s10584-011-0200-z

Fields, S. (2006). The price of gold in Chile. *Environ. Health Perspect.* 114, A536–A539.

Flantua, S. G., Hooghiemstra, H., Vuille, M., Behling, H., Carson, J. F., Gosling, W., et al. (2016). Climate variability and human impact in South America during the

last 2000 years: synthesis and perspectives from pollen records. *Clim. Past* 12, 483–523. doi: 10.5194/cp-12-483-2016

Flores-Aqueveque, V., Rojas, M., Aguirre, C., Arias, P. A., and González, C. (2019). South Pacific Subtropical High from the late Holocene to the end of the 21st century: insights from climate proxies and general circulation models. *Clim. Past* 16, 79–99. doi: 10.5194/cp-16-79-2020

Fountain, A. G., and Tangborn, W. V. (1985). The effect of glaciers on streamflow variations. *Water Resour. Res.* 21, 579–586. doi: 10.1029/wr021i004p00579

Garreaud, R. (2009). The Andes climate and weather. *Adv. Geosci.* 22, 3–11. doi: 10.5194/adgeo-22-3-2009

Garreaud, R. D., Alvarez-Garreton, C., Barichivich, J., Boisier, J. P., Christie, D., Galleguillos, M., et al. (2017). The 2010-2015 megadrought in central Chile: impacts on regional hydroclimate and vegetation. *Hydrol. Earth Syst. Sci.* 21, 6307–6327. doi: 10.5194/hess-21-6307-2017

Garreaud, R. D., Boisier, J. P., Rondanelli, R., Montecinos, A., Sepúlveda, H. H., and Veloso-Aguila, D. (2019). The central Chile mega drought (2010–2018): a climate dynamics perspective. *Int. J. Climatol.* 40, 421–439. doi: 10.1002/joc.6219

Garreaud, R. D., Vuille, M., Compagnucci, R., and Marengo, J. (2009). Present-day South American climate. *Palaeogeogr. Palaeoclimatol. Palaeoecol.* 281, 180–195. doi: 10.1016/j.palaeo.2007.10.032

Gascoin, S., Kinnard, C., Ponce, R., MacDonell, S., Lhermitte, S., and Rabatel, A. (2011). Glacier contribution to streamflow in two headwaters of the Huasco River, Dry Andes of Chile. *Cryosphere* 5, 1099–1113. doi: 10.5194/tc-5-1099-2011

Gascoin, S., Lhermitte, S., Kinnard, C., Bortels, K., and Liston, G. E. (2013). Wind effects on snow cover in Pascua-Lama, Dry Andes of Chile. *Adv. Water Resour.* 55, 25–39. doi: 10.1016/j.advwatres.2012.11.013

Ginot, P., Kull, C., Schotterer, U., Schwikowski, M., and Gäggeler, H. (2006). Glacier mass balance reconstruction by sublimation induced enrichment of chemical species on Cerro Tapado (Chilean Andes). *Clim. Past* 2, 21–30. doi: 10.5194/cp-2-21-2006

Ginot, P., Stampfli, F., Stampfli, D., Schwikowski, M., and Gaggeler, H. (2002). FELICS, a new ice core drilling system for high-altitude glaciers. *Mem. Natl. Inst. Polar Res.* 56, 38–48.

Golder Associates, (2005). *Estudios de Campo de Hielo y Glaciares Proyecto Pascua-Lama, Chile*. Santiago: Golder Associates S.A.

Grumet, N. S., Wake, C. P., Zielinski, G. A., Fisher, D., Koerner, R., and Jacobs, J. D. (1998). Preservation of glaciochemical time-series in snow and ice from the Penny Ice Cap, Baffin Island. *Geophys. Res. Lett.* 25, 357–360. doi: 10.1029/97gl03787

Hock, R. (2005). Glacier melt: a review of processes and their modelling. *Prog. Phys. Geogr.* 29, 362–391. doi: 10.1191/0309133305pp453ra

Hoffmann, G., Ramirez, E., Taupin, J. D., Francou, B., Ribstein, P., Delmas, R., et al. (2003). Coherent isotope history of Andean ice cores over the last century. *Geophys. Res. Lett.* 30:1179. doi: 10.1029/2002GL014870

Houston, J. (2006). Variability of precipitation in the Atacama Desert: its causes and hydrological impact. *Int. J. Climatol.* 26, 2181–2198. doi: 10.1002/joc.1359

Huss, M. (2011). Present and future contribution of glacier storage change to runoff from macroscale drainage basins in Europe. *Water Resour. Res.* 47:W07511.

Iribarren Anacona, P., Mackintosh, A., and Norton, K. P. (2015). Hazardous processes and events from glacier and permafrost areas: lessons from the Chilean and Argentinean Andes. *Earth Surf. Process. Landf.* 40, 2–21. doi: 10.1002/esp.3524

Jansson, P., Hock, R., and Schneider, T. (2003). The concept of glacier storage: a review. *J. Hydrol.* 282, 116–129. doi: 10.1016/s0022-1694(03)00258-0

Jones, J. M., Fogt, R. L., Widmann, M., Marshall, G. J., Jones, P. D., and Visbeck, M. (2009). Historical SAM variability. Part I: Century-length seasonal reconstructions. *J. Clim.* 22, 5319–5345. doi: 10.1175/2009jcli2785.1

Juliá, C., Rahn, D. A., and Rutllant, J. A. (2012). Assessing the influence of the MJO on strong precipitation events in subtropical, semi-arid north-central Chile (30 S). *J. Clim.* 25, 7003–7013. doi: 10.1175/jcli-d-11-00679.1

Kaser, G. (2001). Glacier-climate interaction at low latitudes. *J. Glaciol.* 47, 195–204. doi: 10.3189/172756501781832296

Kinnard, C., Koerner, R. M., Zdanowicz, C. M., Fisher, D. A., Zheng, J., Sharp, M. J., et al. (2008). Stratigraphic analysis of an ice core from the Prince of Wales Icefield, Ellesmere Island, Arctic Canada, using digital image analysis: High-resolution density, past summer warmth reconstruction, and melt effect on ice core solid conductivity. *J. Geophys. Res. Atmos.* 113:D24120. doi: 10.1029/2008JD011083

Koerner, R. M. (1997). Some comments on climatic reconstructions from ice cores drilled in areas of high melt. *J. Glaciol.* 43, 90–97. doi: 10.1017/s0022143000002847

Kronenberg, J. (2013). Linking ecological economics and political ecology to study mining, glaciers and global warming. *Environ. Policy Gov.* 23, 75–90. doi: 10.1002/eet.1605

Kull, C., Grosjean, M., and Veit, H. (2002). Modeling modern and Late Pleistocene glacio-climatological conditions in the north Chilean Andes (29–30). *Clim. Change* 52, 359–381.

Leiva, J., Cabrera, G., and Lenzano, L. (2007). 20 years of mass balances on the Piloto glacier, Las Cuevas river basin, Mendoza, Argentina. *Glob. Planet. Change* 59, 10–16. doi: 10.1016/j.gloplacha.2006.11.018

Lhermitte, S., Abermann, J., and Kinnard, C. (2014). Albedo over rough snow and ice surfaces. *Cryosphere* 8, 1069–1086. doi: 10.5194/tc-8-1069-2014

Lliboutry, L. (1954). The origin of penitents. *J. Glaciol.* 2, 331–338. doi: 10.1017/s0022143000025181

MacDonell, S., Kinnard, C., Mölg, T., Nicholson, L., and Abermann, J. (2013). Meteorological drivers of ablation processes on a cold glacier in the semi-arid Andes of Chile. *Cryosphere* 7, 1513–1526. doi: 10.5194/tc-7-1513-2013

Masiokas, M. H., Christie, D. A., Le Quesne, C., Pitte, P., Ruiz, L., Villalba, R., et al. (2016). Reconstructing the annual mass balance of the Echaurren Norte glacier (Central Andes, 33.5 S) using local and regional hydroclimatic data. *Cryosphere* 10, 927–940. doi: 10.5194/tc-10-927-2016

Masiokas, M. H., Rivera, A., Espizua, L. E., Villalba, R., Delgado, S., and Aravena, J. C. (2009). Glacier fluctuations in extratropical South America during the past 1000 years. *Palaeogeogr. Palaeoclimatol. Palaeoecol.* 281, 242–268. doi: 10.1016/j.palaeo.2009.08.006

Montecinos, A., and Aceituno, P. (2003). Seasonality of the ENSO-related rainfall variability in central Chile and associated circulation anomalies. *J. Clim.* 16, 281–296. doi: 10.1175/1520-0442(2003)016<0281:soterr>2.0.co;2

Moore, J. C., Grinsted, A., Kekonen, T., and Pohjola, V. (2005). Separation of melting and environmental signals in an ice core with seasonal melt. *Geophys. Res. Lett.* 32:L10501. doi: 10.1029/2005GL023039

Naruse, R., and Leiva, J. C. (1997). Preliminary study on the shape of snow penitents at Piloto Glacier, the Central Andes. *Bull. Glacier Res.* 15, 99–104.

Neukom, R., and Gergis, J. (2012). Southern Hemisphere high-resolution palaeoclimate records of the last 2000 years. *Holocene* 22, 501–524. doi: 10.1177/0959683611427335

Nicholson, L., Marín, J., Lopez, D., Rabatel, A., Bown, F., and Rivera, A. (2009). Glacier inventory of the upper Huasco valley, Norte Chico, Chile: glacier characteristics, glacier change and comparison with central Chile. *Ann. Glaciol.* 50, 111–118. doi: 10.3189/172756410790595787

Nuth, C., and Kääb, A. (2011). Co-registration and bias corrections of satellite elevation data sets for quantifying glacier thickness change. *Cryosphere* 5, 271–290. doi: 10.5194/tc-5-271-2011

Oerlemans, J. (2001). *Glaciers and Climate Change*. Hardcover: CRC Press.

Østrem, G., and Brugman, M. (1991). *Glacier Mass balance Measurements: A Manual for Field and Office Work (NHRl Science Report)*. Saskatoon: National Hydrological Research Institute.

Østrem, G., and Haakensen, N. (1999). Map comparison or traditional mass balance measurements: Which method is better? *Geogr. Ann.* 81, 703–713.

Oyarzún, J., and Oyarzún, R. (2011). Sustainable development threats, inter-sector conflicts and environmental policy requirements in the arid, mining rich, northern Chile territory. *Sustain. Dev.* 19, 263–274. doi: 10.1002/sd.441

Peña, H., and Escobar, F. (1987). *Análisis del Aluvión de Mayo de 1985 del Río Manflas, Cuenca del Río Copiapó*. Santiago: Ministerio de Obras Públicas.

Pohjola, V., Moore, J., Isaksson, E., Jauhiainen, T., Van De Wal, R., Martma, T., et al. (2002). Effect of periodic melting on geochemical and isotopic signals in an ice core from Lomonosovfonna, Svalbard. *J. Geophys. Res. Atmos.* 107:4036.

Putman, A. L., Fiorella, R. P., Bowen, G. J., and Cai, Z. (2019). A global perspective on local meteoric water lines: meta-analytic insight into fundamental controls and practical constraints. *Water Resour. Res.* 55, 6896–6910. doi: 10.1029/2019wr025181

Quintana, J., and Aceituno, P. (2012). Changes in the rainfall regime along the extratropical west coast of South America (Chile): 30-43° S. *Atmósfera* 25, 1–22.

Rabatel, A., Castebrunet, H., Favier, V., Nicholson, L., and Kinnard, C. (2011). Glacier changes in the Pascua-Lama region, Chilean Andes (29 ° S): recent mass balance and 50 yr surface area variations. *Cryosphere* 5, 1029–1041. doi: 10.5194/tc-5-1029-2011

Réveillet, M., MacDonell, S., Gascoin, S., Kinnard, C., Lhermitte, S., and Schaffer, N. (2020). Impact of forcing on sublimation simulations for a high mountain catchment in the semiarid Andes. *Cryosphere* 14, 147–163. doi: 10.5194/tc-14-147-2020

Rolstad, C., Haug, T., and Denby, B. (2009). Spatially integrated geodetic glacier mass balance and its uncertainty based on geostatistical analysis: application to the western Svartisen ice cap. *Norway. J. Glaciol.* 55, 666–680. doi: 10.3189/002214309789470950

Rupper, S., and Roe, G. (2008). Glacier changes and regional climate: a mass and energy balance approach. *J. Clim.* 21, 5384–5401. doi: 10.1175/2008jcli2219.1

Sagredo, E., and Lowell, T. (2012). Climatology of Andean glaciers: a framework to understand glacier response to climate change. *Glob. Planet. Change* 86, 101–109. doi: 10.1016/j.gloplacha.2012.02.010

Sagredo, E. A., Rupper, S., and Lowell, T. V. (2014). Sensitivities of the equilibrium line altitude to temperature and precipitation changes along the Andes. *Quat. Res.* 81, 355–366. doi: 10.1016/j.yqres.2014.01.008

Scaff, L., Rutllant, J. A., Rahn, D., Gascoin, S., and Rondanelli, R. (2017). Meteorological interpretation of orographic precipitation gradients along an Andes west slope basin at 30 S (Elqui Valley, Chile). *J. Hydrometeorol.* 18, 713–727. doi: 10.1175/jhm-d-16-0073.1

Schotterer, U., Grosjean, M., Stichler, W., Ginot, P., Kull, C., Bonnaveira, H., et al. (2003). "Glaciers and climate in the Andes between the Equator and 30(S: what is recorded under extreme environmental conditions?" in *Climate Variability and Change in High Elevation Regions: Past, Present & Future*, ed. H. F. Diaz, (Dordrecht: Springer), 157–175. doi: 10.1007/978-94-015-1252-7_9

Schotterer, U., Schwarz, P., and Rajner, V. (1998). "From pre-bomb levels to industrial times: a complete tritium record from an alpine ice core and its relevance for environmental studies," in *Proceedings of the Isotope Techniques in the Study of Environmental Change* (Vienna: International Atomic Energy Agency).

Schulz, N., Boisier, J., and Aceituno, P. (2012). Climate change along the arid coast of northern Chile. *Int. J. Climatol.* 32, 1803–1814. doi: 10.1002/joc.2395

Sinclair, K. E., and MacDonell, S. (2016). Seasonal evolution of penitente glaciochemistry at Tapado Glacier, Northern Chile. *Hydrol. Process.* 30, 176–186. doi: 10.1002/hyp.10531

Smith, C. A., and Sardeshmukh, P. D. (2000). The effect of ENSO on the intraseasonal variance of surface temperatures in winter. *Int. J. Climatol.* 20, 1543–1557. doi: 10.1002/1097-0088(20001115)20:13<1543::aid-joc579>3.0.co;2-a

Stichler, W., Schotterer, U., Fröhlich, K., Ginot, P., Kull, C., Gäggeler, H., et al. (2001). Influence of sublimation on stable isotope records recovered from high-altitude glaciers in the tropical Andes. *J. Geophys. Res.* 106, 22613–22620. doi: 10.1029/2001jd900179

Stigter, E. E., Litt, M., Steiner, J. F., Bonekamp, P. N., Shea, J. M., Bierkens, M. F., et al. (2018). The importance of snow sublimation on a Himalayan glacier. *Front. Earth Sci.* 6:108. doi: 10.3389/feart.2018.00108

Surazakov, A. B., and Aizen, V. B. (2006). Estimating volume change of mountain glaciers using SRTM and map-based topographic data. *IEEE Transact. Geosci. Remote Sens.* 44, 2991–2995. doi: 10.1109/tgrs.2006.875357

Thibert, E., Blanc, R., Vincent, C., and Eckert, N. (2008). Glaciological and volumetric mass balance measurements: error analysis over 51 years for Glacier de Sarennes, French Alps. *J. Glaciol.* 54, 522–532. doi: 10.3189/002214308785837093

Thompson, L. G. (2000). Ice core evidence for climate change in the Tropics: implications for our future. *Quat. Sci. Rev.* 19, 19–35. doi: 10.1016/s0277-3791(99)00052-9

Torrence, C., and Compo, G. P. (1998). A practical guide to wavelet analysis. *Bull. Am. Meteorol. Soc.* 79, 61–78.

Valdés-Pineda, R., Pizarro, R., García-Chevesich, P., Valdés, J. B., Olivares, C., Vera, M., et al. (2014). Water governance in Chile: availability, management and climate change. *J. Hydrol.* 519, 2538–2567.

Viale, M., and Nuñez, M. N. (2011). Climatologyof winter orographic precipitation over the subtropical central Andes and associated synoptic and regional characteristics. *J. Hydrometeorol.* 12, 481–507. doi: 10.1175/2010jhm1284.1

Vimeux, F., Ginot, P., Schwikowski, M., Vuille, M., Hoffmann, G., Thompson, L. G., et al. (2009). Climate variability during the last 1000 years inferred from Andean ice cores: a review of methodology and recent results. *Palaeogeogr. Palaeoclimatol. Palaeoecol.* 281, 229–241. doi: 10.1016/j.palaeo.2008.03.054

Viviroli, D., Dürr, H. H., Messerli, B., Meybeck, M., and Weingartner, R. (2007). Mountains of the world, water towers for humanity: typology, mapping, and global significance. *Water Resour. Res.* 43:W07447.

WGMS, (ed.) (2017). *Global Glacier Change Bulletin No. 2 (2014-2015)*. Zurich: World Glacier Monitoring Service.

Whillans, I., and Grootes, P. (1985). Isotopic diffusion in cold snow and firn. *J. Geophys. Res. Atmos.* 90, 3910–3918.

Wilks, D. S. (2011). *Statistical Methods in the Atmospheric Sciences*. Oxford: Academic press.

Young, G., Zavala, H., Wandel, J., Smit, B., Salas, S., Jimenez, E., et al. (2010). Vulnerability and adaptation in a dryland community of the Elqui Valley Chile. *Clim. Change* 98, 245–276. doi: 10.1007/s10584-009-9665-4

Zemp, M., Thibert, E., Huss, M., Stumm, D., Rolstad Denby, C., Nuth, C., et al. (2013). Reanalysing glacier mass balance measurement series. *Cryosphere* 7, 1227–1245. doi: 10.5194/tc-7-1227-2013

Conflict of Interest: Funding for the mass balance monitoring program and ice coring was provided by the Compañía Minera Nevada in order to implement a Glacier monitoring plan approved by Comisión Regional del Medio Ambiente (Corema) de la Región de Atacama, Chile. The authors declare no personal nor financial conflict of interest related to the results presented in this study.

Copyright © 2020 Kinnard, Ginot, Surazakov, MacDonell, Nicholson, Patris, Rabatel, Rivera and Squeo. This is an open-access article distributed under the terms of the Creative Commons Attribution License (CC BY). The use, distribution or reproduction in other forums is permitted, provided the original author(s) and the copyright owner(s) are credited and that the original publication in this journal is cited, in accordance with accepted academic practice. No use, distribution or reproduction is permitted which does not comply with these terms.

frontiers in Earth Science

ORIGINAL RESEARCH
published: 28 February 2020
doi: 10.3389/feart.2020.00017

Future Meteorological Droughts in Ecuador: Decreasing Trends and Associated Spatio-Temporal Features Derived From CMIP5 Models

Lenin Campozano[1]*, *Daniela Ballari*[2], *Martin Montenegro*[3] and *Alex Avilés*[3]

[1] Departamento de Ingeniería Civil y Ambiental, Escuela Politécnica Nacional, Quito, Ecuador, [2] IERSE, Facultad de Ciencia y Tecnología, Universidad del Azuay, Cuenca, Ecuador, [3] Facultad de Ciencias Químicas, Universidad de Cuenca, Cuenca, Ecuador

Droughts are one of the most spatially extensive disasters that are faced by societies. Despite the urgency to define mitigation strategies, little research has been done regarding droughts related to climate change. The challenges are due to the complexity of droughts and to future precipitation uncertainty from Global Climate Models (GCMs). It is well-known that climate change will have more impact on developing countries. This is the case for Ecuador, which also has the additional challenges of lacking meteorological drought studies covering its three main regions: Coast, Highlands, and Amazon, and of having an intricate orography. Thus, this study assesses the spatio-temporal characteristics of present and future droughts in Ecuador under Representative Concentrations Pathways (RCP) 4.5 and 8.5. The 10 km dynamically downscaled products (DGCMs) from Coupled Model Intercomparison Project 5 (CMIP5) was used. The Standardized Precipitation Index (SPI) for droughts was calculated pixel-wise for present time 1981–2005 and for future time 2041-2070. The results showed a slightly decreasing trend for future droughts for the whole country, with a larger reduction for moderate droughts, followed by severe and extreme drought events. In the Coast and Highland regions, the intra-annual analysis showed a reduction of moderate and severe future droughts for RCP 4.5 and for RCP 8.5 throughout the year. Extreme droughts showed small and statistically non-significant decreases. In the Amazon region, moderate droughts showed increases from May to October, and decreases for the rest of the year. Additionally, severe drought increases are expected from May to December, and decreases from January to April. Finally, extreme drought increases are expected from January to April, with larger increases in October and November. Thus, in the Amazon, the rainy period showed a decreasing trend of droughts, following the wetter in wet- and drier in dry paradigm. Climate change causes decision-making process and calls for adaptation strategies being more challenging. In this context, our study has contributed to better mapping the space-time evolution of future drought risk in Ecuador, thus providing valuable information for water management and decision making as Ecuador faces climate change.

Keywords: climate change, weather research, forecasting models, climate extremes, spatial-temporal projections, tropical region

OPEN ACCESS

Edited by:
Bryan G. Mark,
The Ohio State University,
United States

Reviewed by:
Chenghai Wang,
Lanzhou University, China
Ana Cristina Russo,
University of Lisbon, Portugal

***Correspondence:**
Lenin Campozano
lenin.campozano@epn.edu.ec

Specialty section:
This article was submitted to Atmospheric Science, a section of the journal Frontiers in Earth Science

Received: *15 August 2019*
Accepted: *20 January 2020*
Published: *28 February 2020*

Citation:
Campozano L, Ballari D, Montenegro M and Avilés A (2020) Future Meteorological Droughts in Ecuador: Decreasing Trends and Associated Spatio-Temporal Features Derived From CMIP5 Models. Front. Earth Sci. 8:17. doi: 10.3389/feart.2020.00017

INTRODUCTION

Droughts are a transitory climatic anomaly, where the water availability is below average during a prolonged period of time limiting its supply for human needs and ecosystems. Among the most significant impacts of droughts to the environment are the acceleration of desertification processes, the increase in the risk of forest fires, the reduction of the availability of water resources for domestic and industrial use and the damage done to animals and vegetation (Mishra and Singh, 2010). In addition, droughts in sensitive climate regions have world-wide effects, as it was the case for the 2005 and 2010 Amazon droughts (Espinoza et al., 2011), where the changes in net biomass and mortality of old rainforest affected the CO_2 balance in the most important CO_2 sink of the planet (Phillips et al., 2009). These facts made the complexity of this phenomenon explicit. For instance, droughts are initiated by a meteorological drought, then they generate a hydrological drought, which may produce an agricultural drought and, in cases of prolonged occurrence, may cause a socio-economic drought (Podestá et al., 2015). The final stage of a socio-economic drought may cause negative impacts, such as the loss of crops and livestock, a decrease in hydroelectric generation, migration, landscape degradation or social conflicts, among others (Wilhite et al., 2007).

The last century increase of the global mean temperature is unprecedented in scales from decades to centuries (Mora et al., 2014). Such a temperature increase has produced generalized changes in spatio-temporal precipitation patterns, sea salinity (Heuzé et al., 2015), wind patterns, heat waves, and more intensity in tropical cyclones and droughts (Dai, 2013); all these phenomena are attributed to climate change (CC) (Allen and Ingram, 2002; Mach et al., 2016). Despite that several studies link CC with the increase of droughts' severity and occurrence, it is acknowledged that the impacts of CC are diverse and even contrasting depending on the specific region of study. For instance, some studies (Dai, 2011; Sillmann et al., 2013; Wang and Chen, 2014; Huang et al., 2016) suggest that droughts will be more extreme and frequent, producing an increase of dryland by the end of the century. In addition, Dai (2011) and Sillmann et al. (2013) showed that extreme precipitation will become more frequent, with the Representative Concentrations Pathway (RCP) 8.5 presenting the most extreme changes in Central America, Australia, South Africa and in the Mediterranean region. In east China, Chen and Sun (2017) suggested that droughts could increase by the end of the century by ca. 31% for RCP 4.5 and almost double for RCP 8.5. Burke et al. (2006) reported that projections with the Palmer Drought Severity Index (PDSI) suggest that, compared to the current coverage, droughts may affect ca. 30% of the world land area by the year 2100, which is ∼1% using the A2 scenario. In southern South America, Penalba and Rivera (2013) showed that the occurrence of droughts will be more frequent in the twenty-first century. Also, precipitation is expected to increase in high latitude regions of the northern hemisphere (Feng et al., 2014) under CC conditions.

The few studies conducted in north-western South America present contrasting projections in CC conditions, primarily due to the complex orography of the Andes and several climatic influences such as El Niño Southern Oscillation (ENSO), its tropical location, the Amazon rainforest producing high evapotranspiration rates, and the influence of the easterlies. For instance, for the eastern Amazon, Duffy et al. (2015) show an increase of meteorological droughts under RCP 8.5, while for the western Amazon the opposite was found. Steinhoff et al. (2015) show drier projections for Colombia and Central America and wetter conditions for southwestern Colombia, Ecuador and northern Peru in future CC conditions. Despite these results, no temporal trends are found for the last 50 to 100 years in droughts in the Amazon river. Contrarily, there is evidence that flooding events are becoming more frequent and severe (Barichivich et al., 2018).

More specifically in Ecuador, drought studies are scarce despite the potential impacts that CC and droughts may have on agriculture, energy, biodiversity, forest, marine and hydrologic resources (Fontaine et al., 2008). Identifying the potential spatio-temporal patterns of droughts in Ecuador has major relevance due to its high volume of crops production (Peralta et al., 2018) and due to the country's economy dependence on hydroelectricity. By the year 2000, the water deficit already affected several Ecuadorian river basins like Esmeraldas, Portoviejo, Chone, Jama, Briceño, Pastaza, Paute, Mira, Carchi, and Napo during the dry season. Such events produced losses of ca. 45% of transitory crops and of 11% of perennial crop (Ministerio del Ambiente, 2009). The complexity of drought events added to the conspicuous patterns of precipitation in the three natural regions in Ecuador, i.e., the Coast, the Highlands and the Amazon, makes the study of droughts necessary for an adequate water management in the country.

Studies about drought forecasting in the highlands of Ecuador were conducted by Avilés et al. (2015). They developed a drought index using first and second order Markov chains in the Chulco river sub-basin in the Andes. Additionally, Avilés et al. (2016) compared Markov chains and Bayesian network models for drought predictions. Domínguez-Castro et al. (2018) conducted an interesting study in the highlands in Quito, the capital of Ecuador, using 125 years (period 1891–2015) of precipitation observations from one ground station, and the registry of the rogation ceremonies in the Chapel Acts of Quito, from 1600 to 1822. They inferred that the most important drought periods were 1692–1701, 1718–1723, 1976–1980, 1990–1993, and 2001–2006, nevertheless no climatic evidence was linked to such events. In relation to the influence of ENSO on drought patterns, Vicente-Serrano et al. (2017) showed that drought influence has two patterns: (i) in the Andean mountains where there are no changes in trends of drought severity, linked to teleconnections with Sea Surface Temperature (SST) in El Niño 3.4 region, and (ii) in the coastal region showing trends to less severe and frequent droughts, linked to the local SST in the El Niño 1+2 region. In the same line of research, Zambrano Mera et al. (2018) used ENSO as a predictor of droughts for the coast of Ecuador. Nonetheless, important drought events need further study. For instance, the drought that occurred in 2005 showed anomalously negative precipitation in the coast and in the Amazon, and an above normal precipitation in the highlands, which was related to the anomalously warmed North Tropical Atlantic

(Marengo et al., 2008) producing a northward displacement of the ITCZ and a strong drought in the Amazon. This event showed drought spatial patterns different to those caused by ENSO. Therefore, there is a clear gap of knowledge related to the climatologic characteristics of droughts in Ecuador, and furthermore, a country-wide evaluation of present and future drought projections in Ecuador by GCMs.

Therefore, the aim of this study is 2-fold: (i) assess the representation of droughts from dynamically downscaled GCMs in the present; and (ii) evaluate the spatio-temporal structure and variability of future meteorological droughts in Ecuador under RCP 4.5 and RCP 8.5 scenarios. This is done by using three products (GISS, CSIRO, and IPSL) from the Coupled Model Intercomparison Project 5 (CMIP5) of the Third National Communication on Climate Change. The Standardized Precipitation Index (SPI) was used to characterize extreme, severe and moderate droughts in the present (period 1981–2005) and the future (period 2041–2070). This study contributes to the spatial and temporal characterization of present and future droughts, and offers a contrasting analysis between them.

STUDY AREA

The study area is the continental region of Ecuador (ca. 256.370 km^2), located over the equatorial line in South America (**Figure 1A**). Continental Ecuador presents three natural regions (**Figure 1B**), i.e., the Coastal region which is ca. 100 km wide, located on the western side of the Andes and next to the Pacific Ocean; the inter-Andean region (up to 6,300 m a.s.l.) which acts as a weather divide between the coast and the Amazon; and on the eastern plains of the Andes, the Amazon region, with heights below 300 m a.s.l. (Naranjo, 1981). Around 60% of Ecuador's population (ca. 16.5 million people in total) is dedicated to agriculture, mainly cultivating bananas, flowers, cacao and fruits. Ecuador is one of the 10 biggest producers of bananas in the world, representing ca. 30% of the world's total production (Orozco, 2017). Thus, an increment in the inter-annual variability of precipitation can produce losses in agrobusiness, making it necessary to implement mitigation strategies.

Ecuador's hydroelectric potential is high. Especially in the last two decades, several hydroelectric projects were constructed, such as Coca Codo Sinclair, Sopladora, Manduriaco, Toachi Pilatón among others, producing ca. 90% of the total demand for electricity (Ministerio de Electricidad y Energía Renovable, 2018).

The three main climatic regions of Ecuador (Coast, Highlands and Amazon) have their own climatic characteristics. The large-scale signal of precipitation is regulated by the Inter-Tropical Convergence Zone (ITCZ) producing two rainy seasons, March-April and October-November (Bendix and Lauer, 1992; Campozano et al., 2016b). During these seasons, the influence of the ITCZ enhances convection, producing strong precipitation, especially during afternoons. This regime of precipitation is characteristic for the inter-Andean valleys in the highlands. However, in the coast of Ecuador, the south Pacific anticyclone (Bendix and Lauer, 1992) produces an important modification to the bi-modal influence of the ITCZ, creating a unimodal regime. The inhibition of precipitation during October-November is due to the seasonality of the south Pacific Anticyclone, bringing dry air and stability from the coasts of Chile to the coasts of Ecuador. With respect to the Amazon, in addition to the bi-modal regime of precipitation related to the ITCZ, precipitation is enhanced from June to August due to the increment of the easterlies (Campozano et al., 2016b).

MATERIALS

Precipitation *in-situ* Observations

Monthly observations of precipitation belonging to 172 ground stations were obtained from the Instituto Nacional de Meteorología e Hidrología de Ecuador (INAMHI). Quality control was done in four steps. Firstly, missing data was quantified, selecting stations with <10% of gaps. Despite a recommended bound of 5% (WMO—World Meteorological Organization, 2009), a 10% threshold was applied to keep a useful amount of stations for analysis. Secondly, outliers were identified using interquartile criteria (Campozano et al., 2015). Then, data homogeneity was checked to identify variability due to external factors, such as equipment or location changes for the ground stations. In this case, the analysis developed by

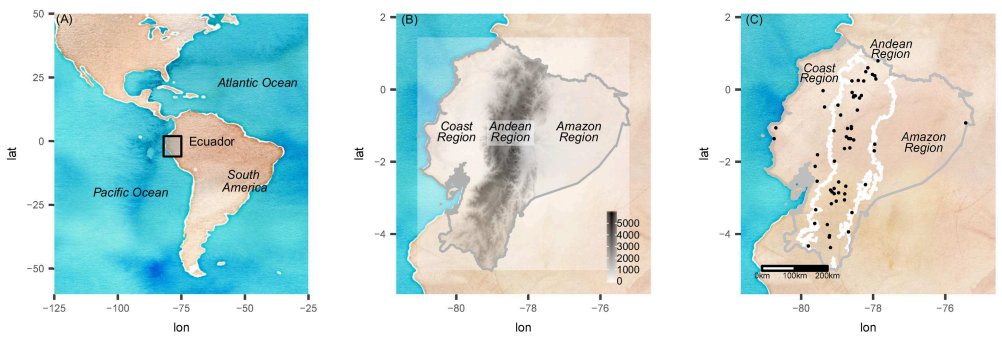


FIGURE 1 | Study area. **(A)** Ecuador is located in South America (left). **(B)** The Highlands are a weather divide between the coast and the Amazon (center). **(C)** Ground rainfall stations (black points) used for this study (right). Due to logistical limitation very few stations are located in the Amazon.

Xiaolan et al. (2013) and by Wang and Feng (2013) was applied. Finally, the infilling of missing data was done following Ureña Mora et al. (2016). After a quality control, the observational data was reduced to 60 stations across the whole country, with a temporal period of 25 years from January 1981 to December 2005. **Figure 1C** shows the location of the stations.

Global Climate Models

The Third National Communication of Climate Change project of Ecuador (TCN), before the Intergovernmental Panel on Climate Change (IPCC), provided GCMs data from three selected models among all GCMs of CMIP5. These three GCMs were selected among the 42 available from CMIP5 in present and future periods, by using statistical metrics evaluated in 137 precipitation stations in the whole country. They were Pearson correlation, bias and RMSE. For details about the GCM selection, see Armenta et al. (2016). The selected GCMs were CSIRO-Mk36, GISS-E2, and IPSL-CM5A-MR. The present study considered the base period from 1981 to 2005 and the future period from 2041 to 2070, analyzing RCP 4.5 and 8.5.

CSIRO

The dynamic/thermodynamic CSIRO-MK3-6-0 (MK36) model was developed by the Commonwealth Scientific and Industrial Research Organization in collaboration with the Queensland Climate Change Centre of Excellence. It presents a horizontal resolution of $1.9^\circ \times 1.9^\circ$. The marine ice is added in the atmospheric model. MK36 has 31 vertical levels and each atmospheric grid is associated to two oceanic layers. MK36 has shown improvements compared to MK35, for example interactive aerosol, actualized radiation, and a layer with properties are included now (Collier et al., 2013).

GISS

The Goddard Institute for Space Studies model (GISS E2) has a horizontal resolution of $2.5^\circ \times 2^\circ$, nine atmosphere layers, and two ground hydrological layers. The radiation scheme includes cloud particles, aerosol, and trace gases. The convective cloud cover is predicted and the calculation of temperature includes both seasonal and diurnal solar cycles. The radiation scheme includes integrated cloud particles, aerosols and radioactive important trace gases. The precipitation occurs whenever supersaturated conditions appear. Surface fluxes change the ocean water and the sea ice temperature in proportion to the covered area for a grid cell (Schmidt et al., 2014).

IPSL

The IPSL-CM5A climate model was developed in the Institute Pierre Simon Laplace and presents a refined horizontal and vertical grid of the atmospheric component. This is the major difference related to the last version IPSL-CM4A. The grid resolution is $2.5^\circ \times 1.25^\circ$. These changes reduce the mean biases in the tropospheric structure. The extended stratosphere scheme, with new parametrization, was increased by adding layer numbers from 19 to 39. This version captures the stratospheric variability and shows stratospheric sudden warmings (Hourdin et al., 2013).

Downscaled Global Climate Models

The TCN published the 10 km dynamically downscaled products of CSIRO-Mk36, GISS-E2, IPSL-CM5A-MR for the base period (1981–2005) and for the future period (2041–2070), analyzing RCP 4.5 and RCP 8.5. For the downscaling, the Weather Research and Forecasting model (WRF) version 3.6.1 was used with the following parameterizations: Microphysics WSM 3-class simple ice; Short Wave Radiation, rrtm; Long Wave Radiation, Dudhia; Surface layer, Monin-Obukhov; Land Surface model, Unified Noah land-surface model; Boundary layer, YSU (Yonsei University) and Kain-Fritsch (new Eta) for cumulus parameterization (Armenta et al., 2016). The downscaled GCMs products will be called from now on: DGCMs. After dynamically downscaling, precipitation data was extracted from NetCDF files with a spatial resolution of 10 Km and with a 6 h temporal resolution. All these products were aggregated to the monthly temporal scale and stored as rasterbrick of the raster library in R (Hijmans, 2017).

METHODS

Four analyses were performed. First, the standardized precipitation index was computed for precipitation data; second, precipitation data and the standardized precipitation index were validated. Then the present and future drought intensities and their probability of occurrence were computed, and finally present and future probability of drought intensities were compared following spatial and temporal approaches. The validation of the precipitation data and of the standardized precipitation index were computed for the ground rain gauge locations. Meanwhile, the following analyses were performed for the whole study area.

The Standardized Precipitation Index

The Standardized Precipitation Index (SPI) is one the most widely used drought indices due to its robustness and versatility for drought monitoring (Morid et al., 2006). The SPI is globally accepted due to its standardized nature (WMO—World Meteorological Organization, 2012), which allows to compare places with different precipitation characteristics, and to make calculations across diverse time scales (Morid et al., 2006). It helps to identify for instance short-term droughts, affecting the agricultural sector through the reduction of soil moisture, as well as large-term droughts affecting hydric balance in rivers and water reservoirs (Rivera, 2014). Even if other variables like temperature, evapotranspiration, atmospheric humidity, and wind, are also related to droughts, SPI only takes into account precipitation. The reason is because precipitation mainly determines the duration, magnitude, and intensity of droughts (Chang and Kleopa, 1991). Thus SPI is applicable to meteorological droughts because it only uses precipitation, and it does not account for interactions with the land surface or temperature (Taylor et al., 2013).

The SPI was calculated in four steps (Paulo et al., 2003). Firstly, cumulative precipitation for each month and each location was calculated using a k-month time scale. In our case, k was 3. The short-term SPI-3 was used, calculated as

the 3 months' precipitation moving window. For instance, the cumulative precipitation for March is computed as the sum of the precipitation of January, February and March. We chose this time scale to account for a seasonal estimation of precipitation. The total precipitation for the month j of the year i and the $k-1$ past consecutive months, with $k \leq 3$, is (Equation 1) (Paulo et al., 2003; Vicente-Serrano, 2006):

$$X_{i,j}^{k} = \begin{cases} \sum_{l=4-k+j}^{3} w_{i-1,l} + \sum_{l=1}^{j} w_{i,j}\,, & j < k \\ \sum_{l=j-k+1}^{j} w_{i,j}\,, & j \geq k \end{cases} \quad (1)$$

Secondly, a two-parameter gamma probability distribution (Equation 2) was fitted, since it well-models the frequencies of accumulated precipitation (Vicente-Serrano et al., 2010). The unbiased Probability Weighted Moments was used as a fitting method, as it was already available in the SPEI R library (Beguería et al., 2014), resulting in the following equation:

$$f(x) = \frac{1}{\beta^{\alpha}\,\Gamma(\alpha)}\, x^{\alpha-1} e^{\frac{x}{\beta}}\,,\quad x > 0 \quad (2)$$

With α and β being the shape and scale parameters, x the precipitation and $\Gamma(\alpha)$ the gamma function.

Thirdly, after α and β were estimated, they were used to calculate the distribution function values for the cumulative precipitation.

$$F(x) = \int_0^x f(t)\,dt = \frac{1}{\hat{\beta}^{\hat{\alpha}}\,\Gamma(\hat{\alpha})} \int_0^x t^{\hat{\alpha}-1} e^{\frac{t}{\hat{\beta}}}\,dt \quad (3)$$

Fourthly, with the obtained value of $F(x)$, the SPI values were computed by transforming the gamma distribution function values into standard normal variable values (Equation 4). In other words, the SPI values were normalized, i.e., standardized with a median of 0 and a standard deviation of 1.

$$SPI_{i,j}^{k} = \frac{X_{i,j}^{k} - \hat{\mu}_{j}^{k}}{\hat{\sigma}_{j}^{k}} \quad (4)$$

As a result, SPI is a dimensionless value that represents the number of standard deviations above or below the median precipitation at a defined location (WMO—World Meteorological Organization, 2012). A positive SPI indicates a greater value than the median precipitation, and a negative one indicates a lower value than the median precipitation. Droughts are considered as SPI values ≤ -1. Additionally, the SPI values can be categorized in different drought severities (McKee et al., 1993) as shown in **Table 1**. For more details on the calculation of SPI we refer the reader to McKee et al. (1993), Lloyd-Hughes and Saunders (2002), Vicente-Serrano et al. (2010), WMO—World Meteorological Organization (2012).

The computation was performed pixel-wise using the SPI function from the SPEI library in R (Beguería and Vicente-Serrano, 2017), considering the 1981–2005 period as the reference which helped to highlight changes between present and future droughts.

TABLE 1 | Drought categories for SPI (WMO—World Meteorological Organization, 2012).

SPI values	Drought category
−1.00 to −1.49	Moderate drought
−1.50 to −1.99	Severe drought
≤−2.00	Extreme drought

Validation of Present Time Precipitation and SPI-3

The present time DGCMs were validated against *in-situ* observations, i.e., 60 stations. This validation was done for monthly precipitation, as well as for the SPI-3 time series. Statistical metrics such as the Root Mean Square Error (RMSE), Pearson correlation (r) and Percentage of Bias (PBIAS %) were calculated for the time series at each specific location corresponding to the meteorological stations; median and Interquartile Range (IQR) were reported. The best present time DGCM models for precipitation and SPI-3 were identified based on the lower median RMSE, the higher median r, and the median PBIAS% closest to 0. The results were also disaggregated for the Coast, Highlands and Amazon regions. This was useful to give insights about the performance of the models for the whole country and for each natural region.

Probability of Present and Future Drought Intensities

Pixel-wise time series of SPI-3 were categorized as moderate, severe or extreme droughts. Then, the probability of the detected drought intensity was calculated as the frequency divided by the time series length (i.e., 298 months because the first 2 months were not computed in SPI-3). This showed the probability of different drought intensity occurrences at the different locations. Afterwards, maps of probability of occurrence were made for present and for future RCPs 4.5 and 8.5. SPI-3 time series of observations were calculated likewise.

In order to compare the present time probability of droughts between observations and DGCMs, the non-parametric Kruskal Wallis test for multiple median comparison was applied. If significant median differences were detected, the *post-hoc* Pairwise Wilcoxon rank sum hypothesis test with Bonferroni correction for adjusting p-values, was calculated. If ties were found, exact p-values were computed by adding a small amount of noise in the data (jitter). $P < 0.05$ showed significant differences between DGCMs and observations. The same criterion was applied to future 4.5 and 8.5 DGCMs, as two samples Wilcoxon test. Additionally, the climatological probability of present and future drought intensities was computed. This allowed us to describe the temporal behavior of the different drought intensities within the different regions of the country.

Comparison of Present and Future Probability of Drought Intensities

Present and future probabilities of moderate, severe or extreme droughts were compared through the map difference at each

pixel. A positive result represented future increment of droughts, while negative results represented future decrement of droughts. This was presented in maps as well as summarized in tables with median values for the entire country and for the three regions. Significant differences from zero were evaluated with the one-sample Wilcoxon test and with a significance level of 0.05. Medians that were non-significantly different from zero were interpreted as no changes in future drought occurrence. Additionally, the difference between future and present monthly probabilities was computed.

RESULTS

Evaluating the Present Time Representation of Precipitation and SPI-3

Evaluating Inter-model Uncertainties

In **Table 2** RMSE, Pearson correlation coefficient, and PBIAS are shown for the period 1981-2005 for precipitation and for SPI-3, comparing observations and DGCMs evaluated over ground stations. In general, the three DGCMs showed a similar performance of monthly precipitation estimates, although the GISS model slightly outperformed the other two. Regarding median RMSE values, the three models showed relatively high median RMSE values, with the lowest median RMSE for GISS with 77.56 mm/month and an IQR of 38.27 mm/month. Correlation coefficients were acceptable, with the highest coefficient for GISS (0.42). Finally, the PBIAS showed overestimation for all DGCMs. CSIRO showed the lowest overestimation with 8.95% while the highest one was GISS with 12.10%. The dispersion from median values measured with interquartile range (IQR) were high with 67.78% for CSIRO and 61.40% for IPSL.

Regarding SPI-3, the three DGCMs showed similar performances, although decreases in the correlation and PBIAS performances were observed. For CSIRO, RMSE and PBIAS showed the lowest values, 1.28 and −18.95%, respectively. As it was observed for precipitation, the high PBIAS's IQR represented variations of models' performance from site to site. PBIAS showed underestimation for the three DGCMs, with low underestimation for CSIRO, medium for IPSL and large for GISS. The lack of agreement in correlation for both precipitation and SPI-3, can be attributed to the smooth in DGCM's extreme values. This will be shown in next section with larger dispersion for observations and smaller for the models.

TABLE 2 | Validation of present time precipitation and SPI-3.

	RMSE (mm/month)		*r*		PBIAS (%)	
GCM Model	**Median**	**IQR**	**Median**	**IQR**	**Median**	**IQR**
PRECIPITATION						
CSIRO	81.58	42.85	0.39	0.27	8.95	67.78
GISS	77.56	38.27	0.42	0.26	12.10	67.28
IPSL	79.30	38.82	0.38	0.25	10.90	61.40
SPI-3						
CSIRO	1.28	0.12	0.11	0.12	−18.95	92.65
GISS	1.34	0.07	0.03	0.15	−77.35	84.83
IPSL	1.39	0.06	−0.01	0.08	−27.15	92.18

Variable units are provided in parentheses or otherwise dimensionless.

Spatial Patterns of Present Time Droughts

The probability of moderate, severe and extreme drought occurrence for *in-situ* observations and DGCMs is presented in **Figure A1** (Supplementary Material). They showed similar behavior displaying larger probabilities of drought occurrence for moderate than for severe and extreme intensities. Nevertheless, probabilities were low with a maximum of 0.13, which means that droughts were not persistent in time, and instead, they occurred as extraordinary events.

Although, the three models showed similar values among the moderate, severe and extreme droughts evaluated in ground stations, the spatial patterns varied among products. For moderate drought, CSIRO in the Amazon and central-south Highlands, GISS in the north Coast and central Highlands and Amazon, and IPSL in central Coast and central-south Highlands, showed larger probabilities of occurrence. However, for moderate drought, the spatial patterns of GISS and IPSL were more similar one to the other than compared with CSIRO. For severe drought, CSIRO showed larger probabilities in the north and south Highlands; GISS in the Highlands and Amazon; while IPSL in the central-south Highlands. Finally, for extreme drought, CSIRO showed larger probabilities in the north and central Highlands; GISS in the Amazon and central and northern Highlands; while IPSL in the Amazon and north Highlands. In Figure A1, it is observed that extreme droughts showed similar spatial structure for GISS and IPSL.

When comparing the probability of observations and DGCMs for moderate, severe and extreme drought at observations points (i.e., meteorological stations), similar values were obtained. In **Table 3**, the median of the probability and the IQR of such probabilities are shown. The general dispersion of probabilities for the whole country is shown in **Figure 2A**. It is interesting to note that observations showed a larger dispersion than DGCMs, as such it can be concluded that DGCMs underrepresented extreme precipitation values. Additionally, models tended to overestimate probabilities of occurrence for moderate and severe droughts, while for extreme droughts, they were slightly underestimated. Among DGCMs, for moderate drought, GISS had the closest median to the observation and IPSL the largest overestimation; for severe drought, IPSL had the closest median to the observation and GISS the largest overestimation; and for extreme drought, IPSL had the closest median to the observation, CSIRO the largest overestimation and GISS the largest underestimation.

The *post-hoc* test for pairwise comparison of observation and models (Pairwise Wilcoxon test with Bonferroni *p*-values adjustment) only showed significant median differences ($p < 0.05$) between observations and IPSL for moderate droughts, between observations and GISS for severe droughts, and there were no significant differences noted for extreme droughts. Similarly, as it was obtained for the monthly precipitation and SPI-3 comparison, there was not a single model that

outperformed in any of the situations. Given the lack of significant median differences, it can be concluded that different GCMs are suitable to be used in the different drought intensities. This is, for moderate droughts CSIRO and IPSL are suitable to be used; for severe droughts, CSIRO and GISS; and for extreme droughts, CSIRO, GISS, and IPSL. Therefore, CSIRO was the only model suitable in all three drought intensities.

Regarding the climatic regions of the country, the models at observation points showed different behaviors (**Figure 2B**). In the Coast, represented by seven observation points, the three models largely overestimated the probability of occurrence for moderate, severe and extreme droughts. The *post-hoc* pairwise test for moderate drought showed significant median differences ($p < 0.05$) between observations and the three models. For severe droughts, significant median differences were found for GISS and IPSL, non-significant differences for CSIRO. For extreme drought, significant differences for IPSL and non-significant differences for CSIRO and GISS were found. This means that CSIRO was the most suitable model with non-significant median differences for severe and extreme droughts.

In the Highlands, represented by 46 observation points, the three models performed similar to the observations at the meteorological stations. The behavior was similar to that for the whole country (**Figure 2A**) because 46 of the 60 total points were located in the Andes. The Kruskal-Wallis test for moderate drought did not show significant median differences for any of the three DGCMs. For severe droughts, the *post-hoc* test showed significant median differences of probability regarding observations and GISS, and non-significant for CSIRO and IPSL. For extreme droughts, significant differences were found only for CSIRO. This means that IPSL, followed by CSIRO, were the most suitable models; with non-significant median differences for moderate, severe and extreme droughts.

TABLE 3 | Probability of occurrence of SPI-3, at observation points.

	Moderate		Severe		Extreme	
Model	**Median**	**IQR**	**Median**	**IQR**	**Median**	**IQR**
Obs	0.08	0.03	0.04	0.02	0.02	0.02
CSIRO	0.09	0.02	0.05	0.03	0.02	0.01
GISS	0.08	0.02	0.05	0.01	0.02	0.01
IPSL	0.09	0.02	0.04	0.02	0.02	0.01

Comparison of measured and modeled data. Units: dimensionless.

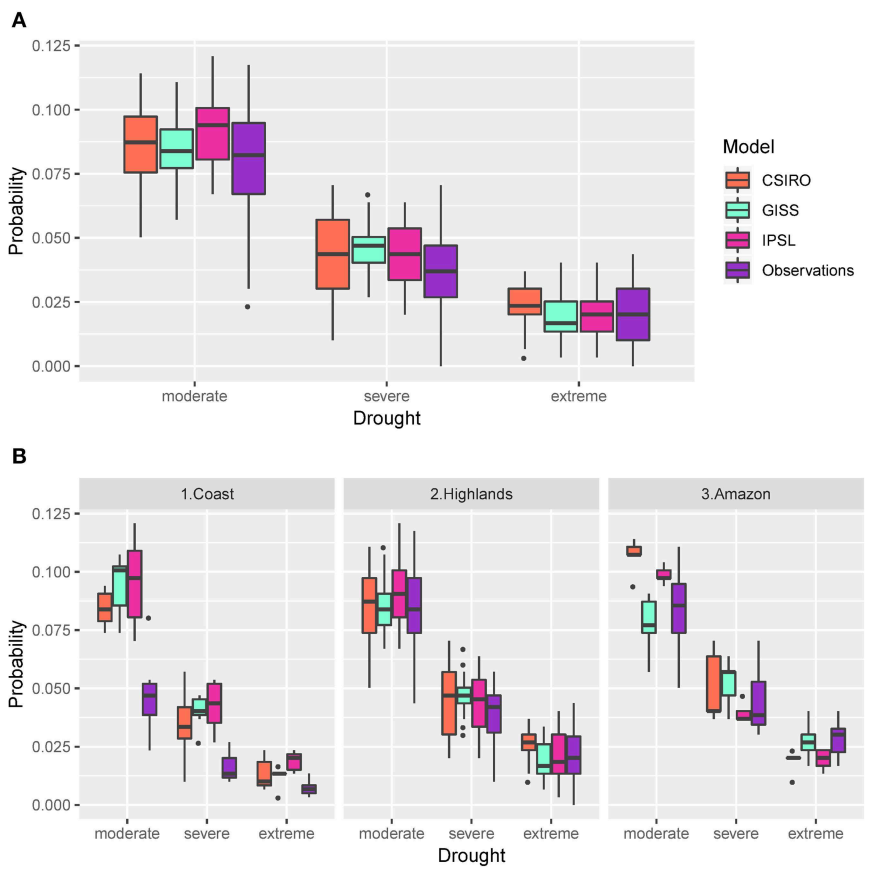


FIGURE 2 | Present time probability of drought occurrence by category for observations and DGCMs evaluated at ground stations. **(A)** for the whole country, **(B)** for each region.

Finally, in the Amazon, represented by only six observation points, for moderate droughts, GISS performed better while for severe droughts the ISPL was better. For extreme droughts, the GISS model outperformed the others. The Kruskal-Wallis test did not show significant median differences for the three droughts categories for any of the three DGCMs. Despite the small validation data size, it can be concluded that the three models are suitable.

Spatio-Temporal Structure of Future Meteorological Droughts Under RCPs 4.5 and 8.5

Future Droughts Trends for RCPs 4.5 and 8.5

The overall future probabilities of occurrence for moderate, severe and extreme drought for all DGCMs and RCPs 4.5 and 8.5 at observation stations for the whole country, are presented in **Figure 3A**. Additionally, they are compared to present observations. In all cases, future probabilities are lower than present ones, meaning that an overall reduction of drought is expected in the future. Regarding RCPs 4.5 and 8.5 comparison, in most cases it is observed that droughts are less frequent in RCP 8.5 than in RCP 4.5. For moderate and severe droughts, CSIRO and GISS 4.5 showed larger probability of occurrence than RCP 8.5, however IPSL showed smaller probability for RCP 4.5 than for RCP 8.5. For severe and extreme drought, GISS and IPSL showed the same behavior, however CSIRO showed greater probability for RCP 8.5 than for RCP 4.5. In all cases, there are significant median differences with $p < 0.05$ according to the Wilcoxon test.

Regarding the climatic regions of the country, the models and scenarios at observation points show different behaviors (**Figure 3B**). In the Coast, similar probabilities of occurrence with 4.5 were observed, while with 8.5 there was a clear reduction. In the Highlands and Amazon, a clear reduction was also observed. The previous trend that droughts tend to be less frequent in 8.5 than in 4.5 RCP, is also observed here.

In the Coast, the three drought categories for CSIRO showed significant differences ($p < 0.05$) between RCPs 4.5 and 8.5. Moderate GISS did not show significant differences,

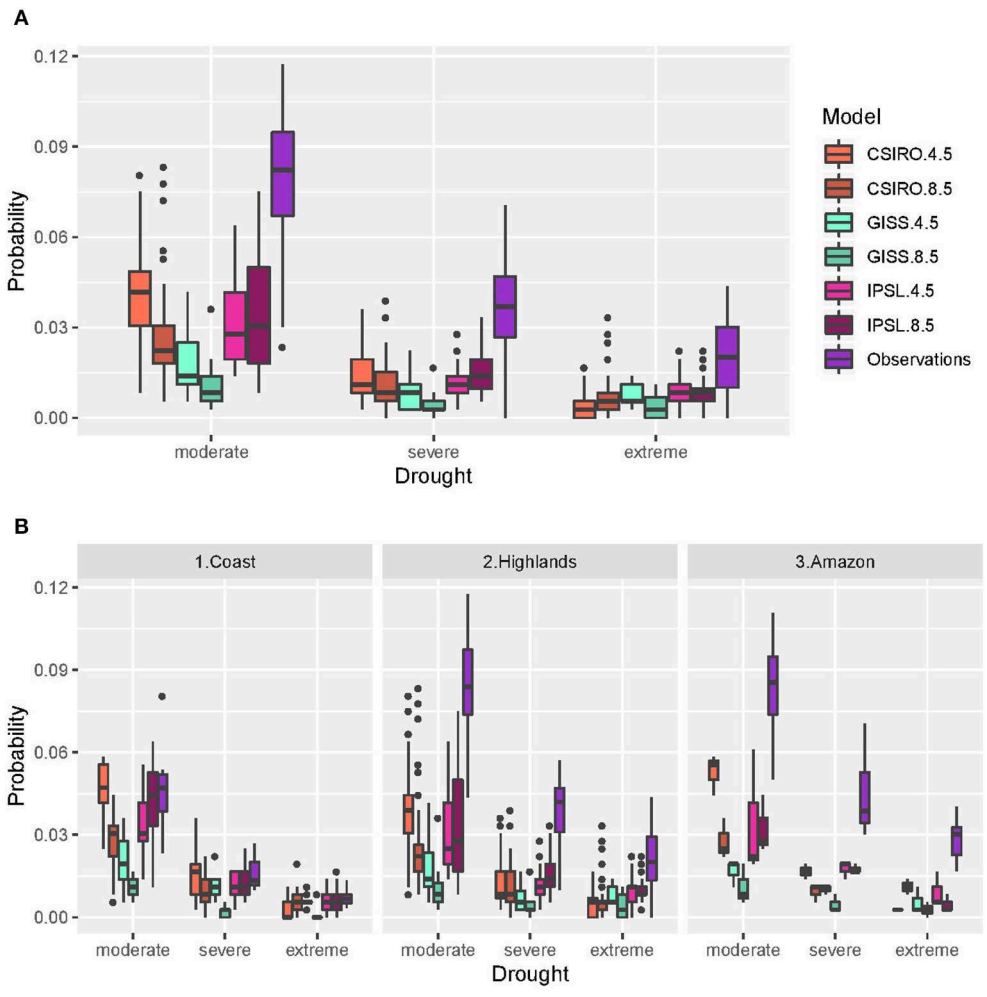


FIGURE 3 | Future probability of drought occurrence at observations points. **(A)** for the whole country, **(B)** for each region.

while severe and extreme did. Finally, IPSL did not show significant differences between RCPs for any of the three drought intensities. In the Highlands, moderate drought for CSIRO showed significant differences RCPs, while no significant differences were observed for severe and extreme droughts. For GISS, all three drought intensities showed significant differences. IPSL showed significant differences for severe, but not for moderate and extreme droughts. Finally, in the Amazon, the six models did not show significant differences between RCPs.

Spatial Structure of Future Droughts in Ecuador

The spatial distribution of future drought probability is shown in **Figure A2** (Supplementary Material), for the three GCMs and for moderate, severe and extreme intensities. CSIRO showed higher probability in the Amazon for all intensities and both RCPs. IPSL displayed greater probability in the Amazon also, but with lower probability values than CSIRO. GISS showed similar probability of drought occurrence in the whole country.

In order to evaluate the spatial structure and trends of droughts in Ecuador, the change of the drought probability was computed as the difference of probability maps between future and present DGCMs for moderate, severe and extreme drought for RCPs 4.5 and 8.5 (see **Figures 4**–**6**). The results revealed a mix of future increments and reductions of droughts in a complex spatial structure. Such variations depended on the region of the country, the DGCM and the RCP. Red/Blue-colored cells represented future drought increments/decrements different from zero (statistically significant, one-sample Wilcoxon tests, $p < 0.05$), understanding zero as no changes in future drought occurrence. Finally, white cells were non-significantly different from zero. Additionally, in **Table 4**, the median differences for the whole country, and by regions are reported. The overall tendency for the whole country was a slight reduction of moderate and severe droughts.

More in detail, the probability change maps for moderate drought (**Figure 4**) show a country-wide downward trend (more blue-colored cells than red-colored ones). DGCMs CSIRO, GISS and IPSL showed reductions of moderate drought especially in the coast and the Andes for RCPs 4.5 and 8.5. In the Amazon, IPSL for RCP 4.5 showed some increase of moderate droughts whereas for RCP 8.5 there was a slight decrease. For CSIRO under both RCPs, there was little to no change in moderate drought tendency, whereas for GISS under RCPs 4.5 and 8.5 there was a clear reduction in moderate drought tendency.

For severe droughts (**Figure 5**), GISS showed a decreasing tendency in the whole country, especially in the Highlands and in the western Ecuadorian Amazon for both RCPs. CSIRO and IPSL showed a slight decrease in the Highlands and Coast region, whereas in the Amazon region CSIRO showed a greater increase in the probability of droughts than IPSL. IPSL showed none to some increasing trend of droughts for RCP 4.5, while almost no trend changes were observed for RCP 8.5.

For extreme droughts (**Figure 6**), GISS showed a small decrease in the Amazon and the eastern regions of the Highlands for both RCPs, and no changes in the Coast. CSIRO showed a clear increasing trend of droughts in the Amazon and the

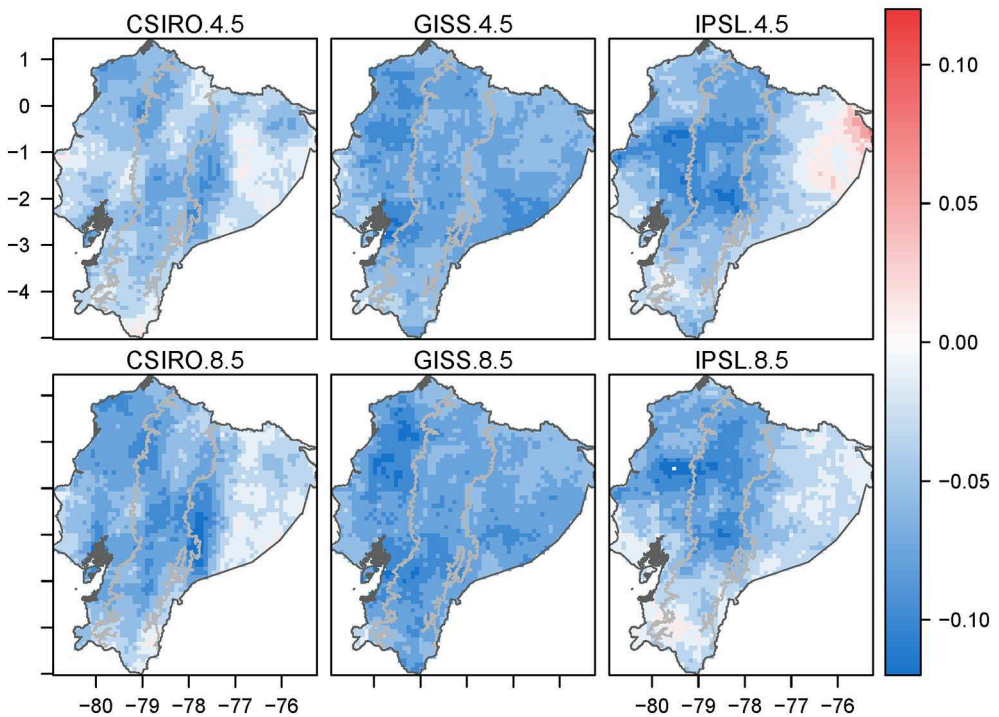


FIGURE 4 | Spatial distribution of change for moderate drought probability. RCP (rows) and GCM (columns). White pixels indicate no change.

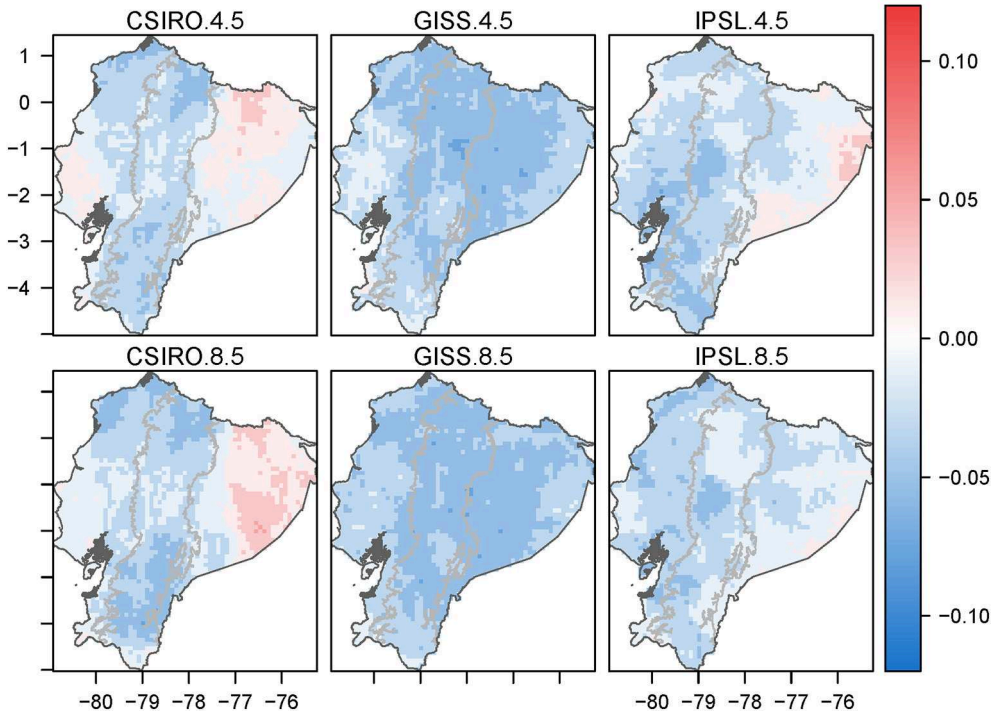


FIGURE 5 | Spatial distribution of change for severe drought probability. RCP (rows) and GCM (columns). White pixels indicate no change.

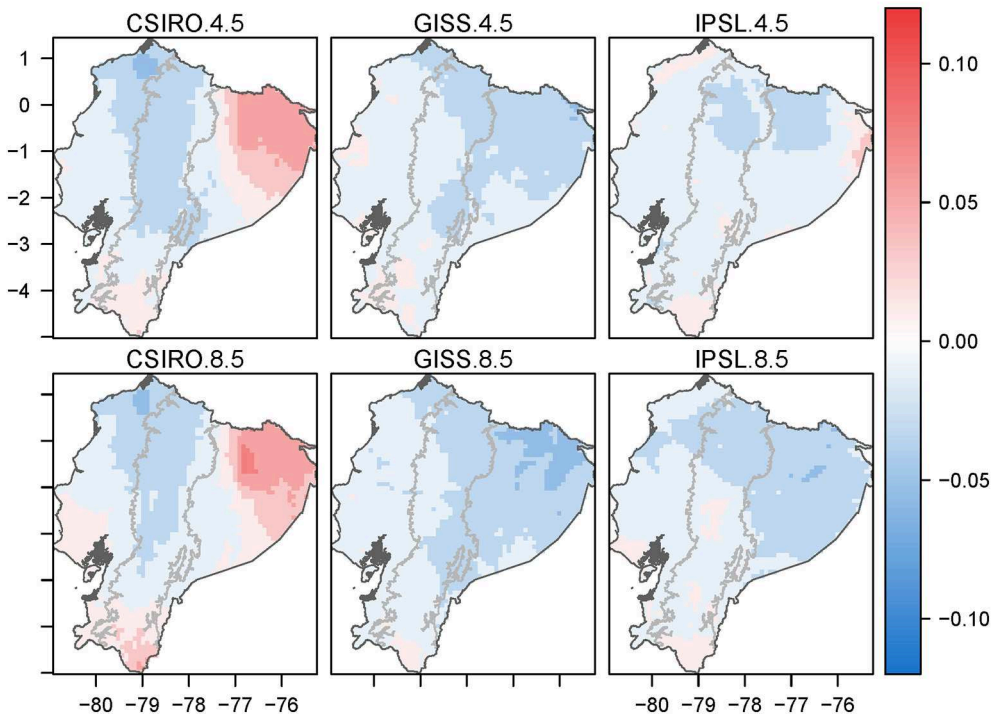


FIGURE 6 | Spatial distribution of change for extreme drought probability. RCP (rows) and GCM (columns). White pixels indicate no change.

TABLE 4 | Change of drought probabilities.

Model	Scenario	Ecuador	Coast	Highlands	Amazon
MODERATE DROUGHT					
CSIRO	4.5	−0.04	−0.04	−0.05	−0.04
	8.5	−0.06	−0.07	−0.06	−0.03
GISS	4.5	−0.06	−0.07	−0.06	−0.06
	8.5	−0.07	−0.08	−0.07	−0.07
IPSL	4.5	−0.05	−0.05	−0.07	−0.03
	8.5	−0.05	−0.06	−0.07	−0.03
SEVERE DROUGHT					
CSIRO	4.5	−0.02	−0.02	-0.03	
	8.5	−0.02	−0.02	−0.03	0.01
GISS	4.5	−0.04	−0.03	−0.04	−0.04
	8.5	−0.04	−0.03	−0.04	0.04
IPSL	4.5	−0.02	−0.03	−0.03	−0.01
	8.5	−0.02	−0.03	−0.02	−0.01
EXTREME DROUGHT					
CSIRO	4.5	−0.01	−0.01	−0.02	0.02
	8.5	−0.01	−0.01	−0.02	0.01
GISS	4.5	−0.01	−0.01	−0.01	−0.03
	8.5	−0.02	−0.01	−0.02	−0.03
IPSL	4.5	−0.01	−0.01	−0.01	−0.01
	8.5	−0.02	−0.01	−0.01	−0.03

Increase (decrease) shown as positive (negative) values. Units: dimensionless.

south of the country for both RCPs. The same DGCM showed a decreasing trend of droughts in the Highlands for RCPs 4.5 and 8.5 and almost no changes in the coast for both RCPs. IPSL showed some decreasing trend in the north of the country for RCP 4.5, while for RCP 8.5 a decreasing trend was noted for the Amazon and the northern Highlands. Almost no changes are expected in the coast.

Monthly Trends of Future Droughts Under RCPs 4.5 and 8.5

Previous sections showed the spatial analysis of future droughts in Ecuador, however in this section the results of the difference between future and present monthly probability of droughts in Ecuador is shown for moderate, severe and extreme droughts in the Coast, Highlands and Amazon, for RCPs 4.5 and 8.5 using CSIRO, GISS and IPSL DGCMs. This information is synthetized in **Tables 5**–**7**.

The analysis of monthly trends of future droughts is valuable information for decision makers and water resource management in general. It is important to highlight that changes in drought trends are dependent on the climatic forcing at synoptic scales which can affect several processes. For instance, on one hand, the wet season in Ecuador is mainly dominated by the ITCZ influence (Goldberg et al., 1987). On the other hand, during the dry season, strong easterlies prevail which may respond differently to the ITCZ (Sulca et al., 2018) in CC conditions, producing an intra-annual differentiated response to CC in addition to spatial variations.

Monthly changes of moderate droughts are shown in **Table 5**. In the Coast region, GISS and IPSL presented very similar trends for RCPs 4.5 and 8.5, showing that less moderate droughts are expected. For CSIRO, similar trends to GISS and IPSL are expected with the exception of July and October, which showed non-significant differences between future and present droughts. In the Highlands, all DGCMs showed a decrease of probability between future and present probabilities of severe droughts for the entire year, for both RCPs, with the exception of CSIRO in August for RCP 4.5 where is non-significant changes are expected. This model showed very low differences from zero in September and October, thus changes were not too evident during the dry season. For the Amazon region, CSIRO showed a slight decrease in the probability of droughts throughout the year, with the exception of August and September for RCP 4.5 which showed a slight increase. For RCP 8.5, all months showed a decrease of probability with the exception of August and October which showed a slight increase. GISS showed a consistent decrease of probability of moderate drought occurrence for RCPs 4.5 and 8.5. IPSL showed a consistent decrease of probability throughout the year with the exception of May and October which showed a slightly increase. For July and October, non-significant differences were found for both RCPs. Thus, moderate droughts in the Coast and in the Highlands are expected to occur less. However, for the Amazon, some models showed a slight increase, especially in boreal summer when the ITCZ is located to the north.

For severe droughts (**Table 6**), in the coast region, CSIRO showed a small decrease of probability from October to April. From May to September, non-significant or slight increases of probability were shown for both RCPs. For GISS, for both RCPs, the whole year showed a slight decrease of probability with the exception of February and November, which showed non-significant changes. For IPSL, the whole year showed a small decrease of probability with the exception of July. In the Highlands, CSIRO showed a decrease of probability from January to April and October and November, and non-significant probability changes from May to September and for December. IPSL and GISS showed a consistent decrease in probability throughout the year for both RCPs. It is interesting to observe that for the Amazon region, a less uniform pattern was displayed. GISS showed a consistent decrease of probability for both RCPs, however, IPSL and CSIRO showed a consistent decrease of probability from January to March, and a mixed occurrence of non-significant, increasing and decreasing probabilities was shown for the rest of the year.

For extreme droughts in the Coast under RCPs 4.5 and 8.5, CSIRO showed a decreasing probability in January and in October, whereas GISS showed an extreme drought probability decrease for February, March and June for both RCPs (**Table 7**). For IPSL, a decreased probability was shown from December to February and for October. Overall, for the coast region, the three DGCMs showed a decreased probability of extreme drought occurrence during the first rainy season. In the Highlands, all DGCMs in both RCPs showed a clear trend of decreasing probability of extreme drought occurrence from December to April and during September and October. These periods are

TABLE 5 | Monthly changes of drought probablity for moderate droughts.

	GCM	Jan	Feb	Mar	Ap	May	Jun	Jul	Aug	Sep	Oct	Nov	Dec
COAST													
RCP 4.5	CSIRO	−0.02	−0.09	−0.05	−0.08	−0.08	−0.09		−0.04	−0.04		−0.08	−0.04
	GISS	−0.08	−0.08	−0.05	−0.08	−0.05	−0.01	−0.05	−0.08	−0.08	−0.04	−0.09	−0.12
	IPSL	−0.04	−0.04	−0.02	−0.02	−0.05	−0.09	−0.04	−0.08	−0.05	−0.08	−0.08	−0.08
RCP 8.5	CSIRO	−0.08	−0.12	−0.08	−0.08	−0.05	−0.05		−0.05	−0.05		−0.08	−0.08
	GISS	−0.08	−0.08	−0.08	−0.08	−0.08	−0.05	−0.08	−0.08	−0.08	−0.04	−0.08	−0.12
	IPSL	−0.04	−0.04	−0.02	−0.02	−0.05	−0.09	−0.04	−0.08	−0.05	−0.08	−0.08	−0.08
HIGHLANDS													
RCP 4.5	CSIRO	−0.05	−0.09	−0.05	−0.04	−0.05	−0.08	−0.05		−0.01	−0.01	−0.08	−0.05
	GISS	−0.05	−0.04	−0.08	−0.12	−0.05	−0.05	−0.05	−0.04	−0.12	−0.04	−0.08	−0.08
	IPSL	−0.09	−0.04	−0.08	−0.05	−0.01	−0.09	−0.05	−0.05	−0.04	−0.08	−0.08	−0.08
RCP 8.5	CSIRO	−0.08	−0.12	−0.08	−0.04	−0.04	−0.09	−0.08	−0.04	−0.01	−0.01	−0.09	−0.05
	GISS	−0.08	−0.04	−0.05	−0.12	−0.05	−0.08	−0.08	−0.08	−0.09	−0.04	−0.05	−0.12
	IPSL	−0.09	−0.04	−0.08	−0.05	−0.01	−0.09	−0.05	−0.05	−0.04	−0.08	−0.08	−0.08
AMAZON													
RCP 4.5	CSIRO	−0.05	−0.06	−0.09	−0.04	−0.03	−0.09	−0.06	0.02	0.01	−0.01	−0.02	−0.05
	GISS	−0.08	−0.04	−0.04	−0.08	−0.09	−0.05	−0.08	−0.08	−0.04	−0.05	−0.08	−0.08
	IPSL	−0.05	−0.02	−0.04	−0.09	0.02	−0.02		−0.08	−0.01	0.02		−0.04
RCP 8.5	CSIRO	−0.06	−0.09	−0.09	−0.01	−0.05	−0.09	−0.08	0.01	−0.03	0.02		
	GISS	−0.05	−0.04	−0.04	−0.08	−0.12	−0.05	−0.08	−0.08	−0.05	−0.08	−0.05	−0.05
	IPSL	−0.05	−0.02	−0.04	−0.09	0.02	−0.02		−0.08	−0.01	0.02		−0.04

White cell indicate no-significant changes. Units: dimensionless. Red/Blue-colored cells represent future drought increments/decrements.

TABLE 6 | Monthly changes of drought probablity for severe droughts.

	GCM	Jan	Feb	Mar	Ap	May	Jun	Jul	Aug	Sep	Oct	Nov	Dec
COAST													
RCP 4.5	CSIRO		−0.04	−0.04	−0.04		0.03				−0.04	−0.04	−0.01
	GISS	−0.04		−0.04	−0.08	−0.04	−0.01		−0.04	−0.04	−0.04		−0.04
	IPSL	−0.04	−0.04	−0.04	−0.04	−0.01	−0.05		−0.04	−0.01	−0.04	−0.04	−0.04
RCP 8.5	CSIRO		−0.04	−0.04	−0.04	0.03					−0.04	−0.04	−0.04
	GISS	−0.04		−0.04	−0.08	−0.04	−0.01	−0.04	−0.04	−0.04	−0.04		−0.04
	IPSL	−0.04	−0.04	−0.04	−0.04	−0.01	−0.05		−0.04	−0.01	−0.04	−0.04	−0.04
HIGHLANDS													
RCP 4.5	CSIRO	−0.04	−0.04	−0.01	−0.04	−0.04	−0.01				−0.04	−0.04	
	GISS	−0.04	−0.04	−0.08	−0.04	−0.04	−0.04	−0.04	−0.04	−0.04	−0.04	−0.04	−0.04
	IPSL	−0.04	−0.01	−0.04	−0.04	−0.04	−0.04	−0.04	−0.04	−0.01	−0.04	−0.04	−0.05
RCP 8.5	CSIRO	−0.08	−0.04	−0.04	−0.04				−0.04		−0.04	−0.04	
	GISS	−0.05	−0.04	−0.08	−0.04	−0.04	−0.04	−0.04	−0.04	−0.04	−0.04	−0.04	−0.04
	IPSL	−0.04	−0.01	−0.04	−0.04	−0.04	−0.04	−0.04	−0.04	−0.01	−0.04	−0.04	−0.05
AMAZON													
RCP 4.5	CSIRO	−0.04	−0.01	−0.01	−0.04	−0.04	0.03	−0.01		0.03		0.02	0.03
	GISS	−0.08	−0.04	−0.04	−0.04	−0.04	−0.04	−0.04	−0.04	−0.04	−0.04	−0.08	−0.04
	IPSL	−0.08	−0.01	−0.04		0.03	−0.01	0.02	−0.04	0.03		0.03	−0.05
RCP 8.5	CSIRO	−0.05	−0.02	−0.01		−0.04	−0.01	−0.01		0.03	0.06	0.03	0.03
	GISS	−0.08	−0.04	−0.04	−0.04	−0.04	−0.04	−0.04	−0.05	−0.04	−0.01	−0.05	−0.04
	IPSL	−0.08	−0.01	−0.04		0.03	−0.01	0.02	−0.04	0.03		0.03	−0.05

White cell indicate no-significant changes. Units: dimensionless. Red/Blue-colored cells represent future drought increments/decrements.

clearly related to the two rainy seasons of the Highlands along the inter-Andean valleys. In the Amazon the patterns of intra-annual variability are more complex. CSIRO showed an increase of probability of extreme drought in October, November, January and February. For May, June, and July, no change is expected, where a lower probability was shown for the rest of the year. GISS under RCP 4.5 showed a decrease of probability from February to April, and from September to December, and

TABLE 7 | Monthly changes of drought probablity for extreme droughts.

	GCM	Jan	Feb	Mar	Ap	May	Jun	Jul	Aug	Sep	Oct	Nov	Dec
COAST													
RCP 4.5	CSIRO	−0.04									−0.04		
	GISS		−0.04	−0.04			−0.01						
	IPSL	−0.04	−0.04			−0.01							−0.04
RCP 8.5	CSIRO	−0.04									−0.04		
	GISS		−0.04	−0.04			−0.04						
	IPSL	−0.04	−0.04			−0.01							−0.04
HIGHLANDS													
RCP 4.5	CSIRO	−0.01		−0.04	−0.04					−0.04	−0.04		−0.05
	GISS		−0.08	−0.04	−0.04		0.03			−0.04	−0.04		
	IPSL	−0.04	−0.04			−0.01				−0.01			
RCP 8.5	CSIRO	−0.01		−0.04	−0.01					−0.04	−0.04		−0.08
	GISS		−0.08	−0.04	−0.04					−0.04	−0.04		
	IPSL	−0.04	−0.04			−0.01				−0.01			
AMAZON													
RCP 4.5	CSIRO	0.03	0.03	−0.04	−0.04				−0.04	−0.04	0.13	0.10	0.06
	GISS		−0.08	−0.08	−0.04	0.03	0.03	0.03		−0.04	−0.04	−0.04	−0.04
	IPSL	−0.01	−0.01	0.03	0.03	−0.01		−0.04		−0.01	−0.04	−0.08	−0.04
RCP 8.5	CSIRO	0.03	0.03	−0.01	−0.01				−0.04	−0.04	0.06	0.17	−0.01
	GISS		−0.08	−0.08	−0.04		−0.01			−0.04	−0.04	−0.04	−0.04
	IPSL	−0.01	−0.01	0.03	0.03	−0.01		−0.04		−0.01	−0.04	−0.08	−0.04

White cell indicate no–significant changes. Units: dimensionless. Red/Blue-colored cells represent future drought increments/decrements.

an increase from May to July. GISS for RCP 8.5 showed a decrease in extreme drought probability from February to April and from September to December. IPSL showed a decrease in probability of extreme drought from September to February for both RCPs, and an increase in March and April, also for both RCPs.

In general, for extreme droughts it is interesting to observe that the first rainy season, from February to April, showed a decrease in probability of extreme drought occurrence across the country. The second rainy season, from October to December, also showed a decrease in the Highlands and the Amazon. The period from May to August showed less variation in the occurrence of extreme drought probability. These results highlight that CC's impact on droughts has an important intra-annual variability, which is related to a different response of several processes toward CC.

DISCUSSION AND CONCLUDING REMARKS

Intra-Model Uncertainties in Future Droughts Projections in Ecuador

The strong differences in present time and projected precipitation among CMIP5 GCMs in the tropical regions is well-known (Hirota and Takayabu, 2013; Mehran et al., 2014). Such differences are still present after dynamically downscaling the results, because downscaled results inherit the main features from the driving GCMs (Di Luca et al., 2015). In order to reduce such intra-model uncertainty, the three downscaled results of CMIP5 GCMs were used (i.e., GISS, IPSL, CSIRO) to study drought representation in Ecuador.

The present time representation of moderate, severe and extreme droughts in Ecuador was better captured for the Highlands and the Amazon, and strongly overestimated in the Coast, especially for moderate and severe droughts. Such difference in the ability of the DGCMs to represent droughts among regions is intrinsically related to the capabilities of the DGCMs to represent the climatic processes in those specific regions (Schiermeier, 2010). For instance, the Eastern Pacific SST is influenced by the eastern Pacific cold tongue and the El Niño and La Niña phenomena, thus modulating the climate in the coastal region (Bendix et al., 2011). However, GCMs underestimate El Niño related precipitation (Steinhoff et al., 2015) which might be responsible for the DGCMs' droughts overestimation. It is important to highlight that the limited representation of precipitation in the Coast of Ecuador might be more related to the limitation of the DGCMs to represent atmospheric processes and teleconnections, than to the low representation of SST in the Eastern Pacific as pointed out by Tedeschi and Collins (2016).

The precipitation in the Coast of Ecuador has two inner regions. One toward the south that is dry and more related to the drying effect of the cold Humboldt current, similar to the climate in the coastal region of northern Perú. The other region is situated toward the north and is wetter due to the influence of the Chocó low level Jet (LLJ) (Poveda and Mesa, 2000; Sierra et al., 2015, 2018). This wetter region is one of the most important climatic features in northern South America, related to the Lloró climate, and one of the rainiest regions on Earth (Poveda and Mesa, 2000). The representation of the Chocó LLJ by 26 Atmosphere-Ocean General Circulation Models (AOGCMs) and 11 atmospheric climate models was evaluated

by Sierra et al. (2018), attributing less skill to models unable to represent the ITCZ strength and location in addition to poor resolution and limited representation of complex orographic features. Such limitations might explain the overestimation of droughts in the Coast of Ecuador.

Present time droughts were better represented by the DGCMs in the Amazon region than in the Coast region. This is remarkable because the climate of Ecuadorian Amazon (78°W−75°11'W) located in the westernmost region of the Amazon basin, shows a complex interaction with the Andes. Along the Andean-Amazon transition region, there is a rainy period during boreal summer (Campozano et al., 2016b), which differs from the typical more uniform precipitation regime toward the east, into the Amazon basin. The increment of precipitation during boreal summer in this region might be related to the Andean Occurrence System, AOS (Bendix et al., 2006). Additionally, using a Lagrangian back trajectory method, Esquivel-Hernández et al. (2019), showed that water vapor is brought from the Caribbean as an influence from the northeastern trade winds to the eastern escarpments of the Andes. Likewise, in the Peruvian Andes-Amazonian transition, Chavez and Takahashi (2017) used reanalysis data to study the physical drivers for precipitation, pointing to the influence of the South American Low-Level Jet, SALLJ. Thus, although the influence of the SALLJ in Ecuador seems plausible, further research is necessary. It is relevant to evaluate GCMs along this region in the Amazon because the rainfall hotspots contribute to ca. 35% of the hydroelectricity generation in Ecuador. Additionally, several cities are located in this region (e.g., Zamora Chinchipe, Morona Santiago, Napo, Sucumbíos, Orellana, Pastaza with a total of population of ca. 750.000 inhabitants), which are vulnerable to extreme precipitation events.

Contrarily, in the central and eastern Amazon region, mostly corresponding to Colombia, Peru and Brazil, there are many studies evaluating GCMs representation of droughts. Regarding to the Amazon basin over all, the droughts are affected by ENSO events and by SST anomalies in the Tropical North Atlantic (Barichivich et al., 2018), which show a good representation in CMIP5 models (Duffy et al., 2015). This agrees with our findings of present time representation of droughts from DGCMs. However, in the Amazon region, an overestimation of total precipitation and an underestimation of consecutive dry days was reported by Sillmann et al. (2013), which might be related to the misrepresentation of atmospheric processes rather than a poor SST representation (Tedeschi and Collins, 2016).

Present time representation of droughts in the Ecuadorian Andes by DGCMs was adequate despite the complex orography. A slight reduction of droughts is expected for RCPs 4.5 and 8.5 in the future. Few studies on the future precipitation evaluation by GCMs have been conducted in the Ecuadorian Andes. For CMIP3 GCMs after applying statistical downscaling in an Inter-Andean basin (Paute basin), Mora et al. (2014) showed that the mean annual rainfall will increase as well as rainfall rates in the period 2045–2065 for A1B, A2, B1 scenarios, in addition to wetter conditions in rainy seasons. These conclusions can be related to our findings of a slight reduction on future droughts in the Andes derived from CMIP5 DGCMs. These results agree with the recent findings of Zhiña et al. (2019), in the same region, where they find a reduction of duration and magnitude using the SPEI drought index for RCPs 4.5 and 8.5.

Buytaert et al. (2010) analyzed the uncertainty between ensembled precipitation projections of several GCMs from the IPCC Third and Fourth Assessment Report, and PRECIS (0.5° resolution) regional climate model results driven by HadAM3p for A2 and B2 scenarios in the Paute basin. They show that biases of GCM ensembled precipitation projections are as large as PRECIS results, however, gradients are better captured by PRECIS. It is important to note that the PRECIS RCM limitations are reduced in the present study due to: i) the use of a better regional climate model, in this case WRF using parameterizations adapted to the study region at a higher resolution (ca. 0.1°); and ii) WRF was driven by GCMs with the best representation among all GCMs from CMIP5 models. Thus, the limitations coming from a cascade of uncertainties involved in climate projections will be present (e.g., intra-model, scenario, downscaling techniques, initial conditions, etc.), and it is highly advisable to try to reduce or at least quantify them when possible.

The findings in the present study that showed the overall future tendency for the Coast and the Highlands as a slight reduction of moderate and severe droughts for both RCPs in the three DGCMs, might be related to the increase in precipitation projections for this region found in other studies (Palomino-Lemus et al., 2015; Steinhoff et al., 2015). On a monthly scale, this reduction is less evident for extreme droughts, whereas for moderate and severe droughts, the decrease is similar throughout the year. In the Amazon region, the projection of droughts is more complex. IPSL and CSIRO for moderate droughts showed some increase in the probability of occurrence from May to October, for severe droughts the increase is expected from May to December, and for extreme droughts increases are expected from January to April and to a greater extent during October and November. Contrarily, for GISS, in the Amazon region, the projections for moderate and severe droughts showed a slight decrease throughout the year for both RCPs, whereas for extreme drought some increase is expected from May to July for RCP 4.5 and no change is projected for RCP 8.5. Thus, for some DGCMs there is some evidence that wet seasons will have less probability of droughts than present time, which may be linked to the results of Barichivich et al. (2018) that wet seasons will be wetter and dry seasons drier.

Future Climatic Processes Affecting Droughts in Ecuador

To better interpret the plausibility of these results, an analysis of the future changes in the climatic processes may be helpful. The increase of future precipitation in Ecuador and southern Colombia might be due to the colder mean state of the Tropical Pacific SST produced by a downward shift of the ITCZ (Karmalkar et al., 2011; Steinhoff et al., 2015). Contrarily, the southward shift of the ITCZ will produce a decrease of precipitation along the coast of Central America during the wet season (Karmalkar et al., 2011). With respect to the western part of the Amazon basin, the projections show increased precipitation especially after 2040, and decreases in future droughts (Duffy et al., 2015), which agrees with our findings. These results might be explained by the colder mean state of

the eastern Pacific, producing more rainfall in the Ecuadorian Andes and Amazon, but may affect the Coast through the dipolar response of rainfall in Ecuador to ENSO (Rossel and Cadier, 2009; Bendix et al., 2011; Campozano et al., 2016a).

Several factors may be determinant for the occurrence of future droughts, highlighting the uncertainty of this complex phenomenon. For instance, despite the fact that GCMs have varying degrees of ENSO representation, Power et al. (2013) claim that robust changes in projected precipitation are expected, with drying- on the western Pacific and increasing trends in the eastern Pacific. Along similar lines, Steinhoff et al. (2015) argue that, despite the underestimation of ENSO related precipitation, GCMs show the same sign anomalies. In addition, the precipitation in the Amazon is highly dependent on regional evapotranspiration, which might be affected under unfavorable land use change conditions increasing the probability of droughts occurrence (Duffy et al., 2015). Other factors such as the weakening and lowering of the south Pacific Anticyclone (Urrutia and Vuille, 2009) might also affect the occurrence of droughts, especially along the western coasts of South-America.

In relation to GCMs uncertainty, Yeh et al. (2014) showed that the representation of Tropical Pacific SST during the second half of the twentieth century shifted from La Niña-like pattern in CMIP3 models to El Niño-like patterns in the CMIP5 models. A plausible explanation of the eastward shift of the SST positive anomalies relies on an increased Bjerknes feedback with SST in the CMIP5 models with respect to CMIP3 counterparts (Yeh et al., 2012). Although such uncertainties affect drought predictability, there are world-wide statistically significant increasing trends in drought hazard in future projections (Carrao et al., 2018), which demands immediate action for adaptation measures and CC mitigation efforts to limit greenhouse gas emissions.

Climate change has important societal implications for both extremes (i.e., droughts and floods) because they produce similar economic losses on an annual basis (Trenberth, 2008). Floods produce higher damage to property, loss of life, and infrastructure, whereas droughts pose tremendous threats to society by negatively impacting agriculture and increasing risks of wildfires and heat waves. Furthermore, Trenberth (2008) reported cases where the impact of floods were more severe after droughts, thus in climate change conditions a more robust assessment for decision making is necessary. This aspect of a changing climate is more challenging for decision-making and adaptation strategies (Lawrence et al., 2013), and implies more dynamical risks for the future. In this context, our study has contributed to better mapping the space-time evolution of future drought risk in Ecuador, thus providing valuable information for water management and decision making as Ecuador faces climate change.

DATA AVAILABILITY STATEMENT

The datasets generated for this study are available on request to the corresponding author.

AUTHOR CONTRIBUTIONS

LC, DB, and MM: conceptual design. DB: scripts development. LC, DB, MM, and AA: article development.

ACKNOWLEDGMENTS

The authors would like to thank INAMHI for providing ground stations data and MAE for sharing downscaled results from the Third National Communication project. AA would like to thank the Direction of Investigation of the University of Cuenca for their support of the project: "Evaluación del riesgo de sequias en cuencas andinas reguladas influenciadas por la variabilidad climática y cambio climático. Caso de estudio en la cuenca del rio Machángara." The authors would also like to thank Freek Everaert from the University of Azuay for the careful English revision.

SUPPLEMENTARY MATERIAL

The Supplementary Material for this article can be found online at: https://www.frontiersin.org/articles/10.3389/feart.2020.00017/full#supplementary-material

REFERENCES

Allen, M. R., and Ingram, W. J. (2002). Constraints on future changes in climate and the hydrologic cycle. *Nature* 419, 228–232. doi: 10.1038/nature01092

Armenta, G., Villa, J., Jácome, P. (2016). *Proyección Climática de Precipitación y Temperatura Para Ecuador Bajo Distintos Escenarios de Cambio Climático*. Quito: Ministerio del Ambiente. Available online at: https://info.undp.org/docs/pdc/Documents/ECU/14ProyeccionesdeClimaFuturoparaEcuadorenbaseaIPCC-AR5.pdf (accessed February 14, 2020)

Avilés, A., Célleri, R., Paredes, J., and Solera, A. (2015). Evaluation of markov chain based drought forecasts in an andean regulated river basin using the skill scores RPS and GMSS. *Water Resour. Manage* 29, 1949–1963. doi: 10.1007/s11269-015-0921-2

Avilés, A., Célleri, R., Solera, A., and Paredes, J. (2016). Probabilistic forecasting of drought events using markov chain-and bayesian network-based models: a case study of an andean regulated river basin. *Water* 8:37. doi: 10.3390/w8020037

Barichivich, J., Gloor, E., Peylin, P., Brienen, R. J. W., Espinoza, J. C., Pattnayak, K. C., et al. (2018). Recent intensification of Amazon flooding extremes driven by strengthened Walker circulation. *Sci. Adv.* 4:eaat8785. doi: 10.1126/sciadv.aat8785

Beguería, S., and Vicente-Serrano, S. M. (2017). *SPEI: Calculation of the Standardised Precipitation-Evapotranspiration Index. R package version 1.7*. Available online at: https://CRAN.R-project.org/package=SPEI. (accessed December 13, 2019).

Beguería, S., Vicente-Serrano, S. M., Reig, F., and Latorre, B. (2014). Standardized precipitation evapotranspiration index (SPEI) revisited: parameter fitting, evapotranspiration models, tools, datasets and drought monitoring. *Int. J. Climatol.* 34, 3001–3023. doi: 10.1002/joc.3887

Bendix, J., and Lauer, W. (1992). Die niederschlagsjahreszeiten in Ecuador und ihreklimadynamische interpretation. *Erdkunde* 46, 118–134. doi: 10.3112/erdkunde.1992.02.04

Bendix, J., Rollenbeck, R., Göttlicher, D., and Cermak, J. (2006). Cloud occurrence and cloud properties in Ecuador. *Climate Res.* 30, 133–147. doi: 10.3354/cr030133

Bendix, J., Trachte, K., Palacios, E., Rollenbeck, R., Göttlicher, D., Nauss, T., et al. (2011). El Niño meets la Niña—anomalous rainfall patterns in the "Traditional" el Niño region of Southern Ecuador. *Erdkunde* 65, 151–167. doi: 10.3112/erdkunde.2011.02.04

Burke, E. J., Brown, S. J., and Christidis, N. (2006). Modeling the recent evolution of global drought and projections for the twenty-first century with the hadley centre climate model. *J. Hydrometeorol.* 7, 1113–1125. doi: 10.1175/JHM544.1

Buytaert, W., Vuille, M., Dewulf, A., Urrutia, R., Karmalkar, A., and Célleri, R. (2010). Uncertainties in climate change projections and regional downscaling in the tropical Andes: implications for water resources management. *Hydrol. Earth Syst. Sci.* 14, 1247–1258. doi: 10.5194/hess-14-1247-2010

Campozano, L., Ballari, D., and Celleri, R. (2016a). *Imágenes TRMM para identificar patrones de precipitación e índices ENSO en Ecuador*. Maskana, 185–191. Available online at: http://dspace.ucuenca.edu.ec/handle/123456789/21368 (accessed February 14, 2020).

Campozano, L., Célleri, R., Trachte, K., Bendix, J., and Samaniego, E. (2016b). Rainfall and cloud dynamics in the andes: a Southern Ecuador Case Study. *Adv. Meteorol.* 2016:15. doi: 10.1155/2016/3192765

Campozano, L., Sánchez, E., Aviles, A., and Samaniego, E. (2015). *Evaluation of Infilling Methods for Time Series of Daily Precipitation and Temperature: The Case of the Ecuadorian Andes*. Maskana, 99–115. Available online at: http://dspace.ucuenca.edu.ec/handle/123456789/5586 (accessed February 14, 2020).

Carrao, H., Naumann, G., and Barbosa, P. (2018). Global projections of drought hazard in a warming climate: a prime for disaster risk management. *Climate Dyn.* 50, 2137–2155. doi: 10.1007/s00382-017-3740-8

Chang, T. J., and Kleopa, X. A. (1991). A proposed method for drought monitoring. *JAWRA* 27, 275–281. doi: 10.1111/j.1752-1688.1991.tb03132.x

Chavez, S. P., and Takahashi, K. (2017). Orographic rainfall hot spots in the Andes-Amazon transition according to the TRMM precipitation radar and *in situ* data. *J. Geophys. Res. Atmos.* 122, 5870–5882. doi: 10.1002/2016JD026282

Chen, H., and Sun, J. (2017). Characterizing present and future drought changes over eastern China. *Int. J. Climatol.* 37, 138–156. doi: 10.1002/joc.4987

Collier, M. A., Rotstayn, L. D., Kim, K.-Y., Hirst, A. C., and Jeffrey, S. J. (2013). Ocean circulation response to anthropogenic-aerosol and greenhouse gas forcing in the CSIRO-Mk3. 6 coupled climate model. *Aust. Meteorol. Oceanogr. J.* 63, 27–39. doi: 10.22499/2.6301.003

Dai, A. (2011). Characteristics and trends in various forms of the Palmer Drought Severity Index during 1900–2008. *J. Geophys. Res.* 116:D12115. doi: 10.1029/2010JD015541

Dai, A. (2013). Increasing drought under global warming in observations and models. *Nat. Clim. Chang.* 3, 52–58. doi: 10.1038/nclimate1633

Di Luca, A., de Elía, R., and Laprise, R. (2015). Challenges in the quest for added value of regional climate dynamical downscaling. *Curr Climate Change Rep.* 1, 10–21. doi: 10.1007/s40641-015-0003-9

Domínguez-Castro, F., García-Herrera, R., and Vicente-Serrano, S. M. (2018). Wet and dry extremes in Quito (Ecuador) since the 17th century. *Int. J. Climatol.* 38, 2006–2014. doi: 10.1002/joc.5312

Duffy, P. B., Brando, P., Asner, G. P., and Field, C. B. (2015). Projections of future meteorological drought and wet periods in the Amazon. *PNAS*. 112, 13172–13177. doi: 10.1073/pnas.1421010112

Espinoza, J. C., Ronchail, J., Guyot, J. L., Junquas, C., Vauchel, P., Lavado, W., et al. (2011). Climate variability and extreme drought in the upper Solimões River (western Amazon Basin): understanding the exceptional 2010 drought. *Geophys. Res. Lett.* 38:L13406. doi: 10.1029/2011GL047862

Esquivel-Hernández, G., Mosquera, G. M., Sánchez-Murillo, R., Quesada-Román, A., Birkel, C., Crespo, P., et al. (2019). Moisture transport and seasonal variations in the stable isotopic composition of rainfall in Central American and Andean Páramo during El Niño conditions (2015–2016). *Hydrol. Proces.* 33, 1802–1817. doi: 10.1002/hyp.13438

Feng, S., Hu, Q., Huang, W., Ho, C.-H., Li, R., and Tang, Z. (2014). Projected climate regime shift under future global warming from multi-model, multi-scenario CMIP5 simulations. *Glob. Planet. Change* 112, 41–52. doi: 10.1016/j.gloplacha.2013.11.002

Fontaine, G., Narváez, I., and Cisneros, P. (2008). *Geo Ecuador 2008: Informe Sobre el Estado del Medio Ambiente*. FLACSO. Quito, Ecuador. Available online at: https://biblio.flacsoandes.edu.ec/libros/digital/41444.pdf (accessed December 13, 2019).

Goldberg, R. A., Tisnado, M., G., and Scofield, R. A. (1987). Characteristics of extreme rainfall events in Northwestern Peru during the 1982–1983 El Nino period. *J. Geophys. Res.* 92, 14225–14241. doi: 10.1029/JC092iC13p14225

Heuzé, C., Heywood, K. J., Stevens, D. P., and Ridley, J. K. (2015). Southern Ocean bottom water characteristics in CMIP5 models. *Geophys. Res. Lett.* 40, 1409–1414. doi: 10.1002/grl.50287

Hijmans, R. (2017). *Raster: Geographic Data Analysis and Modeling. R package version 2.6-7*. Available online at: https://CRAN.R-project.org/package=raster. (accessed December 13, 2019).

Hirota, N., and Takayabu, Y. N. (2013). Reproducibility of precipitation distribution over the tropical oceans in CMIP5 multi-climate models compared to CMIP3. *Climate Dyn.* 41, 2909–2920. doi: 10.1007/s00382-013-1839-0

Hourdin, F., Foujols, M.-A., Codron, F., Guemas, V., Dufresne, J.-L., Bony, S., et al. (2013). Impact of the LMDZ atmospheric grid configuration on the climate and sensitivity of the IPSL-CM5A coupled model. *Climate Dyn.* 40, 2167–2192. doi: 10.1007/s00382-012-1411-3

Huang, J., Yu, H., Guan, X., Wang, G., and Guo, R. (2016). Accelerated dryland expansion under climate change. *Nat. Clim. Chang.* 6, 166–171. doi: 10.1038/nclimate2837

Karmalkar, A. V., Bradley, R. S., and Diaz, H. F. (2011). Climate change in Central America and Mexico: regional climate model validation and climate change projections. *Clim Dyn.* 37:605–629. doi: 10.1007/s00382-011-1099-9

Lawrence, J., Reisinger, A., Mullan, B., and Jackson, B. (2013). Exploring climate change uncertainties to support adaptive management of changing flood-risk. *Environ. Sci. Policy* 33, 133–142. doi: 10.1016/j.envsci.2013.05.008

Lloyd-Hughes, B., and Saunders, M. A. (2002). A drought climatology for Europe. *Int. J. Climatol.* 22, 1571–1592. doi: 10.1002/joc.846

Mach, K. J., Mastrandrea, M. D., Bilir, T. E., and Field, C. B. (2016). Understanding and responding to danger from climate change: the role of key risks in the IPCC AR5. *Climatic Change* 136, 427–444. doi: 10.1007/s10584-016-1645-x

Marengo, J. A., Nobre, C. A., Tomasella, J., Oyama, M. D., de Oliveira, G. S., de Oliveira, R., et al. (2008). The drought of Amazonia in 2005. *J. Clim.* 21, 495–516. doi: 10.1175/2007JCLI1600.1

McKee, T. B., Doesken, N. J., and Kleist, J. (1993). "The relationship of drought frequency and duration to time scales," in *Proceedings of the 8th Conference on Applied Climatology* (Boston, MA: American Meteorological Society), 179–183.

Mehran, A., AghaKouchak A., and Phillips, T. J. (2014). Evaluation of CMIP5 continental precipitation simulations relative to satellite-based gauge-adjusted observations. *J. Geophys. Res. Atmos*. 119, 1695–1707. doi: 10.1002/2013JD021152

Ministerio de Electricidad y Energía Renovable (2018). *Ministra de Electricidad resaltó los logros energéticos alcanzados en el 2017*. Ministerio de Electricidad y Energía Renovable: Quito. Available online at: http://historico.energia.gob.ec/13685-2/. (accessed December 13, 2019).

Ministerio del Ambiente (2009). *Estudio de vulnerabilidad actual a los riesgos climáticos en el sector de los recursos hídricos en las cuencas de los ríos Paute, Jubones, Catamayo, Chone, Portoviejo y Babahoyo*. Ministerio del Ambiente: Quito. Available online at: https://www.researchgate.net/publication/261798786_Estudio_de_vulnerabilidad_actual_a_los_riesgos_climaticos_en_el_sector_de_los_recursos_hidricos_en_las_cuencas_de_los_Rios_Paute_Jubones_Catamayo_Chone_Portoviejo_y_Babahoyo (accessed December 13, 2019).

Mishra, A. K., and Singh, V. P. (2010). A review of drought concepts. *J. Hydrol.* 391, 202–216. doi: 10.1016/j.jhydrol.2010.07.012

Mora, D., Campozano, L., Cisneros, F., Wyseure, G., and Willems, P. (2014). Climate changes of hydrometeorological and hydrological extremes in the Paute basin, Ecuadorean Andes. *Hydrol. Earth Syst. Sci.* 18, 631–648. doi: 10.5194/hess-18-631-2014

Morid, S., Smakhtin, V., and Moghaddasi, M. (2006). Comparison of seven meteorological indices for drought monitoring in Iran. *Int. J. Climatolol.* 26, 971–985. doi: 10.1002/joc.1264

Naranjo, P. (1981). *El Clima del Ecuador*. Quito: Casa de la Cultura Ecuatoriana.

Orozco, R. V. (2017). *El impacto del comercio del Banano en el desarrollo del Ecuador*. Revista AFESE, 53. Available online at: https://afese.com/img/revistas/revista53/comerbanano.pdf. (accessed December 13, 2019).

Palomino-Lemus, R., Córdoba-Machado, S., Gámiz-Fortis, S. R., Castro-Díez, Y., and Esteban-Parra, M. J. (2015). Summer precipitation projections over northwestern South America from CMIP5 models. *Glob. Planet. Change* 131, 11–23. doi: 10.1016/j.gloplacha.2015.05.004

Paulo, A. A., Pereira, L. S., and Matias, P. G. (2003). "Analysis of local and regional droughts in southern Portugal using the theory of runs and the Standardised Precipitation Index," in *Tools for Drought Mitigation in Mediterranean Regions. Water Science and Technology Library*, eds G. Rossi, A. Cancelliere, L. S.

Pereira, T. Oweis, M. Shatanawi, A. Zairi (Dordrecht: Springer), 55–78. doi: 10.1007/978-94-010-0129-8_4

Penalba, O. C., and Rivera, J. A. (2013). Future changes in drought characteristics over southern South America projected by a CMIP5 multi-model ensemble. *Am. J. Climate Change* 2, 173–182. doi: 10.4236/ajcc.2013.23017

Peralta, S. L. P., Aguilar, H. R., Loayza, A. G. E. A., and Morejón, L. A. S. (2018). *Aporte del sector agropecuario a la economía del Ecuador. Análisis crítico de su evolución en el período de dolarización. Años 2000–2016*. Available online at: https://www.revistaespacios.com/a18v39n32/a18v39n32p07.pdf (accessed December 13, 2019).

Phillips, O. L., Aragão, L. E., Lewis, S. L., Fisher, J. B., Lloyd, J., López-González, G., et al. (2009). Drought sensitivity of the Amazon rainforest. *Science* 323:1344–1347. doi: 10.1126/science.1164033

Podestá, G., Skansi, M. M., Herrera, N., and Veiga, H. (2015). *Descripción de índices para el monitoreo de sequía meteorológica implementados por el Centro Regional del Clima para el Sur de América del Sur. Reporte Técnico CRC-SAS-2015-001*. Buenos Aires: Centro Regional del Clima para el Sur de América del Sur. Available online at: http://www.crc-sas.org/es/content/monitoreo/reporte_sequias.pdf (accessed December 13, 2019).

Poveda, G., and Mesa, O. J. (2000). On the existence of Lloró (the rainiest locality on earth): enhanced ocean-land-atmosphere interaction by a low-level jet. *Geophys. Res. Lett.* 27, 1675–1678. doi: 10.1029/1999GL006091

Power, S., Delage, F., Chung, C., Kociuba, G., and Keay, K. (2013). Robust twenty-first-century projections of El Nin o and related precipitation variability. *Nature* 502, 541–5. doi: 10.1038/nature12580

Rivera, J. A. (2014). *Aspectos climatológicos de las sequías meteorológicas en el sur de Sudamérica. Análisis regional y proyecciones futuras* (PhD Thesis). Facultad de Ciencias Exactas y Naturales. Universidad de Buenos Aires, Buenos Aires, Argentina. Available online at: http://hdl.handle.net/20.500.12110/tesis_n5504_Rivera (accessed December 13, 2019).

Rossel, F., and Cadier, E. (2009). El Niño and prediction of anomalous monthly rainfalls in Ecuador. *Hydrol. Process.* 23, 3253–3260. doi: 10.1002/hyp.7401

Schiermeier, Q. (2010). The real holes in climate science. *Nature* 463, 284–287. doi: 10.1038/463284a

Schmidt, G. A., Kelley, M., Nazarenko, L., Ruedy, R., Russell, G. L., Aleinov, I., et al. (2014). Configuration and assessment of the GISS ModelE2 contributions to the CMIP5 archive. *J. Adv. Model. Earth Syst.* 6, 141–184. doi: 10.1002/2013MS000265

Sierra, J. P., Arias, P. A., and Vieira, S. C. (2015). Precipitation over Northern South America and its seasonal variability as simulated by the CMIP5 models. *Adv. Meteorol.* 2015, 1–22. doi: 10.1155/2015/634720

Sierra, J. P., Arias, P. A., Vieira, S. C., and Agudelo, J. (2018). How well do CMIP5 models simulate the low-level jet in western Colombia? *Climate Dyn.* 51, 2247–2265. doi: 10.1007/s00382-017-4010-5

Sillmann, J., Kharin, V. V., Zwiers, F. W., Zhang, X., and Bronaugh, D. (2013). Climate extremes indices in the CMIP5 multimodel ensemble: part 2. Future climate projections. *J. Geophys. Res.* 118, 2473–2493. doi: 10.1002/jgrd.50188

Steinhoff, D. F., Monaghan, A. J., and Clark, M. P. (2015). Projected impact of twenty-first century ENSO changes on rainfall over Central America and northwest South America from CMIP5 AOGCMs Climate *Dynamics* 44, 1329–1349. doi: 10.1007/s00382-014-2196-3

Sulca, J., Takahashi, K., Espinoza, J.-C., Vuille, M., and Lavado-Casimiro, W. (2018). Impacts of different ENSO flavors and tropical Pacific convection variability (ITCZ, SPCZ) on austral summer rainfall in South America, with a focus on Peru. *Int. J. Climatol.* 38, 420–435. doi: 10.1002/joc.5185

Taylor, I. H., Burke, E., McColl, L., Falloon, P. D., Harris, G. R., and McNeall, D. (2013). The impact of climate mitigation on projections of future drought, hydrology and earth system. *Science* 17, 2339–2358. doi: 10.5194/hess-17-2339-2013

Tedeschi, R. G., and Collins, M. (2016). The influence of ENSO on South American precipitation during austral summer and autumn in observations and models. *Int. J. Climatol.* 36, 618–635. doi: 10.1002/joc.4371

Trenberth, K. E. (2008). "The impact of climate change and variability on heavy precipitation, floods, and droughts," in *Encyclopedia of Hydrological Sciences*. eds M. G. Anderson and J. J. McDonnells (New York, NY: John Wiley and Sons), 2–11. doi: 10.1002/0470848944.hsa211

Ureña Mora, P., Alfaro Martínez, E. J., Alfaro, S., and Javier, F. (2016). *Propuestas metodológicas para el rellenado de datos ausentes en series de tiempo geofísicas. Guía Práctica de uso*. Available online at: http://www.kerwa.ucr.ac.cr/handle/10669/28888. (accessed December 13, 2019).

Urrutia, R., and Vuille, M. (2009). Climate change projections for the tropical Andes using a regional climate model: temperature and precipitation simulations for the end of the 21st century. *J. Geophys. Res. Atmos.* 114, 1–15. doi: 10.1029/2008JD011021

Vicente-Serrano, S. M. (2006). Differences in spatial patterns of drought on different time scales: an analysis of the Iberian Peninsula. *Water Resourc. Manage.* 20, 37–60. doi: 10.1007/s11269-006-2974-8

Vicente-Serrano, S. M., Aguilar, E., Martínez, R., Martín-Hernández, N., Azorin-Molina, C., Sanchez-Lorenzo, A., et al. (2017). The complex influence of ENSO on droughts in Ecuador. *Climate Dyn.* 48, 405–427. doi: 10.1007/s00382-016-3082-y

Vicente-Serrano, S. M., Beguería, S., and López-Moreno, J. I. (2010). A Multiscalar drought index sensitive to global warming: the standardized precipitation evapotranspiration index. *J. Climate* 23, 1696–1718. doi: 10.1175/2009JCLI2909.1

Wang, L., and Chen, W. A. (2014). CMIP5 multimodel projection of future temperature, precipitation, and climatological drought in China. *Int. J. Climatol.* 34, 2059–2078. doi: 10.1002/joc.3822

Wang, X. L., and Feng, Y. (2013). *RHtestsV3_UserManual*. Climate Research Division Atmospheric Science and Technology Directorate Science and Technology Branch. Environment Canada Toronto, Ontario, Canada. Available online at: http://etccdi.pacificclimate.org/RHtest/RHtestsV3_UserManual.doc. (accessed December 13, 2019).

Wilhite, D. A., Svoboda, M. D., and Hayes, M. J. (2007). Understanding the complex impacts of drought: a key to enhancing drought mitigation and preparedness. *Water Resour Manage* 21, 763–774. doi: 10.1007/s,11269-006-9076-5

WMO—World Meteorological Organization (2009). *WCDMP, 68. Climate observations and climate data management guidelines, WMO/TD*. Available online at: https://library.wmo.int/index.php?lvl=notice_display&id=16666#.XfTiXWRKhPY. (accessed December 13, 2019).

WMO—World Meteorological Organization (2012). *Standardized Precipitation Index User Guide*. Available online at: http://www.wamis.org/agm/pubs/SPI/WMO_1090_EN.pdf. (accessed December 13, 2019).

Xiaolan, L., Wang, X., and Feng, Y. (2013). *RHtestsV4 User Manual*. Climate Research Division Atmospheric Science and Technology Directorate Science and Technology Branch, Environment Canada Toronto, Ontario, Canada. Available online at: http://etccdi.pacificclimate.org/software.shtml (accessed December 13, 2019).

Yeh, S. W., Ham, Y. G., and Kirtman, B. P. (2014). A possible explanation on the changes in the spatial structure of ENSO from CMIP3 to CMIP5. *Geophys. Res. Lett.* 41, 140–145. doi: 10.1002/2013GL058478

Yeh, S. W., Ham, Y. G., and Lee, J. Y. (2012). Changes in the tropical pacific SST trend from CMIP3 to CMIP5 and its implication of ENSO. *J. Clim.* 25, 7764–7771. doi: 10.1175/JCLI-D-12-00304.1

Zambrano Mera, Y. E., Rivadeneira Vera, J. F., and Pérez-Martín, M. Á. (2018). Linking El Niño Southern Oscillation for early drought detection in tropical climates: the Ecuadorian coast. *Sci. Total Environ.* 643, 193–207. doi: 10.1016/j.scitotenv.2018.06.160

Zhiña, D., Montenegro, M., Montalván, L., Mendoza, D., Contreras, J., Campozano, L., et al. (2019). Climate change influences of temporal and spatial drought variation in the andean high mountain basin. *Atmosphere* 10:558. doi: 10.3390/atmos10090558

Conflict of Interest: The authors declare that the research was conducted in the absence of any commercial or financial relationships that could be construed as a potential conflict of interest.

Copyright © 2020 Campozano, Ballari, Montenegro and Avilés. This is an open-access article distributed under the terms of the Creative Commons Attribution License (CC BY). The use, distribution or reproduction in other forums is permitted, provided the original author(s) and the copyright owner(s) are credited and that the original publication in this journal is cited, in accordance with accepted academic practice. No use, distribution or reproduction is permitted which does not comply with these terms.

frontiers in Earth Science

REVIEW
published: 17 March 2020
doi: 10.3389/feart.2020.00061

Observed and Projected Hydroclimate Changes in the Andes

José Daniel Pabón-Caicedo[1], Paola A. Arias[2], Andrea F. Carril[3,4], Jhan Carlo Espinoza[5], Lluís Fita Borrel[3,4], Katerina Goubanova[6], Waldo Lavado-Casimiro[7], Mariano Masiokas[8], Silvina Solman[9,3,4] and Ricardo Villalba[8,4]*

[1] Departamento de Geografía, Universidad Nacional de Colombia, Bogotá DC, Colombia, [2] Grupo de Ingeniería y Gestión Ambiental (GIGA), Escuela Ambiental, Facultad de Ingeniería, Universidad de Antioquia, Medellín, Colombia, [3] Centro de Investigaciones del Mar y la Atmósfera (CIMA/UBA-CONICET), Ciudad Autónoma de Buenos Aires, Buenos Aires, Argentina, [4] Institut Franco-Argentin d'Etudes sur le Climat et ses Impacts (UMI-IFAECI/CNRS-IRD-CONICET-UBA), Buenos Aires, Argentina, [5] IRD, CNRS, G-INP, IGE (UMR 5001), Université Grenoble Alpes, Grenoble, France, [6] Centro de Estudios Avanzados en Zonas Áridas (CEAZA), La Serena, Chile, [7] Dirección de Hidrología, Servicio Nacional de Meteorología e Hidrología (SENAMHI), Lima, Peru, [8] Instituto Argentino de Nivología, Glaciología y Ciencias Ambientales (IANIGLA), CCT-CONICET Mendoza, Mendoza, Argentina, [9] Departamento de Ciencias de la Atmósfera y los Océanos DCAO-FCEN-UBA, Facultad de Ciencias Exactas y Naturales, Universidad de Buenos Aires, Buenos Aires, Argentina

The Andes is the most biodiverse region across the globe. In addition, some of the largest urban areas in South America are located within this region. Therefore, ecosystems and human population are affected by hydroclimate changes reported at global, regional and local scales. This paper summarizes progress of knowledge about long-term trends observed during the last two millennia over the entire Andes, with more detail for the period since the second half of the 20th century, and presents a synthesis of climate change projections by the end of the 21st century. In particular, this paper focuses on temperature, precipitation and surface runoff in the Andes. Changes in the Andean cryosphere are not included here since this particular topic is discussed in other paper in this Frontiers special issue, and elsewhere (e.g. IPCC, 2019b). While previous works have reviewed the hydroclimate of South America and particular sectors (i.e., Amazon and La Plata basins, the Altiplano, Northern South America, etc.) this review includes for the first time the entire Andes region, considering all latitudinal ranges: tropical (North of 27°S), subtropical (27°S–37°S) and extratropical (South of 37°S). This paper provides a comprehensive view of past and recent changes, as well as available climate change projections, over the entire Andean range. From this review, the main knowledge gaps are highlighted and urgent research necessities in order to provide more mechanistic understanding of hydroclimate changes in the Andes and more confident projections of its possible changes in association with global climate change.

Keywords: hydroclimate of the Andes, global change in the Andes, hydroclimate trends in the Andes, hydroclimate projections of the Andes, climate change in the Andes, climate change scenarios for the Andes

OPEN ACCESS

Edited by:
Bryan G. Mark, The Ohio State University, United States

Reviewed by:
Eduardo Zorita, Helmholtz Centre for Materials and Coastal Research (HZG), Germany
Mario Bruno Rohrer, Meteodat GmbH, Switzerland

****Correspondence:***
José Daniel Pabón-Caicedo
jdpabonc@unal.edu.co

Specialty section:
This article was submitted to Atmospheric Science, a section of the journal Frontiers in Earth Science

Received: *21 October 2019*
Accepted: *19 February 2020*
Published: *17 March 2020*

Citation:
Pabón-Caicedo JD, Arias PA, Carril AF, Espinoza JC, Borrel LF, Goubanova K, Lavado-Casimiro W, Masiokas M, Solman S and Villalba R (2020) Observed and Projected Hydroclimate Changes in the Andes. Front. Earth Sci. 8:61. doi: 10.3389/feart.2020.00061

INTRODUCTION

Earth's environment has experienced long-term changes at planetary and continental scales, including changes of atmospheric circulation, ocean circulation, carbon cycle, nitrogen cycle, water cycle, sea-ice extension, sea level, food chains, biological diversity, air, and water composition, among many others (IPCC, 2013). Currently, these changes in consequence provoke several

environmental impacts such as soil degradation, desertification, water and air pollution, water, energy and food scarcity, and health problems (IPCC, 2014, 2019a,b). In the Andean region, global environmental change has been evidenced mainly in the modification of land cover, land use and hydroclimate. Changes in land cover, which have impacted regional water and energy cycles, involves different time-scales driven by geological and climate processes, which shaped the altitudinal zones (types of vegetation and glaciers) throughout different periods of evolution (Flantua, 2017).

The interaction of regional atmospheric circulation with the Andean orography configures the current spatial and seasonal patterns of regional hydroclimate that are modified during long periods by other processes of the Earth's system, but this interaction varies along the Andes. In the north tropical Andes (North of 8°S; Ecuador, Colombia, and Venezuela) and south tropical Andes (8°S–27°S; Peru, Bolivia), the eastern side (inward) of the Cordillera allows the convergence of the atmospheric moisture provided by the Intertropical Convergence Zone (ITCZ) and by the South American Monsoon System (SAMS), generating a humid environment and a particular feature in the distribution of mass (atmospheric moisture) and energy (latent and sensible heat) (Makarieva and Gorshkov, 2007; Poveda et al., 2014; Espinoza et al., 2015; Chavez and Takahashi, 2017). On the eastern side of the subtropical Andes occur some of the strongest convective phenomena in the world (Altinger de Schwarzkopf and Rosso, 1982; Rasmussen et al., 2014; Zuluaga and Houze, 2015). Warm and wet air from the Amazonian region is transported along the eastern side of the Andes to the south generating a low-level jet. Strong and deep convection is generated when this air is uplifted by the "Sierras de Córdoba" and/or interacts with incoming south cold fronts and upper level disturbances. In the western side of the Southern Andes, the prevailing atmospheric moisture source is the evaporation from the Pacific Ocean (Gimeno et al., 2016). Moreover, the heavy orographic precipitation events during winter over the western slopes of the subtropical (27°S–37°S) and extratropical Andes (South of 37°S; mainly central and southern Chile) are strongly related to the intense water vapor transport from the southern Pacific, associated with extratropical cyclones (Viale and Nuñez, 2011), with the most intense rainfall occurring near and above the top of the mountain range (Falvey and Garreaud, 2007). These features of the Andean hydroclimate have experienced recent changes, as evidenced by several studies.

Previous research has provided new knowledge about Andean environment, allowing a better understanding of regional hydroclimate processes, including changes of hydroclimate patterns in different time scales. Most previous studies have been dedicated to specific regions into the Andes, while an integrated overview of the observed and projected hydroclimatic changes throughout the Andes is still lacking. In addition, there are still several research topics that need further development and surely new research problems have appeared that need to be solved. The review presented here focuses on the progress of knowledge about hydroclimate changes observed during the last two millennia as well as changes throughout the 20th Century, and climate change projections by the 21st Century over the Andes. First, we summarize current knowledge on the hydroclimate changes of the Andes during the last two millennia, followed by the changes during the last decades and a final section related to projected changes. We finalize with a description of the main concluding remarks.

HYDROCLIMATE CHANGES IN THE ANDES DURING THE LAST TWO MILLENNIA

Given the shortness of most instrumental climate records along the Andes, it is highly recommendable to rely on paleoenvironmental records to characterize natural climate variability and place current climate changes in the context of the last hundred to thousand years (Bradley, 2013). Particular emphasis has been given to the study of climatic variations during the last 2000 years, a period in which the conditions of the global climate system have been very similar to those of today (i.e., similar sea levels, approximately the same global ice cover, similar ocean circulation; Abram et al., 2016). In the effort to characterize past climates, the Andes provide a unique opportunity since along the region, the large diversity of paleo-indicators with its long geographic extension can be combined. The diverse topography of the Andes houses numerous high-resolution natural archives (seasonal to decadal information on climate), including ice cores, tree rings, speleothems, sedimentary records, boreholes and historical documents, among others. The Andes mountains constitute the richest region with high-resolution paleoenvironmental records in South America, and possibly in the entire Southern Hemisphere (SH; Villalba et al., 2009). Most of the high-resolution paleoenvironmental records available in the Andes cover the last 200–500 years, but some of them exceed 2000 years (Lara and Villalba, 1993).

One of the major questions that persist in paleoclimate studies over the past millennia is to establish the global imprint of well-documented climate anomalies in the Northern Hemisphere (NH). Periods abundantly documented in Europe and other mid-latitudes in the NH (Bradley, 2013), such as the Medieval Climate Anomaly (MCA, the warm period centered on the first centuries of the last millennium) or the Little Ice Age (LIA, the cold interval between the 15th and 19th centuries), have not yet been conclusively substantiated across South America. It is well known that glaciers advanced in the Andes concurrent with the LIA in Europe, but important differences in the timing of the ice advances along the Andes have already been documented (Masiokas et al., 2009). There is no consensus on the causes of the LIA, but most studies indicate that the LIA event was induced by the combination of frequent volcanic eruptions and weak solar radiation (Ahmed et al., 2013; Brönnimann et al., 2019). The existence of MCA has been proposed for South America for over 30 years (Villalba, 1994), but evidence of its occurrence is still scarce and not always straightforward. In this section, we review a selection of high-resolution (annual or seasonal) paleoclimatic studies

based on records along the Andes to depict long-term variations in temperature and precipitation during the last 2000 years. Although the major emphasis is placed on precipitation changes, we also collect information on past temperature variations to illustrate the occurrence of long-term past climatic events showing major contrasts in hydroclimatic conditions such as droughts and floods.

Temperature and Precipitation Changes in the Tropical Andes (North of 27°S)

High-resolution proxies sensitive to temperature are scarce in the tropical Andes (Villalba et al., 2009). Based on ammonium (NH_4 + concentrations in ice cores from Nevado Illimani (16°37′S, 67°46′W, 6300 m), Bolivia, Kellerhals et al. (2010) reconstructed the temperature variations over the past 1600 years for this sector of tropical South America (**Figure 1C**). The Nevado Illimani temperature record shows relatively warm conditions during the first centuries of the last millennium followed by colder temperature between the 15th and 18th centuries. This record suggests that the MCA and LIA events were not limited to high-latitudes in the NH but also registered at 16°S in tropical South America. Nevertheless, while the LIA cooling in the NH has traditionally been associated with an increase in frequency and intensity of volcanic eruptions concurrent with a reduction in solar radiation (Bradley, 2013; Brönnimann et al., 2019), in the tropical Andes it was likely related to precipitation-temperature interactions. In the tropical Andes, increased cloud cover during wet conditions reduces air temperature, in line with the simultaneous occurrence of wet (dry) and cool (warm) periods in Pumacocha (**Figure 1B**) and Nevado Illimani (**Figure 1C**), respectively. Therefore, the simultaneous occurrence of long-term temperature anomalies at both mid-high NH latitudes and the tropical Andes may have been modulated by different drivers, but they might be dynamically connected. In the Nevado Illimani temperature reconstruction, the last decades of the 20th century are characterized by extremely warm temperatures that seem unprecedented in the context of the last 1600 years (Kellerhals et al., 2010).

Different paleo-indicators suggest that the changes in the SAMS during the last millennia were connected, to some extent, with the inter-hemispheric temperature gradient over the Atlantic Ocean, affecting hydroclimate of the Andes-Amazon region. The $\delta^{18}O$ records from the laminated sediments in Laguna Pumacocha (10°42′S, 76°04′W; **Figure 1**) show that the SAMS underwent in the last 2300 years decadal to multi-decadal scale variability embedded in three main centennial-long intervals. The first period concurrent with the MCA in the NH was characterized by pronounced dryness. It was followed by markedly humid conditions during the LIA and a return to drier conditions since the beginning of the 20th century (**Figure 1B**). This current warm period (CWP) was characterized by the highest positive $\delta^{18}O$ values throughout the 2300-year record (Bird et al., 2011). Thus, in response to pronounced cooling of the NH during the LIA (**Figure 1A**), the ITCZ would have moved toward the south, intensifying the monsoon activity in the Amazon basin and, in general, at the tropical portion of South America, including the tropical Andes (Bird et al., 2011; Vuille et al., 2012). On the contrary, during the warm periods of the MCA and CWP in the NH, the ITCZ migrated northward, reducing the transport of humidity toward the core of the SAMS domain, increasing the dry conditions over the tropical Andes. The long-term temporal oscillations in the $\delta^{18}Ocal$ record from Pumacocha were concurrent with variations recorded in the temperature reconstruction for NH (**Figures 1A,B**) by Moberg et al. (2005), suggesting that long-term changes in SAMS intensity are sensitive to fluctuations in ITCZ latitude on similar time scales (Bird et al., 2011; Novello et al., 2012, 2016; Vuille et al., 2012).

In the most arid southwestern sector of the South American Altiplano (18–22°S, 67–69°S), the *Polylepis tarapacana* tree rings have been successfully used to reconstruct the variations in annual rainfall over the past seven centuries (**Figure 1D**; Morales et al., 2012). In this sector of the Altiplano, summer rains represent more than 80% of total annual precipitation. In the Altiplano, as in other regions of the Andes, El Niño-Southern Oscillation (ENSO) events introduce an enormous interannual variability in precipitation, which somehow masks the long-term oscillations (Christie et al., 2009). However, the reconstruction of precipitation shows persistent long-term periods with abundant or reduced rainfalls (**Figure 1D**). The persistent rainfall reduction since the mid-19th century to the present is the most relevant long-term feature in the reconstruction. Since the 1930s, this persistent negative trend in precipitation has intensified, with the driest years since 1300 AD occurring in the last 70 years.

Precipitation Changes in the Subtropical Andes (27°S–37°S)

Austrocedrus chilensis tree-ring records have recently been used to develop the first millennial reconstruction of rainfall in the subtropical Andes, particularly in central Chile (Garreaud et al., 2017). Similar to the Altiplano, rainfall in central Chile shows large ENSO-induced interannual variability (Montecinos and Aceituno, 2003). This enormous variability hinders to some extent the direct identification of long-term oscillations in rainfall during the last 1000 years, even though some long-term anomalies are well identified (**Figure 1E**). During the 11th and 13th centuries concurrent with the MCA, multi-decadal dry periods were observed. Preceded by a long wet period, the reduction of rainfall from the beginning of the 19th century to the CWP constitutes, as in the Altiplano, the most outstanding long-term feature of the last millennium. On the other hand, the two long-term periods with abundant rainfall do not seem to be associated with the colder (LIA) event, but with the transitions from the MCA to LIA, and from LIA to CWP, centered on the 14th and early 18th centuries (**Figure 1E**).

Temperature and Precipitation Changes in the Extratropical Andes (South of 37°S)

At extratropical latitudes, summer temperature reconstructions derived from *Fitzroya cupressoides tr*ee rings (Villalba, 1990; Lara and Villalba, 1993, and updates) indicate that the 20th century

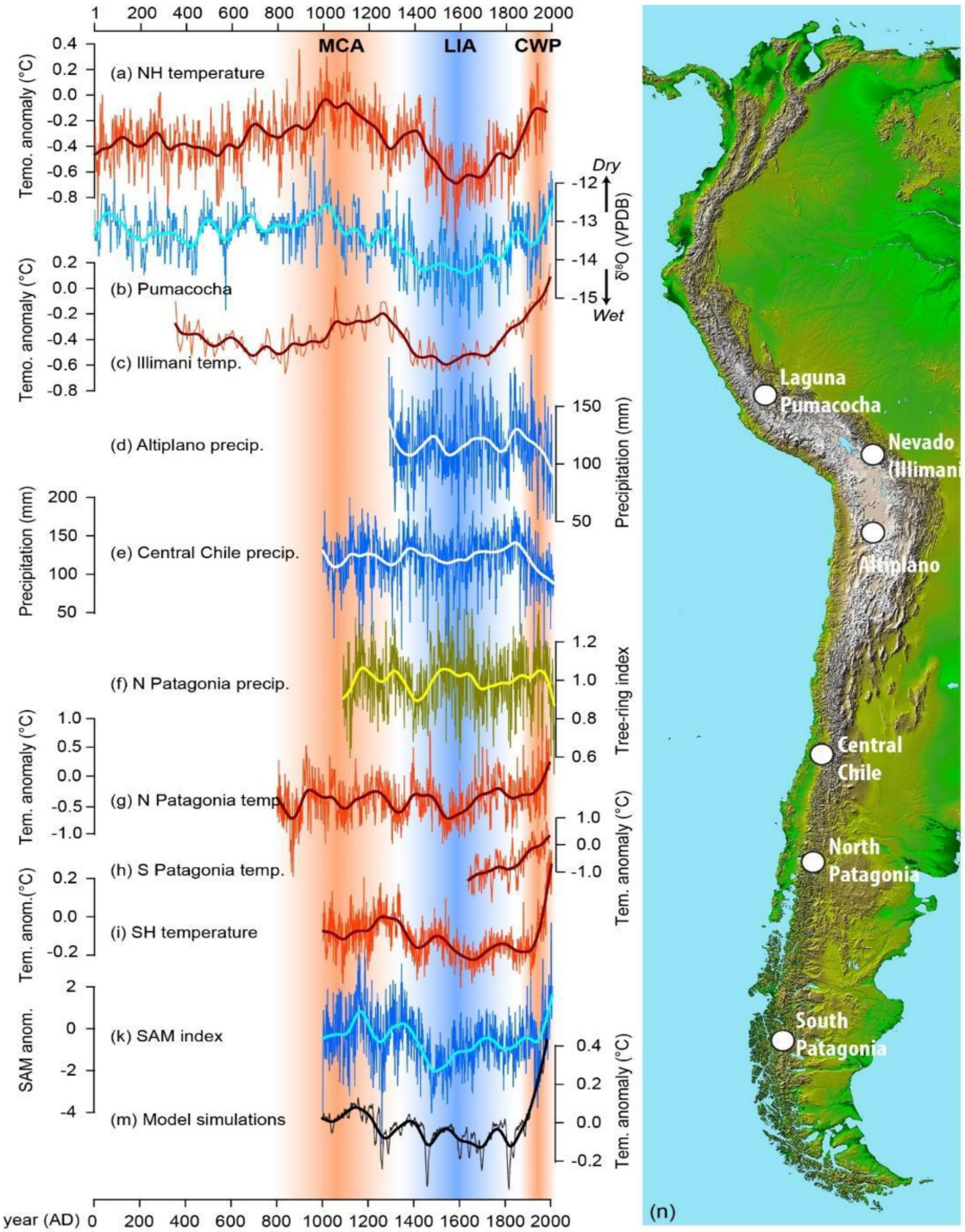


FIGURE 1 | Climatic variations along the Andes during the last 2000 years and their relationships with hemispheric and global forcings of long-term climate variability. **(A)** Reconstruction of NH temperature anomalies (Moberg et al., 2005), **(B)** The Pumacocha $\delta^{18}O$ record of SAMS intensity (Bird et al., 2011); **(C)** Reconstruction of tropical South American temperature anomalies (Kellerhals et al., 2010); **(D)** Annual precipitation reconstruction in the South American Altiplano (Morales et al., 2012); **(E)** Reconstruction of winter–early summer (June–December) normalized precipitation anomalies from Central Chile (Garreaud et al., 2017); **(F)** Precipitation-sensitive chronology from Austrocedrus chilensis in northern Patagonia (Villalba et al., 2012); **(G)** Summer (December-February) temperature reconstruction in northern Patagonia (Villalba, 1990 and updates); **(H)** Annual temperature variations in southern Patagonia (Villalba et al., 2003); **(I)** Ensemble mean temperature reconstruction for the SH relative to the millennium mean (Neukom et al., 2014); **(K)** Summer (December-March) reconstruction of the Southern Annular Mode (Dätwyler et al., 2018); **(M)** Twenty-four member climate model ensemble for temperature variability in the SH (Neukom et al., 2014). To emphasize the long-term variability, all records are also shown in a smoothed version using a 128-year spline filter; **(N)** Map of the western part of South America showing the location of the proxy records and the geographical areas discussed in the text.

has been the warmest interval during the last millennium in the northern Patagonian east of the Andes (**Figure 1G**). The records of stable isotopes from *Fitzroya* extending from AD 1800 to present, also indicate that the 20th century was warmer than the 19th century, recording the highest temperatures of the past 200 years since the mid-1970 (Lavergne et al., 2018). The lowest temperatures in the eastern sector of northern Patagonia were concurrent with the LIA in the NH (**Figure 1A**) and with the period of lowest temperatures in the SH over the last millennium (**Figure 1I**). During the MCA, reconstructed temperatures oscillated around the long-term mean (**Figure 1G**). Most of the long-term periods with low temperatures in northern Patagonia showed abundant precipitations (**Figures 1G,F**), a climatic pattern seen in current instrumental records during summer (Bianchi et al., 2016).

High-resolution reconstructions of temperature variations in southern South America (47–52°S) have been based on *Nothofagus pumilio* tree-ring chronologies and they are limited to the past 200–400 years (Aravena et al., 2002; Villalba et al., 2003). In these records, the lowest temperatures reconstructed during the end of the LIA contrast with the period of high temperatures since the beginning of the 20th century (**Figure 1H**). As in northern Patagonia, temperatures from the 1970s onward are the warmest in the last four centuries. Although current high-resolution paleoclimatic records in the region are limited in temporal coverage, a combination of radiocarbon and dendrochronological dating of *in situ* subfossil trunks buried by glacial deposits support the occurrence of a warmer interval before than the LIA (Masiokas et al., 2009). Trees buried by glacier advances associated with LIA suggest that forests in front of valley glaciers were established during the MCA, when temperatures in southern Patagonia were similar to or even higher than today. These records support the occurrence of cold events during the LIA preceded by warmer events concurrent with the MCA in the southern Patagonian Andes. This pattern of temperature variations is consistent with those recorded in both the NH (**Figure 1A**) and SH (**Figure 1I**) and with Southern Annular Mode (SAM) variations over the last 1000 years showing positive indices from approximately 1000 to 1400 and recently from 1900 to present (**Figure 1K**).

Ten degrees latitude farther south in the Andes, variations in precipitation over the last millennium have also been estimated from *Austrocedrus chilensis* trees at the dry steppe-forest ecotone in northern Patagonia (37–44°S; Villalba et al., 1998, 2012 and updates). Similar to the Altiplano and central Chile, the inter-annual variability in this precipitation-sensitive record is very high, masking somewhat the low-frequency climatic signal in the record (**Figure 1F**). The longest wet period from mid-15th to late-17th centuries in the past millennium was concurrent with the cold period of the LIA recorded in both the NH (**Figure 1A**) and the SH (**Figure 1I**), as well as in northern Patagonia temperature reconstruction (**Figure 1G**). Two prolonged dry periods at the end of the 11th century and centered on the 14th century were recorded during the MCA (**Figure 1F**). These two long-term dry periods have been surpassed in magnitude by the severe droughts in recent decades (**Figure 1F**). Indeed, northern Patagonia has showed the largest reduction in precipitation in the extratropical Andes since the mid-20th century (Quintana and Aceituno, 2012), a negative precipitation trend associated with the persistently positive increase in the SAM (**Figure 1K**). Consistent with the SAM influences on precipitation in northern Patagonia during the instrumental period (Garreaud et al., 2009; Villalba et al., 2012), the long-term interval with abundant precipitation during the LIA was concurrent with the most marked negative trends in SAM during the last millennium (**Figure 1K**; Dätwyler et al., 2018).

Paleoclimate Model Simulations

A 24-member multi-model ensemble for temperature variations during the past millennium in the SH (**Figure 1M**; Neukom et al., 2014) show some common features with proxy-based climate reconstructions. The warmest pre-industrial temperatures are simulated sometime between 1050 and 1250 preceding somewhat the phase of maximum SH pre-industrial warmth in the SH temperature reconstruction (**Figure 1I**; Neukom et al., 2014). Between 1300 and 1900, simulated temperatures are close to the 1000–2000 mean, periodically interrupted by shorter volcanically induced cold excursions. In contrast to the delay in industrial SH warming in the SH temperature reconstruction (**Figure 1I**), the climate model simulations show a mostly synchronous temperature increase after 1850 (**Figure 1M**). The multi-model temperature ensemble shows some similarities with the temporal evolution of the SAM (**Figure 1K**) during the last 1000 years, particularly during the period AD 1000–1500. However, Dätwyler et al. (2018) explicitly stated no link between their reconstructed SAM index and external forcings, suggesting that the apparent trend similarities between simulated SH temperatures and the reconstructed SAM may only be just coincidence. The clearest global cooling signals in response to the volcanic eruptions around years 1450 (likely Reclus volcano; Hartman et al., 2019) and 1258 (Samalas) in the ensemble models are present in the SAM reconstruction (**Figure 1K**), recording two of the most negative indices during these volcanic eruptions.

The number of high-resolution paleoenvironmental records should be increased to achieve a comprehensive view of the long-term climatic variations over the past two millennia across the extensive and topographically complex Andes Mountains. However, the proxy indicators developed so far have initially allowed us to advance our understanding of long-term climate variability in the Andes. The seven selected natural archives shown in **Figure 1**, regardless of type (trees, sedimentary records, ice cores) and parameters evaluated (ring width, chemical or isotopic composition), coincide in showing that the climate during the last decades (to be discussed in the following section) along the Andes is experiencing extreme climatic conditions, many of them unprecedented in the last millennia (**Figure 1**).

HYDROCLIMATE CHANGES IN THE ANDES OBSERVED DURING THE LAST DECADES

Recent hydroclimate changes over the Andes are widely manifested by trends in air surface temperature, precipitation,

glaciers area and volume, runoff and surface land cover. Here, the recent trends on hydroclimate variables in the Andes are reviewed. Cryosphere changes in the Andes are not discussed in this work. This topic is discussed by a paper in this Frontiers special issue, and by the recent Intergovernmental Panel on Climate Change (IPCC) special report on oceans and cryosphere in a changing climate (IPCC, 2019b).

Air Surface Temperature Trends in the Andes

The IPCC Fifth Assessment Report (AR5) summarized scientific literature addressing trends of air surface temperature in South America (IPCC, 2013, 2014). However, since 2012, several regional studies not assessed in the AR5 (Marengo et al., 2012a; Pabón, 2012; de los Skansi et al., 2013; Lavado-Casimiro et al., 2013; Seiler et al., 2013a,b; Carmona and Poveda, 2014; Vuille et al., 2015; Castino et al., 2016; Morán-Tejeda et al., 2016) provide updated analyses and revisit previous trend estimates over different zones in the Andes, as well as point out a number of scientific questions associated with the detected trends.

Among all studies, there is a general agreement in the rising of temperatures from different perspectives and metrics. These studies suggest an overall increase in the number of warm days and nights, as well as a decrease of cold nights and days over western South America (i.e., the Andean belt from Ecuador to Argentina). IPCC (2014) reported an increasing trend of 0.1–0.4°C/decade in monthly mean temperature and an overall increase of temperature extremes on tropical (North of 27°S) and subtropical (27°S–37°S) Andes. Over the tropical Andes minimum and maximum temperatures show a rising trend with a few exceptions in Bolivia and Peru highlands (Martínez et al., 2011). Barkhordarian et al. (2017) attributed an increase of daily maximum and minimum temperatures, especially during the December-January-February (DJF) over the north tropical Andes (North of 8°S), to anthropogenic activity. In addition, over the Amazon rainforest, warming trends have reached values of 0.6–0.7°C over the last 40 years, suggesting 2016 as the warmest year in the region since at least 1950 (Jimenez-Muñoz et al., 2018; Marengo et al., 2018a).

A growing number of studies suggests that the rate of warming may be amplified with elevation (e.g., Rangwala and Miller, 2012; Pepin et al., 2015; Palazzi et al., 2017, 2019). Although there is not yet full agreement on this issue, the elevation-dependent warming (EDW) may have important implications for the mass balance of the high-altitude cryosphere; it can accelerate the rate of change in mountain hydrological regime, ecosystems, and biodiversity. The lack of a dense network of stations along the Andes does not allow addressing comprehensively this issue. However, Russell et al. (2017) show evidence from several reanalysis products of a regional enhancement of mid-tropospheric warming around the south tropical Andes (8°S–27°S) over the past few decades that makes this region stand out as a hotspot within the broader pantropic. On the other hand, a vertical stratification of the temperature trends over recent decades has been documented by a number of regional studies for the tropical Andes and western slopes of the subtropical Andes (27°N–37°N) (Falvey and Garreaud, 2009; Vuille et al., 2015; Burger et al., 2018). Vuille et al. (2015) and Aguilar-Lome et al. (2019) show an EDW of air and land surface temperature in the region, respectively (**Figure 2**). These studies suggest that the tropical Andes (north of 27°S) have suffered a warming trend of 0.15–0.2°C/decade above the 4000 m.a.s.l during the last four decades. Vuille et al. (2015) further suggest that future warming at higher elevations will likely enhance vertical stratification of atmospheric temperature trends, whereas in coastal locations, temperature trends will depend on changes in large-scale circulation controlling near-coastal sea surface temperature (SST), and on the state of Pacific Oscillations, such as the Pacific Decadal Oscillation (PDO).

Climate of the subtropical and extratropical Andes (South of 27°S; Chile and Argentina) has undergone significant changes during the last century. Though the *in situ* data coverage from meteorological and hydrological stations is sparse over the region, several studies dealing with a variety of datasets and analysis show agreement in identifying the temperature increase as the most robust climate signal. However, these trends are not uniform all along the subtropical and extratropical Andes, but highly dependent on regional features. Masiokas et al. (2006); Rusticucci et al. (2014) and Saavedra et al. (2018) reported a sustained warming trend on both sides of the subtropical Andes (27°S-37°S), especially at annual scale and during the warm season in central Chile (DJF).

Table 1 summarizes estimates of air surface temperature trends over different periods in the Andes from previous studies.

Precipitation Trends in the Andes

Trends in annual precipitation exhibit different signs across sectors in the Andes. For instance, annual precipitation trends in north tropical (north of 8°S) and south tropical (8°S–27°S) Andes do not show a homogeneous pattern, ranging between −4%/decade and +4%/decade with respect to the mean annual precipitation volume of a 30-year period at the end of the 20th century. Even within the inter-Andean valleys of northern South America, precipitation trends have opposite signs (Pabón, 2012; Carmona and Poveda, 2014; IDEAM-UNAL, 2018). In particular, precipitation has been increasing over the eastern slopes of the Andes in Colombia, Ecuador and northern Peru. For the 1964–2008 period, Martínez et al. (2011) reported decreasing trends in annual precipitation in the north tropical (north of 8°S) and south tropical (8°S–27°S) Andes with exception of the western cordillera of the Colombian Andes, the Ecuadorian Andes, and a few sites in the southern highlands of Peru. Martínez et al. (2011) also reported a positive trend of relative humidity in northern Ecuador and southern Colombia, and less marked positive trends over southern Peru and western Bolivia. These trends coincide with positive cloud cover trends in the northern tropical Andes during December-January-February, while a negative trend in the southern sector of the tropical Andes is observed. Barry and Seimon (2000) suggested an apparent upward shift in the orographic cloud band over this region, highlighting the

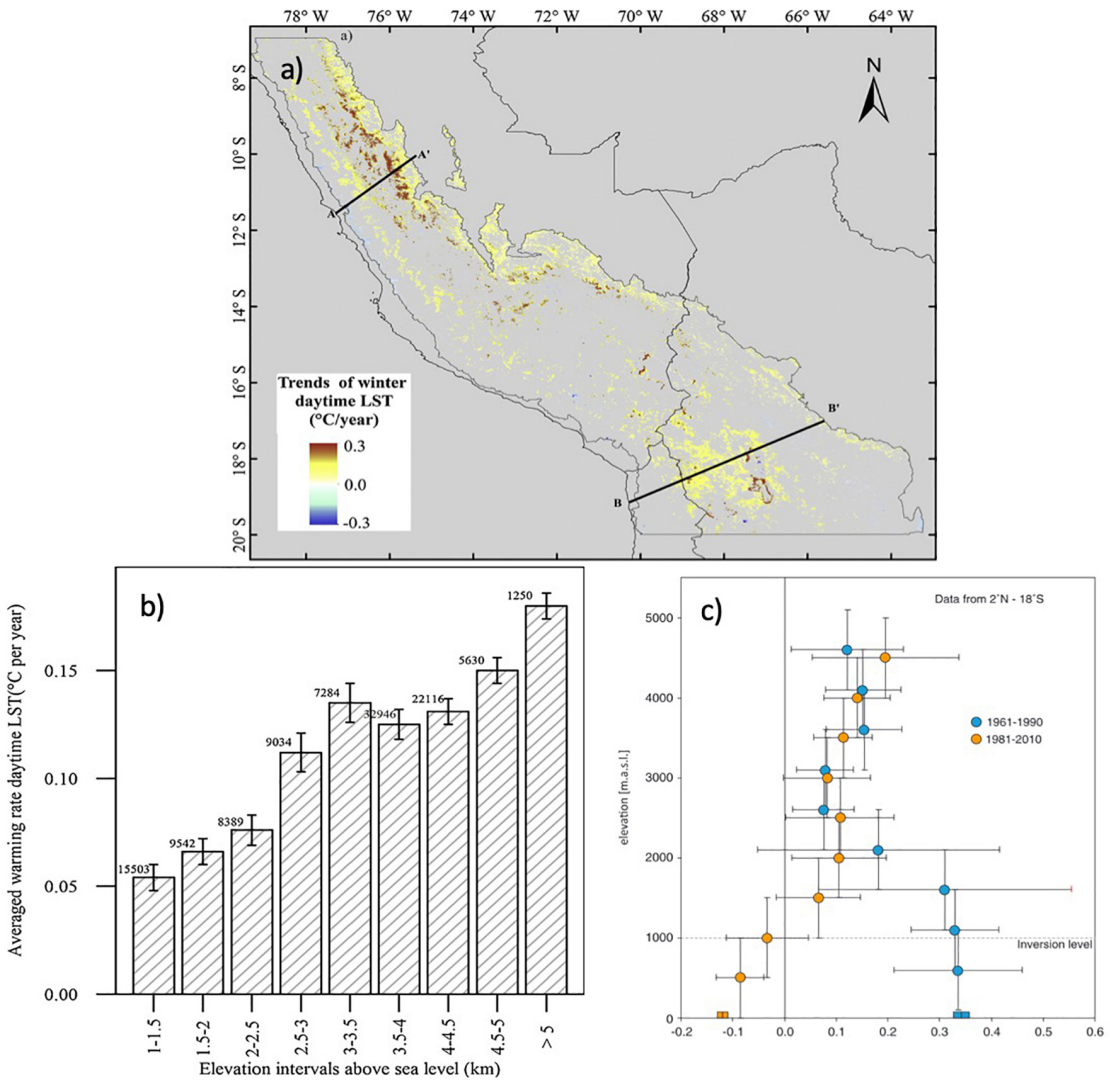


FIGURE 2 | (a) Spatial distribution of the daytime land surface temperature (LST; °C/year) trend in austral winter [June-July-August (JJA)] over the Andes between 7°S and 20°S for the period 2000–2017 (MODIS LST Data). Trends are significant at 95% (p = 0.05) confidence level. **(b)** Averages of winter daytime LST trends at 500-m intervals in the tropical Andes (7°S–20°S). Values at the top of bars indicate the number of MODIS pixels at each elevation range. **(a,b)** Are adapted from Aguilar-Lome et al. (2019). © International Journal of Applied Earth Observation and Geoinformation. Reprinted by permission from Elsevier. **(c)** Air temperature trends versus altitude along the western tropical Andean slopes (2°N–18°S) for the periods 1961–1990 (blue circle) and 1981–2010 (orange circle). Adapted from Vuille et al. (2015). © American Geophysical Union. Reprinted by permission from John Wiley and Sons.

importance of this vertical cloud shift supporting cloud forest and regional natural environment.

The Amazonian side of the north tropical Andes (northern and northwestern Amazon) has experienced wetter conditions since the mid-1990s, particularly during its wet season (December to May) (Espinoza et al., 2009; Gloor et al., 2013; Barichivich et al., 2018; Wang et al., 2018). Increasing rainfall intensity has been related to an enhanced convective activity over this region and the intensification of the Walker cell since the mid-1990s. Wet-day frequency (WDF) significantly increases in the northern Amazon (north of 8°S), producing an estimated rainfall increase during the March-April-May (MAM) season of 17% between 1981 and 2017 (**Figure 3**; Espinoza et al., 2019a). These significant changes in both WDF and rainfall in the northern Amazon have been detected since 1998. After 1998, the increase in MAM WDF and rainfall is explained by enhanced moisture flux from the tropical North Atlantic Ocean and an increase in deep convection over the northern and northwestern Amazon.

Over the central and southern Amazon, the dry-day frequency (DDF) has increased in austral winter and spring, during the 1981–2017 period, particularly for September-October-November (SON) (Espinoza et al., 2019a), which corresponds to the wet season onset in this region (**Figure 3**). Consistently, total rainfall in the southern Amazon during SON also shows a significant decrease of 18% during

TABLE 1 | Trends detected in air temperature and precipitation in the Andes.

Region	Air Temperature	Precipitation	Period Analyzed	Authors
VNZ	Increase of minimum temperature; decrease of diurnal temperature range (last 25 years of their analysis)		1965–1990	Quintana-Gómez, 1999
		Increase of precipitation between 25 and 75 mm/decade	1950–2010	de los Skansi et al., 2013
COL	Increase of mean temperature between 0.01–0.08°C/year	Increase of precipitation over 41% of sites between 0.1 and 7.0 mm/year; decrease in 44% of sites between 0.1–7.4 mm/year	25–50 years	Carmona and Poveda, 2014
	Increase of mean temperature between 0.1 and 0.2°C/decade; slight decrease in number of frost days	Decrease of precipitation in most of the Colombian Andes; increase in some places of the Magdalena river basin slopes	1960–2005	Pabón, 2012
		Increase of precipitation between 25 and 75 mm/decade over the Andes of Colombia; decrease of precipitation between 75 and 25 mm/decade in the Andes of Colombia	1950–2010	de los Skansi et al., 2013
ECU	Increase of maximum and minimum temperatures (average increase of 0.25°C/decade)	Increase of precipitation in most sites of Andes	1966–2011	Morán-Tejeda et al., 2016
	Overall increase of number of warm days and warm nights; reduction of cold days and cold nights	Increase of precipitation between 0.25 and 0.5 mm/year	1950–2010	de los Skansi et al., 2013
		Decrease in rainfall over the Ecuadorian-Peruvian Amazon basin	1971–2004 (at Tamshiyacu basin); 1969–2004 (at Tabatinga basin)	Espinoza et al., 2011; Lavado-Casimiro et al., 2012
PER	Increase of mean temperature of about 0.09°C/decade over the Amazon-Andes basin		1965–2007	Lavado-Casimiro et al., 2013
		Decrease in total annual rainfall in the southern Amazon basin. Decrease in 1-day and 5-day yearly maximum rainfall in the central coast of Peru, with an increase in the number of wet days	1965–2010	Heidinger et al., 2018
		Negative trend in precipitation in central Peruvian Andes of −4%/decade during January–March	1970–2004	Silva et al., 2008
	Overall increase of number of warm days and warm nights; reduction of cold days and cold nights	Slight increase of precipitation (up to 25 mm/decade) at the northern and a small sector at the southern Peruvian Andes; decrease of precipitation (25–75 mm/decade) over the central Peruvian Andes and close to Bolivia	1950–2010	de los Skansi et al., 2013
	Annual minimum (maximum) temperature increase of 0.18 (0.16) °C/decade		1964–2014	Vicente-Serrano et al., 2018
	In Cordillera Blanca (8°S-11°S), an increase of 0.31°C/decade over 1969–1998 and a slowdown in the warming to 0.13°C/decade over 1983–2012		1969–2012	Schauwecker et al., 2014

(Continued)

TABLE 1 | Continued

Region	Air Temperature	Precipitation	Period Analyzed	Authors
BOL	Increase of mean temperature of 0.1°C/decade	Increase of precipitation before 1984 (12% in DJF and 18% in JJA); decrease since 1984 (4% in DJF and 10% in JJA)	1960–2009	Seiler et al., 2013a
	Increase of number of warm nights; decrease of number of cold nights; in some places decrease of warm days and increase of cold days	Decrease of precipitation between 75 and 25 mm/decade at the northern Bolivian Andes; increase precipitation (up to 25 mm/decade) in some places over the central Bolivian Andes	1950–2010	de los Skansi et al., 2013
		Decrease of annual rainfall in southern Bolivian Amazon. Rainfall increase in northern Bolivian Amazon during December-February	1981–2018	Espinoza et al. (2019b)
CHI	Increase of number of warm days and warm nights; reduction of number of cold days and cold nights	Increase of precipitation in some places over central Chilean Andes; decrease of precipitation from central to southern Chile	1950–2010	de los Skansi et al., 2013
		Decrease of annual precipitation about 65 mm/decade (7.1%) in central Chile	1979–2014	Boisier et al., 2016
		Robust drying trend (30°S to 48°S) over 1960–2016	1960–2016	Boisier et al., 2018
		More drought events since the second half of the twentieth century (30–37°S)	1910–2011	González-Reyes et al., 2017
	In central and northern Chile (17°–37°S): strong vertical stratification of temperature trends in the atmosphere west of the Andes: a warming in the Andes (+0.25°C/decade) and surface cooling at coastal stations (−0.2°C/decade)		1979–2006	Falvey and Garreaud, 2009
	Central Chile (30–35°): Significant warming trends in Andes are largely restricted to austral spring, summer and autumn seasons		1979–2015	Burger et al., 2018
ARG		Increase of annual precipitation in the arid, high-elevation southern Andean Plateau; decrease of annual precipitation at low elevations	1979–2014	Castino et al., 2016
	Reduction of number of cold days and cold nights; increase of number of warm days and warm nights	Increase of precipitation in northern and central Argentinian Andes; decrease of precipitation in the southern Argentinian Andes	1950–2010	de los Skansi et al., 2013

the period 1981–2017 (Espinoza et al., 2019a). In agreement, Marengo et al. (2011, 2018a) and Fu et al. (2013) show that the dry season length over the southern Amazon has increased in around 1 month since the 1970s (**Figure 3**), which is associated with a delay in the onset of the SAMS (Arias et al., 2015).

Rainfall trend in the south tropical Andes (8°S–27°S) shows a high sensitivity with respect to the specific region and period considered (Lavado-Casimiro et al., 2012, 2013; Seiler et al., 2013a; Heidinger et al., 2018). In Bolivia, Seiler et al. (2013a) document an increase of rainfall during the 1965–1984 period, and a rainfall decrease since 1984. These results are in agreement with Espinoza et al. (2019a; 2019b) and Molina-Carpio et al. (2017), who report an increase in dry conditions in most of the Bolivian Amazon-Andean rivers since the 1980s. In the Peruvian Andes, including the Pacific coast and the Titicaca basin, no significant rainfall trends are documented (Lavado-Casimiro et al., 2012; Rau et al., 2016); however, decreasing rainfall since 1970 has been reported in the central and southern Peruvian Amazon-Andes (e.g., Silva et al., 2008; Espinoza et al., 2011; Lavado-Casimiro et al., 2012; Heidinger et al., 2018). Over

the subtropical Andes (27°S-37°S), central Chile shows declining precipitation since 1970 partly associated to the variability of the PDO, although at least 25% of this decline is not explained without considering anthropogenic forcing (Boisier et al., 2016). Further analyses confirm this drying trend over central and southern Chile and its link to ozone depletion over the Antarctic (Boisier et al., 2018), affecting regional vegetation and watersheds (Garreaud et al., 2017) and forest fires intensity (Urrutia-Jalabert et al., 2018).

Over the subtropical northwestern Argentinian Andes, Castino et al. (2016) found that precipitation trends are strongly dependent on elevation: low (500 m above sea level -m.a.s.l.), intermediate (500–3000 m), and high-elevation (>30000 m.a.s.l) areas respond differently to changing climate conditions, and the transition zone between low and intermediate elevations is characterized by the most significant positive annual rainfall trends since 1950. At low elevations areas, generalized decreasing trends are observed.

Table 1 summarizes estimates of precipitation trends over the Andes identified from several studies based on different periods and datasets.

Surface Hydrology Trends in the Andes

The sparse and short period of observations of hydrological networks in the Andes hinder the study of hydrological variability and trends in the region. It also hampers hydrological modeling and regional studies (Buytaert and Beven, 2009; Paiva et al., 2011; Zulkafli et al., 2014; Wongchuig-Correa et al., 2017; Zubieta et al., 2017). At the same time, airborne measurement such as satellite-derived precipitation data has large uncertainties in this region, and remote sensing water level data is almost impossible to obtain from the narrow rivers and valleys present in the region. As a consequence, hydrological modeling has been used to extend historical records, simulate land-use and future climate change scenarios and get a better understanding of hydrological processes in the Andes (Buytaert and Beven, 2009; Paiva et al., 2013; Zulkafli et al., 2016; Olsson et al., 2017; Zubieta et al., 2017). Thus, hydrological modeling studies in the region are foreseen to increase.

Despite data shortcomings, several studies based on data from measurements have provided further evidence of hydroclimate changes in the Andes. Carmona and Poveda (2014) found that series of monthly mean river discharge in the tropical Andes of Colombia exhibit significant decreasing trends, although the signal in monthly precipitation records is mixed. Lavado-Casimiro et al. (2012) found no significant trends on mean annual discharge in the western Peruvian Andes and Titicaca Lake tributaries in the northern Altiplano during the 1969–2004 period. Annual river runoff in the western Andes of Colombia, Ecuador, and Chile appeared to increase significantly (Mernild et al., 2018). In the Pauto basin (Ecuador) over the tropical Andes, Mora et al. (2014), found increasing trends in maximum flows and decreasing trends in minimum flows. Espinoza et al. (2011, 2013), Zulkafli et al. (2016); Molina-Carpio et al. (2017) and Wongchuig-Correa et al. (2017) suggest an increasing frequency of droughts and floods in the Andean Amazon region. In the Andes-Amazon region, studies on different specific regions have found diverging trends in river discharge (generally since the 1970s or 1980s). In general, these studies show decreasing discharge trends in the southern Amazon-Andes region (South of Peru and Bolivia) and increased trend in the north (Espinoza et al., 2009; Lavado-Casimiro et al., 2012; Molina-Carpio et al., 2017; Wongchuig-Correa et al., 2017; Ronchail et al., 2018). Some of these changes are associated to both Pacific and Atlantic SST anomalies and atmospheric moisture transport anomalies from the tropical Atlantic into the Amazon basin. In addition, the superposition of northern with Andean western and southern tributaries flood waves have been observed in several extreme floods in this region (Marengo et al., 2012b; Espinoza et al., 2013; Ovando et al., 2016).

The Amazonian side of the north tropical Andes (northern and northwestern Amazon) has experienced an increase in discharge of the northern tributaries of the Amazon River, especially during the period December-May (Espinoza et al., 2009; Gloor et al., 2013; Marengo and Espinoza, 2016; Barichivich et al., 2018), associated with increases of rainfall (see section "Precipitation Trends in the Andes"). Other authors document recent changes in the timing of the annual hydrological cycle in this region. For instance, Ronchail et al. (2018) found a trend to delayed endings and longer duration of the low-water period at Tamshiyacu on the upper Amazon River, as well as a more abruptly ending of the flood recession in this region. Rainfall intensification over the northern Amazon after 1998 (see section "Precipitation Trends in the Andes") has produced a major frequency of extreme floods, as recently confirmed by Barichivich et al. (2018), who showed that flood frequency of the Amazon River during the 1903–2015 period has experienced a significant fivefold increase from roughly one flood every 20 years during the first half of the 20th century to one about every 4 years from the 2000s onward (**Figure 3**). In the Argentinian Andes, Castino et al. (2016) found statistically significant increasing trends in river discharge during the 1940–2015 period, documenting an intensification of the hydrological cycle during this period.

Evidence of hydrological changes are also observed in the subtropical and extratropical Andes as changes of snow cover and glacier extension. The robust pattern of positive trends found in temperature records, together with the generalized recession of glaciers observed in the region, suggest that significant changes in climate have already impacted glacier mass balances in the subtropical and extratropical Andes. Changes in temperature and precipitation are the main drivers of changes in snowpack, which may have a strong socioeconomic impact in the region. In fact, Peru, Bolivia, Chile, and Argentina depend on snow and/or glaciers melt for water supply due to short rainy seasons (Masiokas et al., 2010; Peduzzi et al., 2010; Rabatel et al., 2013). Studies focused on assessing trends in snowpack coverage provide contradictory results, mainly owing to the quality and quantity of snow data. Masiokas et al. (2006) reported no significant trends of snow cover for the period 1951–2004 over the subtropical Andes (from 27°S to 37°S) while Saavedra et al. (2018) revealed a significant negative trend of snow cover between 29°S and 36°S during the period 2000–2016, being this decrease even more pronounced on the eastern side of the Andes. The relevance of identifying trends on snowpack characteristics is clear due to

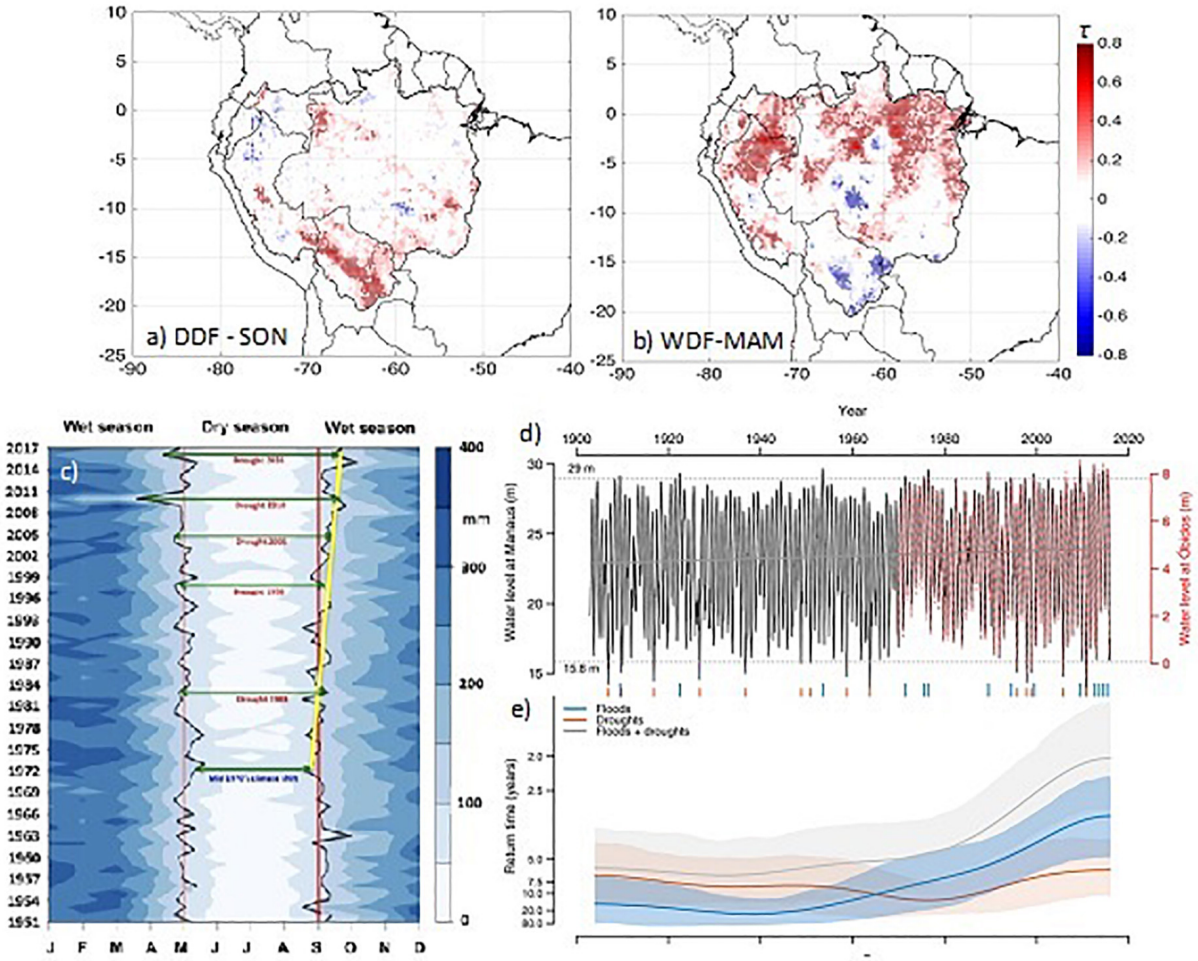


FIGURE 3 | Spatial distribution of Kendall coefficient values ($p < 0.05$ are indicated with a dark dot) showing the trend for: **(A)** 1981–2017 DDF during SON season and **(B)** 1981–2017 WDF during MAM season. DDF (WDF) are defined as days with rainfall <1 mm (>10 mm). Adapted from Espinoza et al. (2019a). © Climate Dynamics. Reprinted by permission from Springer Nature. **(C)** Hovmoller diagram showing monthly rainfall (1951 to 2017) for southern Amazonia (mm/month). The isoline of 100 mm/month is an indicator of dry months in the region (Sombroek, 2001). Drought years are indicated with green lines. Red lines show the average onset and retreat of the rainy season [Adapted from Marengo et al. (2011) and updated to 2017 in Marengo et al. (2018b). © American Geophysical Union. Used with permission]. Yellow line shows the trend to a longer dry season after the mid 1970's climate shift. **(D)** Daily water level of Negro River at Manaus (black; 1903–2015) and Amazon River at Óbidos (red; 1968–2015). The horizontal dotted lines denote the thresholds used to define drought (15.8 m) and flood (29.0 m) events from the Negro River daily water level data. The resulting events are indicated by orange (droughts) and blue (floods) vertical ticks at the bottom of the panel. **(E)** Time-varying frequency of the identified droughts and floods between 1903 and 2015. Adapted from Barichivich et al. (2018). CC licence. © American Association for the Advancement of Science.

its influence on river discharges. However, more extended data records are still needed to provide fully supported evidence of trends in snow pack coverage in the region.

Several studies on monthly and annual mean discharge in the Andes show divergent trends (or no trends at all) and uncertainty is still large. The complexity of hydrological processes along the region, differences in records length, contrasting hydroclimatic variability between regions and the impact of man-induced changes (see section "Vegetation Cover and Land Use Change in the Andes and Its Effect on Regional hydroclimatology") are possible explanations for these divergent trends. For instance, Marengo et al. (1998) identified decreasing trends of minimum flows during the 20th century in the northern Pacific coast of Peru associated to increased water abstraction for irrigation and water supply (Rau et al., 2016). In the Rimac River (the main source of fresh water for Lima city), regulation or hydraulic diversion projects developed in the basin since the 1960s produced significant changes in the hydrological regime. The annual minimum flows increased by 35% while maximum flows decreased by 29% after the regulation data (Vega-Jácome et al., 2017). Souvignet et al. (2012) identified contrasting short and long-term discharge trends in the "Norte Chico" region of Chile (29–32°S). Along the Desaguadero River and Poopo Lake basins in the central Altiplano, a decreasing discharge trend has been identified over the 1966–2012 period (Satgé et al., 2017), associated to increasing

water diversion and transfer, having climate variability as a secondary cause.

Further south, the rivers originating in the Andes between 18° and 55°S also constitute a crucial natural resource and support numerous ecosystems, human populations and a large number of socio-economic activities throughout Chile, western Argentina and southwestern Bolivia. Masiokas et al. (2019) compiled an extensive database of mean monthly streamflow records from these countries to identify the areas with common patterns of hydroclimatic variability during the instrumental era (early 20th century – present). Their results indicate that about 75% of the total variance in the mean annual (April-March) series can be explained by only eight spatially coherent patterns of variations (**Figure 4A**). In the central Andes of Chile and Argentina, the Norte Chico region in Chile, and the northwestern portion of Patagonia, river flows show marked negative trends that culminate in the severe droughts that these regions have been experiencing since 2009–2010. On the contrary, the river flows in northwestern Argentina and southern Bolivia, southern Patagonia (Santa Cruz river), and Tierra del Fuego show positive trends with above-average values in the last decades (**Figure 4**). The ENSO phenomenon in the tropical Pacific can be used to predict between 20% and 45% of the variations observed in the annual streamflows of the Andean basins located between 28° and 46°S. Other large-scale ocean atmospheric indices, such as the SAM or the PDO, also show associations with Andean flows, but their predictive power is weaker than that detected with the El Niño indicators (Masiokas et al., 2019).

Vegetation Cover and Land Use Change in the Andes and Its Effect on Regional Hydroclimatology

The surface land cover of the Andes, a crucial element in water balance, energy budget and climate, has been modified by humans since the beginning of their settlement in high- and mid-altitudes to accomplish their primary needs: shelter, food, and energy. This environmental transformation has been happening during the Holocene (Young, 2009), but became more intense during the last millennium, accelerating about 500 years ago. Currently, diverse ways of land use continue actively producing changes with strong effects on biodiversity, soil dynamics, climate, water resources availability, and hydroclimate extremes. According to Salazar et al. (2015), 3.6 million km^2 of the original natural vegetation cover in non-Amazonian South America (the Andes is a large part of this region) were converted into other types of land use, which is about four times larger than the historical Amazon deforestation. In contrast, land use and land cover (LULC) change processes in non-Amazonian regions have been less studied (Salazar et al., 2015).

Several studies have been conducted in the last decades in order to improve our current knowledge about LULC change dynamics and drivers in the Andes (Etter et al., 2008; Armenteras et al., 2011; Rodriguez-Eraso et al., 2013; Salazar et al., 2015). Rodriguez-Eraso et al. (2013) suggest that cropland, pasture, and secondary vegetation over the north tropical Andes (north of 8°S) showed systematic transitions, changing from a traditional land use to pasture in 1980–2000 period. These authors also note a high spatial variability of transition trends in the region, controlled mainly by attractors and biophysical features. The AR5 (IPCC, 2014), and the Special Report IPCC (2019a) notes that at least for the tropical Andes, the responsible forces of LULC change are deforestation, agriculture, cattle ranching, and gold mining (IPCC, 2014, 2019a), although other socio-political dynamics play important roles in this process (Diaz et al., 2011; Hoffman et al., 2018; Salazar A. et al., 2018).

Celeri and Feyen (2009) explored the hydroclimatic effect of LULC changes in the Andes and established a climate-dependence of conversion from a given land cover to another (for instance, from forest to pastures; from forest to crops; from pastures to crops). Aide et al. (2019) evaluated the change in the distribution of woody vegetation in the tropical Andes for the 2001–2014 period using Moderate Resolution Imaging Spectroradiometer (MODIS) satellite data (250 m pixel resolution) (**Figure 5**). These authors estimated an overall net gain of (∼500,000 ha in woody vegetation. Forest loss dominated the 1,000–1,499 m elevation zone and forest gain dominated above 1,500 m.a.s.l. Forest loss at lower elevations is related to transition from forest to pastures and croplands, while forest gain in abandoned pastures and cropland dominate in mid-elevation areas.

Changes of land cover modify surface radiative properties (albedo and absorption), inducing an effect on surface radiation balance; consequently, LULC changes produce changes in mean surface temperature. Furthermore, LULC changes also have effects on soil-vegetation interactions, which further modifies the hydrological cycle (Bonan et al., 2012). In some cases, for example in transitions from forest to pasture, LULC changes are associated with increasing surface temperature and decreasing soil moisture, precipitation and cloudiness. By contrast, transitions from pastures to coffee crops reduce mean air surface temperature (**Figure 6**) and increase precipitation (Carvajal-Vanegas and Pabón-Caicedo, 2014). These regional effects of LULC change on local hydroclimate may smooth or enhance the signal of global climate change, which result in different impacts on water and energy fluxes as well as on the whole regional environment.

Deforestation has a direct effect on hydrological cycle and energy budget, since forest loss modifies land cover and subsequently hydrological and radiative properties of the soil-vegetation interface. Different studies have addressed deforestation in the Andes at diverse scales. Schoolmeester et al. (2016) compared deforestation rates during two periods (2000–2005 and 2006–2010), finding rate reductions in some Andean countries (Bolivia, Ecuador and Venezuela) and increases in others (Peru and Colombia), although forest loss occurred over the entire region during the overall period of 2000–2014. Later, Armenteras et al. (2017) summarized 369 papers issued within a recent 25 years period and analyzed information with a standardized deforestation rate index in the Andes for tropical mountain forest, subtropical dry forest and subtropical temperate and mixed forests. Their results suggest a high rate of deforestation in the subtropical and extratropical Andes (Chile and Argentina), followed by the tropical Andes (Bolivia, Ecuador, Colombia, and Peru). Deforestation rates vary in the considered

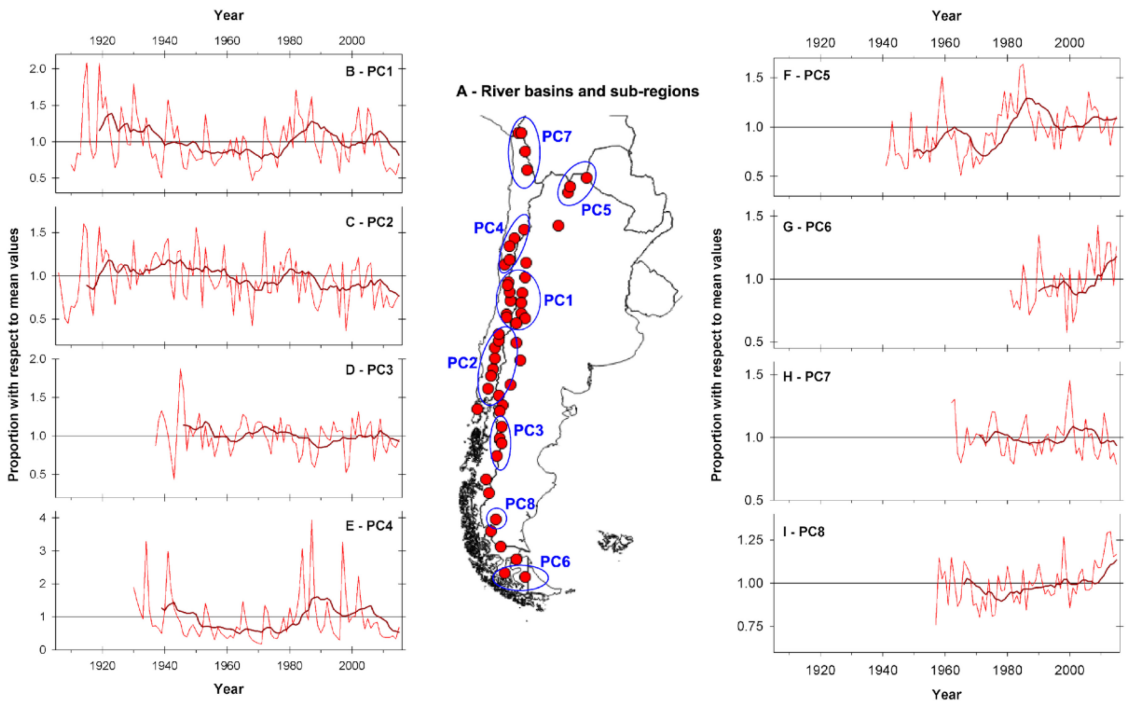


FIGURE 4 | (A) Map showing the location of the selected river basins used to identify the main regional patterns of streamflow variations in the subtropical and extratropical Andes (18–55°S). **(B)** Mean annual (April–March) regionally averaged streamflow record for the PC1 sub-region (thin red line). Ten-year moving averages (thick red line) are also shown to highlight the lower frequency variations in this record. **(C–I)** Same as **(B)**, but for PC2 trough PC8, respectively. See Masiokas et al. (2019) for details.

period, depending on the geophysical and socioeconomic drivers in each country. Furthermore, Armenteras et al. (2017) highlight the convenience of addressing the particular features of each type of forest (dry forest, low-altitude forest, etc.), and not only those related to the main cover forest, in order to assess different analysis regarding water resources as well as hydrological cycle modeling.

Deforestation is one factor that conduces to land degradation (soil loss by water/wind erosion, soil salinization or acidification, soil compaction and drainage suppression), aridization of extended areas, advance of dunes or arid environments (desertification), biological degradation, soil pollution, and landslides, processes that have effect on regional hydroclimate. Several studies have suggested land/soil degradation is related to different causes in different areas along the Andes (e.g., Sayago and Collantes (2016) for Argentina; Preston (2016) for Bolivia; Metternicht and Zinck (2016) and Hugo (2008) for Argentina, Chile, Bolivia, Peru, Ecuador, Colombia, and Venezuela).

At a local scale, deforestation has been related to an increase of the magnitude of floods and droughts (Farley et al., 2005). Bare soils favor runoff, increasing flow velocities and reducing the time for water getting the basin outlet, thus increasing the occurrence and magnitude of peak discharges. On the other side, deforestation reduces infiltration, as well as surface and groundwater storage, leading to the reduction of base flows. These effects are particularly strong in mountain regions and have been extensively modeled (Buytaert and Beven, 2009).

The impacts of forest loss are not limited to areas where land cover changes occur but have a regional influence through atmospheric circulation mechanisms, for instance over the Andes and the Atlantic Ocean (i.e., Boers et al., 2017; Agudelo et al., 2019; Molina et al., 2019). For instance, the Amazon basin provides the Andean region with substantial contributions of water vapor (Sakamoto et al., 2011; Arias et al., 2015; Hoyos et al., 2017, 2018; Salazar J. F. et al., 2018), therefore vegetation changes in the Amazon rainforest modifies atmospheric moisture transport and hydroclimate in the Andes (Builes-Jaramillo et al., 2017; Agudelo et al., 2019; Molina et al., 2019). In this sense, vegetation–atmosphere feedbacks could play a crucial role in future precipitation over the Andes region.

Soil erosion is an immediate effect of deforestation in the Andean slopes. Human-induced soil erosion reduces soil productivity, compromises freshwater ecosystem services and drives geomorphic and ecological change in rivers and floodplains. By combining observations and modeling, Restrepo et al. (2015) estimated that erosion rates within the Magdalena drainage basin in Colombia have increased 33% between 1972 and 2010, increasing the river's sediment load by 44 Mty^{-1}. Much of that river catchment (79%) is under severe erosional conditions due in part to the clearance of more than 70% natural forest between 1980 and 2010. It has been estimated that 9% of the sediment load in the Magdalena River basin is due to deforestation and 482 Mt of sediments was produced due to forest clearance over the last three decades. Extreme

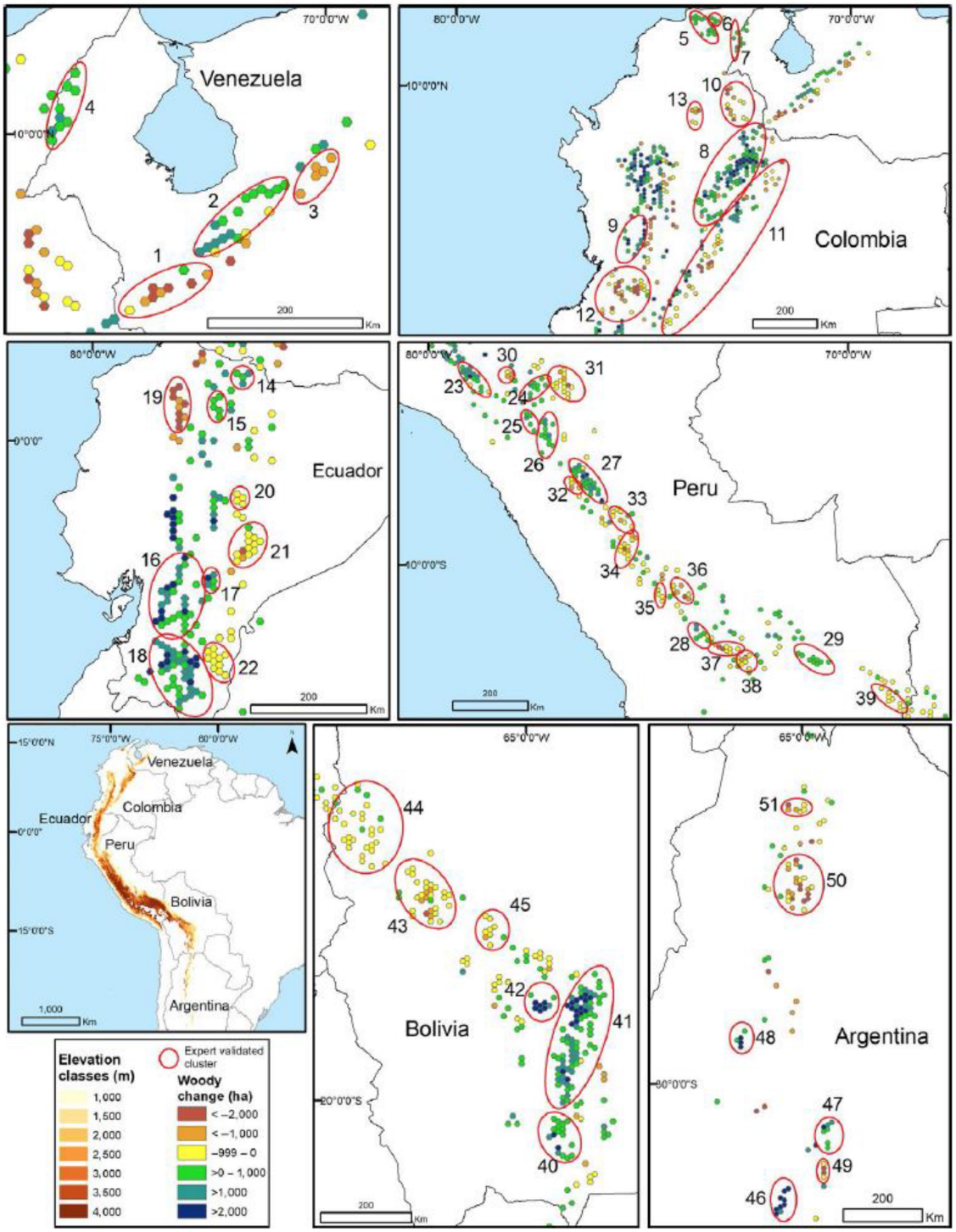


FIGURE 5 | Distribution of elevation classes within the tropical and subtropical Andes and hexagons with a significant 14-year linear increase or decrease in woody vegetation in each country. From Aide et al. (2019).

climate events play also a major role in the production of sediments, such is the case of El Niño events in the Pacific coast of Peru and Ecuador (Morera et al., 2017). The Andean cordillera provides more than 90% of the total of the sediment load observed in the Amazon Basin, with a major contribution from southwestern rivers such as Ucayali and particularly the Madeira River, which accounts for nearly 50% of the total sediment transported into the

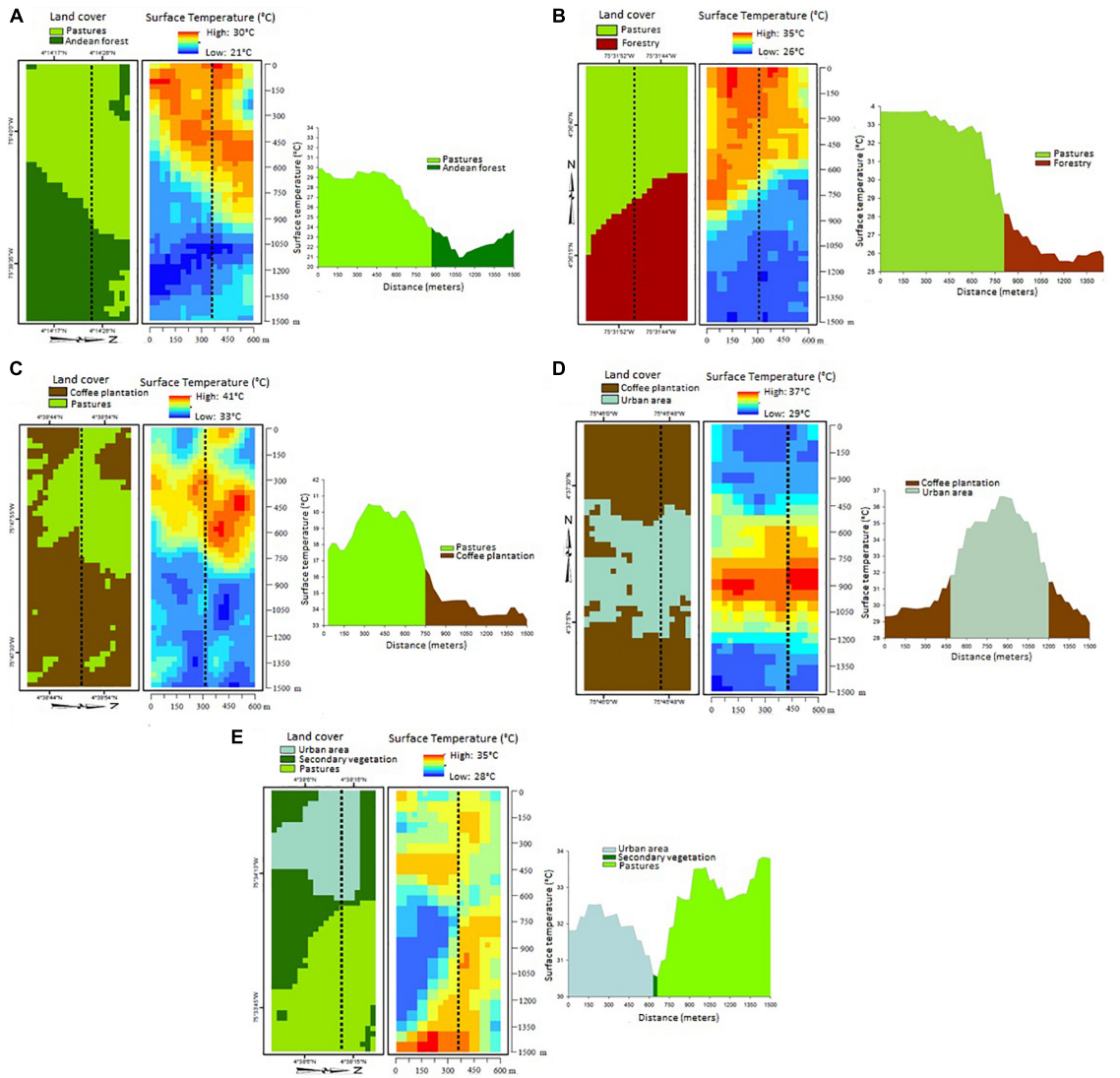


FIGURE 6 | Types of land use and land cover (left) and profiles of surface temperature (right) along the dark dotted line. Note the temperature differences between land use transitions: **(A)** pastures – natural Andean forest; **(B)** pastures – forestry; **(C)** coffee plantations – pastures; **(D)** coffee – urban area; **(E)** urban area – secondary vegetation – pastures. Adapted from Carvajal-Vanegas and Pabón-Caicedo (2014).

Amazon system (Armijos et al., 2013; Santini et al., 2015; Vauchel et al., 2017).

Although deforestation has impacts on water cycle, it has been established that inadequate forestation may also have negative effects on water availability since some exotic tree plantations and a few native species are high-water consumers and may reduce downstream runoff supply (Balthazar et al., 2015; Bonnesoeur et al., 2019). Most of Andean countries have developed several projects regarding restoring vegetation cover and the re-establishment of ecosystem services like water supply, by using alien species (eucalyptus and pine, for example), reducing runoff and water availability. These findings, besides the practical application they may have in planning and environmental management, highlight the importance to take into account details of forest composition, in the sense of considering the role of specific tree species in water budget quantification and hydrological cycle studies.

PROJECTED CHANGES IN THE ANDES DURING THE 21ST CENTURY

Temperature and Precipitation Projections From CMIP3/CMIP5 Models and Associated Uncertainties

Coupled Atmosphere Ocean General Circulation Models (AOGCMs) and Earth System Models (ESMs) (referred hereafter to as Global Climate Models – GCMs) are the main tool for projecting future climate changes. Multi-model ensembles from

coordinated GCMs experiments such as the Coupled Model Intercomparison Projects (CMIP3 and CMIP5) (Meehl et al., 2007; Taylor et al., 2012) have become indispensable for assessing future changes in climate at global and large regional scale and for quantifying their uncertainties. **Figure 7** shows the change of precipitation and air surface temperature in South America projected by the end of the 21st century (2071–2100) under the high emission scenario RCP8.5, considering an ensemble mean of 48 CMIP5 models.

There is a general agreement among the models on the warming over the Andes, which exhibits the lowest values over extratropical latitudes (less than 3°C) and the highest values (up to 5°C) over the central region (**Figure 7B**). The latter is associated with the largest warming over the continent projected for the Amazon river basin (Blázquez and Nuñez, 2013), especially during the dry and dry-to-wet transition seasons (**Figure 7B**). The projected changes in precipitation are associated with large uncertainties (**Figure 7A**). The only Andean region where the CMIP5 models agree on the sign of future changes is central Chile, in the subtropical Andes (**Figure 7A**; SON). As mentioned in section "Precipitation Trends in the Andes," in this region, the large-scale regional drying has been already evidenced as an emerging anthropogenic signal from a background observed variability (Boisier et al., 2016). The drying is projected to pursue in the future (Zazulie et al., 2017) in association with the positive SAM-like circulation change in summer caused by stratospheric ozone depletion which amplifies the effect of the same sigh driven by the greenhouse gas forcing in all seasons (Boisier et al., 2018).

Despite rather low confidence in the CMIP3/CMIP5 ensemble mean projections of precipitation over the tropical northern and southern Andes, some consensus can be found in the literature regarding future changes. Schoolmeester et al. (2016) summarized findings by Vuille et al. (2008) and Magrin et al. (2014) for the tropical Andes, and suggest that the northwestern region of Colombia, Ecuador and Peru will experience more precipitation than that observed in the present climate, while a decrease of precipitation is expected in the northeastern Andes of Venezuela and Colombia, Southern Peru, and Bolivia. A longer dry season is expected over the southern Amazonian Andes (Fu et al., 2013; Guimberteau et al., 2013; Boisier et al., 2015). The Altiplano region will exhibit a strong precipitation decline driven by an increasing westerly flow over the Central Andes (Minvielle and Garreaud, 2011; Thibeault et al., 2012; Neukom et al., 2015). In particular, under the assumption of a stable and linear relationship between precipitation and upper level zonal wind, Neukom et al. (2015) suggest a precipitation decrease of 19–33% for 2071–2100 relative to present-day conditions (RCP8.5).

Due to the coarse spatial resolution of CMIP5 models, projections for the Andes give a generalized picture of changes over extended areas. Within these areas, different sub-regional expressions of climate variability and change may occur and then the area average may not be representative of the actual changes, which may show opposite signals between regions, as evidenced from the recent observed trends (see sections "Air Surface Temperature Trends in the Andes" and "Precipitation Trends in the Andes"). As an example, **Figure 8** illustrates the regional topography of Uyuni Salt Flats (Bolivia), located at heights between 3650 and 5000 meters over a 2 × 2 degree area (19–21°S, 69–67°W). Note that the typical resolution of atmospheric components in CMIP5 models is about 1.5° (Haarsma et al., 2016). By consequence, the maximum height of the plateau in CMIP5 models is 4000 m.a.s.l. Analysis of such region in a GCMs ensemble is a complex task because of different representations of the mountains among the models. Indeed, the Andes produce a huge disturbance of the atmospheric circulation over South America, which organizes particular climates over inward and leeward sides of the range. Since simulated climate has strong dependence on the topographical height assigned to the grid points representing the mountains, spatial distribution of particular climates may strongly differ among models. One possible way to circumvent these limitations, is based on the methodology proposed in Fita et al. (2019), in which an objective classification of the simulated domain is performed by slices, based on three criteria: latitudinal bands, topographical height, and western or eastern side of the mountain range. One of the other advantages of the technique is that no additional interpolation is required.

Taking the example of the 2 × 2 degree box over Uyuni Salt Flats and an ensemble of 25 CMIP5 models (under the RCP8.5 scenario), **Figure 9** shows the precipitation and 2-m maximum and minimum air temperature in the present climate and their future changes for different slices defined by given altitude and mountain range face (uphill, peak and downhill). Therefore, **Figure 9** do not display gradients but integrate information from different sub-ensembles that have been built clustering models according to a dynamical-robustness criteria. Temperature is projected to increase everywhere over the Uyuni box with differences in intensity between changes for maximum and minimum temperature, as well as between the mountains range faces, and between altitudinal zones. Projections for precipitation show negative change, except for the uphill slice at a height of about 3500 m.a.s.l, where positive changes are projected according to the five models that resolve this altitude. It is worth noting that even the detailed analysis of future projections proposed by Fita et al. (2019) that takes into account the geographical specificities of the Andean region, suggests generally a large dispersion between models in terms of future changes in precipitation.

In general, large uncertainties in model projections of precipitation over the Andes are associated with large errors in representations of regional precipitation and their controlling processes. Indeed, whereas CMIP5 models simulate relatively well the near-surface air temperature in different regions of the Andes (Zazulie et al., 2017, 2018), they generally fail in simulating regional precipitation. Sierra et al. (2015, 2017) and Bonilla-Ovallos and Mesa (2017) question the ability of the CMIP5 models to represent precipitation and its seasonal cycle in the northern tropical Andes (North of 8°S). Fu et al. (2013) found large models errors in simulating the dry season length over the Southern Amazon basin and linked them to remotely driven errors in local convective inhibition energy in austral winter and to a general underestimation of the variability in the latitudinal position of the subtropical jet. Zazulie et al. (2017, 2018) show

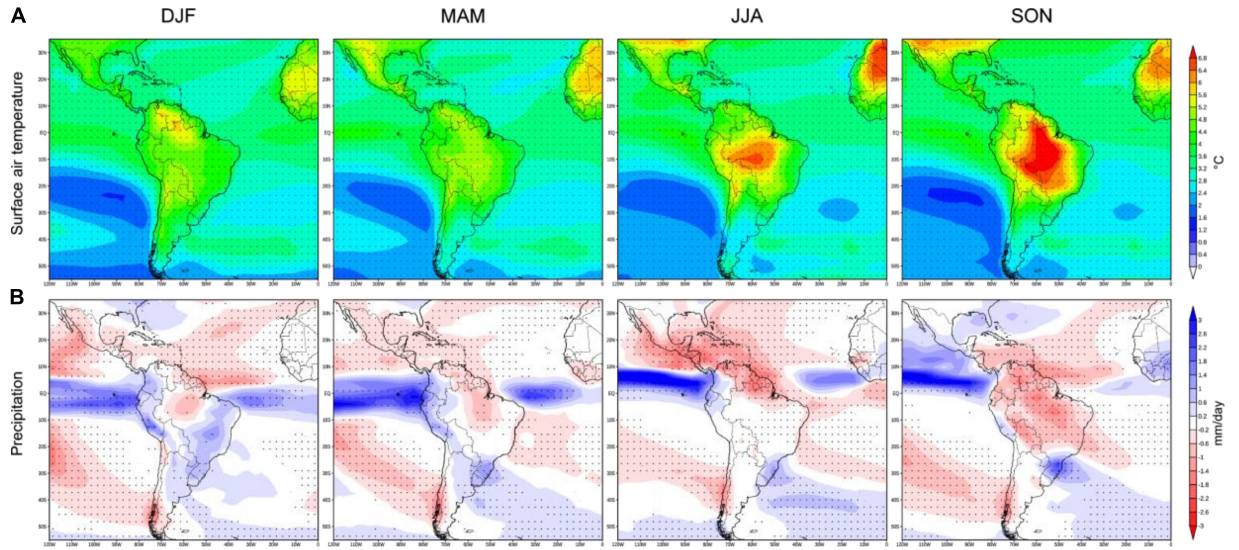


FIGURE 7 | Ensemble mean projected changes of **(A)** air surface temperature (in °C) and **(B)** precipitation (in mm/day) in South America. Change is estimated as the difference between the RCP8.5 projection by the end of the 21st century (2071–2100) and the historical simulation by the end of the 20th century (1971–2000). Ensemble mean is obtained considering 48 CMIP5 models. Dots indicate an agreement in the sign of the projected change among 80% or more of the models.

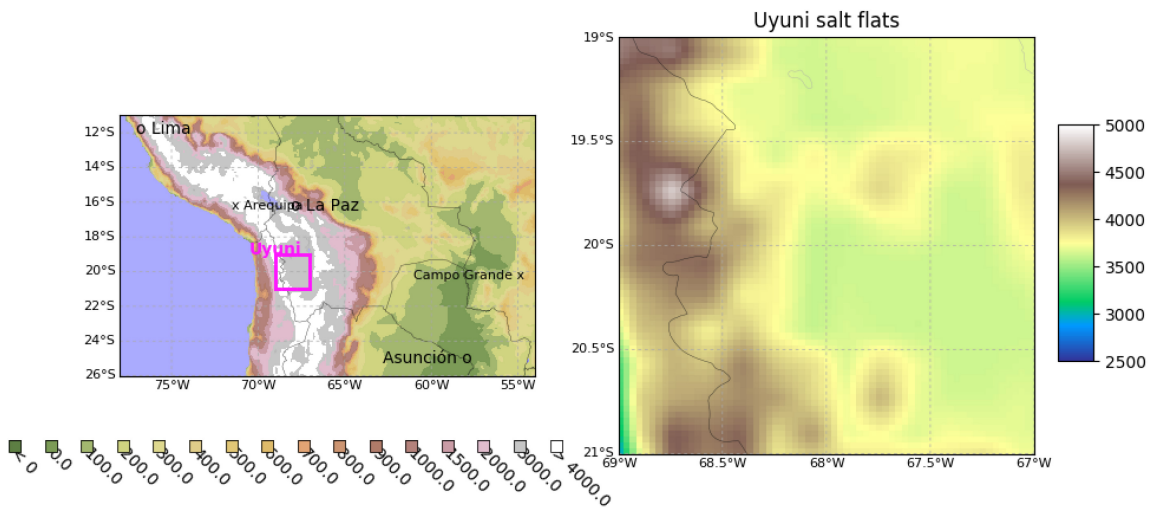


FIGURE 8 | The Uyuni Salt Flats geographical location in Potosi, Bolivia (left). 1-km resolution map of topography (meters) in a 2° × 2° box, shows Uyuni region as represented in CMIP5 models (right).

that the models have deficiencies in reproducing precipitation over the subtropical Andes of Chile and Argentina (30–37°S) especially in summer, the latter being attributed to an unrealistic simulation of the summer low-level jet east of the Andes.

The above-mentioned biases in CMIP-class climate simulations suggest that using precipitation projections for downstream applications and impact studies in the Andes should be done after applying bias correction techniques to the raw GCM outputs (e.g., Mourre et al., 2016; Heredia et al., 2018). In parallel, it is indispensable to improve the representation of the regional specificities of the Andes in any modeling effort, in order to better represent the interaction between main circulation and local complex orography, which is the cause of climate diversity in the Andes.

Regional Climate Downscaling

Since the hydroclimate diversity and complexity of the driving processes of the Andes can be hardly represented by the current generation of global models, dynamical and statistical downscaling techniques are widely used to assess climate change effects at regional scales. Several initiatives have been developed based on the implementation of Regional Climate Models (RCM) to produce high resolution climate simulations over the Andean region. Some of these initiatives are embedded within

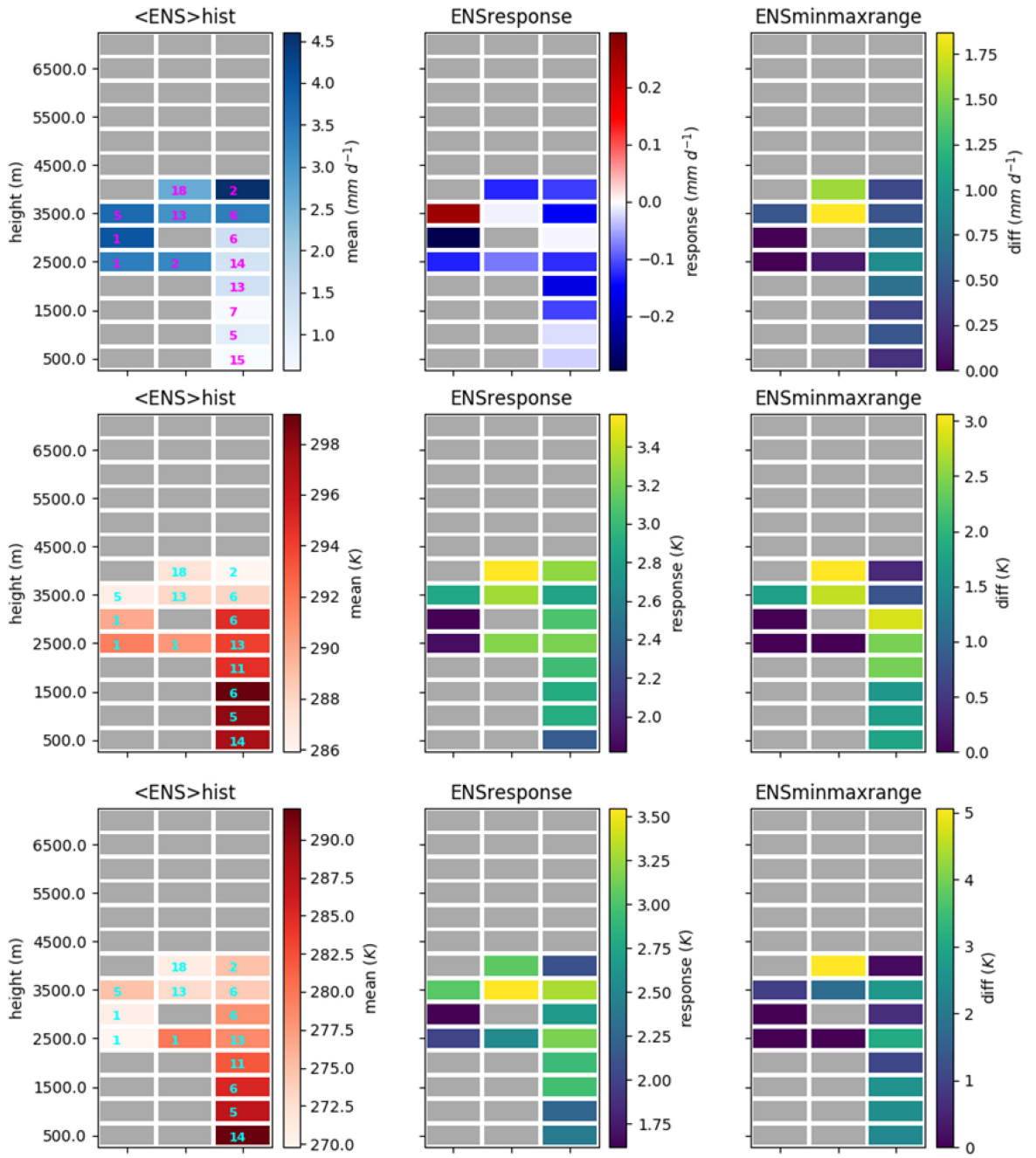


FIGURE 9 | Ensemble mean response to the projected climate change at Uyuni box, as a function of the height (discretized every 500 m) and mountain range face (uphill, peak and downhill represented, respectively, by vertical arrays in each box). Results are from 25 CMIP5 models, and for the scenario RCP8.5. First row is for the precipitation, second row is for the minimum 2-m temperature, and the third row is for the maximum 2-m temperature. Left column presents the ensemble mean value for the historical period (1960—1990), where pink/green numbers indicate how much models provide data for each slice, and slices without data are in gray. Middle column is for the change (2040—2070 minus 1960—1990) response. Right column is for the maximum range of the climate change signal.

a more general dynamical downscaling exercises developed under coordinated frameworks such as the Coordinated Regional Downscaling Experiment (CORDEX; Giorgi et al., 2009) and the CLARIS-LPB project (Solman, 2013; Boulanger et al., 2016), both covering the whole South American domain. This unprecedented set of RCM simulations have been performed with horizontal resolutions of roughly 22 and 50 km. The assessment of the climate change signal for the end of the 21st century over the Andean region, as derived by this set of coordinated simulations, has been performed in several studies, such as Marengo et al. (2012a), Chou et al. (2014), Sánchez et al. (2015), Menéndez et al. (2016), Ambrizzi et al. (2018), and Zaninelli et al. (2019).

Dynamical downscaling exercises over several regional domains covering different Andean subregions have also been performed at either 50 or 25 km horizontal resolution Marengo et al. (2009) for the whole South American continent; Urrutia and Vuille (2009) for tropical South America; Cabré et al. (2016) for southern South America, and Pabón (2012) for Colombia). All these studies based on dynamical downscaling tools agree on projecting a generalized warming over the Andean region by the end of the 21st century, ranging from 1° to 5°, being the magnitude of the warming dependent on the region and the emission scenario used. Moreover, the projected warming is characterized by a complex spatial distribution, given the complexity of the topography in the region. Projected precipitation changes exhibit larger uncertainties (Buytaert et al., 2010), though common features can be highlighted, such as the drying over the western Andes south of 35°S during the SH winter season and the wetting over southern Chile during summer, in agreement with observed trends. For the northern Andes, most of the modeling exercises suggest a future increase in precipitation, though the sign in the projected precipitation change is highly dependent on the models used. The most interesting feature of all these modeling efforts is that the projected precipitation changes are characterized by a complex spatial distribution, with narrow areas of opposite projected changes over the Andes. **Figure 10** displays the projected changes in seasonal mean temperature and precipitation from an ensemble of RCMs from Sánchez et al. (2015). Note that the ensemble (which includes projections from 10 RCMs) displays smooth changes in the temperature field, though the projected change in precipitation displays more complex features, particularly along the Andes. Inspection of changes from individual RCMs suggests more complex spatial patterns that are smooth out when building the ensemble. In addition to the aforementioned dynamical downscaling efforts, some authors have developed regional projections based on a variety of statistical downscaling tools (Minvielle and Garreaud, 2011; Boisier et al., 2015; Palomino-Lemus et al., 2015, 2017, 2018; Bozkurt et al., 2018, 2019). For northern Andes (north of 8°S) Palomino-Lemus et al. (2015, 2017, 2018) show a general increase of precipitation between 5% and 20% under the scenario RCP8.5. For the Altiplano region, Minvielle and Garreaud (2011) suggest a significant reduction (10%–30%) in precipitation by the end of the 21th century under SRES A2 emission scenarios. Over the extratropical Andes, in the Central Chile region, Bozkurt et al. (2018) show large difference in drying between low and high emission scenarios (about −3% in RCP2.6 and −30% in RCP8.5), associated with warming of 1.2°C and 3.5°C, respectively.

The reliability of the projected changes from RCMs may also be built after assessing the extent to which models are able to represent present climate conditions. Several studies have focused on assessing the reliability of regional climate models over the Andes and most of them found that RCMs usually present systematic biases, such as an underestimation of temperature at different altitudes (López-Franca et al., 2016) and a overestimation of precipitation over the mountains, in particular over the eastern Andes slopes (Solman and Blazquez, 2019; see **Figure 2a** in Menéndez et al., 2016). The origin of these biases lies, at least partly, in unresolved topographical forcing which remains too smoothed over the complex terrain of the Andes, limiting the simulation of regional processes such as the interactions between local circulation and orography, a key factor in climate modulation at meso-scale levels. However, even considering these systematic biases, recent studies have confirmed that CORDEX-type RCMs (e.g., with a spatial resolution of 20–50 km) have the potential to add value in the representation of extreme precipitation and mean surface temperature over the Andes (Falco et al., 2018, 2019; Bozkurt et al., 2019).

Enhancing the spatial resolution in regional climate models is crucial in complex topography regions such as Andes, in particular for assessing the elevational dependence of warming, which has been already mentioned in section "Air Surface Temperature Trends in the Andes." Given that change in albedo is one of dominant drivers of EDW (Rangwala and Miller, 2012; Pepin et al., 2015), a realistic simulation of the seasonal transition between snow-covered and snow-free elevation requires fine spatial resolution allowing accurate representation of the topography (Palazzi et al., 2019). Furthermore, future elevation-dependent warming and associated wetting suggested by previous studies (e.g., Giorgi et al., 1997; Palazzi et al., 2017, 2019), may lead to locally enhanced convective activity and therefore affect locally precipitations. For instance, based on an ensemble of regional climate models simulations at approximately 12 km resolution, Giorgi et al. (1997) have demonstrated increasing precipitation in future climate projections over the European Alpine high peaks, whereas the forcing GCMs scenarios suggest reducing precipitation over the region. In order to investigate the role of local processes in the Andean precipitation response to global warming, related in particular to orography-atmosphere and land-atmosphere interactions, it is crucial to apply high-resolution modeling tools allowing resolving gamma-meso-scales (2–20 km). This issue becomes an important point for the regional research agenda. Currently, several projects are exploring the use of RCMs at gamma-mesoscale resolution for climate projections in different regions of the Andes (Bozkurt et al., 2019; Posada-Marín et al., 2019).

Hydrological Projections and Impacts

About surface hydrology projections, several sub-regional and small scale studies have been carried out. Exbrayat et al. (2014), using global climate projection produced for IPCC AR4 and AR5, found for the Ecuadorian Andes a likely increase in annual runoff by 2100 with a large variability between the different combinations of a climate model with a hydrological model, but they pointed out that differences between GCM projections introduced a gradually increasing relative uncertainty throughout the 21st century, and structural differences between applied hydrological models still contribute to a third of the total uncertainty in the late 21st century runoff projections and differences between the two emission scenarios are marginal.

Ragettli et al. (2016), for a catchment in the subtropical Andes of Chile, found that runoff is likely to sharply decrease in the future and the runoff seasonality is sensitive to projected

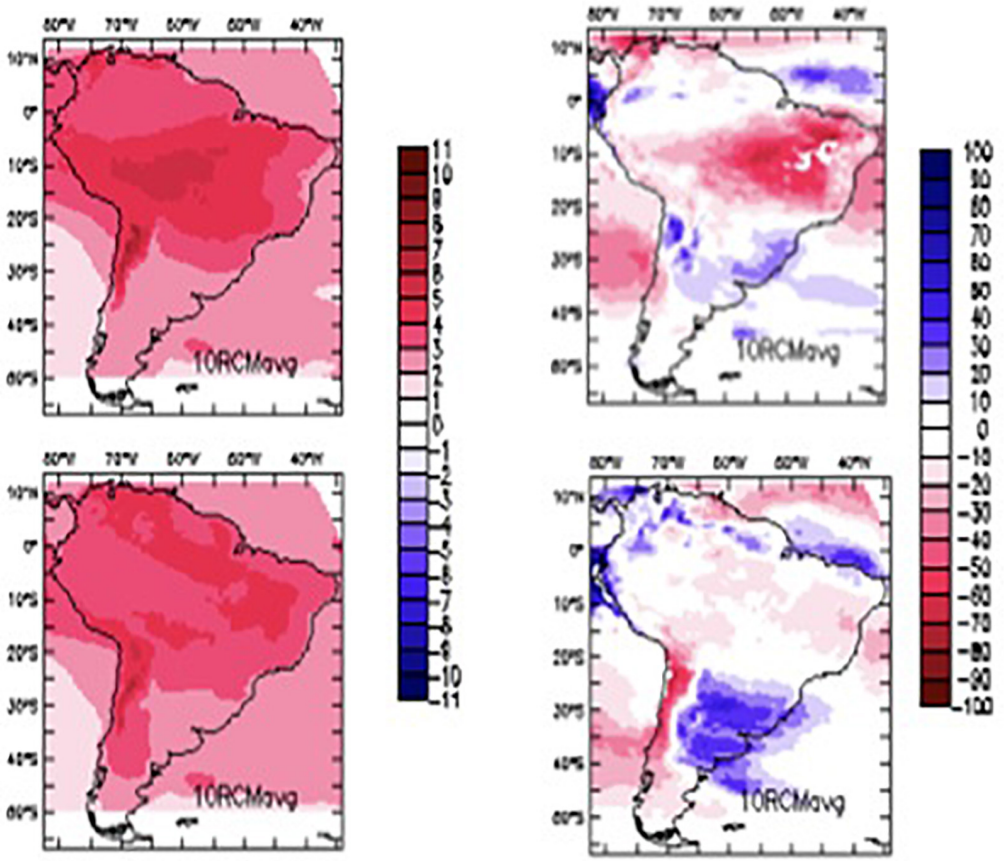


FIGURE 10 | Projections of seasonal mean temperature (left; in °C) and seasonal mean precipitation (right; in%) for the period 2071–2100, according to an ensemble of RCMs for the SRES A1B scenario for JJA (top) and DJF (bottom). Adapted from Sánchez et al. (2015).

climatic changes. Their projections indicate that climate change adaptation in central Chile should focus on a reduction in water availability. Also, for Andean basins in Central Chile, Bozkurt et al. (2017) found that for 21st century droughts would be increased to up to 5 events/century and the probability of having more extended events; additionally, analyzing probability density function of annual maximum daily runoff they found an increase in the frequency of flood events. In the context of future climate change, most studies show a large range of uncertainty, but they project that an intensification of the hydrological cycle is likely to occur in the Amazon-Andes region (Guimberteau et al., 2013; Boisier et al., 2015; Marengo and Espinoza, 2016; Zulkafli et al., 2016). The aforementioned projected effects of climate change in the Andes will impact the ecosystems and human socioeconomic systems of the region (Young et al., 2011).

Large warming during the dry season in the Amazon river basin could shift the southern Amazon area toward a climate more appropriate to seasonal forests or savannah rather than tropical rain-forest (Oyama and Nobre, 2003; Salazar et al., 2007; Malhi et al., 2008; De Faria et al., 2017). Direct human intervention, including land use changes, the construction of new Andean dams in the Amazon basin, among others (e.g., Nobre et al., 2016; Forsberg et al., 2017), is also expected to increase in the future. This scenario represents a high risk of reduction of the atmospheric moisture generated by the Amazon rainforest evapotranspiration and its transport toward neighboring regions, such as the tropical Andes (Lejeune et al., 2015). Combined impacts of Amazon land use and climate changes could be even stronger in the Altiplano (Minvielle and Garreaud, 2011), a semiarid high plateau situated above 3600 m.a.s.l in the south tropical Andes (14–23°S). In addition, the interaction between local-scale and regional-to-global scale processes is a key topic of research to better understand tropical climate change, with surface conditions and water cycle playing a central role in such interactions (e.g., Builes-Jaramillo et al., 2017).

Schoolmeester et al. (2016) suggest that change in mean temperature and precipitation regime in the Andes, as well as glaciers melting, will have a marked effect on runoff and consequently on water availability for drinking, sanitation, agriculture, energy and industry. Mean temperature increase will alter biochemical composition of soil and vegetation, changing their capacity to regulate water flows. The increase and concentration of the water demand (due to population growth and urbanization) will have crucial effects on the water

supply-demand balance, affecting water availability and causing regional conflicts that are necessary to anticipate. In this sense, improving our knowledge and information about these issues becomes extremely necessary.

CONCLUDING REMARKS AND OPEN RESEARCH QUESTIONS

The Andes have been subject of different hydroclimate changes throughout the past two millennia. Over the tropical Andes, paleoclimate evidence shows relatively warm conditions during the first centuries of the last millennium followed by colder temperature between the 15th and 18th centuries, suggesting the influence of MCA and LIA periods over tropical South America. Over the South American Altiplano (south tropical Andes) and central Chile (subtropical Andes), reconstructions indicate a persistent rainfall reduction since the mid-19th century to the beginning of the 21st century. Over the extratropical Andes, temperature reconstructions indicate that the 20th century has been the warmest period during the last millennium in the northern Patagonian, to the east of the Andes.

During the last decades, observational data suggest a general agreement on the occurrence of warmer temperatures over the Andes. However, there is not yet full agreement whether the rate of warming is amplified with elevation, which is particularly important in regions with complex topography, like the Andes. In this sense, the lack of a dense network of stations along the Andes does not allow addressing comprehensively this issue.

In contrast to temperature changes, trends in annual precipitation exhibit different signs across sectors in the Andes. For instance, annual precipitation trends in north tropical (north of 8°S) and south tropical (8°S–27°S) Andes do not show a homogeneous pattern. The Amazonian side of the north tropical Andes (northern and northwestern Amazon) has experienced wetter conditions since the mid-1990s, particularly during its wet season. In opposition, dry conditions have increased in austral winter and spring over the central and southern Amazon. Increases of rainfall during the 1965–1984 period and decreases since 1984 have been documented in Bolivia. In the Peruvian Andes, no significant rainfall trends are documented, although decreasing rainfall since 1970 has been reported by several studies in the central and southern Peruvian Amazon-Andes. Over the subtropical Andes, central Chile shows a robust signal of declining precipitation since 1970. Over the subtropical northwestern Argentinian Andes, precipitation trends are strongly dependent on elevation: the transition zone between low and intermediate elevations is characterized by the most significant positive annual rainfall trends since 1950, whereas at low elevations areas, generalized decreasing trends are observed.

Despite hydrological data shortcomings, several studies have provided further evidence of changes of surface runoff in the Andes. River runoff in the western Andes of Colombia, Ecuador, and Chile appears to increase significantly during the last 4–5 decades. Over Ecuador (tropical Andes), increasing trends in maximum flows and decreasing trends in minimum flows are found. Increasing frequency of droughts and floods in the Andean Amazon region has also been reported. In particular for this region, studies on different specific regions have found diverging trends in river discharge: decreasing discharge trends in the southern Amazon-Andes region (South of Peru and Bolivia) and increased trend in the north. In the Argentinian Andes, significant positive trends in river discharge during the last 5–6 decades are documented. Evidence of hydrological changes are also observed in the subtropical and extratropical Andes as changes of snow cover and glacier extension. The robust pattern of warmer temperatures and the overall recession of glaciers in the region suggest that such changes have impacted glacier mass balances in the subtropical and extratropical Andes, affecting river runoff. However, studies of monthly and annual mean discharge in the Andes show divergent trends (or no trends at all) and uncertainty is still large. In the central Andes of Chile and Argentina, the Norte Chico region in Chile, and the northwestern portion of Patagonia, river flows show marked negative trends. On the contrary, the river flows in northwestern Argentina and southern Bolivia, southern Patagonia, and Tierra del Fuego show positive trends with above-average values in the last decades.

LULC changes influence surface runoff in the Andes. Studies identify that cropland, pasture, and secondary vegetation over the north tropical Andes (north of 8°S) showed systematic transitions, changing from a traditional land use to pasture. In particular, the main responsible forces of LULC change over this region are deforestation, agriculture, cattle ranching, and gold mining, although other socio-political dynamics are involved. High rates of deforestation are detected in the subtropical and extratropical Andes (Chile and Argentina), followed by the tropical Andes (Bolivia, Ecuador, Colombia and Peru). Such changes in LULC modify surface properties, affecting energy and water balances. Detailed studies addressed to understand how LULC changes influence hydroclimate in the Andes at local and regional scales are required.

Climate change projections over the Andes show general agreement on a future warming over the Andes, with the lowest values (less than 3°C) over extratropical latitudes and the highest values (up to 5°C) over the central region. By contrast, projections of precipitation in the Andes exhibit higher spread among models and uncertainties. The only agreement among models in the Andean region is the drying trend over central Chile, located in the subtropical Andes, which has been already evidenced as an emerging anthropogenic signal from a background observed variability.

The difficulty of GCMs to adequately simulate and project precipitation changes in the Andes is highly associated with their coarse spatial resolution. Therefore, downscaling simulations are required in order to provide more detailed information at local scale. This is an ongoing research area. For instance, CORDEX and CLARIS-LPB projects have allowed the development of dynamical downscaling using RCMs for climate change projections in the Andes, whereas different studies have used dynamical and statistical tools suggesting a general increase of precipitation over the northern Andes (north of 8°S) and a significant reduction (10%–30%) in precipitation by the end of the 21th century over the western

subtropical Andes. However, RCMs at CORDEX-type resolution (20–50 km) exhibit biases such as the underestimation of temperature at different altitudes of mountains and the overestimation of precipitation over mountain regions, in particular over the eastern Andes slopes, in association with unresolved topographical forcing which remains too smoothed over the complex terrain of the Andes. Higher-resolution models allowing resolving gamma-meso-scales (2–20 km) are needed for a more accurate representation of the topography of the Andes and by consequence for a more realistic simulation of orography-atmosphere and land-atmosphere interactions.

This review highlights the necessity of strengthening different research areas in order to provide a more comprehensive understanding of past, present and future hydroclimate changes over the Andes. In this sense, it allowed to identify open questions tend to indicate research areas to be pursued by the scientific community. Amongst them, we identify the following topics as the more relevant to be addressed:

- The immense variety of meso-climates of the Andes, as a consequence of the interaction of large-scale circulation with complex topography and regional circulations systems, requires a more detailed assessment in hydroclimate studies. Generalized views of large sub-regions in terms of climate trends and future scenarios is not sufficient to represent the real processes of this environmental diversity. Therefore, a more detailed spatial view is needed in terms of observed trends and projected climate change scenarios in the Andes. This request to put on any regional research agenda the challenge of producing more detailed high-quality data, and the development of very high spatial resolution modeling and dynamically robust methodologies of analysis.
- There are different regional-to-local scale processes which require a further understanding of hydroclimate changes in the Andes. The most relevant are the altitude and latitude dependence on the warming signal and the LULC changes. Efforts are necessary in order to produce more detailed knowledge on these specific topics for a variety of sub-regions, stressing the importance of the impacts of LULC change in the hydrological cycle at local and regional scale. To achieve this objective, several oriented-case studies based on observational and high-resolution numerical modeling approaches have to be promoted.
- Some authors have described diverse mechanisms and feedbacks that could contribute to EDW and at what heights each one plays a role (Rangwala and Miller, 2012; Pepin et al., 2015; Palazzi et al., 2017). It is believed that complex interactions among snow and other land-cover albedo, water vapor changes and latent heat release, surface heat loss, surface water vapor and radiative flux changes, aerosols, among others, could explain the EDW. However, they could play different roles at individual heights and

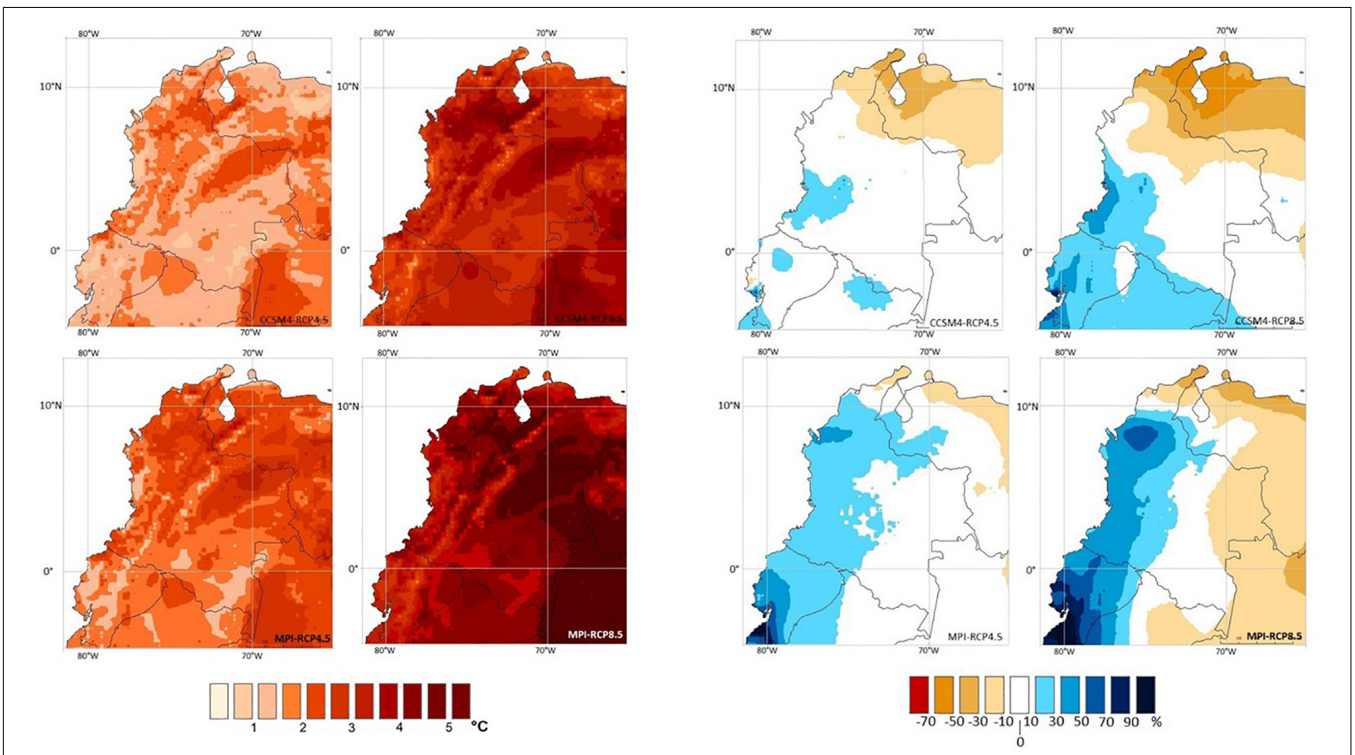


FIGURE 11 | Projected changes in annual temperature (left; in °C) and annual precipitation (right; in% related to annual average 1976–2005 period) over the north tropical Andes as obtained with dynamical downscaling of CCSM4 (top) and MPI (bottom) under RCP4.5 and RCP8.5 scenarios. Weather Research Forecast (WRF) model was used to downscale to spatial resolution 10 × 10 km. After Armenta-Porras and Pabón-Caicedo (2018).

locations, clarifying the contrasting trends documented by different authors (e.g., Vuille and Bradley, 2000; Ohmura, 2012; Wang et al., 2014). On the other hand, the PDO fingerprint is visible on the western Andes at low elevations locations (Vuille et al., 2015): while coastal regions have been recently affected by a cooling along the Andes, inland and higher elevations regions continue to warm. Therefore, the first question to answer is about the capability of simulations with prescribed SSTs (AMIP) to reproduce these mechanisms. Future warming or cooling in the Andes, as well as its EDW, will depend on regional-to-local feedbacks but also on the balance between the global warming forcing and the state of the PDO.

- Regarding climate change projections for the Andes, besides detailed spatial information that represents the diversity of climate conditions, it is necessary to reduce uncertainties in currently produced scenarios. In this sense, efforts are needed for improving the models used to simulate hydroclimate processes over this region, including the impacts of LULC changes in regional atmospheric circulation (e.g., Saavedra et al., 2018). Improvement and innovations are also needed to develop methodologies for downscaling of global/regional models, as well as new analysis methods over regions with complex topography. For instance, **Figure 11** shows an example of ongoing efforts to produce very high resolution (10 km) projections over the north tropical Andes (Armenta-Porras and Pabón-Caicedo, 2018). Also, it is mandatory to take advantage of the information provided by the incoming CMIP6 exercise for a better representation of hydroclimate processes in the Andes. In particular, high resolution downscaling of climate change projections at convective permitting resolutions (higher than 5 km) in a coordinated effort are urgently required.
- There is an urgent need to better understand the impact on the projected climate changes over the Andes, since it holds most of the ecological, social and economic systems in South America. This is primordial to properly design strategies of adaptation and mitigation in order to prevent potential socio-economical conflicts in the entire continent (e.g., Salazar A. et al., 2018).

AUTHOR CONTRIBUTIONS

All authors contributed to the conception, discussion, and refinement of this manuscript.

FUNDING

This review manuscript has been achieved as part of the ANDEX program (www.gewex.org/project/andex/), which is a prospective Regional Hydroclimate Project (RHP) of the GEWEX Hydroclimatology Panel (GHP). JP-C was partially supported by Centro Internacional para la Investigación del Fenómeno de El Niño (CIIFEN). PA was supported by Universidad de Antioquia through the Grant CODI PRG2017-16264. AC also thanks the ANPCyT (Argentina) that partially supported this work through the PICT-2015-3097. JE was supported by the French AMANECER-MOPGA project funded by ANR and IRD (ref. ANR-18-MPGA-0008). MM and RV were funded by Consejo Nacional de Investigaciones Científicas y Técnicas (CONICET) – Argentina. RV was partially supported by BNP Paribas through the project THEMES. Finally, this article has the support of UNESCO's Intergovernmental Hydrological Programme through the Working Group Hydrogeomorphology of the Andes-Amazon Basin in which PA, JE, and WL-C participated. The views presented in this manuscript are those of the authors and do not compromise the Working Group or UNESCO in any way.

ACKNOWLEDGMENTS

The authors acknowledge Geusep Ortega for his help with **Figure 7** and the two reviewers for their insightful comments on this manuscript.

REFERENCES

Abram, N. J., McGregor, H. V., Tierney, J. E., Evans, M. N., McKay, N. P., Kaufman, D. S., et al. (2016). Early onset of industrial-era warming across the oceans and continents. *Nature* 536, 411–418. doi: 10.1038/nature19082

Agudelo, J., Arias, P. A., Vieira, S. C., and Martínez, J. A. (2019). Influence of longer dry seasons in the Southern Amazon on patterns of water vapor transport over northern South America and the Caribbean. *Clim. Dyn.* 52, 2647–2665. doi: 10.1007/s00382-018-4285-1

Aguilar-Lome, J., Espinoza-Villar, R., Espinoza, J.-C., Rojas-Acuña, J., Willems, B. L., and Leyva-Molina, W.-M. (2019). Elevation-dependent warming of land surface temperatures in the Andes assessed using MODIS LST time series (2000–2017). *Int. J. Appl. Earth Observ. Geoinf.* 77, 119–128. doi: 10.1016/j.jag.2018.12.013

Ahmed, M., Anchukaitis, K. J., Asrat, A., Borgaonkar, H. P., Braida, M., Buckle, B. M., et al. (2013). Continental-scale temperature variability during the past two millennia. *Nat. Geosci.* 6, 339–346. doi: 10.1038/ngeo1797

Aide, T. M., Grau, H. R., Graesser, J., Andrade-Nuñez, M. J., Aráoz, E., Barros, A. P., et al. (2019). Woody vegetation dynamics in the tropical and subtropical Andes from 2001 to 2014: satellite image interpretation and expert validation. *Glob. Change Biol.* 25, 2112–2126. doi: 10.1111/gcb.14618

Altinger de Schwarzkopf, M. L., and Rosso, L. C. (1982). "Severe storms and tornadoes in Argentina," in *Proceedings of the 12th Conf. on Severe Local Storms* (San Antonio, TX: Amer. Meteor. Soc), 59–62.

Ambrizzi, T., Reboita, M. S., da Rocha, R. P., and Llopart, M. (2018). The state-of-the-art and fundamental aspects of regional climate modeling in South America. *Ann. N. Y. Acad. Sci.* 1436, 98–120. doi: 10.1111/nyas.13932

Aravena, J. C., Lara, A., Wolodarsky-Franke, A., Villalba, R., and Cuq, E. (2002). Tree-ring growth patterns and temperature reconstruction from Nothofagus pumilio (Fagaceae) forests at the upper tree line of southern Chilean Patagonia. *Rev. Chil. Hist. Nat.* 75, 361–376.

Arias, P. A., Fo, R., Vera, C., and Rojas, M. (2015). A correlated shortening of the North and South American monsoon seasons in the past few decades. *Clim. Dyn.* 45, 3183–3203. doi: 10.1007/s00382-015-2533-1

Armenta-Porras, G. E., and Pabón-Caicedo, J. D., (2018). "Producing high spatial resolution climate scenarios for tropical america and colombia using WRF model," in *CORDEX Central America and South America Training Workshop*

on Downscaling Techniques, La Paz. Available at: http://www.cima.fcen.uba.ar/cordex-2018/poster.php.

Armenteras, D., Rodríguez, N., and Retana, J. (2017). Deforestation dynamics and drivers in different forest types of Latin America: three decades of studies (1980-2010). *Global Environ. Change* 46, 139–147. doi: 10.1016/j.gloenvcha.2017.09.002

Armenteras, D., Rodríguez, N., Retana, J., and Morales, M. (2011). Understanding deforestation in montane and lowland forests of the colombian andes. *Reg. Environ. Change* 11, 693–705. doi: 10.1007/s10113-010-0200-y

Armijos, E., Crave, A., Vauchel, P., Fraizy, P., Santini, W., Moquet, J.-S., et al. (2013). Suspended sediment dynamics in the Amazon River of Peru. *J. S. Am. Earth Sci.* 44, 75–84. doi: 10.1016/j.jsames.2012.09.002

Balthazar, V., Vanacker, V., Molina, A., and Lambin, E. F. (2015). Impacts of forest cover change on ecosystem services in high Andean mountains. *Ecol. Indic.* 48, 63–75. doi: 10.1016/j.ecolind.2014.07.043

Barichivich, J., Gloor, E., Peylin, P., Brienen, R. J. W., Schöngart, J., Espinoza, J. C., et al. (2018). Recent intensification of Amazon flooding extremes driven by strengthened Walker circulation. *Sci. Adv.* 4:eaat8785. doi: 10.1126/sciadv.aat8785

Barkhordarian, A., von Storch, H., Zorita, E., Loikith, P. C., and Mechoso, C. R. (2017). Observed warming over northern South America has an anthropogenic origin. *Clim. Dyn.* 51, 1901–1914. doi: 10.1007/s00382-017-3988-z

Barry, R., and Seimon, A. (2000). Research for mountain area development: climatic fluctuations in the mountains of the Americas and their significance. *Ambio* 29, 364–370. doi: 10.1579/0044-7447-29.7.364

Bianchi, E., Villalba, R., Viale, M., Couvreux, F., and Marticorena, R. (2016). New precipitation and temperature grids for northern patagonia: advances in relation to global climate grids. *J. Meteorol. Res.* 30, 38–52. doi: 10.1007/s13351-015-5058-y

Bird, B. W., Abbott, M. B., Vuille, M., Rodbell, D. T., Rosenmeier, M. F., and Stansell, N. D. (2011). A 2300-year-long annually resolved record of the South American summer monsoon from the Peruvian Andes. *Proc. Natl. Acad. Sci. U.S.A.* 108, 8583–8588. doi: 10.1073/pnas.1003719108

Blázquez, J., and Nuñez, M. N. (2013). Analysis of uncertainties in future climate projections for South America: comparison of WCRP-CMIP3 and WCRP-CMIP5 models. *Clim. Dyn.* 41, 1039–1056. doi: 10.1007/s00382-012-1489-7

Boers, N., Marwan, N., Barbosa, H. M. J., and Kurths, J. (2017). A deforestation-induced tipping point for the South American monsoon system. *Sci. Rep.* 7:41489. doi: 10.1038/srep41489

Boisier, J. P., Alvarez-Garreton, C., Cordero, R., Damian, A., Gallardo, L., Garreaud, R., et al. (2018). Anthropogenic drying in central-southern Chile evidenced by long term observations and climate model simulations. *Elem. Sci. Anth.* 6:74. doi: 10.1525/elementa.328

Boisier, J. P., Ciais, P., Ducharne, A., and Guimberteau, M. (2015). Projected strengthening of Amazonian dry season by constrained climate model simulations. *Nat. Clim. Change* 5, 656–660. doi: 10.1038/nclimate2658

Boisier, J. P., Rondanelli, R., Garreaud, R. D., and Muñoz, F. (2016). Anthropogenic and natural contributions to the southeast Pacific precipitation decline and recent megadrought in central Chile. *Geophys. Res. Lett.* 43, 413–421. doi: 10.1002/2015gl067265

Bonan, G. B., Defries, R. S., Coe, M. T., and Ojima, D. S. (2012). "Land use and climate," in *GUTMAN*, eds G. Gutman, A. C. Janetos, C. O. Justice, E. F. Moran, J. F. Mustard, R. R. Rindfuss, et al. (Dordrecht: Springer), 467,307–320.

Bonilla-Ovallos, C. A., and Mesa, O. J. (2017). Validación de la precipitación estimada por modelos climáticos acoplados del proyecto de intercomparación CMIP5 en Colombia. *Rev. Acad. Colomb. Cienc. Ex. Fis. Nat.* 41, 107–118. doi: 10.18257/raccefyn.27

Bonnesoeur, V., Locatelli, B., Guariguata, M. R., Ochoa-Tocachi, B. F., Vanacker, V., Mao, Z., et al. (2019). Impacts of forests and forestation on hydrological services in the Andes: a systematic review. *For. Ecol. Manage.* 433, 569–584. doi: 10.1016/j.foreco.2018.11.033

Boulanger, J. P., Carril, A. F., and Sánchez, E. (2016). CLARIS-La Plata Basin: the regional climate variability and the analysis of an ensemble of regional hydroclimate scenarios and their uncertainties. *Clim. Res.* 68, 93–94. doi: 10.3354/cr01392

Bozkurt, D., Rojas, M., Boisier, J. B., Rondanelli, R., Garreaud, R., et al. (2019). Dynamical downscaling over the complex terrain of southwest South America: present climate conditions and added value analysis. *Clim. Dyn.* 53, 6745–6767. doi: 10.1007/s00382-019-04959-y

Bozkurt, D., Rojas, M., and Boisier, J. P. (2018). Projected hydroclimate changes over Andean basins in central Chile from downscaled CMIP5 models under the low and high emission scenarios. *Clim. Change* 150:131. doi: 10.1007/s10584-018-2246-7

Bozkurt, D., Rojas, M., Boisier, J. P., and Valdivieso, J. (2017). Climate change impacts on hydroclimatic regimes and extremes over Andean basins in central Chile. *Hydrol Earth Syst. Sci. Discuss.* 2017, 1–29. doi: 10.5194/hess-2016-690

Bradley, R. S. (2013). *Paleoclimatology: Reconstructing Climates of the Quaternary*, 3rd Edn. Amsterdam: Elsevier.

Brönnimann, S., Franke, J., Nussbaumer, S. U., Zumbühl, H. J., Steiner, D., Trachsel, M., et al. (2019). Last phase of the Little Ice Age forced by volcanic eruptions. *Nat. Geosci.* 12, 650–656. doi: 10.1038/s41561-019-0402-y

Builes-Jaramillo, A., Marwan, N., Poveda, G., and Kurths, J. (2017). Nonlinear interactions between the Amazon River basin and the Tropical North Atlantic at interannual timescales. *Clim. Dyn.* 50, 2951–2969. doi: 10.1007/s00382-017-3785-8

Burger, F., Brock, B., and Montecinos, A. (2018). Seasonal and elevational contrasts in temperature trends in Central Chile between 1979 and 2015. *Global Planet. Change* 162, 136–147. doi: 10.1016/j.gloplacha.2018.01.005

Buytaert, W., and Beven, K. (2009). Regionalization as a learning process. *Water Resour. Res.* 45:W11419. doi: 10.1029/2008WR007359

Buytaert, W., Vuille, M., Dewulf, A., Urrutia, R., Karmalkar, A., and Célleri, R. (2010). Uncertainties in climate change projections and regional downscaling in the tropical Andes: implications for water resources management. *Hydrol. Earth Syst. Sci.* 14, 1247–1258. doi: 10.5194/hess-14-1247-2010

Cabré, M. F., Solman, S., and Nuñez, M. (2016). Regional climate change scenarios over southern South America for future climate (2080-2099) using the MM5 Model. Mean, interannual variability and uncertainties. *Atmósfera* 15, 35–60. doi: 10.20937/ATM.2016.29.01.04

Carmona, A. M., and Poveda, G. (2014). Detection of long-term trends in monthly hydro-climatic series of Colombia through Empirical Mode Decomposition. *Clim. Change* 123, 301–313. doi: 10.1007/s10584-013-1046-3

Carvajal-Vanegas, A. F., and Pabón-Caicedo, J. D. (2014). Temperatura de la superficie terrestre en diferentes tipos de cobertura de la región andina colombiana. *Soc. Natureza* 26, 95–112. doi: 10.1590/1982-4513201401 0107

Castino, F., Bookhagen, B., and Strecker, M. R. (2016). Rainfall variability and trends of the past six decades (1950-2014) in the subtropical NW Argentine Andes. *Clim. Dyn.* 48, 1049–1067. doi: 10.1007/s00382-016-3127-2

Celeri, R., and Feyen, J. (2009). The hydrology of tropical andean ecosystems: importance, knowledge status, and perspectives. *Mount. Res. Dev.* 29, 350–355. doi: 10.1659/mrd.00007

Chavez, S. P., and Takahashi, K. (2017). Orographic rainfall hot spots in the Andes-Amazon transition according to the TRMM precipitation radar and in situ data. *J. Geophys. Res.* 112, 5870–5882. doi: 10.1002/2016JD026282

Chou, S. C., Lyra, A., Mourão, C., Dereczynski, C., Pilotto, I., Gomes, J., et al. (2014). Assessment of climate change over South America under RCP 4.5 and 8.5 downscaling scenarios. *Am. J. Clim. Change* 3, 512–525. doi: 10.4236/ajcc.2014.35043

Christie, D. A., Lara, A., Barichivich, J., Villalba, R., Morales, M. S., and Cuq, E. (2009). El Niño-Southern Oscillation signal in the world's highest-elevation tree-ring chronologies from the Altiplano, Central Andes. *Palaeogeogr. Palaeoclimatol. Palaeoecol.* 281, 309–319. doi: 10.1016/j.palaeo.2007.11.013

Dätwyler, C., Neukom, R., Abram, N. J., Gallant, A. J. E., Grosjean, M., Jacques-Coper, M., et al. (2018). Teleconnection stationarity, variability and trends of the Southern Annular Mode (SAM) during the last millennium. *Clim. Dyn.* 51, 2321–2339. doi: 10.1007/s00382-017-4015-0

De Faria, B. L., Brando, P. M., Macedo, M. N., Panday, P. K., Soares-Filho, B. S., and Coe, M. T. (2017). Current and future patterns of fire-induced forest degradation in Amazonia. *Environ. Res. Lett.* 12:095005. doi: 10.1088/1748-9326/aa69ce

de los Skansi, M., Brunet, M., Sigró, J., Aguilar, E., Arevalo Groening, J. A., Bentancur, O. J., et al. (2013). Warming and wetting signals emerging from analysis of changes in climate extreme indices over South America. *Glob. Planet. Change* 100, 295–307. doi: 10.1016/j.gloplacha.2012.11.004

Diaz, I. G., Nahuelhual, L., Echeverría, C., and Marín, S. (2011). Drivers of land abandonment in Southern Chile and implications for landscape planning. *Landsc. Urban Plann.* 99, 207–217. doi: 10.1016/j.landurbplan.2010.11.005

Espinoza, J. C., Chavez, S., Ronchail, J., Junquas, C., Takahashi, K., et al. (2015). Rainfall hotspots over the southern tropical andes: spatial distribution, rainfall intensity, and relations with large-scale atmospheric circulation. *Water Resour. Res.* 51, 3459–3475. doi: 10.1002/2014WR016273

Espinoza, J. C., Guyot, J. L., Ronchail, J., Cochonneau, G., Filizola, N., Fraizy, P., et al. (2009). Contrasting regional discharge evolutions in the Amazon basin (1974-2004). *J. Hydrol.* 375, 297–311. doi: 10.1016/j.jhydrol.2009.03.004

Espinoza, J. C., Ronchail, J., Frappart, F., Lavado, W., Santini, W., and Guyot, J. L. (2013). The major floods in the amazonas river and tributaries (Western Amazon Basin) during the 1970–2012 Period: a Focus on the 2012 Flood*. *J. Hydrometeorol.* 14, 1000–1008. doi: 10.1175/jhm-d-12-0100.1

Espinoza, J. C., Ronchail, J., Guyot, J. L., Junquas, C., Vauchel, P., Lavado, W. S., et al. (2011). Climate variability and extremes drought in the upper Solimões River (Western Amazon Basin): understanding the exceptional 2010 drought. *Geophys. Res. Lett.* 38:L13406. doi: 10.1029/2011GL047862

Espinoza, J. C., Ronchail, J., Marengo, J. A., and Segura, H. (2019a). Contrasting North–South changes in Amazon wet-day and dry-day frequency and related atmospheric features (1981–2017). *Clim. Dyn.* 52, 5416–5430. doi: 10.1007/s00382-018-4462-2

Espinoza, J. C., Sörensson, A., Ronchail, J., Molina-Carpio, J., Segura, H., Gutierrez-Cori, O., et al. (2019b). Regional hydro-climatic changes in the Southern Amazon Basin (Upper Madeira Basin) during the 1982-2017 period. *J. Hydrol. Reg. Stud.* 26:100637. doi: 10.1016/j.ejrh.2019.100637

Etter, A., McAlpine, C., and Possingham, H. (2008). Historical patterns and drivers of landscape change in colombia since 1500: a regionalized spatial approach. *Ann. Assoc. Am. Geograph.* 98, 2–23. doi: 10.1080/00045600701733911

Exbrayat, J.-F., Buytaert, W., Timbe, E., Windhorst, D., and Breuer, L. (2014). Addressing sources of uncertainty in runoff projections for a data scarce catchment in the Ecuadorian Andes. *Clim. Change* 125, 221–235. doi: 10.1007/s10584-014-1160-x

Falco, M., Carril, A. F., Li, L. Z. X., Cabrelli, C., and Menéndez, C. G. (2019). The potential added value of regional climate models in South America using a multiresolution approach. *Clim. Dyn.* 54, 1553–1569. doi: 10.1007/s00382-019-05073-9

Falco, M., Carril, A. F., Menéndez, C. G., Zaninelli, P. G., Laurent, Z., and Li, X. (2018). Assessment of CORDEX simulations over South America: added value on seasonal climatology and resolution considerations. *Clim. Dyn.* 52, 4771–4786. doi: 10.1007/s00382-018-4412-z

Falvey, M., and Garreaud, R. (2007). Wintertime precipitation episodes in Central Chile: associated meteorological conditions and orographic influences. *J. Hydrometeor.* 8, 171–193. doi: 10.1175/jhm562.1

Falvey, M., and Garreaud, R. D. (2009). Regional cooling in a warming world: recent temperature trends in the southeast Pacific and along the west coast of subtropical South America (1979–2006). *J. Geophys. Res.* 114, 1–16. doi: 10.1029/ 2008JD010519

Farley, K. A., Jobba'gy, E. G., and Jackson, R. B. (2005). Effects of afforestation on water yield: a global synthesis with implications for policy. *Global Change Biol.* 11, 1565–1576. doi: 10.1111/j.1365-2486.2005.01011.x

Fita, L., Carril, A. F., Flombaum, P., Menéndez, C., Ruscica, R., Sörensson, A., Zaninelli, P. (2019). "Results of a new methodology to analyze the climate change uncertainty on a high step mountain range. Application at the Andes," in *International Conference on Regional Climate-CORDEX 2019, 14th-18th October*, Beijing.

Flantua, S. G. A., (2017). *Climate Change and Topography as Drivers of Latin American Biome Dynamics*. Doctoral thesis, University of Amsterdam, Amsterdam.

Forsberg, B. R., Melack, J. M., Dunne, T., Barthem, R. B., Goulding, M., Paiva, R. C. D., et al. (2017). The potential impact of new Andean dams on Amazon fluvial ecosystems. *PLoS ONE* 12:e0182254. doi: 10.1371/journal.pone.0182254

Fu, R., Yin, L., Li, W., Arias, P. A., Dickinson, R. E., Huang, L., et al. (2013). Increased dry-season length over southern Amazonia in recent decades and its implication for future climate projection. *Proc. Natl. Acad. Sci. U.S.A.* 110, 18110–18115. doi: 10.1073/pnas.1302584110

Garreaud, R., Alvarez-Garreton, C., Barichivich, J., Boisier, J. P., Christie, D. A., Galleguillos, M., et al. (2017). The 2010–2015 mega drought in Central Chile: impacts on regional hydroclimate and vegetation. *Hydrol. Earth Syst. Sci.* 21, 6307–6327. doi: 10.5194/hess-21-6307-2017

Garreaud, R. D., Vuilles, M., Compagnucci, R., and Marengo, J. A. (2009). Present-day South American climate. *Palaeogeogr. Palaeoclimatol. Palaeoecol.* 281, 180–195. doi: 10.1016/j.palaeo.2007.10.032

Gimeno, L., Dominguez, F., Nieto, R., Trigo, R., Drumond, A., Reason, C. J. C., et al. (2016). Major mechanisms of atmospheric moisture transport and their role in extreme precipitation events. *Annu. Rev. Environ. Resour.* 41, 117–141. doi: 10.1146/annurev-environ-110615-085558

Giorgi, F., Hurrell, J. W., Marinucci, M. R., and Beniston, M. (1997). Elevation dependency of the surface climate change signal: a model study. *J. Clim.* 10, 288–296. doi: 10.1175/1520-0442(1997)010<0288:edotsc>2.0.co;2

Giorgi, F., Jones, C., and Asrar, G. (2009). Addressing climate information needs at the regional level: the CORDEX framework. *WMO Bull.* 58, 175–183.

Gloor, M., Brienen, R. J. W., Galbraith, D., Feldpausch, T. R., Schöngart, J., Guyot, J.-L., et al. (2013). Intensification of the Amazon hydrological cycle over the last two decades. *Geophys. Res. Lett.* 40, 1729–1733. doi: 10.1002/grl.50377

González-Reyes, Á, McPhee, J., Christie, D. A., Le Quesne, C., Szejner, P., Masiokas, M. H., et al. (2017). Spatiotemporal Variations in ydroclimate across the Mediterranean Andes (30–37°?S) since the Early Twentieth Century. *J. Hydrometeorol.* 18, 1929–1942. doi: 10.1175/JHM-D-16-0004.1

Guimberteau, M., Ronchail, J., Espinoza, J. C., Lengaigne, M., Sultan, B., Polcher, J., et al. (2013). Future changes in precipitation and impacts on extreme streamflow over Amazonian sub-basins. *Environ. Res. Lett.* 8:014035. doi: 10.1088/1748-9326/8/1/014035

Haarsma, R. J., Roberts, M. J., Vidale, P. L., Senior, C. A., Bellucci, A., Bao, Q., et al. (2016). High resolution model intercomparison project (HighResMIP v1.0) for CMIP6. *Geosci. Model Dev.* 9, 4185–4208. doi: 10.5194/gmd-9-4185-2016

Hartman, L. H., Kurbatov, A. V., Winski, D. A., Cruz-Uribe, A. M., Davies, S. M., Dunbar, N. W., et al. (2019). Volcanic glass properties from 1459 C.E. volcanic event in South Pole ice core dismiss Kuwae caldera as a potential source. *Sci. Rep.* 9, 1–7. doi: 10.1038/s41598-019-50939-x

Heidinger, H., Calrvalho, L., Jones, C., Posadas, A., and Quiroz, R. (2018). A new assessment in total and extreme rainfall trends over central and southern Peruvian Andes during 1965–2010. *Int. J. Climatol.* 38, e998–e1015. doi: 10.1002/joc.5427

Heredia, M. B., Junquas, C., Prieur, C., and Condom, T. (2018). New Statistical methods for precipitation bias correction applied to WRF model simulations in the antisana region (Ecuador). *J. Hydrometeorol.* 19, 2021–2040. doi: 10.1175/JHM-D-18-0032.1

Hoffman, C., García-Márquez, J. R., and Krueger, T. (2018). A local perspective on drivers and measures to slow deforestation in the Andean-Amazonian foothills of Colombia. *Land Use Policy* 77, 379–391. doi: 10.1016/j.landusepol.2018.04.043

Hoyos, I., Cañón-Barriga, J., Arenas-Suárez, T., Dominguez, F., and Rodríguez, B. A. (2018). Variability of regional atmospheric moisture over Northern South America: patterns and underlying phenomena. *Clim. Dyn.* 52, 893–911. doi: 10.1007/s00382-018-4172-9

Hoyos, I. C., Dominguez, F., Cañón-Barriga, J., Martínez, J. A., Nieto, R., Gimeno, L., et al. (2017). Moisture origin and transport processes in Colombia, northern South America. *Clim. Dyn.* 50, 971–990. doi: 10.1007/s00382-017-3653-6

Hugo, G. (2008). "Trends in land degradation in South America," in *Management of Natural and Environmental Resources for Sustainable Agricultural Development*, eds R. Stefanski, and P. Pasteris, (Portland, OR: World Meteorological Organization).

Ideam-Unal. (2018). *Variabilidad Climática y Cambio Climático en Colombia*. Bogotá, DC: Instituto de Hidrología, Meteorología y Estudios Ambientales – Universidad Nacional de Colombia, 53.

IPCC (2013). "Climate Change 2013: the physical science basis," in *Contribution of Working Group I to the Fifth Assessment Report of the Intergovernmental Panel on Climate Change*, eds T.F. Stocker, D. Qin, G.-K. Plattner, M. Tignor, S.K. Allen, J. Boschung, et al. (Cambridge: Cambridge University Press), 1535.

IPCC (2014). "Summary for policymakers," *Climate Change 2014: Impacts, Adaptation, and Vulnerability. Part A: Global and Sectoral Aspects. Contribution of Working Group II to the Fifth Assessment Report of the Intergovernmental Panel on Climate Change* C.B. Field, V.R. Barros, D.J. Dokken, K.J. Mach, M.D. Mastrandrea, T.E. Bilir, et al. (Cambridge: Cambridge University Press), 1–32.

IPCC (2019a). *Climate Change and Land: An IPCC Special Report on Climate Change, Desertification, Land Degradation, Sustainable Land Management, Food Security, and Greenhouse Gas Fluxes in Terrestrial Ecosystems*. Available online at: https://www.ipcc.ch/srccl/ (accessed September 28, 2019).

IPCC (2019b). *IPCC Special Report on the Ocean and Cryosphere in a Changing Climate*. Available online at: https://www.ipcc.ch/srocc/download/ (accessed September 28, 2019).

Jimenez-Muñoz, J. C., Barichivich, J., Mattar, C., Takahashi, K., Santamaría-Artigas, A., Sobrino, J. A., et al. (2018). Spatio-temporal patterns of thermal anomalies and drought over tropical forests driven by recent extreme climatic anomalies. *Philos. Trans. R. Soc. B Biol. Sci.* 373:20170300. doi: 10.1098/rstb.2017.0300

Kellerhals, T., Brütsch, S., Sigl, M., Knüsel, S., Gäggeler, H. W., and Schwikowski, M. (2010). Ammonium concentration in ice cores: a new proxy for regional temperature reconstruction? *J. Geophys. Res.* 115:D16123. doi: 10.1029/2009JD012603

Lara, A., and Villalba, R. (1993). A 3,620-year temperature reconstruction from Fitzroya cupressoides tree rings in southern South America. *Science* 260, 1104–1106. doi: 10.1126/science.260.5111.1104

Lavado-Casimiro, W., Ronchail, J., Labat, D., Espinoza, J. C., and Guyot, J. L. (2012). A basin-scale analysis of rainfall and runoff in Peru (1969-2004): pacific, Titicaca and Amazonas drainages. *Hydrol. Sci. J.* 57, 41–18. doi: 10.1080/02626667.2012.672985

Lavado-Casimiro, W. S., Labat, D., Ronchail, J., Espinoza, J. C., and Guyot, J. L. (2013). Trends in rainfall and temperature in the Peruvian Amazon-Andes basin over the last 40 years (1965–2007). *Hydrol. Proc.* 41, 2944–2957.

Lavergne, A., Daux, V., Pierre, M., Stievenard, M., Srur, A. M., and Villalba, R. (2018). Past summer temperatures inferred from dendrochronological records of Fitzroya cupressoides on the eastern slope of the northern Patagonian Andes. *J. Geophys. Res. Biogeosci.* 123, 32–45. doi: 10.1002/2017JG003989

Lejeune, Q., Davin, E. L., Guillod, B. P., and Seneviratne, S. I. (2015). Influence of Amazonian deforestation on the future evolution of regional surface fluxes, circulation, surface temperature and precipitation. *Clim. Dyn.* 44, 2769–2786. doi: 10.1007/s00382-014-2203-8

López-Franca, N., Zaninelli, P. G., Carril, A. F., Menéndez, C. G., and Sánchez, E. (2016). Changes in temperature extremes for 21st century scenarios over South America derived from a multi-model ensemble of regional climate models. *Clim. Res.* 68, 151–167. doi: 10.3354/cr01393

Magrin, G. O., Marengo, J. A., Boulanger, J.-P., Buckeridge, M. S., Castellanos, E., Poveda, G., et al. (2014). "Central and South America," in *Climate Change 2014: Impacts, Adaptation, and Vulnerability. Part B: Regional Aspects. Contribution of Working Group II to the Fifth Assessment Report of the Intergovernmental Panel on Climate Change*, eds V. R. Barros, C. B. Field, D. J. Dokken, M. D. Mastrandrea, K. J. Mach, T. E. Bilir, et al. (Cambridge: Cambridge University Press), 1499–1566.

Makarieva, A. M., and Gorshkov, V. G. (2007). Biotic pump of the atmospheric moisture as driver of the hydrological cycle on land. *Hydrol. Earth Syst Sci.* 11, 1013–1033. doi: 10.5194/hess-11-1013-2007

Malhi, Y., Roberts, J. T., Betts, R. A., Killeen, T. J., Li, W., and Nobre, C. A. (2008). Climate change, deforestation, and the fate of the Amazon. *Science* 319, 169–172. doi: 10.1126/science.1146961

Marengo, J. A., Alves, L. M., Alvala, R. C. S., Cunha, A. P., Brito, S., Moraes, O. L. L., et al. (2018a). Climatic characteristics of the 2010-2016 drought in the semiarid Northeast Brazil region. *Anais Acad. Brasil. Ciências* 90(2 Suppl. 1), 1973–1985. doi: 10.1590/0001-3765201720170206

Marengo, J. A., Chou, S. C., Kay, G., Alves, L. M., Pesquero, J. F., Soares, W. R., et al. (2012a). Development of regional future climate change scenarios in South America using the Eta CPTEC/HadCM3 climate change 87 projections: climatology and regional analyses for the Amazon, São Francisco and the Paraná River Basins. *Clim. Dyn.* 38, 9–12, 1829–1848.

Marengo, J. A., Souza, C. M., Thonicke, K., Burton, C., Halladay, K., Betts, R. A., et al. (2018b). Changes in climate and land use over the amazon region: current and future variability and trends. *Front. Earth Sci.* 6:228. doi: 10.3389/feart.2018.00228

Marengo, J. A., Tomasella, J., Soares, W. R., Alves, L. M., and Nobre, C. A. (2012b). Extreme climatic events in the Amazon basin. *Theor. Appl. Climatol.* 107, 73–85. doi: 10.1007/s00704-011-0465-1

Marengo, J. A., and Espinoza, J. C. (2016). Extreme seasonal droughts and floods in Amazonia: causes, trends and impacts. *Int. J. Climatol.* 36, 1033–1050. doi: 10.1002/joc.4420

Marengo, J. A., Jones, R., Alves, L. M., and Valverde, M. C. (2009). Future change of temperature and precipitation extremes in South America as derived from the PRECIS regional climate modeling system. *Int. J. Climatol.* 29, 2241–2255. doi: 10.1002/joc.1863

Marengo, J. A., Tomasella, J., Alves, L. M., Soares, W. R., and Rodriguez, D. A. (2011). The drought of 2010 in the context of historical droughts in the Amazon region. *Geophys. Res. Lett.* 38, L12703. doi: 10.1029/2011gl047436

Marengo, J. A., Tomasella, J., and Uvo, C. (1998). Long-term streamflow and rainfall fluctuations in tropical South America: Amazonia, Eastern Brazil and Northwest Peru. *J. Geophys. Res.* 103, 1775–1178.

Martínez, R., Ruiz, D., Andrade, M., Blacutt, L., Pabón, D., Jaimes, E., et al. (2011). "Synthesis of the climate of the tropical andes," in *Climate Change and Biodiversity in the Tropical Andes*, eds S. Herzog, R. Martinez, P.M. Jorgensen, H. Tiessen, (São José dos Campos – Paris: Inter American Institute for Global Change Research (IAI) – Scientific Committee on Problems of the Environment (SCOPE)), 97–109.

Masiokas, M. H., Cara, L., Villalba, R., Pitte, P., Luckman, B. H., Toum, E., et al. (2019). Streamflow variations across the Andes (18°-55°S) during the instrumental era. *Sci. Rep.* 9:17879. doi: 10.1038/s41598-019-53981-x

Masiokas, M. H., Rivera, A., Espizua, L. E., Villalba, R., Delgado, S., and Aravena, J. C. (2009). Glacier fluctuations in extratropical South America during the past 1000years. *Palaeogeogr. Palaeoclimatol. Palaeoecol.* 281, 242–268. doi: 10.1016/j.palaeo.2009.08.006

Masiokas, M. H., Villalba, R., Luckman, B. H., Le Quesne, C., and Aravena, J. C. (2006). Snowpack variations in the central andes of argentina and chile, (1951)–2005. Large-scale atmospheric influences and implications for water resources in the region. *J. Clim.* 19, 6334–6352. doi: 10.1175/jcli3969.1

Masiokas, M. H., Villalba, R., Luckman, B. H., and Mauget, S. (2010). Intra- to multidecadal variations of snowpack and streamflow records in the andes of chile and argentina between 30° and 37°S. *J. Hydrometeorol.* 11, 822–831. doi: 10.1175/2010jhm1191.1

Meehl, G. A., Covey, C., Delworth, T., Latif, M., McAvaney, B., Mitchell, J. F. B., et al. (2007). The WCRP CMIP3 multimodel dataset: a new era in climate change research. *Bull. Am. Meteorol. Soc.* 88, 1383–1394. doi: 10.1175/bams-88-9-1383

Menéndez, C. G., Zaninelli, P. G., Carril, A. F., and Sánchez, E. (2016). Hydrological cycle, temperature, and land surface–atmosphere interaction in the La Plata Basin during summer: response to climate change. *Clim. Res.* 68, 231–241. doi: 10.3354/cr01373

Mernild, S. H., Liston, G. E., Hiemstra, C. A., Yde, J. C., and Casassa, G. (2018). Annual river runoff variations and trends for the andes cordillera. *J. Hydrometeorol.* 19, 1167–1189. doi: 10.1175/jhm-d-17-0094.1

Metternicht, G., and Zinck, J. A. (2016). "Geomorphic landscape approach to mapping soil degradation and hazard prediction in semi-arid environments: salinization in the cochabamba valleys, bolivia," in *Geopedology*, eds J. A. Zinck, G. Metternicht, G. Bocco, and H. F. Del Valle, (Cham: Springer).

Minvielle, M., and Garreaud, R. D. (2011). Projecting rainfall changes over the south american altiplano. *J. Clim.* 24, 4577–4583. doi: 10.1175/jcli-d-11-00051.1

Moberg, A., Sonechkin, D. M., Holmgren, K., Datsenko, N. M., and Karlen, W. (2005). Highly variable Northern Hemisphere temperatures reconstructed from low- and high-resolution proxy data. *Nature* 433, 613–617. doi: 10.1038/nature03265

Molina, R. D., Salazar, J. F., Martínez, J. A., Villegas, J. C., and Arias, P. A. (2019). Forest-induced exponential growth of precipitation along climatological wind streamlines over the Amazon. *J. Geophys. Res. Atmos.* 124, 2589–2599. doi: 10.1029/2018jd029534

Molina-Carpio, J., Espinoza, J. C., Vauchel, P., Ronchail, J., Gutierrez Caloir, B., Guyot, J.-L., et al. (2017). Hydroclimatology of the Upper Madeira River basin: spatio-temporal variability and trends. *Hydrol. Sci. J.* 62, 911–927. doi: 10.1080/02626667.2016.1267861

Montecinos, A., and Aceituno, P. (2003). Seasonality of the ENSO-related rainfall variability in central chile and associated circulation anomalies. *J. Clim.* 16, 281–296. doi: 10.1175/1520-0442(2003)016<0281:soterr>2.0.co;2

Mora, D. E., Campozano, L., Cisneros, F., Wyseure, G., and Willems, P. (2014). Climate changes of hydrometeorological and hydrological extremes in the Paute basin, Ecuadorean Andes. *Hydrol. Earth Syst. Sci.* 18, 631–648. doi: 10.5194/hess-18-631-2014

Morales, M. S., Christie, D. A., Villalba, R., Argollo, J., Pacajes, J., Silva, J. S., et al. (2012). Precipitation changes in the South American Altiplano since 1300AD reconstructed by tree-rings. *Clim. Past* 8, 653–666. doi: 10.5194/cp-8-653-2012

Morán-Tejeda, E., Bazo, J., López-Moreno, J. I., Aguilar, E., Azorín-Molina, C., Martínez, R., et al. (2016). Climate trends and variability in Ecuador (1966–2011). *Int. J. Climatol.* 36, 3839–3855. doi: 10.1002/joc.4597

Morera, S. B., Condom, T., Crave, A., Steer, P., and Guyot, J. L. (2017). The impact of extreme El Niño events on modern sediment transport along the western Peruvian Andes (1968–2012). *Sci. Rep.* 7:11947. doi: 10.1038/s41598-017-12220-x

Mourre, L., Condom, T., Junquas, C., Lebel, T. E., Sicart, J., Figueroa, R., et al. (2016). Spatio-temporal assessment of WRF, TRMM and in situ precipitation data in a tropical mountain environment (Cordillera Blanca, Peru). *Hydrol. Earth Syst. Sci.* 20, 125–141. doi: 10.5194/hess-20-125-2016

Neukom, R., Gergis, J., Karoly, D. J., Wanner, H., Curran, M., Elbert, J., et al. (2014). Inter-hemispheric temperature variability over the past millennium. *Nat. Clim. Change* 4, 362–367. doi: 10.1038/nclimate2174

Neukom, R., Rohrer, M., Calanca, P., Salzmann, N., Huggel, C., Acuña, D., et al. (2015). Facing unprecedented drying of the Central Andes? Precipitation variability over the period AD 1000–2100. *Environ. Res. Lett.* 10:084017. doi: 10.1088/1748-9326/10/8/084017

Nobre, C. A., Sampaio, G., Borma, L. S., Castilla-Rubio, J. C., Silva, J. S., and Cardoso, M. (2016). Land-use and climate change risks in the Amazon and the need of a novel sustainable development paradigm. *Proc. Natl. Acad. Sci. U.S.A.* 113, 10759–10768. doi: 10.1073/pnas.1605516113

Novello, V. F., Cruz, F. W., Karmann, I., Burns, S. J., Stríkis, N. M., Vuille, M., et al. (2012). Multidecadal climate variability in Brazil's Nordeste during the last 3000 years based on speleothem isotope records. *Geophys. Res. Lett.* 39:L23706. doi: 10.1029/ 2012GL053936

Novello, V. F., Vuille, M., Cruz, F. W., Stríkis, N. M., de Paula, M. S., Edwards, R. L., et al. (2016). Centennial-scale solar forcing of the South American monsoon system recorded in stalagmites. *Sci. Rep.* 6:24762. doi: 10.1038/srep24762

Ohmura, A. (2012). Enhanced temperature variability in high-altitude climate change. *Theor. Appl. Climatol.* 110, 499–508. doi: 10.1007/s00704-012-0687-x

Olsson, T., Kämäräinen, M., Santos, D., Seitola, T., Tuomenvirta, H., Haavisto, R., et al. (2017). Downscaling climate projections for the Peruvian coastal Chancay-Huaral Basin to support river discharge modeling with WEAP. *J. Hydrol. Reg. Stud.* 13, 26–42. doi: 10.1016/j.ejrh.2017.05.011

Ovando, A., Tomasella, J., Rodriguez, D. A., Martinez, J. M., Siqueira-Junior, J. L., Pinto, G. L. N., et al. (2016). Extreme flood events in the Bolivian Amazon wetlands. *J. Hydrol. Reg. Stud.* 5, 293–308. doi: 10.1016/j.ejrh.2015.11.004

Oyama, M. D., and Nobre, C. A. (2003). A new climate-vegetation equilibrium state for tropical South America. *Geophys. Res. Lett.* 30:2199. doi: 10.1029/2003gl018600

Pabón, J. D. (2012). Cambio climático en Colombia: tendencias en la segunda mitad del siglo XX y escenarios posibles para el siglo XXI. *Rev. Acad. Colomb. Cienc.* 36, 127–144.

Paiva, R. C. D., Buarque, D. C., Collischonn, W., Bonnet, M.-P., Frappart, F., Calmant, S., et al. (2013). Large-scale hydrologic and hydrodynamic modeling of the Amazon River basin. *Water Resour. Res.* 49, 1226–1243. doi: 10.1002/wrcr.20067

Paiva, R. C. D., Collischonn, W., and Tucci, C. E. M. (2011). Large scale hydrologic and hydrodynamic modeling using limited data and a GIS based approach. *J. Hydrol.* 406, 170–181. doi: 10.1016/j.jhydrol.2011.06.007

Palazzi, E., Filippi, L., and von Hardenberg. (2017). Insights into elevation-dependent warming in the Tibetan Plateau-Himalayas from CMIP5 model simulations. *J. Clim. Dyn.* 48:3991. doi: 10.1007/s00382-016-3316-z

Palazzi, E., Mortarini, L., Terzago, S., and von Hardenberg, J. (2019). Elevation-dependent warming in global climate model simulations at high spatial resolution. *Clim. Dyn.* 52, 2685–2702. doi: 10.1007/s00382-018-4287-z

Palomino-Lemus, R., Córdoba-Machado, S., Gámiz-Fortis, S. R., Castro-Díez, Y., and Esteban-Parra, M. J. (2015). Summer precipitation projections over northwestern South America from CMIP5 models. *Glob. Planet. Change* 131, 11–23. doi: 10.1016/j.gloplacha.2015.05.004

Palomino-Lemus, R., Córdoba-Machado, S., Gámiz-Fortis, S. R., Castro-Díez, Y., and Esteban-Parra, M. J. (2017). Climate change projections of boreal summer precipitation over tropical America by using statistical downscaling from CMIP5 models. *Environ. Res. Lett.* 12:124011. doi: 10.1088/1748-9326/aa9bf7

Palomino-Lemus, R., Córdoba-Machado, S., Gámiz-Fortis, S. R., Castro-Díez, Y., and Esteban-Parra, M. J. (2018). High-resolution boreal winter precipitation projections over tropical America from CMIP5 models. *Clim. Dyn.* 51, 1773–1792. doi: 10.1007/s00382-017-3982-5

Peduzzi, P., Herold, C., and Silverio, W. (2010). Assessing high altitude glacier thickness, volume and area changes using field, GIS and remote sensing techniques: the case of Nevado Coropuna (Peru). *Cryosphere* 4, 313–323. doi: 10.5194/tc-4-313-2010

Pepin, N., Bradley, R. S., Diaz, H. F., Baraer, M., Caceres, E. B., Forsythe, N., et al. (2015). Elevation-dependent warming in mountain regions of the world. *Nat. Clim. Change* 5:424. doi: 10.1038/nclimate2563

Posada-Marín, J. A., Rendon, A. M., Salazar, J. F., Mejía, J. F., and Villegas, J. C. (2019). WRF downscaling improves ERA-Interim representation of precipitation around a tropical Andean valley during El Niño: implications for GCM-scale simulation of precipitation over complex terrain. *Clim. Dyn.* 52, 3609–3629. doi: 10.1007/s00382-018-4403-0

Poveda, G., Jaramillo, L., and Vallejo, L. F. (2014). Seasonal precipitation patterns along pathways of South American low-level jets and aerial rivers. *Water Resour. Res.* 50, 98–118. doi: 10.1002/2013WR014087

Preston, D. (2016). "Interpreting environmental changes in the southern bolivian andes: rural responses and political actions," in *The End of Desertification? Disputing Environmental Change in the Drylands*, eds R. H. Behnke, and M. Mortimore, (Berlin: Springer).

Quintana, J. M., and Aceituno, P. (2012). Changes in the rainfall regime along the extratropical west coast of South America (Chile): 30-43° S. *Atmósfera* 25, 1–22.

Quintana-Gómez, R. A. (1999). Trends of Maximum and minimum Temperatures in Northern South America. *J. Clim.* 12, 2104–2112. doi: 10.1175/1520-0442(1999)012<2104:tomamt>2.0.co;2

Rabatel, A., Francou, B., Soruco, A., Gomez, J., Caìceres, B., Ceballos, J. L., et al. (2013). Current state of glaciers in the tropical Andes: a multi-century perspective on glacier evolution and climate change. *Cryosphere* 7, 81–102. doi: 10.5194/tc-7-81-2013

Ragettli, S., Immerzeel, W. W., and Pellicciotti, F. (2016). Contrasting climate change impact on river flows from high-altitude catchments in the Himalayan and Andes Mountains. *Proc. Natl. Acad. Sci. U.S.A.* 113, 9222–9227. doi: 10.1073/pnas.1606526113

Rangwala, I., and Miller, J. R. (2012). Climate change in mountains: a review of elevation-dependent warming and its possible causes. *Clim. Change* 114, 527–547. doi: 10.1007/s10584-012-0419-3

Rasmussen, K. L., Zuluaga, M. D., and Houze, R. A. Jr. (2014). Severe convection and lightning in subtropical South America. *Geophys. Res. Lett.* 41, 7359–7366. doi: 10.1002/2014gl061767

Rau, P., Bourrel, L., Labat, D., Melo, P., Dewitte, B., Frappart, F., et al. (2016). Regionalization of rainfall over the Peruvian Pacific slope and coast. *Int. J. Climatol.* 37, 143–158. doi: 10.1002/joc.4693

Restrepo, J. D., Kettner, A. J., and Syvitski, J. P. M. (2015). Recent deforestation causes rapid increase in river sediment load in the Colombian Andes. *Anthropocene* 10, 13–28. doi: 10.1016/j.ancene.2015.09.001

Rodriguez-Eraso, N., Armenteras-Pascual, D., and Retana-Alumbreros, J. (2013). Land use and land cover change in the Colombian Andes: dynamics and future scenarios. *J. Land Use Sci.* 8, 154–174. doi: 10.1080/1747423X.2011.650228

Ronchail, J., Espinoza, J. C., Drapeau, G., Sabot, M., Cochonneau, G., and Schor, T. (2018). The flood recession period in Western Amazonia and its variability during the 1985–2015 period. *J. Hydrol. Reg. Stud.* 15, 16–30. doi: 10.1016/j.ejrh.2017.11.008

Russell, A. M., Gnanadesikan, A., and Zaitchik, B. (2017). Are the central andes mountains a warming hot spot? *J. Clim.* 30, 3589–3608. doi: 10.1175/jcli-d-16-0268.1

Rusticucci, M., Zazulie, N., and Raga, G. B. (2014). Regional winter climate of the southern central Andes: assessing the performance of ERA-Interim for climate studies. *J. Geophys. Res. Atmos.* 119, 8568–8582. doi: 10.1002/2013JD021167

Saavedra, F., Kampf, S., Fassnacht, S. R., and Sibold, J. S. (2018). Changes in Andes snow cover from MODIS data, 2000–2016. *Cryosphere* 12, 1027–1046. doi: 10.5194/tc-12-1027-2018

Sakamoto, M. S., Ambrizzi, T., and Poveda, G. (2011). Moisture sources and life cycle of convective systems over western colombia. *Adv. Meteorol.* 2011, 1–11. doi: 10.1155/2011/890759

Salazar, A., Baldi, G., Hirota, M., Syktus, J., and McAlpine, C. (2015). Land use and land cover change impacts on the regional climate of non-Amazonian South America: a review. *Glob. Planet. Change* 128, 103–119. doi: 10.1016/j.gloplacha.2015.02.009

Salazar, A., Sánchez-Andrade, A., Villegas, J. C., Salazar-Villegas, J. F., Ruiz-Carrascal, D., Sitch, S., et al. (2018). The ecology of peace: preparing Colombia for new political and planetary climates. *Front. Ecol. Environ.* 16:1950. doi: 10.1002/fee.1950

Salazar, J. F., Villegas, J. C., Rendón, A. M., Rodríguez, E., Hoyos, I., Mercado-Bettín, D., et al. (2018). Scaling properties reveal regulation of river flows in the Amazon through a forest reservoir Hydrology and Earth System Sciences. 22, 1735–1748. doi: 10.5194/hess-22-1735-2018

Salazar, L. F., Nobre, C. A., and Oyama, M. D. (2007). Climate change consequences on the biome distribution in tropical South America. *Geophys. Res. Lett.* 34:L09708. doi: 10.1029/2007GL029695

Sánchez, E., Solman, S., Remedio, A. R. C., Berbery, H., Samuelsson, P., Da Rocha, R. P., et al. (2015). Regional climate modelling in CLARIS-LPB: a concerted approach towards twenty first century projections of regional temperature and precipitation over South America. *Clim. Dyn.* 45, 2193–2212. doi: 10.1007/s00382-014-2466-0

Santini, W., Martinez, J.-M., Espinoza-Villar, R., Cochonneau, G., Vauchel, P., Moquet, J.-S., et al. (2015). Sediment budget in the Ucayali River basin, an Andean tributary of the Amazon River. *Proc. IAHS* 367, 320–325. doi: 10.5194/piahs-367-320-2015

Satgé, F., Espinoza, R., Zolá, R., Roig, H., Timouk, F., Molina, J., et al. (2017). Role of climate variability and human activity on poopó lake droughts between 1990 and 2015 assessed using remote sensing data. *Remote Sens.* 9:218. doi: 10.3390/rs9030218

Sayago, J. M., and Collantes, M. M. (2016). "Geopedology and land degradation in north-west argentina," in *Geopedology*, eds J. A. Zinck, G. Metternicht, G. Bocco, and H. F. Del Valle, (Berlin: Springer).

Schauwecker, S., Rohrer, M., Acuña, D., Cochachin, A., Dávila, L. R., Frey, H., et al. (2014). Climate trends and glacier retreat in the Cordillera Blanca, Peru, revisited. *Glob. Planet. Change* 119, 85–97. doi: 10.1016/j.gloplacha.2014.05.005

Schoolmeester, T., Saravia, M., Andresen, M., Postigo, J., Valverde, A., Jurek, M., et al. (2016). *Outlook on Climate Change Adaptation in the Tropical Andes mountains. Mountain Adaptation Outlook Series*. Nairobi, Arendal, Vienna and Lima: United Nations Environment Programme, GRIDArendal and CONDESAN.

Seiler, C., Hutjes, R. W. A., and Kabat, P. (2013a). Climate variability and trends in Bolivia. *J. Appl. Meteorol. Climatol.* 52, 130–146. doi: 10.1175/jamc-d-12-s0105.1

Seiler, C., Hutjes, R. W., and Kabat, P. (2013b). Likely ranges of climate change in bolivia. *J. Appl. Meteor. Climatol.* 52, 1303–1317. doi: 10.1175/jamc-d-12-0224.1

Sierra, J. P., Arias, P. A., and Vieira, S. C. (2015). Precipitation over northern south america and its seasonal variability as simulated by the CMIP5 models. *Adv. Meteorol.* 2015, 21–22.

Sierra, J. P., Arias, P. A., Vieira, S. C., and Agudelo, J. (2017). How well do CMIP5 models simulate the low-level jet in western Colombia? *Clim. Dyn.* 51, 2247–2265. doi: 10.1007/s00382-017-4010-5

Silva, Y., Takahashi, K., and Chávez, R. (2008). Dry and wet rainy seasons in the Mantaro river basin (Central Peruvian Andes). *Adv. Geosci.* 14, 261–264. doi: 10.5194/adgeo-14-261-2008

Solman, S. A. (2013). Regional climate modeling over south america: a review. *Adv. Meteorol.* 2013:504357.

Solman, S. A., and Blazquez, J. (2019). Multiscale precipitation variability over South America: analysis of the added value of CORDEX RCM simulations. *Clim. Dyn.* 53, 1547–1565. doi: 10.1007/s00382-019-04689-1

Sombroek, W. (2001). Spatial and Temporal Patterns of Amazon Rainfall. *AMBIO J. Hum. Environ.* 30, 388–396. doi: 10.1579/0044-7447-30.7.388

Souvignet, M., Oyarzún, R., Verbist, K. M. J., Gaese, H., and Heinrich, J. (2012). Hydrometeorological trends in semi-arid north-central Chile (29−32 °S): water resourcesimplicationsfor a fragileAndean region. *Hydrol. Sci. J.* 57, 479–495. doi: 10.1080/02626667.2012.665607

Taylor, K. E., Stouffer, R. J., and Meehl, G. A. (2012). An overview of CMIP5 and the experiment design. *Bull. Am. Meteorol. Soc.* 93, 485–498. doi: 10.1175/bams-d-11-00094.1

Thibeault, J., Seth, A., and Wang, G. (2012). Mechanisms of summertime precipitation variability in the Bolivian Altiplano: present and future. *Int. J. Climatol.* 32, 2033–2041. doi: 10.1002/joc.2424

Urrutia, R., and Vuille, M. (2009). Climate change projections for the tropical Andes using a regionalclimate model: temperature and precipitation simulations for the end of the 21st century. *J. Geophys. Res. Atmos. Atmos.* 114:D02108. doi: 10.1029/2008JD011021

Urrutia-Jalabert, R., González, M. E., González-Reyes, Á, Lara, A., and Garreaud, R. (2018). Climate variability and forest fires in central and south-central Chile. *Ecosphere* 9:e02171. doi: 10.1002/ecs2.2171

Vauchel, P., Santini, W., Guyot, J. L., Moquet, J. S., Martinez, J. M., Espinoza, J. C., et al. (2017). A reassessment of the suspended sediment load in the Madeira River basin from the Andes of Peru and Bolivia to the Amazon River in Brazil, based on 10 years of data from the HYBAM monitoring programme. *J. Hydrol.* 553, 35–48. doi: 10.1016/j.jhydrol.2017.07.018

Vega-Jácome, F., Lavado-Casimiro, W. S., and Felipe-Obando, O. G. (2017). Assessing hydrological changes in a regulated river system over the last 90 years in Rimac Basin (Peru). *Theor. Appl. Climatol.* 132, 347–362. doi: 10.1007/s00704-017-2084-y

Viale, M., and Nuñez, M. N. (2011). Climatology of winter orographic precipitation over the subtropical central andes and associated synoptic and regional characteristics. *J. Hydrometeorol.* 12, 481–507. doi: 10.1175/2010JHM1284.1

Vicente-Serrano, S. M., López-Moreno, J. I., Correa, K., Avalos, G., Bazo, J., Azorin-Molina, C., et al. (2018). Recent changes in monthly surface air temperature over Peru, 1964–2014. *Int. J. Climatol.* 38, 283–306. doi: 10.1002/joc.5176

Villalba, R. (1990). Climatic Fluctuations in Northern Patagonia during the Last 1000 Years as Inferred from Tree-Ring Records. *Quat. Res.* 34, 346–360. doi: 10.1016/0033-5894(90)90046-n

Villalba, R. (1994). Tree-ring and glacial evidence for the medieval warm epoch and the little ice age in southern South America. *Clim. Change* 26, 183–197. doi: 10.1007/978-94-011-1186-7_4

Villalba, R., Cook, E. R., Jacoby, G. C., D'Arrigo, R. D., Veblen, T. T., and Jones, P. D. (1998). Tree-ring based reconstructions of northern Patagonia precipitation since A.D. 1600. *Holocene* 8, 659–674. doi: 10.1191/095968398669095576

Villalba, R., Grosjean, M., and Kiefer, T. (2009). Long-term multi-proxy climate reconstructions and dynamics in South America (LOTRED-SA): state of the art and perspectives. *Palaeogeogr. Palaeoclimatol. Palaeoecol.* 281, 175–179. doi: 10.1016/j.palaeo.2009.08.007

Villalba, R., Lara, A., Boninsegna, J. A., Masiokas, M., Delgado, S., Aravena, J. C., et al. (2003). Large-scale temperature changes across the southern Andes: 20th-century variations in the context of the past 400 years. *Clim. Change* 59, 177–232. doi: 10.1007/978-94-015-1252-7_10

Villalba, R., Lara, A., Masiokas, M. H., Urrutia, R., Luckman, B. H., Marshall, G. J., et al. (2012). Unusual southern hemisphere tree growth patterns induced by changes in the southern annular mode. *Nat. Geosci.* 5, 793–798. doi: 10.1038/ngeo1613

Vuille, M., and Bradley, R. S. (2000). Mean annual temperature trends and their vertical structure in the tropical Andes. *Geophys. Res. Lett.* 27, 3885–3888. doi: 10.1029/2000gl011871

Vuille, M., Burns, S. J., Taylor, B. L., Cruz, F. W., Bird, B. W., Abbott, M. B., et al. (2012). A review of the south american monsoon history as recorded in stable isotopic proxies over the past two millennia. *Clim. Past* 8, 1309–1321. doi: 10.5194/cp-8-1309-2012

Vuille, M., Francou, B., Wagnon, P., Juen, I., Kaser, G., Mark, B. G., et al. (2008). Climate change and tropical Andean glaciers: past, present and future. *Earth-Sci. Rev.* 89, 79–96. doi: 10.1016/j.earscirev.2008.04.002

Vuille, M., Franquist, E., Garreaud, R., Lavado Casimiro, W. S., and Cáceres, B. (2015). Impact of the global warming hiatus on Andean temperature. *J. Geophys. Res. Atmos.* 120, 3745–3757. doi: 10.1002/2015jd023126

Wang, S., Huang, J., He, Y., and Guan, Y. (2014). Combined effects of the pacific decadal oscillation and el niño-southern oscillation on global land dry-wet changes. *Nat. Sci. Rep.* 4, 1–8. doi: 10.1038/srep06651

Wang, X.-Y., Li, X., Zhu, J., and Tanajura, C. A. S. (2018). The strengthening of Amazonian precipitation during the wet season driven by tropical sea surface temperature forcing. *Environ. Res. Lett.* 13:094015. doi: 10.1088/1748-9326/aadbb9

Wongchuig-Correa, S., Dias, de Paiva, R. C., Espinoza, J. C., and Collischonn, W. (2017). Multi-decadal hydrological retrospective: case study of amazon floods and droughts. 54, 667–684. doi: 10.1016/j.jhydrol.2017.04.019

Young, B., Young, K. R., and Josse, C. (2011). "Vulnerability of tropical Andean ecosystems to climate change," in *Climate Change and Biodiversity in the Tropical Andes*, eds S. K. Herzog, R. Martinez, P. M. Jorgensen, and H. Tiessen, (São José dos Campos – Paris: Inter American Institute for Global Change Research (IAI) – Scientific Committee on Problems of the Environment (SCOPE)), 170–181.

Young, K. N. (2009). Andean land use and biodiversity: humanized landscapes in a time of changes. *Ann. Missouri Bot. Garden* 96, 492–507. doi: 10.3417/2008035

Zaninelli, P. G., Menéndez, C. G., Falco, M., et al. (2019). Future hydroclimatological changes in South America based on an ensemble of regional climate models. *Clim. Dyn.* 52, 819–830. doi: 10.1007/s00382-018-4225-0

Zazulie, N., Rusticucci, M., and Raga, G. B. (2017). Regional climate of the subtropical central Andes using high-resolution CMIP5 models—part I: past performance (1980–2005). *Clim. Dyn.* 49, 3937–3957. doi: 10.1007/s00382-017-3560-x

Zazulie, N., Rusticucci, M., and Raga, G. B. (2018). Regional climate of the Subtropical Central Andes using high-resolution CMIP5 models. Part II: future projections for the twenty-first century. *Clim. Dyn.* 51:2913. doi: 10.1007/s00382-017-4056-4

Zubieta, R., Getirana, A., Espinoza, J. C., Lavado-Casimiro, W., and Aragon, L. (2017). Hydrological modeling of the Peruvian-Ecuadorian Amazon basin using GPM-IMERG satellite-based precipitation dataset. *Hydrol. Earth Syst. Sci.* 21, 3543–3555. doi: 10.5194/hess-21-3543-2017

Zulkafli, Z., Buytaert, W., Manz, B., Rosas, C. V., Willems, P., Lavado-Casimiro, W., et al. (2016). Projected increases in the annual flood pulse of the Western Amazon. *Environ. Res. Lett.* 11:014013. doi: 10.1088/1748-9326/11/1/014013

Zulkafli, Z., Buytaert, W., Onof, C., Manz, B., Tarnavsky, E., Lavado, W., et al. (2014). A comparative performance analysis of TRMM 3B42 (TMPA) versions 6 and 7 for hydrological applications over Andean–Amazon River basins. *J. Hydrometeorol.* 15, 581–592. doi: 10.1175/jhm-d-13-094.1

Zuluaga, M. D., and Houze, R. A. (2015). Extreme convection of the near-equatorial americas, africa, and adjoining oceans as seen by TRMM. *Monthly Weather Rev.* 143, 298–316. doi: 10.1175/mwr-d-14-00109.1

Conflict of Interest: The authors declare that the research was conducted in the absence of any commercial or financial relationships that could be construed as a potential conflict of interest.

Copyright © 2020 Pabón-Caicedo, Arias, Carril, Espinoza, Borrel, Goubanova, Lavado-Casimiro, Masiokas, Solman and Villalba. This is an open-access article distributed under the terms of the Creative Commons Attribution License (CC BY). The use, distribution or reproduction in other forums is permitted, provided the original author(s) and the copyright owner(s) are credited and that the original publication in this journal is cited, in accordance with accepted academic practice. No use, distribution or reproduction is permitted which does not comply with these terms.

frontiers in Earth Science

REVIEW
published: 20 March 2020
doi: 10.3389/feart.2020.00064

Hydroclimate of the Andes Part I: Main Climatic Features

Jhan Carlo Espinoza[1], René Garreaud[2], Germán Poveda[3], Paola A. Arias[4], Jorge Molina-Carpio[5], Mariano Masiokas[6], Maximiliano Viale[6] and Lucia Scaff[7]*

[1] Université Grenoble Alpes, IRD, CNRS, G-INP, IGE (UMR 5001), Grenoble, France, [2] Department of Geophysics, Universidad de Chile, Santiago, Chile, [3] Department of Geosciences and Environment Universidad Nacional de Colombia, Sede Medellín, Colombia, [4] Grupo de Ingeniería y Gestión Ambiental (GIGA), Escuela Ambiental, Facultad de Ingeniería, Universidad de Antioquia, Medellín, Colombia, [5] Instituto de Hidráulica e Hidrología (IHH), Universidad Mayor de San Andrés, La Paz, Bolivia, [6] Instituto Argentino de Nivología, Glaciología y Ciencias Ambientales (IANIGLA) – Consejo Nacional de Investigaciones Científicas y Técnicas (CONICET), Mendoza, Argentina, [7] Global Water Futures, Canada First Research Excellence Fund (CFREF), University of Saskatchewan, Saskatoon, SK, Canada

The Andes is the longest cordillera in the world and extends from northern South America to the southern extreme of the continent (from 11°N to 53°S). The Andes runs through seven countries and is characterized by a wide variety of ecosystems strongly related to the contrasting climate over its eastern and western sides, as well as along its latitudinal extension. This region faces very high potential impacts of climate change, which could affect food and water security for about 90 million people. In addition, climate change represents an important threat on biodiversity, particularly in the tropical Andes, which is the most biodiverse region on Earth. From a scientific and societal view, the Andes exhibits specific challenges because of its unique landscape and the fragile equilibrium between the growing population and its environment. In this manuscript, we provide an updated review of the most relevant scientific literature regarding the hydroclimate of the Andes with an integrated view of the entire Andes range. This review paper is presented in two parts. Part I is dedicated to summarize the scientific knowledge about the main climatic features of the Andes, with emphasis on mean large-scale atmospheric circulation, the Andes-Amazon hydroclimate interconnections and the most distinctive diurnal and annual cycles of precipitation. Part II, which is also included in the research topic "Connecting Mountain Hydroclimate Through the American Cordilleras," focuses on the hydroclimate variability of the Andes at the sub-continental scale, including the effects of El Niño-Southern Oscillation.

Keywords: Sou nailing, Andes (South America), atmospheric circulation, rainfall variability, hydrological cycle

OPEN ACCESS

Edited by:
Wouter Buytaert, Imperial College London, United Kingdom

Reviewed by:
Patricio Javier Crespo, Universidad de Cuenca, Ecuador
Valentijn Pauwels, Monash University, Australia

****Correspondence:***
Jhan Carlo Espinoza
jhan-carlo.espinoza@ird.fr

Specialty section:
This article was submitted to Hydrosphere, a section of the journal Frontiers in Earth Science

Received: *16 October 2019*
Accepted: *20 February 2020*
Published: *20 March 2020*

Citation:
Espinoza JC, Garreaud R, Poveda G, Arias PA, Molina-Carpio J, Masiokas M, Viale M and Scaff L (2020) Hydroclimate of the Andes Part I: Main Climatic Features. Front. Earth Sci. 8:64. doi: 10.3389/feart.2020.00064

INTRODUCTION

The Andes is the longest mountain chain in the world (~7240 km) and the highest within the inner tropics. The Andes extends over South America with a south-north direction from Patagonia to Venezuela. The complexity of the topography and the relative low density/short period of the meteorological network over the Andes have been an inconvenience for a proper characterization of the main atmospheric circulation patterns and their relationships with the main hydroclimatic features, including the spatio-temporal characterization of precipitation over the whole of the Andes chain. Sustainable development in the Andes is currently menaced by changes ranging

from local and regional (land use and deforestation; e.g., Nobre et al., 2016; Aide et al., 2019) to global (climate change; Magrín et al., 2014), which in turn would affect its climate and water resources, from glaciers retreat (Rabatel et al., 2013) to water supply and ecosystem services (Vuille et al., 2018).

During the last two decades, a few studies have summarized the main features of the atmospheric circulation over particular regions in South America, including Barros et al. (2000), focusing on the La Plata Basin in Southeastern South America, and Garreaud and Aceituno (2007), focusing on the subtropical/extratropical part of the continent. Over equatorial and tropical part of South America, several studies have reviewed the main mechanisms associated to the South America Monsoon System (SAMS) (Zhou and Lau, 1998; Vera et al., 2006; Marengo et al., 2012), whereas Vuille et al. (2012) provide a review of changes in this monsoon circulation during the past two millennia. Reviews of the hydroclimate of the Amazon basin have been provided by Figueroa and Nobre (1990), Espinoza et al. (2009b), and more recently by Marengo and Espinoza (2016), with particular focus on extreme hydrological events. At the regional level, Poveda et al. (2006) and Garreaud et al. (2003) have provided review papers on the climate of Northern South America/Southern Mesoamerica and the South American Altiplano, respectively. However, to our knowledge, we still lack of integrated reviews and assessments of the hydroclimate over the entire Andes range.

This contribution makes part of a series of review papers focused on diverse aspects of climate, weather, hydrology and cryosphere of the Andes cordillera. Such reviews are being prepared to provide a state-of-the-art synthesis of current knowledge, as part of the ANDEX initiative. ANDEX is a prospective Regional Hydrological Project (RHP) of the Global Energy and Water Cycle Experiment (GEWEX)[1] project of the World Climate Research Programme (WCRP)[2]. Three international workshops have been held among researchers from Andean countries and elsewhere to discuss the existing knowledge about the Andes hydroclimatology, to identify the research community working on the relevant scientific disciplines and applications, and to start identifying major research gaps. The ANDEX foundational meeting was held in Medellín, Colombia, on 5–7 December 2017; the second one in Santiago, Chile, on 22–24 October 2018; and the third workshop took place in Quito, Ecuador, on 21–24 April 2019. As a result of these activities, three overarching questions have been defined to guide the ANDEX scientific agenda, as follows[3]:

(i) What are the main physical processes driving the water and energy budgets of the Andes (as a singular cordillera), at a broad range of spatial and temporal scales, and their interactions with the Pacific and Atlantic Oceans and major river basins of South America?
(ii) How climate change, deforestation and land use changes are affecting the hydroclimatological functioning of the Andes across the altitudinal and latitudinal gradients, from glaciers to *paramos*, *punas*, cloud montane forests, rainforests, dry forests, and deserts?
(iii) What is the scientific basis underpinning the sustainable development of the Andean region?

In particular, this review aims to assess and discuss recent progress in the knowledge of the Andes hydroclimate, under an integrated view from the Patagonia to the northern Andes, including for the first time all latitudinal ranges: north tropical (north of 8°S), south tropical (8°S–27°S), subtropical (27°S–37°S) and extratropical (south of 37°S). This review considers the interactions Andes-Amazonas, which play a key role controlling hydroclimate over the Andes. This comprehensive approach has allowed better describing the differences and connections among regions, including water and energy fluxes. Also, this manuscript highlights the main research gaps that need to be addressed in order to improve our current understanding of Andean hydroclimate. This manuscript is presented in two parts. Part I is dedicated to summarize (i) the mean large-scale atmospheric circulation that characterize the hydroclimate of the Andes, including zonal flow impinging the Andes, the low-level jets observed over the Andes and the hydroclimatic connectivity between the Amazon and the Andes; and (ii) the regular cycles of precipitation, including the most distinctive diurnal and annual cycles of precipitation. Part II addresses the hydroclimate variability of the Andes at the sub-continental scale, including interannual variability and its relationship with the El Niño-Southern Oscillation (ENSO). Recent progress in the knowledge about impacts of the ENSO on the Andean hydroclimate are also reviewed by Poveda et al. (submitted) in the paper "High Impact Weather Events in the Andes," submitted to this special issue ("Connecting Mountain Hydroclimate Through the American Cordilleras").

MEAN LARGE-SCALE CIRCULATION

The atmospheric circulation over South America and adjacent oceans are major drivers of weather and climate over the Andes, including mean climatic conditions and regular cycles. These large-scale features are in turn affected by the Andean topography, vegetation patterns, the gradually-varying boundary conditions provided by the Pacific and Atlantic oceans, the tropical-extratropical interactions, the Amazon-Andes connection, among other regional-to-local interactions. In the next sections, these main features are described and discussed.

Zonal Flow Impinging the Andes

Figure 1 shows the long-term mean upper and lower tropospheric wind field in South America for January and July from the NCEP-NCAR reanalysis, a rather coarse dataset but fine enough to describe the large-scale circulation interacting with the Andes (see also Garreaud, 2009). To complement the isobaric maps, **Figure 2** displays the latitude-height cross section of the zonal flow at 70°W. Broadly speaking, the mid- and upper-level circulation atop and over the Andes is mostly zonal,

[1] https://www.gewex.org/
[2] https://www.wcrp-climate.org/
[3] www.gewex.org/project/andex/

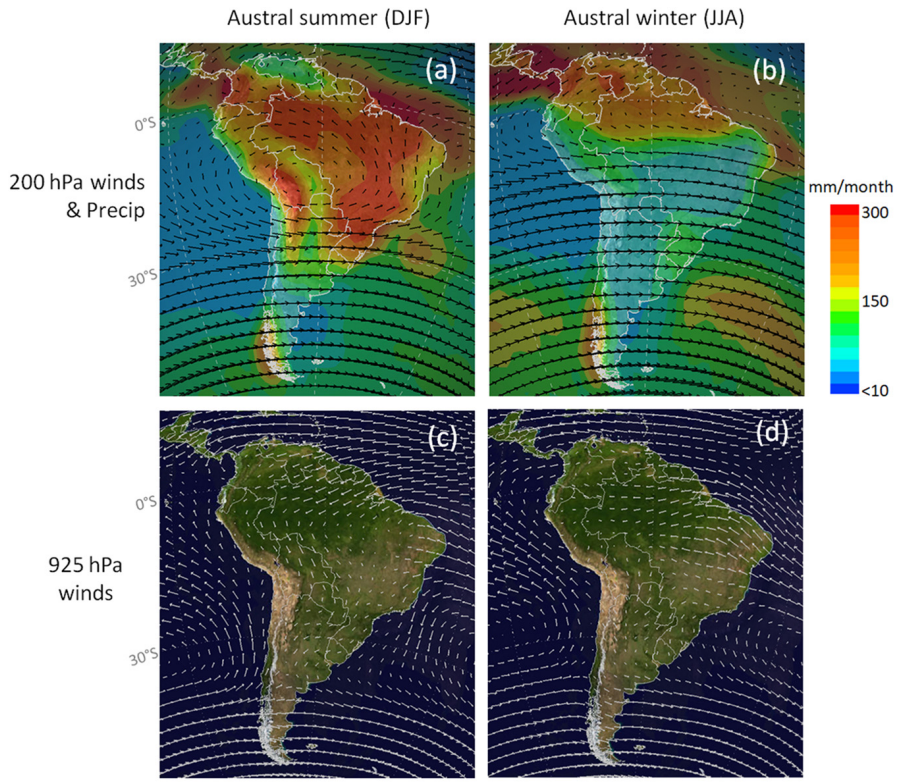


FIGURE 1 | (a,b) Long-term mean (1981–2020) winds at 200 hPa (arrows) and precipitation (shades). **(c,d)** Long-term mean (1981–2020) winds at 925 hPa (arrows) over blue marble. Data from NCEP/NCAR reanalysis.

with westerly flow from 25°S southward and easterly flow at low latitudes. During the austral winter [June-July-August (JJA)], mid-level westerlies reach ∼10°S and the upper-level jet stream is located over the subtropical Andes, at about 30°S. During the summer [December–January–February (DJF)], the zonal flow over South America is disrupted by the Bolivian High (see section 3) but since it is centered over the Altiplano, the flow atop of the cordillera remains mostly easterly (from 20°N to 20°S) or westerly (from 25°S southward, with an upper-level jet stream located over the extratropical Andes at about 45°S). The narrowness and elevation of the mountain range preclude the formation of large-scale stationary waves, because most of the low- and mid-level flow impinging the Andes is blocked and there is little deflection of the horizontal streamlines over the sloping terrain (that otherwise will generate topographic Rossby waves, e.g., Holton, 2002). On the other hand, the interaction of the strong westerly winds with the extratropical Andes (south of 37°S) is capable to produce large-amplitude gravity waves propagating into the stratosphere where they deposit their momentum (e.g., Jiang et al., 2013).

Baroclinic disturbances embedded in the mid-latitude westerly wind belt are responsible for most of the rain and snowfall in the subtropical and extratropical Andes (particularly, central-southern Chile, and western Argentina) due to the spill-over effect. The axis of the southern hemisphere storm track intersect the extratropical Andes at 45–50°S year round (**Figure 1**; Berbery and Vera, 1996; Inatsu and Hoskins, 2004; Hoskins and Hodges, 2005) and recent studies have shown that climate change is responsible for a poleward shift of the storm track (Bengtsson et al., 2006; Chang et al., 2012) with important consequences for the Chile/western Argentina hydroclimate (Boisier et al., 2018).

Near-surface, westerly flow continues to impinge against the Andes at mid-latitudes and easterly flow near the equator. The trans-Andean flow at mid-latitudes -responsible for some of the most marked precipitation gradients on Earth (see Part II)- is possible because of the strong flow and the relatively low topography, even though some blocking occurs at the lowest levels (Viale and Garreaud, 2015). The trans-Andean flow at low latitudes is more difficult to occur given the altitude of the mountains in this region. Indeed, the eastern slopes of the south Tropical Andes (which cover Bolivia, Peru, and Ecuador) act as a topographic barrier for the warm and moist flux from the Amazon region. Moisture advection from the Amazon region is predominant during the austral summer (**Figure 1a**). However, at low latitudes (north of 5°S), where the altitude of the mountains is lower, trans-Andean flows are predominant all year around, producing a complex rainfall regime over this region (Laraque et al., 2007; Espinoza et al., 2009b; Segura et al., 2019).

Because of the topographic blocking, the low-level flow adjacent to the subtropical Andes is mostly meridional: southerly winds to the west and northerly winds to the east. This meridional

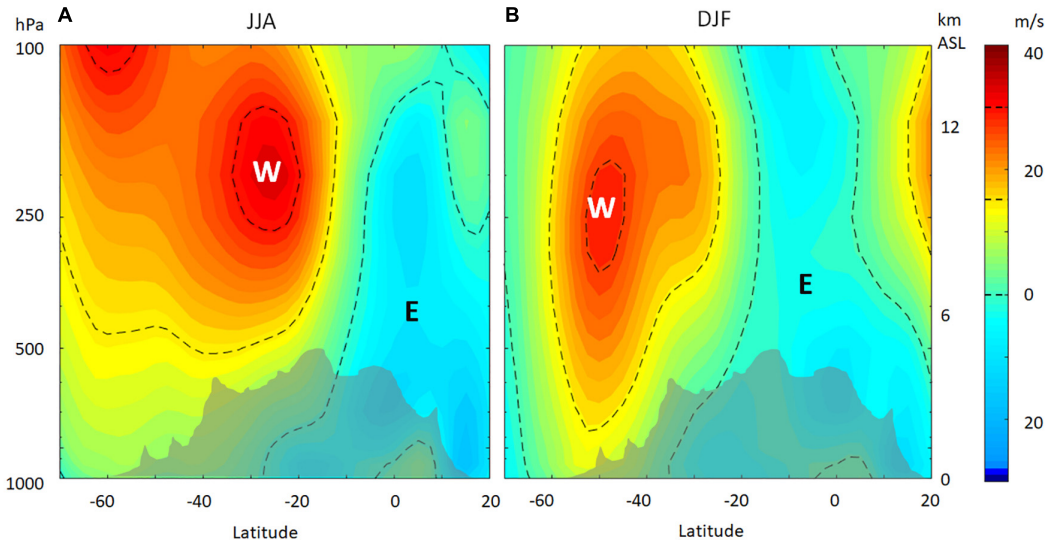


FIGURE 2 | Cross-section of long-term-mean (1981–2020) zonal wind (U) at 70°W for **(A)** austral winter (JJA) and **(B)** summer (DJF). Gray area indicates mean Andes height averaged at 80–60°W. Contours indicate U = 0, 15, and 30 m/s. Data from NCEP-NCAR Reanalysis.

flow pattern is stronger in the austral summer and in quasi-geostrophic balance with the subtropical Pacific anticyclone and the continental low (Seluchi et al., 2003), whose maintenance is partially driven by the Andes (Rodwell and Hoskins, 2001; Takahashi and Battisti, 2007). Near to the western flank of the subtropical Andes, the flow becomes northerly, with a well-defined jet at about 700 hPa within 30 km from the mountain surface (Rutllant and Garreaud, 2004; Garreaud, 2009). The low-level, terrain-parallel flow close to both sides of the Andes often organize in low-level jets (LLJs) described in detail in section Low Level Jets at the Andes Foothills.

The relevance of the Andes cordillera in organizing the tropospheric flow at the continental scale (and so the moisture transport among other consequences) can also be appreciated in numerical experiments in which the Andes is removed, as presented in Insel et al. (2010) and Garreaud et al. (2010). Of particular relevance, the presence of the Andes is instrumental for the existence of the low-level jet east of the Andes, the South American Low-Level jet (SALLJ; see section LLJs to the East of the Andes), that transport humidity from the Amazonian rainforest into the southern plains of the continent, and so it is fundamental for inducing the occurrence of the SAMS during austral summer. The SAMS corresponds to a monsoonal circulation over South America, mainly Bolivia, Peru, Brazil and northern Argentina, covering the Amazon rainforest (e.g., Zhou and Lau, 1998), that exhibits four dominant features: (i) an upper troposphere anticyclone (at 200–300 hPa), located over Bolivia, known as the Bolivian High (see section Regular Cycles of Precipitation); (ii) a northwest-southwest oriented band of cloudiness over the southeast of the continent, known as the South Atlantic Convergence Zone (SACZ); (iii) the occurrence of high surface temperatures over the Atlantic Ocean prior to the wet season onset; and (iv) the presence of the SALLJ to the east of the Andes (see section LLJs to the East of the Andes) (Gan et al., 2004; Vera et al., 2006; Carvalho et al., 2011; Marengo et al., 2012). The evolution of the SAMS is also related to the location and intensity of the Atlantic Intertropical Convergence Zone (ITCZ). For instance, during the onset and mature phases of the SAMS (early-mid austral summer), the ITCZ is confined to the Atlantic region between 5 and 8°N (Zhou and Lau, 1998). During the retreat phase of the SAMS (late austral summer-early austral fall), the deep convection of the Atlantic ITCZ is relatively weak and shows a northward migration (Vera et al., 2006). Therefore, atmospheric circulation over the Andes is partly connected to the dynamics of the SAMS, as discussed throughout the next subsections.

Amazon-Andes Connection

The Amazon-Andes transition region is characterized by a unique landscape and the fragile equilibrium between the growing population and its environment (Myers et al., 2000; Vuille et al., 2018). This region shows an exceptional biodiversity and biogeographical patterns, which are the result of the interplay between contrasted climates and the complexity of Andean topography (Hoorn et al., 2010; Rangel et al., 2018). The eastern Andes and the Amazon River basin constitute an entangled biogeophysical system. The Amazon region exports water vapor and nutrients to the Andes through the moisture-laden trade winds (e.g., Garreaud, 1999; Poveda et al., 2006, 2014; Zemp et al., 2017). The ascent of these winds owing to the orographic effect of the Andes, favors convection and high intensity rainfall rates over the eastern piedmont (e.g., Espinoza et al., 2009b, 2015; Chavez and Takahashi, 2017; Junquas et al., 2018; Kumar et al., 2019), which in turn produces the river runoff draining sediments, pollutants, and nutrients downstream to the Amazon lowlands (Poveda et al., 2006; McClain and Naiman, 2008; Espinoza et al., 2009a; Moquet et al., 2011; Molina-Carpio et al., 2017; Builes-Jaramillo and Poveda, 2018).

The eastern flank of the tropical Andes is the wettest region in the Amazonia (e.g., Figueroa and Nobre, 1990; Espinoza et al., 2009b). From the diurnal to the interdecadal timescale, rainfall variability in the Amazon-Andes transition region is the result of the interplay between regional atmospheric circulation, lowland-highland temperature contrast and the complex Andean topography (Ronchail and Gallaire, 2006; Espinoza et al., 2015; Segura et al., 2016; Chavez and Takahashi, 2017; Junquas et al., 2018). These features produce high rainfall rates of around 6000–7000 mm/year, generally observed at around 400–2000 m.a.s.l (Johnson, 1976; Giovannettone and Barros, 2009; Poveda et al., 2014; Espinoza et al., 2015; Chavez and Takahashi, 2017). As a consequence, the Andean region has the largest runoff per unit area of the Amazon basin (Moquet et al., 2011; Builes-Jaramillo and Poveda, 2018; **Figure 3**) and the extreme hydrological events that occur over this region can have impacts over the entire Amazon basin, as observed during the exceptional 2014 flood in the upper Madeira River basin (Espinoza et al., 2014; Ovando et al., 2016). Studies have documented the key role of the hydrological variability of the Andean-Amazon rivers, such as the Madeira, Ucayali, Marañón and Caquetá-Japura for a broad understanding of hydrological variability of the entire Amazon basin at the seasonal and interannual time scales, including long-term hydrological trends (e.g., Roche and Fernandez Jáuregui, 1988; Espinoza et al., 2009a; Lavado-Casimiro et al., 2013; Molina-Carpio et al., 2017; Wongchuig-Correa et al., 2017; Barichivich et al., 2018), atmospheric and surface water balances (Builes-Jaramillo and Poveda, 2018, **Figure 3**) and the dynamics of the sediments and nutrients at the Amazon basin scale (Guyot et al., 2007; Moquet et al., 2011; Armijos et al., 2013; Bouchez et al., 2017; Vauchel et al., 2017). Multiannual rainfall variability in the Amazon basin, including extreme hydroclimatic events, has been mainly attributed to the sea surface temperatures (SST) variations in both the tropical Pacific and Atlantic oceans, with seasonal and regional specificities. In addition, a reduced vegetation cover in the southern Amazon also contributes to a more frequent occurrence of longer dry seasons over this region (for more details see Debortoli et al., 2015; Marengo and Espinoza, 2016; Barichivich et al., 2018; Builes-Jaramillo and Poveda, 2018; Espinoza et al., 2019; Leite-Filho et al., 2019; Ruiz-Vasquez et al., submitted, among others).

Builes-Jaramillo and Poveda (2018) provide recent estimates of water balance components in the Andes-Amazon transition zone (**Figure 3**). Despite receiving less precipitation, runoff is higher in the Andean part of the Amazon basin than the Amazon lowlands (Moquet et al., 2011). This difference could be related to the spatial variability of rainfall over the Andes-Amazon region, where the rainiest zones are observed ("hotspots"), as well as the steep topography that favors runoff (Espinoza et al., 2014). High rainfall rates on the eastern slopes of the Andes cause strong erosion, particularly over the south tropical Andes, mainly related to climate variability (Pepin et al., 2013; Lowman and Barros, 2014). The erosion of the eastern flank of the tropical Andes provides nearly 100% of the suspended sediment load observed in the Amazon Basin (estimated between 750 and 1200 Mt/year), with a major contribution from southern Amazon rivers such as the Ucayali and Madeira. For instance, the average suspended sediment production of the Madeira River Andean catchment has recently been estimated at 640 Mt/year (Vauchel et al., 2017), but almost a third of that load is deposited in the floodplains before reaching the Amazon (Guyot et al., 2007; Armijos et al., 2013; Santini et al., 2014; Vauchel et al., 2017; Espinoza-Villar et al., 2018; Ayes-Rivera et al., 2019). Andean rivers also control the Amazon basin hydrochemistry, in particular due to the salt rocks and carbonates present in the Marañón and Ucayali basins (Moquet et al., 2011; Bouchez et al., 2017).

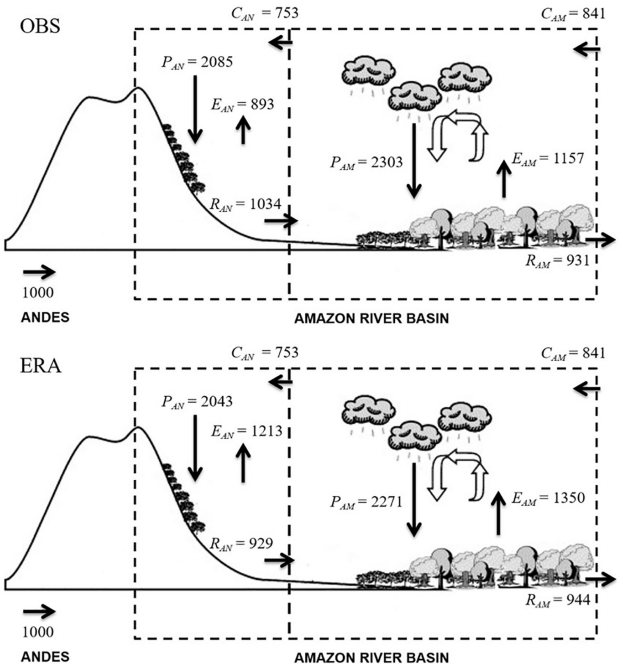


FIGURE 3 | Illustration of the components of surface water balance and atmospheric water balance based on the observations (OBS) and reanalysis (ERA) datasets in the Andes and Amazonia subregions of the Amazon River basin. P, precipitation; E, actual evapotranspiration; R, runoff; C, moisture convergence. Values are in units of mm.y^{-1}. The arrow convention on the bottom left represents 1000 mm.y^{-1}. Source: Builes-Jaramillo and Poveda (2018). © American Geophysical Union. Reprinted by permission from John Wiley and Sons.

The Atlantic Ocean and the Amazon rainforest are, respectively, the main oceanic and continental atmospheric moisture sources for most of the north tropical Andes (north of 8°S) and neighboring regions (Arias et al., 2015; Hoyos et al., 2017; Zemp et al., 2017; **Figures 3**, **4**). On the other hand, the Amazon rainforest is a major supply of humidity for neighboring regions, such as tropical South America, the La Plata river basin and the Andes cordillera (e.g., Berbery and Barros, 2002; Martinez and Dominguez, 2014; Poveda et al., 2014; Arias et al., 2015; Molina et al., 2019; Ruiz-Vasquez et al., submitted). In a recent study, Staal et al. (2018) estimates that around 25–50% of total annual rainfall observed in the tropical Andes might be originated by Amazon tree transpiration transported westward by dominant trade winds (**Figure 4**). For instance, Rodriguez et al. (2018) suggest that environmental change

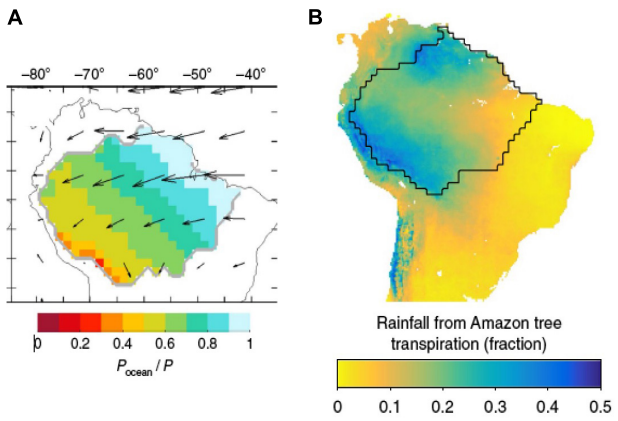


FIGURE 4 | (A) Fraction of total precipitation during the extended dry season (June–November) that last evaporated from the ocean, calculated from atmospheric moisture tracking (1989–2005). Arrows represent vertically integrated moisture fluxes. Source: Zemp et al. (2017), © Nature Communications. CC licence. **(B)** Fraction of mean annual rainfall that has been transpired by trees in the Amazon basin. Source: Staal et al. (2018). © Nature Climate Change. Reprinted by permission from Springer Nature.

(mainly land use change) in the southern and southeastern Amazon basin has reduced its capacity to regulate low flows. Also, according to previous works, Amazonian rainforest is the main source of atmospheric moisture for the subtropical Andes (e.g., Garreaud, 1999; Garreaud et al., 2003; Falvey and Garreaud, 2005; Sorí et al., 2017; Segura et al., 2020).

Consequently, the high rate of Amazonian land-cover change probably will affect the entire hydrological cycle over both the Amazon basin and the Andes. In fact, the existence of two-way biogeophysical feedbacks between the Andes and the Amazon is difficult to overstate. Massive amounts of water vapor are evapotranspired into the atmosphere by the Amazonian rainforest, which are condensed and converted into rainfall (precipitation recycling), and later on evapotranspired several times within the region (**Figure 3**). Such cascade of water vapor is then transported by the trade winds from eastern to central and western Amazonia (**Figure 4A**), to be lifted by the orography of the Andes and then condensed and converted into rainfall. This explains that the rainiest regions of the Amazon river basin are located along the piedmonts of the Andes of Colombia, Ecuador, Peru, and Bolivia (Espinoza et al., 2009b), which in turn feed the extraordinarily high precipitation recycling rates in the Andes (Zemp et al., 2014; Staal et al., 2018). Such high amounts of rainfall along the Andes feed the rivers flowing to the low-lying Amazonia (**Figure 3**). Therefore, deforestation of the low-lying Amazon would reduce the recycling of precipitation, but also the flux of water vapor exported to the Andes, and the surface runoff and sediments exported from the Andes to the low-lying Amazonia, increasing the risks of drought, tree mortality and fires. Such hydrological disruption also threatens the supply of water that is transported from the low-lying Amazon to the tropical Andean glaciers, already undergoing a fast retreat owing to global warming (Sagredo and Lowell, 2012; Rabatel et al., 2013), which in turn impact the ecological dynamics of *paramos, yungas, punas*, and Andean forests (cloud, montane, and rainforests) (Zimmer et al., 2018), and put in peril the water supply for major cities like Bogotá, Lima, Quito, and La Paz, and hundreds of cities and towns along the Andes.

The Bolivian High

During the DJF season (austral summer), the 200 hPa westerlies over South America are mainly observed south of 22°S. Also, the extreme north of the continent is dominated by westerlies (**Figure 5**). An upper-level anticyclonic circulation (around 200–300 hPa), referred as the Bolivian High, is observed over the tropical South American continent (centered at around 15°S–65°W). Downstream, over northeastern Brazil, an upper level cyclonic circulation is observed in complement to the Bolivian High and a convergence region is defined over the Peruvian and Ecuadorian coasts (Virji, 1981; Lenters and Cook, 1997).

Initial studies suggested a thermal origin for the Bolivian High, supported by the strong sensible heating and the liberation of latent heat over the Altiplano and the tropical Andes during the austral summer (Schwerdtfeger, 1961; Gutman and Schwerdtfeger, 1965). Later, a comprehensive modeling study by Lenters and Cook (1997) suggested that the Bolivian High is a dynamical response to the heating of the upper levels of the troposphere produced by the deep convection over the central-western Amazonia. Diabatic heating over the Andes and the Altiplano does not seem crucial for the development of the Bolivian High, while the Andes organize the low-level circulation and convection over tropical South America. Hence, the Bolivian High is now recognized as one of the most prominent regional responses of the tropospheric circulation associated with the strong convection over the Amazon observed during the SAMS in austral summer (e.g., Vera et al., 2006). The Bolivian High contributes actively to the precipitation over the Altiplano and the south tropical Andes during the austral summer because the easterly winds in the upper troposphere favor the transport of moist air from the Amazon lowlands toward the tropical Andes (Garreaud, 1999; Segura et al., 2019). In addition, the Bolivian High is crucial to the strengthening of the SACZ during the DJF season, due to vorticity advection observed upward (Figueroa et al., 1995). During the March-April-May (MAM) season, the southern hemisphere westerlies return to encompass the subtropics and a couple of anticyclones is observed over the tropical part of the continent, in accordance with the convection over the equator.

The Bolivian High experiences strong synoptic and intraseasonal variability (**Figure 5**) in its intensity, position and extent. While the Bolivian High mean-state has been firmly related to convection over the Amazon, it is unclear how both elements are connected at higher frequencies. A confounding factor is extratropical variability that can impact both upper-level winds and low-level conditions affecting continental convection. Of particular relevance is a sub-monthly scale dipole of convection that is often observed in southeastern South America between the La Plata basin and southern Brazil (e.g., Nogués-Paegle and Mo, 1997; Díaz and Aceituno, 2003). Earlier studies

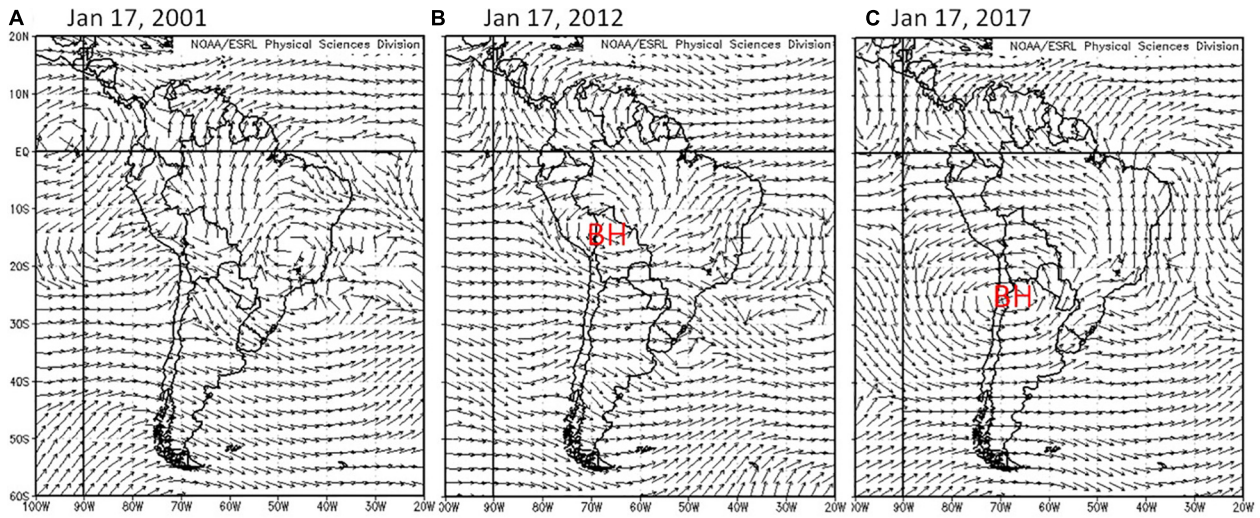


FIGURE 5 | 200 hPa winds for 3 days in austral summer depicting an absent Bolivian High (BH; **A**), a Bolivian High near its climatological position **(B)** and an intense, broad Bolivian High centered well to the south of its mean position **(C)**. Wind data from NCEP-NCAR Reanalysis.

indicate that this dipole is related to distinct changes in intensity and position of the Bolivian High (Vera and Vigliarolo, 2000).

Low Level Jets at the Andes Foothills

Prominent LLJs are observed at both sides of the Andes and at different ranges of latitude, which are induced by mechanical blocking of impinging flow and/or diabatic heating in the mountain slopes. These LLJs are important because they transport vast quantities of moisture along large meridional distances, except for the case of the jets to the west of the Andes at subtropical latitudes. A schematic representation of these LLJs is presented in **Figure 6** and we now examine their main features.

LLJs to the East of the Andes

One of the LLJs to the east to the Andes circulates over northern South America from the Tropical North Atlantic through Guyana and eastern Venezuela. It becomes a LLJ blowing over the Venezuela-Colombian Llanos (plains) of the Orinoco River, so-called Corriente de los Andes Orientales (CAO), the Llanos jet, the Orinoco jet, or the Eastern Andes Jet (Montoya et al., 2001; Torrealba and Amador, 2010; Jiménez-Sánchez et al., 2019; see **Figure 6**). The easterly flow of the CAO reaches the eastern piedmont of the Andes as the northernmost leg of the SALLJ (**Figure 6**). The SALLJ is characterized by northerly surface (850 hPa) wind speeds higher than 12 ms^{-1} (Marengo et al., 2004). This LLJ reaches regions of Bolivia, Paraguay, Southern Brazil, Uruguay and Argentina (Byerle and Peagle, 2002; Campetella and Vera, 2002; Wang and Fu, 2002; Vera et al., 2006; Moraes-Arraut et al., 2012; Poveda et al., 2014) where it delivers vast quantities of moisture transported from the Atlantic or the Amazon basin, feeding severe weather well into subtropical latitudes (e.g., Salio et al., 2007). The SALLJ is promoted by the diabatic heating released in the SAMS region (Vera et al., 2006). This LLJ attracted considerable attention in the early 2000's when a major field experiment (SALLJEX) was conducted in the summer of 2003, mostly over Bolivia and Paraguay[4].

Over the Colombian and Venezuelan Llanos region, the CAO exhibits a clear annual cycle with peak velocities during DJF (8–12 ms^{-1}) and lower velocities during JJA (2–3 ms^{-1}). It is worth noticing that the annual cycle of the CAO wind strength is negatively correlated with rainfall over the Colombian Llanos (Rueda, 2014; Jiménez-Sánchez et al., 2019) and the western Amazon basin (Espinoza et al., 2018) and positively correlated with rainfall over the south tropical Andes and southern Amazonia, where annual rainfall reaches 6000 mm (e.g., Figueroa and Nobre, 1990; Garreaud et al., 2003; Espinoza et al., 2009b; Giovannettone and Barros, 2009; Segura et al., 2019). At the eastern flank of the south tropical Andes, the moisture fluxes provided by the CAO produce high rainfall rates (5000–7000 mm yr^{-1}) over the Andes-Amazon transition zone of Peru and Bolivia (Poveda et al., 2014; Espinoza et al., 2015; Chavez and Takahashi, 2017).

LLJs to the West of the Andes

One of the rainiest places on Earth (Lloró; 5°30′N, 76°32′W) is situated alongside the Pacific coast of Colombia, witnessing mean annual precipitation rates reaching 13,000 mm (Snow, 1976; Meisner and Arkin, 1987; Poveda and Mesa, 1999, 2000; Adler et al., 2000; Mapes et al., 2003; Sakamoto et al., 2011; Zuluaga and Houze, 2015; Jaramillo et al., 2017; King et al., 2017). Such world record precipitation is explained by the dynamics of the Chocó low-level jet (hereafter, Chocó Jet), enhanced by atmosphere-ocean-land surface interactions (Poveda and Mesa, 1999, 2000). The Chocó Jet is a singular southwesterly circulation feature acting over the easternmost tropical Pacific, with origin off the Chilean coast (Sakamoto et al., 2011; Arias et al., 2015; Hoyos et al., 2017). Once the southeasterly trade

[4]https://www.eol.ucar.edu/field_projects/salljex

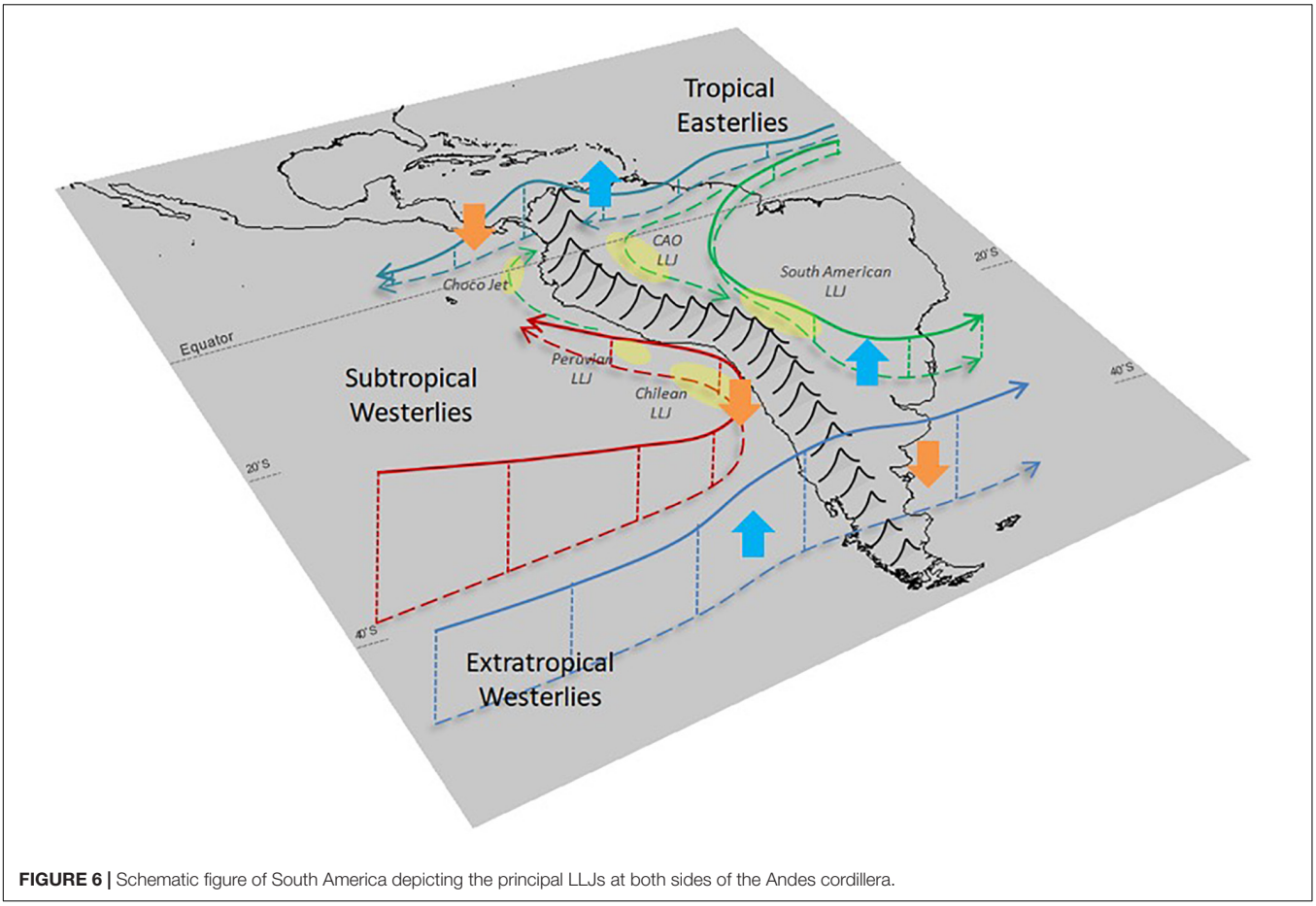


FIGURE 6 | Schematic figure of South America depicting the principal LLJs at both sides of the Andes cordillera.

winds cross the Equator over the eastern Pacific, they enter onshore in the form of a LLJ, which is then lifted up due to the orographic effect of the western north tropical Andes, and interacts aloft with the warmer easterly trade winds to increase deep convection (López and Howell, 1967; Poveda and Mesa, 2000; Mapes et al., 2003; Warner et al., 2003; Poveda et al., 2006; Jaramillo et al., 2017). **Figure 7** depicts the mean seasonal vertical distribution of 925 hPa zonal winds in the tropical Americas with data from MERRA-2 Reanalysis (Gelaro et al., 2017). The Choco jet exhibits a distinctive annual cycle with higher velocities during September–October-November (SON), and lower during February-March, transporting higher amounts of moisture during SON ($\sim$90 ms^{-1} g kg^{-1}), and minimum values during March, according to data from the NCEP/NCAR Reanalysis (Poveda et al., 2006, 2014; Rueda and Poveda, 2006). The Choco jet reaches southern Central America during June to November (Durán-Quesada et al., 2010). The meridional migration exhibited by this LLJ, characterized by a further north location during SON, is related to the seasonal migration of the ITCZ (Sierra et al., 2018). It is also associated with the dynamics of Mesoscale Convective Systems (MCS) off the Colombian Pacific (Velasco and Fritsch, 1987; Poveda and Mesa, 2000; Mapes et al., 2003; Zuluaga and Poveda, 2004; Mejia and Poveda, 2005; Zuluaga and Houze, 2015; Jaramillo et al., 2017; King et al., 2017).

A fourth LLJ in the Andean region forms over the southeastern Pacific, close to the Andean western slope (Garreaud and Muñoz, 2005; Muñoz and Garreaud, 2005). It has been shown that this LLJ is produced by the ageostrophic wind balance between pressure, Coriolis and friction forces within the Marine Boundary Layer. The geostrophic balance is broken down by both the Andes cordillera and a coastal range (Takahashi, 2012). While this southerly LLJ does not transport considerable amounts of moisture, it drives the upwelling of cold but nutrient reach water masses along north-central Chile and southern Peru. Weakening of this southerly LLJ can result in the onset of a Coastal El Niño with dramatic consequences along the Peruvian and Ecuadorian coasts (Garreaud, 2018). This was particularly observed during 2016–2017, when the weakening of this LLJ was remotely forced by anomalously intense deep convection in the far-western Pacific that triggered Rossby wave trains extending across the South Pacific, further inducing the occurrence of a Coastal El Niño event in 2017 (Garreaud, 2018).

REGULAR CYCLES OF PRECIPITATION

Regular cycles of precipitation over the Andes are associated with complex interactions between the above-described large-scale atmospheric features (e.g., latitudinal oscillation of the

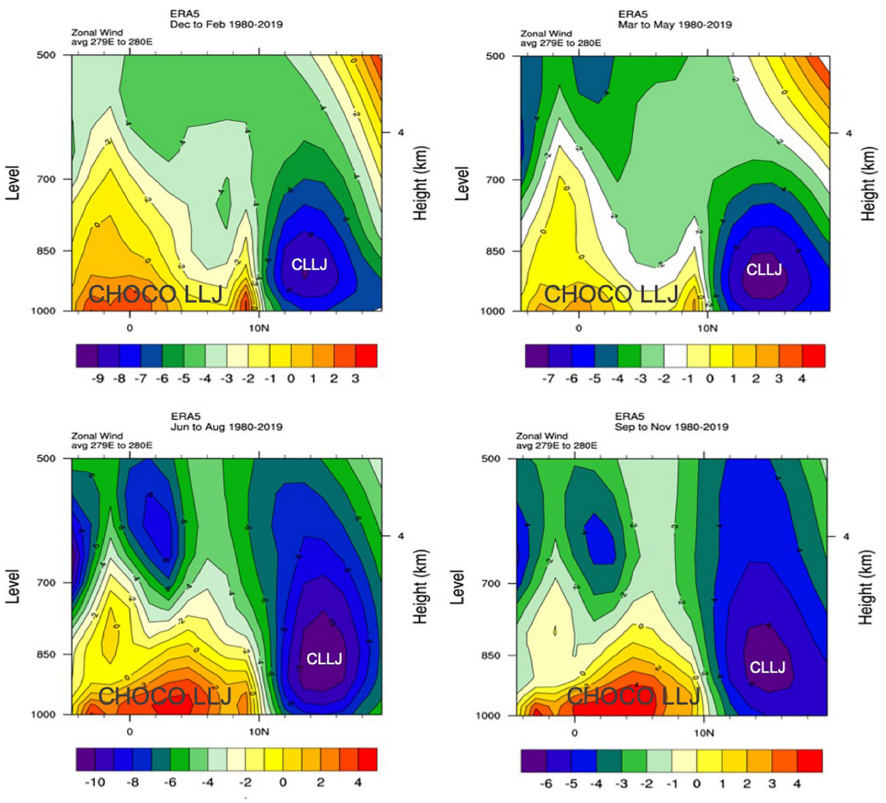


FIGURE 7 | Vertical distribution of mean (1980–2019) zonal winds (m s^{-1}) based on ERA 5 at 79–80°W during **(A)** December–February (DJF), **(B)** March–May (MAM), **(C)** June–August (JJA), and **(D)** September–November (SON). Positive values indicate westerly flow while negative values indicate easterly flow. CLLJ indicates the easterly blowing Caribbean LLJ crossing Central America. The westerly blowing Choco jet is most evident from May through November. Images provided by the NOAA/ESRL Physical Sciences Division, Boulder Colorado from their web site at https://www.esrl.noaa.gov/psd/.

ITCZ and the westerlies) and local patterns, such as the Andean orography, local circulations (e.g., diurnal thermally driven circulations, upslope, and downslope moisture transport) and temperature gradients. Based on the current scientific literature, this section provides a synthesis of diurnal and seasonal cycles of precipitation across the entire Andes.

Diurnal Cycle of Precipitation

The most dominant feature of tropical climatology is the strong amplitude of the diurnal cycle of temperature, which in turn is associated with the formation and development of shallow and deep convective processes generating rainfall. Orography exerts a strong role to control and focus local circulation and temperature gradients, and therefore tropical Andean rainfall exhibits a strong spatiotemporal variability. The diurnal cycle of rainfall in the north tropical Andes of Colombia (north of 8°S) has been studied by Poveda et al. (2001, 2002a,b,c, 2005). **Figure 8** exemplifies the strong variability in the hour of preferential rains over the north tropical Andes of Colombia, which can be unimodal (diurnal) or bimodal (semi-diurnal). The phase of the diurnal cycle of rainfall in the north tropical Andes of Colombia also exhibits a strong spatial variability with respect to the month of the year. Dedicated studies are needed to further understand the physical mechanisms and dynamic and thermodynamic processes that explain such strong spatial variability in the diurnal cycle of rainfall within the seasonal march.

In most of the south tropical Andes (mainly in southern Peru and Bolivia), a clear diurnal cycle has been identified, characterized by maximum precipitation values observed during the day (night) in the western (eastern) flank of the highlands (Chavez and Takahashi, 2017; Junquas et al., 2018; Saavedra et al., 2020). In the eastern valleys of the Amazon-Andes transition region, the maximum (minimum) precipitation is observed during the night (day). This is the case for the valleys in the Cuzco region (**Figure 9**; Junquas et al., 2018). On the other side, a thermally-driven early afternoon maximum (Garreaud, 1999) is frequently observed over the hillslopes, associated to upslope flows that mobilize water vapor from the valley floor. This local circulation pattern has been related to the strong precipitation spatial variability and gradients that occur in many Andean valleys (Molina-Carpio et al., 2019). The use of high-resolution climate models has been proposed to study diurnal variability and thus its relationship with spatial variability at local scales (Junquas et al., 2018).

Over the Altiplano, the maximum precipitation is observed in the early afternoon (13 h LT) associated with the maximum outgoing longwave radiation, the radiative heating and the

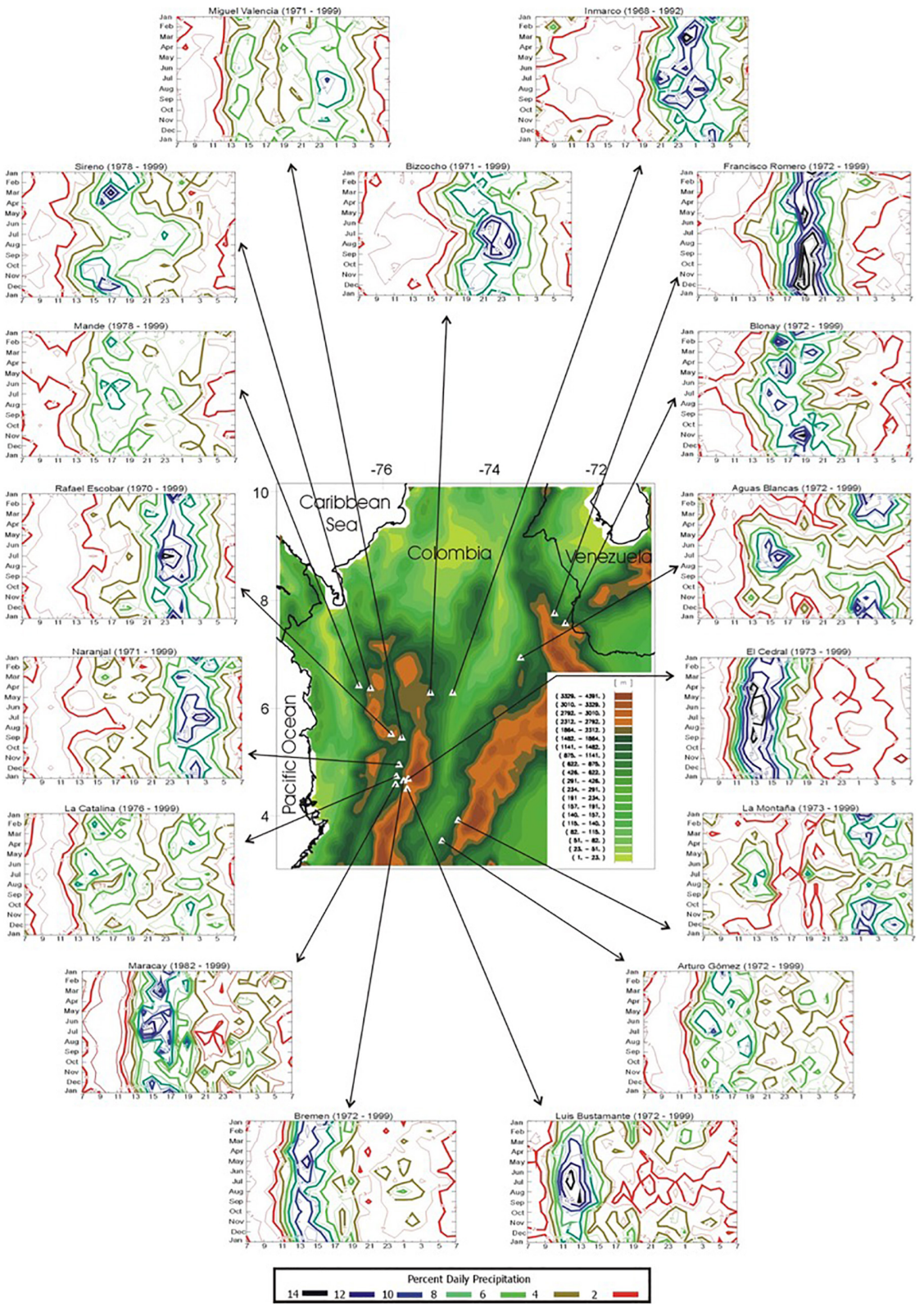


FIGURE 8 | Seasonal march of the diurnal cycle of rainfall at 17 selected stations in the north tropical Andes of Colombia (north of 8°S). The diurnal cycle is defined from 0700 to 0700 local standard time (LST), and interpolated isolines indicate percent of total daily rainfall, with the color scale shown at the bottom. Boundaries of the neighboring (left) Cauca and (right) Magdalena River valleys are shown in white. The inset at the bottom left shows details of rain gauges located in the western flank of the central range of the Colombian Andes. Source: Poveda et al. (2005). © American Meteorological Society. Used with permission.

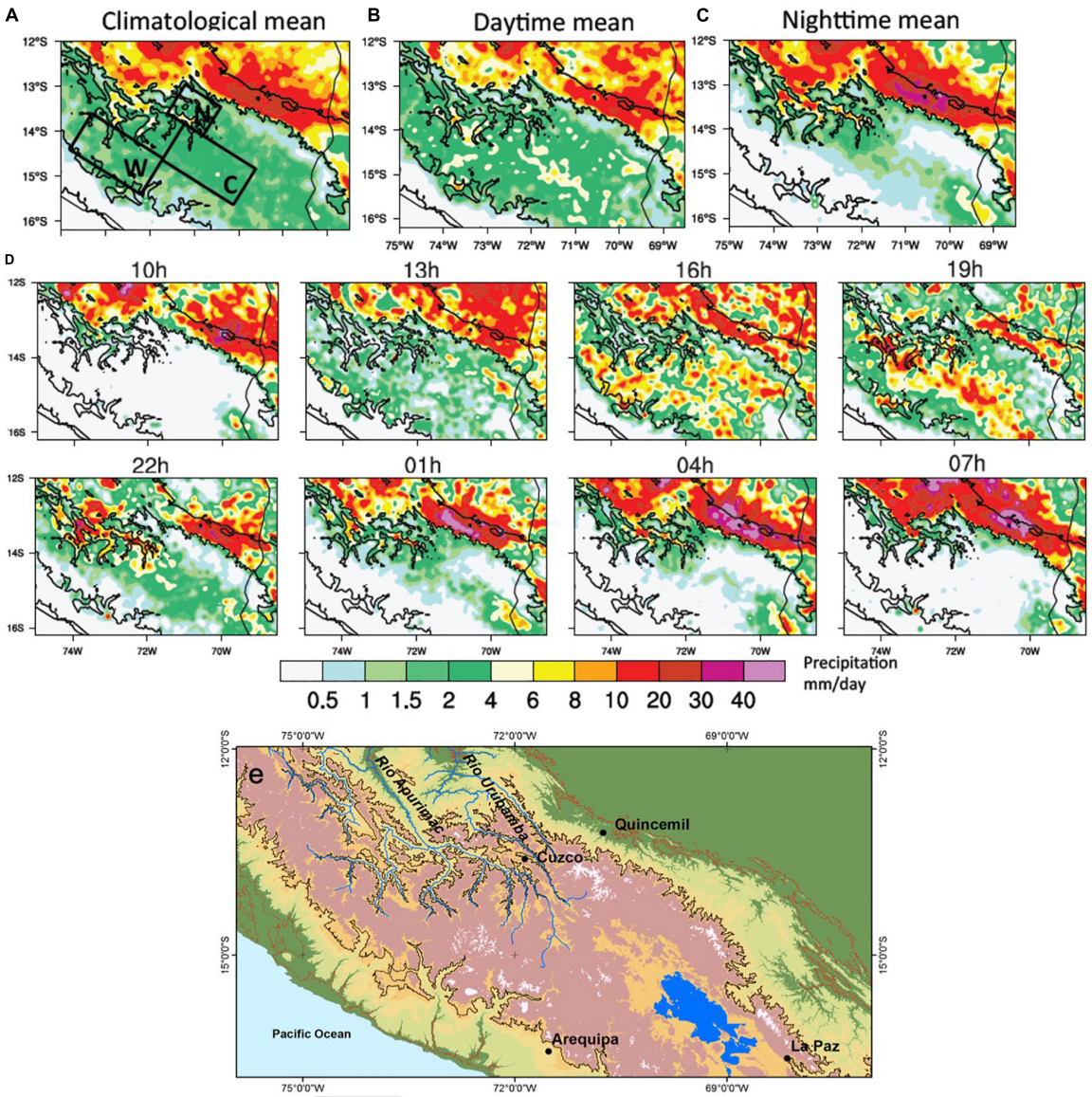


FIGURE 9 | Mean December-February precipitation estimated by the precipitation radar of the Tropical Rainfall Measuring Mission (TRMM-2A25) for the 2000–2014 period (mm/day) in the Peruvian Andes (Cuzco region), corresponding to **(a)** all times step mean, **(b)** daytime mean [7–19 h Local Time (LT)], **(c)** nighttime mean (19–7 h LT), **(d)** 3 h times-step mean. Bold black contours show 500 and 3500 m orography limits. The black boxes indicated in **(a)** define the West (W), Center (C), and North (N) boxes. In **(d)**, the indicated time-step titles are 10 h (7–10 h mean), 13 h (10–13 h mean), 16 h (13–16 h mean), 19 h (16–19 h mean), 22 h (19–22 h mean), 1 h (22–1 h mean), 4 h (1–4 h mean), 7 h (4–7 h mean). In **(e)** the location of the main cities and rivers are indicated. Source: Junquas et al. (2018). © Climate Dynamics. Reprinted by permission from Springer Nature.

upslope flow development in both sides of the Andes (Garreaud, 1999; Garreaud et al., 2009). However, the diurnal cycle of convection and rainfall along the eastern piedmont of the south tropical Andes, one of the rainiest places along the cordillera, is out of phase with the diurnal cycle over the Andes, with maximum occurring at late night/dawn, related to the diurnal thermal valley/mountain circulations, which produce cold air descending downslope and convergence of low-level moisture in the piedmont (Killeen et al., 2007; Chavez and Takahashi, 2017; Junquas et al., 2018).

Further south, the western subtropical Andes have little convective activity during summer, but it is enhanced when rainfall occurs in the late afternoon (Viale and Garreaud, 2014). On the eastern side of the subtropical Andes, a clear summer diurnal cycle is present right at the foothills (Romatschke and Houze, 2013), which corresponds with one of the places with the most intense convection in the world (Zipser et al., 2006; Rasmussen et al., 2014; Liu and Zipser, 2015). Some of these convective systems propagate east characterizing their diurnal life cycle (Rasmussen et al., 2016). The winter rainfall over the

subtropical and extratropical Andes have no diurnal cycle given its frontal nature (Saavedra and Foppiano, 1992). Likewise, the annual cycle of rainfall from 35°S southward is relatively small although one can discern a preference for the austral winter months (Viale and Garreaud, 2015).

Annual Cycle of Precipitation

The latitudinal oscillation of the ITCZ is the principal modulator of the annual cycle of rainfall along the north tropical South America (Mejia et al., 1999; Hastenrath, 2002; Poveda et al., 2006; Killeen et al., 2007; Espinoza et al., 2009b; Alvarez-Villa et al., 2011; Sierra et al., 2015). Thus, the annual cycle of precipitation in western and central Colombia is mostly bimodal, exhibiting two wet seasons (MAM and SON), and two drier seasons (DJF and JJA) (Bendix and Lauer, 1992; Mejia et al., 1999; Ricaurte et al., 2019; **Figure 10**). On the other hand, the annual cycle of rainfall in the Caribbean region of Colombia, over the north tropical Andes (north of 8°S), is mostly unimodal, and thus it cannot be explained only by the ITCZ migration. In particular, precipitation over this region is influenced by the occurrence of synoptic disturbances associated to the African easterly waves and the Caribbean LLJ (Poveda et al., 2006; Arias et al., 2015; Giraldo-Cárdenas et al., 2017).

Over the equatorial Andes, the eastern slope is characterized by a unimodal rainfall annual cycle with maximum values in June–August (**Figures 11e,g**). This pattern is related to an intensification of the westward moisture advection from the equatorial Amazon basin and orographic uplift forced by the Andean topography (Bendix and Lauer, 1992; Rollenbeck and Bendix, 2011; Campozano et al., 2016). Two wet seasons are identified in the highest part of the equatorial Andes (e.g., Guaslán station in **Figure 11g**), corresponding to the February–April and the October–December seasons (Bendix and Lauer, 1992; Laraque et al., 2007; Espinoza et al., 2009b; Rollenbeck and Bendix, 2011; Campozano et al., 2016, 2018).

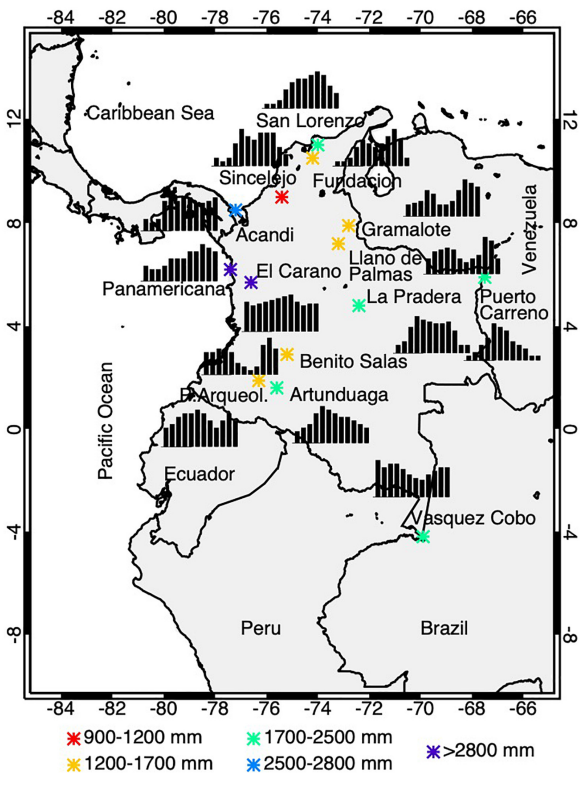


FIGURE 10 | Mean annual cycle of precipitation in different rain gauges over the north tropical Andes of Colombia (north of 8°S). Adapted from Ricaurte et al. (2019).

Over the south tropical Andes/Altiplano, where unimodal rainfall regime predominates (**Figure 11h**), the rainy season extends from November to March with its peak in January, when the establishment of the Bolivian High brings easterly, moist-laden winds from the interior of the continent (Garreaud, 1999). The rest of the year, the south tropical Andes are dominated by westerly flow that brings dry air from the mid-level troposphere over the southeast Pacific (**Figures 11a–d**). In an early study (Garreaud and Wallace, 1998), the frequency of cold clouds was used as a proxy of convection, but more recent climatologists have considered surface rain data, satellite/radar data and more recently lightning data (e.g., Giovannettone and Barros, 2009; Chavez and Takahashi, 2017; Junquas et al., 2018; Kumar et al., 2019).

In a recent study, Segura et al. (2019) identify three zones over the tropical Andes in relation to seasonal rainfall regime using the Climate Hazards group Infrared Precipitation with Stations (CHIRPS) monthly data (**Figures 11h,i**): the equatorial Andes (EA; 5°S-1°N), the transition zone (TZ; 8°S–5°S) and the southern tropical Andes (STA, 20°S–8°S). For this purpose, the maximum spectral precipitation value between 10 and 16.67 months is defined as the unimodal index (PSD12) and the value between 5 and 8 months as the bimodal index (PSD6). Thus, the unimodal and bimodal indices allow us to estimate the relative difference between the unimodal and bimodal regime (PSD12-6, see Equation 3 in Segura et al., 2019). The EA and the TZ are characterized by a same wet season in the February–April period, associated with the seasonal variations of the ITCZ and the Walker cell (i.e., southerly displacement of the ITCZ and the weakened Walker Cell during this season). In addition, strong westward moisture transport from the equatorial Amazon is observed during the October–November wet season in the TZ.

Atop and over the western side of the subtropical and extratropical Andes most of the rainfall is produced by frontal systems in winter crossing the continent (Saavedra and Foppiano, 1992), especially fronts associated with atmospheric rivers (Viale et al., 2018). The fronts are rooted in extratropical cyclones that drift in the westerly wind belt and the collocated storm track. These two features of the general circulation remain between 45 and 55°S year round, producing a precipitation annual cycle of low seasonality over the extratropical Andes. Yet, the meridional displacement of the upper-level jet stream does favor more precipitation during the austral winter (JJA) over the subtropical Andes, causing the wet season in central-southern Chile (Rutllant and Fuenzalida, 1991; Viale and Garreaud, 2015; Viale et al., 2019, **Figure 12**). The mean annual precipitation has a strong latitudinal gradient between 25 and

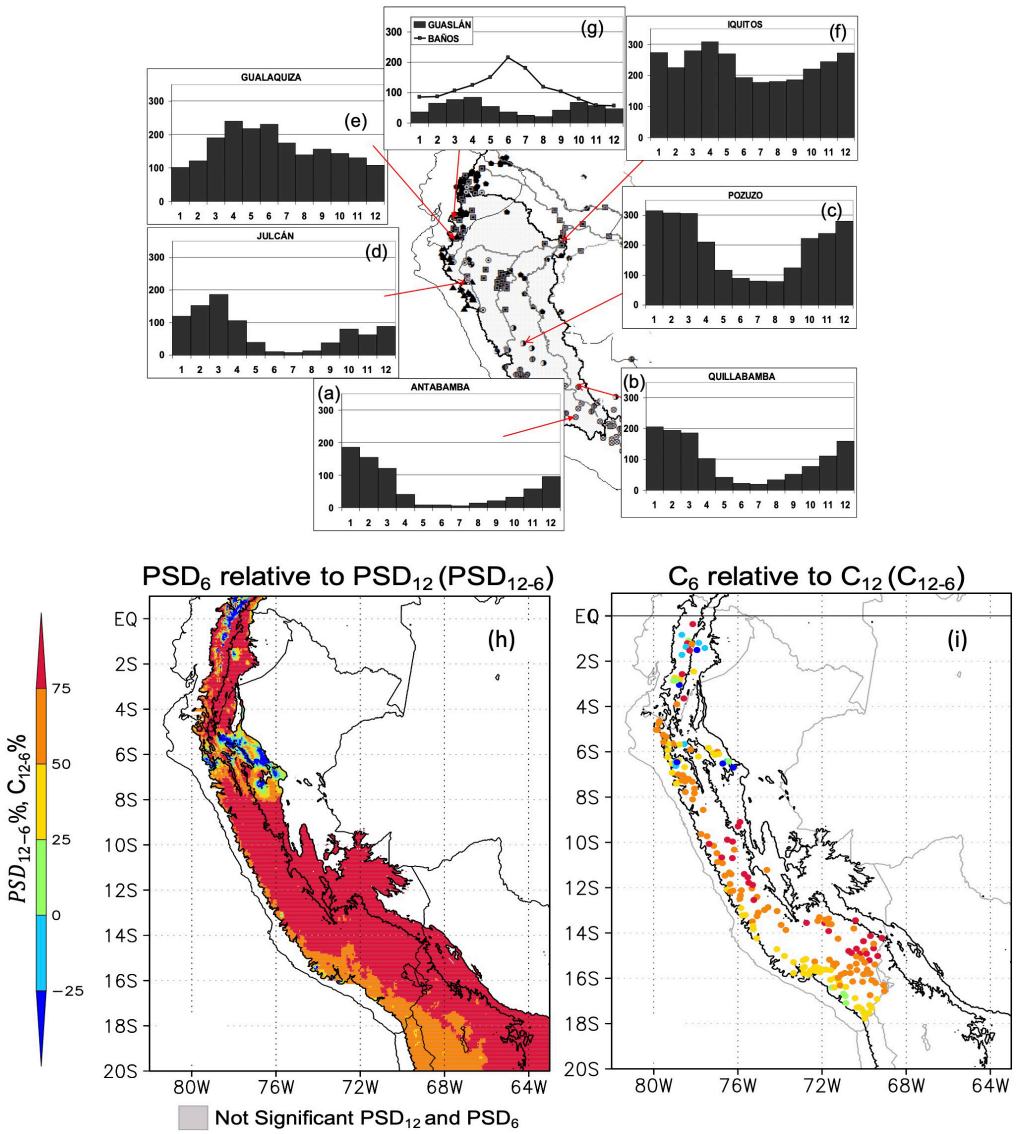


FIGURE 11 | (a–g) Rainfall regimes in eight stations in the south tropical Andes-Amazon region. Adapted from: Espinoza et al. (2009b). © International Journal of Climatology. Reprinted by permission from John Wiley and Sons. **(h)** Relative difference (PSD12-6; shaded) between the maximum spectral value of monthly precipitation from 10 to 16.67 months (defined as the power spectrum density-PSD12-unimodal index) and the maximum spectral value between 5 and 8 months (defined as the PSD6 bimodal index). PSD12 and PSD6 are computed using Equation 3 in Segura et al. (2019) and CHIRPS data set. **(i)** Relative difference between the harmonic of 12 months and the harmonic of 6 month (C12-C6) estimated by using in situ precipitation of 206 rain-gauge stations located in Peru and Ecuador and Equation 6 from Segura et al. (2019). Topography contours of the altitude of 350 and 2000 m.a.s.l are plotted in black solid lines. Source: Segura et al. (2019). © Climate Dynamics. Reprinted by permission from Springer Nature.

40°S (Falvey and Garreaud, 2007; Garreaud, 2009). In Santiago (Chile), at 33°S just west of the Andes, more than 80% of the annual rainfall is concentrated between May and September. On the contrary, the eastern slopes of the subtropical Andes receive most of the precipitation in the austral summer due to convective activity over western Argentina (Viale et al., 2019). South of 40°S, the annual cycle of precipitation over the austral Andes exhibits a low seasonality and it is rather similar between the western and eastern slopes, despite the large difference in precipitation totals at each side of the mountain range (Viale et al., 2019; **Figure 12**).

SUMMARY AND OPEN RESEARCH QUESTIONS

Sustainable development in the Andes is currently menaced by multiscale changes, which affect its climate and water resources from glaciers retreat to ecosystem services and water supply for about 90 million people. Under this context, is crucial to improve our understanding about large-scale controls of the Andes hydroclimate and its interactions with regional and local processes, and therefore enable adaptation to high impacts events

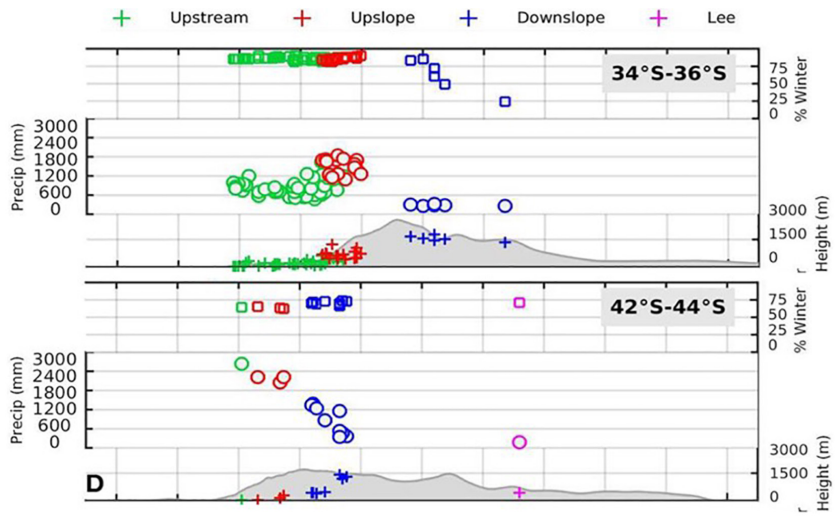


FIGURE 12 | Mean annual precipitation in different rain gauges of the Andes at subtropical (35°S) and extratropical (43°S) latitudes. In both cases, the figure is a west-east cross section including topography (gray shaded), annual mean precipitation (circles) in rain gauges (crosses). The boxes at the top indicate the fraction of precipitation that falls in austral winter (April–September). Adapted from Viale et al. (2019).

related to climate variability and climate change. This manuscript presents a review of the recent progress in the understanding of the Andes hydroclimate based on a unified overview from southern Patagonia to the northern part of the Andes in South America. This section is dedicated to summarizing the most relevant issues stated in the manuscript and the associated research gaps. Two major topics have been summarized in Part I of this paper:

(i) *The mean large-scale atmospheric circulation that characterizes the hydroclimate of the Andes*

Over the Andes, the mid- and upper-level circulation is mostly zonal, with westerly flow southward of 25°S and easterly flow at low latitudes. However, during the austral winter, mid-level westerlies reach around 10°S and the upper-level jet stream is located over the subtropical Andes (27–37°S). At low latitudes (north of 5°S), trans-Andean flows are predominant all year around, producing a complex rainfall regime over this region (north of Peru, Ecuador and Colombia). During the austral summer, when the mature phase of the South American Monsoon System (SAMS) occurs, the mountains of the south tropical Andes (8–27°S) act as a topographic barrier for the warm and moist flux from the Amazonian region. These flows are crucial for moisture advection to the tropical Andes; however, studies suggest that environmental change (e.g., land use change) in the south and southeastern Amazon basin has reduced its capacity to regulate low flows. Further observational and modeling analysis are necessary to improve our understanding of biosphere-atmosphere interactions involving Amazon rainforest and water cycle in the Andes.

Low-level jets (LLJs) are distinctly observed at both sides of the Andes and at different ranges of latitude, which are induced by mechanical blocking of impinging flow and/or diabatic heating in the mountain slopes. At the western side of the Andes, the Chilean and Peruvian LLJ blows equatorward along the subtropical Andes (27–37°S) over the dry Pacific coast of central-northern Chile and Peru, while a LLJ blows poleward along the extratropical Andes (south of 37°S) due to blocking effect of the barrier on low-level winds associated with frontal precipitation system. Some climatological studies (Falvey and Garreaud, 2007; Viale and Garreaud, 2015) suggested that the blocking effect of the extratropical Andes largely modulate precipitation over the Andes and adjacent low lands, but their physical mechanisms are still little understood and deserve further research in future. At the north tropical Andes (north of 8°S), the Chocó LLJ is a singular southwesterly circulation feature acting over the easternmost tropical Pacific and is enhanced by atmosphere-ocean-land surface interactions over the Pacific coast of Colombia. At the northern part of the eastern flank of the Andes, the so-called *Corriente de los Andes Orientales* (CAO), Llanos jet, Orinoco jet, or Eastern Andes Jet circulates from the Tropical North Atlantic through Guyana and eastern Venezuela reaching the northernmost leg of the South American low-level jet (SALLJ). The SALLJ blows poleward over regions of Bolivia, Paraguay, Southern Brazil, Uruguay and Argentina, where it delivers vast quantities of moisture originated in the Atlantic or over the Amazon basin, feeding severe weather well into subtropical latitudes. From reanalysis data, the SALLJ intensity, frequency (Jones, 2019), and moisture flux (Montini et al., 2019) have shown an increase in the last decades in most of the seasons, affecting precipitation in the eastern Andes. Further studies are needed to understand how these changes will be projected in a warmer climate, which will require improvements in global models to better representing the low-level circulation in the region (Barros and Doyle, 2018). In addition, interactions between large-scale atmospheric features (Intertropical Convergence Zone (ITCZ), SAMS, Bolivian High,

Hadley, and Walker cell, etc.), LLJs in South America, biosphere-atmosphere exchanges and atmospheric mechanisms related to local rainfall in the Andes remain little understood. Modeling and observational initiatives on multiscale atmospheric interactions deserve further attention in future research, including both land cover changes and climate change.

(ii) *The regular cycles of precipitation (diurnal and annual cycles)*

The above-mentioned large-scale atmospheric mechanisms, the latitudinal migration of the ITCZ, the westerlies, the complex Andean orography, as well as local circulations and temperature gradients, are the main factors that explain regular cycles of precipitation over the Andes. The annual cycle of precipitation in the western and central Colombian Andes is mostly bimodal, exhibiting two wet (drier) seasons in March–April–May and September–October–November [December–January–February and June–July–August (JJA)]. On the other hand, the annual cycle of rainfall in the eastern and northern Colombian Andes, is mostly unimodal, and thus cannot be explained only by the ITCZ migration but also by the synoptic activity related to the easterly waves over the Atlantic Ocean. Over the equatorial Andes, a unimodal regime with a peak in the JJA period is associated with the intensification of the westward moisture transport from the equatorial Amazon and a forced orographic uplift. However, over the high altitudes, two wet periods are observed in February–April and in October–December, in relation to the latitudinal migration of the ITCZ. However, what determines that the bimodality of the annual cycle is limited to the Andean region of Colombia, Ecuador and northern Peru deserves clarifications in future studies (Ricaurte et al., 2019; Segura et al., 2019). Over the south tropical Andes (8–27°S), the rainy season extends from November to March, when the establishment of the Bolivian High brings easterly, moist-laden winds from the interior of the continent. Dry conditions are observed the rest of the year. Over the western side of the Andes, south of 25°S, most of the rainfall is produced by frontal systems crossing the continent. The meridional displacement of the upper-level jet stream does favor more precipitation during the austral winter (JJA) over the subtropical Andes (27–37°S) causing the wet season in central-southern Chile and central-western Argentina. By the contrary, the eastern slopes of the subtropical Andes receive most of the precipitation in the austral summer due to convective activity over western Argentina. This region is part of today's active research (Seneviratne and Stephens, 2014), as several aspects of the multiscale nature of convection and its impact in the hydrology are not well understood (Varble et al., 2017). The better understanding of how convection initiates, the efficient generation of hail and its propagation, would help to improve forecasting in the Andean region. South of 40°S, the annual cycle is gradually reduced poleward and rather similar between the western and eastern slopes of the Andes, due to the nature of precipitation is not convective and midlatitude frontal precipitation within the westerly circulation and the storm tracks dominate there. Further work is also needed to evaluate how the annual cycle of precipitation (rainfall and snowfall) will change in a warmer climate at different latitudinal and altitudinal ranges of the Andes cordillera. If more model simulations are available, an assessment on the main changes on the annual cycle characteristics would give insights on the impact and tools to evaluate adaptation for sustainable development.

The very high spatial variability of the diurnal cycle of precipitation along the Andes is the result of the interplay among large-scale and local circulation patterns and the complex Andean orography. In particular, diurnal cycles associated to local circulation features in the tropical Andes have been poorly studied (e.g., diurnal thermally driven circulations related to the topography and propagation of off coast convective rainfall). One of the rainiest spots in the World (in Colombia) has been recently center of a field experiment performed to study diverse aspects of the Choco Jet and its effect in convection (Mejia and Poveda, 2005; Yepes et al., 2019). This unique observational data will help to characterize the variability of the diurnal cycle of precipitation and wind circulations in the mesoscale, and the dominant mechanisms of westerly propagation of convection offshore (Yepes et al., submitted). Furthermore, the diurnal cycle of local circulations over the eastern and western Andean slopes are especially interesting as they can be related to the strong precipitation spatial variability and gradients that occur in many Andean valleys, which usually are not identified by the meteorological networks and satellite data. This results in a poor estimation of the precipitation and large residuals (usually negatives) in water balances, even for big Andean basins (Espinoza et al., 2015; Builes-Jaramillo and Poveda, 2018). This research topic could be addressed with the help of high-resolution (both spatial and temporal) climate models that use the relatively scarce sub-daily meteorological data available (e.g., Junquas et al., 2018; Kumar et al., 2019; Saavedra et al., 2020).

Regarding the high relevance of meteorological data in regions of complex topography such as the Andes, recent progress in hydroclimate data in the Andes is reviewed in a specific study by Condom et al. (unpublished), submitted to this special issue ("Connecting Mountain Hydroclimate Through the American Cordilleras").

Due to this strong interdependence, the Amazon-Andes connectivity (**Figures 3**, **4**) represents a specific challenge for the scientific community, which is particularly important in a climate change context and amidst the intensification of seasonal extreme floods and droughts in Amazonia (Gloor et al., 2013; Marengo and Espinoza, 2016; Barichivich et al., 2018; Espinoza et al., 2018; Wang et al., 2018; Haghtalab et al., submitted), including changes in the land surface, related to climate and human forcing activity (Nobre et al., 2016; Aragão et al., 2018; Aide et al., 2019). Thus, changes in Amazon water cycle could locally affect diurnal and annual cycles of precipitation in the Andes (e.g., Segura et al., 2020), including the hydroclimatological functioning of the glaciers, *paramos*, *punas*, cloud montane forests, rainforests, dry forests and deserts. Considering that the annual cycle of precipitation and evapotranspiration is an important research topic for the Andes economical activities, it is crucial to better identify atmospheric mechanisms involving

Amazon-Andes connectivity in terms of evapotranspiration, moisture transport and local convection.

In Part II of this manuscript, which is also included in this special issue, we review the hydroclimate variability of the Andes at the sub-continental scale, including the effects of El Niño-Southern Oscillation.

AUTHOR CONTRIBUTIONS

All authors contributed to the conception, discussion, and refinement of this manuscript.

FUNDING

This review manuscript has been achieved as part of the ANDEX program (www.gewex.org/project/andex/), which is a prospective Regional Hydroclimate Project (RHP) of the GEWEX Hydroclimatology Panel (GHP). JE was supported by the French AMANECER-MOPGA project funded by ANR and IRD (ref. ANR-18-MPGA-0008). PA was supported by the Universidad de Antioquia through the Grant CODI PRG2017-16264. LS would like to acknowledge the financial support from Tri-agency Institutional Programs Secretariat of Canada through the Global Water Futures Program, Canada First Research Excellence Fund. MM was supported by the Consejo Nacional de Investigaciones Científicas y Técnicas (CONICET), Argentina. MV was supported by FONDECYT 11151009 and FONCYT PICT2016-1666. Finally, this article has the support of UNESCO's Intergovernmental Hydrological Programme through the Working Group Hydrogeomorphology of the Andes-Amazon Basin in which participate PA, JE, GP, and JM-C. The views presented in this paper are those of the authors and do not compromise the Working Group or UNESCO in any way.

REFERENCES

Adler, R. F., Huffman, G. J., Bolvin, D. T., Curtis, S., and Nelkin, E. J. (2000). Tropical rainfall distributions determined using TRMM combined with other satellite and rain gauge information. *J. Appl. Meteorol.* 39, 2007–2023. doi: 10.1175/1520-0450(2001)040<2007:trddut>2.0.co;2

Aide, T. M., Grau, H. R., Graesser, J., Andrade-Nunez, M. J., Araoz, E., and Barros, A. P. (2019). Woody vegetation dynamics in the tropical and subtropical Andes from 2001 to 2014: satellite image interpretation and expert validation. *Glob. Change Biol.* 5, 2112–2126. doi: 10.1111/gcb.14618

Alvarez-Villa, O. D., Vélez, J. I., and Poveda, G. (2011). Improved long-term mean annual rainfall fields for Colombia. *Int. J. Climatol.* 31, 2194–2212. doi: 10.1002/joc.2232

Aragão, L. E. O., Anderson, L. O., Fonseca, M. G., Rosan, T. M., Vedovato, L. B., and Wagner, F. H. (2018). 21st Century drought-related fires counteract the decline of Amazon deforestation carbon emissions. *Nat. Commun.* 9:536. doi: 10.1038/s41467-017-02771-y

Arias, P. A., Martínez, J. A., and Vieira, S. C. (2015). Moisture sources to the 2010-2012 anomalous wet season in northern South America. *Clim. Dyn.* 45, 2861–2884. doi: 10.1007/s00382-015-2511-7

Armijos, E., Crave, A., Vauchel, P., Fraizy, P., Santini, W., Moquet, J. S., et al. (2013). Suspended sediment dynamics in the Amazon River of Peru. *J. South Am. Earth Sci.* 44, 75–84. doi: 10.1073/pnas.1907842116

Ayes-Rivera, I., Armijos Cardenas, E., Espinoza-Villar, R., Espinoza, J. C., Molina-Carpio, J., Ayala, J. M., et al. (2019). Decline of fine suspended sediments in the madeira river basin (2003–2017). *Water* 11:514. doi: 10.3390/w11030514

Barichivich, J., Gloor, E., Peylin, P., Brienen, R. J. W., Schönegartn, J., Espinozan, J. C., et al. (2018). Recent intensification of Amazon flooding extremes driven by strengthened Walker circulation. *Sci. Adv.* 4:eaat8785. doi: 10.1126/sciadv.aat8785

Barros, V., Gonzalez, M., Liebmann, B., and Camilloni, I. (2000). Influence of the South Atlantic convergence zone and South Atlantic Sea surface temperature on interannual summer rainfall variability in Southeastern South America. *Theor. Appl. Climatol.* 67, 123–133. doi: 10.1007/s007040070002

Barros, V. R., and Doyle, M. E. (2018). Low-level circulation and precipitation simulated by CMIP5 GCMS over southeastern South America. *Int. J. Climatol.* 38, 5476–5490. doi: 10.1002/joc.5740

Bendix, J., and Lauer, W. (1992). Die Niederschlagsjahreszeiten in Ecuador undihre klimadynamische Interpretation (Rainy Seasons in Ecuador and Their Climate-Dynamic Interpretation). *Erdkunde* 2, 118–134.

Bengtsson, L., Hodges, K. I., and Roeckner, E. (2006). Storm tracks and climate change. *J. Clim.* 19, 3518–3543. doi: 10.1175/jcli3815.1

Berbery, E. H., and Barros, V. (2002). The hydrologic cycle of the La Plata basin in South America. *J. Hydrometeorol.* 3, 630–645. doi: 10.1175/1525-7541(2002)003<0630:thcotl>2.0.co;2

Berbery, E. H., and Vera, C. (1996). Characteristics of the Southern Hemisphere Winter Storm Track with Filtered and Unfiltered Data. *J. Atmos. Sci.* 53, 468–481. doi: 10.1175/1520-0469(1996)053<0468:cotshw>2.0.co;2

Boisier, J. P., Alvarez-Garreton, C., Cordero, R. R., Damian, A., Gallardo, L., Garreaud, R. D., et al. (2018)). Anthropogenic drying in Central-Southern Chile evidenced by long term observations and climate model simulations. *Elem. Sci. Anthropocene* 6:74. doi: 10.1525/elementa.328

Bouchez, J., Moquet, J. S., Espinoza, J. C., Martinez, J. M., Guyot, J. L., Lagane, C., et al. (2017). River mixing in the Amazon as a driver of concentration discharge relationships. *Water Resour. Res.* 53, 8660–8685. doi: 10.1002/2017WR020591

Builes-Jaramillo, L. A., and Poveda, G. (2018). Conjoint analysis of surface and atmospheric water balances in the Andes-Amazon system. *Water Resour. Res.* 54, 3472–3489. doi: 10.1029/2017WR021338

Byerle, L. A., and Peagle, J. (2002). Description of the seasonal cycle of low-level flows flanking the Andes and their interannual variability. *Meteorologica* 27, 71–88.

Campetella, C. M., and Vera, C. (2002). The influence of the Andes mountains on the South American low-level flow. *Geophys. Res. Lett.* 29:1826. doi: 10.1029/2002GL015451

Campozano, L., Célleri, R., Trachte, K., Bendix, J., and Samaniego, E. (2016). Rainfall and cloud dynamics in the Andes: a Southern Ecuador case study. *Adv. Meteorol.* 2016:3192765.

Campozano, L., Trachte, K., Célleri, R., Samaniego, E., Bendix, J., Albuja, C., et al. (2018). Climatology and teleconnections of mesoscale convective systems in an Andean basin in southern Ecuador: the case of the Paute basin. *Adv. Meteorol.* 2018, 1–13. doi: 10.1155/2018/4259191

Carvalho, L. M., Silva, A. E., Jones, C., Liebmann, B., Dias, P. L. S., and Rocha, H. R. (2011). Moisture transport and intraseasonal variability in the South America monsoon system. *Clim. Dyn.* 36, 1865–1880. doi: 10.1007/s00382-010-0806-2

Chang, E. K. M., Guo, Y., and Xia, X. (2012). CMIP5 multimodel ensemble projection of storm track change under global warming. *J. Geophys. Res.* 117:D23118. doi: 10.1029/2012JD018578

Chavez, S. P., and Takahashi, K. (2017). Orographic rainfall hotspots in the Andes-Amazon transition according to the TRMM precipitation radar and in situ data. *J. Geophys. Res.* 122, 5870–5882. doi: 10.1002/2016JD026282

Debortoli, N. S., Dubreuil, V., Funatsu, B., Delahaye, F., Henke de Oliveira, C., Rodrigues-Filho, S., et al. (2015). Rainfall patterns in the Southern Amazon: a chronological perspective (1971– 2010). *Clim. Change* 132, 251–264. doi: 10.1007/s10584-015-1415-1

Díaz, A., and Aceituno, P. (2003). Atmospheric circulation anomalies during episodes of enhanced and reduced convective cloudiness over Uruguay. *J. Clim.* 16, 3171–3185. doi: 10.1175/1520-0442(2003)016<3171:acadeo>2.0.co;2

Durán-Quesada, A. M., Gimeno, L., Amador, J. A., and Nieto, R. (2010). Moisture sources for Central America: Identification of moisture sources using

a Lagrangian analysis technique. *J. Geophys. Res.* 115:D05103. doi: 10.1029/2009JD012455

Espinoza, J. C., Chavez, S., Ronchail, J., Junquas, C., Takahashi, K., and Lavado, W. (2015). Rainfall hotspots over the southern tropical Andes: spatial distribution, rainfall intensity and relations with largescale atmospheric circulation. *Water Resour. Res.* 51, 3459–3475. doi: 10.1002/2014wr016273

Espinoza, J. C., Marengo, J. A., Ronchail, J., Molina, J., Noriega, L., and Guyot, J. L. (2014). The extreme 2014 flood in south-western Amazon basin: the role of tropical-subtropical south Atlantic SST gradient. *Environm. Res. Lett.* 9:124007. doi: 10.1088/1748-9326/9/12/124007

Espinoza, J. C., Guyot, J. L., Ronchail, J., Cochonneau, G., Filizola, N., Fraizy, P., et al. (2009a). Contrasting regional discharge evolutions in the Amazon basin (1974-2004). *J. Hydrol.* 375, 297–311. doi: 10.1016/j.jhydrol.2009.03.004

Espinoza, J. C., Ronchail, J., Guyot, J. L., Cochonneau, G., Naziano, F., Lavado, W., et al. (2009b). Spatio-temporal rainfall variability in the Amazon basin countries (Brazil, Peru, Bolivia, Colombia, and Ecuador). *Int. J. Climatol.* 29, 1574–1594. doi: 10.1002/joc.1791

Espinoza, J. C., Ronchail, J., Marengo, J. A., and Segura, H. (2018). Contrasting North–South changes in Amazon wet-day and dry-day frequency and related atmospheric features (1981–2017). *Clim. Dyn.* 116, 1–18. doi: 10.1007/s00382-018-4462-2

Espinoza, J. C., Sörensson, A., Ronchail, J., Molina-Carpio, J., Segura, H., Gutierrez-Cori, O., et al. (2019). Regional hydro-climatic changes in the Southern Amazon Basin (Upper Madeira Basin) during the 1982–2017 period. *J. Hydrol. Reg. Stud.* 26:10063. doi: 10.1016/j.ejrh.2019.100637

Espinoza-Villar, R., Martinez, J. M., Armijos, E., Espinoza, J. C., Filizola, N., Dos Santos, A., et al. (2018). Spatio-temporal monitoring of suspendent sediment in Solimões River (2000–2014). *C. R. Geosci.* 350, 4–12. doi: 10.1016/j.crte.2017.05.001

Falvey, M., and Garreaud, R. D. (2005). Moisture variability over the South American Altiplano during the South American low level jetexperiment (SALLJEX) observing season. *J. Geophy. Res.* 110:D22105. doi: 10.1029/2005JD006152

Falvey, M., and Garreaud, R. (2007). Wintertime precipitation episodes in central Chile: associated meteorological conditions and orographic influences. *J. Hydrometeorol.* 8, 171–193. doi: 10.1175/JHM562.1

Figueroa, S. N., and Nobre, C. A. (1990). Precipitation distribution over central and western tropical South America. *Climanalise* 6, 36–40.

Figueroa, S. N., Satyamurty, P., and Da Silva Dias, P. L. (1995). Simulations of the summer circulation over the South American region with an Eta coordinate model. *J. Atmos. Sci.* 52, 1573–1584. doi: 10.1175/1520-0469(1995)052<1573:sotsco>2.0.co;2

Gan, M. A., Kousky, V. E., and Ropelewski, C. F. (2004). The South America monsoon circulation and its relationship to rainfall over west-central Brazil. *J. Clim.* 17, 47–66. doi: 10.1175/1520-0442(2004)017<0047:tsamca>2.0.co;2

Garreaud, R., Molina, A., and Farias, M. (2010). Andean uplift and Atacama Hyperaridity: a climate modeling perspective. *Earth Planet. Sci. Lett.* 292, 39–50. doi: 10.1016/j.epsl.2010.01.017

Garreaud, R., and Muñoz, R. (2005). The low-level jet off the subtropical west coast of South America: structure and variability. *Mon. Weather Rev.* 133, 2246–2261. doi: 10.1175/mwr2972.1

Garreaud, R., Vuille, M., and Clement, A. (2003). The climate of the Altiplano: observed current conditions and mechanisms of past changes. *Palaeogeogr. Palaeoclimatol. Palaeoecol.* 194, 5–22. doi: 10.1016/s0031-0182(03)00269-4

Garreaud, R., and Wallace, J. M. (1998). Summertime incursions of midlatitude air into subtropical and tropical South America. *Mon. Weather Rev.* 126, 2713–2733. doi: 10.1175/1520-0493(1998)126<2713:siomai>2.0.co;2

Garreaud, R. D. (1999). Multiscale analysis of the summertime precipitation over the Central Andes. *Mon. Weather Rev.* 127, 901–921. doi: 10.1175/1520-0493(1999)127<0901:maotsp>2.0.co;2

Garreaud, R. D. (2009). The Andes climate and weather. *Adv. Geosci.* 22, 3–11. doi: 10.5194/adgeo-22-3-2009

Garreaud, R. D. (2018). A plausible atmospheric trigger for the 2017 coastal El Niño. *Int. J. Climatol.* 38, 1296–1302.

Garreaud, R. D., and Aceituno, P. (2007). "Atmospheric circulation over South America: mean features and variability," in *The Physical Geography of South America*, eds T. Veblen, K. Young, and A. Orme (Oxford: Oxford University Press), 45–66.

Garreaud, R. D., Vuille, M., Compagnucci, R., and Marengo, J. (2009). Present-day South American climate. *Palaeogeogr. Palaeoclimatol. Palaeoecol.* 281, 180–195. doi: 10.1016/j.palaeo.2007.10.032

Gelaro, R., McCarty, W., Suárez, M. J., Todling, R., Molod, A., and Takacs, L. (2017). MERRA-2 overview: the Modern-Era retrospective analysis for research and applications, version 2 (MERRA-2). *J. Clim.* 30, 5419–5454. doi: 10.1175/JCLI-D-16-0758.1

Giovannettone, J. P., and Barros, A. P. (2009). Probing regional orographic controls of precipitation and cloudiness in the central Andes using satellite data. *J. Hydrometeorol.* 10, 167–182. doi: 10.1175/2008jhm973.1

Giraldo-Cárdenas, S., Arias, P. A., and Vieira, S. C. (2017). "The African Easterly Waves over Northern South America," in *Proceedings of the 2nd International Electronic Conference on Atmospheric Sciences,* Vol. 1, Basel, 165. doi: 10.3390/ecas2017-04151

Gloor, M., Brienen, R. J. W., Galbraithm, D., Feldpauschm, T. R., Schöngartm, J., Guyotm, J. L., et al. (2013). Intensification of the Amazon hydrological cycle over the last two decades. *Geophys. Res. Lett.* 40, 1–5. doi: 10.1002/grl.50377

Gutman, G., and Schwerdtfeger, W. (1965). The role of latent and sensible heat for the development of a high pressure system over the subtropical Andes in the summer. *Meteorol. Rund.* 18, 69–75.

Guyot, J.-L., Bazan, H., Fraizy, P., Ordonez, J. J., Armijos, E., and Laraque, A. (2007). "Suspended sediment yields in the Amazon basin of Peru: a first estimation," in *Water Quality and Sediment Behaviour of the Future: Predictions for the 21st Century*, eds B. W. Webb, and D. De Boer (Wallingford: AISH), 3–10.

Hastenrath, S. (2002). The Intertropical Convergence Zone of the eastern Pacific revisited. *Int. J. Climatol.* 22, 347–356. doi: 10.1002/joc.739

Holton, J. (2002). *An Introduction to Dynamic Meteorology*. San Diego, CA: Academic Press.

Hoorn, C., Wesseling, P., ter Steege, H., Bermudez, M. A., Mora, A., Sevink, J., et al. (2010). Amazonia through time: andean uplift, climate change, landscape evolution, and biodiversity. *Science* 330, 927–931. doi: 10.1126/science.1194585

Hoskins, B. J., and Hodges, K. I. (2005). A new perspective on Southern Hemisphere storm tracks. *J. Clim.* 18, 4108–4129. doi: 10.1175/jcli3570.1

Hoyos, F. I, Dominguez, J., Cañón-Barriga, J. A., Martínez, R., Nieto, L., Gimeno, et al. (2017). Moisture origin and transport processes in Colombia, northern South America. *Clim. Dyn.* 50, 971–990. doi: 10.1007/s00382-017-3653-6

Inatsu, M., and Hoskins, B. J. (2004). The zonal asymmetry of the Southern Hemisphere winter storm track. *J. Clim.* 17, 4882–4891.

Insel, N., Poulsen, C. J., and Ehlers, T. A. (2010). Influence of the Andes mountains on South American moisture transport, convection, and precipitation. *Clim. Dyn.* 35, 1477–1492. doi: 10.1007/s00382-009-0637-1

Jaramillo, L., Poveda, G., and Mejía, J. F. (2017). Mesoscale convective systems and other precipitation features over the tropical Americas and surrounding seas as seen by TRMM. *Intern. J. Climatol* 37, 380–397. doi: 10.1002/joc.5009

Jiang, Q., Doyle, J. D., Reinecke, A., Smith, R. B., and Eckermann, S. D. (2013). A modeling study of stratospheric waves over the Southern Andes and Drake Passage. *J. Atmos. Sci.* 70, 1668–1689. doi: 10.1175/JAS-D-12-0180.1

Jiménez-Sánchez, G., Markowski, P. M., Jewtoukoff, V., Young, G. S., and Stensrud, D. J. (2019). The Orinoco low-level jet: an investigation of its characteristics and evolution using the WRF model. *J. Geophys. Res. Atmos.* 124, 10696–10711. doi: 10.1029/2019JD030934

Johnson, A. M. (1976). "The climate of Peru, Bolivia and Ecuador," in *Climates of Central and South America, World Survey of Climatology*, Vol. 12, ed. W. Schwerdtfeger (Amsterdam: Elsevier), 147–218.

Jones, C. (2019). Recent changes in the South America low-level jet. *npj Clim. Atmos. Sci.* 2, 1–8. doi: 10.1038/s41612-019-0077-5

Junquas, C., Takahashi, K., Condom, T., Espinoza, J. C., Chavez, S., Sicart, J. E., et al. (2018). Understanding the influence of orography over the precipitation diurnal cycle and the associated atmospheric processes in the central Andes. *Clim. Dyn.* 50, 3995–4017. doi: 10.1007/s00382-017-3858-8

Killeen, T. J., Douglas, M., Consiglio, T., Jorgensen, P. M., and Mejía, J. (2007). Dry spots and wet spots in the Andean hotspot. *J. Biogeogr.* 34, 1357–1373. doi: 10.1111/j.1365-2699.2006.01682.x

King, M. J., Wheeler, M. C., and Lane, T. P. (2017). Mechanisms linking global 5-day waves to tropical convection. *J. Atmos. Sci.* 74:36793702. doi: 10.1175/JASD-17-0101.1

Kumar, S., Vidal, Y.-S., Moya-Álvarez, A. S., and Martínez-Castro, D. (2019). Effect of the surface wind flow and topography on precipitating cloud systems over the Andes and associated Amazon basin: GPM observations. *Atmos. Res.* 225, 193–208. doi: 10.1016/j.atmosres.2019.03.027

Laraque, A., Ronchail, J., Cochonneau, G., Pombosa, R., and Guyot, J. L. (2007). Heterogeneous distribution of rainfall and discharge regimes in the Ecuadorian Amazon basin. *J. Hydrometeorol.* 8, 1364–1381. doi: 10.1175/2007jhm784.1

Lavado-Casimiro, W., Labat, D., Ronchail, J., Espinoza, J. C., and Guyot, J. L. (2013). Trends in rainfall and temperature in the Peruvian Amazon-Andes basin over the last 40 years (1965-2007). *Hydrol. Processes* 41, 2944–2957. doi: 10.1002/hyp.9418

Leite-Filho, A. T., de Sousa Pontes, V. Y., and Costa, M. H. (2019). Effects of deforestation on the onset of the rainy season and the duration of dry spells in southern Amazonia. *J. Geophys. Res. Atmos.* 124, 5268–5281. doi: 10.1029/2018jd029537

Lenters, J.-D., and Cook, K.-H. (1997). On the origin of the Bolivian high and related circulation features of the South American climate. *J. Atmos. Sci.* 54, 656–677.

Liu, C., and Zipser, E. J. (2015). The global distribution of largest, deepest, and most intense precipitation systems. *Geophys. Res. Lett.* 42, 3591–3595. doi: 10.1002/2015gl063776

López, M. E., and Howell, W. E. (1967). Katabatic winds in the Equatorial Andes. *J. Atmos. Sci.* 24, 29–35. doi: 10.1175/1520-0469(1967)024<0029:kwitea>2.0.co;2

Lowman, E. L., and Barros, A. P. (2014). Investigating links between climate and orography in the central Andes: coupling erosion and precipitation using a physical-statistical model. *JGR Earth Surf.* 119, 1322–1353. doi: 10.1002/2013JF002940

Magrín, G. O., Marengo, J. A., Boulanger, J.-P., Buckeridge, M. S., Castellanos, E., Poveda, G., et al. (2014). "Central and South America," in *Climate Change 2014: Impacts, Adaptation, and Vulnerability. Part B: Regional Aspects. Contribution of Working Group II to the Fifth Assessment Report of the Intergovernmental Panel on Climate Change*, eds V. R. Barros, C. B. Field, D. J. Dokken, M. D. Mastrandrea, K. J. Mach, T. E. Bilir, et al. (Cambridge: Cambridge University Press), 1499–1566.

Mapes, B. E., Warner, T. T., Xu, M., and Negri, A. J. (2003). Diurnal patterns of rainfall in northwestern South America. Part I: Observations and context. *Mon. Weather Rev.* 131, 799–812. doi: 10.1175/1520-0493(2003)131<0799:dporin>2.0.co;2

Marengo, J. A., and Espinoza, J. C. (2016). Extreme seasonal droughts and floods in Amazonia: causes, trends and impacts. *Int. J. Climatol.* 36, 1033–1050. doi: 10.1002/joc.4420

Marengo, J. A., Liebmann, B., Grimm, A. M., Misra, V., Silva Dias, P. L. D., Cavalcanti, I. F. A., et al. (2012). Recent developments on the South American monsoon system. *Int. J. Climatol.* 32, 1–21.

Marengo, J. A., Soares, W. R., Saulo, C., and Nicolini, M. (2004). Climatology of the low-level jet east of the Andes as derived from NCEP-NCAR reanalyses: characteristics and temporal variability. *J. Clim.* 17, 2261–2280. doi: 10.1175/1520-0442(2004)017<2261:cotlje>2.0.co;2

Martinez, J. A., and Dominguez, F. (2014). Sources of Atmospheric Moisture for the La Plata River Basin. *J. Clim.* 27, 6737–6753. doi: 10.1175/JCLI-D-14-00022.1

McClain, M. E., and Naiman, R. J. (2008). Andean influences on the biogeochemistry and ecology of the Amazon river. *Bioscience* 58, 325–338. doi: 10.1641/b580408

Meisner, B. N., and Arkin, P. A. (1987). Spatial and annual variations in the diurnal cycle of large scale tropical convective cloudiness and precipitation. *Mon. Weather Rev.* 115, 2009–2030.

Mejia, J. F., Mesa, O., Poveda, G., and Velez, J. I. (1999). Distribución espacial y ciclos anual y semianual de la precipitación en Colombia. *Dyna* 127, 7–14.

Mejia, J. F., and Poveda, G. (2005). Atmospheric environments of mesoscale convective systems over Colombia during 1999 using TRMM radar and microwave products and NCEP/NCAR reanalysis [in Spanish]. *Rev. Acad. Colomb. Cienc.* 29:495514.

Molina, R., Salazar, J. F., Martínez, J. A., Villegas, J. C., and Arias, P. A. (2019). Exponential growth of precipitation along a "forest-fed moisture conveyor belt" above the Amazon. *J. Geophys. Res. Atmos.* 124, 2589–2599. doi: 10.1029/2018jd029534

Molina-Carpio, J., Espinoza, J. C., Coritza, E., Salcedo, F., Farfán, C., Mamani, L., et al. (2019). Climate and spatial variability of the humid upper Andes. *Ecol. Boliv.* 54, 40–56.

Molina-Carpio, J., Espinoza, J. C., Vauchel, P., Ronchail, J., Gutierrez, B., Guyot, J. L., et al. (2017). The hydroclimatology of the upper Madeira River basin: spatio-temporal variability and trends (1967-2013). *Hydrol. Sci. J.* 62, 911–927. doi: 10.1080/02626667.2016.1267861

Montini, T. L., Jones, C., and Carvalho, L. M. V. (2019). The South American Low-Level Jet: a new climatology, variability, and changes. *J. Geophys. Res. Atmos.* 124, 1200–1218. doi: 10.1029/2018jd029634

Montoya, G., Pelkowski, J., and Eslava, J. A. (2001). On the northeasterlies trade winds and the existence of a low-level jet along the eastern Andes piedemont [In Spanish]. *Rev. Acad. Colomb. Cienc.* 96, 363–370.

Moquet, J.-S., Crave, A., Viers, J., Selyer, P., Armijos, J., and Bourrel, L. (2011). Chemical weathering and atmospheric/soil CO_2 uptake in the Andean and Foreland Amazon basins. *Chem. Geol.* 287, 1–26. doi: 10.1016/j.chemgeo.2011.01.005

Moraes-Arraut, J., Nobre, C. A., Barbosa, H. M., Obregon, G., and Marengo, J. A. (2012). Aerial rivers and lakes: looking at large-scale moisture transport and its relation to Amazonia and to subtropical rainfall in South America. *J. Clim* 25, 543–556. doi: 10.1175/2011JCLI4189.1

Muñoz, R., and Garreaud, R. (2005). Dynamics of the low-level jet off the subtropical west coast of South America. *Mon. Weather Rev.* 133, 3661–3677. doi: 10.1175/mwr3074.1

Myers, N., Mittermeier, R. A., Mittermeier, C. G., da Fonseca, C. A. B., and Kent, J. (2000). Biodiversity hotspots for conservation priorities. *Nature* 403, 853–858. doi: 10.1038/35002501

Nobre, C. A., Sampaio, G., Borma, L. S., Castilla-rubio, J. C., Silva, J. S., and Cardoso, M. (2016). Land-use and climate change risks in the Amazon and the need of a novel sustainable development Paradigm. *Proc. Natl. Acad. Sci. U.S.A.* 113, 10759–10768. doi: 10.1073/pnas.1605516113

Nogués-Paegle, J., and Mo, K. (1997). Alternating Wet and Dry Conditions over South America during Summer. *Mon. Weather Rev.* 125, 279–291. doi: 10.1175/1520-0493(1997)125<0279:awadco>2.0.co;2

Ovando, A., Tomasella, J., Rodriguez, D. A., Martinez, J. M., Siqueira-Junior, J. L., Pinto, G. L. N., et al. (2016). Extreme flood events in the Bolivian Amazon wetlands. *J. Hydrol. Region. Stud.* 5, 293–308. doi: 10.1016/j.ejrh.2015.11.004

Pepin, E., Guyot, J.-L., Armijos, E., Bazan, H., Fraisy, P., Moquet, J. S., et al. (2013). Climatic control on eastern Andean denudation rates (Central cordillera from Ecuador to Bolivia). *J. South Am. Earth Sci.* 44, 85–93. doi: 10.1016/j.jsames.2012.12.010

Poveda, G., Jaramillo, L., and Vallejo, L. F. (2014). Seasonal precipitation patterns along pathways of South American low-level jets and aerial rivers. *Water Resour. Res.* 50, 98–118. doi: 10.1002/2013WR014087

Poveda, G., and Mesa, O. J. (1999). The CHOCO low-level jet and two others jets over Colombia: climatology and variability during ENSO [in Spanish]. *Rev. Acad. Colomb. Cienc.* 23, 517–528.

Poveda, G., and Mesa, O. J. (2000). On the existence of Lloró (the rainiest locality on Earth): enhanced ocean-atmosphere-land interaction by a low-level jet. *Geophys. Res. Lett.* 27, 1675–1678. doi: 10.1029/1999gl006091

Poveda, G., Mesa, O. J., Agudelo, P. A., Álvarez, J. F., Arias, P. A., Moreno, H. A., et al. (2002a). "Diagnóstico del ciclo diurno de precipitación en los Andes tropicales de Colombia," in *Proceedings of the Memorias XX Congreso Latinoamericano de Hidráulica, ISBN* 959-7160-17-X, Ciudad de La Habana.

Poveda, G., Mesa, O. J., Agudelo, P. A., Álvarez, J. F., Arias, P. A., Moreno, H. A., et al. (2002b). "Influencia del ENSO, oscilación Madden-Julian, ondas del este, huracanes y fases de la luna en el ciclo diurno de la precipitación en los Andes tropicales de Colombia," in *Proceedings of the Memorias XX Congreso Latinoamericano de Hidráulica, ISBN* 959-7160-17-X, Ciudad de La Habana.

Poveda, G., Mesa, O. J., Salazar, L. F., Arias, P. A., Moreno, H. A., Vieira, S. C., et al. (2005). Diurnal cycle of precipitation in the tropical Andes of Colombia. *Mon. Weather Rev.* 133, 228–240. doi: 10.1175/mwr-2853.1

Poveda, G., Mesa, O. J., Toro, V. G., Agudelo, P. A., Álvarez, J. F., Arias, P. A., et al. (2002c). "Diagnóstico del ciclo anual y efectos del ENSO sobre la intensidad máxima de lluvias de duración entre 1 y 24 horas en los Andes de Colombia," in *Proceedings of the Memorias XX Congreso Latinoamericano de Hidráulica, ISBN 959-7160-17-X*, Ciudad de La Habana.

Poveda, G., Moreno, H. A., Vieira, S. C., Agudelo, P., Arias, P. A., Salazar, L. F., et al. (2001). "Caracterización del ciclo diurno de la precipitación en los Andes tropicales de Colombia," in *Proceedings of the Memorias IX Congreso Latinoamericano e Ibérico de Meteorología*, Buenos Aires, 7–11.

Poveda, G., Waylen, P. R., and Pulwarty, R. (2006). Modern climate variability in northern South America and southern Mesoamerica. *Palaeogeogr. Palaeoclimatol. Palaeoecol.* 234, 3–27. doi: 10.1016/j.palaeo.2005.10.031

Rabatel, A., Francou, B., Soruco, A., Gomez, J., Cáceres, B., Ceballos, J. L., et al. (2013). Current state of glaciers in the tropical Andes: a multi-century perspective on glacier evolution and climate change. *Cryosphere* 7, 81–102. doi: 10.5194/tc-7-81-2013

Rangel, T. F., Edwards, N. R., Holden, P. B., Diniz-Filho, J. A. F., Gosling, W. D., and Coelho, M. T. P. (2018). Modeling the ecology and evolution of biodiversity: Biogeographical cradles, museums, and graves. *Science* 361:eaar5452. doi: 10.1126/science.aar5452

Rasmussen, K. L., Chaplin, M. M., Zuluaga, M. D., and Houze, R. A. (2016). Contribution of extreme convective storms to rainfall in South America. *J. Hydrometeorol.* 17, 353–367. doi: 10.1175/jhm-d-15-0067.1

Rasmussen, K. L., Zuluaga, M. D., and Houze, R. A. (2014). Severe convection and lightning in subtropical South America. *Geophys. Res. Lett.* 41, 7359–7366. doi: 10.1002/2014gl061767

Ricaurte, L. F., Patiño, J. E., and Junk, W. J. (2019). A classification system for Colombian wetlands: an essential step forward in open environmental policy-making. *Wetlands* 39, 971–990. doi: 10.1007/s13157-019-01149-8

Roche, M. A., and Fernandez Jáuregui, C. (1988). Water resources, salinity and salt yields of the rivers of the Bolivian Amazon. *J. Hydrol.* 101, 305–331. doi: 10.1016/0022-1694(88)90042-x

Rodriguez, D. A., Tomasella, J., and Linhares, C. (2018). Is the forest conversion to pasture affecting the hydrological response of Amazonian catchments? Signals in the Ji-Paraná Basin. *Hydrol. Processes* 24, 1254–1269. doi: 10.1002/hyp.7586

Rodwell, M. J., and Hoskins, B. J. (2001). Subtropical anticyclones and summer monsoons. *J. Clim.* 14, 3192–3211. doi: 10.1038/srep21346

Rollenbeck, R., and Bendix, J. (2011). Rainfall distribution in the Andes of southern Ecuador derived from blending weather radar data and meteorological field observations. *Atmos. Res.* 99, 277–289. doi: 10.1016/j.atmosres.2010.10.018

Romatschke, U., and Houze, R. A. (2013). Characteristics of precipitating convective systems accounting for the summer rainfall of tropical and subtropical South America. *J. Hydrometeorol.* 14, 25–46. doi: 10.1175/jhm-d-12-060.1

Ronchail, J., and Gallaire, R. (2006). ENSO and rainfall along the Zongo Valley (Bolivia) from the Altiplano to the Amazon Basin. *Int. J. Climatol.* 26, 1223–1236. doi: 10.1002/joc.1296

Rueda, D. C. (2014). Caracterización de la corriente en chorro de bajo nivel de los llanos orientales colombianos. Master's thesis, Universidad Nacional de Colombia, Bogotá.

Rueda, O. A., and Poveda, G. (2006). Variabilidad espacial y temporal del Chorro del Chocó y su efecto en la hidroclimatología del Pacífico Colombiano. *Meteorol. Colomb.* 10, 132–145.

Rutllant, J., and Fuenzalida, H. (1991). Synoptic aspects of the central Chile rainfall variability associated with the Southern Oscillation. *Int. J. Climatol* 11, 63–76. doi: 10.1002/joc.3370110105

Rutllant, J. A., and Garreaud, R. D. (2004). Episodes of strong flow down the western slope of the subtropical Andes. *Mon. Weather Rev.* 132, 611. doi: 10.1175/1520-0493(2004)132<0611:eosfdt>2.0.co;2

Saavedra, M., Junquas, C., Espinoza, J. C., and Silva, Y. (2020). Impacts of topography and land use change on the air surface temperature and precipitation over the central Peruvian Andes. *Atmos. Res.* 234:104711.

Saavedra, N., and Foppiano, A. J. (1992). Monthly mean pressure model for Chile. *Int. J. Climatol.* 12, 469–480. doi: 10.2196/10226

Sagredo, E., and Lowell, T. (2012). Climatology of Andean glaciers: a framework to understand glacier response to climate change. *Glob. Planet. Chang.* 86–87, 101–109. doi: 10.1016/j.gloplacha.2012.02.010

Sakamoto, M., Ambrizzi, T., and Poveda, G. (2011). Moisture sources and life cycle of convective systems over western Colombia. *Adv. Meteorol.* 2011:890759. doi: 10.1155/2011/890759

Salio, P., Nicolini, M., and Zipser, E. J. (2007). Mesoscale convective systems over southeastern South America and their relationship with the South American low-level jet. *Mon. Weather Rev.* 135, 1290–1309. doi: 10.1175/mwr3305.1

Santini, W., Martinez, J. M., Espinoza Villar, R., Cochonneau, G., Vauchel, P., Moquet, J. S., et al. (2014). "Sediment budget in the Ucayali River basin, an Andean tributary of the Amazon River," in *Sediment Dynamics from the Summit to the Sea*, ed. Y. J. Xu (Wallingford: AISH), 320–325. doi: 10.5194/piahs-367-320-2015

Schwerdtfeger, W. C. (1961). Stromings und Temperatufeld der freien Atmosphare uber den Andes. *Meteorol. Rund.* 14, 1–6.

Segura, H., Espinoza, J. C., Junquas, C., Lebel, T., Vuille, M., and Garreaud, R. (2020). Recent changes in the precipitation-driving processes over the southern tropical Andes/western Amazon. *Clim. Dyn.* doi: 10.1007/s00382-020-05132-6

Segura, H., Espinoza, J. C., Junquas, C., and Takahashi, K. (2016). Evidencing Decadal and Interdecadal Hydroclimatic Variability over the Central Andes. *Environ. Res. Lett.* 11:094016. doi: 10.1088/1748-9326/11/9/094016

Segura, H., Junquas, C., Espinoza, J. C., Vuille, M., Jauregui, Y. R., Rabatel, A., et al. (2019). New insights into the rainfall variability in the tropical Andes on seasonal and interannual time scales. *Clim. Dyn.* 53, 405–426. doi: 10.1007/s00382-018-4590-8

Seluchi, M. E., Saulo, A. C., NicoLini, M., and Satyamurthy, P. (2003). The northwestern Argentinean low: A study of two typical events. *Mon. Weather Rev.* 131, 2361–2378. doi: 10.1175/1520-0493(2003)131<2361:tnalas>2.0.co;2

Seneviratne, S. I., and Stephens, G. (2014). "7th International Scientific Conference on the Global Water and Energy Cycle," in *Proceedings of the Highlights of the 7th International GEWEX Conference and Pan-GEWEX Meeting 3*.

Sierra, J. P., Arias, P. A., and Vieira, S. C. (2015). Precipitation over Northern South America and Its Seasonal Variability as Simulated by the CMIP5 Models. *Adv. Meteorol.* 2015:634720.

Sierra, J. P., Arias, P. A., Vieira, S. C., and Agudelo, J. (2018). How well do CMIP5 models simulate the low-level jet in western Colombia? *Clim. Dyn.* 51, 2247–2265. doi: 10.1007/s00382-017-4010-5

Snow, J. W. (1976). "The climate of northern South America," in *Climates of Central and South America*, ed. W. Schwerdtfeger (Amsterdam: Elsevier), 295–403.

Sorí, R., Marengo, J., Nieto, R., Drumond, A., and Gimeno, L. (2017). "Drought and wet episodes in Amazonia: the role of atmospheric moisture transport," in *Proceedings of the 1st International Electronic Conference on Hydrological Cycle (CHyCle-2017)*, Basel.

Staal, A., Tuinenburg, O., Bosmans, J., and Dekker, S. C. (2018). Forest-rainfall cascades buffer against drought across the Amazon. *Nat. Clim. Chang.* 8, 539–543. doi: 10.1038/s41558-018-0177-y

Takahashi, K. (2012). Thermotidal and land-heating forcing of the diurnal cycle of oceanic surface winds in the eastern tropical Pacific. *Geophys. Res. Lett.* 39:L15809. doi: 10.1029/2011GL050692

Takahashi, K., and Battisti, D. (2007). Processes controlling the mean Tropical Pacific precipitation pattern. Part II: the SPCZ and the Southeast Pacific Dry Zone. *J. Clim.* 20, 5696–5706. doi: 10.1175/2007jcli1656.1

Torrealba, E. R., and Amador, J. A. (2010). La corriente en chorro de bajo nivel sobre los Llanos Venezolanos de Sur America. *Rev. Climatol.* 10, 1–20.

Varble, A., Steve, N., Paola, S., Edward, Z., Susan, V. D. H., and Greg, M. (2017). *Cloud, Aerosol and Complex Terrain Interactions (CACTI) Preliminary Science Plan*. Washington, DC: United States Department of Energy.

Vauchel, P., Santini, W., Guyot, J. L., Moquet, J. S., Martinez, J. M., and Espinoza, J. C. (2017). A reassessment of the suspended sediment load in the Madeira River Basin from the Andes of Peru and Bolivia to the Amazon River in Brazil, based on 10 years of data from the HYBAM monitoring programme. *J. Hydrol.* 553, 35–48. doi: 10.1016/j.jhydrol.2017.07.018

Velasco, I., and Fritsch, J. M. (1987). Mesoscale convective complexes in the Americas. *J. Geophys. Res.* 92, 9591–9613. doi: 10.1002/97811187820 71.ch7

Vera, C., Higgins, W., Amador, J., Ambrizzi, T., Garreaud, R., and Gochis, D. (2006). Toward a unified view of the American monsoon systems. *J. Clim.* 19, 4977–5000. doi: 10.1175/jcli3896.1

Vera, C. S., and Vigliarolo, P. K. (2000). A diagnostic study of cold-air outbreaks over South America. *Mon. Weather Rev.* 128, 3–24. doi: 10.1175/1520-0493(2000)128<0003:ADSOCA>2.0.CO;2

Viale, M., Bianchi, E., Cara, L., Ruiz, L. E., Villalba, R., and Pitte, P. (2019). Contrasting Climates at Both Sides of the Andes in Argentina and Chile. *Front. Environ. Sci.* 7:69. doi: 10.3389/fenvs.2019.00069

Viale, M., and Garreaud, R. (2015). Orographic effects of the subtropical and extratropical Andes on upwind precipitating clouds. *J. Geophys. Res. Atmos.* 120, 4962–4974. doi: 10.1002/2014jd023014

Viale, M., and Garreaud, R. D. (2014). Summer precipitation events over the western slopes of the subtropical Andes. *Mon. Weather Rev.* 142, 1074–1092. doi: 10.1175/mwr-d-13-00259.1

Viale, M., Valenzuela, R., Garreaud, R., and Ralph, F. M. (2018). Impacts of Atmospheric Rivers on Precipitation in Southern South America. *J. Hydrometeorol.* 19, 1671–1687. doi: 10.1111/gcb.14128

Virji, H. (1981). A preliminary study of summertime tropospheric circulation patterns over South America estimated from cloud winds. *Mon. Weather Rev.* 109, 599–610. doi: 10.1175/1520-0493(1981)109<0599:apsost>2.0.co;2

Vuille, M., Burns, S. J., Taylor, B. L., Cruz, F. W., Bird, B. W., Abbott, M. B., et al. (2012). A review of the South American monsoon history as recorded in stable isotopic proxies over the past two millennia. *Clim. Past* 8, 1309–1321. doi: 10.5194/cp-8-1309-2012

Vuille, M., Carey, M., Huggel, C., Buytaert, W., Rabatel, A., Jacobsen, D., et al. (2018). Rapid decline of snow and ice in the tropical Andes – impacts, uncertainties and challenges ahead. *Earth Rev.* 176, 195–213. doi: 10.1016/j.earscirev.2017.09.019

Wang, H., and Fu, R. (2002). Cross-equatorial flow and seasonal cycle of precipitation over South America. *J. Clim.* 15, 1591–1608. doi: 10.1175/1520-0442(2002)015<1591:cefasc>2.0.co;2

Wang, X.-Y., Li, X., Zhu, J., and Tanajura, C. (2018). The strengthening of Amazonian precipitation during the wet season driven by tropical sea surface temperature forcing. *Environ. Res. Lett.* 13:094015. doi: 10.1088/1748-9326/aadbb9

Warner, T. T., Mapes, B. E., and Xu, M. (2003). Diurnal patterns of rainfall in northwestern South America. Part II: Model simulations. *Mon. Weather Rev.* 131, 813–829. doi: 10.1175/1520-0493(2003)131<0813:dporin>2.0.co;2

Wongchuig-Correa, S., de Paiva, R. C. D., Espinoza, J. C., and Collischonn, W. (2017). Multi-decadal hydrological retrospective: case study of Amazon floods and droughts. *J. Hydrol.* 549, 667–684. doi: 10.1016/j.jhydrol.2017.04.019

Yepes, J., Poveda, G., Mejía, J. F., Moreno, L., and Rueda, C. (2019). CHOCO-JEX. A Research Experiment Focused on the Chocó Low-Level Jet over the Far Eastern Pacific and Western Colombia. *Bull. Am. Meteorol. Soc.* 100, 779–796. doi: 10.1175/bams-d-18-0045.1

Zemp, D. C., Schleussner, C. F., Barbosa, H. M., Hirota, M., Montade, V., Sampaio, G., et al. (2017). Self-amplified Amazon forest loss due to vegetation-atmosphere feedbacks. *Nat. Commun.* 8:14681. doi: 10.1038/ncomms14681

Zemp, D. C., Schleussner, C. F., Barbosa, H. M. J., van der Ent, R. J., Donges, J. F., Heink, J., et al. (2014). On the importance of cascading moisture recycling in South America. *Atmos. Chem. Phys.* 14, 13337–13359. doi: 10.5194/acp-14-13337-2014

Zhou, J., and Lau, K. M. (1998). Does a monsoon climate exist over South America? *J. Climate* 11, 1020–1040. doi: 10.1371/journal.pone.0199457

Zimmer, A., Meneses, R. I., Rabatel, A., Soruco, A., Dangles, O., and Anthelme, F. (2018). Time lag between glacial retreat and upward migration alters tropical alpine communities. *Perspect. Plant Ecol. Evol. Syst.* 30, 89–102. doi: 10.1016/j.ppees.2017.05.003

Zipser, E. J., Cecil, D. J., Liu, C., Nesbitt, S. W., and Yorty, D. P. (2006). Where are the most intense thunderstorms on Earth? *Bull. Am. Meteorol. Soc.* 87, 1057–1071. doi: 10.1038/ncomms12786

Zuluaga, M. D., and Houze, R. A. (2015). Extreme Convection of the Near-Equatorial Americas, Africa, and Adjoining Oceans as seen by TRMM. *Mon. Weather Rev.* 143, 298–316. doi: 10.1175/mwr-d-14-00109.1

Zuluaga, M. D., and Poveda, G. (2004). Diagnostics of mesoscale convective systems over Colombia and the eastern tropical Pacific during 1998-2002 [in Spanish]. *Av. Recur. Hidráulicos* 11, 145–160.

Conflict of Interest: The authors declare that the research was conducted in the absence of any commercial or financial relationships that could be construed as a potential conflict of interest.

Copyright © 2020 Espinoza, Garreaud, Poveda, Arias, Molina-Carpio, Masiokas, Viale and Scaff. This is an open-access article distributed under the terms of the Creative Commons Attribution License (CC BY). The use, distribution or reproduction in other forums is permitted, provided the original author(s) and the copyright owner(s) are credited and that the original publication in this journal is cited, in accordance with accepted academic practice. No use, distribution or reproduction is permitted which does not comply with these terms.

frontiers in Earth Science

REVIEW
published: 09 April 2020
doi: 10.3389/feart.2020.00092

Climatological and Hydrological Observations for the South American Andes: *In situ* Stations, Satellite, and Reanalysis Data Sets

Thomas Condom[1], Rodney Martínez[2], José Daniel Pabón[3], Felipe Costa[2], Luis Pineda[4], Juan Jose Nieto[2], Freddy López[2] and Marcos Villacis[5]*

[1] *Institut des Geosciences de l'Environnement – UMR 5001, IRD, CNRS, Université Grenoble Alpes, Grenoble, France,* [2] *Department of Climate Services, Centro Internacional para la Investigación del Fenómeno de El Niño, Guayaquil, Ecuador,* [3] *Department of Geography, Universidad Nacional de Colombia, Bogota, Colombia,* [4] *Escuela de Ciencias de la Tierra, Energía y Ambiente, Universidad Yachay Tech, Urcuquí, Ecuador,* [5] *Departamento de Ingeniería Civil y Ambiental, Escuela Politécnica Nacional, Quito, Ecuador*

OPEN ACCESS

Edited by:
Alfonso Fernandez, University of Concepcion, Chile

Reviewed by:
Oliver Meseguer-Ruiz, Universidad de Tarapacá, Chile
Eric Sproles, Montana State University, United States

***Correspondence:**
Thomas Condom
thomas.condom@ird.fr

Specialty section:
This article was submitted to Hydrosphere, a section of the journal Frontiers in Earth Science

Received: *31 October 2019*
Accepted: *17 March 2020*
Published: *09 April 2020*

Citation:
Condom T, Martínez R, Pabón JD, Costa F, Pineda L, Nieto JJ, López F and Villacis M (2020) Climatological and Hydrological Observations for the South American Andes: In situ Stations, Satellite, and Reanalysis Data Sets. Front. Earth Sci. 8:92. doi: 10.3389/feart.2020.00092

Modern hydrology relies on multiple sources of information combined with climatological, hydrological and glaciological data. These data can be collected through various sources such as private initiatives by companies, research programs, and both national and international organisms. They also vary by types, e.g., *in situ* measurements, satellite, reanalysis and simulated data. Recently the ANDEX research project, as a GEWEX regional program, was created to understand the processes related to the hydrological cycle and energy fluxes in the Andean region from Colombia to Patagonia. It is quite challenging to carry out this program given the complex orography and diversity of climates from tropical to sub-polar climates. This review article is a compilation of the various databases that are useful for hydrometeorological research in the South American Andes. The National Meteorological and Hydrological Services in Bolivia, Chile, Colombia, Ecuador, Peru, Venezuela and Argentina provide a large amount of data however the high-elevation areas are poorly instrumented and the number of stations varies greatly between the countries. National databases are only partially shared with the international bodies responsible for summarizing the existing data; this causes problems in term of data product assimilation. Across the entire continent, too few radiosondes are being used despite the fact that these data are crucial for validating and identifying problems in the atmospheric models. An increasing number of satellite data are available but it is difficult to assimilate them into the hydroclimatological models suited to the adjusted spatial and temporal resolutions. Specifically, for precipitation, we recommend merged products that account for the high spatial and temporal variability across the Andes. Finally, the international ANDEX program could be an excellent opportunity to increase the knowledge of the hydrological processes in the Andes.

Keywords: ANDEX program, South America, hydrology, climatology, mountain

INTRODUCTION

Modern hydrology relies on multiple sources of information given that, in recent decades, data availability has increased thereby contributing to a new paradigm with data intensive science (Butler, 2014; Chen and Wang, 2018). This study is related to the ANDEX a prospective Regional Hydrological Project (RHP) of the Global Energy and Water Cycle Experiment (GEWEX[1]) project of the World Climate Research Program (WCRP[2]). This RHP aims to understand the processes related to the hydrological cycle and energy fluxes in the Andean region that extends from Venezuela to Patagonia and cover a large range of climates from tropical to sub-polar (Garreaud et al., 2009; Sarricolea et al., 2017).

To accomplish this, ANDEX requires bio-geophysical data, such as air temperature, precipitation, evaporation, evapotranspiration, runoff, as well as data on the vegetation, glaciers, etc. Due to the complex physiographic characteristics of the region, additional high resolution data are needed on the topography, soils, land cover and land use. This would allow for a more detailed and accurate representation of the hydrological processes in basins. Therefore, it is necessary to create an inventory of the sources of data and information. The goal of this review is to compile the existing hydrological and meteorological information for the South American Andes. The assessment of the data and observations is based on publications by the World Meteorological Organization (WMO) (WMO, 2007, 2010), the portals of various international and national institutions or universities, as well as information provided by the National Meteorological and Hydrological Services (NMHSs) from Bolivia, Chile, Colombia, Ecuador, Peru, Venezuela and Argentina. With the exception of Colombia, information taken from private networks was not included in this study, mainly because this information was not available or reported by the NMHSs. In addition to these *in situ* measurements, we present a compilation of the satellite based products and reanalysis data useful for climatological and hydrological purposes in the Andes. The purpose of this article is to provide a concise review of the available sources of information that are useful or relevant for the objectives of the ANDEX program. This inventory besides showing the data availability, also identifies the gaps to be filled and the current limitations that must be addressed, in order to implement new research programs on the water cycle and energy balance in the Andean region. The available data sources and information are separated according to their types: *in situ* observations and measurements from the current hydrometeorological network operated by governmental institutions (**Section 2**); remote sensing data (satellite sensors) (**Section 3**); re-analysis data (**Section 4**); physiographic and morpho-topographic data (**Section 5**). The main knowledge gaps and some research are presented in **Section 6**. Finally, we conclude with research opportunities through the ANDEX program (**Section 7**). Although this is a renewed effort to update the inventory of existing observations, it cannot be considered as complete. The data relative to future climatological and hydrological scenarios for the Andes are beyond the scope of this article.

[1]https://www.gewex.org/

[2]https://www.wcrp-climate.org/

IN SITU OBSERVATION AND MEASUREMENTS

The following information is available for different time periods and different spatial and temporal resolutions. On the one hand, data for some places and regions have been obtained through regular observations or measurements over long periods, while other data are obtained by specific research programs over a limited time period. Regular observations/measurements of hydrometeorological variables have been made by governmental institutions in countries in this region under the standard methods used by the WMO for its operational Integrated Global Observing System (WIGOS). These observations include, among others, the Regional Basic Synoptic Network (RBSN) and the Regional Basic Climatological Networks (RBCN). A description of the whole Integrated Global Observing System may be found in WMO (2017). For the Andes, these regional networks are operated by Argentina, Bolivia, Chile, Colombia, Ecuador, Peru and Venezuela; i.e., countries that are members of the WMO Regional Association III (RA-III) (WMO, 2018).

Observing Systems Capability Analysis and Review Tool – OSCAR

The official information from the NMHSs is compiled in the Observing Systems Capability Analysis and Review Tool (OSCAR)[1]. This database is developed by the WMO at the global scale in support of Earth Observation applications, and provides physical variables related to weather, water and climate. Additionally, the portal details information concerning all earth observation satellites. However, for South America, OSCAR has a limited number of observations included by the NMHSs. For the seven Andean countries mentioned, there are only 451 stations that collect hydrometeorological variables. In **Table 1**, the stations reported to OSCAR are broken down by country (NMHS) and by variable. Argentina is the country with the highest number of stations in the system with 147 stations, while Bolivia has the lowest number of stations with 39. In general, almost all of the stations reported temperature and precipitation measurements with different time steps (hourly, daily, and monthly). Argentina, Chile, Colombia and Venezuela measure the Potential Evaporation and Solar Insolation while Ecuador just measures the Potential Evaporation, Peru measures the Insolation and Bolivia does not include these variables in the OSCAR system. This could be due to the lack of records or because the data was not downloaded in the OSCAR system. Very few glaciers are reported in the database along the Andes from Colombia to Patagonia. None of the Andean countries reported river/lake level and discharge observations to OSCAR, indicating a lack of information for these two critical hydrological components.

TABLE 1 | Number of surface hydrometeorological stations operated by the National Meteorological and Hydrological Services in the Andean Region reported in OSCAR.

Country	NMHS	Total #Stations	Temp	Pr	EVP	Insol	Lev	Disch	Glacier
Argentina	SMN	147	116	111	28	88	0	0	13
Bolivia	SENAMHI	39	37	38	0	0	0	0	1
Chile	DMC	58	36	36	8	27	0	0	2
Colombia	IDEAM	59	51	51	17	28	0	0	5
Ecuador	INAMHI	49	43	42	7	0	0	0	0
Peru	SENAMHI	55	50	50	0	8	0	0	6
Venezuela	INAMEH	44	38	44	36	37	0	0	0

Variables: ***Temp*** *– surface air temperature;* ***Pr*** *– Precipitation;* ***EVP*** *– Evaporation;* ***Insol*** *– Insolation;* ***Lev*** *– River/Lake levels;* ***Disch*** *– River/Lake discharges;* ***Glacie****r – Glacier variables. Source: OSCAR/Surface WMO's official repository of WIGOS metadata https://oscar.wmo.int/surface//index.html#/.*

TABLE 2 | Total number of stations (meteorological and hydrological) per country and altitude range based on the reports received from the NMHSs in Bolivia, Colombia, Chile, Ecuador, Peru, Venezuela, and Argentina.

Country	Altitude range (# Stations)					
	0 to 1,000 m (% of stations for each country)	1,001 to 2,000 m (% of stations for each country)	2,001 to 3,000 m (% of stations for each country)	>3,000 m (% of stations for each country)	Total	OSCAR Total
Bolivia	39 (23.5)	12 (7.2)	35 (21.1)	80 (48.2)	**166**	39
Chile	773 (80.6)	86 (8.9)	42 (4.4)	58 (6.0)	**959**	58
Colombia	4,288 (48.4)	2,448 (27.6)	1,743 (19.7)	379 (4.3)	**8,858**	59
Ecuador	765 (52.9)	172 (11.9)	291 (20.1)	219 (15.1)	**1,447**	49
Peru	785 (35.1)	245 (11)	315 (14.1)	891 (39.8)	**2,236**	55
Venezuela	767 (93.5)	47 (5.7)	5 (1)	1 (0.1)	**820**	44
Argentina	54 (49.5)	43 (39.4)	5 (4.6)	7 (6.4)	**109**	147
Total	**7,471**	**3,053**	**2,436**	**1,635**	**14,595**	**451**

National Meteorological and Hydrological Services Data

OSCAR is an official repository but there is a lack of meteorological and hydrological data for South America. To estimate the available information in western South American countries, the direct information provided by the NMHS and through their official website has been compiled. The summary of this information from Bolivia, Chile, Colombia, Ecuador, Peru, Venezuela and Argentina indicate a total of 14,595 stations (meteorological and hydrological), which is much higher than the number of stations reported to OSCAR. The details of this compilation, broken down by country and altitude range, are presented in **Table 2**. The stations are distributed as follows: 7,471 stations between an altitude of 0 and 1,000 m; 3,053 stations between 1,001 and 2,000 m; 2,436 stations between 2,001 and 3,000 m and 1,635 stations above an altitude of 3,000 m. Colombia has a total of 8,858 stations, representing 60.7% of the total stations. It is the sole country to have made records from the available private stations, which explains the difference with the other countries. Peru follows with 2,236 stations (15.3%); Ecuador is the third country with 1,447 stations (9.9%); Chile has 959 stations (6.6%); Venezuela has 820 stations (5.6%); next comes Bolivia with a total of 166 stations, representing 1.1% of the total and Argentina rank last with a total of 109 stations, which represents 0.7% of the total. In general terms, the spatial density of the stations could be determined by considering the local geographical such as the presence of deserts and extended plains and how easy is to access these areas to acquire data.

Observations Between 0 and 1,000 m

The percentage of stations between 0 to 1,000 m in comparison with the total per country is given in **Table 2**. Chile, Ecuador, Peru and Venezuela have very similar values at this level, representing close to 10% for each country. Colombia has the highest number of stations at this altitude range with 57.4% of the total stations, while Bolivia and Argentina represent less than 1.0%. For Chile, Colombia, Ecuador and Venezuela, the majority of the stations are located in the 0–1,000 altitude range. For Venezuela and Chile, this range is important as it represents 93.5 and 80.6%, respectively, of its total stations. The spatial distribution of the stations between 0 and 1,000 m is shown in **Figure 1**. In this altitude range, a good coverage is found in the Caribbean basins (Colombia and Venezuela) and on the western slope of the Andean mountains to the coast. This dense meteorological station network contrasts with the network on the eastern slope and the Orinoco and Amazon basins. The same pattern is observed in Ecuador and Peru, where most of the stations are located from the western slope of Andes to the coast and only few stations are located in the Amazon Basin. In Bolivia, the density of stations is relatively low with major gaps depending on the

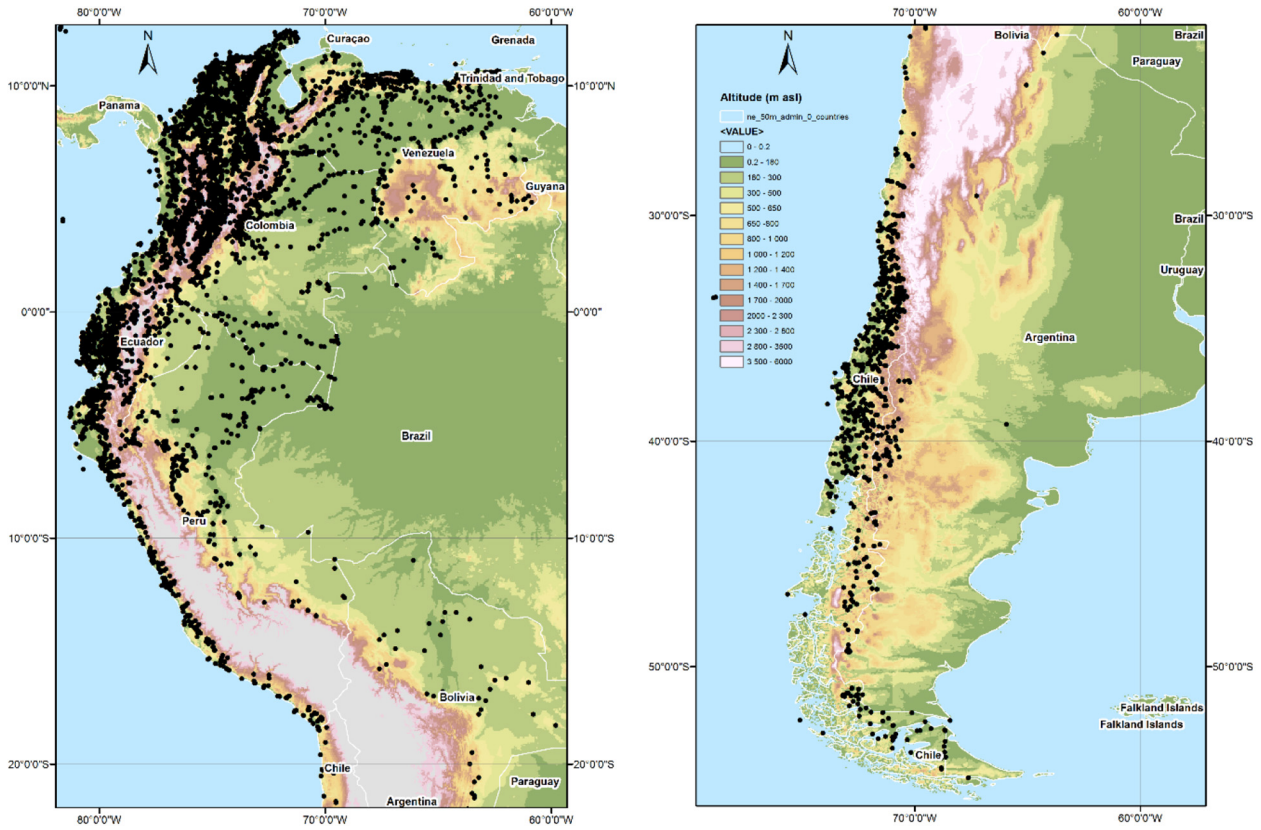


FIGURE 1 | Total number of surface stations (meteorological and hydrological) between 0 and 1000 m. Source: National Meteorological and hydrological Services from Bolivia, Chile, Colombia, Ecuador, Peru, Venezuela, and Argentina.

region. Chile shows a lower density of stations in the northern and southern regions in comparison with the central region of the country. The highest density of stations in Argentina is in the central-western region.

Observations Between 1,001 and 2,000 m

Once again, Columbia has the highest percentage of stations between 1,001 and 2,000 m out of the total number for the Andean region compared to the other countries. The spatial distribution of the stations for this altitude range is shown in **Figure 2**, where we observe a good coverage with a dense network of stations for Colombia. A significant gap exists over the Guiana Shield ("Macizo Guayanés") located in southern Venezuela. A low density is also observed in the Andean region of Ecuador, and the southern Andes of Peru and Bolivia and Chile. Once again, Argentina shows a higher density of stations in its western-central region, on the eastern side of the Andes.

Observations Between 2,001 and 3,000 m

The percentage of stations between 2,001 to 3,000 m is shown in **Table 2**. For this altitude range, the countries with the fewest number of stations at this range, compared to the other ranges, are Chile, Argentina and Venezuela. Conversely, Colombia stands out as having the highest percentage compared with the other countries (71.5% of the total). The spatial distribution of the stations for this altitude range is shown in **Figure 3** and there is a lack of stations over the Andean Cordillera in Bolivia, Chile and Venezuela. On the contrary, there is a high density of stations over the Andean Cordillera in Colombia, Ecuador and Peru.

Observations Above 3,000 m

In general very few stations exist above 3,000 m along the Andes. Nevertheless, this percentage represents 48.2% of Bolivia's total number of stations, and 39.8% of Peru's total number of stations. In contrast, Argentina, Colombia and Venezuela have the fewest number of stations in this range with a total of 6.4, 4.3, and 0.1% in each country, respectively. Colombia still has more stations than Argentina, Bolivia, Chile Ecuador and Venezuela (with only one station) in this altitude range. The spatial distribution of stations above 3,000 m is illustrated in **Figure 4** where we generally note a low density of stations. In the case of Chile, the stations are only located in the northern region due to the orography.

Reported Observations for the WMO Information System

CLIMAT is an additional database in which each station has a code for reporting the monthly climatological data assembled at land-based meteorological surface observation sites

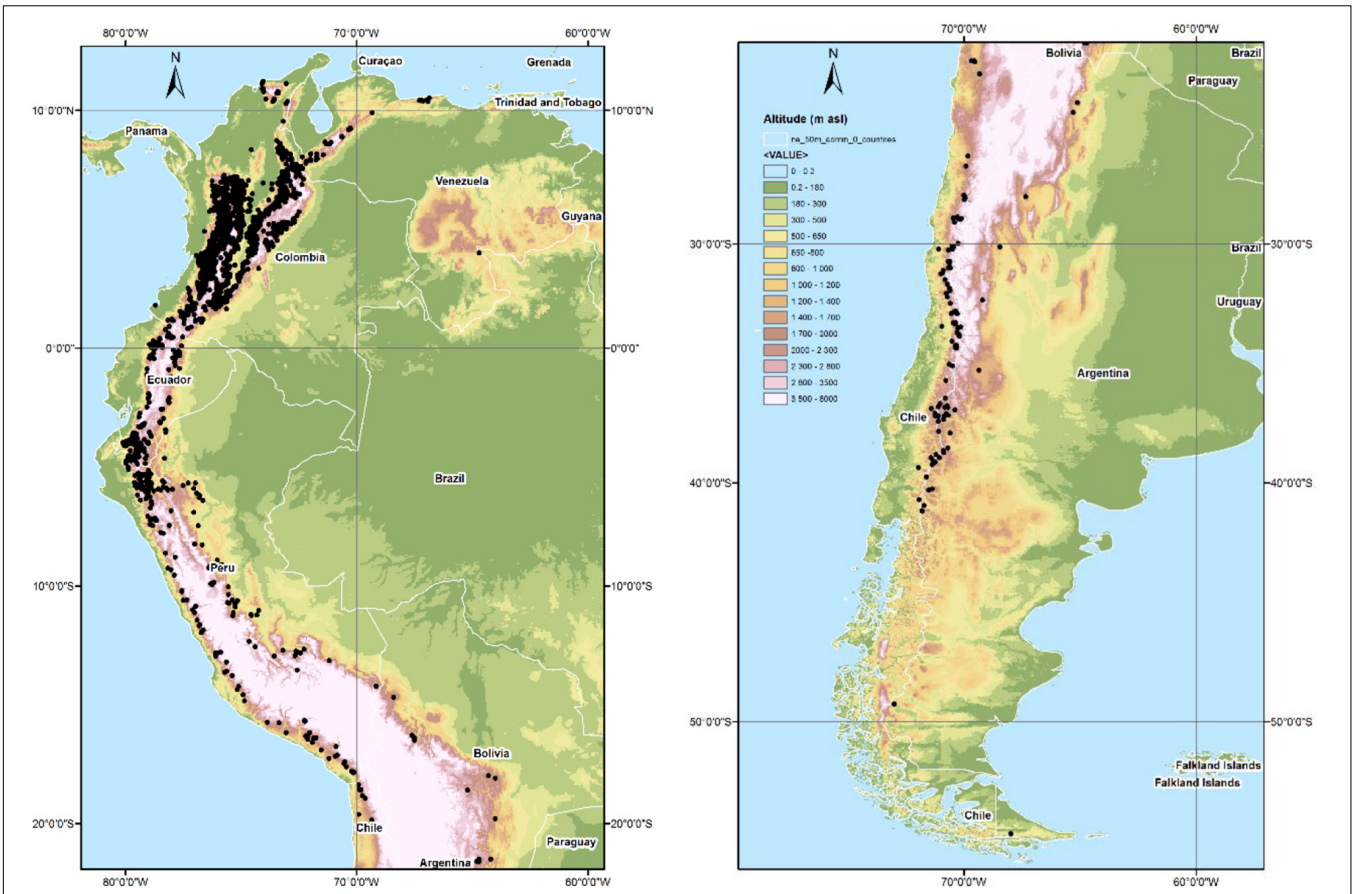


FIGURE 2 | Total number of surface stations (meteorological and hydrological) between 1,001 to 2,000 m. Source: National Meteorological and hydrological Services from Bolivia, Chile, Colombia, Ecuador, Peru, Venezuela, and Argentina.

to data centers. Each NMHS exchanges data via the Global Telecommunication System (GTS) (WMO, 2017). The stations reported in CLIMAT are a subset of the NMHS's stations mentioned in the previous section. **Figure 5** shows the percentage of stations that are part of the Global Climate Observing System Surface Network (GSN)[2] and which report data to the CLIMAT[3] database from June 2018 to May 2019. Although the observational capacity in the Andean countries has increased over time, the availability of data transmitted through the CLIMAT Reports is limited in countries such as Ecuador, Peru and Venezuela. This example illustrates how the number of available stations and the existing gaps could be exacerbated by the operational limitations.

Global Precipitation Climatology Centre – GPCC

The GPCC provides three datasets (Schneider et al., 2011). The first quality-controlled dataset compiles the information from 7,000 stations and covers the period from 2007 to the present. The second one is a quality-controlled dataset from 67,200 stations worldwide with recording duration of at least 10 years over the 1901–2013 period (Full Data Product, V7). This product contains the gridded monthly rainfall with spatial resolutions of 0.5°, 1.0°, and 2.5°. The last product, a near real-time first guess, is a gridded product with spatial resolution of 1.0° at daily time-scale. The problem is that it is based on a limited number of stations. These three gridded products are not yet bias-corrected for systematic gauge measurements, e.g., wind undercatch. Nevertheless, the GPCC provides the number of gauges used to generate the grids as well as the climatological estimates of error. All of the products can be downloaded on the GPCC[3] portal. A limitation of the GPCC dataset in South America, and the Andes in particular, is the number of stations used for the gauge interpolation. The number of stations has declined considerably during the last two decades (**Figures 6A,B**). **Figure 6B** illustrates the scarcity of data along the Andes. It can be seen that more data are available in the Northern Andes. Because gauges are scarce in this region, this has implications for the gridded product which could be non-homogeneous. Problems can be observed in mountainous areas when the satellite-based rainfall estimates (SREs), such as TMPA (TRMM Multi-satellite Precipitation Analysis), use GPCC to adjust their estimates. Finally, this could degrade the results of the hydrological modeling using this data.

[3]https://tandemx-science.dlr.de/

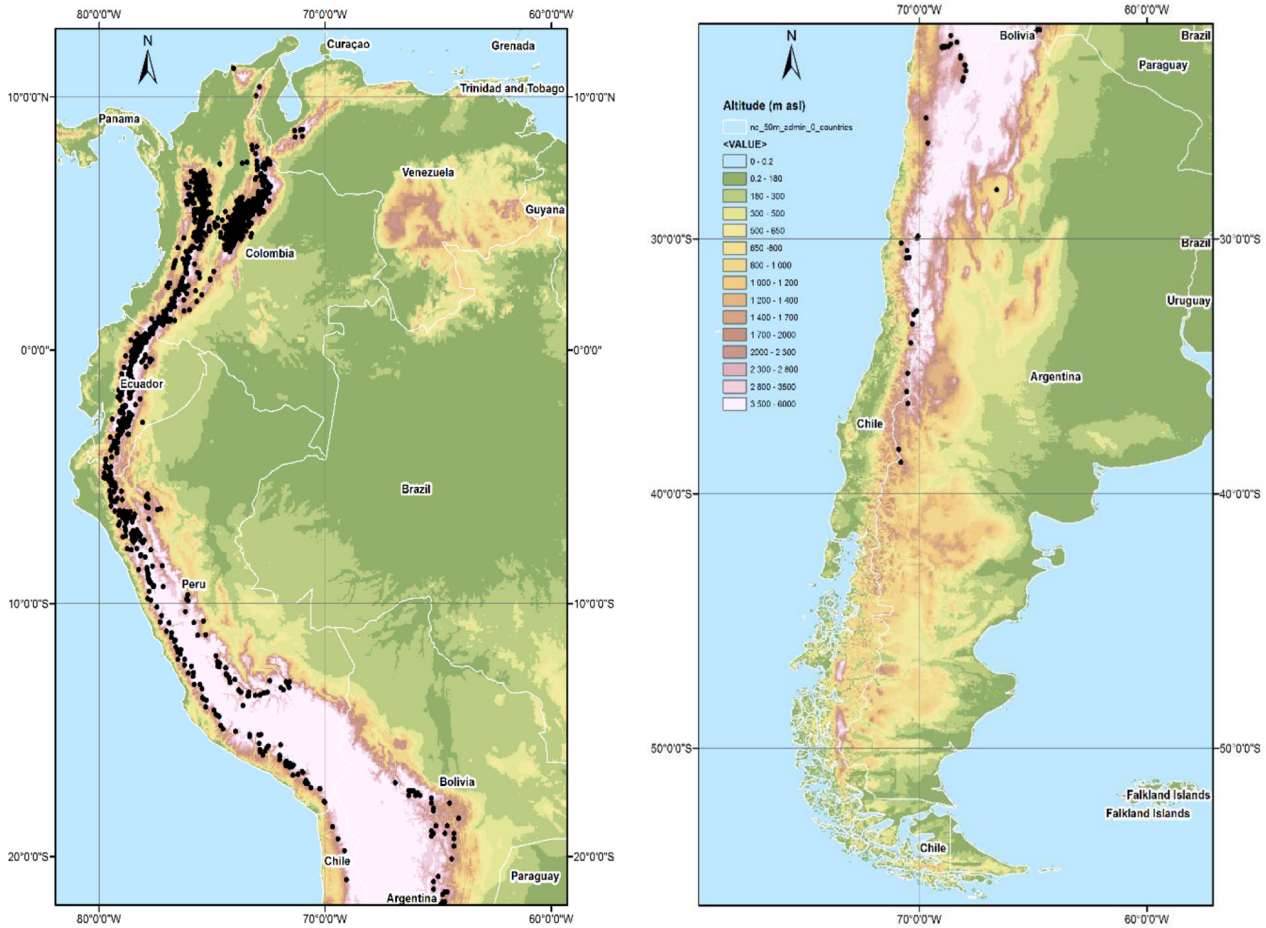


FIGURE 3 | Total of surface stations (meteorological and hydrological) between 2,001 to 3,000 m. Source: National Meteorological and hydrological Services from Bolivia, Chile, Colombia, Ecuador, Peru, Venezuela, and Argentina.

Radiosonde

The punctual upper-air measurements for a given time and date can be taken using a radiosonde. This instrument, carried by a balloon through the troposphere, is equipped with devices to measure one or several meteorological variables (pressure, temperature, humidity, horizontal wind) at different altitudes, and is equipped with a radio transmitter for sending this information to the observing station usually at a fixed location (WMO, 2014). Radiosondes take measurements at one location, ideally twice a day, up to heights of roughly 25 to 35 km. The ascending velocities are comprised between 5 and 8 m s^{-1}. Biases exist for each variable: 1 hPa for pressure, 0.4 to 1 K for temperature and 5 to 14% for relative humidity, respectively. One of the strengths of this data is its precise location into the atmospheric column. These data are used in forecast models as well as in reanalysis. Some limitations for sending the radiosondes exist due to high and labor-intensive costs. In the Andean region and nearby adjacent areas there are only 16 points for five countries with regular upper air measurements with a mean frequency equal to 1 per day (**Table 3**). Generally, the launch time is at 12Z. Data from these radiosonde stations may be accessed in each NMHS or through the University of Wyoming[5], by searching in South America or using the station code number. Only five stations are launched at an altitude higher than 1000 meters above sea level, demonstrating the need for developing more scientific projects and programs in the Andes. If intensive radiosonde campaigns were to be carried out in the Andean region, this would lead to a better understanding of the vertical structure of precipitation events and cloud microphysical processes (Perry et al., 2014).

Hydrological Data

The hydrological used and disseminated by the NMHS are also collected, processed and analyzed according to the WMO's standard methodologies as part of the WMO Hydrological Observing System (WHOS[6]), the hydrological component of WIGOS. The concept of this resource is to pool and share historical and real-time data from water information systems. In the web portal[3] is possible to have access to each NMHS database and the corresponding website. In addition to the NMHS, other institutions and specific research programs also operate hydrometeorological stations based on the concept of

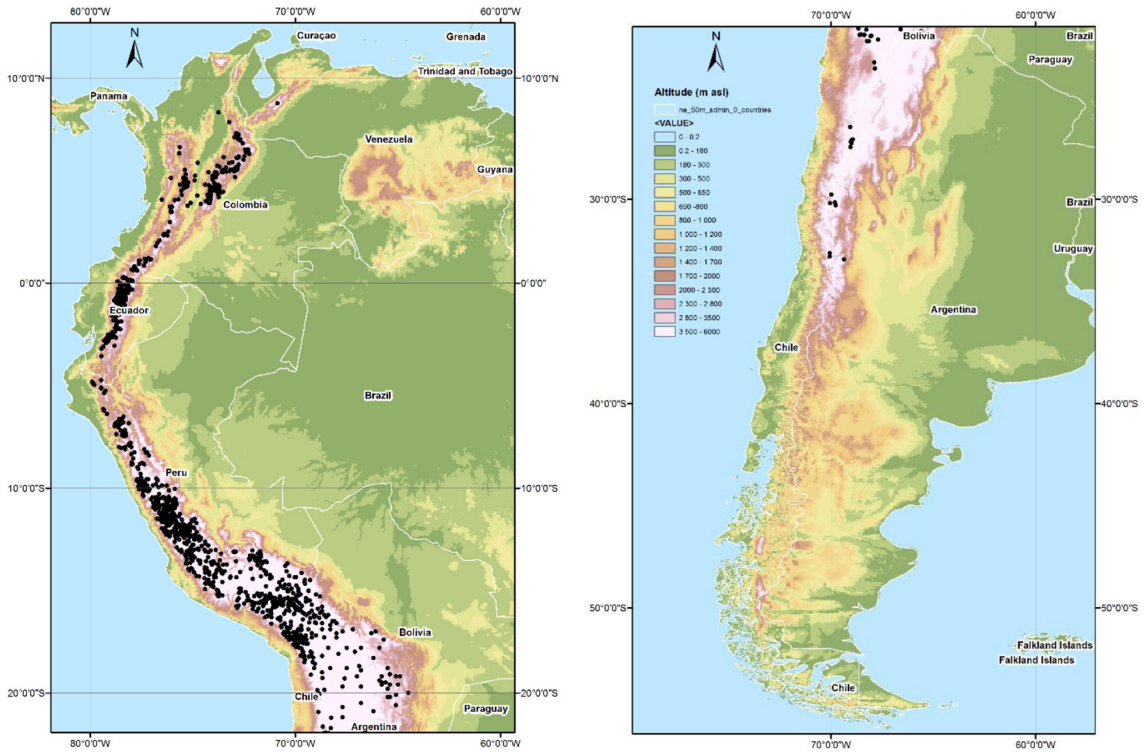


FIGURE 4 | Total number of surface stations (meteorological and hydrological) above 3000 m. Source: National Meteorological and hydrological Services from Bolivia, Chile, Colombia, Ecuador, Peru, and Venezuela.

citizen science, which implies that stakeholders help to define the research or application objectives for this kind of network. For example, few years ago, Celleri et al. (2010) proposed an Andean Network of Research for a participatory-based (or collaborative) hydrological monitoring network, including the collection, processing, storage and dissemination of data for research and application purposes; this network should include (a) densely-instrumented basins for identifying and quantifying hydrological processes and their spatial variability and (b) baseline instrumented basins managed by local stakeholders. More recently, Ochoa-Tocachi et al. (2017) presented the initial results of the Regional Initiative for Hydrological Monitoring of Andean Ecosystems (iMHEA), a network with over 30 local stakeholders at 15 sites located in Bolivia, Ecuador, Peru and Venezuela. iMHEA has produced data for precipitation, stream flows, meteorological variables (temperature, humidity and wind speed/direction), soil properties, geological characterizations, land use and tracer monitoring. The data and analyses tools generated by iMHEA are freely available on internet (Ochoa-Tocachi et al., 2018). Other initiatives in Chile spearheaded by the Center for Climate and Resilience Research share a free extensive hydro-meteorological database through their portal[7]. These data can be used to improve knowledge about hydrological processes in a much detailed manner than the scale provided by the NMHS. The Global Runoff Data Centre (GRDC[8]) provides another free hydrological database compiling runoff data at the global scale. The GRDC is an international data center operating under the auspices of the World Meteorological Organization (WMO) that was established in 1988 to support research on global and climate change and integrated water resources management. Furthermore, cryosphere monitoring provides relevant information for hydrology, especially in the Andean region. To share this information, the WMO created an international mechanism for supporting *in situ* and remote sensing observations: the Global Cryosphere Watch (GCW), which is also a component of WIGOS. The objective is to group and share the raw data, information and analyses on the past, present and future state of the cryosphere. As part of WMO, data obtained from extensive monitoring are collected through standardized measurements[9].

Regional Climate Centers of South America

In addition to the NMHS, South America has two Regional Climate Centers (RCC): the RCC for Western South America (RCC-WSA[10]), which includes Bolivia, Chile, Colombia, Ecuador, Peru and Venezuela and is coordinated by the International Research Center on El Niño (CIIFEN[11]); and the RCC for Southern South America (RCC-SSA[12]) coordinated by the National Meteorological Service of Argentina and the National Institute of Meteorology of Brazil, that have Bolivia, Chile, Paraguay and Uruguay as active members. These institutions are WMO members, which they have a series

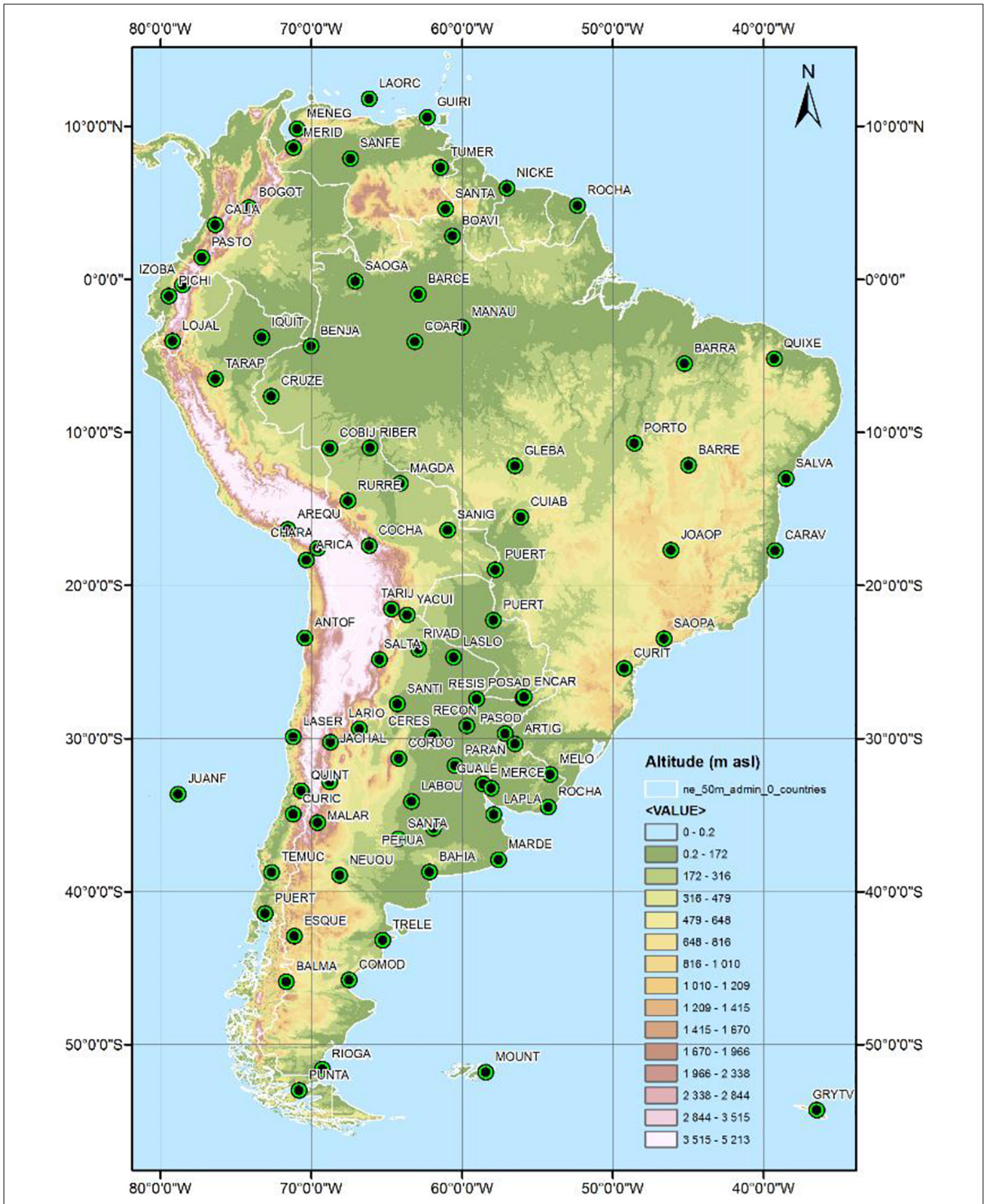


FIGURE 5 | GSN-stations (black points) in the CLIMAT database.

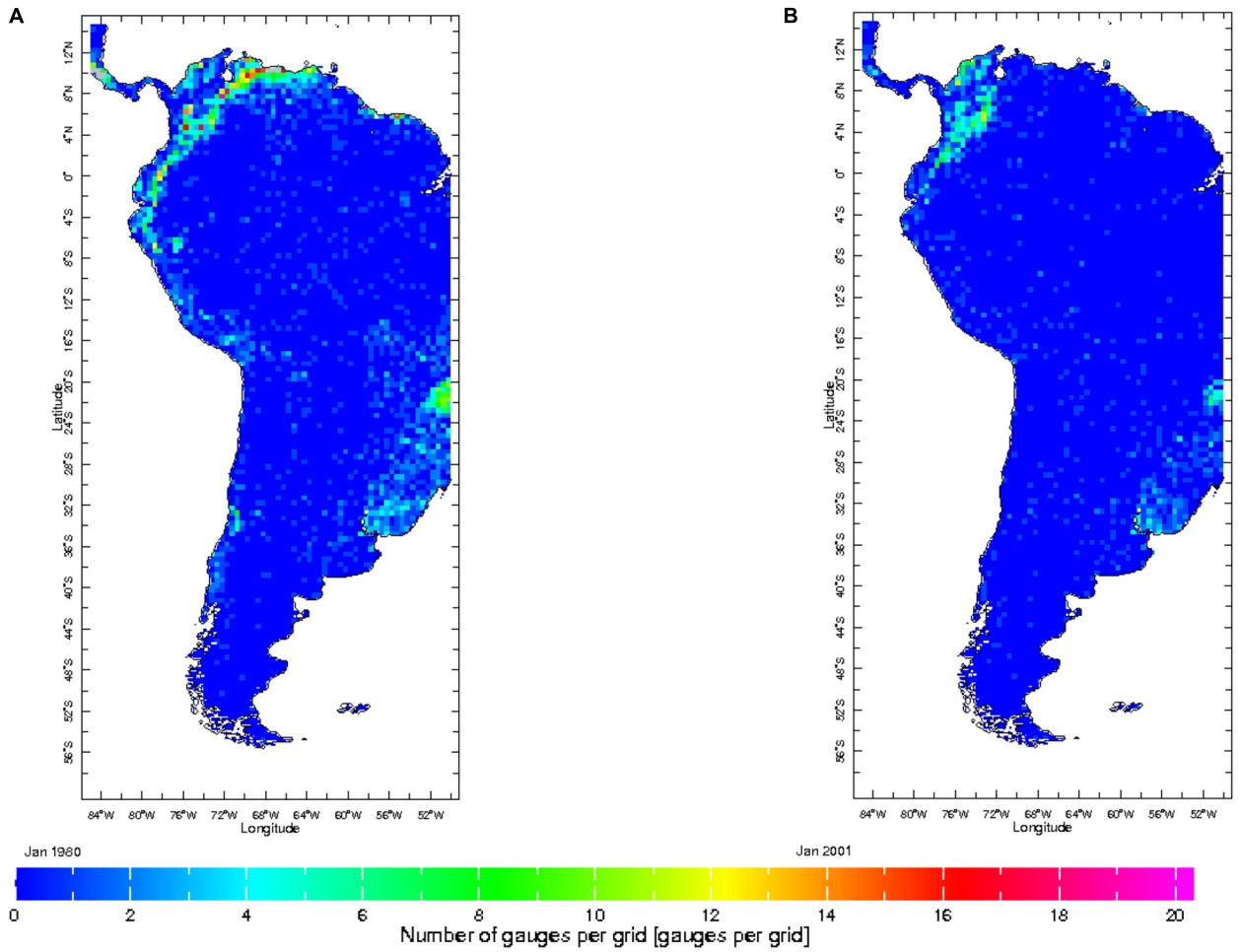


FIGURE 6 | Spatial distribution of the average number of rain gauges per grid used in GPCC[4] over the period **(A)** 1980–2000 and **(B)** 2001–2018.

TABLE 3 | Stations with upper air measurements located in the Andes region or in nearby adjacent areas.

	Code	Country	Name	Latitude	Longitude	Elevation (meters above sea level)
1	87344	Argentina	Córdoba Airport	−31,19	−64,13	474
2	87418	Argentina	Mendoza El Plumeril	−32,5	−68,47	704
3	87715	Argentina	Neuquen Airport	−38,57	−68,08	271
4	87047	Argentina	Salta Airport	−24,51	−65,29	1216
5	87623	Argentina	Santa Rosa Airport	−36,34	−64,16	191
6	85442	Chile	Antofagasta Cerro	−23,26	−70,26	120
7	85574	Chile	Pudauel Arturo Mendoza	−33,23	−70,47	476
8	85543	Chile	Puerto Montt Tepual	−41,25	−73,05	86
9	80222	Colombia	Bogotá Eldorado	4,42	−74,08	2548
10	80094	Colombia	Bucaramanga Airport	7,06	−73,12	1189
11	80259	Colombia	Cali Airport	3,543	−76,381	978
12	80210	Colombia	Pereira	4,813	−75,739	1401
13	84377	Peru	Iquitos Secada	−3,45	−80,36	126
14	84628	Peru	Lima	−12	−77	13
15	84658	Peru	Puerto Maldonado	−12,38	−69,12	266
16	80462	Venezuela	Santa Elena Uarien	4,36	−61,07	907

University of Wyoming[5].

of obligatory functions to create regional climate products, including prediction, and to support climate activities at regional and national scales. In western South America, a relevant source of information is the Latin American Climate Assessment & Dataset (LACA&D[13]) that receives data from nine member countries with 1,225 weather stations. They present information on rainfall rates, rainfall extremes and climatic trends. These data are shared by the NMHSs from their official databases. RCC-WSA also is responsible for receiving and publishing the seasonal prediction made by the NMHS with monthly *in situ* measured data. Similarly, the RCC-SSA has their own database with information from the meteorological stations of the member countries. This information is updated on a monthly basis and can be used to analyze the climate diagnosis. The historical information in this database may be also used for hydroclimatological studies. Additionally, both institutions develop climate analyses from global and regional data in order to provide a better understanding of the impacts of extreme climate events and climate variability and change in the region.

The present challenges for the different Centers are: (i) to have a system of data rescue and to provide high quality essential climate variables datasets up to date; (ii) to create new gridded time series products merging station data, reanalysis and satellite observations; (iii) to work with sector-based research team to develop applications models.

DATA FROM SATELLITE SENSORS

In addition to the data produced by *in situ* observations and measurements, data are also generated by remote sensors placed in satellite platforms. By scanning the Earth's surface and atmosphere, these devices produce data on the surface temperature, soil and air moisture, water vapor, cloudiness, precipitation and several indices that represent the vegetation and the soil. This methodology provides new and useful information for monitoring and modeling hydroclimatic variables, due to the higher spatial resolution and longer time ranges of the data generated. Considering that huge amounts of data are becoming increasingly available, cloud computing is becoming increasingly necessary as a result. These data can be accessed through portals such as Google Earth Engine, NASA Earth Exchange (NEX) and/or Earth Observation Data for Water Resources Monitoring (EODC) (Chen and Wang, 2018). Satellite-derived precipitation estimates use indirect data and do not accurately represent the precipitation in mountainous areas where orography plays an important role (Derin and Yilmaz, 2014). The article published by Sun et al. (2018) gives a review of Global Precipitation Data Sets, witch estimated 30 different products and highlighted that large differences exist, particularly in complex mountain areas. One recent study Nijzink et al. (2018) highlights the advantage of taking various information sources into account in order to better understand the hydrological processes. Using five different conceptual hydrological models applied to 27 catchments with areas comprised between 91 and 1587 km^2, these authors demonstrated that the models became more accurate with an increasing number of data sources include Advanced Microwave Scanning Radiometer, Earth Observing System and Advanced Scattermeter soil moisture, gravity measurements and Moderate Resolution Imaging Spectroradiometer (MODIS) data. **Table 4**, modified from McCabe et al. (2017), compiles the most used satellite data to study the water cycle and we detail each of them in sections 3.1 to 3.6.

Details are provided regarding the most used satellite precipitation based products and the MODIS data (**Table 5**). These devices are on board the Terra (EOS AM-1) and Aqua (EOS PM-1) satellites. Since the early 1990s, they have been producing data on the land, oceans and lower atmosphere. Until now, data time series are available for these variables over a 25 year period, with a spatial resolution from 500 meters to 1 kilometer. Some of the variables measured by these different components are presented in the **Table 4**.

Rainfall, Snowfall, Land Surface Temperature, and Evaporation

Tropical Rainfall Measuring Mission (TRMM) and Global Precipitation Measurement – Integrated Multi-SatellitE Retrievals (GPM – IMERG)

A highly valuable source of data for hydroclimate studies is the Tropical Rainfall Measuring Mission (TRMM), a joint program of the National Aeronautics and Space Administration (NASA) and the Japan Aerospace Exploration Agency (JAXA) (Huffman et al., 2007). The use of a Microwave Sounder Unit (MSU) emplaced in a research satellite, covering tropical and subtropical regions, generated operational data on the total available precipitation. There is 3-hourly data points over a 25-year period with a spatial resolution of 0.5° × 0.5°. There are several versions of TRMM data and many studies have been conducted on the Andes to determine their usefulness for hydrological applications (Collischonn et al., 2008). Depending on the TRMM product, some corrections for the high zones are needed (Condom et al., 2011). A relevant study from Zulkafli et al. (2014) demonstrates the interest of version 7 of the TRMM 3B42 precipitation estimates (or TRMM Multi-satellite Precipitation Analysis – TMPA) as forcing data for hydrological modeling in Andean-Amazon River Basins. The TRMM 3B43-V7 product is also able to reproduce the spatio-temporal variability of the precipitation for the Pacific slope of Ecuador but tends to overestimate the ground observation (Erazo et al., 2018).

In addition, Ochoa et al. (2014) found that for the Pacific-Andean River Basins in Ecuador, TMPA accurately represents the rainfall amounts related to advective-convective precipitation regimes in southern Ecuador. The TMPA data are available on the Precipitation Measurement Mission's (PMM) web page[14]. Manz et al. (2017) showed that the Integrated Multi-satellitE Retrievals for GPM (IMERG) has better detection levels and can provide better quantitative rainfall intensity estimates than TMPA (TRMM Multi-satellite Precipitation Analysis), particularly in the high Andes of Ecuador and Peru. However, IMERG did not show any improvement in terms of either rainfall detection or rainfall rate estimation along the dry Peruvian coastline. Another study carried out by Palomino-Angel et al. (2019) aims to evaluate the TRMM-3B42V7 (from 2012 to 2015) and IMERG (from 2014 to

TABLE 4 | (non-exhaustive overview) Hydrological variables corresponding to current and planned (in italic) satellite remote sensing missions.

Hydrological variables	Missions/instruments	Standard spatial resolution (km)	Standard temporal resolution (days)	Launch year	Sensor type
Rainfall	GPM -IMERG	5	0.125	2014	R and S
	CHIRPS	5	1	1981	O
	TRMM	27	0.125	1998	S and R
	CMORPH	27	0.125	1998	O
	PERSIANN-CCS	5	0.5	1983	S and T and O
	PERSIANN-CDR	27	0.042	1983	O
Snowfall	GPM -IMERG	5	0.125	2014	R and S
	CHIRPS	5	1	1981	O
	CloudSat	1.5	1	2006	R
Evaporation	Terra/MODIS	0.5	1	1999	O
	Aqua/MODIS	0.5	1	2002	O
	Suomi/VIIRS	0.5	1	2013	R
	LSA-SAF	3	1	2005	O and R
	Landsat 8	0.5	1	2013	O and T
	Landsat 9	*0.5*	*1*	*2023*	O and T
Snow cover	Terra/MODIS	0.5	1	1999	O
	Aqua/MODIS	0.5	1	2002	O
	Suomi/VIIRS	0.5	1	2013	R
	Sentinel-1 A/B	0.1–0.005	6	2014/2016	R
	SPOT 1-7	0.4—0.005	26	1986	O
	Sentinel-2 A/B	0.01—0.06	5	2015/2017	O
Snow density, depth, or water equivalent	GCOM-W/AMSR2	30	1	2012	R
Surface soil moisture	SMOS	36	3	2009	R
	SMAP (radiometer)	36	3	2015	R
	ASCAT-SWI	25	1	2006	S
	GCOM-W/AMSR2	50	1	2012	R
	Sentinel-1A/1B	0.1–0.005	12	2014/2016	R
Deep soil moisture	*Biomass*	*0.2*	*18*	*2021*	S
Altimetry/Surface water elevation	Jason-3	0.5	10	2016	L and R
	SARAL/Altika	0.5	35	2013	L and R
	SWOT	*0.1*	*11*	*2021*	S and R and L
	Sentinel-3A/B	0.3	27	2016/2018	O and R and S
	TOPEX/Poseidon	0.6	10	1992	S and R
	Cryosat-2	local	10	2010	R
	ICESat	0.07	91	2003	L
	ICESat-2	1.5	90	2018	L
Terrestrial water storage change	GRACE	220	30	2002	G
	GRACE-FO	180	30	2017	G
Vegetation/landcover/irrigated area	Terra/MODIS	0.5	1	1999	O
	Aqua/MODIS	0.5	1	2002	O
	Suomi/VIIRS	0.5	1	2013	R
	Landsat 8	0.03	16	2013	O and T
	Landsat 9	0.03	16	2023	O and T
	Sentinel-2A/2B	0.02	10	2015/2017	O
	SPOT 1-7	0.4—0.005	26	1986	O
	Sentinel-3A/3B	0.3	27	2016/2018	O and R and S
	Proba-V	0.35	2	2013	O
Vegetation stress	ISS/ECOSTRESS	0.07	4	2018	O
Photosynthesis/Vegetation indices	*FLEX*	*0.3*	*0.5*	*2022*	*O*
	GOES	3	0.01	1975	O
Water vapor	Aqua/AIRS	13.5	1	2002	O

(Continued)

TABLE 4 | Continued

Hydrological variables	Missions/instruments	Standard spatial resolution (km)	Standard temporal resolution (days)	Launch year	Sensor type
Albedo	Terra/MODIS	0.5	1	1999	O
	Aqua/MODIS	0.5	1	2002	O
	AVHRR	1	10	2015	R
Land surface temperature	AVHRR	1	10	2015	R
	Terra/MODIS	0.5	1	1999	O
	Aqua/MODIS	0.5	1	2002	O
	ISS/ECOSTRESS	0.07	4	2018	R
Flooded area	GIEMS-D3	25	30	1993	O

Sensor types: L/laser; O/optical; R/radiometer; S/radar; G/gravimeter; T/thermal (see Joyce et al., 2004 for details regarding the CMORPH product).

TABLE 5 | Available products from MODIS.

Land	Ocean	Atmosphere
Surface Reflectance	Sea Surface Temperature	Aerosol
Land Surface Temperature	Remote Sensing Reflectance	Total Precipitable Water
Land Cover Products	Chlorophyll-a Concentration	Cloud Products
Vegetation Indices (NDVI and EVI)	Diffuse Attenuation at 490 nm	Atmospheric Profiles
Thermal Anomalies/Fires	Particulate Organic Carbon	Atmosphere Joint Products
Evapotranspiration	Particulate Inorganic Carbon	Atmosphere Gridded Products
Gross Primary Productivity	Normalized Fluorescence Line Height (FLH)	Cloud Mask
Albedo	Instantaneous Photosynthetically Available Radiation	
Vegetation Continuous Fields	Daily Mean Photosynthetically Available Radiation	
Water Mask		
Burned Area Product		
Snow Cover and Ice surface temperature	Sea Ice	

https://modis.gsfc.nasa.gov/data/.

2017) daily precipitation products over the northwestern South America Andean region (Colombia) using *in situ* observations from 185 rain-gauges. Both products are able to capture the spatial and temporal distribution of the daily mean precipitation however the amounts are biased with an overestimation over the Andes Mountains and an underestimation in areas with medium to low altitudes that also correspond to areas with very high levels of precipitation near the coast of the Pacific Ocean. Over southern South America (Chile/Argentina) Hobouchian et al. (2017) carried out a systematic evaluation of satellite estimates of the daily precipitation in relation to terrain complexity. Over a period of 7 years and using more than 400 *in situ* weather stations as a reference, they found that CMORPH, TRMM3B42RT (real-time version) and TRMM3B42-V7 (research version) are able to reproduce the spatio-temporal variability of the precipitation with more accurate estimates in the wettest and coldest season (June-July-August). The bias is not the same depending on the altitude with an underestimation at low land elevations and an overestimation at high altitudes. More generally, the best performances of the estimate are found downwind of the terrain. These studies underlined the necessity to evaluate the bias for the different satellite precipitation estimates for each Andean region (from Venezuela to Patagonia) and eventually correct them before using these estimates in hydrological models.

Climate Hazards Group InfraRed Precipitation With Station (CHIRPS)

CHIRPS[15] is a global (maximum latitudes of 50°N-50°S) precipitation dataset from 1981 to the present. The dataset is a combination of a climatology developed from predictors of precipitation such as topography, elevation, geography, and estimated precipitation data from meteorological stations and satellites with current *in situ* data from stations and satellites. The result is a blended gridded dataset with a spatial resolution of 0.05° and temporal resolution of 1 day. The CHIRPS station blending procedure is a modified Inverse Distance Weighting (IDW) algorithm that has several unique characteristics. The first version of these is the use of climatology to define a local decorrelation distance; this distance is where the estimated point-to-point correlation is zero (Funk et al., 2015). This dataset has a rapid preliminary version followed by a final version made available at a slightly later time. The first version is available within a 1 day, while the final version is available sometime after the 15th of the following month. Similar to the GPCC, the limitation of CHIRPS is also the number of stations included in the blended final data, especially for South America. However, as a quasi-global dataset, it can be used to carry out an analysis at a regional scale (Segura et al., 2019).

Precipitation Estimation From Remotely Sensed Information Using Artificial Neural Networks-Climate Data Record (PERSIANN-CDR)

The PERSIAN-CDR[16] product is developed in two steps, first by applying a PERSIANN algorithm using an artificial neural network on the Gridded Satellite Infrared Data (GridSat-B1) and secondly by correcting the bias with the 2.5° grid of monthly Global Precipitation Climatology Project (GPCP) (Sorooshian et al., 2000; Ashouri et al., 2015). The final product covers the major part of the world (60°S–60°N), has a daily time-step and has a spatial resolution of 0.25°. The data are available

through the Climate Data Record of the National Oceanic and Atmospheric Administration's (CDR NOAA) website[17].

Snowfall

Snowfall estimates are still challenging in mountainous regions. This is particularly true for estimating precipitation from space. Three main satellite estimates can be used to quantify this variable: CHIRPS, GPM-IMERG and CloudSat. In the following part, we will focus on the last two products because CHIRPS has a poor ability of detecting snowfall (Bai et al., 2018). Through its design with a dual-wavelength precipitation radar (DPR) at 13.6 and 35.5 GHz, GPM was designed to have high sensitivity to detect low amounts of precipitation and to discriminate solid precipitation from liquid precipitation (You et al., 2017). For CloudSat, at a global scale, Kulie et al. (2016) propose a separation between the different kinds of clouds generating snowfalls, i.e., shallow cumuliform or nimbostratus clouds. Only a few regions are investigated in detail (e.g., Greenland, inland Russia, among others). As there have been no evaluations comparing this with ground measurements, they conclude that the next steps should be to use reanalysis and ground based observational datasets to identify and quantify the dataset biases. Skofronick-Jackson et al. (2019) compare active and passive snowfall estimates for GPM and CloudSat at the global scale with an exhaustive analysis of the differences arising from classification, sampling, instrumentation and algorithm differences and they propose a unified approach to evaluate the global snowfall datasets. Furthermore, they also concluded that it is necessary to validate the GPM and CloudSat estimates with ground-based observations over contrasting regions and with different kinds of surfaces. At the Andean scale, the problem with this is that such data are scarce. Kidd and Levizzani (2019) recently provide an exhaustive analysis of the Precipitation Estimation from the Earth Observation Satellite. These authors highlight the good accuracy and mention that the resolution (spatial and temporal) is suitable for hydrological modeling and water resource assessment. They also list the future improvements that are needed. The TRMM PR and CloudSat radar systems will be added to the upcoming radars on the GPM-core satellites and the European Space Agency's Clouds, Aerosol and Radiation Explorer (EarthCare). Finally, to improve the identification and quantification of frozen precipitation, effort should be made to correctly quantify the radiative transfer modified by the snow particles. This would be possible by combining both active and passive radar observations. The high variability of the surface ground state (rugosity, type of soil cover and humidity) will have to be considered.

Land Surface Temperature and Evaporation

In the hydrological cycle, the Land Surface Temperature (LST) is essential for discerning the physical processes occurring on the Earth's surface at the regional and global scale. The variability of LST is due to soil-surface-atmosphere interactions and is important for environmental studies and water management (Li et al., 2013). More specifically, LST can be used to quantify climate warming. In this context, MODIS LST is commonly used to estimate the air temperature (Zhang et al., 2016b) because Terra and Aqua satellites both pass over land at approximately the same local time each day data and therefore, the data representing the daylight conditions are comparable between days (Mao et al., 2017). Nevertheless, caution should be taken with cloudy scenes because the cloud cover affects the relationship between LST and air temperature (Zhang et al., 2016b). Aguilar-Lome et al. (2019) used MODIS LST on the Andes (between 7 and 20°S) over 2000–2017 period at a resolution of 1 km with monthly data to characterize the regional air temperature trends and determine the altitude dependence. They limit their study to the austral winter (June-July-August) to avoid problems with the clouds. The main conclusions are that, at the regional scale, the temperature trend is positive in most areas with an average rate of 1.0°C/decade and that this increase is dependent on the elevation and is more pronounced for higher elevations. This kind of analysis could be planned for the whole Andean regions as temperature changes affect Andean ecosystems. Basically, the actual evaporation (E) and evapotranspiration (ET) are calculated using the atmospheric states (T°, humidity, wind, etc.), the land cover type (vegetation, bare soil, bare rocks, open water, etc.) and the soil moisture. Three approaches are used to calculate the actual evapotranspiration from remote sensing imagery (Zhang et al., 2016a): (i) Land Surface Temperature Vegetation Index (LST-VI) space methods; (ii) empirical methods; and (iii) Surface Energy Balance (SEB) methods. Chen and Liu (2020) propose a review of these methods and one of their conclusions is the need to improve the regional ET *in situ* monitoring capacity. Two satellites are mostly used to calculate E and ET: MODIS and Landsat (7 and 8). Olivera-Guerra et al. (2020) propose a simple model to estimate the daily root zone soil moisture as well as ET with Landsat 7 and 8 data and show that the model is suitable at a monthly time scale but has some limits due to the frequency of the Landsat images. MODIS is more suitable at the regional scale and can be used to calculate daily ET (Zou et al., 2020). All of the methods based on remote sensing imagery to estimate ET require a large amount of storage and calculating capacities. New efforts are being made to parallelize the algorithm that can be used on either public or private clouds (Cunha et al., 2020). Furthermore, future requirements to refine the hydrological modeling would include reducing the revisit time satellites that will be launched in the future.

Snow Cover

At high altitudes, snowfall, accumulation and melt are important in the hydrological cycle. Remote sensing data are useful in snow cover evolution estimates and the main satellites for this field are MODIS, VIIRS, SPOT, Landsat and SENTINEL, among others. The major advantage of MODIS is the time step, resolution and duration of the time series that could be use to calculate the climatic trends. For instance, over the 2000–2016 period for the Andes (8 to 36°S), Saavedra et al. (2018) identify a significant rising of the snowline by approximately 10–30 $m.y^{-1}$ south of 30°S. Concerning the snow persistence (the fraction of time with snow cover for 1 year) over the same period, a distinction should be made between the region situated to the north of 29°S which has limited snow cover and areas found between 29 and 36°S that have significant seasonal snow cover. For this region, the season presents a decrease of 5 days over the period. Malmros

et al. (2018) provide details concerning the central Chilean and Argentinean Andes for the same period. They use the MODIS MOD10A1 C6 daily snow product in a hydrological model. The Snow Cover Extent (SCE) and the snow persistence decrease by an average of ± 2% and 43 ± 20 days. Snapir et al. (2019) used a data fusion technique with MODIS and Sentinel-1 data for a huge Himalayan catchment extending 55,000 km^2 over ∼2.5 years to characterize the changed in the snow cover area as well as its fraction of wet snow. These kind of data are pertinent as input data to feed hydrological models and will allow to improve runoff analyses (water resources, flood risk, etc.). This methodology could be applied in the Andean region when SENTINEL data are available. For the Andes in Bolivia, Chile and Argentina, Foster et al. (2009) used passive microwave satellite from the Scanning Multichannel Microwave Radiometer for the Nimbus-7 satellite and the Special Sensor Microwave Radiometer of the Defense Meteorological Satellite Program to quantify the snow cover and the snow mass evolutions over the 1979–2006 period. The results identify a significant inter-annual variability for these two variables but, contrary to other studies mentioned above, no long-term trend is detected.

Water Storage in Soils

Soil moisture evolutions and groundwater storage changes are a crucial component of the hydrological cycle and essential for water management. At a large spatial scale, two recent studies aimed to characterize the changes in water storage in the soil using GRACE data (Khaki and Awange, 2019; Ndehedehe and Ferreira, 2020). In the first study, South America is divided into 15 major catchments and the water balance is calculated for each one using a hydrological model at a 3 × 3° spatial resolution and a monthly time step. In this model, the assimilation of GRACE and SMOS data improve the quality of the simulations. Nevertheless, this superior analysis cannot be completed for small mountainous catchments due to low temporal and spatial resolutions. In the second study, the groundwater changes in the floodplain is analyzed in detail but some discrepancies between the simulations and observations in the arid zone highlight the difficulty to quantify complex hydrogeological processes from space where an anthropogenic influence could play an important role.

Vegetation Indices and Land Cover Changes

Land use and land cover change affect regional climate through modifications in the water balance and energy budget. Remote sensing data offer a great opportunity to quantify these changes at the regional scale. For example, MODIS provides time series of vegetation indices (MODIS – VI) and a normalized difference vegetation index at 1 km and 500 m, respectively (Tucker et al., 2005). Huete et al. (2002), demonstrate the performance of these two indices with *in situ* measurements for the semi-arid grass, shrub, savanna and tropical forest biomes. For small mountainous catchments, some limitations exist due to the relatively low spatial resolution of the products. One possibility is to use the Landsat 5TM, Landsat 7ETM + and Landsat 8 data, as shown by López et al. (2017) which aims to investigate the connections between land use and climate variation at decadal time scale for the Cotopaxi region in Ecuador between 1976 and 2013. On the other hand, Salazar et al. (2015) propose an exhaustive analysis of the land use and land cover change at the continental scale over South America with a link to the climatic variability. The data used, MODIS and Landsat TM, can be used to precisely quantify where severe changes in the region occurred over the past few decades, e.g., the Amazon deforestation, the Chilean Matorral or the Atlantic forest. In the conclusion, they highlight the fact that more studies are needed in order to estimate the changes in non-Amazonian South America and to ascertain the link with the duration and intensity of climate extremes.

DATA PRODUCED BY RE-ANALYSIS AND MODELING

Reanalysis is a systematic approach to produce datasets for climate monitoring and this option can be used in hydroclimatic studies (Van den Hurk, 2012). Reanalysis are created by processing observational data with an assimilation scheme and by models, which ingest all available observations every 3–6–12 h over the period being analyzed. Produced data in a grid for a given spatial resolution provides a dynamically consistent estimate of the climate state at each time step. However, it is necessary to know the technical specifications and to be aware of the limitations (Parker, 2016). The main reanalysis products are detailed in the following section (see Sun et al., 2018 for an exhaustive list).

European Centre for Medium-Range Weather Forecast (ECMWF; ERA-Interim and ERA5 Data)

The European Centre uses its forecast systems to generate global data sets for the atmosphere, land, surface and oceans. The reanalysis data highlighted for this institution are ERA-Interim and ERA5 data. ERA-INTERIM are global atmospheric data with a 6-h analysis window, a spatial resolution of approximately 80 km and a time period of 1979–2019. These reanalysis products are updated once a month with a delay of 2 months to guarantee quality and to correct any possible technical problems. In 2017, a new version of the ECMWF reanalysis data (ERA5) was released, with a spatial resolution of 30 × 30 km and with improved data quality, which includes information about uncertainties for all variables. Compared with ERA-Interim data, this new data has a higher spatial and temporal resolution, a better tropospheric description, a better global balance between precipitation and evaporation, better precipitation over land and in the tropical zone, better soil moisture and more consistent Sea Surface Temperature and sea ice. It also covers a longer time from 1950 until the present. ERA5 data will eventually replace ERA-Interim and uncertainty estimate for ERA5 can be found in Laloyaux et al. (2018). These data can be downloaded on the Copernicus webpage[18].

NCEP/NCAR Reanalysis 1 Project

The NCEP/NCAR reanalysis is available from 1948 to the present with a temporal resolution equal to 6 h intervals. This reanalysis is produced by an analysis/forecast system with the assimilation of *in situ* data. However, the data from 1948 to 1957 are different compared with the rest of the time series due to time step differences. The data and related technical specifications can be found on the PSD webpage[19].

JRA-55 Japanese Reanalysis

The Japanese global atmospheric reanalysis project covers 55 years, extending back to 1958. The data were produced in a regular latitude-longitude Gaussian grid (320 latitudes by 640 longitudes, nominally 0.56 degree). For detailed information about this project, see Kobayashi et al. (2015). JRA-55 data and technical information can be consulted on the University Corporation for Atmospheric Research (UCAR) webpage[20].

Multi-Source Weighted-Ensemble Precipitation (MSWEP)

Another important precipitation dataset developed for hydrology is the Multi-Source Weighted-Ensemble Precipitation (MSWEP; Beck et al., 2017). The latest version of MSWEP provides a fully global historic precipitation dataset (1979–2017) with a 3-hourly temporal and 0.1° spatial resolution. The key feature of the MSWEP product is that it provides a precipitation estimate worldwide merging seven complementary precipitation estimates with three satellite remote sensing, two gauge observations and two atmospheric reanalysis datasets. For each grid cell, the weight assigned to the gauge-based estimates is calculated from the gauge network density, while the weights assigned to the satellite and reanalysis based estimates are calculated from their comparative performance at the surrounding gauges[21].

The long-term mean of MSWEP is based on Climate Hazards Group's Precipitation Climatology (CHPclim) dataset. It includes also a correction for gauge under-catch and orographic effects.

Modern-Era Retrospective Analysis for Research and Applications Version 2 (MERRA-2)

The MERRA-2 product, provided by the NASA's Global Modeling and Assimilation Office (GMAO), has a spatial resolution of 50 km, an hourly temporal resolution, and is available from 1980 to the present. Assimilation observation types (GPS-Radio, GEOS model, among others) are assimilated into MERRA-2. Data are available at the Goddard Space Flight Center[22] and detailed information concerning this product can be found in Gelaro et al. (2017).

Global Land Evaporation Amsterdam Model (GLEAM v3)

GLEAM is a set of algorithms that separately estimate the different components of land evaporation at the global scale. The eight products are: (i) transpiration, (ii) bare-soil evaporation, (iii) interception loss, (iv) open-water evaporation, (v) sublimation, (vi) surface and root-zone soil moisture, (vii) potential evaporation, and (viii) evaporative stress conditions. Basically, the algorithm, based on the Priestley and Taylor equation, uses observations of surface net radiation and near-surface air temperature to calculate the potential evaporation of the tall and short canopy and the land fractions of bare soil. Then, these potential evaporation estimates are converted into actual evaporation using a multiplicative evaporative stress factor based on observations of microwave Vegetation Optical Depth (VOD) and estimates of root-zone soil moisture. Two recent products are available at daily resolution and 25 km spatial resolution: GLEAM v3.3a (1980–2018 period) and GLEAM v3.3b (2003–2018), which are mainly based on satellite data. Some limitations are inherent to this kind of global product for mountainous regions due to the spatial resolution and the limited knowledge of the soil properties. Details concerning the data can be found in Miralles et al. (2011) and Martens et al. (2017) and data can be download on the GLEAM website[23].

PHYSIOGRAPHIC AND MORPHO-TOPOGRAPHIC DATA

Several global and open datasets are available to estimate physiographic data relevant for hydrology. Recently, land cover and land use data with a 30-meter resolution was released by the Global Land Cover Characterization (GLCC) Project. This land cover map is one of the best available open datasets. GLCC is based on 1-year Advanced Very High Resolution Radiometer (AVHRR) using an unsupervised classification. Data are available on the GISGeography webpage[24]. Simultaneously, most of the physiographic catchment characteristics can be estimated from the European Space Agency (ESA) Climate Change Initiative (CCI) program or from the NASA among others. The global databases cover the principal physical controlling factors of the hydrological cycle with land cover characteristics, soils properties, glaciers, water bodies (lakes, rivers, etc.) and flooded areas. These databases are listed in **Table 6** (non-exhaustive list).

In addition, Digital Elevation Models (DEM) are crucial in climatological and hydrological studies; they can be used to delineate the catchment limits, to determine flow routings, aspects, etc. The most common DEMs are: (i) the Global Digital Elevation Model - GDEM v2, with a resolution of 30 m; (ii) the Shuttle Radar Topographic Mission - SRTM v4 with a resolution of 90 m (Satgé et al., 2015); (iii) the JAXA's Global ALOS 3D world with a resolution of 30m; and (iv) the TanDEM-X DEM with a resolution of 12 m distributed by the German Aerospace Center DLR[3]. Since 2010, higher spatial resolution DEMs at the decimetric scale can be obtained with the Pleiades satellites. In addition, the Global Width Database for Large Rivers (GWD-LR) with a resolution of three arcseconds (Yamazaki et al., 2014) can be used for flow routing.

KNOWLEDGE GAPS AND NEXT STEPS

A recent evaluation of multiple satellite products in Chile reported that CHIRPS and MSWEP data are quite promising

TABLE 6 | Datasets available for the physiographic data estimation.

Type	Dataset/Link	Provider/References
Land cover characteristics	ESA CCI Landcover v 1.6.1 epoch 2010 (300 m) – https://www.esalandcover-cci.org/?q~=~node/169	ESA Climate Change Initiative – Land Cover project
Glaciers	Randolph Glacier Inventory (RGI) v 6.0 – https://www.glims.org/RGI/randolph60.html	RGI Consortium
Glaciers	Global Terrestrial Network for Glaciers https://www.gtn-g.ch	World Glacier Monitoring Service (WGMS), United States National Snow and Ice Data Center (NSIDC), Global Land Ice Measurements from Space (GLIMS)
Lakes	ESA CCI-LC Waterbodies 150 m 2000 v 4.0 – https://www.esalandcover-cci.org/?q~=~node/169	ESA Climate Change Initiative – Land Cover project Lakes Global Lake and Wetland Database 1.1 (GLWD) (Lehner and Döll, 2004)
Lake depths	Global Lake Database v2 (GLDB) http://www.flake.igbberlin.de/ep-data.shtml	Kourzeneva, 2010; Choulga et al., 2014
Reservoirs and dams	Global Reservoir and Dam database v 1.1 (GRanD) http://www.gwsp.org/products/grand-database.html	Lehner et al., 2011
Irrigation	GMIA v5.0	Portmann et al., 2010; Siebert et al., 2013
	http://www.fao.org/nr/water/aquastat/irrigationmap/index10.stm	
	MIRCA v1.1 http://www.unifrankfurt.de/45218031/data_download	
Geology	GLIM V1.0	Hartmann and Moosdorf, 2012
	https://www.geo.uni-hamburg.de/en/geologie/forschung/geochemie/glim.html	
Soil permeability	GLHYMPS	Gleeson et al., 2014
	http://crustalpermeability.weebly.com/glhymps.html	
Soils/Bedrock characteristics		Hengl et al., 2017
	https://soilgrids.org/	Shangguan et al., 2017
		Pelletier et al., 2016
Soil characteristics	Harmonized World Soil Database V1.2	Food and Agriculture Organization of the United Nations, FAO/IIASA/ISRIC/ISS-CAS/JRC, 2012
	http://www.fao.org/soils-portal/soil-survey/soil-maps-and-databases/harmonized-world-soil-database-v12/en/	
Water Bodies	ASTER Global Water Bodies Database	Sensor Information Laboratory Corp. (SILC) in Tokyo
	https://lpdaac.usgs.gov/products/astwbdv001/	
	https://search.earthdata.nasa.gov/search	
Flooded area	GIEMS-D3	Aires et al., 2017

when compared with other satellite-based rainfall estimates. CHIRPSv2 was found to be the best performing SRE and is recommended for use in hydrology because it has a low latency (1 day–3 weeks, depending on the product), a long data record (1981-present), and high spatial resolution (0.05°). The MSWEP also performed well, particularly in southern Chile. In contrast, an adjusted version of PERSIANN for Chile, the PERSIANN-CCS-Adj, near real-time data was considered to be less suitable for use in hydrological applications due to large biases when validated against observations. This is probably due to the fact that it has been corrected using only the regional climatology (Zambrano-Bigiarini et al., 2017). Another recent study compared and evaluated 12 different satellite-based precipitation products with gauges measurements in the central Andes (71°W–68°W/14°S–17°S) and used these products for the hydrological modeling of four mountainous catchments (Satgé et al., 2019). These authors identified CHIRP v.2, CHIRPS v.2, CMORPH-BLD v.1, MSWEP v2.1, PERSIANN-CDR, and TMPA-Adj v.7 as the best products for a good representation of the hydrological processes. This region-specific methodology could be extended to other Andean regions in order to see if the same ranking between the different products exists along the Andes. More generally, other initiatives exist, with different regional high-resolution datasets produced within the framework of research projects and experimental field campaigns (Poveda et al., 2007; Nunes, 2012).

It is still challenging to study precipitation in a mountainous context not only because of the frequency and intensity needed but also due to the partitioning between solid and liquid precipitation. It is difficult to quantify precipitation due to the complex terrain, high altitudes, large climatic gradients and both sparse and scarce data.

One way to address the complexity of spatio-temporal patterns is to use dynamical downscaling in global climate models for South America as done in the CORDEX/CLARIS project (Solman, 2013). It is also possible to use the Weather Research Forecast Model (WRF) as done in the study by Armenta-Porras and Pabón Caicedo (2016) where a data-set of meteorological and hydrological variables was produced for the northern Andes at a horizontal resolution of 10 × 10 kilometers, over 39 levels, and a 3-hourly time step. Finally this kind of Regional Climate Model can be used to describe the spatio-temporal variability of the precipitation, the orography taking into account (Trachte et al., 2018); however any biases should be corrected before using these data in hydro-glaciological models (Mourre et al., 2016). A recent atmospheric modeling framework was proposed over the Himalayas and Middle Eastern mountains at the kilometer scale and can be used to reproduce the effect of the orography on atmospheric flow (Van Niekerk et al., 2018). This kind of methodology could guide future studies at the scale of the Andes. To date, the development of precipitation products tends to combine the strengths of multiple and complementary data sources: gauge, satellite and reanalysis-based data, as well as model simulations in order to produce reliable precipitation estimates (Heredia et al., 2018). Combined products with local weather stations and TRMM data can also integrate the normalized difference vegetation index as shown by Yarleque et al. (2016) in the Peruvian Andes.

CONCLUSION AND PERSPECTIVES

Despite the asymmetries among countries and capabilities in the Andean region, there is strong evidence of increasing observational capacity and data availability. However, in several meetings of the RA III (WMO, 2018), the NMHS identified that some of the current limitations on weather and climate prediction are related with the limited understanding of the physical processes that define weather and climate in particular regions. Data availability could be increased by identifying and prioritizing scientific questions so that a sound research agenda for the region can be put into place where the NMHSs would acquire the data and sent it to the OSCAR database. Since one of the main challenges in the region is the sustainability of the observations networks and the increase in available data for applications and research, potential activities should be focused on promoting and facilitating meeting points between the operational community represented by the NMHS and the scientific community in the region. ANDEX could be a suitable opportunity to foster this approach in order to discuss all together the relevance and urgent need to address the societal needs, save lives, reduce the adverse impacts of hydrometeorological hazards and adapt to a changing climate. This is particularly challenging in the Andean region where many scientific questions are still open with the subsequent impact on prediction and early warnings limitations.

The international context provides a unique opportunity to moving forward. The new WCRP Strategic Plan 2019–2029, the recently approved WMO Strategy and the current reform in the organization aim to promote a better and more efficient interaction between the operational and research communities with a strong focus in the regions. The current Regional Climate centers operating in South America: CIIFEN/RCC-WSA and RCC-SSA are suitable infrastructures which could be used by ANDEX to work together and foster hydroclimate research. It is highly recommended to meet the operational and the research community to work together and demonstrate the relevance of ANDEX to the Governments and funding agencies. This will help maintain and enhance the NMHS's capabilities and will help obtain the necessary funding to foster research activities in this field. Considering the increasing GSM network, future efforts should be made to obtain more remote data transmission. This would be a prerequisite for near-real time forecasts in climatology and hydrology. Data on the physical processes involved in the climatological processes in mountainous regions could be improved if there were more radiosondes in the area. In addition, from a hydrological point of view, scientific programs could focus on a better understanding of groundwater and water use data as this is crucial in the hydrological cycle but is still poorly known.

NOTES

(1) OSCAR – https://www.wmo-sat.info/oscar/
(2) GSN – https://gcos.wmo.int/en/networks/atmospheric/gsn
(3) CLIMAT – https://library.wmo.int/index.php?lvl=notice_display&id=11989
(4) GPCC data – https://opendata.dwd.de/climate_environment/GPCC/html/download_gate.html
(5) University of Wyoming – http://weather.uwyo.edu/upperair/sounding.html
(6) WHOS – http://www.wmo.int/pages/prog/hwrp/chy/whos/index.php
(7) http://www.cr2.cl/bases-de-datos/
(8) GRDC – https://www.bafg.de/GRDC/EN/Home/homepage_node.html
(9) GCW – https://globalcryospherewatch.org/
(10) RCC-WSA http://crc-osa.ciifen.org
(11) CIIFEN – www.ciifen.org
(12) RCC-SSA – www.crc-sas.org/
(13) LACA&D – http://lacad.ciifen.org/
(14) PMM – https://pmm.nasa.gov/data-access/downloads/trmm
(15) CHIRPS – https://earlywarning.usgs.gov/fews/datadownloads/Global/CHIRPS%202.0
(16) PERSIAN-CDR – www.ncdc.noaa.gov/cdr/operationalcdrs.html
(17) CDR NOAA – https://www.ncdc.noaa.gov/cdr/atmospheric/precipitation-persiann-cdr
(18) Copernicus webpage – https://www.ecmwf.int/en/forecasts/datasets/browse-reanalysis-datasets

(19) PSD webpage – https://www.esrl.noaa.gov/psd/data/gridded/data.ncep.reanalysis.html
(20) University Corporation for Atmospheric Research webpage – https://rda.ucar.edu/datasets/ds628.0/
(21) Multi-Source Weighted-Ensemble Precipitation – http://www.gloh2o.org/
(22) Modern-Era Retrospective analysis for Research and Applications version 2 – https://gmao.gsfc.nasa.gov/reanalysis/MERRA-2/
(23) GLEAM v3 – https://www.gleam.eu/
(24) GISGeography webpage – https://gisgeography.com/free-global-land-cover-land-use-data/

AUTHOR CONTRIBUTIONS

RM requested station data from the NMHSs in Bolivia, Colombia, Chile, Ecuador, Peru, Venezuela, and Argentina. He also analyzed the collected data. JP helped describe the hydrological data and the hydrometeorological Andean network. FC incorporated and described the OSCAR data. FL generated the maps with GIS processing. LP, TC, and JN incorporated the satellite information and physiographic datasets used in hydrology. All of the authors helped writing the article.

FUNDING

This review paper has been achieved as part of the ANDEX program (www.gewex.org/project/andex/), which is a prospective Regional Hydroclimate Project (RHP) of the GEWEX Hydroclimatology Panel (GHP). This study was supported by the 'Centro Internacional para la Investigación del Fenómeno de El Niño,' the 'Universidad Nacional de Colombia,' the 'Universidad Yachay Tech,' the 'Escuela Politécnica Nacional,' and the French 'Institut de Recherche pour le Développement' (IRD) through the Andean part of the French glacier observatory service, GLACIOCLIM (https://glacioclim.osug.fr/spip.php?rubrique30&lang=en). It was conducted in the framework of the International Joint Laboratory GREAT-ICE, a joint initiative of the IRD and universities and institutions in Bolivia, Peru, Ecuador, and Colombia.

ACKNOWLEDGMENTS

All the contributing authors acknowledge the contribution of NMHSs of Bolivia, Chile, Colombia, Ecuador, Peru, Venezuela, and Argentina.

REFERENCES

Aguilar-Lome, J., Espinoza-Villar, R., Espinoza, J. C., Rojas-Acuña, J., Willems, B. L., and Leyva-Molina, W. M. (2019). Elevation-dependent warming of land surface temperatures in the Andes assessed using MODIS LST time series (2000-2017). *Int. J. Appl. Earth Obs. Geoinform.* 77, 119–128. doi: 10.1016/j.jag.2018.12.013

Aires, F., Miolane, L., Prigent, C., Pham, B., Fluet-Chouinard, E., Lehner, B., et al. (2017). A global dynamic long-term inundation extent dataset at high spatial resolution derived through downscaling of satellite observations. *J. Hydrometeorol.* 18, 1305–1325. doi: 10.1175/JHM-D-16-0155.1

Armenta-Porras, G. E., and Pabón Caicedo, J. D. (2016). "Producing high spatial resolution climate scenarios for tropical America using WRF model," in *Proceedings of the International Conference on Regional Climate CORDEX*-2016, Stockholm, 197.

Ashouri, H., Hsu, K. L., Sorooshian, S., Braithwaite, D. K., Knapp, K. R., Cecil, L. D., et al. (2015). PERSIANN-CDR: daily precipitation climate data record from multisatellite observations for hydrological and climate studies. *Bull Ame.Meteorol. Soc.* 96, 69–83.

Bai, L., Shi, C., Li, L., Yang, Y., and Wu, J. (2018). Accuracy of chirps satellite-rainfall products over Mainland China. *Remote Sens.* 10:362. doi: 10.3390/rs10030362

Beck, H. E., van Dijk, A. I. J. M., Levizzani, V., Schellekens, J., Miralles, D. G., Martens, B., et al. (2017). MSWEP: 3-hourly 0.25° global gridded precipitation (1979–2015) by merging gauge, satellite, and 771 reanalysis data. *Hydrol. Earth Syst. Sci.* 21, 589–615. doi: 10.5194/hess-21-589-2017

Butler, D. (2014). Earth Observation enters next phase. *Nature* 508, 160–161.

Celleri, R., Buytaert, W., De Bièvre, B., Tobón, C., Crespo, P., Molina, J., et al. (2010). "Understanding the hydrology of tropical andean ecosystems through an andean network of basins," In: *Status and Perspectives of Hydrology in Small Basins Proceedings of the Workshop held at Goslar-Hahnenklee*, Germany: IAHS Publ. 336, 209–212.

Chen, J. M., and Liu, J. (2020). Evolution of evapotranspiration models using thermal and shortwave remote sensing data. *Remote Sens. Environ.* 237:111594. doi: 10.1016/j.rse.2019.111594

Chen, L., and Wang, L. (2018). Recent advance in earth observation big data for hydrology. *Big Earth Data* 2, 86–107. doi: 10.1080/20964471.2018.1435072

Choulga, M., Kourzeneva, E., Zakharova, E., and Doganovsky, A. (2014). Estimation of the mean depth of boreal lakes for use in numerical weather prediction and climate modelling. *Tellus A: Dyn. Meteorol. Oceanogr.* 66:1. doi: 10.3402/tellusa.v66.21295

Collischonn, B., Coollischonn, W., and Tucci, C. E. M. (2008). Daily hydrological modeling in the Amazon basin using TRMM rainfall estimates. *J. Hydrol.* 360, 207–216.

Condom, T., Rau, P., and Espinoza, J. C. (2011). Correction of TRMM 3B43 monthly precipitation data over the mountainous areas of Peru during the period 1998–2007. *Hydrol. Process.* 25, 1924–1933.

Cunha, J., Pereira, T. E., Pereira, E., Rufino, I., Galvão, C., Valente, F., et al. (2020). A high-throughput shared service to estimate evapotranspiration using Landsat imagery. *Comput. Geosci.* 134. doi: 10.1016/j.cageo.2019.104341

Derin, Y., and Yilmaz, K. K. (2014). Evaluation of multiple satellite-based precipitation products over complex topography. *J. Hydrometeorol.* 15, 1498–1516.

Erazo, B., Bourrel, L., Frappart, F., Chimbrazo, O., Labat, D., Dominguez-Granda, L., et al. (2018). Validation of satellite estimates (tropical rainfall measuring mission, TRMM) for rainfall variability over the pacific slope and coast of ecuador. *Water* 10:213. doi: 10.3390/w10020213

FAO/IIASA/ISRIC/ISS-CAS/JRC (2012). *Harmonized World Soil Database (version 1.2)*. Rome: FAO.

Foster, J. L., Hall, D. K., Kelly, R. E. J., and Chiu, L. (2009). Seasonal snow extent and snow mass in South America using SMMR and SSM/I passive microwave data (1979–2006). *Remote Sens. Environ.* 113, 291–305. doi: 10.1016/j.rse.2008.09.010

Funk, C., Peterson, P., Landsfeld, M., Pedreros, D., Verdin, J., Shukla, S., et al. (2015). The climate hazards infrared precipitation with stations—a new environmental record for monitoring extremes. *Sci. Data* 2:150066. doi: 10.1038/sdata.2015.66

Garreaud, R. D., Vuille, M., Compagnucci, R., and Marengo, J. (2009). Present-day South American climate. *Palaeogeogr. Palaeoclimatol. Palaeoecol.* 281, 180–195.

Gelaro, R., McCarty, W., Suárez, M. J., Todling, R., Molod, A., Takacs, L., et al. (2017). The modern-era retrospective analysis for research and applications, version 2 (MERRA-2). *J. Clim.* 30, 5419–5454.

Gleeson, T., Moosdorf, N., Hartmann, J., and van Beek, L. P. H. (2014). A glimpse beneath earth's surface: global hydrogeology MaPS (GLHYMPS) of permeability and porosity. *Geophys. Res. Lett.* 41:GL059856. doi: 10.1002/2014gl059856pdf

Hartmann, J., and Moosdorf, N. (2012). The new global lithological map database GLiM: a representation of rock properties at the Earth surface. *Geochem. Geophys. Geosys.* 13:Q12004. doi: 10.1029/2012GC004370

Hengl, T., Mendes, de Jesus, J., Heuvelink, G. B. M., Ruiperez Gonzalez, M., Kilibarda, M., et al. (2017). SoilGrids250m: global gridded soil information based on machine learning. *PLoS One* 12:e0169748. doi: 10.1371/journal.pone.0169748

Heredia, M. B., Junquas, C., Prieur, C., and Condom, T. (2018). New Statistical Methodologies of precipitation bias correction applied to WRF model simulations in the antisana region (Ecuador). *J. Hydrometeorol.* 19, 2021–2040. doi: 10.1175/JHM-D-18-0032.1

Hobouchian, M. P., Salio, P., Skabar, Y. G., Vila, D., and Garreaud, R. (2017). Assessment of satellite precipitation estimates over the slopes of the subtropical Andes. *Atmosph. Res.* 190, 43–54. doi: 10.1016/j.atmosres.2017.02.006

Huete, A., Didan, K., Miura, T., Rodriguez, E. P., Gao, X., and Ferreira, L. G. (2002). Overview of the radiometric and biophysical performance of the MODIS vegetation índices. *Remote Sens. Environ.* 83, 195–213.

Huffman, G. J., Bolvin, D. T., Nelkin, E. J., Wolff, D. B., Adler, R. F., Gu, G., et al. (2007). The TRMM Multisatellite Precipitation Analysis (TMPA): quasi-global, multiyear, combined-sensor precipitation estimates at fine scales. *J. Hydrometeorol.* 8, 38–55.

Joyce, R., Janowiak, J. E., Arkin, P. A., and Xie, P. (2004). CMORPH : a method that produces global precipitation estimates from passive microwave and infrared data at high spatial and temporal resolution. *J. Hydrometeorol.* 5, 487–503. doi: 10.1175/1525-7541(2004)005<0487:CAMTPG>2.0.CO;2

Khaki, M., and Awange, J. (2019). Improved remotely sensed satellite products for studying Lake Victoria's water storage changes. *Sci. Total Environ.* 652, 915–926. doi: 10.1016/j.scitotenv.2018.10.279

Kidd, C., and Levizzani, V. (2019). "Chapter one – quantitative estimation from satellite observations, book chapter," in *Extreme Hydroclimatic Events and Multivariate Hazards in a Changing Environment*, eds V. Maggioni and C. Massari (Amsterdam: Elsevier), 3–19.

Kobayashi, S., Ota, Y., Harada, Y., Ebita, A., Moriya, M., Onoda, H., et al. (2015). The JRA-55 reanalysis: general specifications and basic characteristics. *J. Met. Soc. Jap.* 93, 5–48. doi: 10.2151/jmsj.2015-001

Kourzeneva, E. (2010). External data for lake parameterization in numerical weather prediction and climate modeling. *Boreal Environ. Res.* 15, 165–177.

Kulie, M. S., Milani, L., Wood, N. B., Tushaus, S. A., Bennartz, R., and L'Ecuyer, T. S. (2016). A shallow cumuliform snowfall census using spaceborne radar. *J. Hydrometeor.* 17, 1261–1279. doi: 10.1175/JHM-D-15-0123.1

Laloyaux, P., de Boisseson, E., Balmaseda, M., Bidlot, J., Broennimann, S., Buizza, R., et al. (2018). CERA-20C: a coupled reanalysis of the twentieth century. *J. Adv. Model. Earth Syst.* 10, 1172–1195. doi: 10.1029/2018MS001273

Lehner, B., and Döll, P. (2004). Development and validation of a global database of lakes, reservoirs and 879 wetlands. *J. Hydrol.* 296, 1–22. doi: 10.1016/j.jhydrol.2004.03.028

Lehner, B., Reidy Liermann, C., Revenga, C., Vorosmarty, C., Fekete, B., Crouzet, P., et al. (2011). *Global Reservoir and Dam Database, Version 1 (GRanDv1): Dams, Revision 01*. Palisades, NY: NASA Socioeconomic Data and Applications Center (SEDAC). Available online at: https://doi.org/10.7927/H4N877QK

Li, Z., Tang, H., Wu, H., Ren, H., Yan, G., Wan, Z., et al. (2013). Satellite derived land surface temperature: current status and perspectives. *Remote Sens. Environ.* 131, 14–37.

López, S., Wright, C., and Costanza, P. (2017). Environmental change in the equatorial Andes: linking climate, land use, and land cover transformations. *Remote Sens., Appl. Soc. Environ.* 8, 291–303. doi: 10.1016/j.rsase.2016.11.001

Malmros, J. K., Mernild, S. H., Wilson, R., Tagesson, T., and Fensholt, R. (2018). Snow cover and snow albedo changes in the central andes of chile and argentina from daily MODIS observations (2000–2016). *Remote Sens. Environ.* 209, 240–252. doi: 10.1016/j.rse.2018.02.072

Manz, B., Páez-Bimos, S., Horna, N., Buytaert, W., Ochoa-Tocachi, B., Lavado-Casimiro, W., et al. (2017). Comparative ground validation of IMERG and TMPA at variable spatiotemporal scales in the tropical andes. *J. Hydrometeor.* 18, 2469–2489. doi: 10.1175/JHM-D-16-0277.1

Mao, K. B., Ma, Y., Tan, X. A., Shen, X. Y., Liu, G., Li, Z. L., et al. (2017). Global surface temperature change analysis based on MODIS data in recent twelve years. *Adv. Space Res.* 59, 503–512.

Martens, B., Miralles, D. G., Lievens, H., van der Schalie, R., de Jeu, R. A. M., Fernández-Prieto, D., et al. (2017). GLEAM v3: satellite-based land evaporation and root-zone soil moisture. *Geosci. Model Dev.* 10, 1903–1925. doi: 10.5194/gmd-10-1903-2017

McCabe, M. F., Rodell, M., Alsdorf, D. E., Miralles, D. G., Uijlenhoet, R., Wagner, W., et al. (2017). The future of Earth observation in hydrology. *Hydrol. Earth Syst. Sci.* 21, 3879–3914. doi: 10.5194/hess-21-3879-2017

Miralles, D. G., Holmes, T. R. H., de Jeu, R. A. M., Gash, J. H., Meesters, A. G. C. A., and Dolman, A. J. (2011). Global land-surface evaporation estimated from satellite-based observations. *Hydrol. Earth Syst. Sci.* 15, 453–469. doi: 10.5194/hess-15-45.

Mourre, L., Condom, T., Junquas, C., Lebel, T., Sicart, J.-E., Figueroa, R., et al. (2016). Spatio-temporal assessment of WRF, TRMM and in situ precipitation data in a tropical mountain environment (Cordillera Blanca, Peru). *Hydrol. Earth Syst. Sci.* 20, 125–141.

Ndehedehe, C. E., and Ferreira, V. G. (2020). Assessing land water storage dynamics over South America. *J. Hydrol.* 580:124339. doi: 10.1016/j.jhydrol.2019.124339

Nijzink, R. C., Almeida, S., Pechlivanidis, I. G., Capell, R., Gustafssons, D., Arheimer, B., et al. (2018). Constraining conceptuel hydrological models with multiple information sources. *Water Ressour. Res.* 54, 8332–8362. doi: 10.1029/2017WR021895

Nunes, A. (2012). *Regional Reanalysis for Climate Research Applications: South American Hydroclimate Reconstruction*. Geneva: Gewex News.

Ochoa, A., Pineda, L., Crespo, P., and Willems, P. (2014). Evaluation of TRMM 3B42 precipitation estimates and WRF retrospective precipitation simulation over the Pacific–Andean region of Ecuador and Peru. *Hydrol. Earth Syst. Sci.* 18, 3179–3193. doi: 10.5194/hess-18-3179-2014

Ochoa-Tocachi, B. F., Buytaert, W., Antiporta, J., Acosta, L., Bardales, J. D., Célleri, R., et al. (2018). High-resolution hydrometeorological data from a network of headwater catchments in the tropical Andes. *Sci. Data* 5:180080. doi: 10.1038/sdata.2018.80

Ochoa-Tocachi, B. F., Buytaert, W., and De Bièvre, B. (2017). "Chapter 6: participatory monitoring of the impact of watershed interventions in the tropical andes," in *Andean Hydrology*, eds D. A. Rivera, A. Godoy-Faundez, and M. Lillo Saavedra (Taylor: CRC Press), 126–163.

Olivera-Guerra, L., Merlin, O., and Er-Raki, S. (2020). Irrigation retrieval from Landsat optical/thermal data integrated into a crop water balance model: a case study over winter wheat fields in a semi-arid region. *Remote Sens. Environ.* 239:111627. doi: 10.1016/j.rse.2019.111627.b

Palomino-Angel, S., Anaya-Acevedo, J. A., and Botero, B. A. (2019). Evaluation of 3B42V7 and IMERG daily-precipitation products for a very high-precipitation region in northwestern South America. *Atmos. Res.* 217, 37–48. doi: 10.1016/j.atmosres.2018.10.012

Parker, W. S. (2016). Reanalysis and observations: what's the difference? *Am. Met. Soc.* 97, 1565–1572. doi: 10.1175/BAMS-D-14-00226.1

Pelletier, J. D., Broxton, P. D., Hazenberg, P., Zeng, X., Troch, P. A., Niu, G. Y., et al. (2016). A gridded global data set of soil, immobile regolith, and sedimentary deposit thicknesses for regional and global land surface modeling. *J. Adva. Model., Earth Sys.* 8, 41–65.

Perry, B., Seimon, A., and Kelly, G. M. (2014). Precipitation delivery in the tropical high Andes of southern Peru: new findings and paleoclimatic implications. *Inte. J. Climatol.* 34, 197–215.

Portmann, F. T., Siebert, S., and Döll, P. (2010). MIRCA2000 – Global monthly irrigated and rainfed 925 crop areas around the year 2000: a new high-resolution data set for agricultural and hydrological 926 modeling. *Global. Bio. Cycles* 24:GB1011.

Poveda, G., Mesa, O. J., Vélez, J. I, Mantilla, L., Ramirez, J. L., Hernández, O. O., et al. (2007). HidroSIG: an interactive digital atlas of Colombia's hydroclimatology. *J. Hydroinform.* 9, 145–156.

Saavedra, F. A., Kampf, S. K., Fassnacht, S. R., and Sibold, J. S. (2018). Changes in andes snow cover from MODIS data, 2000–2016. *Cryosphere* 12, 1027–1046.

Salazar, A., Baldi, G., Hirota, M., Syktus, J., and McAlpine, C. (2015). Land use and land cover change impacts on the regional climate of non-Amazonian South America: a review. *Global Planet. Change* 128, 103–119. doi: 10.1016/j.gloplacha.2015.02.009

Sarricolea, P., Herrera-Ossandon, M., and Meseguer-Ruiz, O. (2017). Climatic regionalisation of continental Chile. *J. Maps* 13, 66–73. doi: 10.1080/17445647.2016.1259592

Satgé, F., Bonnet, M. P., Timouk, F., Calmant, S., Pillco, R., Molina, J., et al. (2015). Accuracy assessment of SRTM v4 and ASTER GDEM v2 over the Altiplano watershed using ICESat/GLAS data. *Int. J. Remote Sens.* 36, 465–488. doi: 10.1080/01431161.2014.999166

Satgé, F., Ruelland, D., Bonnet, M. P., Molina, J., and Pillco, R. (2019). Consistency of satellite-based precipitation products in space and over time compared with gauge observations and snow-hydrological modelling in the Lake Titicaca region. *Hydrol. Earth Syst. Sci.* 23, 595–619. doi: 10.5194/hess-23-595-2019

Schneider, U., Andreas, B., Peter, F., Anja, M.-C., Bruno, R., et al. (2011). *GPCC Full Data Reanalysis Version 6.0 at 0.5°: Monthly Land-Surface Precipitation From Rain-Gauges Built on GTS-Based and Historic Data.* Silver Spring, MA: NOAA.

Segura, H., Junquas, C., Espinoza, J. C., Vuille, M., Jauregui, Y., Rabatel, A., et al. (2019). New insights into the rainfall variability in the tropical Andes on seasonal and interannual time scales. *Clim. Dyn.* 53, 405–426. doi: 10.1007/s00382-018-4590-8

Shangguan, W., Hengl, T., de Jesus, J. M., Yuan, H., and Dai, Y. (2017). Mapping the global depth to bedrock for land surface modeling. *J. Adv. Model. Earth Syst.* 9, 65–88.

Siebert, S., Henrich, V., Frenken, K., and Burke, J. (2013). *Global Map of Irrigation Areas Version 5. Rheinische 944*. Bonn: Friedrich-Wilhelms-University.

Skofronick-Jackson, G., Kulie, M., Milani, L., Munchak, S. J., Wood, N. B., and Levizzani, V. (2019). Satellite estimation of falling snow: a global precipitation measurement (GPM) core observatory perspective. *J. Appl. Meteor. Climatol.* 58, 1429–1448. doi: 10.1175/JAMC-D-18-0124.1

Snapir, B., Momblanch, A., Jain, S. K., Waine, T. W., and Holman, I. P. (2019). A method for monthly mapping of wet and dry snow using Sentinel-1 and MODIS: application to a Himalayan river basin. *Int. J. Appl. Earth Observ. Geoinform.* 74, 222–230. doi: 10.1016/j.jag.2018.09.011

Solman, S. S. (2013). Regional climate modeling over south america: a review. *Adv. Meteorol.* 2013, 504357. doi: 10.1155/2013/504357

Sorooshian, S., Hsu, K. L., Gao, X., Gupta, H. V., Imam, B., et al. (2000). *Evaluation of PERSIANN System Satellite-Based Estimates of Tropical Rainfall. Bulletin of the*. American Meteorological Society, 81.

Sun, Q., Miao, C., Duan, Q., Ashouri, H., Sorooshian, S., and Hsu, K.-L. (2018). A review of global precipitation data sets: data sources, estimation, and intercomparisons. *Rev. Geophys.* 56, 79–107. doi: 10.1002/2017RG000574

Trachte, K., Seidel, J., Figueroa, R., Otto, M., and Bendix, J. (2018). Cross-scale precipitation variability in a semiarid catchment area on the western slopes of the central andes. *J. Appl. Meteorol. Climatol.* 57, 675–694. doi: 10.1175/JAMC-D-17-0207.1

Tucker, C. J., Pinzon, J. E., Brown, M. E., Slayback, D. A., Pak, E. W., Mahoney, R., et al. (2005). An extended AVHRR 8-km NDVI dataset compatible with MODIS and SPOT vegetation NDVI data. *Int. J. Remote Sens.* 26, 4485–4498.

Van den Hurk, B. (2012). *Reanalysis and Their Applicability for Climate Research*. Geneva: Gewex News.

Van Niekerk, A., Sandu, I., and Vosper, S. (2018). The circulation response to resolved versus parametrized orographic drag over complex mountain terrains. *J. Adv. Model. Earth Syst.* 10, 2527–2547. doi: 10.1029/2018MS001417

WMO (2007). *Guide to the Global Observing System. WMO-No. 488*, 3rd Edn. Geneva: WMO, 170.

WMO (2010). *Manual on the Global Telecommunication System. Annex III to the WMO Technical Regulations. WMO-No*. Geneva: WMO, 386.

WMO (2014). *Updated in 2017, guide to meteorological instruments and methods of observation. WMO-No. 8* Geneva: WMO, 1177.

WMO (2017). *Guide to the WMO Integrated Global Observing System. WMO-No*. Geneva: WMO., 1165.

WMO (2018). *Regional Association III (South America): Abridged Final Report of the Seventeenth Session. WMO-No*. Geneva: WMO, 1128.

Yamazaki, D., O'Loughlin, F., Trigg, M. A., Miller, Z. F., Pavelsky, T. M., and Bates, P. D. (2014). Development of the global width database for large rivers. *Water Resour. Res.* 50, 3467–3480. doi: 10.1002/2013WR014664

Yarleque, C., Vuille, M., Hardy, D. R., Posadas, A., and Quroz, R. (2016). Multiscale assessment of spatial precipitation variability over complex mountain terrain using high-resolution spatiotemporal wavelet reconstruction method. *J. Geophys. Res. Atmos.* 121, 198–112. doi: 10.1002/2016JD025647

You, Y., Wang, N. Y., Ferraro, R., and Rudlosky, S. (2017). Quantifying the snowfall detection performance of the global precipitation measurement (GPM) microwave imager channels over land. *J. Hydrometeorol.* 18, 729–751. doi: 10.1175/JHM-D-16-0190.1

Zambrano-Bigiarini, M., Nauditt, A., Birkel, C., Verbist, K., and Ribbe, L. (2017). Temporal and spatial evaluation of satellite-based rainfall estimates across the complex topographical and climatic gradients of Chile. *Hydrol. Earth Syst. Sci.* 21, 1295–1320. doi: 10.5194/hess-21-1295-2017

Zhang, K., Kimball, J. S., and Running, S. W. (2016a). A review of remote sensing based actual evapotranspiration estimation. *Wiley Interdiscip. Rev. Water* 3, 834–853. doi: 10.1002/wat2.1168

Zhang, H., Zhang, F., Zhang, G., He, X., and Tian, L. (2016b). Evaluation of cloud effects on air temperature estimation using MODIS LST based on ground measurements over the Tibetan Plateau. *Atmos. Chem. Phys.* 16, 13681–13696.

Zou, J., Ding, J., Welp, M., Huang, S., and Liu, B. (2020). Using MODIS data to analyse the ecosystem water use efficiency spatial-temporal variations across Central Asia from 2000 to 2014. *Environ. Res.* 182:108985. doi: 10.1016/j.envres.2019.108985

Zulkafli, Z., Buytaert, W., Onof, C., Manz, B., Tarnavsky, E., Lavado, W., et al. (2014). A comparative performance analysis of TRMM 3B42 (TMPA) versions 6 and 7 for applications over andean–amazon river basins. *Am. Meterolo. Soc.* 15, 581–592.

Conflict of Interest: The authors declare that the research was conducted in the absence of any commercial or financial relationships that could be construed as a potential conflict of interest.

Copyright © 2020 Condom, Martínez, Pabón, Costa, Pineda, Nieto, López and Villacis. This is an open-access article distributed under the terms of the Creative Commons Attribution License (CC BY). The use, distribution or reproduction in other forums is permitted, provided the original author(s) and the copyright owner(s) are credited and that the original publication in this journal is cited, in accordance with accepted academic practice. No use, distribution or reproduction is permitted which does not comply with these terms.

frontiers in Earth Science

ORIGINAL RESEARCH
published: 12 May 2020
doi: 10.3389/feart.2020.00136

Detecting the Effects of Sustained Glacier Wastage on Streamflow in Variably Glacierized Catchments

R. D. Moore[1]*, *Ben Pelto*[2], *Brian Menounos*[2] and *David Hutchinson*[3]

[1] Department of Geography, University of British Columbia, Vancouver, BC, Canada, [2] Geography Program and Natural Resources and Environmental Studies Institute, Prince George, BC, Canada, [3] Environment and Climate Change Canada, Vancouver, QC, Canada

This study focused on the effects of glacier wastage on streamflow in the Canadian portion of the Columbia River headwaters over the period 1977 to 2017. Between 1985 and 2013, glacier coverage decreased by up to 2% of catchment area for the 35 study catchments. The mean wastage flux contribution to streamflow had a positive relation with fractional glacier coverage and an inverse relation with catchment water yield. Glacier mass change estimates suggest that wastage flux contributions declined between 1985–1999 and 2000–2018, but the estimates are subject to substantial uncertainty. Annual wastage flux contributions over a four-year period for two study catchments ranged from 8 to 13% of annual water yield for a catchment with 17% glacier cover, with glaciers extending below treeline, and 9–19% for a smaller alpine catchment with 57% glacier cover. After accounting statistically for climatic forcing and non-glacial contributions to streamflow, August runoff from glacierized catchments decreased through time at a rate that was linearly related to loss of glacier cover. The analyses suggest that glacier-melt contributions to August runoff have already have passed peak water, and that these reductions have exacerbated a regional climate-driven trend to decreased August streamflow contributions from unglacierized areas.

Keywords: glacier retreat, glacier cover, streamflow, peak water, trend analysis, Columbia River

OPEN ACCESS

Edited by:
Bryan G. Mark,
The Ohio State University,
United States

Reviewed by:
Matthias Huss,
ETH Zürich, Switzerland
Feiteng Wang,
Chinese Academy of Sciences, China

***Correspondence:**
R. D. Moore
dan.moore@ubc.ca

Specialty section:
This article was submitted to Hydrosphere, a section of the journal Frontiers in Earth Science

Received: *24 October 2019*
Accepted: *14 April 2020*
Published: *12 May 2020*

Citation:
Moore RD, Pelto B, Menounos B and Hutchinson D (2020) Detecting the Effects of Sustained Glacier Wastage on Streamflow in Variably Glacierized Catchments. Front. Earth Sci. 8:136. doi: 10.3389/feart.2020.00136

1. INTRODUCTION

Glaciers make significant contributions to streamflow and water resources in many parts of the world (Barnett et al., 2005; Kaser et al., 2010). Contributions of glaciers to streamflow are particularly important during periods of warm, dry weather, and have been detected even for glacier cover as low as about 1 or 2% (Stahl and Moore, 2006; Huss, 2011). Glaciers in many regions are experiencing sustained negative mass balance conditions, which are expressed to varying degrees by thinning and/or terminal retreat (Zemp et al., 2015; IPCC, 2019), and the hydrological consequences are of interest for both scientific and practical reasons.

It is generally accepted that glacier contributions to streamflow in the presence of climatic warming should follow a trajectory that begins with an initially increasing phase associated with rising snowlines and loss of firn, with streamflow eventually peaking and then declining as glaciers retreat either until they disappear or reach a new glacio-climatic equilibrium (Jansson et al., 2003; Moore et al., 2009; Baraer et al., 2012). An important question relates to the duration of the various phases, particularly when using historical hydrological records to plan for future land use, water allocation or infrastructure development. Based on a review of 15 studies from around the world, Casassa et al. (2009) observed that increasing trends tended to be found in high-elevation

catchments or those with high glacier coverage, while decreasing trends tended to be found in low-elevation catchments or those with low glacier coverage. In simulations using future climate projections, Huss and Hock (2018) found that peak water occurs later in basins with larger glaciers and higher ice-cover fractions. Carnahan et al. (2019) developed a numerical model using idealized glacier geometry and climatic forcing to explore the time scale of the peak water cycle, including the effect of vegetation succession on deglaciated forelands. Their study suggests that the duration of the rising phase can last from a few decades to over a century and scales with glacier response time, which they found to vary with climatic conditions and basin slope.

The modeling domains of Huss and Hock (2018) and Carnahan et al. (2019) focused on the drainage area associated with the outlet of the glacier at the start of the simulation period, although their simulations did include the effects of runoff generation from the deglaciated areas exposed by glacier retreat. However, neither study explored how glacier changes, in conjunction with trends in streamflow production from pre-existing non-glacier areas, would be expressed as streamflow variability at the outlets of partially glacierized catchments.

Recent studies that applied detailed process-based numerical models with dynamic glacier routines and realistic boundary conditions (e.g., vegetation, topography, and atmospheric forcing) to partially glacierized catchments suggest that the response of streamflow to climate-forced glacier changes may be more complex than the simplified "peak water cycle" outlined by Jansson et al. (2003) and Moore et al. (2009). Frans et al. (2016) and Frans et al. (2018) demonstrated that decadal-scale climatic variability can generate secondary cycles superimposed on that generated by a longer-term climatic trend. They also demonstrated that there can be substantial variation among catchments within a region.

Model-based approaches, such as applied by Frans et al. (2018), explicitly resolve effects of both glacier retreat and trends in streamflow production from unglacierized parts of a catchment. However, they involve substantial investments in time and expert resources, and are also subject to a range of uncertainties related to model structure, model parameterization, and input data. Unfortunately, due to the significant computing time required to run process-based, spatially distributed models, it is not feasible to conduct comprehensive multi-objective testing and uncertainty analyses as is possible with simpler models (Schaefli and Huss, 2011; Jost et al., 2012; Finger et al., 2015).

While empirical approaches may be, in some ways, easier to apply than model-based analyses for studying the glacier-driven peak water cycle, a complication in trying to use empirical approaches is that measured streamflow represents the integrated contributions from both the glaciers and the unglacierized portions of a catchment. While it is possible to separate these contributions using tracers, as done by Nolin et al. (2010), such information is not widely available, especially for regional scales and multi-decadal time series. Another complication with empirical studies is that trends associated with glacier changes can be confounded by trends in climatic forcing. Therefore, any interpretation of empirical trend analyses must explicitly address both these sources of variability.

The objective of this study was to determine the current status of streamflow trends in glacier-fed catchments in the Canadian portion of the Columbia River headwaters, which have glacier-cover fractions from 0 to almost 0.2, and which have experienced widespread glacier retreat over the last four decades (Bolch et al., 2010). This study uses a regional statistical approach to gain insights into the effect of glacier changes relative to the effects of streamflow contributions from the unglacierized portions of the catchments. However, unlike the regional studies by Fleming et al. (2006) and Stahl and Moore (2006), who only drew upon streamflow and climatic data, we also draw upon information on glacier area and mass changes during the study period to help inform the interpretation of streamflow trends.

2. DATA AND METHODS

2.1. Study Area

This study focused on the Canadian portion of the upper Columbia River basin, located in southeastern British Columbia, Canada (**Figure 1**). The topography of the Columbia River headwaters is dominated by the Columbia Mountains, which comprise the Monashee, Selkirk, and Purcell Mountains (in order from west to east), with the western slope of the Rocky Mountains defining the eastern boundary. Elevations range from below 1,000 m above sea level (masl) in the main valley bottoms to over 3,000 masl on the mountain peaks.

The regional climate is dominated in autumn and winter by the passage of frontal-cyclonic weather systems that travel eastward across the north Pacific before traversing southern BC. In summer, anticyclonic systems tend to dominate, leading to extended spells of clear, dry weather (Moore et al., 2010). The mountain chains are oriented roughly perpendicular to the dominant westerly circulation. The Monashees, Selkirks, and the west slope of the Purcells are dominated by cool to cold, moderately wet winters and warm, moderately dry summers (Chilton, 1981). The east slope of the Purcells and the Rocky Mountains tend to be drier with colder winters than the western part of the catchment.

Based on outlines from 2005, there were 2,078 glaciers in the Columbia River basin covering 1,750 km^2 (Bolch et al., 2010). These glaciers ranged from 1,300 to 3,140 m a.s.l. with a mean elevation range of 2,290–2,700 m a.s.l. Glacier areas ranged from the minimum mapped area of 0.05 km^2 to a maximum of 44 km^2, with an average of 0.84 km^2. Using the ice thickness estimates of Farinotti et al. (2019), estimated ice volume for year 2000 in the upper Columbia River basin was 103 km^3.

The dominant vegetation cover is coniferous forest that extends up to about 1,800 masl. Forest cover characteristics reflect the effects of disturbances associated with mining and forest harvesting, which extend back over a century, as well as fires and, over the last two decades, mortality associated with Mountain Pine Beetle.

2.2. Streamflow Data

This study was based on records of streamflow at gauges operated by the Water Survey of Canada (WSC), which were obtained through Environment and Climate Change Canada's National Water Archive (Environment Climate Change

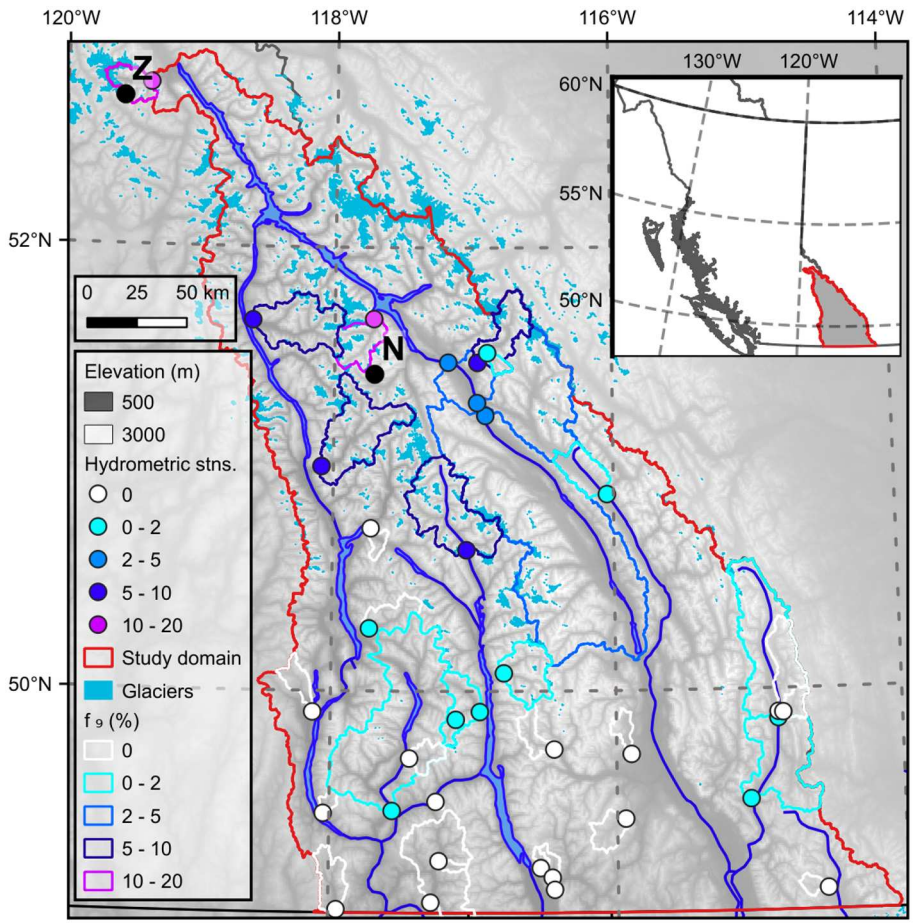


FIGURE 1 | The study area showing hydrometric stations used in this analysis, including gauge locations and associated catchment divides along with major rivers, lakes, and reservoirs (blue lines and polygons), glaciers (blue filled polygons), and the boundary of the study domain (red polygon). Symbols for gauging station locations and catchment divides are colour-coded based on the percent glacier cover in the catchment. The inset map shows the study area located within British Columbia, Canada. The letters "Z" and "N" indicate the locations of Zillmer Glacier (within the Canoe River catchment) and Nordic Glacier.

Canada, 2018). Hydrometric data were accessed using the R package **tidyhydat**.

Analyses focused on the period from 1977 to present to avoid potential complications associated with the 1976–1977 shift in the Pacific Decadal Oscillation, which influenced streamflow throughout western North America (Whitfield et al., 2010). The period from 1977 to present has been dominated by persistently negative mass balance throughout western North America (Moore et al., 2009; Naz et al., 2014; Pelto, 2018; O'Neel et al., 2019). Use of a common period of record within a region helps to ensure that all catchments experienced similar climatic variability.

Stations were selected from the WSC network based on the following criteria: (1) currently active, (2) established prior to 1977, (3) unregulated flow, (4) drainage area less than 10,000 km^2, and (5) at least 36 years of record from 1977 to present to maximize statistical power and ensure the stations represent a common period of record. In addition, this record length permits the application of multiple regression models with three predictor variables. A total of n = 35 stations met all the criteria (**Figure 1**).

The subset of hydrometric gauges selected for analysis monitor varying contributions from glaciers, from non-glacierized to a maximum of 19% glacier cover in 1985 (for Canoe River, WSC station number 08NC004) (**Figure 2**). Generally, gauges on non-glacierized catchments are located in the southwestern portion of the Columbia Basin and have lower median elevations (**Figures 1**, **2**). Catchments with glacier cover are generally greater than 100 km^2 in area and have median elevations above 1,600 masl (**Figure 2**). Further information on the catchments is provided in the file "cbt_metadata.xlsx," which has been posted on the zenodo.org repository (see data availability statement for the URL).

2.3. Climate Data

Time series of monthly mean air temperature and total monthly precipitation for each gauging station were extracted from the ClimateWNA application for locations corresponding to the

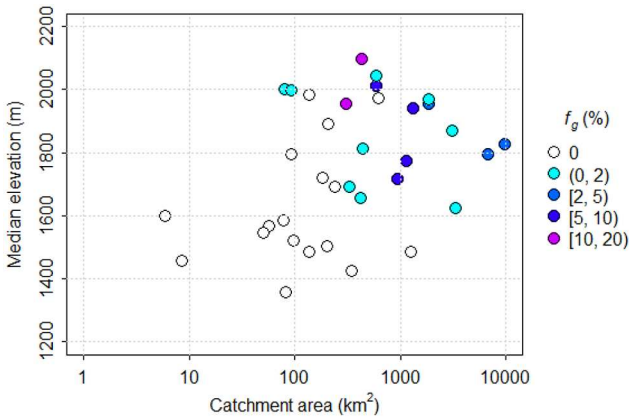


FIGURE 2 | Scatterplot of median catchment elevation vs. drainage area for the subset of catchments used in this analysis. Symbol color indicates catchment glacier cover.

gauging stations (Hamann et al., 2013). ClimateWNA is based on the PRISM gridded climate product (Daley et al., 2008), and can generate monthly time series for 1899 to near present for air temperature, precipitation, and several derived variables for specified point locations via interpolation from the baseline grid. Because these values were used only as indices of the interannual variability of climatic conditions rather than as representative values for the catchment area, it was deemed not necessary to correct for elevation differences.

2.4. Glacier Extent

The earliest glacier extents and elevations used in this analysis were based on photogrammetric analysis by the BC Government through the Terrain Resource Information Management (TRIM) program (Schiefer et al., 2007). The aerial photographs spanned the period 1982–1988, with a median date weighted by mapped area of 1985. Bolch et al. (2010) corrected these glacier polygons for gross errors and used them with additional polygons derived from Landsat imagery to yield glacier extents for the period 1985 and 2005. We updated extents determined by Bolch et al. (2010) using the same methods (ratio of Landsat bands 5 and 7). The uncertainties will be similar to those described in Bolch et al. (2010).

Fractional glacier cover within the study catchments was calculated by intersecting the glacier polygons with catchment polygons, which were accessed via Government of Canada (2019). All spatial analyses were conducted within R using the **raster** and **sf** packages. In some of the analyses described below, we used an approximate mean glacier cover over the period, computed as the average of the values for 1985 and 2013.

2.5. Glacier Mass Change

Glacier mass change for gauged catchments within the Columbia River headwaters was derived through differencing of sequential digital elevation models (DEMs) for two periods, 1985–1999 and 2000–2018. For both periods, height changes were converted to mass changes per unit area by multiplying by an assumed glacier density of 850 kg·m^{-3} (Huss, 2013).

For the 2000–2018, we used repeat stereo imagery from the Advanced Spaceborne Thermal Emission and Reflection Radiometer (ASTER) visible and near infrared instrument for the period of 2000–2018 and trend analyses from them (Menounos et al., 2019). For 1985–1999, we used results derived by Schiefer et al. (2007). For 1985, Schiefer et al. (2007) used the TRIM DEM, which was derived from aerial photography with a horizontal resolution of 25 m. The reported horizontal and vertical accuracies of TRIM elevation data are ± 10 and ± 5 m, respectively (British Columbia Ministry of Environment, Land and Parks, 1992). For 1999, Schiefer et al. (2007) used the Shuttle Radar Topography Mission (SRTM) DEM. As described in Schiefer et al. (2007), the SRTM DEM likely reflects the elevation of the glaciers at the end of the 1999 ablation season. Height changes derived by Schiefer et al. (2007) were converted to mass changes per unit area by multiplying by an assumed glacier density of 850 kg·m^{-3} (Huss, 2013).

Radar penetration associated with the STRM DEM could cause an overestimate in mass loss from the 1985 to 1999 period estimated by Schiefer et al. (2007), as penetration up to 10 m may have occurred in the accumulation zones (Rignot et al., 2001). Schiefer et al. (2007) bias-corrected the SRTM elevations by removing elevation trends off glaciers, but there remains the possibility that some positive bias exists in the estimates of mass loss in regions of substantial radar penetration.

Annual geodetic balance for the Nordic Creek and Canoe River catchments was calculated from 2015 to 2018 using coregistered late summer DEMs derived from Lidar and distributed estimates of density based on surface classification of ice, snow, and firn surfaces. See Pelto et al. (2019) for details of the methods.

2.6. Wastage Flux Contribution to Streamflow

When glaciers experience a net mass loss at the catchment scale, the lost glacier storage represents a net contribution to catchment outflow. Some of this glacier wastage may be lost to evaporation (e.g., from lakes downstream of the glaciers), and some may exit a catchment as groundwater. If evaporation of glacial meltwater and losses via groundwater are negligible, then the wastage flux contribution to streamflow, Q_{wf}, can be assumed to equal $-\Delta S_g$, where ΔS_g is the net mass change from glaciers over some time interval. When viewed as a streamflow contribution, ΔS_g is commonly expressed as an average depth of water over the catchment area.

Wastage flux contributions were computed from glacier storage changes determined for the periods 1985–1999 and 2000–2018, as described in the preceding section. The value of the wastage flux contribution to streamflow for each catchment was then converted to a fraction of the total outflow from the catchment for each period, Q, computed from streamflow data and expressed as an average depth of water.

To explore the interannual variability of wastage flux contributions, they were also calculated on an annual time step

TABLE 1 | Catchment characteristics for Canoe River and Nordic Creek, including Water Survey of Canada station number, catchment area, fractional glacier coverage and the minimum (z_0), median (z_{50}) and maximum (z_{100}) elevations.

Catchment	WSC ID	A (km^2)	f_g (1985)	f_g (2005)	f_g (2013)	z_0 (m)	z_{50} (m)	z_{100} (m)
Canoe River	08NC004	305	0.189	0.177	0.170	963	1,955	3298
Nordic Creek	08NB020	7.49	0.669	0.591	0.577	1,864	2,399	2972

using geodetic mass balance for the Canoe River and Nordic Creek catchments (**Table 1**). In this analysis, catchment-scale glacier storage change was computed as

$$\Delta S_g = f_g \cdot B_a \quad (1)$$

where f_g is the fractional glacier coverage in the catchment and B_a is the annual specific glacier net balance (mm) derived by Pelto et al. (2019).

2.7. Regression Analysis of August Streamflow

This analysis broadly followed the approach applied to all of BC by Stahl and Moore (2006). However, whereas Stahl and Moore (2006) standardized monthly streamflow data and predictor variables, we converted each monthly streamflow value from a mean discharge in m^3s^{-1} to a runoff depth in mm, and retained the predictor variables in their original units.

Following Stahl and Moore (2006), we focused on August streamflow for two reasons. First, glacier-melt contributions to streamflow generally peak in August due to the combination of relatively high energy supply and high snowlines. Earlier in the year (May–July), seasonal snowmelt is a major cause of streamflow variability from year to year, and can obscure the role of glacier-melt contributions. Later in the year (September and October), energy supply declines and the influence of precipitation (both rain and snow) increases in the study region. Second, August is often a period of low flows and high water temperatures in unglacierized catchments, so that glacier-melt contributions can become critical in terms of water supply and fish habitat, particularly for cold- and cool-water species such as salmon (Moore, 2006; Moore et al., 2013; Parkinson et al., 2016).

Regression analysis was used to understand the drivers of interannual variability in August runoff (Q_{Aug}) (mm) by relating it to the following predictor variables: runoff in the preceding month (Q_{Jul}) (mm), mean August air temperature (T_{Aug}) (°C), and total August precipitation (P_{Aug}) (mm). The underlying logic is that the inclusion of July runoff helps to account for effects of carry-over storage, air temperature is an index of the magnitude of snow and ice melt as well as evapotranspiration from non-glacierized surfaces, and August precipitation represents the streamflow contribution from rainfall.

The regression model is:

$$Q_{Aug}(t) = a_0 + a_1 \cdot Q_{Jul}(t) + a_2 \cdot T_{Aug}(t) + a_3 \cdot P_{Aug}(t) + e(t) \quad (2)$$

where a_i are the estimated coefficients, t indicates year, and $e(t)$ is the residual from the regression.

Drawing on the degree-day melt model concept as an analogy, the sensitivity of glacier melt runoff to air temperature can be expressed as follows:

$$M_{Aug} = k_m \cdot n_d \cdot f_g \cdot (T_{Aug} - T_0) \quad (3)$$

where M_{Aug} is the glacier meltwater contribution to streamflow in August (mm), k_m is an apparent degree-day factor (mm · d^{-1} °C^{-1}), and n_d is the number of days in August (31), and T_0 is a base temperature, below which there is no glacier melt (°C). Based on the assumption that the air temperature term in Equation (2) represents the contribution of glacier melt, and if the value of k_m is assumed to be approximately constant across glaciers, we can equate the coefficient a_2 with $k_m \cdot n_d \cdot f_g$ to compute an apparent degree-day factor by combining Equations (2) and (3) and differentiating with respect to f_g:

$$k_m = \frac{1}{n_d} \frac{da_2}{df_g} \quad (4)$$

where da_2/df_g is the slope of a linear relation between a_2 and f_g. We acknowledge that the analogy is not perfect when using monthly mean temperatures because the effect of daily temperatures lower than T_0 is not explicitly accounted for. In addition, the value of k_m will reflect the combination of both snow and ice melt in proportions that vary from year to year.

2.8. Trend Analyses

Trend analyses for the August runoff time series were conducted by computing the Spearman correlation coefficient between August runoff and year, which requires no assumptions about data distributions or linearity of trends. The test has similar power to the Mann–Kendall test (Yue et al., 2002). Trend magnitudes were estimated using the Theil–Sen slope estimator, which is robust to outliers and lack of normality of the residuals (Helsel and Hirsch, 2002).

A trend analysis was also performed for the residuals from the regression model. The logic underlying this analysis is that the three predictors account for external hydroclimatic influences and non-glacial storage influences, and that the residuals should contain information about any effects caused by internal changes in the catchment, particularly glacier retreat.

3. RESULTS

3.1. Hydroclimatic Variability Over the Study Period

Variations in August air temperature and precipitation display a high degree of regional coherence, especially for air temperature,

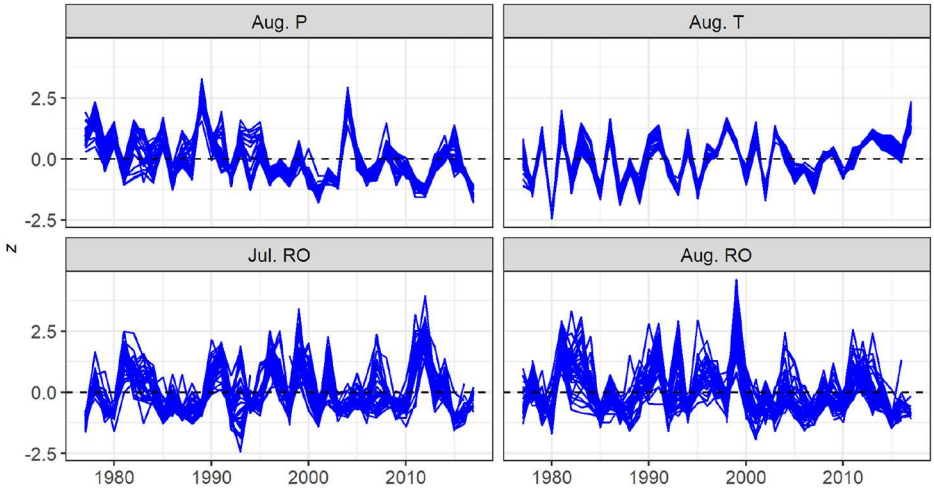


FIGURE 3 | Time series of August precipitation, August air temperature, and July and August runoff from 1977 to 2017. Each trace represents a station. Time series for each station were standardized prior to plotting by subtracting the mean and dividing by the standard deviation.

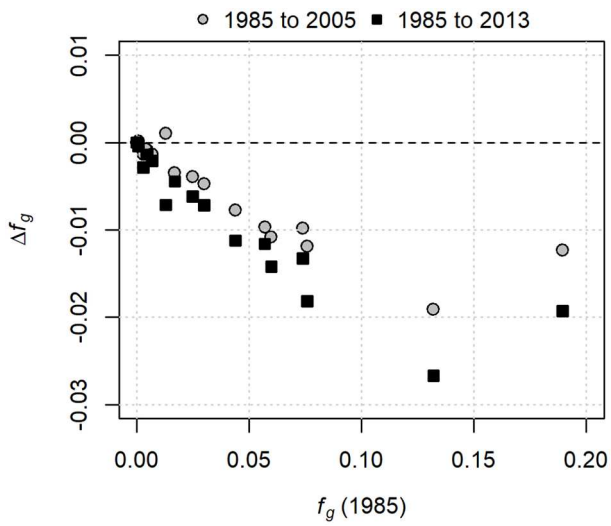


FIGURE 4 | Changes in glacier cover between 1985 and 2005, and 1985 and 2013, plotted against glacier cover in 1985.

while July and August runoff are somewhat less consistent among stations (**Figure 3**). August air temperature exhibited positive trends ranging from 0.022 to 0.032°C · yr^{-1}, with a median value of 0.025 °C · yr^{-1}. These trends represent an increase of about 1°C over the 41-year study period. However, none of the trends is significant at $p < 0.05$.

Trends for August precipitation ranged from −1.09 mm · yr^{-1} to −0.43 mm · yr^{-1} with a median value of −0.78 mm · yr^{-1}, equivalent to a decrease of about 30 mm over the study period. Of these trends, 31 of 35 were significant at $p < 0.05$.

3.2. Changes in Glacier Extent and Volume

In 1985, fractional glacier cover ranged among catchments from 0 to 0.19. **Figure 4** presents the magnitude of the change in glacier cover in 2005 and 2013, relative to 1985. Although glaciers in one catchment appeared to advance slightly from 1985 to 2005 ($\Delta f_g > 0$), the rest exhibited retreat of up to about 0.02. However, the apparent increase in glacier cover is probably a reflection of measurement uncertainty, given that there is no evidence that any glaciers advanced during the study period. By 2013, all glaciers retreated, with all showing a net negative change relative to 1985. With the exception of the heavily glacierized Canoe River catchment, the amount of change in glacier cover generally varied linearly with the glacier cover in 1985, representing about a 20% decrease in glacier coverage between 1985 and 2013. Between 1985 and 1999, mass changes derived from the digital elevation models indicate a mean rate of glacier storage loss that varied among catchments from about 0.1–0.9 m w.e. a^{-1}, with a mean of 0.55 ± 0.13 m w.e. a^{-1}.

3.3. Glacier Contributions to Streamflow

Figure 5 illustrates daily streamflow responses for 2 years with contrasting climatic conditions. For both years, catchments with and without glacier cover track reasonable well during the snowmelt freshet up to about the time of the freshet peak flow. Following the peak, streamflow for the glacier-fed catchments diverges from that for the unglacierized catchments and eventually converges in October. These composite hydrographs suggest that glaciers make substantial contributions to streamflow beginning some time in June and extending through September. However, some of the apparent contribution represents the extended snowmelt from the high-elevation portions of the glacier-fed catchments, as well as orographically enhanced rainfall. The contribution from glaciers is least complicated by rainfall and carry-over storage from the preceding month in August. Only a portion of the apparent contributions from glaciers constitutes a non-sustainable wastage flux; the remainder represents a lag in response to precipitation associated with transient glacier storage on seasonal to interannual scales.

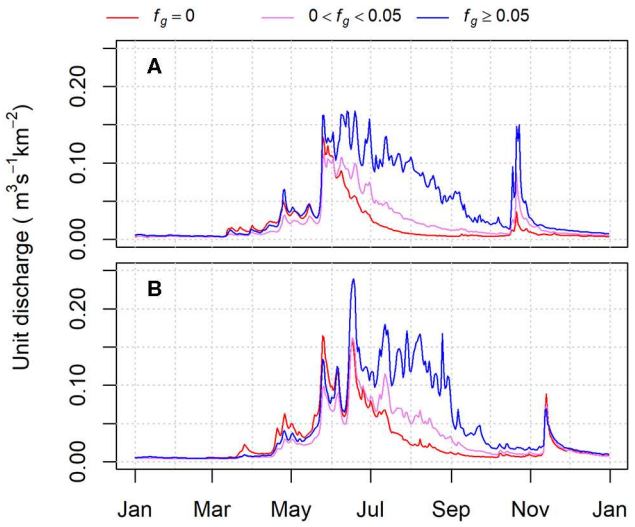


FIGURE 5 | Composite daily hydrographs of unit discharge for catchments with and without glacier cover. **(A)** is for 2003, a year dominated by summer drought conditions; **(B)** is for 1999, a year with heavy winter snow accumulation and more frequent summer rainfall.

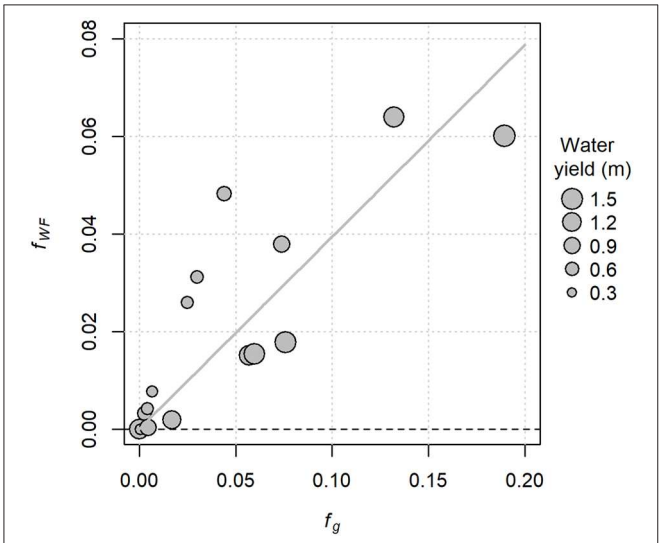


FIGURE 6 | Computed contributions of glacier wastage to streamflow as a fraction of annual water yield (f_{WF}), plotted against the glacier coverage in 1985. The trend line is a linear fit through the origin.

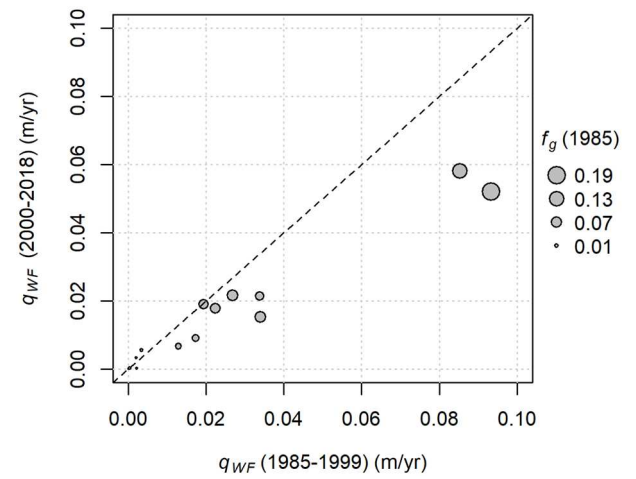


FIGURE 7 | Comparison of wastage flux contributions to streamflow (q_{WF}) on a mean annual basis for two periods. Wastage is expressed as an average depth of water over the catchment area. Symbol sizes are scaled to fractional glacier coverage in 1985. The dashed line indicates perfect agreement.

TABLE 2 | Glacier contributions to streamflow for Nordic Creek and Canoe River.

Year	Catchment	B_a (m)	*WY* (m)	Q_{wf} (m)	Q_{wf} (%)
2015	Canoe	−1.066	1.739	0.181	10.4
2016	Canoe	−0.830	1.645	0.141	8.6
2017	Canoe	−0.720	1.549	0.122	7.9
2018	Canoe	−1.080	1.405	0.184	13.1
2015	Nordic	−1.310	3.925	0.756	19.3
2016	Nordic	−0.490	3.125	0.283	9.0
2017	Nordic	−0.900	2.852	0.519	18.2
2018	Nordic	−0.590	2.629	0.340	13.0

B_a is annual net balance, WY is annual water yield, and Q_{wf} is the glacier wastage flux contribution to annual water yield.

Glacier mass loss between the mid-1980s and 1999 translates into wastage flux contributions that range up to just over 0.06 as a fraction of annual water yield (**Figure 6**). The distribution of points above and below the best-fit relation indicates that the fractional contribution to streamflow by glacier wastage is inversely related to annual water yield.

The relative wastage flux contributions to streamflow among catchments were consistent between 1985–1999 and 2000–2018 (**Figure 7**). It appears that the contributions were lower during the second period, which would be consistent with a post-peak-water scenario. However, we acknowledge that there is substantial uncertainty in geodetic estimates of mass loss. In particular, the effect of radar penetration on the SRTM DEM could cause an overestimate of mass loss for the early period, potentially accounting for the apparent discrepancy in wastage flux between the two periods. Therefore, it is not appropriate to draw a firm conclusion from this analysis.

Wastage flux contributions to Canoe River streamflow ranged from 8 to 13% of annual water yield (**Table 2**), higher than the long-term estimate for the mid-1980s to 1999 period (**Figure 6**), in which Canoe River corresponds to the point with f_g = 0.19. Wastage flux contributions in the more heavily glacierized, higher-elevation Nordic Creek catchment ranged from 9 to 19% of annual water yield. The coefficient of variation for annual flow for the 4 years was 0.09 for Canoe River and 0.18 for Nordic Creek. Although the coefficient of variation based on only 4 years of data will be subject to substantial sampling variability, the relative difference between the two catchments should be reasonable considering the use of a common period of record.

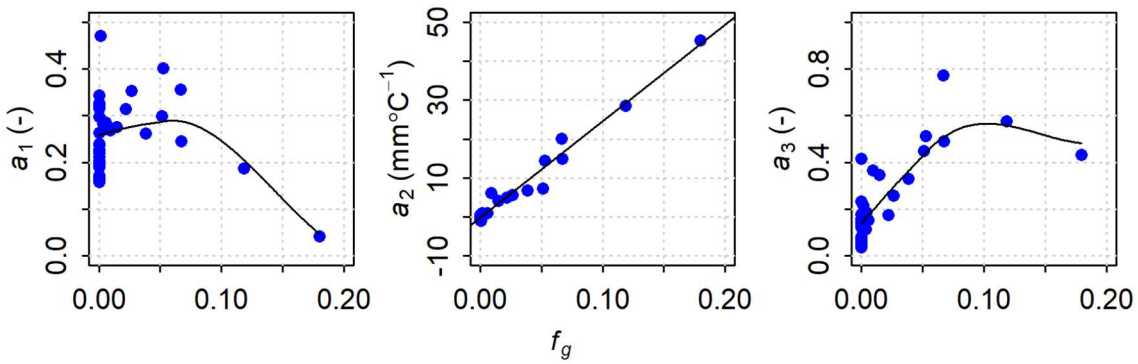


FIGURE 8 | Plot of fitted regression coefficients (a_i) against fractional glacier cover (f_g), computed as the average of the values for 1985 and 2013. The coefficients a_1 to a_3 correspond to July runoff, August air temperature and August precipitation, respectively. The trend lines for a_1 and a_3 were generated using the loess algorithm (span = 1, degree = 1); the trend line for a_2 is a linear regression fit.

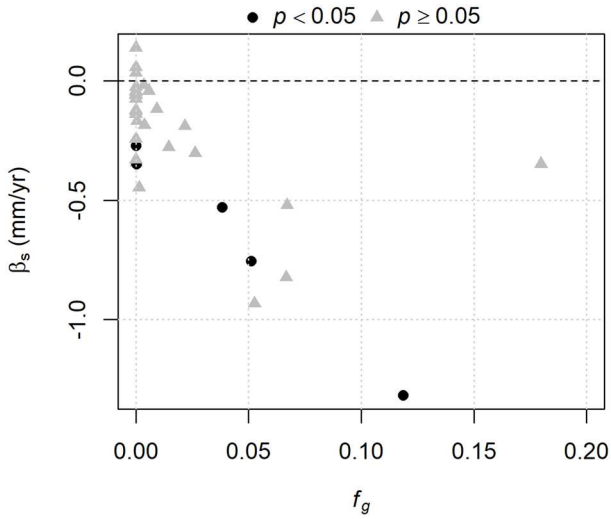


FIGURE 9 | Relation between the Sen slope estimator for August streamflow (β_s) and the mean fractional glacier cover from 1985 to 2013. Significance is based on the Spearman correlation test for each series.

3.4. Multiple Regression Analysis of August Streamflow

The regression model provided reasonable fits for the catchments with no or minimal (f_g < 0.01) glacier cover; adjusted R^2 ranges from 0.50 to 0.86, with a median of 0.70. The regression fits are less strong for the catchments with $f_g \geq 0.01$, with a range from 0.37 to 0.56 and a median of 0.49. It appears that a model including measures of climatic forcing and non-glacial storage explains more variability for the catchments with minimal glacier cover.

The fitted regression coefficients exhibit varying relations with fractional glacier cover (**Figure 8**). Coefficient a_1, which represents the effect of carry-over storage and is analogous to a recession constant, averages roughly 0.3 for most catchments, but appears to decline for catchments with greater glacier coverage. This result is consistent with our process understanding, in that high flows in July would be associated, in many years, with heavy snow accumulation and a late disappearance of snow. In unglacierized catchments, late disappearance of snow would be associated with enhanced streamflow in July and August. On the other hand, persistence of snow on glaciers would reduce glacier melt runoff in August due to the higher albedo of snow relative to exposed glacier ice. Another possible cause of the nonlinear relation is that higher-elevation, more heavily glacierized catchments may have less storage potential due to shallower soils and lack of extensive aquifers.

Coefficient a_3, which reflects the effects of rainfall-runoff in August, tends to increase with glacier cover. This relation is consistent with the tendency for more heavily glacierized catchments to have higher elevations, and thus a greater orographic enhancement of precipitation. Note that the relation appears to flatten out for higher fractional glacier coverages. This pattern might reflect a nonlinear relation between precipitation and elevation or the tendency for higher-elevation areas to receive precipitation as snow, which would suppress glacier melt.

Coefficient a_2 displays a linear relation with fractional glacier coverage with a slope of 247 mm · °C^{-1}. That is, the sensitivity of August water yield to August air temperature increases linearly with fractional glacier coverage, consistent with the conceptual model based on a degree-day melt model (Equation 3).

3.5. Trend Analyses

Most stations exhibited negative trends for August streamflow, although only five are significant at $p < 0.05$ (**Figure 9**). There is a general tendency to increasingly negative trend with increasing glacier cover, except for the most heavily glacierized catchment (Canoe River).

When the August runoff trends are plotted against the change in glacier cover (**Figure 10**, left panel), there is a more consistent relation than shown in **Figure 9**. The model has adjusted R^2 = 0.69, and the intercept and slope are −0.093 and 38.2 mm · yr^{-1}, respectively, both significant at $p < 0.05$. When considering trends for the residuals from the regression

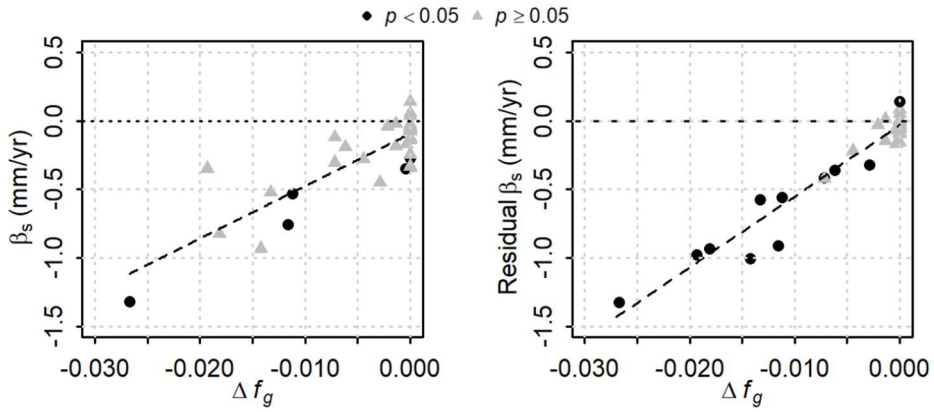


FIGURE 10 | Trend magnitudes as a function of the change in fractional glacier cover from 1985 to 2013. The Sen slope estimator (β_s) is shown for August streamflow in the left panel, and for the residuals from the multiple regression model in the right panel. Significance is based on the Spearman correlation test for each series. Dashed lines are fitted regressions.

model (Equation 2), there is less scatter about the regression line (adjusted R^2 = 0.93), and the trends are significant for 11 of the 35 catchments (**Figure 10**, right panel). The intercept, −0.031 mm·yr^{-1}, is not significantly different from 0 (p = 0.12), while the slope, 51.8 mm·yr^{-1}, is significant at well less than $p < 0.001$.

4. DISCUSSION

On a decadal time scale, the fractional contribution of glacier wastage had a positive relation with fractional glacier coverage and an inverse relation with annual water yield. The maximum contributions were about 6 % of annual water yield for the mid-1980s to 1999 period (**Figure 6**), and were somewhat lower for the 2000–2018 period (**Figure 7**). While the fractional contribution may seem minor on an annual time scale, the contributions during August would be higher. Based on simulations with and without glacier cover, Jost et al. (2012) concluded that ice melt contributed up to 6% of annual streamflow and up to 25% of August streamflow in the Mica Basin of the Columbia River headwaters, which has about 5% glacier cover.

The annual mass balances for 2015–2018 for the Nordic Creek and Canoe River catchments indicate higher losses than for the two longer-term periods, but this difference likely relates to the fact that August tended to be warmer and drier in recent years compared to longer term conditions (**Figure 3**). Indeed, results presented by Menounos et al. (2019) suggested that mass loss on a per-unit-area basis in the Columbia headwaters (Region 5 in their **Figure 4**) was higher in 2009–2018 than in either 1985–1999 or 2000–2009, consistent with the climatic trends shown in **Figure 3**.

Wastage flux contributions on an annual scale were less variable for Canoe River than for Nordic Creek. This difference likely reflects the fact that glaciers in the Canoe River catchment extend below treeline, such that a substantial portion of bare ice is exposed each summer regardless of the final snowline elevation. At Nordic Creek, on the other hand, where the glacier is entirely above treeline, there is likely to be greater relative interannual variation in the amount of bare ice exposed during the ablation season. This contrasting behavior between alpine glaciers and those extending to lower elevations contributes to inter-catchment variation in the glacier compensation effect, over and above the effect of fractional glacier coverage. The coefficient of variation for Nordic Creek was double that for Canoe River. This contrast is consistent with the high coefficient of variation of annual streamflow for the alpine-glacier-fed Vernagtbach catchment as compared to other catchments in the European Alps, which have glaciers extending to lower elevations (Tiel et al., 2020).

Based on the relation between the a_2 coefficient and fractional glacier cover, it appears that fractional glacier coverage of only about 0.01 is required to shift a catchment in this region from being relatively insensitive to August air temperature to having a positive response. This temperature-sensitivity for catchments with low glacier coverage could be partially due to melting of late-lying snow at high elevations, given that catchments with even low levels of glacier coverage tend to be at higher elevations than unglacierized catchments. However, late-lying snow would also reduce melt from the glaciers, so it is difficult to make a definitive statement about its role in the temperature sensitivity of streamflow.

The slope of the relation between a_2 and fractional glacier coverage corresponds to an apparent melt factor of k_m = 7.97 mm · day^{-1}·°C^{-1}. This value is higher than melt factors for ice derived for glaciers in western Canada by Shea et al. (2009), which averaged 4.6 mm · day^{-1}·°C^{-1}. However, the values derived by Shea et al. (2009) were for the entire ablation season, whereas the value of k_m derived here is based only on August. Also, the temperature-dependence could be higher because, in terms of streamflow production, glacier cover not only provides an ice surface available for melt, but also reduces losses by evapotranspiration that would occur from unglacierized areas (Carnahan et al., 2019).

All but three of the 35 catchments exhibited negative trends in August streamflow (although only five were significant), and the trend magnitudes have a significant linear relation with the change in glacier cover from 1985 to 2013. The intercept of the relation is negative and significantly different from 0, suggesting that there was a climate-driven negative trend in August streamflow for the unglacierized catchments, consistent with the dominance of significant negative trends in precipitation and widespread but not significant positive trends in air temperature. The relation between trend magnitude and Δf_g indicates stronger trends for catchments with greater loss of glacier cover, suggesting that decreases in glacier-melt contributions to streamflow augmented the climate-driven decreases from unglacierized portions of the catchments.

After accounting for the effects of external hydroclimatic forcing and non-glacial storage change through the regression model, the residuals had significant trends for 11 of the 35 stations, including most of the catchments that experienced a decrease in fractional glacier coverage of 0.002 or more. The intercept of the relation is not significantly different from zero, suggesting that the regression model has effectively accounted for climate-driven trends for unglacierized catchments.

Projections by Clarke et al. (2015) indicated that peak water in the Columbia River headwaters may occur around 2020 or later, depending on the climate scenario. The pattern of points in **Figure 9** suggests that, for all but the most heavily glacierized catchment, declining trends in glacier-melt contributions to streamflow added to the climate-driven negative trend in August runoff for unglacierized portions of the catchments. The most heavily glacierized catchment appears to have experienced a weaker negative trend than the lesser-glacierized catchments. This pattern is broadly consistent with the observations by Casassa et al. (2009) and Huss and Hock (2018) that more heavily glacierized catchments should have a longer rising phase. Overall, it appears that the Columbia River headwaters region is already in the process of beginning a post-peak-water decline, and the magnitude and significance of the declines may get stronger over the coming decades, unless there is an increase in summer rainfall to compensate for reduced glacier melt.

The residual trends indicate that there has been a decrease in what Moyer et al. (2016) called "realized streamflow"; that is, observed streamflow has been declining relative to the streamflow that would have been recorded if glaciers had not been retreating. There are two important implications in relation to a decrease in realized streamflow caused by glacier retreat. The first is that hydrological models based on out-of-date glacier information would tend to over-predict summer streamflow. Therefore, agencies tasked with making streamflow forecasts for glacier-fed catchments should ensure that they use up-to-date glacier cover information when setting up their models, which should be updated on a regular basis. The second is that periods with high air temperature would be accompanied by reduced streamflow, which would likely lead to higher stream temperatures considering that stream temperature response to surface energy exchange is inversely related to discharge (Gu et al., 1998; Webb et al., 2003).

5. CONCLUSIONS

The glacier wastage flux contribution to annual water yield had a positive relation with fractional glacier coverage and an inverse relation with catchment water yield. For catchments with over 10% glacier cover, glacier wastage contributed about 6% of the annual water yield over the period from the mid-1980s to 1999. For the heavily glacierized Nordic Creek and Canoe River catchments, the glacier wastage flux contributed on the order of 10 and 15% of annual water yield, on average, for the period 2015–2019. The fractional contribution varied from year to year, particularly for the high-elevation, highly glacierized Nordic Creek catchment.

Trend analyses suggest that glacier-melt contributions to streamflow have already passed peak water in the Columbia River headwaters. The trend analysis of the residuals from the regression with climate-related variables indicates that there is a clear declining trend in realized streamflow—that is, the streamflow that would have been observed if glaciers had not retreated—which can have implications for streamflow forecasting and summer water temperature response during hot, dry weather.

The study design employed here focused on a set of stations with a range of glacier cover, but with all catchments experiencing similar patterns of climatic variability over a common period of record. This design, along with consideration of climatic variability and changes in glacier cover, facilitated the partitioning of observed streamflow trends into components associated with climate-driven trends from unglacierized areas and those associated with glacier changes. This approach should be useful for application to other regions.

It would be valuable to complement this empirical study with the application of a process-based model, similar to the approach taken by Frans et al. (2018). While the empirical analysis provides robust information about the spatio-temporal patterns of response and permits inferences regarding the roles of glaciers and glacier retreat in those patterns, interrogation of model output and sensitivity analyses could generate more detailed understanding of the hydrological interactions underlying the response and provide a basis for making projections under varying climatic scenarios.

DATA AVAILABILITY STATEMENT

Data and code used in the execution of this study are publicly available via http://doi.org/10.5281/zenodo.3779279.

AUTHOR CONTRIBUTIONS

All authors contributed to the development of the research question and general conceptual approach. RM developed and applied the statistical analysis and led the writing and production of the manuscript. DH assisted with access to hydrological data and generated summaries of catchment characteristics. BM developed the glacier-cover outlines and mass change calculations. BP provided annual mass-balance data for Nordic

Creek and Canoe River catchments. All authors reviewed and edited the manuscript.

ACKNOWLEDGMENTS

This research was supported by the Natural Sciences and Engineering Research Council of Canada, the Canada Research Chair Program, the Columbia Basin Trust, and the Tula Foundation. We acknowledge the developers of open source software tools used for data wrangling and analysis, including the R programming language (R Core Team, 2019) and the following packages: **tidyverse** (Wickham, 2017), **sf** (Pebesma, 2018), **raster** (Hijmans, 2019), **bcmaps** (Teucher et al., 2019) and **tidyhydat** (Albers, 2017).

REFERENCES

Albers, S. (2017). tidyhydat: Extract and tidy Canadian hydrometric data. *J. Open Source Softw.* 2:511. doi: 10.21105/joss.00511

Baraer, M., Mark, B. G., McKenzie, J. M., Condom, T., Bury, J., Huh, K.-I., et al. (2012). Glacier recession and water resources in Peru's Cordillera Blanca. *J. Glaciol.* 58, 134–150. doi: 10.3189/2012JoG11J186

Barnett, T. P., Adam, J. C., and Lettenmaier, D. P. (2005). Potential impacts of a warming climate on water availability in snow-dominated regions. *Nature* 438, 303–309. doi: 10.1038/nature04141

Bolch, T., Menounos, B., and Wheate, R. (2010). Landsat-based inventory of glaciers in western Canada, 1985–2005. *Remote Sens. Environ.* 114, 127–137. doi: 10.1016/j.rse.2009.08.015

British Columbia Ministry of Environment, Land and Parks (1992). *British Columbia Specifications and Guidelines for Geomatics, Release 2.0* Victoria, BC: British Columbia Ministry of Environment, Land and Parks.

Carnahan, E., Amundson, J. M., and Hood, E. (2019). Impact of glacier loss and vegetation succession on annual basin runoff. *Hydrol. Earth Syst. Sci.* 23, 1667–1681. doi: 10.5194/hess-23-1667-2019

Casassa, G., Löpez, P., Pouyaud, B., and Escobar, F. (2009). Detection of changes in glacial run-off in alpine basins: examples from North America, the Alps, central Asia and the Andes. *Hydrol. Process.* 23, 31–41. doi: 10.1002/hyp.7194

Chilton, R. H. (1981). *A Summary of Climate Regimes of British Columbia.* Victoria, BC: B.C. Ministry of Environment.

Clarke, G. K. C., Jarosch, A. H., Anslow, F. S., Radić, V., and Menounos, B. (2015). Projected deglaciation of western Canada in the twenty-first century. *Nat. Geosci.* 8, 372–377. doi: 10.1038/ngeo2407

Daley, C., Halbleib, M., Smith, J. I., Gibson, D., W. P., and Curtis, J. (2008). Physiographically sensitive mapping of temperature and precipitation across the conterminous United States. *Int. J. Climatol.* 28, 2031–2064. doi: 10.1002/joc.1688

Environment and Climate Change Canada (2018). *National Water Data Archive: HYDAT*. Available online at: https://www.canada.ca/en/environment-climate-change/services/water-overview/quantity/monitoring/survey/data-products-services/national-archive-hydat.html.

Farinotti, D., Huss, M., Fürst, J. J., Landmann, J., Machguth, H., Maussion, F., et al. (2019). A consensus estimate for the ice thickness distribution of all glaciers on Earth. *Nat. Geosci.* 12, 168–173. doi: 10.1038/s41561-019-0300-3

Finger, D., Vis, M., Huss, M., and Seibert, J. (2015). The value of multiple data set calibration versus model complexity for improving the performance of hydrological models in mountain catchments. *Water Resour. Res.* 51, 1939–1958. doi: 10.1002/2014WR015712

Fleming, S. W., Moore, R. D., and Clarke, G. K. C. (2006). Glacier-mediated streamflow teleconnections to the Arctic Oscillation. *Int. J. Climatol.* 26, 619–636. doi: 10.1002/joc.1273

Frans, C., Istanbulluoglu, E., Lettenmaier, D. P., Clarke, G., Bohn, T. J., and Stumbaugh, M. (2016). Implications of decadal to century scale glacio-hydrological change for water resources of the Hood River basin, OR, USA. *Hydrol. Process.* 30, 4314–4329. doi: 10.1002/hyp.10872

Frans, C., Istanbulluoglu, E., Lettenmaier, D. P., Fountain, A. G., and Riedel, J. (2018). Glacier recession and the response of summer streamflow in the Pacific Northwest United States, 1960–2099. *Water Resour. Res.* 54, 6202–6225. doi: 10.1029/2017WR021764

Government of Canada (2019). *National Hydrometric Network Basin Polygons*. Available online at: https://open.canada.ca/data/en/dataset/0c121878-ac23-46f5-95df-eb9960753375 (accessed January 14, 2019).

Gu, R., Montgomery, S., and Austin, T. A. (1998). Quantifying the effects of stream discharge on summer river temperature. *Hydrol. Sci. J.* 43, 885–904.

Hamann, A., Wang, T., Spittlehouse, D. L., and Murdock, T. Q. (2013). A comprehensive, high-resolution database of historical and projected climate surfaces for western North America. *Bull. Am. Meteorol. Soc.* 94, 1307–1309. doi: 10.1175/BAMS-D-12-00145.1

Helsel, D. R., and Hirsch, R. M. (2002). *Statistical Methods in Water Resources, Techniques of Water Resources Investigations, Book 4, Chapter A3*. U.S. Geological Survey. doi: 10.13140/RG.2.2.36048.10248

Hijmans, R. J. (2019). *raster: Geographic Data Analysis and Modeling*. Available online at: https://CRAN.R-project.org/package=raster.

Huss, M. (2011). Present and future contribution of glacier storage change to runoff from macroscale drainage basins in Europe. *Water Resour. Res.* 47:W07511. doi: 10.1029/2010WR010299

Huss, M. (2013). Density assumptions for converting geodetic glacier volume change to mass change. *Cryosphere* 7, 877–887. doi: 10.5194/tc-7-877-2013

Huss, M., and Hock, R. (2018). Global-scale hydrological response to future glacier mass loss. *Nat. Clim. Change* 8, 135–140. doi: 10.1038/s41558-017-0049-x

IPCC (2019). "Summary for policymakers," in *International Governmental Panel on Climate Change Special Report on the Ocean and Cryosphere in a Changing Climate*, eds H. O. Pörtner, D. C. Roberts, V. Masson-Delmotte, P. Zhai, M. Tignor, E. Poloczanska, et al. (IPCC).

Jansson, P., Hock, R., and Schneider, T. (2003). The concept of glacier storage: a review. *J. Hydrol.* 282, 116–129. doi: 10.1016/S0022-1694(03)00258-0

Jost, G., Moore, R. D., Menounos, B., and Wheate, R. (2012). Quantifying the contribution of glacier runoff to streamflow in the upper Columbia River Basin, Canada. *Hydrol. Earth Syst. Sci.* 16, 849–860. doi: 10.5194/hess-16-849-2012

Kaser, G., Großhauser, M., and Marzeion, B. (2010). Contribution potential of glaciers to water availability in different climate regimes. *Proc. Natl. Acad. Sci. U.S.A.* 107, 20223–20227. doi: 10.1073/pnas.1008162107

Menounos, B., Hugonnet, R., Shean, D., Gardner, A., Howat, I., Berthier, E., et al. (2019). Heterogeneous changes in western North American glaciers linked to decadal variability in zonal wind strength. *Geophys. Res. Lett.* 46, 200–209. doi: 10.1029/2018GL080942

Moore, R. D. (2006). Stream temperature patterns in British Columbia, Canada, based on routine spot measurements. *Can. Water Resour. J.* 31, 41–56. doi: 10.4296/cwrj3101041

Moore, R. D., Fleming, S. W., Menounos, B., Wheate, R., Fountain, A., Stahl, K., et al. (2009). Glacier change in western North America: implications for hydrology, geomorphic hazards and water quality. *Hydrol. Process.* 23, 42–61. doi: 10.1002/hyp.7162

Moore, R. D., Nelitz, M., and Parkinson, E. (2013). Empirical modelling of maximum weekly average stream temperature in British Columbia, Canada, to support assessment of fish habitat suitability. *Can. Water Resour. J.* 38, 135–147. doi: 10.1080/07011784.2013.794992

Moore, R. D., Spittlehouse, D. L., Whitfield, P. H., and Stahl, K. (2010). "Weather and climate," in *Land Management Handbook 66*, eds R. Pike, T. E. Redding, R. D. Moore, R. D. Winkler, and K. D. Bladon (Kamloops, BC; Victoria, BC: B.C. Ministry of Forest; Range, Forest Science Program; FORREX Forum for Research; Extension in Natural Resources), 47–84.

Moyer, A. N., Moore, R. D., and Koppes, M. N. (2016). Streamflow response to the rapid retreat of a lake-calving glacier. *Hydrol. Process.* 30, 3650–3665. doi: 10.1002/hyp.10890

Naz, B. S., Frans, C. D., Clarke, G. K. C., Burns, P., and Lettenmaier, D. P. (2014). Modeling the effect of glacier recession on streamflow response using a coupled glacio-hydrological model. *Hydrol. Earth Syst. Sci.* 18, 787–802. doi: 10.5194/hess-18-787-2014

Nolin, A. W., Phillippe, J., Jefferson, A., and Lewis, S. L. (2010). Present-day and future contributions of glacier runoff to summertime flows in a Pacific Northwest watershed: implications for water resources. *Water Resour. Res.* 46:W12509. doi: 10.1029/2009WR008968

O'Neel, S., McNeil, C., Sass, L. C., Florentine, C., Baker, E. H., Peitzsch, E., et al. (2019). Reanalysis of the US Geological Survey Benchmark Glaciers: long-term insight into climate forcing of glacier mass balance. *J. Glaciol.* 65, 850–866. doi: 10.1017/jog.2019.66

Parkinson, E., Lea, E. V., Nelitz, M., Knudson, J. M., and Moore, R. D. (2016). Identifying temperature thresholds associated with fish community changes in British Columbia, Canada, to support identification of temperature sensitive streams. *River Res. Appl.* 32, 330–347. doi: 10.1002/rra.2867

Pebesma, E. (2018). Simple Features for R: standardized support for spatial vector data. *R J.* 10, 439–446. doi: 10.32614/RJ-2018-009

Pelto, B. M., Menounos, B., and Marshall, S. J. (2019). Multi-year evaluation of airborne geodetic surveys to estimate seasonal mass balance, Columbia and Rocky Mountains, Canada. *Cryosphere* 13, 1709–1727. doi: 10.5194/tc-13-1709-2019

Pelto, M. S. (2018). How unusual was 2015 in the 1984-2015 period of the North Cascade Glacier annual mass balance? *Water* 10:543. doi: 10.5194/tc-20 17-62

R Core Team (2019). *R: A Language and Environment for Statistical Computing*. Vienna: R Foundation for Statistical Computing Available online at: https:// www.R-project.org/.

Rignot, E., Echelmeyer, K., and Krabill, W. (2001). Penetration depth of interferometric synthetic-aperture radar signals in snow and ice. *Geophys. Res. Lett.* 28, 3501–3504. doi: 10.1029/2000GL012484

Schaefli, B., and Huss, M. (2011). Integrating point glacier mass balance observations into hydrologic model identification. *Hydrol. Earth Syst. Sci.* 15, 1227–1241. doi: 10.5194/hess-15-1227-2011

Schiefer, E., Menounos, B., and Wheate, R. (2007). Recent volume loss of British Columbian glaciers, Canada. *Geophys. Res. Lett.* 34, 1–6. doi: 10.1029/2007GL030780

Shea, J. M., Stahl, K., and Moore, R. D. (2009). Derivation of melt factors from glacier mass-balance records in western Canada. *J. Glaciol.* 55, 123–130. doi: 10.3189/002214309788608886

Stahl, K., and Moore, R. D. (2006). Influence of watershed glacier coverage on summer streamflow in British Columbia, Canada. *Water Resour. Res.* 42:W06201. doi: 10.1029/2006WR005022

Teucher, A., Hazlitt, S., and Albers, S. (2019). *Bcmaps: Map Layers and Spatial Utilities for British Columbia*. Available online at: https://CRAN.R-project.org/ package=bcmaps

Tiel, M. van, Kohn, I., Van Loon, A. F., and Stahl, K. (2020). The compensating effect of glaciers: Characterizing the relation between interannual streamflow variability and glacier cover. *Hydrol. Process.* 34, 553–568. doi: 10.1002/hyp.13603

Webb, B. W., Clack, P. D., and Walling, D. E. (2003). Water–air temperature relationships in a Devon river system and the role of flow. *Hydrol. Process.* 17, 3069–3084. doi: 10.1002/hyp.1280

Whitfield, P. H., Moore, R., Fleming, S. W., and Zawadski, A. (2010). Pacific Decadal Oscillation and the hydroclimatology of Western Canada - review and prospects. *Can. Water Resour. J.* 35, 1–28. doi: 10.4296/cwrj3501001

Wickham, H. (2017). *Tidyverse: Easily Install and Load the 'Tidyverse'*. Available online at: https://CRAN.R-project.org/package=tidyverse

Yue, S., Pilon, P., and Cavadias, G. (2002). Power of the Mann-Kendall and Spearman's rho test for detecting monotonic trends in hydrological series. *J. Hydrol.* 259, 254–271. doi: 10.1016/S0022-1694(01)00594-7

Zemp, M., Frey, H., Gärtner-Roer, I., Nussbaumer, S. U., Hoelzle, M., Paul, F., et al. (2015). Historically unprecedented global glacier decline in the early 21st century. *J. Glaciol.* 61, 745–762. doi: 10.3189/2015JoG15J017

Conflict of Interest: The authors declare that the research was conducted in the absence of any commercial or financial relationships that could be construed as a potential conflict of interest.

Copyright © 2020 Moore, Pelto, Menounos and Hutchinson. This is an open-access article distributed under the terms of the Creative Commons Attribution License (CC BY). The use, distribution or reproduction in other forums is permitted, provided the original author(s) and the copyright owner(s) are credited and that the original publication in this journal is cited, in accordance with accepted academic practice. No use, distribution or reproduction is permitted which does not comply with these terms.

frontiers in Earth Science

REVIEW
published: 29 May 2020
doi: 10.3389/feart.2020.00162

High Impact Weather Events in the Andes

Germán Poveda[1], Jhan Carlo Espinoza[2], Manuel D. Zuluaga[1], Silvina A. Solman[3,4], René Garreaud[5] and Peter J. van Oevelen[6]*

[1] Department of Geosciences and Environment, Universidad Nacional de Colombia, Medellín, Colombia, [2] Université Grenoble Alpes, IRD, CNRS, G-INP, IGE (UMR 5001), Grenoble, France, [3] Universidad de Buenos Aires, Facultad de Ciencias Exactas y Naturales, Departamento de Ciencias de la Atmósfera y los Océanos, Buenos Aires, Argentina, [4] CONICET - Universidad de Buenos Aires, Centro de Investigaciones del Mar y la Atmósfera (CIMA), Buenos Aires, Argentina, [5] Department of Geophysics, Universidad de Chile, Santiago, Chile, [6] International GEWEX Project Office, Washington, DC, United States

Owing to the extraordinary latitudinal extent, a strong orographic variability with very high mountain tops, and the presence of deep valleys and steep slopes, the Andes and the population of the region are highly prone and vulnerable to the impacts of a large suite of extreme weather events. Here we provide a review of the most salient events in terms of losses of human and animal lives, economic and monetary losses in costs and damages, and social disruption, namely: (1) extreme precipitation events and related processes (Mesoscale Convective Systems, lightning), (2) cold spells, frosts, and high winds, (3) the impacts of ENSO on extreme hydro-meteorological events, (4) floods, (5) landslides, mudslides, avalanches, and (6) droughts, heat waves and fires. For our purposes, we focus this review on three distinctive regions along the Andes: Northern tropical (north of 8°S), Southern tropical (8°S-27°S) and Extratropical Andes (south of 27°S). Research gaps are also identified and discussed at the end of this review. It is very likely that climate change will increase the vulnerability of the millions of inhabitants of the Andes, impacting their livelihoods and the sustainable development of the region into the twenty first century amidst urbanization, deforestation, air, soil and water pollution, and land use changes.

Keywords: Andes, extreme weather, storms, ENSO, floods, landslides, droughts, fires

OPEN ACCESS

Edited by:
Bryan G. Mark, The Ohio State University, United States

Reviewed by:
Francina Dominguez, University of Illinois at Urbana-Champaign, United States
Mario Bruno Rohrer, Meteodat GmbH, Switzerland

****Correspondence:***
Germán Poveda
gpoveda@unal.edu.co

Specialty section:
This article was submitted to Hydrosphere, a section of the journal Frontiers in Earth Science

Received: *04 November 2019*
Accepted: *29 April 2020*
Published: *29 May 2020*

Citation:
Poveda G, Espinoza JC, Zuluaga MD, Solman SA, Garreaud R and van Oevelen PJ (2020) High Impact Weather Events in the Andes. Front. Earth Sci. 8:162. doi: 10.3389/feart.2020.00162

INTRODUCTION

Rapid rates of human encroachment, urbanization, deforestation and land use changes are taking place along the Andes (**Figure 1**). These developments make the region and their populations highly vulnerable to extreme weather events and impose a huge toll in terms of socioeconomic, environmental and ecological impacts. Such high vulnerability is associated with diverse natural hazards and risks, poor (or non-existent) preventive and adaptive capabilities and fragile governance. **Figures 2A,B** illustrate the impacts of weather and hydrological extreme events over the Andes. Floods and cold spells lead the rank in human lives losses in the region. Between 1985 and 2014 occurred 150 disasters in the Andes triggered by these extreme events, causing economic losses of 3,138.4 million of US dollars, killing 6,664 people and affecting more than 12 million people (Stäubli et al., 2017). It is highly likely that climate change will increase such vulnerability throughout the Andes (Magrin et al., 2014).

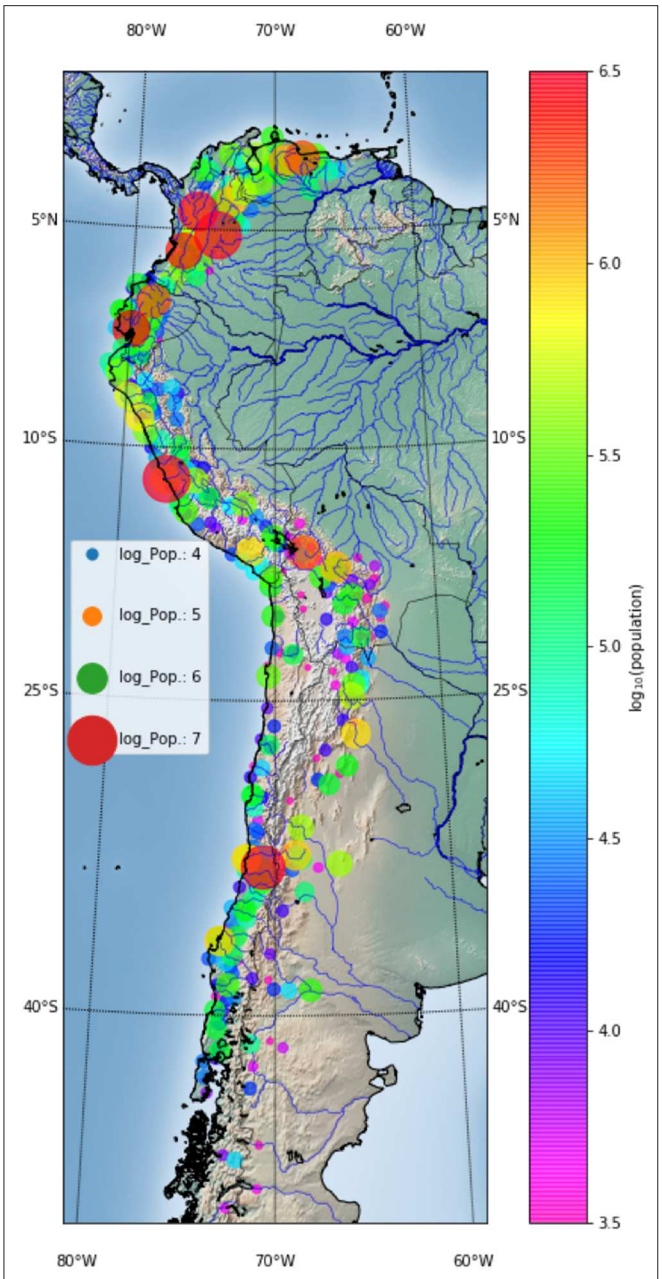


FIGURE 1 | Location and population of cities and towns along the Andes, whose populations are greater that 10,000 inhabitants. Data source: World Cities Database (https://simplemaps.com/data/world-cities).

This paper reviews high impact weather events affecting the livelihoods of millions of people, and compromise the sustainable development of the Andean region amid climate change, urbanization, deforestation, and land use changes. It is a contribution in a series of six to this special issue of Frontiers in Earth Science focused on the Andes climate, weather, hydrology and cryosphere (Condom et al., 2020; Espinoza et al., 2020; Masiokas et al., 2020; Pabón-Caicedo et al., 2020), arising from ANDEX, a prospective Regional Hydroclimate Project (RHP) of the Global Energy and Water Cycle Experiment (GEWEX; https://www.gewex.org/).

For our purposes, the Andean region is divided into three distinctive regions: Northern Tropical (north of 8°S), Southern Tropical (27°S-8°S) and Extratropical Andes (south of 27°S). The work is distributed as follows. Section Extreme Precipitation and Related Processes is focused on extreme precipitation and storm events and related processes, including mesoscale convective systems and lightning. Section Cold Spells, Frosts, and High Winds deals with cold spells, frosts, and high winds, while section ENSO Impacts on Extreme Events discusses the impacts of ENSO on extreme hydro-meteorological events. Section Floods is related to floods, while section Landslides, Mudslides, Avalanches with landslides, mudslides, and avalanches, and section Droughts, Heat Waves and Fires reviews droughts, heat waves and fires. Section Research Gaps provides a summary of main research gaps regarding the monitoring, understanding, modeling, and prediction of the studied processes and phenomena, and some final remarks are pointed out in section Final Remarks.

EXTREME PRECIPITATION AND RELATED PROCESSES

Northern Tropical Andes

Very localized intense storms occur in the tropical Andes during the (annual or semi-annual) wet seasons, with a diurnal cycle shifting with the seasons (Poveda et al., 2005; Bedoya-Soto et al., 2019). Over the Andes of Colombia and Venezuela, most intense storms occur during the two maxima of the annual cycle (April-May and September-November) (Espinoza et al., 2020). The most salient feature of intense storms is a strong spatiotemporal variability, which is caused by steep orography and topographic roughness, local circulations, small and large-scale convective cloud systems acting at different timescales, local circulations and regional valley/mountain breeze systems, katabatic winds (López and Howell, 1967; Bendix et al., 2009), evapotranspiration from the bottom of intra-Andean valleys, orographically-driven moisture transport (Rollenbeck and Bendix, 2011), and anabatic circulations (Bedoya-Soto et al., 2019), which in turn are influenced by synoptic mesoscale and continental conditions. Over the eastern slopes of the Ecuadorian Andes, nocturnal convection and clouds develop in spite of unfavorable large-scale conditions (Bendix et al., 2009; Trachte et al., 2010). Precipitation recycling in the tropical Andes can be 70–90% of total precipitation (Zemp et al., 2014; Bedoya-Soto et al., 2019). The strong variability of tropical Andean storms is evidenced in their fractal and multifractal properties (Poveda and Mejía, 2004; Gómez and Poveda, 2008; Hurtado and Poveda, 2009; Poveda, 2011; Mesa and Peñaranda, 2015; Posadas et al., 2015; Poveda and Salas, 2015; Yarleque et al., 2016; Duffaut-Espinosa et al., 2017).

Intense storms over the tropical Andes are also associated with Mesoscale Convective Systems (MCS) over western Colombia and the far eastern tropical Pacific (Velasco and Fritsch, 1987; Houze et al., 2015; Zuluaga and Houze, 2015). These large and intense convective systems are seen to contribute to explain

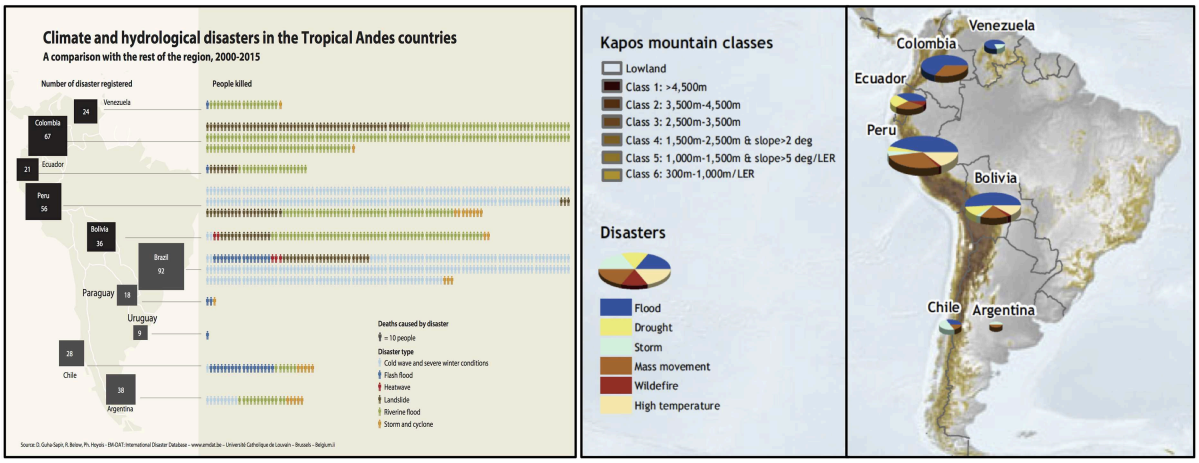


FIGURE 2 | (A) Climate and hydrological disasters in the Andean countries and human fatalities during the period spanning from 2000 to 2015. Source: Schoolmeester et al. (2016), from a figure made by GRID-Arendal and Cartografare il Presente/Riccardo Pravettoni (https://www.grida.no/resource). **(B)** Disasters along the Andes caused by storms, floods, mass movements, extreme temperatures, droughts and wild fires, based on EM-DAT (Guha-Sapir et al., 2015). Cartography by Jürg Krauer, Centre for Development and Environment (CDE), University of Bern, Switzerland. Adapted from Stäubli et al. (2017) by permission from Springer, *Climate Change Extreme Events and Disaster Risk Reduction*, by S. Mal, R. B. Singh, and C. Huggel (eds.), Copyright, 2018.

the existence of one of the rainiest spots on Earth over the Pacific coast of Colombia with average rain rates of 10,000–13,000 mm per year (Poveda and Mesa, 1999; Poveda et al., 2014; Yepes et al., 2019). Over Colombia's far eastern Pacific, the cross-equatorial flow become the south-westerly CHOCO LLJ that interacts with the western Andes (Poveda and Mesa, 2000; Bedoya-Soto et al., 2019; Yepes et al., 2019), exhibiting weaker winds in February-March and stronger winds during September-November (**Figure 3**). Such enhanced ocean-atmosphere-land interactions by the CHOCO LLJ produce world-record breaking rainfall intensities over western Colombia inland and off-shore (Poveda and Mesa, 1999, 2000; Yepes et al., 2019). Mostly focused on the Caribbean and the Orinoco LLJs, easterly trade winds prevail, and their interaction with the ITCZ produce large amounts of rainfall in the Orinoco basin, and the Upper Amazon river basins in Colombia, Venezuela and Brazil (**Figure 3**).

Figure 4 shows the distribution of average (1998–2013) rainfall over most South America during JJA and DJF, using data from the Tropical Rainfall Measuring Mission (TRMM). Most of this rain is produced by different types of convective organization at the regional scale (Houze et al., 2015; Rasmussen et al., 2016), which are often part of large MCSs at different stages. Such types can be classified using reflectivity echoes from the TRMM 3B42 product (Kummerow et al., 1998, 2000; Houze et al., 2007, 2015; Romatschke et al., 2010). **Figure 5A** shows the probability of TRMM Precipitation Radar (PR) observing a wide convective core (WCC), with pixels exceeding 40 dBZ reflectivity over 1,000 km^2 during JJA (Houze et al., 2015). The WWC tend to maximize in the Pacific coast of Colombia and Panama, in the northern region of the Andes of Colombia, as well as in the Orinoco and parts of the Upper Amazon river basin. **Figures S1**, **S2** show the MCS that triggered the flooding of Mocoa, Colombia, in April 1st, 2017, killing at least 336 people, injuring 332, and 70 others missing.

Rainfall over north-western South America exhibits different precipitation features (PF) containing elements associated with their convective life cycle, such as those with and without ice scattering and MCSs. The former two maximize in the afternoon from 12:00 to 18:00 LT at the west of the western Colombian Andes, and the eastern slope of the eastern Andes. The former occurs by the effect of Pacific sea breeze along the valley floor and upslope to the top of the Andes in the afternoon (López and Howell, 1967; Yepes et al., 2019), but also from the Orinoco LLJ during the afternoon. On the other hand, PFs with MCSs mainly occur in the morning (00:00–06:00 LT) offshore in the Pacific at 77.5°W (Mapes et al., 2003; Yepes et al., 2019). Large precipitation features (PFs) associated with MCSs represent <1% of PFs in the eastern Amazonian slopes of the Andes (Jaramillo et al., 2017). The most common PFs exhibit small areas and contribute about 15% to total precipitation, while MCS are observed least but produce more than 50% of the total along the eastern slope of the Central Andes below 2000 m a.s.l. (Chávez and Takahashi, 2017).

Some mesoscale convective units may become broad areas of stratiform rain (BSR; TRMM echoes covering more than 50,000 km^2) at the later stage of MCS (Houze, 2004) (**Figure 5B** for JJA). They are concentrated over the eastern Pacific near Colombia, and less in the Orinoco and Upper Amazon basin. Furthermore, very deep and intense convective cores (DCC) develop over continental regions, with maxima during JJA over the north-eastern Andes of Colombia and Venezuela. **Figure 5C** shows DCCs higher than 10 km, associated with severe weather, lightning and flash floods (Rasmussen and Houze, 2011; Zuluaga and Houze, 2015; Hoyos et al., 2019).

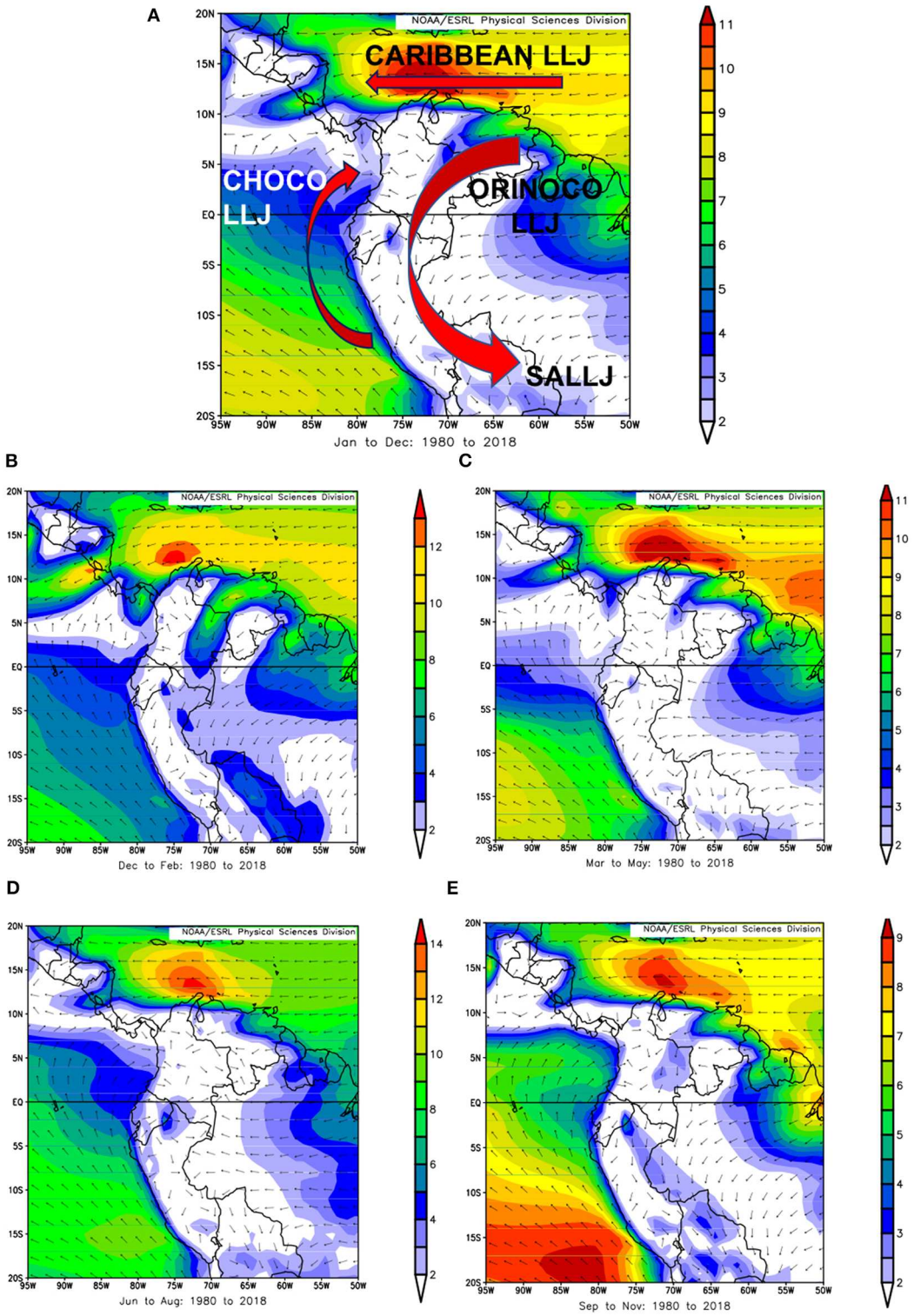


FIGURE 3 | Distribution of the long-term mean (1980-2018) horizontal wind speed (m/s) at 950 hPa over northern South America; **(A)** Mean annual values showing the Choco, Caribbean, and Orinoco low-level jets, and the SALLJ. Mean seasonal values during **(B)** December-January-February; **(C)** March-April-May; **(D)** June-July-August; and **(E)** September-October-November. Images prepared from the NOAA/ESRL Physical Sciences Division, Boulder Colorado; https://www.esrl.noaa.gov/psd/.

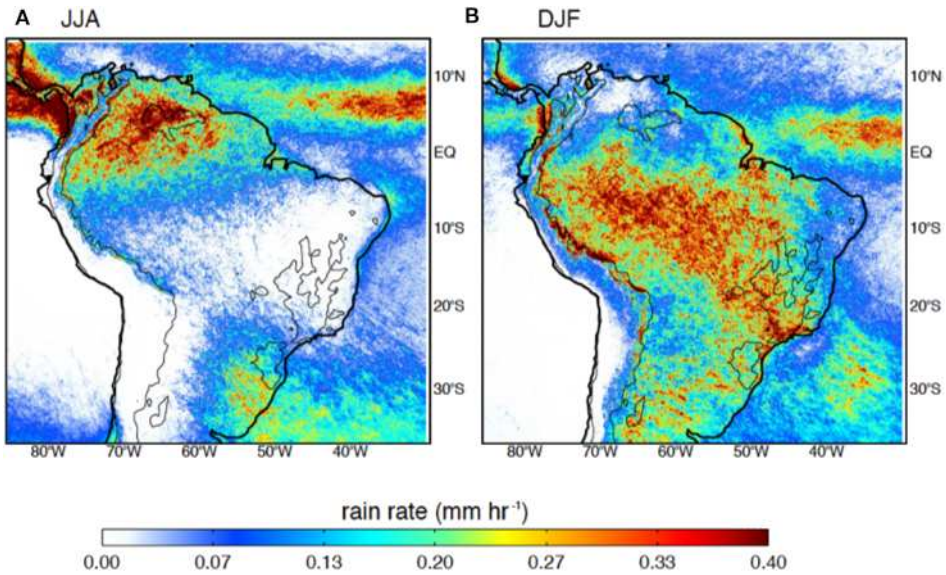


FIGURE 4 | Average rain rate from TRMM distinguishable rain areas during the months of **(A)** JJA and **(B)** DJF from 1998 to 2013. The black thin contour characterizes the 700 m elevation. Adapted from Houze et al. (2015).

After convective systems get organized, they migrate away from the topography. Usually, the migration of organized convective systems is favored by the prevailing mid- to upper level wind. Over northern western Colombia and southern Panama, organized systems tend to move westward away from the topography toward the east Pacific Ocean by the easterly flow (Mapes et al., 2003; Zuluaga and Houze, 2015). Some authors attribute the speed of flow to a gravity wave triggered by the afternoon heating of the Andes (Mapes et al., 2003), and others to the easterly wave migration over the east Pacific (Rydbeck and Maloney, 2015).

Northern South America is also affected by synoptic-scale processes favoring convective organization over the tropical Andes such as the African Easterly Waves (AEWs). These perturbations are associated with convective activity and the occurrence of storm events in northern Colombia and Venezuela (León et al., 2001; Poveda et al., 2002; Dominguez et al., 2020). To the west of the tropical Andes (north of Peru and Ecuador), rain is associated with an onshore westerly low-level flow from the equatorial Pacific, which triggers convection forced by orographic lifting of the Andes (e.g., Takahashi, 2004).

The most active regions of lightning in the world are found in the low-lands of the tropical Andes of Colombia and Venezuela (Albrecht et al., 2016), with flash rate density (FRD) of 233 flashes per km^2 per year (**Figure S3**). Lightning flash density is inversely correlated with altitude along the Andes of Colombia (Herrera et al., 2018), causing high human and livestock mortality (Cristancho et al., 2017), with 757 deaths from 2000 to 2009, or 1.78 per million per year (Cruz et al., 2013; Navarrete-Aldana et al., 2014). Also, between 2003 and 2012, 282 casualties were reported among soldiers of the Colombian Army in 149 events with 72 deaths and 210 injuries. Lightning also affect the power transmission systems in Colombia (Aranguren et al., 2017).

Southern Tropical Andes

Most of moisture reaching the Andes highlands come from the Atlantic Ocean and the Amazon River basin via easterly aerial rivers (Poveda et al., 2014). Westerly winds from the Pacific are not infrequent over the Andes from Colombia to Peru, and occur following the seasonal movement of the ITCZ and the strength of the Bolivian High Sakamoto et al. (2011); Poveda et al. (2014); Makowski Giannoni et al. (2016); Trachte (2018); Espinoza et al. (2020). Boers et al. (2015a,b, 2016) studied different types of extreme storms events over the southern tropical Andes, and found that events north of 20°S are typically generated in the Amazon Basin, whereas storms over the foothills of the eastern Andes south of 20°S, including the Puna High Plateau, originate over the southeastern part of the continent. Such propagation during the monsoon season (December to March) is explained by mid-latitude alternating pressure anomalies embedded in a westerly Rossby wave-train in combination with a low-pressure center located over northwestern Argentina, creating favorable conditions for intense storms (Liebmann et al., 2004; Espinoza et al., 2012a; Boers et al., 2015b; Paccini et al., 2017). Over the northern part of the south tropical Andes (10°S-5°N), the eastward propagation of the MJO convective core during the Austral summer (DJF), modulates sub-seasonal precipitation, producing positive rainfall anomalies up to 50% compared with the climatology (Recalde-Coronel et al., 2020).

Extreme rainfall in the valleys of the southern tropical Andes results from the interplay between the Amazon and the Pacific Ocean flows, influenced by orography (Junquas et al., 2016, 2018; Trachte, 2018). Kumar et al. (2019) show that

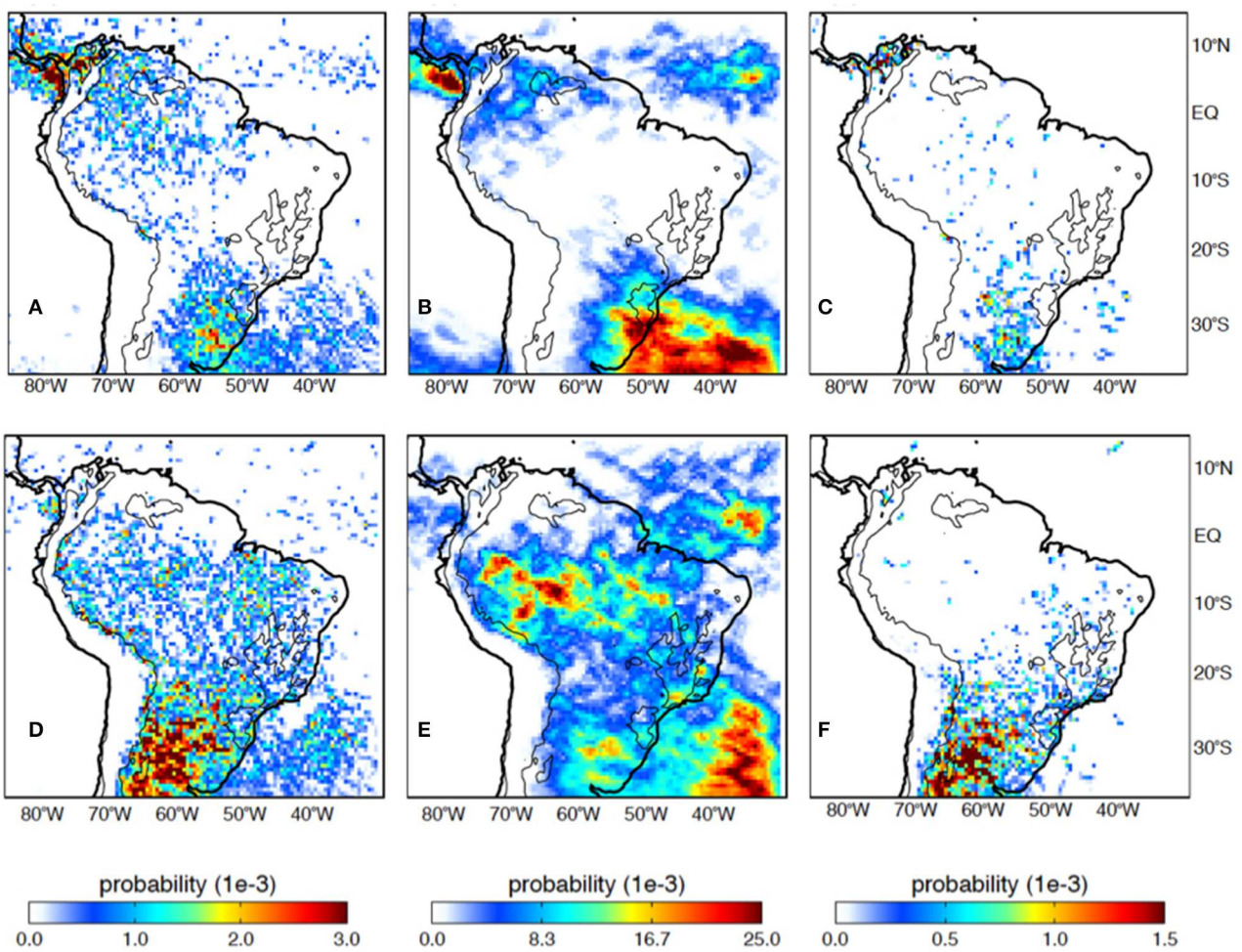


FIGURE 5 | Geographical distribution of the probability of finding **(A)** a wide convective core; **(B)** a broad stratiform region; and **(C)** a deep convective core during the months of JJA from 1998 to 2003. **(D)** same as **(A)**; **(E)** same as **(B)**; and **(F)** same as **(C)** but for DJF, respectively. The black contour inside the continental regions represents the 700 m elevation. Figure adapted from Zuluaga and Houze (2015).

precipitating cloud systems (PCs) in the Andes and western Amazon are largely affected by the directional surface flows. In particular, larger PCs (>2,000 km^2) are more frequent at the western flank of the Andes during southerly and easterly surface flows, while along the eastern flank, northerly and easterly surface winds are predominant during high and large PCs (**Figures 6A–D**). According to Villalobos et al. (2019), convection and cloud systems are deeper over the central Andes regions than in the Amazon-Andes transition region. The central Andes witness convective (30%) and stratiform (70%) precipitation, contributing with 63.3 and 36.7% of total rain, whereas in the Amazon-Andes transition those percentages and the contribution to cumulative rain attain similar values (31 and 69%, respectively). Over the central Peruvian Andes, and using a vertically pointed profile rain radar installed in the Mantaro Basin, Kumar et al. (2020) show that most of the bright band height (an indication for the melting zone) over this region vary between 4.3 and 4.7 km. An example of the vertical profile of radar reflectivity is shown in **Figures 6E,F**.

The eastern Andes foothills located at windward conditions are among the rainiest regions in the Amazon basin (4,000–7,000 mm yr^{-1}; Roche et al., 1990; Espinoza et al., 2015), resulting from the interaction between large-scale humidity transport from the Atlantic Ocean, Amazonian evapotranspiration and moisture recycling, and the steep Andes topography (Killeen et al., 2007; Espinoza et al., 2009; Zemp et al., 2014). Highest values of this orographic rainfall are located along the foothills of the eastern Andes of Peru and Bolivia (e.g., **Figure 6B**), mainly during the austral summer (Romatschke and Houze, 2010; Espinoza et al., 2015). Most rainfall intensification has been associated to the direction of 850 hPa winds (**Figure 6G**), with excessive rainfall during a north-easterly wind regime originating in subtropical South America (Garreaud and Wallace, 1998; Laurent et al., 2002; Rickenbach et al., 2002; Espinoza et al., 2015; Chávez and Takahashi, 2017; Kumar et al., 2019; Moya-Álvarez et al.,

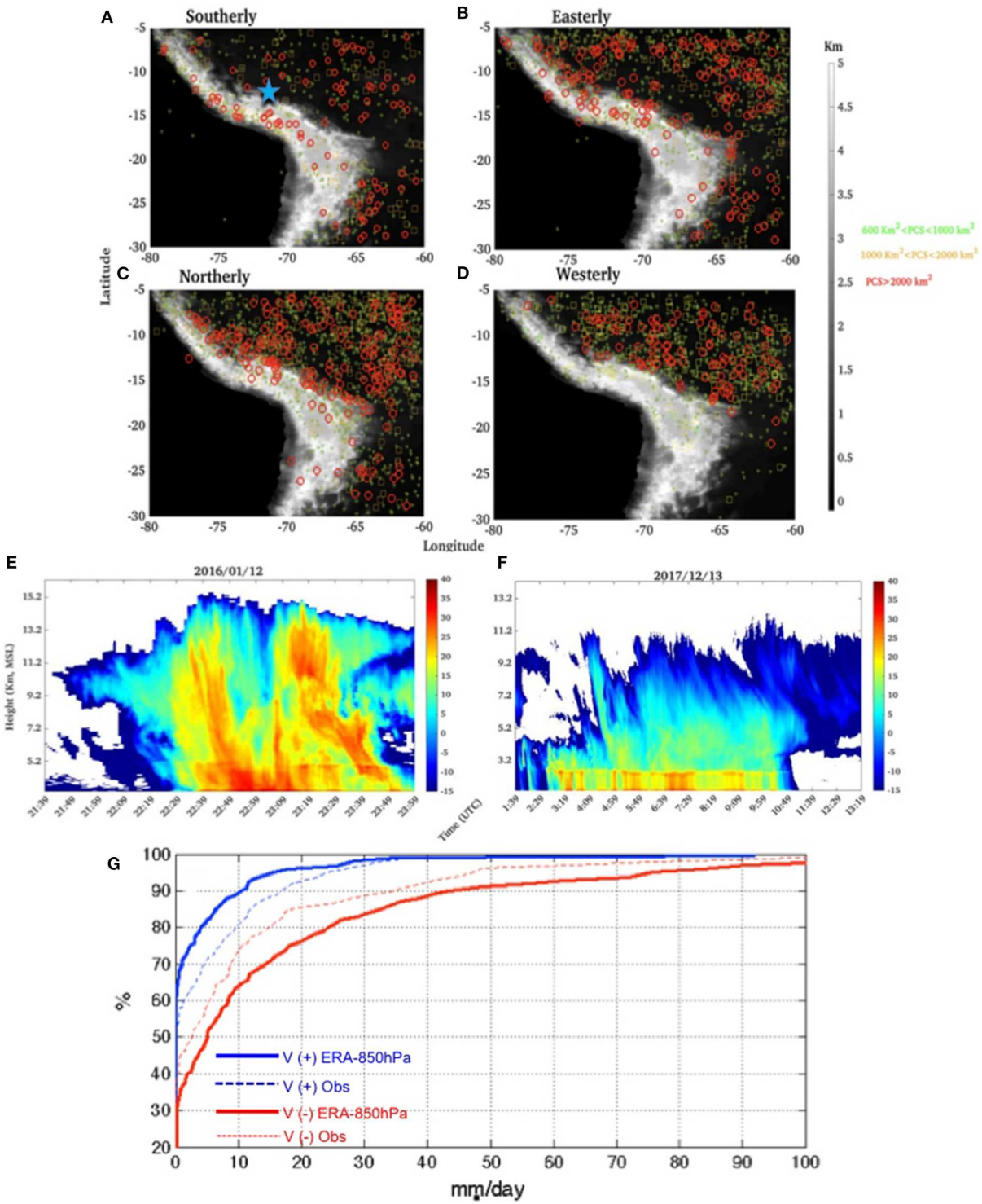


FIGURE 6 | Locations of the precipitation cloud systems for different wind regimes: **(A)** Southerly, **(B)** Easterly, **(C)** Northerly, and **(D)** Westerly. The size of the precipitation cloud systems is represented by different colors (in red, precipitation cloud systems larger than 2,000 km^2). Source: Kumar et al. (2019). © Atmospheric Research. Reprinted by permission from Elsevier. **(E,F)** Radar reflectivity measured by a meteorological Ka band cloud radar installed in the Mantaro Basin, Peru (12.04°S, 75.32°W, 3,322 m a.s.l.) during **(A)** a convective rainfall event (12 January 2016), and **(B)** a stratiform rainfall (13 February 2017). Source Kumar et al. (2020). © Atmosphere – MDPI. CC license. **(G)** Probability distribution function of June-August rainfall over the Quincemil-San Gabán stations in the Amazon-Andes transition zone, southern Peru (blue star, **A**) during different regimes: southerly (V+, blue line), and northerly (V–, red line). 850 hPa winds from ERA-40 and from the meteorological station at Iquitos, Peru, are used to estimate wind regimes (solid and dashed lines, respectively). Adapted from Espinoza et al. (2015). © Water Resources Research. Reprinted by permission from John Wiley and Sons.

2019). Wet episodes over these regions are frequently related to large and medium MCSs, triggered by the orographic lifting of the moist South American low-level jet (SALLJ, Bendix et al., 2009; Giovannettone and Barros, 2009; Romatschke and Houze, 2013; Junquas et al., 2018). Below 2000 m, intraseasonal rainfall variability is mainly modulated by the interplay between SALLJ, cross-equatorial low-level flow and southern winds intrusion toward low latitudes (Wang and Fu, 2002; Espinoza et al., 2015; Chávez and Takahashi, 2017). In the north-western Amazon-Andes transition region (Peru, Ecuador and Colombia) intense storms are more frequent under southerly low-level winds regime, particularly from June to November (Wang and Fu, 2002; Paccini et al., 2017).

Figure 5D shows how the Andes foothills region in Central South America witness localized maxima of storms containing wide convective cores (WCC). These storms are organized at the mesoscale, producing the accumulated rainfall concentrated in the hotspots shown in **Figure 5B**). The region also experiences storms with extensive broad areas of stratiform rain (BSR) as shown in **Figure 5E**, mainly localized in the Andes foothills south of Peru and northern Bolivia. Diurnal analysis of the occurrence of these storms show how WCC peaks during the evening hours while storms containing BSRs peak in the early morning, which suggest that both are part of similar MCSs in either early or later stages of their convective life cycles (Romatschke and Houze, 2010). Chávez and Takahashi (2017) found that surface precipitation over these rainfall "hotspots" at the eastern flank of the Peruvian Andes is characterized by maximum values at 01–06 LT and organizes into MCSs that represent with at least 50% of daily rainfall. Few storms containing deep convective elements are found in the central Andes foothills region (**Figure 5F**), which suggests the orographically-driven moderate convective nature of storms. This observation agrees with the notion that convection here is highly influenced by the proximity to the convection in the Amazon basin, which tends to have less deep, more maritime-like and weaker convection (Houze et al., 2015).

MCSs in the region are observed in about 86% of the cases (Jaramillo et al., 2017) by the moisture transport that converges in the Andes foothills, in association with a stronger SALLJ. In the Central Andes, MCSs mainly occur from December to March, as in the northern part of the La Plata River basin (Jaramillo et al., 2017). The other 14% of the cases are associated with cold surges coming from south-eastern South America. These MCSs show a strong relationship with the diurnal cycle of rainfall in the Amazon-Andes transition region; in the upper Andes and lower Amazon precipitation tends to peak in the afternoon (Killeen et al., 2007), On the eastern slopes of the Andes (800–2,000 m a.s.l.), convection is developed and organized into MCSs during the night and a peak of precipitation is observed at 01–06 LT. These then move downslope (∼700 m) and precipitation declines during the morning (Chávez and Takahashi, 2017).

Extratropical Andes

Intense precipitation events over the extratropical Andes are different than those over the northern and central Andes, and occur both in summer and winter. Most precipitation is delivered by deep stratiform clouds rooted along frontal systems (Falvey and Garreaud, 2007; Viale and Nuñez, 2011), although deep convection associated with cut-off lows (COL) also occur. These weather systems reach the extratropical Andes year-round, and are strongly distorted by the mountains (Barrett et al., 2009). In particular, the cordillera produces a west-east precipitation gradient such that precipitation increases by a factor 2–4 over the western slope of the Andes to sharply decrease to the east of the continental divide (Viale and Garreaud, 2014). The upstream precipitation enhancement and downstream rain shadow across the southern Andes cordillera creates one of the most extreme precipitation gradients on Earth. In frontal cases, the amount of precipitation over the mountains and adjacent lowlands scales directly with the integrated water vapor transported by the westerly winds toward the western Andes (Falvey and Garreaud, 2007). Recent research shows that such transport maximizes in the core of atmospheric rivers (Ralph et al., 2016; Nieto et al., 2019) that landfall between 35 and 45° along the west coast of South America 3–4 times per month (Viale et al., 2018). After making landfall, the ARs face the Andes cordillera where they deliver most of their precipitating. Thus, ARs account for up to 50% of the precipitation in the western slope of the Andes and are associated with about half of the extreme precipitation events in this region (Viale et al., 2018), thus being responsible for the majority of extreme precipitation events along the west slopes of the extratropical Andes (Valenzuela and Garreaud, 2019). A dramatic example of this situation is illustrated with the integrated water vapor and accumulated rainfall on Dec. 17, 2017, which triggered a major flooding causing more than 20 fatalities in the Santa Lucia village in southern Chile (**Figure 7**).

The thermal structure of weather systems is also relevant in triggering extreme hydrological events over the extratropical Andes. In most storms (at least two thirds of the events) precipitation over the central valleys begins almost simultaneously with the arrival of the cold front, so the bulk of the storm accumulation occurs under cold conditions (post-frontal precipitation) with a freezing level altitude around 2,200 m (Garreaud, 2013). This level is well below the Andes crest height between 27 and 37°S (>5,000 m a.s.l.), contributing to the build-up of a seasonal snow pack that eventually melt during spring-summer. Indeed, many cold fronts arriving to central Chile during winter produce a minor increase in the flow of the rivers draining the Andes cordillera. A few winter storms, however, feature warm conditions causing a freezing level as high as 4,000 m a.s.l. and increasing the pluvial area up to a factor 4 relative to average conditions. This winter warm storm, often associated with an AR, can cause large floods downstream (Garreaud, 2013).

Cut-off lows (COL) can cause substantial precipitation near the western slope of the Andes, because the ascent in its leading edge is reinforced by the forced ascent over the terrain. In contrast to cold fronts, COLs can reach subtropical latitudes (northern Chile to southern Peru). An extraordinary COL situation happened in March 22–24, 2015, after warm waters established along the western coast of South America since early March, providing ample moisture in this otherwise dry region. The result was a major rainstorm over the Atacama region, the most arid desert in the world: up to

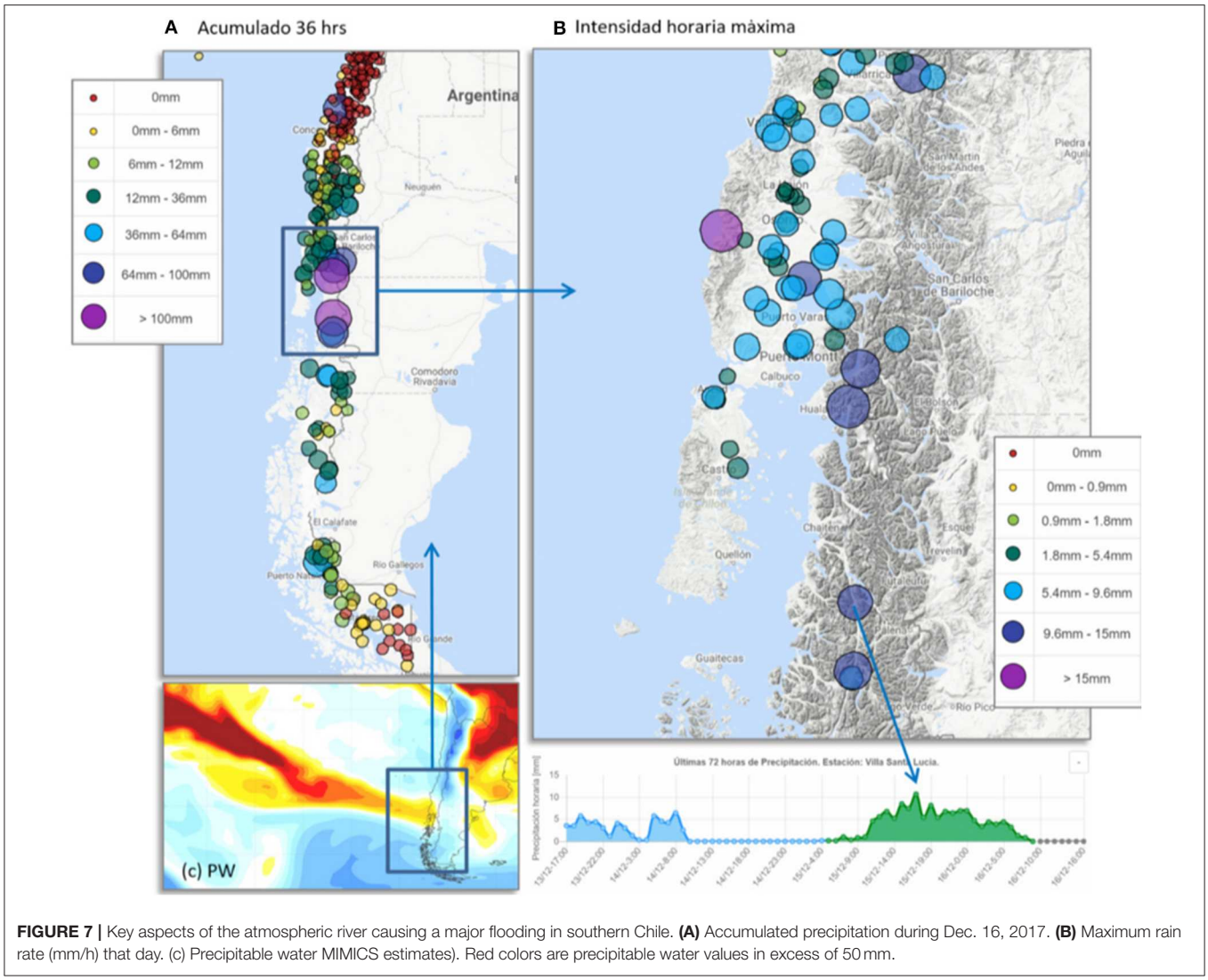


FIGURE 7 | Key aspects of the atmospheric river causing a major flooding in southern Chile. **(A)** Accumulated precipitation during Dec. 16, 2017. **(B)** Maximum rain rate (mm/h) that day. (c) Precipitable water MIMICS estimates). Red colors are precipitable water values in excess of 50 mm.

100 mm during 3 days and rainfall intensities in excess of 10 mm/h at some stations (**Figure 8**). The 2015 Atacama flooding episode is among the worst hydrometeorological disasters in Chile in terms of losses of human lives (more than 60 fatalities) and infrastructure damage (Bozkurt et al., 2016).

Convective rainfall events also occur during dry austral summer months in the northern sector of the extratropical Andes (30–40°S), when liquid precipitation occur as high as 4,000 m a.s.l, triggering landslides and debris flows and damaging infrastructure and international highways (Sepúlveda and Padilla, 2008; Garreaud and Viale, 2014). The synoptic conditions for these summer events are characterized by easterly winds atop of the Andes, opposing the climatological westerly flow that transport moist air toward the mountains (**Figure 9**). The approach of an upper level trough (or COL) is necessary to overcome the large-scale subsidence, thus contributing to exacerbate the intensity of storms (Garreaud and Rutllant, 1997; Viale and Garreaud, 2014).

The southern region of South America experience one of the deepest, and most intense convective systems on Earth (Zipser et al., 2006; Rasmussen et al., 2016), mainly over the region of Mendoza, along the Andes of Argentina. Most of this precipitation occurs in the austral spring and summer (e.g., **Figure 5B**), and concentrates to the east of the Andes in the La Plata River basin (Zipser et al., 2006; Salio et al., 2007; Romatschke and Houze, 2010; Rasmussen and Houze, 2011, 2016). An on-going research effort is under way to monitor and understand the life cycle of convective storms associated with high impact weather in the lee side of the Andes of Argentina (Provinces of Córdoba and Mendoza), known as RELAMPAGO (Remote sensing of Electrification, Lightning, And Mesoscale/microscale Processes with Adaptive Ground Observations; https://www.eol.ucar.edu/field_projects/

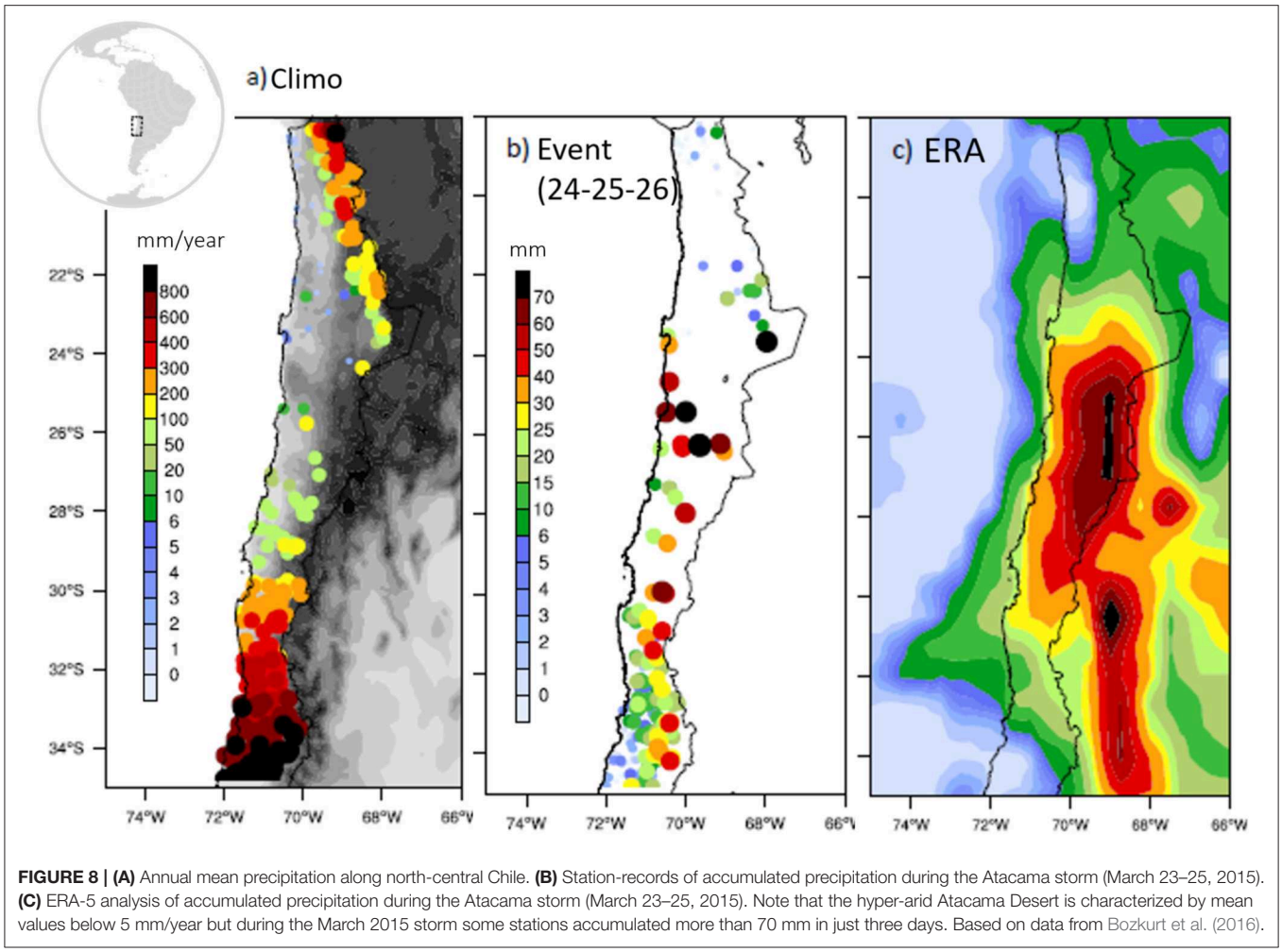


FIGURE 8 | (A) Annual mean precipitation along north-central Chile. **(B)** Station-records of accumulated precipitation during the Atacama storm (March 23–25, 2015). **(C)** ERA-5 analysis of accumulated precipitation during the Atacama storm (March 23–25, 2015). Note that the hyper-arid Atacama Desert is characterized by mean values below 5 mm/year but during the March 2015 storm some stations accumulated more than 70 mm in just three days. Based on data from Bozkurt et al. (2016).

relampago). It is a joint effort between USA, Brazil and Argentina which had an Extended Observing Period from June 1st 2018 to April 30th, 2019, and an Intensive Observing Period from November 1st to December 18th, 2018. This region experiences multicellular storms which rank among the most intense convective systems in the world, exhibiting high tops, large hail, and strong lightning activity. Most of the storms initiate and develop in the early afternoon and late evening hours near and just east of the Sierras de Córdoba, and are predominant during the austral summer (December to February), with large CAPE and weak low-level vertical wind shear (Mulholland et al., 2018). The RELAMPAGO project involve collaboration with CACTI (Clouds, Aerosols, and Complex Terrain Interactions), a USA funded project to study orographic clouds and their representation in multi-scale models (Varble et al., 2019).

Farther downstream of the extratropical Andes, the lowlands of the La Plata River Basin region experience an exceptionally number of localized and widespread convective storms near the La Plata River basin, just east of the Andes ranges (**Figures 5D–F**). There exists a preference for initial deep convective cells to be triggered near the foothills of the Andes close to Sierra de Cordoba in Argentina (e.g., DCCs shown in **Figure 5F**), under a strong topographically-driven convective initiation and maintenance. Although the Amazonian moisture source for the SALLJ does not seem to be as significant as originally thought (Yang and Dominguez, 2019), it is sometimes capped by leeside subsidence of the midlevel dry air that flows over the Andes from the eastward synoptic disturbances. The breaking of this cap triggers the release of convective instability and deep convection leading to tornadoes, hail and floods along the plains between the Andes and the Atlantic coast (Grandoso, 1966; Nascimento and Marcelino, 2005; Matsudo and Salio, 2011; Rasmussen and Houze, 2011; Mezher et al., 2012; Rasmussen et al., 2014). Associated mechanisms of hail occurrence include intense convection with sufficiently high warm and moist updrafts to increase super-cooled water content in the cloud, convergence of moist enthalpy near the ground, and the passage of cold fronts that trigger instabilities favoring upward motion on the warm side of the front, and facilitating the growth of deep convection (Teitelbaum and D'Andrea, 2015).

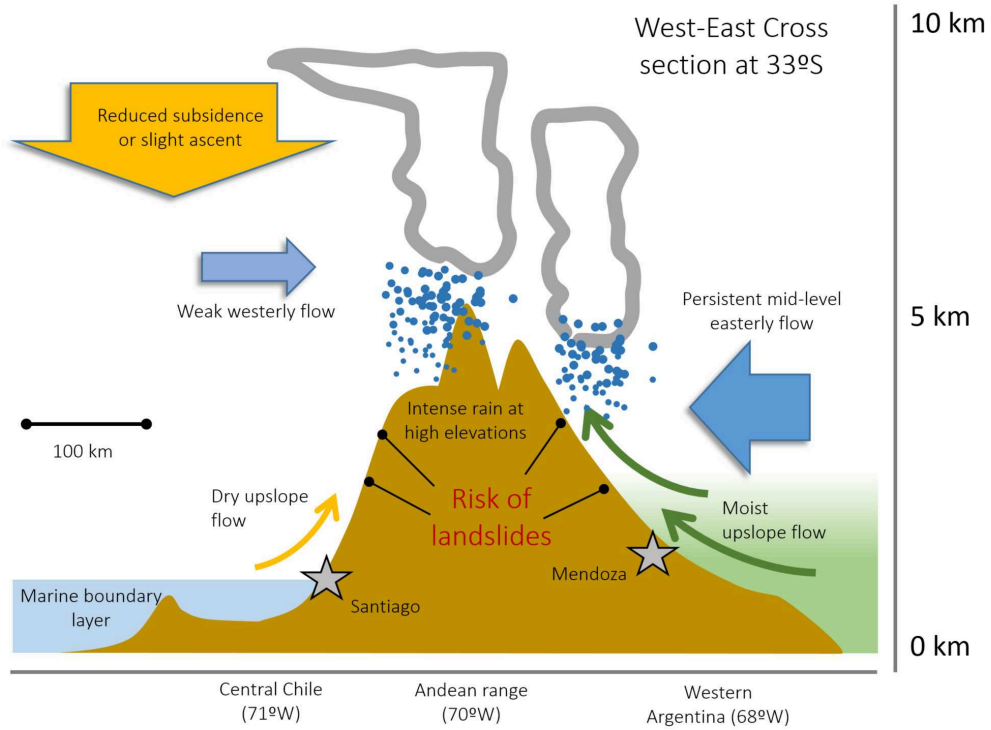


FIGURE 9 | Schematic west-east cross section during summer storms over the extratropical Andes (30-37°S). This is the most frequent type of storm (2/3) associated with an approaching weak trough aloft and easterly winds over the Argentinean side. Adapted from Viale and Garreaud (2014).

COLD SPELLS, FROSTS, AND HIGH WINDS

Northern Tropical Andes

Higher elevations in the tropical Andes pose a challenge for their communities which have to adapt to the occurrence of frosts, as is the case in the northern Andes of Colombia above 2,500 m a.s.l. Such events are typical during dry seasons due to intense radiative cooling of the ground during the night in association with very low cloud cover (**Figure S4**). The occurrence of intense frosts events causes large economic losses to agricultural communities in the Andes by destroying crops and pastures (Bermúdez, 1990; Holmann et al., 2005).

Southern Tropical Andes

Metz et al. (2013) find that along the Andes corridor, extreme cold events reduce 925-hPa temperatures up to 17°C below normal. During these events 925-hPa southerly winds are intensified from 0 to 10 m s^{-1} and the 925–700 hPa lapse rates is low (−3°C km^{-1}). Cold surges, also known as *Friajes* or *Surazos* in Spanish (*Friagems*, in Portuguese), propagate equatorward reaching the Bolivian and southern Peruvian Amazon, causing sudden and severe drops in temperature, up to 10°C in few hours, affecting people, livestock and crops (Marengo, 1983; Ronchail, 1989a,b; Marengo et al., 1997; Garreaud and Wallace, 1998; Pezza and Ambrizzi, 2005; Quispe, 2010; Sulca et al., 2018). Incursions of low-level cold southerly winds from southern South America are also associated with rainy episodes on the Amazon-Andes transition region (Chávez and Takahashi, 2017; Paccini et al., 2017), as well as formation of thick clouds in the Zongo glacier region in Bolivia (16°S, 5,060 m a.s.l.), particularly during the austral winter and spring (Sicart et al., 2015). Hurley et al. (2015) showed that around 70% of the total accumulated snow on the Quelccaya glacier (Peruvian Andes; 5,680 m) is associated with these southern cold air intrusions.

In the central Peruvian Andes, radiative frosts are a major hazard to agriculture. They are caused by low cloud cover, surface air humidity, and soil moisture (Saavedra and Takahashi, 2017), and tend to occur at night times and early morning of the dry and cold seasons (June–August) (Saavedra and Takahashi, 2017; Sulca et al., 2018). During the austral summer, extreme cold events in the Mantaro Valley (central Peruvian Andes, around 500–5,300 m a.s.l.) are caused by intrusions of air masses along the east of the Andes through equatorward displacement of extratropical Rossby waves, negative temperature advection and southeasterly surface wind anomalies, positive OLR anomalies, and possibly influenced by the Madden-Julian Oscillation.

Extratropical Andes

Severe weather events associated with intense downslope wind episodes are observed in the eastward slope of the subtropical Andes and are commonly referred to as Zonda wind events (Norte, 2015). Zonda is a high-speed warm and very dry downslope wind occurring on the lee side of the Andes characterized by very strong wind-gusts affecting several western Argentina areas. Zonda episodes are more frequent during winter

and spring. The occurrence of Zonda events is often associated with large damages on a variety of systems. These damages can be either socio-economical or ecological, such as blowing off roofs, toppling of trees, downing of power electricity supply and communication lines, among others. Because of its association with dry and very warm conditions, it also favors the occurrence of fire events and damage in crops. At high altitudes over the mountains, its occurrence affects the hydrological cycle, by accelerating snow melt and evaporation, and may trigger the occurrence of avalanches (Norte et al., 2008). The classical Zonda episode, described in Norte (2015) occurs in a synoptic environment characterized by a cold front approaching the western coast of South America and the associated migratory depression, as well as a moderate northern flow over central Argentina associated with the presence of the north-western Argentinean low and a warm front located over north-eastern Argentina. These ingredients induce strong baroclinicity, intense vertical wind shear and strong wind components that are transversal to the Andes. In addition, the presence of a warm front downstream the region where the Zonda develops favors its dynamics. Hence, the Zonda is produced by the topographically and dynamically forced ascent of humid air upslope of the Andes and a subsequent orographic descent of a prefrontal air mass which is strongly baroclinic. On the basis of the knowledge of the favorable conditions for Zonda events occurrence, Otero et al. (2018) have constructed a probability index for surface Zonda wind occurrence at the city of Mendoza (Argentina), including the estimation of the onset of the event, as a tool for predicting its probability of occurrence. However, Zonda events have been less investigated over the northern part of the extratropical Andes, where several strong episodes were identified (Otero et al., 2018).

ENSO IMPACTS ON EXTREME EVENTS

El Niño-Southern Oscillation (ENSO) is the most important modulator of the global hydro-climatology at interannual timescales. Its two phases, El Niño and La Niña, trigger a large suite of hydrological and meteorological extreme events worldwide (McPhaden et al., 2006), and particularly in South America and the Andean region (Aceituno, 1988; Waylen and Poveda, 2002; Aceituno et al., 2009; Cai et al., 2020), affecting the livelihoods of societies and imposing a huge socio-economic and environmental burden to the region.

Northern Tropical Andes

During El Niño, the Andes of Colombia experience long and intense droughts, heat waves, and forest fires, while La Niña triggers intense storms, landslides, floods, avalanches and inundations (Poveda and Mesa, 1996, 1997; Poveda et al., 2001a, 2006, 2011; Hoyos et al., 2013; Bedoya-Soto et al., 2018, 2019). **Figure 10** shows the annual cycle of the probability distribution function (box-plots) of maximum intensity 1-h rainfall events in 19 rain gauges on the Colombian Andes (Poveda et al., 2002), including monthly maximum events during both extreme ENSO phases, and also *maxima* events (MME). In general, maximum rainfall intensities are larger (smaller) during La Niña (El Niño), although the MME are not necessarily directly associated with either ENSO phase. Similar conclusions are obtained for storm durations from 1 to 24 h (Poveda et al., 2002). El Niño and La Niña also affect the diurnal cycle of rainfall over the Colombian Andes, by increasing (decreasing) the amplitude during La Niña (El Niño), although the phase remains unchanged (Poveda et al., 2005).

Soil moisture over the Andes of Colombia is affected consistently by both phases of ENSO. **Figure 11** shows soil moisture data gathered at nearby plots covered by shaded coffee, sunlit coffee and secondary forest. Results indicate that the annual seasonal cycle exhibits a strong coupling to interannual (ENSO) variability. Soil moisture exhibited minimum values during the two drier seasons (July through September 1997, and December 1997 through March 1998), amidst the 1997–1998 El Niño event. On the other hand, the bi-modal annual cycle of soil moisture disappeared during the following 1998–1999 La Niña event, exhibiting saturation values throughout the rest of that year. Sunlit coffee plants exhibited stronger water deficits than forest and shaded coffee plants, thus pointing out the relevance of vegetation and land use in controlling water stress (Poveda et al., 2001a, 2011).

Atmospheric teleconnections are part of the physical mechanisms that explain the establishment and persistence of drought in the northern Andes (Poveda et al., 2006, 2011). For instance, droughts in the Andes of Ecuador during El Niño (La Niña) are associated with clear-cut westerly (easterly) surface wind anomalies over the central tropical Pacific and the reverse flow in the higher troposphere (Wang, 2002; Vicente-Serrano et al., 2017). The significant negative correlation between SST anomalies in the central tropical Pacific and precipitation anomalies over the glaciers of Ecuador showcase their strong dependence to both phases of ENSO (Favier et al., 2004; Francou et al., 2004; Vuille et al., 2008; Rabatel et al., 2013).

Southern Tropical Andes

The general effect of ENSO on precipitation in the Southern Tropical Andes tends to be the opposite to the Northern Tropical Andes, with positive (negative) anomalies during El Niño (La Niña). Different ENSO types involve a large range of impacts worldwide through atmospheric teleconnections, in addition to land-atmosphere feedbacks (e.g., Larkin and Harrison, 2005; Ashok et al., 2007; Sun et al., 2013; Bedoya-Soto et al., 2018). In Peru, rainfall anomalies are associated with different types of ENSO, usually denoted as with the EP (Eastern Pacific) and CP (Central Pacific) indices (Yu and Kao, 2007; Kao and Yu, 2009; Takahashi et al., 2011; Lavado-Casimiro and Espinoza, 2014; Sulca et al., 2017; Takahashi and Martínez, 2019). SST warming in the eastern (central) equatorial Pacific is frequently associated with enhanced (reduced) coastal (Andean and Amazonian) rainfall, which can occur, with varying relative magnitudes, during El Niño or, with opposite sign, during La Niña (Lagos et al., 2008; Lavado-Casimiro et al., 2013; Lavado-Casimiro and Espinoza, 2014; Rau et al., 2016; Sulca et al., 2017; Imfeld et al., 2019). Both EP and CP indices are associated with weakened upper-level easterly flow over Peru, more so over the central/southern Peruvian Andes (Sulca et al., 2017). Moreover, during EP El Niño events extreme droughts in the southern

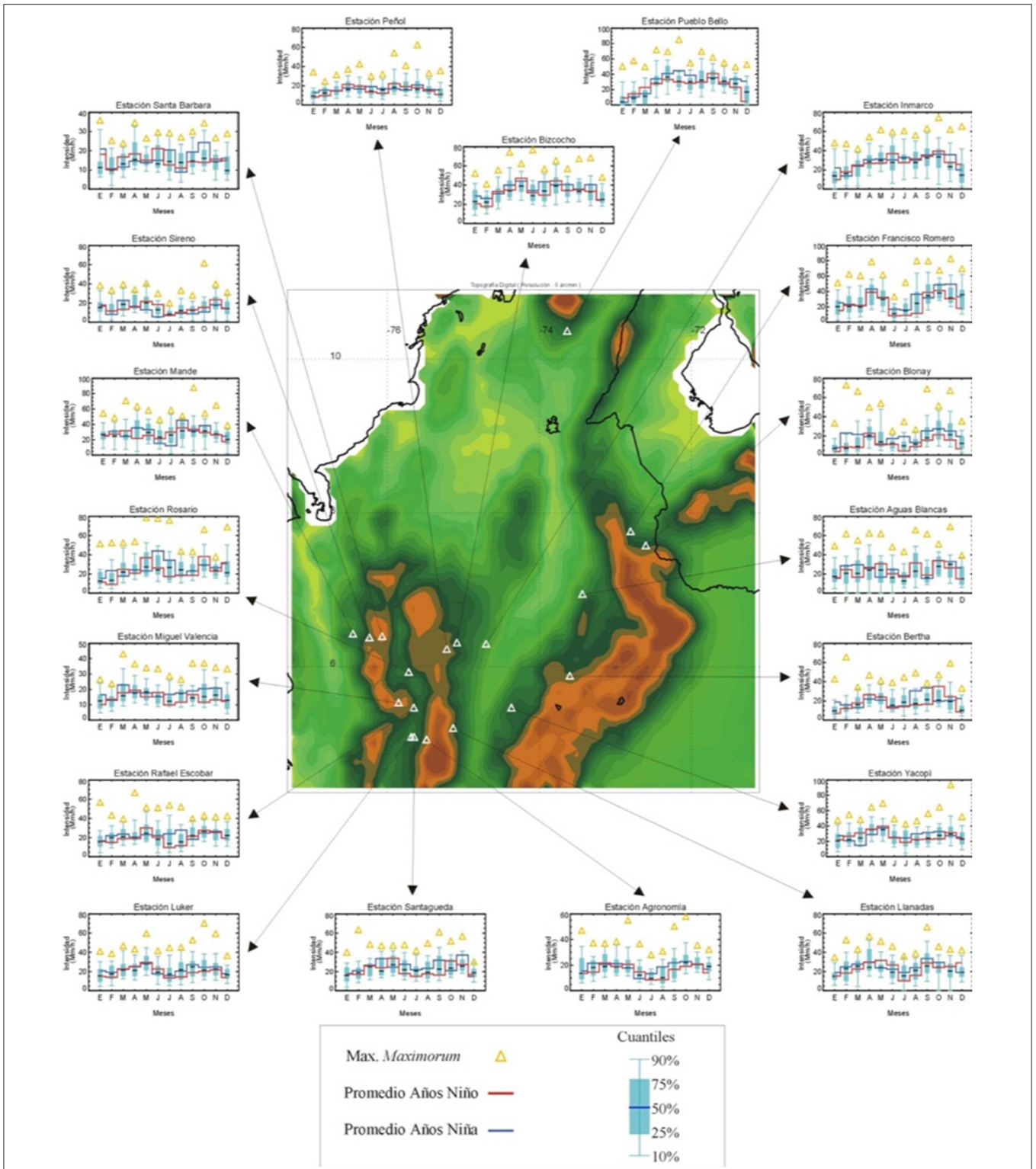


FIGURE 10 | Long-term mean annual cycle of the probability distribution function of 1 h rainfall events, including average values during El Niño (red line) and La Niña (blue line), and maxima values (yellow triangles) recorded at selected rain gauges along the Colombian Andes. Source: Poveda et al. (2002).

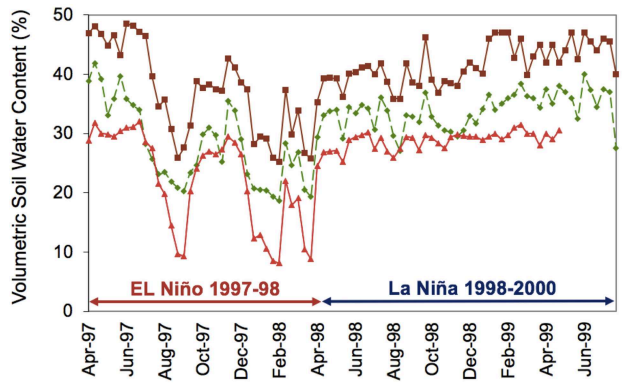


FIGURE 11 | Temporal dynamics of 10-day mean values of volumetric soil water content at 40 cm depth, recorded at three nearby parcels in the Central Andes of Colombia under different vegetation types: shaded coffee (brown), secondary forest (green), and sunlit coffee (red). The studied period (March 1997–August 1999) was under the influence of the 1997–98 El Niño and 1998–99 La Niña events. Adapted from Poveda et al. (2001b).

Peruvian Andes are associated with a stronger warming in the troposphere above the central Pacific Ocean (Imfeld et al., 2019). However, not all extreme droughts over the region are explained by El Niño. The Bolivian High and moisture advection from the Amazon play an important role (e.g., Segura et al., 2016, 2020; Imfeld et al., 2019).

Over the Peruvian coast, El Niño is the main modulator of rainfall variability at interannual scale. The strong 1982–83 and 1997–98 El Niño events were characterized by an enhancement of convective activity in the eastern Pacific (Takahashi et al., 2011; Takahashi and Dewitte, 2016; Jauregui and Takahashi, 2017), and intense storms leading to floods in the central and northern Peruvian coast (e.g., Woodman, 1985, 1999; Lavado-Casimiro et al., 2013; Bourrel et al., 2015; Rau et al., 2016). Rainfall and streamflow records in the Piura River basin (5.2°S, 80.6°W, 40 m a.s.l.; **Figure 12A**) characterize El Niño impacts (e.g., Deser and Wallace, 1987; Takahashi and Martínez, 2019). For instance, while the mean annual discharge is around 28 m^3/s (Lavado et al., 2012), it reached values of 442 m^3/s and 364 m^3/s during the 1998 and 1983 El Niños, respectively (Takahashi and Martínez, 2019). Accordingly, during extreme El Niño events suspended sediment yield in the Peruvian coast increases by 3 to 60 times compared to the 1968–2012 multiyear average (**Figure 12B**; Morera et al., 2017). In turn, Rodriguez-Morata et al. (2018) estimated that 21% of the total hydro-geomorphic disasters reported in Peru during the 1970–2013 period (including generic rainfall-related damage such as muddy areas, structural damage, holes, etc.) were related to the 1972–1973, 1982–1983, and 1997–1998 El Niño events. The 1997–1998 El Niño-driven flood damages were estimated to be around USD 1 billion, primarily along the northern coast of Peru (OPS, 2000).

A complex relationship is observed between ENSO variability and rainfall over the Peruvian coast (Bourrel et al., 2015). The so-called "coastal El Niño" strongly impacts the hydrology of Peru, such as in 1891, 1925, and 2017, characterized by warm SST anomalies over the easternmost tropical Pacific, and cold SST anomalies in the central tropical Pacific. Costal El Niño events of 1925 and 2017 are documented in Takahashi and Martínez (2019) and in Garreaud (2018a), respectively. According to Rodriguez-Morata et al. (2019) the 2017 Coastal El Niño produced rainfall records in northern Peru that can only be compared to the extraordinary El Niño events of the last 40 years, namely 1982–83 and 1997–98.

Over the Altiplano a dominant negative (positive) relationship between El Niño (La Niña) and summer (DJF) rainfall has been identified (Vuille et al., 2000; Garreaud et al., 2009). This signal becomes rather weak to the north of the Altiplano and to the sub-Andean valleys of the southwestern Amazon below 1,500 m a.s.l. (Ronchail and Gallaire, 2006). The ENSO-Altiplano rainfall emerges from the changes in the zonal wind atop of the Andes during austral summer. During El Niño years the subtropical jet stream is enhanced thus reducing the transport of moist air from the continent toward the mountains (Garreaud, 1999). The opposite situation occurs during La Niña years, when weaker westerlies in the mid troposphere foster the intrusion of moist air from the eastern lowlands toward the Altiplano. In a recent study, a second mechanism associated with upward motion over the western Amazon, has been proposed to explain the interannual precipitation variability over the Altiplano (Segura et al., 2020). The authors show a slight increase in rainfall over the past two decades, in association with the strengthening of upward motion over the western Amazon.

Seiler et al. (2013) investigated interannual climate variability in Bolivia. Temperatures were found to be higher in the Andes during El Niño, as well as during the positive phase of PDO and the Antarctic Oscillation (AAO). During the positive phase of the PDO the total annual rainfall and the frequency of intense storms were higher, regardless of ENSO phase in the lowlands. During December-February, El Niño was associated with drier conditions in the Andes with more variable precipitation.

Extratropical Andes

ENSO is a major modulator of interannual precipitation along the extratropical Andes (25–40°S), exhibiting positive (negative) anomalies during the occurrence of El Niño (La Niña). While most precipitation in this area occurs during austral winter, it does not coincide with the peak of ENSO. Yet, the correlation coefficient between Niño3.4 index and annual rainfall is about 0.6 across this region (Montecinos and Aceituno, 2003), which mostly relies on rainfall over the western slope of the Andes (central Chile). In this region, the probability of having an extreme precipitation event (>40 mm/day) is twice as large during El Niño events compared to neutral conditions. Contrary, the probability of extreme events does not decrease substantially during La Niña events.

On the eastern side of the Andes, El Niño (La Niña) is associated with positive (negative) anomalies in precipitation, river runoff and landslides (Compagnucci and Vargas, 1998; Moreiras, 2005) during both winter and summer months. Significant differences in the frequency of occurrence of extreme precipitation events have also been identified over western Argentina during winter and late spring, with increased

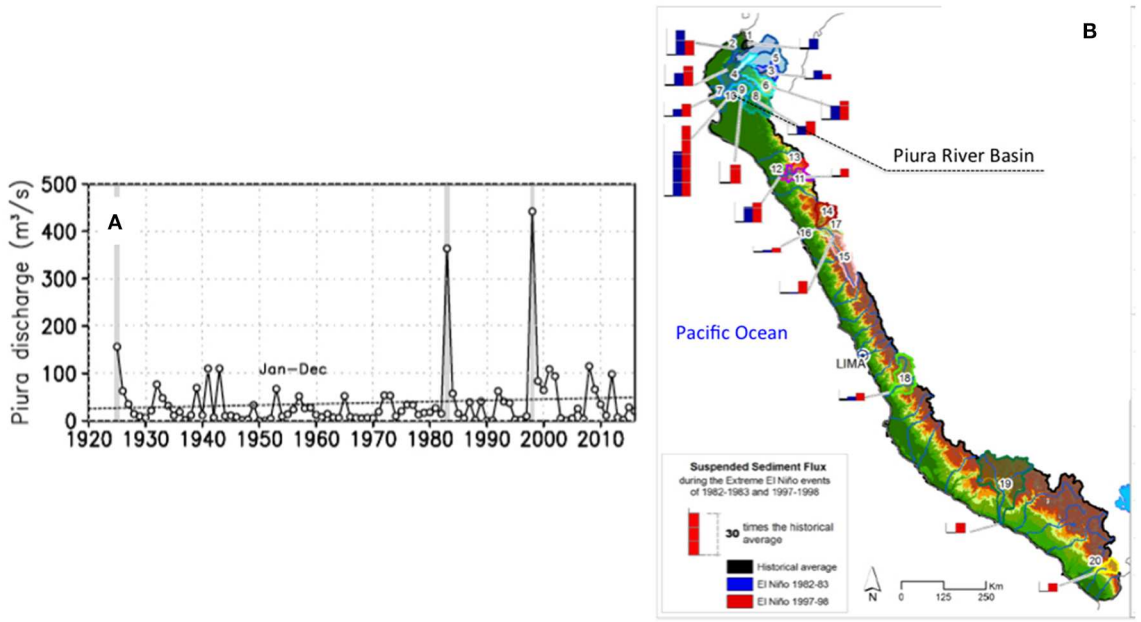


FIGURE 12 | (A) January-December mean discharge of the Piura River during the 1925–2015 period. The linear trend is indicated in dashed line. Vertical gray lines indicate the strong El Niño events of 1925, 1983, and 1998. Adapted from Takahashi and Martínez (2019). © Springer Nature. CC license. **(B)** Suspended sediment flux observed in the Peruvian coast. Black bars represent climatological sediment flux, red and blue bars display sediment flux during El Niño years of 1982–83 and 1997–98, respectively. Each cube on the bar represents the sediment flux transported over 10 normal years. Adapted from Morera et al. (2017). © Springer Nature. CC license.

(decreased) number of extreme events during El Niño (La Niña) (Grimm and Tedeschi, 2009).

FLOODS

Northern Tropical Andes

Colombia ranks first in Latin America and the Caribbean in losses and damages (per 100,000 inhabitants), from natural hazards during 1999–2013 (UNISDR, 2016). Most of them are associated with massive flooding during La Niña events (Poveda and Mesa, 1996, 1997; Poveda et al., 2001a, 2002, 2006; Hoyos et al., 2013; Bedoya-Soto et al., 2018). During the 2010–11 La Niña event, widespread flooding caused damages and losses in excess of 6 Billion US dollars, or 2% of Colombia's GDP for 2011. One reason is the intensification of the CHOCO low-level jet during La Niña, which transport large amounts of atmospheric moisture from the far eastern Pacific onshore, thus providing extra moisture for the development of MCSs and intense storms that can lead to widespread flooding along the Andes of Colombia and Ecuador. Typically, such steep river basins witness intense storms that produce flash floods, as the Guayas River in Ecuador during El Niño years (Frappart et al., 2017). Flooding mechanisms in tropical Andean cities depend on the preceding 24-h rainfall, baseflow, urbanization patterns, soil types and saturation conditions, as in the case of Quito (Perrin et al., 2001).

On the other hand, flash flood emergencies have also been observed to occur in periods with negative monthly precipitation anomalies associated with El Niño conditions as was the case of 18 May, 2015 in La Liboriana basin in the Municipality of Salgar, Colombia, causing more than 100 casualties and significant infrastructural damage. The meteorological factors associated with the emergency showed the role of successive precipitation pulses in relatively short periods that were intensified as deep convective cores interacted with the steep topography (Hoyos et al., 2019). These results show the challenges to opportunely pinpoint convective intensification over complex mountainous terrain from observations and forecast models to improve local risk reduction strategies over vulnerable regions of the tropical Andes.

Southern Tropical Andes

Floods in the central Andes can be triggered by intense storms and/or rapid glacier melting during the spring-summer of the austral hemisphere (Huggel et al., 2015). Flash floods commonly originate in moraine-dammed lakes threatening communities located in the Cordillera Blanca of Peru (Emmer, 2017). In addition, urbanization is increasing the risks of flash floods (Bourges et al., 1995; Méndez et al., 2016). In the valleys of Urubamba and Vilcanota in the Cuzco region, extreme rainfall and floods occurred in January and February 2010 causing USD 200M in damages and losses (Lavado-Casimiro et al., 2010) See **Figure S5**.

In the Peruvian Coast and most of the western flank of the Peruvian Andes, extreme floods have been associated with El Niño dating back to pre-Inca societies (e.g., Takahashi, 2004;

Manners et al., 2007; Lavado-Casimiro and Espinoza, 2014; Rau et al., 2016). Three distinctive flooding responses to El Niño have been found over the western Andes of the Chancay River north of Lima (Peru): coastal desert, Lomas, and mountain desert. The mountain desert and valleys of the Pacific slopes are devastated by catastrophic floods and torrential rains during El Niño. However, less abundant precipitation is observed in Lomas, favoring the development of vegetation during the austral winter (Kalicki et al., 2014).

Besides the strong impacts of El Niño on the Peruvian coast, extreme rainfall in Peru has also been reported during La Niña and neutral conditions in the equatorial Pacific (Ronchail et al., 2002; Espinoza et al., 2012b; Lavado-Casimiro and Espinoza, 2014; Sulca et al., 2017; Recalde-Coronel et al., 2020). Indeed, excessive rainfall over the central and western Amazon have been related to La Niña events, and to warm anomalies in the tropical South Atlantic Ocean (TSA), in association with extreme rainfall and floods, as reported in 2009, 2012 and 2014 (Ronchail et al., 2005; Marengo et al., 2010, 2011, 2013; Satyamurty et al., 2013). Rodriguez-Morata et al. (2018) documented that more than 36% of the hydro-geomorphic disasters reported in Peru during the 1970–2013 period were associated with La Niña and neutral conditions in the equatorial Pacific. The very unusual wet 2014 austral-summer period originated in the eastern slope of the Peruvian and Bolivian Andes and flooded the southern Amazon (Espinoza et al., 2014; Ovando et al., 2016; **Figure 13**). This exceptional event has been associated with warm anomalies in the western Pacific-Indian Ocean and over the subtropical South Atlantic Ocean.

Extratropical Andes

Highly intense and short storms regularly trigger severe flash floods in the Andes of Mendoza, Argentina. Although previous studies have been unsuccessful in simulating peak discharges, factors such as storms characteristics and soil variability (quasi-impervious areas) play a key role, along with vegetation, surface storage capacity, and antecedent soil moisture (Braud et al., 1999). Other studies have proposed that surface, perimeter, basin length, elevations, and slope can be useful to predict floods over that region (Perucca and Angilieri, 2011). Flash floods in the Patagonian Andes have been reconstructed from dendrochronological studies (Casteller et al., 2015).

Along the western slopes of the southern Andes (continental Chile) floods occurs mostly during winter storms with significant precipitation (>50 mm/day), and have warm characteristics (thus producing a high freezing level) or last for more than 3 days. Recent events have been observed in northern, central and southern Chile (Valenzuela and Garreaud, 2019) and they are associated either with atmospheric rivers (Viale et al., 2018) or cut-off lows (COLs), as described in section Extratropical Andes.

A trend analysis was performed on annual peak river flows between 1975 and 2008 for rivers in the semi-arid (29−32°S) and temperate (36−38°S) zone of the Chilean Andes (Pizarro et al., 2014). Negative trends were identified in 87% of the stations in the semi-arid zone while positive trends were found in 57% of the stations in the temperate zone. Differences in trends sign seem to be associated with the positive trend in the altitude of the zero-degree isotherm in this region.

LANDSLIDES, MUDSLIDES, AVALANCHES

The Andes, as all high mountain regions worldwide are subject to landslides, mudslides, rockslides, debris flows, and avalanches due to the steep topography, the soil and rock characteristics, land cover/land use change, and climate and weather patterns (Hermanns et al., 2012; Stahr and Langenscheidt, 2015). Intense storms, likely exacerbated by global warming and increased climate variability are the most important cause of landslides in the Andes (Moreiras, 2006; Sepúlveda and Petley, 2015).

Rainfall-triggered landslides cause large number of fatalities, damages and losses along the Andean, affecting human and animal lives, civil infrastructure, roads, crops, and the provision of public services (Nossin, 1999; Moreiras, 2006; Michoud et al., 2016; Younes-Cárdenas and Erazo-Mera, 2016), pipelines (Lee et al., 2009; Pettinger and Sykora, 2011; Bustinza et al., 2013; Contreras et al., 2013; García et al., 2013; Oliveros et al., 2017), and water supply systems. See **Figure S6**. Also, infrastructure development and construction favor the occurrence of landslides in the Andes (Brenning et al., 2015). On the other hand, meteorological conditions also determine the type and intensity of snow avalanches in the Andes of Argentina (Naaim et al., 2002).

These risks are particularly enhanced by the combined effects of rock avalanches causing temporal lakes and the ensuing dam failures (Ferrer, 1999; Hermanns et al., 2004). Intense storms exacerbate sediment production by slope movement on hillslopes, directly affecting their transport and deposition in downstream rivers and dams, as well as producing morphological changes in stream channels. The role of vegetation is critical on the stability of runoff and sediment yield and for example deforestation of the Andes plays a deleterious role (Braud et al., 2001). The Multinational Andean Project (MAP:GAC 2002–2008) have set forward regional guides for landslide studies and mapping, and have conformed the first regional group of researchers for landslide studies in the Andes (GEMMA) (Jaramillo, 2008).

Northern Tropical Andes

The combination of intense storms and steep terrain are major causes of landslides in the tropical Andes. For instance, a 3 h rainfall event (208 mm) on September 21, 1990, triggered more than 800 landslides along the Andes of Colombia (Aristizábal et al., 2015). The SHALSTAB model (Montgomery and Dietrich, 1994) was able to capture the physics involved in such landslides. López Salgado (2016) studied mass movements in the upper Coello River basin in the Central Andes of Colombia and identified that they result from the combination of high rainfall, steep slopes, and unstable volcanic ash cover.

There is also a strong connection between deforestation and land use change with erosion and landslides in the tropical Andes. Erosion rates in the Magdalena River basin, located between the central and eastern ranges of the Colombian Andes, have shown

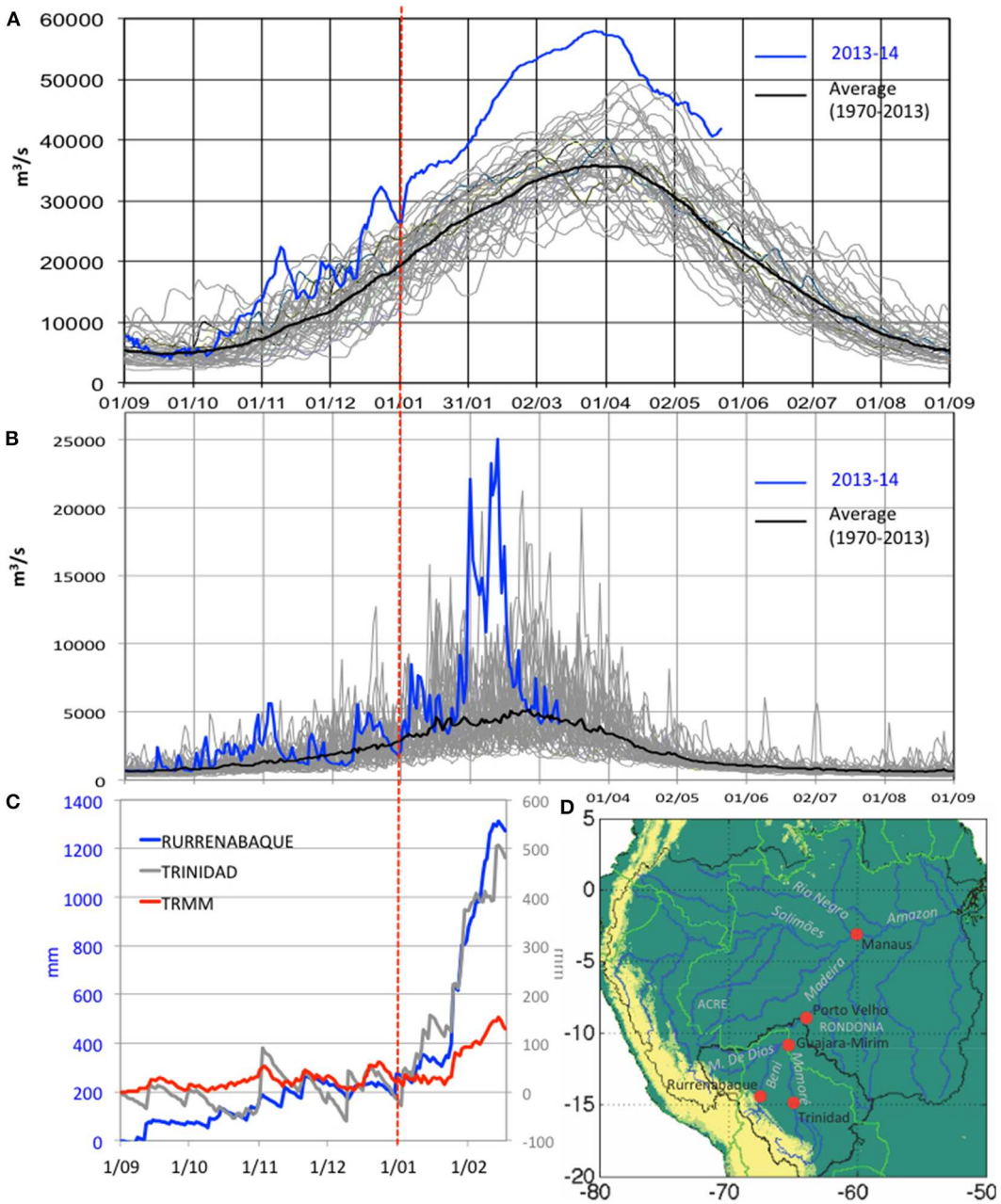


FIGURE 13 | Daily discharge at **(A)** Porto Velho on the upper Madeira River, and **(B)** Rurrenabaque on the upper Beni River during the period of 1970–2013 (gray lines). Mean discharge values and discharge during the 2013–14 hydrological year are displayed in black and blue lines, respectively. **(C)** Cumulative rainfall anomalies in Rurrenabaque (blue, left Y axis) and Trinidad (gray, right Y axis), and area average rainfall in the Porto Velho River basin computed with TRMM-RT 3B42 V7 (red, right Y axis), for the 01/09/2013–17/02/2014 period. **(D)** Location of stations and main rivers. Adapted from Espinoza et al. (2014). © ERL. CC license.

an increase from 550 ton km^{-2} y^{-1}, in the years previous to 2000, to 710 t km^{-2} y^{-1} between 2000 and 2010, as well as sediment load (average increase of 44 Mt y^{-1}), coinciding with a forest loss of 40%, and an increase of 65% in areas dedicated to agriculture and pastures (Restrepo and Escobar, 2018).

Deforestation and land use change significantly alter the landslide frequency-area distributions in the Andes of Ecuador (Guns and Vanacker, 2014). A strong increase in the frequency of small landslides in anthropogenic environments explains in part the observed enhancement in landslide denudation rates in this region (Vanacker et al., 2003, 2013; Molina et al., 2012; Guns and Vanacker, 2013, 2014). Marie and Veerle (2013) suggest that deforestation causes major changes in soil properties and hydrology, accelerating landslide activity. In other cases, vegetation contributes to destabilize slopes owing to its contribution to the organic layer mass, and promotes

a new cycle of vegetation succession. Vanacker et al. (2007) show evidence that the steepness of topography contributes more than human activities or land use practices to the occurrence of infrequent large landslides over the Andes of Ecuador.

Although many landslides in the Andes are triggered by highly intense storms, Soto et al. (2017a) found that only 24% landslides in the Loja River basin (southern Ecuador) were triggered by intense storms whose return periods exceed 1 year, and less for the 76% of landslides. Also, rainfall events that are not exceptionally intense can reactivate these landslides (Soto et al., 2017b).

Erosion processes in the Andean river basins yield large concentrations of suspended sediment to the western part of the low-lying Amazonia. For example, as is the case of the Napo River in the Amazonian regions of Ecuador and Peru, where annual mean erosion rates are approximately 1,160 t km^{-2} (Laraque et al., 2009; Clark et al., 2016).

Younes-Cárdenas and Erazo-Mera (2016) developed an explanatory model to predict the degree of susceptibility of landslides along the E-20 highway in Ecuador, and concluded that the distribution of landslides was far from random, and clearly associated with several geological and environmental factors, including zones of active erosion processes, volcanic sandstones, granitic rocks and mean annual rainfall values between 1500 and 1750 mm. The non-random nature of landslides in space and time has been confirmed by Muñoz et al. (2017) who showed the multifractal space-time characteristics of landslides in the Andes of Colombia.

The main source of sediments (and nutrients) to the lower Amazon River basin is located along the Andes. Townsend-Small et al. (2008) studied the production and transport of sediments and suspended organic matter along the Chorobamba River in the central region of the Andes-Amazon transition of Peru. At least 80% of total annual suspended sediment, 74% of organic carbon, and 64% of organic nitrogen transport was concentrated in 10 days of the year, with significant seasonal changes in sources of organic matter. The latter indicates that extreme events are the main origin for this process.

Southern Tropical Andes

Global warming linked to intense storms and stronger El Niño events, along with permafrost degradation and glacier retreat promote slope instability in the Central Andes, thus increasing the frequency and intensity of landslides. These processes can modify the spatial distribution of landslides, shifting initial points of slope instability to higher altitudes, and triggering more complex and larger landslides (Moreiras and Pont, 2017). Furthermore, large mass movements that originated as rock/ice falls from the glacierized Andes can become high-volume high-velocity mud-rich debris flows, such as the 1962 and 1970 events in Nevado Huscarán (Cordillera Blanca, Peru) (Evans et al., 2009).

Landslides play an important ecological role (Restrepo et al., 2009; Smith, 2011). An inventory over the Andes of Peru indicated turn over times of 1,320 years (Clark et al., 2016), removing 264 tC km^{-2} yr^{-1} of organic carbon mostly from soils (80 %) in 25 years. A single storm event in March 2010 was responsible for 27% of the total landslide area reported, and produced 26% of the organic carbon flux associated with landslides during such 25-yr period (Huggel et al., 2015). Heavy rainfall reported during the austral summer of 2010 in Cuzco region caused economic losses estimated to be around 250 million US dollars. Landslide and flash floods destroyed around 5,000 houses, 16,300 ha of farmlands, 6.15 km of the Cusco-Machu Picchu railway line and 21 bridges (Lavado-Casimiro et al., 2010; **Figure S5**).

Lowman and Barros (2014) investigated the links between precipitation and erosion in the central Andes, and estimated mean erosion rates of 2.1–8.5 mm per year, which happens to be 1 to 2 orders of magnitude larger than long-term estimates (1,000 to 1 million years) for the central Andes. On the other hand, erosion rates in the Eastern Cordillera (northern Bolivia) have been estimated as 5–14 mm per year (Blodgett and Isacks, 2007).

The ratio of sediment transport between hillslopes and channels in the Peruvian Andes influences geomorphological features and the morphology and dynamics along the channel network (Schneider et al., 2008). The headwaters of river channel networks exhibit rough and high-relief surfaces with deep incisions and dense drainage density. Thus, storminess influences the production and transport of sediments on hillslopes and channels, reflected into landscape morphometry.

Extratropical Andes

Rock avalanches along the northwest Andes of Argentina are produced by active tectonics, in addition to lithologic, structural and topographic conditions, and climate change (Hermanns and Niedermann, 2006). Landslides in the Andes of Argentina and Chile have been linked to intense summer storms, in particular during El Niño (Trauth et al., 2000; Espizua and Bengochea, 2002; Marwan et al., 2003; Moreiras, 2005; Sepúlveda et al., 2014a,b; Moreiras and Sepúlveda, 2015; Moreiras et al., 2018). The most dangerous are caused by the zero-isotherm lifting in smaller basins exhibiting debris-rock glaciers, so-called "ENSO-climate change" landslides (ECCL; Moreiras et al., 2018).

The melting of snow accumulated in the winter conductive to saturation of soils and landslides in the following spring and summer seasons (December to February) is the major cause of slope instability in the Aconcagua Park, as evidenced in the high significant correlation between landslides and river discharges, and a weak relationship between landslide and temperature records (Moreiras et al., 2012).

DROUGHTS, HEAT WAVES, AND FIRES

ENSO is a major driver of droughts in various regions of South America (Zhou and Lau, 2001; Kane, 2006; McPhaden et al., 2010; Cai et al., 2020), in particular El Niño is associated with droughts over large parts of Colombia, Venezuela, some regions of the high Andes of Ecuador, Peru and Bolivia (Francou, 1985; Caviedes and Endlicher, 1989). At the same time, La Niña is

associated with droughts in other regions of Ecuador, Bolivia, Chile and Argentina.

Northern Tropical Andes

Multiple studies have shown that droughts in the northern tropical Andes are associated with the occurrence of El Niño (section ENSO Impacts on Extreme Events, Northern Tropical Andes) through changes in the Hadley circulation (Poveda et al., 2006, 2011; Arias et al., 2015), the Walker circulation (Kousky et al., 1984; Vuille, 1999; Vuille et al., 2000; Francou et al., 2004; Poveda et al., 2006, 2011; Vicente-Serrano et al., 2011a,b, 2017), as well as to land surface-atmosphere feedbacks (Poveda and Mesa, 1997; Bedoya-Soto et al., 2018, 2019). Such droughts have deleterious impacts on water supply for humans and livestock, crops failure, and contribute to intensify forest fires, heat waves, as well as outbreaks of malaria, dengue and other vector-borne diseases, and electricity shortages owing to the importance of hydropower generation.

Tropical cloud forests are facing huge threats from fires, deforestation and climate change (Mutke et al., 2017). Deforestation and land use/land change also affect the dynamics of soil moisture in the Andes of Colombia, reducing water storage capacity and leading to higher peak flows (Ramírez et al., 2017).

The frequency and duration of dry periods in Quito has been increasing since the middle of the last century, compared to the last 400 years (Domínguez-Castro et al., 2018). The strongest dry periods occurred in 1692–1701 (the severest one), 1718–723, 1976–1980, 1990–1993, and 2001–2006. The great drought that lasted from 1692 to 1701 caused generalized famine in Quito and affected the majority of population of the central Andes. Such dry periods affect water supply, agriculture and have strong ecological impacts (Chirino et al., 2017).

The unique tundra ecosystems above 3,500 m in the neotropical Andes, *páramos*, play a fundamental ecological and hydrological role below the snow line in the high Andes, in terms of ecosystem services, such as water retention for human and animal consumption, irrigation, and hydropower. Droughts have a strong impact on the hydrological dynamics of *páramos*, such that the recovery from droughts are fundamentally determined by the aridity index (Iñiguez et al., 2016).

The dynamics of fires in the Andes of Colombia is highly controlled by the occurrence of El Niño (Becerra and Poveda, 2006). On the other hand, fires in Ecuador, Peru and Bolivia (Paramo, Yungas, and Puna, respectively) do not show a significant relation to ENSO, but to periodic weather patterns of precipitation: increased rainfall the year before fire-peak seasons followed by very dry periods and unusual low temperatures during the fire-pike (Román-Cuesta et al., 2011, 2014).

Southern Tropical Andes

Over the Altiplano region century-scale dry periods have been identified using a 707-yr dendrochronological reconstruction (Morales et al., 2012). A persistent negative trend in precipitation has been identified from 1930s to date. At interannual to multidecadal time scales, those authors also identified an ENSO-like pattern. Severe drought condition in the Altiplano region were reported during 1983 and 1992 El Niño years (Garreaud et al., 2003; Segura et al., 2016). During the 2015–2016 El Niño event, extreme dry conditions were reported over the Altiplano (Marengo et al., 2017). Severe drought affected central and southern Bolivia, with deficits of rainfall surpassing 30%. Low river discharges were documented in the northern part of the Titicaca basin (Peru) (Jiménez-Muñoz et al., 2016).

The Western Amazon has suffered three periods of extreme droughts since the beginning of the XXI Century (2005, 2010, and 2016; Espinoza et al., 2011; Jiménez-Muñoz et al., 2016), with deleterious ecological consequences (Maeda et al., 2015).

During extreme drought years, impacts on the vegetation have been identified over this region, such as reduction in vegetation activity (measured using NDVI index) and forest fires during the 2005, 2010, and 2016 droughts (Fernandes et al., 2011; Espinoza et al., 2016; Jiménez-Muñoz et al., 2016). Peaks of active fires in Amazonia have been more related to extreme drought than deforestation (Aragão et al., 2018), although the intense fire 2019 summer season was indeed related with deregulation policies in the Brazilian Amazon and the concomitant deforestation (Amigo, 2000; Lovejoy and Nobre, 2019; MAAP, 2019; Wheeling, 2019). These fires and the resulting smoke and soot can reach the highest Andes, contributing to accelerate their on-going rapid melting and disappearance (Allen, 2020). Espinoza et al. (2019) documented an increase in the dry day frequency (DDF) over the central and southern Peruvian Amazon, as well as in the Bolivian Amazon, considering the 1981–2017 period. See also Espinoza et al. (2020).

Various studies document the demise and collapse of pre-Columbian civilizations due to extensive droughts in the Central Andes. For instance, during the sixth century, major cultural disturbances were reported on the northern Peruvian coast, including the Mochica culture that was conditioned by severe sixth-century droughts, spanning from 562 to 594 CE (Shimada et al., 1991). Likewise, the Tiwanaku state, in the south-central Andes, disintegrated between c. AD 1000–1100, after 700 years of growth and colonial expansion. Such droughts impacted irrigation-based agriculture in the low-altitude colonies and the groundwater-dependent raised-field systems in the Altiplano (Ortloff and Kolata, 1993).

In the central Peruvian Andes, dry spells during the wet season (December to March) are associated with a weakened convective activity over the western tropical Pacific, that is in accord with the impacts of El Niño over the region (Sulca et al., 2016). The authors also show that westerly wind anomalies over the upper troposphere reduce moisture flow from the Amazon basin, producing dry events over the Peruvian Andes. Reduced snowfall from suppressed frontal activity in the Central Andes of Argentina is another mechanism that propagates droughts into river flows, mainly driven by La Niña-like conditions in the Pacific Ocean (Rivera et al., 2017b).

Extratropical Andes

The semiarid, Mediterranean-like climate of the extratropical Andes (30-40°S) makes this region drought-prone. Most of the annual precipitation is concentrated in few rain events. This region exhibits high year-to-year variability and

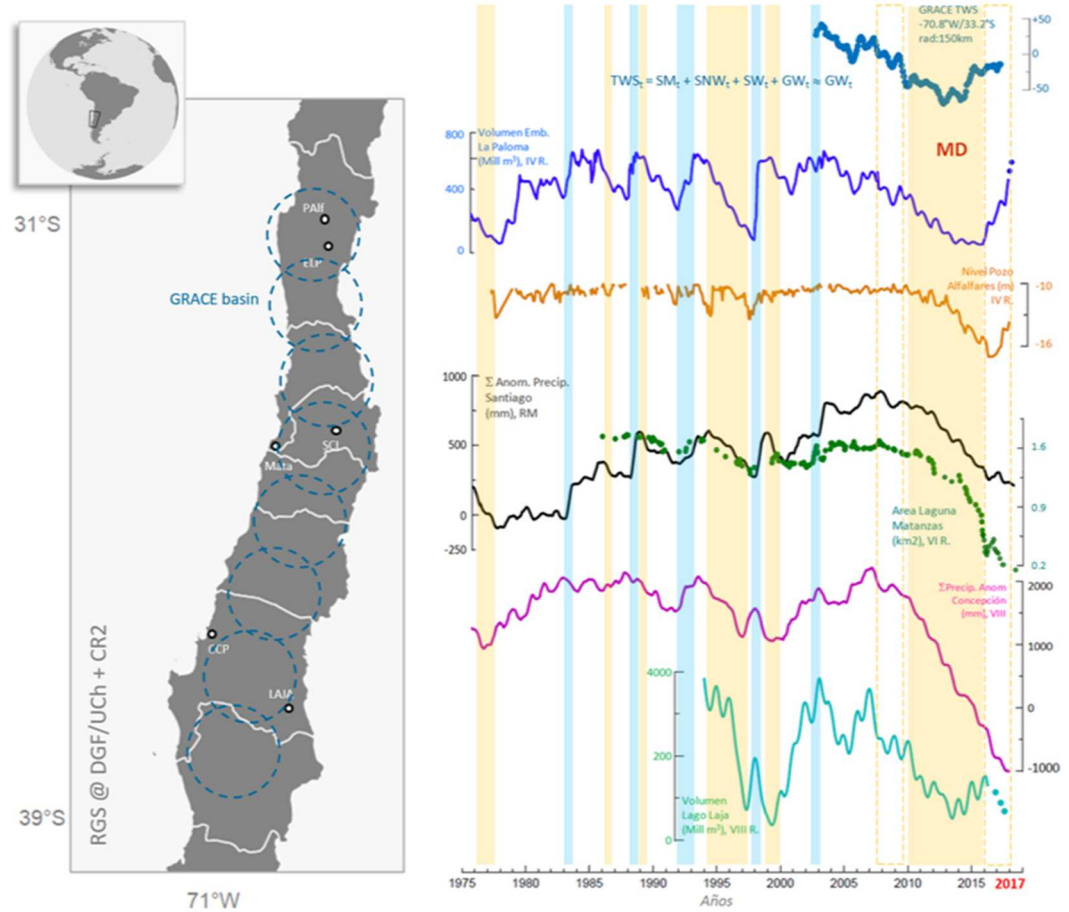


FIGURE 14 | Evolution of the water volume in selected reservoirs in central Chile (extratropical Andes) during the last four decades. Dry periods are marked by the yellow vertical bars. The ongoing megadrought is the dry spell that began in 2010.

is punctuated by severe droughts (30–60% deficits; Núñez-Cobo et al., 2018), lasting 1 year (winter season) and in some cases up to 2–3 years. An exceptional "megadrought" has been occurring in central Chile since 2010 (**Figure 14**; Garreaud et al., 2017).

Winter season droughts are accompanied by a reinforced subtropical anticyclone and deeper than average Amundsen-Bellingshausen Seas Low that conspire to weaken the westerly flow impinging in the southern Andes and restrict the number of fronts (Montecinos et al., 2011; Garreaud et al., 2017). Most drought years occur under La Niña conditions (Montecinos and Aceituno, 2003), and less under ENSO neutral conditions. Indeed, the "megadrought" has occurred mostly under near normal conditions in the equatorial Pacific and it even resisted the strong 2015–16 El Niño event (Garreaud et al., 2017).

Droughts in the southern Andes affect agriculture in central Chile and central-western Argentina (Núñez-Cobo et al., 2018), but also the water supply and hydro-electricity generation, and sets the stage for forest fires (González et al., 2018; Urrutia-Jalabert et al., 2018). The ecology of rivers flowing to the Pacific is also affected (Masotti et al., 2018), as exemplified in the summer of 2016 when the drought triggered the worst ever recorded harmful algal bloom in the coastal areas of Patagonia (Garreaud, 2018b).

Amoroso et al. (2018) developed a 525 year-long reconstruction from the Chubut River basin in Patagonia, finding the most severe droughts in 1680–1705, 1813–1828, 1900–1920, 1993–2002, and from 2011 to the present, in association with forest fires since the 1850s with a 12 year return interval, and a lack of fire for the last 94 years.

Droughts exhibit two distinct temporal regional behaviors in terms of duration and severity between North and Central Patagonia (Rivera et al., 2018). Diverse macro-climatic phenomena such as SAM, ENSO and the Pacific Decadal Oscillation (PDO) affect the interannual and interdecadal variability of droughts in Patagonia (Rivera et al., 2018). Droughts have shown to be more persistent in Argentina, with important regional differences (Minetti et al., 2010).

Extreme droughts have been on the rise in the Temperate-Mediterranean transition (TMT) zone of the Andes (35.5°-39.5°S) during the last century with respect to the previous six

centuries (Christie et al., 2011). The identified changes are related to the north-south oscillations in moisture conditions between the Mediterranean and temperate Andean regions, resulting from the latitudinal position of the storm tracks forced by large-scale circulation modes. In turn, moisture conditions are linked to tropical and high-latitude ocean-atmospheric forcing, with the Palmer Drought Severity Index (PDSI) positively related to Niño-3.4 SST during spring and strongly negatively correlated with the Antarctic Oscillation (AAO) during summer. Extreme dry years exhibit a strong negative PDSI vs. AAO correlation.

In addition to droughts, years of above average moisture availability precede fire years in northern Patagonia (Veblen and Kitzberger, 2002), by enhancing the growth of herbaceous plants which increases the quantity of fine fuels during the fire season a few years later. The short-term variability of available moisture leading to massive burning is linked to El Niño, due to greater moisture availability in spring, causing fires in the following years. Warmer and drier conditions during La Niña in the spring exacerbate the drying of fuels, and fire events.

Regarding heat waves, Jacques-Coper et al. (2016) identified 201 cases in south-eastern Patagonia during 1872–2010, with mean duration of 2 weeks and temperature peak of 4.3°C on day 0 (the warmest day in the mean signal), affecting both sides of the Andes. The warming results from temperature advection and enhanced radiative heating, following a high-pressure system over southern South America, from a wave-train-like pattern along the South Pacific. Two thirds of the heat wave events are linked to enhanced ascent in the South Atlantic Convergence Zone (SACZ).

During the 2010–2015 period, the eastern flank of the southern Andes (37°S—31°S) experienced one of the most severe hydrological droughts on record with large socioeconomic impacts. Moreover, since snowmelt is the most important source of water, the reduced snowfall over the mountains propagated the drought signal through the streamflow in the adjacent foothills east of the Andes (Rivera et al., 2017a,b).

RESEARCH GAPS

There is a plethora of challenges toward understanding, modeling and, let alone, predicting the studied high impact weather events.

Much of the current knowledge about extreme climate and weather events in the Andes are based upon limited observational data in particular in the higher Andes. For instance, there are just eight permanent atmospheric sounding sites operating near or in the Andes: Palonegro and Bogotá located on the eastern Andes of Colombia, Alfonso Bonilla-Aragón near Cali (Colombia), Quito (Ecuador), Lima-Callao (Perú), Antofagasta (Chile), Mendoza (Argentina), and Santo Domingo (Chile). This is a meager set of atmospheric measurements to understand the spatiotemporal dynamics of extreme weather patterns in a region characterized by steep slopes, deep valleys, and strong ecological gradients from north to south and from west to east. The situation of meteorological radars is even worse, given the need of high spatiotemporal precipitation estimates in the Andes (Guallpa et al., 2019), and that just a few are operating in the region: Bogotá and Medellín (Colombia), the network of three radars in Cajas, Loja, and Guachaurco in southern Ecuador (Bendix et al., 2017), another in Piura that covers a small region of the north-western Peruvian Andes, three radars in the Province of Mendoza (San Martín, Tunuyan y San Rafael), and one in Jujuy, Argentina, which are active during the hail storm season (October to April).

Regarding the monitoring network of other hydrological, meteorological and climatic variables, the situation is better with respect to *in-situ* rainfall data, although large regions remain uncovered. Something similar can be said about river discharges. The network is highly deficient with respect to weather and climate data sets required to estimate evapotranspiration, and almost non-existent for soil moisture and groundwater, and for all the processes that make part of the surface energy budget. Satellite and Unmanned Aerial Vehicles (UAV) type remotely sensed observations can help improve our understanding in this region, but still require appropriate *in situ* evaluation. Satellite data alone is also insufficient to detect the occurrence and quantify the magnitude of extreme events given their short timescales and small spatial resolution. For instance, diverse ground-validation studies show the poor skill of the TRMM satellite to capture rainfall over the Andes (e.g., Ochoa et al., 2014; Zambrano-Bigiarini et al., 2017; Vallejo-Bernal et al., 2020). Our modeling efforts and the much-needed establishment of early warning systems and disaster prevention efforts are similarly limited by the lack of observational data and data networks. A thorough discussion of the observational and monitoring hydrometeorological network in the Andes is presented by Condom et al. (2020).

Many scientific questions arise about the spatiotemporal dynamics of the high impact weather and climate events discussed herein. For example, what are the dynamics and thermodynamics of the ocean-atmosphere-land interactions that explain the wettest spot on Earth over the Pacific coast of Colombia, in association with MCSs and other rainfall-generating mechanisms leading to intense storms, flooding and landsliding over the Andes of Colombia.

The very topic of rainfall-runoff processes and the formation of floods along the Andes has been largely overlooked, which is more concerning given that floods constitute the most impacting events in terms of human lives and socio-economic losses in the region. The framework of statistical scaling provides a tool to understand and predict the occurrence of floods from intense storms (Gupta and Dawdy, 1995; Menabde and Sivapalan, 2001; Furey and Gupta, 2007; Mandapaka et al., 2009; Gupta et al., 2010; Ayalew et al., 2015), but also to estimate annual peak discharges of different return periods, relevant in hydrologic design (Poveda et al., 2007). Scaling properties need to be explained in terms of the physical processes and predicted by hydrologic models (Nguyen et al., 2015; Quintero et al., 2016; Wu et al., 2017; Salazar et al., 2018; Pérez et al., 2019).

Major knowledge gaps still remain regarding the non-linear interactions and synchronicity (e.g., Boers et al., 2014, 2016; Salas et al., 2020) between the dynamics of the CHOCO, Caribbean and Orinoco LLJs, and the SALLJ with other macroclimatic phenomena and modes of variability at a wide range of temporal scales, and their association with the occurrence of extreme

TABLE 1 | Summary of High-Impact Weather Events in the Andes.

Region	Type of event	Sub-region	Leading synoptic pattern	Consequences	Seasonality	Interannual variability
Northern tropical andes	Large precipitation accumulation	Far East Pacific Ocean near Colombian and Panama Coast	Dynamics of Choco and Caribbean LLJ	Flooding, Hurricanes formation in East Pacific	Boreal summer—autumn	Decrease during El Niño years
	Large precipitation accumulation	Slopes of Tropical Andes	Dynamics of mesoscale circulations favoring MCS	Flooding, soil saturation, landslides	Boreal spring—autumn	Increase during La Niña years
	Intense rainfall rates	Slopes of Tropical Andes	Regional circulation with topographical intensification of convection	Landslides, Flash floods	Boreal spring—autumn	Strong interannual variability associated with ENSO. Location-specific
	Deep Convection	Northern Andes	Monsoonal type interaction with Caribbean Ocean	Landslides; Very intense Lighting	Summer	Increase during La Niña and decrease during El Niño
	Drought	Colombia and Ecuador	Dynamics of the CHOCO LLJ Moisture transport from Amazonia	Forest fires. Impacts on agriculture, water supply, hydroelectricity, human health, fluvial navigation	Intensified in boreal winter	Extreme cases during El Niño events
	Frost	Higher elevation of the Andes, above 2,500 m a.s.l.	Intense radiative cooling associated with low cloud cover	Negative impacts on agriculture and cattle ranching	Dry season	Increase during El Niño
Southern tropical andes	Large precipitation accumulation	Western slope of the Andes, mainly 5°S-2°N	Atmospheric Rivers; MCs	Extreme Flooding, Landslides	Austral summer	Increase during El Niño years
	Large precipitation accumulation	Eastern slope of the Andes (>2,000 masl)	Atmospheric Rivers; MCs; SA Monsoon	Flash floods, Landslides	Year round but more notable in austral summer	Increase during La Niña years
	Intense rainfall rates	Atop of South Tropical Andes (10°S—27°S)	COLs, SA Monsoon, intensification of the BH.	Landslides, hailstorms	Austral summer	Tend to coincide with La Niña
	Heavy Convection	Eastern slope of the Andes -western Amazon	MCs; Pre-frontal condition, SA Monsoon	Landslides; Lighting, flash floods	Year round but more notable in austral summer	Tend to increase during La Niña years
	Drought	Atop of South Tropical Andes (8°S-27°S, >2,000 m asl)	Reduced eastern moisture advection	Impacts on agriculture, water supply, forest fires, hydroelectricity, ecosystems	Austral summer	Tend to coincide with El Niño
	Drought	Eastern slope of the Andes -western Amazon	Reduced eastern moisture advection	Impacts on Forest fires, fluvial transport, wildlife, agriculture, water supply	Austral winter and spring	Increase during El Niño years and during warm conditions in the tropical Atlantic
	Frost	Atop of South Tropical Andes (8°S-27°S, >3,000 m)	Low cloud cover, Post frontal conditions	Negative impacts on agriculture, human health, cattle health.	Winter and spring	Unknown
	Cold spell	Eastern slope of the Andes -western Amazon	Post frontal conditions	Negative impacts human health.	Austral winter and spring	Unknown
Extratropical andes	Large precipitation accumulation	Western slope of the Andes, mainly 35–45°S	Atmospheric Rivers; Cold fronts	Flooding, extreme snow accumulation	Austral winter	Increase during El Niño years
	Intense rainfall rates	Western slope of Subtropical Andes	ARs, COLs	Landslides, hailstorms	Austral fall-winter-spring	Unknown
	Heavy Convection	Atop of Subtropical Andes (27°-37°S)	COLs, extension of the SA Monsoon	Landslides; Lighting, hailstorms	Summer	Unknown
	Drought	Subtropical Andes and adjacent lowlands	N/A	Forest fires, impacts on agriculture, water supply	Year round but more notable in winter	Tend to coincide with La Niña events
	Frost	Subtropical Andes and adjacent lowlands	Post frontal	Negative impacts on agriculture	Winter and spring	Unknown
	Wind events (Zonda winds)	East side of the subtropical Andes	Pre-frontal condition	Unseasonal heat waves, dust storms	Austral fall-winter-spring	Unknown

events, including PDO, AMO, NAO, IOD, QBO, SAM, and the Tropical Atlantic SST Dipole. Also, the interplay between high-frequency variability modes (e.g., equatorial waves, gravity waves, MJO, etc.) and ENSO, and how such interactions modulate extreme events over the Andes.

There is the need to understand the role of the diurnal cycle on the formation of storms over the Andes, and its dynamics during the aforementioned diverse modes of climate variability. In that regard, what is the role of land surface-atmosphere interactions in explaining the water and energy budgets across timescales, from the interdecadal to the diurnal, and the extraordinarily high percentage (70–90%) of precipitation recycling in the Andes (Zemp et al., 2014).

Land use changes have been intense during the last decades over the Andes and the Amazon rainforest. Deforestation, agriculture, urbanization, large infrastructure development and extractive industry exacerbate these problems, such that the tropical Andes have been identified as the most critical biodiversity hotspot worldwide (Myers et al., 2000; Marchese, 2015; Hrdina and Romportl, 2017). The functioning of the coupled Andes-Amazon system (Builes-Jaramillo and Poveda, 2018) requires a thorough investigation, including how the modification in local and regional land conditions affect: (*i*) the frequency and magnitude of extreme weather events, owing to the alteration of the hydrological cycle and the energy budget across river basins of increasing scales, and (*ii*) the vulnerability of populations under risks of avalanches, flash floods, landslides, droughts, etc.

Extreme events are most often related to a local (mesoscale) intensification of extreme conditions (e.g., high rainfall rates, strong winds) embedded in broader synoptic systems (e.g., forced convection along a cold front). Most of the research in the last decades has focused on the synoptic-scale aspects of these extreme events, but examination of their mesoscale features is largely hindered by the aforementioned shortcomings of the observational network in space and time. Thus, we do not know much yet about the triggers and mechanism behind extreme precipitation events (say, brief periods with more than 20 mm/h) over the extratropical Andes.

Another limitation is the short, limited and non-systematic record of landslides, avalanches, flash floods and other ground-level manifestations of extreme weather events. Recall that south of 20°S the Andes is sparsely populated (most people live in the lowlands immediately to the west or east of the range). The record is composed of events that somehow reached the lowlands or interrupted some roads and railways crossing the Andes. Therefore, we may face a substantial underestimation of geo-climatic hazards in this region of extremely complex terrain.

Multiple scientific questions need to be answered regarding the dynamics and spatiotemporal persistence of droughts along the Andes, including the role of vegetation, precipitation, evapotranspiration, river flows, soil moisture and groundwater, net surface radiation and the fluxes of latent and sensible heat. This is also valid for the case of wild fires and heat waves.

Given the large socio-economic toll of high impact weather events in the Andes, the need of assessing their projected changes in future climate scenarios is evident, having in mind diverse adaptation strategies. Though there are studies focusing on the impacts of climate change in the Andes (e.g., Pabón-Caicedo et al., 2020), there is a lack of studies focusing on projected changes of high impact weather events over the region. One of the reasons for this may be the lack of reliability of climate models in reproducing the current climate conditions. Models exhibit large biases mostly in near-surface variables such as temperature, winds and precipitation and, hence, large discrepancies may be found when looking at extreme weather events. Consequently, there is a clear need on assessing the quality of climate models in reproducing high-impact events in the Andes and on assessing how these events are expected to change under future warmer conditions. The state-of-the-art climate models, either Global or Regional, operating at horizontal resolutions in a range from 100 to 20 km, are not expected to capture the high-impacts events themselves, but the large scale forcings and their interaction with the complex orography. Hence, there is also the need to evaluate the skill of convection-permitting models in terms and their capability in reproducing triggering synoptic-scale mechanisms, and the occurrence of diverse extreme events.

FINAL REMARKS

We have provided an in-depth review of the most important high impact weather events along the Andes, summarized in **Table 1**. It is not possible to overstate their socio-economic, environmental and ecological deleterious impacts. Such knowledge is fundamental to assess the relevant knowledge gaps and monitoring needs, but also toward the development of associated human capabilities, the implementation of scientific networks that involve the Andean scientific community and the transfer of scientific knowledge to public policies, which are particularly necessary and particularly challenging amidst population growth and climate change, as well as deforestation and urbanization trends throughout the Andes.

AUTHOR CONTRIBUTIONS

All authors listed have made a substantial, direct and intellectual contribution to the work, and approved it for publication.

FUNDING

GP was supported by Universidad Nacional de Colombia at Medellín. JE was supported by the French AMANECER-MOPGA project funded by ANR and IRD (ref. ANR-18-MPGA-0008). MZ was supported by Patrimonio Autónomo Fondo Nacional de Financiamiento para la Ciencia, la Tecnología y la Innovación, Francisco José de Caldas (ref. 80740-128-2019). Support for the Twentieth Century Reanalysis Project version 3 dataset is provided by the U.S. Department of Energy, Office of Science Biological and Environmental Research (BER), by the National Oceanic and Atmospheric Administration Climate Program Office, and by the NOAA Earth System Research Laboratory Physical Sciences Division.

ACKNOWLEDGMENTS

We are grateful to the Global Water and Energy Exchanges Programme (GEWEX) of WCRP, in particular to Fernande Vervoort, and also to Universidad Nacional de Colombia at Medellín, and to Centro de Ciencia del Clima y la Resiliencia $(CR)^2$ of Universidad de Chile in Santiago (FONDAP Grant 15110009), for supporting the three regional workshops of ANDEX (https://www.gewex.org/project/andex/home/), as a prospective Regional Hydroclimate Project (RHP).

SUPPLEMENTARY MATERIAL

The Supplementary Material for this article can be found online at: https://www.frontiersin.org/articles/10.3389/feart.2020.00162/full#supplementary-material

REFERENCES

Aceituno, P. (1988). On the functioning of the southern oscillation in the South American sector: surface, climate. *Mon. Weather. Rev.* 116, 505–524.

Aceituno, P., Prieto, M. D. R., Solari, M. E., Martínez, A., Poveda, G., and Falvey, M. (2009). The 1877-1878 El Niño episode: associated impacts in South America. *Clim. Change* 92, 389–416. doi: 10.1007/s10584-008-9470-5

Albrecht, R. I., Goodman, S. J., Buechler, D. E., Blakeslee, R. J., and Christian, H. J. (2016). Where are the lightning hotspots on Earth? *Bull. Am. Meteor. Soc.* 97, 2051–2068. doi: 10.1175/BAMS-D-14-00193.1

Allen, M. (2020, January 13). Amazon fires contribute to Andean glacier melting. *Eos*.

Amigo, I. (2000). The Amazon's fragile future. *Nature* 578, 505–507. doi: 10.1038/d41586-020-00508-4

Amoroso, M. M., Speer, J. H., Daniels, L. D., Villalba, R., Cook, E., Stahle, D., et al. (2018). South American dendroecological field week 2016: exploring dendrochronological research in Northern Patagonia. *Tree Ring Res.* 74, 120–131. doi: 10.3959/1536-1098-74.1.120

Aragão, L. E. O. C., Anderson, L. O., Fonseca, M. G., Rosan, T. M., Vedovato, L. B., Wagner, F. H., et al. (2018). 21st Century drought-related fires counteract the decline of Amazon deforestation carbon emissions. *Nat. Commun.* 9:536. doi: 10.1038/s41467-017-02771-y

Aranguren, D., González, J., Cruz, A., Inampués, J., Torres, H., and Pérez-Tobón, P. S. (2017). "Lightning strikes on power transmission lines and lightning detection in Colombia," in *International Symposium on Lightning Protection, XIV SIPDA 2017* (Natal), 273–278.

Arias, P. A., Fu, R., Vera, C., and Rojas, M. (2015). A correlated shortening of the North and South American monsoon seasons in the past few decades. *Clim. Dyn.* 45, 3183–3203. doi: 10.1007/s00382-015-2533-1

Aristizábal, E., García, E., and Martí-nez, C. (2015). Susceptibility assessment of shallow landslides triggered by rainfall in tropical basins and mountainous terrains. *Nat. Hazards* 78, 621–634. doi: 10.1007/s11069-015-1736-4

Ashok, K., Behera, S., Rao, S. A., Weng, H., and Yamagata, T. (2007). El Niño modoki and its possible teleconnection. *J. Geophy. Res.* 112:3798. doi: 10.1029/2006JC003798

Ayalew, T. B., Krajewski, W. F., and Mantilla, R. (2015). Analyzing the effects of excess rainfall properties on the scaling structure of peak discharges: insights from a mesoscale river basin. *Water Resour. Res.* 51, 3900–3921. doi: 10.1002/2014WR016258

Barrett, B., Garreaud, R., and Falvey, M. (2009). Impacts of the Andes cordillera on precipitation from a midlatitude cold front. *Mon. Weather Rev.* 9, 3092–3109. doi: 10.1175/2009MWR2881.1

Becerra, A., and Poveda, G. (2006). Variabilidad anual, interanual y escalamiento temporal de los incendios forestales en la Amazonía. *Meteorol. Colombiana* 10, 121–131. Available online at: http://gfnun.unal.edu.co/fileadmin/content/geociencias/revista_meteorologia_colombiana/numero10/10_11.pdf

Bedoya-Soto, J. M., Aristizábal, E., Carmona, A. M., and Poveda, G. (2019). Seasonal shift of the diurnal cycle of rainfall over Medellin's valley, central Andes of Colombia (1998–2005). *Front. Earth Sci.* 7:92. doi: 10.3389/feart.2019.00092

Bedoya-Soto, J. M., Poveda, G., Trenberth, K., and Vélez, J. J. (2018). Interannual hydroclimatic variability and the 2009–2011 extreme ENSO phases in Colombia: from Andean glaciers to Caribbean lowlands. *Theor. Appl. Climatol.* 135, 1531–1544. doi: 10.1007/s00704-018-2452-2

Bendix, J., Fries, A., Zárate, J., Trachte, K., Rollenbeck, R., Pucha-Cofrep, F., et al. (2017). RadarNet-Sur first weather radar network in tropical high mountains. *Bull. Am. Meteor. Soc.* 98, 1235–1254. doi: 10.1175/BAMS-D-15-00178.1

Bendix, J., Trachte, K., Cermak, J., Rollenbeck, R., and Naub, T. (2009). Formation of convective clouds at the foothills of the tropical eastern Andes (South Ecuador). *J. Appl. Meteorol. Climatol.* 48, 1682–1695. doi: 10.1175/2009JAMC2078.1

Bermúdez, O. (1990). "Study into frosts in the Bogota savanna," in *Economic and Social Benefits of Meteorological and Hydrological Services. Proceedings Conference* (Geneva), 409–412.

Blodgett, T. A., and Isacks, B. L. (2007). Landslide erosion rate in the eastern cordillera of northern Bolivia. *Earth Interact.* 11, 1–30. doi: 10.1175/2007EI222.1

Boers, N., Barbosa, H. M. J., Bookhagen, B., Marengo, J. A., Marwan, N., and Kurths, J. (2015b). Propagation of strong rainfall events from southeastern South America to the Central Andes. *J. Clim.* 28, 7641–7658. doi: 10.1175/JCLI-D-15-0137.1

Boers, N., Bookhagen, B., Barbosa, H. M., Marwan, N., Kurths, J., and Marengo, J. A. (2014). Prediction of extreme floods in the eastern Central Andes based on a complex networks approach. *Nat. Commun.* 5:5199. doi: 10.1038/ncomms6199

Boers, N., Bookhagen, B., Marengo, J., Marwan, N., Storch, J. -S. V., and Kurths, J. (2015a). Extreme rainfall of the South American monsoon system: a dataset comparison using complex networks. *J. Clim.* 28, 1031–1056. doi: 10.1175/JCLI-D-14-00340.1

Boers, N., Bookhagen, B., Marwan, N., and Kurths, J. (2016). Spatiotemporal characteristics and synchronization of extreme rainfall in South America with focus on the Andes mountain range. *Clim. Dyn.* 46, 601–617. doi: 10.1007/s00382-015-2601-6

Bourges, J., Ribstein, P., Dietze, C., Guyot, J. -L., and Hoorelbeck, R. (1995). Flows and exceptional floods on a small Andean river, or the negative impact of urbanisation [Flux et crues singulieres d'un petit cours d'eau andin ou les effets pervers de l'urbanisation]. *Rev. Geogr. Alpine* 83, 111–126. doi: 10.3406/rga.1995.3793

Bourrel, L., Rau, P., Dewitte, B., Labat, D., Lavado, W., Coutaud, A., et al. (2015). Low-frequency modulation and trend of the relationship between ENSO and precipitation along the northern to centre Peruvian Pacific coast. *Hydrol. Process.* 29, 1252–1266. doi: 10.1002/hyp.10247

Bozkurt, D., Rondanelli, R., Garreaud, R., and Arriagada, A. (2016). Impact of warmer eastern tropical Pacific SST on the March 2015 Atacama floods. *Mon. Weather Rev.* 144, 4441–4460. doi: 10.1175/MWR-D-16-0041.1

Braud, I., Fernandez, P., and Bouraoui, F. (1999). Study of the rainfall-runoff process in the Andes region using a continuous distributed model. *J. Hydrol.* 216, 155–171. doi: 10.1016/S0022-1694(98)00292-3

Braud, I., Vich, A. I. J., Zuluaga, J., Fornero, L., and Pedrani, A. (2001). Vegetation influence on runoff and sediment yield in the Andes region: observation and modelling. *J. Hydrol.* 254, 124–144. doi: 10.1016/S0022-1694(01)00500-5

Brenning, A., Schwinn, M., Ruiz-Páez, A. P., and Muenchow, J. (2015). Landslide susceptibility near highways is increased by 1 order of magnitude in the Andes of southern Ecuador, Loja province. *Nat. Hazard Earth Syst.* 15, 45–57. doi: 10.5194/nhess-15-45-2015

Builes-Jaramillo, L. A., and Poveda, G. (2018). Conjoint analysis of surface and atmospheric water balances in the Andes-Amazon system. *Water Resour. Res.* 54, 3472–3489. doi: 10.1029/2017WR021338

Bustinza, J. A., Rocca, R. J., Zeballos, M. E., and Terzariol, R. E. (2013). "Rerouting of a pipeline due to landslide reactivation in an Andean valley," in *ASME 2013 International Pipeline Geotechnical Conference (IPG)* (Bogotá).

Cai, W., McPhaden, M., Grimm, A., Rodrigues, R., Taschetto, A., Garreaud, R., et al. (2020). Climate impacts of El Niño-Southern Oscillation on South America. *Nat. Rev. Earth Environ.* 1, 215–231. doi: 10.1038/s43017-020-0040-3

Casteller, A., Stoffel, M., Crespo, S., Villalba, R., Corona, C., and Bianchi, E. (2015). Dendrogeomorphic reconstruction of flash floods in the Patagonian Andes. *Geomorphology* 228, 116–123. doi: 10.1016/j.geomorph.2014.08.022

Caviedes, C., and Endlicher, W. (1989). The precipitation in northern Peru during the El Nino oscillation of 1983 [Die Niederschlagsverhaltnisse in Nordperu wahrend des El-Nino oscillation-ereignisses von 1983]. *Erde* 120, 81–87.

Chávez, S. P., and Takahashi, K. (2017). Orographic rainfall hotspots in the Andes-Amazon transition according to the TRMM precipitation radar and *in situ* data. *Geophys. Res. Atmos.* 122, 5870–5882. doi: 10.1002/2016JD026282

Chirino, E., Ruiz-Yanetti, S., Vilagrosa, A., Mera, X., Espinoza, M., and Lozano, P. (2017). Morpho-functional traits and plant response to drought conditions in seedlings of six native species of Ecuadorian ecosystems. *Flora* 233, 58–67. doi: 10.1016/j.flora.2017.05.012

Christie, D. A., Boninsegna, J. A., Cleaveland, M. K., Lara, A., Le Quesne, C., Morales, M. S., et al. (2011). Aridity changes in the Temperate-Mediterranean transition of the Andes since AD 1346 reconstructed from tree-rings. *Clim. Dyn.* 36, 1505–1521. doi: 10.1007/s00382-009-0723-4

Clark, K. E., West, A. J., Hilton, R. G., Asner, G. P., Quesada, C. A., Silman, M. R., et al. (2016). Storm-triggered landslides in the Peruvian Andes and implications for topography, carbon cycles, and biodiversity. *Earth Surf. Dyn.* 4, 47–70. doi: 10.5194/esurf-4-47-2016

Compagnucci, R. H., and Vargas, W. (1998). Inter-annual variability of the Cuyo rivers' streamflow in the Argentinean Andean mountains and ENSO events. *Int. J. Climatol.* 18, 1593–1609.

Condom, T., Martínez, R., Pabón, J. D., Costa, F., Pineda, L., Nieto, J. J., et al. (2020). Climatological and hydrological observations for the South American Andes: *in-situ* stations, satellite and reanalysis data sets. *Front. Earth Sci.* 8:92. doi: 10.3389/feart.2020.00092

Contreras, M. F., Vergara, C., Pereira, M., Colonia, J. D., and Garcí-a, H. (2013). "Pipeline integrity assessment and mitigation techniques in unstable soil conditions based on comparison of in line inspection results," in *ASME 2013 International Pipeline Geotechnical Conference (IPG)* (Bogotá).

Cristancho, C. J. A., Suárez, H., Urbano, Y., and Román, F. (2017). "Fatal livestock lightning accident in Colombia," in: *2017 International Symposium on Lightning Protection (XIV SIPDA)* (Natal), 295–298.

Cruz, C., Rentería, E., and Román, F. (2013). "Statistics of the Colombian National Army lightning accidents," in *2013 International Symposium on Lightning Protection (XII SIPDA)* (Belo Horizonte), 324–328.

Deser, C., and Wallace, J. M. (1987). El Niño events and their relation to the Southern Oscillation: 1925–1986. *J. Geoph. Res.* 92, 14189–14196. doi: 10.1029/JC092iC13p14189

Dominguez, C., Done, J. M., and Bruyère, C. L. (2020). Easterly wave contributions to seasonal rainfall over the tropical Americas in observations and a regional climate model. *Clim. Dyn.* 54, 191–209. doi: 10.1007/s00382-019-04996-7

Domínguez-Castro, F., Garcí-a-Herrera, R., and Vicente-Serrano, S. M. (2018). Wet and dry extremes in Quito (Ecuador) since the 17th century. *Inter. J. Clim.* 38, 2006–2014. doi: 10.1002/joc.5312

Duffaut-Espinosa, L. A., Posadas, A. N., Carbajal, M., and Quiroz, R. (2017). Multifractal downscaling of rainfall using Normalized Difference Vegetation Index (NDVI) in the Andes plateau. *PLoS ONE* 12:e0168982. doi: 10.1371/journal.pone.0168982

Emmer, A. (2017). Geomorphologically effective floods from moraine-dammed lakes in the Cordillera Blanca, Peru. *Quat. Sci. Rev.* 177, 220–234. doi: 10.1016/j.quascirev.2017.10.028

Espinoza, J. C., Chavez, S., Ronchail, J., Junquas, C., Takahashi, K., and Lavado, W. (2015). Rainfall hotspots over the southern tropical Andes: spatial distribution, rainfall intensity, and relations with large-scale atmospheric circulation, *Water Resour. Res.* 51, 3459–3475. doi: 10.1002/2014WR016273

Espinoza, J. C., Garreaud, R., Poveda, G., Arias, P. A., Molina-Carpio, J., Masiokas, M., et al. (2020). Hydroclimate of the Andes Part I: main climatic features. *Front. Earth Sci.* 8:64. doi: 10.3389/feart.2020.00064

Espinoza, J. C., Lengaigne, M., Ronchail, J., and Janicot, S. (2012a). Large-scale circulation patterns and related rainfall in the Amazon Basin: a neuronal networks approach. *Clim. Dyn.* 38:121. doi: 10.1007/s00382-011-1010-8

Espinoza, J. C., Marengo, J. A., Ronchail, J., Molina, J., Noriega, L., and Guyot, J. L. (2014). The extreme 2014 flood in south-western Amazon basin: the role of tropical-subtropical south Atlantic SST gradient. *Environ. Res. Lett.* 9:124007. doi: 10.1088/1748-9326/9/12/124007

Espinoza, J. C., Ronchail, J., Guyot, J. L., Cochonneau, G., Naziano, F., Lavado, W., et al. (2009). Spatio-temporal rainfall variability in the Amazon basin countries (Brazil, Peru, Bolivia, Colombia, and Ecuador). *Int. J. Climatol.* 29, 1574–1594. doi: 10.1002/joc.1791

Espinoza, J. C., Ronchail, J., Guyot, J. L., Junquas, C., Drapeau, G., Martinez, J. M., et al. (2012b). From drought to flooding: understanding the abrupt 2010-2011 hydrological annual cycle in the Amazonas River and tributaries. *Environ. Res. Lett.* 7:024008. doi: 10.1088/1748-9326/7/2/024008

Espinoza, J. C., Ronchail, J., Guyot, J. L., Junquas, C., Vauchel, P., Lavado, W. S., et al. (2011). Climate variability and extremes drought in the upper Solimões River (Western Amazon Basin): understanding the exceptional 2010 drought. *Geophys. Res. Lett.* 38:L13406. doi: 10.1029/2011GL047862

Espinoza, J. C., Ronchail, J., Marengo, J. A., and Segura, H. (2019). Contrasting north-south changes in Amazon wet-day and dry-day frequency and related atmospheric features (1981–2017). *Clim. Dyn.* 52, 5413–5430. doi: 10.1007/s00382-018-4462-2

Espinoza, J. C., Segura, H., Ronchail, J., Drapeau, G., and Gutierrez-Cori, O. (2016). Evolution of wet- and dry-day frequency in the western Amazon basin: relationship with the atmospheric circulation and impacts on the vegetation. *Water Resour. Res.* 52, 8546–8560. doi: 10.1002/2016WR019305

Espizua, L. E., and Bengochea, J. D. (2002). Landslide hazard and risk zonation mapping in the Rí-o Grande basin, Central Andes of Mendoza, Argentina. *Mt. Res. Dev.* 22, 177–185. doi: 10.1659/0276-4741(2002)022[0177:LHARZM]2.0.CO;2

Evans, S. G., Bishop, N. F., Fidel Smoll, L., Valderrama Murillo, P., Delaney, K. B., and Oliver-Smith, A. (2009). A re-examination of the mechanism and human impact of catastrophic mass flows originating on Nevado Huascarán, Cordillera Blanca, Peru in 1962 and 1970. *Eng. Geol.* 108, 96–118. doi: 10.1016/j.enggeo.2009.06.020

Falvey, M., and Garreaud, R. (2007). Wintertime precipitation episodes in Central Chile: associated meteorological conditions and orographic influences. *J. Hydromet.* 8, 171–193. doi: 10.1175/JHM562.1

Favier, V., Wagnon, P., Chazarin, J. -P., Maisincho, L., and Coudrain, A. (2004). One-year measurements of surface heat budget on the ablation zone of Antizana Glacier 15, Ecuadorian Andes. *J. Geophys. Res.* 109:D18105. doi: 10.1029/2003JD004359

Fernandes, K., Baethgen, W., Bernardes, S., deFries, R., DeWitt, D. G., Goddard, L., et al. (2011). North Tropical Atlantic influence on western Amazon fire season variability. *Geophys. Res. Lett.* 38:L12701. doi: 10.1029/2011GL047392

Ferrer, C. (1999). Dammed and failure of natural dams and its relations with coseismic events: some examples from the Venezuelan Andes [Represamientos y rupturas de embalses naturales (lagunas de obturación) como efectos cósmicos: algunos ejemplos en los Andes venezolanos]. *Rev. Geog. Venez.* 40, 109–121.

Francou, B. (1985). El Nino and the drought in the High Central Andes of Peru and Bolivia. [El Nino y la sequia en los altos Andes Centrales: Peru y Bolivia.] *Bull. Inst.Francais des Etudes Andines.* 14, 1–18.

Francou, B., Vuille, M., Favier, V., and Cáceres, B. (2004). New evidence for an ENSO impact on low-latitude glaciers: Antizana, Andes of Ecuador. *J Geophys. Res.* 109:D18106. doi: 10.1029/2003JD004484

Frappart, F., Bourrel, L., Brodu, N., Salazar, X. R., Baup, F., Darrozes, J., et al. (2017). Monitoring of the spatio-temporal dynamics of the floods in the Guayas watershed (Ecuadorian pacific coast) using global monitoring ENVISAT ASAR images and rainfall data. *Water* 9:12. doi: 10.3390/w9010012

Furey, P., and Gupta, V. K. (2007). Diagnosing peak-discharge power laws observed in rainfall-runoff events in Goodwin Creek experimental watershed. *Adv. Water Res.* 30, 2387–2399. doi: 10.1016/j.advwatres.2007.05.014

García, H., Nieves, C., and Colonia, J. D. (2013). "Integrity management program for geo-hazards in the OCENSA pipeline system," in *ASME 2013 International Pipeline Geotechnical Conference (IPG)* (Bogotá).

Garreaud, R. (2013). Warm winter storms in central Chile. *J. Hydrometeor*. 14, 1515–1534. doi: 10.1175/JHM-D-12-0135.1

Garreaud, R., Vuille, M., and Clement, A. (2003). The climate of the Altiplano: observed current conditions and mechanism of past changes. *Paleogeogr. Palaeoclimatol. Palaeoecol*. 194, 5–22. doi: 10.1016/S0031-0182(03)00269-4

Garreaud, R. D. (1999). Multiscale analysis of the summertime precipitation over the central Andes. *Mon. Weather. Rev.* 127, 901–921.

Garreaud, R. D. (2018a). A plausible atmospheric trigger for the 2017 coastal El Niño. *Int. J. Climatol.* 38, e1296–e1302. doi: 10.1002/joc.5426

Garreaud, R. D. (2018b). Record-breaking climate anomalies lead to severe drought and environmental disruption in Western Patagonia in 2016. *Clim. Res.*74, 217–229. doi: 10.3354/cr01505

Garreaud, R. D., Alvarez-Garreton, C., Barichivich, J., Boisier, J. P., Christie, D. A., Galleguillos, M., et al. (2017). The 2010-2015 megadrought in Central Chile: impacts on regional hydroclimate and vegetation. *Hydrol. Earth Syst. Sci.* 21, 6307–6327. doi: 10.5194/hess-21-6307-2017

Garreaud, R. D., and Rutllant, J. (1997). Precipitación estival en los Andes de Chile central: aspectos climatológicos. *Atmósfera* 10, 191–211.

Garreaud, R. D., and Viale, M. (2014). Análisis de los fenómenos meteorológicos y climáticos que afectan la cuenca del río Maipo. *Aquae Papers* 5, 17–29.

Garreaud, R. D., Vuille, M., Compagnucci, R., and Marengo, J. (2009). Present-day South American climate. *Palaeogeo. Palaeoclim. Palaeoecol*. 281, 180–195. doi: 10.1016/j.palaeo.2007.10.032

Garreaud, R. D., and Wallace, J. M. (1998). Summertime incursions of midlatitude air into subtropical and tropical South America. *Mon. Weather Rev.* 126, 2713–2733.

Giovannettone, J. P., and Barros, A. P. (2009). Probing regional orographic controls of precipitation and cloudiness in the central andes using satellite data. *J. Hydromet*. 10, 167–182. doi: 10.1175/2008JHM973.1

Gómez, J. D., and Poveda, G. (2008). Estimación del espectro multifractal para series de precipitación horaria en los Andes tropicales de Colombia. *Revista Acad. Colomb. Ci. Exact*. 32, 483–502. Available online at: http://www.accefyn.com/revista/Vol_32/125/483-502.pdf

González, M. E., Gómez-González, S., Lara, A., Garreaud, R. D., and Díaz-Hormazábal, I. (2018). The 2010-2015 Megadrought and its influence on the fire regime in central and south central Chile. *Ecosphere* 9:e2300. doi: 10.1002/ecs2.2300

Grandoso, H. N. (1966). Distribución temporal y geográfica del granizo en la Provincia de Mendoza y su relación con algunos parámetros meteorológicos. *Serie Meteorológica*. 1, 49.

Grimm, A. A., and Tedeschi, R. G. (2009) ENSO and extreme rainfall events in South America. *J. Clim.* 22,1590–1609. doi: 10.1175/2008JCLI2429.1

Guallpa, M., Orellana-Alvear, J., and Bendix, J. (2019). Tropical Andes radar precipitation estimates need high temporal and moderate spatial resolution. *Water* 11:1038. doi: 10.3390/w11051038

Guha-Sapir, D., Below, R., and Hoyois, P. (2015). *EM-DAT: The CRED/OFDA International Disaster Database*. Brussels: Université Catholique de Louvain. Retrieved from: http://www.emdat.be/database (accessed October 30, 2015).

Guns, M., and Vanacker, V. (2013). Forest cover change trajectories and their impact on landslide occurrence in the tropical Andes. *Environ. Earth Sci.* 70, 2941–2952. doi: 10.1007/s12665-013-2352-9

Guns, M., and Vanacker, V. (2014). Shifts in landslide frequency-area distribution after forest conversion in the tropical Andes. *Anthropocene* 6, 75–85. doi: 10.1016/j.ancene.2014.08.001

Gupta, V. K., and Dawdy, D. (1995). Physical interpretations of regional variations in the scaling exponents of flood quantiles. *Hydrol. Process.* 9, 347–361. doi: 10.1002/hyp.3360090309

Gupta, V. K., Mantilla, R., Troutman, B. M., Dawdy, D., and Krajewski, W. F. (2010). Generalizing a nonlinear geophysical flood theory to medium-sized river networks. *Geophys. Res. Lett.* 37:L11402. doi: 10.1029/2009GL041540

Hermanns, R. L., and Niedermann, S. (2006). Rock avalanching in the NW argentine Andes as a result of complex interactions of lithologic, structural and topographic boundary conditions, climate change and active tectonics. *Landslides* 49, 497–520. doi: 10.1007/978-1-4020-4037-5_27

Hermanns, R. L., Niedermann, S., Ivy-Ochs, S., and Kubik, P. W. (2004). Rock avalanching into a landslide-dammed lake causing multiple dam failure in las conchas valley (NW Argentina) - evidence from surface exposure dating and stratigraphic analyses. *Landslides* 1, 113–122. doi: 10.1007/s10346-004-0013-5

Hermanns, R. L., Valderrama, P., Fauqu, L., Penna, I. M., Sepúlveda, S., Moreiras, S., et al. (2012). Landslides in the Andes and the need to communicate on an interandean level on landslide mapping and research [Deslizamientos en los Andes y la necesidad de comunicar a nivel interandino sobre el mapeo y la investigación de deslizamientos]. *Rev. Assoc. Geol.* 69, 321–327. Available online at: http://ppct.caicyt.gov.ar/index.php/raga/article/view/1824

Herrera, J., Younes, C., and Porras, L. (2018). Cloud-to-ground lightning activity in Colombia: a 14-year study using lightning location system data. *Atmos. Res.* 203, 164–174. doi: 10.1016/j.atmosres.2017.12.009

Holmann, F., Rivas, L., Urbina, N., Rivera, B., Giraldo, L. A., Guzman, S., et al. (2005). The role of livestock in poverty alleviation: an analysis of Colombia. *Livest. Res. Rural Dev.* 17. Retrieved from: http://www.lrrd.org/lrrd17/1/holm17011.htm (accessed May 16, 2020).

Houze, R. A. Jr., Wilton, D. C., and Smull, B. F. (2007). Monsoon convection in the Himalayan region as seen by the TRMM precipitation radar. *Quart. J. Roy. Meteor. Soc.* 133, 1389–1411.

Houze, R. A. Jr. (2004). Mesoscale convective systems. *Rev. Geophys.* 42:150. doi: 10.1029/2004RG000150

Houze, R. A. Jr., Rasmussen, K. L., Zuluaga, M. D., and Brodzik, S. R. (2015). The variable nature of convection in the tropics and subtropics: a legacy of 16 years of Tropical rainfall measuring mission satellite. *Rev. Geophys.* 53, 994–1021. doi: 10.1002/2015RG000488

Hoyos, C. D., Ceballos, L. I., Pérez-Carrasquilla, J. S., Sepúlveda, J., López-Zapata, S. M., Zuluaga, M. D., et al. (2019). Meteorological conditions leading to the 2015 Salgar flash flood: lessons for vulnerable regions in tropical complex terrain. *Nat. Hazards Earth Syst. Sci.* 19, 2635–2665. doi: 10.5194/nhess-19-2635-2019

Hoyos, N., Escobar, J., Restrepo, J. C., Arango, A. M., and Ortiz, J. C. (2013). Impact of the 2010-2011 La Niña phenomenon in Colombia, South America: the human toll of an extreme weather event. *Appl. Geogr.* 39, 16-25. doi: 10.1016/j.apgeog.2012.11.018

Hrdina, A., and Romportl, D. (2017). Evaluating global biodiversity hotspots – very rich and even more endangered. *J. Lands Ecol.* 10, 108–115. doi: 10.1515/jlecol-2017-0013

Huggel, C., Raissig, A., Rohrer, M., Romero, G., Diaz, A., and Salzmann, N. (2015). How useful and reliable are disaster databases in the context of climate and global change? A comparative case study analysis in Peru. *Nat. Hazards Earth Syst. Sci.* 15, 475–485. doi: 10.5194/nhess-15-475-2015

Hurley, J. V., Vuille, M., Hardy, D. R., Burns, S. J., and Thompson, L. G. (2015). Cold air incursions, $\delta^{18}O$ variability, and monsoon dynamics associated with snow days at Quelccaya ice cap, Peru. *J. Geophys. Res. Atmos.* 120, 7467–7487. doi: 10.1002/2015JD023323

Hurtado, A. F., and Poveda, G. (2009). Linear and global space-time dependence and Taylor hypotheses for rainfall in the tropical Andes. *J. Geophys. Res.* 114: D10105. doi: 10.1029/2008JD011074

Imfeld, N., Schuller, C. B., Marrou, K. M. C., Jaques-Cooper, M., Sedlmeier, K., Gubler, S., et al. (2019). Summertime precipitation deficits in the southern Peruvian highlands since 1964. *Int. J. Climatol.* 39, 4497–4513. doi: 10.1002/joc.6087

Iñiguez, V., Morales, O., Cisneros, F., Bauwens, W., and Wyseure, G. (2016). Analysis of the drought recovery of Andosols on southern Ecuadorian Andean páramos. *Hydrol. Earth Sys. Sci*. 20, 2421–2435. doi: 10.5194/hess-20-2421-2016

Jacques-Coper, M., Bronnimann, S., Martius, O., Vera, C., and Cerne, B. (2016). Summer heat waves in Southeastern Patagonia: an analysis of the intraseasonal timescale. *Int. J. Climatol.* 36, 1359–1374. doi: 10.1002/joc.4430

Jaramillo, L., Poveda, G., and Mejía, J. F. (2017). Mesoscale convective systems and other precipitation features over the tropical Americas and surrounding seas as seen by TRMM. *Int. J. Climatol.* 37, 380–397. doi: 10.1002/joc.5009

Jaramillo, M. M. (2008). Guidelines for landslide hazard mapping in the Andes: speaking one language. *Geol. Soc. Spec. Publ.* 305, 53–61. doi: 10.1144/SP305.6

Jauregui, Y. R., and Takahashi, K. (2017). Simple physical-empirical model of the precipitation distribution based on a tropical sea surface temperature threshold and the effects of climate change. *Clim. Dyn.* 50:2217. doi: 10.1007/s00382-017-3745-3

Jiménez-Muñoz, J. C., Mattar, C., Barichivich, J., Santamaría-Artigas, A., Takahashi, K., Malhi, Y., et al. (2016). Record-breaking warming and extreme drought in the Amazon rainforest during the course of El Niño 2015-2016. *Sci. Rep*. 6:33130. doi: 10.1038/srep33130

Junquas, C., Li, L., Vera, C. S., Le Treut, H., and Takahashi, K. (2016). Influence of South America orography on summertime precipitation in Southeastern South America. *Clim. Dyn*. 46, 3941–3963. doi: 10.1007/s00382-015-2814-8

Junquas, C., Takahashi, K., Condom, T., Espinoza, J. C., Chavez, S., Sicart, J. E., et al. (2018). Understanding the influence of orography over the precipitation diurnal cycle and the associated atmospheric processes in the central Andes. *Clim. Dyn*. 50, 3995–4017. doi: 10.1007/s00382-017-3858-8

Kalicki, P., Kalicki, T., and Kittel, P. (2014). The influence of El Niño on settlement patterns in Lomas de Lachay, central coast, Peru. *Interdis. Archaeol*. 5, 147–160. doi: 10.24916/iansa.2014.2.5

Kane, R. P. (2006). El Niño effects on rainfall in South America: comparison with rainfalls in India and other parts of the world. *Adv. Geosci*. 6, 35–41. doi: 10.5194/adgeo-6-35-2006

Kao, H., and Yu, J. (2009). Contrasting Eastern-Pacific and Central-Pacific types of ENSO. *J. Clim*. 22, 615–632. doi: 10.1175/2008JCLI2309.1

Killeen, T. J., Douglas, M., Consiglio, T., Jørgensen, P. M., and Mejia, J. (2007). Dry spots and wet spots in the Andean hotspot. *J. Biogeogr*. 34, 1357–1373. doi: 10.1111/j.1365-2699.2006.01682.x

Kousky, V. E., Kayano, M. T., and Cavalcanti, I. F. A. (1984). A review of the Southern Oscillation: oceanic–atmospheric circulation changes and related rainfall anomalies. *Tellus Ser A* 36, 490–504. doi: 10.1111/j.1600-0870.1984.tb00264.x

Kumar, S., Castillo-Velarde, C. D., Valdivia Prado, J. M., Flores Rojas, J. L., Callañaupa Gutierrez, S. M., Moya Alvarez, A. S., et al. (2020). Rainfall Characteristics in the Mantaro Basin over tropical Andes from a vertically pointed profile rain radar and *in-situ* field campaign. *Atmosphere* 11:248. doi: 10.3390/atmos11030248

Kumar, S., Vidal, S.-Y., Moya-Álvarez, A. S., and Martínez-Castro, D. (2019). Effect of the surface wind flow and topography on precipitating cloud systems over the Andes and associated Amazon basin: GPM observations. *Atmos. Res*. 225, 193–208. doi: 10.1016/j.atmosres.2019.03.027

Kummerow, C., Barnes, W., Kozu, T., Shiue, J., and Simpson, J. (1998). The Tropical Rainfall Measuring Mission (TRMM) sensor package. *J. Atmos. Oceanic Technol*. 15, 809–817.

Kummerow, C. J., Simpson, J., Thiele, O., Barnes, W., Chang, A. T., Hou, A., et al. (2000). The status of the Tropical Rainfall Measuring Mission (TRMM) after two years in orbit. *J. Appl. Meteorol*. 39, 1965–1982. doi: 10.1175/1520-0450(2001)040<1965:TSOTTR>2.0.CO;2

Lagos, P., Silva, Y., Nickl, E., and Mosquera, K. (2008). El Niño-related precipitation variability in Perú. *Adv. Geosci*. 14, 231–237. doi: 10.5194/adgeo-14-231-2008

Laraque, A., Bernal, C., Bourrel, L., Darrozes, J., Christophoul, F., Armijos, E., et al. (2009). Sediment budget of the Napo River, Amazon Basin, Ecuador and Peru. *Hydrol. Proc*. 23, 3509–3524. doi: 10.1002/hyp.7463

Larkin, N. K., and Harrison,. D. E. (2005). Global seasonal temperature and precipitation anomalies during El Niño autumn and winter. *Geophys. Res. Lett*. 32:L13705. doi: 10.1029/2005GL022738

Laurent, H., Machado, L. A. T., Morales, C., and Durieux, L. (2002). Characteristics of the Amazonian mesoscale convective systems observed from satellite and radar during the WETAMC/LBA experiment. *J. Geophys. Res*. 107:8054. doi: 10.1029/2001JD000337

Lavado, W., Ronchail, J., Labat, D., Espinoza, J. C., and Guyot, J. L. (2012). A basin-scale analysis of rainfall and runoff in Peru (1969-2004): Pacific, Titicaca and Amazonas drainages. *Hydrol. Sci. J*. 57, 625–642. doi: 10.1080/02626667.2012.672985

Lavado-Casimiro, W., and Espinoza, J. C. (2014). Impactos de El Niño y La Niña en las lluvias del Perú (1965–2007). *Rev. Brasil. Meteo*. 29, 171–182. doi: 10.1590/S0102-77862014000200003

Lavado-Casimiro, W., Felipe, O., Silvestre, E., and Bourrel, L. (2013). ENSO impact on hydrology in Peru. *Adv. Geos*. 33, 33–39. doi: 10.5194/adgeo-33-33-2013

Lavado-Casimiro, W. S., Silvestre, E., and Pulache, W. (2010). Tendencias en los extremos de lluvias cerca a la ciudad del Cusco y su relación con las inundaciones de Enero del 2010. (Extreme rainfall trends around Cusco and its relationship with the floods in January). *Rev. Peruana Geoatmos*. 2,89–98. Available online at: https://web2.senamhi.gob.pe/rpga/pdf/2010_vol02/art8.pdf

Lee, E. M., Audibert, J. M. E., Hengesh, J. V., and Nyman, D. J. (2009). Landslide-related ruptures of the Camisea pipeline system, Peru. *Q. J. Eng. Geol. Hydrog*. 42, 251–259. doi: 10.1144/1470-9236/08-061

León, G., Zea, J., and Eslava, J. (2001). Ondas del este en Colombia y algunos aspectos relevantes de los ciclones tropicales. *Meteorol. Colomb*. 3, 137–141. Available online at: http://gfnun.unal.edu.co/fileadmin/content/geociencias/revista_meteorologia_colombiana/numero03/03_15.pdf

Liebmann, B., Kiladis, G. N., Vera, C. S., Saulo, A. C., and Carvalho, L. M. V. (2004). Subseasonal variations of rainfall in South America in the vicinity of the low-level jet east of the Andes and comparison to those in the South Atlantic convergence zone. *J. Clim*. 17, 3829–3842. doi: 10.1175/1520-0442(2004)017<3829:SVORIS>2.0.CO;2

López Salgado, H. J. (2016). "Assessing soil susceptibility to mass movements: case study of the Coello river basin, Colombia," in: *Geopedology: An Integration of Geomorphology and Pedology for Soil and Landscape Studies*, eds J. A. Zinck, G. Metternicht, G. Bocco, and H. F. Del Valle (Cham: Springer International Publisher), 411–424.

López, M. E., and Howell, W. E. (1967). Katabatic winds in the Equatorial Andes. *J. Atmos. Sci*. 24, 29–35.

Lovejoy, T., and Nobre, C. A. (2019). Winds of will: tipping change in the Amazon. *Sci. Adv*. 5:eaba2949. doi: 10.1126/sciadv.aba2949

Lowman, L. E. L., and Barros, A. P. (2014). Investigating links between climate and orography in the central Andes: coupling erosion and precipitation using a physical-statistical model. *J. Geophys. Res. Earth Surf*. 119, 1322–1353. doi: 10.1002/2013JF002940

MAAP (2019). *Major Finding - Many Brazilian Amazon Fires Follow 2019 Deforestation*. Available online at: https://maaproject.org/2019/amazon-fires-deforestation/ (accessed March 9, 2020).

Maeda, E. E., Kim, H., Aragão, L. E. O. C., Famiglietti, J. S., and Oki, T. (2015). Disruption of hydroecological equilibrium in southwest Amazon mediated by drought. *Geophys. Res. Lett*. 42, 7546–7553. doi: 10.1002/2015GL065252

Magrin, G. O., Marengo, J. A., Boulanger, J.-P., Buckeridge, M. S., Castellanos, E., Poveda, G., et al. (2014). "Central and South America," in: *Climate Change 2014: Impacts, Adaptation, and Vulnerability. Part B: Regional Aspects. Contribution of Working Group II to the Fifth Assessment Report of the Intergovernmental Panel on Climate Change*, eds V. R. Barros, C. B. Field, D. J. Dokken, M. D. Mastrandrea, K. J. Mach, T. E. Bilir, M. Chatterjee, K. L. Ebi, Y. O. Estrada, R. C. Genova, B. Girma, E. S. Kissel, A. N. Levy, S. MacCracken, P. R. Mastrandrea, and L.L. White (Cambridge, UK; New York, NY: Cambridge University Press), 1499–1566.

Makowski Giannoni, S., Trachte, K., Rollenbeck, R., Lehnert, L., Fuchs, J., and Bendix, J. (2016). Atmospheric salt deposition in a tropical mountain rainforest at the eastern Andean slopes of south Ecuador-Pacific or Atlantic origin? *Atmos. Chem. Phys*. 16, 10241–10261. doi: 10.5194/acp-16-10241-2016

Mandapaka, P. V., Krajewski, W. F., Mantilla, R., and Gupta, V. K. (2009). Dissecting the effect of rainfall variability on the statistical structure of peak flows. *Adv.Water Res*. 32, 1508–1525. doi: 10.1016/j.advwatres.2009.07.005

Manners, R. B., Magilligan, F. J., and Goldstein, P. S. (2007). Floodplain development, El Niño, and cultural consequences in a hyperarid Andean environment. *Ann. Assoc. Am. Geogr*. 97, 229–249. doi: 10.1111/j.1467-8306.2007.00533.x

Mapes, B. E., Warner, T. T., and Xu, M. (2003). Diurnal patterns of rainfall in northwestern South America. Part III: diurnal gravity waves and nocturnal convection offshore. *Mon. Weather Rev*. 131, 830–844. doi: 10.1175/1520-0493(2003)131<0830:DPORIN>2.0.CO;2

Marchese, C. (2015). Biodiversity hotspots: a shortcut for a more complicated concept. *Glob. Ecol. Conserv*. 3, 297–309. doi: 10.1016/j.gecco.2014.12.008

Marengo, J. (1983). Estudios Agroclimático de la zona de Genaro Herrera (Requena-Loreto) y climático en la selva baja norte del Perú. Tesis UNALM. *Ing. Meteorólogo. Lima*. p. 464.

Marengo, J., Cornejo, A., Satymurty, P., Nobre, C., and Sea, W. (1997). Cold surges in tropical and extratropical South America: the strong event in June 1994. *Mon. Weather Rev*. 125, 2759–2786.

Marengo, J. A., Alves, L. M., Soares, W. R., Rodriguez, D. A., Camargo, H., Paredes, M., et al. (2013). Two contrasting seasonal extremes in tropical South America

in 2012: flood in Amazonia and drought in Northeast Brazil. *J. Clim.* 26, 9137–9154. doi: 10.1175/JCLI-D-12-00642.1

Marengo, J. A., Espinoza, J. C., Ronchail, J., Alves, L. M., and Baez, J. (2017). [Regional Climates] Central South America [in "State of the Climate in 2016"]. *Bull. Am. Meteorol. Soc.* 98, S187–S190. doi: 10.1175/2017BAMSStateoftheClimate.1

Marengo, J. A., Tomasella, J., Alves, L. M., Soares, W., and Rodriguez, D. A. (2011). The drought of 2010 in the context of historical droughts in the Amazon region. *Geophys. Res. Lett.* 38, 1–5. doi: 10.1029/2011GL047436

Marengo, J. A., Tomasella, J., Soares, W., Alves, L. M., and Nobre, C. A. (2010). Extreme climatic events in the Amazon basin: climatological and hydrological context of previous floods. *Theor. Appl. Climatol.* 85, 1–5. doi: 10.1007/s00704-011-0465-1

Marie, G., and Veerle, V. (2013). "Landslide controlling factors in catchments with high deforestation," in *Landslide Science and Practice.* eds C. Margottini, P. Canuti, and K. Sassa (Berlin; Heidelberg: Springer), 227–233.

Marwan, N., Trauth, M. H., Vuille, M., and Kurths, J. (2003). Comparing modern and Pleistocene ENSO-like influences in NW Argentina using nonlinear time series analysis methods. *Clim. Dyn.* 21, 317–326. doi: 10.1007/s00382-003-0335-3

Masiokas, M. H., Rabatel, A., Rivera, A., Ruiz, L., Pitte, P., Ceballos, J. L., et al. (2020). Current state and recent changes of the cryosphere in the Andes. *Front Earth Sci.* 8:99. doi: 10.3389/feart.2020.00099

Masotti, I., Aparicio-Rizzo, P., Yevenes, M. A., Garreaud, R., Belmar, L., and Farías, L. (2018). The influence of river discharge on nutrient export and phytoplankton biomass off the central Chile coast (33°-37°S): seasonal cycle and interannual variability. *Front. Mar. Sci.* 5:423. doi: 10.3389/fmars.2018.00423

Matsudo, C. M., and Salio, P. (2011). Severe weather reports and proximity to deep convection over Northern Argentina. *Atmos. Res.* 100, 523–537. doi: 10.1016/j.atmosres.2010.11.004

McPhaden, M. J., Vera, C. S., and Martnez Guingla, R. (2010). Climate variability and change in South America. *Eos* 91:473. doi: 10.1029/2010EO490006

McPhaden, M. J., Zebiak, S. E., and Glantz, M. H. (2006). ENSO as an integrating concept in Earth science. *Science* 314, 1740–1745. doi: 10.1126/science.1132588

Menabde, M., and Sivapalan, M. (2001). Linking space-time variability of river runoff and rainfall fields: a dynamic approach. *Adv. Water Res.*, 24, 1001–1014. doi: 10.1016/S0309-1708(01)00038-0

Méndez, W., Rivas, L., Fernández, E., Díaz, Y., Arévalo, M., and Correa, N. (2016). Hydro-geomorphological hazard in catchments of the Waraira Repano national park south hillside, Distrito Capital, Venezuela [Amenaza hidrogeomorfológica en microcuencas de la vertiente sur del Parque Nacional Waraira Repano, Distrito Capital, Venezuela]. *Rev. Geog. Venez.* 57, 70–91. Available online at: http://www.saber.ula.ve/handle/123456789/41975

Mesa, O. J., and Peñaranda, V. M. (2015). Complejidad de la estructura espacio-temporal de la precipitación. *Rev. Acad. Colomb. Cienc. Ex. Fis. Nat.* 39, 304–320. doi: 10.18257/raccefyn.196

Metz, N. D., Archambault, H. M., Srock, A. F., Galarneau, T. J. Jr., and Bosart, L. F. (2013). A comparison of South American and African preferential pathways for extreme cold events. *Mon. Weather. Rev.* 141, 2066–2086. doi: 10.1175/MWR-D-12-00202.1

Mezher, R. N., Doyle, M., and Barros, V. (2012). Climatology of hail in Argentina. *Atmos. Res.* 114–115, 70–82. doi: 10.1016/j.atmosres.2012.05.020

Michoud, C., Baumann, V., Lauknes, T. R., Penna, I., Derron, M. -H., and Jaboyedoff, M. (2016). Large slope deformations detection and monitoring along shores of the Potrerillos dam reservoir, Argentina, based on a small-baseline InSAR approach. *Landslides* 13, 451–465. doi: 10.1007/s10346-015-0583-4

Minetti, J. L., Vargas, W. M., Poblete, A. G., de la Zerda, L. R., and Acuña, L. R. (2010). Regional droughts in southern South America. *Theor. Appl. Clim.* 102, 403–415. doi: 10.1007/s00704-010-0271-1

Molina, A., Vanacker, V., Balthazar, V., Mora, D., and Govers, G. (2012). Complex land cover change, water and sediment yield in a degraded andean environment. *J. Hydrol.* 472–473, 25–35. doi: 10.1016/j.jhydrol.2012.09.012

Montecinos, A., and Aceituno, P. (2003). Seasonality of the ENSO-related rainfall variability in central Chile and associated circulation anomalies. *J. Clim.* 16, 281–296. doi: 10.1175/1520-0442(2003)016<0281:SOTERR>2.0.CO;2

Montecinos, A., Kurgansky, M. V., Muñoz, C., and Takahashi, K. (2011). Non-ENSO interannual rainfall variability in central Chile during austral winter. *Theor. Appl. Climatol.* 106, 557–568. doi: 10.1007/s00704-011-0457-1

Montgomery, D. R., and Dietrich, W. E. (1994). A physically based model for the topographic control on shallow landsliding. *Water Resour. Res.* 30, 1153–1171. doi: 10.1029/93WR02979

Morales, M. S., Christie, D. A., Villalba, R., Argollo, J., Pacajes, J., Silva, J. S., et al. (2012). Precipitation changes in the South American Altiplano since 1300 AD reconstructed by tree-rings. *Clim. Past* 8, 653–666. doi: 10.5194/cp-8-653-2012

Moreiras, S., Lisboa, M. S., and Mastrantonio, L. (2012). The role of snow melting upon landslides in the central Argentinean Andes. *Earth Surf. Proc. Land.* 37, 1106–1119. doi: 10.1002/esp.3239

Moreiras, S. M. (2005). Climatic effect of ENSO associated with landslide occurrence in the Central Andes, Mendoza Province, Argentina. *Landslides* 2, 53–59. doi: 10.1007/s10346-005-0046-4

Moreiras, S. M. (2006). Frequency of debris flows and rockfall along the Mendoza river valley (Central Andes), Argentina: associated risk and future scenario. *Q Intern.* 158, 110–121. doi: 10.1016/j.quaint.2006.05.028

Moreiras, S. M., and Pont, I. P. V. D. (2017). Climate change driving greater slope instability in the Central Andes. *Adv. Cult. Liv. Landsl.* 5, 191–197. doi: 10.1007/978-3-319-53483-1_22

Moreiras, S. M., Pont, I. V. D., and Araneo, D. (2018). Were merely storm-landslides driven by the 2015-2016 Niño in the Mendoza River valley? *Landslides* 15:997. doi: 10.1007/s10346-018-0959-3

Moreiras, S. M., and Sepúlveda, S. A. (2015). Megalandslides in the Andes of central Chile and Argentina (32°-34°S) and potential hazards. *Geol. Soc. Spec. Publ.* 399, 329–344. doi: 10.1144/SP399.18

Morera, S. B., Condom, T., Crave, A., Steer, P., and Guyot, J. L. (2017). The impact of extreme El Niño events on modern sediment transport along the western Peruvian Andes (1968-2012). *Sci. Rep.* 7:11947. doi: 10.1038/s41598-017-12220-x

Moya-Álvarez, A. S., Martínez-Castro, D., Kumar, S., Estevan, R., and Silva, Y. (2019). Response of the WRF model to different resolutions in the rainfall forecast over the complex Peruvian orography. *Theor. Appl. Clim.* 137:2993. doi: 10.1007/s00704-019-02782-3

Mulholland, J. P., Nesbitt, S. W., Trapp, R. J., Rasmussen, K. L., and Salio, P. V. (2018). Convective storm life cycle and environments near the Sierras de Córdoba, Argentina. *Mon. Weather Rev.* 146, 2541–2557. doi: 10.1175/MWR-D-18-0081.1

Muñoz, E., Poveda, G., Ochoa, A., and Caballero, H. (2017). "Multifractal analysis of spatial and temporal distributions of landslides in Colombia," in *Advancing Culture of Living With Landslides,* eds M. Mikos, B. Tiwari, Y. Yin, K. Sassa (Cham: Springer International Publishing), 1073–1079.

Mutke, J., Bohnert, T., and Weigend, M. (2017). Climate change: save last cloud forests in western Andes. *Nature* 541:157. doi: 10.1038/541157e

Myers, N., Mittermeier, R. A., da Fonseca, C. G., Gustavo, A. B., and Kent, J. (2000). Biodiversity hotspots for conservation priorities. *Nature* 403, 853–858. doi: 10.1038/35002501

Naaim, M., Furdada, G., and Martínez, H. (2002). Calibration and application of the MN2D dynamics model to the avalanches of Las Leñas (Argentina). *Nat. Hazards Earth Sys. Sci.* 2, 221–226. doi: 10.5194/nhess-2-221-2002

Nascimento, E. L., and Marcelino, I. P. V. O. (2005). Preliminary analysis of the 3 January 2005 tornadoes in Criciuma/SC. *Bull. Braz. Meteorol. Soc.* 29, 33–44.

Navarrete-Aldana, N., Cooper, M. A., and Holle, R. L. (2014). Lightning fatalities in Colombia from 2000 to 2009. *Nat. Hazards* 74, 1349–1362. doi: 10.1007/s11069-014-1254-9

Nguyen, P., Thorstensen, A., Sorooshian, S., Hsu, K., and AghaKouchak, A. (2015). Flood forecasting and inundation mapping using hiresflood-uci and near-real-time satellite precipitation data: the 2008 Iowa flood. *J. Hydrometeorol.* 16, 1171–1183. doi: 10.1175/JHM-D-14-0212.1

Nieto, R., Ciric, D., Vázquez, M., Liberato, M. L. R., and Gimeno, L. (2019). Contribution of the main moisture sources to precipitation during extreme peak precipitation months. *Adv. Water Resour.* 131:103385. doi: 10.1016/j.advwatres.2019.103385

Norte, F. A. (2015). Understanding and forecasting Zonda wind (Andean Foehn) in Argentina: a review. *Atmos. Clim. Sci.* 5, 163–193. doi: 10.4236/acs.2015.53012

Norte, F. A., Ulke, A., Simonelli, S., and Viale, M. (2008). The severe Zonda wind event of 11 July 2006 east of the Andes Cordillera (Argentine): a case study using the BRAMS model. *Met. Atmos. Phys.* 102, 1–14. doi: 10.1007/s00703-008-0011-6

Nossin, J. J. (1999). Monitoring of hazards and urban growth in Villavicencio, Colombia, using scanned air photos and satellite imagery. *Geo J.* 49, 151–158. doi: 10.1023/A:1006939519722

Núñez-Cobo, J., Garreaud, R., and Verbist, K. (2018). "Sequias en Chile," in *Atlas de Sequía de América Latina y el Caribe*. ed J. K. Núñez Cobo (Paris; La Serena: Verbist UNESCO and CAZALAC), 204.

Ochoa, A., Pineda, L., Crespo, P., and Willems, P. (2014). Evaluation of TRMM 3B42 precipitation estimates and WRF retrospective precipitation simulation over the Pacific–Andean region of Ecuador and Peru. *Hydrol. Earth Syst. Sci.* 18, 3179-3193. doi: 10.5194/hess-18-3179-2014

Oliveros, F., Hernández, E., and Soto, G. (2017). "Application of geotechnical criteria for the occurrence of earth flows (avalanches) on the right of way of pipeline transportation system of Camisea in the coast zone of Peru," in *ASME 2017 International Pipeline Geotechnical Conference (IPG)* (Lima).

OPS (2000). *Perú: Fenómeno El Niño, 1997-1998.* Washigton, DC: Organización Panamericana de la Salud. Fenómeno El Niño, 1997-1998.

Ortloff, C. R., and Kolata, A. L. (1993). Climate and collapse: agro-ecological perspectives on the decline of the Tiwanaku State. *J. Archaeol. Sci.* 20, 195–221. doi: 10.1006/jasc.1993.1014

Otero, F., Norte, F., and Araneo, D. (2018). A probability index for surface zonda wind occurrence. *Theor. Appl. Climatol.* 131, 213. doi: 10.1007/s00704-016-1983-7

Ovando, A., Tomasella, J., Rodriguez, D. A., Martinez, J. M., Siqueira-Junior, J. L., Pinto, G. L. N., et al. (2016). Extreme flood events in the Bolivian Amazon wetlands. *J. Hydrol. Reg. Stu.* 5, 293–308. doi: 10.1016/j.ejrh.2015.11.004

Pabón-Caicedo, J. D., Arias, P. A., Carril, A. F., Espinoza, J. C., Fita, L., Goubanova, K., et al. (2020). Observed and projected hydroclimate changes in the Andes. *Front. Earth Sci.* 8:61. doi: 10.3389/feart.2020.00061

Paccini, L., Espinoza, J. C., Ronchail, J., and Segura, H. (2017). Intraseasonal rainfall variability in the Amazon basin related to large-scale circulation patterns: a focus on western Amazon-Andes transition region. *Int. J. Clim.* 38, 2386–2399. doi: 10.1002/joc.5341

Pérez, G., Mantilla, R., Krajewski, W. F., and Wright, D. B. (2019). Using physically based synthetic peak flows to assess local and regional flood frequency analysis methods. *Water Resour. Res.* 55, 8384–8403. doi: 10.1029/2019WR024827

Perrin, J. L., Bouvier, C., Janeau, J. L., Mánez, G., and Cruz, F. (2001). Rainfall/runoff processes in a small peri-urban catchment in the Andes mountains. The Rumihurcu Quebrada, Quito (Ecuador). *Hydrol. Process.* 15, 843–854. doi: 10.1002/hyp.190

Perucca, L. P., and Angilieri, Y. E. (2011). Morphometric characterization of del Molle Basin applied to the evaluation of flash floods hazard, Iglesia Department, San Juan, Argentina. *Q. Int.* 233, 81–86. doi: 10.1016/j.quaint.2010.08.007

Pettinger, A. M., and Sykora, D. W. (2011). Landslide risk assessment for pipeline systems in mountainous regions. *J. Pipeline Syst. Eng.* 10, 161–171.

Pezza, A. B., and Ambrizzi, T. (2005). Dynamical conditions and synoptic tracks associated with different types of cold surge over tropical South America. *Int. J. Climatol.* 25, 215–241. doi: 10.1002/joc.1080

Pizarro, R., Vera, M., Valdés, R., Helwig, B., and Olivares, C. (2014). Multi-decadal variations in annual maximum peak flows in semi-arid and temperate regions of Chile. *Hydrol. Sci. J.* 59, 300–311. doi: 10.1080/02626667.2013.803182

Posadas, A., Duffaut Espinosa, L. A., Yarlequé, C., Carbajal, M., Heidinger, H., Carvalho, L., et al. (2015). Spatial random downscaling of rainfall signals in Andean heterogeneous terrain, Nonlin. *Process. Geophys.* 22, 383–402. doi: 10.5194/npg-22-383-2015

Poveda, G. (2011). Mixed memory, (non) Hurst effect, and maximum entropy of rainfall in the tropical Andes. *Adv. Water Res.* 34, 243–256. doi: 10.1016/j.advwatres.2010.11.007

Poveda, G., Álvarez, D. M., and Rueda, O. A. (2011). Hydro-climatic variability over the Andes of Colombia associated with ENSO: a review of climatic processes and their impact on one of the Earth's most important biodiversity hotspots. *Clim. Dyn.* 36, 2233–2249. doi: 10.1007/s00382-010-0931-y

Poveda, G., Jaramillo, A., Gil, M. M., Quiceno, N., and Mantilla, R. I. (2001a). Seasonality in ENSO related precipitation, river discharges, soil moisture, and vegetation index (NDVI) in Colombia. *Water Resour. Res.* 37, 2169–2178. doi: 10.1029/2000WR900395

Poveda, G., Jaramillo, A., and Mantilla, R. (2001b). "Asociación Entre el Fenómeno El Niño y las anomalías de humedad de suelo y del índice "NDVI" en Colombia," in *Memorias IX Congreso Latinoamericano e Ibérico de Meteorología* (Buenos Aires), 7–11.

Poveda, G., Jaramillo, L., and Vallejo, L. F. (2014). Seasonal precipitation patterns along pathways of South American low-level jets and aerial rivers. *Water Resour. Res.* 50, 98–118. doi: 10.1002/2013WR014087

Poveda, G., and Mejía, J. F. (2004). Escalamiento espacial de sistemas convectivos de mesoescala sobre Colombia y el Pacífico Oriental en 1998 según la Misión TRMM. *Avances en Recursos Hidráulicos* 11, 131–143. Available online at: http://bdigital.unal.edu.co/6108/1/No._11-2004-4.pdf

Poveda, G., and Mesa, O. J. (1996). Las fases extremas del fenómeno ENSO (El Niño y La Niña) y su influencia sobre hidrología de Colombia. *Ing. Hidrául. Méx.* 1, 21–37.

Poveda, G., and Mesa, O. J. (1997). Feedbacks between hydrological processes in tropical South America and large scale oceanic atmospheric phenomena. *J. Clim.* 10, 2690–2702.

Poveda, G., and Mesa, O. J. (1999). La corriente de chorro superficial del oeste ("del CHOCÓ") y otras dos corrientes de chorro atmosféricas sobre Colombia: Climatología y Variabilidad durante las fases del ENSO. *Revista Acad. Colomb. Ci. Exact.* 23, 517–528.

Poveda, G., and Mesa, O. J. (2000). On the existence of Lloró (the rainiest locality on earth): enhanced ocean-land-atmosphere interaction by a low-level jet. *Geophys. Res. Lett.* 27, 1675–1678. doi: 10.1029/1999GL006091

Poveda, G., Mesa, O. J., Arias, P. A., Salazar, L. F. Moreno, H., Vieira, S. C., et al. (2005). The diurnal cycle of precipitation in the tropical Andes of Colombia. *Mon. Weather. Rev.* 133, 228–240. doi: 10.1175/MWR-2853.1

Poveda, G., Mesa, O. J., Toro, V. G., Agudelo, P. A., Álvarez, J. F., Arias, P. A., et al. (2002). Diagnostics of the anual cycle and ENSO effects on 1 to 24-hr rainfall events over the Andes of Colombia [In Spanish]. *Meteorol. Colombiana.* 5, 67–74.

Poveda, G., and Salas, H. D. (2015). Statistical scaling, Shannon entropy and generalized space-time q-entropy of rainfall fields in tropical South America. *Chaos* 25:075409. doi: 10.1063/1.4922595

Poveda, G., Vélez, J. I., Mesa, O. J., Cuartas, A., Barco, J., Mantilla, R., et al. (2007). Linking long-term water balances and statistical scaling to estimate river flows along the drainage network of Colombia. *J. Hydrol. Eng.* 12, 4–13. doi: 10.1061/(ASCE)1084-0699(2007)12:1(4)

Poveda, G., Waylen, P. R., and Pulwarty, R. (2006). Modern climate variability in northern South America and southern Mesoamerica. *Palaeogeo. Palaeoclim. Palaeoecol.* 234, 3–27. doi: 10.1016/j.palaeo.2005.10.031

Quintero, F., Krajewski, W. F., Mantilla, R., Small, S., and Seo, B. (2016). A spatial–dynamical framework for evaluation of satellite rainfall products for flood prediction. *J. Hydrometeorol.* 17, 2137-2154. doi: 10.1175/JHM-D-15-0195.1

Quispe, N. (2010). Estructura dinámica de una baja fría. *Rev. Peruana Geo-Atmos.* 1, 125–133. Available online at: https://web2.senamhi.gob.pe/rpga/pdf/2009_vol01/

Rabatel, A., Francou, B., Soruco, A., Gomez, J., Cáceres, B., Ceballos, J. L., et al. (2013). Current state of glaciers in the tropical Andes: a multi-century perspective on glacier evolution and climate change. *Cryosphere* 7, 81–102. doi: 10.5194/tc-7-81-2013

Ralph, F. M., Prather, K. A., Cayan, D., Spackman, J. R., DeMott, P., Dettinger, M., et al. (2016). CalWater field studies designed to quantify the roles of atmospheric rivers and aerosols in modulating US West Coast precipitation in a changing climate. *Bull. Am. Meteorol. Soc.* 97, 1209–1228. doi: 10.1175/BAMS-D-14-00043.1

Ramírez, B. H., van der Ploeg, M., Teuling, A. J., Ganzeveld, L., and Leemans, R. (2017). Tropical montane cloud forests in the orinoco river basin: the role of soil organic layers in water storage and release. *Geoderma* 298,14–26. doi: 10.1016/j.geoderma.2017.03.007

Rasmussen, K. L., Chaplin, M. M., Zuluaga, M. D., and Houze, R. A. Jr. (2016). Contribution of extreme convective storms to rainfall in south america. *J. Hydrometeorol.* 17, 353–367. doi: 10.1175/JHM-D-15-0067.1

Rasmussen, K. L., and Houze, R. A. Jr. (2011). Orogenic convection in subtropical South America as seen by the TRMM satellite. *Mon. Weather Rev.* 139, 2399–2420. doi: 10.1175/MWR-D-10-05006.1

Rasmussen, K. L., and Houze, R. A. Jr. (2016). Convective initiation near the Andes in subtropical South America. *Mon. Weather Rev*. 144, 2351–2374. doi: 10.1175/MWR-D-15-0058.1

Rasmussen, K. L., Zuluaga, M. D., and Houze, R. A. Jr. (2014). Severe convection and lightning in subtropical South America. *Geophys. Res. Lett*. 41, 7359–7366. doi: 10.1002/2014GL061767

Rau, P., Bourrel, L., Labat, D., Melo, P., Dewitte, B., Frappart, F., et al. (2016). Regionalization of rainfall over the Peruvian Pacific slope and coast. *Int. J. Climatol.* 37, 143–158. doi: 10.1002/joc.4693

Recalde-Coronel, G. C., Zaitchik, B., and Pan, W. K. (2020). Madden–Julian oscillation influence on sub-seasonal rainfall variability on the west of South America. *Clim. Dyn.* 54, 2167–2185. doi: 10.1007/s00382-019-05107-2

Restrepo, C., Walker, L. R., Shiels, A. B., Bussmann, R., Claessens, L., Fisch, S., et al. (2009). Landsliding and its multiscale influence on mountainscapes. *Bioscience* 59, 685–698. doi: 10.1525/bio.2009.59.8.10

Restrepo, J. D., and Escobar, H. A. (2018). Sediment load trends in the Magdalena River basin (1980–2010): anthropogenic and climate-induced causes. *Geomorphology* 302, 76–91. doi: 10.1016/j.geomorph.2016.12.013

Rickenbach, T. M., Ferreira, R. N., Halverson, J. B., Herdies, D. L., and Silva Dias, M. A. F. (2002). Modulation of convection in the southwestern Amazon basin by extratropical stationary fronts. *J. Geophys. Res.* 107:8040. doi: 10.1029/2000JD000263

Rivera, J. A., Araneo, D. C., and Peñalba, O. C. (2017a). Threshold level approach for streamflow drought analysis in the Central Andes of Argentina: a climatological assessment. *Hydrol. Sci. J.* 62, 1949–1964. doi: 10.1080/02626667.2017.1367095

Rivera, J. A., Araneo, D. C., Penalba, O. C., and Villalba, R. (2018). Regional aspects of streamflow droughts in the Andean rivers of Patagonia, Argentina. Links with large-scale climatic oscillations. *Hydrol. Res*. 49, 134–149. doi: 10.2166/nh.2017.207

Rivera, J. A., Penalba, O. C., Villalba, R., and Araneo, D. C. (2017b). Spatio-temporal patterns of the 2010-2015 extreme hydrological drought across the Central Andes, Argentina. *Water* 9:652. doi: 10.3390/w9090652

Roche, M. A., Aliaga, A., Campos, J., Pena, J., Cortes, J., and Rocha, N. (1990). "Hétérogénéité des précipitations sur la cordillère des Andes boliviennes," in *Hydrology in Mountainous Regions: International Association of Hydrological Sciences,* ed H. Lang (Wallingford*:* IAHS Publication), 381–388.

Rodriguez-Morata, C., Ballesteros-Canovas, J. A., Rohrer, M., Espinoza, J. C., Beniston, M., and Stoffel, M. (2018). Linking atmospheric circulation patterns with hydro geomorphic disasters in Peru. *Int. J. Climatol.* 38, 3388–3404. doi: 10.1002/joc.5507

Rodriguez-Morata, C., Díaz, H. F., and Ballesteros-Canovas, J. A. (2019). The anomalous 2017 coastal El Niño event in Peru. *Clim Dyn*. 52, 5605–5622. doi: 10.1007/s00382-018-4466-y

Rollenbeck, R., and Bendix, J. (2011). Rainfall distribution in the Andes of southern Ecuador derived from blending weather radar data and meteorological field observations. *Atmos. Res*. 99, 277–289. doi: 10.1016/j.atmosres.2010.10.018

Román-Cuesta, R. M., Carmona-Moreno, C., Lizcano, G., New, M., Silman, M., Knoke, T., et al. (2014). Synchronous fire activity in the tropical high Andes: an indication of regional climate forcing. *Glob. Change Biol.* 20, 1929–1942. doi: 10.1111/gcb.12538

Román-Cuesta, R. M., Salinas, N., Asbjornsen, H., Oliveras, I., Huaman, V., Gutiérrez, Y., et al. (2011). Implications of fires on carbon budgets in Andean cloud montane forest: the importance of peat soils and tree resprouting. *Forest Ecol. Manag.* 261, 1987–1997. doi: 10.1016/j.foreco.2011.02.025

Romatschke, U., and Houze, R. A. (2013). Characteristics of precipitating convective systems accounting for the summer rainfall of tropical and subtropical South America. *J. Hydrometeorol.* 14, 25–46. doi: 10.1175/JHM-D-12-060.1

Romatschke, U., and Houze, R. A. Jr. (2010). Extreme summer convection in South America. *J. Clim.* 23, 3761–3791. doi: 10.1175/2010JCLI3465.1

Romatschke, U., Medina, S., and Houze, R. A. Jr. (2010). Regional, seasonal, and diurnal variations of extreme convection in the South Asian region. *J. Climate* 23, 419–439. doi: 10.1175/2009JCLI3140.1

Ronchail, J. (1989a). Advections Polaires en Bolivie: mise en évidence et caractérisation des effets climatiques. *Hydrol. Cont*. 4, 49–56.

Ronchail, J. (1989b). "Climatological winter effects of southern advections in Bolivia and north-west Brazil (1973–1984)," *Paper Read at Third International Conference on Southern Hemisphere Meteorology and Oceanography*. (Buenos Aires).

Ronchail, J., Bourrel, L., Cochonneau, G., Vauchel, P., Phillips, L., Castro, A., et al. (2005). Climate and inundations in the Mamoré basin (South-Western Amazon-Bolivia). *J. Hydrol*. 302, 223–238. doi: 10.1016/j.jhydrol.2004.07.005

Ronchail, J., Cochonneau, G., Molinier, M., Guyot, J. -L., de Miranda Chaves, G. A., Guimarães, V., et al. (2002). Interannual rainfall variability in the Amazon Basin and sea surface temperatures in the equatorial Pacific and the tropical Atlantic Oceans. *Int. J. Climatol*. 22, 1663–1686. doi: 10.1002/joc.815

Ronchail, J., and Gallaire, R. (2006). ENSO and rainfall along the Zongo Valley (Bolivia) from the Altiplano to the Amazon Basin. *Int. J. Climatol*. 26, 1223–1236. doi: 10.1002/joc.1296

Rydbeck, A. V., and Maloney, E. D. (2015). On the Convective coupling and moisture organization of east Pacific easterly waves. *J. Atmos. Sci*. 72, 3850–3970. doi: 10.1175/JAS-D-15-0056.1

Saavedra, M., and Takahashi, K. (2017). Physical controls on frost events in the central Andes of Peru using in situ observations and energy flux models. *Agric. For. Met*. 239, 58–70. doi: 10.1016/j.agrformet.2017.02.019

Sakamoto, M. S., Ambrizzi, T., and Poveda, G. (2011). Moisture sources and life cycle of convective systems over western Colombia. *Adv. Meteorol*. 2011:890759. doi: 10.1155/2011/890759

Salas, H. D., Poveda, G., Mesa, O. J., and Marwan, N. (2020). Generalized synchronization between ENSO and hydrological variables in Colombia: a recurrence quantification approach. *Front. Appl. Math. Stat*. 6:3. doi: 10.3389/fams.2020.00003

Salazar, J. F., Villegas, J. C., Rendón, A. M., Rodríguez, E., Hoyos, I., Mercado-Bettín, D., et al. (2018). Scaling properties reveal regulation of river flows in the Amazon through a "forest reservoir". *Hydrol. Earth Syst. Sci.* 22, 1735–1748. doi: 10.5194/hess-22-1735-2018

Salio, P., Nicolini, M., and Zipser, E. J. (2007). Mesoscale convective systems over southeastern South America and their relationship with the South American low-level jet. *Mon. Weather Rev*. 135, 1290–1309. doi: 10.1175/MWR3305.1

Satyamurty, P., da Costa, C. P. W., Manzi, A. O., and Candido, L. A. (2013). A quick look at the 2012 record flood in the Amazon basin. *Geophys. Res. Lett*. 40, 1396–1401. doi: 10.1002/grl.50245

Schneider, H., Schwab, M., and Schlunegger, F. (2008). Channelized and hillslope sediment transport and the geomorphology of mountain belts. *Int. J. Earth Sci*. 97, 179–192. doi: 10.1007/s00531-006-0164-9

Schoolmeester, T., Saravia, M., Andresen, M., Postigo, J., Valverde, A., Jurek, M., et al. (2016). "*Outlook on Climate Change Adaptation in the Tropical Andes mountains*," in *Mountain Adaptation Outlook Series.United Nations Environment Programme, GRID-Arendal and CONDESAN*. Nairobi, Arendal, Vienna and Lima. Available online at: www.unep.org, www.grida.no, www.co.

Segura, H., Espinoza, J. C., Junquas, C., Lebel, T., Vuille, M., and Garreau, R. (2020). Recent changes in the precipitation-driving processes over the southern tropical Andes/western Amazon. *Clim. Dyn.* 54, 2613-2631. doi: 10.1007/s00382-020-05132-6

Segura, H., Espinoza, J. C., Junquas, C., and Takahashi, K. (2016). Evidencing decadal and interdecadal hydroclimatic variability over the central Andes. *Environ. Res. Lett*. 11:094016. doi: 10.1088/1748-9326/11/9/094016

Seiler, C., Hutjes, R. W. A., and Kabat, P. (2013). Climate variability and trends in Bolivia. *Jour. Appl. Meteorol. Clim*. 52, 130–146. doi: 10.1175/JAMC-D-12-0105.1

Sepúlveda, S. A., Moreiras, S. M., Lara, M., and Alfaro, A. (2014a). Debris flows in the Andean ranges of central Chile and Argentina triggered by 2013 summer storms: characteristics and consequences. *Landslides* 12, 115–133. doi: 10.1007/s10346-014-0539-0

Sepúlveda, S. A., and Padilla, C. (2008). Rain-induced debris and mudflow triggering factors assessment in the Santiago cordilleran foothills, Central Chile. *Nat. Hazards* 47, 201–215. doi: 10.1007/s11069-007-9210-6

Sepúlveda, S. A., and Petley, D. N. (2015). Regional trends and controlling factors of fatal landslides in Latin America and the Caribbean. *Nat. Hazards Earth Syst. Sci.* 15, 1821–1833. doi: 10.5194/nhess-15-1821-2015

Sepúlveda, S. A., Rebolledo, S., McPhee, J., Lara, M., Cartes, M., Rubio, E., et al. (2014b). Catastrophic, rainfall-induced debris flows in Andean villages of Tarapacá, Atacama desert, northern Chile. *Landslides* 11, 481–491. doi: 10.1007/s10346-014-0480-2

Shimada, I., Schaaf, C. B., Thompson, L. G., and Mosley-Thompson, E. (1991). Cultural impacts of severe droughts in the prehistoric Andes: application of a 1,500-year ice core precipitation record. *World Archaeol.* 22, 247–270. doi: 10.1080/00438243.1991.9980145

Sicart, J. E., Espinoza, J. C., Queno, L., and Medina, M. (2015). Radiative properties of clouds over a tropical Bolivian glacier: seasonal variations and relationship with regional atmospheric circulation. *Int. J. Clim.* 36, 3116–3128. doi: 10.1002/joc.4540

Smith, M. D. (2011). The ecological role of climate extremes: current understanding and future prospects. *J. Ecol.* 99, 651–655. doi: 10.1111/j.1365-2745.2011.01833.x

Soto, J., Galve, J. P., Palenzuela, J. A., Azaín, J. M., Tamay, J., and Irigaray, C. (2017b). A multi-method approach for the characterization of landslides in an intramontane basin in the Andes (Loja, Ecuador). *Landslides* 14, 1929–1947. doi: 10.1007/s10346-017-0830-y

Soto, J., Palenzuela, J. A., Galve, J. P., Luque, J. A., Azaín, J. M., Tamay, J., et al. (2017a). Estimation of empirical rainfall thresholds for landslide triggering using partial duration series and their relation with climatic cycles. An application in southern Ecuador. *Bull. Eng. Geol. And Environ.* doi: 10.1007/s10064-017-1216-z

Stahr, A., and Langenscheidt, E. (2015). *Landforms of High Mountains*. Berlin; Heidelberg: Springer-Verlag.

Stäubli, A., Nussbaumer, S. U., Allen, S. K., Huggel, C., Arguello, M., Costa, F., et al. (2017). "Analysis of weather- and climate-related disasters in mountain regions using different disaster databases," in: *Climate Change, Extreme Events and Disaster Risk Reduction. Sustainable Development Goals Series.* eds S. Mal, R. Singh, and C. Huggel (Cham: Springer), 17–41.

Sulca, J., Takahashi, K., Espinoza, J. C., Vuille, M., and Lavado-Casimiro, W. (2017). Impacts of different ENSO flavors and tropical Pacific convection variability (ITCZ, SPCZ) on austral summer rainfall in South America, with a focus on Peru. *Int. J. Climatol.* 38, 420–435. doi: 10.1002/joc.5185

Sulca, J., Vuille, M., Roundy, P., Takahashi, K., Espinoza, J. C., Silva, Y., et al. (2018). Climatology of extreme cold events in the central Peruvian Andes during austral summer: origin, types, and teleconnections. *Q J. R Meteorol. Soc.* 144, 2693–2714. doi: 10.1002/qj.3398

Sulca, J., Vuille, M., Silva, Y., and Takahashi, K. (2016). Teleconnections between the Peruvian central Andes and Northeast Brazil during extreme rainfall events in austral summer. *J. Hydrometeorol.* 17, 499–515. doi: 10.1175/JHM-D-15-0034.1

Sun, D., Xue, F., and Zhou, T. J. (2013). Impacts of two types of El Niño on atmospheric circulation in the Southern Hemisphere. *Adv. Atmos. Sci.* 30, 1732–1742. doi: 10.1007/s00376-013-2287-9

Takahashi, K. (2004). The atmospheric circulation associated with extreme rainfall events in Piura, Peru, during the 1997–1998 and 2002 El Niño events. *Ann. Geophys.* 22, 3917–3926. doi: 10.5194/angeo-22-3917-2004

Takahashi, K., and Dewitte, B. (2016). Strong and moderate nonlinear El Niño regimes. *Clim. Dyn.* 46, 1627–1645. doi: 10.1007/s00382-015-2665-3

Takahashi, K., and Martínez, A. G. (2019). The very strong coastal El Niño in 1925 in the far-eastern Pacific. *Clim. Dyn.* 52, 7389–7415. doi: 10.1007/s00382-017-3702-1

Takahashi, K., Montecinos, A., Goubanova, K., and Dewitte, B. (2011). ENSO regimes: reinterpreting the canonical and Modoki El Niño. *Geophys. Res. Lett.* 38:L10707. doi: 10.1029/2011GL047364

Teitelbaum, H., and D'Andrea, F. (2015). Deep convection east of the Andes Cordillera: four hailstorm cases. *Tellus* 67:26806. doi: 10.3402/tellusa.v67.26806

Townsend-Small, A., McClain, M. E., Hall, B., Noguera, J. L., Llerena, C. A., and Brandes, J. A. (2008). Suspended sediments and organic matter in mountain headwaters of the Amazon River: results from a 1-year time series study in the central Peruvian Andes. *Geochim. Cosmochim. Acta* 72, 732–740. doi: 10.1016/j.gca.2007.11.020

Trachte, K. (2018). Atmospheric moisture pathways to the highlands of the tropical Andes: analyzing the effects of spectral nudging on different driving fields for regional climate modeling. *Atmosphere* 9:456. doi: 10.3390/atmos9110456

Trachte, K., Rollenbeck, R., and Bendix, J. (2010). Nocturnal convective cloud formation under clear-sky conditions at the eastern Andes of south Ecuador. *J. Geophys. Res. Atmos.* 115D:24203. doi: 10.1029/2010JD014146

Trauth, M. H., Alonso, R. A., Haselton, K. R., Hermanns, R. L., and Strecker, M. R. (2000). Climate change and mass movements in the NW Argentine Andes. *Earth Planet. Sci. Lett.* 179, 243–256. doi: 10.1016/S0012-821X(00)00127-8

UNISDR (2016). *Oficina de las Naciones Unidas para la Reducción del Riesgo de Desastres 2016: Impacto de los Desastres en América Latina y El Caribe, 1990-2013.* Agencia Española de Cooperación Internacional para el Desarrollo y Corporación OSSO.

Urrutia-Jalabert, R., González, M. E., González-Reyes, Á., Lara, A., and Garreaud, R. (2018). Climate variability and forest fires in central and south-central Chile. *Ecosphere* 9:e02171. doi: 10.1002/ecs2.2171

Valenzuela, R. A., and Garreaud, R. D. (2019). Extreme daily rainfall in central-southern Chile and its relationship with low-level horizontal water vapor fluxes. *J. Hydrometeorol.* 20, 1829–1850. doi: 10.1175/JHM-D-19-0036.1

Vallejo-Bernal, S. M., Urrea, V., Bedoya-Soto, J. M., Posada, D., Olarte, A., Cárdenas-Posso, Y., et al. (2020). Ground validation of TRMM 3B43 V7 precipitation estimates over Colombia. Part I: Monthly and seasonal timescales. *Int. J. Climatol.* doi: 10.1002/joc.6640

Vanacker, V., Balthazar, V., and Molina, A. (2013). Anthropogenic activity triggering landslides in densely populated mountain areas. *Landslide Sci.Pract.* 4, 163–167. doi: 10.1007/978-3-642-31337-0_21

Vanacker, V., Molina, A., Govers, G., Poesen, J., and Deckers, J. (2007). Spatial variation of suspended sediment concentrations in a tropical Andean river system: the Paute River, southern Ecuador. *Geomorphology* 87, 53–67. doi: 10.1016/j.geomorph.2006.06.042

Vanacker, V., Vanderschaeghe, M., Govers, G., Willems, E., Poesen, J., Deckers, J., et al. (2003). Linking hydrological, infinite slope stability and land-use change models through GIS for assessing the impact of deforestation on slope stability in high Andean watersheds. *Geomorphology* 52, 299–315. doi: 10.1016/S0169-555X(02)00263-5

Varble, A., Nesbitt, S., Salio, P., Avila, E., Borque, P., deMott, P., et al. (2019). *Cloud, Aerosol, and Complex Terrain Interactions (CACTI) Field Campaign Report.* Ed Stafford R (ARM user facility). DOE/SC-ARM-19-028.

Veblen, T. T., and Kitzberger, T. (2002). Inter-hemispheric comparison of fire history: the Colorado Front Range, U.S.A., and the northern Patagonian Andes, Argentina. *Plant Ecol.* 163, 187–207. doi: 10.1023/A:1020905823901

Velasco, I., and Fritsch, J. M. (1987). Mesoscale convective complexes in the Americas. *J. Geophys. Res. Atmos.* 92, 9591–9613. doi: 10.1029/JD092iD08p09591

Viale, M., and Garreaud, R. (2014). Summer precipitation events over the western slope of the subtropical Andes. *Mon. Weather Rev.* 142, 1074-1092. doi: 10.1175/MWR-D-13-00259.1

Viale, M., and Nuñez, M. N. (2011). Climatology of winter orographic precipitation over the subtropical central Andes and associated synoptic and regional characteristic. *J. Hydrometeorol.* 12, 481–507. doi: 10.1175/2010JHM1284.1

Viale, M., Valenzuela, R., Garreaud, R., and Ralph, F. (2018). Impacts of atmospheric rivers on precipitation in Southern South America. *J. Hydrometeorol.* 19, 1671–1686. doi: 10.1175/JHM-D-18-0006.1

Vicente-Serrano, S. M., Aguilar, E., Martínez, R., Martín-Hernández, N., Azorin-Molina, C., Sanchez-Lorenzo, A., et al. (2017). The complex influence of ENSO on droughts in Ecuador. *Clim. Dyn.* 48, 405–427. doi: 10.1007/s00382-016-3082-y

Vicente-Serrano, S. M., Beguería, S., and López-Moreno, J. I. (2011b). Comment on "Characteristics and trends in various forms of the Palmer Drought Severity Index (PDSI) during 1900–2008" by A. *Dai. J. Geophys. Res. Atmos.* 116:D19112. doi: 10.1029/2011JD016410

Vicente-Serrano, S. M., López-Moreno, J. I., Gimeno, L., Nieto, R., Morán-Tejeda, E., Lorenzo-Lacruz, J., et al. (2011a) A multi-scalar global evaluation of the impact of ENSO on droughts. *J. Geophys. Res. Atmos.* 116:D20109. doi: 10.1029/2011JD016039

Villalobos, E. E., Martinez-Castro, D., Kumar, S., Silva, Y., and Fashe, O. (2019). Study of convective storms in the Peruvian central Andes using PR-TRMM and KuPR-GPM radars (In Spanish). *Rev. Cubana Meteorol.* 25, 59–75. Available online at: http://rcm.insmet.cu/index.php/rcm/article/view/454/673

Vuille, M. (1999). Atmospheric circulation over the Bolivian Altiplano during dry and wet periods and extreme phases of the southern oscillation. *Int. J. Climatol.* 19, 1579–1600.

Vuille, M., Bradley, R., and Keimig, F. (2000). Interannual climate variability in the central Andes and its relation to tropical Pacific and Atlantic forcing. *J. Geophys. Res. Atmos.* 105, 12447–12460. doi: 10.1029/2000JD900134

Vuille, M., Francou, B., Wagnon, P., Juen, I., Kaser, G., Mark, B., et al. (2008). Climate change and tropical Andean glaciers: past, present and future. *Earth Sci. Rev*. 89, 79–86. doi: 10.1016/j.earscirev.2008.04.002

Wang, C. (2002). Atmospheric circulation cells associated with the El Niño–Southern Oscillation. *J. Climate* 15, 399–419. doi: 10.1175/1520-0442(2002)015<0399:ACCAWT>2.0.CO;2

Wang, H., and Fu, R. (2002) Cross-equatorial flow and seasonal cycle of precipitation over South America. *J. Clim.* 15, 1591–1608. doi: 10.1175/1520-0442(2002)015<1591:CEFASC>2.0.CO;2

Waylen, P. R., and Poveda, G. (2002). El Niño-Southern oscillation and aspects of western South America hydro-climatology. *Hydrol. Process*. 16, 1247–1260. doi: 10.1002/hyp.1060

Wheeling, K. (2019, October 10). Deforestation could Exacerbate Drought in the Amazon. *Eos.*

Woodman, R. F. (1985). "Recurrencia del Fenòmeno del Niño con intensidad comparable a la del Niño 1982–1983. El Fenòmeno El Niño," in *Proceedings of the Seminario Regional Ciencia, Tecnología y Agresiòn Ambiental* (Lima: CONCYTEC), 301–332.

Woodman, R. F. (1999). "Modelo estadístico de pronòstico de las precipitaciones en la costa norte del Perú. El Fenòmeno El Niño. Investigaciòn para una prognosis," in *1er encuentro de Universidades del Pacífico Sur: Memoria* (Lima), 93–108.

Wu, H., Adler, R. F., Tian, Y., Gu, G., and Huffman, G. J. (2017). Evaluation of quantitative precipitation estimations through hydrological modeling in floods river basins. *J. Hydrometeorol.* 18, 529–553. doi: 10.1175/JHM-D-15-0149.1

Yang, Z., and Dominguez, F. (2019). Investigating land surface effects on the moisture transport over south america with a moisture tagging model. *J. Clim.* 32, 6627–6644. doi: 10.1175/JCLI-D-18-0700.1

Yarleque, C., Vuille, M., Hardy, D. R., Posadas, A., and Quiroz, R. (2016). Multiscale assessment of spatial precipitation variability over complex mountain terrain using a high-resolution spatiotemporal wavelet reconstruction method. *J. Geophys. Res. Atmos.* 121, 198–216. doi: 10.1002/2016JD025647

Yepes, J., Poveda, G., Mejía, J. F., Moreno, L., and Rueda, C. (2019). CHOCO-JEX: a research experiment focused on the Chocó low-level jet over the far eastern Pacific and western Colombia. *Bull. Am. Meteorol. Soc.* 100, 779–796. doi: 10.1175/BAMS-D-18-0045.1

Younes-Cárdenas, N., and Erazo-Mera, E. (2016). Landslide susceptibility analysis using remote sensing and GIS in the western Ecuadorian Andes. *Nat. Hazards* 81, 1829–1859. doi: 10.1007/s11069-016-2157-8

Yu, J. -Y., and Kao, H. -Y. (2007). Decadal changes of ENSO persistence barrier in SST and ocean heat content indices: 1958–2001. *J. Geophys. Res*. 112:D13106. doi: 10.1029/2006JD007654

Zambrano-Bigiarini, M., Nauditt, A., Birkel, C., Verbist, K., and Ribbe, L. (2017). Temporal and spatial evaluation of satellite-based rainfall estimates across the complex topographical and climatic gradients of Chile. *Hydrol. Earth Syst. Sci*. 21, 1295–1320. doi: 10.5194/hess-21-1295-2017

Zemp, D., Schleussner, C. -F., Barbosa, H., van Der Ent, R., Donges, J. F., Heinke, J., et al. (2014). On the importance of cascading moisture recycling in South America. *Atmos. Chem. Phys*. 14, 13337–13359. doi: 10.5194/acp-14-13337-2014

Zhou, J., and Lau, K.-M. (2001). Principal modes of interannual and decadal variability of summer rainfall over South America (2001). *Int. J. Clim*. 21, 1623–1644. doi: 10.1002/joc.700

Zipser, E. J., Liu, C., Cecil, D. J., Nesbitt, S. W., and Yorty, D. P. (2006). Where are the most intense thunderstorms on Earth? *Bull. Am. Meteorol. Soc*. 87, 1057–1071. doi: 10.1175/BAMS-87-8-1057

Zuluaga, M. D., and Houze, R. A. Jr. (2015). Extreme convection of the near-equatorial Americas, Africa, and adjoining oceans as seen by TRMM. *Mon. Weather Rev*. 143, 298–316. doi: 10.1175/MWR-D-14-00109.1

Conflict of Interest: The authors declare that the research was conducted in the absence of any commercial or financial relationships that could be construed as a potential conflict of interest.

Copyright © 2020 Poveda, Espinoza, Zuluaga, Solman, Garreaud and van Oevelen. This is an open-access article distributed under the terms of the Creative Commons Attribution License (CC BY). The use, distribution or reproduction in other forums is permitted, provided the original author(s) and the copyright owner(s) are credited and that the original publication in this journal is cited, in accordance with accepted academic practice. No use, distribution or reproduction is permitted which does not comply with these terms.

frontiers in Earth Science

REVIEW
published: 23 June 2020
doi: 10.3389/feart.2020.00099

A Review of the Current State and Recent Changes of the Andean Cryosphere

M. H. Masiokas[1], A. Rabatel[2], A. Rivera[3,4], L. Ruiz[1], P. Pitte[1], J. L. Ceballos[5], G. Barcaza[6], A. Soruco[7], F. Bown[8], E. Berthier[9], I. Dussaillant[9] and S. MacDonell[10]*

[1] *Instituto Argentino de Nivología, Glaciología y Ciencias Ambientales (IANIGLA), CCT CONICET Mendoza, Mendoza, Argentina,* [2] *Univ. Grenoble Alpes, CNRS, IRD, Grenoble-INP, Institut des Géosciences de l'Environnement, Grenoble, France,* [3] *Departamento de Geografía, Universidad de Chile, Santiago, Chile,* [4] *Instituto de Conservación, Biodiversidad y Territorio, Universidad Austral de Chile, Valdivia, Chile,* [5] *Instituto de Hidrología, Meteorología y Estudios Ambientales (IDEAM), Bogotá, Colombia,* [6] *Instituto de Geografía, Pontificia Universidad Católica de Chile, Santiago, Chile,* [7] *Facultad de Ciencias Geológicas, Universidad Mayor de San Andrés, La Paz, Bolivia,* [8] *Tambo Austral Geoscience Consultants, Valdivia, Chile,* [9] *LEGOS, Université de Toulouse, CNES, CNRS, IRD, UPS, Toulouse, France,* [10] *Centro de Estudios Avanzados en Zonas Áridas (CEAZA), La Serena, Chile*

The Andes Cordillera contains the most diverse cryosphere on Earth, including extensive areas covered by seasonal snow, numerous tropical and extratropical glaciers, and many mountain permafrost landforms. Here, we review some recent advances in the study of the main components of the cryosphere in the Andes, and discuss the changes observed in the seasonal snow and permanent ice masses of this region over the past decades. The open access and increasing availability of remote sensing products has produced a substantial improvement in our understanding of the current state and recent changes of the Andean cryosphere, allowing an unprecedented detail in their identification and monitoring at local and regional scales. Analyses of snow cover maps has allowed the identification of seasonal patterns and long term trends in snow accumulation for most of the Andes, with some sectors in central Chile and central-western Argentina showing a clear decline in snowfall and snow persistence since 2010. This recent shortage of mountain snow has caused an extended, severe drought that is unprecedented in the hydrological and climatological records from this region. Together with data from global glacier inventories, detailed inventories at local/regional scales are now also freely available, providing important new information for glaciological, hydrological, and climatological assessments in different sectors of the Andes. Numerous studies largely based on field measurements and/or remote sensing techniques have documented the recent glacier shrinkage throughout the Andes. This observed ice mass loss has put Andean glaciers among the highest contributors to sea level rise per unit area. Other recent studies have focused on rock glaciers, showing that in extensive semi-arid sectors of the Andes these mountain permafrost features contain large reserves of freshwater and may play a crucial role as future climate becomes warmer and drier in this region. Many relevant issues remain to be investigated, however, including an improved estimation of ice volumes at local scales, and detailed assessments of the hydrological significance of the different components of the cryosphere in Andean river basins. The impacts of future climate changes on the Andean cryosphere also need to be studied in more detail, considering the contrasting

OPEN ACCESS

Edited by:
Bryan G. Mark,
The Ohio State University,
United States

Reviewed by:
Tom Holt,
Aberystwyth University,
United Kingdom
Lukas Arenson,
BGC Engineering, Canada

****Correspondence:***
M. H. Masiokas
mmasiokas@mendoza-conicet.gob.ar

Specialty section:
This article was submitted to Cryospheric Sciences, a section of the journal Frontiers in Earth Science

Received: *09 October 2019*
Accepted: *20 March 2020*
Published: *23 June 2020*

Citation:
Masiokas MH, Rabatel A, Rivera A, Ruiz L, Pitte P, Ceballos JL, Barcaza G, Soruco A, Bown F, Berthier E, Dussaillant I and MacDonell S (2020) A Review of the Current State and Recent Changes of the Andean Cryosphere. Front. Earth Sci. 8:99. doi: 10.3389/feart.2020.00099

climatic scenarios projected for each region. The sustained work of various monitoring programs in the different Andean countries is promising and will provide much needed field observations to validate and improve the analyses made from remote sensors and modeling techniques. In this sense, the development of a well-coordinated network of high-elevation hydro-meteorological stations appears as a much needed priority to complement and improve the many glaciological and hydro-climatological assessments that are being conducted across the Andes.

Keywords: glaciers, mountain permafrost, seasonal snow, Andes Cordillera, tropical Andes, southern Andes

INTRODUCTION

The Andes Cordillera extends for almost 8,000 km along the western portion of South America, from ca. 11°N in northern Colombia and Venezuela to ca. 55°S in southern Chile and Argentina. Over this extensive latitudinal range, the Andes portray an impressive variety of topographic and climatic conditions that result in a vast and diverse cryosphere. In fact, no other mountainous region on Earth contains such a diversity of cryospheric features. The Andes contain the largest extension of tropical glaciers on Earth (many located above 5,000 m a.s.l.; Kaser and Osmaston, 2002). In the semi-arid subtropical Andes of Chile and Argentina one of the greatest areas of rock glaciers exists (Zalazar et al., 2017). In south-western Patagonia and Tierra del Fuego, extensive temperate glaciers and icefields terminate into terrestrial, lacustrine and marine environments. The Andes also include the largest glacierized area in the Southern Hemisphere outside Antarctica (the South Patagonian Icefield alone covers ca. 12,200 km^2), and they have the greatest extension of seasonal snow and mountain permafrost in this part of the globe (RGI Consortium, 2017; Hammond et al., 2018; Jones et al., 2018).

Recent global estimates suggest that Andean glaciers are probably one of the highest contributors per unit area to sea level rise (e.g., Braun et al., 2019; Dussaillant et al., 2019; Wouters et al., 2019; Zemp et al., 2019), and many scientific assessments have used the Andean ice mass loss as a clear indicator of climate change. Furthermore, in vast semi-arid regions from Peru-Bolivia to central Chile and Argentina, the meltwater originating from different components of the Andean cryosphere represents a crucial water resource for sustaining human consumption, agriculture, mountain ecosystems, hydro-electric generation, and numerous industrial activities in the adjacent lowlands (e.g., Masiokas et al., 2013; Soruco et al., 2015; Dangles et al., 2017; Schoolmeester et al., 2018; Vuille et al., 2018; Zimmer et al., 2018). It is noteworthy that in the tropical regions, perennial and seasonal snow covers are limited or absent, strengthening the importance of glaciers to maintain water availability in the dry periods of the year (Kaser et al., 2010). Andean glaciers are also considered valuable natural elements of the landscape that attract hundreds of thousands of tourists each year and generate significant revenues for the local and regional economies (e.g., Schoolmeester et al., 2018; Vuille et al., 2018). On the other hand, the recent ice mass loss and the associated destabilization of slopes in the vicinity of newly formed proglacial lakes can also pose potential hazards and threaten the human populations and infrastructure located downvalley in the Andes (e.g., Worni et al., 2012; Cook et al., 2016; Wilson et al., 2018).

The diversity of glaciological and geocryological features and conditions briefly mentioned above demonstrate the enormous potential for cryospheric studies of the Andes Cordillera. In this paper we provide an overview of the Andean cryosphere by describing the current understanding and recent advances in the study of seasonal snow, glaciers and mountain permafrost (with a focus on rock glaciers) in this region. We also discuss recent trends observed in these main components of the Andean cryosphere in an attempt to put the more recent results in a longer term perspective. This review concludes with the discussion of some pending issues regarding the current understanding and potential future directions in the study of the major elements of the Andean cryosphere, hoping they can motivate and promote additional new scientific research in this mountain range.

SEASONAL SNOW

One of the typical characteristics of the Andes is the accumulation of variable amounts of snow on the ground in different periods of the year (**Figure 1**). This seasonal natural process constitutes a major feature in the Andean hydro-climatic system and is crucial for the distribution and preservation of other components of the cryosphere. For many Andean river basins, and in particular those in semi-arid climates in Chile and Argentina, this seasonal accumulation and subsequent melting of snow during warmer months provides a significant portion of the surface runoff (e.g., Masiokas et al., 2006; Favier et al., 2009) and is one of the most important sources of water for the maintenance of mountain ecosystems, for the recharge of aquifers, and for numerous human populations that rely on Andean waters for human consumption, irrigation, industries, and hydro-power generation. According to Masiokas et al. (2006), over 85% of the interannual variability in Andean streamflows between 30° and 37°S can be explained by variations in winter snow accumulation alone.

The interaction between the main atmospheric circulation patterns and the orographic barrier of the Andes modulates the spatial and temporal distribution of solid precipitation across western South America, creating specific hydro-climatic regimes at different latitudes (Garreaud, 2009; Viale et al., 2019; Espinoza et al., 2020).

In the tropical Andes most of the moisture has an Atlantic origin and is transported to the mountains by the dominant easterly circulation in a series of convection-driven precipitation events. This general pattern is in turn governed by the seasonal latitudinal changes of the Inter-Tropical Convergence Zone (ITCZ), which moves the zone of highest convective activity southward in late spring - summer (December-February), and equatorward during the winter (May-August). Thus in the inner tropical Andes of Ecuador, Colombia and Venezuela, humidity remains high throughout the year but two wetter seasons can be discerned in spring (October to November) during the southward passage of the ITCZ, and in autumn (April to May) when the belt of convective activity moves northward. In contrast, further south in the outer tropical Andes of Bolivia and Peru, most of the solid and liquid precipitation occurs when the ITCZ reaches these latitudes during the summer months (for more details see Espinoza et al., 2020). It is important to note, however, that the snow that falls outside of the glacier limits typically lasts for only a few days due to the high solar radiation which exists throughout the year, and thus the seasonal snow cover is almost entirely limited to the glacierized areas (Lejeune et al., 2007; Wagnon et al., 2009; Vuille et al., 2018).

Precipitation in the subtropical Andes (i.e., ca. 18°–29°S) is also of predominantly Atlantic origin and occurs during the austral summer months, but is driven primarily by the tropical easterlies associated with the South American summer monsoon (Garreaud, 2009). At the southernmost reaches of the subtropical region some precipitation can have a Pacific origin, but overall the precipitation amounts are comparatively much lower than those observed further north in the tropical Andes. In northernmost Chile (ca. 18–18.5°S), precipitation totals for upper Andean river basins range between ca. 150 and 400 mm a^{-1}, but further south at 27–28°S these values can decrease to 40 mm a^{-1} (Alvarez-Garreton et al., 2018). These small precipitation amounts are clearly evidenced by the arid conditions of the region and the very limited number and extent of glaciers and snow patches in southwestern Bolivia, northern Chile and northwestern Argentina, despite the high elevation of the Andes at these latitudes.

South of ca. 29°S most of the precipitation reaching the Andes has a predominantly Pacific origin and is modulated by a series of frontal systems embedded in the dominant westerly circulation. At these latitudes the location of the subtropical Pacific anticyclone plays a major role in the intensity of the westerlies and precipitation seasonality. The equatorward displacement of this high pressure center allows the westerly storm tracks to move northward and result in a peak in precipitation in winter in the central Andes of Chile and Argentina and also in the north Patagonian Andes. At high elevations this peak in precipitation usually falls as snow and remains frozen until the onset of the melting season in the spring (September to October). Typical annual precipitation totals for upper Andean river basins in Chile (Alvarez-Garreton et al., 2018) increase from 150 to 200 mm a^{-1} around 30°S to 1600–2200 mm a^{-1} at 35°S. Further south, the Andes are exposed to the westerlies throughout the year and thus precipitation is more uniformly distributed in the different seasons, with a more mixed pattern of rain and snow that depends on the annual cycle of temperatures and the overall conditions during each specific precipitation event (Garreaud et al., 2009; Saavedra et al., 2017).

The extensive and persistent cloud cover associated with large precipitation amounts that are common in the latitudinal extremes of the Andes (i.e., in the inner Tropics and in southern Patagonia and Tierra del Fuego) have limited the use of optical satellite images to derive large-scale snow cover assessments in these regions. Saavedra et al. (2017) developed a detailed Andean snow climatology based on daily moderate resolution imaging spectroradiometer (MODIS) satellite images for the 8°–39°S latitude range. They found, for example, that in the tropics until ca. 23°S the snow cover is largely constrained to elevations above 5,000 m. Their analyses also showed that between 8° and 14°S snow cover has minimal seasonal variability but further south (14°–23°S) it peaks in late summer-early fall at the end of the wet season. At higher latitudes (south of 23°S) the highest snow coverage coincides with the austral winter months. The high elevation of the Andes and the relatively high precipitation that occurs between 28° and 37°S determine the greatest concentration of seasonal and permanent snow covered areas in this region (Saavedra et al., 2017; **Figure 1**). At higher latitudes, the southward decrease in elevation of the Andes also determines a concomitant gradual lowering of the regional snow line (Nogami, 1972; Rabassa, 1981; Saavedra et al., 2017). These regional patterns explain, to a large extent, the limited glacierization of the high arid Andes of northern Chile and Argentina, and the extensive glaciers and icefields in southern Patagonia, where greater and more frequent snow accumulation can be observed all year long (Aniya et al., 1997; Lliboutry, 1998; Garreaud, 2009; Bravo et al., 2019a; Durand et al., 2019).

ENSO and Seasonal Snow

The El Niño – Southern Oscillation phenomenon, and the associated ocean-atmosphere conditions in the tropical Pacific, constitute major factors modulating the interannual variability of the solid and liquid precipitation that reaches the Andes. The impacts of ENSO on Andean glaciers and snowfall records are well known in western South America and have been described using a variety of indicators, including *in situ* measurements (e.g., Masiokas et al., 2006; Maussion et al., 2015), and more recently data derived from remote sensing (e.g., Cortés and Margulis, 2017; Saavedra et al., 2017; Cordero et al., 2019) and snow mass balance models (Réveillet et al., 2020).

In the tropical Andes, El Niño events associated with warm conditions in the tropical Pacific usually result in reduced and delayed snow accumulation and higher temperatures in the mountains, which ultimately produce significant ice mass loss in glaciers during these years (e.g., Wagnon et al., 2001; Francou et al., 2003, 2004; Maussion et al., 2015; Vuille et al., 2018). In contrast, La Niña events are often associated with higher snow accumulation and colder temperatures that tend to lead to less negative or even slightly positive glacier mass balances across this region. In the southern Andes, numerous studies have reported a significant association between ENSO and winter snow

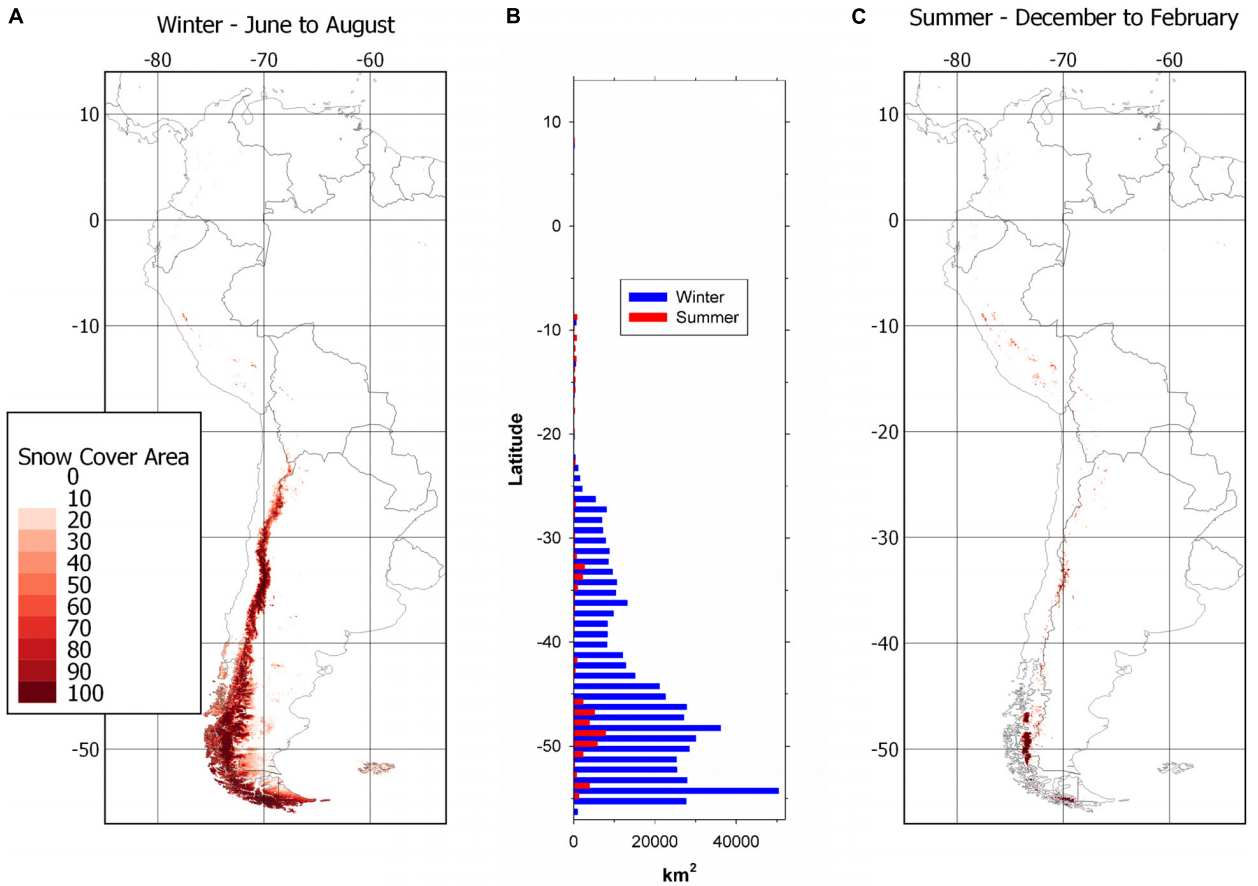


FIGURE 1 | (A,C) Percentage of snow covered area in the Andes, averaged for the winter (June to August) and summer (December to February) seasons, respectively, and derived from MODIS sensors over the period 2000–2019. **(B)** Surface area covered with snow (NDSI > 0.4) during the two seasons mentioned above. Note the substantial differences in snow covered area at different times of the year. Source: NASA NSDIC DAAC (https://doi.org/10.5067/MODIS/MOD10CM.006).

accumulation. However, the impacts of ENSO have an opposite effect than that observed in the tropical Andes. In the central Andes of Chile and Argentina between ca. 29° and 37°S, above-average snowfall anomalies tend to occur during the warm phases of ENSO (El Niño years), and below-average snow conditions during the cold ENSO phases (La Niña events; Masiokas et al., 2006; Rivera et al., 2017). This relationship is nonetheless not straightforward and does not necessarily apply in all warm or cold ENSO years (Masiokas et al., 2006). This non-linear relationship was also observed by Saavedra et al. (2017) using snow cover data derived from MODIS imagery, and by Garreaud et al. (2017) based on precipitation series from central Chile. They showed that although ENSO appears as a main climate driver in the region, not all El Niño (La Niña) years result in above-average (below-average) precipitation anomalies in the Andes at these latitudes. Cordero et al. (2019) found a discernible influence of ENSO in dry season snow patterns.

Recent Snow Trends

The magnitude and spatial patterns of the snow accumulated each year in many tropical, subtropical and extratropical Andean basins have remained largely unknown until very recently. This limited knowledge is likely due to the sheer magnitude of the Andes Cordillera as a whole, the systematic lack of snowpack measurements at high elevations, and the great diversity in topographic and climatic conditions that exist over this mountain range. In this regard, the freely available data from the MODIS sensors have become useful for the study and characterization of snow cover variations across large areas, providing new important information for many previously unstudied regions throughout the Andes. Several recent studies (e.g., Cara et al., 2016; Cortés et al., 2016; Cortés and Margulis, 2017; Saavedra et al., 2018) have used the MODIS dataset, other remote sensing sources (such as Landsat imagery), in situ snowpack measurements and/or modeling approaches to assess recent changes in snow cover across the Andes. Saavedra et al. (2018), for example, assessed snow cover patterns using 2000–2016 daily MODIS data from the region between 8° and 36°S (further north and south, the high frequency of clouds precluded detailed assessments). One prominent finding of their analyses is the identification of an extensive area in the Andes between 29° and 36°S where snow cover has decreased at an average rate of 2–5

fewer days per year, and where the snowline elevation increased at an annual rate of 10–30 m a^{-1}. Cordero et al. (2019) used Landsat images from the Andes between 18° and 40°S, and found that despite significant interannual variability, dry-season snow cover in this extensive region has declined at an average annual rate of −12% $decade^{-1}$ between 1968 and 2018.

Given that snowfall is a major component of the glacier mass balance in the tropical Andes, the recent decline in tropical glacier mass could be associated, at least partly, with a decreasing trend in snow accumulation at high elevations. However, as stressed by Vuille et al. (2018), snowfall measurements at these sites are quite scarce and the spatio-temporal patterns of this climatic variable are virtually unknown, highlighting the need to improve the measurements and characterization of this crucial climatic process in this region. In contrast, further south in the central Andes of Chile and Argentina, the recent decline in winter snow accumulation is relatively well known and is being monitored with concern on both sides of the international divide. Particularly because since 2010, this region has been experiencing the most extreme dry period since at least the beginning of the 20th century. Due to its severity and duration, this sustained dry period has been termed the "Megadrought" (Garreaud et al., 2017; Rivera et al., 2017). This drought (which still persists in 2020) is apparently unprecedented even in a tree-ring based precipitation reconstruction that spans the last millennium (Garreaud et al., 2017), and is readily observable not only on the snowpack records, but also on streamflow series and glacier mass balance records (Masiokas et al., 2016; Rivera et al., 2017; Dussaillant et al., 2019).

The widespread retreat reported for most Patagonian glaciers (see section "Glaciers" below) could also be partly associated with a decrease in winter snow accumulation. However, although this is probably true for the north Patagonian region (Masiokas et al., 2008; Garreaud et al., 2009), the assessment is much more uncertain further south where there is a serious lack of direct *in situ* snowfall measurements. A recent study by Falaschi et al. (2019) showed a clear atmospheric warming and a reduction in precipitation in the eastern side of the North Patagonian Icefield (hereafter NPI) in the last 5–6 decades. Other studies have used modeling approaches combined with reanalysis data to derive spatially resolved precipitation maps (e.g., Lenaerts et al., 2014; Schaefer et al., 2015). Bravo et al. (2019a) assessed spatial and temporal patterns in snow accumulation in the NPI and the South Patagonian Icefield (hereafter SPI) using a regional climate model, four phase partitioning methods, and few short-term snow accumulation observations. They found a marked contrast between the wetter western side vs. the drier eastern side at both icefields, and no significant trend during the 1980–2015 period for all seasons except in the austral autum. In this season they found a positive (negative) trend in snow accumulation in the western (eastern) side of the SPI. Further south, Aguirre et al. (2018) used MODIS snow cover products and historical climate data to reconstruct snow cover changes in the Brunswick Peninsula around the city of Punta Arenas in southwestern Patagonia (ca. 53°S, 71°W). Their analyses showed that snow extent in this region has decreased ca. 20% between 1972 and 2016, and that this pattern could be related to the long-term warming observed at Punta Arenas during the cold season.

GLACIERS

Tropical Andes (11°N – 17.5°S)

The tropical Andes can be divided into two zones with different climate characteristics (Troll, 1941). The inner tropics with more or less continuous precipitation throughout the year, and the outer tropics characterized by a dry, a wet and a transition season. From a glaciological point of view, one can consider that glaciers from 11°N in Colombia and Venezuela to about 5°S in the northern part of Peru belong to the inner tropics, whereas glaciers located south of 5°S in Peru to 17.5°S in Bolivia belong to the outer tropics. Homogeneous air temperature conditions in average prevail throughout the year but with a slight seasonality in the outer tropics (1 to 2°C higher temperatures during the austral summer). The incident solar radiation is also more or less constant throughout the year (∼200 W m^{-2}), as the seasonality of the extraterrestrial irradiance in the outer tropics is attenuated by pronounced cloud seasonality (Sicart et al., 2005). In the inner tropics, humidity remains almost unchanged throughout the year (e.g., ∼80 ± 10% at Antisana glacier in Ecuador), whereas the outer tropics are characterized by notable seasonal differences in humidity and increased precipitation during the wet season. These climate features lead to specificities in the glacier surface mass and energy balance regimes (e.g., Rabatel et al., 2012, 2013; Vuille et al., 2018).

Tropical glaciers are characterized by large vertical mass balance gradients in the ablation area (e.g., Kaser et al., 1996; Favier et al., 2004; Soruco et al., 2009; Vincent et al., 2018), implying a significant contribution of the lowest areas of the glacier to total ablation. For example, for the Zongo glacier in Bolivia, the ablation area (one third of the glacier surface at the low elevation ranges) contributes with 80% to the yearly specific mass balance of the glacier (Soruco et al., 2009). Distributed simulation of the energy fluxes at the glacier scale showed that the frequent changes in snow cover throughout the ablation season are the main explanation for the marked vertical mass balance gradients of tropical glaciers (Sicart et al., 2011). In addition, tropical glaciers have year-round ablation conditions close to the glacier snout. Indeed, the ablation is almost constant in Ecuador (around 25 to 30 cm on average per month at about 4950 m a.s.l., Francou et al., 2004) but toward the outer tropics the melt rate seasonality is more evident. In the inner tropics, the sensitivity of Ecuadorian and Colombian glaciers to climate is closely linked to the absence of temperature seasonality. The 0°C isotherm constantly oscillates through the ablation zone of the glaciers, and a minor variation in air temperature can influence the melt processes by determining the phase of precipitation and consequently affect the surface albedo in the ablation zone. The frequency and intensity of snowfall, which can occur all year long, play a major role in attenuating the melt processes. The interannual variability of ablation is mainly controlled by year-to-year variations in air temperature (Francou et al., 2004), which determine the snowline altitude.

In the outer tropics, where liquid precipitation is rare on glaciers, the surface mass balance is closely related to the total amount and the seasonal distribution of precipitation (Wagnon et al., 2001; Francou et al., 2003; Sicart et al., 2005). Concerning the evolution of melt at the glacier surface throughout the year, three seasons can be distinguished for outer tropical glaciers (Sicart et al., 2011; Rabatel et al., 2012): (1) the transition season from September to December, when accumulation is still limited and the ablation of ice gradually increases to reach its maximum in November; (2) the rainy season from January to April, which corresponds to the period of accumulation, where in the lower part of the glacier, snow ablation predominates; and (3) the dry season from May to August, where ablation, although reduced, is largely present by sublimation over the entire surface of the glacier. Finally, the annual surface mass balance depends largely on the beginning of the wet season, which interrupts the period of high melt caused by solar radiation (Sicart et al., 2011). Any delay in the onset of the wet season and the concurrent accumulation of snow causes a very negative surface mass balance due to the existence of exposed ice and high ablation rates in the lower portion of the glaciers.

Recent Glacier Changes in the Tropical Andes

Rabatel et al. (2013) made an extensive review of the glacier changes in the tropical Andes over recent decades. The information between the early 1940s and the early 1960s is scarce but the available evidence from Peru, Bolivia and Colombia indicates a moderate retreat, followed by a relatively stable period from the mid-1960s to the second half of the 1970s (and even with some glacier snouts advancing during this interval; e.g., Zongo glacier; Soruco et al., 2009). In the late 1970s a clear shift toward increased ice mass wastage occurred and glacier volumes, lengths and surface areas started to decrease substantially. The glacier shrinkage in the three last decades appears to be unprecedented at a multi-secular scale (Rabatel et al., 2013).

Rabatel et al. (2013) and more recent works have shown that glaciers in Venezuela have almost completely disappeared. Morris et al. (2006) reported that glacier surface area decreased from 2.03 km^2 in 1952 to 0.3 km^2 in 2003, representing a total loss of 87%. In Colombia, Rabatel et al. (2018a) reported an overall glacier extent of about 42.4 $\pm$ 0.71 km^2 in 2016 distributed in four glacierized mountain ranges. This is 36% less than in the mid-1990s, 62% less than in the mid-twentieth century and almost 90% less than the Little Ice Age (LIA) maximum extent. Considering the strong imbalance with the current climate conditions, the limited altitudinal extent of these glaciers and their reduced accumulation areas, most of the Colombian glaciers will likely disappear in the coming decades whatever the considered climate scenario. Only the largest ones located on the highest summits will probably persist, covering a reduced area, until the second half of the twenty-first century.

In Ecuador, results obtained by Jordan et al. (2005) using photogrammetry on the Cotopaxi Volcano (5897 m a.s.l.) showed that Cotopaxi glacier area remained stable between 1956 and 1976 and then decreased by approximately 30% between 1976 and 1997. Recent updates are mostly based on satellite imagery (LANDSAT, ASTER, and ALOS), and show that over the 1962–1997 period, the surface area of the glaciers on Chimborazo (6268 m a.s.l.) decreased 57% from 27.7 to 11.8 km^2 (Caceres, 2010). For Cotopaxi and Antisana (5753 m a.s.l.) volcanoes, the loss in surface area was 37% and 33% for the period 1979–2007, respectively (Caceres, 2010). Intermediate data indicate that the retreat increased since the early 1990s (Basantes, 2010; Collet, 2010).

In Peru, four national inventories were produced since the 1960s. The first one used aerial photographs from 1962 and presented a total glacierized area of 2042 km^2, but in many sectors of the Andes the glacier data were incomplete. These data were reanalyzed and completed recently with Landsat images from 1975, and the glacier area for 1962/1975 estimated to 2399 km^2 (INAIGEM, 2018). The second inventory was performed in 1997 using Landsat satellite images, resulting in a total area of 1595 km^2 (CONAM, 2001). The third inventory (using Landsat, ASTER and SPOT satellite images from 2003 to 2010) showed a further decrease in the total glacierized area to 1298 km^2 (ANA, 2014). Finally, the fourth inventory showed that by 2016 the glacierized area of Peru had reduced to 1114 km^2 (INAIGEM, 2018). The INAIGEM report (2018) indicates that the northern, central and southern cordilleras lost 1285 km^2 (54%) of ice cover between 1962 and 2016. The northern cordilleras (Blanca, Huallanca, Huayhuash, and Raura) lost 40% during this period, whereas the central cordilleras (Huagoruncho, La Viuda, Central, Huaytapallana and Chonta) showed much larger glacier shrinkages reaching up to 70% of areal loss. Finally, in the southern cordilleras (Ampato, Vilcabamba, Urubamba, Huanzo, Chila, La Raya, Vilcanota, Carabaya and Apolobamba) the glacier areal loss was ca. 60% (INAIGEM, 2018).

Other studies have shown a similar pattern of glacier recession in Peru: in the Cordillera Blanca areal changes were relatively low from the 1950s to the 1970s, but were followed by a sharp glacier retreat (e.g., Hastenrath and Ames, 1995; Salzmann et al., 2013). A twenty-seven percent areal loss was reported for the entire Cordillera Blanca between the 1960s and the 2000s (UGRH, 2010), with a glacier surface area shrinking from 723 to 527 km^2. For the second largest glacierized mountain range in Peru (the Cordillera Vilcanota), Salzmann et al. (2013) reported a 32% glacier area loss between 1962 and 2006 (from 440 to 297 km^2), with changes concentrated mostly after 1985. More recently, Drenkhan et al. (2018) estimated for this region a rate of glacier area loss of about 1% a^{-1} between 2010 and 2016.

In Bolivia, Jordan (1991) published the first and almost complete (excluding the Cordillera Occidental) glacier inventory using aerial photographs from 1975. The total glacierized area was estimated to about 560 km^2. Many additional studies have been presented in the following decades, all showing alarming degrees of deglaciation in different sectors of the Bolivian Andes (**Table 1**). The most recent estimate indicates that in Bolivia the total glacierized area is ca. 266 km^2 (Veettil et al., 2018).

Multi-decadal time series of surface mass balance in the Tropical Andes are scarce (**Figure 2**) and have been complemented with the geodetic method that uses the differences

TABLE 1 | Compilation of studies based on aerial photographs and/or satellite imagery showing the recent glacier changes in Bolivia.

Region	Period	Changes in glacier area (%)	References
Cordillera Oriental	1986–2014	−43	Cook et al., 2016
Nevado Cololo, Cordillera de Apolobamba	1975–2011	−42	Sanches, 2013
Nevado Cololo, Cordillera de Apolobamba	1986–2014	−43	Cook et al., 2016
Apolobamba region	1975–2015	−57	Veettil and Kamp, 2017
Cordillera Real	1963–2006	−43	Soruco et al., 2009
Northern side of Cordillera Real	1963–2006	−49	Bicca, 2012
Cordillera Real	1987–2010	−30	Liu et al., 2013
Nevado Condoriri (Cordillera Real)	1988–2010	−40	Morizawa et al., 2013
Nevado Illimani (Cordillera Real)	1969–2009	−35	Ribeiro et al., 2013
Cordillera Tres Cruces	1986–2014	−42	Cook et al., 2016
Cordillera Tres Cruces	1972–1999	−33	Ribeiro et al., 2005
Cordillera Tres Cruces	1975–2009	−49	Albert et al., 2014
Nevado Santa Vera Cruz	1986–2014	−47.3	Cook et al., 2016
Cordillera de Apolobamba	1975–2016	−48.8	Veettil et al., 2018
Cordillera Real	1975–2016	−50.7	Veettil et al., 2018
Tres Cruces and Santa Vera Cruz	1975–2016	−59.4	Veettil et al., 2018
Entire Cordillera Oriental	1975–2016	−51	Veettil et al., 2018

in surface elevation derived from digital elevation models (DEMs) from different dates. The available information clearly indicates a predominant pattern of glacier mass loss over the past 50 years. As reported in Rabatel et al. (2013), this information would also suggest that in the last decades of the 20th century, glaciers in the tropical Andes experienced highly negative mass balances, particularly from the late 1970s to the early 2000s. A break point in the late 1970s is clearly discernible in the series of mean annual mass balances, which decreased from −0.2 m w.e. yr^{-1} during 1964–1975 to −0.76 m w.e. yr^{-1} during 1976–2010. Rabatel et al. (2013) compared mass balance records from glaciers at different elevations and showed that glaciers with a maximum elevation located above 5400 m a.s.l (i.e., approximately the uppermost altitude reached by the equilibrium line during very negative mass balance years) showed an average trend of −0.6 m w.e. yr^{-1} from the mid-1970s to the late 2000s. In contrast, glaciers with a maximum elevation lower than 5400 m a.s.l. showed much stronger negative trends with an average of −1.2 m w.e. yr^{-1}. The negative trend in the observed mass balances has continued until recent times (**Figure 2**).

A recent study by Dussaillant et al. (2019) used multi-temporal DEMs based on stereo-pairs of ASTER satellite optical images (Raup et al., 2000) to quantify the overall ice mass changes along the Andes over the 2000–2018 period. The authors showed that glaciers of the Tropical Andes have lost ice at an almost constant rate of -1.0 ± 0.5 Gt yr^{-1} between 2000 and 2018 (corresponding to a mass balance of −0.42 m w.e. yr^{-1}). Braun et al. (2019) estimated roughly half of this value using satellite radar data, a discrepancy that can be partly explained by a lower spatial coverage in the latter study (56% vs. 90% of glacierized area considered in Dussaillant et al., 2019). Differences between the two estimates might also be related to the respective uncertainties of the methods that used different satellite data (optical for Dussaillant et al., vs. radar for Braun et al.) and to the data processing (e.g., filtering of outliers, gap-filling). Please refer to Dussaillant et al. (2019) for an in-depth analysis of these issues.

Southern Andes (17.5° – 55°S)

The southern Andes cover more than 4500 km from northernmost Chile to the southern tip of South America in Tierra del Fuego. According to the glacio-climatological regions proposed by Lliboutry (1998), this region can be divided into the Dry Andes (17.5° – 35°S) and the Wet Andes (35° – 55°S). The Dry Andes include the Desert (17.5° – 31°S) and the Central Andes (31° – 35°S) regions, whereas the Wet Andes are divided here into the North Patagonian (35° – 45.5°S) and the South Patagonian Andes (45.5° – 55°S). Over this extensive range the Andes contain a wide variety of glaciers including permanent snowfields or glacierets, mountain glaciers, valley glaciers, outlet glaciers, piedmont glaciers, icecaps, and extensive icefields (**Figure 3**).

Dry Andes (17.5° – 35°S)

The Dry Andes constitute a high elevation semi-arid region where the high inter-annual variability in seasonal snow accumulation (e.g., Masiokas et al., 2006; Garreaud, 2009) is likely the main driver of the inter-annual variability in glacier mass balance (Masiokas et al., 2016; Farías-Barahona et al., 2019). Indeed, in dry years, the regional snowline is usually above the upper limits of many glaciers, exposing their entire surface to ablation and ice mass loss. In contrast, during snowier years, the regional snowline descends below the glacier fronts and thus many of these glaciers accumulate mass over their entire surface. This particular phenomenon lead Lliboutry (1965) to term these ice masses as "reservoir glaciers" and complicates their study using classical techniques as it is usually difficult to define the ablation and accumulation areas and the equilibrium-line altitude (ELA) of these glaciers. The large year-to-year variability of

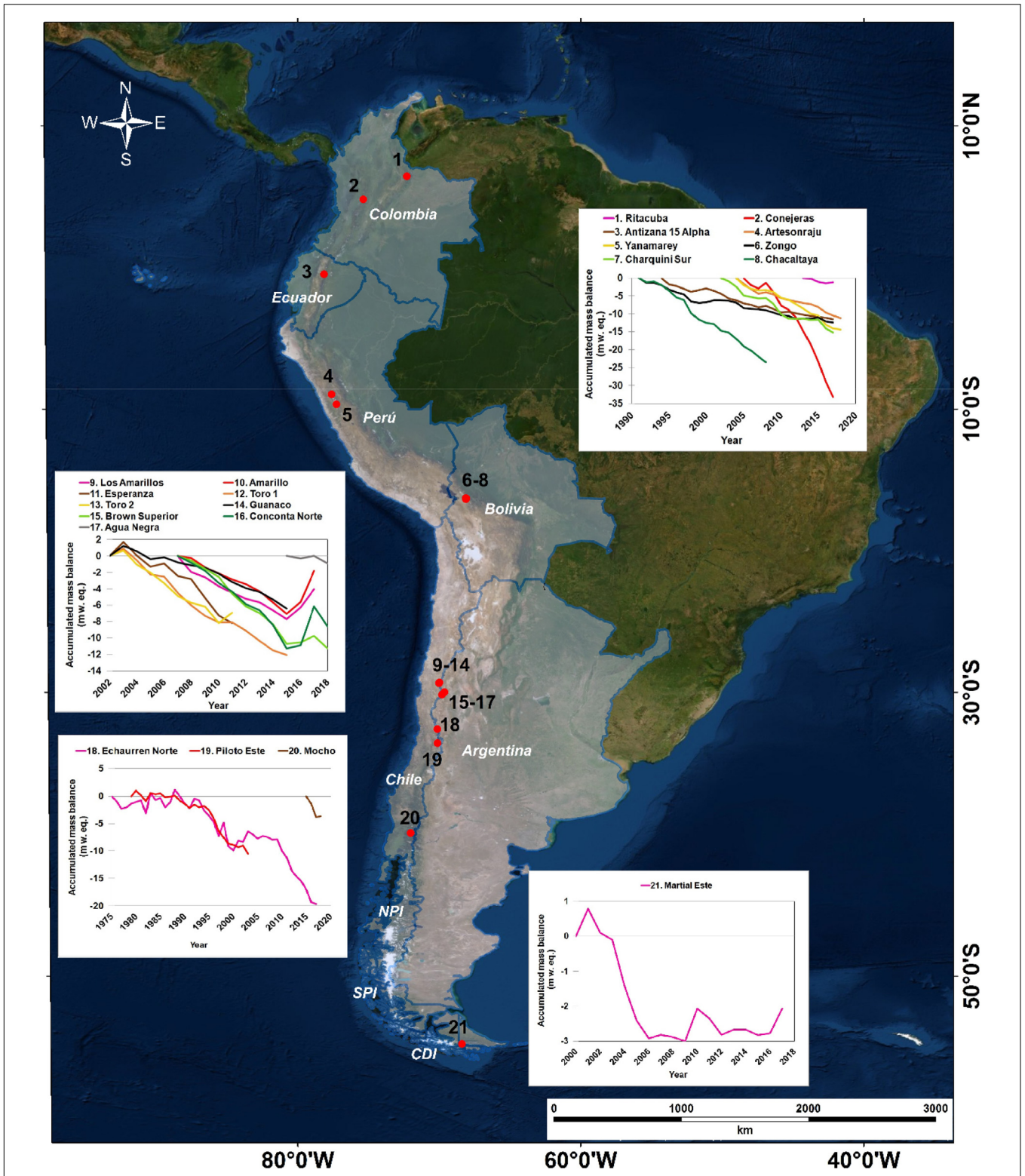


FIGURE 2 | Location of the glaciers with long (>5 years) series of mass balance measurements in the Andes. Note that only the Echaurren Norte series is longer than 30 years. Source: Official glacier mass balance data provided by the national correspondents and published by the World Glacier Monitoring Service (https://wgms.ch/).

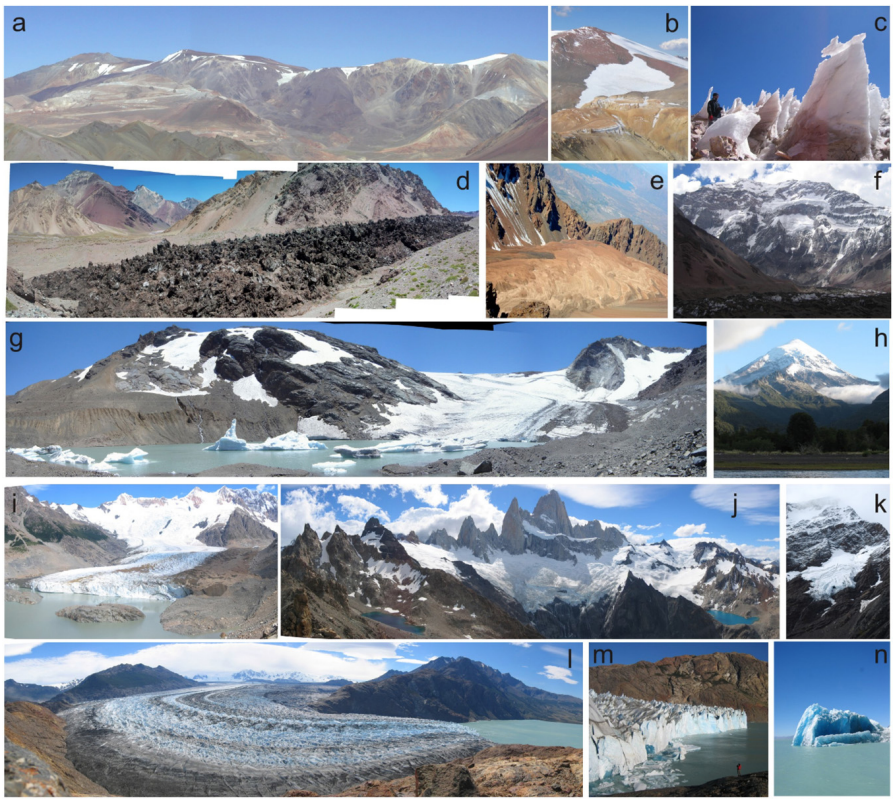


FIGURE 3 | Different types of ice masses that can be found in the Southern Andes. **(a,b)** snowfields/glacierets and mountain glaciers, Desert Andes, **(c)** ice penitent on mountain glacier, Desert Andes, **(d)** debris-covered, surging glacier, Central Andes, **(e)** rock glacier, Central Andes, **(f)** hanging and debris-covered glaciers, Central Andes, **(g)** calving valley glacier, Central Andes, **(h)** dome-shaped glacier, North Patagonian Andes, **(i,j)** valley and mountain glaciers, South Patagonian Andes, **(k)** hanging glacier, South Patagonian Andes, **(l,m)** outlet glacier and calving front, South Patagonian Andes, **(n)** iceberg from calving glacier front, South Patagonian Andes. Photos provided by IANIGLA-CONICET.

precipitation and the wind drifting of snow (Gascoin et al., 2013) also result in weak altitudinal gradients of snow accumulation and glacier mass balance in this region (Rabatel et al., 2011; Pitte, 2014).

Other characteristic features of this region are the so-called "penitentes" (Lliboutry, 1954; Corripio and Purves, 2005; Cathles et al., 2014; **Figure 3c**). Penitentes are irregular blades of snow and/or glacier ice, oriented east-west and leaning toward the sun (north in the Southern Hemisphere). They are created as the result of long periods of high shortwave radiation acting on a snow or ice surface exposed to a cold and dry atmosphere (Lhermitte et al., 2014). Differential sublimation and melting rates gradually increase the size of the penitentes, which can reach up to a few meters in height (**Figure 3c**) and be observed throughout the austral summer across the Dry Andes (Nicholson et al., 2016; Sinclair and MacDonell, 2016). In fact, the lower latitudinal limit of generalized distribution of penitentes (ca. 35°S) marks the southern limit of the Dry Andes. These features also show that in this region, sublimation is often a non-negligible factor: ice mass loss by sublimation has been estimated to represent more than 50% of the total ablation at some sites (Ginot et al., 2006; MacDonell et al., 2013; Ayala et al., 2017; Réveillet et al., 2020).

The glaciers in the Dry Andes constitute a crucial water reserve and can play a significant hydrological role during extended dry periods or at the end of the warm season when most of the seasonal snow has disappeared from the mountains (Gascoin et al., 2011; Radić and Hock, 2014; Huss and Hock, 2018). Although it is well known that in normal or snowy years the seasonal snow provides the largest proportion of surface runoff in this region (e.g., Masiokas et al., 2006, 2013; Favier et al., 2009), the current lack of snow due to the "megadrought" that started in 2010 has put additional pressure on the limited water resources and on the permanent ice masses of this region. A recent study by Dussaillant et al. (2019) reported that, after 2009, surface runoff in four of the main river basins of the Dry Andes decreased between 28 and 46%, and was accompanied by a substantial increase in glacier mass loss. Their calculations also showed that the ice mass loss partly helped to mitigate the impacts of the widespread drought by contributing with 3 to 8% of the total discharge in these four rivers (Dussaillant et al., 2019). These glacial contribution values, which represent quasi-decadal estimates, would very likely be larger if considered seasonally at the end of the summer (Gascoin et al., 2011; Radić and Hock, 2014; Ayala et al., 2016, 2017).

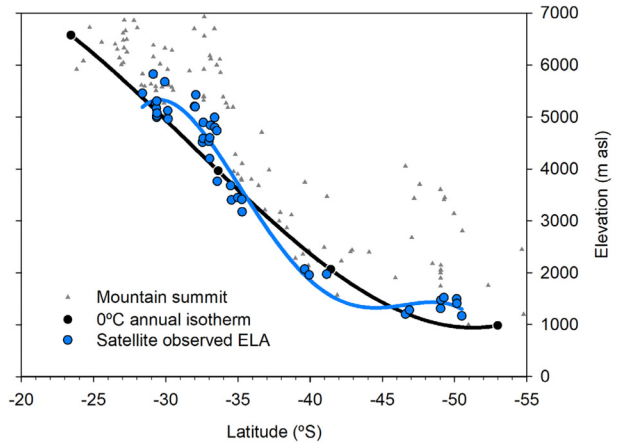


FIGURE 4 | Gradient along the southern Andes of the 0°C isotherm and the equilibrium-line altitude (ELA) of glaciers estimated from climatic variables. Individual summits are shown in triangles. Adapted from Carrasco et al. (2008).

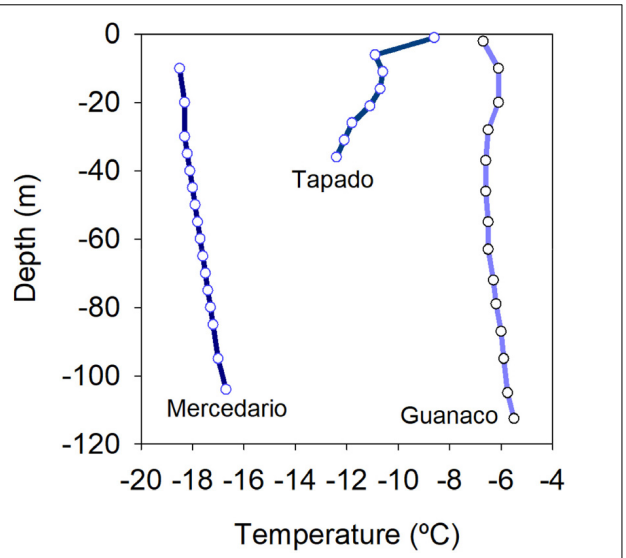


FIGURE 5 | Temperatures measured in glacier boreholes in the Desert Andes. The Mercedario glacier is located at ca. 32°S, Tapado at ca. 30°S, and Guanaco at 29.3°S (adapted from Pitte, 2014).

Debris covered glaciers are prevalent throughout the central parts of the Dry Andes (Janke et al., 2015), but are largely underrepresented in glaciological studies. Ayala et al. (2016) presented the first modeling comparison of debris-covered and debris-free glaciers for the Dry Andes, and found that the spatial mass balance patterns were vastly different. In their study debris-free glaciers followed a classical positive altitudinal mass balance gradient, whilst the debris-covered glacier displayed no obvious gradient. However, the two glacier types showed similar contributions to streamflow in the studied catchment, although discharge from the debris-covered glacier began earlier in the season, possibly due to the fact that debris-covered surfaces are located at lower elevations.

In the Desert Andes, the predominantly cold and dry conditions produce an ELA that is usually several hundred meters above the 0°C isotherm (ca. 4500 m a.s.l. in the northern sectors of the Desert Andes; **Figure 4**). This determines that ice and snow only persists on the highest peaks or in protected high elevation sites, ultimately resulting in a low glacier coverage and an extended distribution of mountain permafrost with numerous rock glaciers and other periglacial features (Nicholson et al., 2009). The climatic contrasts that exist between both sides of the Andes at these latitudes are also reflected in glacier distribution: on the western drier flanks, mountain glaciers, glacierets and permanent snowfield were mapped with a total area of 71 km^2 (Barcaza et al., 2017). In contrast, on the eastern more humid slopes, the analyses identified three times the total surface covered with ice (217 km^2; Ianigla-Conicet and Mayds, 2018). In general, glaciers in this region (and throughout the Southern Andes) have a dominant southeastern orientation that reflects the differential insolation patterns of mountain regions in the Southern Hemisphere.

The high, semi-arid plateau known as "Altiplano" extends from southern Peru and southwestern Bolivia to Chile and Argentina until ca. 28°S. This plateau has a mean elevation of ca. 4,000 m a.s.l. and on the western margin it contains some very high (over 6,000 m a.s.l.) isolated volcanoes with permanent snow patches or glacierets on their summits. To the east, the Cordillera Oriental forms a more continuous mountain range where rock glaciers are relatively common and only few debris-free ice surfaces can be observed. Glaciers in this region are usually located above 5900 m a.s.l. in the northern sectors but descend to 4600–4800 m a.s.l. in the south, where the Andes become a set of parallel, generally north-south oriented ranges and small to mid-size (1–10 km^2) glaciers start to become more common. Here most ice masses can be considered to be cold based, with ice temperatures several degrees below 0 °C and almost no liquid water at the base (**Figure 5**; Bolius et al., 2006; Ginot et al., 2006).

In the Central Andes the combination of the overall high elevation of the mountains with increasing precipitation levels from the Pacific produces one of the largest concentrations of glaciers in South America (Rivera et al., 2016; Barcaza et al., 2017; Zalazar et al., 2017). Many peaks in this region are above 6,000 m a.s.l., and together with other lower elevation massifs they host a large variety of glaciers that includes snowfields/glacierets, mountain glaciers, hanging glaciers, and large debris-covered and clean-ice glaciers. This region also contains the largest concentration of rock glaciers in the Andes (Barcaza et al., 2017), and includes many complex units that start as clean-ice glaciers at high elevations, gradually turn into debris-covered glaciers further down, and finally end as rock glaciers at the lowest sectors (Monnier and Kinnard, 2015, 2017; Zalazar et al., 2017). Recent inventories in this region (Barcaza et al., 2017; Ianigla-Conicet and Mayds, 2018) identified ca. 1700 km^2 of glacier surface area, with large valley glaciers descending to ca. 3,000 m a.s.l. in the west but only reaching 3500 m a.s.l. on the eastern drier side of the Andes. These recent inventories also

indicate that most of the glacier area in this region is concentrated between 3,600 and 4,000 m a.s.l. and with a predominant southeastern orientation.

Recent Glacier Variations in the Dry Andes

Glaciers in the Dry Andes have shown an overall thinning and areal reduction in the last century. The longest available series of glacier length fluctuations show retreating trends at both sides of the Andes with some minor advances (Masiokas et al., 2009; Rivera, 2019). The reconstruction of mean annual mass balance records from this region (Masiokas et al., 2016) also show some periods with positive mass balances and minor glacier advances around the 1920s–1930s, the 1980s, and in the first decade of the 21st century. Several mass balance monitoring sites are maintained in the north-central Andes of Chile and Argentina (**Figure 2**). The record from the Echaurren Norte glacier in Central Chile (33°S) is the longest series in the region and in the entire Andes, and constitutes the only Andean reference series in the World Glacier Monitoring Service (WGMS) dataset. Since 1975/76 this glacier has lost ca. 20 m w.e., a critical amount that puts this small glacier at the risk of disappearing in the next decades (Farías-Barahona et al., 2019). The overall glacier mass loss pattern described above appears to be related to the recent decreasing trend in precipitation observed in the subtropical region, which has clearly intensified since 2010 (e.g., Rabatel et al., 2011; Garreaud et al., 2017). Indeed, modeling exercises of mass balance observations at Glacier Echaurren Norte suggest that precipitation variability is the dominant forcing at this site, with temperature variations likely playing a secondary role (Masiokas et al., 2016). Interestingly, some of the glaciers in the Desert Andes have shown positive mass balances in recent years and a marked increase in their cumulative record (**Figure 2**). We hypothesize that this pattern is probably associated with slightly positive snow accumulation anomalies observed in this region in 2015 and 2016.

Dussaillant et al. (2019) showed that over the period 2000/2001–2017 the glaciers in the Desert and Central Andes have experienced moderate thinning rates of -0.12 ± 0.17 and -0.31 ± 0.19 m w.e. yr^{-1}, respectively. When this interval is split and assessed for changes before and after 2009, the Desert Andes maintain these relatively stable annual rates during both periods (0.00 ± 0.22 m w.e. yr^{-1} for 2000–2008, and -0.11 ± 0.20 m w.e. yr^{-1} for 2009–2017). In contrast, the glaciers in the Central Andes show stable to positive ice mass change rates (0.17 ± 0.23 m w.e. yr^{-1}) between 2001 and 2008, but much more negative values between 2009 and 2017 (-0.40 ± 0.21 m w.e. yr^{-1}; Dussaillant et al., 2019). It is important to note, however, that these values represent regional estimates and that specific cases will likely differ from these estimates. This is clearly demonstrated in recent detailed studies (Pitte et al., 2016; Falaschi et al., 2018), which identified up to 21 cases of surge-type glaciers with well documented advancing fronts embedded within the recent regional pattern of glacier thinning in the Central Andes. Burger et al. (2019) also found that, in the Central Andes, debris-covered glaciers have been more heavily impacted by the recent drought than debris-free glaciers, noting that the differential response of these glacier types to climate forcings has a direct impact on the hydrological role these features play in their catchments.

Wet Andes

The Wet Andes are located south of 35°S, where the elevation of most peaks and massifs usually does not exceed 4,000 m a.s.l. This lower elevation of the mountain range, together with the more intense influence of the westerly circulation from the Pacific, result in markedly higher precipitation amounts. Some high peaks in the north Patagonian Andes can receive 3–5 m w.e. of precipitation per year (Schaeffer et al., 2017), and further south these values increase to 4–7 m w.e. yr^{-1} on the Patagonian icefields (Schaefer et al., 2015). Seasonality is gradually reduced southward, with higher amounts concentrated during the winter months in the north, but a more regular precipitation regime throughout the year in Tierra del Fuego (Sagredo and Lowell, 2012). The Wet Andes are also characterized by strong precipitation gradients, with clear contrasts between the wetter western slopes and the much drier conditions only a few tens of km to the east of the mountains in Argentina (Viale et al., 2018). The presence of numerous rivers, lakes, and an extensive forest cover is also characteristic of the Wet Andes, where some 4800 km^2 of the former extent of large glaciers are now occupied by more than 4,000 lakes (Wilson et al., 2018). In this region the mean annual 0°C isotherm decreases in elevation from about 3,000 in the north to less than 1,000 m a.s.l. in Tierra del Fuego (Condom et al., 2007; Carrasco et al., 2008). The topographic and climatological conditions mentioned above allow the development of numerous and extensive glacierized areas, which are mostly concentrated in the South Patagonian Andes and constitute the largest glacierized surface in South America. Most glaciers in the Wet Andes have their ELA below the mean annual 0°C isotherm (**Figure 4**).

The hydrological significance of glaciers in the Wet Andes is comparatively lower than that in the Dry Andes. This is largely due to the much higher precipitation amounts in the Wet Andes, making most rivers dependent on rainfall and snowmelt patterns (Masiokas et al., 2019). However, the very large size of some of the glacierized areas in the South Patagonian Andes does have a noticeable hydrological signature on some of the most important rivers of the region. This is the case of the Baker and Santa Cruz rivers, which drain large portions of the NPI and SPI, respectively, and are sporadically affected by huge amounts of meltwater draining after the rapid collapse of ice-dammed lakes in the icefields (Pasquini and Depetris, 2011; Dussaillant et al., 2012).

In the North Patagonian Andes, glaciers are comparatively smaller than those located further south (i.e., from a few km^2 to tens of km^2, compared to glaciers that can cover tens to hundreds of km^2 in the south). The north Patagonian glaciers are usually found on isolated volcanoes and high peaks (Reinthaler et al., 2019), forming small ice caps with a dominant radial flow (**Figure 3h**). The elevated precipitation levels of the region (up to a few meters per year), the relatively mild temperatures (annual

means ranging between 0° and 10°C; Alvarez-Garreton et al., 2018), and the steep average slopes of most glaciers in the region result in high ice mass turnover rates and fast ice velocities, which can reach several hundred meters per year for some of these temperate glaciers (Ruiz et al., 2015). The total glacierized area in the North Patagonian Andes is ca. 1800 km^2. At 35°S the glaciers do not descend below 3,000 m a.s.l., but their fronts can reach 700 m a.s.l. at 45°S (Barcaza et al., 2017; Zalazar et al., 2017).

The glaciers in the South Patagonian Andes have historically received a great deal of attention from scientists and explorers, and many reviews are already available in the literature (Warren and Sugden, 1993; Glasser et al., 2008, 2011; Aniya, 2013). This region contains a very large number of mountain glaciers, outlet glaciers, and icefields, including the NPI, the SPI, and the icefield of Cordillera Darwin (hereafter CDI) in the southwestern corner of Tierra del Fuego (**Figure 3**). The SPI alone is formed by 139 glaciers larger than 5 km^2, and in total this ice mass currently covers an area of ca. 12200 km^2 (De Angelis, 2014; Meier et al., 2018). The NPI is ca. 3700 km^2 (Dussaillant et al., 2018), and the icefield at Cordillera Darwin is ca. 2300 km^2 (Bown et al., 2014). Other minor ice caps can be found at Mount San Lorenzo (ca. 140 km^2; Falaschi et al., 2013) and Gran Campo Nevado (ca. 200 km^2; Schneider et al., 2007; Weidemann et al., 2013).

Recent Glacier Changes and Ice Dynamics in the Wet Andes

The assessment of areal glacier changes during the last decades in the Wet Andes has been discussed by many studies. These studies have focused on different study areas and periods of time, and have sometimes used different methodologies, but in most cases they have relied on early historical records, aerial photographs, and/or satellite imagery to assess recent glacier variations (see e.g., Masiokas et al., 2009; Lopez et al., 2010; Davies and Glasser, 2012; Paul and Moelg, 2014; Meier et al., 2018; and references therein). Despite their inherent differences, the results from these studies largely point to a widespread pattern of recent glacier recession that is consistent with what has been observed in the Andes further north (**Figures 6**, **7**). This inequivocal recent trend toward increasingly smaller glaciers started sometime after the occurrence of the LIA, which was an extended period of generalized glacier growth and frontal advances that culminated between the 17th and 19th centuries (see e.g., Masiokas et al., 2009; Davies and Glasser, 2012; and references therein). Most LIA glacier advances in the Wet Andes can be associated with vegetation trimlines and/or lateral and frontal moraines with varying degrees of forest recolonization that provide valuable evidence for assessing glacier recession patterns over the past centuries (e.g., Villalba et al., 1990; Masiokas et al., 2009; Ruiz et al., 2012). Davies and Glasser, 2012 used this geomorphological evidence and Landsat imagery to map the LIA glacier extent in the Andes south of 41°S, estimating that by the year 2011, the glaciated area had decreased by ca. 15%. Meier et al. (2018) used a similar approach to estimate glacier changes south of 45.5°S, and found that the overall area covered by glaciers during the LIA (ca. 28100 km^2) had shrank almost 20% by the year 2016. According to their results, the SPI alone lost ca. 13% during the same period, reducing its area from ca. 14200 km^2 during the LIA to ca. 12230 km^2 in present times (**Figure 8**).

Ruiz et al. (2012) presented a detailed dendro-geomorphological record of LIA and post-LIA fluctuations for Esperanza Norte glacier in the North Patagonian Andes (ca. 42°S), and compared these fluctuations with those reported for Frías glacier (Villalba et al., 1990; Leclercq et al., 2012) ca. 110 km to the north. They conclude that both glaciers probably reached a peak LIA position during the early-mid 17th century and since then have had roughly similar patterns of recession, with changes during the 20th century occurring much more rapidly than in the previous interval. In a larger-scale study of 1985–2011 glacier changes in the North Patagonian Andes (40.5°–44.5°S), Paul and Moelg (2014) found a total glacier area reduction of ca. 25% and a concomitant marked increase in the number and surface area of proglacial lakes. Further south, Lopez et al. (2010) studied the length fluctuations of 72 glaciers of the NPI, SPI, and CDI between 1945 and 2005 using historical maps, aerial photographs and satellite images. They found a considerable frontal retreat for most glaciers during this 60-yr period, with the highest retractions for each icefield recorded at San Rafael Glacier in the NPI (5.7 km frontal retreat), O'Higgins glacier in the SPI (11.6 km retreat), and Marinelli glacier in the CDI (12.2 km retreat). White and Copland (2015) used ASTER and Landsat images from the mid-1970s to the early 2000s to compile glacier changes of 130 SPI glaciers concluding that nearly 4% (542 km^2) of the original area was lost with some indications of acceleration in the ice mass loss rates in recent years. This acceleration was also reported recently by the large-scale study of Meier et al. (2018): since the LIA and until 1986, the annual glacier areal loss for the Andes south of 45.5°S was $-0.10 \pm 0.04\%$ a^{-1}, increasing to $-0.33 \pm 0.28\%$ a^{-1} between 1986 and 2005, and to $-0.25 \pm 0.50\%$ a^{-1} for the period 2005–2016.

It is interesting to note, however, that there are few exceptions to this century-long trend of ice mass loss in the Wet Andes. The most remarkable case is probably Pío XI glacier (the largest outlet of the SPI), which has shown a net advance of 11 km since 1945 (Wilson et al., 2016; Rivera, 2018; **Figure 9**). In this period this glacier formed a prominent moraine overridding 400 yr-old trees located in the glacier forefield. Another anomalous case is Perito Moreno glacier on the eastern side of the SPI, which has shown a relatively stable frontal position with several re-advances during the last century (Guerrido et al., 2014; Minowa et al., 2015). Contrasting glacier behavior has also been observed at Cordillera Darwin in Tierra del Fuego, where some glaciers like Marinelli have retreated markedly but others like Garibaldi have shown clear frontal advances in recent times (Melkonian et al., 2013).

Due to logistic and meteorological constraints for conducting the direct surface mass balance measurements (Rivera et al., 2016), many studies have also applied the geodetic method to investigate recent ice mass changes in the Wet Andes. The existence of the freely available Shuttle Radar Topography Mission (SRTM; 90 m horizontal resolution) DEM for the year 2000 has provided a very valuable and reliable reference that has been compared to other DEMs, such as the ASTER-GDEM

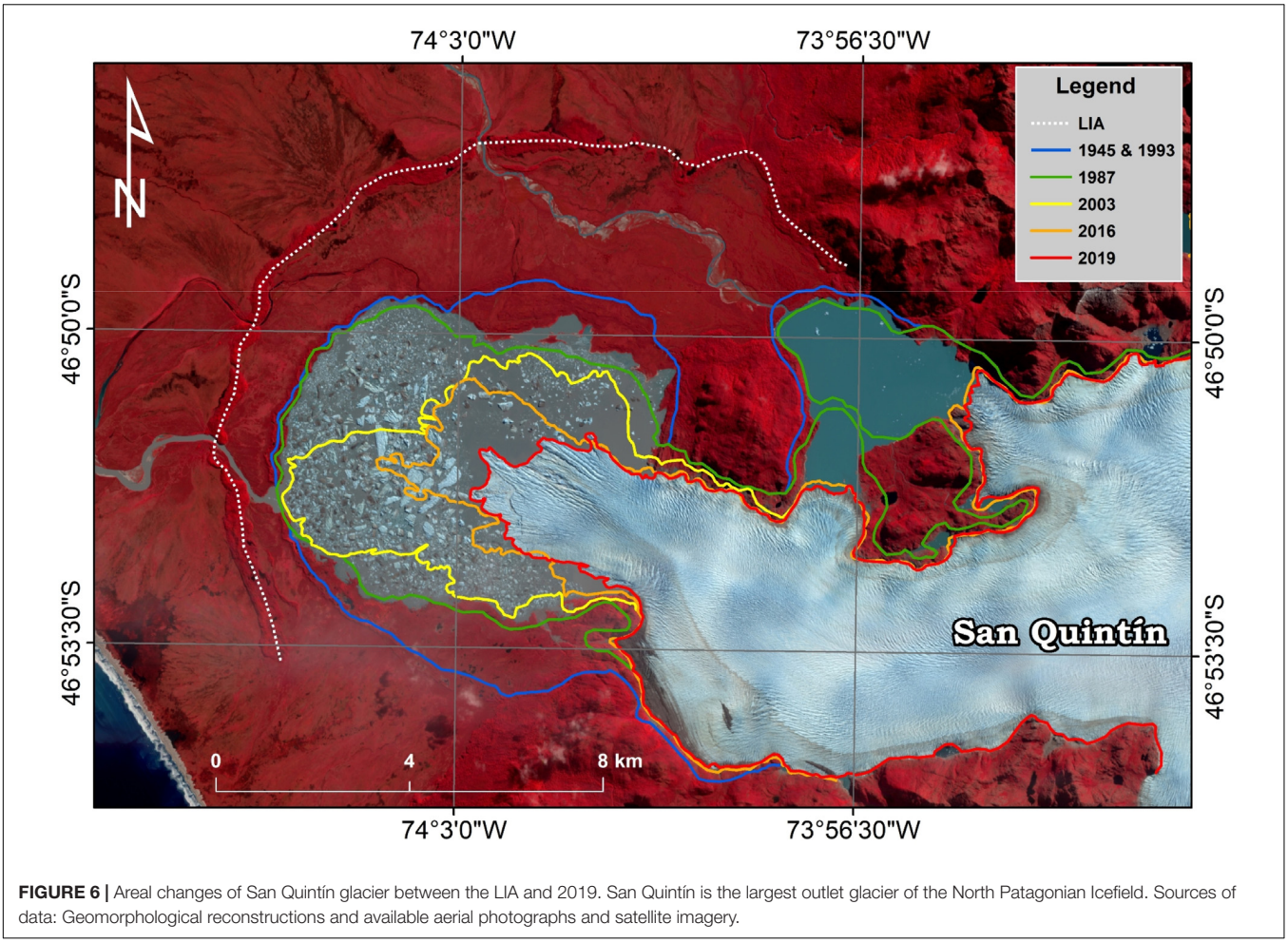


FIGURE 6 | Areal changes of San Quintín glacier between the LIA and 2019. San Quintín is the largest outlet glacier of the North Patagonian Icefield. Sources of data: Geomorphological reconstructions and available aerial photographs and satellite imagery.

(30 m horizontal resolution). Melkonian et al. (2013) used this approach in Cordillera Darwin, southernmost Chile, and Willis et al. (2012a,b; **Figure 10**) in the SPI and the NPI, respectively. More recently, Dussaillant et al. (2019) applied this methodology for the whole Andes Cordillera including the large glaciated areas in Patagonia (**Figure 10**). The SRTM has also been compared to SPOT5 DEMs (40 m horizontal resolution; Korona et al., 2009), Dussaillant et al. (2018) in the NPI, and Falaschi et al. (2017) in Monte San Lorenzo glaciers to the east of the Patagonian icefields.

In contrast, studies using topographic data prior to SRTM are very scarce in the southern Andes (e.g., Rignot et al., 2003, who used 1975 regular cartography in the SPI). Falaschi et al. (2019) used historical vertical and oblique aerial photographs to generate topographic information for Monte San Lorenzo glaciers for the years 1958 and 1981, and subsequently compared these early DEMs with those derived from the SRTM mission and recent Pléiades (Berthier et al., 2014) and Spot 5 (Korona et al., 2009) imagery. Their analyses show strong negative glacier mass balances (between −0.78 and −1.65 m w.e. a^{-1}) in this region during the last six decades. The SRTM DEM was also compared to the TanDEM-X mission, for example by Malz et al. (2018) for the whole SPI, or by Abdel Jaber et al. (2019) for both the NPI and SPI. Foresta et al. (2018) used Cryosat-2 to study the 2011–2017 elevation changes of the Patagonian icefields. In this case the results have a coarse spatial definition but high temporal resolution, allowing the retrieval of elevation changes at seasonal scales.

The increasing availability of satellite images and the application of automatized methods has also resulted in marked improvements in our knowledge of the ice velocity and dynamics of many Patagonian glaciers (e.g., Rivera et al., 2012b; Muto and Furuya, 2013; Sakakibara and Sugiyama, 2014; Mouginot and Rignot, 2015; Ruiz et al., 2015; Euillades et al., 2016; Lenzano et al., 2018; Lo Vecchio et al., 2018; Moragues et al., 2018). Cross-correlation of radar remote sensing data (SAR) has revealed that surface velocities of some SPI glaciers can reach several hundred meters per year, placing these glaciers among the fastest on Earth (only exceeded by some glaciers in Greenland, Alaska and Antarctica; Howat et al., 2007; Moon et al., 2012; Gardner et al., 2018). Indeed, in some sectors of the Pío XI, Upsala and O'Higgins glaciers, ice can move a few km per year (**Figure 11**), suggesting a dominant role of basal sliding in the dynamics of these large SPI outlet glaciers (Sugiyama et al., 2011; Bown et al., 2019). These remote sensing data also show that the longitudinal velocity profiles of these outlet glaciers are typical of calving glaciers, with low speeds at the ice divides and increasing values

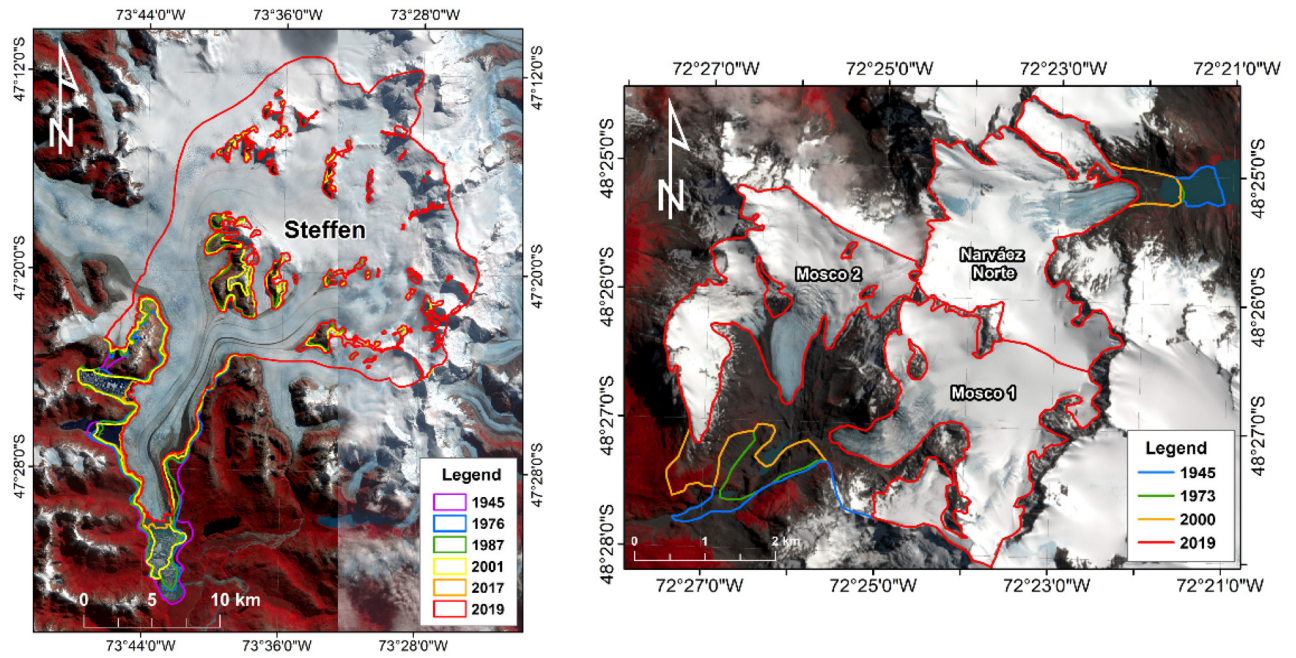


FIGURE 7 | Areal recession of south Patagonian glaciers between 1945 and 2019. Sources: Available aerial photographs and satellite imagery.

toward their snout (e.g., Euillades et al., 2016). This pattern is very different from that of mountain glaciers, which show low velocities at the ice divides and the glacier front but maximum speeds at the ELA due to the maximum glacier thickness in this area. Other analyses (Sakakibara et al., 2013; Sakakibara and Sugiyama, 2014; Mouginot and Rignot, 2015) indicate a recent acceleration of some calving glaciers, which may suggest a possible destabilization of these ice masses. These glaciers show an acceleration and recession of the ice front, and accelerating patterns that extend to the upper central plateaus and along the ice divides of the SPI.

Calving has been frequently addressed in the region since many of the largest glaciers in southern Patagonia terminate in fjords or lakes (Warren and Sugden, 1993). According to Rivera et al. (2012c), many of these calving glaciers follow the so-called Tidewater Glacier Calving Cycle, that in general is controlled by mass balance and water depth at the glacier front. An example of a glacier in the advancing phase of this cycle is Pío XI glacier (Wilson et al., 2016), whereas an example of a glacier reaching new equilibrium after fast retreat is the Upsala glacier (Sakakibara et al., 2013). Other calving glaciers, such as Jorge Montt, are currently in the retreating or collapsing phase of the cycle due to near buoyant conditions when the ice front ends in deep waters (Bown et al., 2019).

Recently published global models of ice thickness and volumes (Huss and Farinotti, 2012; Carrivick et al., 2016; Farinotti et al., 2019) provide valuable information in this region and can work relatively well in mountain glaciers with well-defined tongues. However, these models have some limitations when dealing with large icefields such as the NPI and SPI, because the modeled subglacial topographies are often unrealistic and may contain many artifacts. Patagonian glaciers have been occasionally surveyed with radar methods that are able to reach up to 700 m of ice thickness, with penetration ranges restrained by the temperate conditions of the ice and the presence of crevasses and water (Zamora et al., 2017). Gravity methods (e.g., Gourlet et al., 2016) offer one option to overcome this limitation as they have no limits in ice thickness determinations, but they need to be validated and controlled by more accurate methods, such as radar. This combined approach has been applied in Patagonia (Millan et al., 2019), resulting in an improved ice thickness distribution coverage and the first comprehensive subglacial topography of the whole NPI and the northern part of the SPI.

Information on ice thickness, subglacial topography, and ice flux, among others, are critical parameters for a proper modeling and understanding of the observed glacier changes and their contrasting behaviors between adjacent basins, and for forecasting future responses to climate change. Collao-Barrios et al. (2018) applied a physically based model that relies on surface climatic data plus ice fluxes from ice thickness and surface velocities to estimate the surface mass balance of San Rafael glacier in the NPI. This analysis showed that the mass balance is slightly positive (0.08 ± 0.06 Gt a^{-1}) between 2000 and 2012, with an ice discharge of ca. -0.83 Gt a^{-1}. These numbers seems to contradict previous surface mass balance models for San Rafael based mainly on climatic data (mainly reanalysis since automatic weather stations are very scarce) and calving fluxes based on geodetic measurements, that obtained a much higher surface mass balance of 1.19 Gt a^{-1} between 1979 and 2011 (Schaefer et al., 2013) and 0.72 ± 0.37 Gt a^{-1} (Koppes et al., 2011), and also higher ice discharges of -1.68 and -1.04 Gt a^{-1} by Schaefer et al. (2013) and Koppes et al. (2011), respectively. Using a coupled

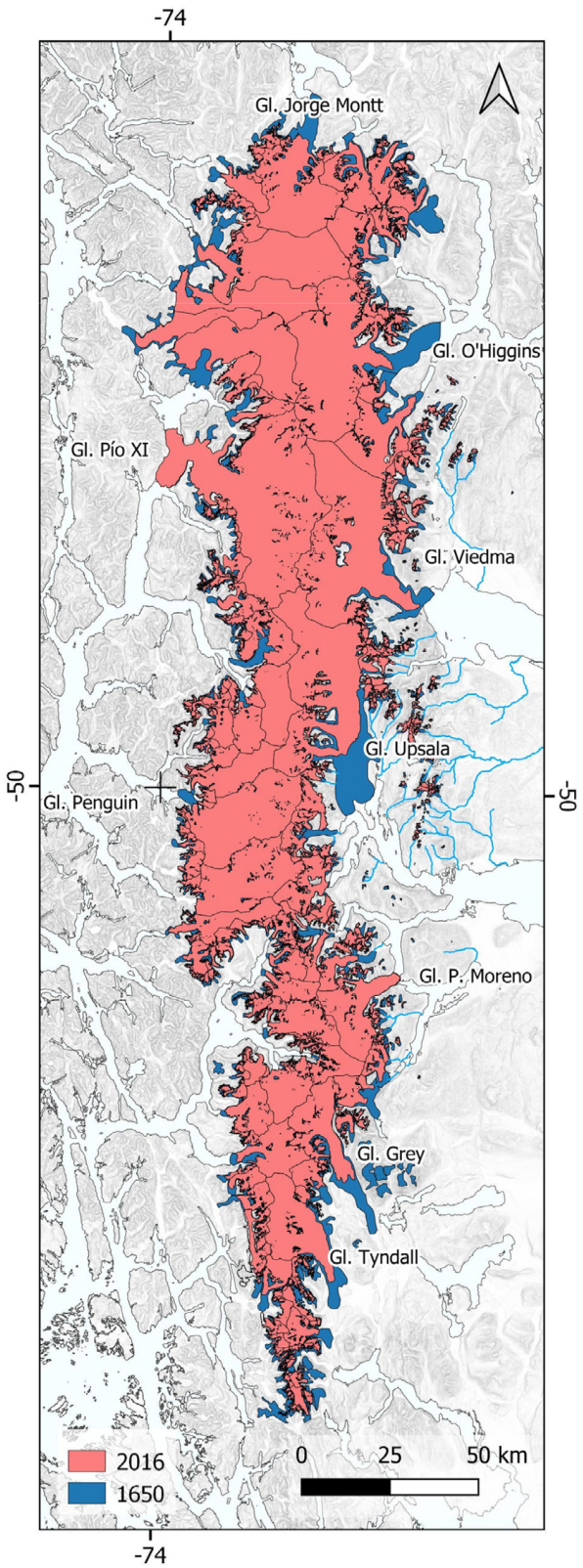


FIGURE 8 | Areal fluctuations of the SPI between the LIA and 2016 derived from reconstructions based on geomorphology and recent optical remote sensing data (Davies and Glasser, 2012; Meier et al., 2018).

snow and ice energy and mass balance model, Weidemann et al. (2018a) concluded that the Tyndall and Gray glaciers, located at the southern tip of the SPI, experienced a 2000–2014 climatic mass balance $+1.02 \pm 0.52$ m w.e. a^{-1} and $+0.68 \pm 0.54$ m w.e. a^{-1}, respectively. These positive numbers are, however, counterbalanced by strong ablation at the calving ice fronts, yielding an overall mass balance of -1.05 ± 0.18 m w.e. a^{-1} and 2.58 ± 0.28 m w.e. a^{-1} for Gray and Tyndall glaciers, respectively. Schaefer et al. (2015) modeled the surface mass balance for the entire SPI during the period 1975–2011. They estimated an average annual acumulation on the SPI of ca. 67.7 km^3, an average ice surface melt of ca. 36.5 km^3, and a strong increase in annual ice mass losses due to calving between 1975–2000 and 2000–2011 (changing from 44.4 to 61.3 km^3 of ice).

Important limitations still remain, however, due to the serious lack of in situ validation data, especially of precipitation/accumulation in the upper plateaus, temperature/melt patterns on the ice, and calving fluxes and dynamics at many more sites throughout the region. To partly overcome the lack of basic climatic information, many modeling studies have used data from the ERA or NCEP/NCAR climate reanalyses (Lenaerts et al., 2014; Weidemann et al., 2018b), and more recently the WRF simulations (e.g., Villarroel et al., 2013; Schaefer et al., 2015). Meteorological stations from lowlands away from glaciers have also been used, but the scarcity and lack of continuity remains a serious problem in this region (Masiokas et al., 2015; Bravo et al., 2019b).

One of the consequences of the ongoing shrinkage of Patagonian glaciers (**Figures 7**–**9**) is the formation and expansion of lakes in lands recently abandoned by ice. For example, at the NPI, Loriaux and Casassa (2013) detected an increase in glacial lake area of 66 km^2 between 1945 and 2011. At Monte San Lorenzo, south-east of the NPI, Falaschi et al. (2019) measured a three-fold increase in the number of lakes and 5 km^2 of new lake area formed between 1958 and 2018. The retreating glaciers are also uncovering rock outcrops and nunataks with unknown geological information. The regional geological maps show little information about these areas but recent works revealed tectonic features that extend under the ice and are controlling present glacier location and flow (Georgieva et al., 2016).

MOUNTAIN PERMAFROST

Mountain permafrost, i.e., ground which remains at or below 0°C for at least two consecutive years (Harris et al., 1998), is widespread in the high Andes mountains where the air temperature is at freezing temperatures most of the year. However, as only a few instrumented permafrost boreholes have been published in the Andes, our ability to analyze the current state of Andean permafrost is limited (e.g., Trombotto, 2014). The local variations in topography, solar radiation, snow cover, ground surface type, subsurface hydrology and geology, and their differential influences on smaller scale ground temperature patterns, determine a predominant discontinuous mountain permafrost distribution in the Andes (Haeberli and Gruber, 2009). However, given the practical and technical

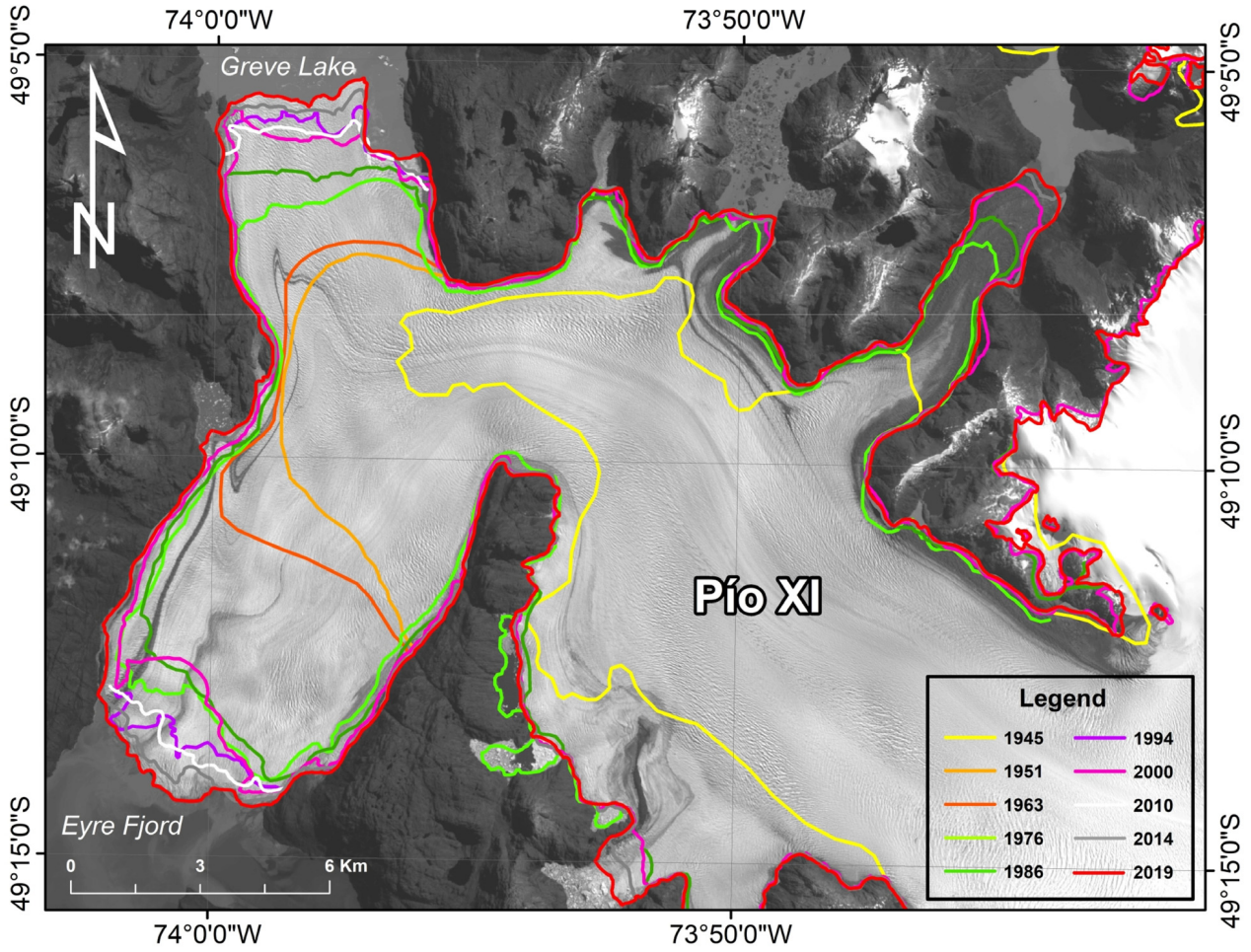


FIGURE 9 | Changes in surface area of Pío XI glacier between 1945 and 2019. This glacier is the largest outlet glacier of the SPI and unlike most of the glaciers in the region, it has shown an anomalous behavior with an advancing front over most of the last century. Sources: Available aerial photographs and satellite imagery.

difficulties in the identification and mapping of permafrost (defined, as indicated above, by the thermal condition of the ground), most of the efforts to assess the extent of permafrost along the Andes have been based on modeling approaches (Arenson and Jakob, 2010a; Gruber, 2012; Ruiz and Trombotto, 2012; Azócar et al., 2017; Esper Angillieri, 2017) and/or the recognition and mapping of ice-rich permafrost landforms such as rock glaciers (Barcaza et al., 2017; Zalazar et al., 2017). In this sense, the publication of local and regional inventories of perennial ice masses that includes rock glaciers represents a substantial improvement in our efforts to characterize and understand the distribution of permafrost in the Andes. Rock glaciers are formed by permanently frozen ground which is supersaturated in ice, favoring the movement and creeping of the permafrost in specific mountain slopes (Haeberli, 1985; Barsch, 1996). This movement and creeping generates the characteristic transverse and longitudinal ridges and furrows on the surface of rock glaciers, which resemble viscous lava flows and allow the identification of these cryoforms in aerial photographs and satellite images (Haeberli, 1985; Trombotto Liaudat et al., 2014; Jones et al., 2019).

The first estimation of mountain permafrost distribution in the Andes was conducted by Trombotto Liaudat (2000), who identified the areas of seasonally frozen, discontinuous and continuous permafrost surfaces using the elevation of 5°C, 0°C and −5°C isotherms, respectively. Although no areal extents were presented, this simple approach showed that it is possible to find permafrost conditions from Venezuela to Tierra del Fuego. Gruber (2012) presented the first global model of permafrost extent using DEMs and gridded air temperatures. The study provided a Permafrost Zonation Index (PZI) map which indicated the possibility of finding permafrost (from very low to high possibilities) and showed that, in the Andes, it is much more likely to find permafrost conditions south of 18°S with most of the area (∼70%) concentrated between 23° and 36°S. Arenson and Jakob (2010a) developed a mountain permafrost distribution model primarily based on physical evidence (elevation, slope aspect and angles, and potential solar radiation) and field observations, and showed promising results in local tests in the

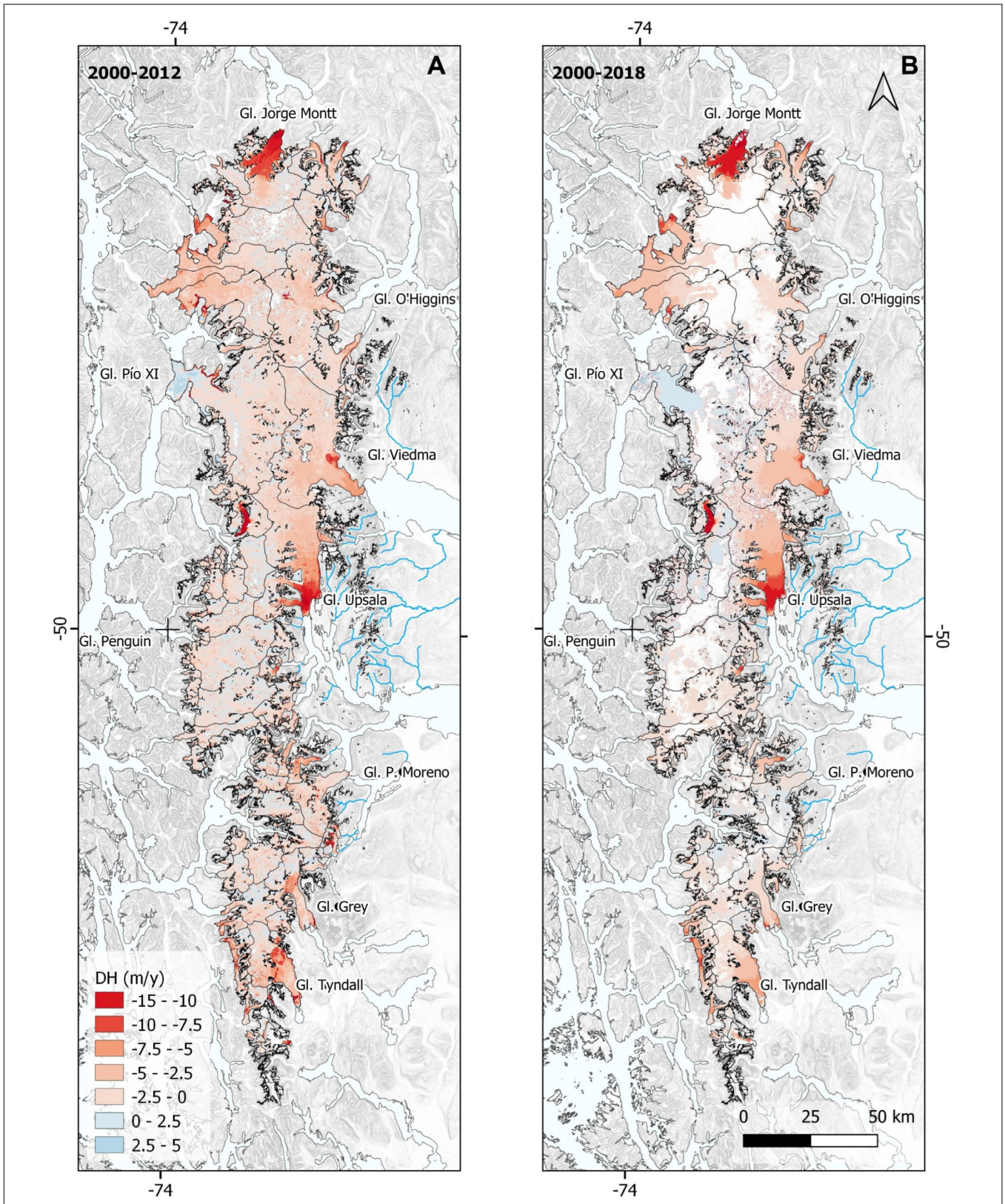


FIGURE 10 | (A) Mean annual ice thickness changes for the SPI between 2000 and 2012, derived from the SRTM and ASTER DEMs (Willis et al., 2012a). Note that the ice loss is larger in the tongues of the large outlet glaciers and, in many cases it extends toward the higher sectors near the ice divides. **(B)** Same as A, but for the period 2000–2018 (Dussaillant et al., 2019). The anomalous behavior of Pío XI glacier is also evident in these maps.

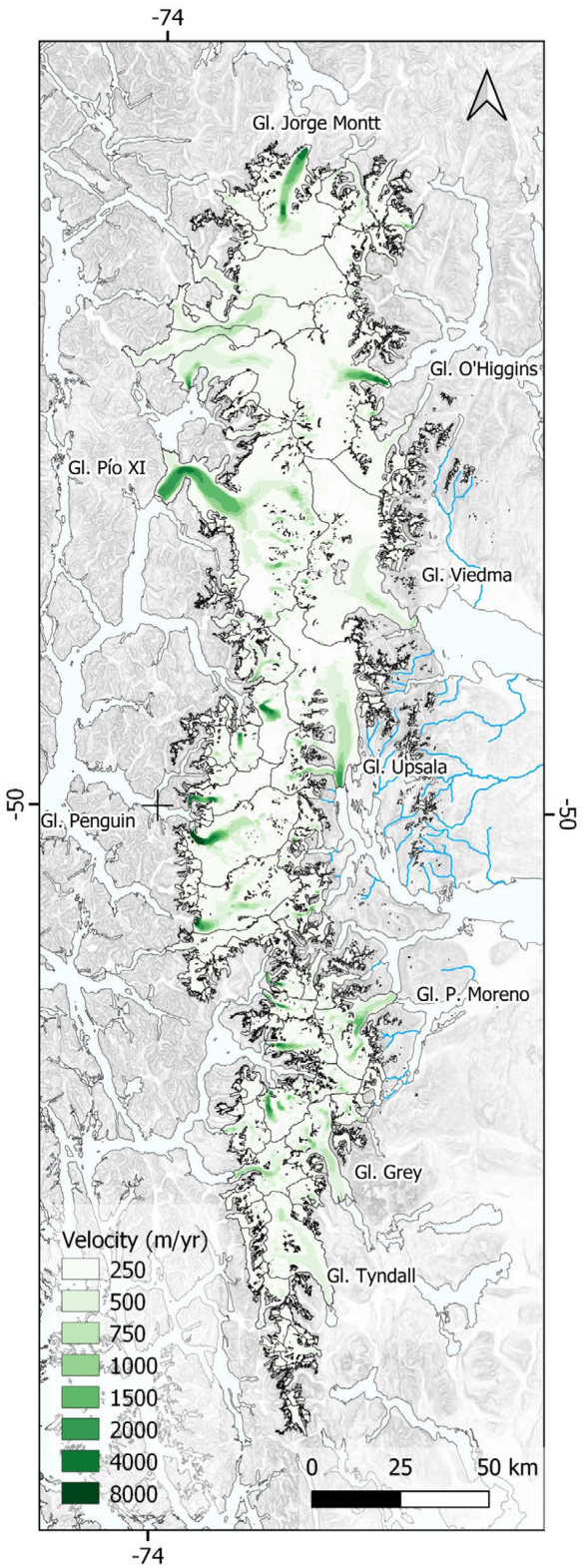


FIGURE 11 | Mean annual surface ice velocity of SPI glaciers between 2000 and 2012, derived from synthetic aperture radar (SAR; Mouginot and Rignot, 2015). High velocities can be observed along the central flowline of some of the largest outlet glaciers.

Dry Andes at ca. 31.6°S. Other local efforts have used statistical permafrost distribution models such as the Bottom Temperature of the Snow Cover (BTS) model (Ruiz and Trombotto, 2012) to identify the presence of permafrost conditions in the eastern margin of the North Patagonian Andes at 42°S. Azócar et al. (2017) presented an empirical model of mountain permafrost favorability, with a spatial resolution of 30 m, for the semi-arid Andes of central Chile (29°–32°S). The model is based on rock glacier activity and temperature data, and similarly to Gruber (2012), their results provide a permafrost favorability index. They found conditions highly favorable for permafrost presence over 1051 km^2 (2.7% of the total investigated area) and favorable conditions for 2636 km^2 (6.8% of the total area). Esper Angillieri (2017) presented a high resolution (30 m pixel size) permafrost probability model for the Andes of the San Juan province in central-western Argentina based on the presence and activity of rock glaciers and their relationship with topoclimatic variables such as altitude, aspect, mean annual air temperature, mean annual precipitation and potential incoming solar radiation. Based on this model and using the 70% threshold for the probability of rock glacier occurrence, they estimated an extent of permafrost of ca. 10772 km^2 in this province.

In the inner Tropical Andes, Trombotto Liaudat (2000) reported evidence of patterned ground and other periglacial environments in the Páramo ecosystem and in the highest volcanoes of Ecuador. Rangecroft et al. (2014) presented the first rock glacier inventory for the Bolivian Andes (15–22°S) based on remote sensing and field validation data. They found 94 rock glaciers (57% classified as active and the remaining as relict) which cover a total area of 11 km^2 with a mean size of 0.12 km^2. Based on the mean minimum altitude of rock glacier fronts, they approximate the lower limit of permafrost at 4700 m a.s.l. in the Bolivian Andes. Barcaza et al. (2017) presented the first glacier inventory of the Chilean Andes based on remote sensing data. They found a total of 2831 rock glaciers covering a total area of 369 km^2 and spanning from 17°S to 37°S. The mean area of the Chilean rock glaciers is 0.13 km^2, and their mean minimum elevation decreases from ca. 4800 m a.s.l. at around 18°–23°S, to a minimum of ca. 2500 m a.s.l. at 37°S. Zalazar et al. (2017) presented the first glacier inventory of Argentina, including a detailed description of rock glaciers, expanding the classification to include their genesis (permafrost-related or glacial related), form, activity, and other characteristics. In the Andes of Argentina there are almost 7600 rock glaciers (almost 75% classified as active) that cover an area of ca. 673 km^2 between 21° and 55°S. These rock glaciers have a mean surface area of 0.08 km^2, and their mean minimum elevation decreases from 4800 to 4500 m a.s.l. between 22° and 28°S, to less than 1,000 m a.s.l. in the south of Tierra del Fuego (55°S). Interestingly, these new regional-scale rock glacier inventories from Chile and Argentina show that the region from ca. 28° to 36°S concentrates almost 90% of the total area covered by rock glaciers in South America.

Falaschi et al. (2014, 2015, 2016) and Perucca and Esper Angillieri (2008), among others, also provide inventories and detailed descriptions of rock glaciers in the northern, central and southern sectors of the Andes of Argentina. The existence

of rock glaciers in southern Patagonia and even in Tierra del Fuego has been confirmed in recent studies (e.g., Falaschi et al., 2015; Masiokas et al., 2015; Zalazar et al., 2017) and is an interesting characteristic of these regions, which are usually appreciated by their numerous and extensive glaciers and a persistent cloud cover throughout the year. In these southern regions these periglacial features are usually concentrated toward the eastern drier margin sectors of the mountain ranges (Ruiz and Trombotto, 2012; Falaschi et al., 2015, 2016; Masiokas et al., 2015; Zalazar et al., 2017). This new evidence provides solid information of these southernmost rock glaciers that contributes to a more comprehensive understanding of the cryosphere and the mountain climatology in these regions.

The role of rock glaciers as long-term water reserves and short-term sources of freshwater in many semi-arid sectors across the southern Andes has also received an increasing attention in recent years (Azócar and Brenning, 2010; e.g., Arenson and Jakob, 2010b; Jones et al., 2018, 2019; Schaffer et al., 2019). These permanent ice masses are inherently more resilient to changes in climate than clean-ice glaciers, and can provide a relatively steady amount of freshwater in many catchments where glacier ice is absent or very scarce, especially during extended dry periods when precipitation is also reduced to a minimum (Schaffer et al., 2019). Recently, Jones et al. (2018, 2019) estimated that the water volume equivalent stored within rock glaciers on a near-global scale is around 83.7 $\pm$ 16.7 Gt (ca. 68–102 trillion litres), with rock glaciers in the Andes contributing with almost 40% (i.e., 32.84 $\pm$ 6.57 Gt; the highest percentage of all individual regions). At a local scale, studies using empirical methods have estimated that, in total, rock glaciers may account for more stored ice than glaciers in the Central Andes (Azócar and Brenning, 2010; Janke et al., 2017), but more measurements are required to confirm these results (Arenson and Jakob, 2010b). Also, as rock glacier formation processes are still up for debate (Monnier and Kinnard, 2015, 2016, 2017), determining ice content of glaciogenic vs. cryogenic, or active vs. inactive rock glaciers is still contentious.

Besides the global estimates discussed above, determining the specific hydrological role of rock glaciers has been even more elusive, as few methods have been validated in the scientific literature to quantify the hydrological contribution of rock glaciers or to understand their wider impact on drainage system processes. Using seasonal discharge measurements in the La Laguna catchment (30°S), Schaffer et al. (2019) estimated that rock glaciers are likely to contribute around 10% of streamflow for this basin. Due to the paucity of published cores from rock glaciers (Monnier and Kinnard, 2013) and discharge measurements in headwater catchments, such estimations should be treated with caution.

DISCUSSION AND CONCLUSION

The information discussed above highlights the impressive richness and diversity of cryospheric features and conditions that can be found along the Andes from Venezuela and Colombia to Tierra del Fuego. Along this vast region, the cryosphere plays an important hydrological, climatological and socio-economic role providing, for example, a large proportion of the water that is consumed by the numerous human populations living near the Andes (Schoolmeester et al., 2018). This combination puts the Andes Cordillera in a very prominent position as a relatively pristine natural laboratory where many glaciological, geocryological, hydrological, climatological, ecological and socio-economic processes and phenomena can be assessed from different points of view. In this last section we discuss some pending issues that could improve the current knowledge of the Andean cryosphere and the potential application in related disciplines and studies.

Accurate Quantification of Glacier Ice Thickness

One of the main issues to better quantify the future changes of Andean glaciers, their contribution to sea level rise, and their hydrological contribution to glacierized watersheds is the complexity to quantify the ice thicknesses and glacier volumes. Unfortunately, accurate ice thickness quantifications are limited to very few glaciers (less than 1% at global scale) where *in situ* thickness measurements have been realized (Welty et al., 2020). To overcome this limitation, several methods have taken advantage of the increasing availability of morpho-topographic glaciological data from repeated glacier inventories, digital elevation models of the glacier surface, surface mass balance data, and more recently surface flow velocity data. The Working Group of the International Association of Cryospheric Sciences (IACS)[1] conducted the Ice Thickness Models Intercomparison eXperiment (ITMIX). Farinotti et al. (2017, 2019) presented a review of existing methods together with the first results of the intercomparison experiment. One interesting finding was the possibility of using glacier surface flow velocities to faithfully represent the thickness distribution at the glacier scale. In contrast, approaches based on the shear stress (i.e., using the surface slope) provided less accurate results. Indeed, Rabatel et al. (2018b) strongly encouraged the use of glacier surface flow velocities to improve the quantification of glacier ice thickness distribution and underlined the need of at least a few *in situ* measured thickness data. The methods using the glacier surface slope as input data (e.g., Huss and Farinotti, 2012; Linsbauer et al., 2012) should be used with caution because of the strong uncertainties associated with this variable. Certain particular considerations are probably also needed if these methods are applied in regions such as the Desert Andes where cold-based glaciers are common.

Updated Simulations of Future Glacier Changes

Studies of projections of potential future changes of glaciers in the Andes have been regional/global in scale (e.g., Marzeion et al., 2012; Radić and Hock, 2014; Huss and Hock, 2015; Huss et al., 2017), or site-specific (e.g., Frans et al., 2015; Réveillet et al., 2015; Yarleque et al., 2018). The different approaches range from simple extrapolations of past surface or length changes,

[1] http://cryosphericsciences.org/

to complex modeling of glacier mass balance and ice flow dynamics. All studies indicate an important reduction of glacier ice volume in the Andes by the end of the 21st century, and even the disappearance of many glaciers. Small glaciers are likely to completely disappear in the coming decades (e.g., Rabatel et al., 2018a for Colombia), and even the largest tropical ice cap (the Quelccaya ice cap in the Cordillera de Vilcanota, Peru; Yarleque et al., 2018). Given the limited altitudinal extent of many glaciers, even if air temperature is assumed to stabilize by the second half of this century according to the most optimistic climate scenario, such glaciers will not reach a new equilibrium with climate and will likely disappear or shrink substantially.

For improved estimations of future glacier evolution, ice dynamics models will need to be coupled to adequate representations of glacier surface mass balance. Application of models able to resolve the full energy balance is thus required (e.g., Bravo et al., 2017). However, such models need accurate projections of atmospheric variables, and thus decreasing the uncertainties in future projections of atmospheric variables and improving their downscaling at the glacier scale are two other important issues. Finally, a better quantification of the impact of supraglacial debris and related feedbacks will also be required as many glacier tongues are covered by debris especially in the southern Andes.

Development of a Coordinated Network of High Elevation Hydro-Meteorological Stations

The current lack of an extended, well-coordinated network of permanent, complete and reliable meteorological stations at high elevations in the Andes constitutes a very important limitation to properly understand the atmospheric processes and phenomena that affect the cryosphere and many other natural systems in this mountain range. Very few automatic weather stations (AWS) that measure the whole range of relevant variables including snow accumulation are located near glacierized areas, and thus many studies have relied on remote stations and/or gridded datasets that do not necessarily capture the local processes in a proper manner. In many cases the different research groups have installed and maintain AWS at their study sites, but currently there is no coordinated effort to integrate this dispersed information for improved analyses of glacier-climate relationships and climate change related studies. Additionally, very few discharge gauging stations exist in glacierized zones, which greatly limits our ability to validate runoff models, as well as accurately estimate the cryospheric contribution to streamflow.

Geological Impacts of Deglaciation

The deglaciation that is widespread across the Andes (Braun et al., 2019; Dussaillant et al., 2019; Reinthaler et al., 2019) has important associated impacts that include the increase in frequency of landslides due to slope instabilities, possible moraine dam failures, various effects on volcanic activity, and glacio-isostatic rebounds. In view of the observed increases in proglacial lake areas due to glacier shrinkage (Wilson et al., 2018), the occurrence of glacial lake outburst floods (GLOFs) due to the sudden release of glacier- or moraine-dammed lakes poses a real and growing threat in some sectors of the Andes. In many cases these lakes have experienced GLOF events with strong impacts in downstream valleys and in the runoff of the outlet rivers (Dussaillant et al., 2012). According to Harrison et al. (2018), these processes are expected to increase in the future as the glacier retreat continues along the Andes. Thus the monitoring of this phenomenon should be established as a precautionary measure in places where human populations and infrastructure are located downstream from potentially dangerous sites. In steep terrains, thawing of mountain permafrost can also influence the frequency and magnitude of gravitational natural hazards with consequences for local communities and infrastructure (Arenson and Jakob, 2015; Deline et al., 2015). To date, only few studies have focused on the issue of volcanic activity and ice-volcano interactions (Rivera et al., 2012a; Rivera and Bown, 2013). This is particularly relevant in the region south of 46°S, where there are three active volcanoes (Lautaro, Reclus and Burney) that contain glaciers but with very little direct information on their impacts and interactions (Martinic, 2016).

Hydrological Significance of Rock Glaciers

As discussed above, the recent publication of up-to-date inventories of glaciers and rock glaciers has improved substantially the knowledge about their current state and distribution in the Andes. An increasing number of studies has focused on quantifying the amount of ice present in rock glaciers (Monnier and Kinnard, 2013; Janke et al., 2017; Jones et al., 2018), and on the possible impacts of climate change on rock glacier dynamics (Deline et al., 2015; Iribarren et al., 2015). Increasingly, both regionally (Rangecroft et al., 2015; Schaffer et al., 2019), and globally (Jones et al., 2018, 2019), the importance of rock glaciers as water reserves is being recognized in semi-arid areas (Rangecroft et al., 2013; Jones et al., 2019). However, as very few studies are available that provide rock glacier depths, the estimations of the ice volume contained in rock glaciers must be considered preliminary.

Long-term monitoring sites are showing that permafrost temperatures appear to be increasing (Trombotto, 2014), and modeling exercises indicate that temperatures will likely continue to increase in the coming decades. This permafrost warming may become a relevant issue especially in arid and semi-arid areas of the Andes as this could promote the degradation of permafrost and affect the rock glacier contribution to the water supply in these areas. A coordinated effort is urgently needed to determine the ice content in rock glaciers, how this ice is changing through time, and the implications for catchment hydrology.

More ground temperature and active layer thickness measurements along the Andes are also needed to have a better understanding of the role of ground fabric, air temperature, radiative fluxes, snow cover, and turbulent heat fluxes on the surface energy balance and on the current presence and the future extent of mountain permafrost. Most of the data from ground temperature and active layer thicknesses are restricted

to the Central Andes of Argentina and Chile, in many cases collected by mining companies, but a substantially larger network is needed to better understand the ground temperature patterns in permafrost sites across the Andes.

Final Thoughts

The wide range of studies and analyses discussed above clearly shows that our knowledge about the different components of the Andean cryosphere has improved substantially in the last 1–2 decades. In this relatively short period of time, an astounding number of assessments have become available tackling increasingly complex patterns and phenomenons pertaining to the snow, glaciers and/or mountain permafrost in specific sectors of the Andes, or involving the Andes Cordillera as a whole. Certainly, the increasing availability of medium to high resolution data from remote sensors has played a critical role in this process. These remote sensing data have been particularly useful, for example, for developing local and regional-scale glacier inventories and for assessing glacier changes with greater temporal and spatial detail. Combined with the increasing capabilities of numerical models, this detailed information has allowed in many cases the faithful simulation of specific cryospheric processes that were previously unknown or extremely difficult to estimate using the very limited set of in situ measurements that are usually available for most sectors of the Andes. These combined approaches are most certainly welcome and needed in many regions, but we nonetheless would like to stress the overarching need for continued and renewed efforts to expand the sets of direct cryospheric measurements across the Andes. It is only through the careful comparison with direct in situ measurements that many of the remote sensing analyses and modeling exercises can reliably validate their results and provide solid evidence to further our understanding of many of the complex snow and ice processes that occur in the Andes.

AUTHOR CONTRIBUTIONS

MM, ARa, ARi, LR, and PP wrote most sections of the manuscript. All authors contributed with material and suggestions on different revisions the text.

FUNDING

MM, PP, and LR acknowledge the support from IANIGLA-CONICET. ARa acknowledges the support of the Service National d'Observation GLACIOCLIM (https://glacioclim.osug.fr) (UGA, CNRS, IRD, INRAE, IPEV), the LMI GREAT ICE (IRD), and the LabEx OSUG@2020 (Investissements d'avenir, Grant Number ANR-10-LABX56). ARi acknowledges the support of FONDECYT 1171832. EB and ID acknowledge the France Space Agency (CNES), and the Région Occitanie for the Ph.D. fellowship of ID. SM acknowledges the support from ANID-Programa Regional R16a10003.

ACKNOWLEDGMENTS

This review manuscript has been achieved as part of the ANDEX program (www.gewex.org/project/andex/), which is a prospective Regional Hydroclimate Project (RHP) of the GEWEX Hydroclimatology Panel (GHP). We thank the National Correspondents of the WGMS and the Snow and Ice Working Group (GTNH) of Latinamerica and Caribe/IHP UNESCO for the updated glacier mass balance data. L. Cara from IANIGLA-CONICET helped with the analyses shown in **Figure 1**. The numerous and constructive comments and suggestions provided by the two reviewers helped to improve the final version of the manuscript and are greatly appreciated.

REFERENCES

Abdel Jaber, W., Rott, H., Floricioiu, D., Wuite, J., and Miranda, N. (2019). Heterogeneous spatial and temporal pattern of surface elevation change and mass balance of the Patagonian ice fields between 2000 and 2016. *The Cryosphere* 13, 2511–2535. doi: 10.5194/tc-13-2511-2019

Aguirre, F., Carrasco, J., Sauter, T., Schneider, C., Gaete, K., Garín, E., et al. (2018). Snow cover change as a climate indicator in Brunswick Peninsula. Patagonia. *Front. Earth Sci.* 6:130. doi: 10.3389/feart.2018.00130

Albert, T., Klein, A., Kincaid, J. L., Huggel, C., Racoviteanu, A. E., Arnaud, Y., et al. (2014). "Remote sensing of rapidly diminishing tropical glaciers in the northern Andes," in *Global Land Ice Measurements from Space*, eds M. P. Bishop, G. J. Leonard, and B. H. Raup (Berlin: Springer), 609–638. doi: 10.1007/978-3-540-79818-7_26

Alvarez-Garreton, C., Mendoza, P. A., Boisier, J. P., Addor, N., Galleguillos, M., and Zambrano-Bigiarini, M. (2018). The CAMELS-CL dataset: catchment attributes and meteorology for large sample studies – Chile dataset. *Hydrol. Earth Syst. Sci.* 22, 5817–5846. doi: 10.5194/hess-22-5817-2018

ANA (2014). *Inventario Nacional de Glaciares y lagunas (in Spanish). Autoridad Nacional del Agua, Dirección de Conservación y Planeamiento de Recursos Hídricos*. Peru: Unidad de Glaciología y Recursos Hídricos.

Aniya, M. (2013). Holocene glaciations of Hielo Patagónico (Patagonia Icefield), South America: a brief review. *Geochem. J.* 47, 97–105. doi: 10.2343/geochemj.1.0171

Aniya, M., Sato, H., Naruse, R., Skvarca, P., and Casassa, G. (1997). Recent Variations in the Southern Patagonia Icefield, South America. *Arctic Alpine Res.* 29, 1–12.

Arenson, L. U., and Jakob, M. (2010a). "A New GIS based mountain permafrost distribution model," in *Proceedings of the 62nd Canadian Geotechnical Conference*, Calgary, AB, 452–458.

Arenson, L. U., and Jakob, M. (2010b). The significance of rock glaciers in the dry Andes - A discussion of Azócar and Brenning (2010) and Brenning and Azócar (2010). *Permafrost Periglacial Process.* 21, 286–288. doi: 10.1002/ppp.693

Arenson, L. U., and Jakob, M. (2015). "Periglacial Geohazard Risks and Ground Temperature Increases," in *Engineering Geology for Society and Territory – Volume 1: Climate Change and Engineering Geology*, Vol. 1, eds G. Lollino, A. Manconi, J. Clague, W. Shan, and M. Chiarle (Cham: Springer International Publishing), 233–237. doi: 10.1007/978-3-319-09300-0

Aster Gdem Validation Team (2009). *ASTER global DEM Validation Summary Report*. Tokyo: METI & NASA, 28.

Ayala, A., Pellicciotti, F., MacDonell, S., McPhee, J., and Burlando, P. (2017). Patterns of glacier ablation across North-Central Chile: identifying the limits of empirical melt models under sublimation-favorable conditions. *Water Resour. Res.* 53, 5601–5625. doi: 10.1002/2016WR020126

Ayala, A., Pellicciotti, F., MacDonell, S., McPhee, J., Vivero, S., Campos, C., et al. (2016). Modelling the hydrological response of debris-free and debris-covered glaciers to present climatic conditions in the semiarid Andes of central Chile. *Hydrol. Process.* 30, 4036–4058. doi: 10.1002/hyp.10971

Azócar, G. F., and Brenning, A. (2010). Hydrological and geomorphological significance of rock glaciers in the dry Andes, Chile (27°-33°S). *Permafrost Perigl. Process.* 21, 42–53. doi: 10.1002/ppp.669

Azócar, G. F., Brenning, A., and Bodin, X. (2017). Permafrost distribution modelling in the semi-arid Chilean Andes. *Cryosphere* 11, 877–890. doi: 10.5194/tc-11-877-2017

Barcaza, G., Nussbaumer, S. U., Tapia, G., Valdés, J., García, J.-L., Videla, Y., et al. (2017). Glacier inventory and recent glacier variations in the Andes of Chile, South America. *Ann. Glaciol.* 58, 166–180. doi: 10.1017/aog.2017.28

Barsch, D. (1996). *Rock-glaciers. Indicators for the Present and Former Geoecology in High Mountain Environments*. Berlin: Springer.

Basantes, R. (2010). *Análisis Espacio-Temporal de Comportamiento Geométrico de los glaciares del Volcán Antisana y su Relación con la Variabilidad Climática*. Master Thesis, University of Nice, France.

Berthier, E., Vincent, C., Magnússon, E., Gunnlaugsson, Á Þ, Pitte, P., Le Meur, E., et al. (2014). Glacier topography and elevation changes derived from Pléiades sub-meter stereo images. *Cryosphere* 8, 2275–2291. doi: 10.5194/tc-8-2275-2014

Bicca, C. E. (2012). *Variações nas geleiras da porção norte da Cordilheira Real durante o período de 1984 a 2010 através do Sensoriamento Remoto (in Portuguese)*. Master dissertation, Federal University of Rio Grande do Sul, Porto Alegre.

Bolius, D., Schwikowski, M., Jenk, T., Gaggeler, H. W., Casassa, G., and Rivera, A. (2006). A first shallow firn core record from Glaciar La Ollada on Cerro Mercedario in the Central Argentinean Andes. *Ann. Glaciol.* 43, 14–22. doi: 10.3189/172756406781812474

Bown, F., Rivera, A., Pêtlicki, M., Bravo, C., Oberreuter, J., and Moffat, C. (2019). Recent ice dynamics and mass balance of Jorge Montt Glacier, Southern Patagonia Icefield. *J. Glaciol.* 65, 732–744. doi: 10.1017/jog.2019.47

Bown, F., Rivera, A., Zenteno, P., Bravo, C., and Cawkwell, F. (2014). "First glacier inventory and recent glacier variation on Isla Grande de Tierra del Fuego and adjacent islands in Southern Chile," in *Global Land Ice Measurements from Space*, eds M. P. Bishop, G. J. Leonard, and B. H. Raup (Berlin: Springer-Praxis), 661–674. doi: 10.1007/978-3-540-79818-7_28

Braun, M. H., Malz, P. H., Sommer, C. H., Farías-Barahona, D., Sauter, T., Casassa, G., et al. (2019). Constraining glacier elevation and mass changes in South America. *Nat. Clim. Change* 9, 130–136. doi: 10.1038/s41558-018-0375-7

Bravo, C., Bozkurt, D., Gonzalez-Reyes, Á, Quincey, D. J., Ross, A. N., Farías-Barahona, D., et al. (2019a). Assessing snow accumulation patterns and changes on the patagonian icefields. *Front. Environ. Sci.* 7:30. doi: 10.3389/fenvs.2019.00030

Bravo, C., Quincey, A., Ross, A., Rivera, B., Brock, E., and Silva, M. A. (2019b). Air temperature characteristics, distribution and impact on modeled ablation for the South Patagonia Icefield. *J. Geophys. Res.* 124, 907–925. doi: 10.1029/2018JD028857

Bravo, C., Loriaux, T., Rivera, A., and Brock, B. (2017). Assessing glacier melt contribution to streamflow at Universidad Glacier, central Andes of Chile. *Hydrol. Earth Syst. Sci.* 21, 3249–3266. doi: 10.5194/hess-21-3249-2017

Burger, F., Ayala, A., Farias, D., MacDonell, S., Shaw, T., Brock, B., et al. (2019). Interannual variability in glacier contribution to runoff from high-elevation Andean catchments: understanding the role of debris cover in glacier hydrology. *Hydrol. Process.* 33, 214–229. doi: 10.1002/hyp.13354

Caceres, B. (2010). *Actualización del Inventario de Tres Casquetes Glaciares del Ecuador*. Master Thesis, University of Nice, France.

Cara, L., Masiokas, M. H., Viale, M., and Villalba, R. (2016). Análisis de la cobertura nival de la cuenca superior del río Mendoza a partir de imágenes MODIS. *Rev. Meteorol.* 41, 21–36.

Carrasco, J., Osorio, R., and Casassa, G. (2008). Secular trend of the equilibrium-line altitude on the western side of the southern andes, derived from radiosonde and surface observations. *J. Glaciol.* 54, 538–550. doi: 10.3189/002214308785837002

Carrivick, J. L., Davies, B. J., James, W. H. L., Quincey, D. J., and Glasser, N. F. (2016). Distributed ice thickness and glacier volume in southern South America. *Glob. Planet. Change* 146, 122–132. doi: 10.1016/j.gloplacha.2016.09.010

Cathles, L. M., Abbot, D. S., and MacAyeal, D. R. (2014). Intra-surface radiative transfer limits the geographic extent of snow penitents on horizontal snowfields. *J. Glaciol.* 60, 147–154. doi: 10.3189/2014jog13j124

Collao-Barrios, G., Gilliet-Chaulet, F., Favier, V., Casassa, G., and Berthier, E. (2018). Ice flow modelling to constrain the surface mass balance and ice discharge of San Rafael Glacier, Northern Patagonia Icefield. *J. Glaciol.* 64, 568–582. doi: 10.1017/jog.2018.46

Collet, M. (2010). *Suivi Spatio-Temporel des Calottes Glaciaires de l'Antisana et du Cotopaxi (Equateur). Analyse par télédétection dans un Contexte de Changement Climatique*. Master Thesis, University of Rennes, France.

CONAM (2001). *National communication of Peru to the United Nations Framework Convention on Climate change (UNFCCC)*. Lima: National Council on the Environment.

Condom, T., Coudrain, A., Sicart, J.-E., and Théry, S. (2007). Computation of the space and time evolution of equilibrium-line altitudes on Andean glaciers (10°N-55°S). *Glob. Planet. Change* 59, 189–202. doi: 10.1016/j.gloplacha.2006.11.021

Cook, S. J., Kougkoulos, I., Edwards, L. A., Dortch, J., and Hoffmann, D. (2016). Glacier change and glacial lake outburst flood risk in the Bolivian Andes. *Cryosphere*, 10:239.

Cordero, R. R., Asencio, V., Feron, S., et al. (2019). Dry-season snow cover losses in the andes (18°–40°S) driven by changes in large-scale climate modes. *Sci. Rep.* 9:16945. doi: 10.1038/s41598-019-53486-7

Corripio, J. G., and Purves, R. S. (2005). "Surface energy balance of high altitude glaciers in the Central Andes: the effect of snow penitentes," in *Climate and Hydrology in Mountain Areas*, ed. C. de Jong (London: Wiley & Sons), 15–27. doi: 10.1002/0470858249.ch3

Cortés, G., Girotto, M., and Margulis, S. (2016). Snow process estimation over the extratropical Andes using a data assimilation framework integrating MERRA data and Landsat imagery. *Water Resour. Res.* 52, 2582–2600. doi: 10.1002/2015wr018376

Cortés, G., and Margulis, S. (2017). Impacts of El Niño and La Niña on interannual snow accumulation in the Andes: Results from a high-resolution 31 year reanalysis. *Geophys. Res. Lett.* 44, 6859–6867. doi: 10.1002/2017gl073826

Dangles, O., Rabatel, A., Kraemer, M., Zeballos, G., Soruco, A., Jacobsen, D., et al. (2017). Ecosystem sentinels for climate change? Evidence of wetland cover changes over the last 30 years in the high Bolivian Andes. *PLoS One* 12:e0175814. doi: 10.1371/journal.pone.0175814

Davies, B. J., and Glasser, N. F. (2012). Accelerating shrinkage of Patagonian glaciers from the "Little Ice Age" (c. AD 1870) to 2011). *J. Glaciol.* 58, 1063–1084. doi: 10.3189/2012JoG12J026

De Angelis, H. (2014). Hypsometry and sensitivity of the mass balance to changes in equilibrium-line altitude: the case of the Southern Patagonia Icefield. *J. Glaciol.* 60, 14–28. doi: 10.3189/2014JoG13J127

Deline, P., Gruber, S., Delaloye, R., Fischer, L., Hasler, A., Kirkbride, M., et al. (2015). "Ice loss and slope stability in high-mountain regions," in *Snow and Ice-Related Hazards, Risks and Disasters*, eds W. Haeberli, C. Whiteman, and J. F. Shroder (Amsterdam: Elsevier), 521–561. doi: 10.1016/B978-0-12-394849-6.00015-9

Drenkhan, F., Guardamino, L., Huggel, C., and Frey, H. (2018). Current and future glacier and lake assessment in the deglaciating Vilcanota-Urubamba basin, Peruvian Andes. *Glob. Planet. Change* 169, 105–118. doi: 10.1016/j.gloplacha.2018.07.005

Durand, M., Rivera, A., Geremia-Nievinski, F., Lenzano, M. G., Galera, J. F., Paredes, P., et al. (2019). GPS reflectometry study detecting snow height changes in the Southern Patagonia Icefield. *Cold Reg. Sci. Technol.* 166:102840. doi: 10.1016/j.coldregions.2019.102840

Dussaillant, A., Wouter, B., Claudio, M., and Fabián, E. (2012). Hydrological regime of remote catchments with extreme gradients under accelerated change: the Baker basin in Patagonia. *Hydrol. Sci. J.* 57, 1530–1542. doi: 10.1080/02626667.2012.726993

Dussaillant, I., Berthier, E., and Brun, F. (2018). Geodetic Mass Balance of the Northern Patagonian Icefield from 2000 to 2012 using two independent methods. *Front. Earth Sci.* 6:8. doi: 10.3389/feart.2018.00008

Dussaillant, I., Berthier, E., Brun, F., Masiokas, M., Hugonnet, R., and Favier, V. (2019). Two decades of glacier mass loss along the Andes. *Nat. Geosci.* 12, 802–808. doi: 10.1038/s41561-019-0432-5

Esper Angillieri, M. Y. (2017). Permafrost distribution map of San Juan Dry Andes (Argentina) based on rock glacier sites. *J. S. Am. Earth Sci.* 73, 42–49. doi: 10.1016/j.jsames.2016.12.002

Euillades, L., Euillades, P., Riveros, N., Masiokas, M., Ruiz, L., Pitte, P., et al. (2016). Detection of glaciers displacement time-series using SAR. *Remote Sens. Environ.* 184, 188–198. doi: 10.1016/j.rse.2016.07.003

Espinoza, J. C., Garreaud, R., Poveda, G., Arias, P. A., Molina-Carpio, J., Masiokas, M., et al. (2020). Hydroclimate of the andes part I: main climatic features. *Front. Earth Sci.* 8:64. doi: 10.3389/feart.2020.00064

Falaschi, D., Bolch, T., Lenzano, M. G., Tadono, T., Lo Vecchio, A., and Lenzano, L. (2018). New evidence of glaciar surges in the Central Andes of Argentina and Chile. *Prog. Phys. Geog.* 42, 792–825. doi: 10.1177/0309133318803014

Falaschi, D., Bolch, T., Rastner, P., Lenzano, M. G., Lenzano, L., Lo Vecchio, A., et al. (2017). Mass changes of Alpine Glaciers at the Eastern Margin of the Northern and Southern Patagonian Icefields between 2000 and 2012. *J. Glaciol.* 63, 258–272. doi: 10.1017/jog.2016.136

Falaschi, D., Bravo, C., Masiokas, M. H., Villalba, R., and Rivera, A. (2013). First glacier inventory and recent changes in glacier area in the Monte San Lorenzo region (47°S), southern Patagonian Andes, South America. *Arctic Antarctic Alpine Res.* 45, 19–28. doi: 10.1657/1938-4246-45.1.19

Falaschi, D., Castro, M., Masiokas, M. H., Tadono, T., and Ahumada, A. L. (2014). Rock glacier inventory of the Valles Calchaquíes region (∼25° S), Salta, Argentina, derived from ALOS data. *Permafrost Periglacial Process.* 25, 69–75. doi: 10.1002/ppp.1801

Falaschi, D., Lenzano, M. G., Villalba, R., Bolch, T., Rivera, A., and Lo Vecchio, A. (2019). Six Decades (1958–2018) of Geodetic Glacier Mass Balance in Monte San Lorenzo, Patagonian Andes. *Front. Earth Sci.* 7:326. doi: 10.3389/feart.2019.00326

Falaschi, D., Masiokas, M. H., and Tadono, T. (2016). ALOS-derived glacier and rock glacier inventory of the Volcán Domuyo region (∼36°S), southernmost Central Andes, Argentina. *Zeitschrift Geomorphol.* 60, 195–208. doi: 10.1127/zfg/2016/0319

Falaschi, D., Tadono, T., and Masiokas, M. H. (2015). Rock glaciers in the Patagonian Andes: an inventory for the Monte San Lorenzo (Cerro Cochrane) massif, 47°S. *Geogr. Ann.* 97, 769–777. doi: 10.1111/geoa.12113

Farías-Barahona, D., Vivero, S., Casassa, G., Schaefer, M., Burger, F., Seehus, T., et al. (2019). Geodetic Mass Balances and Area Changes of Echaurren Norte Glacier (Central Andes, Chile) between 1955 and 2015. *Remote Sens.* 11:260. doi: 10.3390/rs11030260

Farinotti, D., Brinkerhoff, D. J., Clarke, G. K., Fürst, J., Frey, H., Gantayat, P., et al. (2017). How accurate are estimates of glacier ice thickness? Results from ITMIX, the Ice Thickness Models Intercomparison eXperiment. *Cryosphere* 11, 949–970.

Farinotti, D., Huss, M., Fürst, J. J., Landmann, J., Machguth, H., Maussion, F., et al. (2019). A consensus estimate for the ice thickness distribution of all glaciers on Earth. *Nat. Geosci.* 12:168. doi: 10.1038/s41561-019-0300-3

Favier, V., Falvey, M., Rabatel, A., Praderio, E., and Lopez, D. (2009). Interpreting discrepancies between discharge and precipitation in high altitude area of Chile's Norte Chico region (26°S-32°S). *Water Resour. Res.* 45:W02424. doi: 10.1029/2008WR006802

Favier, V., Wagnon, P., Chazarin, J.-P., Maisincho, L., and Coudrain, A. (2004). One-year measurements of surface heat budget on the ablation zone of Antizana glacier 15, Ecuadorian Andes. *J. Geophys. Res* 109:18105. doi: 10.1029/2003JD004359

Foresta, L., Gourmelen, N., Weissgerber, F., Nienow, P., Williams, J. J., Shepherd, A., et al. (2018). Heterogeneous and rapid ice loss over the patagonian ice fields revealed by Cryosat-2 Swath Radar altimetry. *Remote Sens. Environ.* 211, 441–455. doi: 10.1016/j.rse.2018.03.041

Francou, B., Vuille, M., Favier, V., and Cáceres, B. (2004). New evidence for an ENSO impact on low-latitude glaciers: Antizana 15, Andes of Ecuador, 0°28′ S. *J. Geophys. Res.* 109:D18106. doi: 10.1029/2003JD004484

Francou, B., Vuille, M., Wagnon, P., Mendoza, J., and Sicart, J. E. (2003). Tropical climate change recorded by a glacier in the central Andes during the last decades of the twentieth century: Chacaltaya. Bolivia, 16°S. *J. Geophys. Res.* 108:4154. doi: 10.1029/2002JD002959

Frans, C., Istanbulluoglu, E., Lettenmaier, D. P., Naz, B., Clarke, G., Condom, T., et al. (2015). Predicting glacio-hydrologic change in the headwaters of the Zongo River, Cordillera Real, Bolivia. *Water Resour. Res.* 51, 9029–9052. doi: 10.1002/2014WR016728

Gardner, A. S., Moholdt, G., Scambos, T., Fahnstock, M., Ligtenberg, S., van den Broeke, M., et al. (2018). Increased West Antarctic and unchanged East Antarctic ice discharge over the last 7 years. *Cryosphere* 12, 521–547. doi: 10.5194/tc-12-521-2018

Garreaud, R. D. (2009). The Andes climate and weather. *Adv. Geosci.* 22, 3–11. doi: 10.5194/adgeo-22-3-2009

Garreaud, R. D., Camila, A. G., Jonathan, B., Juan, P. B., Duncan, C., Carlos, L., et al. (2017). The 2010–2015 megadrought in central Chile: impacts on regional hydroclimate and vegetation. *Hydrol. Earth Syst. Sci.* 21, 6307–6327. doi: 10.5194/hess-21-6307-2017

Garreaud, R. D., Vuille, M., Compagnucci, R., and Marengo, J. (2009). Present-day South American climate. *Palaeogeogr. Palaeoclimatol. Palaeoecol.* 281, 180–195. doi: 10.1016/j.palaeo.2007.10.032

Gascoin, S., Kinnard, C., Ponce, R., Rabatel, A., Lhermitte, S., et al. (2011). Glacier contribution to streamflow in two headwaters of the Huasco River, Dry Andes of Chile. *Cryosphere* 5, 1099–1113. doi: 10.5194/tc-5-1099-2011

Gascoin, S., Lhermitte, S., Kinnard, C., Borstel, K., and Liston, G. E. (2013). Wind effects on snow cover in Pascua-Lama, Dry Andes of Chile. *Adv. Water Resour.* 55, 25–39. doi: 10.1016/j.advwatres.2012.11.013

Georgieva, V., Melnick, D., Schildgen, T. F., Ehlers, T. A., Lagabrielle, Y., Enkelmann, E., et al. (2016). Tectonic control on rock uplift, exhumation, and topography above an oceanic ridge collision: Southern Patagonian Andes (47°S). *Chile. Tecton.* 35, 1317–1341. doi: 10.1002/2016tc004120

Ginot, P., Kull, C., Schotterer, U., Schwikowski, M., and Gaggeler, H. W. (2006). Glacier mass balance reconstruction by sublimation induced enrichment of chemical species on Cerro Tapado (Chilean Andes). *Clim. Past* 2, 21–30. doi: 10.5194/cp-2-21-2006

Glasser, N. F., Harrison, S., Jansson, K. N., Anderson, K., and Cowley, A. (2011). Global sea-level contribution from the Patagonian Icefields since the Little Ice Age maximum. *Nat. Geosci.* 4, 303–307. doi: 10.1038/ngeo1122

Glasser, N. F., Jansson, K. N., Harrison, S., and Kleman, J. (2008). The glacial geomorphology and Pleistocene history of South America between 38°S and 56°S. *Q. Sci. Rev.* 27, 365–390. doi: 10.1016/j.quascirev.2007.11.011

Gourlet, P., Rignot, E., Rivera, A., and Casassa, G. (2016). Ice thickness of the northern half of the Patagonia Icefields of South America from high-resolution airborne gravity surveys. *Geophys. Res. Lett.* 43, 241–249. doi: 10.1002/2015GL066728

Gruber, S. (2012). Derivation and analysis of a high-resolution estimate of global permafrost zonation. *Cryosphere* 6, 221–233. doi: 10.5194/tc-6-221-2012

Guerrido, C. M., Villalba, R., and Rojas, F. (2014). Documentary and tree-ring evidence for a long-term interval without ice impoundments from Glaciar Perito Moreno, Patagonia, Argentina. *Holocene* 24, 1686–1693. doi: 10.1177/0959683614551215

Haeberli, W. (1985). *Creep of Muntain Permafrost: Internal Structure and Flow of Alpine Rock Glaciers. Mitteilungen der Versuchsanstalt für Wasserbau*. Zürich: ETH Zürich.

Haeberli, W., and Gruber, S. (2009). "Global warming and mountain Permafrost," in *Permafrost soils. Soil Biology*, Ed. M. Rosa (Berlin: Springer Berlin Heidelberg), 205–218. doi: 10.1007/978-3-540-69371-0_14

Hammond, J. C., Saavedra, F. A., and Kampf, S. K. (2018). Global snow zone maps and trends in snow persistence 2001–2016. *Int. J. Climatol.* 38, 4369–4383. doi: 10.1002/joc.5674

Harris, S. A., French, H. M., Heginbottom, J. A., Johnston, G. H., Ladanyi, B., Sego, D. C., et al. (1998). *Glossary of Permafrost and Related Ground Ice Terms*. Ottawa, ON: National Research Council of Canada.

Harrison, S., Kargel, J. S., Huggel, C., Reynolds, J., Shugar, D. H., Betts, R. A., et al. (2018). Climate change and the global pattern of moraine-dammed glacial lake outburst floods. *Cryosphere* 12, 1195–1209. doi: 10.5194/tc-12-1195-2018

Hastenrath, S., and Ames, A. (1995). Recession of Yanamarey Glacier in Cordillera Blanca, Peru, during the 20th century. *J. Glaciol.* 41, 191–196. doi: 10.1017/s0022143000017883

Howat, I. M., Joughin, I., and Scambos, T. A. (2007). Rapid changes in ice discharge from Greenland outlet glaciers. *Science* 315, 1559–1561. doi: 10.1126/science.1138478

Huss, M., and Farinotti, D. (2012). Distributed ice thickness and volume of all glaciers around the globe. *J. Geophys. Res.* 117:F04010. doi: 10.1029/2012JF002523

Huss, M., and Hock, R. (2015). A new model for global glacier change and sea-level rise. *Front. Earth Sci.* 3:54. doi: 10.3389/feart.2015.00054

Huss, M., and Hock, R. (2018). Global-scale hydrological response to future glacier mass loss. *Nat. Clim. Change* 8, 135–140. doi: 10.1038/s41558-017-0049-x

Huss, M., Huggel, C., Jacobsen, D., Bradley, R. S., Clague, J. J., Vuille, M., et al. (2017). Toward mountains without permanent snow and ice. *Earth's Future* 5, 418–435. doi: 10.1002/2016ef000514

Ianigla-Conicet, and Mayds (2018). *Resumen ejecutivo de los resultados del Inventario Nacional de Glaciares*. Mendoza: IANIGLA-CONICET, 27.

INAIGEM (2018). *Inventario Nacional de Glaciares*. Huaraz: INAIGEM.

Iribarren, A. P., Mackintosh, A., and Norton, K. P. (2015). Hazardous processes and events from glacier and permafrost areas: lessons from the Chilean and Argentinean Andes. *Earth Surf. Process. Landf.* 40, 2–21. doi: 10.1002/esp.3524

Janke, J. R., Bellisario, A. C., and Ferrando, F. A. (2015). Classification of debris-covered glaciers and rock glaciers in the Andes of central Chile. *Geomorphology* 241, 98–121. doi: 10.1016/j.geomorph.2015.03.034

Janke, J. R., Ng, S., and Bellisario, A. (2017). An inventory and estimate of water stored in firn fields, glaciers, debris-covered glaciers, and rock glaciers in the Aconcagua River Basin, Chile. *Geomorphology* 296, 142–152. doi: 10.1016/j.geomorph.2017.09.002

Jones, D. B., Harrison, S., Anderson, K., and Betts, R. A. (2018). Mountain rock glaciers contain globally significant water stores. *Sci. Rep.* 8:2834.

Jones, D. B., Harrison, S., Anderson, K., and Whalley, W. B. (2019). Rock glaciers and mountain hydrology: a review. *Earth Sci. Rev.* 193, 66–90. doi: 10.1016/j.earscirev.2019.04.001

Jordan, E. (1991). *Die Gletscher der Bolivianischen Anden: eine photogrammetrisch-kartographische Bestandsaufnahme der Gletscher Boliviens als Grundlage für klimatische Deutungen und Potential für die wirtschaftliche Nutzung*. Stuttgart: Franz Steiner Verlag.

Jordan, E., Ungerechts, L., Caceres, B., Penafiel, A., and Francou, B. (2005). Estimation by photogrammetry of the glacier recession on the Cotopaxi Volcano (Ecuador) between 1956 and 1997. *Hydrol. Sci. J.* 50:94.

Kaser, G., Großhauser, M., and Marzeion, B. (2010). Contribution potential of glaciers to water availability in different climate regimes. *PNAS* 107, 20223–20227. doi: 10.1073/pnas.1008162107

Kaser, G., Hastenrath, S., and Ames, A. (1996). Mass balance profiles on tropical glaciers. *Z. Gletscherkd. Glazialgeol.* 32, 75–81.

Kaser, G., and Osmaston, H. (2002). *Tropical Glaciers*. New York, NY: Cambridge University Press, 207.

Koppes, M., Conway, H., Rasmussen, L., and Chernos, M. (2011). Deriving calving variations from reanalysis data and sparse observations, Glaciar San Rafael, northern Patagonia, 1950–2005. *Cryosphere* 5, 791–808. doi: 10.5194/tc-5-791-2011

Korona, J., Berthier, E., Bernard, M., Remy, F., and Thouvenot, E. (2009). SPIRIT. SPOT 5 stereoscopic survey of Polar Ice: reference Images and Topographies during the fourth International Polar Year (2007-2009). *ISPRS J. Photogramm.* 64, 204–212. doi: 10.1016/j.isprsjprs.2008.10.005

Leclercq, P. W., Pitte, P., Giesen, R. H., Masiokas, M. H., and Oerlemans, J. (2012). Modelling and climatic interpretation of the length fluctuations of Glaciar Frías (north Patagonian Andes, Argentina) 1639-2009 AD. *Clim. Past* 8, 1385–1402. doi: 10.5194/cp-8-1385-2012

Lejeune, Y., Bouilloud, L., Etchevers, P., Wagnon, P., Chevallier, P., Sicart, J. E., et al. (2007). Melting of snow cover in a tropical mountain environment in Bolivia: processes and modeling. *J. Hydrometeorol.* 8, 922–937. doi: 10.1175/jhm590.1

Lenaerts, J. T. M., Van den Broeke, M. R., Van Wessem, J. M., and Van de Berg, W. J. (2014). Extreme precipitation and climate gradients in Patagonia revealed by high-resolution regional atmospheric climate modeling. *J. Clim.* 27, 4607–4621. doi: 10.1175/JCLI-D-13-00579.1

Lenzano, M. G., Lannutti, E., Toth, C., Rivera, A., and Lenzano, L. (2018). Detecting glacier surface motion by optical flow. *Photogrammetr. Eng. Remote Sens.* 84, 33–42. doi: 10.14358/PERS.84.1.33

Lhermitte, S., Abermann, J., and Kinnard, C. (2014). Albedo over rough snow and ice surfaces. *Cryosphere* 8, 1069–1086. doi: 10.5194/tc-8-1069-2014

Linsbauer, A., Paul, F., and Haeberli, W. (2012). Modeling glacier thickness distribution and bed topography over entire mountain ranges with GlabTop: application of a fast and robust approach. *J. Geophys. Res.* 117:F03007. doi: 10.1029/2011JF002313

Liu, T., Kinouchi, T., and Ledezma, F. (2013). Characterization of recent glacier decline in the Cordillera Real by LANDSAT, ALOS, and ASTER data. *Remote Sens. Environ.* 137, 158–172. doi: 10.1016/j.rse.2013.06.010

Lliboutry, L. (1954). The origin of penitents. *J. Glaciol.* 2, 331–338. doi: 10.3189/s0022143000025181

Lliboutry, L. (1965). *Traité de glaciologie, tome 2: Glaciers, variations du climat, sols gelés [Treatise of Glaciology, v. 2: Glaciers, Climatic Variations, Frozen Ground]*. Paris: Masson et Cie, 612.

Lliboutry, L. (1998). "Glaciers of chile and Argentina," in *Satellite Image Atlas of Glaciers of the World, Geological Survey Professional Paper 1386-I-6*, eds R. Williams and J. Ferrigno (Reston, VA: USGS)

Lo Vecchio, A., Lenzano, M. G., Durand, M., Lanutti, E., Bruce, R., and Lenzano, L. (2018). Estimation of surface flow speed and ice surface temperature from optical satellite imagery at Viedma glacier. Argentina. *Glob. Planet. Change* 169, 202–213. doi: 10.1016/j.gloplacha.2018.08.001

Lopez, P., Chevallier, P., Favier, V., Pouyaud, B., Ordenes, F., and Oerlemans, J. (2010). A regional view of fluctuations in glacier length in southern South America. *Glob. Planet. Change* 71, 85–108. doi: 10.1016/J.GLOPLACHA.2009.12.009

Loriaux, T., and Casassa, G. (2013). Evolution of Glacial Lakes from the Northern Patagonia Icefield and Terrestrial Water Storage in a Sea-Level Rise Context. *Glob. Planet. Change* 102, 33–40. doi: 10.1016/j.gloplacha.2012.12.012

MacDonell, S., Kinnard, C., Mölg, T., Nicholson, L., and Abermann, J. (2013). Meteorological drivers of sublimation and melt on a cold glacier in the semi-arid Andes of Chile. *Cryosphere* 7, 1513–1526. doi: 10.5194/tc-7-1513-2013

Malz, P., Meier, W., Casassa, G., Jaña, R., Skvarca, P., and Braun, M. H. (2018). Elevation and mass changes of the Southern Patagonia icefield derived from TanDEM-X and SRTM data. *Remote Sens.* 10:188. doi: 10.3390/rs10020188

Martinic, M. (2016). La erupción del volcán de los Gigantes (Lautaro) en 1883. Algunas consideraciones. *Magallania* 44, 65–68. doi: 10.4067/s0718-22442016000200003

Marzeion, B., Jarosch, A. H., and Hofer, M. (2012). Past and future sea-level change from the surface mass balance of glaciers. *Cryosphere* 6, 1295–1322. doi: 10.5194/tc-6-1295-2012

Masiokas, M. H., Cara, L., Villalba, R., Pitte, P., Christie, D. A., Le Quesne, C., et al. (2019). Streamflow variations across the Andes (18°-55°S) during the instrumental era. *Sci. Rep.* 9:17879.

Masiokas, M. H., Christie, D. A., Le Quesne, C., Pitte, P., Ruiz, L., Villalba, R., et al. (2016). Reconstructing the annual mass balance of the Echaurren Norte glacier (Central Andes, 33.5° S) using local and regional hydroclimatic data. *Cryosphere* 10, 927–940. doi: 10.5194/tc-10-927-2016

Masiokas, M. H., Delgado, S., Pitte, P., Berthier, E., Villalba, R., Skvarca, P., et al. (2015). Inventory and recent changes of small glaciers on the northeast margin of the South Patagonian Icefield, Argentina. *J. Glaciol.* 61, 511–523. doi: 10.3189/2015jog14j094

Masiokas, M. H., Rivera, A., Espizua, L. E., Villalba, R., Delgado, S., and Aravena, J. C. (2009). Glacier fluctuations in extratropical South America during the past 1000 years. *Palaeogeogr. Palaeoclimatol. Palaeoecol.* 281, 242–268. doi: 10.1016/j.palaeo.2009.08.006

Masiokas, M. H., Villalba, R., Luckman, B., Delgado, S., Lascano, M., and Stepanek, P. (2008). 20th century glacier recession and regional hydroclimatic changes in northwestern Patagonia. *Glob. Planet. Change* 60, 85–100. doi: 10.1016/j.gloplacha.2006.07.031

Masiokas, M. H., Villalba, R., Luckman, B., LeQuesne, C., and Aravena, J. C. (2006). Snowpack variations in the central Andes of Argentina and Chile, 1951-2005: large-scale atmospheric influences and implications for water resources in the region. *J. Clim.* 19, 6334–6352. doi: 10.1175/jcli3969.1

Masiokas, M. H., Villalba, R., Luckman, B. H., Montaña, E., Betman, E., Christie, D., et al. (2013). "Recent and historic Andean snowpack and streamflow variations and vulnerability to water shortages in central-western Argentina," in *Climate Vulnerability: Understanding and Addressing Threats to Essential Resources*, Vol. 5, eds R. A. Pielke, J. Adegoke, D. Niyogi, G. Kallos, T. R.

Seastedt, and F. Hossain (Amsterdam: Elsevier Inc), 213–227. doi: 10.1016/b978-0-12-384703-4.00522-0

Maussion, F., Gurgiser, W., Großhauser, M., Kaser, G., and Marzeion, B. (2015). ENSO influence on surface energy and mass balance at Shallap Glacier, Cordillera Blanca, Peru. *Cryosphere* 9, 1663–1683. doi: 10.5194/tc-9-1663-2015

Meier, W. J. H., Grießinger, J., Hochreuther, P., and Braun, M. H. (2018). An updated multi-temporal glacier inventory for the Patagonian Andes with changes between the Little Ice Age and 2016. *Front. Earth Sci.* 6:62. doi: 10.3389/feart.2018.00062

Melkonian, A. K., Willis, M. J., Pritchard, M. E., Rivera, A., Bown, F., and Bernstein, S. A. (2013). Satellite-derived volume loss rates and glacier speeds for the Cordillera Darwin Icefield, Chile. *Cryosphere* 7, 823–839. doi: 10.5194/tc-7-823-2013

Millan, R., Rignot, E., Rivera, A., Martineau, V., Mouginot, J., Zamora, R., et al. (2019). Ice thickness and bed elevation of the Northern and Southern Patagonian Icefields. *Geophys. Res. Lett.* 46, 6626–6635. doi: 10.1029/2019GL082485

Minowa, M., Sugiyama, S., Sakakibara, D., and Sawagaki, T. (2015). Contrasting glacier variations of Glaciar Perito Moreno and Glaciar Ameghino, Southern Patagonia Icefield. *Ann. Glaciol.* 56, 26–32. doi: 10.3189/2015AoG70A020

Monnier, S., and Kinnard, C. (2013). Internal structure and composition of a rock glacier in the Andes (upper Choapa valley, Chile) using borehole information and ground-penetrating radar. *Ann. Glaciol.* 54, 61–72. doi: 10.3189/2013AoG64A107

Monnier, S., and Kinnard, C. (2015). Reconsidering the glacier to rock glacier transformation problem: new insights from the central Andes of Chile. *Geomorphology* 238, 47–55. doi: 10.1016/j.geomorph.2015.02.025

Monnier, S., and Kinnard, C. (2016). Interrogating the time and processes of development of the Las Liebres rock glacier, central Chilean Andes, using a numerical flow model. *Earth Surf. Process. Landf.* 41, 1884–1893. doi: 10.1002/esp.3956

Monnier, S., and Kinnard, C. (2017). Pluri-decadal (1955–2014) evolution of glacier–rock glacier transitional landforms in the central Andes of Chile (30–33° S). *Earth Surf. Dyn.* 5, 493–509. doi: 10.5194/esurf-5-493-2017

Moon, T., Joughin, I., Smith, B., and Howat, I. (2012). 21st-century evolution of Greenland outlet glacier velocities. *Science* 336, 576–578. doi: 10.1126/science.1219985

Moragues, S. M., Lenzano, M. G., Lo Vecchio, A., Falaschi, D., and Lenzano, L. (2018). Surface velocities of Upsala Glacier, Southern Patagonian Andes using cross correlation satellite imagery: 2013-2014 Period. *Andean Geol.* 45, 87–103.

Morizawa, K., Asaoka, Y., Kazama, S., and Gunawardhana, L. N. (2013). Temporal glacier area changes correlated with the El Niño/La Niña Southern Oscillation using satellite imagery. *Hydrol. Res. Lett.* 7, 18–22. doi: 10.3178/hrl.7.18

Morris, J. N., Poole, A. J., and Klein, A. G. (2006). "Retreat of tropical glaciers in Colombia and Venezuela from 1984 to 2004 as measured from ASTER and Landsat images," in *Proceeding of the 63rd Eastern Snow Conference*, Newark, 181–191.

Mouginot, J., and Rignot, E. (2015). Ice motion of the Patagonian Icefields of South America: 1984–2014. *Geophys. Res. Lett.* 42, 1441–1449. doi: 10.1002/2014GL062661

Muto, M., and Furuya, M. (2013). Surface velocities and ice-front positions of eight major glaciers in the southern Patagonian Ice Field, South America, from 2002 to 2011. *Remote Sens. Environ.* 139, 50–59. doi: 10.1016/j.rse.2013.07.034

Nicholson, L., Marín, J., Lopez, D., Rabatel, A., Bown, F., and Rivera, A. (2009). Glacier inventory of the upper Huasco valley, Norte Chico, Chile: glacier characteristics, glacier change and comparison to central Chile. *Ann. Glaciol.* 50, 111–118. doi: 10.3189/172756410790595787

Nicholson, L., Petlicki, M., Partan, B., and MacDonell, S. (2016). 3-D surface properties of glacier penitentes over an ablation season, measured using a Microsoft Xbox Kinect. *Cryosphere* 10, 1897–1913. doi: 10.5194/tc-10-1897-2016

Nogami, M. (1972). The snow line and climate during the last glacial period in the Andes mountains. *Q. Res.* 11, 71–80. doi: 10.4116/jaqua.11.71

Pasquini, A. I., and Depetris, P. J. (2011). Southern Patagonia's Perito Moreno Glacier, Lake Argentino, and Santa Cruz River hydrological system: An overview. *J. Hydrol.* 405, 48–56. doi: 10.1016/j.jhydrol.2011.05.009

Paul, F., and Moelg, N. (2014). Hasty retreat of glaciers in northern Patagonia from 1985 to 2011. *J. Glaciol.* 60, 1033–1043. doi: 10.3189/2014JoG14J104

Perucca, L. P., and Esper Angillieri, M. Y. (2008). A preliminary inventory of periglacial landforms in the Andes of La Rioja and San Juan, Argentina, at about 28°S. *Q. Int.* 190, 171–179. doi: 10.1016/j.quaint.2007.10.007

Pitte, P. (2014). *Fluctuaciones de Los Glaciares, en Los Últimos 50 años, en las Cuencas Amarillo, Turbio, Canito y Potrerillos, San Juan, Argentina (in Spanish)*. PhD Thesis, Universidad Nacional de Córdoba, Argentina.

Pitte, P., Berthier, E., Masiokas, M. H., Cabot, V., Ruiz, L., Ferri Hidalgo, L., et al. (2016). Geometric evolution of the Horcones Inferior Glacier (Mount Aconcagua, Central Andes) during the 2002-2006 surge. *J. Geophys. Res. Earth Surf.* 121, 111–127. doi: 10.1002/2015JF003522

Rabassa, J. (1981). Inventario de glaciares y cuerpos de nieve permanentes en los Andes Patagónicos Septentrionales, Argentina (in Spanish). *Actas VIII Congr. Geol. Argentino Actas* 4, 109–122.

Rabatel, A., Bermejo, A., Loarte, E., Soruco, A., Gomez, J., Leonardini, G., et al. (2012). Can the snowline be used as an indicator of the equilibrium line and mass balance for glaciers in the outer tropics? *J. Glaciol.* 58, 1027–1036. doi: 10.3189/2012JoG12J027

Rabatel, A., Castebrunet, H., Favier, V., Nicholson, L., and Kinnard, C. (2011). Glacier changes in the Pascua-Lama region, Chilean Andes (29° S): recent mass balance and 50 yr surface area variations. *Cryosphere* 5, 1029–1041. doi: 10.5194/tc-5-1029-2011

Rabatel, A., Ceballos, J. L., Micheletti, N., Jordan, E., Braitmeier, M., Gonzalez, J., et al. (2018a). Toward an imminent extinction of Colombian glaciers? Geografiska Annaler: Series A. *Phys. Geogr.* 100, 75–95. doi: 10.1080/04353676.2017.1383015

Rabatel, A., Sanchez, O., Vincent, C., and Six, D. (2018b). Estimation of glacier thickness from surface mass balance and ice flow velocities: a case study on Argentière Glacier, France. *Front. Earth Sci.* 6:112. doi: 10.3389/feart.2018.00112

Rabatel, A., Francou, B., Soruco, A., Gomez, B., Caceres, J. L., Ceballos, R., et al. (2013). Current state of glaciers in the tropical Andes: a multi-century perspective on glacier evolution and climate change. *Cryosphere* 7, 81–102. doi: 10.5194/tc-7-81-2013

Radić, V., and Hock, R. (2014). Glaciers in the Earth's hydrological cycle. Assessments of glacier mass and runoff changes on global and regional scales. *Surv. Geophys.* 35, 813–837. doi: 10.1007/s10712-013-9262-y

Rangecroft, S., Harrison, S., and Anderson, K. (2015). Rock glaciers as water stores in the Bolivian Andes: an assessment of their hydrological importance. *Arctic Antarctic Alpine Res.* 47, 89–98. doi: 10.1657/AAAR0014-029

Rangecroft, S., Harrison, S., Anderson, K., Magrath, J., Castel, A. P., and Pacheco, P. (2013). Climate change and water resources in arid mountains: an example from the Bolivian Andes. *AMBIO* 42, 852–863. doi: 10.1007/s13280-013-0430-6

Rangecroft, S., Harrison, S., Anderson, K., Magrath, J., Castel, A. P., and Pacheco, P. (2014). A first rock glacier inventory for the Bolivian Andes. *Permafrost Periglacial Process.* 25, 333–343. doi: 10.1002/ppp.1816

Raup, B. H., Kieffer, H. H., Hare, T. M., and Kargel, J. S. (2000). Generation of data acquisition requests for the ASTER satellite instrument for monitoring a globally distributed target: glaciers. *IEEE Trans. Geosci. Remote Sens.* 38, 1105–1112.

Reinthaler, J., Paul, F., Granados, H., Rivera, A., and Huggel, C. (2019). Area changes of glaciers on active volcanoes in Latin America between 1986 and 2015 observed from multi-temporal satellite imagery. *J. Glaciol.* 65, 542–556. doi: 10.1017/jog.2019.30

Réveillet, M., MacDonell, S., Gascoin, S., Kinnard, C., Lhermitte, S., and Schaffer, N. (2020). Impact of forcing on sublimation simulations for a high mountain

catchment in the semiarid Andes. *Cryosphere* 14, 147–163. doi: 10.5194/tc-14-147-2020

Réveillet, M., Rabatel, A., Gillet-Chaulet, F., and Soruco, A. (2015). Simulations of changes to Glacier Zongo, Bolivia (16S), over the 21st century using a 3-D full-Stokes model and CMIP5 climate projections. *Ann. Glaciol.* 56, 89–97. doi: 10.3189/2015aog70a113

RGI Consortium (2017). *Randolph Glacier Inventory – A Dataset of Global Glacier Outlines: Version 6.0*. Technical Report, Global Land Ice Measurements from Space, Colorado, doi: 10.7265/N5-RGI-60

Ribeiro, R., Simões, J. C., and Bremer, U. F. (2005). "Application of remote sensing in the estimate of the retraction of the Bolivian glaciers," in *Proceedings of XIIth Brazilian Remote Sensing Symposium*, Goiânia, 669–671.

Ribeiro, R. D. R., Ramirez, E., Simões, J. C., and Machaca, A. (2013). 46 years of environmental records from the Nevado Illimani glacier group, Bolivia, using digital photogrammetry. *Ann. Glaciol.* 54, 272–278. doi: 10.3189/2013aog63a494

Rignot, E., Rivera, A., and Casassa, G. (2003). Contribution of the Patagonia Icefields of South America to Sea Level Rise. *Science* 302, 434–437. doi: 10.1126/science.1087393

Rivera, A. (2018). Glaciar Pío XI: La excepción a la tendencia de desglaciación en Patagonia. *Rev. Geogr. Chile Terra Aust.* 54, 1–12. doi: 10.23854/07199562.2018541rivera1

Rivera, A. (2019). "Los glaciares de Chile central a seis décadas de los trabajos de Louis Lliboutry," in *El Hombre Que Descifró los Glaciares Louis Lliboutry*, ed. M. Turrel (Santiago: Aguas Andinas), 250–255.

Rivera, A., and Bown, F. (2013). Recent glacier variations on active ice capped volcanoes in the Southern Volcanic Zone (37° 46°S), Chilean Andes. *J. South Am. Earth Sci.* 45, 345–356. doi: 10.1016/j.jsames.2013.02.004

Rivera, A., Bown, F., Napoleoni, F., Muñoz, C., and Vuille, M. (2016). *Balance de Masa Glaciar*. Valdivia: Ediciones CECs, 203.

Rivera, A., Bown, F., Carrión, D., and Zenteno, P. (2012a). Glacier responses to recent volcanic activity in Southern Chile. *Environ. Res. Lett.* 7:014036. doi: 10.1088/1748-9326/7/014036

Rivera, A., Corripio, J., Bravo, C., and Cisternas, S. (2012b). Glaciar Jorge Montt dynamics derived from photos obtained by fixed cameras and satellite image feature tracking. *Ann. Glaciol.* 53, 147–155. doi: 10.3189/2012aog60a152

Rivera, A., Koppes, M., Bravo, C., and Aravena, J. (2012c). Little Ice Age advance and retreat of Glaciar Jorge Montt, Chilean Patagonia. *Clim. Past* 8, 403–414. doi: 10.5194/cp-8-403-2012

Rivera, J. A., Penalba, O. C., Villalba, R., and Araneo, D. C. (2017). Spatio-temporal patterns of the 2010–2015 extreme hydrological drought across the Central Andes, Argentina. *Water* 9:652. doi: 10.3390/w9090652

Ruiz, L., Berthier, E., Masiokas, M., Pitte, P., and Villalba, R. (2015). First surface velocity maps for glaciers of Monte Tronador, North Patagonian Andes, derived from sequential Pléiades satellite images. *J. Glaciol.gy* 61, 908–922. doi: 10.3189/2015JoG14J134

Ruiz, L., Masiokas, M. H., and Villalba, R. (2012). Fluctuations of Glaciar Esperanza Norte in the north Patagonian Andes of Argentina during the past 400 yr. *Clim. Past* 8, 1079–1090. doi: 10.5194/cp-8-1079-2012

Ruiz, L., and Trombotto, D. (2012). "Mountain permafrost distribution in the Andes of Chubut (Argentina) based on a statistical model," in *Proceedings of the 10th International Permafrost Conference*, Salekhard, 365–370.

Saavedra, F. A., Kampf, S. K., Fassnacht, S. R., and Sibold, J. S. (2017). A snow climatology of the Andes Mountains from MODIS snow cover data. *Int. J. Climatol.* 37, 1526–1539. doi: 10.1002/joc.4795

Saavedra, F. A., Kampf, S. K., Fassnacht, S. R., and Sibold, J. S. (2018). Changes in Andes snow cover from MODIS data, 2000–2016. *Cryosphere* 12, 1027–1046. doi: 10.5194/tc-12-1027-2018

Sagredo, E. A., and Lowell, T. V. (2012). Climatology of Andean glaciers: a framework to understand glacier response to climate change. *Glob. Planet. Change* 8, 101–109. doi: 10.1016/j.gloplacha.2012.02.010

Sakakibara, D., and Sugiyama, S. (2014). Ice-front variations and speed changes of calving glaciers in the southern patagonia icefield from 1984 to 2011. *J. Geophys. Res. Earth Surf.* 119, 2541–2554. doi: 10.1002/2014JF003148

Sakakibara, D., Sugiyama, S., Sawagaki, T., Marinsek, S., and Skvarca, P. (2013). Rapid retreat, acceleration, and thinning of Glaciar Upsala in the Southern Patagonia Icefield, initiated in 2008. *Ann. Glaciol.* 54, 131–138. doi: 10.3189/2013aog63a236

Salzmann, N., Huggel, C., Rohrer, M., Silverio, W., Mark, B. G., Burns, P., et al. (2013). Glacier changes and climate trends derived from multiple sources in the data scarce Cordillera Vilcanota region, southern Peruvian Andes. *Cryosphere* 7, 103–118. doi: 10.5194/tc-7-103-2013

Sanches, A. M. (2013). *Variações na extensão da cobertura de gelo do Nevado Cololo, Bolívia*. Doctoral dissertation, Federal University of Rio Grande do Sul, Porto Alegre.

Schaefer, M., MacHguth, H., Falvey, M., and Casassa, G. (2013). Modeling past and future surface mass balance of the Northern Patagonia icefield. *J. Geophys. Res. Earth Surf.* 118, 571–588. doi: 10.1002/jgrf.20038

Schaefer, M., MacHguth, H., Falvey, M., Casassa, G., and Rignot, E. (2015). Quantifying mass balance processes on the Southern Patagonia icefield. *Cryosphere* 9, 25–35. doi: 10.5194/tc-9-25-2015

Schaeffer, M., Rodriguez, J., Scheiter, M., and Casassa, G. (2017). Climate and surface mass balance of Mocho Glacier, Chilean Lake District, 40°S. *J. Glaciol.* 63, 218–228. doi: 10.1017/jog.2016.129

Schaffer, N., MacDonell, S., Réveillet, M., Yáñez, E., and Valois, R. (2019). Rock glaciers as a water resource in the semiarid Chilean Andes in a changing climate. *Reg. Environ. Change* 19, 1263–1279. doi: 10.1007/s10113-018-01459-1453

Schoolmeester, T., Johansen, K. S., Alfthan, B., Baker, E., Hesping, M., and Verbist, K. (2018). *The Andean Glacier and Water Atlas – The Impact of Glacier Retreat on Water Resources*. Arendal: UNESCO and GRID-Arendal. Available online at: https://unesdoc.unesco.org/ark:/48223/pf0000265810

Schneider, C., Schnirch, M., Acuña, C., Casassa, G., and Kilian, R. (2007). Glacier inventory of the Gran Campo Nevado Ice Cap in the Southern Andes and glacier changes observed during recent decades. *Glob. Planet. Change* 59, 87–100. doi: 10.1016/j.gloplacha.2006.11.023

Sicart, J. E., Hock, R., Ribstein, P., Litt, M., and Ramirez, E. (2011). Analysis of seasonal variations in mass balance and meltwater discharge of the Tropical Zongo Glacier by application of a distributed energy balance model. *J. Geophys. Res.* 116:D13105. doi: 10.1029/2010JD015105

Sicart, J. E., Wagnon, P., and Ribstein, P. (2005). Atmospheric controls of heat balance of Zongo Glacier (16°S. Bolivia). *J. Geophys. Res.* 110:D12106. doi: 10.1029/2004JD005732

Sinclair, K., and MacDonell, S. (2016). Seasonal evolution of penitente geochemistry at Tapado Glacier, northern Chile. *Hydrol. Process.* 30, 176–186. doi: 10.1002/hyp.10531

Soruco, A., Vincent, C., Francou, B., Ribstein, P., Berger, T., Sicart, J. E., et al. (2009). Mass balance of Glaciar Zongo, Bolivia, between 1956 and 2006, using glaciological, hydrological and geodetic methods. *Ann. Glaciol.* 50:2009.

Soruco, A., Vincent, C., Rabatel, A., Francou, B., Thibert, E., Sicart, J. E., et al. (2015). Impacts of glacier shrinkage on water resources of La Paz city, Bolivia (16°S). *Ann. Glaciol.* 56, 147–154. doi: 10.3189/2015AoG70A001

Sugiyama, S., Skvarca, P., Naito, N., Enomoto, H., Tsutaki, S., Tone, K., et al. (2011). Ice speed of a calving glacier modulated by small fluctuations in basal water pressure. *Nature Geosci.* 4, 597–600. doi: 10.1038/ngeo1218

Troll, C. (1941). *Studien zur Vergleichenden Geographie der Hochgebirge der Erde*. Bonn: Bonner Mitteilungen, 1941.

Trombotto, L. (2014). *Environmental Status of the Cryogenic Permafrost Conditions in the Last Decade in the Central Andes, one Example*. Mendoza: IANIGLA – CCT CONICET, 27–29.

Trombotto Liaudat, D. (2000). Survey of cryogenic processes, periglacial forms and permafrost conditions in South America. *Rev. Inst. Geol.* 21, 33–55. doi: 10.5935/0100-929X.20000004

Trombotto Liaudat, D., Wainstein, P., and Arenson, L. (2014). *Guía Terminológica de la Geocriología Sudamericana*. Buenos Aires: Vazquez Mazzini.

UGRH (2010). *Unidad de Glaciología y Recursos Hídricos [UGRH]: Inventario de glaciares, Cordillera Blanca, Perú*. Huaraz: Autoridad Nacional del Agua, 81.

Veettil, B. K., and Kamp, U. (2017). Remote sensing of glaciers in the tropical Andes: a review. *Int. J. Remote Sens.* 38, 7101–7137. doi: 10.1080/01431161.2017.1371868

Veettil, B. K., Wang, S., Simões, J. C., and Pereira, S. F. R. (2018). Glacier monitoring in the eastern mountain ranges of Bolivia from 1975 to 2016 using Landsat and Sentinel-2 data. *Environ. Earth Sci.* 77:452.

Viale, M., Bianchi, E., Cara, L., Ruiz, L. E., Villalba, R., Pitte, P., et al. (2019). Contrasting climates at both sides of the Andes in Argentina and Chile. *Front. Environ. Sci.* 7:69. doi: 10.3389/fenvs.2019.00069

Villalba, R., Leiva, J., Rubulls, S., Suarez, J., and Lenzano, L. (1990). Climate, Tree-Ring, and Glacial Fluctuations in the Rio Frias Valley, Rio Negro, Argentina. *Arctic Alpine Res.* 22, 215–232. doi: 10.2307/1551585

Villarroel, C., Carrasco, J., Casassa, G., and Falvey, M. (2013). Modeling near-surface air temperature and precipitation using WRF with 5-km resolution in the Northern Patagonia Icefield: a pilot simulation. *Int. J. Geosci.* 4, 1193–1199. doi: 10.4236/ijg.2013.48113

Vincent, C., Soruco, A., Azam, F., Basantes-Serrano, R., Jackson, M., Kjollmoen, B., et al. (2018). A non-linear statistical model for extracting a climatic signal from glacier mass-balance measurements. *J. Geosphys. Res. Earth Surf.* 123, 2228–2242. doi: 10.1029/2018JF004702

Vuille, M., Carey, M., Huggel, C., Buytaert, W., Rabatel, A., Jacobsen, D., et al. (2018). Rapid decline of snow and ice in the tropical Andes–Impacts, uncertainties and challenges ahead. *Earth Sci. Rev.* 176, 195–213. doi: 10.1016/j.earscirev.2017.09.019

Wagnon, P., Lafaysse, M. Lejeune, Y. Maisincho, L. Rojas, M., and Chazarin, J. P. (2009). Understanding and modeling the physical processes that govern the melting of snow cover in a tropical mountain environment in Ecuador. *J. Geophys. Res.* 114:D19113. doi: 10.1029/2009JD012292

Wagnon, P., Ribstein, P., Francou, B., and Sicart, J. E. (2001). Anomalous heat and mass balance budget of Glaciar Zongo, Bolivia, during the 1997/98, El Nino year. *J. Glaciol.* 47, 21–28. doi: 10.3189/172756501781832593

Warren, C., and Sugden, D. (1993). The Patagonian icefields: a glaciological review. *Arctic Alpine Res.* 25, 316–331.

Weidemann, S., Sauter, T., Schneider, L., and Schneider, C. (2013). Impact of two conceptual precipitation downscaling schemes on mass-balance modeling of Gran Campo Nevado ice cap, Patagonia. *J. Glaciol.* 59, 1106–1116. doi: 10.3189/2013JoG13J046

Weidemann, S. S., Sauter, T., Kilian, R., Steger, D., Butorovic, N., and Schneider, C. (2018b). A 17-year Record of Meteorological Observations Across the Gran Campo Nevado Ice Cap in Southern Patagonia, Chile, Related to Synoptic Weather Types and Climate Modes. *Front. Earth Sci.* 6:53. doi: 10.3389/feart.2018.00053

Weidemann, S. S., Sauter, T., Malz, P., Jaña, R., Arigony-Neto, J., Casassa, G., et al. (2018a). Glacier mass changes of lake-terminating grey and tyndall glaciers at the southern patagonia icefield derived from geodetic observations and energy and mass balance modeling. *Front. Earth Sci.* 6:81. doi: 10.3389/feart.2018.00081

Welty, E., Zemp, M., Navarro, F., Huss, M., Fürst, J. J., Gärtner-Roer, I., et al. (2020). Worldwide version-controlled database of glacier thickness observations. *Earth Syst. Sci. Data Discuss.* (in press). doi: 10.5194/essd-2020-87

White, A., and Copland, L. (2015). Decadal-Scale Variations in Glacier Area Changes Across the Southern Patagonian Icefield Since the 1970s. *Arctic Antarctic Alpine Res.* 47, 147–167. doi: 10.1657/AAAR0013-102

Willis, M., Melkonian, A., Pritchard, M., and Rivera, A. (2012a). Ice loss from the Southern Patagonian Ice Field, South America, between 2000 and 2012. *Geophys. Res. Lett.* 39, L17501. doi: 10.1029/2012GL053136

Willis, M. J., Melkonian, A. K., Pritchard, M. E., and Ramage, J. M. (2012b). Ice loss rates at the Northern Patagonian Ice Field derived using a decade of satellite remote sensing. *Remote Sens. Environ.* 117, 184–198. doi: 10.1016/j.rse.2011.09.017

Wilson, R., Carrión, D., and Rivera, A. (2016). Detailed dynamic, geometric and supraglacial moraine data for Glaciar Pio XI, the only surge-type glacier of the Southern Patagonia Icefield. *Ann. Glaciol.* 57, 119–130. doi: 10.1017/aog.2016.32

Wilson, R., Glasser, N. F., Reynolds, J. M., Harrison, S., Iribarren Anacona, P., Schaefer, M., et al. (2018). Glacial lakes of the Central and Patagonian Andes. *Glob. Planet. Change* 162, 275–291. doi: 10.1016/j.gloplacha.2018.01.004

Worni, R., Stoffel, M., Huggel, C., Volz, C., Casteller, A., and Luckman, B. (2012). Analysis and dynamic modeling of a moraine failure and glacier lake outburst flood at Ventisquero Negro, Patagonian Andes (Argentina). *J. Hydrol.* 444–445, 134–145. doi: 10.1016/j.jhydrol.2012.04.013

Wouters, B., Gardner, A. S., and Moholdt, G. (2019). Global Glacier Mass Loss During the GRACE Satellite Mission (2002-2016). *Front. Earth Sci.* 7:96. doi: 10.3389/feart.2019.00096

Yarleque, C., Vuille, M., Hardy, D. R., Timm, O. E., De la Cruz, J., Ramos, H., et al. (2018). Projections of future disappearance of the Quelccaya, the largest tropical ice cap on Earth. *Nat. Sci. Rep.* 8:15564.

Zalazar, L., Ferri Hidalgo, L., Castro, M., Gargantini, H., Giménez, M., Pitte, P., et al. (2017). Glaciares de Argentina: Resultados Preliminares del Inventario Nacional de Glaciares. *Rev. Glac. Ecosist. Montaña* 2, 13–22.

Zamora, R. J., Uribe, J., and Rivera, O. A. (2017). "Ice thickness surveys of the Southern Patagonian Ice Field using a low frequency ice penetrating radar system," in *Proceedings of the First IEEE International Symposium of Geoscience and Remote Sensing (GRSS-CHILE)*, Valdivia, doi: 10.1109/GRSS-CHILE.2017.7996003

Zemp, M., Huss, M., Thibbert, E., and Cogley, J. G. (2019). Global glacier mass changes and their contributions to sea-level rise from 1961 to 2016. *Nature* 568:E9. doi: 10.1038/s41586-019-

Zimmer, A., Meneses, R., Rabatel, A., Soruco, A., and Anthelme, F. (2018). Time lag between glacial retreat and upward migration alters tropical alpine communities. *Perspect. Plant Ecol. Evol. Syst.* 30, 89–102. doi: 10.1016/j.ppees.2017.05.003

Conflict of Interest: The authors declare that the research was conducted in the absence of any commercial or financial relationships that could be construed as a potential conflict of interest.

Copyright © 2020 Masiokas, Rabatel, Rivera, Ruiz, Pitte, Ceballos, Barcaza, Soruco, Bown, Berthier, Dussaillant and MacDonell. This is an open-access article distributed under the terms of the Creative Commons Attribution License (CC BY). The use, distribution or reproduction in other forums is permitted, provided the original author(s) and the copyright owner(s) are credited and that the original publication in this journal is cited, in accordance with accepted academic practice. No use, distribution or reproduction is permitted which does not comply with these terms.

frontiers in Earth Science

ORIGINAL RESEARCH
published: 14 July 2020
doi: 10.3389/feart.2020.00292

Mountain Temperature Changes From Embedded Sensors Spanning 2000 m in Great Basin National Park, 2006–2018

Emily N. Sambuco[1], Bryan G. Mark[1], Nathan Patrick[2], James Q. DeGrand[1], David F. Porinchu[3], Scott A. Reinemann[4], Gretchen M. Baker[5] and Jason E. Box[6]*

[1] Department of Geography, The Ohio State University, Columbus, OH, United States, [2] California Nevada River Forecast Center, National Oceanic and Atmospheric Administration, National Weather Service, Sacramento, CA, United States, [3] Department of Geography, University of Georgia, Athens, GA, United States, [4] Geography, Sinclair Community College, Dayton, OH, United States, [5] Great Basin National Park, National Park Service, Baker, NV, United States, [6] Geological Survey of Denmark and Greenland, Copenhagen, NY, United States

Mountains of the arid Great Basin region of Nevada are home to critical water resources and numerous species of plants and animals. Understanding the nature of climatic variability in these environments, especially in the face of unfolding climate change, is a challenge for resource planning and adaptation. Here, we utilize an Embedded Sensor Network (ESN) to investigate landscape-scale temperature variability in Great Basin National Park (GBNP). The ESN was installed in 2006 and has been maintained during uninterrupted annual student research training expeditions. The ESN is comprised of 29 Lascar sensors that record hourly near-surface air temperature and relative humidity at locations spanning 2000 m and multiple ecoregions within the park. From a maximum elevation near 4000 m a.s.l. atop Wheeler Peak, the sensor locations are distributed: (1) along a multi-mountain ridgeline to the valley floor, located ∼2000 m lower; (2) along two streams in adjoining eastern-draining watersheds; and (3) within multiple ecological zones including sub-alpine forests, alpine lakes, sagebrush meadows, and a rock glacier. After quality checking all available hourly observations, we analyze a 12-year distributed temperature record for GBNP and report on key patterns of variability. From 2006 to 2018, there were significantly increasing trends in daily maximum, minimum and mean temperatures for all elevations. The average daily minimum temperature increased by 2.1°C. The trend in daily maximum temperatures above 3500 m was significantly greater than the increasing trends at lower elevations, suggesting that daytime forcings may be driving enhanced warming at GBNP's highest elevations. These results indicate that existing weather stations, such as the Wheeler Peak SNOTEL site, alone cannot account for small-scale variability found in GBNP. This study offers an alternative, low-cost methodology for sustaining long-term, distributed observations of conditions in heterogeneous mountainous environments at finer spatial resolutions. In arid mountainous regions with vulnerable water resources and fragile ecosystems, it is imperative to maintain and extend existing networks and observations as climate change continues to alter conditions.

Keywords: Great Basin, climate, mountain, warming, sensor network, lapse rate

OPEN ACCESS

Edited by:
David Glenn Chandler, Syracuse University, United States

Reviewed by:
Ulf Mallast, Helmholtz Centre for Environmental Research (UFZ), Germany
Scotty Strachan, University of Nevada, Reno, United States

***Correspondence:**
Bryan G. Mark
mark.9@osu.edu

Specialty section:
This article was submitted to Hydrosphere, a section of the journal Frontiers in Earth Science

Received: *01 November 2019*
Accepted: *23 June 2020*
Published: *14 July 2020*

Citation:
Sambuco EN, Mark BG, Patrick N, DeGrand JQ, Porinchu DF, Reinemann SA, Baker GM and Box JE (2020) Mountain Temperature Changes From Embedded Sensors Spanning 2000 m in Great Basin National Park, 2006–2018. Front. Earth Sci. 8:292. doi: 10.3389/feart.2020.00292

INTRODUCTION

Great Basin National Park (GBNP) comprises a mid-latitude, semi-arid mountain landscape, where sharp vertical gradients underscore the vitality of water access and where biophysical indicators record the impacts of past and present climate change on Park ecosystems (Porinchu et al., 2007; Reinemann et al., 2009). The Great Basin desert region stretches between the Sierra Nevada Range in California and the Wasatch Mountain Range in Utah, encapsulating North America's largest number of contiguous, endorheic watersheds, and numerous mountain ranges. The topography is shaped by regional uplift and extensional tectonics dating to the Cenozoic that resulted in N-S faulting up-thrusted mountain ranges bounding flat valleys characteristic of the "Basin and Range" landscape, wherein Nevada contains the largest number of mountain ranges of all States in the United States (Dickinson, 2006).

Concerns for this region and ongoing climate changes center on the vertically distributed biodiversity and available ecosystem services, particularly water. Lying in the Sierra Nevada rain shadow, the Great Basin region receives limited annual precipitation, with orographic processes resulting in most precipitation falling in the form of snow, which provides critical meltwater to streams during spring and summer (Wise, 2012). Total annual snowfall at high elevations can reach 6–9 m (Baker, 2012). The mountains thus provide a source of water to the arid basins, comprising literal water towers. This landscape has experienced notable hydroclimate variability during the late Quaternary, with highlands shaped by glaciation (Osborn and Bevis, 2001) and basins filled with pluvial lakes, e.g., Bonneville and Lahontan (Reheis et al., 2014). There is also a noticeable imprint of human intervention in the regional hydrology as intensifying groundwater use and a proposed pipeline to transport groundwater from the Snake Valley aquifers to rapidly expanding urban development in Las Vegas comprises a legal transboundary apportionment precedent (Hall and Cavataro, 2013; Masbruch, 2019).

Previous observational studies have documented warming trends over the 20th century in the Great Basin region consistent in magnitude and pattern with an enhanced greenhouse effect. Using records from 93 COOP weather stations spanning the Great Basin from California to Utah, Tang and Arnone (2013) identified a +1°C increase in annual average daily mean temperature characterized the region between 1901 and 2010. This warming featured asymmetry in diurnal patterns, with the more rapid increase in daily minimum temperature contributing to a decrease in the diurnal range of 0.8°C. The asymmetry in the diurnal patterns occurred in all seasons but was most pronounced in the winter. The trend in monthly averaged daily maximum temperatures remained insignificant in all seasons, excepting the most recent five decades that show significant increasing trends in daily maximum temperature during the spring and summer. Similarly, the number of frost days and cool nights per year declined, while numbers of warm nights increased.

Globally, these mountain environments have been shown to be potentially more vulnerable to changes since warming seems to be enhanced at elevation (Diaz and Bradley, 1997; Pederson et al., 2010; Rangwala and Miller, 2012; Pepin et al., 2015; Wang et al., 2016; Minder et al., 2018; Palazzi et al., 2019; Williamson et al., 2020). Nevertheless, monitoring is hampered by the lack of distributed and continuous observations. Near-surface lapse rates are not commonly described by in-situ measurements. Instrumental observations from the Great Basin region are relatively sparse. New instruments have been established, such as the NevCAN (McEvoy et al., 2014), but often gridded products are relied upon (e.g., PRISM).

In an effort to document changes and microclimatic variability at the landscape scale and examine if the hypothesized elevation dependent warming seen in mountains globally is evidenced in the Great Basin, we installed an Embedded Sensor Network (ESN) comprising multiple temperature logging instruments distributed over a range of elevations. We have maintained this network during annual visits to GBNP with undergraduate and graduate students as part of an educational research experience we have entitled, "GBEX (Great Basin Expedition)." Here we present findings collected from over a decade of hourly temperature observations (2006–2018). We aim to: present our ESN and evaluate the data quality; summarize and describe the seasonal to annual distributions of temperatures at different elevations and topographic settings; and explore multi-annual trends in our dataset. Specifically, we report on how consistently our ESN instrumentation resolves temperature variability relative to nearby weather stations and compare our observations with regional gridded climate data to examine emergent patterns of elevation-dependent variability.

STUDY SITE

Great Basin National Park (39°N, 114°W) is located in the Snake Mountain Range in sparsely populated eastern Nevada. The Park encloses a landscape that ranges in elevation from ∼1500 m to ∼4000 m a.s.l., culminating at the highest point of Wheeler Peak (3958 m a.s.l.), and features asymmetric hypsometry with notable geological and ecological diversity (**Figure 1**). Average year-round temperature in GBNP varies between 11 and 14°C (Baker, 2012) with large annual, seasonal and diurnal temperature ranges. The dominant surface weather conditions across the Great Basin are strongly modified by topography, resulting in diverse environments spanning vertical gradients (Tang and Arnone, 2013). The Snake Range region experiences winter-dominated precipitation, while occasional summer monsoonal convection brings a second maximum (Mensing et al., 2013). The Snake Range also sits at a transition zone in the Great Basin, and more broadly the western United States, characterized by a strong winter precipitation dipole (Wise, 2010). The precipitation dipole is typified by a north to south seesaw pattern of winter precipitation in the western United States, centered around 40°N latitude and controlled primarily by the El Niño Southern Oscillation (ENSO) and the Pacific Decadal Oscillation (PDO) (Brown and Comrie, 2004; Wise, 2010). Wise (2010) delineates a transition zone in the central Great Basin that separates winter precipitation maxima in the northern Great Basin from the

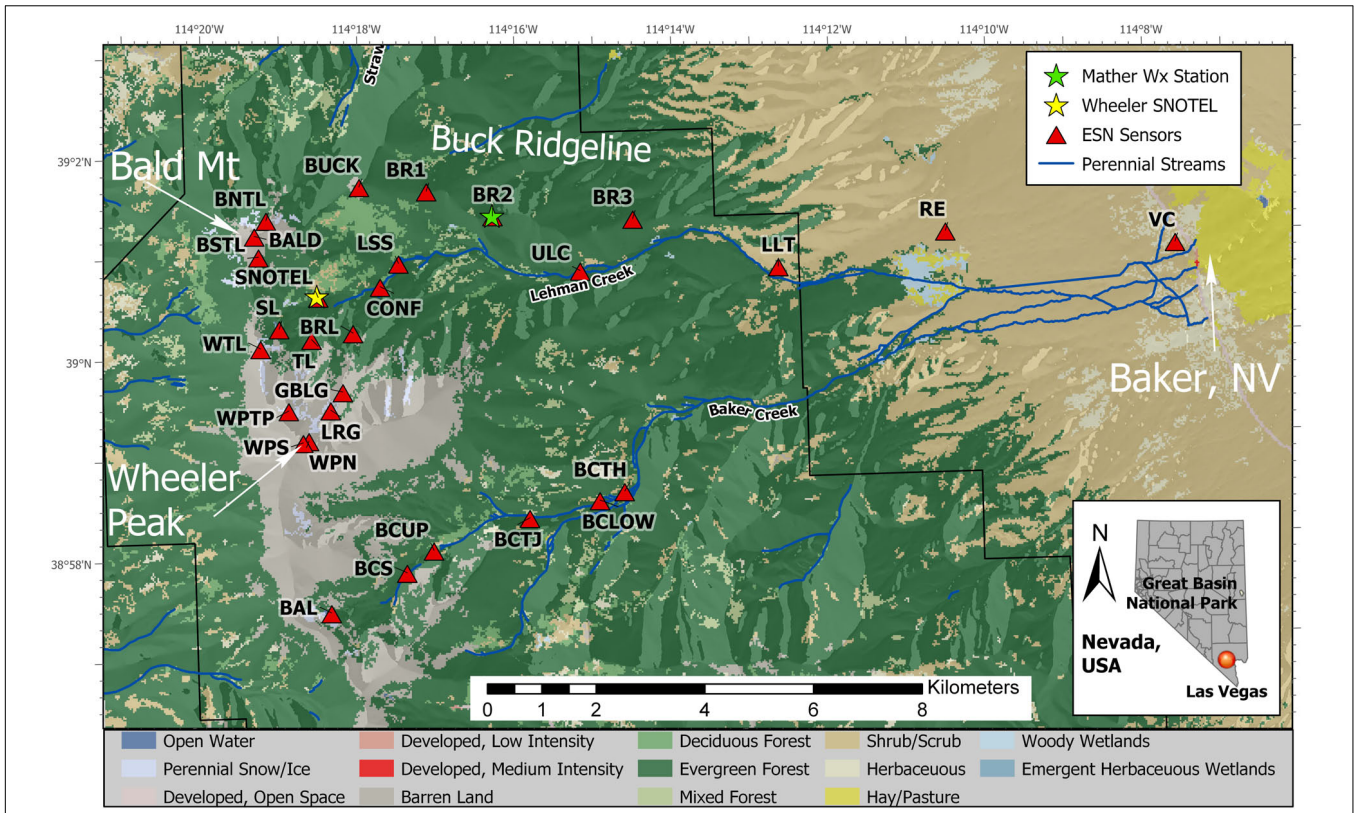


FIGURE 1 | Hillshade map of GBNP illustrating sensor locations along Lehman and Baker creeks below Wheeler Peak. Colors depict landcover type, identified in key. Nearby weather stations, location of Baker, NV (nearest town) and general stream hydrography are also illustrated. Sensors are identified by codes relating to **Table 1** and **Figure 2**. Location of GBNP and Las Vegas (red circle) are shown in inset map of Nevada.

summer precipitation maxima in the southern Great Basin. The region is prone to cold air pooling in valley locations due to stable nighttime boundary layer conditions (Lundquist et al., 2008; McEvoy et al., 2014). Perennial snow cover is present throughout the higher elevations in GBNP and typically remains throughout the spring and summer, melting and feeding the park's stream systems. Due to the arid, high-desert climate, daily and seasonal temperatures experience extreme fluctuations. On average, the Great Basin region experiences annual average temperature of 8.6°C, maximum temperature of 14.9°C, and minimum temperature of 2.3°C. Mean precipitation reaches ∼36 cm annually based on the most recent Climate Normal (1981–2010) (WRCC, 2019).

The steep elevation-related gradients in temperature and precipitation define ecological zones and influence the composition of the diverse biotic communities, with the eastern drainages of Lehman and Baker Creeks having more gradual elevation gradients and larger basins than the west (Baker, 2012). Microclimate heterogeneity within this complex terrain defines niches for vegetation responding to climate variables (Ford et al., 2013). Likewise, heterogeneous vegetation communities exert a coupled feedback within such areas of complex terrain, influencing local climate (Beniston, 2003; Ford et al., 2013; Xiang et al., 2014; Mutiibwa et al., 2015; Strachan et al., 2016; Devitt et al., 2018). Within GBNP, cold desert scrub and salt flats can be found at the lowest elevations. Above the valley floor, sagebrush meadows and open grasslands transition to Pinyon Pine and Juniper stands. Above this arid zone, a montane forest consisting of mixed conifer species and aspen groves is found; many of the park's hydrologic features, such as riparian zones and alpine lakes are also located in this zone. Subalpine forest is found above the montane forest, above which subalpine tree species transition to a rocky, exposed alpine environment in the highest reaches of the park. The Park is also home to unusual geologic features, including the Wheeler Peak Rock Glacier and an extensive limestone cave system (Baker, 2012).

MATERIALS AND METHODS

Embedded Sensor Network (ESN) and Data Quality Control

The ESN was initiated during GBEX excursions in 2005 and 2006. At this time, a series of Lascar EL-USB-2 temperature and humidity micro-loggers within identical radiation shields ("beehives") were emplaced at locations spanning a 2000 m elevation range in GBNP (**Figure 2**, **Table 1**). Lascars are stand-alone data loggers that can record more than 16,000 temperature readings over a −35 to +80°C (−31 to +176°F) range, with an internal resolution of 0.5°C. They are powered with 3.6V batteries

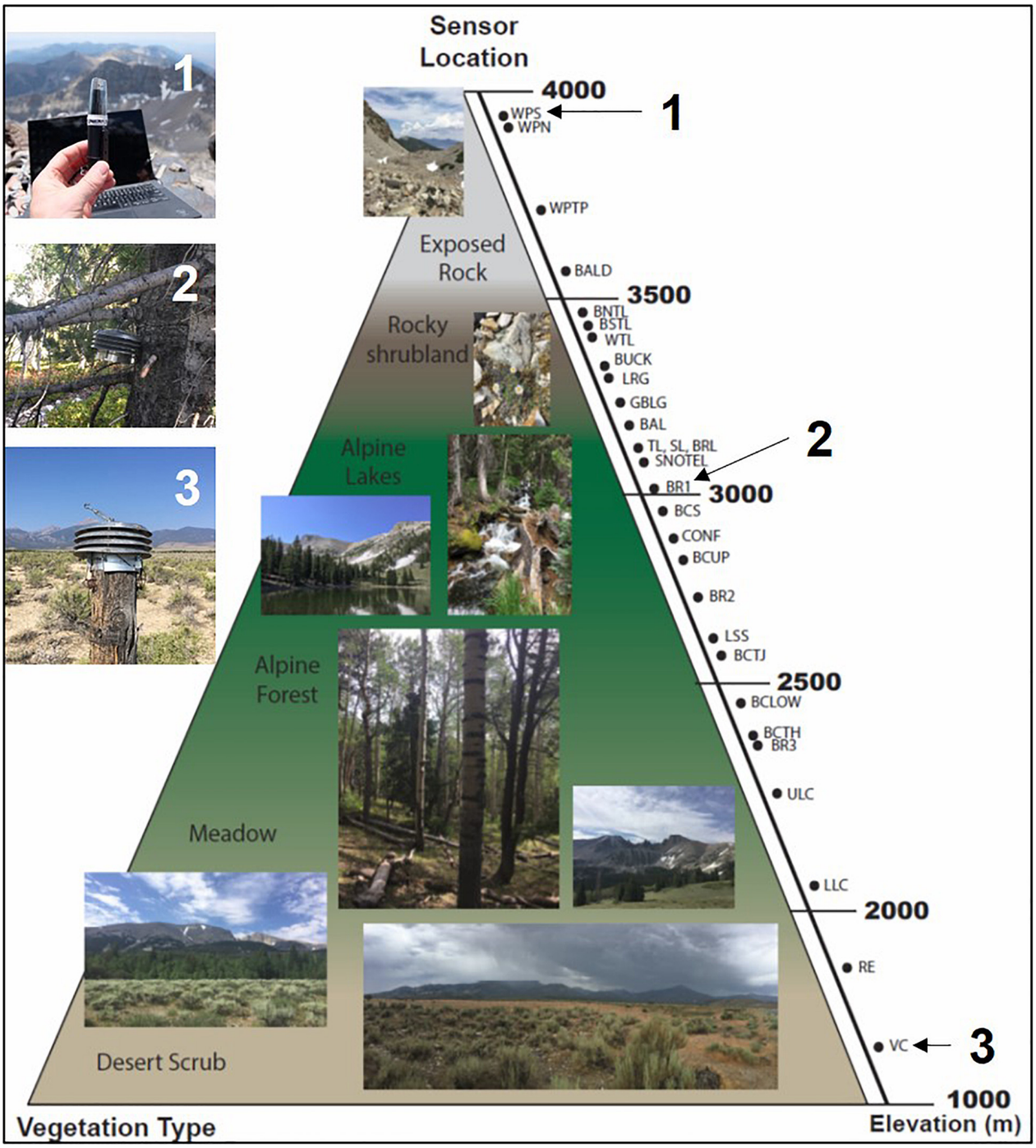


FIGURE 2 | Vertical schematic representing the ESN sensor location by elevation and ecosystem. Numbered panels show Lascar radiation shields for three locations, also identified by number and elevation: (1) WPS, 3976 m a.s.l.; (2) BR1, 3034 m a.s.l; and (3) VC, 1639 m a.s.l.

that are replaced annually. Sensor locations were selected based on the following criteria: (1) accessibility for continued sensor maintenance; (2) proximity to prominent features of interest, such as alpine lakes, the Wheeler Peak Rock Glacier in the Lehman Creek watershed, hereafter the Lehman Rock Glacier (LRG), and the NPS Visitor Center; and (3) the establishment of ridge and valley transects capturing notable topographic variation. Three transects were established: along the Lehman Creek stream valley floor to the alpine lakes (Brown, Teresa, and Stella Lakes); along the Baker Creek trail to Baker Lake; and along the exposed Buck Ridgeline. Sensors were also placed at upper treeline limits and summits of both Wheeler Peak

TABLE 1 | Sensor Information table, including site name, site ID, elevation, coordinates, mounting location, surrounding area, and local ecosystem type corresponding to **Figures 1**, **2**.

Site name	Site ID	Elevation (m)	Latitude (°)	Longitude (°)	Mounting location	Surrounding area	Local ecosystem
NPS visitor center	VC	1639	39.01475	−114.12753	Post	Scrub	Salt desert scrub
Ranch exhibit	RE	1832	39.01768	−114.17623	Tree	Scrub	Salt desert scrub/Mountain scrub
Lehman lower treeline	LLT	2045	39.01262	−114.21190	Tree	Scrub	Pinyon-Juniper forest/Mountain scrub
Upper lehman campground	ULC	2339	39.01288	−114.25399	Tree	Stream	Pinyon-Juniper forest
Buck ridge 3	BR3	2397	39.02123	−114.24253	Tree	Trees	Pinyon-Juniper forest
Baker creek near trailhead	BCTH	2411	38.97617	−114.24595	Tree	Stream	Mountain scrub
Baker creek lower snow course	BCLOW	2479	38.97480	−114.25125	Tree	Meadow	Montane forest
Baker creek near trail junction	BCTJ	2649	38.97220	−114.26622	Tree	Stream	Mixed conifer/aspen forest
Lehman spring	LSS	2692	39.01495	−114.29252	Tree	Trees	Mixed conifer/aspen forest
Buck ridge 2	BR2	2826	39.02234	−114.27226	Tree	Trees	Pinyon-Juniper Forest
Baker creek upper snow course	BCUP	2898	38.96728	−114.28678	Tree	Meadow	Mixed conifer/aspen forest
Dead lake	DEAD	2915	38.93553	−114.27422	Tree	Lake	Montane forest
Lehman creek confluence	CONF	2923	39.01119	−114.29657	Tree	Stream	Deciduous forest
Baker creek stream	BCS	2968	38.96372	−114.29260	Tree	Stream	Mixed conifer/aspen forest
Buck ridge 1	BR1	3034	39.02679	−114.28618	Tree	Trees	Mixed conifer/aspen forest
Wheeler SNOTEL	SNOTEL	3093	39.00970	−114.30977	Tree	Trees	Mixed conifer/aspen forest
Brown lake	BRL	3105	39.00364	−114.30259	Tree	Lake	Sub-alpine forest
Stella lake	SL	3122	39.00465	−114.31823	Tree	Lake	Sub-alpine forest
Teresa lake	TL	3131	39.00275	−114.31144	Tree	Lake	Sub-alpine forest
Baker lake	BAL	3213	38.95740	−114.30887	Tree	Lake	Sub-alpine forest
Grove below lehman glacier	GBLG	3255	38.99392	−114.30512	Tree	Rock	Alpine tundra/Coniferous forest
Lehman rock glacier	LRG	3332	38.99088	−114.30787	Post	Rock	Alpine tundra
Buck mountain summit	BUCK	3346	39.02783	−114.30043	Post	Trees/rock	Alpine tundra/Coniferous forest
Wheeler treeline	WTL	3413	39.00145	−114.32232	Tree	Trees/rock	Coniferous forest
Bald mtn south treeline	BSTL	3423	39.01665	−114.32221	Tree	Trees/rock	Alpine tundra/Coniferous forest
Bald north treeline	BNTL	3439	39.02272	−114.32039	Tree	Trees/rock	Alpine tundra/Coniferous forest
Bald mtn Wx station	BALD	3516	39.02013	−114.32298	Post	Rock	Alpine tundra
Wheeler peak tundra plateau	WPTP	3696	38.99103	−114.31672	Post	Rock	Bare rock/ground
Wheeler peak north	WPN	3965	38.98603	−114.31261	Rock	Rock	Bare rock/ground
Wheeler peak south	WPS	3976	38.98571	−114.31389	Rock	Rock	Bare rock/ground

and Bald Mountain. Since 2006, the ESN has evolved through expansion, replacement of sensors when lost and ongoing sensor maintenance. The network currently has sensors at 29 locations in the park, with the majority of sensors providing more than 10 years of hourly near-surface temperature data. Unit costs of the Lascars and radiation shields are <$100 each, and annual costs to keep the network running include travel for a small crew from Ohio for a week of camping. The sensors are visited

annually during the late summer for data recovery and routine maintenance or replacement when needed. Detailed information regarding sensor locations is provided in the **Supplementary Material**. While the diverse sensor locations introduce inherent sources of variability in temperatures, individual sensor sites were held constant over the entire span of observations.

In 2010, we performed an in-situ relative calibration comparison in GBNP at a calibration elevation of ∼3048 m a.s.l. to assess the performance and dependability of the Lascars (Patrick, 2014). Thirteen new unused Lascars were deployed and co-located alongside two Campbell Scientific T107, two Campbell Scientific HMP45C and two thermocouple fine wire probes in identical radiation shield beehives. Nine hundred sixty synchronous 1-min temperature observations captured daily maximum and daily minimum temperatures. A combination of Student-t tests and Kruskal-Wallis tests were used to test null hypotheses that mean temperatures were equal among the sensors for both 1-min observations and aggregated hourly values.

Following the relative calibration, we deployed ten of the thirteen new Lascars alongside existing Lascars in the ESN at a broad sample of locations spanning elevations from 1639 to 3131 m a.s.l. to test sensor drift from August 2010 – August 2011. Student-t tests were used to test the null hypothesis of equal mean temperatures at each of the ten locations for hourly pairs and aggregated days.

We compiled all the hourly temperatures from the ESN and conducted all analyses using R (R Core Team, 2018). To maintain consistency throughout the study period, we standardized the time for all Lascar measurements to UTC, unless otherwise noted. We used the standard statistical outlier definition to identify outliers as any observation exceeding 1.5*IQR (Interquartile Range). We removed all outliers exceeding a 0.1% proportion of the dataset.

We addressed an additional source of potential sensor error resulting from the variable snow accumulation that characterizes GBNP annually. Higher elevations commonly receive substantial amounts of winter snow that can persist into the late spring or early summer. Lascar sensors were situated approximately 1.5 m above the ground surface (within trees and atop wooden stakes) as an initial approach to avert burial of the sensor by snow. However, given evidence of snow burial in some sensors, we employed a conservative data evaluation approach after downloading Lascars to determine if and when sensors were compromised due to snow burial. We developed an algorithm to identify any sensor observations meeting all of the following criteria: (1) relative humidity surpassing 95%; (2) temperature at or below 0°C; and (3) a diurnal temperature range less than 5°C. All temperature observations meeting the above criteria were assumed to have been influenced by snow burial and were removed from the sensor dataset.

ESN Validation With Comparative Data

Since confounding factors (e.g., snow-cover, sensor malfunction) could potentially influence the accuracy of Lascar sensor temperature measurements in the field, we validated sensor measurements by comparing to simultaneously collected temperature data from nearby calibrated weather stations within GBNP.

Wheeler Peak SNOTEL: We obtained data from the Wheeler Peak SNOTEL site (number 1147) through the U.S. Department of Agriculture (USDA) Natural Resources Conservation Service online portal[1]. The site was established by the National Water and Climate Center and has been reporting data since October 1, 2010. This site records accumulated precipitation, snow depth, snow water equivalent, air temperature, soil moisture and soil temperature aggregated to daily time steps and controlled for quality assurance. The site is located on the eastern slope below Wheeler Peak at an elevation of 3066 m a.s.l. Temperature is recorded with a shielded thermistor with 0.1°C precision.

Mather Weather Station (MWx): We procured additional data from GBNP's Mather Remote Automatic Weather Station (RAWS; NWS Location ID MTHN2), located near the Mather Overlook area. The weather station data were obtained using Iowa State University's Iowa Environmental Mesonet (IEM) Data Download Server[2]. The station is located at an elevation of about 2750 m a.s.l, overlooking the Lehman Creek watershed as it tracks eastward from Wheeler Peak. MWx records air temperature, liquid precipitation, wind direction and speed, relative humidity, and total downward solar radiation, with data available from 2002.

We made direct comparisons of recorded temperatures between the meteorological stations and the nearest Lascar sensor from the ESN. An ESN Lascar sensor is located within ∼10 m of the Wheeler SNOTEL Site (S1147). Both S1147 and the Lascar sensor have a common period of temperature observations extending from 2012-08-16 to the present. We obtained daily S1147 temperature data to compare to daily Lascar data. We used a non-parametric Wilcoxon signed-rank test to compare paired samples of Tmean, Tmin, and Tmax from both sensors. This test determines whether two dependent samples are selected from populations having the same distribution and provides significance levels. We also employed this method while comparing Lascar sensor data to the nearby MWx, which is located less than 5 m away from one of the Buck Ridgeline lascar sensors (BR2) and records temperature and humidity observations. Using the same statistical testing, we compared daily statistics, Tmean, Tmin, and Tmax, between the BR2 and MWx sensors.

PRISM precipitation and temperature normals: To explore continuity with long-term observations, we used vertically interpolated climate data from the Parameter-elevation Relationships on Independent Slopes Model (PRISM) (PRISM Climate Group, Oregon State University[3]). PRISM assumes that for a local region, elevation is the most significant influence on climate parameters. PRISM incorporates nearby meteorological station data to generate a local regression function for the climatological variable of interest. PRISM aims to parameterize the physiographic complexity of the Earth's surface through a series of interpolation methods. PRISM makes use of point

[1]http://www.wcc.nrcs.usda.gov/snow/

[2]https://mesonet.agron.iastate.edu/request/dcp/fe.phtml?network=NV_DCP

[3]http://prism.oregonstate.edu

station data, Digital Elevation Models (DEMs), other spatial data sets, and an encoded spatial climate knowledge base to produce a gridded dataset of the distribution of climate variables (Daly et al., 2008). We used R and PRISM (Hart and Bell, 2015) to obtain 30-year Climate Normals for Tmean, Tmin, Tmax, and precipitation from the nearest 800 m PRISM grid cell containing ESN Lascar locations within GBNP. We used these PRISM normals as both supplementary precipitation information and a basis for comparison with the ESN.

We compared the PRISM 30-year monthly temperature normals to ESN sensor data for Lascar sites (n = 20) with continuous monthly records spanning longer than 10 years. We compared sensor data using root mean square error (RMSE) and mean absolute error (MAE) calculations in Metrics (Hamner and Frasco, 2018). We also calculated monthly, annual, and decadal Tmean anomalies as observational data minus predicted values (i.e., PRISM 30-year normals subtracted from ESN monthly Tmean observations).

Compiling ESN Climatologies and Near-Surface Lapse Rates Analysis

We calculated summaries for all 29 sensor locations for all data in the 2006–2018 interval that passed our quality control screening using the criteria described above. First, we calculated daily temperature statistics using hourly sensor data. Only sensors with 24 h observations per day were incorporated into these daily statistics; we calculated daily Tmean as the average temperature of all 24 daily observations, while we calculated Tmin and Tmax as the minimum and maximum hourly temperatures recorded for the day, respectively. Then, we computed monthly statistics, but only for sensors encompassing greater than or equal to 25 daily summaries per month. We defined seasonal aggregations, using the months December–February as winter, March–May as spring, June–August as summer, and September–November as fall. We incorporated only sensors with greater than 2 monthly observations per season into the overall seasonal averages. For annual averages, we limited our calculations to sensors having 11 months or more of measurements available.

To quantify the known impact of elevation on temperature, we computed near-surface lapse rates using the ESN, incorporating only sensors containing full records of observations during our selected interval (n = 20). We developed a simple linear model using temperature as the dependent variable and elevation as the independent predictor variable. We calculated Tmean, Tmin, and Tmax lapse rates at daily, monthly, seasonal, and annual timescales, assuming a significance level of p-value < 0.05. Additionally, we explored the extent to which topographic positioning of the sensors impact temperature regimes by contrasting seasonal Tmean lapse rates (using average Tmean values for January and July) for sensors located along an interfluve (Buck Ridgeline) against those along the stream valleys of both Lehman and Baker Creeks. For reference, the Buck Ridgeline is aligned with the crest that connects Bald and Buck Mountains and descends toward the northeast, delineating the northern boundary of the Lehman watershed (**Figure 1**). Each of these transects includes at least four loggers hung in trees spanning >750 m.

Analysis of Temperature Trends and Landscape Variability

We analyzed decadal trends from daily, monthly and annual temperature aggregations by using simple linear regression, testing for significance. Additionally, we decomposed temperature time series data from selected sensors to explore systematically seasonal and trend components. To determine statistical significance of hypothesized temperature variations caused by local factors within the ESN, we used the non-parametric Kruskal-Wallis Test (Kruskal and Wallis, 1952) followed by a *post hoc* Dunn Test (Dunn, 1964) to determine specific differences between sites. Initially, we conducted this test using elevation as the independent predictor group. Then, we grouped ESN sensors to analyze the influence of relative landscape positioning on temperature regimes. We made three specific tests to examine: (1) aspect influences atop Wheeler Peak and Bald Mountain; (2) exposure influences along the Buck Ridgeline; and (3) hydrological influences in and around riparian zones.

RESULTS

Sensor Quality Validation

The 2010 instrument inter-comparisons between Lascars and Campbell sensors showed that with respect to 1 min temporal resolution, the null hypothesis was rejected by the Lascars but upheld by the HMP45C and T107 sensors. For the aggregated hourly samples, the Kruskal Wallis test affirmed the null hypothesis of equal mean hourly temperatures for all sensors. As a collective group, the thirteen Lascars had an hourly p-value of 0.996. Differences among the Lascars were within manufacturer specifications of internal resolution, typical error and maximum error. For the year-long paired Lascar tests, at the hourly temporal resolution, five locations affirmed the null hypothesis and five locations rejected the null hypothesis. At the daily temporal resolution, all locations affirmed the null hypothesis with computed p-values ranging from 0.194 to 0.819. Based on the results of the relative calibration and drift study we found non-significant sensor drift had taken place within the ESN and results were within manufacturer specifications. These results confirm that the Lascars are reliable for analyses at a daily temporal resolution or greater.

Of all sensor observations, fewer than 1% were filtered out according to quality control criteria. Fewer than 0.1% of all observations failed to meet acceptable outlier thresholds. Similarly, 0.7% of downloaded data failed the test for being possibly covered by snow and were removed from subsequent analyses.

Lascar temperatures demonstrated close parity with the daily temperature distributions at the SNOTEL site. The Lascar observations were not significantly different from those of S1147, and comparisons of all three daily temperature statistics (Tmean, Tmin, and Tmax) revealed p-values well below the 0.05 threshold.

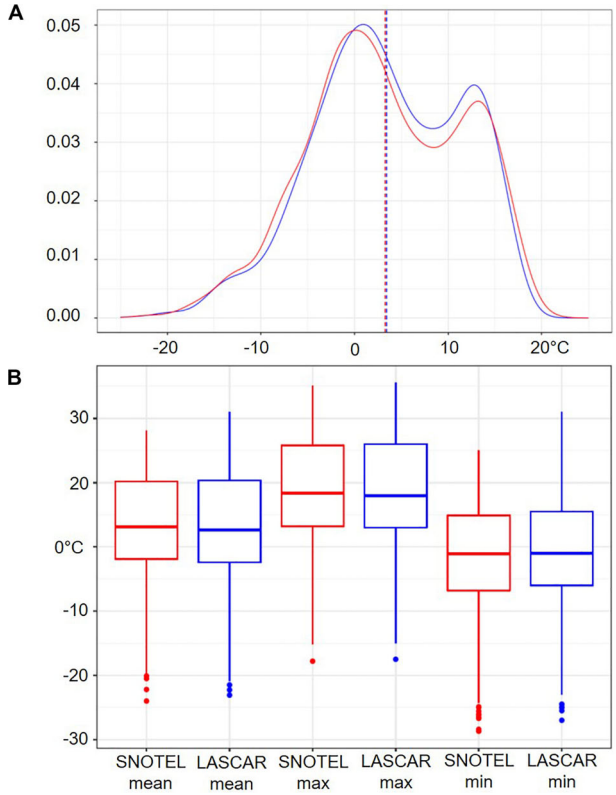


FIGURE 3 | (A) Density plot comparing daily Tmean of Lascar sensor (blue) and S1147 sensor (red). Mean values of each distribution are illustrated with a dashed line. **(B)** Boxplot illustrating Tmean, Tmin, and Tmax recorded by the sensors. Sensor values are depicted in blue and red for the Lascar and S1147, respectively.

Temperature distributions from both sensors were similar in bimodal pattern and spread (**Figure 3A**). Distributions of Tmean, Tmin, and Tmax had nearly similar sample mean values, with Lascar Tmean observations occurring with higher frequency in the mid-range of temperatures relative to S1147 (**Figure 3B**).

No significant difference was noted between the MWx and the BR2 Lascar observations for Tmean, Tmin, and Tmax and average RH. All comparisons resulted in *p*-values less than 0.05. The correspondence between the MWx and the BR2 Lascar observations was strongest for Tmean, with a correlation coefficient greater than 0.99 (**Figure 4A**). BR2 and MWx are located at a similar height above the ground surface and both sites are surrounded by vegetation of similar density and structure. Monthly values between sensors are highly correlated and are characterized by low MAE and RMSE values (**Figure 4B**).

Monthly Tmean from BR2 and MWx were compared to PRISM-derived monthly Tmean to determine if a significant deviation from 30-year average exists (**Figure 4C**). The lowest MAE and RMSE values (0.0024 and 0.0028, respectively) exist between the BR2 and MWx monthly Tmean. Comparing the BR2 and MWx with PRISM normals results in similar MAE and RMSE values. A MAE of 1.7315 and RMSE of 2.0995 were found between BR2 and PRISM normals. A MAE of 1.7312 and RMSE of 2.0991 were found between MWx and PRISM normals. This suggests that both the BR2 and MWx observations of local near-surface temperature and humidity are consistent and provides support for the robustness of Lascar observations.

As an additional check on consistency, we compared mean temperatures from the 20 ESN sensors with enough data to compute monthly statistics with the PRISM 30-year normals. Monthly, annual, and decadal Tmean anomalies were calculated as observational data minus predicted values (i.e., PRISM 30-year normals subtracted from ESN monthly Tmean observations). Comparison between annual average temperatures revealed small deviations between ESN data and PRISM normals (**Supplementary Figure 1**). All ESN Tmean measurements (monthly and annual) tracked closely with the 800 m resolution PRISM normals (monthly and annual). When averaged over the past decade, no anomalies exceeded ± 2.5°C and 60% had decade-averaged Tmean anomalies less than ± 1°C. Most sites indicated no significant difference between PRISM normals and ESN Tmean values (85%; p-value < 0.05).

Sensor Climatologies and Near-Surface Lapse Rates

The ESN features large contrasts (>15°C range in Tmean) in temperature across GBNP that conform to elevation and surface environmental conditions (**Figure 5**). While individual sensor records depict similar ranges of temperature, there is a discernible decrease in Tmean with increasing elevation. There is increased variability and a greater number of outliers associated with higher elevation sites or sites located on rocky exposures subjected to additional snow cover. Temperature distributions show consistent contrasts between seasons, with a temperature consistency (narrower histograms) occurring in summer and winter (**Figure 6**). Temperature distributions across GBNP indicate strong bi-modal patterns, due to extreme seasonal shifts. Temperature variability is enhanced during spring and fall. The most extreme temperature shift occurs in fall, with temperatures ranging from above 20°C to well below 0°C.

From 2006 to 2018, GBNP experienced an average near-surface lapse rate of 5.81°C/km. GBNP experiences steepest near-surface temperature lapse rates in the spring, although summer Tmax lapse rates are largest in magnitude (**Table 2**). Winter lapse rates are less steep, with less than 4°C decrease in Tmean per km. Only summer Tmean lapse rates approached the average environmental lapse rate of 6.5°C/km. Summer lapse rates contain the largest range, with a 4.5°C/km difference between Tmin and Tmax. Winter lapse rates exhibit a reduced range between Tmin and Tmax equal to 2.6°C/km.

The near-surface Tmean lapse rates along the more exposed Buck Ridgeline interfluve were steeper and more seasonally contrasting than those along the stream valleys of Lehman and Baker creek. For the Buck Ridgeline, the average July Tmean lapse rate was 8.7°C/km and the average January Tmean lapse rate was 5.1°C/km. In contrast, these values for the stream valleys in July and January, respectively, were 5.3 and 4.3°C/km along Lehman Creek and 5.3 and 3.4°C/km along Baker Creek.

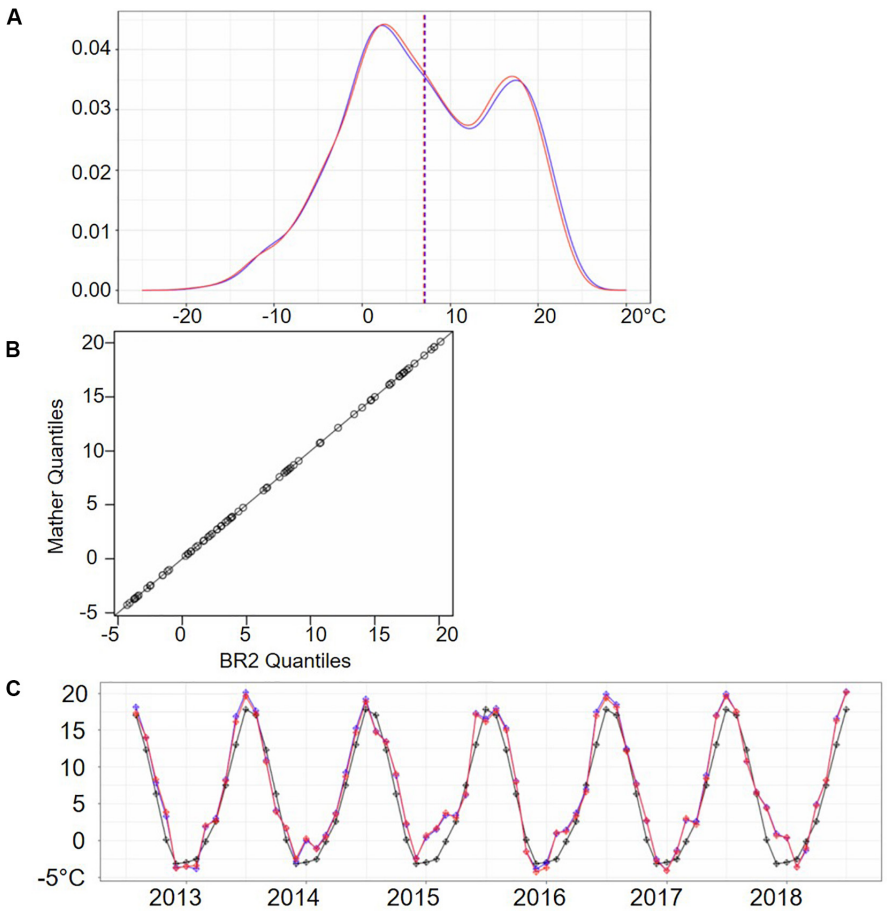


FIGURE 4 | (A) Density plot comparing daily T_{mean} of Lascar sensor (blue) and MWx Station sensor (red). Mean values of each distribution are shown with dashed line. **(B)** Q-Q plot displaying monthly T_{mean} from MWx data and the BR2 Lascar sensor. Line displays 1:1 value ratio. **(C)** Monthly T_{mean} timeseries from 2012 to 2018, depicting monthly values for BR2 sensor (blue), MWx Station (red), and PRISM 30-year normals (black). Deviations in the BR2 and MWx trends correspond to the PRISM 30-year normals.

Decadal Temperature Trends

There is a significant increasing trend in annual temperature anomalies throughout GBNP (i.e., ESN deviations from PRISM 30-year normals) from 2006 to 2018. When averaged over the year and incorporating all sensors with continuous data, monthly Tmean is shown to have significantly deviated from the 30-year normal value over the past decade. Anomalies were incorporated into a simple linear model, yielding an averaged increased anomaly of 0.128°C per year ($p < 0.000001$). Out of 20 calculated ESN anomaly trends (**Figure 7**), 18 sensors indicated significant increases in temperature anomalies over the last decade ($p < 0.05$). The WTL and SNOTEL sensors also document increasing trends in temperature, but these trends were not significant. Our decomposition of the monthly time series showed clear seasonal patterns that vary by sensor, as well as trend components (**Supplementary Figure 2**).

Overall, average daily Tmin in GBNP has increased by 2.06°C between 2006 and 2018. Daily Tmean and Tmax have increased by 1.95 and 1.39°C, respectively. Daily temperature range has decreased by 0.47°C on average. Tmean, Tmin, and Tmax at all sites, excluding Lehman Rock Glacier (LRG), experienced increasing rates of temperature change during the study period (**Figure 8**). At LRG, Tmax decreased by more than 1°C since 2006, contrary to the slight increase in Tmin at that site. Generally, the ESN sensors document larger rates of increase in Tmin (blue, **Figure 8**) than in Tmax (red, **Figure 8**), consistent with literature highlighting nighttime warming.

In contrast, the sensors in our ESN located above the tree line (**Figure 1**) show a reversed warming signal. BALD, WPN, and WPS show greater increases in Tmax than in Tmin. In addition, BALD has experienced the greatest rate of temperature change in the ESN. These are the most exposed sensors in the ESN: the sensors are mounted atop wooden poles and fastened to rocky outcrops.

It should be noted that, due to the variation in exposure to insolation by sensor installation (**Figure 1**), there are limitations when drawing significant conclusions between contrasting sensors. To evaluate this effect, we grouped sensors together according to installation type and height from ground. Tree

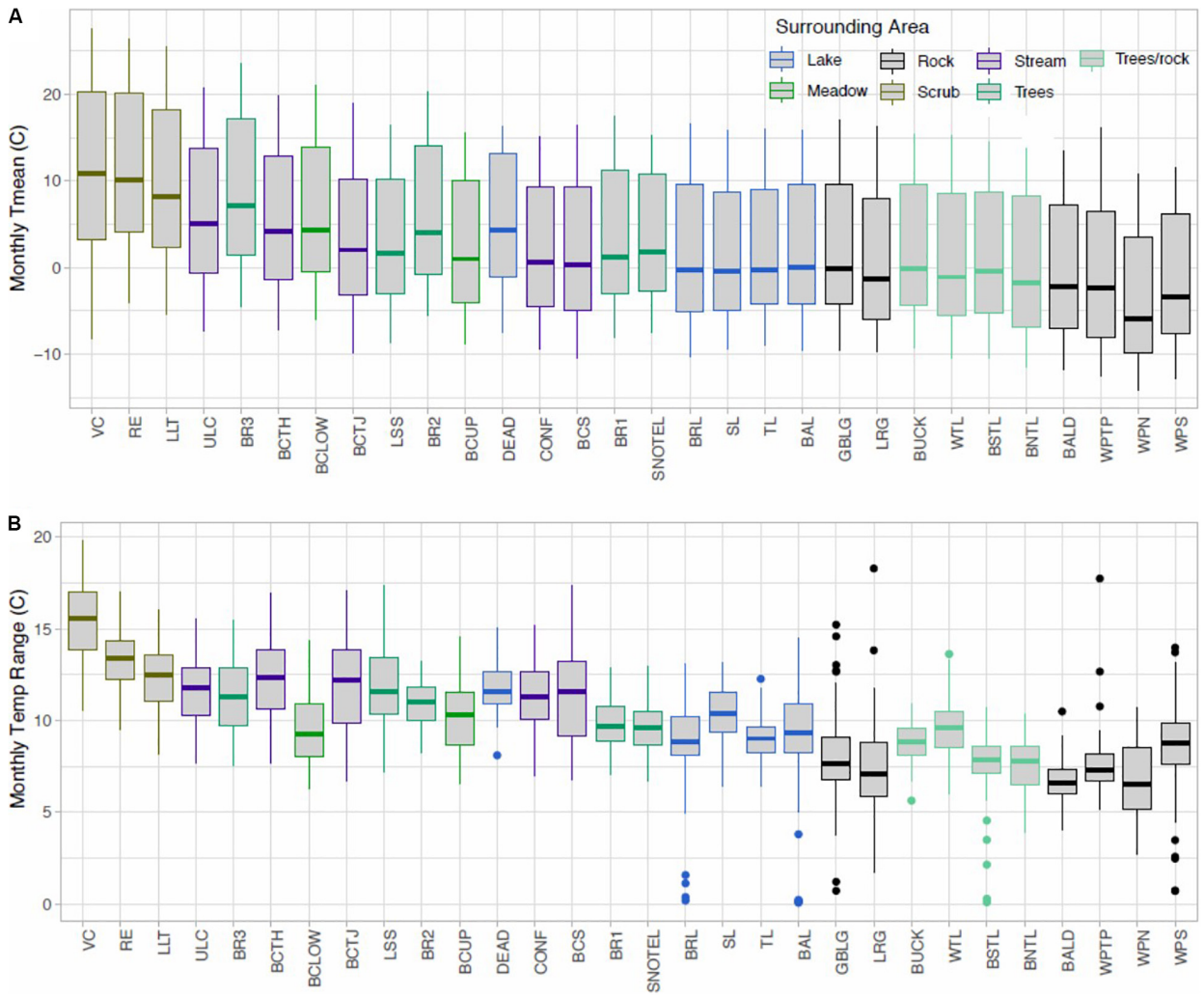


FIGURE 5 | Boxplots of monthly T_{mean} (**A**, top) and T_{range} (**B**, bottom) distributions for all the available Lascar sensors within the ESN, including data from 2006–2018. Colors describe the local environment surrounding each sensor.

installations showed on average a 0.1°C weaker increasing Tmean trend, a 0.2°C weaker increasing Tmax trend, and no difference in Tmin trend. When grouping sensors by installation height >1.5 and 1.5 m and below, the higher sensors showed 0.4–0.5°C stronger warming trends for Tmean, Tmin, and Tmax. Sensors located at summits on posts or fastened close to rock faces showed the strongest warming trends, when grouped together. WPN and WPS are both situated on steep slopes under rock overhangs atop Wheeler Peak and are thus subject to very different thermal regimes than other sensors.

All sensors exhibited a warming trend in daily Tmin. Most sensors are located below the treeline and are shaded by foliage and the tree canopy. Sensors located near sources of water indicated striking Tmin increases compared to Tmax. Baker stream sensors (BCTH, BCTJ, BCUP, and BCS) and lake sensors (SL, TL, BAL) indicate larger rates of Tmin increase than Tmax. The overall effect is to reduce the daily range of temperature, as seen in **Table 3**.

To further investigate signals of Elevation Dependent Warming (EDW), we grouped temperature trends by sensor elevation range and tested for significant differences (**Figure 9**). The sensor groups are numbered sequentially by elevation: Group 1 – less than 2500 m a.s.l.; Group 2 – between 2500 and 2999 m a.s.l.; Group 3 – between 3000 and 3249 m a.s.l.; Group 4 – between 3250 and 3499 m a.s.l.; and Group 5 – 3500 m a.s.l. and above. There is an indication that EDW is evident in the ESN data, as there is an increasing rate of warming with higher elevation, most strongly expressed by increases in Tmax between groups 4 and 5. The increasing trend in Tmax for elevations above 3500 m a.s.l. was greater than the increasing trends between 3251 – 3499 m a.s.l. This may suggest daytime forcings are driving enhanced warming at GBNP's highest elevations.

Seasonally, there is evidence for differential warming during the cold season. The winter shows the greatest number of significant temperature trends throughout the ESN (**Table 4**). Both winter Tmean and Tmin show increasing change at a

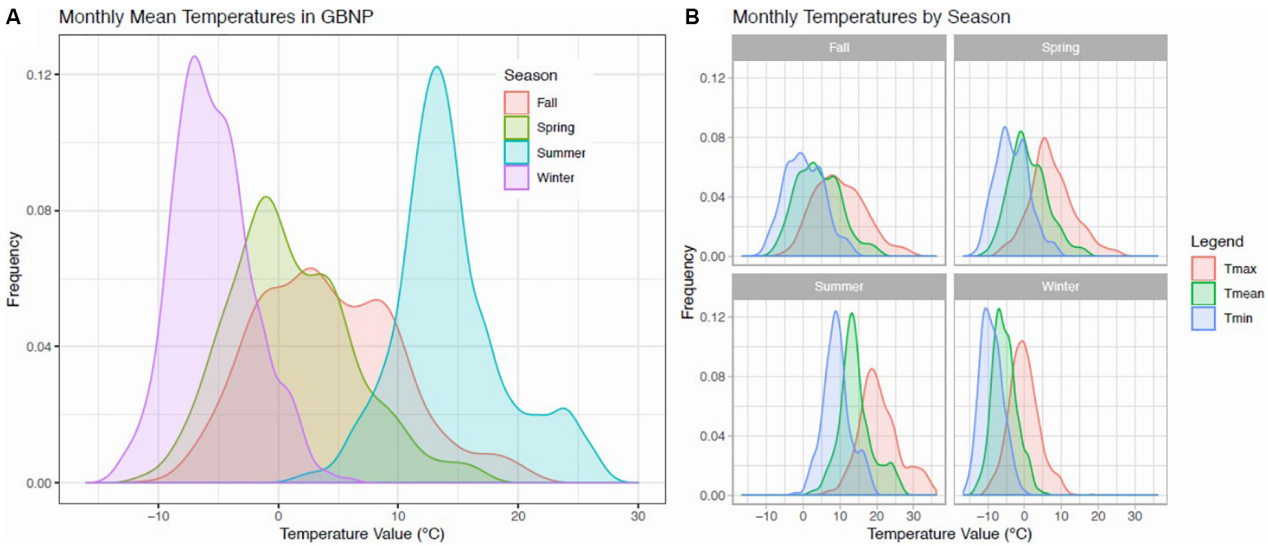


FIGURE 6 | (A) Histogram illustrating the frequency of monthly T_{mean} across GBNP by season, including all ESN sensors; **(B)** Histograms displaying the frequency of mean, minimum, and maximum temperature occurrences during fall, spring, summer, and winter.

large number of sensors. The BALD and WPS sites document increasing summer temperature but no significant trends in any other season. Due to extreme temperature variability in fall, no significant trends were able to be discerned throughout the ESN. Spring can also be relatively variable in temperature, with one sensor (RE) illustrating a significant increase in Tmin.

Landscape Temperature Variability

Local near-surface temperature is controlled by many factors, most notably by elevation within the ESN. There is a clear elevational influence on near-surface temperatures, with Tmean, Tmin, and Tmax generally decreasing with elevation. Sensor temperature distributions are distinct from one another throughout the ESN. Temperature statistics (Tmean, Tmin, Tmax, and Trange) on all time scales (daily, monthly, and annual) indicated significant differences when compared across groups. There appears to be a fairly consistent temperature trend with elevation (**Figure 10**). However, certain sensors show a slight deviation in this trend, implying local features (i.e., landcover) modify the regional temperature variability. This observation prompted us to supplement our investigation with an examination of how localities of specific sensors in different microclimates vary, namely the sensors located on Wheeler Peak (WPN and WPS), Buck Ridgeline (BR1, BR2, BR3) and in riparian zones.

TABLE 2 | Seasonal near-surface lapse rates (°C/km).

Season	Tmax	Tmean	Tmin
Spring	8.60	7.03	5.20
Summer	8.91	6.88	4.40
Fall	7.28	5.34	3.54
Winter	5.44	3.98	2.87

Site radiation exposure and slope aspect comprise important factors in moderating local temperature. The daily temperature statistics for the Wheeler Peak sensors were significantly different from one another; this difference was largely a function of aspect (**Supplementary Figure 3A**). WPS had a higher daily Tmean, Tmin, Tmax, and Trange than WPN. Monthly averages indicated significant differences between Tmax and Trange, with WPS higher than WPN on average. Annual averages also displayed a difference between Tmean and Tmin, with the WPS values much higher than the WPN values.

The Bald Mountain sensors (BALD, BNTL, and BSTL) exhibited significant differences in temperature statistics with respect to aspect (**Supplementary Figure 3B**). The BALD sensor is located atop Bald Mountain, at an elevation of 3516 m a.s.l. BNTL (3420 m a.s.l.) and BSTL (3440 m a.s.l.) are located at tree line on the north and south sides of the mountain, respectively. Daily Tmax was significantly different between all three sensors, with BSTL observing the highest daily Tmax and BALD observing the lowest daily Tmax. The daily temperature range was different amongst the sensors. BSTL had the largest range in daily temperatures, followed by BNTL and then BALD with the smallest range. On monthly timescales, BALD Trange indicated significant deviation from BSTL and BNTL Trange. Annual averages were more congruent between sensors, excluding annual BALD and BSTL Tmax values. BSTL indicated significantly higher annual Tmax values than BALD.

In addition to showing steeper near-surface lapse rates, the three Buck Ridgeline sensors (BR1, BR2, and BR3) document an anomalous increase in temperature relative to sensors at similar elevations elsewhere in the ESN. The three ESN sensors placed along this ridgeline are relatively more exposed to atmospheric forcings and further from riparian or lacustrine environments, as compared to the more sheltered ESN sensors that are located along the Lehman and Baker creeks.

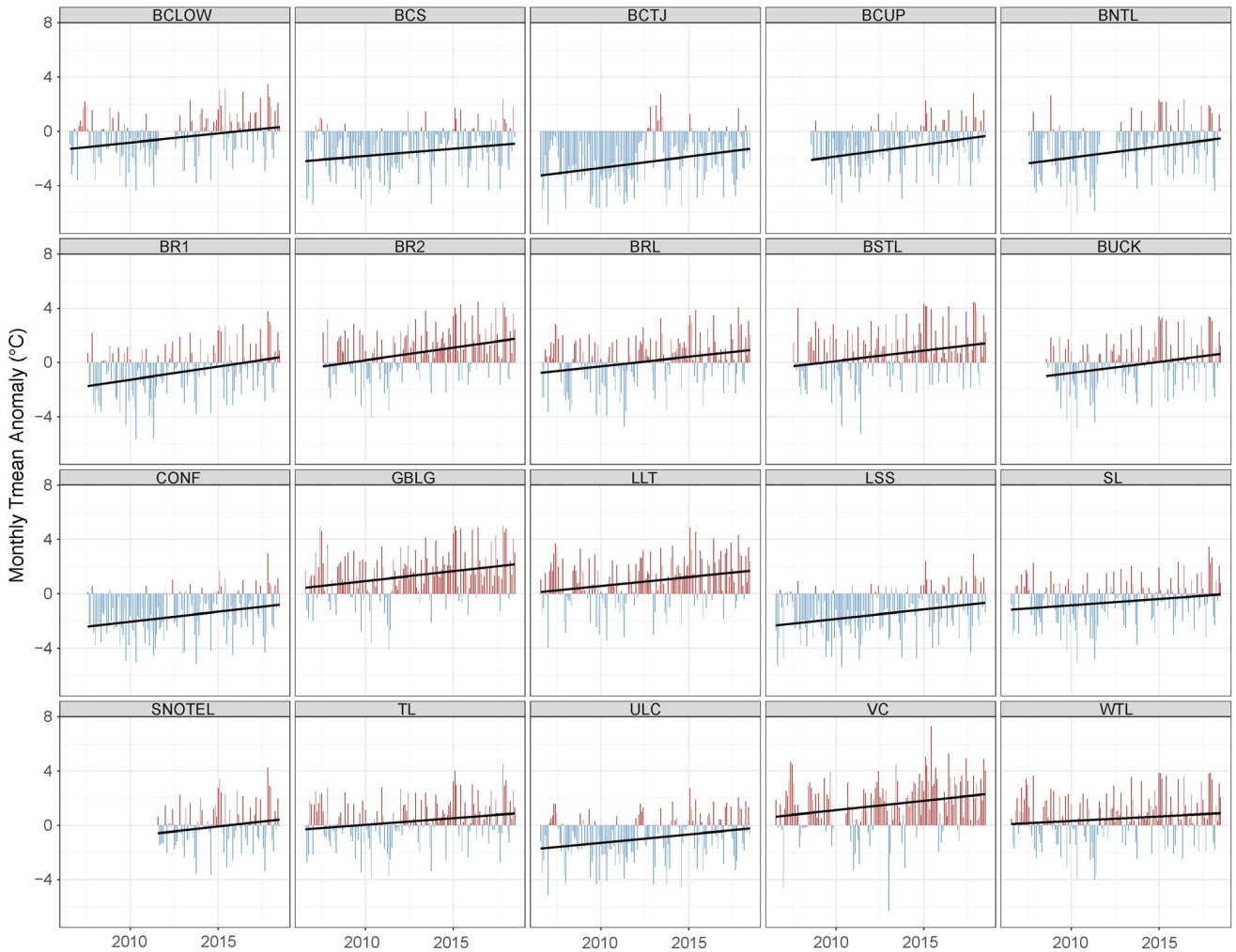


FIGURE 7 | Matrix of monthly T_{mean} time series of anomalies at 20 ESN sensor sites. Red bars represent positive anomaly values and blue bars represent negative anomaly values. Overall anomaly trendlines are shown with a solid black line. SNOTEL and WTL sites have positive but not significant trends.

Buck Ridgeline daily temperatures (BR1, BR2, and BR3) were compared to temperature distributions from sensors at similar elevations but located in valleys along streams in order to determine if variance in temperature is related to exposure. With respect to elevation, BR3 – the lowest of the Buck Ridgeline sensors – is located between ULC (58 m below) on Lehman Creek and BCTH (14 m above) along Baker Creek. BR2 is located between LSS (134 m below) and BCUP (72 m above). BR1 – the highest Buck Ridgeline sensor – is located between BCS (66 m below) and the SNOTEL site (59 m above).

BR3 indicated significant deviation from similar sensors when comparing daily Tmean, Tmin, Tmax, and Trange (**Supplementary Figure 4**). However, when comparing ULC and BCTH with each other, no significant difference is evident. BR3 had higher Tmean, Tmin, and Tmax on average and similar average Trange to the other sensors, though slightly narrower distribution. BR2 also indicated significant deviations from stations at similar elevations, LSS and BCUP; BR2 had significantly higher Tmean, Tmin, and Tmax on average and lower Trange on average than both LSS and BCUP. Likewise, BR1 displayed a significant difference in Tmean, Tmin, and Tmax relative to the sensors closest in elevation, BCS and SNOTEL. Regarding Trange, there was deviation between BCS and BR1 values but no significant difference between SNOTEL and BR1 values. When comparing SNOTEL and BCS, temperature statistics generally differed from one another aside from similar Tmax.

To investigate potential influences on local weather due to proximity to hydrologic features, we compared Brown Lake (BRL) temperatures to those from the SNOTEL lascar sensor (**Supplementary Figure 5**). BRL is located at 3105 m a.s.l., and the SNTOEL site is at 3093 m a.s.l. The BRL sensor is located on the southwest edge of Brown Lake, hanging from a tree. The SNOTEL sensor is hung in a tree, located nearby the SNOTEL snow pillow. BRL was found to have significantly lower daily Tmean, Tmin, Tmax and Trange than the SNOTEL site.

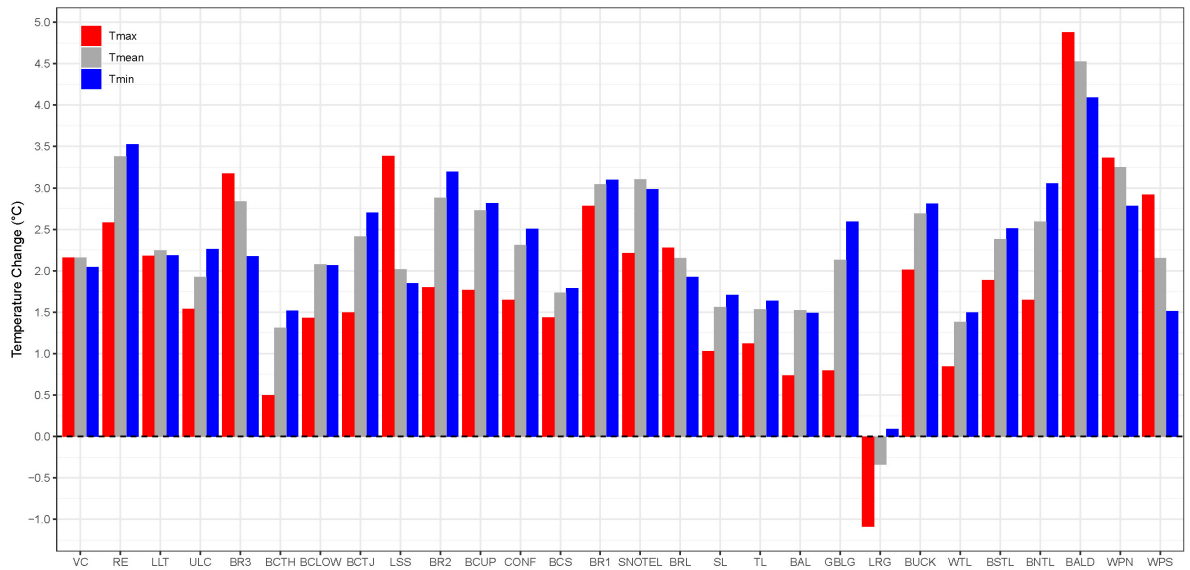


FIGURE 8 | Overall study period temperature changes from 2006–2018 at each sensor location, arranged by elevation. Changes of maximum temperature (red), mean temperature (gray), and minimum temperature (blue) were calculated using linear regressions of daily temperature values.

However, BRL temperatures exhibit a wider range than SNOTEL values. Monthly Trange was also shown to be significantly lower at BRL than at the SNOTEL site.

TABLE 3 | Significant changes in T_{range} for the ESN sensors, including daily T_{range} from 2006–2018.

Sensor	ΔTrange in °C (2006–2018)
GBLG	−1.68
BNTL	−1.40
BR2	−1.38
BCUP	−1.06
BCTJ	−1.04
BCTH	−1.03
RE	−0.87
BUCK	−0.81
CONF	−0.81
BAL	−0.75
LRG	−0.74
ULC	−0.70
SL	−0.69
BCLOW	−0.63
WTL	−0.63
BSTL	−0.63
TL	−0.53
BALD	0.57
BR3	1.00
WPN	1.03
LSS	1.30
WPS	1.50

The majority of sensors experienced a decrease in the daily diurnal temperature range; five sensors experienced an increase in the daily diurnal temperature range.

DISCUSSION

ESN Reliability

This study demonstrates that ESN data are both reliable and consistent with expected local near-surface temperature conditions, providing new insights into temperature variability and change within GBNP. Acknowledging that differential radiation exposure is the largest source of variance in meteorological instrumentation positions (i.e., World Meteorological Organization, 1983), we have shown how the ESN features variable shading that impacts ranges of temperatures. The consistency of the Lascar sensors is evident with our side-to-side comparisons to both MWx and S1147 records. Yet the discrepancy between Lascar sensors and the proximal station may relate to the relative positioning of sensors within the surrounding environment. For example, the S1147 instrument suite is located atop a ∼5 m pole and located in the center of an open clearing, away from tree canopy influence. Conversely, the Lascar sensor is located ∼10 m away, hung in a conifer tree 2 m above the ground surface. Site characteristics of the S1147 temperature sensor could potentially result in lower Tmax values (**Figure 3**), due in part to wind exposure and reduced local albedo (Strachan and Daly, 2017). The branches surrounding the Lascar sensor act as an additional radiation shield and refuge, reducing solar heating and protecting the Lascar sensor from wind exposure. This would moderate Tmax and Tmin significantly, in direct contrast to the exposed S1147 sensor suite. Temperature and humidity values are more consistent at the MWx and BR2 sites (**Figure 4**) relative to the Wheeler Peak SNOTEL site. This is likely due to the greater similarity in the sensor's placement and immediate environment.

In general, the ESN observations were characterized by high levels of consistency relative to 30-year PRISM

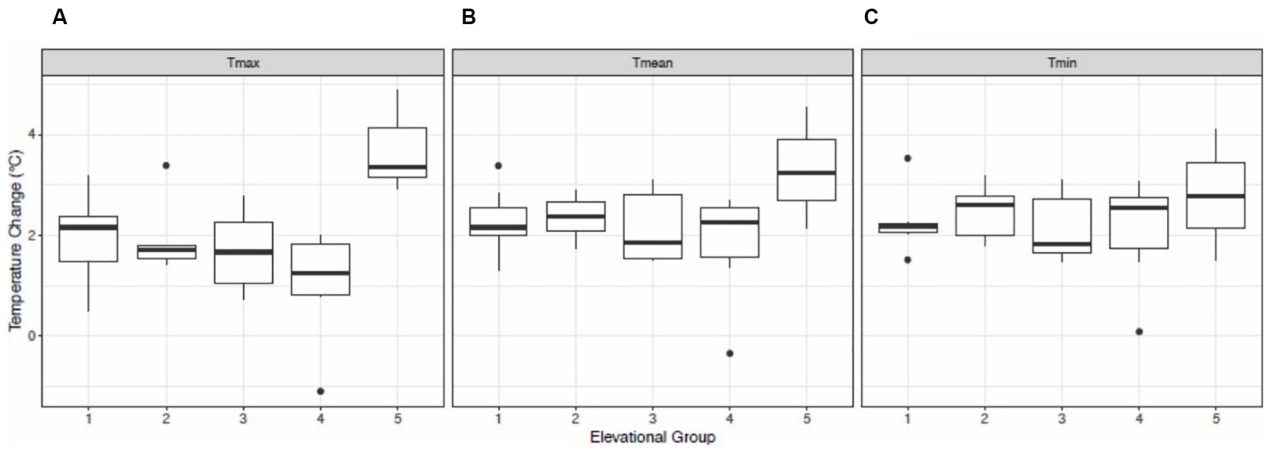


FIGURE 9 | Boxplots illustrating temperature change (°C) at each sensor over the study period, grouped by elevation, separating trends in: **(A)** T_{max}; **(B)** T_{mean}; and **(C)** T_{min}. Group 1 – less than 2500 m, Group 2 – between 2500 and 2999 m, Group 3 – between 3000 and 3249 m, Group 4 – between 3250 and 3499 m, Group 5 – 3500 m and above. All elevations in m. a. s. l.

TABLE 4 | Sensors capturing significant seasonal trends in T_{mean}, T_{min}, and T_{max} (2006–2018).

	Spring	Summer		Winter		
Sensor	**Tmin**	**Tmax**	**Tmean**	**Tmax**	**Tmean**	**Tmin**
BALD	–	0.1649	0.1373	–	–	–
BCLOW	–	–	–	–	0.0856	0.0918
BCS	–	–	–	–	0.0649	0.0709
BCTH	–	–	–	0.1178	0.1148	0.1076
BCTJ	–	–	–	–	0.1033	0.1204
BNTL	–	–	–	–	0.1031	0.1150
BR1	–	–	–	0.1012	0.1104	0.1125
BR2	–	–	–	–	0.1084	0.1203
BR3	–	–	–	0.1188	0.1005	0.0883
BRL	–	–	–	0.0778	0.0917	0.0881
BSTL	–	–	–	–	0.1002	0.1066
CONF	–	–	–	–	0.0850	0.0932
GBLG	–	–	–	–	0.0923	0.1098
LLT	–	–	–	0.1101	0.1033	0.0990
LSS	–	0.1489	–	0.0643	0.0777	0.0859
RE	0.1413	–	–	0.1316	0.1341	0.1247
TL	–	–	–	–	0.0633	–
ULC	–	–	–	0.0795	0.0951	0.1143
WPN	–	0.1206	–	–	–	–

Numbers correspond to positive seasonal temperature trends over time (°C/year).

temperature normals. On average, no annual sensor anomalies exceeded ± 2.5°C. However, due to the coarse spatial resolution (when compared to the distribution of the ESN), as well as uncertainties of PRISM, bias could be introduced when comparing sensor data to PRISM 30-year normals. All ESN sensors fell within their own unique 800 m grid cell, but in some cases the elevation of the ESN sensor elevation could be unrepresentative of the grid cell's average elevation.

Overall, the ESN provides a relatively low-cost, distributed complement to more complete and certified single-point weather stations in mountainous environments. The ESN is relatively inexpensive and easy to design, implement and maintain for multiple years. When compared to state-of-the-art stations such as S1147, ESN sensors are able to capture more local variability in biophysical conditions and vegetation found in heterogeneous, complex mountain environments and therefore, are likely to be more representative of near-surface controls on microclimate. Beyond the practical affordability and ease of maintaining the ESN, the main advantage is the ability to sample small-scale spatial variability. This additional fine-grain data can assist with downscaling coarser data sets, elaborate and integrate the spatial uncertainty of coarser data sets such as PRISM, and

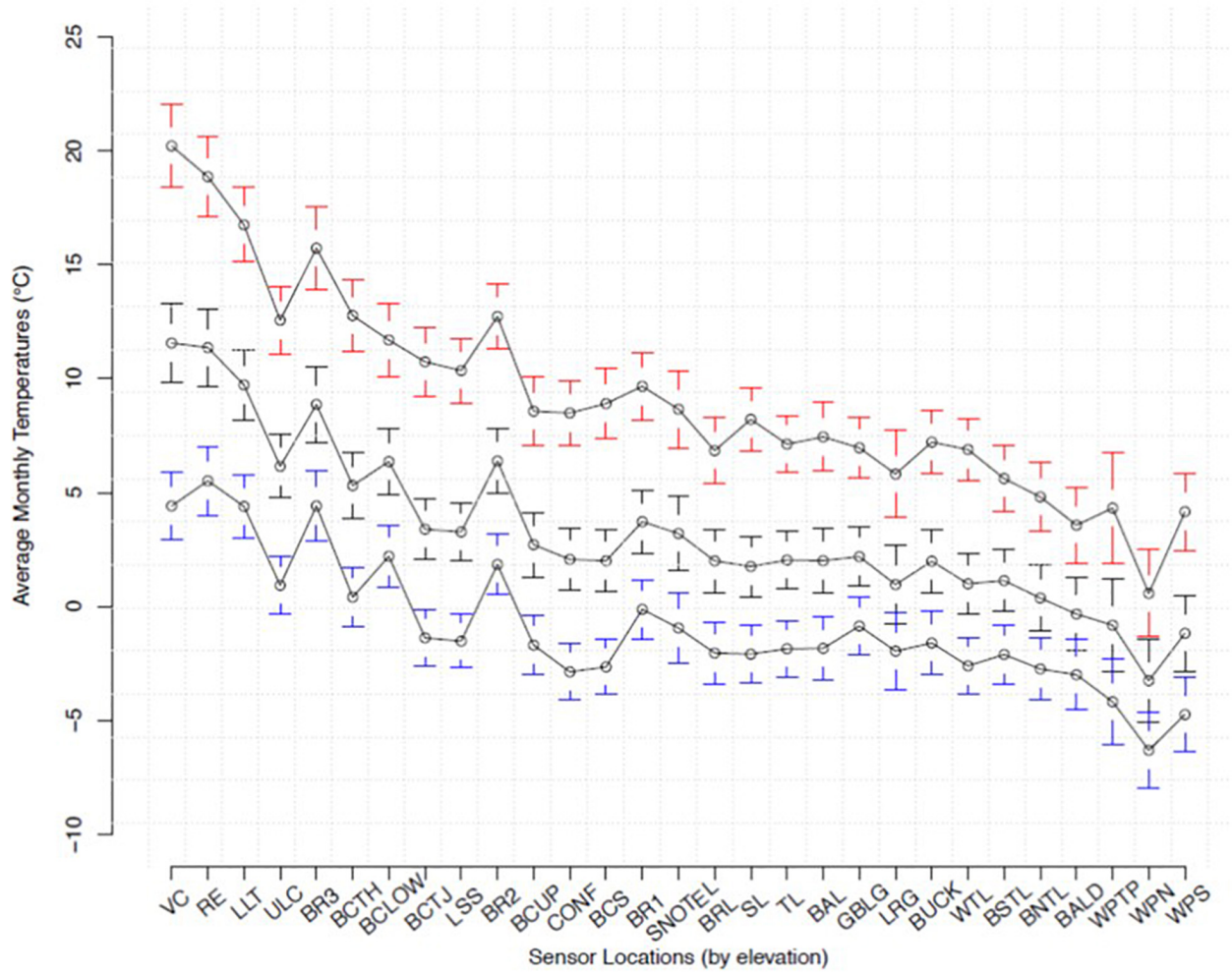


FIGURE 10 | Average monthly T_{mean} (black), T_{min} (blue), and T_{max} (red) of ESN sensors. Plot shows sensors ordered by elevation, from the lowest sensor (VC) on left to highest sensor (WPS) on right.

thus provide a unique calibration and validation potential given its nested design. Unlike traditional weather instrumentation, micro-loggers provide an additional benefit of site location flexibility. Research initiatives such as the ESN project offer ample opportunities for student-led research and involvement.

GBNP Mountain Climatology and Near-Surface Lapse Rates

Great Basin National Park generally exhibits decreasing temperature with elevation, as well as a decrease in diurnal temperature range. Seasonal changes in GBNP have a robust influence on near-surface temperatures. Temperatures largely fluctuate between summer and winter, with significant amounts of variability occurring in spring and fall. All ESN sensors exhibit strong bi-modal temperature distributions due to seasonality. These results are in agreement with other nearby distributed sensor observations from NevCAN (Mensing et al., 2013).

Eastern Nevada encompasses numerous Koeppen-Geiger climate classification zones, but most prevalent within GBNP are BWk (cold arid desert/mid-latitude desert) and BSk (cold arid steppe/mid-latitude steppe), and ESN temperatures are representative of these zones. Small extents of Dsb/Dfb (humid, warm continental), and ET (alpine tundra) are also found in the park. In recent decades, high-elevation regions of the southwest United States have experienced significant reductions in ET extent due to increasing monthly average temperatures (Diaz and Eischeid, 2007). ET may still be present at the highest elevations in GBNP, as the ESN documented monthly temperatures between 0 and 10°C on Wheeler Peak (WPN and WPS). It should be noted that both Wheeler Peak sensors have observed a warming trend in monthly temperatures over the study period, which may lead to the continued contraction of "alpine tundra" in GBNP in coming decades.

Near-surface lapse rates in GBNP have been found to differ considerably from the commonly accepted environmental lapse rate of 6.5°C/km. Previous research indicates an average GBNP lapse rate of 6°C/km and a range from 3.8°C/km in January to 7.3°C/km in June (Patrick, 2014). Seasonally, spring experiences

the steepest Tmean and Tmin lapse rates (7.0 and 5.2°C/km, respectively). The steepest Tmax lapse rate occurs in summer at 8.91°C/km. During much of the year, near-surface Tmean lapse rates are lower than 6.5°C/km. Tmin lapse rates are almost always lower than the environmental lapse rate. No significant variation in near-surface temperature lapse rate trend was observed between 2006 and 2018.

Analysis of near-surface lapse rates in other mountain ranges also reveal striking differences in lapse rates, seasonally and spatially. The Colorado Rockies and Yellowstone National Park were shown to have 6.2°C/km summer and 4.1°C/km winter lapse rates, slightly suppressed compared to GBNP (Huang et al., 2008). The Cascades have been found to have much shallower lapse rates, at 4.9°C/km (Minder et al., 2010) and 4°C/km (O'Neal et al., 2010). The Sierra Nevada has the most similar near-surface lapse rate to GBNP, at an averaged 5.8°C/km (Dobrowski et al., 2009). Lapse rates differ regionally, indicating the importance of local understanding of near-surface temperature change with elevation and changes in vegetation cover (Pepin and Lundquist, 2008).

Temperature Trends in GBNP From 2006 to 2018

Temperatures in GBNP have significantly increased over the last decade. Tmin has changed the most, increasing 2.06°C during this interval. Tmean and Tmin have also increased, increasing 1.95 and 1.39°C, respectively. The diurnal temperature range has decreased on average by 0.47°C from 2006–2018. All sensor locations show an increasing trend in temperature throughout the study period, excluding the Lehman Rock Glacier (LRG). This site shows an increasing trend in Tmin but decreasing trends in Tmean and Tmax. LRG is located atop the Lehman Rock Glacier, located within the larger Lehman Rock Glacier cirque and enclosed by the Wheeler Peak ridgeline to the west-southwest. This area is prone to drainage of cold air due to the topography. The influence of topography and associated cold air drainage could account for the observed reduction in temperature at LRG.

Most ESN sensors show a larger increase in Tmin than in Tmax, consistent with other studies (Tang and Arnone, 2013), but there were noteworthy exceptions. Considering the ongoing and projected influence of climate change in the Great Basin, the differential positive response of daily Tmin was expected over the study period (USGRP, 2017). However, the highest-elevation sensors (BALD, WPN, WPS) show a larger increase in Tmax rather than in Tmin. Larger increases in Tmin occurred at a wide range of sensors, encompassing alpine lakes, riparian zones, and treeline, among other locations. The mountaintop sensors may be more exposed to atmospheric forcing and higher amounts of insolation. The larger increase in Tmax at these sites may be due to these locations having greater exposure to warming tropospheric temperatures (Pepin and Lundquist, 2008). As the free atmosphere warms, the more exposed regions of GBNP may warm at an accelerated rate. VC, LLT, BR3, LSS, and BRL also experienced higher rates of Tmax increase. Longer snowpack coverage at higher elevations may also influence Tmin due to radiative cooling. Future work should focus on the relationship between free atmosphere influence and high elevation warming in the Great Basin.

Elevation dependent warming is a complex process (Rangwala and Miller, 2012). Many mechanisms have been invoked to account for EDW including: snow-ice albedo feedback (Minder et al., 2018); cloud patterns and cover (Yan et al., 2016); aerosol loading (Lau et al., 2010) and water vapor modulation of downward thermal radiation (Rangwala et al., 2013). In general, the largest air temperature trend was during the winter season. Of particular note, given our results, is the finding that elevated winter-season temperatures in the mid-latitudes of the northern hemisphere are positively correlated with elevation dependent increases in water vapor (Rangwala et al., 2016). An increasing trend over the past decade in GBNP is evident when comparing ESN sensor data to PRISM 30-year normal temperatures. On average, there has been an increase in the annual temperature by 0.128°C/year. All sensors indicated an increasing trend in monthly Tmean anomalies, indicating that the observed ESN temperatures have steadily increased relative to the PRISM 30-year normal temperatures. Decomposing the monthly averages confirmed warming trends throughout the ESN, with an oscillation pattern becoming more apparent at a multi-year scale. This supports southwestern patterns in warming and cooling.

Microclimates in GBNP

All sensors demonstrated the persistent elevational influence on temperature, but other local drivers on temperature were also evident. For example, the south-facing slopes of Wheeler Peak and Bald Mountain experienced significantly higher Tmean, Tmin, Tmax, and Trange than the north-facing sides of these mountains at the same elevations. The differences were most pronounced on daily and monthly timescales. Mean annual temperatures were not significantly different when aspect was taken into account. The Buck Ridgeline sensors exhibited differences due to local relative exposure with BR1, BR2, and BR3 having higher temperatures and lower Trange than sensors located at similar elevations throughout the Park. The contrasting diminished and seasonally similar lapse rates seen along the Lehman and Baker Creeks provide additional indication that the distributed locations of ESN sensors allows for distinguishing differential sensitivity to topographic positioning. Cold air pooling and more shading along the stream valleys diminishes temperature contrasts seen along similar ranges of elevation along the exposed interfluve. The average July Tmean lapse rate along the Buck Ridgeline interfluve was 3°C/km greater than in January, while the lapse rates along Baker and Lehman Creeks stayed within 1 and 2°C/km, respectively. Proximity to hydrological features also seemed to influence local temperature throughout the ESN. When comparing a lake sensor (BRL) with a similar-elevation sensor further from a water source (SNOTEL), Trange was found to be narrower near the lake. Tmean, Tmin, and Tmax, were lower and wider ranging at BRL than at SNOTEL. This is contradictory to what might be expected since BRL is in closer proximity to water (Brown Lake) that might dampen fluctuations in temperature. However, it is located under the steep NE cirque below Wheeler Peak that contains the rock

glacier, so likely receives more cold air pooling. Moreover, the lake is very shallow and likely freezes fully in winter.

Future Directions

Anthropogenic climate change suggests the likelihood for temperatures to continue increasing and along with increasing temperatures, other changes to environmental conditions in the Park (Chambers, 2008; Gonzalez et al., 2018). The stability of water resources and environmental and biotic refugia appear to face increasing threats due to ongoing climate warming. In order to better understand the near-surface climate controls in high-elevation regions and their interconnection with local water resources, further work is warranted. Future analyses will likewise focus on the ESN relative humidity data that were recorded simultaneously with the temperatures reported here.

This study exemplifies the use of relatively low-cost, distributed ESNs as a viable option for extending near-surface climate monitoring at high spatial resolution in complex mountainous environments over decadal timescales. Smaller, denser networks of embedded sensors complement single point weather stations like SNOTEL and capture a more distributed and accurate depiction of changes across these complex mountain landscapes. Elevation dependent warming may be examined further if additional high-elevation climate data were made available.

DATA AVAILABILITY STATEMENT

The datasets generated for this study are available on request to the corresponding author.

AUTHOR CONTRIBUTIONS

ES compiled data, conducted analyses, and wrote the initial draft for her Master's thesis at Ohio State University (OSU). BM served as primary advisor to ES, supervised research design, ESN installation, and data acquisition, and revised the manuscript for submission. NP pioneered research on the ESN, conducted sensor calibration, computed near-surface lapse rates, reviewed prior research, and revised the manuscript. JD co-advised ES, assisted in research design, supervised ESN maintenance and data acquisition, directed calibration and validation experiments, and guided writing. DP assisted with ESN design, data acquisition, and manuscript revision. SR assisted with ESN design and maintenance, data acquisition, and manuscript revision. GB supervised research design, data acquisition, and permitting within GBNP. JB assisted with ESN installation, research design, data acquisition, and analyses. All authors contributed to the article and approved the submitted version.

FUNDING

The Western National Parks Association and Department of Geography at Ohio State University provided funding for ESN maintenance during annual GBEx expeditions to GBNP.

ACKNOWLEDGMENTS

We gratefully acknowledge: the National Park Service and staff at GBNP for supporting and giving permission for this long-term study; the WNPA and the Departments of Geography at Ohio State University and University of Georgia for support of annual GBEx activities; the citizens of Baker, NV, especially the Baker family and owners of T&Ds for provisions, help, and hospitality; and more than 30 GBEx students who have assisted over the years with field work. We also thank the reviewers UM and SS for providing very constructive reviews that helped us improve our manuscript.

SUPPLEMENTARY MATERIAL

The Supplementary Material for this article can be found online at: https://www.frontiersin.org/articles/10.3389/feart.2020.00292/full#supplementary-material

REFERENCES

Baker, G. M. (2012). *Great Basin National Park: A Guide to the Park and Surrounding Area*. Logan, UT: Utah State University Press.

Beniston, M. (2003). Climatic change in mountain regions: a review of possible impacts. *Clim. Change* 59, 5–31. doi: 10.1007/978-94-015-1252-7_2

Brown, D. P., and Comrie, A. C. (2004). A winter precipitation 'dipole'in the western United States associated with multidecadal ENSO variability. *Geophys. Res. Lett.* 31:L09203.

Chambers, J. C. (2008). "Climate Change and the Great Basin," in *Collaborative Management and Research in the Great Basin - Examining the Issues and Developing a Framework for Action. Gen. Tech. Rep. RMRS-GTR-204*, eds J. C. Chambers, N. Devoe, and A. Evenden (Fort Collins, CO: U.S. Department of Agriculture), 29–32.

Daly, C., Smith, J. I., Wayne, P. G., Jan, C., Taylor, G. H., Pasteris, P. P., et al. (2008). Physiographically sensitive mapping of climatological temperature and precipitation across the conterminous United States. *Int. J. Climatol.* 28, 2031–2064. doi: 10.1002/joc.1688

Devitt, D., Bird, B., Brad, F. L., Jay, A., Scott, A. M., Saito, L., et al. (2018). Assessing near surface hydrologic processes and plant response over a 1600 m mountain valley gradient in the Great Basin, NV, U.S.A. *Water* 10:420. doi: 10.3390/w10040420

Diaz, H. F., and Bradley, R. S. (1997). Temperature variations during the last century at high elevation sites. *Clim. Change* 36, 253–279.

Diaz, H. F., and Eischeid, J. K. (2007). Disappearing "alpine tundra" Köppen climatic type in the western United States. *Geophys. Res. Lett.* 34:L18707.

Dickinson, W. R. (2006). Geotectonic evolution of the Great Basin. *Geosphere* 2, 353–368.

Dobrowski, S. Z., Abatzoglou, J. T., Greenberg, J. A., and Schladow, S. G. (2009). How much influence does landscape-scale physiography have on air temperature in a mountain environment? *Agric. For. Meteorol.* 149, 1751–1758. doi: 10.1016/j.agrformet.2009.06.006

Dunn, O. J. (1964). Multiple comparisons using rank sums. *Technometrics* 6, 241–252. doi: 10.1080/00401706.1964.10490181

Ford, K. R., Ettinger, A. K., Lundquist, J. D., Raleigh, M. S., and Hille Ris Lambers, J. (2013). Spatial heterogeneity in ecologically important climate variables at

coarse and fine scales in a high-snow mountain landscape. *PLoS One* 8:e65008. doi: 10.1371/journal.pone.0065008

Gonzalez, P., Garfin, G. M., Brooks, K. M., Brown, H. E., Huntly, N., Udall, B. H., et al. (2018). "Southwest," in *Impacts, Risks, and Adaptation in the United States: Fourth National Climate Assessment. Fourth National Climate Assessment*, ed. D. R. Reidmiller (Washington, DC: U.S. Global Change Research Program), 1101–1184.

Hall, N. D., and Cavataro, B. (2013). Interstate groundwater law in the snake valley: equitable apportionment and a new model for transboundary aquifer management. *Utah Law Rev.* 6, 1553–1626.

Hamner, B., and Frasco, M. (2018). *Metrics: Evaluation Metrics for Machine Learning. R Package Version 0.1.4*.

Hart, E., and Bell, K. (2015). *prism: Access Data from the Oregon State Prism Climate Project*. Genèva: Zenodo.

Huang, S., Rich, P. M., Crabtree, R. L., Potter, C. S., and Fu, P. (2008). Modeling monthly near-surface air temperature from solar radiation and lapse rate: application over complex terrain in Yellowstone National Park. *Phys. Geogr.* 29, 158–178. doi: 10.2747/0272-3646.29.2.158

Kruskal, W. H., and Wallis, W. A. (1952). Use of ranks in one-criterion variance analysis. *J. Am. Stat. Assoc.* 47, 583–621. doi: 10.1080/01621459.1952.10483441

Lau, W. K., Kim, M. K., Kim, K. M., and Lee, W. S. (2010). Enhanced surface warming and accelerated snow melt in the Himalayas and Tibetan Plateau induced by absorbing aerosols. *Environ. Res. Lett.* 5:025204. doi: 10.1088/1748-9326/5/2/025204

Lundquist, J. D., Pepin, N., and Rochford, C. (2008). Automated algorithm for mapping regions of cold-air pooling in complex terrain. *J. Geophys. Res. Atmos.* 113:D22107.

Masbruch, M. D. (2019). *Numerical Model Simulations of Potential Changes in Water Levels and Capture of Natural Discharge from Groundwater Withdrawals in Snake Valley and Adjacent Areas, Utah and Nevada*. Reston, VA: USGS.

McEvoy, D. J., Mejia, J. F., and Huntington, J. L. (2014). Use of an observation network in the great basin to evaluate gridded climate data. *J. Hydrometeorol.* 15, 1913–1931. doi: 10.1175/jhm-d-14-0015.1

Mensing, S., Jay, A., Lynn, F., Dale, D., Bird, B., Eric, F., et al. (2013). A network for observing great basin climate change. *EOS Trans. Am. Geophys. Union* 94, 105–106. doi: 10.1002/2013eo110001

Minder, J. R., Letcher, T. W., and Liu, C. (2018). The character and causes of elevation-dependent warming in high-resolution simulations of Rocky Mountain climate change. *J. Clim.* 31, 2093–2113. doi: 10.1175/jcli-d-17-0321.1

Minder, J. R., Mote, P. W., and Lundquist, J. D. (2010). Surface temperature lapse rates over complex terrain: lessons from the Cascade Mountains. *J. Geophys. Res. Atmos.* 115:13.

Mutiibwa, D., Strachan, S., and Albright, T. (2015). Land surface temperature and surface air temperature in complex terrain. *IEEE J. Select. Topics Appl. Earth Observ. Remote Sens.* 8, 4762–4774. doi: 10.1109/jstars.2015.2468594

O'Neal, M. A., Roth, L. B., Hanson, B., and Leathers, D. J. (2010). A field-based model of the effects of landcover changes on daytime summer temperatures in the North Cascades. *Phys. Geogr.* 31, 137–155. doi: 10.2747/0272-3646.31.2.137

Osborn, G., and Bevis, K. (2001). Glaciation in the great basin of the Western United States. *Q. Sci. Rev.* 20, 1377–1410. doi: 10.1016/s0277-3791(01)00002-6

Palazzi, E., Mortarini, L., Terzago, S., and Von Hardenberg, J. (2019). Elevation-dependent warming in global climate model simulations at high spatial resolution. *Clim. Dyn.* 52, 2685–2702. doi: 10.1007/s00382-018-4287-z

Patrick, N. (2014). *Evaluating Near Surface Lapse Rates Over Complex Terrain Using an Embedded Micrologger Sensor Network in Great Basin National Park*. Columbus, OH: Ohio State University.

Pederson, G. T., Graumlich, L. J., Fagre, D. B., Kipfer, T., and Muhlfeld, C. C. (2010). A century of climate and ecosystem change in Western Montana: what do temperature trends portend? *Clim. Change* 98, 133–154. doi: 10.1007/s10584-009-9642-y

Pepin, N., Bradley, R. S., Baraer, M., Palazzi, E., Miller, J. R., Ning, L., et al. (2015). Elevation-dependent warming in mountain regions of the world. *Nat. Clim. Change* 5, 424–430. doi: 10.1038/nclimate2563

Pepin, N. C., and Lundquist, J. D. (2008). Temperature trends at high elevations: patterns across the globe. *Geophys. Res. Lett.* 35:L14701.

Porinchu, D. F., Moser, K. A., and Munroe, J. S. (2007). Development of a midge-based summer surface water temperature inference model for the great basin of the Western United States. *Arctic Antarctic Alpine Res.* 39, 566–577. doi: 10.1657/1523-0430(07-033)%5Bporinchu%5D2.0.co;2

R Core Team (2018). *R: A Language and Environment for Statistical Computing*. Vienna: R Foundation for Statistical Computing.

Rangwala, I., and Miller, J. R. (2012). Climate change in mountains: a review of elevation-dependent warming and its possible causes. *Clim. Chang.* 114, 527–547. doi: 10.1007/s10584-012-0419-3

Rangwala, I., Sinsky, E., and Miller, J. R. (2013). Amplified warming projections for high altitude regions of the northern hemisphere mid-latitudes from CMIP5 models. *Environ. Res. Lett.* 8:024040. doi: 10.1088/1748-9326/8/2/024040

Rangwala, I., Sinsky, E., and Miller, J. R. (2016). Variability in projected elevation dependent warming in boreal midlatitude winter in CMIP5 climate models and its potential drivers. *Clim. Dyn.* 46, 2115–2122. doi: 10.1007/s00382-015-2692-0

Reheis, M. C., Adams, K. D., Oviatt, C. G., and Bacon, S. N. (2014). Pluvial lakes in the Great Basin of the western United States—a view from the outcrop. *Q. Sci. Rev.* 97, 33–57. doi: 10.1016/j.quascirev.2014.04.012

Reinemann, S. A., Porinchu, D. F., Bloom, A. M., Mark, B. G., and Box, J. E. (2009). A multi-proxy paleolimnological reconstruction of Holocene climate conditions in the Great Basin, United States. *Q. Res.* 72, 347–358. doi: 10.1016/j.yqres.2009.06.003

Strachan, S., and Daly, C. (2017). Testing the daily PRISM air temperature model on semiarid mountain slopes. *J. Geophys. Res. Atmos.* 122, 5697–5715. doi: 10.1002/2016jd025920

Strachan, S., Eric, P. K., Brown, R. F., Fred, H., Kent, G., David, S., et al. (2016). Filling the data gaps in mountain climate observatories through advanced technology, refined instrument siting, and a focus on gradients. *Mountain Res. Dev.* 36, 518–527. doi: 10.1659/mrd-journal-d-16-00028.1

Tang, G., and Arnone, J. A. III (2013). Trends in surface air temperature and temperature extremes in the Great Basin during the 20th century from ground-based observations. J. Geophys. Res. Atmos. 118, 3579Ű3589.

USGRP (2017). *Climate Science Special Report*. Washington, DC: United States Global Change Research Program.

Wang, Q., Fan, X., and Wang, M. (2016). Evidence of high-elevation amplification versus Arctic amplification. *Sci. Rep.* 6, 1–8.

Williamson, S. N., Zdanowicz, C., Anslow, F. S., Clarke, G. K., Copland, L., Danby, R. K., et al. (2020). Evidence for elevation-dependent warming in the St. Elias Mountains, Yukon, Canada. *J. Clim.* 33, 3253–3269. doi: 10.1175/jcli-d-19-0405.1

Wise, E. K. (2010). Spatiotemporal variability of the precipitation dipole transition zone in the western United States. *Geophys. Res. Lett.* 37:L07706.

Wise, E. K. (2012). Hydroclimatology of the US intermountain west. *Prog. Phys. Geogr.* 36, 458–479. doi: 10.1177/0309133312446538

World Meteorological Organization (1983). *World Weather Report No. 38. "Very Short-Range Forecasting - Observations, Methods and Systems." WMO No. 621*. Geneva: World Meteorological Organization.

WRCC (2019). *Western Regional Climate Center*. Reno: WRCC.

Xiang, T., Vivoni, E. R., and Gochis, D. J. (2014). Seasonal evolution of ecohydrological controls on land surface temperature over complex terrain. *Water Resour. Res.* 50, 3852–3874.

Yan, L., Liu, Z., Chen, G., Kutzbach, J. E., and Liu, X. (2016). Mechanisms of elevation-dependent warming over the Tibetan plateau in quadrupled CO_2 experiments. *Clim. Chang.* 135, 509–519. doi: 10.1007/s10584-016-1599-z

Conflict of Interest: Lead author ES is currently employed by the company Liberty Mutual, but completed the research while a graduate student at Ohio State University.

The remaining authors declare that the research was conducted in the absence of any commercial or financial relationships that could be construed as a potential conflict of interest.

Copyright © 2020 Sambuco, Mark, Patrick, DeGrand, Porinchu, Reinemann, Baker and Box. This is an open-access article distributed under the terms of the Creative Commons Attribution License (CC BY). The use, distribution or reproduction in other forums is permitted, provided the original author(s) and the copyright owner(s) are credited and that the original publication in this journal is cited, in accordance with accepted academic practice. No use, distribution or reproduction is permitted which does not comply with these terms.

frontiers in Earth Science

ORIGINAL RESEARCH
published: 28 July 2020
doi: 10.3389/feart.2020.00261

Atmospheric Rivers Contribution to the Snow Accumulation Over the Southern Andes (26.5° S–37.5° S)

Felipe Saavedra[1]*, *Gonzalo Cortés*[2], *Maximiliano Viale*[3], *Steven Margulis*[4] and *James McPhee*[1,5]

[1] Advanced Mining Technology Center, Universidad de Chile, Santiago, Chile, [2] Cetaqua, Centro Tecnológico del Agua, Santiago, Chile, [3] Instituto Argentino de Nivología, Glaciología y Ciencias Ambientales (IANIGLA) – Consejo Nacional de Investigaciones Científicas y Técnicas (CONICET), Mendoza, Argentina, [4] Civil and Environmental Engineering Department, University of California, Los Angeles, Los Angeles, CA, United States, [5] Departamento de Ingenieria Civil, Universidad de Chile, Santiago, Chile

This paper quantifies the climatological contribution of atmospheric rivers (ARs) to annual snow accumulation in the Andes Cordillera between 26.5° S and 36.5° S. An AR identification algorithm, and a high-resolution (0.01°) snow reanalysis dataset, both especially developed for this mountainous region, are used for this quantification over the 1984–2014 period. Results show that AR snowfall events explain approximately 50% of the annual snow accumulation over the study area, and are 2.5 times more intense than non-AR snowfall events. Due to orographic precipitation enhancement on the western slopes and a prominent rain shadow effect on the eastern slopes, annual snow accumulation and AR storms contribution to this accumulation are, on average, 7 and 12 times larger on western than on eastern slopes of the mountain range, respectively. Areas with lower peak elevations see more spillover snowfall over the eastern slopes of the mountain range, especially south of 35° S. Analysis of teleconnections with El Niño Southern Oscillation shows a reduction in the AR frequency across the study area during La Niña episodes and, consequently, a lower contribution to snow accumulation. Conversely, weak and moderate El Niño episodes show an increase in AR frequency, and consequently more snowfall.

Keywords: atmospheric rivers, Andes Cordillera, snow accumulation, ENSO, El Niño, rain shadow, South America

OPEN ACCESS

Edited by:
Bryan G. Mark,
The Ohio State University,
United States

Reviewed by:
Ulf Mallast,
Helmholtz Centre for Environmental Research (UFZ), Germany
Wei Zhang,
University of Iowa, United States

***Correspondence:**
Felipe Saavedra
fesaaved@uchile.cl

Specialty section:
This article was submitted to Hydrosphere, a section of the journal Frontiers in Earth Science

Received: *02 September 2019*
Accepted: *10 April 2020*
Published: *28 July 2020*

Citation:
Saavedra F, Cortés G, Viale M, Margulis S and McPhee J (2020) Atmospheric Rivers Contribution to the Snow Accumulation Over the Southern Andes (26.5° S–37.5° S). Front. Earth Sci. 8:261. doi: 10.3389/feart.2020.00261

1. INTRODUCTION

Snowmelt in the subtropical Andes Cordillera (25°–38° S) is the primary source of surface runoff during spring and summer months, having important implications for water supply and the local economy. Since 1970, an increase in the snow line elevation can be observed in this region, with a consequent decrease on average snow-covered area (Casassa et al., 2003; Carrasco et al., 2005). Since 2010, an unprecedented sequence of winter accumulation deficits has been observed, in what has come to be known as the Andean megadrought period (CR2, 2015; Boisier et al., 2016; Garreaud et al., 2019), this drought persists at the time of writing.

The accumulation of snow on the mid-latitudes Andes is usually produced by cold frontal systems originating in the Pacific Ocean, mostly during winter (Escobar and Aceituno, 1998). When cold fronts make landfall, the orographic effect of the Andes strongly enhance and reduce precipitation over the western and eastern side of the continental divide, respectively (e.g., Falvey and Garreaud, 2007; Viale et al., 2013). In addition, the strongest snowfall events are usually related

to intense water vapor transport from the Pacific Ocean in the pre-cold-front environment of cold frontal systems, which take the form of atmospheric rivers (ARs) (Viale and Nuñez, 2011).

ARs are narrow and elongated streams of intense water vapor that play an important role in the global water cycle and the local hydroclimate. In fact, they account for 84–88% of the total meridional Integrated Vapor Transport (IVT), covering 10% of Earth's circumference at midlatitudes (Zhu and Newell, 1998; Guan and Waliser, 2015). In California and western Europe, a contribution of 20–50% to annual precipitation and runoff has been estimated (e.g., Dettinger et al., 2011; Lavers and Villarini, 2015). Moreover, ARs are responsible for floods, extreme winds and related damages over the western U.S. and Europe (Ralph et al., 2006; Leung and Qian, 2009; Dettinger et al., 2011; Lavers et al., 2011, 2012; Neiman et al., 2011, 2013). Dettinger (2013) reports that ARs may also play a critical role in ending drought events on the coast of the Western United States.

On the west coast of South America, recent work by Viale et al. (2018) introduced a climatology of landfalling ARs and evaluated their impacts on precipitation. Landfalling ARs are most frequent between 38° and 50° S, averaging 35–40 AR days/year, and decrease rapidly to the north with just 10 AR days/year at 31° S. AR contributions to annual precipitation in subtropical Chile (32° S–38° S) is estimated to be 50%-65%, and median daily and hourly AR-related precipitation is 2–3 times larger than that of other storms. North of 32° S, the contribution reduces to <8% on the western side (Pacific-draining) of the Andes, while on the eastern side of the Andes ARs are infrequent, contributing less than 15% to annual precipitation.

Interannual variation of Precipitation in Central Chile is strongly influenced by El Niño Southern Oscillation (ENSO) phases, where more extreme precipitation events occur during El Niño (warm) and fewer during La Niña (cold) conditions (Escobar and Aceituno, 1998; Montecinos and Aceituno, 2003; Grimm and Tedeschi, 2009; Quintana and Aceituno, 2012). ENSO is also an important driving mechanism of year to year variations in snowpack accumulation (Rutllant and Fuenzalida, 1991; Escobar and Aceituno, 1998; Masiokas et al., 2010), and explains 25% of peak Snow Water Equivalent (SWE) variability (Cortés et al., 2016) with significant correlations between peak SWE and ENSO only in El Niño phase (Cortés and Margulis, 2017). In the western US coast, AR precipitation is modulated by ENSO, Madden-Julian Oscillation (MJO), Arctic Oscillation (AO), and Pacific/North American (PNA) teleconnections. In addition, combinations of MJO and the quasi-biennial oscillation (QBO) provide sub-seasonal predictive skill for anomalous AR activity in the west coast of North America (Guan and Waliser, 2015; Baggett et al., 2017; Mundhenk et al., 2018)

Past studies have suggested a considerable contribution of ARs to the snowpack in mountain regions. For example, over the Sierra Nevada, California Guan et al. (2013) reported that the high volume of snowpack accumulated during the 2010/2011 winter season was related to a positive anomaly in the number of AR snow events during that season. In addition, AR snow events contributed to 30–40% of the annual SWE accumulation in most years for that region, with that fraction determined in many cases by just one or two extreme events (Guan et al., 2010). In Antarctica, four and five ARs reaching the coastal Dronning Maud Land contributed 74–80% of the outstanding ice sheet surface mass balance during 2009 and 2011 (Gorodetskaya et al., 2014). By using only six snow measurement sites in the central Andes (30° S–35° S), Viale et al. (2018) reported that ARs contribute between 43 and 55% of observed snow accumulation between 2001 and 2015. However, the influence of ARs on snowpack spatiotemporal patterns over the full extent of the subtropical Andes is still largely unknown.

In this paper, a high-resolution snow reanalysis data set for the Andes is analyzed in conjunction with an AR catalog to determine the contribution of ARs to snow accumulation. In light of scarce snow measurements across the study domain, the use of a snow reanalysis provides an opportunity for improving our understanding of the influence of AR on the spatial patterns of snow accumulation. Given the important effect of ENSO on snowpack accumulation (Cortés and Margulis, 2017), the effects of AR events on the spatiotemporal variability of SWE during different ENSO phases are also analyzed.

2. GEOGRAPHICAL SETTING, DATA, AND METHODS

2.1. Geographic and Climatic Setting

Our study domain extends from 26.5° S to 37.5° S, and from 72° W to 68° W, spanning the subtropical Andes region and including the headwaters of 24 watersheds in Chile and Argentina (**Figure 1A**). These mountain catchments supply water for highly populated cities and important agricultural and industrial areas in both countries. **Figures 1B,C** show that snow accumulation on the western slopes is quite larger than on the eastern slopes of the subtropical Andes, and that most of the snow falls in winter as midlatitudes storm-tracks and AR storms migrate toward the equator (e.g., Hoskins and Hodges, 2005; Falvey and Garreaud, 2007). The crest of the Andes varies largely from 2,300 to 5,300 m.a.s.l. from 37.5° S to 26.5° S, which imply variations in cross-barrier orographic effects on precipitation. To the east of the crest, precipitation amounts are considerably reduced due to the rain shadow effect, which is greater between 32° and 34.5° S than between 35° and 36.5° S, probably due to lower crest altitude (Viale and Nuñez, 2011). To the west of the continental divide, annual precipitation increases from the Pacific coast to the western slopes by a factor of 1.8 ± 0.3 (Viale and Garreaud, 2015). In along-barrier direction, there is also a climatic gradient on the western side of the Andes, going from arid conditions (300–400 mm) at 26.5° S to more humid conditions (∼1,000–1,500 mm) at 37.5° S due to more baroclinic activity (e.g., Boisier et al., 2018).

2.2. AR and Snow Reanalysis Data

The occurrence of ARs landfall on western South America was obtained from an AR catalog derived from an AR detection algorithm for the South American region. This algorithm was developed by Viale et al. (2018) and uses the Integrated Vapor Transport variable from the Climate Forecast System Reanalysis (CFSR, Saha et al., 2010) gridded dataset. The CFSR grid has an 0.5° horizontal resolution, a temporal span from 1979 to present every 6-h timestep, and uses a coupled ocean–atmosphere–land

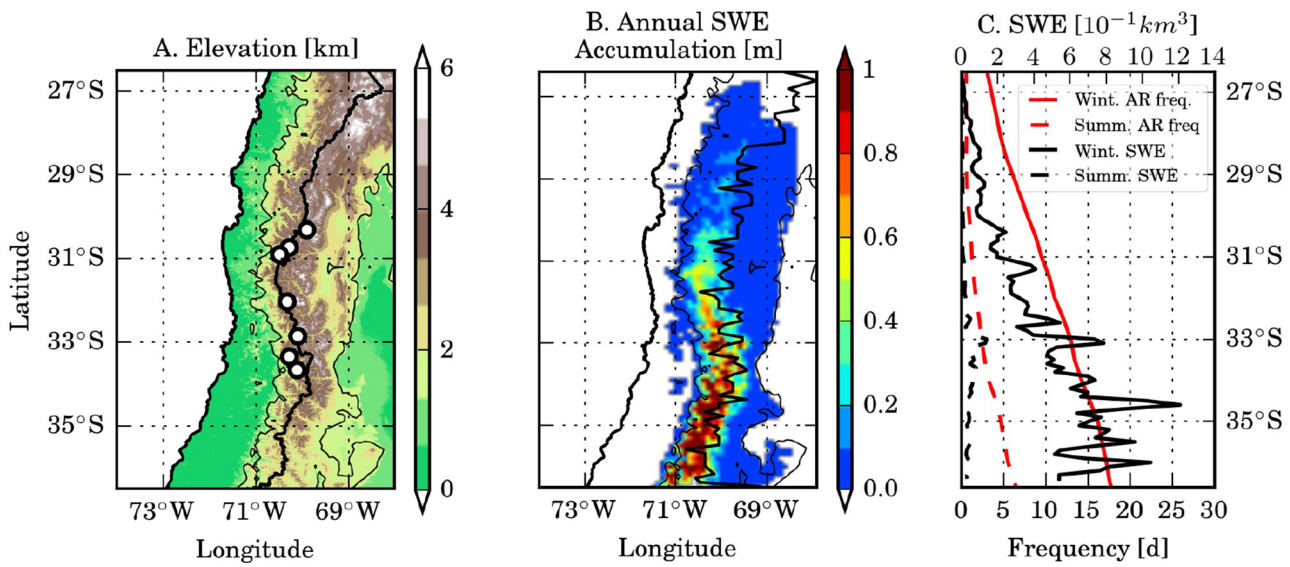


FIGURE 1 | (A) Topographic map of the Subtropical Andes. Surface snow measurement sites are indicated by white circles and the thick black lines indicate the border between Argentina and Chile and the coastline, while the thin black line indicate the 2,000 m elevation for reference. **(B)** Climatology of the Snow Water Equivalent (SWE) derived from the snow reanalysis over the 1984–2014 period [adapted from Cortés and Margulis (2017)]. Black thick lines show the coast line and the crest of Andes (maximum altitudes in snow reanalysis dataset); the 2,000 m elevation line is also indicated. **(C)** Variations with latitude of the Atmospheric River frequency along the Pacific coast (red lines) and of the areal mean SWE (black lines) for winter (Apr-Sep) and summer (Oct-Mar) seasons (continuous and dashed lines, respectively).

model to assimilate observations. Although the AR identification algorithm is described in detail in Viale et al. (2018), a brief explanation is given here. The algorithm follows as close as possible the definition of an AR which appeared in 2017 in the glossary of meteorology of the American Meteorological Society (AMS, Ralph et al., 2019). This is essentially a long and narrow corridor of intense water vapor transport usually associated with a midlatitude cold front. The algorithm detects a long and narrow corridor of intense IVT as an AR when its IVT values are greater than the 85th monthly percentile values in each grid cell, its length is larger than 2,000 km and its earth surface area to length ratio is greater than 2 (i.e., a metric for its width). Finally, the corridor must be associated with a near-surface frontal zone following the procedure proposed by Jenkner et al. (2010). We computed AR frequency as the number of AR time steps for a given period.

The Andean SWE Reanalysis (ASR) dataset developed by Cortés and Margulis (2017) and Cortés et al. (2014) was employed to analyze SWE variations. The dataset is generated using a particle batch smoother assimilation framework (Margulis et al., 2015). The land surface model (LSM) SSiB3 and a depletion curve model (DCM) were used to obtain prior estimates of SWE and fractional snow covered area (fSCA) respectively. Posteriorly fSCA values obtained from a Landsat imagery were assimilated to improve SWE estimations. Further details in the ASR development can be consulted in Margulis et al. (2016) and Cortés et al. (2016).

The ASR has daily data from April 1984 to March 2015 with a 0.001° spatial resolution. We aggregated SWE to a 0.1° resolution by the simple average for all analyzes. We estimate yearly peak SWE values as the maximum annual SWE value per pixel, in order to calculate annual correlations with AR frequency. In addition, we use maximum SWE annual values from 7 snow pillows from the Chilean national water agency (DGA, **Figure 1A**) to compute annual correlations with AR frequency. Daily accumulation from the SWE reanalysis was calculated by subtracting the SWE values of the previous day for each cell, keeping only positive values. This assumption neglects the effects of daily snow gravitational and wind transport between pixels.

2.3. AR Attribution to Snowpack Variations

Daily snow amount variations derived from the SWE reanalysis data was related to the presence of an AR by using the AR catalog. Since both products have different grid spacings and time steps, the AR catalog with coarser grid spacing (0.5°) was refined using a nearest neighbor interpolation to the 0.1° grid spacing of the SWE product.

By comparing both AR and SWE datasets with the same grid spacing and time period (1984-2014), a snowfall day was counted as AR-related when AR conditions were present at any grid cell on any of the four 6-h time steps that day. Then, if this criterion was met in 1 day, the snowfall in the day before and after were also related to the AR, in order to account for lead- and lag-time response between AR conditions and snowfall. A similar methodology was also used by Guan et al. (2010), Viale et al. (2018), and Huning et al. (2017, 2019). Additionally, high resolution (0.1°) topographic data from USGS was used

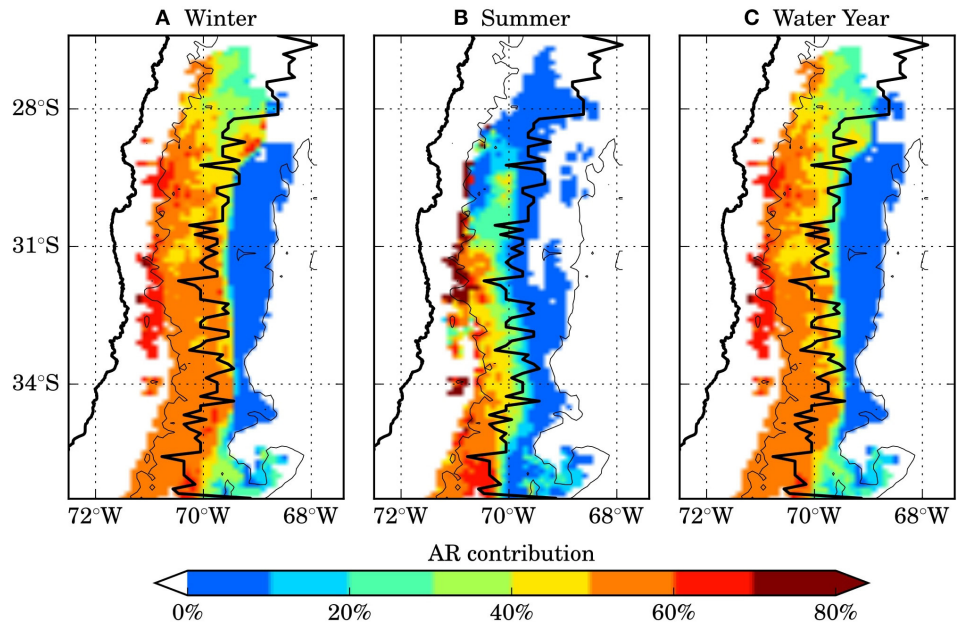


FIGURE 2 | Percentage AR contribution to **(A)** winter (Apr-Sep), **(B)** summer (Oct-Mar), and **(C)** annual total snow accumulation over the Subtropical Andes during the 1984–2014 period. Thick black lines show the crest of Andes and the coast line, while thin lines show the 2,000 m elevation for reference.

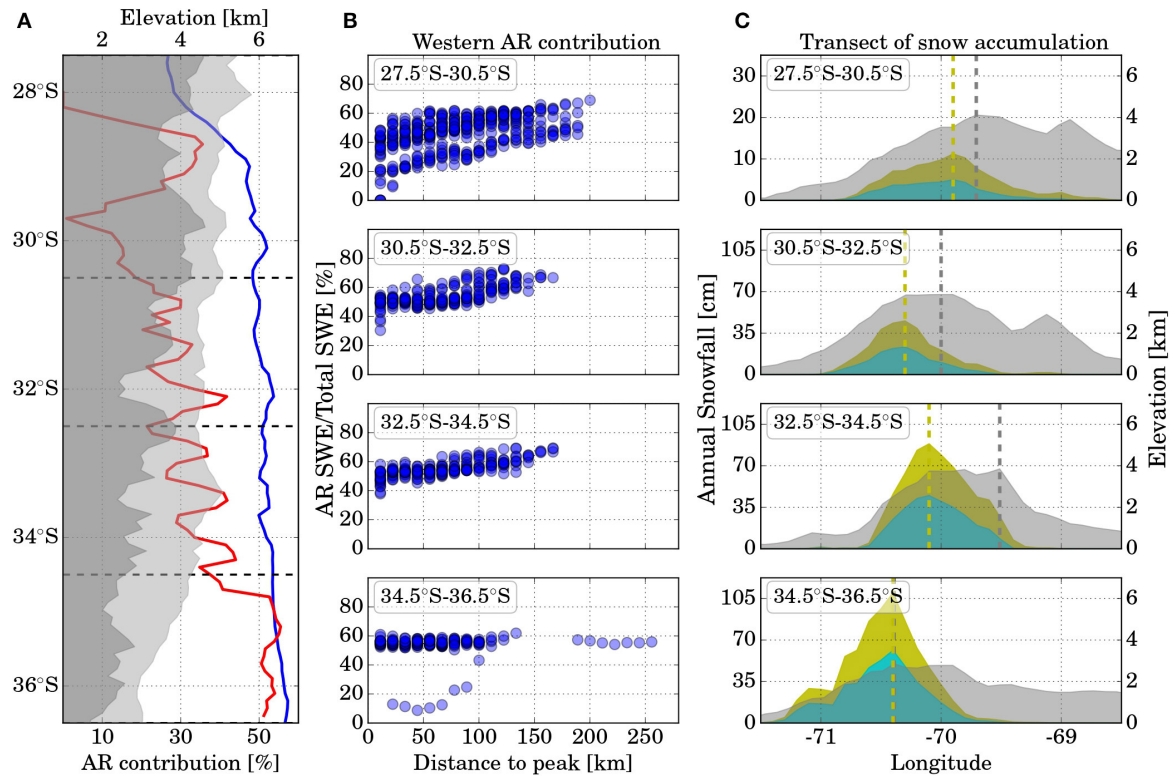


FIGURE 3 | (A) Variations with latitude (i.e., along-barrier direction) of the crestline (light gray), of the topographic altitude 40 km to the west (upwind) of the crest of the Andes (dark gray), and of the AR contribution to the annual snow accumulation on the western (blue line) and eastern (red line) slopes, respectively. Transects showing the variations in cross-barrier direction of **(B)** the AR contribution on pixel scales over the western (blue circles), and **(C)** the annual total (yellow) and AR-related (green) annual snow accumulation. The meridionally-averaged peak of the snow accumulation and of the maximum topographic elevation (crest) are shown as dotted yellow and gray lines, respectively.

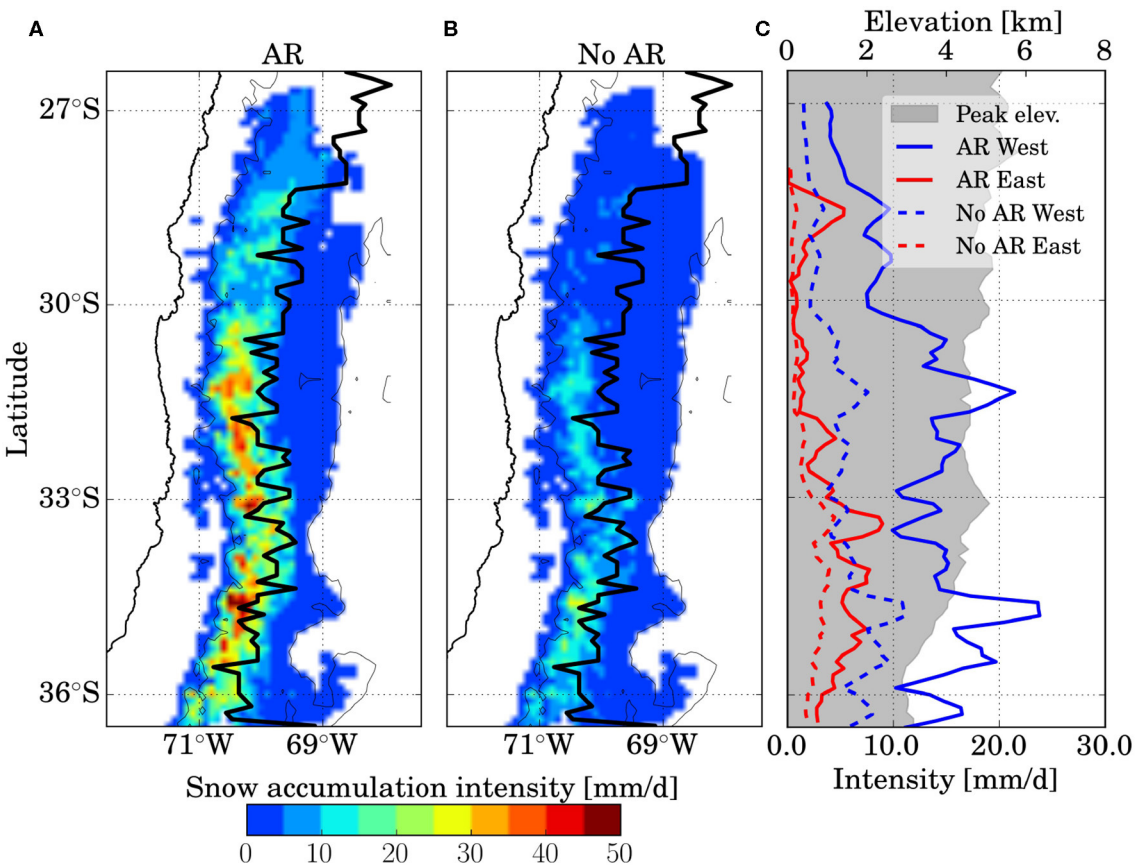


FIGURE 4 | Mean daily snowfall intensity for **(A)** the AR and **(B)** the non-AR snowfall events on pixel scales. The crest of the Andes and the 2,000 m topographic line are plotted by thick and thin black lines, respectively. **(C)** Variations with latitude of the altitude of the crestline (shaded in gray) and of the mean daily snowfall intensity on the western (blue lines) and eastern (red lines) slopes for the AR (continuous lines) and non-AR (dashed lines) snowfall event.

to determine the crest of the Andes chain at different latitudes in order to compare AR influences on snow over western and eastern slopes of the Andes.

The ENSO correlation with SWE and AR frequency is explored to understand variability in AR contribution. ENSO teleconnections were analyzed by classifying years based on the Oceanic Niño Index (ONI). An ENSO phase (El Niño or La Niña) is defined when a minimum of five consecutive overlapping months are above/below ±0.5°C, following NOAA Climate Prediction methodology (http://www.cpc.ncep.noaa.gov). In this study, we use an arbitrary classification scheme from Cortés and Margulis (2017), in order to further define the year categorization. Taking into account the months between April and October (including AMJ, MJJ, JJA, and JAS values), we define a Moderate to Strong El Niño (MSE) if the ENSO 3.4 anomaly value is over 1°C; a Weak El Niño (WE) if ENSO 3.4 is between 0.5 and 1°C; a Weak La Niña (WL) if ENSO 3.4 is between −0.5 and −1°C; and Moderate to Strong La Niña (MSL) for ENSO 3.4 values lower than −1°C. This classification yields 4 MSL, 7 WL, 4 WE, and 3 MSE years within the study period.

3. RESULTS

3.1. ARs Contribution to Snowpacks

Coherent with climatic conditions described above, ARs make landfall on the subtropical west coast of South America mostly during winter, and increases from <10 AR days at 26.5° S to 30 AR days at 37.5° S annually (see also Figure 7 of Viale et al., 2018). Despite the large spatial variation of snow accumulation in the study domain, the overall contribution of ARs to the annual total snow accumulation on the western and immediate eastern sides of the crest of the Andes is estimated to be 51% (**Figure 2C**). Farther east of the crest, the snowfall drops drastically down to near zero values due to a prominent rain shadow effect, and so does the AR contribution. AR contribution to snow accumulation is greater in the wet, winter season (53%) than in the dry, summer season (<30%), further highlighting the great importance of ARs in supplying water in the region (c.f, **Figures 2A,B**). Although the snow accumulation maximum is observed on the high western slopes close to the crest, both seasonal and annual total AR contribution plots of **Figure 2** show that the AR contribution is slightly larger on lower western (windward) slopes than on high terrain close to the crest. This

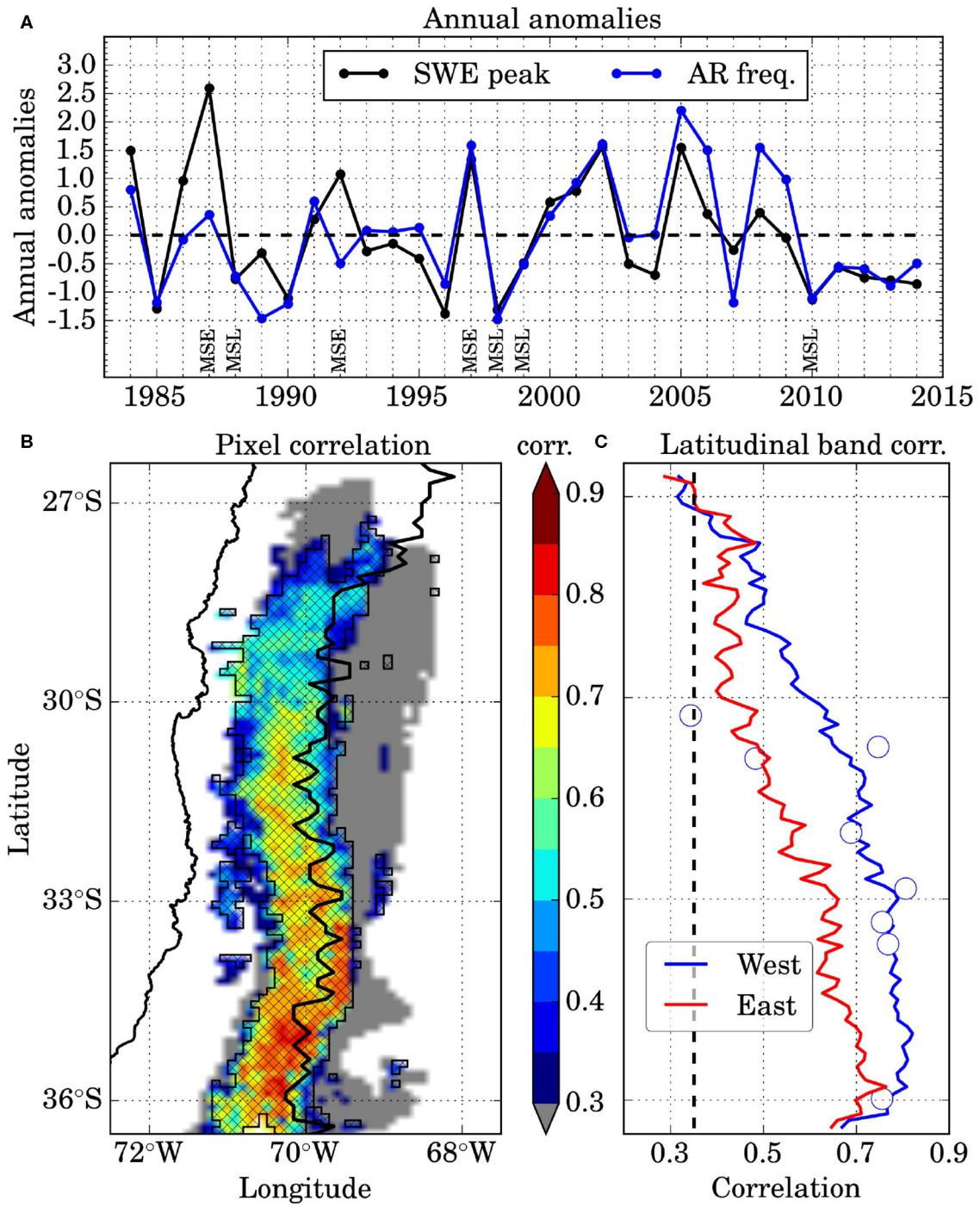


FIGURE 5 | (A) Time series of annual standardized anomalies of the regional SWE peak and AR contribution to snow accumulation. **(B)** Correlation between annual time series of peak SWE peak and AR frequency on the pixel scale (dashed pixels indicate significant correlation). Thick black line indicates the crest of the Andes. **(C)** Variation with latitude of correlations between annual time series of SWE peak and AR frequency latitudinally averaged on the western (blue) and eastern (red) slopes. The correlations at some available Snow pillows sites are shown by the circles. Dashed black lines represent the 95% significance level for the correlations.

feature is further demonstrated in transects of **Figure 3C**, and could be a response of greater orographic enhancement of precipitation on the first rise of the strong, cross-barrier moisture flux from ARs as has been suggested by other studies on the coastal western mountains of North America (Neiman et al., 2017; Zagrodnik et al., 2018, 2019).

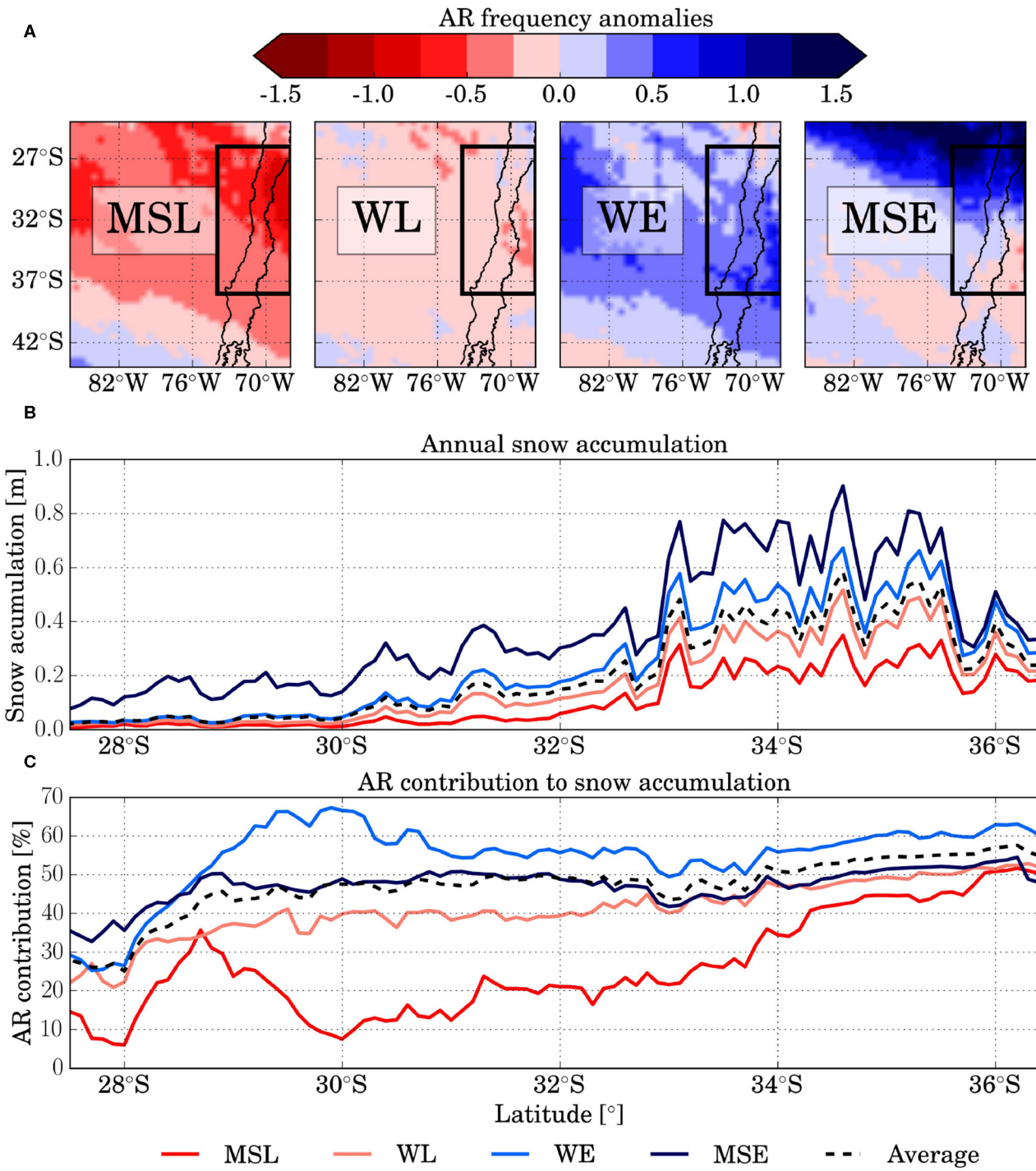


FIGURE 6 | (A) Standardized anomalies of AR frequency for different ENSO phases: moderate to strong La Niña (MSL), weak La Niña (WL), weak El Niño (WE) and moderate to strong El Niño (MSE). The black rectangles delimit the study zone and black lines show coastline and political border between Chile and Argentina. **(B)** Variation with latitude of latitudinally-averaged snow accumulation for the different ENSO phases and average year. **(C)** Same as **(B)** but for AR contribution to the annual snow accumulation.

Figure 3 illustrates the strong orographic effects of the Andes on the snow accumulation and the ARs contribution to this accumulation in along- and cross-barrier directions. While the AR contribution on the western slopes varies gradually from 30% at 27.5° S to 60% at 36.5° S, the AR contribution on the eastern slopes alternates between sectors with 0x and 50% of contribution

(**Figure 3A**). This variation seems to follow closely changes in the Andes height. North of 34° S, where the mountain range is higher (>4,000 m), areas with near zero contribution correspond to high peaks (>5,000 m) where westerly moisture transporting airflow are unable overpass to the lee; areas with increased contribution correspond to low valleys or passageways where westerly airflow is able to overpass. South of 34° S where the Andes are lower on average (<4,000 m), the highest contribution on eastern slopes are observed (50%) being similar to those on the western slopes (**Figure 3A**) and almost never reaching such low values as on the northern subdomain. Cross-barrier plots in **Figure 3C** highlight the large difference in snow accumulation between both sides of the Andes, which is about 2–15 times larger (7 on average) on the western than on the eastern slopes for the different subdomains and for AR storms it is about 1.5–40 times larger (12 on average). The transects also show how the maximum in accumulation occurs farther upstream from the crest of the Andes as the height of the crest increases (c.f, **Figures 3A–D**). While the maximum snow accumulation occurs close to the crest of the Andes between 35 and 37° S, this maximum occurs between 50 km and 100 km upstream of the crest north of 35° S. This result is in line with previous studies documenting orographic precipitation pattern in other mountain ranges (e.g., Roe, 2005), and responds to the physical Clausius-Clapeyron phenomenon, which explains how the holding capacity of water vapor drops abruptly with temperature. In other words, as temperature decreases strongly with altitude, the capacity of the atmosphere to hold unsaturated water vapor reduces abruptly, and so the amount of condensate and freezing liquid water (snow) on higher western slopes.

In order to evaluate the snowfall intensity under AR conditions, mean daily snow accumulation per pixel was computed using days with $\Delta SWE>0$ for AR and non-AR events (**Figure 4**). Domain-averaged snowfall intensity during AR events is 8.1 mm/day, which is 2.5 times more intense than snowfall intensity during non-AR events (3.2 mm/day). The highest snowfall intensities are observed upwind of the crest and south of 31° S during AR storms (**Figure 4A**). On both sides of the crest, there is an increase in snowfall intensity during AR storms compared with non-AR storms, although the overall snowfall intensities are quite lower on the eastern than on the western slopes regardless of the presence of AR.

3.2. Interannual Variability and ENSO Teleconnections

The interannual variability of snowpacks in the subtropical Andes and their connections with AR frequency and the ENSO phenomenon are explored in this section. To this end, the correlation between SWE and AR frequency is analyzed in **Figure 5**. In particular, at the regional scale, the correlation between the anomalies of the annual peak SWE areal average and AR frequency is high (0.73) and significative (**Figure 5A**), suggesting a strong dependence of the annual peak SWE on AR occurrence over this region of the Andes. Consistent with the previous analysis, the spatial correlation between annual peak SWE and AR frequency at the pixel scale shows higher (significative) correlation values on the western than on the eastern slopes of the Andes (**Figures 5B,C**), ranging from 0.9 to less than 0.3, respectively. These results denote a stronger dependence of annual snow accumulation on AR occurrence toward the southern sector and on the western (windward side) slopes. Interestingly, the estimated highest values of AR contribution on the lower western slopes (**Figure 2**) do not correspond with high values in correlation, which may be explained by the relatively low altitude of this sector on the foothills, where an alternation between liquid and solid precipitation depending on temperature may be frequent. This phenomenon may degrade the correlation as the few AR snowfall events contribute largely to the annual total snow.

The connection between the different ENSO phases, AR frequency, and snow accumulation is analyzed in **Figure 6**. During the warm (cold) phase AR landfalls frequency in the central Chilean coast increase (decrease) (**Figure 6A**). This behavior is consistent with some previous results. For example, Montecinos and Aceituno (2003) documented wet (dry) conditions in central Chile (30°–35° S) during the warm (cold) phase of ENSO associated with an equatorward (poleward) displacement of wintertime storm track (e.g., Karoly, 1989; Seager et al., 2005). This ENSO-related pattern has a resemblance to those documented by Zhang and Villarini (2018) in the North Pacific, which also produce more AR activity and precipitation in the southwest of the US, a region with climatic features very similar to those in central Chile. More recently, Guan and Waliser (2015) reported an increase (decrease) of AR frequency in our study area under El Niño (La Niña) conditions and linked this pattern to an anomaly in the South Pacific Convergence Zone (SPCZ). For the warm (cold) phase of ENSO, it has been also reported a northeastward (southwestward) shift of the SPCZ as a result of ENSO derived meridional sea surface temperature gradients variations (Folland et al., 2002; Widlansky et al., 2013; Sulca et al., 2018).

Large absolute differences in snow accumulation can be seen across the study area during Moderate to Strong el Niño (MSE) conditions, with a stronger effect on the northern subdomain. Conversely, AR contribution is higher during Weak El Niño (WE) conditions, particularly between 29° and 31° S, indicating an "optimum" in which for warmer ENSO 3.4 conditions, other precipitation-originating fronts take relevance as moisture sources. Conversely, for cold anomaly conditions (La Niña), AR contribution decreases sharply north of 34° S. This result is in strong agreement with previous findings, which point at a sharp precipitation gradient located approximately at 34° S (Aravena and Luckman, 2009; González-Reyes et al., 2017). A more consistent regime of AR south of this latitude is likely to explain this transition.

4. CONCLUSIONS

The contribution of ARs to the snow accumulation in the southern Andes (27.5°–37.5° S) has been quantified in this study by using an AR catalog and a snow reanalysis dataset both specifically developed for this South American region. Results show that AR events play an important role in snow

accumulation, contributing, on average, 51% of annual total snow accumulation across the entire study area. This estimation is similar to those (43–55%) provided by Viale et al. (2018) based on a few snow pillows located between 30° S and 36° S, and are also comparable with those obtained for the Sierra Nevada by Huning et al. (2017, 2019), who estimate 52–62% using a similar methodology, whereas Guan et al. (2013) found a lower contribution of 37%.

In this study, AR snowfall events are shown to be 2.5 times more intense than non-AR snowfall events, in agreement with previous results in other mountain ranges, such as the Sierra Nevada and the Cascades in US (Neiman et al., 2008; Guan et al., 2010), and in the same Andean region (Viale et al., 2018). Due to the strong orographic effects of the Andes on precipitation, the snow accumulation and the AR storms contribution to this accumulation is, on average, 7 and 12 times larger on the western than on the eastern slopes, respectively. The basic physical mechanism that explains this main result is the orographic ascend and descend of the large-scale westerly airflow associated with snowstorms that follow the shape of the barrier, and favored an orographic precipitation enhancement and reduction of snow on the western and eastern slopes of the Andes, respectively. Some variations with latitude in this orographic effects are observed caused by variations in the height of the Andes, especially south of 35° S where they are lower and more spillover snowfall is observed on the eastern slopes. Unlike the few snow measurement sites available in the Andes, the snow reanalysis dataset has allowed this detailed description of snow distribution and the role of ARs on it over the entire Andes range. Overall, our findings are coherent with orographic precipitation patterns observed on other mountain ranges [e.g., see the review of Roe (2005)].

AR activity and snow accumulation show large interannual variability in the study region. We found significant positive correlations between peak SWE and AR activity, showing the potential of estimating peak SWE based on AR data. Interannual SWE variability is found to be modulated by ENSO in agreement with previous studies (e.g., Cortés and Margulis, 2017). During La Niña episodes there is a decrease in AR activity and a smaller AR influence in snow accumulation. El Niño phase is known to promote more snowfall. For weak El Niño episodes AR activity and their snow contribution increase in the entire study area. However, we find that moderate to strong El Niño episodes displace AR landfall northward reducing the partial contribution south of 32° S. This can be explained due to the equatorward shift of the wintertime storm tracks during ENSO warm phase and bears a resemblance with ENSO-related patterns founded in northern Pacific.

The findings of this study agree with previous research that shows midlatitude frontal systems to be connected with atmospheric rivers encountering mountainous coastal terrains, such as the west coast of North America and Europa. These storms are well-known to potentially produce heavy orographic precipitation and provide a large fraction of water resources. Previous results in the Andes have confirmed these findings using only a few snow sites and our results here have moved forward by using a high-resolution snow dataset that covers the entire mountain range. This paper expands the understanding of the AR contribution to snow and water supply over different sectors of the Andes, such as their contribution on the first rise or different eastern and western slopes of the range, which may be useful for water management agencies in both countries, Chile and Argentina. In addition, new knowledge about the relationship between the AR storms and the large-scale ENSO phenomena, which is one of the main drivers of interannual snow accumulation, is provided here. For a whole understanding of the ARs in the modulation of snapbacks on this sector of the Andes, future works may deal with the role of AR in relation to rain-on-snow events, which has been proven to be significant in other mountain ranges.

DATA AVAILABILITY STATEMENT

The datasets generated for this study are available on request to the corresponding author.

AUTHOR CONTRIBUTIONS

All authors contributed conception and design of the study. GC and MV provided and organized source data. All authors contributed to manuscript writing, revision, read, and approved the submitted version.

FUNDING

This research was supported by CONICYT Project AFB180004 and FONDECYT Project 1171032. MV was supported by FONDECYT 11151009.

ACKNOWLEDGMENTS

Snow pillow data was obtained from Direccion General de Aguas (DGA) from Chile. We thank Pablo Mendoza, Thomas Shaw, and two reviewers for valuable contributions that have improved the original manuscript.

REFERENCES

Aravena, J.-C., and Luckman, B. H. (2009). Spatio-temporal rainfall patterns in Southern South America. *Int. J. Climatol.* 29, 2106–2120. doi: 10.1002/joc.1761

Baggett, C. F., Barnes, E. A., Maloney, E. D., and Mundhenk, B. D. (2017). Advancing atmospheric river forecasts into subseasonal-to-seasonal time scales. *Geophys. Res. Lett.* 44, 7528–7536. doi: 10.1002/2017GL074434

Boisier, J. P., Alvarez-Garretón, C., Cordero, R. R., Damiani, A., Gallardo, L., Garreaud, R. D., et al. (2018). Anthropogenic drying in central-southern Chile evidenced by long-term observations and climate model simulations. *Elem. Sci. Anth.* 6:74. doi: 10.1525/elementa.328

Boisier, J. P., Rondanelli, R., Garreaud, R. D., and Muñoz, F. (2016). Anthropogenic and natural contributions to the Southeast Pacific precipitation decline and recent megadrought in central Chile. *Geophys. Res. Lett.* 43, 413–421. doi: 10.1002/2015GL067265

Carrasco, J. F., Casassa, G., and Quintana, J. (2005). Changes of the 0°C isotherm and the equilibrium line altitude in central Chile during the last quarter of the 20th century / Changements de l'isotherme 0°C et de la ligne d'équilibre des neiges dans le Chili central durant le dernier quart du 20éme siécle. *Hydrol. Sci. J.* 50, 933–948. doi: 10.1623/hysj.2005.50.6.933

Casassa, G., Rivera, A., Escobar, F., Acuña, C., Carrasco, J., and Quintana, J. (2003). Snow line rise in central Chile in recent decades and its correlation with climate. *Geophys. Res. Abstr.* 5:14395.

Cortés, G., Girotto, M., and Margulis, S. (2016). Snow process estimation over the extratropical Andes using a data assimilation framework integrating MERRA data and Landsat imagery. *Water Resour. Res.* 52, 2582–2600. doi: 10.1002/2015WR018376

Cortés, G., Girotto, M., and Margulis, S. A. (2014). Analysis of sub-pixel snow and ice extent over the extratropical Andes using spectral unmixing of historical Landsat imagery. *Remote Sens. Environ.* 141, 64–78. doi: 10.1016/j.rse.2013.10.023

Cortés, G., and Margulis, S. (2017). Impacts of El Niño and La Niña on interannual snow accumulation in the Andes: results from a high-resolution 31 year reanalysis. *Geophys. Res. Lett.* 44, 6859–6867. doi: 10.1002/2017GL073826

CR2 (2015). *Report to the Nation. The 2010-2015 Mega-Drought: A Lesson for the Future*. Center for Climate and Resilience Research (CR2), 28.

Dettinger, M. D. (2013). Atmospheric rivers as drought busters on the U.S. West Coast. *J. Hydrometeorol.* 14, 1721–1732. doi: 10.1175/JHM-D-13-02.1

Dettinger, M. D., Ralph, F. M., Das, T., Neiman, P. J., and Cayan, D. R. (2011). Atmospheric rivers, floods and the water resources of California. *Water* 3, 445–478. doi: 10.3390/w3020445

Escobar, F., and Aceituno, P. (1998). Influencia del fenomeno ENSO sobre la precipitacion nival en el sector andino de Chile Central durante el invierno. *Mech. Ageing Dev.* 4, 201–213.

Falvey, M., and Garreaud, R. (2007). Wintertime precipitation episodes in central Chile: associated meteorological conditions and orographic influences. *J. Hydrometeorol.* 8, 171–193. doi: 10.1175/JHM562.1

Folland, C. K., Renwick, J. A., Salinger, M. J., and Mullan, A. B. (2002). Relative influences of the Interdecadal Pacific Oscillation and ENSO on the South Pacific Convergence Zone. *Geophys. Res. Lett.* 29, 21-1–21-4. doi: 10.1029/2001GL014201

Garreaud, R. D., Boisier, J. P., Rondanelli, R., Montecinos, A., Sepúlveda, H. H., and Veloso-Aguila, D. (2019). The Central Chile Mega Drought (2010-2018): A climate dynamics perspective. *Int. J. Climatol.* 40, 421–439. doi: 10.1002/joc.6219

González-Reyes, Á., McPhee, J., Christie, D. A., Quesne, C. L., Szejner, P., Masiokas, M. H., et al. (2017). Spatiotemporal variations in hydroclimate across the Mediterranean Andes (30°-37° S) since the early twentieth century. *J. Hydrometeorol.* 18, 1929–1942. doi: 10.1175/JHM-D-16-0004.1

Gorodetskaya, I. V., Tsukernik, M., Claes, K., Ralph, M. F., Neff, W. D., and Van Lipzig, N. P. M. (2014). The role of atmospheric rivers in anomalous snow accumulation in East Antarctica. *Geophys. Res. Lett.* 41, 6199–6206. doi: 10.1002/2014GL060881

Grimm, A. M., and Tedeschi, R. G. (2009). ENSO and extreme rainfall events in South America. *J. Clim.* 22, 1589–1609. doi: 10.1175/2008JCLI2429.1

Guan, B., Molotch, N. P., Waliser, D. E., Fetzer, E. J., and Neiman, P. J. (2010). Extreme snowfall events linked to atmospheric rivers and surface air temperature via satellite measurements. *Geophys. Res. Lett.* 37, 2–7. doi: 10.1029/2010GL044696

Guan, B., Molotch, N. P., Waliser, D. E., Fetzer, E. J., and Neiman, P. J. (2013). The 2010/2011 snow season in California's Sierra Nevada: role of atmospheric rivers and modes of large-scale variability. *Water Resour. Res.* 49, 6731–6743. doi: 10.1002/wrcr.20537

Guan, B., and Waliser, D. E. (2015). Detection of atmospheric rivers: Evaluation and application of an algorithm for global studies. *J. Geophys. Res. Atmos.* 120, 12514–12535. doi: 10.1002/2015JD024257

Hoskins, B. J., and Hodges, K. I. (2005). A new perspective on Southern Hemisphere storm tracks. *J. Clim.* 18, 4108–4129. doi: 10.1175/JCLI3570.1

Huning, L. S., Guan, B., Waliser, D. E., and Lettenmaier, D. P. (2019). Sensitivity of seasonal snowfall attribution to atmospheric rivers and their reanalysis-based detection. *Geophys. Res. Lett.* 46, 794–803. doi: 10.1029/2018GL080783

Huning, L. S., Margulis, S. A., Guan, B., Waliser, D. E., and Neiman, P. J. (2017). Implications of detection methods on characterizing atmospheric river contribution to seasonal snowfall across Sierra Nevada, USA. *Geophys. Res. Lett.* 44, 10445–10453. doi: 10.1002/2017GL075201

Jenkner, J., Sprenger, M., Schwenk, I., Schwierz, C., Dierer, S., and Leuenberger, D. (2010). Detection and climatology of fronts in a high-resolution model reanalysis over the Alps. *Meteorol. Appl.* 17, 1–18. doi: 10.1002/met.142

Karoly, D. J. (1989). Southern hemisphere circulation features associated with El Niño-southern oscillation events. *J. Clim.* 2, 1239–52. doi: 10.1175/1520-0442(1989)002h1239:SHCFAWi2.0.CO;2

Lavers, D. A., Allan, R. P., Wood, E. F., Villarini, G., Brayshaw, D. J., and Wade, A. J. (2011). Winter floods in Britain are connected to atmospheric rivers. *Geophys. Res. Lett.* 38, 1–8. doi: 10.1029/2011GL049783

Lavers, D. A., and Villarini, G. (2015). The contribution of atmospheric rivers to precipitation in Europe and the United States. *J. Hydrol.* 522, 382–390. doi: 10.1016/j.jhydrol.2014.12.010

Lavers, D. A., Villarini, G., Allan, R. P., Wood, E. F., and Wade, A. J. (2012). The detection of atmospheric rivers in atmospheric reanalyses and their links to British winter floods and the large-scale climatic circulation. *J. Geophys. Res. Atmos.* 117, 1–13. doi: 10.1029/2012JD018027

Leung, L. R., and Qian, Y. (2009). Atmospheric rivers induced heavy precipitation and flooding in the western U.S. simulated by the WRF regional climate model. *Geophys. Res. Lett.* 36:L03820. doi: 10.1029/2008GL036445

Margulis, S. A., Cortés, G., Girotto, M., and Durand, M. (2016). A landsat-era Sierra Nevada snow reanalysis (1985-2015). *J. Hydrometeorol.* 17, 1203–1221. doi: 10.1175/JHM-D-15-0177.1

Margulis, S. A., Girotto, M., Cortés, G., and Durand, M. (2015). A particle batch smoother approach to snow water equivalent estimation. *J. Hydrometeorol.* 16, 1752–1772. doi: 10.1175/JHM-D-14-0177.1

Masiokas, M. H., Villalba, R., Luckman, B. H., and Mauget, S. (2010). Intra- to multidecadal variations of snowpack and streamflow records in the Andes of Chile and Argentina between 30° and 37° S. *J. Hydrometeorol.* 11, 822–831. doi: 10.1175/2010JHM1191.1

Montecinos, A., and Aceituno, P. (2003). Seasonality of the ENSO-related rainfall variability in central Chile and associated circulation anomalies. *J. Clim.* 16, 281–296. doi: 10.1175/1520-0442(2003)016<0281:SOTERR>2.0.CO;2

Mundhenk, B. D., Barnes, E. A., Maloney, E. D., and Baggett, C. F. (2018). Skillful empirical subseasonal prediction of landfalling atmospheric river activity using the Madden-Julian oscillation and quasi-biennial oscillation. *NPJ Clim. Atmos. Sci.* 1:20177. doi: 10.1038/s41612-017-0008-2

Neiman, P. J., Gaggini, N., Fairall, C. W., Aikins, J., Spackman, J. R., Leung, L. R., et al. (2017). An analysis of coordinated observations from NOAA's Ronald H. Brown ship and G-IV aircraft in a landfalling atmospheric river over the North Pacific during CalWater-2015. *Mthly. Weather Rev.* 145, 3647–3669. doi: 10.1175/MWR-D-17-0055.1

Neiman, P. J., Ralph, F. M., Moore, B. J., Hughes, M., Mahoney, K. M., Cordeira, J. M., et al. (2013). The landfall and inland penetration of a flood-producing atmospheric river in Arizona. Part I: observed synoptic-scale, orographic, and hydrometeorological characteristics. *J. Hydrometeorol.* 14, 460–484. doi: 10.1175/JHM-D-12-0101.1

Neiman, P. J., Ralph, F. M., Wick, G. A., Lundquist, J. D., and Dettinger, M. D. (2008). Meteorological characteristics and overland precipitation impacts of atmospheric rivers affecting the West Coast of North America based on eight years of SSM/I satellite observations. *J. Hydrometeorol.* 9, 22–47. doi: 10.1175/2007JHM855.1

Neiman, P. J., Schick, L. J., Ralph, F. M., Hughes, M., and Wick, G. A. (2011). Flooding in Western Washington: the connection to atmospheric rivers*. *J. Hydrometeorol.* 12, 1337–1358. doi: 10.1175/2011JHM1358.1

Quintana, J. M., and Aceituno, P. (2012). Changes in the rainfall regime along the extratropical west coast of South America (Chile): 30-43º S. *Atmósfera* 25, 1–22. Available online at: http://www.scielo.org.mx/scielo.php?script=sci_arttext&pid=S0187-62362012000100001&lng=es&tlng=en

Ralph, F. M., Neiman, P. J., Wick, G. A., Gutman, S. I., Dettinger, M. D., Cayan, D. R., et al. (2006). Flooding on California's Russian River: Role of atmospheric rivers. *Geophys. Res. Lett.* 33:L13801. doi: 10.1029/2006GL026689

Ralph, F. M., Rutz, J. J., Cordeira, J. M., Dettinger, M., Anderson, M., Reynolds, D., et al. (2019). A scale to characterize the strength and impacts of atmospheric rivers. *Bull. Amer. Meteor. Soc.* 100, 269–289. doi: 10.1175/BAMS-D-18-0023.1

Roe, G. H. (2005). Orographic precipitation. *Annu. Rev. Earth Planet. Sci.* 33, 645–671. doi: 10.1146/annurev.earth.33.092203.122541

Rutllant, J., and Fuenzalida, H. (1991). Synoptic aspects of the central Chile rainfall variability associated with the Southern Oscillation. *Int. J. Climatol.* 11, 63–76. doi: 10.1002/joc.3370110105

Saha, S., Moorthi, S., Pan, H.-L., Wu, X., Wang, J., Nadiga, S., et al. (2010). The NCEP climate forecast system reanalysis. *Bull. Am. Meteorol. Soc.* 91, 1015–1058. doi: 10.1175/2010BAMS3001.1

Seager, R., Harnik, N., Robinson, W. A., Kushnir, Y., Ting, M., Huang, H.-P., et al. (2005). Mechanisms of ENSO-forcing of hemispherically symmetric precipitation variability. *Q. J. R. Meteorol. Soc.* 131, 1501–27. doi: 10.1256/qj.04.96

Sulca, J., Takahashi, K., Espinoza, J.-C., Vuille, M., and Lavado-Casimiro, W. (2018). Impacts of different ENSO flavors and tropical Pacific convection variability (ITCZ, SPCZ) on austral summer rainfall in South America, with a focus on Peru. *Int. J. Climatol.* 38, 420–435. doi: 10.1002/joc.5185

Viale, M., and Garreaud, R. (2015). Orographic effects of the subtropical and extratropical Andes on upwind precipitating clouds. *J. Geophys. Res. Atmos.* 120, 4962–74. doi: 10.1002/2014JD023014

Viale, M., Houze, R. A., and Rasmussen, K. L. (2013). Upstream orographic enhancement of a narrow cold-frontal rainband approaching the Andes. *Mthly. Weather Rev.* 141, 1708–1730. doi: 10.1175/MWR-D-12-00138.1

Viale, M., and Nuñez, M. N. (2011). Climatology of winter orographic precipitation over the subtropical central Andes and associated synoptic and regional characteristics. *J. Hydrometeorol.* 12, 481–507. doi: 10.1175/2010JHM1284.1

Viale, M., Valenzuela, R., Garreaud, R. D., and Ralph, F. M. (2018). Impacts of atmospheric rivers on precipitation in southern south America. *J. Hydrometeorol.* 19, 1671–1687. doi: 10.1175/JHM-D-18-0006.1

Widlansky, M. J., Timmermann, A., Stein, K., McGregor, S., Schneider, N., England, M. H., et al. (2013). Changes in South Pacific rainfall bands in a warming climate. *Nat. Clim. Change* 3, 417–423. doi: 10.1038/nclimate1726

Zagrodnik, J. P., McMurdie, L. A., and Houze, R. A. (2018). Stratiform precipitation processes in cyclones passing over a coastal mountain range. *J. Atmos. Sci.* 75, 983–1004. doi: 10.1175/JAS-D-17-0168.1

Zagrodnik, J. P., McMurdie, L. A., Houze, R. A., and Tanelli, S. (2019). Vertical structure and microphysical characteristics of frontal systems passing over a three-dimensional coastal mountain range. *J. Atmos. Sci.* 76, 1521–1546. doi: 10.1175/JAS-D-18-0279.1

Zhang, W., and Villarini, G. (2018). Uncovering the role of the East Asian jet stream and heterogeneities in atmospheric rivers affecting the western United States. *Proc. Natl. Acad. Sci. U. S. A.* 115, 891–96. doi: 10.1073/pnas.1717883115

Zhu, Y., and Newell, R. E. (1998). A proposed algorithm for moisture fluxes from atmospheric rivers. *Mthly. Weather Rev.* 126, 725–735. doi: 10.1175/1520-0493(1998)126<0725:APAFMF>2.0.CO;2

Conflict of Interest: The authors declare that the research was conducted in the absence of any commercial or financial relationships that could be construed as a potential conflict of interest.

Copyright © 2020 Saavedra, Cortés, Viale, Margulis and McPhee. This is an open-access article distributed under the terms of the Creative Commons Attribution License (CC BY). The use, distribution or reproduction in other forums is permitted, provided the original author(s) and the copyright owner(s) are credited and that the original publication in this journal is cited, in accordance with accepted academic practice. No use, distribution or reproduction is permitted which does not comply with these terms.

frontiers in Earth Science

ORIGINAL RESEARCH
published: 02 October 2020
doi: 10.3389/feart.2020.00328

WRF High Resolution Dynamical Downscaling of Precipitation for the Central Andes of Chile and Argentina

Vanucia Schumacher[1], Alfonso Fernández[2,3], Flavio Justino[1] and Alcimoni Comin[1]*

[1] Department of Agriculture Engineering, Universidade Federal de Viçosa, Viçosa, Brazil, [2] Department of Geography & Mountain GeoScience Group, Universidad de Concepción, Concepción, Chile, [3] Department of Geological Sciences, University of Texas at San Antonio, San Antonio, TX, United States

This study evaluates the skill of the Weather Research and Forecasting (WRF) model to reproduce the variability of precipitation over the Central Andes of Chile and Argentina, a region characterized by complex topography. The simulation corresponds to a dynamical downscaling of ERA-Interim, in the period between 1996 and 2015, performed with two nested grids, at 9 and 3 km horizontal resolution. Precipitation data from 62 rain gauges from Chile and Argentina were used to evaluate the performance of WRF simulations carried out at the annual and warm-cold season analysis. The results of this study indicate that WRF at 9 and 3 km is able to reproduce the main characteristics of seasonal and interannual precipitation variability along the study area. On the windwards slopes of the Andes, however, WRF at 9 km presents a wet bias in relation to observation and WRF at 3 km. Additionally, WRF at 3 km achieves better performance of precipitation as elevation increases, most likely due to the better-resolved topography. To our knowledge, this is the first study that compares performance between nested domains on mountain areas that found a better match between the model and observations, as elevations increased.

Keywords: WRF model, downscaling, precipitation, spatio-temporal validation, Andes

OPEN ACCESS

Edited by:
Frédéric Frappart, UMR5566 Laboratoire d'études en Géophysique et Océanographie Spatiales (LEGOS), France

Reviewed by:
Francina Dominguez, University of Illinois at Urbana-Champaign, United States
Angela Maria Rendon, University of Antioquia, Colombia
Maria Dillon, Consejo Nacional de Investigaciones Científicas y Técnicas (CONICET), Argentina

****Correspondence:***
Vanucia Schumacher
vanucia-schumacher@hotmail.com

Specialty section:
This article was submitted to Hydrosphere, a section of the journal Frontiers in Earth Science

Received: *02 October 2019*
Accepted: *15 July 2020*
Published: *02 October 2020*

Citation:
Schumacher V, Fernández A, Justino F and Comin A (2020) WRF High Resolution Dynamical Downscaling of Precipitation for the Central Andes of Chile and Argentina. Front. Earth Sci. 8:328. doi: 10.3389/feart.2020.00328

1. INTRODUCTION

Atmospheric conditions in the Central Andes of Chile and Argentina are particularly distinct as a result of the interplay of complex topography and large-scale synoptic systems (Garreaud, 2009). While on the west slope there is a marked seasonality of dry-warm summers and wet-cold orographically intensified winters (Falvey and Garreaud, 2007; Viale and Nuñez, 2011), the eastern side is wetter during summers due to the development of the South America Low Level Jet (SALLJ) which originates in the Brazilian Plateau (Garreaud et al., 2009). This makes this section of the Andes a crucial water reservoir for socio-economic activities in this region (Mark et al., 2015) that need to be monitored to support better adaptation for future challenges associated with global climate warming. However, precise values of precipitation are scarce, as the natural barrier of the Andes makes it difficult to install, maintain, and expand a network of meteorological stations, resulting in the lack of reliable measurements of long-term historical observations.

In recent years, several gridded datasets such as a reanalysis have been used for climate assessment on regional and global scales. However, in most cases these datasets have coarse horizontal resolutions, leading to misinterpretation of dynamical processes of regional and local climate variability—limitations that are higher in complex terrains such as the mountainous region of the Andes (e.g., Ward et al., 2011; Soares et al., 2012).

Regional climate modeling can help overcome the dearth of records and the problem with coarse spatial resolution in the Andes, as dynamical downscaling can support a better understanding of the spatio-temporal patterns that the discrete nature of sparse meteorological networks do not provide. Downscaling approaches are widely used to provide climatic information at fine spatial resolutions. Regional climate models (RCMs) have been applied for dynamical downscaling with an initial and lateral boundary taken from global to regional/local scales. This strategy has frequently been used in mountainous regions in an attempt to reduce scale mismatches—a relevant problem between model output describing large-scale climate and the scale required to characterize regions of complex topography (Mög and Kaser, 2011; Hughes et al., 2017; Ambrizzi et al., 2019).

Increasing availability of regional climate from initiatives such as the COordinated Regional Climate Downscaling EXperiment (CORDEX) have demonstrated the potential of RCMs to support description of synoptic patterns and dynamical processes of climate in the complex Andean terrain, while also providing more detailed projection scenarios (Ambrizzi et al., 2019). Nevertheless, these simulations are still too coarse, about 50 km for South America (Solman and Blázquez, 2019), relative to the intricate Andean climate. To date, higher resolution downscaling in the Andes has been mostly restricted to short periods (e.g., Mourre et al., 2016), with very few recent studies carrying out long-term simulations (Bozkurt et al., 2019).

The aim of this study is to assess the skill of a simulation performed with the Weather Research and Forecasting Model (WRF) at high resolution (9 and 3 km), relative to observations of precipitation along the complex terrain in the Central Andes of Chile and Argentina, over a 20-year period. The WRF model is widely used by the scientific community to dynamically downscale coarse global climate model output. The model has reasonably simulated precipitation patterns and variability in several complex topography regions (Cardoso et al., 2013; Fathalli et al., 2016; Comin et al., 2018). Posada-Marín et al. (2019) demonstrated that the WRF downscaling outperforms ERA-Interim reanalysis in the representation of precipitation, due to a better representation of orographic effects, over the tropical Cauca river valley in Colombia. However, little information is available on the performance of the downscaling method in the Andean mountain region. This paper is organized as follows: section 2 presents the study area, data and methods, Section 3 the results and the discussion of the main findings, and the conclusion are presented in section 4.

2. DATA AND METHODS

2.1. Study Area

The high-Andes of central Chile and Argentina (**Figure 1**), have a high concentration of glaciers and glacial lakes, which are the main source of water for important rivers that provide fresh water to more than 10 million people in Chile and more than 2 million in Argentina (Malmros et al., 2018). The Andean topography leads to significant differences in precipitation distribution between its eastern and western slopes, for example, in the transition between the tropics and extratropics, annual precipitation and cloud frequency are more pronounced on the western slopes and reduced on the eastern slopes of the Andes (Viale et al., 2019).

In the semi-arid Central Andes of Chile, the climate is characterized by wet and cold winters (April-September), with snow accumulation at high elevations. This contrasts with warm and dry summers (October-March) with almost zero precipitation and low relative humidity. This region is also commonly referred to as having a Mediterranean-type climate (32°S–38°S) (Falvey and Garreaud, 2007; Bown et al., 2008; Bravo et al., 2017). These climate features are mainly associated with the northward-southward displacement of high-pressure in the Pacific Ocean, which generally inhibits precipitation during the warm season, but allows the passage of westerlies and the occurrence of frontal precipitation during the cold season (Masiokas et al., 2009). In contrast, the eastern slopes of the Andes (Argentinean side) is wetter during summer, enhanced by warm and humid air transported by a low-level jet (e.g., Garreaud et al., 2009; Espinoza et al., 2015). From a longitudinal profile along the 33°S, the annual average precipitation ranges from 459 mm in Valparaiso (33.02°S, 71.63°W, 41 m) to 356 mm in Santiago (33.45°S, 70.70°W, 520 m) on the Chilean side, and 180 mm in Mendoza (32.89°S, 68.83°W, 769 m) on the Argentinean side (Corripio and Purves, 2005), clearly indicating the effect of topography.

2.2. WRF Simulation

The model used in this study is the WRF model with its Advanced Research WRF dynamical solver (Skamarock et al., 2008) version 3.5.1. The WRF model was setup with two nested grids (**Figure 1B**), with high regional resolution at 9 km (WRF9km) and 3 km (WRF3km) horizontal grid spacing, using a two-way nesting technique and Mercator projection. Two-way nesting ensures dynamical interaction domains. Both grids are centered in the Central Andes of Chile and Argentina, with the 9-km domain extending 70 x 70 grid points, and 82 x 106 for the higher-resolution 3-km inner nest. Both domains have 28 vertical levels from the surface to 50 hPa. To maximize the development of internal dynamics within the domains, the selection of domain sizes and the number of grid points was dictated by a trade-off between computational constrains and the resolution of the boundary conditions (see next paragraph). The WRF9km domain covers a region of 630 x 630 km, assimilating several points from the initial and boundary conditions, while the size of the WRF3km is 246 x 318 km.

The WRF model run, simulated 20 years, from 1996 to 2015, using initial and lateral boundary conditions taken from the European Center for Medium-Range Weather Forecasts (ECMWF), ERA-Interim reanalysis (ERA-I) (Dee et al., 2011). Lateral forcing was updated every 6 h at 0.75° horizontal resolution and 17 pressure levels. The physical parameterizations used include the WRF Single Moment 6-class (WSM6, Hong et al., 2010). This scheme performed better when compared to the other schemes in the high complex topography of the Andes (Comin et al., 2018). The radiation schemes of Rapid Radiative Transfer Model (RRTM, Mlawer et al., 1997) for longwave and

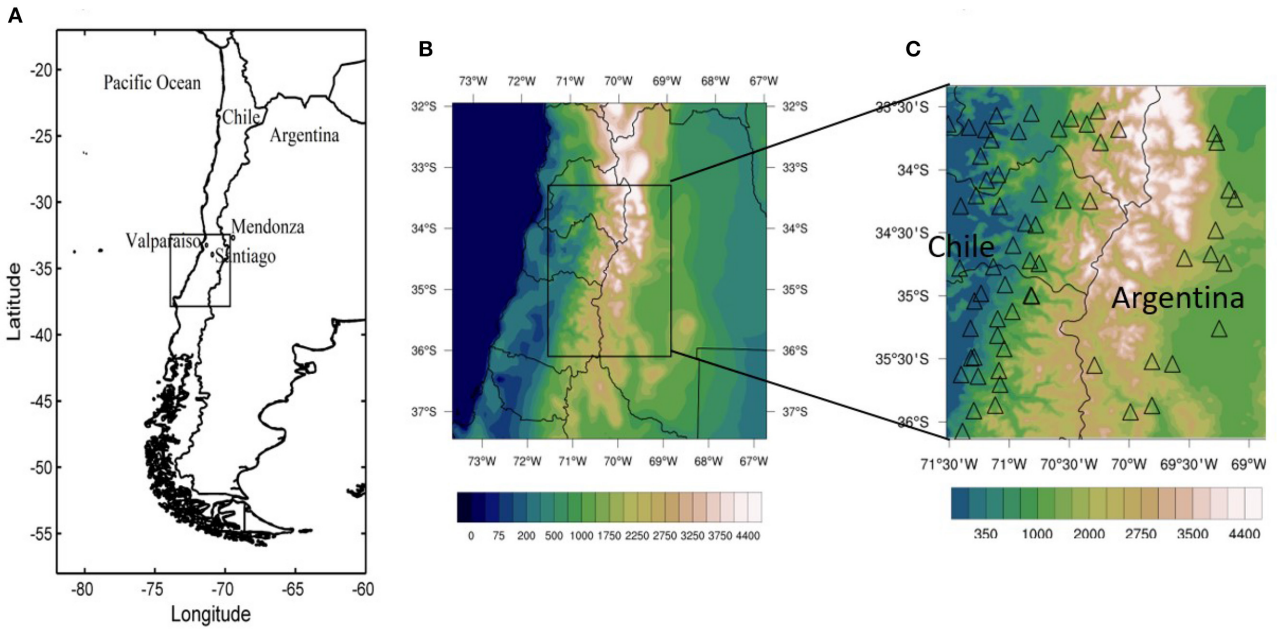


FIGURE 1 | (A) Location of the 9 km WRF model domain within Chile **(B)** WRF at 9 km (full map) and 3 km (black rectangle), and **(C)** geographic positions of the weather stations located within the 3 km domain, with the main topographic features.

the Dudhia scheme (Dudhia, 1989) for shortwave was used. The MM5 similarity surface layer scheme (Paulson, 1970) and the thermal diffusion scheme was used for land surface. This land surface scheme is a Land Surface Model based on the MM5 5-layer soil temperature model with an energy budget that includes radiation, sensible, and latent heat flux (Huang et al., 2014). The Yonsei University parameterization of the planetary Boundary Layer (Hong et al., 2010). The Kain-Fritsch scheme to atmospheric convection (Kain, 2004) are applied for the outer domain but turned off for the inner domain in order to explicitly resolve precipitation processes.

2.3. Observational Datasets

Daily precipitation data in Central Chile and Argentina were used. The observations were provided by the Direccin General de Aguas (DGA) of Chile (http://snia.dga.cl/) and the Water Resources Agency of Argentina (Subsecretara de Recursos Hdricos (SSRH); http://bdhi.hidricosargentina.gob.ar/). We selected all records within the study domain with at least 90% of non-missing data available. Observations were checked for consistency and continuity, retaining 48 stations for Chile and 14 for Argentina for the period between 1996 to 2015 (**Table 1**). **Figure 1C** presents the distribution of precipitation stations.

2.4. Comparison Methods

In order to quantify WRF's ability to represent annual and seasonal precipitation, under distinct spatial resolutions, statistical metrics were computed, namely the percent bias (PB), the mean absolute error (MAE), the Pearson correlation coefficient (PC) and the Willmott index of Agreement (d). Positive values of PB indicate an overestimation of modeled precipitation in respect to observed values, whereas negative values indicate underestimation. The MAE provides information on the average magnitude of simulation errors, considering both systematic and random errors, where 0 is the perfect match. The PC corresponds to the linear relationship between the model output and observations, where 1 is most desirable. Willmott's index is a standardized measure of the degree of model temporal-prediction error and varies between 0 and 1, where value of 1 indicates a perfect match, and 0 no agreement. A more detailed description of these methods can be found in Wilks (2011). Analyses and comparisons are performed using the nearest grid point of the model to observations. Model daily precipitation is computed from 12 to 12 UTC. In this study, the analysis is developed for the annual period as well as for the warm (October-March) and cold (April-September) seasons.

3. RESULTS

3.1. Annual and Seasonal Precipitation Over Central Andes

The observed annual precipitation pattern is marked by a significant latitudinal gradient with high precipitation values (more than 2000 mm/year) concentrated southward of 35°S in the Chilean side. On the other hand, observations in Argentina ranges from 500 to less than 200 mm/year, with maximum values north of 34°S and southernmost of 35°S (**Figure 2A**). This difference in precipitation magnitude is characteristic of the rain shadow effect in this section of the Andes, determining a west-east contrast between the Chilean and Argentinian sides.

TABLE 1 | Geographical characteristics of the selected weather stations for (WS1-WS47) Chile and (WS48-WS61) Argentina.

Indice	Name	Lat (°S)	Lon (°W)	Elevation (m.a.s.l)	Period
WS1	Maitenes Bocatoma	33.53	70.26	1,143	1996-2015
WS2	Fundo Marruecos	33.55	70.81	430	1996-2015
WS3	Mallarauco	33.56	71.11	176	1996-2015
WS4	La Obra Recinto Emos	33.59	70.48	796	1996-2015
WS5	Cerrillos De Leyda	33.63	71.51	182	1996-2015
WS6	San Jose De Maipo Reten	33.63	70.35	943	1996-2015
WS7	Estero Puanque En Ruta78	33.66	71.34	93	1996-2015
WS8	Pirque	33.67	70.58	659	1996-2015
WS9	El Yeso Embalse	33.67	70.08	2,475	1996-2015
WS10	Melipilla	33.68	71.19	168	1996-2015
WS11	El Vergel	33.69	70.92	340	1996-2015
WS12	Carmen De Las Rosas	33.75	71.15	165	1996-2015
WS13	San Gabriel	33.78	70.23	1,266	1996-2015
WS14	Los Guindos	33.89	71.24	125	1996-2015
WS15	Villa Alhue	34.03	71.09	197	1996-2015
WS16	Barrera Loncha	34.08	71.18	144	1996-2015
WS17	Rancagua Cachapoal-Dcp	34.19	70.75	515	1996-2015
WS18	Cocalan	34.2	71.27	120	1996-2015
WS19	Canal Sauzal En Puente	34.24	70.55	750	2006-2015
WS20	Rio Pangal En Pangal	34.24	70.32	1,500	2002-2015
WS21	Pichidegua	34.28	71.4	110	1996-2015
WS22	Coltauco	34.28	71.08	253	1996-2015
WS23	Rengo	34.42	70.86	310	1996-2015
WS24	Popeta	34.43	70.77	480	1996-2015
WS25	San Fernando	34.59	70.96	350	1996-2015
WS26	Rio Tinguiririca Bajos	34.71	70.82	560	1996-2015
WS27	La Rufina	34.74	70.75	743	1996-2015
WS28	Convento Viejo	34.76	71.13	239	1996-2015
WS29	La candelaria	34.78	71.41	213	1996-2015
WS30	Santa Susana	34.91	71.03	410	1996-2015
WS31	Curico	34.98	71.23	195	1996-2015
WS32	Rio Teno Despues De Junta	34.99	70.82	647	2000-2015
WS33	Los Quees	35	70.81	663	1996-2015
WS34	Lontue	35.04	71.29	199	1996-2015
WS35	Monte Oscuro	35.12	70.97	632	1996-2015
WS36	Potrero Grande	35.18	71.09	445	1996-2015
WS37	El Guindo	35.25	71.32	250	1996-2015
WS38	Agua Fria	35.31	71.09	560	1996-2015
WS39	Fundo El Radal	35.41	71.04	685	1996-2015
WS40	Huapi	35.48	71.29	250	1996-2015
WS41	El Durazno	35.49	71.31	275	1996-2015
WS42	Vilches Alto	35.59	71.08	1,058	1996-2015
WS43	Colbun (Maule Sur)	35.62	71.4	280	1996-2015
WS44	Coloroado	35.63	71.26	420	1996-2015
WS45	Armerillo	35.7	71.07	492	1996-2015
WS46	Hornillo	35.86	71.11	810	1996-2015
WS47	Ancoa Embalse	35.91	71.29	421	1996-2015
WS48	Juan Amigo	36.07	71.39	460	1996-2015
WS49	La Remonta	33.71	69.29	1,360	1996-2015
WS50	Valle de Uco	33.78	69.27	1,199	1996-2015
WS51	Yaucha	34.16	69.17	1,471	1996-2015
WS52	Puesto Papagayos	34.23	69.12	1,529	1996-2015
WS53	Arroyo Hondo	34.48	69.28	1,900	1996-2015
WS54	La Jaula	34.67	69.32	1,457	1996-2015
WS55	Las Aucas	34.7	69.54	1,800	1996-2015
WS56	Juncalito	34.74	69.21	1,593	1996-2015
WS57	Loma Negra	35.26	69.25	1,365	2003-2015
WS58	Pincheira	35.52	69.81	1,775	1996-2015
WS59	Dique	35.54	69.64	1,524	1996-2015
WS60	Los Mayines	35.55	70.29	1,663	1996-2015
WS61	Bardas Blancas	35.87	69.81	1,445	1996-2015
WS62	Arroyo La Vaina	35.92	69.99	1,550	1996-2015

The seasonal variability is also dictated by the contrast between the two sides of the Andean mountain range (**Figure 2**). In the warm season, whereas the amount of precipitation decreases northward of 35°S in Chile, a gradual increase characterizes the Argentinian sector. The occurrence of precipitation is associated with convective activity on both slopes. However, the incursion of warm and moist air from the Amazon basin by the SALLJ favors higher precipitation in the eastern slopes of the Central Andes (Marengo et al., 2004; Castañeda and Ulke, 2015). On the other hand, the incursion of the winter frontal systems leads to a significant increase in precipitation on the Chilean side. In Argentina, higher precipitation is observed to the north of 35°S during the cold season, compared to the mild precipitation values north of this point.

Figure 3 shows topography and precipitation features based on the WRF simulations and ERA-I. The spatial pattern of annual and seasonal precipitation is well-captured by WRF3km as well as the WRF9km. Both simulations are able to capture the latitudinal gradient of precipitation, and the seasonal contrast between warm-cold seasons. Overall, WRF3km and WRF9km present similar patterns, although it is notable that in some regions or particular points, precipitation is overestimated at 9 km with respect to observations and WRF3km, likely due to the model topography in the WRF9km. Modeling studies in steep terrain have shown that by smoothing topographic features results an increase of precipitation in lower resolutions (e.g., Soares et al., 2012). This is clearly noticeable in the spatial pattern shown by ERA-I, precipitation features of which are oversmoothed due to the complete absence of the orographic effect (see **Figures 3A–C**). However, this reinforces the relevant added value of downscaling with increasing resolution.

To further illustrate differences in the representation of the annual and seasonal precipitation between the WRF, ERA-I and observations, **Figures 4–8** shows the metrics used to quantify the reliability of the WRF simulations. For Chile (**Figure 4A**) the values of PB show that WRF3km tends to underestimate precipitation in relation to observations by up to 50% at annual

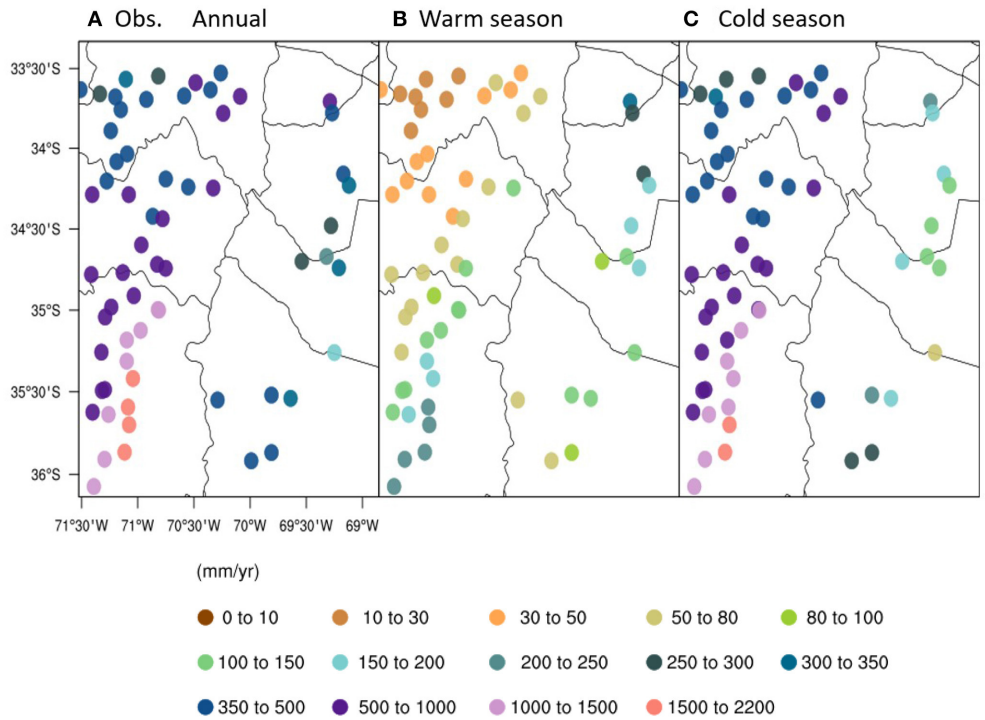


FIGURE 2 | (A–C) Spatial distribution of annual and warm-cold season accumulated precipitation from observations, between 1996 and 2015. The vertical black line represents the border between Chile and Argentina.

scale as well as in warm-cold seasons, mostly on the west of windward stations in Chilean side (west of 71°W) (**Figure 5**). By spatial PB analysis, a wet bias is clearly seen in the nearest locations to windward mountain range, with large bias values to the north of 35°S depicted by both WRF simulations. This wet bias is extended in almost all locations to windward of the Andes by the WRF9km, and also for some stations on the Argentine side, while the WRF9km have larger variability, the majority of stations show negative bias, however, about 33% of stations show positive bias at annual and seasonal scales.

ERA-I overestimates precipitation at all scales as expected due to its low spatial resolution and smooth topography. Both WRF3km and WRF9km have smaller PB variability during the warm season, most likely associated with lower distribution of precipitation during this period as shown in **Figure 3**. On the other hand, in Argentina (**Figure 4E**) the PB distribution shows good performance of both WRF simulations, especially in WRF3km. On the contrary, ERA-I overestimates precipitation in Argentina more than in Chile at annual and seasonal scales (see **Figures 4**, **5**).

Large values of bias (negative or positive) are accompanied by limited performance of the WRF simulations as revealed by the MAE (**Figures 4B,F**, **6**). Higher errors are observed at the annual and cold season periods, while errors are smaller during the warm season and on the Argentina side, associated with lower rainfall variability. Based on PC distribution (**Figures 4C,G**) higher correlation at the annual duration and cold season in both WRF simulations, above 0.7, contrast with the low correlations computed for Argentina during the warm season, especially to the north of 35°S (**Figure 7**). Conversely, the spatial distribution of d is well-simulated for the warm season in both Chile and Argentina (**Figures 4D,H**), especially for WRF3km. Poor performance is shown in almost all locations in western Chile (west of 71°W), especially insofar as annual and cold season are concerned (**Figure 8**). ERA-I shows a high range for PC although low performance is delivered by d in Chile, while on the Argentine side, low performance is noticed by both PC and d values.

In general, both WRF simulations have similar performances and the differences between them are not discrepant. The skill of the WRF3km, and both simulations compared to the ERA-I denotes that the high-resolution terrain features improve precipitation estimates, being able to cancel a positive bias exhibited in the ERA-I as input in downscaling.

3.2. Annual Cycle and Extremes Precipitation

The annual cycle of precipitation from observational and the WRF simulations in Chile and Argentina are depicted in **Figure 9**. On the Chilean side, the seasonal characteristics of precipitation are clearly well-simulated. During the warm months low precipitation dominates, while the maximum values occur during the cold months, especially between May to August. Monthly variability ranges from 300 to 600 mm/month. On the Argentinian side the seasonal variability is not as marked as in Chile. Maximum values of accumulated

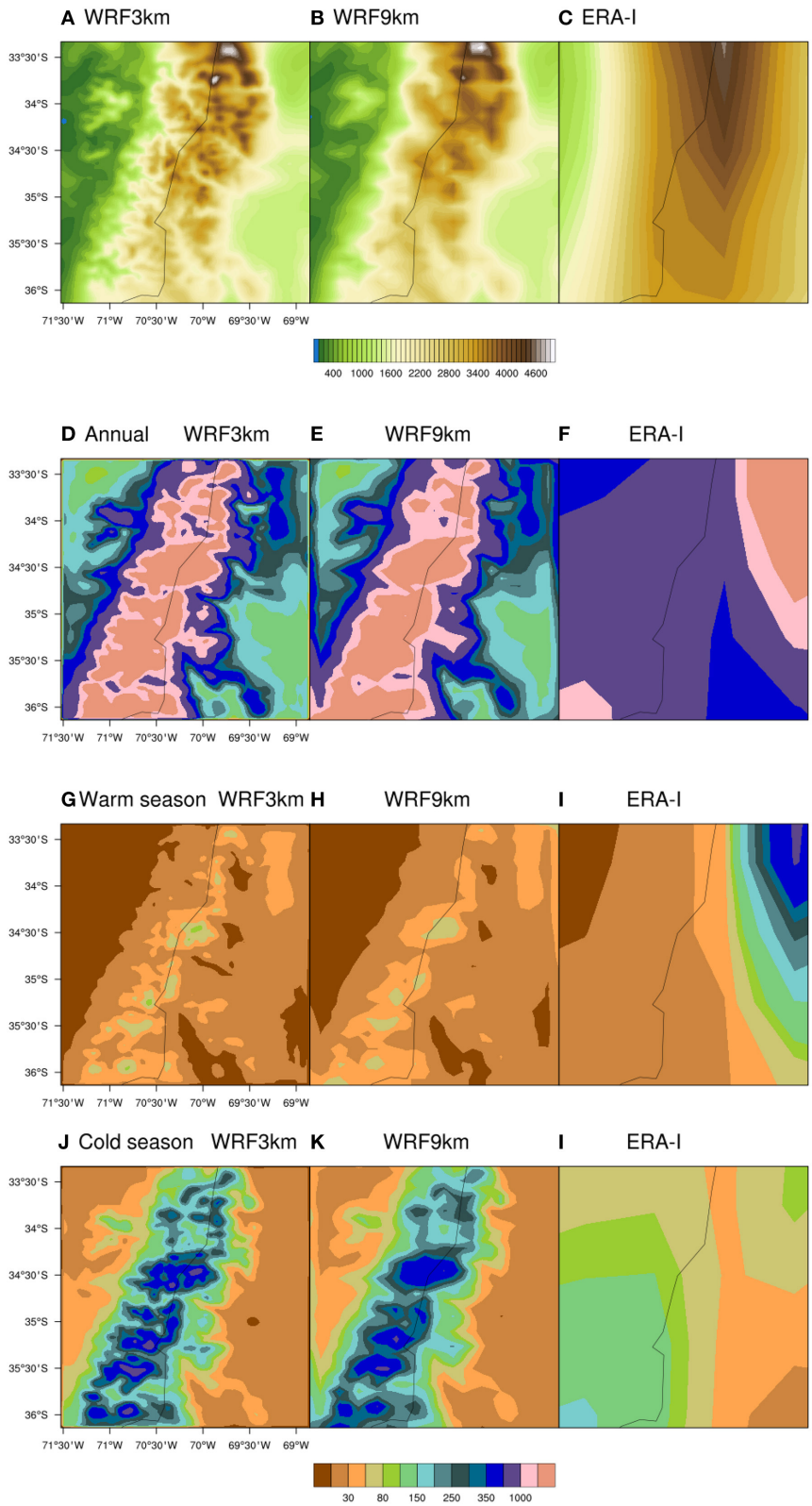


FIGURE 3 | (A–C) Models topographies and spatial distribution of annual and warm-cold season accumulated precipitation (mm), from **(D–F)** WRF3km, **(G–I)** WRF9km, and **(J–L)** ERA-I. The black line represents the border between Chile and Argentina.

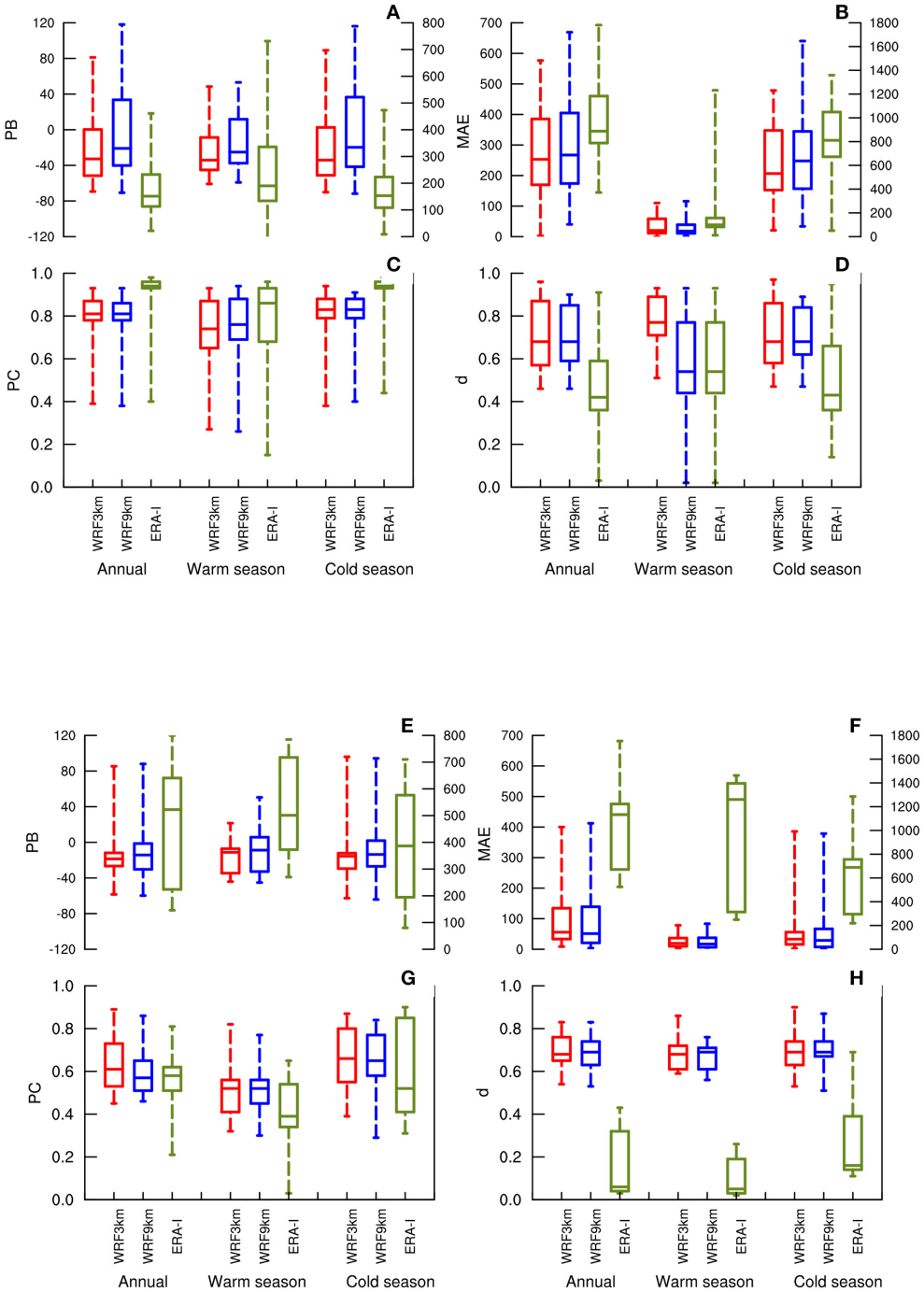


FIGURE 4 | Boxplot of the **(A)** bias and **(B)** mean absolute error, **(C)** coefficient correlation and **(D)** Willmott Index of Agreement (d) between observations and WRF3km (red), WRF9km (blue) and ERA-I (green) estimations for annual and warm-cold season precipitation. **(A–D)** relative to Chile and **(E–H)** for Argentina. Each boxplot shows the first, median, and third quartiles, while the whiskers indicate variability outside the lower and upper quartiles. Y-axis (right axis)is referent to ERA-I values, only for **(A,B,E,F)**.

precipitation occur especially in June, July, and August. Similar behavior is shown by Rivera et al. (2018) for the central region of Argentina from the La Jaula station (34.67°S, 69.32°W). These features in Argentina may likely be related to small scale atmospheric systems that exhibit a sub-seasonal dominant spectrum.

Chilean seasonality of precipitation is properly reproduced in the WRF3km as well as in the WRF9km, although variability

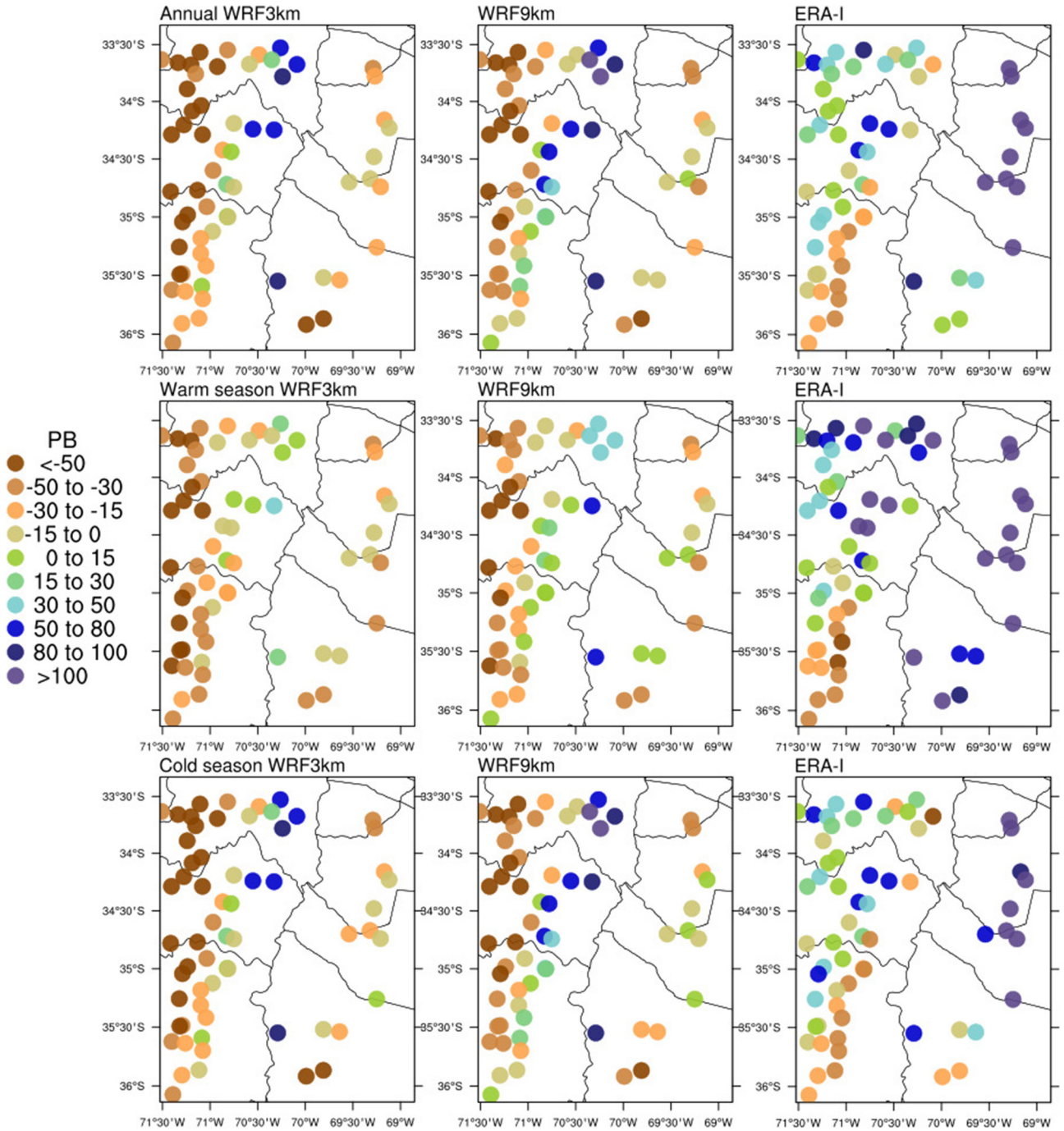


FIGURE 5 | Spatial distribution of percent bias for annual and warm-cold season precipitation.

of precipitation (interquartile range) during the cold months are slightly overestimated in WRF9km, whereas WRF3km underestimates it in relation to observations, especially during May, July, and August. This is probably associated with the smoothing of topographic features; as noted, WRF9km tends to overestimate precipitation compared to WRF3km, showing a slightly positive bias (see **Figure 4**). The lower spatial resolution in WRF9km induces the smoothing of the Andes effect, as a consequence this should enhance the weather systems, such as the upper-level trough and incursion of frontal systems increasing the amount of precipitation during the cold season as compared to WRF3km (Barrett et al., 2009). However, the median and maximum values are underestimated in both WRF simulations in almost all months. And this again is due to the

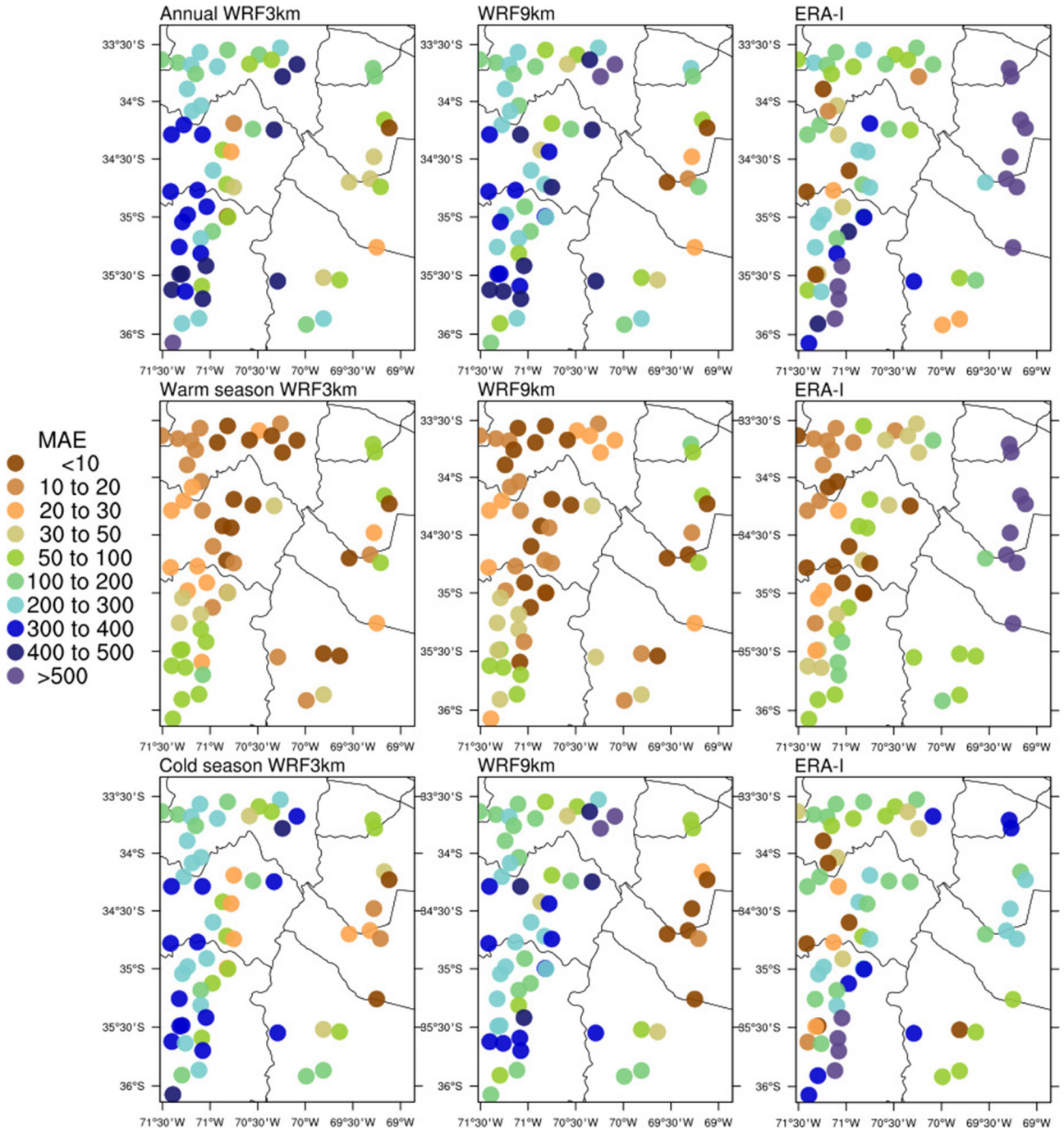


FIGURE 6 | Spatial distribution of mean absolute error for annual and warm-cold season precipitation.

fact that both simulations do not reproduce the complex terrain of the Andes in a realistic way because the resolution is not high enough for higher precipitation rates relative to observation (e.g., Cardoso et al., 2013).

Variability of monthly precipitation totals in Argentina is also well-represented by the WRF simulations, with slight underestimation of median values during the warm months in relation to observations. The maximum values of precipitation are generally underestimated by WRF simulations, except for February and October, when they are overestimated. This larger variability of precipitation during transition months may be associated with enhanced convective precipitation favored by the intensification of the low-level jet during the warm season (Marengo et al., 2004), while the smaller variability during cold

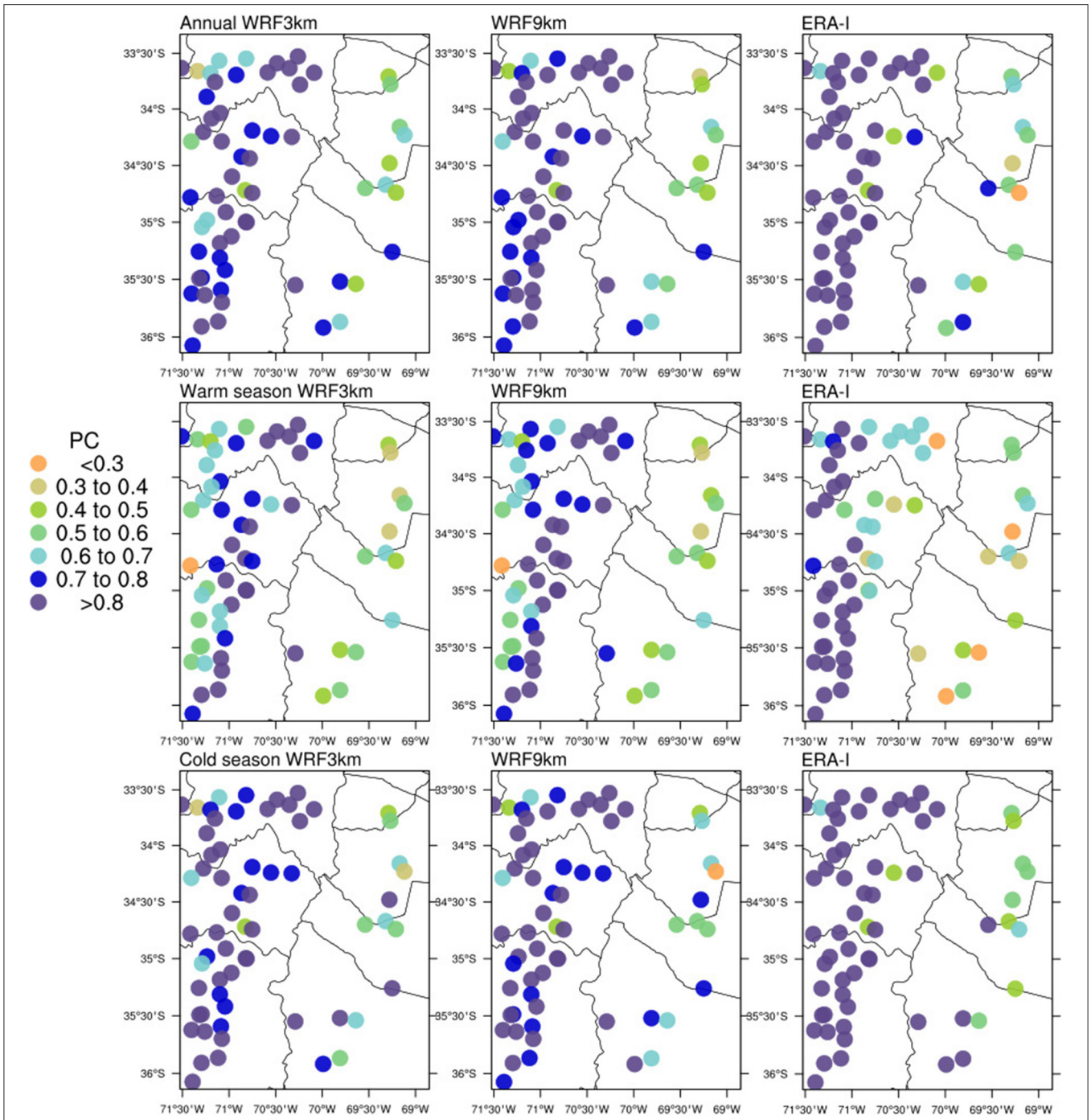


FIGURE 7 | Spatial distribution of coefficient correlation for annual and warm-cold season precipitation.

months can be due to representation of orographic uplift by the WRF simulations, showing a smaller amplitude of precipitation variability on the eastern side of the Andes. It is evident that the topography plays an important role in precipitation distribution leading to better or poorer performance from the WRF simulations according to the representation of the dominant precipitation systems, which are strongly modulated by the height and steepness of the Andes (e.g., Heikkilä et al., 2011; Bozkurt et al., 2019). On the other hand, ERA-I exceeds nearly twice the amount of monthly precipitation compared to WRF simulations on both sides of the Andes. In order to illustrate the performance of the WRF model in representing precipitation extremes, daily precipitation percentile ranges (10th, 25th, 50th, 75th, 90th, 95th, and 99th) were calculated

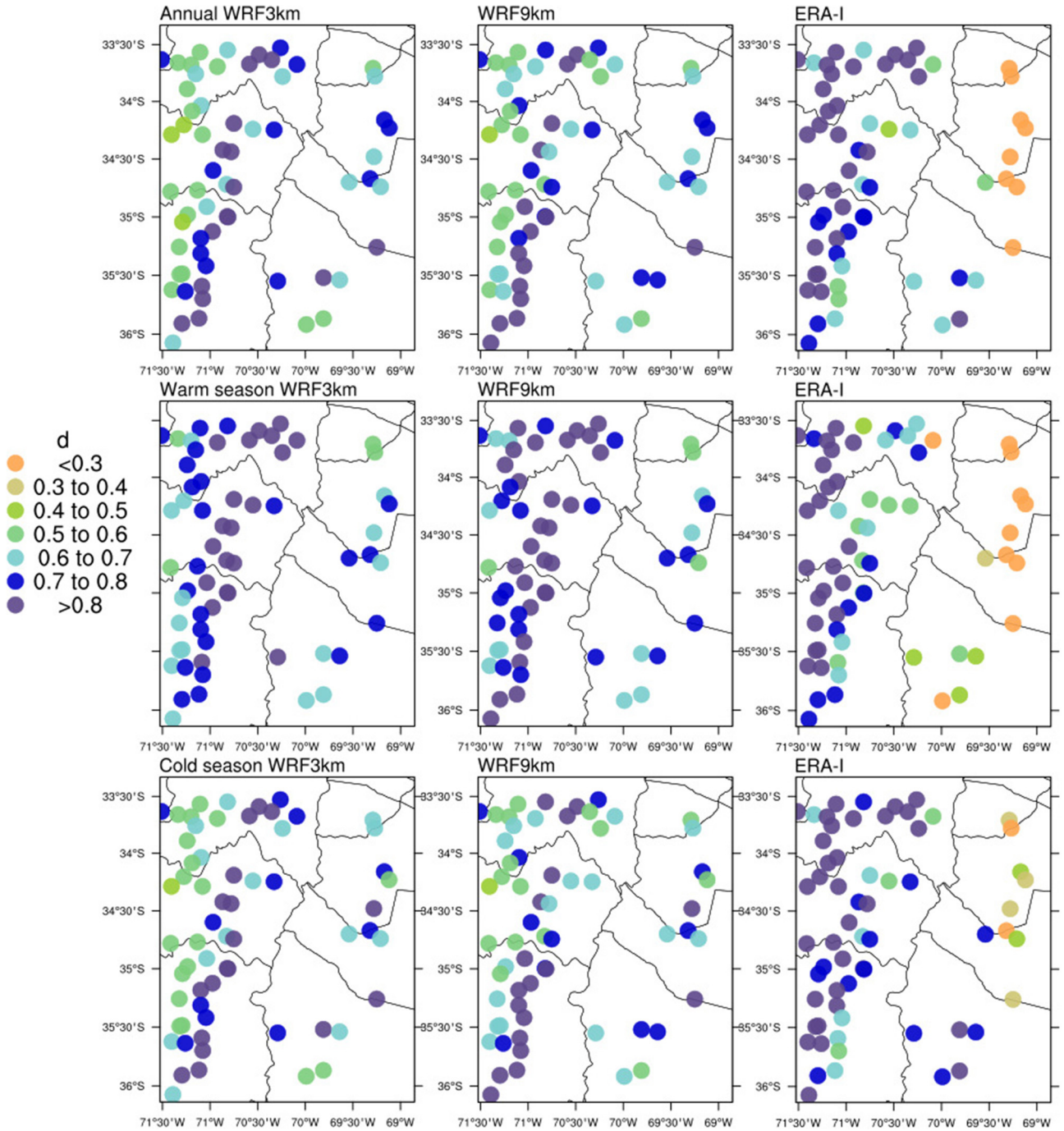


FIGURE 8 | Spatial distribution of Willmott Index of Agreement (d) for annual and warm-cold season precipitation.

for each station's location and compared statistically with the simulations (**Table 2**). In general, both WRF simulations show a good agreement in reproducing precipitation extremes according to the percentiles, with PC values above 0.8. It is interesting to note that there is no variation in the statistical performance (PB, PC, and d) from the 10th to 75th percentiles, however, MAE values increase in most cases according to the percentile range.

Concerning moderating precipitation, (percentiles below the 75th), improvement is noticed in WRF3km relative to WRF9km, especially for lower PB values, from 19.91 to 34.84% respectively. On the other hand, precipitation extremes between the 90th

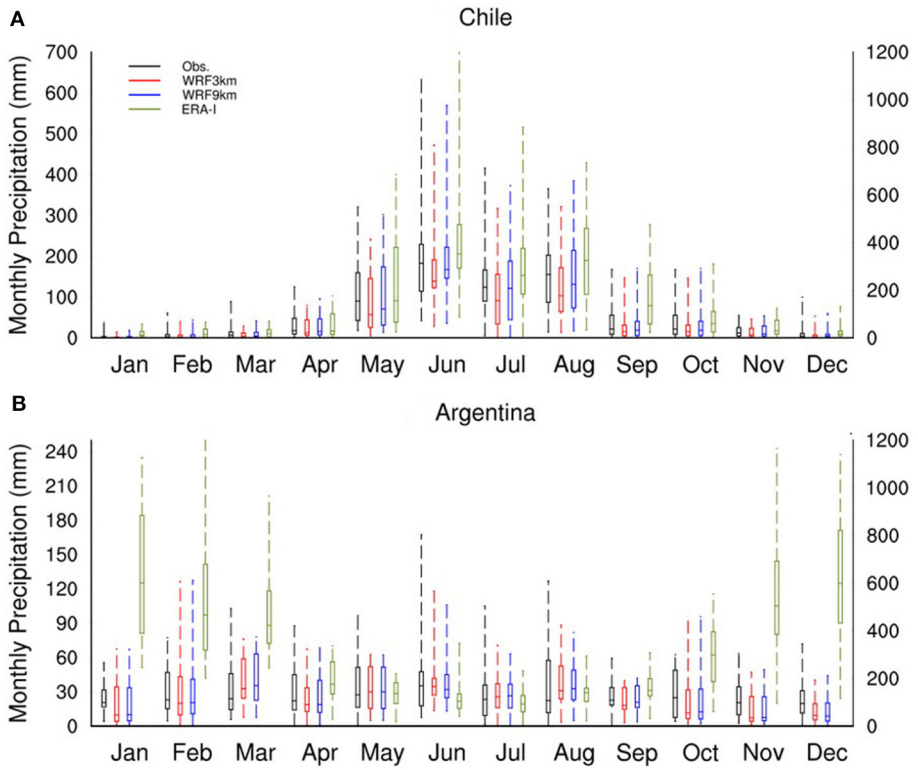


FIGURE 9 | Boxplot of the total monthly precipitation from ensemble of the weather stations in the Chile and Argentina. **(A,B)** Y-axis (right axis) is referent to ERA-I.

TABLE 2 | Performance of the WRF3km, WRF9km, and ERA-I in relation to percentiles range, 10th, 25th, 50th, 75th, 90th, 95th, and 99th.

		Percentiles						
Metrics	**Data**	**P10**	**P25**	**P50**	**P75**	**P90**	**P95**	**P99**
PB	WRF3km	19.91	19.91	19.91	19.91	34.13	–37.5	–12.5
MAE		0.03	0.07	0.14	0.22	1.04	4.54	5.12
PC		0.82*	0.82*	0.82*	0.82*	0.82*	0.85*	0.85*
d		0.81	0.81	0.81	0.81	0.76	0.85	0.89
PB	WRF9km	34.84	34.84	34.84	34.84	15.08	–20.6	0.12
MAE		0.05	0.12	0.25	0.38	0.46	2.49	0.05
PC		0.80*	0.80*	0.80*	0.80*	0.87*	0.85*	0.84*
d		0.73	0.73	0.73	0.73	0.9	0.91	0.87
PB	ERA-I	154.62	151.60	153.76	296.16	374.92	181.29	134.5
MAE		0.21	0.54	1.11	3.22	11.48	21.93	55.07
PC		–0.17	–0.17	–0.16	–0.20	0.06	0.16	0.14
d		0.18	0.18	0.17	0.02	0.15	0.30	0.32

Asterisks are significant at the 5% level.

and 99th percentiles show better performance in WRF9km. This improvement is clearly seen from PB and MAE values. Likewise, a reasonable match of the WRF9km relative to observations is shown in relation to the 99th percentile, with 0.12% for PB and 0.05 for MAE. However, the 95th percentile shows a slightly larger disagreement compared to the 90th and 99th percentiles in both WRF simulations. Poor performance is noticeable by ERA-I.

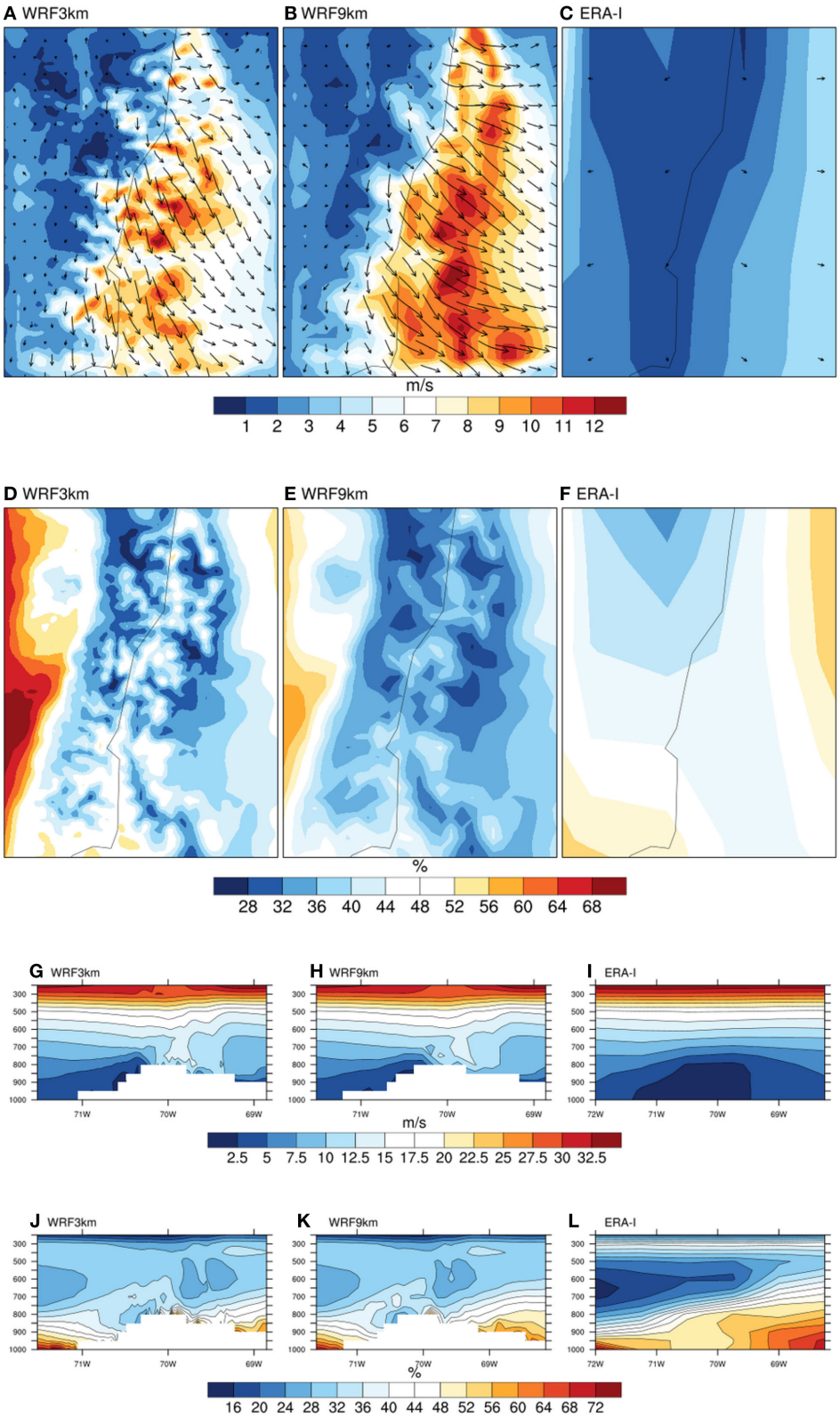


FIGURE 10 | (A–F) Spatial distribution at surface and **(G–L)** vertical distribution of wind speed (m/s) and relative humidity (%) between 1,000 and 200 hPa.

TABLE 3 | Performance of the WRF3km, WRF9km,and ERA-I in different elevation levels.

			Elevation (m.a.s.l.)			
Metrics	**Model**	**Time**	**0–300**	**300–600**	**600–1,300**	**> 1,300**
PB	WRF3km	Monthly	–56.27	–24.13	–2.93	–1.42
		Daily	–56.85	–24.3	–3.38	–1.58
MAE		Monthly	26.21	18.22	2.39	0.49
		Daily	0.88	0.60	0.09	0.02
PC		Monthly	0.91	0.92	0.94	0.83
		Daily	0.80	0.84	0.89	0.61
d		Monthly	0.78	0.93	0.97	0.91
		Daily	0.80	0.91	0.94	0.76
PB	WRF9km	Monthly	–49.79	–9.22	22.51	4.46
		Daily	–50.45	–9.43	21.98	3.31
MAE		Monthly	23.19	6.96	18.33	1.54
		Daily	0.78	0.23	0.59	0.05
PC		Monthly	0.91	0.92	0.93	0.81
		Daily	0.80	0.86	0.88	0.59
d		Monthly	0.82	0.95	0.94	0.90
		Daily	0.82	0.93	0.91	0.75
PB	ERA-I	Monthly	179.54	115.59	130.35	679.49
		Daily	175.82	115.11	129.18	678.31
MAE		Monthly	83.64	87.27	106.15	234.05
		Daily	2.72	2.86	3.74	7.68
PC		Monthly	0.97	0.98	0.94	0.01
		Daily	0.52	0.60	0.60	0.34
d		Monthly	0.69	0.80	0.82	0.11
		Daily	0.50	0.62	0.67	0.24

3.3. Synoptic Features by the WRF Simulations

In an attempt to elucidate differences between WRF3km, WRF9km, and ERA-I, **Figure 10** shows climatological values of wind speed (m/s) and relative humidity (%) for the surface and different levels of pressure. These results clearly show orographic dependence, for example, the coarse resolution of the ERA-I leads to the complete absence of the Andes, and consequently smooth gradients of these variables, which are important drives for the precipitation field.

The poor representation of the Andes by ERA-I induces a large amount of humidity toward the leeward, this implicates overestimated values of precipitation on the Argentine side, as shown by **Figure 9**. The WRF9km also presents a steeper gradient of wind speed on the leeward of the Andes in comparison to the WRF3km, this is due to topography smoothing and consequently influences moisture transport and precipitation on the Argentine side.

3.4. WRF Performance at Different Elevations

A fundamental aspect to validate regional climate models' output is to verify and understand their performance in a complex terrain. In order to add details to the performance of the WRF simulations relative to elevation, the weather stations were classified into four groups according to altitude: between 0–300 m (19 stations), 300–600 m (14 stations), 600–1,300 m (14 stations), and above 1,300 m (15 stations). The performance of the WRF at 3 and 9 km against observations is shown in **Table 3**. Based on the PB and MAE values, the best performance is detected in WRF3km. The reduction of errors is systematic according to the increase in altitude at daily and monthly scales. For example, between 0 and 300 m the PB (MAE) values go from –56.27% (26.21) to –1.42% (0.49) following the increase elevation. These results are in line with PC and d values, although higher values are observed between 600 and 1,300 m, and reduced values are noted above 1,300 m.

It is interesting to note that WRF3km shows a persistent negative bias across all altitude ranges. On the other hand, WRF9km shows a dry bias at stations located between 0 and 600 m, whereas a wet bias is shown above 600 m. This may be understood as a limited performance of the WRF model at 9 km between 600 and 1,300 m that is reproduced by the increase of PB and MAE values. It has to be noted that better performance is achieved at stations above 1,300 m, although larger errors are found compared to WRF3km. The ratio of the MAE values between the WRF9km and WRF3km above 1,300 m shows a

difference of 250% on a daily scale and 314% at a monthly scale, accompanied by slightly lower values of PC and d in relation to high resolution at 3 km. However, it is important to highlight that despite the opposite sign of the bias above 600 m, in absolute values both simulations present the same trend of reduction of bias toward higher elevations. Moreover, ERA-I increases the error and PB with increasing elevation almost systematically. ERA-I also presents good performance for PC and d values up to 1,300 m altitude. Poor performance is noted above this threshold.

The apparent inverse relationship between bias and elevation on the WRF simulations and the weak performance of ERA-I can be further explored by comparing relative humidity at pressure levels that cover the elevation range between the surface and 3,000 m (see **Figure 10**). Between 1,000 and 700 hPa, ERA-I is generally more saturated than the WRF simulations on both slopes, and in fact the temporal trend shows that relative humidity in the WRF3km and WRF9km is consistently 66% of ERA-I from 900 to 700 hPa (about 900 to 3,000 m).

4. DISCUSSION

Overall, both WRF simulations properly reproduce several characteristics of precipitation along the Central Andes. Although there are some differences among the simulations and observations, good performance is obtained in reproducing the spatial variability of the annual and seasonal precipitation. The WRF simulations biases may result from a variety of sources, such as initial conditions, physical configuration of the model, and terrain complexity, among others. Furthermore, main differences between the two simulations cannot only be explained by statistical errors and it is extremely complex to measure.

Differences discussed previously between WRF simulations can be associated with the cumulus scheme. Chawla et al. (2018) has shown that the cumulus scheme modulates the magnitude of simulated precipitation. Sikder and Hossain (2016) also showed that the finer spatial resolution (3 km) without cumulus parameterization schemes did not result in significant improvements in monsoon precipitation. For instance, the presence of this scheme in the simulation at 9 km could be responsible for the improvement of precipitation extremes in comparison to WRF at 3 km (see **Table 3**). Argüeso et al. (2011) also demonstrate that physics configuration plays an important role in reproducing precipitation extremes in terms of percentiles, through the representation of convective and non-convective processes of precipitation and feedback between the cumulus and microphysic scheme. Conversely, Zheng et al. (2015) demonstrated that the explicit treatment of convection—no cumulus parameterization—at 3 km can adequately predict convective systems and precipitation, consistent with many results.

In order to illustrate the convective precipitation behavior by the WRF simulation, **Figure 11** shows the analysis of convective and large-scale precipitation by the WRF9km. This allowed for demonstrating that convective precipitation is less important (magnitude) than large-scale precipitation. This result implies that, on the Argentine side, convection is almost absent, as demonstrated by simulation at 9 km, while large-scale precipitation is well distributed during the seasonal cycle. Although, on the eastern side of the Andes there are fewer gauges available, and thus can lead to larger uncertainty in convection location captured for the WRF9km (**Figure 11B**; see Yair et al., 2010), but the impact on the overall evaluation should be minimal. On the other hand, convective precipitation on the Chilean side presents the same behavior as large-scale precipitation, with maximums during winter, but with smaller magnitudes (differences up to 300 mm/month). However, the influence and connection between the parameterizations used may be a fundamental question but falls outside of the objectives of this study.

Our results also show that high resolution leads to a better performance of precipitation field as elevation increases, most likely due to the better resolved orography. WRF simulation at 3 km has shown good accuracy for precipitation at high elevations, clearly associated with better reproduction of the topographic characteristics of the region compared to resolution at 9 km, which tends to smooth the terrain. This effect is even more noticeable in ERA-I, where the absence of orography greatly exceeds the amount of precipitation compared to observations and WRF simulations. In **Figure 3** there is a noticeable difference in precipitation, with ERA-I exhibiting significant amounts on the NE quadrant. We assess that the lower ERA-I topography allows more water vapor to cross toward the leeward side. In **Figure 10**, relative humidity at 800 hPa, about 2,000 m, close to the summit of the ERA-I topography doubles the values from the WRF simulations, which probably determines more precipitation there.

Thus, an improvement in simulation skill seems to correlate with high resolution in the complex terrain of the Central Andes, as evidenced by more satisfactory statistical metrics. Differences between the simulations are pronounced along windward slopes of the mountain range, in which WRF9km presents a wet bias in relation to observation and WRF3km. In that regard, a salient result that seems intriguing is the relatively better performance of WRF9km at elevations below 600 m and the turn to positive bias at higher locations as revealed by the analysis presented in **Table 3**.

As stated above, studies show that smoother topography in coarse resolution modeling may enhance precipitation (Soares et al., 2012). However, there are very few places in the world featuring the relative extreme elevations of the Andes where this effect can be analyzed in detail and thus literature proposing an explanation for this effect is not abundant. A previous study that compared WRF convection-permitting simulations with and without cumulus parameterizations showed that precipitation was higher in the former case (Wootten et al., 2016). In the present study, WRF9km (with cumulus parameterization) tended to be more positively biased than WRF3km, relative to observations across all elevations. An argument against this explanation is that most convection, when it occurs, is more prevalent on the western side of the Andes (**Figure 11**).

Another option is that the difference in topographic representation between both domains resulted in orographic

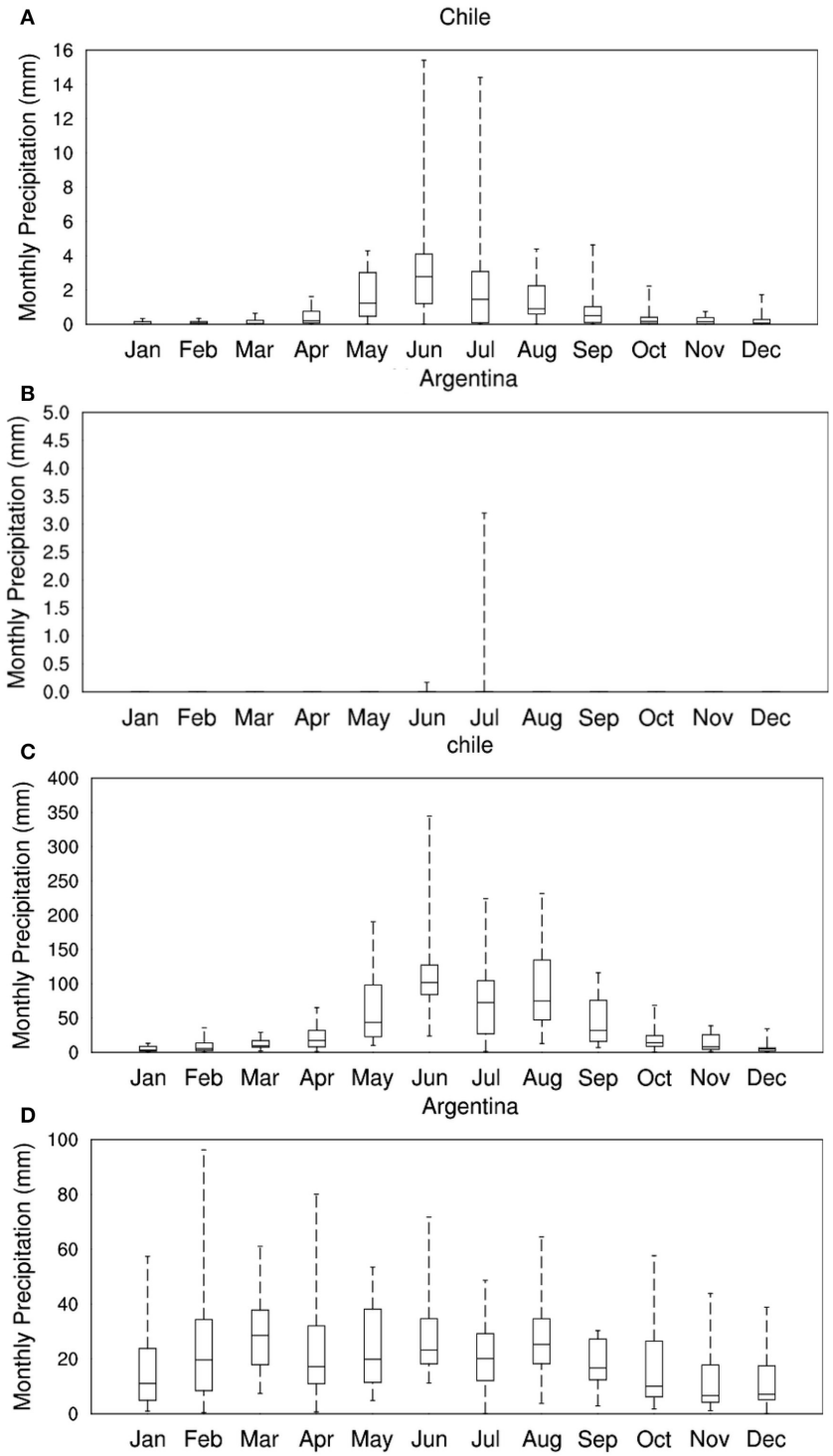


FIGURE 11 | Boxplot of **(A,B)** convection and **(C,D)** large-scale precipitation from the WRF9km for **(A,C)** Chile and **(C,D)** Argentina.

enhancement of precipitation in the coarser domain. **Figure 12A** shows elevation profiles for each domain calculated by averaging all grid boxes pertaining to the same longitude. A remarkable difference can be observed on the windward slope, where the western tip of the WRF3km is lower than WRF9km by about 300 m on average. This difference in elevation results in the WRF9km having a steeper gradient, as demonstrated in the slopes featured in the **Figure 12B**.

Theory, observations, and modeling suggest that precipitation enhancement by topography is dependent upon wind speed,

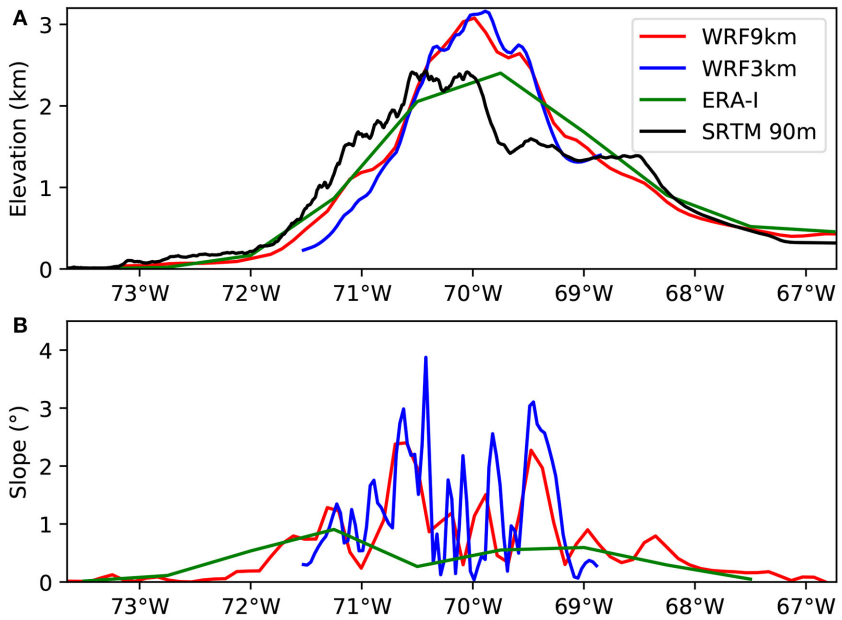


FIGURE 12 | Elevation profiles from the WRF3km and WRF9km, **(A)** elevation (km) and **(B)** slope (°).

slope, and elevation (Roe, 2005). Given that most of the precipitation on the west side of the Andes in this region comes from frontal systems during winter (Falvey and Garreaud, 2007), it is possible that the steeper slope in WRF9km, located just west of the boundary of WRF3km, produced a stronger orographic enhancement which may result in more rainfall in the coarser domain. This is reinforced by the fact that windward winds exhibit higher speeds in WRF9km while wind direction in WRF3km tends to be deflected toward the SSE relative to WRF9km (**Figure 10**), suggesting that the upslope accent in WRF9km is better developed. Considering that the differences in relative humidity are minimal, compared to the respective differences relative to ERA-I (**Figure 10**), allows for the inference that the effect of topography on winds makes precipitation more likely. A consequence of the higher precipitation in WRF9km may be a drier lateral forcing for WRF3km, leading to a systematic underestimation in the latter.

5. CONCLUSION

The present study contributes to an evaluation of high-resolution precipitation simulations over the Central Andes at 3 and 9 km spatial resolution. A state-of-the-art numerical weather prediction model— WRF—driven by the ERA-Interim reanalysis has been used to downscale precipitation over a 20-year long period (1996-2015). The WRF simulations were compared with observations from 62 Chilean and Argentinian weather stations at the annual and warm-cold season analysis.

To our knowledge, this is the first study comparing performance between nested domains on mountain areas that found an improvement in high elevations, despite the fact that availability of long-term instrumental data is sparse at elevations above 2,000 m (see **Table 1**). In a previous study that targeted precipitation using the WRF model and observations in the Nahuelbuta Mountains, part of the Chilean coastal range at 38°S with elevations above 1,300 m, Garreaud et al. (2016) found a uniform 50% bias from the surface to the top of the mountains on both slopes.

Our results show a good agreement between the WRF simulations and observations for seasonal and interannual variability. The WRF simulations, both at 3 and 9 km, outperforms ERA-I with improvement of topographic enhancement, leading to the best accuracy of precipitation amount both on the windward and leeward side of the Andes.

The ability of the WRF simulations to capture the seasonal accumulated precipitation is higher in the warm season than in the cold season, as revealed by the relatively lower PB and MAE values. In addition, WRF improvement varies according to precipitation extremes. WRF3km captures the moderate precipitation (lower-percentiles) more realistically than precipitation extremes. On the contrary, WRF9km represents better performance in relation to precipitation extremes, but represents larger errors in moderate precipitation events.

This study provides important results and implications for precipitation in complex terrains, indicating topographic influences. The higher resolution allows for a better representation of precipitation fields as elevation increases, which is more related with representation of regional processes such as wind and humidity intrinsic by the orographic dependence. Additionally, we have shown that both WRF simulations capture precipitation with good accuracy, therefore a resolution of 9 km may be a good option when elevation or complex terrain is not relevant, alleviating operational costs.

The analyses presented in the current study are subject to a few limitations that could be tested in the future and may vary the results: (a) the need to consider a greater number of weather

stations to expand the study area and (b) evaluation of different physics parameterization schemes of the WRF model, in order to better understand the differences between the simulations and errors. Finally, this has produced a long term, high resolution dataset that can be a useful tool for understanding the climate in mountainous areas, as well as in extreme events. The results contribute to additional data in the region and can be used for hydrological studies.

DATA AVAILABILITY STATEMENT

Publicly available datasets were analyzed in this study. This data can be found here: http://snia.dga.cl, http://bdhi.hidricosargentina.gob.ar.

AUTHOR CONTRIBUTIONS

VS implemented and conducted numerical climatic simulations (using the WRF model), data analysis, and wrote the manuscript. AF cooperated in planning, data analysis, discussion of results, and writing of the manuscript. FJ cooperated in the planning and discussion of results. AC revised and discussed the results. All authors contributed to the article and approved the submitted version.

FUNDING

This study was supported by Fondecyt 1201429 and National Geographic CP-119R-17.

ACKNOWLEDGMENTS

The authors want to thank the Coordination for the Improvement of Higher Education Personnel (CAPES), CNPq project number 306181/2016-9 and FAPEMIG grant PPM-00773-18, and the FONDECYT Projects 11160454 and 1171065 from the Chilean Government.

REFERENCES

Ambrizzi, T., Reboita, M. S., da Rocha, R. P., and Llopart, M. (2019). The state of the art and fundamental aspects of regional climate modeling in South America. *Ann. N. Y. Acad. Sci.* 1436, 98–120. doi: 10.1111/nyas.13932

Argüeso, D., Hidalgo-Muñoz, J. M., Gámiz-Fortis, S. R., Esteban-Parra, M. J., Dudhia, J., and Castro-Díez, Y. (2011). Evaluation of WRF parameterizations for climate studies over southern Spain using a multistep regionalization. *J. Clim.* 24, 5633–5651. doi: 10.1175/JCLI-D-11-00073.1

Barrett, B. S., Garreaud, R. D., and Falvey, M. (2009). Effect of the Andes Cordillera on precipitation from a midlatitude cold front. *Mon. Weather Rev.* 137, 3092–3109. doi: 10.1175/2009MWR2881.1

Bown, F., Rivera, A., and Acuña, C. (2008). Recent glacier variations at the Aconcagua basin, Central Chilean Andes. *Ann. Glaciol.* 48, 43–48. doi: 10.3189/172756408784700572

Bozkurt, D., Rojas, M., Boisier, J. P., Rondanelli, R., Garreaud, R., and Gallardo, L. (2019). Dynamical downscaling over the complex terrain of southwest South America: present climate conditions and added value analysis. *Clim. Dyn.* 53, 6745–6767. doi: 10.1007/s00382-019-04959-y

Bravo, C., Loriaux, T., Rivera, A., and Brock, B. W. (2017). Assessing glacier melt contribution to streamflow at Universidad Glacier, Central Andes of Chile. *Hydrol. Earth Syst. Sci.* 21, 3249–3266. doi: 10.5194/hess-21-3249-2017

Cardoso, R. M., Soares, P. M., Miranda, P. M., and Belo-Pereira, M. (2013). WRF high resolution simulation of Iberian mean and extreme precipitation climate. *Int. J. Climatol.* 33, 2591–2608. doi: 10.1002/joc.3616

Castañeda, M. E., and Ulke, A. G. (2015). Analysis of atmospheric conditions associated to CHACO events of the Low Level Jet East of the Andes and their implications for regional transport. *Int. J. Climatol.* 35, 4126–4138. doi: 10.1002/joc.4272

Chawla, I., Osuri, K. K., Mujumdar, P. P., and Niyogi, D. (2018). Assessment of the Weather Research and Forecasting (WRF) model for simulation of extreme rainfall events in the upper Ganga Basin. *Hydrol. Earth Syst. Sci.* 22, 1095–1117. doi: 10.5194/hess-22-1095-2018

Comin, A. N., Schumacher, V., Justino, F., and Fernández, A. (2018). Impact of different microphysical parameterizations on extreme snowfall events in the Southern Andes. *Weather Clim. Extremes* 21, 65–75. doi: 10.1016/j.wace.2018.07.001

Corripio, J. G., and Purves, R. S. (2005). *Surface Energy Balance of High Altitude Glaciers in the Central Andes: the Effect of Snow Penitentes*. London: Wiley \& Sons.

Dee, D. P., Uppala, S. M., Simmons, A. J., Berrisford, P., Poli, P., Kobayashi, S., et al. (2011). The ERA-Interim reanalysis: configuration and performance of the data assimilation system. *Q. J. R. Meteorol. Soc.* 137, 553–597. doi: 10.1002/qj.828

Dudhia, J. (1989). Numerical study of convection observed during the winter monsoon experiment using a mesoscale two-dimensional model. *J. Atmos. Sci.* 46, 3077–3107.

Espinoza, J. C., Chavez, S., Ronchail, J., Junquas, C., Takahashi, K., and Lavado (2015). Rainfall hotspots over the southern tropical Andes: spatial distribution, rainfall intensity, and relations with large-scale atmospheric circulation. *Water Resour. Res.* 51, 3459–3475. doi: 10.1002/2015WR017200.A

Falvey, M., and Garreaud, R. (2007). Wintertime precipitation episodes in Central Chile: associated meteorological conditions and orographic influences. *J. Hydrometeorol.* 8, 171–193. doi: 10.1175/JHM562.1

Fathalli, B., Pohl, B., Castel, T., and Safi, M. J. (2016). Dynamical downscaling of temperature variability over Tunisia: evaluation a 21-year-long simulation performed with the WRF model. *J. Climatol. Weather Forecast.* 4, 1–8. doi: 10.4172/2332-2594.1000166

Garreaud, R., Falvey, M., and Montecinos, A. (2016). Orographic precipitation in Coastal Southern Chile: mean distribution, temporal variability, and linear contribution. *J. Hydrometeorol.* 17, 1185–1202. doi: 10.1175/JHM-D-15-0170.1

Garreaud, R. D. (2009). The Andes climate and weather. *Adv. Geosci.* 22, 3–11. doi: 10.5194/adgeo-22-3-2009

Garreaud, R. D., Vuille, M., Compagnucci, R., and Marengo, J. (2009). Present-day South American climate. *Palaeogeogr. Palaeoclimatol. Palaeoecol.* 281, 180–195. doi: 10.1016/j.palaeo.2007.10.032

Heikkilä, U., Sandvik, A., and Sorteberg, A. (2011). Dynamical downscaling of ERA-40 in complex terrain using the WRF regional climate model. *Clim. Dyn.* 37, 1551–1564. doi: 10.1007/s00382-010-0928-6

Hong, S.-Y., Lim, K.-S. S., Lee, Y.-H., Ha, J.-C., Kim, H.-W., Ham, S.-J., et al. (2010). Evaluation of the WRF double-moment 6-class microphysics scheme for precipitating convection. *Adv. Meteorol.* 2010, 1–10. doi: 10.1155/2010/707253

Huang, M., Huang, B., and Huang, A. H. (2014). Implementation of 5-layer thermal diffusion scheme in weather research and forecasting model with Intel Many Integrated Cores. *High Perform. Comput. Remote Sens. IV* 9247:924709. doi: 10.1117/12.2069426

Hughes, M., Lundquist, J. D., and Henn, B. (2017). Dynamical downscaling improves upon gridded precipitation products in the Sierra Nevada, California. *Clim. Dyn.* 55, 111–129. doi: 10.1007/s00382-017-3631-z

Kain, J. S. (2004). The Kain–Fritsch convective parameterization: an update. *J. Appl. Meteorol.* 43, 170–181. doi: 10.1175/1520-0450(2004)043<0170:TKCPAU>2.0.CO;2

Malmros, J. K., Mernild, S. H., Wilson, R., Tagesson, T., and Fensholt, R. (2018). Snow cover and snow albedo changes in the central Andes of Chile and

Argentina from daily MODIS observations (2000–2016). *Remote Sens. Environ.* 209, 240–252. doi: 10.1016/j.rse.2018.02.072

Marengo, J. A., Soares, W. R., Saulo, C., and Nicolini, M. (2004). Climatology of the low-level jet east of the Andes as derived from the NCEP-NCAR reanalyses: characteristics and temporal variability. *J. Clim.* 17, 2261–2280. doi: 10.1175/1520-0442(2004)017<2261:COTLJE>2.0.CO;2

Mark, B. G., Baraer, M., Fernandez, A., Immerzeel, W., Moore, R. D., and Weingartner, R. (2015). "Glaciers as water resources," in *The High-Mountain Cryosphere: Environmental Changes and Human Risks*, eds C. Huggel, M. Carey, J. J. Clague, and A. Kaab (Cambridge: Cambridge University Press), 184–203.

Masiokas, M. H., Rivera, A., Espizua, L. E., Villalba, R., Delgado, S., and Aravena, J. C. (2009). Glacier fluctuations in extratropical South America during the past 1000years. *Palaeogeogr. Palaeoclimatol. Palaeoecol.* 281, 242–268. doi: 10.1016/j.palaeo.2009.08.006

Mlawer, E. J., Taubman, J., Brown, P. D., Iacono, M. J., and Clough, S. A. (1997). Radiative transfer for inhomogeneous atmospheres: RRTM, a validated correlatedk model for the longwave. *J. Geophys. Res.* 102, 16663–16682.

Mög, T., and Kaser, G. (2011). A new approach to resolving climate-cryosphere relations: Downscaling climate dynamics to glacier-scale mass and energy balance without statistical scale linking. *J. Geophys. Res. Atmos.* 116, 1–13. doi: 10.1029/2011JD015669

Mourre, L., Condom, T., Junquas, C., Lebel, T., Sicart, E. J., Figueroa, R., et al. (2016). Spatio-temporal assessment of WRF, TRMM and *in situ* precipitation data in a tropical mountain environment (Cordillera Blanca, Peru). *Hydrol. Earth Syst. Sci.* 20, 125–141. doi: 10.5194/hess-20-125-2016

Paulson, C. A. (1970). The mathematical representation of wind speed and temperature profiles in the unstable atmospheric surface layer. *J. Appl. Meteorol.* 9, 857–861.

Posada-Marín, J. A., Rendón, A. M., Salazar, J. F., Mejía, J. F., and Villegas, J. C. (2019). WRF downscaling improves ERA-Interim representation of precipitation around a tropical Andean valley during El Niño: implications for GCM-scale simulation of precipitation over complex terrain. *Clim. Dyn.* 52, 3609–3629. doi: 10.1007/s00382-018-4403-0

Rivera, J. A., Marianetti, G., and Hinrichs, S. (2018). Validation of CHIRPS precipitation dataset along the Central Andes of Argentina. *Atmos. Res.* 213, 437–449. doi: 10.1016/j.atmosres.2018.06.023

Roe, G. H. (2005). Orographic Precipitation. *Annu. Rev. Earth Planet. Sci.* 33, 645–671. doi: 10.1146/annurev.earth.33.092203.122541

Sikder, S., and Hossain, F. (2016). Assessment of the weather research and forecasting model generalized parameterization schemes for advancement of precipitation forecasting in monsoon-driven river basins. *J. Adv. Model. Earth Syst.* 8, 1248–1269. doi: 10.1002/2016MS000689

Skamarock, W. C., Klemp, J. B., Dudhia, J., Gill, D. O., Barker, D. M., Duda, M. G., et al. (2008). *A Description of the Advanced Research WRF Version 3*. NCAR Tech. Note NCAR TN- 475_STR, 113.

Soares, P. M., Cardoso, R. M., Miranda, P. M., de Medeiros, J., Belo-Pereira, M., and Espirito-Santo, F. (2012). WRF high resolution dynamical downscaling of ERA-Interim for Portugal. *Clim. Dyn.* 39, 2497–2522. doi: 10.1007/s00382-012-1315-2

Solman, S. A., and Blázquez, J. (2019). Multiscale precipitation variability over South America: analysis of the added value of CORDEX RCM simulations. *Clim. Dyn.* 53, 1547–1565. doi: 10.1007/s00382-019-04689-1

Viale, M., Bianchi, E., Cara, L., Ruiz, L. E., Villalba, R., Pitte, P., et al. (2019). Contrasting climates at both sides of the Andes in Argentina and Chile. *Front. Environ. Sci.* 7:69. doi: 10.3389/fenvs.2019.00069

Viale, M., and Nuñez, M. N. (2011). Climatology of winter orographic precipitation over the subtropical Central Andes and associated synoptic and regional characteristics. *J. Hydrometeorol.* 12, 481–507. doi: 10.1175/2010JHM1284.1

Ward, E., Buytaert, W., Peaver, L., and Wheater, H. (2011). Evaluation of precipitation products over complex mountainous terrain: a water resources perspective. *Adv. Water Resour.* 34, 1222–1231. doi: 10.1016/j.advwatres.2011.05.007

Wilks, D. S. (2011). *Statistical Methods in the Atmospheric Sciences*. Oxford: Academic Press.

Wootten, A., Bowden, J. H., Boyles, R., and Terando, A. (2016). The sensitivity of WRF downscaled precipitation in puerto rico to cumulus parameterization and interior grid nudging. *J. Appl. Meteorol. Climatol.* 55, 2263–2281. doi: 10.1175/JAMC-D-16-0121.1

Yair, Y., Lynn, B., Price, C., Kotroni, V., Lagouvardos, K., Morin, E., et al. (2010). Predicting the potential for lightning activity in Mediterranean storms based on the Weather Research and Forecasting (WRF) model dynamic and microphysical fields. *J. Geophys. Res. Atmos.* 115, 1–13. doi: 10.1029/2008JD010868

Zheng, Y., Alapaty, K., Herwehe, J. A., Del Genio, A. D., and Niyogi, D. (2015). Improving high-resolution weather forecasts using the Weather Research and Forecasting (WRF) model with an updated Kain–Fritsch Scheme. *Mon. Weather Rev.* 144, 833–860. doi: 10.1175/mwr-d-15-0005.1

Conflict of Interest: The authors declare that the research was conducted in the absence of any commercial or financial relationships that could be construed as a potential conflict of interest.

Copyright © 2020 Schumacher, Fernández, Justino and Comin. This is an open-access article distributed under the terms of the Creative Commons Attribution License (CC BY). The use, distribution or reproduction in other forums is permitted, provided the original author(s) and the copyright owner(s) are credited and that the original publication in this journal is cited, in accordance with accepted academic practice. No use, distribution or reproduction is permitted which does not comply with these terms.

frontiers in Earth Science

ORIGINAL RESEARCH
published: 29 October 2020
doi: 10.3389/feart.2020.519975

High-Resolution Precipitation Gridded Dataset on the South-Central Zone (34° S–41° S) of Chile

Francisco-J. Alvial Vásquez[1,2]*, *Rodrigo Abarca-del-Río*[2] *and Andrés I. Ávila*[3]

[1]Faculty of Sciences in Physical and Mathematical, University of Concepción, Concepción, Chile, [2]Department of Geophysics, Faculty of Sciences in Physical and Mathematical, University of Concepción, Concepción, Chile, [3]Department of Mathematical Engineering, Faculty of Engineering and Sciences, University of La Frontera, Temuco, Chile

Chile is well known as a narrow and long country (over 4,000 km) that encompasses many climate zones and that presents significant west–east gradients as altitudes change from sea level to several thousand meters. Although Chile is recognized as one of the most affected countries by climate change, it is also one of the least covered by hydrometeorological measuring instruments. This data scarcity prevents thorough characterization of hydrological basins. To solve this problem, we constructed a decade-long (2000–2011) high-resolution (~ 800 m) monthly gridded precipitation product for the central-southern zone (34° S–41° S) covering regions from O'Higgins to Los Ríos. These regions contain most of Chile's agricultural land, livestock, forestry, and hydroelectric production. The study zone covers a variety of topographies and climates, including eight hydrological basins: Rapel, Mataquito, Maule, Itata, BioBío, Imperial, Toltén, and Valdivia. We develop a dynamic topo-climatic methodology that includes local and global data. We combined a dynamic downscaling and a spatial-temporal multivariate model over different geographical areas that considered high-resolution precipitation fields from model data, *in situ* stations, and different global precipitation datasets that also understand satellite observations. Results show that most of the precipitation spatial-temporal variability is well-captured by the model in the north and central regions, from O'Higgins to Biobío, with the goodness of fit (R^2) fluctuating around 0.86 and 0.82, respectively. Toward the south, Araucanía and Los Ríos, the goodness of fit (R^2) decreased to values around 0.74 and 0.72, respectively. Both the modified Willmott coefficient (d) and the *nse* indicated a good model skill, with values over 0.8 and 0.7, respectively. Meanwhile, the σ_e, *nrmse*, and *pbias* changed between 0.04–0.2, 0.35–0.52, and 12–22%, respectively. This database is freely available to different regional or national institutions and will help the development of a better understanding and management of local and regional hydrology.

Keywords: weather research and forecasting model, gridded and station data, multiple linear regression, center-south of Chile, topo-climatic modeling

OPEN ACCESS

Edited by:
Bryan G. Mark,
The Ohio State University,
United States

Reviewed by:
Santos J. González-Rojí,
University of Bern, Switzerland
Scott Robeson,
Indiana University, United States

***Correspondence:**
Francisco-J. Alvial Vásquez
franciscojalvia@udec.cl

Specialty section:
This article was submitted to Hydrosphere, a section of the journal Frontiers in Earth Science

Received: *13 December 2019*
Accepted: *24 August 2020*
Published: *29 October 2020*

Citation:
Alvial Vásquez F-J, Abarca-del-Río R and Ávila AI (2020) High-Resolution Precipitation Gridded Dataset on the South-Central Zone (34° S–41° S) of Chile. Front. Earth Sci. 8:519975. doi: 10.3389/feart.2020.519975

1. INTRODUCTION

Meteorological spatial data consistent with observational information are critical for several scientific fields: environmental, hydrology, agriculture, application of renewable energy, biology, economy, and sociology, among others (Parra et al., 2004; Hijmans et al., 2005; Abatzoglou, 2013; Cannon et al., 2015; Liu et al., 2017; Sun et al., 2018). Within weather variables, precipitation is the driver of the hydrological cycle and the most difficult to estimate (Michaelides et al., 2009; Kidd and Levizzani, 2011; Tapiador et al., 2012; Beck et al., 2017b). Precipitation datasets provide information for hydrological models such as SWAT or TOPMODEL (Berezowski et al., 2016) and environmental verification (Ji et al., 2015; Berezowski et al., 2016; Brinckmann et al., 2016; Fick and Hijmans, 2017).

Interpolation methods use information from local weather networks, atmospheric reanalysis products, weather radar, satellite data, or a combination of these products to construct global or local gridded rainfall datasets because each one has its negative sides, in particular precipitation. For instance, datasets based only on instrumental observation networks depend on the spatiotemporal distribution, quality, and length of records (Sun et al., 2014). Atmospheric reanalyses, on the other hand, are at low resolution and sometimes inadequately parameterize sub-grid processes, leading to misrepresentation of synoptic-scale and convective dynamics (Roads, 2003; Ebert et al., 2007; Kidd et al., 2013). Another example is weather radar, since it provides data at high temporal and spatial resolution, but of limited spatial coverage (Koistinen, 1991; Kitchen and Blackall, 1992; Chen et al., 2008; Beck et al., 2017a). Satellite data allow for direct coverage of large areas (~ 0.25˚) (Sorooshian et al., 2014; Ashouri et al., 2015) but are partly insensitive to light rainfall or drizzle events, sensitive to systematic error, and also unfitted for snow- and ice-covered surfaces on mountain areas (Ferraro et al., 1998; Ebert et al., 2007; Kidd and Levizzani, 2011; Kidd et al., 2012; Laviola et al., 2013; Beck et al., 2017a).

Some of these sources for obtaining precipitation grids (satellite, reanalysis, atmospheric modeling, or statistical downscaling techniques) may present problems in areas of complex topography where high spatial-temporal heterogeneity is difficult to estimate, as for example Chile (Daly et al., 1994; Chen et al., 2014; Herold et al., 2016; Beck et al., 2017a; Zambrano M. et al., 2017). Several studies have assessed the insufficiency of these datasets (e.g., Nastos et al., 2016; Beck et al., 2017b; Camera et al., 2017; Liu et al., 2017; Hu et al., 2018; Sun et al., 2018; Timmermans et al., 2019) including some zones in Chile (Muñoz et al., 2011; Ward et al., 2011). Just recently, this problem has been addressed at the national level in Chile (Zambrano F. et al., 2017; Zambrano M. et al., 2017).

High-resolution datasets properly covering Chile are scarce. This is surprising, given that the country is among those most affected by climate change (Kreft et al., 2016), although the complex topography and multiplicity of climates make development of these datasets difficult. Besides, precipitation coverage is inadequate and inhomogeneous, limiting water resources studies (Hosseini-Moghari et al., 2018). To date, datasets are available only in specific regions by local weather stations (Román and Andrés, 2010; Zambrano, 2011; Jacquin and Soto-Sandoval, 2013; Reyes, 2013; Castro et al., 2014; Sijinaldo, 2015; Cifuentes, 2017) or from low-resolution gridded datasets (Morales-Salinas et al., 2012).

Despite these difficulties, there are known methods that allow for building high-resolution databases in an efficient way. Among statistical downscaling techniques for spatial interpolation, regression-based methods are computationally cheap to run, easy to understand, and statistically efficient and straightforward (Semenov et al., 1998; Dibike and Coulibaly, 2005; Hashmi et al., 2011; Pahlavan et al., 2018). Thus, interpolation methods based on functions describing spatial changes of the target variable (Brinckmann et al., 2016) generate continuous spatial data (e.g., Hay et al., 1998; Marquínez et al., 2003; Ceccherini et al., 2015; Beck et al., 2017b).

The main goal of this study was to improve, quantify, and offer a new basis for average monthly precipitation at high spatial resolution (~ 800 m) using a dynamic-statistical method. We focus this analysis on the central-south zone of Chile (**Figure 1**) in the period 2000–2011. We structured this article as follows: in **Section 2**, we describe the regional climate and topography. **Section 3** includes description of the dynamic topo-climatic model and the datasets used. This is followed by **Section 4**, which reports the major findings. The article ends with a discussion and conclusion on the robustness of our model and main findings.

2. STUDY AREA

Variability of the South Pacific subtropical anticyclone and high-latitude pressure centers dominates Chile's synoptic climate (Fuenzalida, 1982; Rojas, 2016). The narrow width (180 km on average) between the Pacific coast and the Andes (https://www.gob.cl/nuestro-pais/), along with a north–south extension of 4,000 km, contributes to a variety of climates (Valdés et al., 2016a). Chile holds a distinct climatic characteristic from low to high moisture from north to south. Because of the orographic effect, the main precipitation pattern shows an annual accumulation moving to the south and the Andes (Pizarro et al., 2012; Quintana and Aceituno, 2012; Valdés-Pineda et al., 2014; Valdés et al., 2016a), with annual precipitations in the north 30˚S of about 100 mm increasing up to 3,000 mm in the south 40˚S (Pizarro et al., 2012; Barrett and Hameed, 2017). Since elevation increases from the sea level in the west to some thousand meters in a few hundred kilometers to the east, Andean precipitation can double coastal rainfall (Viale and Garreaud, 2015; Barrett and Hameed, 2017).

Within Chile, our study area corresponds to the center-south zone of the country between latitudes (34˚S–41˚S), from O'Higgins to Los Ríos regions (**Figure 1**). This region presents a well-defined annual cycle characterized by a peak of precipitation in austral winter and lower values in austral summer (Valdés et al., 2016a; Valdés et al., 2016b). Besides, this is one area with the highest humidity in the southern hemisphere (Miller, 1976) and one of the extra-tropical areas

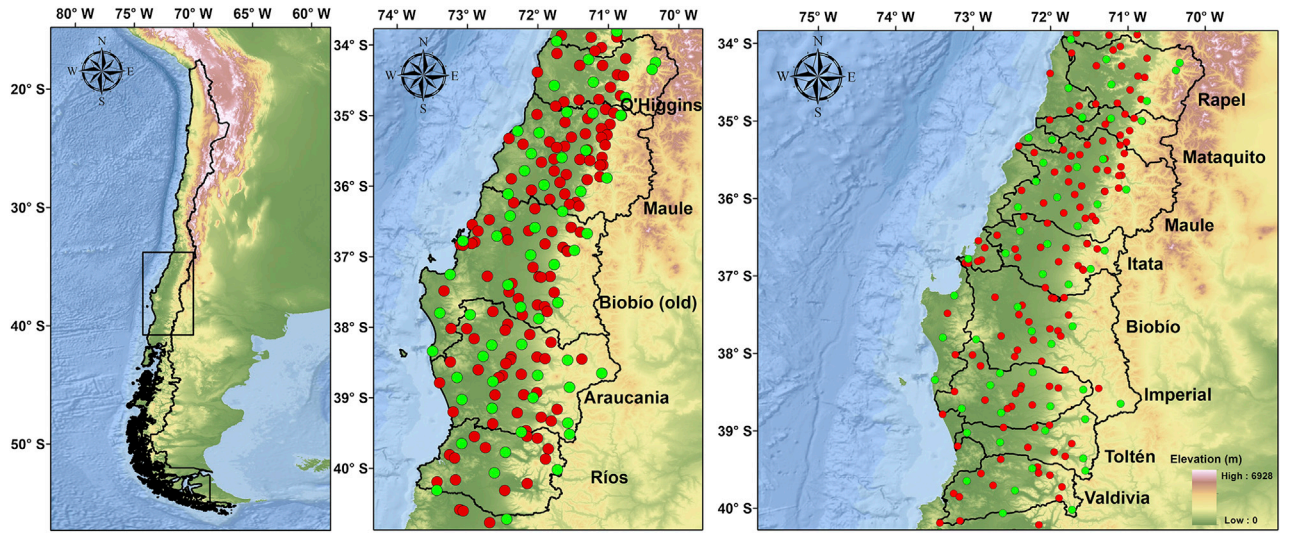


FIGURE 1 | (A) Study area in central-southern Chile (O'Higgins–Los Ríos). **(B)** River basins used for spatial yield analysis of the weather research and forecasting model, the gridded precipitation sets (**Table 2**), and the topo-climatic model. The red dots indicate the 136 stations used as input for the topo-climatic model and the 60 green dots indicate the stations used for performance analysis.

most affected by El Niño and La Niña events (Grimm et al., 2000; Waylen and Poveda, 2002). Due to its transitional location between subtropical and high-latitude temperatures, climate is characterized by a significant interannual rainfall variability (Aceituno et al., 1993; Quintana, 2004; Le Quesne et al., 2009). The El Niño Southern Oscillation, mostly in the northern section, and the Pacific Decadal Oscillation to the south affect hydrological regimes (Arumí-Ribera and Oyarzún-Lucero, 2006; Araya-Ojeda and Isla, 2016). The south-central zone presents yearly accumulated precipitation between 100 and 3000 mm from the north to south (Quintana and Aceituno, 2012; Valdés et al., 2016a). This is a zone of active recharge for surface and groundwaters as a result of infiltration and transport processes in valleys, channels, and fractured systems in the high zones and the pre-mountain ranges (Arumí et al., 2012; Carling et al., 2012). Along the Andes, particularly toward the south, where the role of oceanic fronts is prominent, the orographic effect increases rainfall.

3. METHODOLOGY

The choice and organization of observed precipitation data are presented in **Section 3.1**. **Section 3.2** shows the development and execution of the atmospheric model, and then the adjustment and selection (which considers the database presented in **Section 3.1** of the modeled precipitation fields). The collection of global gridded precipitation sets and their later data choice are discussed in **Section 3.3**. **Section 3.4** presents the structure and procedure in the construction of the topo-climatic dynamic model. The statistical analysis strategy required for the process of calibration and validation of the atmospheric model, choice of global gridded data and topo-climatic dynamic model, and final construction of the high-resolution gridded product is addressed in **Section 3.5**.

3.1. Instrumental Database

The Dirección General de Aguas and the Dirección Meteorológica de Chile (DMC) support Chile's meteorological station network. Although these data are reliable and cover several decades, many stations are conventional (report only daily accumulation) and at low elevations (Garreaud et al., 2016). Also, in most records (**Figure 2**), data gaps are common (Zambrano M. et al., 2017b). Within the study zone, we initially considered 301 stations reporting daily observations

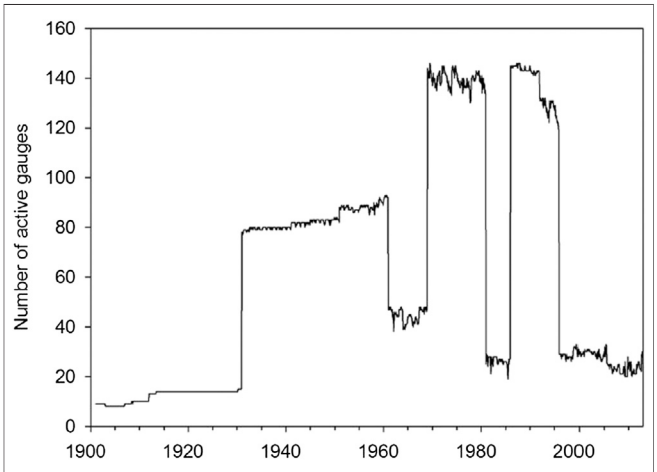


FIGURE 2 | Number of precipitation stations in Chile used by Global Precipitation Climatology Centre dataset (Schamm et al., 2015). Source: Zambrano M. et al. (2017).

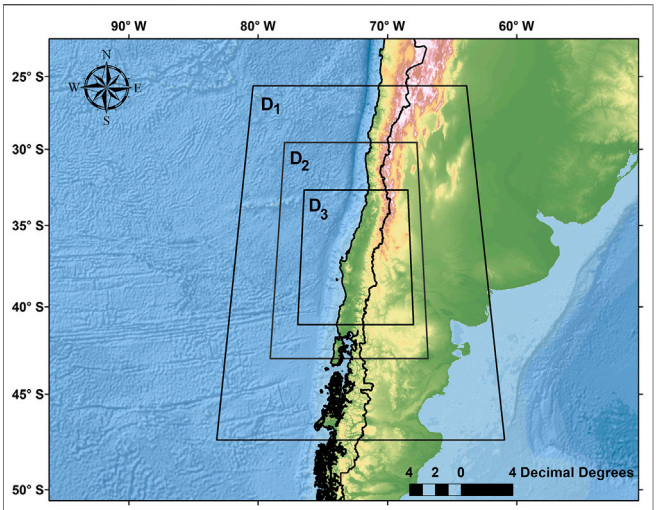


FIGURE 3 | Display of the domains used in weather research and forecasting model. D_1: parent domain with 36-km resolution. D_2: first nesting with 12-km resolution (1/3 parent domain size). D_3: second nesting, with 4-km resolution (1/9 parent domain size).

(**Figure 1**). We eliminated stations with more than 30% monthly data gaps between 2000 and 2011 (105 stations). From the remaining stations (196), 136 correspond to input for model calibration and 60 for validation.

3.2. Atmospheric Modeling

An atmospheric numerical simulation was developed using the Weather Research and Forecasting model (WRF), version 3.6 (Skamarock et al., 2008) for the period 2000–2011 to obtain a high-resolution robust precipitation dataset. The simulation was initialized in October 1999 and run through December 2014, with the first 3 months discarded as model spin-up. As recommended by the DMC (DMC, 2015), this model must consider a domain covering some parts of the Pacific Ocean to capture the phenomena approaching the continent (Yáñez-Morroni et al., 2018). We used three nested domains for downscaling (**Figure 3**). The largest domain, D_1, at 36 km resolution, contained two nested domains, D_2 and D_3, each with a ratio of 1/3 relative to its respective parent (**Table 1**). Initial and boundary conditions for the D_1 domain correspond to the ERA-Interim global reanalysis, at a spatial grid resolution of $0.75^\circ \times 0.75^\circ$ latitude–longitude and 60 vertical hybrid levels (Dee et al., 2011). Ingestion of ERA-Interim's atmospheric fields was every 6 hours. The twelve-year simulation took about 22 real computational months in the Troquil cluster at the Center of Excellence of Scientific Modeling and Computing at Universidad de La Frontera. In atmospheric numerical simulations, parameterizations strongly influence the patterns of simulated precipitation (Wang and Seaman, 1997; Gallus and William, 1999; Jankov et al., 2005) and also affect model response to changes in grid spacing (Gallus and William, 1999) or soil moisture (Gallus and William, 1999; Gallus et al., 2000). A summary of the settings used is shown in **Table 1**, selected following recommendations of the DMC (DMC, 2015).

TABLE 1 | Domain configuration and parameterization schemes selected for the weather research and forecasting model.

Domain	Δx, km	No. of points	Topographic resolutions
D1	36	69 × 48	5′
D2	12	126 × 84	2′
D3	4	234 × 189	30′
Physics		**Parameterization**	**References**
Microphysics		WSM3 scheme	Hong et al. (2004)
Longwave radiation		RRTM scheme	Mlawer et al. (1997)
Shortwave radiation		Dudhia scheme	Dudhia (1989)
Surface layer physics		MM5 Monin–Obukhov scheme	Zhang and Anthes (1982)
Boundary layer physics		Yonsei University (YSU) scheme	Hong et al. (2006)
Soil physics		Noah scheme	Chen (2007)

We implemented a method for systematic error correction (bias) applied to every WRF's generated precipitation field within each regional domain (**Figure 1A**). We calculated the relationship between the average monthly precipitation of a station and its nearest grid point of the WRF model (a virtual station). For each regional domain, **Eq. 1** determined selection of WRF's virtual stations. Next, we obtained and applied a fit factor $\mu(P_o^s)/\mu(P_{wrf}^s)$ to each grid point in the region (**Eq. 1**). Finally, each adjusted grid point was reevaluated and discarded as input to the dynamic topo-climatic model if it did not meet the requirement of **Eq. 1**.

$$P_{wrf}^{cs} = \begin{cases} P_{wrf} & \text{if } P_{min}^o - 0.05 \times P_{min}^o \le P_{wrf} \le P_{max}^o + 0.05 \times P_{max}^o \ (a) \\ \dfrac{\mu(P_o^s)}{\mu(P_{wrf}^s)} P_{wrf} & \text{if } P_{wrf} < P_{min}^o - 0.05 \times P_{min}^o \ (b) \\ \dfrac{\mu(P_o^s)}{\mu(P_{wrf}^s)} P_{wrf} & \text{if } P_{wrf} > P_{max}^o + 0.05 \times P_{max}^o \ (c) \end{cases}, \tag{1}$$

where P_{min}^o and P_{max}^o are the minimum and maximum observed rainfall, respectively; $\mu(P_o^s)$ is the monthly observed average of stations; $\mu(P_{wrf}^s)$ is the monthly average of the nearest virtual stations delivered by the WRF model; P_{wrf} is the computed gridbox; and P_{wrf}^{cs} is the bias-corrected precipitation.

3.3. Global Gridded Datasets

Our compilation includes eight precipitation products from diverse sources (observation, reanalysis, satellite, or mix) and present different spatial and temporal resolutions, and coverage (semiglobal or global, **Table 2**). We did not bias-correct these precipitation products as this was performed by the teams that built them. Therefore, each product's dynamics depends entirely on its source. Three precipitation sets were based on satellite data (TRMM, CMOPRH, and SM2RAIN), one set was based exclusively on observed data (CRUv4.01), and four sets were built with satellite data, reanalysis, and observations (PGFv3, CHIRPSv2.0, PERSIANN – CDR, and MSWEPv1.2).

In order to minimize the difference in bias from these precipitation products (Zhang et al., 2019; Yeh et al., 2020), each gridded precipitation product used in this study was

TABLE 2 | Description of the 8 (quasi) global (sub-)precipitation grids used in this study.

	Dataset	Name and detail	Source	Spatial resolution	Spatial coverage	Temporal resolution	Temporal coverage	References
1	TMPA (3B42)	TRMM Multi-satellite Precipitation Analysis (TMPA) product 3B42 version 7 https://mirador.gsfc.nasa.gov/	S	0.25°	50°N–50°S	3 h, daily	1998–present	Huffman et al. (2007)
2	CHIRPSv2.0	Climate Hazards Group Infrared Precipitation (CHIRPS) V2.0 http://chg.ucsb.edu/data/chirps/	S, R	0.05°	50°N–50°S	Daily, pentadal and monthly	1981–present	Funk et al. (2015)
3	CMORPH	CPC MORPHing (CMORPH) https://rda.ucar.edu/datasets/ds502.0/	S	0.07°, 0.25°	60°N–60°S	3 h, daily	December 2002–present	Joyce et al. (2004) and NOAA (2011)
4	CRUv4.01	Climate Research Unit Time Series version 4.01 http://www.cru.uea.ac.uk/data	I	0.5°	Global	Monthly	1901–2016	Harris et al. (2014) and Harris and Jones (2017)
5	PERSIANN-CDR	Precipitation Estimation from Remotely Sensed Information using Artificial Neural Networks (PERSIANN) Climate Data Record (CDR) http://chrs.web.uci.edu/	S, I	0.25°	60°N–60°S	Daily	1983–present	Sorooshian et al. (2014) and Ashouri et al. (2015)
6	MSWEPv1.2	Multi-Source Weighted-Ensemble Precipitation (MSWEP) v1.2 http://www.gloh2o.org/	I, S, R	0.25°	90°N–90°S	Daily	1979–2014	Beck et al. (2017a)
7	PGFv3	Princeton University Global Meteorological Forcing version 3 http://hydrology.princeton.edu/home.php	R, I	0.25°	Global	3 h	1948–2012	Sheffield et al. (2006) and Peng et al. (2016)
8	SM2RAIN-CCI	Rainfall Satellite Soil Moisture CCI http://hydrology.irpi.cnr.it/download-area/sm2rain-data-sets/	S	0.25°	Global	Daily	1998–2015	Brocca et al. (2013) and (2014)

The abbreviations in the Source column, defined as I, S, R are the abbreviations of the derived products: in situ*, satellite, and reanalysis, respectively.*

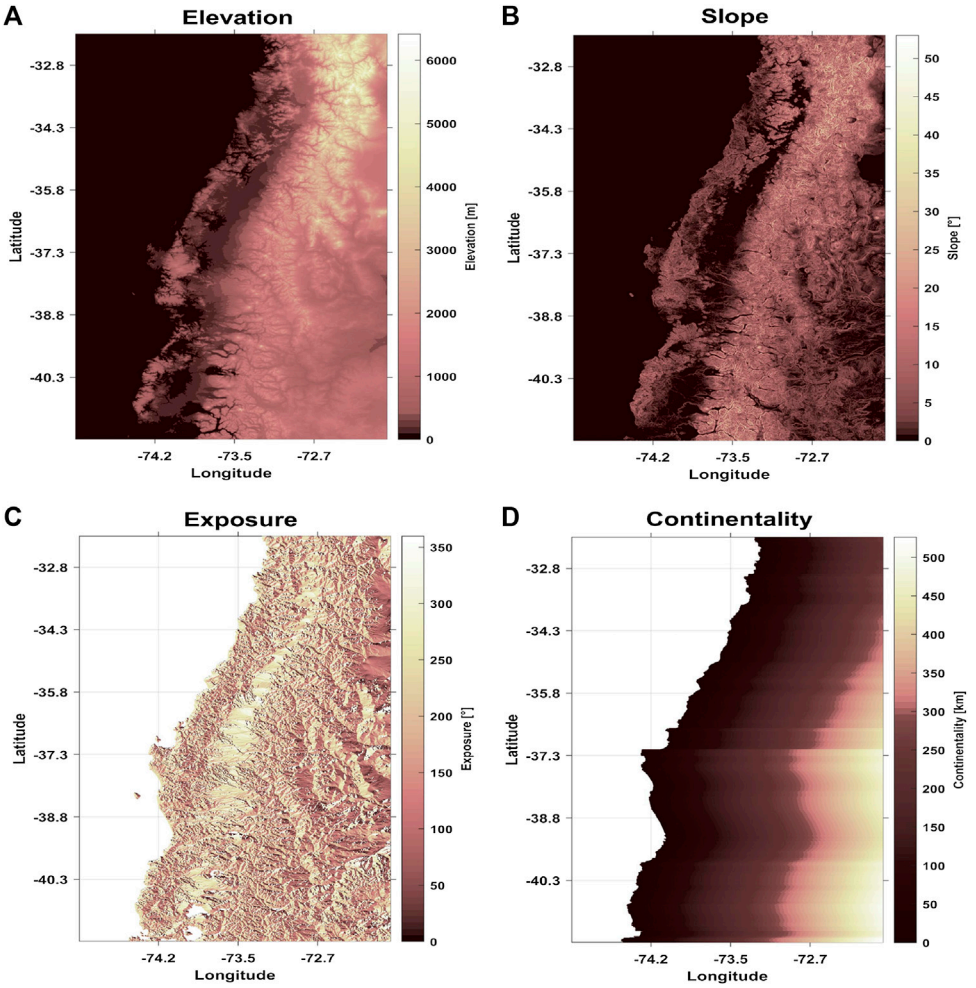


FIGURE 4 | Digital terrain model with independent variables: **(A)** elevation, **(B)** slope, **(C)** exposure, and **(D)** continentality.

evaluated according to **Eq. 2**, where every point was discarded when it was either under or over 5% of the respective minimum and maximum precipitation observed within the respective regional domain (**Figure 1A**). This procedure tries to cover areas where atmospheric modeling precipitation grids are discarded (see **Section 3.2**). Thus, once the best set for each regional domain was obtained, no overlap of data with the WRF model was sought. Otherwise, that is, if overlap happens, the one with the smallest difference in minimum and maximum precipitation bias is selected according to **Eq. 2**. Note that if neither atmospheric nor the gridded data met the admissibility conditions, that place is not used.

$$P_g^s = \begin{cases} P_g & \text{if } P_{min}^o - 0.05 \times P_{min}^o \le P_g \le P_{max}^o + 0.05 \times P_{max}^o \\ NaN & \text{if } P_g < P_{min}^o - 0.05 \times P_{min}^o \\ NaN & \text{if } P_g > P_{max}^o + 0.05 \times P_{max}^o \end{cases}, \tag{2}$$

where P_g is the precipitation gridbox of each set in **Table 2**, P_g^s is the selected gridbox of the grid set, and P_{min}^o and P_{max}^o are the minimum and maximum precipitation of each subregion, respectively. Otherwise, we delete this gridbox.

3.4. Dynamic Topo-Climatic Model

Our model is a multiple linear regression between precipitation as the dependent variable (Swain et al., 2017; Navid and Niloy, 2018; Devi et al., 2020) and the following independent variables: elevation, slope, exposure, continentality, latitude, and longitude (Zambrano, 2011; Camera et al., 2014; Cifuentes, 2017). The model fits the observed values by a least square procedure between the observed and predicted values (Delbari et al., 2019). The linear dependence function is given by

$$P = \alpha + \beta_1 \cdot \text{elev} + \beta_2 \cdot \text{exp} + \beta_3 \cdot \text{slp} + \beta_4 \cdot \text{cont} + \beta_5 \cdot \text{lat} + \beta_6 \cdot \text{lon}, \tag{3}$$

where α is the intercept, and the values $\beta_i, i = 1, ., p$ are called regression coefficients associated with the variables elevation

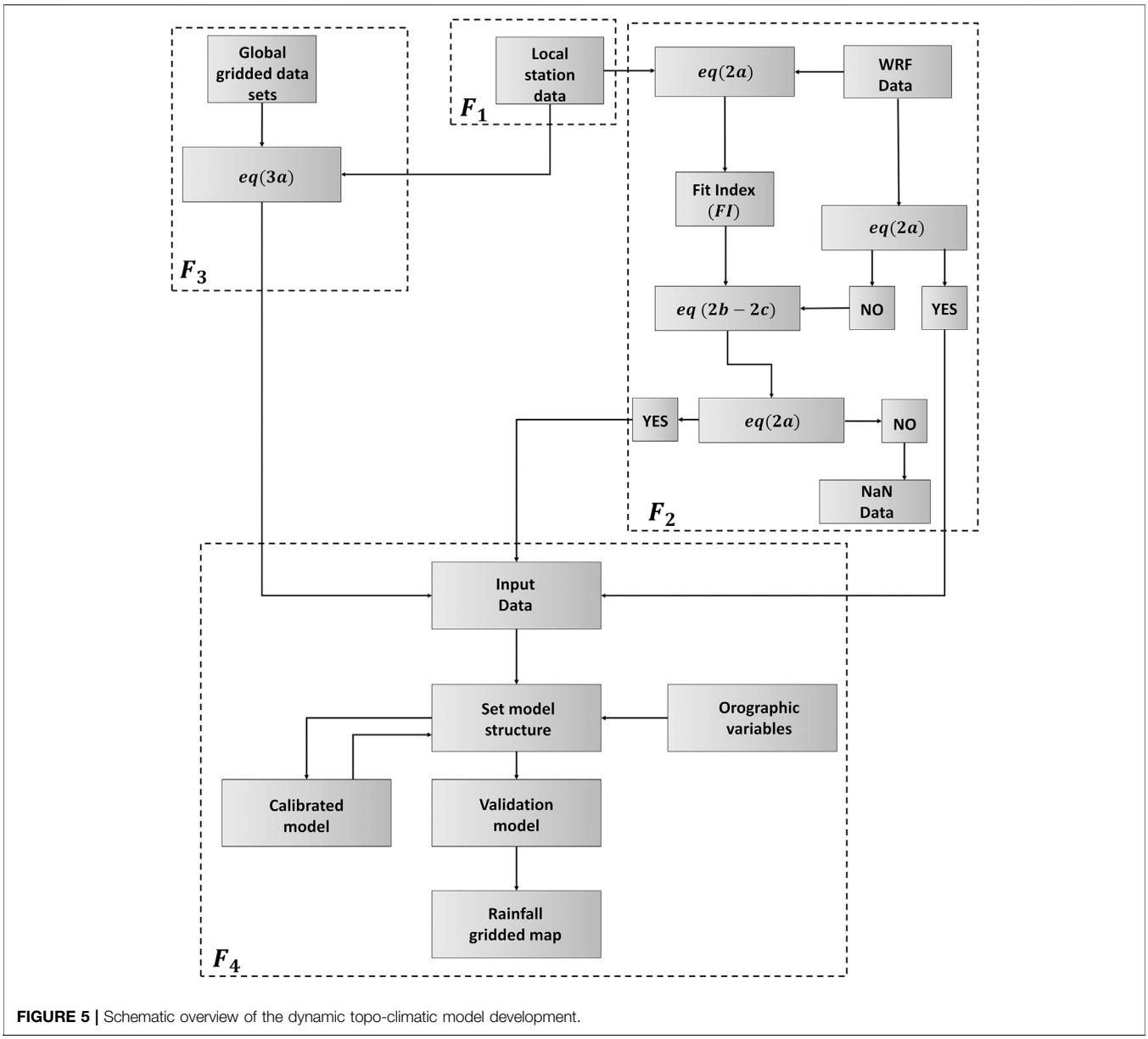


FIGURE 5 | Schematic overview of the dynamic topo-climatic model development.

(elev), exposure (exp), slope (slp), continentality (cont), latitude (lat), and longitude (lon).

To get the dataset gridded at 800 m, we used the Shuttle Radar Topography Mission digital elevation model (Farr et al., 2007) at 90-m spatial resolution. This digital elevation model is aggregated to an 800-m resolution (**Figure 4**). Note that the model domain covers five administrative regions: O'Higgins, El Maule, Biobío (now Biobío and Ñuble), La Araucanía, and Los Ríos (**Figure 1A**). However, the domains correspond to regional boundaries (**Figure 1A**), along with a 25% increase in the contribution from the neighboring regions. With this, we ensured that basins shared between different regions are covered. Also, mutual covering between domains ensures greater consistency and homogeneity to the global solution. Each month, data used for the construction of the field change with input data (**Sections 3.2** and **3.3**).

For each regional domain, we solve the topo-climatic model monthly, trying different configurations of the independent variables described in **Eq. 3**. We carry out tests in which either a single topographic variable or a set of them is eliminated. Thus, each month, six (6!), different tests can be performed. The structure is tested monthly, and at the end of the 12-year period (144 months), the most effective model is used as the basis for the calculation of the monthly topo-climatic model coefficient. Because it plays a significant role in a topo-climatic model, elevation is the only variable used in all calculations. Similarly, the different tests indicated that the elevation and exposure variables are necessary for all regional domains. In the following, only the most representative models are shown.

Each model developed is labeled according to the variables in **Eq. 3**: (*all*), all the variables; (*wexp*), without exposure; (*wslp*), without slope; (*wlat*), without latitude; (*wlon*), without longitude; and (*wcon*), without continentality variable. Subsequently, each model was evaluated through an analysis of variance (ANOVA) test and a residual analysis. We use different statistics to determine the most appropriate structure for each regional domain, namely, the standardized standard deviation (σ_e, **Eq. 6**), standardized mean square error (*nrmse*, **Eq. 7**), percentage of the standardized systematic error (*pbias*, **Eq. 9**), correlation coefficient (ρ_{xy}, **Eq. 8**), Nash–Sutcliffe coefficient (*nse*, **Eq. 10**), and the modified Willmott coefficient (*d*, **Eq. 11**).

Figure 5 depicts the three phases carried out for the construction of the dynamic topo-climatic model. The first phase (*F*1) determines the number of local precipitation stations and their subsequent selection (**Section 3.1**). The second phase (*F*2) corresponds to climatic modeling that produces precipitation fields, which are then bias-corrected (**Section 3.2**) using the local data (**Section 3.1**). The third phase (*F*3) (**Section 3.3**) selects the global precipitation gridded sets which are used alternatively for the locally adjusted precipitation modeled fields. Finally, within the fourth phase (*F*4) (**Section 3.4**), on each geographical domain, the tests allow the choice of the coefficients of variables (elevation, slope, exposure, continentality, latitude, and longitude) to develop the high-resolution fields.

3.5. Statistical Analysis

This section presents the statistical analysis strategy required for the atmospheric model correction and adjusting process, global gridded dataset selection, the topo-dynamic model calibration and validation, and the final high-resolution gridded product construction.

Spatial fitting, selection of monthly fields from the WRF model, and spatial selection of the best monthly products of global grid precipitation are analyzed for each regional domain (**Figure 1A**): The results of these processes are displayed for eight hydrological basins (**Figure 1B**). Our strategy uses a range of statistics following Cardoso et al. (2013), Ji et al. (2015), and Akhter et al. (2019): standardized standard deviation (σ_e, **Eq. 6**), standardized mean square error (*nrmse*, **Eq. 7**), correlation coefficient (ρ_{xy}, **Eq. 8**), percentage of the standardized systematic error (*pbias*, **Eq. 9**), Nash–Sutcliffe coefficient (*nse*, **Eq. 10**), and modified Willmott coefficient (*d*, **Eq. 11**). We used six indices in the data comparison because each of them quantifies only one aspect of data agreement or disagreement.

Once the selection of the best grid points is completed, a different monthly topo-climatic model is constructed over each regional domain. For this process, a calibration phase is followed by a validation phase. As previously indicated, we used 70% of the local rainfall data (136 stations) for calibration and 30% (60 stations) for validation. In both processes, due to the stations' inhomogeneous distribution and notorious inadequate coverage in mountainous areas, the spatial distribution of the local stations chosen tried to maximize homogeneous coverage of each regional domain.

Calibration of the dynamic topo-climatic model includes application of an ANOVA test, and the goodness-of-fit parameters R^2 (**Eq. 4**) and R_j^2 (**Eq. 5**) with the respective residual analysis. For the validation stage, the following statistics are used: standardized standard deviation (σ_e, **Eq. 6**), standardized mean square error (*nrmse*, **Eq. 7**), correlation coefficient (ρ_{xy}, **Eq. 8**), percentage of the standardized systematic error (*pbias*, **Eq. 9**), Nash–Sutcliffe coefficient (*nse*, **Eq. 10**), and the modified Willmott coefficient (*d*, **Eq. 11**). We also analyze results using Taylor's diagrams (Taylor, 2001), to visualize results model behavior relative to observations in terms of the spatial structure generated by the Pearson correlation coefficient (ρ_{xy}), standardized mean square error (*nrmse*), and absolute standardized standard deviation ($|\sigma_e|$). Also, we used boxplot diagrams to visualize standard deviation scores (σ_e), the mean systematic error percentage (*pbias*), coefficient of Nash–Sutcliffe (*nse*), and modified Willmott coefficient (*d*). This calibration and validation processes are performed monthly, thus generating every month a different topo-climate model. Calibration and validation results presented here correspond to the average of all these months. Also, given that the whole domain includes a climatic transition zone, the results of the eight basins are summarized in three subdivisions: northern, central, and southern areas (**Figure 1B**).

The statistics used are defined in the following equations:

$$R^2 = \frac{\sum_{i=1}^{n}\left(Y_i - \overline{X}\right)^2}{\sum_{i=1}^{n}\left(X_i - \overline{X}\right)^2}, \tag{4}$$

$$R_j^2 = 1 - \frac{(n-1)\sum_{n=1}^{n}(X_i - Y_i)^2}{(n-k-1)\sum_{n=1}^{n}\left(X_i - \overline{X}\right)^2}, \tag{5}$$

$$\sigma_e = 1 - \sqrt{\frac{\sum_{i=1}^{n}\left(Y_i - \overline{Y}\right)^2}{\sum_{i=1}^{n}\left(X_i - \overline{X}\right)^2}}, \tag{6}$$

$$nrmse = \frac{\sqrt{\frac{\sum_{i=1}^{n}(X_i - Y_i)^2}{n}}}{\sigma}, \tag{7}$$

$$\rho_{xy} = \frac{\sum_{i=1}^{n}\left(X_i - \overline{X}\right)\left(Y_i - \overline{Y}\right)}{\sqrt{\sum_{i=1}^{n}\left(X_i - \overline{X}\right)^2}\sqrt{\sum_{i=1}^{n}\left(Y_i - \overline{Y}\right)^2}}, \tag{8}$$

$$pbias = \frac{\sum_{i=1}^{n}(X_i - Y_i)}{\sum_{i=1}^{n}X_i} \times 100, \tag{9}$$

$$nse = 1 - \frac{\sum_{i=1}^{n}(X_i - Y_i)^2}{\sum_{i=1}^{n}\left(X_i - \overline{X}\right)^2}, \tag{10}$$

$$d = 1 - \frac{\sum_{i=1}^{n}|Y_i - X_i|}{\sum_{i=1}^{n}\left(\left|Y_i - \overline{X}\right| + \left|X_i - \overline{X}\right|\right)}, \tag{11}$$

where X and Y are observed and simulated precipitation, respectively.

4. RESULTS

In **Sections 4.1** and **4.2**, the average precipitation behavior of the adjusted atmospheric model (see **Section 3.2**) and the selected global gridded products (see **Section 3.3**) is presented over three zones (north, center, and south), covering eight basins (**Figure 1B**). All local stations (196) are used, and these are presented using Taylor and boxplot diagrams (see **Section 3.5**).

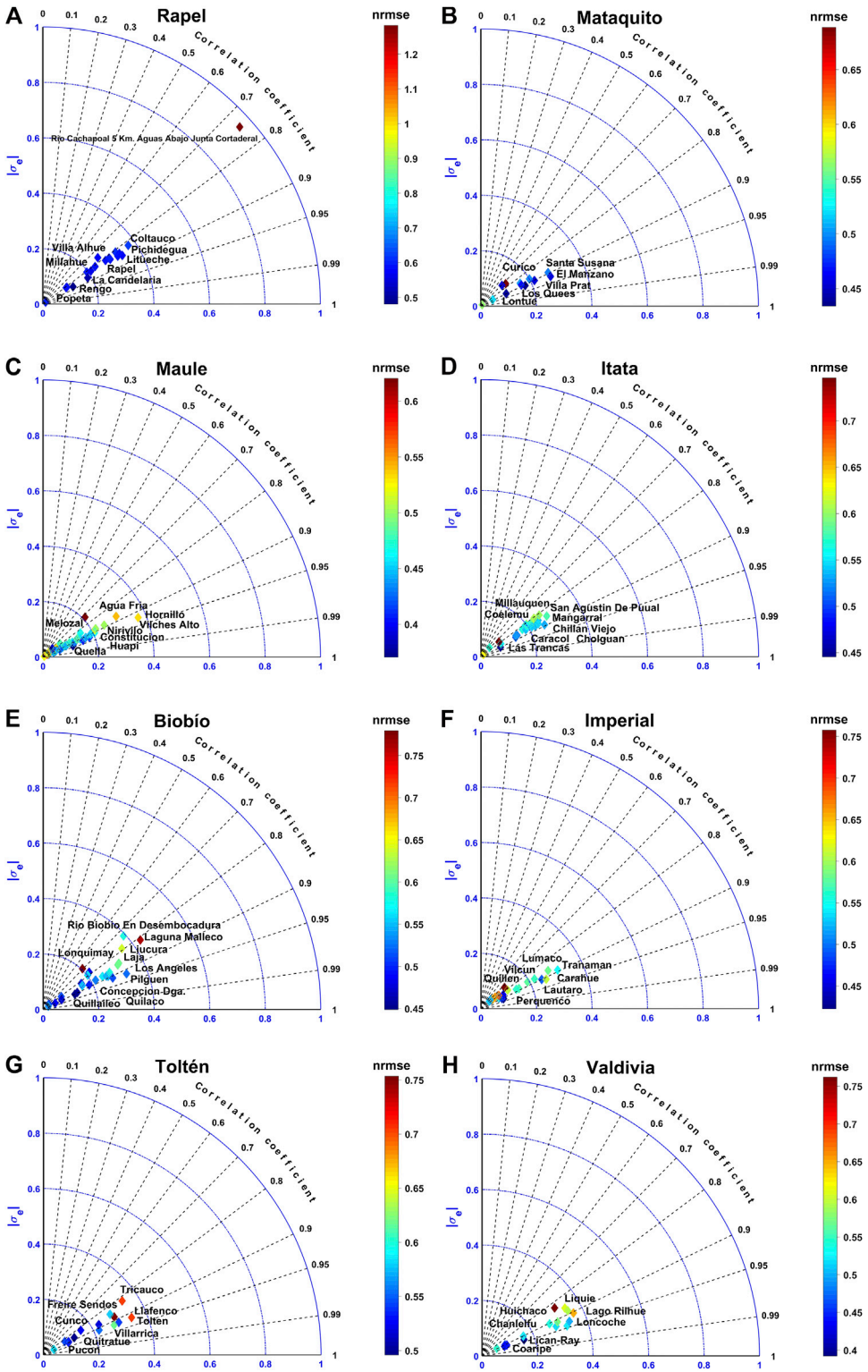


FIGURE 6 | Taylor's diagrams corresponding to weather research and forecasting model performance (**Table 1**) once fitted (**Eq. 1**) in basins: **(A)** Rapel, **(B)** Mataquito, **(C)** Maule, **(D)** Itata, **(E)** Biobío, **(F)** Imperial, **(G)** Toltén, and **(H)** Valdivia.

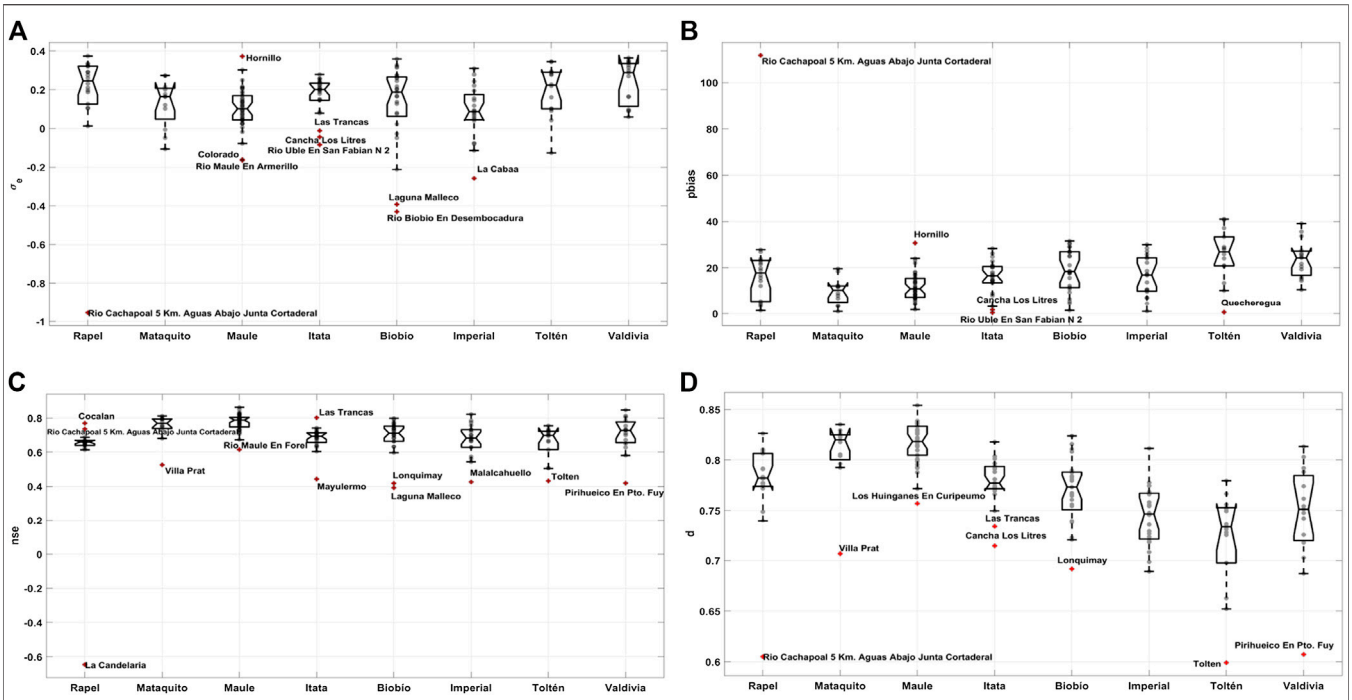


FIGURE 7 | Box diagrams corresponding to the fit of the weather research and forecasting model, once adjusted (**Eq. 1**) on the river basins of the area under study (**Figure 1B**). **(A)** Standardized standard deviation (σ_e), **(B)** percentage of the systematic error (*pbias*), **(C)** Nash–Sutcliffe coefficient (*nse*), and **(D)** Willmott coefficient (*d*).

Section 4.3 presents the best results associated with the calibration process of the dynamic topographic-climatic model within each regional domain (**Section 4.3.1**) using 132 precipitation stations (**Section 3.1**). The model validation stage of the chosen model using 60 stations in **Section 4.3.2** is presented for the eight basins (**Figure 1B**). This part of the article ends by showing the annual accumulation of the constructed monthly climatology.

4.1. Atmospheric Model

In the northern zone (**Figures 6A-C**), ρ_{xy} shows an average of 0.85, but we can appreciate atypical cases with values below 0.65. Meanwhile, *nmrse* shows agreements close to 0.65, although all basins present cases above 0.5. For σ_e (**Figure 7A**), the average agreement is close to 0.1, with Rapel showing some cases above 0.3. Finally, *pbias* (**Figure 7B**) gives an average agreement of 14%, with Mataquito presenting the lowest values since 75% of the analyzed stations there are close to 10%.

Results for the central zone (**6D,E**) indicate an average for ρ_{xy} of 0.83 and 0.55 for *nrmse*, although with several cases well above 0.65. For σ_e (**Figure 7A**), average is 0.14, with the Biobío basin showing values above 0.25. For *pbias* (**Figure 7B**), the 17% average is punctuated by certain basins exceeding 25%.

Good estimation for ρ_{xy} characterizes the southern region (**Figures 6F-G**), averaging a value of 0.87. Within this region, Valdivia shows cases close to 0.6. *nrsme* exhibits an average of 0.56, although all basins have cases above 0.7. In turn, σ_e (**Figure 7A**) shows an average of 0.15, with Imperial and Toltén above 0.3. Finally, *pbias* (**Figure 7B**) shows an average of 9%. Toltén gives the lowest average estimate with 7%.

We show the *nse* and Willmott coefficient (*d*) results in all regions (and basins) in **Figure 7D**. In all basins, the average value for *nse* is greater than 0.7; only Rapel and Maule show values smaller than 0.6. The Willmott coefficient (*d*) shows values close to 0.8 in the north zone (Rapel, Mataquito, and Maule) and a value of 0.75 for the central zone (Itata and Biobío), whereas for the southern zone (Imperial, Toltén, and Valdivia) 25% of stations show values below 0.75 with a large spread.

4.2. Global Precipitation Datasets

In the northern zone (**Figures 8A-C**), ρ_{xy} presents an average value of 0.74. However, CMORPH and SM2RAIN show ρ_{xy} values under 0.6 in all zones. Variations in *nrmse* show an average of 0.4, with Mataquito and Maule displaying 0.5 for the PERSIAN dataset. For σ_e, the average is 0.27, while for CMORPH and SM2RAIN the values are higher than 0.6 for the whole zone (**Figure 9A**). *pbias* (**Figure 9B**) shows an average of 20%, with anomalous estimates (over 30%) in Mataquito and Maule.

Over the central zone (**Figures 8D,E**), ρ_{xy} presents an average of 0.74. Again, CMORPH and SM2RAIN show the worst results for ρ_{xy}, with scores under 0.6. Meanwhile, *nrsme* gives an average of 0.44, although the entire area shows values above 0.3. Continuing with σ_e (**Figure 9A**), the average is 0.34. As above, CMORPH and SM2RAIN give estimates fairly different relative to the average, higher than 0.5. Here, *pbias* (**Figure 9B**) shows an

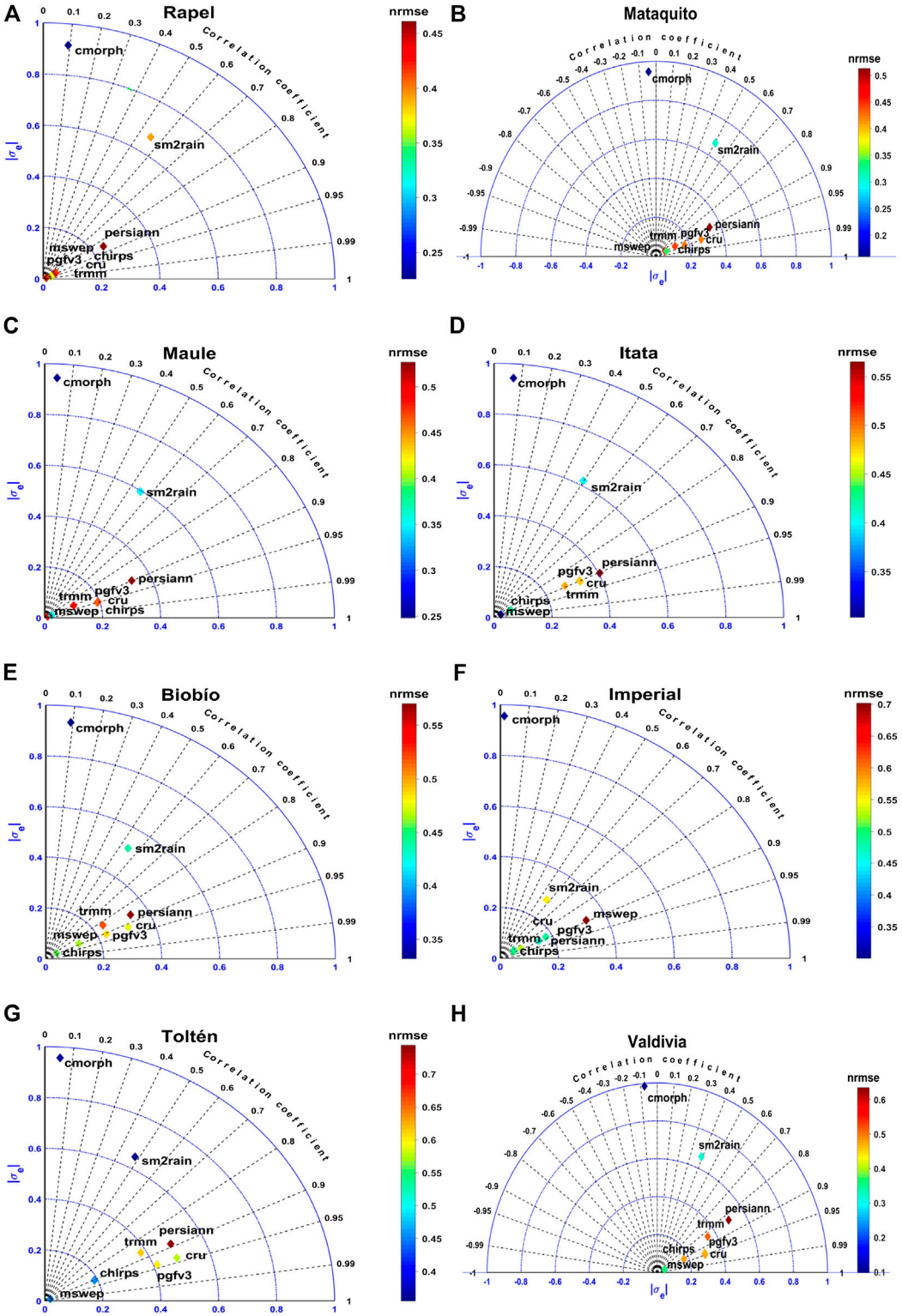


FIGURE 8 | Taylor's diagrams corresponding to the gridded set performance (**Table 2**), once fitted (**Eq. 2**) on the river basins of **(A)** Rapel, **(B)** Maule, **(C)** Itata, **(D)** Biobío, **(E)** Imperial, **(F)** Toltén, **(G)** Mataquito, and **(H)** Valdivia.

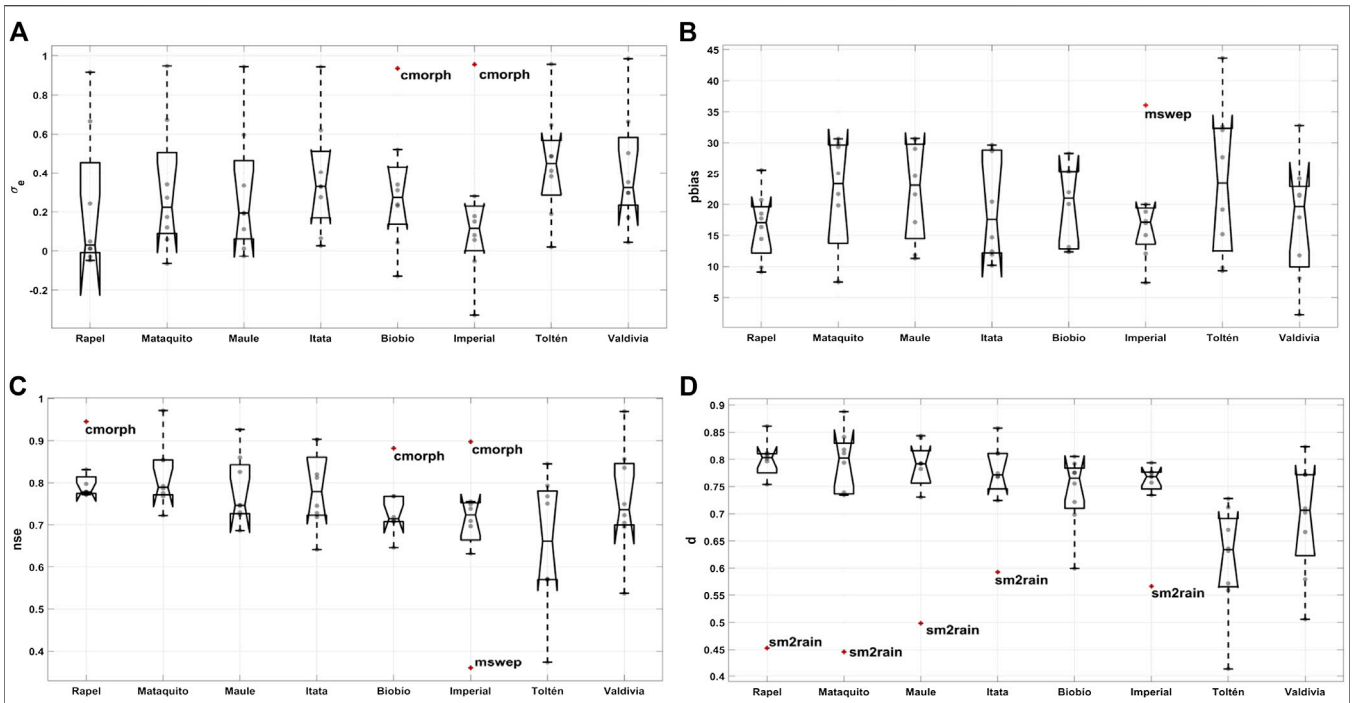


FIGURE 9 | Box diagrams corresponding to the gridded set performance (**Table 2**), once adjusted (**Eq. 2**) on the river basins of the area under study (**Figure 1B**). **(A)** Standardized standard deviation (σ_e), **(B)** percentage of the systematic error (*pbias*), **(C)** Nash–Sutcliffe coefficient (*nse*), and **(D)** Willmott coefficient (*d*).

average error of 20%, while the highest estimates are below 30% in the Itata and Biobío basins.

For the southern zone (**Figures 8F-H**), ρ_{xy} shows an average of 0.73. Similar to that described in the previous paragraph, CMORPH and SM2RAIN show the worst results with estimates for ρ_{xy} under 0.6. A high *nrmse* in all basins delivers an average of 0.48. MSWEP and PERSIAN show the highest *nrmse* with values above 0.6. The average σ_e is 0.34, with CMORPH and SM2RAIN above 0.6 (**Figure 9A**). Meanwhile, *pbias* (**Figure 9B**), exhibits an average of 20%. In this case, it is important to highlight that in all basins, the different datasets present errors more significant than 30%.

The Nash–Sutcliffe (*nse*) and Willmott (*d*) coefficients are displayed for all basins (**Figures 9C,D**). Here, *nse* shows a mean adjustment of about 0.6 from the Rapel to the Imperial basin. There is a larger spread for Toltén and Valdivia, with the minima below 0.55. The Willmott coefficient (*d*) exhibits a similar distribution from Rapel to Imperial, with almost 90% of the datasets above 0.7. We again see more heterogeneity in the Toltén and Valdivia basins with values below 0.5. SM2RAIN shows the weakest performance for all basins.

4.3. Dynamic Topo-Climatic Precipitation

4.3.1. Regional Domain Analysis

The average fit of the dynamic topo-climatic model for each regional domain is shown in **Figure 10**. The coefficient of determination (R^2) (**Figure 10A**) shows an excellent model performance in O'Higgins and Biobío regions with values above 0.8 and in Araucanía and Los Ríos regions with values below 0.77. The adjusted coefficient of determination (R_j^2) (**Figure 10B**) also shows skilled fitting (over 0.8) from O'Higgins to Biobío regions, although the Maule basin shows the lowest estimate for R_j^2. The same occurs in Araucanía and Los Ríos regions. The F_{value} from the ANOVA shows an excellent fit of the model with a P_{value} less than 0.05 (**Figure 10C**). In turn, the average model performance for ρ_{xy} is higher than 0.9 in all domains (**Figure 10H**). We also find an average *pbias* below 22%, with O'Higgins and Biobío below 15% (**Figure 10F**). The outliers identified for σ_e (**Figure 10G**) exhibit an error below 0.22, supporting that the model is skilled. *nrmse* (**Figure 10E**) shows average model values below 0.4, while values above 0.48 are shown in Araucanía and Los Ríos. In these regions, a high error confirms the model is more uncertain in estimating extreme precipitation events. **Table 3** shows the results for the calibrated model configuration (R^2, R_j^2, F_{value}, and P_{value}) and error estimate (σ_e, *nrmse*, *pbias*, and ρ_{xy}) for each regional domain.

4.3.2. Zonal and Basin Analysis

The northern zone (**Figures 11A-C**) shows an average ρ_{xy} of 0.88, although some stations in Rapel get values close to 0.6. Meanwhile, the *nrmse* exhibits an average of 0.46, although in Rapel and Maule some cases are above 0.55. Interestingly, σ_e (**Figure 12A**) shows an average fit of 0.07, with that in Maule below −0.4. *pbias* (**Figure 12B**) shows an average adjustment of 18%, but Rapel and Maule show the most considerable difference with an estimate over 50%.

The central zone (**Figures 11D,E**), ρ_{xy} shows an average of 0.89 and Biobío exhibits values below 0.8. The *nrmse* displays an average of 0.52, while Biobío shows an irregular value greater than

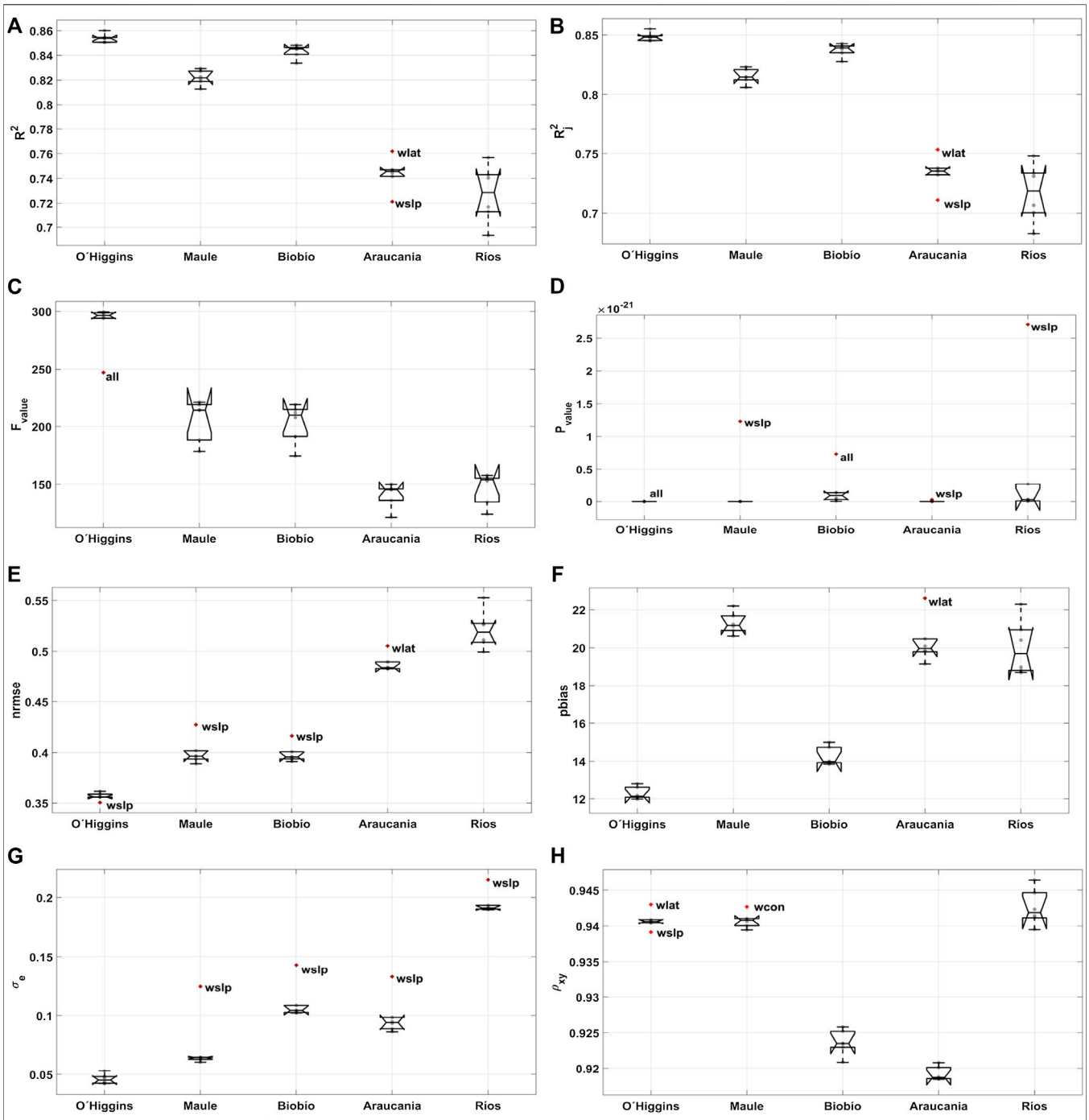


FIGURE 10 | Box diagrams corresponding to the adjustment of the topo-climatic model on the domains in execution. **(A)** Multiple determination coefficient (R^2), **(B)** adjusted multiple determination coefficient R_j^2, **(C)** value *F*, **(D)** value *P*, **(E)** standardized mean square error (*nrmse*), **(F)** percentage of systematic error (*pbias*), **(G)** standardized standard deviation (σ_e), **(H)** Pearson correlation coefficient (ρ_{xy}).

1. The average for σ_e is 0.1 (**Figure 12A**) with only Biobío being below −0.5. For *pbias* (**Figure 12B**) there is a 24% average error with Biobío showing an estimate below 100%.

The southern zone (**Figures 11F-H**) exhibits an average ρ_{xy} over 0.9, while the lowest estimates are above 0.85. *nrsme* shows an average of 0.52, with all basins having some values above 0.66. On the other hand, while σ_e (**Figure 12A**) shows an average of 0.1, only the Imperial basin exhibits a low estimate of −0.2. *pbias* (**Figure 12B**) shows an average of 24%. *nse* shows an average above 0.7 in all basins (**Figure 12C**); only two atypical cases are detected in Maule and Biobío with values of 0.5 and −1, respectively. On the other hand, *d* (**Figure 12D**) shows an

TABLE 3 | Statistical summary of the type of topo-climatic model chosen by the political domain of each region. (wslp), (wcost), (all), (wcon).

Region	Model	R^2	R_j^2	F_{value}	P_{value}	σ_e	nrmse	pbias	ρ_{xy}
O'Higgins	*wslp*	0.860	0.855	298.77	1.1×10^{-29}	5	0.35	11.99	0.94
Maule	*wcon*	0.829	0.823	221.00	1.4×10^{-31}	6	0.38	20.90	0.94
Biobío	*wcon*	0.848	0.843	218.93	1.3×10^{-22}	10	0.39	13.96	0.93
Araucanía	*all*	0.747	0.736	121.35	6.3×10^{-26}	9	0.48	19.84	0.92
Ríos	*wcon*	0.757	0.748	155.13	4.1×10^{-24}	19	0.50	18.81	0.95

O'Higgins is built with a model without a slope (wslp), Maule and Biobío (old) with a model without continentality (wcon), Araucanía by means of a model with all the descriptive variables (all), and Los Ríos by a model with continentality (wcon).

average fitting of 0.75. Only Biobío exhibits an outlier in the Liucura station with a value below 0.5.

On each regional domain, a different monthly model is adjusted to the calibration data and checked using validation points. This allows us to construct a monthly solution for each regional domain, delivering a dataset of monthly fields covering the period 2000–2011 that subsequently are used to produce monthly climatologies from January to December. **Figure 13** shows the observed accumulated annual rainfall and the one obtained by the topo-climatic dynamic model over the study area (34°S–41°S). **Figure 13B** indicates an adequate distribution of precipitation from north to south and from the ocean to the Andes. There is a progressive increase from north to south and drastic increases in mountain areas, particularly along the Andes and the coastal cordillera. Thus, in sectors close to the coast (from 38°S), an abundant annual precipitation is identified, sometimes reaching over 2,000 mm. Throughout the Andean areas, the accumulated annual rainfall can reach and exceed 3,000 mm per year. Finally, between the coast and the Andes below 36°S, it is possible to identify a decrease in annual precipitation.

5. DISCUSSION AND CONCLUSION

High-resolution precipitation spatial variability is significant in different fields such as hydrology, environment, forestry, and agriculture. In Chile, several authors worked on gridded precipitation datasets built only with the information available from local stations in some areas of the country (Román and Andrés, 2010; Jacquin and Soto-Sandoval, 2013; Reyes, 2013; Castro et al., 2014; Sijinaldo, 2015). Also, in some cases, datasets were generated from observed data and low-resolution gridded data higher than 0.25° (Morales-Salinas et al., 2012) or even poorer quality datasets. Thus, these high-resolution datasets are inadequate to study large areas and/or the whole country. Moreover, the insufficient spatial distribution of the pluviometric network (Muñoz et al., 2018) precludes real hydro-climatic impact under current environmental conditions.

Therefore, we assert that the dataset will be useful for different communities in Chile. It will be useful for agricultural, forestry, and livestock planning, for example, and for national institutions such as the Dirección General de Aguas (DGA), the Instituto de Investigaciones Agropecuarias (INIA), and the Instituto Forestal de Chile (INFOR), among others. This product can serve as a basis of comparison for studies aimed at investigating future climate or agricultural changes (Orrego et al., 2016), allowing investigation of the role of and Antartic Oscillation and many climatic phenomena on some local precipitation-related aspects (Fustos et al., 2020b), which is beyond the scope of this study.

To get an improved dataset and to quantify precipitation, we built a high-resolution dynamic statistical gridded precipitation product at ~ 800 m. Its development involved time series of local precipitation and different global precipitation grid sets (as shown in **Table 2**). To detect spatial-temporal variability of precipitation, we performed numerical modeling of the atmosphere over the study area at 4 km spatial resolution for the period 2000–2011. These outputs are a powerful tool for statistical scale reduction (Widmann et al., 2003; Schmidli et al., 2006; González-Rojí et al., 2019). Also, within each region, according to **Eqs. 1 and 2** requirements, we performed a month-by-month data selection. We also evaluated precipitation time series belonging to eight basins to estimate the responses of the best products that entered our dynamic topo-climatic model (**Figure 11**).

We evaluated some precipitation grids and the results are presented in **Table 2**. To classify the optimal precipitation estimates and reduce uncertainty, we used a selection criterion (**Eq. 2**). As shown by Zambrano F. et al. (2017) and Zambrano M. et al. (2017), the performance of many is unsatisfactory. The products CHIRPS, MSWEP, and PGFv3 show the most accurate estimations ($\rho_{xy} > 0.8$). Meanwhile, CMORPH and SM2RAIN provide the worst performance over the whole study area (< 0.6), and the average of σ_e displays a similar distribution in all basins. However, the CMORPH set exhibits the highest mismatches, with estimates close to 1 in Biobío and Imperial. *pbias* shows a similar distribution along all basins between 10 and 30%. The Nash–Sutcliffe coefficient (*nse*) shows a decreasing yield from Rapel to Itata (> 0.7) along with an increasing dispersion. For example, at Biobío and Imperial, the adjustment is centered on 0.7 with low dispersion. Also, Toltén and Valdivia have an average of 0.7, but with high dispersion. On the other hand, Willmott (*d*) does not show an improvement in the performance of the datasets, although it shows a similar pattern as *nse* (> 0.7). For all basins, we notice that SM2RAIN shows low values. However, model fitting results for some datasets should be seen with caution, since we eliminated any value above or below 5% of the respective maximal or minimal observed precipitation. Therefore, cleaned data improve the estimates of these sets.

Atmospheric dynamic models, like WRF, simulate precipitation based on convective and large-scale processes (such as precipitation from cumulonimbus fronts or clouds), generating an improved distribution of precipitation as well as other fields such as temperature (Pope and Stratton, 2002; Jung et al., 2006; Gent et al., 2010). However, there are still errors attributed to feedback processes, which are not necessarily reduced by increasing the model spatial resolution. As these errors are pronounced on rough terrain, and even more so in mountainous areas, to take that possibility into account, it was necessary to add a 5% correction. Despite this, the limited density of observation along the Andes incorporates a high degree of uncertainty, preventing homogeneous fit, thus making the construction of a correct

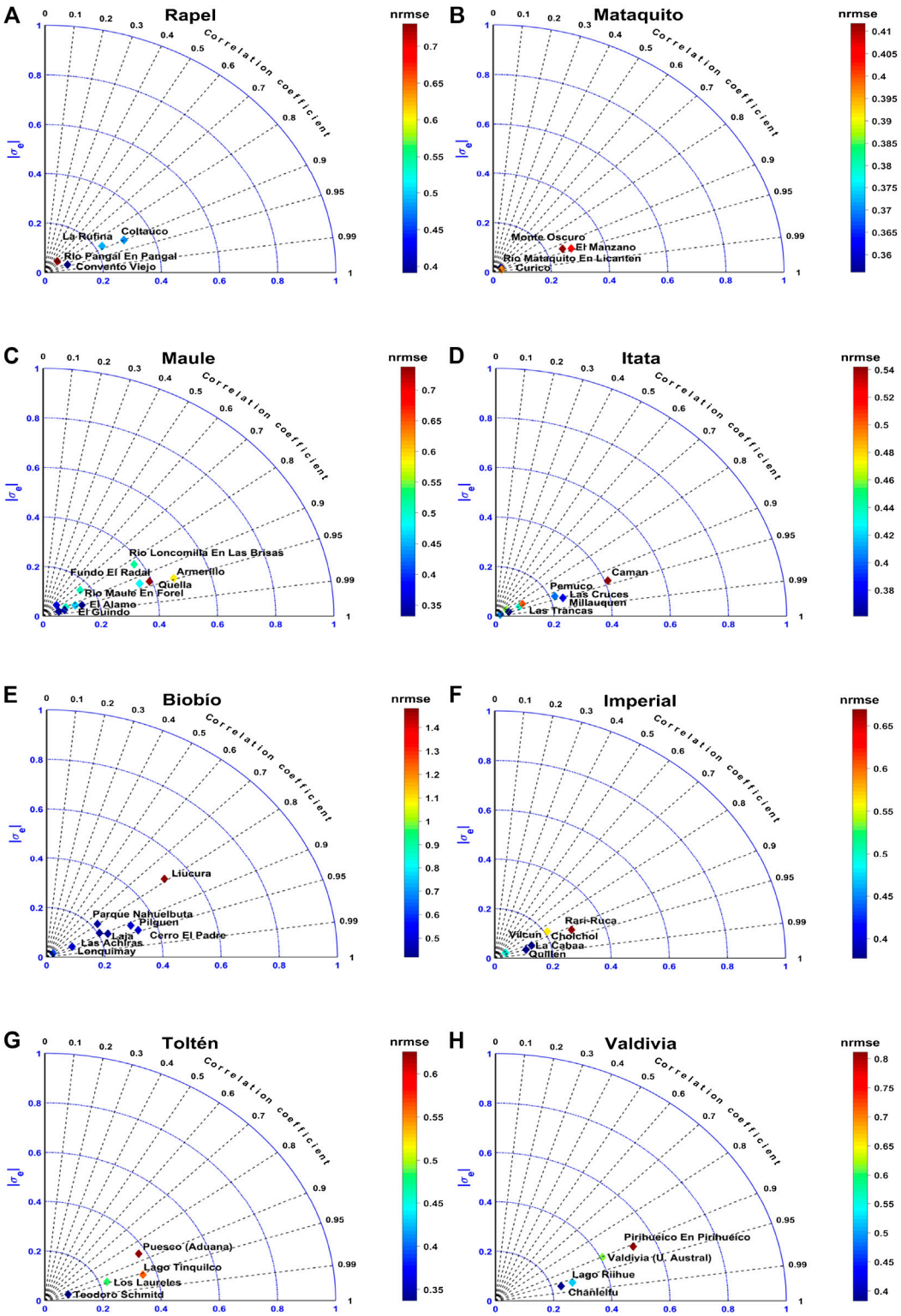


FIGURE 11 | Taylor diagrams corresponding to the performance of the topo-climatic model on the river basins (**Figure 1B**): **(A)** Rapel, **(B)** Mataquito, **(C)** Maule, **(D)** Itata, **(E)** Biobío, **(F)** Imperial, **(G)** Toltén, and **(H)** Valdivia.

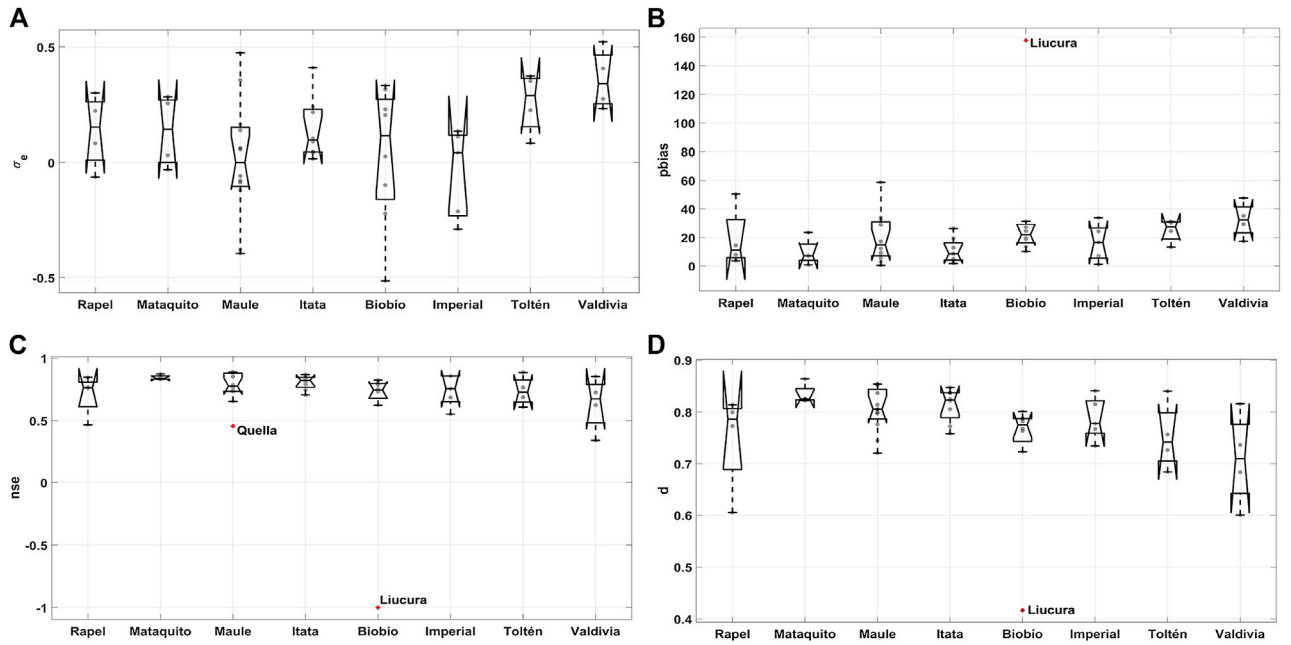


FIGURE 12 | Box diagrams corresponding to the adjustment of the topo-climatic model on the domains in execution. **(A)** Standardized standard deviation (σ_e), **(B)** percentage of the systematic error (*pbias*), **(C)** Nash–Sutcliffe coefficient (*nse*), and **(D)** Willmott coefficient (*d*).

model at high altitude difficult. Taylor and boxplot diagrams show that the model presents a remarkable performance in the northern zone (**Figures 6**, **7**). As far as the central zone is concerned, adequate fitting is again obtained for ρ_{xy}, *nse*, and *d*.

To construct our dynamic geostatistical model, we used global precipitation grids and a local atmospheric model (**Table 2**) in addition to regional domains (**Figure 1B**). This is a nontrivial process, particularly in regions with a great variety of space–time patterns (Zhang et al., 2016). During the precipitation reconstruction phase, we verified the elevation coefficients relative to each regional domain with available local information. For the mountains, the little local information available prevents adequate correction and adjustment of the WRF model or the gridded data. Consequently, in the heights, the precipitations should generally be overestimated. Each month, the adjustment provides different elevation coefficients for each regional domain. However, for the entire domain, the solution that imposed a single elevation coefficient, considering all the information from north to south, turned out to be the best.

The results of the model chosen for each region (**Table 3**) show reasonable skill in the assessed basins (**Figures 11**, **12**). However, the model is unable to satisfactorily represent extreme precipitation events, which gradually increase from north to south. It is essential

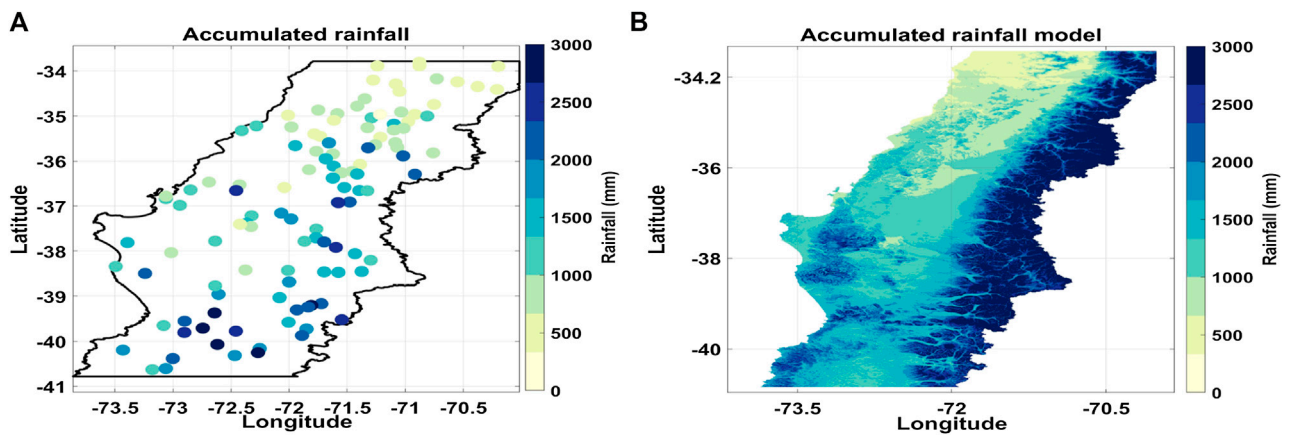


FIGURE 13 | Annual cumulative rainfall. **(A)** Rainfall observed and **(B)** dynamic topo-climatic model.

to note that the choice of the regression model is conditioned by the input data selection and the domain used. Only numerical modeling and satellite information are the ones that provide adequate spatial coverage and persistence. In turn, statistical downscaling can improve the accuracy of discrete meteorological measurements (Diez et al., 2005; Fernández-Ferrero et al., 2009; Le Roux et al., 2018; González-Rojí et al., 2019). To our knowledge, this kind of study is scarce in Chile, not only in the construction of grilled climatic data but also in the analysis and comparison of different methodologies for an optimal statistical scale reduction model or the domain type needed to carry this out.

The database presented in this study results from atmospheric modeling, corrected, adjusted, and ported to higher resolution by a dynamic topo-climatic method using data from local meteorological stations and satellite fields. Note that to improve the accuracy of database selection by different statistical methodologies, we visually inspected each dataset in detail and month by month. However, we still depend on the quality of the atmospheric modeling, which is not reality, and that of the satellite fields and local data. Therefore, we would like to point out that although we are confident that the method used and the resolution will allow a better understanding of local hydrological variability, this database does not replace reality. That is why, contrary to several global gridded databases, which do not stipulate it, we recommend within each basin to check against local data and correct any existing bias.

Of course, there are still many improvements to be made. Note that we will always be dependent on the distribution of the local weather network, which is the only one that allows the calibration and validation process. It is fundamental to improve the quality in many places, notably in the slopes of the Coastal and Andean mountain ranges, where weather coverage is almost nonexistent. A nonhomogeneous distribution of altitude data, used to build a solution over the mountains, may not represent the different mechanisms in both cordilleras, sometimes separated by less than 100 km. Thus, specific measurement campaigns are needed to support, for example, model calibration during brief periods and on a local scale. However, many phenomena throughout Chile develop at high frequencies, where the monthly value does not allow for a correct description (Fustos et al., 2020a). Thus, while it is necessary to expand time–space coverage, north–south and up to 2020, in addition to build other high-resolution grids of essential hydro-climatic parameters (such as temperature), it is also imperative to focus on daily grid products.

DATA AVAILABILITY STATEMENT

The datasets generated for this study are available on request to the corresponding author.

AUTHOR CONTRIBUTIONS

RA assisted the first author (FA) at different levels of research, such as conception, design, analysis, and editing of the manuscript. Although RA is responsible for the overall concept and design of the research, data collection, development of atmospheric modeling, and statistical analysis of this manuscript was performed by FA; RA and AA contributed to the technical implementation required for atmospheric modeling; and AA improved the mathematical interpretation of the results and participated in the review of the submitted manuscript.

ACKNOWLEDGMENTS

We appreciate and are indebted to both the reviewers' outstanding work, whose rigor and scientific culture helped us improve both form and substance. We are very grateful and indebted to our colleague A. Fernandez, for careful proofreading of the manuscript. We are also grateful for advices by B. Mark. We are grateful for funding support received from the PhD in Physical Sciences program from the Faculty of Physical and Mathematical Sciences, the Research Directorate (DRINV), and Postgraduate Directorate of the University of Concepción. This research was partially supported by the supercomputing infrastructure of the NLHPC (ECM-02) at Centro de Modelación y Computacion Científica, Universidad de La Frontera, CMCC-UFRO.

REFERENCES

Abatzoglou, J. T. (2013). Development of gridded surface meteorological data for ecological applications and modelling. *Int. J. Climatol.* 33, 121–131. doi:10.1002/joc.3413

Aceituno, P., Fuenzalida, H., and Rosenblüth, B. (1993). "Climate along the extratropical west coast of south America," in *Earth system responses to global change*. Editors H. A. Mooney, E. R. Fuentes, and B. I. Kronberg (San Diego, CA: Academic Press), 61–69.

Akhter, J., Das, L., Meher, J. K., and Deb, A. (2019). Evaluation of different large-scale predictor-based statistical downscaling models in simulating zone-wise monsoon precipitation over India. *Int. J. Climatol.* 39, 465–482. doi:10.1002/joc.5822

Araya-Ojeda, M., and Isla, F. I. (2016). Variabilidad hidrológica en la región del biobío: los eventos el niño en zonas templadas de Chile. *Revista Universitaria de Geografía* 25, 31–55.

Arumí-Ribera, J., and Oyarzún-Lucero, R. (2006). Las aguas subterráneas en Chile. *Bol. Geol. Min.* 117, 37–45

Arumí, J. L., Rivera, D., Muñoz, E., and Billib, M. (2012). Interacciones entre el agua superficial y subterránea en la región del bío bío de Chile. *Obras y proyectos.*, 4–13. doi:10.4067/s0718-28132012000200001. "https://www.researchgate.net/publication/241157980_Las_aguas_subterraneas_en_Chile/stats" and "https://dialnet.unirioja.es/servlet/articulo?codigo=1710339"

Ashouri, H., Hsu, K.-L., Sorooshian, S., Braithwaite, D. K., Knapp, K. R., Cecil, L. D., et al. (2015). Persiann-CDR: daily precipitation climate data record from multisatellite observations for hydrological and climate studies. *Bull. Am. Meteorol. Soc.* 96, 69–83. doi:10.1175/bams-d-13-00068.1

Barrett, B. S., and Hameed, S. (2017). Seasonal variability in precipitation in central and southern Chile: modulation by the South Pacific High. *J. Clim.* 30, 55–69. doi:10.1175/JCLI-D-16-0019.1

Beck, H. E., Van Dijk, A. I., Levizzani, V., Schellekens, J., Gonzalez Miralles, D., Martens, B., et al. (2017a). Mswep: 3-hourly 0.25 global gridded precipitation (1979-2015) by merging gauge, satellite, and reanalysis data. *Hydrol. Earth Syst. Sci.* 21, 589–615. doi:10.5194/hess-21-589-2017

Beck, H. E., Vergopolan, N., Pan, M., Levizzani, V., Van Dijk, A. I., Weedon, G. P., et al. (2017b). Global-scale evaluation of 22 precipitation datasets using gauge

observations and hydrological modeling. *Hydrol. Earth Syst. Sci.* 21, 6201–6217. doi:10.5194/hess-21-6201-2017

Berezowski, T., Szcześniak, M., Kardel, I., Michałowski, R., Okruszko, T., Mezghani, A., et al. (2016). CPLFD-GDPT5: high-resolution gridded daily precipitation and temperature data set for two largest polish river basins. *Earth Syst. Sci. Data*. 8, 127–139. doi:10.5194/essd-8-127-2016

Brinckmann, S., Krähenmann, S., and Bissolli, P. (2016). High-resolution daily gridded data sets of air temperature and wind speed for Europe. *Earth Syst. Sci. Data*. 8, 491–516. doi:10.5194/essd-8-491-2016

Brocca, L., Ciabatta, L., Massari, C., Moramarco, T., Hahn, S., Hasenauer, S., et al. (2014). Soil as a natural rain gauge: estimating global rainfall from satellite soil moisture data. *J. Geophys. Res.: Atmos.* 119, 5128–5141. doi:10.1002/2014JD021489

Brocca, L., Moramarco, T., Melone, F., and Wagner, W. (2013). A new method for rainfall estimation through soil moisture observations. *Geophys. Res. Lett.* 40, 853–858. doi:10.1002/grl.50173

Camera, C., Bruggeman, A., Hadjinicolaou, P., Pashiardis, S., and Lange, M. A. (2014). Evaluation of interpolation techniques for the creation of gridded daily precipitation (1×1 km^2); Cyprus, 1980–2010. *J. Geophys. Res.: Atmos.* 119, 693–712. doi:10.1002/2013jd020611

Camera, C., Bruggeman, A., Hadjinicolaou, P., Michaelides, S., and Lange, M. A. (2017). Evaluation of a spatial rainfall generator for generating high resolution precipitation projections over orographically complex terrain. *Stoch. Environ. Res. Risk Assess.* 31, 757–773. doi:10.1007/s00477-016-1239-1

Cannon, D. J., Brayshaw, D. J., Methven, J., Coker, P. J., and Lenaghan, D. (2015). Using reanalysis data to quantify extreme wind power generation statistics: a 33 year case study in Great Britain. *Renew. Energy.* 75, 767–778. doi:10.1016/j.renene.2014.10.024

Cardoso, R., Soares, P., Miranda, P., and Belo-Pereira, M. (2013). WRF high resolution simulation of Iberian mean and extreme precipitation climate. *Int. J. Climatol.* 33, 2591–2608. doi:10.1002/joc.3616

Carling, G. T., Mayo, A. L., Tingey, D., and Bruthans, J. (2012). Mechanisms, timing, and rates of arid region mountain front recharge. *J. Hydrol.* 428–429, 15–31. doi:10.1016/j.jhydrol.2011.12.043

Castro, L. M., Gironás, J., and Fernández, B. (2014). Spatial estimation of daily precipitation in regions with complex relief and scarce data using terrain orientation. *J. Hydrol.* 517, 481–492. doi:10.1016/j.jhydrol.2014.05.064

Ceccherini, G., Ameztoy, I., Hernández, C. P. R., and Moreno, C. C. (2015). High-resolution precipitation datasets in South America and West Africa based on satellite-derived rainfall, enhanced vegetation index and digital elevation model. *Rem. Sens.* 7, 6454–6488. doi:10.3390/rs70506454

Chen, F., Liu, Y., Liu, Q., and Li, X. (2014). Spatial downscaling of TRMM 3b43 precipitation considering spatial heterogeneity. *Int. J. Rem. Sens.* 35, 3074–3093. doi:10.1080/01431161.2014.902550

Chen, F. (2007). "The noah land surface model in WRF: a short tutorial," in NCAR, LSM group meeting, Boulder, Colorado, April 17, 2007.

Chen, M., Shi, W., Xie, P., Silva, V. B. S., Kousky, V. E., Higgins, R. W., et al. (2008). Assessing objective techniques for gauge-based analyses of global daily precipitation. *J. Geophys. Res.: Atmos.* 113, D04110. doi:10.1029/2007JD009132

Cifuentes, J. C. G. (2017). Modelación atmosférica de la cuenca del río Baker mediante el modelo WRF, e implicaciones de la temperatura en superficie en un modelo de regresión lineal. PhD thesis. Concepción (Chile): Universidad de Concepción.

Daly, C., Neilson, R. P., and Phillips, D. L. (1994). A statistical-topographic model for mapping climatological precipitation over mountainous terrain. *J. Appl. Meteorol.* 33, 140–158. doi:10.1175/1520-0450(1994)033<0140:astmfm>2.0.co;2

DMC [Dataset] (2015). Análisis de los resultados convenio alta dirección pública, director, dirección meteorológica de Chile, objetivo n3.

Dee, D. P., Uppala, S., Simmons, A., Berrisford, P., Poli, P., Kobayashi, S., et al. (2011). The Era-Interim reanalysis: configuration and performance of the data assimilation system. *Q. J. Roy. Meteorol. Soc.* 137, 553–597. doi:10.1002/qj.828

Delbari, M., Sharifazari, S., and Mohammadi, E. (2019). Modeling daily soil temperature over diverse climate conditions in Iran—a comparison of multiple linear regression and support vector regression techniques. *Theor. Appl. Climatol.* 135, 991–1001. doi:10.1007/s00704-018-2370-3

Devi, U., Shekhar, M., Singh, G., and Dash, S. (2020). Statistical method of forecasting of seasonal precipitation over the northwest Himalayas: North Atlantic oscillation as precursor. *Pure Appl. Geophys.* 177, 3501–3511. doi:10.1007/s00024-019-02409-8

Dibike, Y. B., and Coulibaly, P. (2005). Hydrologic impact of climate change in the Saguenay watershed: comparison of downscaling methods and hydrologic models. *J. hydrol.* 307, 145–163. doi:10.1016/j.jhydrol.2004.10.012

Diez, E., Primo, C., Garcia-Moya, J., Gutiérrez, J., and Orfila, B. (2005). Statistical and dynamical downscaling of precipitation over Spain from demeter seasonal forecasts. *Tellus A Dyn. Meteorol. Oceanogr.* 57, 409–423. doi:10.1111/j.1600-0870.2005.00130.x

Dudhia, J. (1989). Numerical study of convection observed during the winter monsoon experiment using a mesoscale two-dimensional model. *J. Atmos. Sci.* 46, 3077–3107. doi:10.1175/1520-0469(1989)046<3077:nsocod>2.0.co;2

Ebert, E. E., Janowiak, J. E., and Kidd, C. (2007). Comparison of near-real-time precipitation estimates from satellite observations and numerical models. *Bull. Am. Meteorol. Soc.* 88, 47–64. doi:10.1175/bams-88-1-47

Farr, T. G., Rosen, P. A., Caro, E., Crippen, R., Duren, R., Hensley, S., et al. (2007). The shuttle radar topography mission. *Rev. Geophys.* 45, RG2004. doi:10.1029/2005rg000183

Fernández-Ferrero, A., Sáenz, J., Ibarra-Berastegi, G., and Fernández, J. (2009). Evaluation of statistical downscaling in short range precipitation forecasting. *Atmos. Res.* 94, 448–461. doi:10.1016/j.atmosres.2009.07.007

Ferraro, R. R., Smith, E. A., Berg, W., and Huffman, G. J. (1998). A screening methodology for passive microwave precipitation retrieval algorithms. *J. Atmos. Sci.* 55, 1583–1600. doi:10.1175/1520-0469(1998)055<1583:asmfpm>2.0.co;2

Fick, S. E., and Hijmans, R. J. (2017). Worldclim 2: new 1-km spatial resolution climate surfaces for global land areas. *Int. J. Climatol.* 37, 4302–4315. doi:10.1002/joc.5086

Fuenzalida, H. (1982). *Un país de extremos climáticos en Chile: Esencia y evolucion*. Santiago: Inst. de Estud. Reg., Univ. de Chile, 27–35.

Funk, C., Peterson, P., Landsfeld, M., Pedreros, D., Verdin, J., Shukla, S., et al. (2015). The climate hazards infrared precipitation with stations–a new environmental record for monitoring extremes. *Sci Data*. 2, 150066. doi:10.1038/sdata.2015.66

Fustos, I., Abarca-del Río, R., Mardones, M., González, L., and Araya, L. (2020a). Rainfall-induced landslide identification using numerical modelling: a southern Chile case. *J. S. Am. Earth Sci.* 101, 102587. doi:10.1016/j.jsames.2020.102587

Fustos, I., Abarca-del-Rio, R., Moreno-Yaeger, P., and Somos-Valenzuela, M. (2020b). Rainfall-induced landslides forecast using local precipitation and global climate indexes. *Nat. Hazards.* 102, 115–131. doi:10.1007/s11069-020-03913-0

Gallus, J., and William, A. (1999). ETA simulations of three extreme precipitation events: sensitivity to resolution and convective parameterization. *Weather Forecast.* 14, 405–426. doi:10.1175/1520-0434(1999)014<0405:esotep>2.0.co;2

Gallus, J., William, A., and Segal, M. (2000). Sensitivity of forecast rainfall in a Texas convective system to soil moisture and convective parameterization. *Weather Forecast.* 15, 509–525. doi:10.1175/1520-0434(2000)015<0509:sofria>2.0.co;2

Garreaud, R., Falvey, M., and Montecinos, A. (2016). Orographic precipitation in coastal southern Chile: mean distribution, temporal variability, and linear contribution. *J. Hydrometeorol.* 17, 1185–1202. doi:10.1175/jhm-d-15-0170.1

Gent, P. R., Yeager, S. G., Neale, R. B., Levis, S., and Bailey, D. A. (2010). Improvements in a half degree atmosphere/land version of the CCSM. *Clim. Dynam.* 34, 819–833. doi:10.1007/s00382-009-0614-8

González-Rojí, S. J., Wilby, R. L., Sáenz, J., and Ibarra-Berastegi, G. (2019). Harmonized evaluation of daily precipitation downscaled using SDSM and WRF + WRFDA models over the Iberian Peninsula. *Clim. Dynam.* 53, 1413–1433. doi:10.1007/s00382-019-04673-9

Grimm, A. M., Barros, V. R., and Doyle, M. E. (2000). Climate variability in southern South America associated with El Niño and La Niña events. *J. Clim.* 13, 35–58. doi:10.1175/1520-0442(2000)013<0035:cvissa>2.0.co;2

Harris, I., and Jones, P. (2017). *CRU TS4. 00: climatic research unit (CRU) time-series (TS) version 4.00 of high resolution gridded data of month-by-month variation in climate (Jan 1901–Dec 2015)*. Centre for Environmental Data Analysis, 25.

Harris, I., Jones, P. D., Osborn, T. J., and Lister, D. H. (2014). Updated high-resolution grids of monthly climatic observations–the CRU TS3.10 dataset. *Int. J. Climatol.* Oxford Rd, United Kingdom. 34, 623–642. doi:10.1002/joc.3711

Hashmi, M. Z., Shamseldin, A. Y., and Melville, B. W. (2011). Comparison of SDSM and LARS-WG for simulation and downscaling of extreme precipitation events in a watershed. *Stoch. Environ. Res. Risk Assess.* 25, 475–484. doi:10.1007/s00477-010-0416-x

Hay, L., Viger, R., and McCABE, G. (1998). Precipitation interpolation in mountainous regions using multiple linear regression. *IAHS Publ. Series Proc. Reports-Intern. Assoc. Hydrol. Sci.* 248, 33–38

Herold, N., Alexander, L., Donat, M., Contractor, S., and Becker, A. (2016). How much does it rain over land? *Geophys. Res. Lett.* 43, 341–348. doi:10.1002/2015gl066615

Hijmans, R. J., Cameron, S. E., Parra, J. L., Jones, P. G., and Jarvis, A. (2005). Very high resolution interpolated climate surfaces for global land areas. *Int. J. Climatol.* 25, 1965–1978. doi:10.1002/joc.1276

Hong, S.-Y., Dudhia, J., and Chen, S.-H. (2004). A revised approach to ice microphysical processes for the bulk parameterization of clouds and precipitation. *Mon. Weather Rev.* 132, 103–120. doi:10.1175/1520-0493(2004)132<0103:aratim>2.0.co;2

Hong, S.-Y., Noh, Y., and Dudhia, J. (2006). A new vertical diffusion package with an explicit treatment of entrainment processes. *Mon. Weather Rev.* 134, 2318–2341. doi:10.1175/mwr3199.1

Hosseini-Moghari, S.-M., Araghinejad, S., and Ebrahimi, K. (2018). Spatio-temporal evaluation of global gridded precipitation datasets across Iran. *Hydrol. Sci. J.* 63, 1669–1688. doi:10.1080/02626667.2018.1524986

Hu, Z., Zhou, Q., Chen, X., Li, J., Li, Q., Chen, D., et al. (2018). Evaluation of three global gridded precipitation data sets in Central Asia based on rain gauge observations. *Int. J. Climatol.* 38, 3475–3493. doi:10.1002/joc.5510

Huffman, G. J., Bolvin, D. T., Nelkin, E. J., Wolff, D. B., Adler, R. F., Gu, G., et al. (2007). The TRMM multisatellite precipitation analysis (TMPA): quasi-global, multiyear, combined-sensor precipitation estimates at fine scales. *J. Hydrometeorol.* 8, 38–55. doi:10.1175/jhm560.1

Jacquin, A. P., and Soto-Sandoval, J. C. (2013). Interpolation of monthly precipitation amounts in mountainous catchments with sparse precipitation networks. *Chil. J. Agric. Res.* 73, 406–413. doi:10.4067/s0718-58392013000400012

Jankov, I., Gallus, W. A., Jr, Segal, M., Shaw, B., and Koch, S. E. (2005). The impact of different WRF model physical parameterizations and their interactions on warm season MCS rainfall. *Weather Forecast.* 20, 1048–1060. doi:10.1175/waf888.1

Ji, L., Senay, G. B., and Verdin, J. P. (2015). Evaluation of the global land data assimilation system (GLDAS) air temperature data products. *J. Hydrometeorol.* 16, 2463–2480. doi:10.1175/jhm-d-14-0230.1

Joyce, R. J., Janowiak, J. E., Arkin, P. A., and Xie, P. (2004). CMORPH: a method that produces global precipitation estimates from passive microwave and infrared data at high spatial and temporal resolution. *J. Hydrometeorol.* 5, 487–503. doi:10.1175/1525-7541(2004)005<0487:camtpg>2.0.co;2

Jung, T., Gulev, S., Rudeva, I., and Soloviov, V. (2006). Sensitivity of extratropical cyclone characteristics to horizontal resolution in the ECMWF model. *Q. J. R. Meteorol. Soc.* 132, 1839–1857. doi:10.1256/qj.05.212

Kidd, C., Bauer, P., Turk, J., Huffman, G., Joyce, R., Hsu, K.-L., et al. (2012). Intercomparison of high-resolution precipitation products over northwest Europe. *J. Hydrometeorol.* 13, 67–83. doi:10.1175/jhm-d-11-042.1

Kidd, C., Dawkins, E., and Huffman, G. (2013). Comparison of precipitation derived from the ECMWF operational forecast model and satellite precipitation datasets. *J. Hydrometeorol.* 14, 1463–1482. doi:10.1175/jhm-d-12-0182.1

Kidd, C., and Levizzani, V. (2011). Status of satellite precipitation retrievals. *Hydrol. Earth Syst. Sci.* 15, 1109–1116. doi:10.5194/hess-15-1109-2011

Kitchen, M., and Blackall, R. (1992). Representativeness errors in comparisons between radar and gauge measurements of rainfall. *J. Hydrol.* 134, 13–33. doi:10.1016/0022-1694(92)90026-r

Koistinen, J. (1991). "Operational correction of radar rainfall errors due to the vertical reflectivity profile," in 25th international conference on radar meteorology, Paris, France, June 24–28, 1991, American Meteor Society, Vol. 9194.

Kreft, S., Eckstein, D., and Melchior, I. (2016). *Global climate risk index 2017: Who suffers most from extreme weather events? Weather-related loss events in 2015 and 1996 to 2015*. Berlin: Germanwatch Nord-Süd Initiative eV.

Laviola, S., Levizzani, V., Cattani, E., and Kidd, C. (2013). The 183-WSL fast rain rate retrieval algorithm. Part II: validation using ground radar measurements. *Atmos. Res.* 134, 77–86. doi:10.1016/j.atmosres.2013.07.013

Le Quesne, C., Acuña, C., Boninsegna, J. A., Rivera, A., and Barichivich, J. (2009). Long-term glacier variations in the central andes of Argentina and Chile, inferred from historical records and tree-ring reconstructed precipitation. *Palaeogeogr. Palaeoclimatol. Palaeoecol.* 281, 334–344. doi:10.1016/j.palaeo.2008.01.039

Le Roux, R., Katurji, M., Zawar-Reza, P., Quénol, H., and Sturman, A. (2018). Comparison of statistical and dynamical downscaling results from the WRF model. *Environ. Model. Software.* 100, 67–73. doi:10.1016/j.envsoft.2017.11.002

Liu, X., Yang, T., Hsu, K., Liu, C., and Sorooshian, S. (2017). Evaluating the streamflow simulation capability of PERSIANN-CDR daily rainfall products in two river basins on the Tibetan plateau. *Hydrol. Earth Syst. Sci.* 21, 169–181. doi:10.5194/hess-21-169-2017

Marquínez, J., Lastra, J., and García, P. (2003). Estimation models for precipitation in mountainous regions: the use of GIS and multivariate analysis. *J. Hydrol.* 270, 1–11. doi:10.1016/s0022-1694(02)00110-5

Michaelides, S., Levizzani, V., Anagnostou, E., Bauer, P., Kasparis, T., and Lane, J. E. (2009). Precipitation: measurement, remote sensing, climatology and modeling. *Atmos. Res.* 94, 512–533. doi:10.1016/j.atmosres.2009.08.017

Miller, A. (1976). The climate of Chile. *World Survey Climatol.* 12, 113–145. doi:10.1002/qj.49710343520

Mlawer, E. J., Taubman, S. J., Brown, P. D., Iacono, M. J., and Clough, S. A. (1997). Radiative transfer for inhomogeneous atmospheres: RRTM, a validated correlated-k model for the longwave. *J. Geophys. Res. Atmos.* 102, 16663–16682. doi:10.1029/97jd00237

Morales-Salinas, L., Parra-Aravena, J. C., Lang-Tasso, F., Río, R. A.-D., and Jorquera-Fontena, E. (2012). Simple linear algorithm to estimate the space-time variability of precipitable water in the Araucanía region, Chile. *J. Soil Sci. Plant Nutr.* 12, 295–302. doi:10.4067/s0718-95162012000200009

Muñoz, E., Álvarez, C., Billib, M., Arumí, J. L., and Rivera, D. (2011). Comparison of gridded and measured rainfall data for basin-scale hydrological studies. *Chil. J. Agric. Res.* 71, 459–468. doi:10.4067/S0718-58392011000300001

Muñoz, E., Acuña, M., Lucero, J., and Rojas, I. (2018). Correction of precipitation records through inverse modeling in watersheds of south-central Chile. *Water* 10, 1092. doi:10.3390/w10081092

Nastos, P., Kapsomenakis, J., and Philandras, K. (2016). Evaluation of the TRMM 3b43 gridded precipitation estimates over Greece. *Atmos. Res.* 169, 497–514. doi:10.1016/j.atmosres.2015.08.008

Navid, M., and Niloy, N. (2018). Multiple linear regressions for predicting rainfall for Bangladesh. *Communications* 6, 1–4. doi:10.11648/j.com.20180601.11

NOAA (2011). NOAA CPC morphing technique (CMORPH) global precipitation analyses. [Dataset].

Orrego, R., Abarca-Del-Río, R., Ávila, A., and Morales, L. (2016). Enhanced mesoscale climate projections in TAR and AR5 IPCC scenarios: a case study in a Mediterranean climate (Araucanía Region, south central Chile). *SpringerPlus* 5, 1669. doi:10.1186/s40064-016-3157-6

Pahlavan, H., Zahraie, B., Nasseri, M., and Varnousfaderani, A. M. (2018). Improvement of multiple linear regression method for statistical downscaling of monthly precipitation. *Int. J. Environ. Sci. Technol.* 15, 1897–1912. doi:10.1007/s13762-017-1511-z

Parra, J. L., Graham, C. C., and Freile, J. F. (2004). Evaluating alternative data sets for ecological niche models of birds in the Andes. *Ecography* 27, 350–360. doi:10.1111/j.0906-7590.2004.03822.x

Peng, L., Sheffield, J., and Verbist, K. (2016). "Merging station observations with large-scale gridded data to improve hydrological predictions over Chile" in AGU fall meeting abstracts, San francisco, California, USA, December 12–16, 2016.

Pizarro, R., Valdés, R., García-Chevesich, P., Vallejos, C., Sangüesa, C., Morales, C., et al. (2012). Latitudinal analysis of rainfall intensity and mean annual precipitation in Chile. *Chil. J. Agric. Res.* 72, 252–261. doi:10.4067/s0718-58392012000200014

Pope, V., and Stratton, R. (2002). The processes governing horizontal resolution sensitivity in a climate model. *Clim. Dynam.* 19, 211–236. doi:10.1007/s00382-001-0222-8

Quintana, J., and Aceituno, P. (2012). Changes in the rainfall regime along the extratropical west coast of South America (Chile): 30-43°S. *Atmósfera* 25, 1–22. http://www.scielo.org.mx/scielo.php?script=sci_arttext&pid=S0187-62362012000100001

Quintana, J. (2004). *Estudio de los factores que explican la variabilidad de la precipitación en Chile en escalas de tiempo interdecadal*. Magister thesis. Santiago de Chile: Universidad de Chile.

Reyes, M. I. (2013). Análisis y aplicación del método geoestadístico kriging ordinario, en estaciones pluviográficas de la región metropolitana, maule y bíobío. https://journals.ametsoc.org/jhm/article/4/5/826/5173/The-NCEP-NCAR-NCEP-DOE-

and-TRMM-Tropical and https://doi.org/10.1175/1525-7541(2003)004<0826:TNNATT>2.0.CO;2

Roads, J. (2003). The NCEP–NCAR, NCEP–DOE, and TRMM tropical atmosphere hydrologic cycles. *J. Hydrometeorol.* 4, 826–840. doi:10.1175/1525-7541(2003)004<0826:TNNATT>2.0.CO;2. https://journals.ametsoc.org/jhm/article/4/5/826/5173/The-NCEP-NCAR-NCEP-DOE-and-TRMM-Tropical and https://doi.org/10.1175/1525-7541(2003)004<0826:TNNATT>2.0.CO;2

Rojas, Y. G. (2016). Eventos extremos de precipitación diaria en Chile central [Dataset]. https://www.dgeo.udec.cl/investigacion/centro-de-publicaciones/tesis/

Román, N., and Andrés, F. (2010). *Elaboración de la cartografía climática de temperaturas y precipitación mediante redes neuronales artificiales: caso de estudio en la región del libertador bernardo o" higgins*. http://repositorio.uchile.cl/handle/2250/112354

Schamm, K., Ziese, M., Raykova, K., Becker, A., Finger, P., Meyer-Christoffer, A., et al. (2015). GPCC full data daily version 1.0 at 1.0°: daily land-surface precipitation from rain-gauges built on GTS-based and historic data [Dataset] , Boulder CO: Research Data Archive at the National Center for Atmospheric Research, Computational and Information Systems Laboratory, 2016. https://doi.org/10.5065/D6V69GRT

Schmidli, J., Frei, C., and Vidale, P. L. (2006). Downscaling from gcm precipitation: a benchmark for dynamical and statistical downscaling methods. *Int. J. Climatol.* 26, 679–689. doi:10.1002/joc.1287

Semenov, M. A., Brooks, R. J., Barrow, E. M., and Richardson, C. W. (1998). Comparison of the WGEN and LARS-WG stochastic weather generators for diverse climates. *Clim. Res.* 10, 95–107. doi:10.3354/cr010095

Sheffield, J., Goteti, G., and Wood, E. F. (2006). Development of a 50-year high-resolution global dataset of meteorological forcings for land surface modeling. *J. Clim.* 19, 3088–3111. doi:10.1175/jcli3790.1

Sijinaldo, T. J. (2015). Análisis geoestadístico para la confección de mapasde precipitaciones máximas para la Región del Libertador General Bernardo O'Higgins. PhD thesis.. Chile: Universidad Católica de la Santísima Concepción.

Skamarock, W. C., Klemp, J. B., Dudhia, J., Gill, D. O., Barker, D. M., Wang, W., et al. (2008). A description of the advanced research WRF version 3. University Corporation for Atmospheric Research. NCAR technical note-475+ STR

Sorooshian, S., Hsu, K., Braithwaite, D., and Ashouri, H.; NOAA CDR Program (2014). NOAA climate data record (CDR) of precipitation estimation from remotely sensed information using artificial neural networks (PERSIANN-CDR), version 1, revision 1. Available at: https://gis.ncdc.noaa.gov/geoportal/catalog/search/resource/details.

Sun, Q., Miao, C., Duan, Q., Ashouri, H., Sorooshian, S., and Hsu, K.-L. (2018). A review of global precipitation data sets: data sources, estimation, and intercomparisons. *Rev. Geophys.* 56, 79–107. doi:10.1002/2017RG000574

Sun, Q., Miao, C., Duan, Q., Kong, D., Ye, A., Di, Z., et al. (2014). Would the 'real' observed dataset stand up? A critical examination of eight observed gridded climate datasets for China. *Environ. Res. Lett.* 9, 015001. doi:10.1088/1748-9326/9/1/015001

Swain, S., Patel, P., and Nandi, S. (2017). "A multiple linear regression model for precipitation forecasting over Cuttack district, Odisha, India," in 2017 2nd international conference for convergence in technology (I2CT) (New York, NY: IEEE, Mumbai, India), 355–357. doi:10.1109/I2CT.2017.8226150

Tapiador, F. J., Turk, F. J., Petersen, W., Hou, A. Y., García-Ortega, E., Machado, L. A., et al. (2012). Global precipitation measurement: methods, datasets and applications. *Atmos. Res.* 104–105, 70–97. doi:10.1016/j.atmosres.2011.10.021

Taylor, K. E. (2001). Summarizing multiple aspects of model performance in a single diagram. *J. Geophys. Res. Atmos.* 106, 7183–7192. doi:10.1029/2000jd900719

Timmermans, B., Wehner, M., Cooley, D., O'Brien, T., and Krishnan, H. (2019). An evaluation of the consistency of extremes in gridded precipitation data sets. *Clim. Dynam.* 52, 6651–6670. doi:10.1007/s00382-018-4537-0

Valdés, R., Valdes, J. B., Diaz, H. F., and Pizarro-Tapia, R. (2016a). Analysis of spatio-temporal changes in annual and seasonal precipitation variability in South America-Chile and related ocean–atmosphere circulation patterns. *Int. J. Climatol.* 36, 2979–3001. doi:10.1002/joc.4532

Valdés, R., Pizarro, R., Valdes, J. B., Carrasco, J. F., Garcia-Chevesich, P., and Olivares, C. (2016b). Spatio-temporal trends of precipitation, its aggressiveness and concentration, along the pacific coast of South America (36–49 s). *Hydrol. Sci. J.* 61, 2110–2132. doi:10.1080/02626667.2015.1085989

Valdés-Pineda, R., Pizarro, R., García-Chevesich, P., Valdés, J. B., Olivares, C., Vera, M., et al. (2014). Water governance in Chile: availability, management and climate change. *J. Hydrol.* 519, 2538–2567. doi:10.1016/j.jhydrol.2014.04.016

Viale, M., and Garreaud, R. (2015). Orographic effects of the subtropical and extratropical Andes on upwind precipitating clouds. *J. Geophys. Res. Atmos.* 120, 4962–4974. doi:10.1002/2014JD023014. 2014JD023014

Wang, W., and Seaman, N. L. (1997). A comparison study of convective parameterization schemes in a mesoscale model. *Mon. Weather Rev.* 125, 252–278. doi:10.1175/1520-0493(1997)125<0252:ACSOCP>2.0.CO;2

Ward, E., Buytaert, W., Peaver, L., and Wheater, H. (2011). Evaluation of precipitation products over complex mountainous terrain: a water resources perspective. *Adv. Water Resour.* 34, 1222–1231. doi:10.1016/j.advwatres.2011.05.007

Waylen, P., and Poveda, G. (2002). El niño–southern oscillation and aspects of western South American hydro-climatology. *Hydrol. Process.* 16, 1247–1260. doi:10.1002/hyp.1060

Widmann, M., Bretherton, C. S., and Salathé, E. P., Jr (2003). Statistical precipitation downscaling over the northwestern United States using numerically simulated precipitation as a predictor. *J. Clim.* 16, 799–816. doi:10.1175/1520-0442(2003)016<0799:SPDOTN>2.0.CO;2

Yáñez-Morroni, G., Gironás, J., Caneo, M., Delgado, R., and Garreaud, R. (2018). Using the weather research and forecasting (WRF) model for precipitation forecasting in an Andean region with complex topography. *Atmosphere* 9, 304. doi:10.3390/atmos9080304

Yeh, N.-C., Chuang, Y.-C., Peng, H.-S., and Hsu, K.-L. (2020). Bias adjustment of satellite precipitation estimation using ground-based observation: mei-yu front case studies in Taiwan. *Asia-Pacific J. Atmos. Sci.* 56, 485–492. doi:10.1007/s13143-019-00152-7

Zambrano, F., Wardlow, B., Tadesse, T., Lillo-Saavedra, M., and Lagos, O. (2017). Evaluating satellite-derived long-term historical precipitation datasets for drought monitoring in Chile. *Atmos. Res.* 186, 26–42. doi:10.1016/j.atmosres.2016.11.006

Zambrano, M., Nauditt, A., Birkel, C., Verbist, K., and Ribbe, L. (2017). Temporal and spatial evaluation of satellite-based rainfall estimates across the complex topographical and climatic gradients of Chile. *Hydrol. Earth Syst. Sci.* 21, 1295–1320. doi:10.5194/hess-21-1295-2017

Zambrano, M. G. (2011). Balance Hídrico del Lago General Carrera y su variabilidad climática asociada. PhD thesis. Chile: Universidad de Concepción.

Zhang, D., and Anthes, R. A. (1982). A high-resolution model of the planetary boundary layer—sensitivity tests and comparisons with sesame-79 data. *J. Appl. Meteorol.* 21, 1594–1609. doi:10.1175/1520-0450(1982)021<1594:AHRMOT>2.0.CO;2

Zhang, Y., Moges, S., and Block, P. (2016). Optimal cluster analysis for objective regionalization of seasonal precipitation in regions of high spatial–temporal variability: application to western Ethiopia. *J. Clim.* 29, 3697–3717. doi:10.1175/JCLI-D-15-0582.1

Zhang, Y., Sun, A., Sun, H., Gui, D., Xue, J., Liao, W., et al. (2019). Error adjustment of TMPA satellite precipitation estimates and assessment of their hydrological utility in the middle and upper Yangtze River basin, China. *Atmos. Res.* 216, 52–64. doi:10.1016/j.atmosres.2018.09.021

Conflict of Interest: The authors declare that the research was conducted in the absence of any commercial or financial relationships that could be construed as a potential conflict of interest.

Copyright © 2020 Alvial-Vasquez, Abarca-del-Río and Ávila B. This is an open-access article distributed under the terms of the Creative Commons Attribution License (CC BY). The use, distribution or reproduction in other forums is permitted, provided the original author(s) and the copyright owner(s) are credited and that the original publication in this journal is cited, in accordance with accepted academic practice. No use, distribution or reproduction is permitted which does not comply with these terms.

frontiers in Earth Science

ORIGINAL RESEARCH
published: 19 January 2021
doi: 10.3389/feart.2020.539905

Development and Validation of a Model to Evaluate the Water Resources of a Natural Protected Area as a Provider of Ecosystem Services in a Mountain Basin in Southern Chile

Sandra Fernández-Alberti[1]*, *Rodrigo Abarca-del-Río*[2], *Cristian Bornhardt*[1,3] and *Andres Ávila*[1,4]

[1]PhD Engineering Program, Universidad de La Frontera, Temuco, Chile, [2]Department of Geophysics, Universidad de Concepción, Concepción, Chile, [3]Department of Chemical Engineering, Universidad de La Frontera, Temuco, Chile, [4]Modeling and Scientific Computing Excellence Center, Universidad de La Frontera, Temuco, Chile

OPEN ACCESS

Edited by:
Nils Moosdorf,
Leibniz Centre for Tropical Marine Research (LG), Germany

Reviewed by:
David R. Purkey,
Stockholm Environment Institute (Latin America Center), Colombia
Sebastian Vicuna,
Pontificia Universidad Católica de Chile, Chile

***Correspondence:**
Sandra Fernández-Alberti
sandra.fernandez@ufrontera.cl

Specialty section:
This article was submitted to Hydrosphere, a section of the journal Frontiers in Earth Science

Received: 02 March 2020
Accepted: 23 November 2020
Published: 19 January 2021

Citation:
Fernández-Alberti S, Abarca-del-Río R, Bornhardt C and Ávila A (2021) Development and Validation of a Model to Evaluate the Water Resources of a Natural Protected Area as a Provider of Ecosystem Services in a Mountain Basin in Southern Chile. Front. Earth Sci. 8:539905. doi: 10.3389/feart.2020.539905

The objective of this work is to validate a model to characterize and evaluate the water resources (supply and downstream demands) of the hydrological basins associated with the Conguillío National Park, located in the Andes Mountains in central-southern Chile (38°14'–38°54'S). This area is part of the Chilean biodiversity hotspot, of the first geopark in Chile, and constitutes the core of the Araucaria biosphere reserve, which provides multiple ecosystem services. To describe the behavior of the water resources in the four main river sub-basins originating in the park, the Water Evaluation and Planning System (WEAP) software was used, which was calibrated and validated with local hydrological data from 2000 to 2015. The WEAP System allows to quantify parameters involved in the hydrological cycle and water consumption of the different user sectors, and their interrelationships, to establish the water balance of the basins. Water is supplied by rain and snow, which occurs from June to December upstream in the Andes, and feeds the rivers Cautín, Allipén, Quepe and Lonquimay, which maximum flows occur between June and September, and minimum flows between January and April. The evolution of the water demand during the year was determined for each sub-basin for the following user sectors: human consumption, agriculture, livestock, industry, electricity production, aquaculture and other uses. As expected, the main water consuming sector is agriculture, with an average of 79.4 Mm^3/yr. Considering that mountain ecosystems are areas of high productivity value, but are very fragile and vulnerable to anthropic and climatic effects, the use of the obtained data and the calibrated/validated model describing and characterizing these resources, will allow future studies under different socio-economic and climate change scenarios, to assess the importance of mountain basin ecosystem services, providing an example for equivalent studies throughout South America.

Keywords: mountain basin, natural protected areas, ecosystem services, water evaluation and planning, water resources, water balance

INTRODUCTION

Freshwater resources are essential both for society (human consumption, agriculture, and other uses) and for ecosystems. Sustainable water management promotes their development and protection, as socio-economic benefits are provided in a fair balance with environmental sustainability (Clark et al., 2004; Liu et al., 2008; Maliehe and Mulungu, 2017). Water provides various Ecosystem Services (from now on ES), like drinking water supply, recreation, and dilution of pollution discharges (Brauman et al., 2007). The future capacity of natural systems to provide these services will depend on water availability and quality (Sample et al., 2016). "Ecosystem services" are defined as the benefits that people obtain from ecosystems (MEA, 2005), and the direct and indirect contributions that ecosystems make to human well-being. Several studies (Yang et al., 2015; Fan et al., 2016; Liu et al., 2017; Momblanch et al., 2017) indicate that mainly human activity is responsible for the decline in ES. Changes in land use/land cover affect the hydrological cycle, e.g., infiltration (Nelson et al., 2009), evapotranspiration, and groundwater recharge (Fan et al., 2016). There exist few watershed studies in protected areas that analyze the effects of land-use change and climate change (Fan et al., 2016).

Given its biogeographical condition, Chile is endowed with a great and unique diversity (Valdés-Pineda et al., 2014) of terrestrial, marine, coastal, glacial, river, lake, wetland and island ecosystems, hosting nearly 30 thousand endemic species which transform large areas of the territory in dedicated natural laboratories (Rubilar 1994; MMA 2014; MMA, 2015). The natural protected areas have been very significant and effective for ecosystems conservation, such as the different species present (Jorquera-Jaramillo et al., 2012). Each ecosystem, based on its functioning and interactions, provides a series of ecosystem services, ranging from the regulation of the hydrological cycle to the provision of direct goods and services for society (MMA, 2015). A study (Figueroa, 2009; Figueroa, 2010) estimated a value of US$ 1,368 million per year of the ecosystem services provided by the natural protected areas in Chile, and noted that these areas contribute to the country with 0.5% of its GDP.

Different studies point out the importance of mountains as providers of a large number of ES of fundamental importance for life (Bauhus et al., 2010; Decocq et al., 2016; Mori et al., 2017). Studies by Gao et al. (2020) indicate that mountains contribute greatly to the planet's terrestrial biodiversity, hosting 85% of the world's wildlife within 25% of the earth's surface (Rahbek et al., 2019a; Rahbek et al., 2019b). The rich biodiversity of mountains is due to the complex topography, which creates acute vertical heterogeneity in climate, soil and vegetation (Chaplin, 2005). Canedoli et al. (2020) point out that mountain ecosystems are fragile and vulnerable and face serious threats due to climate change, changes in land use or unsustainable exploitation of resources, as well as political decisions and socio-economic pressures (see also Kurz et al., 2008; Huber et al., 2013).

In this context, Protected Areas are very important for Chile, which protect the existing natural heritage, representing a unique biodiversity in the world CONAF, Corporación Nacional Forestal (2012). The distribution from north to south, the altitudinal gradient and the extension of the coast provide the country with a great variety of habitats, being one of the most threatened, according to the global index 200 of WWF and the (World Bank 2011, WWAP, 2014). It should be noted that Chile's economy is heavily dependent on the exploitation and export of natural resources, including resources from sectors that affect or are affected by the condition of biodiversity and the provision of ecosystem services, such as the mining, agricultural, fisheries and forestry sectors (MMA, 2016). In this sense, Chile has the challenge of being able to develop these industries without undermining the biodiversity that sustains them, both because of the wealth of biological diversity that it possesses, and because of its relevance to the economy itself.

Biodiversity, water resources, built infrastructure and economic sectors may be adversely affected by the global climate change within this century (Santibañez et al., 2013). Chile, including its mountain ecosystems, is highly vulnerable to climate change, fulfilling seven of the nine characteristics defined by the UNFCCC (Universidad de Chile, 2007; Universidad de Chile, 2012; CEPAL, 2012). For example, in the central-south zone of the country, in the last 10 years a statistically significant decrease in rainfall has been observed (Schulz et al., 2011; Quintana and Aceituno, 2012; Boisier et al., 2016).

On the other hand, in Chile there is an evident lack of water resources management and there exist only few planning skills to face climate variability and uncertainty. It is urgent to implement strategies for its use in many regions, considering also the country's most important watersheds, which are located within protected areas and at high altitudes. Besides, the allocation of water resources is limited for agricultural and industrial use, and human consumption.

Chile's 1981 Water Code defines water as a "national good of public use," but at the same time as an "economic good." It authorizes the privatization of water through the concession of free use rights in perpetuity (it does not set limits to the concession of use rights). It establishes a system of water redistribution through transactions between private parties, thus creating a Water Market, and favors the concentration of ownership of this resource. In this context, several investigations have reported that in Chile there is no adequate water management, and the water use rights are granted more or less in an arbitrary manner, generating that there is no equity in its distribution (Larraín et al., 2010; Larraín, 2012).

Historically, water management has been the responsibility of the Ministry of Public Works (MOP, 2016), with its ministerial departments (General Direction), the Direction of Hydraulic Works, the Direction of Irrigation, the Direction of Planning, and the Department of River Defense, among others. The Ministry of Economy, Development and Reconstruction, through the National Irrigation Commission (CNR), also has a relationship with water. Thus, water resources involve a set of institutions and government agencies that are responsible for water or regulate the actions of users within a basin, making this finally such an intricate and complicated subject, that at the end it is ineffective. As an example we cite the conservation of river

flows: the only existing measure is the ecological flow, established with the reform of the Water Code in 2005; but this is very limited and insufficient to preserve the diversity and integrity of the watersheds.

One of the major challenges at national level is the systematization of data and monitoring of water quality and biodiversity in these ecosystems, where the main threats are pressure on water resources. At the global level, this pressure is also present and is occurring in the water-energy-food relationship. In this context, several studies (Biggs et al., 2015; Zhang et al., 2016; Tidwell and Moreland, 2016) pointed out the need to establish a balance between the supply of natural resources and human demand on the environment to promote sustainability.

Insufficient knowledge of the hydrology of a basin can lead to deficiencies in water supply and a failure to meet the water demands of users. It is necessary to know the evolution of the water balance, especially during dry seasons, and to develop allocation and management strategies. Maliehe and Mulungu (2017) reported that basin-scale assessments provide essential information for water resources management, in particular predictions of water supply and demand. There exists high uncertainty in water resource management when it comes to describing future conditions (Forni et al., 2016a; Medellín-Azuara et al., 2016). For these purposes, simulation models are indispensable, which can consider the interaction of different variables in a basin, representing their spatio-temporal dependencies and the effects of climate change and human activities on environmental systems (Bhave et al., 2014). Several studies have been performed to capture various aspects of water resources planning in several parts of the world, using hydrological models (Condom et al., 2011; Bhave et al., 2014; Forni et al., 2016a; Medellín-Azuara et al., 2016).

The Water Evaluation and Planning (WEAP) tool is an integrated model for water resource planning (Yates et al., 2005a; Purkey et al., 2008). Several articles (Yates et al., 2005, Yates et al., 2009) describe how watersheds are integrated into WEAP. A set of climate forcing data (precipitation, temperature, relative humidity, and wind speed) is uniformly applied across each catchment, which is fractionally divided into land use/land cover classes (Yates et al., 2005b). Thus, the WEAP model is a useful tool for advising on water resources development and management alternatives (Forni et al., 2016a; Medellín-Azuara et al., 2016; Maliehe and Mulungu, 2017). It is widely used to support water resources planning, providing an analytical and management framework for decision-makers in an open planning process (Yates et al., 2005a; Forni et al., 2016b; Galaitsi et al., 2016), particularly in Africa (e.g., Mulungu and Taipe, 2012; Droogers et al., 2014), because it can be applied at the basin and sub-basin levels (Bhave et al., 2014; Maliehe and Mulungu, 2017). Also, it has been used at the basin level in Chile (Vicuña et al., 2011) and in California (Yates et al., 2007; Young et al., 2009; Forni et al., 2016a; Medellín-Azuara et al., 2016).

This work focuses on the water network of a natural protected area located in the pre-Andean mountain range of the Araucanía Region. Here is located the Conguillío National Park, formed by the mountain range at a variable height between 750 and 3,125 masl, where the Sierra Nevada and the Llaima Volcano stand out, being one of the most active and voluminous volcanoes of the Southern Andes, with 29 km^2 of glaciers (Naranjo and Moreno, 2005). This park has two UNESCO nominations, is the core zone of the Araucaria Biosphere Reserve, and is the first Geopark in the country. It is considered to be of great ecosystemic importance, given the diverse environments typical of this mountain zone, where forests, wetlands, slag heaps, and high peaks are found. Besides, this park is one of the most visited in the country, due to its excellent landscape value. In this context, the magazine National Geographic (2018) chose this park in the fourth place among the ten most beautiful forests on the planet.

The administration and management of Chile's Natural Protected Areas is responsibility of the National Forestry Corporation (CONAF), which is an entity belonging to the Ministry of Agriculture. Its main objective is to protect the preservation of nature and environmental heritage. In this sense, CONAF, Corporación Nacional Forestal (2009) carried out a study to evaluate a management plan for this natural protected area and raised a baseline, which states that within all studies to be conducted (for example studies of flora and fauna, geomorphology, landscape, tourism, archaeological sites, and others), it is necessary to conduct a hydrological study to determine the productive capacity of this area, and the supply and demand of water for the population benefiting from the resource in the sub-basins of the Allipén, Lonquimay, Quepe and Cautín rivers, respectively. It is worth mentioning the importance of this park as a source of water production, since it feeds several communes, providing at the same time countless opportunities for product development. However, they point out the importance of complementing the study with climatological and water quality information that best approximates the reality of the sub-basins. Until now, this study had not been carried out, and this is one of the reasons for our work.

Furthermore, this study is part of a work that includes having a validated model to support the sustainable management of wild protected areas. It will allow for the implementation of proper decision-making strategies in different scenarios, with a focus on sustainable development. Noteworthy, it may allow us to propose and evaluate measures to ensure the ecosystem services sustainability provided by the Conguillío National Park, such as water and landscape resources. In this context, with this study we want to provide a tool that integrates hydrology with the administration and operation of water resource systems, which can be used in micro-basins as well as in big basins.

Thus, the objective of this study is to stablish the actual water balance of the water requirements within the sub-basins fed by the Conguillío National Park.

This requires the following stages

(1) Characterization of the basins, considering the meteorological data required by the model (rainfall, temperature, wind speed, relative humidity, river flows and land cover of the study area) (see *Study Area and Local Data*).

(2) Calibration and validation of the WEAP model for the period 2000 to 2015 (see *Water Evaluation and Planning Calibration and Validation*).
(3) Determination of water requirements at different demand sites and catchment descriptions (see *Demand sites and Catchment Description*).
(4) Estimation of the water balance of the study area (see *Water Balance Estimation Methodology*).

METHODS

Study Area and Local Data

The study area (Conguillío National Park) is located in the Araucanía Region of south-central Chile (38°14'-38°49'S) (**Figure 1A**) (BCN, 2019). It is characterized by its mountainous landscapes, with the presence of active volcanoes in the pre-Andean mountain range, which extends from low valleys to highlands with steep slopes, across an elevation range from 450 to > 3,000 masl (BCN, 2019), with a variety of climatic conditions. The natural forests are composed of *Nothofagus sp.* (CONAF, 2011), as well as *Araucaria araucana*, a vulnerable endemic species recognized as a natural monument in Chile, recognized by UNESCO with the nomination of Araucaria Biosphere Reserve (Moreira-Muñoz and Troncoso, 2014). It also plays an essential role for Mapuche indigenous people (Miranda et al., 2015).

Rainfall in Chile tends to increase with latitude and altitude. Thus, in south central Chile, annual rainfall increases southward from around 100 mm at 30°S to nearly 2000 mm at 40°S. The annual precipitation increases with elevation, up to a maximum of 3,000 mm annually above 1,200 masl in the Andes (Luebert and Pliscoff, 2006). The Andes range isolates this region from the influence of continental air masses (Valdés-Pineda et al., 2014). Thus, south-central Chile has an annual rainfall cycle with a peak in the winter season and lower values in summer, gradually increasing towards the south. In the region under study, climate is characterized by moderate, cold rain with Mediterranean influence under a prominent role by the Pacific Anticyclone, which is the main protection against torrential rainfall in Chile (Garreaud et al., 2009; Orrego et al., 2016), characterized by a significant decrease in rainfall during the summer months, when the highest temperatures are present (Armesto et al., 2008). Rainfall is mainly concentrated in the month's May to September, and climate variability is influenced by the El Niño Southern Oscillation (ENSO) phenomenon (Falvey and Garreaud, 2009; Demaria et al., 2013; Valdés-Pineda et al., 2014; Orrego et al., 2016). ENSO events in central-southern Chile (38°–41°S) are associated with higher than average spring rainfall (35°–38°S) and lower than average summer rainfall (Garreaud et al., 2009; Valdés-Pineda et al., 2014; Orrego et al., 2016). The average annual temperature in the study area is 10.2°C, with a mean maximum of 15.8°C in January and February, and a mean minimum of 4.7°C in June and July (DGA, 2016). An example of this climate is that recorded by the Lonquimay meteorological station (38°45'50''S - 71°36'19''W) located at 900 masl in the Andean range, with a mean annual temperature of 8.4°C and annual precipitation of 1,850 mm.

On the other hand, studies by Rubio-Alvarez and McPhee (2010) on the patterns of spatial and temporal variability of river flows in south-central Chile for the period 1952–2003 reported the time series of annual and seasonal flows of 44 rivers in southern Chile, covering the ecoregion between 34°S and 45°S. They found a significant correlation with climatic indexes at different spatial and temporal scales, with El Niño–Southern Oscillation (ENSO) influence being stronger at the northern subregion, and notably, the Antarctic Oscillation (AAO) and the Pacific Decadal Oscillation (PDO), showing strong correlation with summer flows in the southern subregion. Also, they found significant decreasing trends affecting a region between 37.5°S and 40°S. These were consistent with decreasing trends observed in precipitation in the area, and also with a decreasing trend observed in the Southern Oscillation Index (SOI). Also, the drought affecting central Chile is evident, as indicated by studies conducted by Boisier et al. (2016) on the anthropogenic and natural contributions to the decrease in rainfall in the Southeast Pacific and the mega-drought affecting Central Chile.

Chile's natural heritage is protected by the National System of State Natural Protected Areas (SNASPE). It currently includes 105 units, with 41 national parks, covering an area of approximately 18.6 million hectares (21.3% of Chile's continental territory). It should be noted that the study area (Parque Nacional Conguillio) has two UNESCO designations, is part of the Araucaria Biosphere Reserve, and also is part of the first Geopark in Chile around the Llaima volcano. It is worth mentioning that Chile possesses ten (10) Biosphere Reserves (UNESCO, 1995). Three of them are located in the pre-mountain range of the Andes Mountains, as is our study zone, with heights above 3,000 m above sea level and the presence of permanent snow in winter above 1,100 masl. It is also part of a world biodiversity hotspot, defined as regions where a large amount of species biodiversity is concentrated, and where the original habitat has been strongly impacted and threatened by human actions. Only thirty-five hotspots that meet these characteristics have been defined worldwide (Mittermeier et al., 2004). The "Chilean winter rainfall-Valdivian forests" hotspot is located mainly in Chile. It extends from the Pacific coast to the Andean peaks between 25°S and 47°S (Arroyo et al., 2004).

There are several State-Protected Natural Areas (SPA) in the region; one of these is the Conguillío National Park (CNP) (38°30'S; 71°30'W), with an area of 60,833 ha, where we started our study (**Figure 1A**). The CNP has four defined natural environments: mountain, volcanic slag, forests, and water bodies (rivers, streams, lagoons, lakes, and wetlands). It is characterized by its water network composed of streams, rivers, lagoons, and large lakes, fed by snow-melt, rain, and groundwater. It has two UNESCO distinctions: the Araucaria Biosphere Reserve, and the Kutralkura Geopark, which presents interesting geological characteristics. The landscape and ecological value of the park is dominated by Sierra Nevada

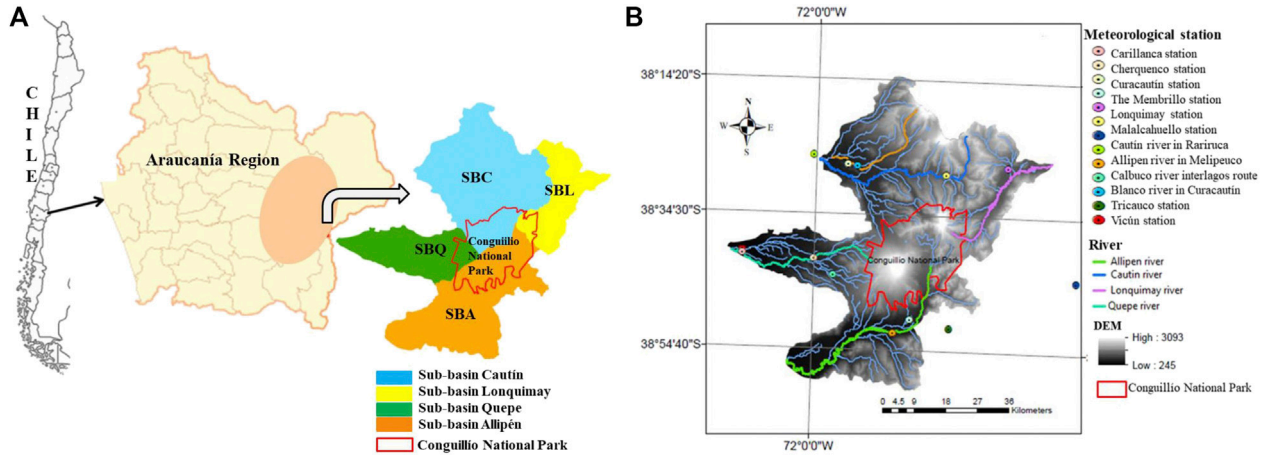


FIGURE 1 | (A) Map of Chile, Araucanía Region, sub-basins of the study area, and Conguillío National Park. **(B)** Geographical data of the study area, including location of meteorological stations and the rivers Cautín, Quepe, Lonquimay and Allipén.

and Llaima volcano CONAF, Corporación Nacional Forestal (2012). The presence of the active Llaima volcano, which occupies a large part of the park, has formed the geomorphological characteristics of the park, rising from 700 masl at its base to the crater rim at 3,125 masl. Historically, it is one of the most active volcanoes in South America, with its last recorded eruption in 2008–2009 (Bathke et al., 2011) and one of the largest in the Southern Andes, with more than 29 km^2 of glaciers (Naranjo and Moreno, 2005).

Basin Characterization

The Araucanía Region contains two large basins: the Imperial River Basin and the Toltén River Basin. Additionally, it includes a small part of the Bío-Bío River Basin. The main tributaries are the following: of the Imperial river: Cautín, Blanco, Quepe, Calbuco and Vilcún; of the Toltén river: Truful-Truful and Allipén; and of the Bío Bío river: Lonquimay. The study zone covers an area of 3,365 km^2 (IDE, 2017; Universidad de Chile, 2017).

For this study, the basins system was grouped in four sub-basins, with the following notation (associated to the main river of each of them) (see **Figure 1A**):

- **SBA:** Sub-basin of the Allipén river
- **SBQ:** Sub-basin of the Quepe river
- **SBC:** Sub-basin of the Cautín river
- **SBL:** Sub-basin of the Lonquimay river

These rivers were selected despite the limitations of data availability in each case. **Figure 1B** shows the Digital Elevation Model (DEM) of the study area and the meteorological stations of the four sub-basins selected for this study.

Land Uses

Table 1 shows the distribution of land uses, representing the dominant land cover categories present in each sub-basin, each component in km^2, which were geo-referenced from the National Native Forests Inventory CONAF, Corporación Nacional Forestal (2012). Bare lands include rocky areas and dunes. Forest plantations are exotic species for timber and paper production, such as *Pinus radiata* and *Eucalyptus spp*. The native forest is represented mainly by the genus *Nothofagus,* mixed with *Araucaria araucana*, and old-growth native forest (Miranda et al., 2015). Water bodies include rivers, lakes, and estuaries identifiable to the resolution of the images. Farmland and forests have dominated the composition of the landscape in the study area. Currently, pine and eucalyptus plantations have overtaken the area covered by native forests (Miranda et al., 2015). Cover change is spatiotemporally heterogeneous, as significant relationships are found between the spatial distribution of land cover types and different biophysical variables (Schulz et al., 2011; Nahuelhual et al., 2012). These changes in the landscape of south-central Chile are related to the expansion of agriculture and the introduction of exotic tree plantations (Aguayo et al., 2009; Little et al., 2009; Echeverría et al., 2012). The most abundant land cover is the native forest, which predominates in all the catchments of the study area, and crops in SBQ, SBC, and SBA. Next, shrublands are important for SBL and SBC; this class includes both arborescent shrublands of *Nothofagus* species or other native woody species, as well as shrublands formed by exotic species. Forest plantations are also important in SBA, SBC, and SBQ. Finally, SBA has the most extensive grassland coverage. SBA and SBC are located at higher altitudes. They include large areas of volcanic slag from Llaima Volcano, covered with snow during the year. **Table 1** shows that the SBC and SBA sub-basins have the most significant cover by native forest, scrublands, snow, and water bodies, suggesting that they also have a greater volume of water resources.

Processing of Climatic Data

Some of the meteorological stations run by DGA (General Directorate of Waters) and AGROMET (National Agroclimatic Network of Chile) have only operated for a few years, while other records cover different periods. There are significant gaps, extending from a few days to several years.

TABLE 1 | Land uses in the sub-basins Cautín river (SBC), Lonquimay river (SBL), Allipén river (SBA) and Quepe river (SBQ).

Basin	SBC	SBL	SBA	SBQ	Σkm^2
Surface (km^2)	1,291.4	464	1,052.7	556.5	3,364.6
Native forest	698.5	281.6	475.5	221	1,676.6
Agricultural crops	188.1	2.3	80.5	190.1	461
Bare land	2.1	5.1	3.3	0.8	11.3
Shrublands	143.3	76.8	79.1	41.5	340.7
Forest plantations	32.2	0	92.1	34.9	159.2
Grassland	59.5	13.9	122.2	24.6	220.2
Volcanic slag	104.5	39.1	135.2	31.1	309.9
Urban zone	4.4	0.1	3.1	4.2	11.8
Snow	44	15.7	38.5	5.3	103.5
Water bodies	9.8	1.1	5.7	1.8	18.4
Wetland	6.4	28.7	17.2	1.3	53.6

TABLE 2 | Meteorological Stations and Streamflow gauging stations (DGA Station) and meteorological stations (AGROMET Station).

Sub-Basin	DGA station	Latitude	Longitude	Elevation (m)
	Stations gauges			
SBA	Allipén river in Melipeuco	38°51′5″S	71°44′0″W	450
SBQ	Quepe river in Vilcún	38°41′0″S	72°13′6″W	292
SBL	Lonquimay river in front of Bio Bio River	38°26′0″S	71°14′0″W	0
SBC	Cautín river in Rari-ruca Station (pp, T°)	38°25′4″S	72°00′3″W	425
SBC	Malalcahuello	38°28′2″S	71°34′4″W	950
SBC	Malalcahuello	38°28′2″S	71°34′4″W	950
SBC	Curacautín	38°27′2″S	71°53′5″W	535
SBQ	Calbuco river Interlake Route	38°43′4″S	71°56′1″W	640
SBQ	Cherquenco	38°41′1″S	72°00′9″W	500
————[a]	Tricauco AGROMET station Station (T°, RH, Wd)	38°51′1″S	71°33′9″W	520
SBQ	Carillanca	38°41′3″S	72°25′0″W	200
SBA	The Membrillo	38°43′5″S	71°08′2″W	1084
————[a]	Marimenuco	38°50′0″S	71°40′5″W	527

Dsch, discharge; Pp, Precipitatios; T°, Temperature; RH, Relative Humidity; Wd, Wind.
[a]*Station outside the study area.*

After a preliminary review of these data, a small number were evaluated for data quality, consistency, and extension (Iroumé and Palacios, 2013). Nine precipitation stations were finally selected (see **Table 2**), covering the four basins (DGA, 2016; Orrego et al., 2016). There are few stations with temperature records (**Table 2**). We included other AGROMET stations close to the study zone.

The temperature-elevation gradient was estimated considering the average temperature values for stations located at different elevations, based on two index stations for the basin, as suggested by Vicuña et al. (2011). Where there are no station data to estimate the temperature gradient, we used the values generally used in Chile: −0.5°C/m when there is precipitation, and −0.65°C/m when there is no precipitation (Cortes, 2010; DGA, 2017).

The entire watershed contains four (4) stream gauges with records from at least 2000 to 2015. **Table 2** shows the location of these gauges (see also **Figure 1B**). These are the Rari-Ruca gauging station for Cautín river, the Melipeuco gauging station for Allipén river, the Vilcún gauging station for Quepe river, and the Lonquimay river gauging station just arriving the Bío-Bío river.

Wind speed and relative humidity (RH) data were obtained from two AGROMET stations. The average monthly wind speed at that location was 5.1 m/s, and the relative humidity (RH) 81%. WEAP requires this information in each hydrological unit or sub-basin (catchment).

Water Evaluation and Planning Model

Basic Description of the Water Evaluation and Planning Model

The Water Evaluation and Planning (WEAP) model was developed initially by The Stockholm Environment Institute at Boston, United States (Van Loon and Droogers, 2006). It presents an integrated system of water resources planning by connecting hydrological processes and their operations in a single analytical platform (Forni et al., 2016a; Medellín-Azuara et al., 2016). It also uses a scenario-based method to determine water supply and demand and their priorities for current and future periods. Within these features, WEAP software can simulate catchment hydrology as surface runoff, evaporation and infiltration, and evaluate water availability (Sieber et al., 2005).

The model is based on a one-dimensional soil water accounting scheme with two storage tanks, which uses empirical quasi-physical functions (Yates et al., 2005) that describe evapotranspiration (potential evapotranspiration is derived using a Penman-Monteith formulation (Maliehe and Mulungu, 2017), surface runoff or interflow, and deep percolation (Vicuña et al., 2011).

The model input information includes the following parameters: precipitation, temperature, relative humidity, wind speed, melting point, freezing point, and land cover. These are required to estimate the water balance components of evapotranspiration, infiltration, surface runoff, and baseflow, providing the framework for the water models system operations (Forni et al., 2016a; Medellín-Azuara et al., 2016).

WEAP can integrate the water supplies generated through hydrological processes from a water management model (Yates et al., 2005; Yates et al., 2007; CCG, 2009). Mass balance equations are the basis of WEAP's monthly water accounting, considering total inflows, total outflows, and storage in reservoirs and aquifers (see **Eq. 1** and **Figure 2**).

$$\sum \text{Inflow} - \sum \text{Outflow} - \sum \text{AdditionToStorage} = 0 \quad (1)$$

The term *AdditionToStorage* only applies to reservoirs and aquifers. *AdditionToStorage* is positive for an increase in storage and negative for a decrease in storage. Outflow includes consumption and losses (http://www.weap21.org/). Every node and link in WEAP has a mass balance equation, and some have additional equations that constrain their flows. Each mass balance equation becomes a constraint in the linear program (LP). Every flow from one point to another is represented by a variable in the LP (http://www.weap21.org/). For example, assume Demand Site

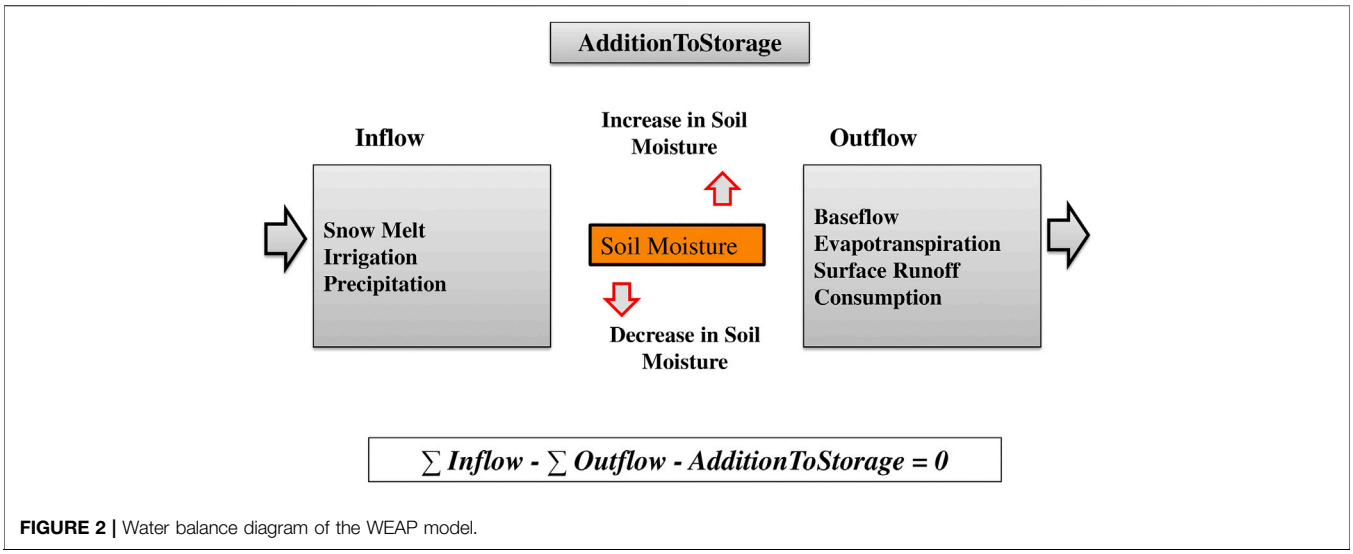


FIGURE 2 | Water balance diagram of the WEAP model.

TABLE 3A | (A) Goodness-of-fit statistical criteria for the calibration and validation of the WEAP model to simulate the streamflow of each river. (B)

A		Rivers		
Calibration	**Cautín**	**Allipén**	**Quepe**	**Lonquimay**
Period (years)		2000–2007		
Bias	0.08	0.04	0.19	0.2
NSE	0.86	0.84	0.8	0.83
R^2	0.9	0.86	0.94	0.91
RMSE	0.02	0.02	0.03	0.03
Validation				
Period (years)		2008–2015		
Bias	0.1	0.08	0.23	0.15
NSE	0.83	0.84	0.77	0.81
R^2	0.89	0.88	0.96	0.93
RMSE	0.02	0.02	0.03	0.02

A draws from Supplies B and C and returns water to those same supplies, as well as consumes some of the water (http://www.weap21.org/), as described in **Eq. 2**.

$$\left[\text{Inflow}_{B,A} + \text{Inflow}_{C,A}\right] - \left[\text{Outflow}_{A,B} + \text{Outflow}_{A,C}\right] - \left[\text{Consumption}_{A}\right] = 0 \quad (2)$$

$Inflow_{B,A}$ is the inflow from supply B to demand site A.

The current accounts, key assumptions, and scenarios were defined during the model set up. Key assumptions can be built into current accounts (Maliehe and Mulungu, 2017), to represent policy, supply, and hydrology. For our study, irrigation needs for agriculture and water demands for human consumption were included in the characterization of the basins. The definition of the study with the WEAP model includes several steps, such as the spatial-temporal boundaries, all system components, the establishment of the water supply and demand, and the problem configuration. Thus, scenarios based on current accounts allow exploring the impacts of alternative assumptions (Maliehe and Mulungu, 2017). For example, for instance modifying the "key Units Domestic", "water use", "irrigation water needs" and "population growth rate" (Van Loon and Droogers, 2006).

The Soil Moisture Method is used for each study basin (http://www.weap21.org/). It represents the basin with two soil layers (Yates et al., 2005) and the potential accumulation of snow (Vicuña et al., 2011). For each catchment, rainfall-runoff processes (Yates et al., 2005) are simulated using a 2-bucket representation of a root zone layer and a deep layer formulation of rainfall-runoff hydrology (Yates et al., 2005; http://www.weap21.org/). The variability of land covers in each catchment

TABLE 3B | Results of the flows in each station: annual Q (m^3/s); Coefficient of variation; max and min flows (m^3/s) of the study rivers.

Station name	Latitude S	Longitude W	Elevation (masl)	Area (Km^2)	Annual Q (m^3/s)	SD	Cv[a]	Maximum flow (m^3/s)	SD	Minimum flow (m^3/s)	SD
Allipén river in Melipeuco	38°51′55″	71°44′01″	450	747	69.6	25.2	0.4	86.8	31.3	46.1	6
Cautín river in Rari-ruca	38°25′4″	72°00′38″	425	1365	85.3	49	0.6	146.2	50.8	36.7	6.7
Lonquimay river in front of Bio Bio River	38°26′00″	71°14′00″	0	463	26.8	19.9	0.7	47	30.3	8.3	2.4
Quepe river in Vilcún	38°41′00″	72°13′60″	292	386	27	16.6	0.6	50	18.6	11.4	2.5

[a]*Coefficient of variation*

is represented by subdividing the area into representative land cover types that are parameterized individually. Finally, demand priorities and supply preferences are established using linear programming to increase water demand satisfaction as an alternative to the multi-criteria weighting or logical approaches based on rules and scenarios (Yates et al., 2005). The model gives an overall water balance for the entire study area.

Hydrological Set-Up

For the construction of the WEAP model in the study basin, the water system was characterized by water demand sites and flow-gauge stations. The demand sites are represented by nodes and connected to the rivers through transmission and return links. These nodes were created in the diagrammatic view of the WEAP model (Maliehe and Mulungu, 2017), and the demand priority set and supply preferences were established. WEAP computes a mass balance of all water entering and leaving one or more demand sites for every node, linking the system in monthly steps (Purkey et al., 2008; Condom et al., 2011; Harma et al., 2012). **Figure 1B** shows each of the basins Digital Elevation Model (DEM). Geographic Information System (GIS) data on elevations, catchment, and land cover were obtained and used to define and characterize each basin (Mehta et al., 2013). Elevation data were extracted from the DEM provided by the U.S. Geological Survey (USGS, 2016). To compute water resource systems, the analysis included monthly rainfall, temperature, wind speed, and relative humidity information, where month-to-month variations produce interannual variations in flow rates. In this context, modelling can incorporate climatic factors such as wind, humidity and temperature, and variations in evapotranspiration (Bhave et al., 2014). Thus, this model supports the analysis of the hydrological characteristics of a basin for future scenarios of climate change, land use (Mehta et al., 2013), and water demand (Bhave et al., 2014).

Water Evaluation and Planning Calibration and Validation

The WEAP model was calibrated and validated using data of the four streamflow gauging stations located in the study area (see **Table 2**), which represent the natural streamflow of the region. A monthly time step was used for calibration and validation analyses to cover the residence time of the survey area, during which all flows are assumed to occur (Purkey et al., 2008; Bhave et al., 2014). The calibration period extended from January 2000 to December 2007, while the validation period considers from January 2008 to December 2015. The period is the same for all four catchments based on data availability.

The model was manually calibrated to maximize the fit between the observed and simulated flow (Vicuña et al., 2011; Bhave et al., 2014). As shown in **Table 3A**, four well known statistical criteria were used to evaluate the ability of the model to simulate the measured streamflows. For the Root Mean Squared Error (RMSE), the lower the number, the better the model performance, with a zero RMSE indicating a perfect fit between the model and the observed data. The Nash-Sutcliffe Efficiency (NSE) can vary from minus infinity to 1 (Mehta et al., 2013; Bhave et al., 2014). When it is lower than 0, the mean predicts the variable better than the model; when it is between 0 and 1, the model works with standard cases, and the closer to 1, the better the correspondence between observed and modelled data. Also, lower values of Bias represent better correspondence between observed and modelled data. A positive Bias indicates overestimation and a negative Bias indicates an underestimation of flows (Condom et al., 2011). The coefficient of determination R^2 represents how well a linear model fits the data. It varies in the range $0 \leq R^2 \leq 1$; a value of 1 means a perfect linear fit, and a value of 0 indicates that the linear model is not representative (Bhave et al., 2014; Maliehe and Mulungu, 2017).

Calibration was performed by comparing the observed and modelled monthly streamflows at the outlets of the four sub-basins or study catchments (**Figures 1A,B** and **Table 2**).

Demand sites and Catchment Description

As explained in *Basin Characterization*, four hydrological units were defined as catchments (sub-basins).

Demand for Human Use

Urban demand was characterized according to the number of inhabitants, population growth rate, and per capita consumption. To estimate the water requirements of the demand sites for human use, eight urban domestic demand sites were identified, composed of small towns with populations of approximately 1,000 to 16,000 people: Vilcún, San Patricio, Cherquenco, Melipeuco, Conguillío National Park, Lonquimay, Malalcahuello, and Curacautín (see **Table 4A**). According to data from the Chilean General Water Agency (DGA, 2007; DGA, 2016) and the National Institute of Statistics (INE, 2014), the average annual water consumption in Chile is 54.8 m^3/person/year. However, in the study area, the average consumption is slightly lower (47 m^3/person/year). It is important to note that the estimate of human water consumption is obtained from official sources and companies that provide this service, supported by the last census conducted on the number of population (INE, 2007).

Demand for Irrigation

The irrigation needs of the considered sub-basins were determined by selecting the land cover and the annual irrigation requirements. The covers (crops, meadows, and forest plantations) were calculated in ArcGIS 10 (**Table 1**), as described in *Land Uses*. The irrigation water demands, together with crop area records and information on their requirements, were obtained from AGRIMED (Universidad de Chile, 2015) and the National Irrigation Commission (CNR, 2011). Agricultural demand sites were created in WEAP to assess irrigation demands. Basins with significant percentages of crop cover, forest plantations, and grassland were considered. The main crops in the study area are cereals, mainly oat and wheat. The forest plantations are *Pinus radiata* and *Eucalyptus globulus* (INE, 2014), and the forage grasslands mainly consist of grasses, fescue, and clover. The irrigated area (ha) also was defined.

TABLE 4A | Water requirements of each demand site for human consumption (m^3/yr).

Demand sites	Population (N° persons)	Domestic water consumption (m^3/year)	Sub-basin
Curacautín	16,221	7,62,387	SBC
Malalcahuello	1,000	47,000	SBC
Lonquimay	10,957	5,14,979	SBL
Cherquenco	5,534	2,60,098	SBQ
San Patricio	2,490	1,17,030	SBQ
Vilcún	13,835	6,50,245	SBQ
Melipeuco	5,837	2,74,339	SBA
Conguillio National Park	1,500	70,500	SBA

TABLE 4B | Total area (Ha), planted area (Ha), irrigated area (Ha) and coverage of the demand (%)

Sub_basin	Surface (ha)	Surface planted (ha)	Irrigation (ha)	Demand coverage (%)
SBA	1,05,270	29,483	4,353	14.7
SBC	1,29,110	27,938	4,330	15.5
SBQ	55,650	24,963	3,870	15.5
SBL	46,430	1,617	0	0

Demands for Hydropower and Other Uses (Livestock, Aquaculture, Industry)

We can point out that in Chile there are more than 140 hydroelectric plants operating, considering reservoirs, run-of-river and mini run-of-river hydraulics. In total, they exceed 6,600 MW of installed power. The participation of hydroelectricity (reservoir and run-of-river) in the electrical matrix by December 2016 covers 28.8% of the energy generation at the national level (www.cne.cl). Thus, through the use of the WEAP model, we estimate the water demand for hydroelectric use of the four sub-basins under study (SBA, SBC, SBQ and SBL). This information was obtained mainly by reviewing reports from the Environmental Assessment Service (SEIA) of the Ministry of the Environment.

In addition, the water demand for livestock production was calculated, which represents 10.4% of the country's production (ODEPA, 2018). To make this estimation, our calculation base was obtained from the Agricultural Census (INE, 2007), where it is estimated that a cattle consumes 45.4 L per day, a cow that produces milk 132 L per day and poultry between 0.2 and 0.4 L per day.

With respect to water demand for aquaculture, information was obtained from official reports of DGA (2007) and permits granted by this state institution, as well as for industrial and other uses (e.g., manufacturing, agro-industry, tourism, etc.).

Finally, there is no public information available for all the economic activities classified as manufacturing industry, which allows to determine or estimate their use and consumption of water. Therefore, an estimate of the water demand for these uses is constructed by integrating information of the sub-sectors from different public and private entities.

Water Balance Estimation Methodology

As the basins investigated are mountain basins, the climate forcing gradient was studied with extrapolation at higher elevations (see *Processing of Climatic Data*). Where a fluviometric record exists, these gradients were adjusted to obtain an acceptable discrepancy term. The estimation of the water balance is based on the mass conservation equation (DGA, 2017), where the main hydrological processes of the system inputs and outputs are precipitation (P), runoff (Q), and evapotranspiration (ET). A discrepancy term is also considered (η). In simplified form, this **Eq. (3)** can be expressed as follows:

$$(P) + (Q) = (ET) - \eta \quad (3)$$

The above equation is applied to a given area and period.

As noted above, the WEAP hydrological model was calibrated for the period 2000–2007, and validated for the period 2008–2015 for the four basins under study, using the Soil Moisture Method, which was developed to model the hydrological processes with a quasi-physical representation, but in a robust method (see **Figure 2**).

RESULTS AND DISCUSSION

After calibrating (2000–2007) and validating (2008–2015) the WEAP model, we computed the efficiency criteria (*Water Evaluation and Planning Modelling Results and Analysis of Efficiency Criteria*). We calculated the water resources supply and demand for human consumption (*Demand for Human Use*), irrigation for agriculture (*Irrigation Demand*), livestock production, industry, aquaculture and other uses (*Livestock Production Demand*), and electricity production (*Demand for Hydropower*). Finally, the whole water resources and demand balance and its components (precipitation, evapotranspiration and runoff) were established for each month in the four basins (*Water Balance*) throughout the study period.

Water Evaluation and Planning Modelling Results and Analysis of Efficiency Criteria

To calibrate and validate the model and test the validity of the different simulation scenarios, the four efficiency criteria presented in *Water Evaluation and Planning Calibration and Validation* were used to assess the model accuracy to simulate the observed streamflow at each of the four stations (Bhave et al., 2014). The obtained values are summarized in **Table 3**. According to all the goodness-of-fit statistical criteria, the model shows an outstanding representation of all rivers, with the best fit to the Quepe river. The best results in the efficiency criterion NSE was obtained for the Cautín river. The Allipén river presents a poorer fit for the R^2 adjustment criteria. However, the R^2 was higher than 0.86 in both the calibration and validation, which is considered quite significant (Condom et al., 2011; Yan et al., 2015). Thus, these results indicate a more than reasonable ability of the WEAP hydrological model to simulate the flows.

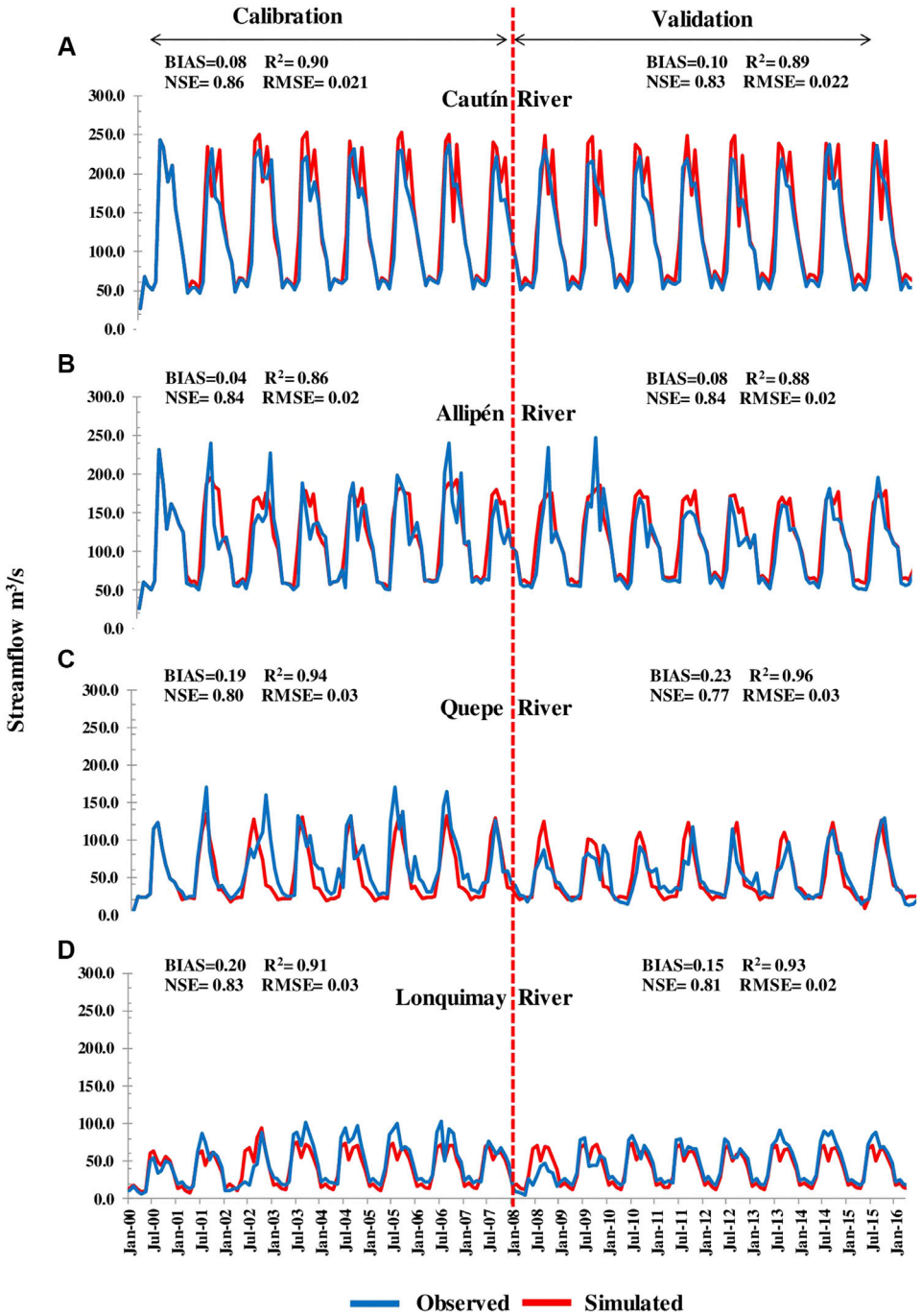


FIGURE 3 | Average monthly streamflow time series (m^3/s) for the calibration and validation period, comparing observed (blue) and WEAP-simulated (red) data. **(A)** SBC basin: Cautín river at the Rari-Ruca station. **(B)** SBA basin: Allipén river at the Melipeuco station. **(C)** SBQ basin: Quepe river at the Vilcún station. **(D)** SBL basin: Lonquimay river at the station located before its junction with the Bío-Bío river. For more details see also **Table 2**.

Considering the sensibility of the WEAP model, the factors that most affected the calibration of the streamflows were the Land Use module factors (deep-water capacity, runoff resistance factor, deep conductivity, and preference flow direction) and the Climate module factors (freezing point, melting point, and albedo).

Figure 3 (A, B, C and D) shows the average monthly river flow time series for the calibration (2000–2007) and validation (2008–2015) periods. It compares the measured (in blue) and simulated (in red) values for the four rivers (Cautín, Allipén, Quepe and Lonquimay) with the respective values of the efficiency criteria, corroborating the good performance of the

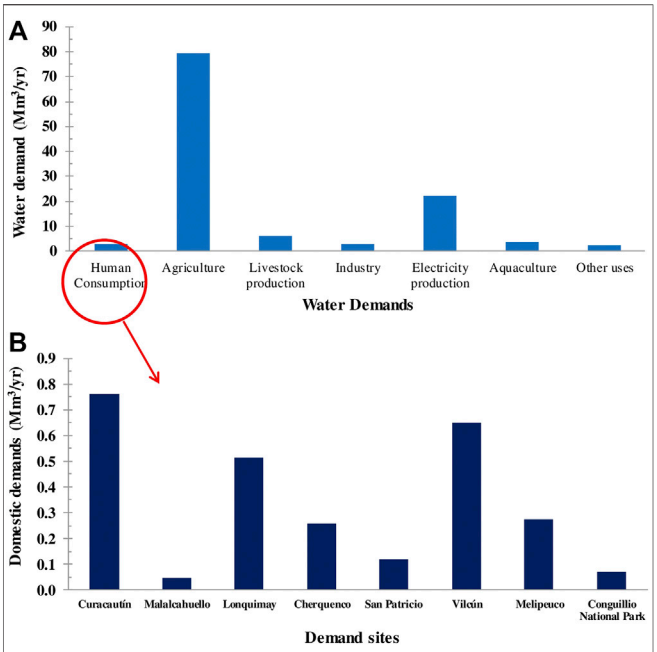


FIGURE 4 | (A) Water Demands for different uses (Mm^3/yr). **(B)** Annual domestic water demand of demand sites (Mm^3/yr).

WEAP model. **Table 3B** summarizes the river's average annual flow and the monthly historical maximum and minimum flows. The Cautín river (SBC) is the most important water body in the study area, followed by the Allipén river (SBA).

From both the figures and the tables, and as expected, the highest flows occur each year between June and September, and the lowest flows between January and April. Thus, the four rivers showed their historical maximum monthly flow in July 2001 and their historical minimum monthly flow in March 2009. We reported a mean maximum flow of 146 m^3/s for the Cautín River, and 50 m^3/s for the Quepe River, while the minimum mean flow was 36.7 m^3/s and 11.4 m^3/s respectively.

Note that the study of Rubio-Alvarez and McPhee (2010) shows an interannual variability of 0.4 (for the Rio Cautín station in Rari-Ruca and Quepe River station in Vilcún) and an annual flow of 107 m^3/s for the Cautín River in Rari-Ruca and 34 m^3/s for the Quepe River in Vilcún. Their results correspond to an average over 50 years of data (1952–2003). In our 16-years study (2000–2015), for these same river stations, the variability is 0.6 (for Cautín and Quepe Rivers), and the annual flows are 85.3 m^3/s and 27 m^3/s, respectively. Therefore, we can point out that in both cases, there is a more significant variability (0.6 greater than 0.4), and, in addition, for both rivers the annual flows decreased by 20%.

Water Demand

First it is important to note that, as specified in *Land Uses* and *Demand for Irrigation*, the model uses land cover information, which is a crucial element for water usage in irrigation. Based on the information showed in **Table 1**, we can point out that the sub-basin with the largest surface area is the Cautín river basin (SBC, 1,291 km^2), of which 54% is native forest, 19% is agricultural use and 2.5% is forest plantations (mainly pine and eucalyptus). With respect to SBA (Allipén river, 1,052.7 km^2), 45% is native forest, 19.3% is agricultural use and 8.7% is forest plantations. The information related to land uses for the other sub-basins is also included in **Table 1**.

The characteristics of the study area suggest the following types of activities that generate water demands: Human consumption, Agriculture (irrigation), Livestock production, Industry, Electricity production, Aquaculture, and Other uses. In **Figure 4A**, the annual water demands for each activity are shown in millions of cubic meters per year (hereinafter Mm^3/yr). **Figure 4B** shows the domestic demand of the different demand sites. As expected, the highest demand is generated for agricultural uses, mainly irrigation of crops and meadows. Additionally, **Figures 5 B, C, D, E and F** show the monthly distribution of the average water demand of the main activities for each sub-basin. The distribution of the results over all the basins is as follows: Agriculture: 79.4 Mm^3/yr; Electricity production: 22.3 Mm^3/yr; Livestock production: 6.2 Mm^3/yr; Industry: 2.79 Mm^3/yr; Aquaculture: 3.58 Mm^3/yr; Human consumption: 2.69 Mm^3/yr; and other uses: 2.4 Mm^3/yr. It can be observed, that the highest demands are produced in agriculture and electricity production. However, results reveal a series of differences between the sub-basins. For example, human consumption is associated mainly to the Quepe and Cautín sub-basins, which correlates with the demands for industrial and other uses, and with its population settlements (**Table 4A**). Livestock demand is highest for the Cautín and Lonquimay sub-basins. In contrast, agricultural demand is associated mainly with the Allipén sub-basin, which also has the largest surface with agricultural uses (crops, forest plantations, and grassland, as shown in **Table 1** and **Table 4B**). The highest variability during the year is observed in irrigation uses, since it only is required during the dry season, from November to April.

Considering its relevance, in the following sections the demand for human uses, irrigation, hydropower and livestock are described in more detail.

Demand for Human Use

As described in *Demand for Human Use*, the water demand for human uses is associated with the eight urban areas identified in **Table 4A**, where also its water requirements are shown, which correlate with its population. Therefore, the highest demand is recorded in Curacautín (762,387 m^3/yr), and the lowest in Malalcahuello (47,000 m^3/yr). The Conguillío National Park (70,500 m^3/yr) has to be considered as a particular demand site, since it receives many visitors in the summer months (more than 100,000), when the water demand increases significantly. With respect to water consumption at the sub-basin level (**Figure 5B**), the monthly consumption of these basins is shown: SBQ is the largest with 1,027,373 m^3/yr; then SBC with 809,387 m^3/yr; then SBL with 514,979 m^3/yr, and finally SBA,

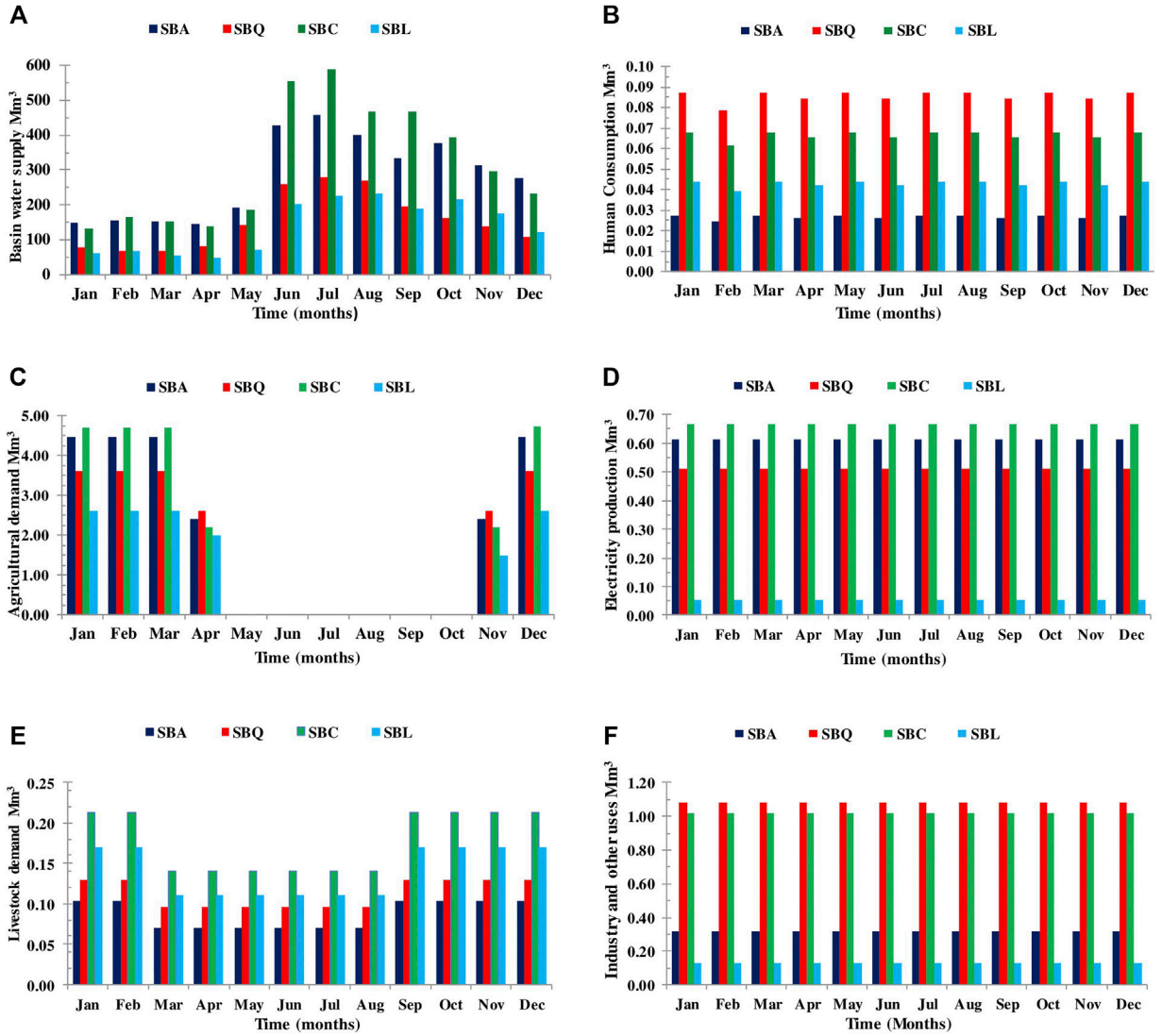


FIGURE 5 | (A) Water supply in study sub-basins (Mm^3/month); **(B)** Water demands for human consumption in each basin (Mm^3/yr); **(C)** Water demands for agricultural uses in each basin (Mm^3/yr); **(D)** Electricity production in each basin ((Mm^3/yr); **(E)** Water demands for livestock farming in each basin (Mm^3/yr); **(F)** Water demands for industry and other uses in each basin (Mm^3/yr).

which demand increases considerably due to visitors to Conguillío National Park during the summer. Without considering these months, the SBA has a demand of 274,339 m^3/yr, which increases in the summer period to 344,839 m^3/yr.

Irrigation Demand

According to the 2007 Census, the Araucanía Region covers 20.6% of the national surface area dedicated to the forestry and agricultural sector (916,993 ha). The main use corresponds to forestry plantations, with 64.3% of this total, followed by cereals with 18.5% and fodder plants with 9.8%. These three items concentrate 92.6% of the hectares of forestry and agricultural use in the region. At the same time, the region presents great importance, at national level, in six items: industrial crops, cereals, forest plantations, legumes and tubers, seedbeds and fodder plants. With respect to cereals, legumes and tubers, of the total area of the country dedicated to these crops, 52.7% is located in the Araucanía Region, (ODEPA, 2015). It is also important to take full advantage of the excellent soil and climate conditions of the region, such as the yield of cereal crops in Chile, compared to the world, due to the quality of its soil, mainly in this region, which has volcanic soil with a high percentage of organic matter (Fernandez-Alberti et al., 2012). Taking a base of more than 50 years, in the world the yield has increased by 200% and in Chile more than 350% (FAO, 2015).

Table 4B shows the distribution of different types of surfaces associated with irrigation demands. The sub-basin with the largest planted area is SBA (28%), followed by SBC (22%). Thus, the largest sub-basin is the Cautín area, with a total

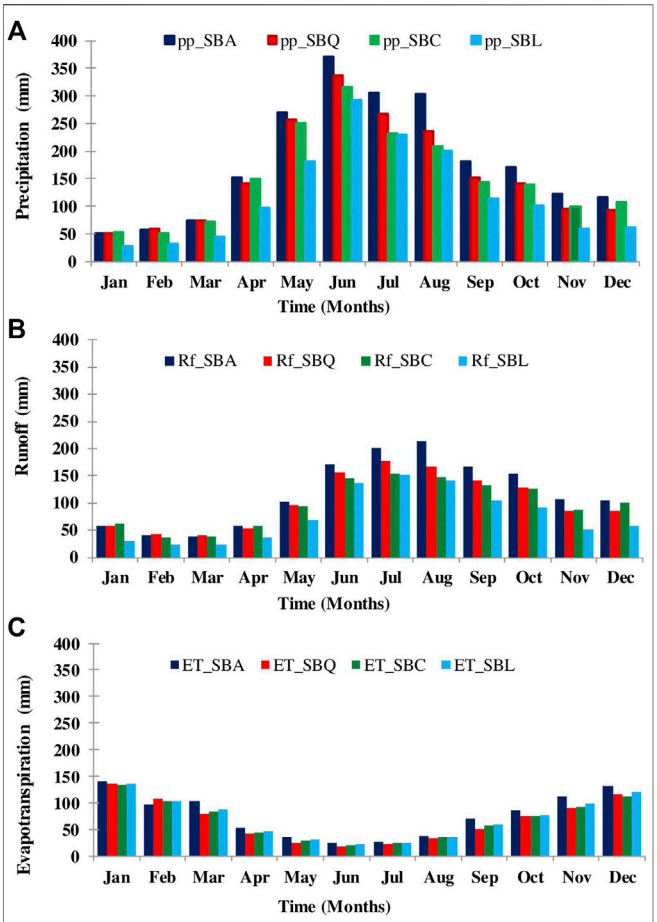


FIGURE 6 | Results of the WEAP simulations: Calculated terms of the monthly water balance for each sub-basin (mm). **(A)** Precipitations (pp). **(B)** Runoff (Rf). **(C)** Evapotranspiration (ET).

surface of approx. 130,000 ha. About one-third of SBA and SBC correspond to cultivated area (84,000 ha), which potentially may need irrigation. In the case of SBQ, it happens that it has a smaller area than the previous basins (55,650 ha), but its ratio in terms of planted area is 45%, and finally SBL only 3%. However, and this is very important, the area effectively irrigated (12,553 ha) represents only 15% of the potential irrigation demand.

To understand this, it is necessary to know the following: The Office of Agrarian Studies and Policies (INE, 2007; ODEPA, 2015) considers a fixed water demand of 2,700 m^3/ha for irrigation during the dry season (November to April). This implies a real irrigation demand of approximately 227 Mm^3/yr. On the other hand, the irrigation water effectively authorized for these basins is only 11 Mm^3/yr. These facts allow us to suggest that there exists a significant gap between the water effectively used for irrigation purposes, and the potential needs of water resources to cover the future potential demands.

As shown in **Figure 5C**, which presents the monthly irrigation demands at sub-basin level, the irrigation requirements are associated only to the dry season. At regional level, 21% (634.5 ha) of the territory has a water deficit, with the northern sector of the region being associated with land under strong pressure for agricultural and forestry use, (ODEPA, 2015). This poses the typical challenge of an adequate water resources management system, which inevitably requires the implementation of artificial water reservoirs, and the use of water balance models like WEAP to develop an effective management strategy.

Livestock Production Demand

The Araucanía region has approximately 1,000,000 ha of grasslands of excellent quality, which constitute the base for the breeding and feeding of cattle and sheep, and, on a smaller scale, horses and goats. As reported by ODEPA (2018), the region represents 10.4% of the livestock production of the country, and occupies the second place nationally in importance in the bovine mass. Specifically in the area of beef, the region has the necessary conditions to become an important producer - exporter of meat. In 2016, the region contributed with 18% of the country's cattle profit, measured in tons of meat (39,828 tons). In 2015, the region contributed with 7.7% of the milk received by the country's largest dairy industry plants (ODEPA, 2018). **Figure 5E** shows the average monthly water demand for livestock production during the year. The total demand in the entire basin is 6.2 Mm^3/yr, and the highest demand is for SBC (2.12 Mm^3/yr), mainly cattle production, followed by SBL (1.68 Mm^3/yr) mainly sheep and goat production. It should be noted that the surface area destined to pasture in these sub-basins is 4.6% and 3% respectively.

Demand for Hydropower

The results of our study for water demand for electricity production was 22.3 Mm^3/year (see **Figure 5D**). The SBC and SBA subbasins have the highest value of water use for hydroelectric production (8.14 and 7.95 Mm^3/year, respectively), and the SBL has a very small value (0.01 Mm^3/year). It should be noted that energy demand or consumption also has a relevant spatial component. For example, the Toltén river basin (where the SBA sub-basin is included) has a total hydroelectric potential of 1,123 MW distributed relatively evenly among all the sub-basins that make up the Toltén river basin and ranging from 100 to 500 MW (Energia, 2016).

In addition, when mapping the basin and its respective sub-basins, it was established that the areas with greatest potential for hydroelectric use, coincide with zones where natural protected areas are located. Therefore, there should be greater restrictions on use. However, today the greatest opposition to the installation of small hydroelectric plants are related with areas of important heritage (national parks) and, mainly, associated with cultural aspects of the native Mapuche people. So, the optimization model used seeks to know how much hydroelectric potential does not overlap with natural protected areas.

Water Balance

An essential aspect of estimating the water availability in a specific area is to have reliable data of the local precipitations behavior. This is the leading term of the inflow streams of any water balance

model (see **Figure 2**). **Figure 5A** shows the average (2000–2015) monthly water supply of the total watershed under study, subdivided into the four sub-basins. This supply is the accumulated water, product of rainfall and snow upstream in the Andean mountain range, mainly in the periods from June to December, with the highest values from June to August.

The main components of the water balance are precipitation, runoff, and evapotranspiration. The monthly behavior of these terms for each catchment area, as simulated by the WEAP model using the available input data, is shown in **Figures 6 A, B and C**, respectively. It can be observed that the catchment which presents the highest precipitation, runoff, and evapotranspiration for the entire period is the Allipén sub-basin (SBA). This catchment shows a well-marked rainfall regime since most of the runoff occurs in the winter months. Precipitation is around 2,175 mm/yr, with higher values in winter, while runoff and evapotranspiration reach 1,420 and 919 mm/yr, respectively. Thus, the runoff factor of the basin is close to 65%, and the evapotranspiration factor is 42%. In principle, the runoff component may be utilized to cover different water demands. However, if there is no adequate infrastructure to accumulate this freshwater, in a few hours, it will flow directly into the ocean. Also, Viviroli et al. (2020) point out that in many parts of the world mountain areas provide excessively high runoff. However, it is projected that 1.5 billion people (24% of the world's lowland population) will be critically dependent on contributions from mountain runoff (39% of the world's land mass) by the middle of the 21st century.

According to DGA studies (2017), the Toltén River basin, of which the SBA catchment forms part, receives less than 15% of its precipitation in the form of snow, since the elevation of the Andes Mountain Range is lower in these latitudes. Almost the entire precipitation of the basin falls in liquid form, causing a marked pluvial regime in the flows.

Changes in the water balance during the cold, wet season (April-September) dominated those in the hot, dry season (October-March). Precipitation was higher between May and September in all the sub-basins, also causing a consistent runoff increase in that period. The essential point of the model is that supply can be summarized as the sum of direct runoff from precipitation, snow-melt, and baseflow. At the same time, evapotranspiration extracts water stored in the unsaturated subsoil (Yates et al., 2005).

CONCLUSION AND RECOMMENDATIONS

This research aimed to advance in the understanding of the behavior of the mountain basins of the Andean mountain range in south-central Chile. Mountain basins are the primary sources of its freshwater supply (Momblanch et al., 2017) and also for the main watersheds of the Araucanía Region, in addition to providing ecosystem services. The study focused on four watersheds of a protected natural area (Conguillío National Park) located in the pre-Andean range of the Southern Andes. These basins drain their water to different communities, which use it as water resources. Using the different local hydroclimatic data available, the WEAP hydrological model was calibrated and validated, allowing not only to correctly determine the water balance, but also its usage.

Our results show that the total water available in the basin almost all the year is greater than the water consumption in the study area. On the other hand, downstream of the study area, the distribution of water is more complex, since the demand for consumption increases due to the fact that in the lower zones (valleys) there are significant human settlements (cities with populations greater than 100,000 persons), large agricultural and forested areas, and various industries. These conditions have to be considered in a territorial planning strategy, preferably based on watershed management. Unfortunately, at this time, the territorial planning based on watersheds is not yet a common practice in Chile. It is limited mainly to academic initiatives (Larrain et al., 2010).

Even if the obtained results of this study agree with the general behavior expected for this type of systems, to the best of our knowledge it is the first time in Chile that hydroclimatic and related data is processed, systematized, and used to validate a water management model. Therefore, this study developed a highly valuable planning skill to support strategic decision-making in the allocation of water resources to various sectors, including the corresponding investment requirements for water regulation infrastructure. This is a fundamental issue to face successfully the challenges raised by the different potential future changes, both in climate as in water demand for human activities. The increase in demand and changes in cropping patterns, combined with the effects of climate change, could present serious problems for agriculture if this activity and its irrigation demand are not planned.

In the context of global climate change, it is expected that Chile will be affected significantly (Valdés-Pineda et al., 2014). Future scenarios indicate a considerable decrease in precipitations (20–50%) and an increase in temperatures (1–3°C) (Orrego et al., 2016), which will have a dramatic impact on the natural and socio-economic environment, mainly in agro-industry. Droughts and floods may cause crop damage, while increased population growth (INE, 2015) will intensify pressure on freshwater supplies. Indeed, in the near-future global water supply will not be sufficient to cover the increasing demand. It is crucial to develop a public strategy to adapt to this uncertain new conditions (Valdés-Pineda et al., 2014; DGA, 2017).

On the other hand, in Chile the existence of several institutions related to water regulation means that the legal framework is fragmented, which generates coordination and financing problems. The use and management of water resources are regulated by the Water Code of 1981, which focuses on Water Rights. The Water Code defines water as a "national good of public use" but at the same time as an "economic good". It authorizes water privatization through the free use rights in perpetuity concession (it does not set limits to the concession of use rights). It establishes a system of water redistribution through transactions between private

parties, thus creating a Water Market, and favors the concentration of ownership of this resource (Larraín et al., 2010; Larraín, 2012). Currently, a great debate takes place in Chile regarding the legislation change concerning water use and management. This debate requires correct knowledge of the distribution of water for different uses.

Therefore, a recommendation is that Chile should have a single institution that regulates and assigns water rights for different uses. For these reasons, a thorough review of the water legislation through the Water Code is needed.

In this context, obtaining calibrated results of a water balance through a water management model, allows to determine the different usages (domestic, agricultural, livestock, fish farming, hydroelectric, and industrial uses). It can be inferred that these sub-basins have a high use value, allowing the supply of water to different communes of the region demanding this resource, providing at the same time abundant opportunities for the development of different economic activities. Besides, it will contribute to a satisfactory and responsible decision-making process, allowing strategies implementation against the different current and future scenarios, such as land-use changes, industrial activities demands (fish farming, hydroelectric, and many others.), and thus will also ensure the Conguillío National Park ecosystem services sustainability.

From an ecosystemic point of view, the presence of these water bodies allows for the maintenance of a balance in the water balance of the basin, controlling runoff, reducing overflows and drying up of downstream flows, offering a high potential for the development of productive activities such as tourism, sport fishing, irrigation and many others CONAF, Corporación Nacional Forestal (2009). Furthermore, protected natural areas are important not only for Chile, since the existing natural heritage is made up of a unique global biodiversity (Mittermeier et al., 2004; Arroyo et al., 2006). Thus, these mountain ecosystems are areas of high production value. However, they are very fragile (Canedoli et al., 2020) and vulnerable to anthropic and climatic effects (Gao et al., 2020; Immerzeel et al. 2020).

Finally, nothing in hydrology can be correctly established without an accurate, modern, and homogeneous network of measurements, both meteorologically and hydrologically. It does not exist in Chile today, even for its most important watersheds. Therefore, it is recommended that the pertinent authorities implement policies oriented to meet the basic needs that allow the reliable follow-up of water flows, both in surface and subsurface, and push forward to effective implementation of watershed-based territorial planning strategies. The results and skills developed in this study are a valuable contribution to these objectives, since the WEAP water resource planning model provides accurate information for decision-making facing different future socio-economic scenarios, such as population growth, land-use changes, forestry, and agricultural use, and of course, those associated with climate change that will influence all the others (de Marsily and Abarca-del-Rio, 2016; Konapala et al., 2020).

DATA AVAILABILITY STATEMENT

The datasets generated for this study are available on request to the corresponding author.

AUTHOR CONTRIBUTIONS

SF-A is the main author who developed her Ph.D.-Thesis in the subject and obtained the results and data. CB is the adviser of the mentioned Ph.D.-Thesis. AÃ. and R-A-d-R are co-advisers of the PhD-Thesis. The co-authors R-A-d-R and CB assisted the first author in different levels of research, such as research design, interpretation of results and editing the manuscript. SF-A and R-A-d-R were in charge of the calibration and software validation.

ACKNOWLEDGMENTS

The first author was supported by the Modeling and Scientific Computing Excellence Center (CEMCC) of Universidad de La Frontera, Temuco, Chile, through a Ph.D. program in Engineering at this University.

REFERENCES

Aguayo, M., Pauchard, A., Azocar, G., and Parra, O. (2009). Land use change in the south Central Chile at the end of the 20th century. Understanding the spatiotemporal dynamics of the landscape. *Rev. Chil. Hist. Nat.* 82 (3), 361–374. doi:10.4067/S0716-078X2009000300004

Armesto, J., Arroyo, M., and Hinojosa, L. (2008). "The Mediterranean environment of central Chile," in *The physical geography of South America*. Editors T. Vablen, K. Young, and A. Orme New York: Oxford University Press.

Arroyo, M. T. K., Marquet, P., Marticorena, C., Simonetti, J., Cavieres, L., Squeo, F., et al. (2006). "El Hotspot Chileno, prioridad mundial para la conservación," in *Comisión Nacional del Medioambiente*. Editors B. de Chile and P. Y. Desafíos Santiago de Chile: Ocho Libros Editores Ltd., 94–97.

Bathke, H., Shirzaei, M., and Walter, T. R. (2011). Inflation and deflation at the steep-sided Llaima stratovolcano (Chile) detected by using InSAR. *Geophys. Res. Lett.* 38, L10304. 10.1029/2011GL047168

Bauhus, J., Pokorny, B., van der Meer, P. J., Kanowski, P. J., and Kanninen, M. (2010). "Ecosystem goods and services–the key for sustainable plantations," in *Ecosystem goods and services from plantation forests*. London, UK: Routledge, 221–243.

BCN (2019). Biblioteca del Congreso Nacional de Chile Información Territorial. Available at: https://www.bcn.cl/siit/nuestropais/region9

Bhave, A. G., Mishra, A., and Raghuwanshi, N. (2014). A combined bottom-up and topdown approach for assessment of climate change adaptation options. *J. Hydrol.* 518, 150–161. 10.1016/j.jhydrol.2013.08.039

Biggs, E. M., Bruce, E., Boruff, B., Duncan, J. M. A., Horsley, J., Pau, N., et al. (2015). Sustainable development and the water-energy-food nexus: a perspective on livelihoods. *Environ. Sci. Policy* 54, 389–397. 10.1016/j.envsci.2015.08.002

Boisier, J. P., Rondanelli, R., Garreaud1, R. D., and Muñoz, F. (2016). anthropogenic and natural contributions to the Southeast pacific precipitation decline and recentmegadrought in central Chile. *AGU Geophys. res. let.* 43, 413–421. doi:10.1002/2015GL067265

Brauman, K. A., Daily, G. C., Duarte, T. K., and Mooney, H. A. (2007). The nature and value of ecosystem services: an overview highlighting hydrologic services. *Annual Rev. Environ. Res.* 32, 67–98. doi:10.1016/j.advwatres.2011.02.010

Canedolia, C., Ferrèa, Ch., Khair, D., Comollia, R., Ligaa, C., Mazzucchellia, F., et al. (2020). Evaluation of ecosystem services in a protected mountain area: soil organic carbon stock and biodiversity in alpine forests and grasslands. *Ecosystem Serv.* 44, 101135. doi:10.1016/j.ecoser.2020.101135

CCG (2009). Centro. de Cambio Global-Universidad Católica de Chile, Stockholm Environment Institute Guía Metodológica – modelación Hidrológica y de Recursos Hídricos con el Modelo WEAP. Available at: http://www.weap21.org/index.asp?action=40

CEPAL (2012). La economía del cambio climático en Chile. Available at: http://repositorio.cepal.org/bitstream/handle/11362/35372/S2012058_es.pdf?sequence

Chaplin, G. (2005). Physical geography of the Gaoligong Shan area of southwest China in relation to biodiversity. *Proc. Calif. Acad. Sci.* 56, 527–556.

Universidad de Chile (2007). Variabilidad climática de Chile para el siglo XXI". Departamento de Geofísica, Santiago de Chile.

Universidad de Chile (2012). Estado del arte de modelos para la investigación del cambio global. Departamento de Geofísica, Santiago de Chile.

Universidad de Chile (2015). AGRIMED, centro de Estudios de Agricultura y medioambiente Atlas Agroclimático de Chile.

Clark, S., Abbett, E., and Nandagopal, S. (2004). Water resources: Agricultural and environmental issues, *Bioscience* 54 (10), 909–918. doi:10.1641/0006-3568(2004)054[0909:WRAAEI]2.0.CO;2

CNR (2011). Comisión Nacional de Riego política nacional de Riego, una mirada a largo plazo. Available at: www.cnr.gob.cl

CONAF, Corporación Nacional Forestal (2009). Unidad de Gestión patrimonio silvestre. Sección parques nacionales y monumentos naturales. Región de la Araucanía de la Araucanía, Chile. Plan de manejo de Parque Nacional Conguillío.

CONAF, Corporación Nacional Forestal (2012). Catastro de los Recursos Vegetacionales Nativos de Chile. Monitoreo de cambios y actualizaciones. Período 1997-2011. Corporación Nacional Forestal, 30.

Condom, T., Escobar, M., Purkey, D., Pouget, J. C., Suarez, W., Ramos, C., et al. (2011). Modelling the hydrologic role of glaciers within a water evaluation and planning system (WEAP): a case study in the Rio santa watershed (Peru). *Hydrol. Earth Syst. Sci. Discuss.* 8, 869–916. doi:10.5194/hessd-8-869-2011

Código de Aguas, (1981). Decreto con Fuerza de Ley 1122. Libro Primerode las Aguas y del Derecho de Aprovechamiento. Ministerio de Justicia.

Cortés, G. (2010). "Evaluación de un modelo hidrológico semi distribuido para la estimación de la escorrentía de deshielo en el río Juncal," in *Memoria para optar al título de Ingeniero Civil*. Chile: Universidad de Chile. Available at: www.cybertesis.uchile.cl/tesis/uchile/2010/cf-cortes_gs/pdfAmont/cf-cortes_gs.pdf

de Marsily, G., and Abarca-del-Rio, R. (2016). Water and food in the twenty-first century. *Surv. Geophys.* 37, 503–527. 10.1007/s10712-015-9335-1

Decocq, G., Andrieu, E., Brunet, J., Chabrerie, O., De Frenne, P., De Smedt, P., et al. (2016). Ecosystem services from small forest patches in agricultural landscapes. *Curr. Forest. Reports* 2 (1), 30–44. doi:10.1007/s40725-016-0028-x

Demaría, E. M. C., Maurer, E. P., Thrasher, B., Vicuña, S., and Meza, F. J. (2013). Climate change impacts on an alpine watershed in Chile: do new model projections change the story?. *J. Hydrol.* 502, 128–138. 10.1016/j.jhydrol.2013.08.027

DGA (2007). Dirección. General de Aguas. *Evaluación de Recursos Hídricos. Informe Técnico. Departamento de Administración y Recursos Hídricos*. Santiago, SDT No 248.

DGA (2016). Dirección General de Aguas. Available at: http://snia.dga.cl/BNAConsultas/reportes

DGA (2017). Dirección General de Aguas, División de Estudios y Planificación, Ministerio de Obras Públicas Metodología para la Actualización del Balance Hídrico Nacional. Ministerio de Obras Públicas de Chile.

Droogers, P., de Boer, F., and Terink, W. (2014). "Water allocation models for the umbeluzi river basin, Mozambique," in *Wetter Skip Frystan and ARA-Sul Report Future Water*, Netherlands, 132.

Echeverría, C., Newton, A., Nahuelhual, L., Coomes, D., and Rey-Benayas, J. M. (2012). How landscapes change: integration of spatial patterns and human processes in temperate landscapes of southern Chile. *Appl. Geogr.* 32, 822–831. doi:10.1016/j.apgeog.2011.08.014

Energía, M. d. (2016). *Estudio de cuencas. Análisis de las condicionantes para el desarrollo hidroeléctrico en las cuencas del Maule, Biobío, Toltén, Valdivia, Bueno, Puelo, Yelcho, Palena, Cisnes, Aysén, Baker y Pascua*. Santiago: Gobierno de Chile, 104.

Falvey, M., and Garreaud, R. D. (2009). Regional cooling in a warming world: recent temperature trends in the southeast Pacific and along the west coast of subtropical South America (1979–2006). *J. Geophys. Res. Atmos* 114, D04102. 10.1029/2008JD010519

Fan, M., Hideaki, S., and Wang, Q. (2016). Optimal conservation planning of multiple hydrological ecosystem services under land use and climate changes in Teshio river watershed, northernmost of Japan. *Ecol. Indicat.* 62, 1–13. 10.1016/j.ecolind.2015.10.064

FAO (2015). Organización de Las naciones Unidad para la Alimentación y la Agricultura. Estudio: Perspectivas de la Agricultura y del Desarrollo Rural en las Américas 2015–2016. ISBN 978-92-9248-577-1. San José, Costa Rica 2015.

Fernández-Alberti, S., Rubilar, O., Tortella, G. R., and Diez, M. C. (2012). Chlorpyrifos degradation in a Biomix: effect of pre-incubation and water holding capacity. *J. Soil Sci. Plant Nutr.* 12 (4), 785–799. doi:10.4067/S0718-95162012005000032

Figueroa, E. (2010). *Valorización Económica Detallada de las Áreas Protegidas. Proyecto GEF SNAP "Creación de un Sistema Nacional Integral de áreas protegidas*. Santiago Chile.

Figueroa, E. (2009). "Valor Económico de la Contribución Anual del Sistema Nacional de Áreas Protegidas de Chile y Análisis de su Financiamiento"; en Comisión Nacional del Medioambiente-Chile (CONAMA), Programa de Naciones Unidas para el Desarrollo (PNUD) y World Bank-Global Environmental Facility (GEF)," in *Creación de un Sistema Nacional Integral de Áreas Protegidas para Chile. Net impresores SpA*. Santiago, Chile, 107–280.

Forni, L. G., Galaitsi, S. E., Mehta, V. K., Escobar, M. I., Purkey, D. R., Depsky, N. J., et al. (2016b). Exploring scientific information for policy making under deep uncertainty. *Environ. Model. Software* 86, 232–247. doi:10.1016/j.envsoft.2016.09.021

Forni, L. G., Medellín-Azuara, J., Tansey, M., Young, Ch., Purkey, D., and Howitta, R. (2016a). Integrating complex economic and hydrologic planning models: an application for drought under climate change analysis. *Water Res. Econom.* 16, 15–27. doi:10.1016/j.wre.2016.10.002

Gao, Y., Zhang, S. X., Geng, R. T., Ren, G. P., Cui, L. W., and Xiao, W. (2020). Control selection for the assessment of protected areas in the hengduan mountains: a case study in yunlong tianchi national nature reserve, China. *Global Ecology and Conservation* 23, e01170. doi:10.1016/j.gecco.2020.e01170

Garreaud, R., Vuille, M., Compagnucci, R., and Marengo, J. (2009). Present-day south American climate. *Palaeogeogr. Palaeoclimatol. Palaeoecol.* 281 (3), 180–195. doi:10.1016/j.palaeo.2007.10.032

Harma, K. J., Johnson, M. S., and Cohen, S. J. (2012). Future water supply and demand in the Okanagan Basin, British Columbia: a scenario-based analysis of multiple, interacting stressors. *Water Resour. Manage* 26, 667–689. doi:10.1007/s11269-011-9938-3

Huber, R., Rigling, A., Bebi, P., Brand, F. S., Briner, S., Buttler, A., et al. (2013). Sustainable land use in mountain regions under global change: synthesis across scales and disciplines. *Ecol. Soc.* 18 (3), 36. doi:10.5751/ES-05499-180336

IDE (2017). Infraestructura de Datos Geoespaciales de Chile. Available at: www.ide.cl.

Immerzeel, W., Lutz, A., Andrade, M., Bahl, A., Biemans, H., Bolch, T., et al. (2020). Importance and vulnerability of the world's water towers. *Nature* 577, 364–369. doi:10.1038/s41586-019-1822-y

INE (2007). Instituto. Nacional de Estadísticas Chile Censo agrícola. Santiago, Chile. Available at: http://www.ine.cl/canales/chile_estadistico/censos_agropecuarios/censo_agropecuario_07.php.

INE (2014). Instituto. Nacional de Estadísticas Chile tablas generales de Estadísticas de Población y vitales. ISBN: 978-956-323-178-6.

INE (2015). Instituto. Nacional de Estadísticas Chile tablas generales de Estadísticas de Población y vitales. ISBN: 978-956-323-166-3.

Iroumé, A., and Palacios, H., (2013). Afforestation and changes in forest composition affect runoff in large river basins with pluvial regime and Mediterranean climate, *Chile J. Hydrol.* 505, 113–125. 10.1016/j.jhydrol.2013.09.031

Jorquera-Jaramillo, C., Vega, J.M., Jaime Aburto, J., Martínez-Tillería, K., León, M.F., Pérez, M.A., et al. (2012). Biodiversity conservation in Chile: new challenges and opportunities in terrestrial and marine coastal ecosystems. *Rev. Chil. Hist. Nat.* 85, 267–280. doi:10.4067/S0716-078X2012000300002

Konapala, G., Mishra, A. K., Wada, Y., and Mann, M. E. (2020). Climate change will affect global water availability through compounding changes in seasonal precipitation and evaporation. *Nat. Commun.* 11 (1), 3044. doi:10.1038/s41467-020-16757-w

Kurz, W. A., Stinson, G., Rampley, G. J., Dymond, C. C., and Neilson, E. T. (2008). Risk of natural disturbances makes future contribution of Canada's forests to the global carbon cycle highly uncertain. *Proc. Nat. Acad. Sci.* 105, 1551–1555. doi:10.1073/pnas.0708133105

Larraín, S. (2012). Water in Chile: Inbetween human rights and the rules of market. *Polis Revista Latinoamenricana*. Available at: http://journals.openedition.org/polis/5091.

Larraín, S., Aedo, M., Navarrete, K., and Villarroel, C. (2010). *Marco Jurídico para la Gestión del Agua en Chile. Diagnóstico y Desafíos. Programa Chile Sustentable and Fundación Heinrich Böll*. I.S.B.N.: 978-956-7889-44-0.

Little, C., Lara, A., McPhee, J., and Urrutia, R. (2009). Revealing the impact of forest exotic plantations on water yield in large scale watersheds in South-Central Chile. *J. Hydrol.* 374, 162–170. doi:10.1016/j.jhydrol.2009.06.011

Liu, J., Li, J., Qin, K., Zhou, Z., Yang, X., and Li, T. (2017). Changes in land-uses and ecosystem services under multi-scenarios simulation. *Sci. Total Environ.* 586, 522–526. 10.1016/j.scitotenv.2017.02.005

Liu, Y., Gupta, H., Springer, E., and Wagener, T. (2008). Linking science with environmental decision making: experiences from an integrated modeling approach to supporting sustainable water resources management. *Environ. Model. Software* 23, 846–858. doi:10.1016/j.envsoft.2007.10.007

Luebert, F., and Pliscoff, P. (2006). Sinopsis bioclimática y vegetacional de Chile. Editorial Universitaria. Instituto de Geografía. Pontificia Universidad Católica de Chile. ISBN 9789561125759.

Maliehe, M., and Mulungu, D. M. (2017). Assessment of water availability for competing uses using SWAT and WEAP in South Phuthiatsana catchment, Lesotho. *Phys. Chem. Earth* 100, 305–316. doi:10.1016/j.pce.2017.02.014

MEA (2005). *Ecosystems and human well-being: synthesis*. Washington DC: Island Press.

Mehta, V. K., Haden, V. R., Joyce, B. A., Purkey, D. R., and Jackson, L. E. (2013). Irrigation demand and supply, given projections of climate and land-use change, in Yolo County, California. Agric. *Water Manag.* 117, 70–82. 10.1016/j.agwat.2012.10.021

MOP (2016). Dirección general de Aguas (DGA), Atlas del agua en Chile. I.S.B.N. 978-956-7970-30-8.

MMA (2014). *Quinto Informe Nacional de Biodiversidad de Chile ante el Convenio sobre la Diversidad Biológica (CBD)*. Chile, 140.

MMA (2015). Available at: http://www.mma.gob.cl/1304/articles-50880_docomunicadoCambioClimatico.pdf.

MMA (2016). Anteproyecto Plan de Acciótn Nacional de Cambio Climático (2017-2022), Departamento de Cambio Climáttico. Ministerio del Medio Ambiente.

Miranda, A., Altamirano, A., Cayuela, L., Pincheira, F., and Lara, A. (2015). Different times, same story: native forest loss and landscape homogenization in three physiographical areas of south-central Chile. *Appl. Geogr.* 60, 20–28. doi:10.1016/j.apgeog.2015.02.016

Mittermeier, R. A., Gil, P. R., Hoffmann, M., Pilgrim, J., Brooks, T., Mittermeier, C. G., et al. (2004). Hotspots revisted: earth's biologically wealthiest and most threatened ecosystems. México D.F.: CEMEX, 99–103.

Momblanch, A., Paredes-Arquiola, J., and Andreu, J. (2017). Improved modelling of the freshwater provisioning ecosystem service in water scarce river basins. *Environ. Model. Software* 94, 87–99. 10.1016/j.envsoft.2017.03.033

Moreira-Muñoz, A., and Troncoso, J. (2014). "Representatividad biogeográfica de las Reservas de la Biosfera de Chile," in *Reservas de la Biósfera de Chile: laboratorios para la Sustentabilidad*. Editors A. Moreira-Muñoz and A. Borsdorf, Santiago: serie Geolibros, Academia de Ciencias Austriaca, Pontificia Universidad Católica de Chile, Instituto de Geografía, 17, 24–61.

Mori, A. S., Lertzman, K. P., and Gustafsson, L. (2017). Biodiversity and ecosystem services in forest ecosystems: a research agenda for applied forest ecology. *J. Appl. Ecol.* 54 (1), 12–27. doi:10.1111/1365-2664.12669

Mulungu, D. M., and Taipe, C. I. (2012). "Water evaluation and planning in wami river -basin: application of the WEAP model," in *Bioenergy and Food Security e the BEFS Analysis for Tanzania FAO*, Editor E. Beall 54, 47–69.

Nahuelhual, L., Carmona, A., Lara, A., Echeverría, C., and Gonzalez, M. E. (2012). Land-cover change to forest plantations: proximate causes and implications for the landscape in South-Central Chile. *Landsc. Urban Plann.* 107 (1), 12–20.

Naranjo, J. A., and Moreno, H. Y. (2005). *Geología del volcán Llaima, Región de la Araucanía. Servicio nacional de Geología y minería, Carta Geológica de Chile, Serie Geología Básica*. Santiago Chile.

Nelson, E., Mendoza, G., Regetz, J., Polasky, S., Tallis, H., and Cameron, D. R. (2009). Modeling multiple ecosystem services, biodiversity conservation, commodity production, and tradeoffs at landscape scales. *Front. Ecol. Environ.* 7, 4–11. doi:10.1890/080023

ODEPA (2015). Ministerios de Agricultura. Estudio: "Región de la Araucanía información regional 2015

ODEPA (2018). Ministerios de Agricultura Información regional. Región de La Araucanía.

Orrego, R., Abarca del Río, R., Ávila, A., and Morales, L. (2016). Enhanced mesoscale climate projections in TAR and AR5 IPCC scenarios: a case study in a Mediterranean climate (Araucanía Region, south central Chile). *SpringerPlus* 5, 1669. doi:10.1186/s40064-016-3157-6

Purkey, D., Joyce, B., Vicuna, S., Hanemann, M., Dale, L., Yates, D., et al. (2008). Robust analysis of future climate change impacts on water for agriculture and other sectors: a case study in the sacramento valley. *Climatic Change* 87 (Suppl. 1), S109–S122. doi:10.1007/s10584-007-9375-8

Qintana, J., and Aceituno, P. (2012). Changes in the rainfall regime along the extratropical west coast of South America (Chile): 30-43°S. *Atmósfera* 25 (3450), 1–22.

Rahbek, C., Borregaard, M. K., Antonelli, A., Colwell, R. K., Holt, B. G., Nogues-Bravo, D., et al. (2019b). Building mountain biodiversity: geological and evolutionary processes. *Science* 365 (6458), 1114–1119. 10.1126/science.aax0151

Rahbek, C., Borregaard, M. K., Colwell, R. K., Dalsgaard, B., Holt, B. G., Morueta-Holme, N., et al. (2019a). Humboldt's enigma: what causes global patterns of mountain biodiversity? *Science* 365 (6458), 1108–1113. 10.1126/science.aax0149

Rubilar, A. (1994). Diversidad ictiológica en depósitos continentales miocenos de la Formación Cura-Mallín, Chile (37-39°S): implicancias paleogeográficas. *Rev. Geol. Chile* 21 (1), 3–29. 10.5027/andgeoV21n1-a01

Rubio-Álvarez, E., and McPhee, J. (2010). Patterns of spatial and temporal variability in streamflow records in south central Chile in the period 1952–2003. *Water Resour. Res.* 46, W05514. doi:10.1029/2009WR007982

Sample, J. E., Baber, I., and Badger, R. (2016). A spatially distributed risk screening tool to assess climate and land use change impacts on water-related ecosystem services. *Environ. Model. Softw.* 83, 12–26. 10.1016/j.envsoftdoi:.2016.05.011

Santibáñez, F., Santibáñez, P., Caroca, C., González, P., Gajardo, N., Pery, P., Simonetti, J. Y., and Pliscoff, P. (2013). Plan de acción para la adaptación y conservación de la biodiversidad en un contexto de adaptación al cambio climático. Fundación facultad de Ciencias Agronómicas Universidad de Chile, Santiago de Chile.

Schulz, J. J., Cayuela, L., Benayas, Rey., J. M.and Schroeder, B. (2011). Factors influencing vegetation cover change in Mediterranean Central Chile (1975-2008). *Appl. Veg. Sci.* 14, 571–582. doi:10.1111/j.1654-109X.2011.01135.x

Sieber, J., Swartz, C., and Huber-Lee, D. (2005). *WEAP water evaluation and planning system user guide for WEAP21*. Stockholm: Environment Institute.

Tidwell, V., and Moreland, B. (2016). Mapping water consumption for energy production around the Pacific Rim. *Environ. Res. Lett.* 11, 094008. doi:10.1088/1748-9326/11/9/094008

UNESCO-MAB, Schaaf, T. (1995). "Integrated mountain research and environmental conservation," in Conference paper No. 21 of EuroMAB IV symposium on mountain zonality facing global change. Editor En A. Breymeyer. Institute of Geography and Spatial Organization, 9-16.

USGS (2016). Geological surveyscience for a changing world. Available at: www.usgs.gov/

Valdés-Pineda, R., Pizarro, R., García-Chevesich, P., Valdés, J. B., Olivares, C., Vera, M., et al. (2014). Water governance in Chile: availability, management and climate change. *J. Hydrol.* 519, 2538–2567. 10.1016/j.jhydrol.2014.04.016

Van Loon, A., and Doogers, P. (2006). Water evaluation and planning system. Kitui Kenya-report N° 2. Kenya.

Vicuña, S., Garreaud, R. D., and McPhee, J. (2011). Climate change impacts on the hydrology of a snowmelt driven basin in semiarid Chile. *Clim. Change* 105, 469–488. doi:10.1007/s10584-010-9888-4

Viviroli, D., Kummu, M., Meybeck, M., Kallio, M., and Wada, Y. (2020). Increasing dependence of lowland populations on mountain water resources. *Nature Sust.* 3, 917–928. 10.1038/s41893-020-0559-9

World Bank (2011). Departamento de Medio Ambiente y Desarrollo Sostenible Región para América Latina y el Caribe. Chile, Diagnóstico de la gestión de los recursos hídricos.

WWAP (2014). Programa Mundial de Evaluación de los Recursos Hídricos. Informe Mundial sobre el Desarrollo de los Recursos Hídricos 2014: agua y

energía. Available at: http://www.unesco.org/new/es/natural-sciences/environment/water/wwap/wwdr/

Yan, D., Wernersa, S. E., Ludwiga, F., and Huang, H. Q. (2015). Hydrological response to climate change: the Pearl River, China under different RCP scenarios. *J. Hydrol. Reg. Stud.* 4, 228–245. doi:10.1016/j.ejrh.2015.06.006

Yang, X., Li, J., Qin, K., Li, T., and Liu, J. (2015). Trade-offs between ecosystem services in guanzhong-tianshui economic region. *Acta geograph. Sin.* 4, 1762–1773. doi:10.11821/dlxb201511006

Yates, D., Purkey, D., Sieber, J., Huber-Lee, A., and Galbraith, H. (2005a). WEAP21 – a Demand-,Priority-, and preference-driven water planning model. Part 2: aiding freshwater ecosystem service evaluation. *Water Int.* 30 (4), 501–512. doi:10.1080/02508060508691894

Yates, D., Sieber, J., Purkey, D., and Huber-Lee, A. (2005b). WEAP21-A demand-, priority-, and preference-Driven Water Planning Model: Part 1: model characteristics. *Water Int.* 30 (4), 487–500. doi:10.1080/02508060508691893

Yates, D., Purkey, D., Sieber, J., Huber-Lee, A., Galbraith, H., West, J., et al. (2007). A physically-based, water resource planning model of the Sacramento Basin, California USA. *ASCE J. Water Res. Manag.* (inpress)

Yates, D., Purkey, D., Sieber, J., Huber-Lee, A., Galbraith, H., West, J., et al. (2009). Climate driven water resources model of the sacramento basin, California. J. Water Resour. Plan. Manag. 135.

Young, C. A., Escobar, M. I., Fernandes, M., Joyce, B., Kiparsky, M., Mount, J. F., et al. (2009). Modeling the hydrology of climate change in California's Sierra Nevada for subwatershed scale. Adaptation1. *J. Am. Water Resour. Assoc.* 45, 1409–1423. doi:10.1111/j.1752-1688.2009.00375.x

Zhang, J. C., Zhong, R., Zhao, P., Zhang, H. W., Wang, Y., and Mao, G. Z. (2016). International energy trade impacts on water resource crises: an embodied water flows perspective. *Environ. Res. Lett.* 11, 074023. doi:10.1088/1748-9326/11/7/074023

Conflict of Interest: The authors declare that the research was conducted in the absence of any commercial or financial relationships that could be construed as a potential conflict of interest.

Copyright © 2021 Fernández-Alberti, Abarca-del-Río, Bornhardt, and Ávila. This is an open-access article distributed under the terms of the Creative Commons Attribution License (CC BY). The use, distribution or reproduction in other forums is permitted, provided the original author(s) and the copyright owner(s) are credited and that the original publication in this journal is cited, in accordance with accepted academic practice. No use, distribution or reproduction is permitted which does not comply with these terms.

frontiers in Earth Science

REVIEW
published: 18 February 2021
doi: 10.3389/feart.2020.505467

Hydroclimate of the Andes Part II: Hydroclimate Variability and Sub-Continental Patterns

Paola A. Arias[1], René Garreaud[2], Germán Poveda[3], Jhan Carlo Espinoza[4], Jorge Molina-Carpio[5], Mariano Masiokas[6], Maximiliano Viale[6], Lucia Scaff[7] and Peter J. van Oevelen[8]*

[1]Grupo de Ingeniería y Gestión Ambiental (GIGA), Escuela Ambiental, Facultad de Ingeniería, Universidad de Antioquia, Medellín, Colombia, [2]Department of Geophysics, Universidad de Chile, Santiago, Chile, [3]Department of Geosciences and Environment, Universidad Nacional de Colombia, Medellín, Colombia, [4]Université Grenoble Alpes, IRD, CNRS, G-INP, IGE (UMR 5001), Grenoble, France, [5]Instituto de Hidráulica e Hidrología (IHH), Universidad Mayor de San Andrés, La Paz, Bolivia, [6]Instituto Argentino de Nivología, Glaciología y Ciencias Ambientales (IANIGLA), CCT CONICET, Mendoza, Argentina, [7]Global Water Futures, CFREF, University of Saskatchewan, Saskatoon, SK, Canada, [8]International GEWEX Project Office, George Mason University, Fairfax, VA, United States

This paper provides an updated review of the most relevant scientific literature related to the hydroclimate of the Andes. The Andes, the longest cordillera in the world, faces major challenges regarding climate variability and climate change, which impose several threats to sustainable development, including water supply and the sustainability of ecosystem services. This review focuses on hydroclimate variability of the Andes at a sub-continental scale. The annual water cycle and long-term water balance along the Andes are addressed first, followed by the examination of the effects of orography on convective and frontal precipitation through the study of precipitation gradients in the tropical, subtropical and extratropical Andes. In addition, a review is presented of the current scientific literature on the climate variability in the Andes at different timescales. Finally, open research questions are presented in the last section of this article.

Keywords: Andes, hydroclimate, hydrological cycle, climate variability, orographic precipitation

OPEN ACCESS

Edited by:
David Glenn Chandler, Syracuse University, United States

Reviewed by:
Mario Cordova, Universidad de Cuenca, Ecuador
James P. McNamara, Boise State University, United States

****Correspondence:***
Paola A. Arias
paola.arias@udea.edu.co

Specialty section:
This article was submitted to Hydrosphere, a section of the journal Frontiers in Earth Science

Received: *16 October 2019*
Accepted: *01 December 2020*
Published: *18 February 2021*

Citation:
Arias PA, Garreaud R, Poveda G, Espinoza JC, Molina-Carpio J, Masiokas M, Viale M, Scaff L and van Oevelen PJ (2021) Hydroclimate of the Andes Part II: Hydroclimate Variability and Sub-Continental Patterns. Front. Earth Sci. 8:505467. doi: 10.3389/feart.2020.505467

INTRODUCTION

Due to its latitudinal extension and its prominent topography, the Andes Cordillera is characterized by a wide variety of mountain climates, from very humid conditions like the cloud forest and paramo in the tropics and the western Patagonia in the extratropics, to the hyper arid conditions in the subtropics, like the Atacama Desert. The Andes provides ecosystem services, such as the provision of fresh water to near 90 million people in seven countries (Venezuela, Colombia, Ecuador, Peru, Bolivia, Chile and *Argentina*) (Schoolmeester et al., 2018). At the same time, the Andes range sets the stage for the occurrence of disasters due to the presence of steep terrains, hydrometeorological extreme events that are exacerbated by hydroclimate variability, climate change, deforestation and land use changes (Poveda et al., 2020).

Given the importance of the Andes in terms of biodiversity and ecosystem services provided to largely populated regions in South America, an adequate understanding of the regional hydroclimate is mandatory. Few studies have provided comprehensive reviews of current knowledge regarding the hydroclimate variability in the Andes. Among them, Rabatel et al. (2013), Vuille et al. (2018), and Masiokas et al. (2020) focused on the Andean cryosphere. In addition, Berbery and Barros (2002)

described the hydrologic cycle of the La Plata basin in Southeastern South America. Marengo and Espinoza (2016) reviewed the hydroclimatic variability of the Amazon river basin, including the eastern flank of the Andes, with a particular emphasis on observed and projected extreme hydrological events.

The current study is part of a series of review papers focused on the diverse aspects of climate, weather, hydrology and cryosphere of the Andes cordillera. Among them, Pabón-Caicedo et al. (2020) provided a review on observed and projected changes in the hydroclimate of the Andes including temperature and precipitation variability in the Andes throughout the last two millennia. Poveda et al. (2020) reviewed the climatological occurrence of high impact weather events in the Andes and Condom et al. (2020) discussed the current observational and monitoring hydrometeorological networks in the Andes. These reviews provide a state-of-the-art synthesis of current knowledge, as part of the ANDEX initiative. ANDEX is a prospective Regional Hydrological Project (RHP) of the Global Energy and Water Cycle Exchanges (GEWEX; https://www.gewex.org/) project of the World Climate Research Program (WCRP; https://www.wcrp-climate.org/). For more details, see Part I (Espinoza et al., 2020).

In this study, recent advances regarding the Andean hydroclimate are assessed and discussed. An integrated overview from the northern Andes to Patagonia is taken into account. This study is presented in two parts. Part I (Espinoza et al., 2020) is dedicated to summarize the mean large-scale atmospheric circulation that characterizes the hydroclimate of the Andes and the annual cycles of precipitation and runoff. This second part addresses the hydroclimate variability of the Andes at a sub-continental scale. Here, the annual long-term water balance and the annual cycle of hydrological fluxes (precipitation and runoff) along the Andes are addressed. Then the effects of orography on precipitation through the study of precipitation gradients at low and mid-latitudes are discussed. Finally, the current knowledge on climate variability in the Andes at subseasonal, interannual and decadal timescales are presented.

HYDROLOGICAL PROCESSES

Surface hydrology in the Andes exhibits a variety of annual cycles along the entire cordillera. Following Espinoza et al. (2020), this paper is focused on the following subregions: north tropical Andes (north of 8°S), south tropical Andes (8°S-27°S), subtropical Andes (27°S-37°S) and extratropical Andes (south of 37°S). This section provides a review of the main features of the annual water cycle in the Andes, with focus on river discharges and its link to spatio-temporal behavior of rainfall presented in Espinoza et al. (2020). The contributions from glacier melting over the south tropical and extratropical Andes are also discussed.

River Flows

Mean Annual River Flows

The latitudinal and longitudinal contrasts that exist in the mean annual flows of the rivers originating in the Andes are clearly reflected in **Figure 1**. In the north tropical Andes and along the eastern portion of the south tropical Andes, the overall humid conditions result in numerous large to very large rivers with mean annual flows in the order of several hundreds or thousands of cubic meters per second. This is the case, for example, of most rivers draining the upper Amazon and Orinoco basins. Substantially lower flows and smaller rivers can be found on the western, drier portion of the south tropical Andes, where rivers reaching the coasts of Peru usually show mean annual values in the order of tens of cubic meters per second (**Figure 1A**). The contrast between the eastern and western basins is clearly evident along the southern sector of the south tropical Andes: the eastern margins of the Andes in Bolivia and northwestern *Argentina* are characterized by lush mountain rainforests ("yungas") drained by large rivers, but conditions change dramatically to the west, where the extreme arid conditions of the Atacama desert and adjacent regions in northern Chile only allow very few rivers and creeks with small annual flows in the order of 0.1–2 cubic meters per second (**Figure 1A**).

In some upper basins of the south tropical Andes, glacier melt can contribute to the river discharges. Soruco et al. (2015) showed that glaciers contribute around 15% of water resources to the La Paz city (Bolivia) annually, and 14 and 27% during the wet and dry seasons, respectively. Buytaert et al. (2017) estimated the relative contribution of glacial melt to the water supply of selected main cities of the south tropical Andes characterized by different meteorological conditions, finding a mean annual glacier melt contribution of 2.2% in Quito (Ecuador), <1% in *Lima* (Peru), and 19% in Huaraz (located in the upper Santa River basin in Peru). Glacier contribution to local water supply is clearly sensitive to the occurrence of extreme droughts, increasing its relevance during dry years when precipitation over the basin is reduced to a minimum (e.g., Dussaillant et al., 2019; Masiokas et al., 2020). The increasing frequency of these events, overlapped with the ongoing shrinking trend in Andean glaciers (Masiokas et al., 2020), will impact the resilience of the local water management systems in the future (Buytaert et al., 2017).

The flows of most rivers on both sides of the subtropical Andes show a strong dependence on seasonal accumulation and subsequent melting of snow in the upper basins (e.g., Masiokas et al., 2006). Here, the drier conditions in the northern basins support smaller rivers than further south, and the longitudinal contrasts between the eastern and western margins of the Andes are not as marked as described above for the south tropical Andes (**Figure 1**). Common mean annual values for the most important rivers in this region range between 10 and 150 cubic meters per second (**Figure 1A**). The Andes at these latitudes contain extensive areas covered by glaciers and permanent ice-rich permafrost features such as rock glaciers (Azócar and Brenning, 2010; Zalazar et al., 2017). Melt water from these ice masses can play an important hydrological role, as shown by a recent study of the Maipo river basin (Ayala et al., 2020). These authors estimated that between 1955 and 2016 glaciers contributed, on average, with ca. 37% of the annual runoff of the basin. This glacier contribution can become especially important during extended dry periods such as those observed in the subtropical Andes region since 2010 (Garreaud et al., 2017; Rivera et al., 2017; Dussaillant et al., 2019).

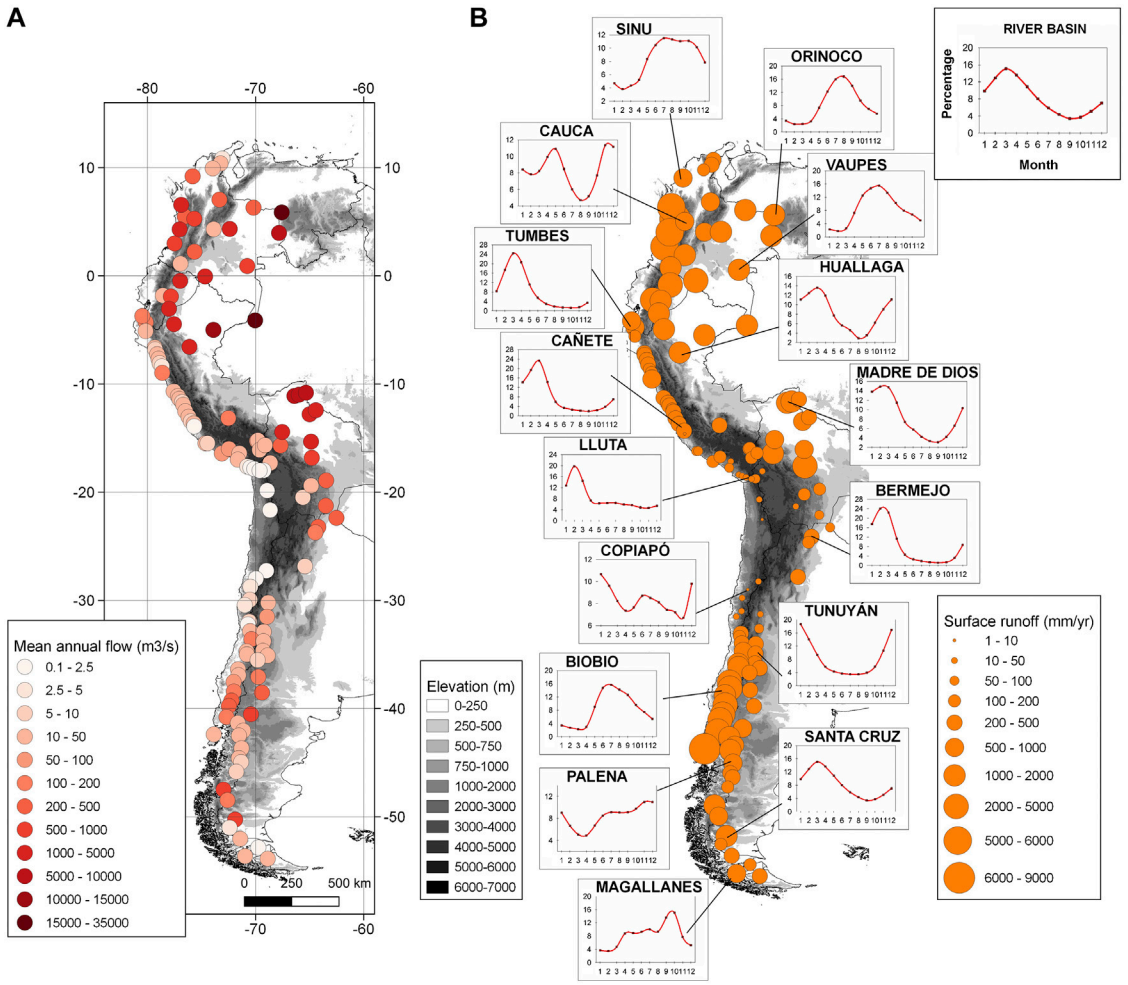


FIGURE 1 | (A) Mean annual streamflow for selected rivers along the Andes. **(B)** Mean annual surface runoff of the same selected rivers. The annual cycles (expressed as monthly percentages relative to the annual totals) are also shown for characteristic river basins to illustrate the marked contrasts that exist along the Andes. Note that these diagrams have different Y-axis scales to highlight the characteristic seasonal variability at each site. X-axis indicates the month of the year (from 1: January to 12: December). Also note that as the period of records can vary among stations (**Table 1**), the values in the figure only provide an overall indication of the long-term mean annual and monthly conditions at each site.

To the south, the extratropical Andes in Patagonia and Tierra del Fuego are lower in elevation and conditions become more humid, usually resulting in larger river flows than those found immediately to the north (**Figure 1A**). Normal mean annual streamflow values can reach several tens to a few hundreds of cubic meters per second for the largest rivers. These values usually depend on the variable amounts of solid and liquid precipitation that falls in the upper basins. In these regions, few cases exist where the glacier cover is extensive enough to have a discernible signal in the annual river flows (Pasquini and Depetris, 2007; Pasquini and Depetris, 2011; Masiokas et al., 2019).

Seasonal Variations in River Flows

The north tropical Andes exhibits unimodal or bimodal regimes on river discharge that respond to the annual cycle of precipitation in the different sectors (see Espinoza et al. (2020) and **Figure 1B**). In Colombia, many river basins located north of the Andes exhibit a bimodal annual cycle with two wet seasons (April-May and September-November; see e.g., the Cauca river in **Figure 1B**) associated with similar patterns in rainfall, evapotranspiration and soil moisture (Mejia et al., 1999; Poveda, 2004; Poveda et al., 2011; Urrea et al., 2019). The bimodal annual cycle of rainfall on the Andes of Colombia results from the combination of the meridional oscillation of the Intertropical Convergence Zone (ITCZ), atmospheric moisture advection by the Choco, Caribbean and Orinoco low-level jets, and strong land surface-atmospheric interactions (Poveda et al., 2014, Poveda et al., 2020; Arias et al., 2015; Hoyos et al., 2017; Bedoya-Soto et al., 2019; Espinoza et al., 2020). Rivers along the Colombian Pacific coast, such as the San Juan river, show discharge peaks around October-November (Velásquez-Restrepo and Poveda, 2019). This pattern is similar to that shown by the Sinu river further north (**Figure 1B**).

Rivers of the eastern Andean basins in Colombia and Ecuador, in contrast, are characterized by unimodal cycles with peaks in

TABLE 1 | General information of the selected runoff gauges corresponding to the mean annual cycles shown in **Figure 1B**.

Id	Country	Station	Lat	Lon	Elevation (m.a.s.l)	Period
BERMEJO	*Argentina*	BERMEJO-POZO SARMIENTO	−23.22	−64.20	296	1986–2015
TUNUYAN	*Argentina*	TUNUYAN-VALLE DE UCO	−33.78	−69.27	1,200	1986–2015
SANTA CRUZ	*Argentina*	SANTA CRUZ-CHARLES FUHR	−50.27	−71.89	206	1986–2015
PALENA	*Argentina*	CARRENLEUFU-LA ELENA	−43.68	−71.30	783	1986–2015
MADRE DE DIOS	Bolivia	MIRAFLORES	−11.11	−66.41	125	1985–2013
LLUTA	Chile	LLUTA EN ALCERRECA	−18.00	−69.63	3,550	1986–2015
COPIAPO	Chile	COPIAPO EN PASTILLO	−28.00	−69.97	1,300	1986–2015
BIO	Chile	DUQUECO EN VILLUCURA	−37.55	−72.03	228	1986–2015
MAGALLANES	Chile	SAN JUAN EN DESEMBOCADURA	−53.65	−70.97	8	1986–2015
SINU	Colombia	PALMA CENTRAL	9.20	−75.82	6	1991–2010
CAUCA	Colombia	IRRA	5.27	−75.67	745	1972–2013
ORINOCO	Colombia	RONCADOR	5.86	−67.58	62	1991–1998
VAUPES	Colombia	LOS CERROS	0.90	−70.77	195	1990–2013
TUMBES	Perú	EL TIGRE	−3.72	−80.47	40	1969–2004
CAÑETE	Perú	SOCSI	−13.03	−76.2	330	1969–2004
HUALLAGA	Perú	CHAZUTA	−6.57	−76.12	150	1986–2010

July-August (see e.g., the Orinoco and Vaupes rivers in **Figure 1B**; Laraque et al., 2007; Arrieta-Castro et al., 2020). These unimodal regimes are associated with low advective shallow clouds causing precipitation, influenced by the advection of water vapor from the Amazon basin and enhanced easterlies during boreal summer (Campozano et al., 2016; Segura et al., 2019). The Ecuadorian Andes, however, also exhibit a large spatial variability in river discharge seasonality and cases with bimodal annual cycles peaking around March-April and October can be found in many intra-Andean basins (Laraque et al., 2007; Campozano et al., 2018). In the lowlands of these intra-Andean basins, the discharge peaks around June-July and October-November (Laraque et al., 2007). These patterns reflect the occurrence of bimodal rainfall regimes, with dry conditions during boreal summer, caused by strong subsidence that inhibits the formation of convective clouds (Campozano et al., 2016; Segura et al., 2019). Rivers of the western Andean basins in Ecuador and northern Peru are characterized by a unimodal pattern with peaks around March-April (see Tumbes river in **Figure 1B**). In this region, the wet season occurs from late December through May, corresponding to the southerly position of the ITCZ (Recalde-Coronel et al., 2014; Rau et al., 2017; Segura et al., 2019).

In the south tropical Andes, the seasonal discharges are usually characterized by unimodal cycles peaking between January and March along both the eastern and western flanks of the mountain range (**Figure 1B**). This pattern reflects the occurrence of the rainy and the dry seasons in December-March and June-August, respectively, and is partly associated with the South American Monsoon (see Espinoza et al. (2020) and *Influence of the Andes Topography on Precipitation*; also Vera, 2006; Espinoza et al., 2011; Lavado-Casimiro et al., 2012; Rau et al., 2017; Molina-Carpio et al., 2017). This relatively consistent unimodal seasonal pattern can be observed in the hydrographs of the Cañete and Lluta river basins along the western, drier portion of the region, and also in the records from the Huallaga, Madre de Dios and Bermejo rivers, located in the upper and much wetter Amazon and La Plata river basins (**Figure 1B**).

In the high subtropical Andes, precipitation usually falls as snow in winter and remains frozen until the onset of the melting season in the spring (October-November). In this sector, most rivers on both sides of the Andes show a unimodal snowmelt-dominated regime with a peak during the warmer months in December-January (see e.g., the Copiapó and Tunuyán rivers in **Figure 1B**; and Masiokas et al., 2006, 2019). Further south in Patagonia and Tierra del Fuego, the extratropical Andes are exposed to the westerlies during most of the year (Garreaud, 2009; Garreaud et al., 2013). This results in a more uniform seasonal distribution of precipitation with mixed contributions of rain and snow, depending on the annual cycle of temperatures and the overall elevation of the different sectors. Rivers in these regions reflect this rather complex hydroclimatic nature of the Andes: some sectors show a single discharge peak due to the higher precipitation levels in winter (e.g., the Bio river in **Figure 1B**), while others also show a peak in spring-early summer due to snowmelt (e.g., the Palena and Magallanes basins, **Figure 1B**; see also Pasquini and Depetris, 2007; Lara et al., 2008; Mundo et al., 2012; Krogh et al., 2015; Masiokas et al., 2019). The two largest rivers of this southernmost portion of the Andes are the Baker and the Santa Cruz rivers, which drain extensive parts of the north and nouth Patagonian Icefields, respectively. The Santa Cruz river, in particular (see **Figure 1B**), drains ca. 3,000 km^2 of glaciated areas and shows a discernible peak in the late summer–early fall largely due to the contribution of ice melt (Pasquini and Depetris, 2007; Pasquini and Depetris, 2011; Masiokas et al., 2019).

Evapotranspiration

The exceptional height of the Andes Mountains conditions the atmospheric circulation at low elevations, and clearly divides the atmospheric moisture sources east and west of the water divide. The Atlantic Ocean as well as the Orinoco, Magdalena and Amazon River basins are the main oceanic and continental water vapor sources for most of the tropical Andes (Sakamoto et al., 2011; Arias et al., 2015; Hoyos et al., 2017) and neighboring regions such as the Altiplano and the Andean part of the La Plata

River basin (Garreaud, 1999; Garreaud et al., 2003; Falvey and Garreaud, 2005; Martinez and Dominguez, 2014; Staal, 2018; Sori et al., 2019; Segura et al., 2020), through the low-level moisture transport. The important Amazon source means that the hydrological cycle and water balance of the tropical Andes system could be particularly sensitive to Amazon land-cover change (see Espinoza et al., 2020). The Pacific Ocean is an important atmospheric moisture source for the western Andes of Colombia (Sakamoto et al., 2011; Arias et al., 2015; Hoyos et al., 2017), northern Peruvian and Ecuadorian Andes (Segura et al., 2019), and the main source for the subtropical and extratropical regions of *Argentina* and Chile (Garreaud et al., 2009).

If changes in storage over time are considered negligible in the long term, the surface (SWB) and atmospheric (AWB) water balance become, respectively:

$$\langle R \rangle = \langle P \rangle - \langle E \rangle$$
$$\langle C \rangle = \langle P \rangle - \langle E \rangle$$

where P is precipitation rate [LT^{-1}], E is evapotranspiration rate [LT^{-1}], R is runoff rate [LT^{-1}] and C is the net moisture convergence (or the moisture that is stored in the atmosphere) (C = -ΛQ, where ΛQ is the net vertically integrated moisture divergence). $\langle\ \rangle$ denotes the long-term mean (Builes-Jaramillo and Poveda, 2018).

Recent water balance estimates by Builes-Jaramillo and Poveda (2018) show that for the Andes-Amazon system, the water balance components are of the same order of magnitude (**Figure 2** of Espinoza et al., 2020). In spite of receiving less precipitation, runoff is higher in the Andean rivers than in the lowland Amazon (Moquet, 2011). This is probably related to the Andes-Amazon spatial rainfall variability. The rainiest Amazon basin regions ("hotspots") occur in the Andes (Espinoza et al., 2015; Chavez and Takahashi, 2017), and also the presence of steep topography that favors higher runoff (Espinoza et al., 2014). Large negative residuals (P-E-R < 0) were detected in two important Andean sub-catchments: Borja (Marañón River) and Rurrenabaque (Andean Beni River) for both the surface and atmospheric water balance. As the uncertainty of runoff records is relatively low, the SWB imbalance in these basins reflects mainly the high spatial variability of P and E (particularly the former) and the low density of meteorological networks. The AWB imbalance (both internally and related to SWB) reflects the uncertainties in the reanalysis data source (Builes-Jaramillo and Poveda, 2018). SWB negative residuals have been also found for many smaller Andean basins (Molina-Carpio et al., 2007; Lavado-Casimiro et al., 2012), suggesting that the study of the components of the water balance in the Andes remains an important research topic. In this sense, the different issues that need to be addressed to better understand the hydrological cycle in the Andes are: 1) the spatial variability of precipitation at different spatial scales and the associated causes (see the following sections); 2) the low density of rainfall and runoff observations in the region (Condom et al., 2020); 3) the generalized lack of permanent atmospheric sounding stations, meteorological radars, and other atmospheric observations (Condom et al., 2020); 4) the combined roles of diverse atmospheric low-level jets and atmospheric rivers in the transport of atmospheric moisture to the Andes (e.g., Sakamoto et al., 2011; Arias et al., 2015; Chavez and Takahashi, 2017; Hoyos et al., 2017; Kumar et al., 2019; Segura et al., 2020); 5) evapotranspiration and moisture recycling processes from the rainforest to the Andes (e.g, Molina et al., 2019; Ampuero et al., 2020; Ruiz-Vasquez et al., 2020); 6) the high amounts of precipitation recycling in the tropical Andes (70–90%) (e.g., Zemp et al., 2014; Zemp et al., 2017; Staal, 2018); 7) the land-atmosphere interactions in the Andes (e.g., Saavedra et al., 2020); 8) the role of groundwater processes in the Andes (karts dynamics, for instance) and its influence on surface hydrology and sediment transport processes (e.g., Tovar Pacheco et al., 2006; Ayes Rivera et al., 2003–2016; Olarinoye et al., 2020); 8) the effects of climate change, deforestation, and land use changes on different water fluxes and storages along the Andes (e.g., Pabón-Caicedo et al., 2020); 9) the physical processes controlling the formation of floods and droughts along the Andes; among others.

Long-Term Water Balance

The mean annual value of reference evapotranspiration (ET_0) (i.e. the rate at which water, if available, would be removed from the soil and plant surface of a specific crop (FAO, 1998)), ranging from 900 to more than 2000 mm/yr, is greater than annual precipitation in the Altiplano region (Chaffaut, 1998; Molina-Carpio et al., 2014). In the northern Altiplano, the Lake Titicaca plays an important regulation role for the local climate and hydrology. In the arid southern Altiplano, extremely arid northern Chile and northwestern *Argentina*, which are the regions on Earth that receive the greater net solar radiation (e.g., Rondanelli et al., 2015), ET_0 is at least one order of magnitude bigger than precipitation (Molina-Carpio, 2007). In most of these regions, runoff can only occur in relation to groundwater storage (aquifers). Thus, more than 95% of surface water comes from groundwater dated to some thousands of years (Aravena, 1995; Chaffaut, 1998; Molina-Carpio, 2007).

Furthermore, the Altiplano is very sensitive to climate (Coudrain et al., 2002; Garreaud et al., 2003) and anthropogenic changes (Minvielle and Garreaud, 2011; Satgé et al., 2017). Even small changes in the water cycle components can put at risk the Altiplano hydrological and natural systems and its population. Given the lack of outlet drainage, the surface water storage in endorheic catchments depends critically on the equilibrium among precipitation, evapotranspiration and groundwater exchange. This equilibrium is affected, for example, by increases in agricultural land and irrigation in the Altiplano, which intensifies evapotranspiration water losses (Torres-Batlló et al., 2020). Evaporation from lakes and soils may also be exacerbated by warming temperatures, which is a trend already detected for the region (Hunziker et al., 2018). In a recent study, Segura et al. (2020) documented that rainfall variability over the Altiplano is also modulated by deep convection in the western Amazon, particularly since 2000. All this highlights the urgent need for proper water management at the basin scale.

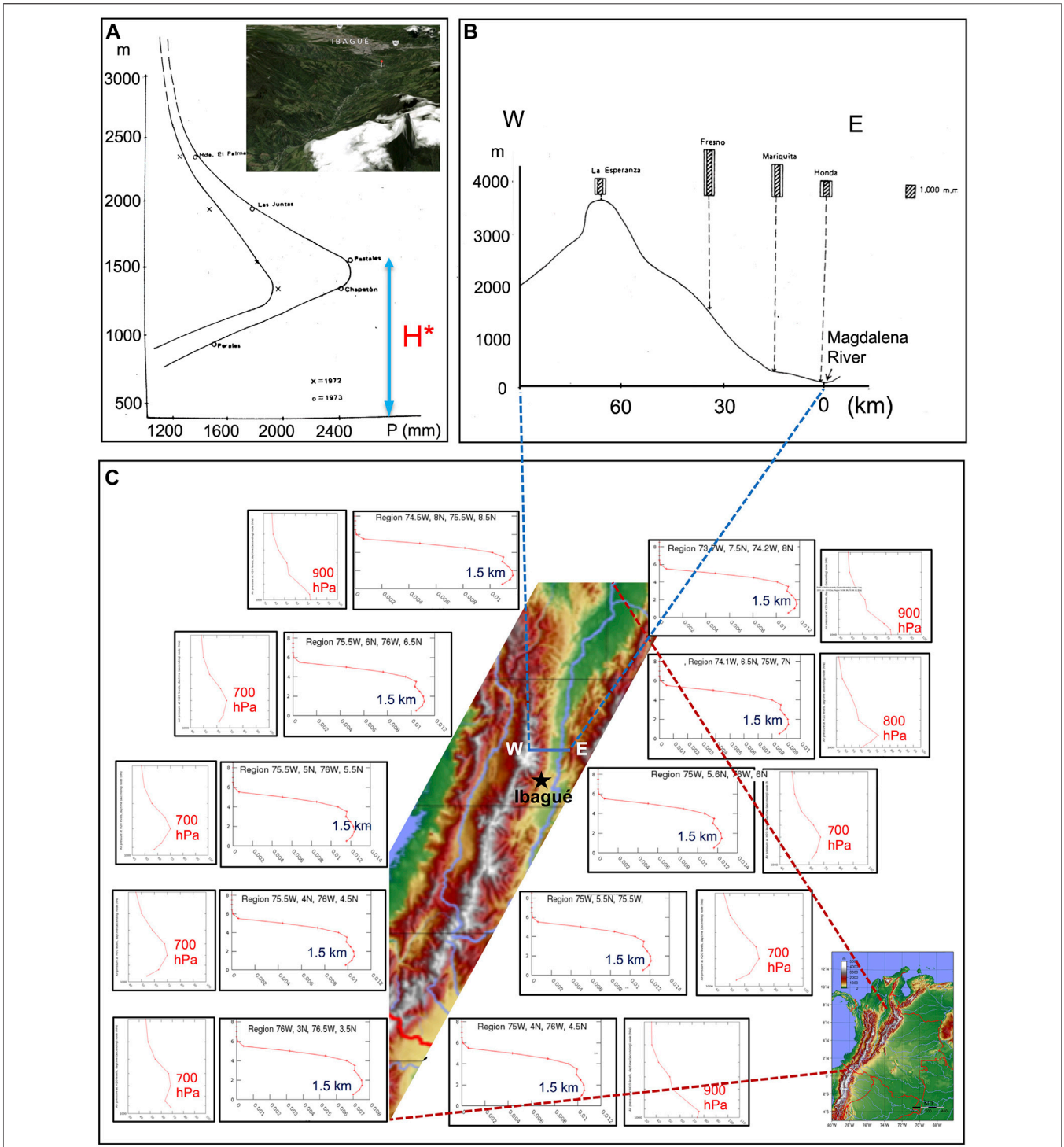


FIGURE 2 | (A) Distribution of rainfall with elevation during 1972 and 1973 along the western slope of the intra-Andean valley of the Combeima River basin, located along the eastern slope of the Central range of Colombian Andes. Adapted from Oster (1979). The inset shows the Combeima River valley and the city of Ibagué, denoted with a black star on panel **(C)**. Source: Google Maps. **(B)** Distribution of long-term mean annual rainfall with elevation and distance to the floor of the Magdalena River valley along the eastern slope of the Central Andes of Colombia around 5°N (W-E transect on panel **(C)**. Adapted from Oster (1979). **(C)** Vertical cross-sections of long-term mean TRMM rainfall data (3A12 V7) and relative humidity (AIRX3STM v006), along diverse transects over the western and eastern slopes of the Central Andes of Colombia. These figures were produced using the Giovanni online tool (https://giovanni.gsfc.nasa.gov/giovanni/).

Considering the large spatial variability of water availability on both sides of the Peruvian Andes, actual evapotranspiration shows high differences according to the relative magnitude of the local water balance components. Few studies have estimated evapotranspiration in the Peruvian Andes. For instance, Lavado-Casimiro et al. (2011), using the modified Hargreaves–Samani method, found a mean annual evapotranspiration of 564 mm/yr and 996 mm/yr in the Vilcanota and Urubamba river basins (Cuzco), respectively. In the Mantaro basin (central Peruvian Andes), these authors estimate that the mean annual evapotranspiration is 648 mm/yr. Due to increased water availability in the Amazonian region, evapotranspiration increases, reaching 1,230 mm/yr and 1,030 mm/yr in average over the Ucayali and Huallaga basins, respectively (Lavado-Casimiro et al., 2011). In the basins of the arid Pacific coast of Peru, evapotranspiration varies from 300 to 500 mm/yr, with the greatest values in the Moche and upper Santa river basins in the central Peruvian Andes (Rau et al., 2017). Using a set of meteorological sensors of latent heat fluxes installed in a gradient tower 30 m high in the Huancayo observatory (central Peruvian Andes, 3,312 m.a.s.l.), Flores-Rojas et al. (2019a) show a clear annual cycle of latent heat fluxes with monthly maximum in February-March and monthly minimum in June-July. In the Peruvian Pacific drainage, ET_0 is higher than precipitation over most of the year (with exception of the December-March rainy season). Consequently, river runoff in the central and southern Pacific basins occurs most of the year in relation to changes in groundwater storage and, in some cases, to glacier contributions (Buytaert et al., 2017). In relation to these hydrological characteristics, agriculture over this region is highly dependent on national special irrigation projects that regulate the annual water availability (e.g., ANA, 2012). In the arid Pacific coast of Peru, groundwater is largely exploited for supply to the population and agriculture, such as the case of *Lima* and Ica regions (Tovar Pacheco et al., 2006). In the Peruvian Andes, UNESCO (2006) estimated that the available surface water (difference between rainfall and evapotranspiration) is 16.5 mm/yr in the basins of the Pacific watershed, 130 mm/yr in the Titicaca basins, and 2,700 mm/yr in the Peruvian Amazon, considering the 1969–2009 period.

In the extremely dry environment of the subtropical Andes, snow accumulated over altitudes above 2000 m.a.s.l is subject to high levels of intensive sublimation, a process that represents a significant loss of water for this semiarid region. Unfortunately, the lack of micro-meteorological data in this region precludes a detailed assessment of sublimations rates, as reported by Réveillet et al. (2019). The contribution of melt and sublimation to total ablation has been studied at both the point-scale (MacDonell et al., 2013) and catchment scale (Gascoin et al., 2013) in one catchment in the semi-arid Andes. MacDonell et al. (2013) estimated that the sublimation fraction was 90% of total ablation at altitudes above 5,000 m.a.s.l., in an extreme environment with predominantly sub-freezing temperatures and strong local wind speeds. On the basis of snow modeling, Gascoin et al. (2013) found that the total contribution of sublimation to total ablation in the Pascua-Lama area (29.3° S, 70.1°W; 2,600–5,630 m.a.s.l.) was 71%.

INFLUENCE OF THE ANDES TOPOGRAPHY ON PRECIPITATION

The Andes exhibits a complex topography that induces spatio-temporal hydroclimate variability at different scales. In particular, precipitation in the Andes is strongly influenced not only by the large-scale weather patterns, including the low-level jets (as described in Espinoza et al., 2020), but also by the interaction of these atmospheric moisture fluxes with orography. This section reviews the main orographic effects on convective (over the tropics and the subtropics) and frontal (over the subtropics and the extratropics) precipitation in the Andes.

Orographic Effects on Convective Precipitation Systems in the Tropical and Subtropical Andes

The orography of the Andes plays a key role on the initiation and evolution of convective precipitation systems, which dominate over and around the tropical and subtropical Andes. The orography strongly modulates the availability of atmospheric moisture and contributes ascending air masses aloft the mountain range, two key ingredients for convection initiation year-round in the tropics and during summer in the subtropics. Terrain-forced and thermally driven diurnal mountain winds are the two main forms of orographic lifting by which topography influences convective activity (e.g., chapters 2 and 3 of Chow et al., 2013). Terrain-forced winds occur when large-scale circulation, normally continental easterly winds in the tropics, encounter the topography and are forced to ascent following the shape of the terrain. The origin of thermal diurnal mountain winds is the strong solar radiation heating on the surface, which in turn induces temperature gradients that generate the diurnal circulations between the air immediately above the mountain terrain, and the air surrounding the mountain terrain at the same level. As a general rule, air moves upward (anabatic winds) during daytime from lower sectors, adjacent plains and valley floor, to higher elevations of the mountain range, following the slope and valley shapes (Bedoya-Soto et al., 2019). The opposite behavior occurs during late afternoon and nighttime (katabatic winds) (e.g., Lopez and Howell, 1967; Bendix et al., 2009; Junquas et al., 2018). Over inter-Andean valleys, there is a strong non-monotonic relationship between precipitation and altitude above the valley floor. Annual precipitation increases with elevation, reaching a maximum at an altitude known as the "Pluviometric Optimum" (PO), and decreasing upwards (Oster, 1979). The PO is observed at both tropical and subtropical regions in the Andes. As an illustration, **Figure 1A** shows the distribution of precipitation with elevation along the western flank of the Combeima River basin, located on the eastern slope of the central Andes of Colombia (approximately at 75°W, 4°N), during the years 1972 and 1973. The elevation of the PO denoted as H^* shows variability among consecutive years, within an altitudinal range of several hundred meters. At monthly timescales, the situation is much more complex. Thus, analyses of long-term mean data are required in order to better understand the governing processes. **Figure 1B** shows

the distribution of long-term mean annual precipitation along the eastern slope of the central Andes of Colombia around 5°N, with respect to elevation and distance to the floor of the Magdalena River valley. The PO is located at the elevation of the Fresno rain gauge. But here too the situation is much more complex. For instance, an in-depth analysis indicates the presence of two POs or even the presence of a pluviometric minimum along different transects of the intra-Andean valleys of the Colombian Andes (Oster, 1979; Poveda et al., 2019). Such strong local and regional variability observations constitute an excellent ground truth for validating convection-permitting models in tropical mountain settings. The challenge is also valid for satellite rainfall, given, for instance, the low-skill of the TRMM data in capturing rainfall over the Andes of Colombia (Vallejo-Bernal et al., 2020). **Figure 1C** shows the long-term mean vertical distribution of rainfall and relative humidity across diverse transects along the central Andes of Colombia. Rainfall data corresponds to TRMM 3A12 V7, at a 0.5° spatial resolution, for the period spanning from December 1997 to March 2015. Relative humidity corresponds to AIRS (AIRX3STM v006) data on board the Aqua satellite, from January 2003 to December 2015 (Poveda et al., 2019). The panels in **Figure 1C** evidence that TRMM satellite rainfall is able to capture important differences in the vertical distribution of rainfall, although rather simplistically given that it locates the PO everywhere at 1,500 m (~850 hPa), and that AIRS data show a maximum amount of relative humidity around 700 hPa, suggesting the existence of a relative humidity optimum at that height, which deserves further investigation.

Local wind circulations contribute to explain the PO location, as well as the strong variability found in the diurnal cycle of rainfall in the Andes of Colombia (Poveda et al., 2005). A simplified depiction of the predominant nocturnal and diurnal wind circulations (4°N- 5°N) is shown in **Figure 2A**. In addition, transects of long-term mean annual precipitation across the three ranges of the Colombian Andes around 6°N, shown in **Figure 2** (reproduced from Alvarez-Villa et al., 2011), clearly illustrates some of the above-mentioned orographic effects. For instance, the nearly constant value of long-term mean annual precipitation over the flat terrain of the Orinoco region differs from the largely variable values within the Andes. Also, the two greatest values are observed on both slopes of the outermost ranges, which receive important atmospheric moisture contributions from Amazonia and the Pacific Ocean. The lowest values coincide with the valley floors within the Andes cordillera.

Past studies (Oster, 1979; Alpert, 1986) indicate that the location of the PO depends on diverse factors, such as: 1) altitude of the valley floor and mountain top above sea level, 2) absolute humidity, 3) local air circulations, 4) evapotranspiration on the valley floor, 5) temporal scale of analysis, 6) presence of pre-orographic rains, and 7) the corresponding landform, valley or hillside. Precipitation below the PO is lower due to less evaporative input, and above the PO due to a decrease in air humidity with altitude. Depending on the orography and altitude of the mountaintop, a secondary (sometimes primary) maximum could occur over the same mountain range at higher elevations (Roche et al., 1990; Molina-Carpio et al., 2019). The association of a PO at 2,700–3,500 m.a.s.l with the existence of the perhumid cloud forest and subparamo ecoregions within the tropical Andes is of particular interest for Andean hydrologists and biologists. The relative dominance of regional or local air circulation patterns has been recently identified as a key factor for the location (elevation) of the PO and it can also be related with the precipitation and wind diurnal cycles (Chavez and Takahashi, 2017; Molina-Carpio et al., 2019). A thorough understanding of the location and variability of the PO constitutes a fundamental scientific challenge.

At the dry western flank of the Peruvian Andes, mean annual rainfall is estimated to be about 15–20 mm/yr below the 500 m.a.s.l, but this value increase slightly up to 90 mm/yr in the northern Pacific coast of Peru. The large-scale subsidence related to the downward motion of the Walker circulation is the primary cause of the stable and dry conditions along the Pacific Peruvian coast (Houston and Hartley, 2003; Takahashi and Battisti, 2007; Garreaud, 2009). Above the inversion layer, rainfall is generally more abundant (Dollfus, 1964; Johnson, 1976) but very little rainfall may also be recorded at high altitude (Lavado-Casimiro et al., 2012; Rau et al., 2016). Annual precipitation can exceed 1,000 mm/yr around 1,000–3,000 m.a.s.l on the western slopes of the Peruvian Andes. Above 3,000 m.a.s.l, however, rainfall ranges from 500 to 750 mm/yr (**Figure 3**) (Lavado-Casimiro et al., 2012; Rau et al., 2016).

At the eastern flank of the tropical Andes, the windward or leeward exposure of the rain gauges to the dominant moist wind generates a more complex relationship between rainfall and altitude (Johnson, 1976; Roche et al., 1990; Guyot, 1993; Pulwarty et al., 1998; Buytaert et al., 2006; Ronchail and Gallaire, 2006; Laraque et al., 2007; Bookhagen and Strecker, 2008; Espinoza et al., 2009b; Espinoza et al., 2009a; Rollenbeck and Bendix, 2011). Extreme rainfall occurs generally at locations that favor strong air uplift, as Churuyacu (500 m.a.s.l; 5,500 mm/yr) in Colombia, close to a steep slope, and Reventador (1,470 m.a.s.l; 6,200 mm/yr), a remote volcano in the Andean-Amazon transition region in Ecuador. Over the Ecuadorian and northern Peruvian Amazon-Andes region, the convergence of nocturnal drainage down the eastern slope of the Andes, interacting with the warm moist air from the Amazon basin, triggers mesoscale convective systems (MCS; Bendix et al., 2009; Trachte et al., 2010a; Trachte et al., 2010b; Trachte and Bendix, 2012; Kumar et al., 2020a). In addition, the occurrence of katabatic flows during nighttime interacting with the concave terrain in the south tropical Andes of Ecuador cause the development of surface cold fronts, initiating the ascent of air masses to its lifting condensation level and the formation of cloud clusters (Bendix et al., 2009; Trachte et al., 2010a; Trachte et al., 2010b; Trachte and Bendix, 2012).

In the eastern flank of the south tropical Andes and the western Amazonia, high rainfall rates of around 4,000–7,000 mm/yr are observed in windward conditions (e.g., Quincemil, San Gabán and Chipiriri stations, **Figure 4**). Orographic effects and the exposure to easterly winds produce a strong annual rainfall gradient between the lowlands and the

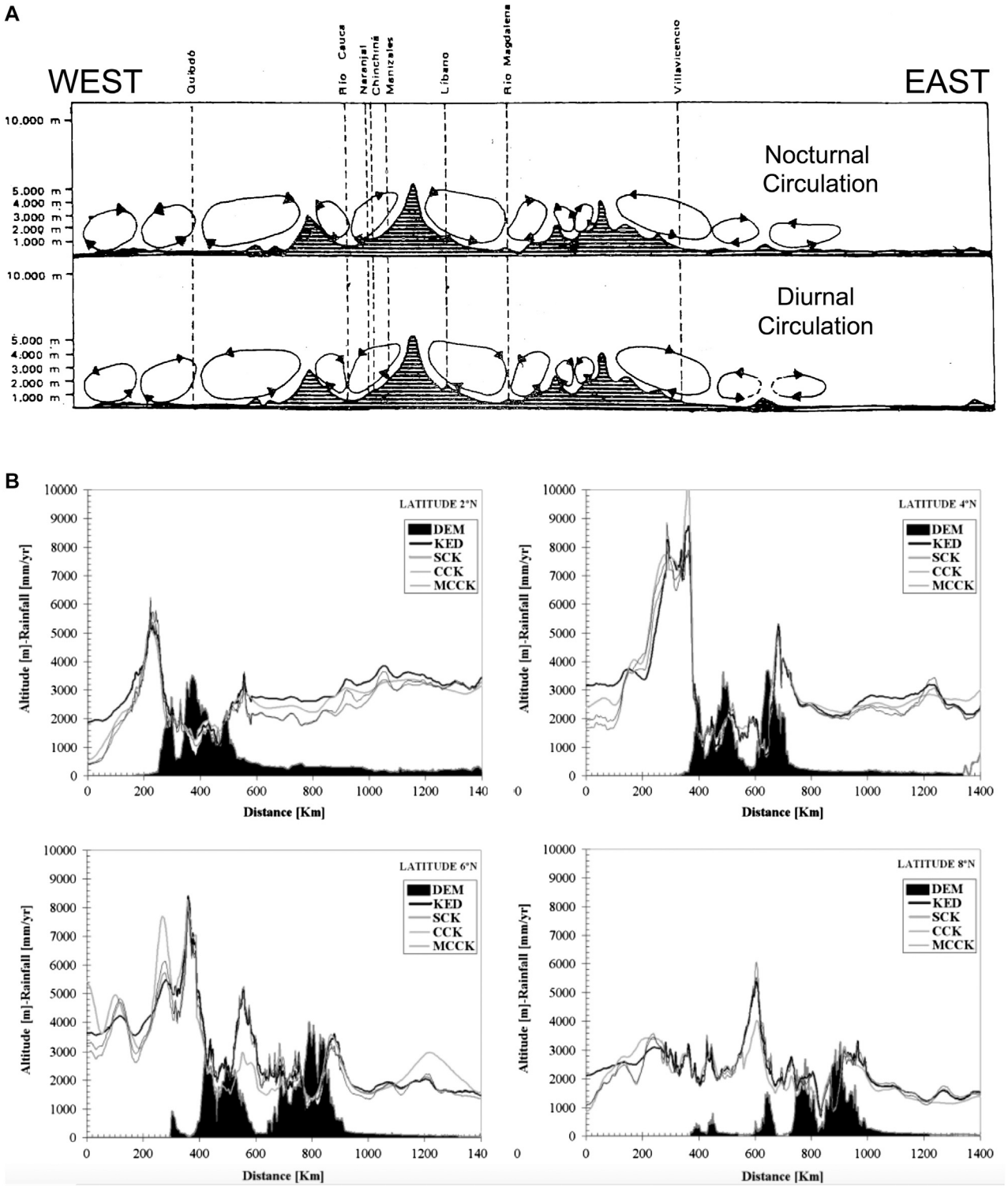


FIGURE 3 | (A) Schematics of local wind circulations among the intra-Andean valleys of the three ranges of the Colombian Andes during night **(top)** and day **(bottom)**. Adapted from Oster (1979). **(B)** Distribution of the long-term mean annual rainfall along four transects (2°N, 4°N, 6°N, 8°N) covering the three ranges of the Colombian Andes (filled in black), showing the location of the pluviometric optima in the intra-Andean valleys. Results were obtained using diverse variants of Kriging interpolation at 4-km resolution for all Colombia, denoted with different line types, with information from 1,180 rain gauges covering the period 1950–2005, and satellite data from the tropical rainfall measuring mission (TRMM) for the period 1999–2005. Source: Alvarez-Villa et al. (2011).

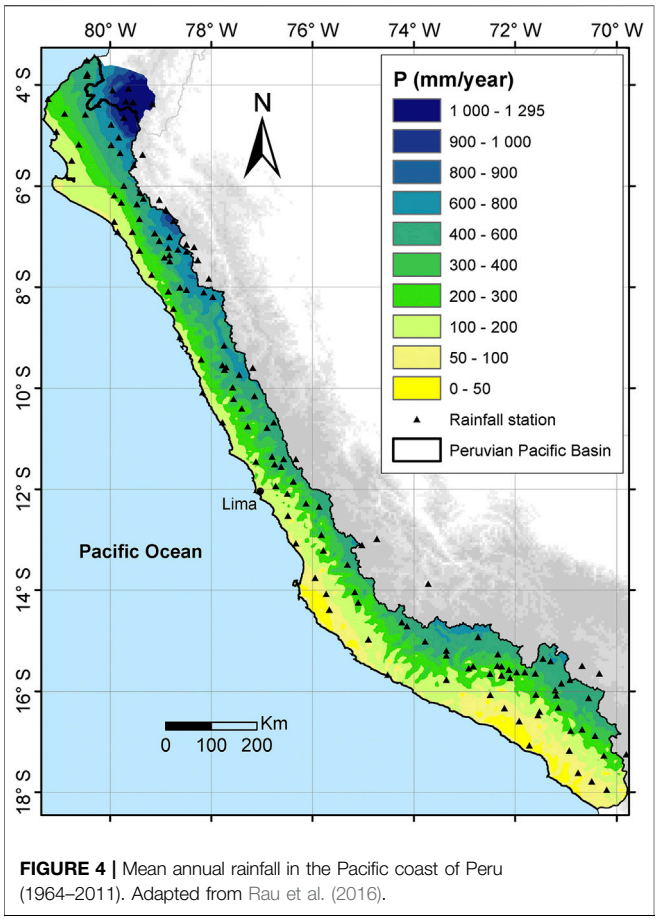


FIGURE 4 | Mean annual rainfall in the Pacific coast of Peru (1964–2011). Adapted from Rau et al. (2016).

Andes that can reach 190 mm/km (Espinoza et al., 2015). Using 15 years of TRMM precipitation data and ground-based stations, Chavez and Takahashi (2017) propose a relationship between terrain elevation and mean surface precipitation, with a mean precipitation peak at an elevation of around 1,000 m.a.s.l. This peak can be explained by the vertical profile of the atmospheric moisture transport by the South American low-level jet (SALLJ). The rainfall-elevation relation from TRMM is similar to the one suggested by rain gauge observations. However, the TRMM measurements underestimates precipitation compared to observations (Espinoza et al., 2015; Chavez and Takahashi, 2017).

Wet episodes over this region are frequently related to large and medium MCS, with greater amount of wide convective and broad stratiform areas that can be triggered by the orographic lifting of the moist SALLJ (e.g., Giovannettone and Barros, 2009; Romatschke and Houze, 2013; Junquas et al., 2018; Kumar et al., 2019). Above surface elevations of 1,000 m.a.s.l, the largely stable dry-to-arid environment of the south tropical Andes limits the development and organization of the MCS (Mohr et al., 2014). Analyzing the triggering mechanisms of severe thunderstorms in the central Peruvian Andes (Mantaro Valley) during the 2015–2016 wet season, Flores-Rojas et al. (2019b) found that thunderstorms are associated with mesoscale convergence of atmospheric moisture flux generated by the intrusion of the sea-breeze from the Pacific Ocean, coupled with upper and middle westerly winds, and moisture advection from low-level winds at the east of the Andes. In addition, using observations from a vertically-pointed profile radar in the Mantaro basin, Kumar et al. (2020b) show that stratiform precipitation in the central Peruvian Andes is more common and lasts longer, but with low accumulated precipitation amounts.

Orographic Effects on Frontal Precipitation Systems in the Subtropical and Extratropical Andes

The orography of the Andes modifies frontal precipitation systems coming from the Pacific Ocean within the westerlies, as they move over the subtropical Andes (mostly in the winter), as well as in the extratropical Andes. Precipitation is mainly enhanced when the strong westerly (cross-barrier) winds associated with the Pacific fronts, are forced to ascent over the windward slopes of the Andes (Chile, e.g., **Figure 5**). Precipitation is then reduced when the westerly flow is forced to descend over the leeward slopes of the subtropical and extratropical Andes. The orographic precipitation enhancement has been estimated in several studies over the windward slopes of the Andes (Chile) using surface observations, as the ratio of mean annual precipitation in the upper part with respect to the lower part of the slopes. They have reported values of 1.51 along the Santiago Basin at ~33.5°S (Falvey and Garreaud, 2007), 1.43 between 32.5°S and 37°S (Viale and Nuñez, 2011), 1.8 between 33° and 44°S (Viale and Garreaud, 2015), and as a linear precipitation gradient over the terrain elevation of 6.3 mm/km at 30°S (Scaff et al., 2017). Estimates of orographic precipitation reduction ratios range between 5 and 10, when comparing precipitation on the leeward slopes of the Andes to those in the windward slopes of the Andes (Viale and Nuñez, 2011; Viale et al., 2019).

Different studies and field experiments allowed for a better understanding of the physical processes associated with frontal systems moving over the Andes. The strong blocking effect of the high subtropical Andes (up to 6,000 m.a.s.l; Falvey and Garreaud, 2007; Barrett et al., 2011; Viale and Nuñez, 2011) can lead to a negative orographic precipitation gradient on the northern extend of the frontal system (Scaff et al., 2017). The low-level blocking effect can produce an enhancement of precipitation upstream of the barrier. This can happen through a strengthening of the frontal convergence zones and a modulation of the feeder-seeder mechanism in the pre-frontal and frontal environment (Barrett et al., 2009; Viale et al., 2013), changing the precipitation gradient upwind of the barrier. The thermodynamical processes and the dynamics of the blocking effect produced by the Andes on frontal systems still need to be better understood to further predict the amount and the spatial distribution of precipitation, especially over the extratropical Andes. The northerly flow associated with the blocking and the cyclonic circulation can transport large amounts of atmospheric moisture. This moisture transport can produce convective instability and a complex interaction with the flow aloft the mountain, resulting in convection (Bozkurt et al., 2016). Mesoscale processes affecting convective initiation in the interior of valleys embedded in frontal systems need to be studied in more detail, not only to explain

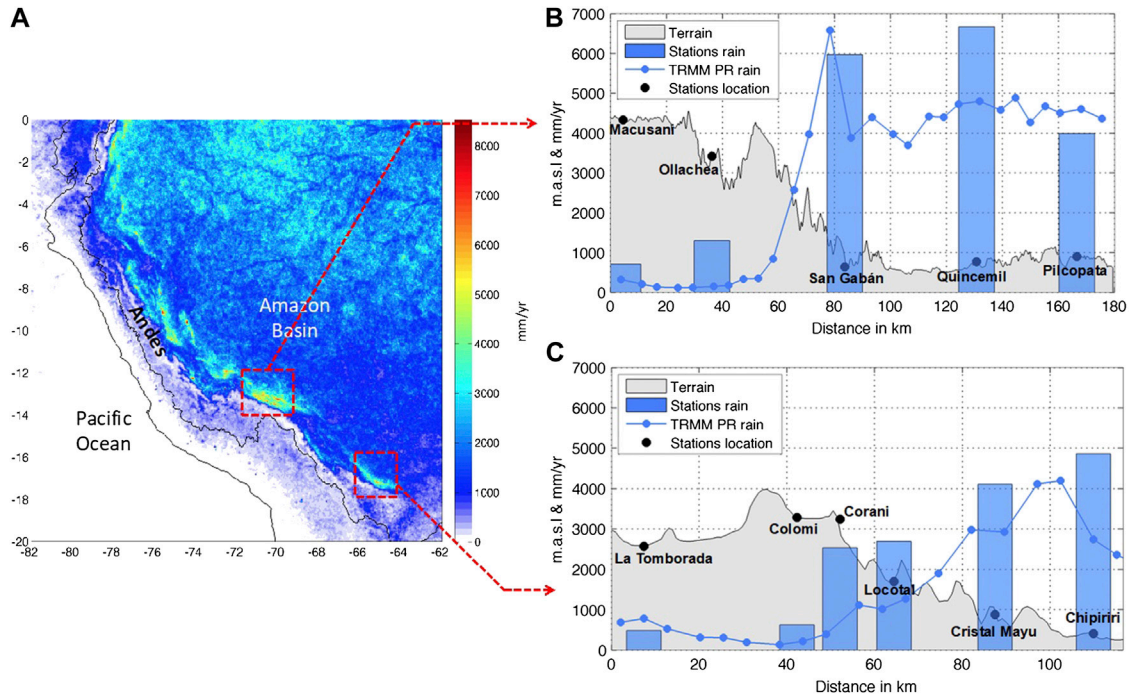


FIGURE 5 | (A) Mean annual rainfall in western tropical South America (mm/yr, 1998–2012) estimated using TRMM 2A25. **(B)** Topographical profile (gray) and total annual rainfall from Macusani to Pilcopata meteorological stations (Peru). The x-axis represents the horizontal distance and the y-axis the altitude (m.a.s.l) and the mean total rainfall (mm/yr) from observations (blue bars) and TRMM 2A25 (blue line). **(C)** As in **(B)** but for the La Tamborada-Chipiriri profile in Bolivia highlands. Adapted from Espinoza et al. (2015) © Water Resources Research. Reprinted by permission from John Wiley and Sons.

extreme precipitation events, but also to better describe postfrontal instabilities. At a monthly scale, a relatively linear regime characterizes the orographic effect in the Nahuelbuta coastal mountains at~37°S (Garreaud et al., 2016) and makes the rain shadow on the leeside more variable. Understanding the temporal and spatial variability of the main processes modulating the rain shadowing downhill remains a great scientific challenge.

Our knowledge of how the upstream flow and successive rainbands associated with a frontal system are affected by the Andes, is also incomplete (Viale et al., 2013; Garreaud et al., 2016). The characterization of the properties of the precipitating clouds moving over and adjacent to the Andes at mid-latitudes has shown significant differences in the along- and cross-barrier directions, suggesting different microphysical processes in orographic precipitation operating at different sectors of the Andes (Viale and Garreaud, 2015). The microphysical processes involved in the orographic enhancement have only been recently explored. A field experiment during 2015 provided a better understanding of the frequency of occurrence of cold or warm orographic rain over the Nahuelbuta coastal mountains, as well as the changes of drop size in function of the rain type (Massmann et al., 2017). The influence of maritime, continental and urban aerosols on the orographic precipitation over the coastal and the Andes Mountains has not been explored yet and needs to be addressed.

Summer precipitation has a minimum within the Andes at mid-latitudes, but the orographic effects are key in the summer convection initiation at their eastern foothills through diurnal thermally-driven mountain winds. Once convection is initiated on the foothills of the Andes, it develops into deep convective storms farther east in central *Argentina* (e.g., Zipser et al., 2006; Rasmussen and Houze 2011). The initiation and development of convection in this region is still under investigation and big efforts are now focused on field experiments. Two campaigns have been performed during the austral summer between 2018 and 2019: the Cloud, Aerosol, and Complex Terrain Interactions (CACTI), and the Remote sensing of Electrification, Lightning, And Mesoscale/microscale Processes with Adaptive Ground Observations (RELAMPAGO). These campaigns have been designed to provide a better understanding of the orographic effects of the Andes and the Sierras de Córdoba on the initiation, development and propagation of convection. The Andes Mountains also modulate the SALLJ and the atmospheric moisture transport that converges over the foothills. Besides diurnal thermally-driven mountain winds, other orographic mechanisms could be important to the initiation of convection, such as the presence of strong atmospheric moisture gradients (Ziegler and Rasmussen, 1998; Bechis et al., 2020), cold-pool gravity currents (Rotunno et al., 1988), the inertial-gravity waves (Li and Smith, 2010; Hierro et al., 2013), and the initiation of elevated convection due to other wave-types like bores (Geerts, 2017).

The lack of reliable measurements of solid precipitation in the Andes, at heights above 2000 m.a.s.l, has been an important

drawback to many of the previous studies in the region (e.g., Falvey and Garreaud, 2007; Viale and Garreaud, 2015; Scaff et al., 2017; Condom et al., 2020). The uncertainty in the precipitation amount and phase is still proven to be a critical issue to properly characterize the observed and modeled distribution of precipitation over the Andes for seasonal water availability in agricultural activities, natural resources extraction, hydropower generation, and municipal consumption.

HYDROCLIMATE VARIABILITY IN THE ANDES AT SUBSEASONAL, INTERANNUAL AND DECADAL TIMESCALES

Hydroclimate variability in the Andes is modulated by different large-scale phenomena occurring within the Earth system at different timescales. Among them, El Niño-Southern Oscillation (ENSO), the Southern Annular Mode (SAM), and the variability of Atlantic sea surface temperatures (SST) impose distinctive interannual variability in the water cycle along the Andes. At longer timescales, the decadal and multidecadal modes of SST variability in the Pacific and Atlantic oceans, such as the Pacific Decadal Oscillation (PDO) and the Atlantic Multidecadal Oscillation (AMO), are among the main modulators of the Andean hydroclimate. At shorter timescales, the Madden-Julian Oscillation (MJO), the African easterly waves, and the high frequency variability of cross-equatorial low-level winds and the low-level jets are associated with the intraseasonal variability of different hydroclimatic variables in the Andes. Multiple studies have addressed the influence of these phenomena on the Andean hydroclimate. Recently, Cai et al. (2020) provide a review of the state of the art regarding the climatic impacts of ENSO in South America. Poveda et al. (2020) discuss the influence of ENSO on the occurrence of extreme hydrometeorological events along the Andes. This section reviews the main aspects of hydroclimate variability in the Andes related to ENSO and other phenomena influencing regional hydroclimate in the Andes at subseasonal, interannual and decadal timescales.

Subseasonal Variability

At subseasonal timescales, the MJO is among the main modulators of climate variability in the tropics (Madden and Julian, 1994). Over the north tropical Andes (north of 8°S), the MJO is related to enhanced (reduced) amplitude of the diurnal cycle of precipitation during its westerly (easterly) phase (Poveda et al., 2005). Also, the MJO has been identified as a driver of extreme temperature and rainfall events in the south tropical Andes and the western Amazonia (Shimizu and Ambrizzi, 2016; Sulca et al., 2018; Grimm, 2019; Mayta et al., 2019; Recalde-Coronel et al., 2020). The occurrence of eastward-propagating equatorially confined MJO events that do not evolve through a complete life cycle are associated with suppressed rainfall conditions over the tropical Andes (Mayta et al., 2019; Recalde-Coronel et al., 2020). Moreover, in the Andes-Amazon transition region, the MJO convection modulates the basic response of ENSO on extreme precipitation events in this region, favoring dry (wet) extreme events when the MJO convection over Indonesia is enhanced (suppressed) (Shimizu and Ambrizzi, 2016; Shimizu et al., 2016). The interactions between ENSO and MJO are of particular relevance since precipitation and temperature anomalies observed in the south tropical Andes during the different ENSO phases, without the simultaneous occurrence of the MJO, are modified during events when ENSO and MJO occur simultaneously (Shimizu and Ambrizzi, 2016).

Over the south tropical Andes (between 8°S and 27°S), incursions of low-level southern winds from southern South America are related to the variability of the cloud cover in the Cordillera Real in Bolivia (Sicart et al., 2016). In addition, southerly incursions of cold and dry air along the eastern the Andes, low cloud cover, surface specific humidity, and soil moisture are key factors controlling the day-to-day variability of minimal temperature in the central Peruvian Andes (Saavedra and Takahashi, 2017; Sulca et al., 2018). During the austral summer, subseasonal rainfall variability over south tropical Andes is in part related to the variability of the South Atlantic Convergence Zone (SACZ) and the Bolivian High–Nordeste Low system, as discussed in Espinoza et al. (2020) and Jones and Carvalho (2002). Dry and wet spells in the Peruvian Andes show a dipole pattern with precipitation anomalies of the opposite sign over northeastern Brazil, which is related to large-scale changes in the upper-troposphere circulation over the Bolivian high–Nordeste low system, in association with northward-propagating extratropical Rossby wave trains (Sulca et al., 2016). The active easterly winds at upper troposphere related to the Bolivian High enhance moisture flux from the lowland Amazon, which favors wet conditions in the tropical Andes (Garreaud et al., 2003; Sulca et al., 2016; Chavez and Takahashi, 2017; Junquas et al., 2018). On the eastern flank of the south tropical Andes (Peru and Bolivia) and in regions below 2000 m.a.s.l, intraseasonal rainfall variability has been related to the southerly low-level winds regime (Wang and Fu, 2002) and to the intensification of the low-level circulation (Espinoza et al., 2015; Chavez and Takahashi, 2017; Paccini et al., 2017).

Outside the tropical band, the effect of the MJO upon precipitation is less clear and mediated by Rossby wave activity propagating across the South Pacific. Yet, recent studies have shown that rainfall in northern and central Chile tends to increase during active MJO phases near the central equatorial Pacific (Barrett et al., 2012; Juliá et al., 2012). These findings support studies that speculated the Pacific South American (PSA) teleconnection mode (Mo and Higgins, 1998; Grimm and Ambrizzi, 2009) was activated when deep convection moved from the maritime continent into the central Pacific region, where most precipitation concentrates to the south of the equator. The role of the MJO in setting the stage for episodes of heavy precipitation along the subtropical Andes was particularly evident in late March 2015, when the MJO reached its largest amplitude on record. Linked to that activity, a strong blocking anticyclone, sited in the Bellingshausen Sea, caused extreme high SSTs in southwestern South America and the Antarctic Peninsula (Rondanelli et al., 2019). At the same time, a cut-off low crossed over northern Chile causing copious rain in the otherwise hyper arid Atacama Desert and subtropical Andes, resulting in flashflood that caused more than 60 fatalities

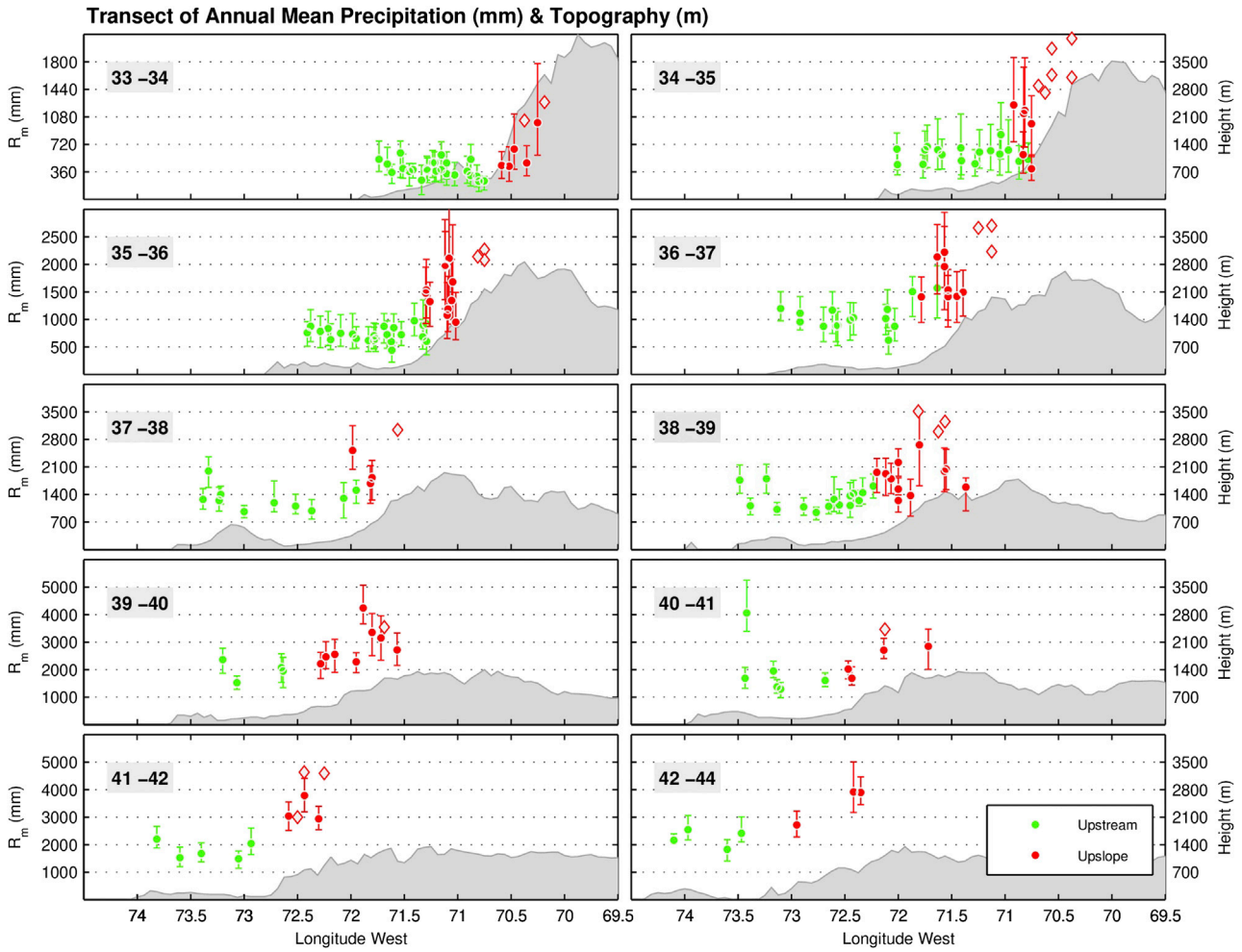


FIGURE 6 | Transect of annual mean precipitation (Rm, in millimeters) in the subtropical and extratropical Andes, from the upstream to the upslope zone (both in the windward side of the Andes). Transects are 1°latitude width (except for the 42°–44° transect due to data availability) and extend from the 33°S to the 44°S, where surface data were available. The circles correspond to the mean values and the bars to the minimum and maximum annual means over a 10-years period (2002–2011). The diamond corresponds to the mean annual precipitation estimated from river discharge gauges on upslope sector. Adapted from Viale and Garreaud (2015). © Journal Geophysical Research–Atmosphere. Reprinted by permission from John Wiley and Sons.

and severe damage in infrastructure (Kreft et al., 2016; Rondanelli et al., 2019). To our best knowledge, no studies have been conducted relating the MJO to rainfall variability in the extratropical Andes, but rainfall episodes do exhibit some clustering during periods of blocking in high latitudes with intrinsic subseasonal periodicity (Rutllant and Fuenzalida, 1991).

Interannual Variability

Interannual climate variability in the Andes is strongly modulated by ENSO. For instance, over the north tropical Andes (mainly Colombia and Venezuela), warm ENSO events (El Niño) are associated with reduced diurnal, seasonal and annual precipitation, while cold ENSO events (La Niña) are related with increased precipitation, runoff and soil moisture (e.g., Poveda et al., 2005; Poveda et al., 2006; Poveda et al., 2011; Bedoya-Soto et al., 2018). The largest ENSO influence in the region is observed during December-January-February (DJF), although such influence is stronger (weaker) over the northwestern (northeastern) Andes (Poveda et al., 2011; Navarro-Monterroza et al., 2019). The impact of ENSO on the Colombian Andes relates to weaker (stronger) SST and surface pressure gradients between the coast of Peru and Ecuador and the Colombian Pacific (Poveda et al., 2006; Cai et al., 2020) that induces a weaker (stronger) atmospheric moisture transport to the region during El Niño (La Niña) (Hoyos et al., 2017; Sierra et al., 2018; Morales et al., 2020). However, the diversity of ENSO events also implies a wide range of atmospheric teleconnections worldwide (e.g., Larkin and Harrison, 2005; Ashok et al., 2007; Sun et al., 2015; Tedeschi et al., 2013). In the north tropical Andes, mainly Colombia, Canonical El Niño events, that are characterized by positive SST anomalies located over the tropical eastern Pacific, are associated with largest reductions of precipitation in the region, compared to El Niño Modoki events, that are characterized by positive SST anomalies located

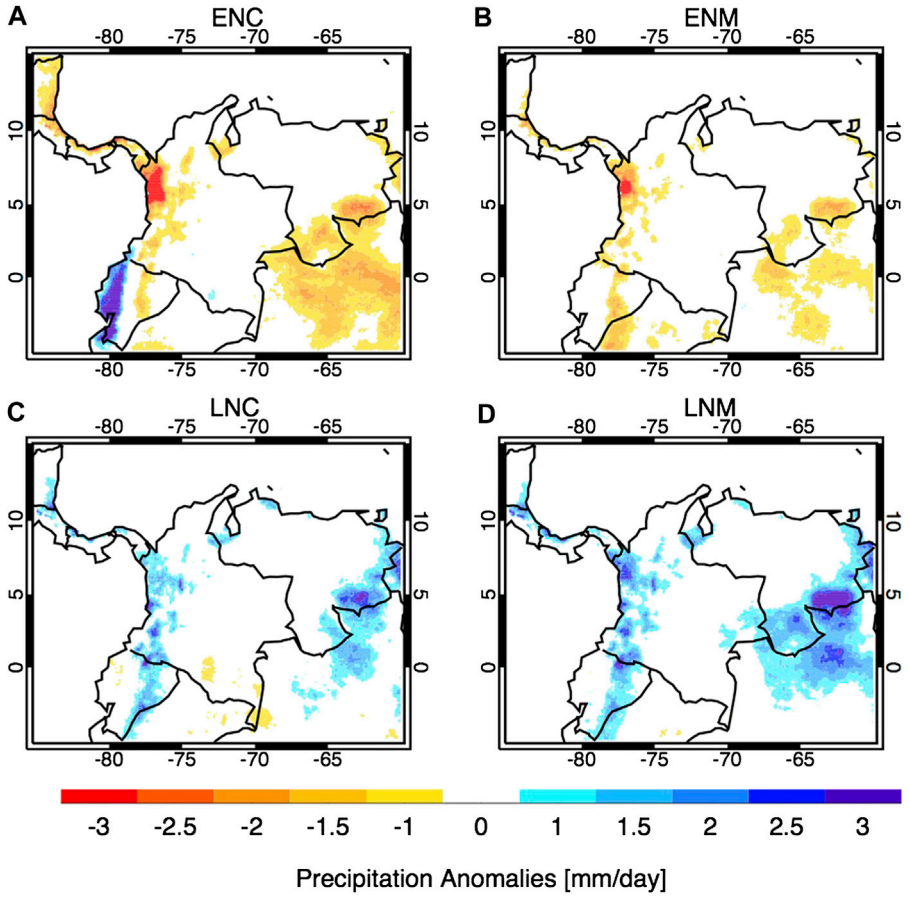


FIGURE 7 | Precipitation anomalies in the north tropical Andes during **(A)** Canonical El Niño (ENC), **(B)** El Niño Modoki (ENM), **(C)** Canonical La Niña (LNC), and **(D)** La Niña Modoki (LNM) for DJF according to CHIRPS data. ENSO years are considered according to Navarro-Monterroza et al. (2019) for the period 1981–2015.

over the tropical central Pacific (Navarro-Monterroza et al., 2019; **Figure 6**). However, the increases of precipitation over the north tropical Andes during La Niña Modoki events are larger than those observed during Canonical La Niña episodes (Navarro-Monterroza et al., 2019). This influence in precipitation is in part associated with changes in the Caribbean and the Choco low-level jets (see Espinoza et al., 2020; Poveda and Mesa, 2000; Serna et al., 2018; Sierra et al., 2018).

Although ENSO dominates interannual climate variability in the north tropical Andes, it is not the only source of interannual variability in the region. The interannual variability of SSTs over the tropical north Atlantic (TNA) also has influence on the regional hydroclimatology The TNA is the main source of atmospheric moisture for the north tropical Andes (Sakamoto et al., 2011; Arias et al., 2015; Hoyos et al., 2017). In particular, a warmer TNA is associated with enhanced precipitation in Colombia and Venezuela, as well as with a weaker Caribbean low-level jet, which favors atmospheric water vapor transport toward northern South America (Arias et al., 2015; Arias et al., 2020). Farther south, precipitation variability over the eastern Andes of Ecuador relates to a dipole-like correlation pattern in the north tropical Atlantic (Vuille et al., 1999). Moreover, to the east of the Paute river in Ecuador, within the south tropical Andes, the variability of MCSs is positively correlated to the south tropical Atlantic SST anomalies, due to the variability of the South Atlantic subtropical high, exhibiting departures from this relationship when ENSO-related anomalies occur in the tropical Pacific (Campozano et al., 2018). In the western side of the Andes in Ecuador and northern Peru, El Niño events are associated with intense convective activity related to warm SST conditions in the eastern equatorial Pacific (e.g., Recalde-Coronel, 2014; Takahashi and Martínez, 2017; **Figure 7**). In this region, El Niño is the main modulator of interannual hydrological variability and catastrophic floods have been associated with this phenomenon (see Takahashi and Martínez (2017), Poveda et al. (2020), and Cai et al. (2020) for more details).

Regarding ENSO effects over the south tropical Andes, different studies document negative (positive) rainfall anomalies over the Peruvian Andes during El Niño (La Niña) (e.g., Lagos et al., 2008; Espinoza et al., 2011; Lavado and Espinoza, 2014; Sulca et al., 2016; **Figure 8**). In Peru, different studies have analyzed the different rainfall impacts associated with Canonical and Modoki El Niño events, synthetized by the eastern Pacific (E) and central Pacific (C) El Niño indices,

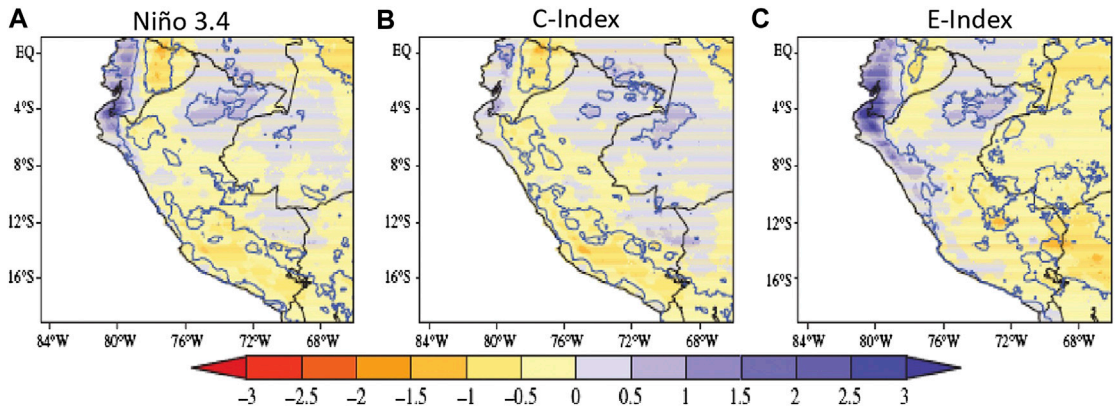


FIGURE 8 | Linear regression coefficients between ENSO indices (Niño 3.4, C-El Niño Modoki, and E-Canonical El Niño) and PISCO precipitation data (**A–C**, respectively) in the south tropical Andes. Values are in mm day−1 for one standard deviation of each corresponding ENSO index. Blue (Red) shading represents positive (negative) precipitation anomalies in intervals of 0.5 (−0.5) mm day−1 per standard deviation. Black contour represents the climatological isoline of 4 mm day−1. Blue contours represent significant correlation between ENSO indices and precipitation at the 95% confidence level. Analysis based on the period 1980–2016. Adapted from Sulca et al. (2017). © International Journal of Climatology. Reprinted by permission from John Wiley and Sons.

respectively (Takahashi et al., 2011). Enhanced coastal and reduced Andean/Amazonian rainfall is associated with surface warming in the eastern (Canonical El Niño) and central equatorial Pacific (El Niño Modoki), respectively (**Figure 7**). Both anomalies can occur, with varying relative magnitudes, during El Niño or (with the opposite sign) during La Niña (Lagos et al., 2008; Lavado-Casimiro et al., 2013; Lavado and Espinoza, 2014; Rau et al., 2016; Sulca et al., 2017; Imfeld et al., 2019; Segura et al., 2019). Both Canonical El Niño and El Niño Modoki events are associated with a weakened upper-level easterly flow over Peru, but they are more restricted to the central and southern Peruvian Andes (Sulca et al., 2017).

A weak (strong) and northward (southward) displacement of the Bolivian High is associated with westerly (easterly) anomalies at 200 hPa over the south tropical Andes, which inhibits (enhances) atmospheric moisture influx from the east, thereby increasing (reducing) atmospheric stability and reducing (increasing) precipitation over upper-elevation regions of the Andes (Garreaud, 1999; Garreaud et al., 2003; Vuille and Keimig, 2004; Neukom et al., 2015). Segura et al. (2019) detected a relationship between precipitation at higher elevations in the Andes north of 10°S and easterly winds at 200 hPa during February–April. In addition, westerly (easterly) anomalies at 200 hPa over the south tropical Andes are strongly associated with warm (cold) SST anomalies in the central Pacific (see updated studies from Sulca et al., 2017; Segura et al., 2019; Imfeld et al., 2019). In fact, over the Altiplano, a dominant negative (positive) relationship of summer (DJF) rainfall with El Niño (La Niña) events has been identified (Garreaud et al., 2003; Vuille et al., 2008; Huerta and Lavado-Casimiro, 2020). This signal becomes rather weak to the north of the Altiplano and to the sub-Andean valleys of the southwestern Amazon below 1,500 m.a.s.l (Ronchail and Gallaire, 2006). During the drier austral winter, negative relationships with the TNA SST appear for the eastern Andean foothills and adjacent southwestern Amazonian lowlands (Espinoza et al., 2011; Marengo and Espinoza, 2016; Molina-Carpio et al., 2017), which are not always mediated by ENSO.

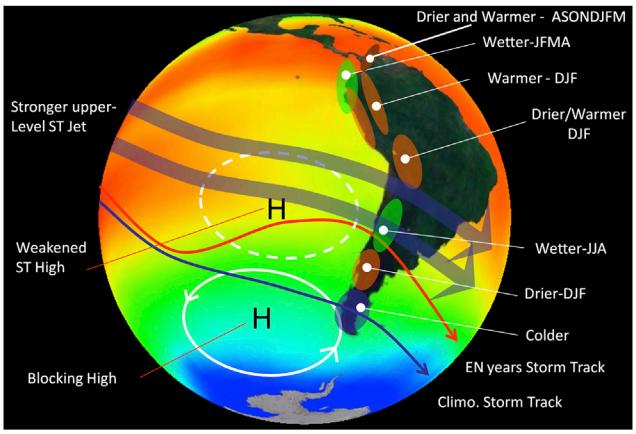


FIGURE 9 | Schematics of the El Niño impacts in precipitation over the Andes. Climate alterations during La Niña events are roughly opposite. "DJF" corresponds to the December-January season, "JJA" to June-August, "JFMA" to January-April, and "ASONDJFM" to August-March. "EN" denotes El Niño while "ST" denotes subtropical.

Segura et al. (2019) show that extreme monthly wet events in the northern Peruvian Andes are related to convection over the equatorial Amazon during February–April period, showing an atmospheric relationship between the Amazon and the Andes (**Figure 9**). Extreme monthly dry events over the Equatorial Andes (north of 8°S) during the February–April period are related to a strengthened Walker Cell, especially in the eastern Pacific. The extreme wet (dry) events over this region are associated with an anomalous southward (northward) displaced eastern Pacific ITCZ.

The influence of ENSO on climate variability in central-southern Chile, thus affecting part of the subtropical Andes (27°S-37°S), has been known for a long time. Many studies

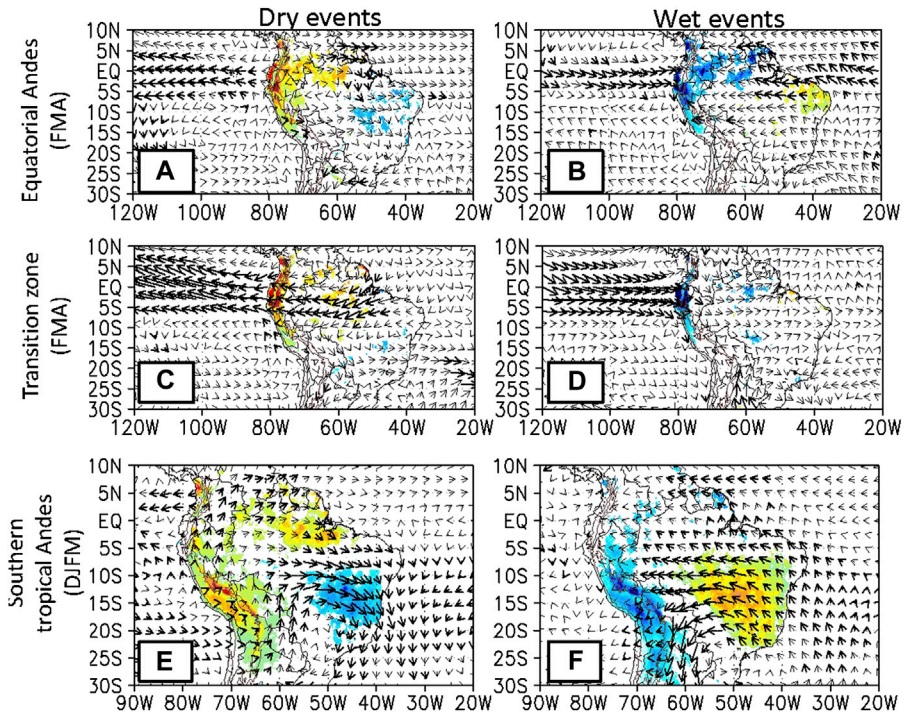


FIGURE 10 | (A) Composite for CHIRPS precipitation (shaded; $p < 0.05$ according to a Cramér test) and vertically integrated water vapor flux (vectors) using a Kramer test with a p-value of 0.05. **(B)** Similar to **(A)** but for wet events in the northern Peruvian Andes from February to april. **(C,D)** Similar to **(A,B)**, respectively, but for dry and wet events in the transition zone from February to april. **(E)** Anomalies considering monthly dry events from February to april in the equatorial Andes. Only significant precipitation anomalies are shown and bold vectors represent significant meridional or zonal vertically integrated water vapor flux anomalies. **(F)** similar to **(A,B)**, respectively, but for dry and wet events in the south tropical Andes from December to March. Adapted from Segura et al. (2019). © Climate Dynamics. Reprinted by permission from Springer Nature.

have confirmed the existence of a warm–wet/cold–dry relation between rainfall in central Chile and SST anomalies in the tropical Pacific related to ENSO (**Figure 8**) (e.g., Rubin 1955; Pittock 1980; Quinn and Neal 1983; Aceituno 1988; Montecinos et al., 2000; Montecinos and Aceituno 2003). The interannual variability of rainfall at lower elevations over central Chile is tightly coupled with the snowfall accumulation over the Andes immediately to the east of this region (e.g., Garreaud et al., 2017; González-Reyes et al., 2017).

Rutllant and Fuenzalida (1991) gave an initial discussion of the physical mechanisms behind the aforementioned relationship. Their synoptic analysis found that major winter storms in central Chile during El Niño episodes are related to persistent anticyclonic anomalies (i.e., blocking conditions) over the Amundsen - Bellingshausen Seas (ABS) to the west of the Antarctic Peninsula. Blocking over the ABS is not infrequent (Renwick and Revell, 1999) and often associated with wave trains triggered by atmospheric heating in the tropical Pacific in what is known as the Pacific–South American (PSA) teleconnection pattern. Frequent ABS blocking in conjunction with the widespread weakening of the PSA during El Niño years leads to a equatorward displacement of the storm track (Solman and Menéndez, 2002) and hence more precipitation in central Chile and the adjacent cordillera (30°S–35°S). A stronger subtropical jet stream and enhanced atmospheric moisture availability over the southeastern Pacific during El Niño years may also contribute to the rainfall and snowfall surplus (Montecinos and Aceituno, 2003). Approximately, the opposite large-scale configuration takes place during La Niña years. Enhanced cyclonic activity over the ABS, stronger PSA and weaker mid-level westerlies produce rainfall deficit in central Chile during the cold phase of ENSO.

Farther south, between 38°S and 45°S, ENSO-related precipitation anomalies are still marked, but they occur in summer, when El Niño (La Niña) years often bring less (more) precipitation than normal over western Patagonia and the adjacent sectors of the Austral Andes (Montecinos and Aceituno, 2003; Garreaud, 2018). Farther south, the impact of ENSO begins to fade at the same time that modulation by the SAM becomes more prominent. Indeed, SAM has a significant correlation with rainfall (and possibly snowfall) such that its positive polarity leads to precipitation deficit across much of the southernmost part of the Andes cordillera (Gillett et al., 2006; Garreaud et al., 2009; Silvestri and Vera, 2009). Historically, the influence of SAM and ENSO on precipitation over the austral Andes has counteracted each other. Nonetheless, there are some years in which both effects can couple, as during the summer of 2016, when a strong El Niño event and a positive phase of SAM were conducive to one of the worst droughts over western Patagonia and the adjacent Andes (**Figure 10** and **Figure 11**), with dramatic environmental impacts (Garreaud, 2018).

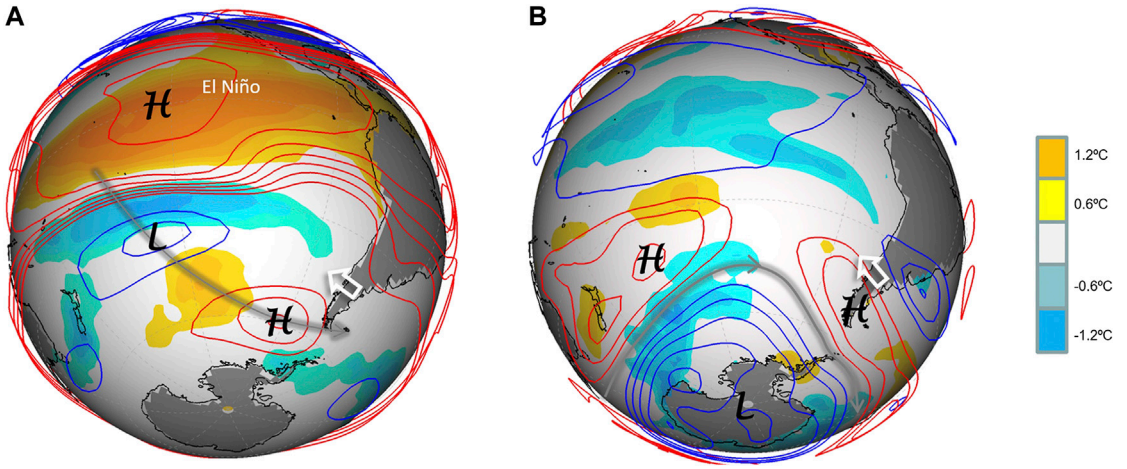


FIGURE 11 | (A) Sea surface temperature anomalies (shaded) and 200 hPa geopotential height anomalies (contoured every 25 m: positive in red, negative in blue contours) during El Niño austral summer (Dec-Feb). **(B)** As **(A)** but for summers with the Southern Annular Mode (SAM) in its positive phase (SAM Index >1). Note how both modes produce easterly wind anomalies over the Austral Andes (white arrow) conducive to dry conditions in the otherwise hyper humid western Patagonia.

Decadal Variability

Despite the lack of long-term measurements of hydroclimatic variables in the Andes (Condom et al., 2020), different studies have studied the decadal and multidecadal variability of Andean hydroclimate. For instance, Kayano and Capistrano (2014) indicate that the cold (warm) phase of AMO strengthens El Niño (La Niña) events due to the presence of a negative inter-Pacific-Atlantic SSTs. Kayano et al. (2019) found that the low-frequency anomalous SST cooling (warming) of the tropical Pacific during the PDO cold phase (warm phase) favors (inhibits) the settling of the La Niña-related negative SST anomalies in the tropical Pacific. Moreover, La Niña events are favored during the simultaneous occurrence of the AMO warm phase and the PDO cold phase (Kayano et al., 2019). From the mid-1970s to late 1990s, a positive phase of the PDO was related with more frequent strong central Pacific La Niña and strong eastern Pacific El Niño events, including the 1982–83 and 1997–98 Superniños (Cai et al., 2020). Afterward, the negative phase of the PDO features more central Pacific El Niño events (El Niño Modoki), which are smaller in amplitude. This modulation of decadal modes of variability on ENSO in turn modulates the teleconnections with rainfall in northern South America, including the Andes.

Over the north tropical Andes, the PDO and AMO influence precipitation due to alterations of the Caribbean and Choco low-level jets (Loaiza Cerón et al., 2020). In particular, the occurrence of cold SST anomalies in the Pacific during the occurrence of the AMO warm phase observed during 1998–2016 strengthened (weakened) the Choco (Caribbean) low-level jet, increasing atmospheric moisture transport and precipitation in the north tropical Andes. Moreover, the strengthening of the Choco jet observed after 1997 is found to be partially related to the occurrence of La Niña events during the simultaneous occurrence of a PDO cold phase and an AMO warm phase (Loaiza Cerón et al., 2020).

Decadal variations in rainfall in the Ecuadorian Andes have been detected. Mora and Willems (2012) show the occurrence of positive precipitation anomalies during 1969–1974 in the Paute river basin, within the lowlands of the Ecuadorian Andes, while the opposite is observed during 1983–1986. Also, in the high paramo regions of the Ecuadorian Andes, increased (reduced) rainfall is observed during 1978–1981 (1965–1974) (Mora and Willems, 2012). Along the Peruvian Pacific coast, fluctuations in the ENSO - rainfall relationship has been identified at decadal timescales considering the 1964–2011 period (Bourrel et al., 2015). The authors show shifts in this relationship in the 1970s and the 2000s, over which main ENSO characteristics significantly changed (e.g., Canonical and Modoki modes).

Silva et al. (2008), Marengo (2009), Espinoza et al. (2009b), and Lavado-Casimiro et al. (2012) identified that multidecadal variations of rainfall in the western Amazon/eastern tropical Andes might be linked to SSTs in the subtropical Atlantic. The AMO affects hydroclimate in this region through alterations of the SALLJ, with active SALLJ days during negative AMO phases in association with negative precipitation anomalies over the Andes-Amazon transition region and the Atlantic ITCZ (Jones and Carvalho, 2018). More recently, Campozano et al. (2020) highlight that PDO modulates the ENSO influence on precipitation in the eastern Ecuadorian Andes, where the PDO warm phase enhances (reduces) precipitation when in phase with El Niño (La Niña). Furthermore, the PDO warm phase influences the connection between ENSO Canonical events and precipitation in the eastern Ecuadorian Andes while this link is not affected for the ENSO Modoki events (Campozano et al., 2020). Over the northern Altiplano, Segura et al. (2016) documented a significant decadal variability on hydroclimate variables (including the water levels of the Titicaca lake). These authors show that this decadal variability is related to low frequency variability of both the western Pacific

SSTa and the zonal wind at 200 hPa above the Central Andes. In the northern Altiplano and the southern Peruvian Andes, a slightly increase in summer precipitation has been recently identified (Imfeld et al., 2020; Segura et al., 2020), associated with an enhanced upward atmospheric moisture from the western Amazon (Espinoza et al., 2019). This change in the atmospheric circulation has been related to warming conditions over the north tropical Atlantic SST during the last two decades (Segura et al., 2020).

The same signal documented for the northern Altiplano is detected for the precipitation in the humid valleys (Yugas) between 1,000 and 4,000 m.a.s.l in the eastern Andean slopes in Bolivia (Ronchail and Gallaire, 2006; Molina-Carpio et al., 2019). Decadal variability identified by Segura et al. (2016) shows a very significant negative correlation with the low frequency variability of the central Pacific ENSO, particularly with the SSTs in the Niño four region (Stuecker, 2018). The results of Seiler et al. (2013) suggest that, in relation to the northern Altiplano, the southwestern Altiplano exhibits a decadal variability of opposite sign. Decadal precipitation variability during the drier winter season (JJA) has been identified in the eastern Altiplano, the eastern Andean foothills below 1,000 m.a.s.l and the adjacent southwestern Amazonian lowlands. This variability has been associated with the TNA SST, as for the interannual variability (Espinoza et al., 2011; Molina-Carpio et al., 2017; Espinoza et al., 2019). Several authors, as cited by Stuecker (2018), relate both interannual and decadal tropical north Atlantic with central Pacific SST variability.

Along the subtropical and part of the extratropical Andes, rainfall also exhibits low frequency phenomena, particularly related to the PDO. Given the ENSO-like structure of the teleconnections in the southern hemisphere (Garreaud, 1999), its cold (warm) phase tends to produce drier (wetter) periods with respect to long term mean (Garreaud et al., 2009; Masiokas et al., 2010; Muñoz et al., 2016; González-Reyes et al., 2017). The statistical relationship between PDO and rainfall in central Chile is modest ($r \approx 0.4$) but such analysis is based on only a few PDO multi-year blocks during the 20th century (Garreaud et al., 2020). In any case, the positive phase of the PDO initiated after the shift in the mid-1970s (Jacques-Coper and Garreaud, 2014) seems partially responsible for the rainy conditions in this region in the 1980's and 1990's. Since then, the PDO has been trending toward its negative polarity thus contributing to the drying trend observed in the extratropical Andes between 30 and 40°S (Boisier et al., 2016) and the maintenance of the central Chile megadrought since 2010 (Garreaud et al., 2020). The positive phase of the PDO also seems to produce a slight warming in the Andes to the south of 40°S (Garreaud et al., 2009; Jacques-Coper and Garreaud, 2014), presumably in connection with the excessive insolation when anticyclonic conditions prevail over the Patagonia. For a further discussion of hydroclimate variability in the Andes on longer timescales, Pabón-Caicedo et al. (2020) discussed the hydroclimate variability over the entire Andes throughout the last two millennia, including multidecadal changes.

SUMMARY AND OPEN RESEARCH QUESTIONS

Due to its long latitudinal extension and its prominent topography, a large variety of mountain climates are documented in the Andes Cordillera. These climates vary strongly across and along the approximately 7,240 km of the range: from northern South America to southern Patagonia and Tierra del Fuego, crossing seven countries (Venezuela, Colombia, Ecuador, Peru, Bolivia, Chile and *Argentina*). Due to climate change and the growing human population in this region (more than 80 million people), the exposure of the Andean societies to disasters from hydrometeorological extremes is frequently discussed in the scientific literature. Poveda et al. (2020) provided a comprehensive review of the main high impact events associated with hydroclimate variability in the Andes.

Changes in the regional hydrological cycle brought about from climate variability, climate change and land use changes are of particular importance because of their impacts on human and ecological systems. The Andes exhibits a large variety of hydrological regimes (**Figure 1**), which are partially influenced by large and regional-scale climatological conditions, as discussed in Part I of this two-part review (Espinoza et al., 2020). For instance, annual cycles of river discharge in the north tropical Andes (north of 8°S) exhibit unimodal or bimodal regimes, depending on the annual cycle of precipitation, the dynamics of atmospheric low-level jets and the land surface-atmosphere interactions. Rivers of the inner Andes of Colombia have a bimodal discharge annual cycle whereas rivers draining into the Caribbean, Orinoco and Amazon basins exhibit a unimodal annual regime. In the northern Peruvian and Ecuadorian Amazon, the hydrological seasonality is more complex (e.g., bimodal or unimodal) due to the influence of several rainfall regimes. Rivers of the equatorial Andes of the Pacific drainage have a unimodal discharge annual cycle, with a peak in March-April in association with southerly position of the ITCZ. Therefore, it is relevant to understand the physical processes involved in the bimodal rainfall annual cycle, restricted on the north tropical and equatorial Andes, while unimodal cycles are observed southward in the tropical Andes.

Rivers in the south tropical Andes (between 8°S and 27°S) are characterized by discharge peaks during February and March, associated with the wet season in the mature phase of the South American Monsoon system. Between the southern end of the Altiplano (27°S) and about 35°S, most rivers also show a unimodal annual cycle characterized by an austral summer discharge peak, but in this case largely related to the melting of the winter snow accumulated in the upper basins. Some rivers in this region also receive important contributions from glaciers and permanent ice-rich permafrost features such as rock glaciers. Further south in the extratropical Andes (south of 37°S), some sectors show a single discharge peak due to higher precipitation during austral winter, while others also show a secondary peak in spring-early austral summer due to snowmelt. Only a few river basins with large glaciated areas (such as those draining the north and south Patagonian Icefields) show a discernible glacier melt signal on

river flows. Masiokas et al. (2020) presented a detailed discussion on recent changes in the Andean cryosphere.

Despite the clear identification of the different regional patterns of runoff cycles in the Andes, there are still gaps limiting a complete understanding of runoff variability in the region. Particularly, further research is required to explain the role of precipitation recycling, soil moisture, evapotranspiration, vegetation, groundwater and aquifers, as well as glaciers and snowpack, in regulating the annual runoff cycle over the Andes. Moreover, how climate change will alter these water fluxes and reservoirs, and how the current warming would affect river flows at subtropical and extratropical latitudes, are still open questions. To understand long-term changes (from decades to centuries) in the Andean hydroclimate, we need further research on the long-term water and energy balances over the Andes. For instance, we need to identify if the surface and the atmospheric water balances exhibit a closure in the long-term. Moreover, we need to estimate the strength of the coupling between the surface and the atmospheric water and energy budgets along the different river basins of the Andes. In addition, we need to determine if the hydrological variables over the Andes exhibit long-term trends and/or non-stationaries and their effects on the water balance closure. Here it is relevant to separate the impacts of climate change from those arising from low-frequency natural variability and those related to land use changes.

Local orography strongly modulates the availability of atmospheric moisture and produces local circulations, which are key elements to trigger convection in the tropical and subtropical Andes. In general, air moves upward (downward) during daytime (nighttime) from lower (higher) sectors, adjacent plains and valley floor, to upper (lower) sectors of the tropical and subtropical Andes following slope and valleys, shaping different diurnal cycles of precipitation. In the subtropics and extratropics, frontal precipitation dominates in winter, when orography modifies precipitation systems coming from the Pacific Ocean. In particular, orography affects the precipitating clouds within a passing frontal system and enhances precipitation in the windward (western) side of the Andes by a factor 2–3 with respect to coastal and lowland values at the same latitude. Despite the substantial differences in mountain height and incoming moist-laden westerly flow, still, the mechanisms involved are not clear. Precipitation is, on the other hand, greatly reduced downstream of the Andes, creating a very marked precipitation gradient between southern Chile (>3,000 mm/year) and southwestern *Argentina* (<300 mm/year). However, the lack of sufficient number of spatially distributed ground-based measurements of precipitation and other hydroclimatic variables over the Andes (Condom et al., 2020), including the strong limitations of satellite estimates over the Andes (Vallejo-Bernal et al., 2020), severely limits the understanding of the local processes involved in precipitation and surface hydrology in the region. This results in a poor estimation of the precipitation and large residuals (usually negative) in water balances, even for large Andean river basins. An alternative approach to partially tackle both, the role of local processes and the high spatial variability in the Andes is the use of high-resolution (both spatial and temporal) climate model simulations. They could be calibrated in the few regions with dense meteorological networks and with the use of the relatively scarce sub-daily meteorological data available to study the diurnal cycles of diverse hydroclimatic variables. The development of high-resolution simulations in the Andes could provide insights to understand and predict the dynamical and thermodynamic processes, explaining the location of the rain hotspots over regions largely influenced by orographic processes, such as western Colombia, the Amazon-Andes transition zone and western Patagonia. Even more, the role of the vegetation on these rain hotspots zones needs to be deeply explored, and that can be potentially addressed using climate simulations and improving the observational network, as well as improving the observational networks in these regions.

Hydroclimate in the Andes is also modulated by different large-scale phenomena such as the tropical easterly waves, aerial and atmospheric rivers, low-level jets, and climatic oscillations, such as MJO, ENSO, SAM, Atlantic SST variability, PDO, and AMO. Although ENSO is the dominant mode of interannual variability of hydroclimate in the Andes, different spatial patterns of SST anomalies over the tropical oceans, like those associated with the ENSO Modoki events in the equatorial Pacific, may induce divergent responses in the Andean hydroclimate. The influence of the tropical North Atlantic has been particularly demonstrated as relevant in the northern Andes and during the winter season in the southern tropical Andes; however, the influences of the South Atlantic Ocean conditions on the hydroclimate on the Andes are largely unknown. Longer time-scale phenomena such as the PDO or the AMO also modulate hydroclimate variability in the Andes. In general, further studies focused on this hydroclimate variability in the Andes are relevant for seasonal and subseasonal forecasts in the region.

The current knowledge about the hydroclimatological processes over the Andes highlights the necessity to better understand different phenomena from local to regional scales, and their interactions at different timescales. In addition to the research gaps highlighted in the previous paragraphs of this section, other research necessities emerge. For instance, the Andes are affected by the activity of different low-level jets (see Espinoza et al., 2020; Poveda et al., 2020); therefore, a better understanding is needed on how these low-level circulations influence the spatiotemporal variability of rainfall, evapotranspiration, soil moisture and streamflows. The occurrence of mesoscale convective and midlatitude stratiform precipitation systems, and their interactions with these low-level jets and orography in the Andes, needs to be further investigated (e.g., Vera, 2006; Viale et al., 2013; Poveda et al., 2020). In addition, the land-atmosphere interaction among surrounding regions are relevant for the Andes hydroclimate. For example, how changes in the Amazon's vegetation (deforestation or savanization) affect surface and atmosphere water and energy budgets over the Andes across scales is of utmost importance. Moreover, we need to better understand the interconnection of the hydrometeorological, climatological and biogeochemical feedbacks between the Andes, the Amazon and the Pacific Ocean. Finally, since local processes play a key role in the Andes, further research is required on the mechanisms controlling the high amounts of precipitation recycling over the tropical Andes and how much water is sublimated from the dry, snow-capped Andes in the subtropics.

The above summarized research and knowledge gaps need to be tackled in the ANDEX research agenda. In particular, the improvement of the observational and monitoring networks in the Andes, as well as the development of high-resolution modeling studies, are necessary in order to fill the major research questions related to recurrent local-scales and orographically-induced physical processes in the Andean hydroclimate. In this context, two additional major technical questions emerge: 1) what are the observational requirements (in terms of what to measure and the spatio-temporal scales) to better understand the hydrometeorological processes under climate change in the Andes?, and 2) what is the proper level of complexity and resolution required to tackle the previous research gaps? It is required to address these and other research gaps to improve our understanding of the Andean hydroclimate and its vulnerability to natural variability and human-induced changes.

AUTHOR CONTRIBUTIONS

All authors listed have made a substantial, direct, and intellectual contribution to the work and approved it for publication.

FUNDING

This review paper has been achieved as part of the ANDEX program (www.gewex.org/project/andex/), which is a prospective Regional Hydroclimate Project (RHP) of the GEWEX Hydroclimatology Panel (GHP). PA was supported by Universidad de Antioquia through the Grant CODI PRG 2017–16264. JE was supported by the French AMANECER-MOPGA project funded by ANR and IRD (ref. ANR-18-MPGA-0008). MM was funded by Consejo Nacional de Investigaciones Científicas y Técnicas (CONICET)–*Argentina*. LS would like to acknowledge the financial support from Tri-agency Institutional Programs Secretariat of Canada through the Global Water Futures Program, Canada First Research Excellence Fund. MV was supported by FONDECYT 11151009 and FONCYT PICT 2016–1666.

ACKNOWLEDGMENTS

We acknowledge Pedro Rau for providing **Figure 3**.

REFERENCES

Aceituno, P. (1988). On the functioning of the Southern Oscillation in the South American sector. Part I: surface climate. *Mon. Weather Rev.* 116, 505–524. doi:10.1175/1520-0493(1988)116<0505:otfots>2.0.co;2

Alpert, P. (1986). Mesoscale indexing of the distribution of orographic precipitation over high mountains. *J. Clim. Appl. Meteorol.* 25, 532–545. doi:10.1175/1520-0450(1986)025<0532:miotdo>2.0.co;2

Alvarez-Villa, O. D., Vélez, J. I., and Poveda, G. (2011). Improved long-term mean annual rainfall fields for colombia. *Int. J. Climatol.* 31, 2194–2212. doi:10.1002/joc.2232

Ampuero, A., Strikis, N., Apaéstegui, J., Vuille, M., Novello, V. F., Espinoza, J. C., et al. (2020). The forest effects on the isotopic composition of rainfall in the northwestern Amazon Basin. Journal of Geophysical Research:. *Atmosphere* 125, e2019JD031445. doi:10.1029/2019JD031445

Aravena, R. (1995). Hidrología isotópica y geoquímica de las aguas subterráneas del norte de chile. *Bull. Inst. Fr. Études Andines*. 24 (3), 495–504.

Arias, P. A., Martínez, J. A., Mejía, J. D., Pazos, M. J., and Espinoza, J. C. (2020). Changes in normalized difference vegetation index in the orinoco and amazon river basins: links to tropical atlantic surface temperatures. *J. Clim.* 33 (19), 8537–8559. doi:10.1175/jcli-d-19-0696.1

Arias, P. A., Martínez, J. A., and Vieira, S. C. (2015). Moisture sources to the 2010-2012 anomalous wet season in northern south america. *Clim. Dynam.* 45 (9-10), 2861–2884. doi:10.1007/s00382-015-2511-7

Arrieta-Castro, M., Donado-Rodríguez, A., Acuña, G. J., Canales, F. A., Teegavarapu, R. S. V., and Kaźmierczak, B. (2020). Analysis of streamflow variability and trends in the meta river, colombia. *Water* 12, 1451. doi:10.3390/w12051451

ANA, (2012). Recursos Hídricos en el Peru, 2nd Edn. Ministerio de Agricultura. Autoridad Nacional del Agua, Lima, 45–189.

Ashok, K., Behera, S. K., Rao, S. A., Weng, H., and Yamagata, T. (2007). El Niño Modoki and its possible teleconnection. *J. Geophys. Res.* 112, C11007. doi:10.1029/2006JC003798

Ayala, Á., Farías-Barahona, D., Huss, M., Pellicciotti, F., McPhee, J., and Farinotti, D. (2020). Glacier runoff variations since 1955 in the maipo river basin, in the semiarid andes of central chile. *Cryosphere* 14, 2005–2027. doi:10.5194/tc-14-2005-2020

Ayes Rivera, I., Callau Poduje, A. C., Molina-Carpio, J., Ayala, J. M., Armijos, E., Espinoza-Villar, R., et al. (2003–2016). On the relationship between suspended sediment concentration, rainfall variability and groundwater: an empirical and probabilistic analysis for the andean beni river. *Bolivia Water* 2019 (11), 2497. doi:10.3390/w11122497

Azócar, G. F., and Brenning, A. (2010). A. Hydrological and geomorphological significance of rock glaciers in the dry andes, chile (27°-33°S). *Permafr. Periglac. Process.* 21 (1), 42–53. doi:10.1002/ppp.669

Barrett, B. S., Krieger, D. B., and Barlow, C. P. (2011). Multiday circulation and precipitation climatology during winter rain events of differing intensities in central chile. *J. Hydrometeorol.* 12, 1071–1085. doi:10.1175/2011jhm1377.1

Barrett, B. S., Carrasco, J. F., and Testino, A. P. (2012). Madden–julian oscillation (MJO) modulation of atmospheric circulation and chilean winter precipitation. *J. Clim.* 25, 1678–1688. doi:10.1175/JCLI-D-11-00216.1

Barrett, B. S., Garreaud, R., and Falvey, M. (2009). Effect of the Andes cordillera on precipitation from a midlatitude cold front. *Mon. Weather Rev.* 137 (9), 3092–3109.

Bechis, H., Salio, P., and Ruiz, J. J. (2020). Drylines in Argentina: synoptic climatology and processes leading to their genesis. *Mon. Weather Rev.* 148, MWR-D-19–0050.1. doi:10.1175/MWR-D-19-0050.1

Bedoya-Soto, J. M., Aristizábal, E., Carmona, A. M., and Poveda, G. (2019). Seasonal shift of the diurnal cycle of rainfall over medellin's valley, central andes of colombia (1998–2005). *Front. Earth Sci.* 7, 92. doi:10.3389/feart.2019.00092

Bedoya-Soto, J. M., Poveda, G., Trenberth, K., and Vélez, J. J. (2018). Interannual hydroclimatic variability and the 2009–2011 extreme ENSO phases in colombia: from andean glaciers to caribbean lowlands. *Theor. Appl. Climatol.* 135, 1531–1544. doi:10.1007/s00704-018-2452-2

Bendix, J., Trachte, K., Cermak, J., Rollenbeck, R., and Nauss, T. (2009). Formation of convective clouds at the foothills of the tropical eastern andes (south Ecuador). *J. Appl. Meteorol.* 48, 1682–1695. doi:10.1175/2009jamc2078.1

Berbery, E. H., and Barros, V. (2000). The hydrologic cycle of the La Plata basin in South America. *J. Hydrometeorol.* 3, 630–645.

Bookhagen, B., and Strecker, M. R. (2008). Orographic barriers, high-resolution TRMM rainfall, and relief variations along the eastern andes. *Geophys. Res. Lett.* 35, L06403. doi:10.1029/2007GL032011

Boisier, J. P., Rondanelli, R., Garreaud, R. D., and Muñoz, F. (2016). Anthropogenic and natural contributions to the Southeast Pacific precipitation decline and recent megadrought in central Chile. *Geophys. Res. Lett.*, 43, 413–421. doi:10.1002/2015GL067265–1266

Bourrel, L., Rau, P., Dewitte, B., Labat, D., Lavado, W., Coutaud, A., et al. (2015). Ordoñez JLow-frequency modulation and trend of the relationship between ENSO and precipitation along the northern to centre peruvian pacific coast. *Hydrol. Process.* 29 (6), 1252. doi:10.1002/hyp.10247–1266.

Bozkurt, D., Rondanelli, R., Garreaud, R., and Arriagada, A. (2016). Impact of warmer eastern tropical pacific SST on the march 2015 atacama floods. *Mon. Weather Rev*. 144 (11), 4441–4460. doi:10.1175/mwr-d-16-0041.1

Builes-Jaramillo, L. A., and Poveda, G. (2018). Conjoint analysis of surface and atmospheric water balances in the andes-amazon system. *Water Resour. Res*. 54 (5), 3472–3489. doi:10.1029/2017WR021338

Buytaert, W., Celleri, R., Willems, P., De Bièvre, B., and Wyseure, G. (2006). Spatial and temporal rainfall variability in mountain areas: a case study from the south ecuadorian andes. *J. Hydrol*. 329, 413–421. doi:10.1016/j.jhydrol.2006.02.031

Buytaert, W., Moulds, S., Acosta, L., de Bievre, B., Olmos, C., Villacis, M., et al. (2017). Glacial melt content of water use in the tropical andes. *Environ. Res. Lett*. 12, 114014. doi:10.1088/1748-9326/aa926c

Cai, W., McPhaden, M., Grimm, A., Rodrigues, R., Taschetto, A., Garreaud, R., et al. (2020). Climate impacts of el niño-southern oscillation on south america. *Nat. Rev. Earth Environ*. 1, 215–231. doi:10.1038/s43017-020-0040-3

Campozano, L., Celleri, R., Trachte, K., Bendix, J., and Samaniego, E. (2016). Rainfall and cloud dynamics in the andes: a southern ecuador case study. *Adv. Meteorol*. 2016, 3192765. doi:10.1155/2016/3192765

Campozano, L., Robaina, L., and Samaniego, E. (2020). The Pacific decadal oscillation modulates the relation of ENSO with the rainfall variability in coast of ecuador. *Int. J. Climatol*. 40 (13), 5801–5812. doi:10.1002/joc.6525

Campozano, L., Trachte, K., Célleri, R., Samaniego, E., Bendix, J., Albuja, C., et al. (2018). Climatology and teleconnections of mesoscale convective systems in an andean basin in southern Ecuador: the case of the paute basin. *Adv. Meteorol*. 2018, 1–13. doi:10.1155/2018/4259191

Chaffaut, I. (1998). "Precipitations d´altitude, eaux souterraines et changements climatiques de l´altiplano nord-chilien. these presenté pour obtenir le grade de docteur en sciences," in *Université paris XI orsay, octubre 1998*. Editors J. Araya, P. Pierre, A. Marc, A. Covarrubias, R. Espejo, L. Nelda, L. Vargas. (Paris).

Chavez, S. P., and Takahashi, K. (2017). Orographic rainfall hotspots in the andes-amazon transition according to the TRMM precipitation radar and *in situ* data. *J. Geophys. Res. Atmos*. 122 (11), 5870–5882. doi:10.1002/2016JD026282

Chow, F. K., De Wekker, S. F. J., and Snyder, B. J. (2013). "Recent progress and current challenges," in *Mountain weather research and forecasting*. The Netherlands: Springer, 750.

Condom, T., Martínez, R., Pabón, J. D., Costa, F., Pineda, L., Nieto, J. J., et al. (2020). Climatological and hydrological observations for the south american andes: *in-situ* stations, satellite and reanalysis data sets. *Front. Earth Sci*. 8, 92. doi:10.3389/feart.2020.00092

Coudrain, A., Loubet, M., Condom, T., Talbi, A., Ribstein, P., Pouyaud, B., et al. (2002). Donnees isotopiques (87Sr/86Sr) et changements hydrologiques depuis 15 000 ans sur l'altiplano andin. *Hydrol. Sci. J*. 47, 293–306. doi:10.1080/02626660209492931

Dollfus, O. (1964). Cambios climáticos cuaternarios en los andes peruanos. boletin de la sociedad geografica. *Lima*. 83, 65–74.

Dussaillant, I., Berthier, E., Brun, F., Masiokas, M., Hugonnet, R., and Favier, V. (2019). Two decades of glacier mass loss along the andes. nat. *Geoscience* 12, 802–808. doi:10.1038/s41561-019-0432-5

Espinoza, J. C., Chavez, S., Ronchail, J., Junquas, C., Takahashi, K., and Lavado, W. (2015). Rainfall hotspots over the south tropical andes: spatial distribution, rainfall intensity and relations with largescale atmospheric circulation. *Water Resour. Res*. 51, 3459–3475. doi:10.1002/2014wr016273

Espinoza, J. C., Garreaud, R., Poveda, G., Arias, P. A., Molina-Carpio, J., Masiokas, M., et al. (2020). Hydroclimate of the andes. Part I: main climatic features. *Front. Earth Sci*. 8, 64. doi:10.3389/feart.2020.00064

Espinoza, J. C., Ronchail, J., Guyot, J. L., Cochonneau, G., Naziano, F., Lavado, W., et al. (2009a). Spatio-temporal rainfall variability in the amazon basin countries (Brazil, Peru, Bolivia, Colombia, and Ecuador). *Int. J. Climatol*. 29, 1574–1594. doi:10.1002/joc.1791

Espinoza, J. C., Guyot, J. L., Ronchail, J., Cochonneau, G., Filizola, N., Fraizy, P., et al. (2009b). Contrasting regional discharge evolutions in the amazon basin (1974-2004). *J. Hydrol*. 375, 297–311. doi:10.1016/j.jhydrol.2009.03.004

Espinoza, J. C., Ronchail, J., Guyot, J. L., Junquas, C., Vauchel, P., Lavado, W., et al. (2011). Climate variability and extreme drought in the upper solimões River (western Amazon Basin): understanding the exceptional 2010 drought. *Geophyisical Res. Lett*. 38, 1–6. doi:10.1029/2011GL047862

Espinoza, J. C., Marengo, J. A., Ronchail, J., Molina, J., Noriega, L., and Guyot, J. L. (2014). The extreme 2014 flood in south-western amazon basin: the role of tropical-subtropical south atlantic SST gradient. *Environ. Res. Lett*. 9, 124007. doi:10.1088/1748-9326/9/12/124007

Espinoza, J. C., Ronchail, J., Marengo, J. A., and Segura, H. (2019). Contrasting North–South changes in Amazon wet-day and dry-day frequency and related atmospheric features (1981–2017). *Clim. Dynam*. 52 (9-10), 5413–5430. doi:10.1007/s00382-018-4462-2

Falvey, M., and Garreaud, R. D. (2005). Moisture variability over the South American Altiplano during the South American low level jetexperiment (SALLJEX) observing season. *J. Geophy. Res*. 110, D22105. doi:10.1029/2005JD006152

Falvey, M., and Garreaud, R. (2007). Wintertime precipitation episodes in central Chile: associated meteorological conditions and orographic influences. *J. Hydrometeorol*. 8 (2), 171–193. doi:10.1175/jhm562.1

FAO (1998). Crop evapotranspiration–guidelines for computing crop water requirements–FAO Irrigation and drainage. Available at: http://www.fao.org/3/x0490e/x0490e00.htm#Contents (Accessed May 20, 2020).

Flores-Rojas, J. L., Cuxart, J., Piñas-Laura, M., Callañaupa, S., Suárez-Salas, L., Kumar, S., et al. (2019a). Seasonal and diurnal cycles of surface boundary layer and energy balance in the central andes of perú, mantaro valley. *Atmosphere* 10, 779. doi:10.3390/atmos10120779

Florez-Rojas, J. L., Alvarez, A. S. M., Kumar, S., Castro, D. M., Puma, E. V., and Silva, F. Y. (2019b). Analysis of possible triggering mechanisms of severe thunderstorms in the tropical central andes of peru, mantaro valley. *Atmosphere* 10, 301. doi:10.3390/atmos10060301

Garreaud, R., Alvarez-Garreton, C., Barichivich, J., Boisier, J. P., Christie, D., Galleguillos, M., et al. (2017). The 2010–2015 mega drought in central chile: impacts on regional hydroclimate and vegetation. *Hydrol. Earth Syst. Sci*. 21, 6307–6327. doi:10.5194/hess-2017-191

Garreaud, R. D. (1999). Multiscale Analysis of the summertime precipitation over the central andes. *Mon. Weather Rev*. 127, 901–921. doi:10.1175/1520-0493(1999)127<0901:maotsp>2.0.co;2

Garreaud, R. D. (2009). The Andes climate and weather. *Adv. Geosci*. 22, 3–11. doi:10.5194/adgeo-22-3-2009

Garreaud, R. D. (2018). A plausible atmospheric trigger for the 2017 coastal el niño. *Int. J. Climatol*. 38, 1296–1302. doi:10.1002/joc.5426

Garreaud, R. D., Vuille, M., Compagnucci, R., and Marengo, J. (2009). Present-day south american climate. *Palaeogeogr. Palaeoclimatol. Palaeoecol*. 281, 180–195. doi:10.1016/j.palaeo.2007.10.032

Garreaud, R., Vuille, M., and Clement, A. (2003). The climate of the Altiplano: observed current conditions and mechanisms of past changes. *Palaeogeogr. Palaeoclimatic. Palaeoecol*. 194, 5–22.

Garreaud, R., Lopez, P., Minvielle, M., and Rojas, M. (2013). Large scale control on the Patagonia climate. *J. Clim*. 26, 215–230.

Garreaud, R., Falvey, M., and Montecinos, A. (2016). Orographic precipitation in coastal southern Chile: mean distribution, temporal variability, and linear contribution. *J. Hydrometeorol*. 17 (4), 1185–1202.

Garreaud, R. D., Boisier, J. P., Rondanelli, R., Montecinos, A., Sepúlveda, H. H., and Veloso-Aguila, D. (2020). The central chile mega drought (2010 -2018): a climate dynamics perspective. *Int. J. Climatol*. 40, 421–439. doi:10.1002/joc.6219

Gascoin, S., Lhermitte, S., Kinnard, C., Bortels, K., and Liston, G. E. (2013). Wind effects on snow cover in Pascua-Lama, dry andes of chile. *Adv. Water Resour*. 55, 25–39. doi:10.1016/j.advwatres.2012.11.013

Geerts, B. (2017). The 2015 Plains Elevated Convection at Night Field Project. *Bull. Amer. Meteor. Soc*. 98, 767–786. doi:10.1175/BAMS-D-15-00257.1

Gillett, N. P., Kell, T. D., and Jones, P. D. (2006). Regional climate impacts of the southern annular mode. *Geophys. Res. Lett*. 33 (23). doi:10.1029/2006GL027721

Giovannettone, J. P., and Barros, A. P. (2009). Probing regional orographic controls of precipitation and cloudiness in the central Andes using satellite data. *J. Hydrometeorol*. 10, 167–182.

González-Reyes, A., McPhee, J., Christie, D. A., Le Quesne, C., Szejner, P., Masiokas, M. H., et al. (2017). Spatiotemporal variations in hydroclimate across the mediterranean andes (30°–37°S) since the early twentieth century. *J. Hydrometeorol*. 18, 1929–1942. doi:10.1175/JHM-D-16-0004.1

Grimm, A. M. (2019). Madden–julian oscillation impacts on south american summer monsoon season: precipitation anomalies, extreme events,

teleconnections, and role in the MJO cycle. *Clim. Dynam*. 53, 907–932. doi:10.1007/s00382-019-04622-6

Grimm, A. M., and Ambrizzi, T. (2009). Teleconnections into South America from the tropics and extratropics on interannual and intraseasonal timescales. In: Vimeux, F., Sylvestre, F. and Khodri, M., editors. Past climate variability in South America and surrounding regions: from the last glacial maximum to the Holocene, Springer, Apeldoorn, 159-191. Available at: http://dx.doi.org/10.1007/978-90-481-2672-9_7

Guyot, J. L. (1993). *Hydrogéochimie des fleuves de l'amazonie bolivienne, editions de l'ORSTOM*. (Paris: INSTITUT FRANCAIS DE RECHERCHE SCIENTIFIQUE POUR LE DÉVELOPPEMENT EN COOPÉRATION) 261.

Hierro, R., Pessano, H., Llamedo, P., de la Torre, A., Alexander, P., and Odiard, A. (2013). Orographic effects related to deep convection events over the Andes region. Atmos. *Atmos. Res*. 120–121. doi:10.1016/j.atmosres.2012.08.020

Houston, J., and Hartley, A. J. (2003). The central Andean west-slope rainshadow and its potential contribution to the origin of hyper-aridity in the atacama desert. Int. *J. Climatol*. 322 (23), 1453–1464. doi:10.1002/joc.938

Hoyos, I., Dominguez, F., Cañón-Barriga, J., Martínez, J. A., Nieto, R., Gimeno, L., et al. (2017). Moisture origin and transport processes in colombia, northern south america. *Clim. Dynam*. 1–20. doi:10.1007/s00382-017-3653-6

Huerta, A., and Lavado-Casimiro, W. (2020). Trends and variability of precipitation extremes in the peruvian altiplano (1971–2013). *Int. J. Clim*. [Epub ahead of print]. doi:10.1002/joc.6635

Hunziker, S., Brönnimann, S., Calle, J., Moreno, I., Andrade, M., Ticona, L., et al. (2018). Effects of undetected data quality issues on climatological analyses. *Clim. Past*. 14, 1–20. doi:10.5194/cp-14-1-2018

Imfeld, N., Schuller, C. B., Marrou, K. M. C., Jaques-Cooper, M., Sedlmeier, K., Gubler, S., et al. (2019). Summertime precipitation deficits in the southern peruvian highlands since 1964. *Int. J. Climatol*. 39 (11), 4497–4513. doi:10.1002/joc.6087

Imfeld, N., Sedlmeier, K., Gubler, S., Marrou, K. C., Davila, C. P., Huerta, A., et al. (2020). A combined view on precipitation and temperature climatology and trends in the southern andes of peru. *Int. J. Climatol*. 1–20. doi:10.1002/joc.6645

Jacques-Coper, M., and Garreaud, R. D. (2015). Characterization of the 1970s climate shift in South America. *Int. J. Climatol*. 35, 2164–2179. doi:10.1002/joc.4120

Johnson, A. M. (1976). "The climate of peru, bolivia, and ecuador. climates of central and south america," in *World survey of climatology*. (New York: Elsevier Scientific Publishing Company), Chap. 4, Vol. 12, 147–218.

Jones, C., and Carvalho, L. M. V. (2002). Active and break phases in the south american monsoon system. *J. Clim*. 15, 905–914. doi:10.1175/1520-0442(2002)015<0905:aabpit>2.0.co;2

Jones, C., and Carvalho, L. M. V. (2018). The influence of the atlantic multidecadal oscillation on the eastern andes low-level jet and precipitation in south america. *NPJ Clim. Atmos. Sci*. 1, 1–7. doi:10.1038/s41612-018-0050-8

Juliá, C., Rahn, D. A., and Rutllant, J. A. (2012). Assessing the influence of the MJO on strong precipitation events in subtropical, semi-arid north-central chile (30°S). *J. Clim*. 25, 7003–7013. doi:10.1175/JCLI-D-11-00679.1

Junquas, C., Takahashi, K., Condom, T., Espinoza, J. C., Chavez, S., Sicart, J. E., et al. (2018). Understanding the influence of orography over the precipitation diurnal cycle and the associated atmospheric processes in the central andes. *Clim. Dynam*. 50 (11-12), 3995–4017. doi:10.1007/s00382-017-3858-8

Kayano, M. T., Andreoli, R. V., and Souzade, R. A. F. (2019). El niño–southern oscillation related teleconnections over south America under distinct atlantic multidecadal oscillation and pacific interdecadal oscillation backgrounds: la niña. *Int. J. Climatol*. 39, 1359–1372. doi:10.1002/joc.5886

Kayano, M. T., and Capistrano, V. B. (2014). How the atlantic multidecadal oscillation (AMO) modifies the ENSO influence on the south american rainfall. *Int. J. Climatol*. 34, 162–178. doi:10.1002/joc.3674

Kreft, S., Eckstein, D., and Melchior, I. (2016). *Global climate risk index 2017: who suffers most from extreme weather events, Weather-related loss events in 2015 and 1996 to 2015*. Berlin: Germanwatch e.V.

Krogh, S. A., Pomeroy, J. W., and McPhee, J. (2015). Physically based mountain hydrological modeling using reanalysis data in patagonia. *J. Hydrometeorol*. 16 (2007), 172–193. doi:10.1175/JHM-D-13-0178.1

Kumar, S., Vidal, S.-Y., Moya-Álvarez, A. S., and Martínez-Castro, D. (2019). Effect of the surface wind flow and topography on precipitating cloud systems over the andes and associated amazon basin: GPM observations. *Atmos. Res*. 225, 193–208. doi:10.1016/j.atmosres.2019.03.027

Kumar, S., Moya-Álvarez, A. S., Castillo-Velarde, C. D., Martinez-Castro, D., and Silva, Y. (2020a). Effect of low-level flow and Andes mountain on the tropical and mid-latitude precipitating cloud systems: GPM observations. *Theor. Appl. Climatol*. 141, 157–172. doi:10.1007/s00704-020-03155-x

Kumar, S., Castillo-Velarde, C. D., Prado, V. J. M., Rojas, F. J. L., Gutierrez, C. S. M., Moya Alvarez, A. S., et al. (2020b). Rainfall characteristics in the mantaro basin over tropical andes from a vertically pointed profile rain radar and *in-situ* field campaign. *Atmosphere* 11, 248. doi:10.3390/atmos11030248

Lagos, P., Silva, Y., Nickl, E., and Mosquera, K. (2008). El Niño –related precipitation variability in peru. *Adv. Geosci*. 14, 231–237. doi:10.5194/adgeo-14-231-2008

Lara, A., Villalba, R., and Urrutia, R. (2008). A 400-year tree-ring record of the Pueblo River summer–fall streamflow in the valdivian rainforest eco-region, chile. *Clim. Change* 86, 331–356. doi:10.1007/s10584-007-9287-7

Laraque, A., Ronchail, J., Cochonneau, G., Pombosa, R., and Guyot, J. L. (2007). Heterogeneous distribution of rainfall and discharge regimes in the ecuadorian amazon basin. *J. Hydrometeorol*. 8, 1364–1381. doi:10.1175/2007jhm784.1

Larkin, N. K., and Harrison, D. E. (2005). On the definition of El Niño and associated seasonal average U.S. weather anomalies. *Geophys. Res. Lett*. 32, L13705. doi:10.1029/2005GL022738

Lavado, W., and Espinoza, J. C. (2014). Impactos de El Niño y La Niña en las lluvias del perú (1965-2007). *Revista Brasileira de Meteorologia* 29, 171–182. doi:10.1590/S0102-77862014000200003

Lavado-Casimiro, W., Labat, D., Guyot, J. L., and Ardoin-Bardin, S. (2011). Assessment of climate change impacts on the hydrology of the peruvian amazon–andes basin. *Hydrol. Process*. 25 (24), 3721–3734. doi:10.1002/hyp.8097

Lavado-Casimiro, W., Labat, D., Ronchail, J., Espinoza, J. C., and Guyot, J. L. (2013). Trends in rainfall and temperature in the Peruvian Amazon-Andes basin over the last 40 years (1965-2007). *Hydrol. Process*. 41, 2944–2957. doi:10.1002/hyp.9418

Lavado-Casimiro, W. S., Ronchail, J., Labat, D., Espinoza, J. C., and Guyot, J. L. (2012). Basin-scale analysis of rainfall and runoff in Peru (1969–2004): Pacific, Titicaca and Amazonas drainages. *Hydrol. Sci. J*. 57. doi:10.1080/02626667.2012.672985

Li, Y., and Smith, R. B. (2010). The detection and significance of diurnal pressure and potential vorticity anomalies east of the rockies. *J. Atmos. Sci*. 67, 2734–2751. doi:10.1175/2010JAS3423.1

Loaiza Cerón, W., Andreoli, R. V., Kayano, M. T., Ferreira de Souza, R. A., Jones, C., and Carvalho, L. M. V. (2020). The influence of the atlantic multidecadal oscillation on the choco low-level jet and precipitation in colombia. *Atmosphere* 11, 174. doi:10.3390/atmos11020174

López, M. E., and Howell, W. E. (1967). Katabatic winds in the Equatorial Andes, *J. Atmos. Sci*. 24 (1), 29–35.

MacDonell, S., Kinnard, C., Mölg, T., Nicholson, L., and Abermann, J. (2013). Meteorological drivers of ablation processes on a cold glacier in the semi-arid andes of chile. *Cryosphere* 7, 1513–1526. doi:10.5194/tc-7-1513-2013

Madden, R. A., and Julian, P. R. (1994). Observations of the 40–50-day tropical oscillation—a review. *Mon. Weather Rev*. 122, 814–837. doi:10.1175/1520-0493(1994)122<0814:ootdto>2.0.co;2

Marengo, J. A. (2009). Long-term trends and cycles in the hydrometeorology of the amazon basin since the late 1920s. *Hydrol. Process*. 23, 3236–3244. doi:10.1002/hyp.7396

Marengo, J. A., and Espinoza, J. C. (2016). Extreme seasonal droughts and floods in amazonia: causes, trends and impacts. *Int. J. Climatol*. 36 (3), 1033–1050. doi:10.1002/joc.4420

Martinez, J. A., and Dominguez, F. (2014). Sources of atmospheric moisture for the la plata river basin. *J. Clim*. 27, 6737–6753. doi:10.1175/JCLI-D-14-00022.1

Masiokas, M. H., Cara, L., Villalba, R., Pitte, P., Luckman, B. H., Toum, E., et al. (2019). Streamflow variations across the andes (18°-55°S) during the instrumental era. *Sci. Rep*. 9, 17879. doi:10.1038/s41598-019-53981-x

Masiokas, M. H., Villalba, R., Luckman, B. H., Le Quesne, C., and Aravena, J. C. (2006). Snowpack variations in the central andes of argentina and chile, 1951–2005: large-scale atmospheric influences and impli-cations for water resources in the region. *J. Clim*. 19, 6334–6352. doi:10.1175/jcli3969.1

Massmann, A., Minder, J., Garreaud, R., Kingsmill, D., Valenzuela, R., Montecinos, A., Fults, S., and Snider, J. (2017). The chilean coastal orographic precipitation experiment: observing the influence of microphysical rain regime on coastal orographic precipitation. *J. Hydrometeorol.* 18 (10), 2723–2743. doi:10.1175/jhm-d-17-0005.1

Mauget, M. H., Rabatel, A., Rivera, A., Ruiz, L., Pitte, P., Ceballos, J. L., et al. (2020). Current state and recent changes of the cryosphere in the andes. *Front. Earth Sci.* 8, 99. doi:10.3389/feart.2020.00099

Mayta, V. C., Ambrizzi, T., Espinoza, J. C., and Silva Dias, P. L. (2019). The role of the madden–julian oscillation on the amazon basin intraseasonal rainfall variability. *Int. J. Climatol.* [Epub ahead of print]. doi:10.1002/joc.5810

Mejía, J. F., Mesa, O. J., Poveda, G., Vélez, J., Hoyos, C., Mantilla, R., et al. (1999). Distribución espacial y ciclos anual y semianual de la precipitación en colombia. *Dyna.* 127, 7–26.

Minvielle, M., and Garreaud, R. D. (2011). Projecting rainfall changes over the south american altiplano. *J. Clim.* 24 (17), 4577–4583. doi:10.1175/jcli-d-11-00051.1

Mo, K. C., and Higgins, R. W. (1998). The Pacific -South American modes and tropical convection during the Southern Hemisphere Winter. *Mon. Weather Rev.* 126 (6), 1581–1596.

Mohr, K. I., Slayback, D., and Yager, K. (2014). Characteristics of precipitation features and annual rainfall during the TRMM era in the central andes. *J. Clim.* 27 (11), 3982–4001. doi:10.1175/jcli-d-13-00592.1

Molina, R., Salazar, J. F., Martínez, J. A., Villegas, J. C., and Arias, P. A. (2019). Exponential growth of precipitation along a "forest-fed moisture conveyor belt" above the amazon. *J. Geophys. Res. Atmos.* 124, 2589–2599. doi:10.1029/2018JD029534

Molina-Carpio, J. (2007). *Agua y Recurso Hídrico en el Sudoeste de Potosí.* Cochabamba: Publicación FOBOMADE, 72.

Molina-Carpio, J., Espinoza, J. C., Coritza, E., Salcedo, F., Farfán, C., Mamani, L., et al. (2019). Climate and spatial variability of the humid upper andes. *Ecología en Bolivia.* 54 (1), 40–56.

Molina-Carpio, J., Espinoza, J. C., Vauchel, P., Ronchail, J., Gutierrez, B., Guyot, J. L., et al. (2017). The hydroclimatology of the upper madeira river basin: spatio-temporal variability and trends (1967-2013). *Hydrol. Sci. J.* 62 (6), 911–927. doi:10.1080/02626667.2016.1267861

Molina-Carpio, J., Salcedo, F., and Vauchel, P. (2007). *Balance hídrico de cuencas montañosas húmedas. 2a reunión científica ORE-HYBAM.* Manaus.

Molina-Carpio, J., Satgé, F., and Pillco, R. (2014). "Los recursos hídricos del sistema TDPS," in *Línea base de conocimientos sobre los recursos hidrológicos e hidrobiológicos en el sistema TDPS con enfoque en la cuenca del Lago Titicaca*. Editors M. Pouilly, X. Lazzaro, and D. Point (Quito: IUCN-IRD), 19–43.

Montecinos, A., and Aceituno, P. (2003). Seasonality of the ENSO-related rainfall variability in central Chile and associated circulation anomalies. *J. Clim.* 16, 281–296. doi:10.1175/1520-0442(2003)016<0281:soterr>2.0.co;2

Montecinos, A., Díaz, A., and Aceituno, P. (2000). Seasonal diagnostic and predictability of rainfall in subtropical south america based on tropical pacific SST. *J. Clim.* 13, 746–758. doi:10.1175/1520-0442(2000)013<0746:sdapor>2.0.co;2

Moquet, J.-S. (2011). Chemical weathering and atmospheric/soil CO2 uptake in the andean and foreland amazon basins. *Chem. Geol.* 287 (1–2), 1–26. doi:10.1016/j.chemgeo.2011.01.005

Mora, D. E., and Willem, P. (2012). Decadal oscillations in rainfall and air temperature in the Paute River Basin –Southern Andes of Ecuador. *Theor Appl. Climatol.* 108, 267–282. doi:10.1007/s00704-011-0527-4

Morales, J. S., Arias, P. A., Martínez, J. A., and Durán-Quesada, A. M. (2020). The role of low-level circulation on water vapor transport to central and northern south america: insights from a 2D Lagrangian approach. *Int. J. Climatol.* [Epub ahead of print]. doi:10.1002/joc.6873

Mundo, I., Masiokas, M., Villalba, R., Morales, M., Neukom, R., Quesne, C., et al. (2012). Multi-century tree-ring based reconstruction of the neuquén river streamflow, northern patagonia, argentina. *Clim. Past.* 8, 815–829. doi:10.5194/cp-8-815-2012

Muñoz, A. A., González-Reyes, A., and Lara, A. (2016). Streamflow variability in the Chilean temperate-mediterranean climate transition (35°S -42°S) during the last 400 years inferred from tree-ring records. *Clim. Dyn.* 47, 4051–4066. doi:10.1007/s00382-016-3068-9

Navarro-Monterroza, E., Arias, P. A., and Vieira, S. C. (2019). El Niño-oscilación del sur, fase modoki, y sus efectos en la variabilidad espacio-temporal de la precipitación en colombia. revista de la acadamia colombiana de ciencias exactas. *Físicas y Naturales.* 43 (166), 120–132. doi:10.18257/raccefyn.704

Neukom, R., Rohrer, M., Calanca, P., Salzmann, N., Huggel, C., Acuña, D., et al. (2015). Facing unprecedented drying of the central Andes? Precipitation variability over the period AD 1000–2100. *Environ. Res. Lett.* 10, 084017. doi:10.1088/1748-9326/10/8/084017

Olarinoye, T., Gleeson, T., and Marx, V. (2020). Global karst springs hydrograph dataset for research and management of the world's fastest-flowing groundwater. *Sci. Data.* 7 (59), 4090. doi:10.1038/s41597-019-0346-5

Oster, R. (1979). Las precipitaciones en colombia. revista colombia geográfica, instituto agustín codazzi. *Bogotá.* VI, 5–147.

Pabón-Caicedo, J. D., Arias, P. A., Carril, A. F., Espinoza, J. C., Goubanova, K., Lavado, W., et al. (2020). Observed and projected hydroclimate changes in the andes. *Front. Earth Sci.* 8, 61. doi:10.3389/feart.2020.00061

Paccini, L., Espinoza, J. C., Ronchail, J., and Segura, H. (2017). Intraseasonal rainfall variability in the Amazon basin related to large-scale circulation patterns: a focus on western amazon-andes transition region. *Int. J. Climatol.* [Epub ahead of print]. doi:10.1002/joc.5341

Pasquini, A., and Depetris, P. (2007). Discharge trends and flow dynamics of South American rivers draining the southern atlantic seaboard: an overview. *J. Hydrol.* 333, 385–399. doi:10.1016/j.jhydrol.2006.09.005

Pasquini, A., and Depetris, P. (2011). Southern patagonia's perito moreno glacier, lake argentino, and santa cruz river hydrological system: an overview. *J. Hydrol.* 405, 48–56. doi:10.1016/j.jhydrol.2011.05.009

Pittock, A. B. (1980). Pattern of climate variability in argentina and chile-I: precipitation, 1931-60. *Mon. Weather Rev.* 108, 1347–1361.

Poveda, G. (2004). La hidroclimatología de colombia: una síntesis desde la escala interdecadal hasta la escala diurna. Revista academia colombiana de ciencias exactas. *Físicas y Naturales.* 28 (107), 201–222.

Poveda, G., Álvarez, D. M., and Rueda, O. A. (2011). Hydro-climatic variability over the andes of colombia associated with ENSO: a review of climatic processes and their impact on one of the Earth's most important biodiversity hotspots. *Clim. Dynam.* 36 (11-12), 2233–2249. doi:10.1007/s00382-010-0931-y

Poveda, G., Espinoza, J. C., Zuluaga, M. D., Solman, S. A., Garreaud, R., and van Oevelen, P. J. (2020). High impact weather events in the andes. *Front. Earth Sci.* 8, 162. doi:10.3389/feart.2020.00162

Poveda, G., Jaramillo, L., and Vallejo, L. F. (2014). Seasonal precipitation patterns along pathways of South American low-level jets and aerial rivers. *Water Resour. Res.* 50, 98–118. doi:10.1002/2013WR014087

Poveda, G., and Mesa, O. J. (2000). On the existence of Lloró (the rainiest locality on Earth): enhanced ocean-atmosphere-land interaction by a low-level jet. *Geophys. Res. Lett.* 27, 1675–1678. doi:10.1029/1999gl006091

Poveda, G., Mesa, O. J., Salazar, L. F., Arias, P. A., Moreno, H. A., Vieira, S. C., et al. (2005). Diurnal cycle of precipitation in the tropical andes of colombia. *Mon. Weather Rev.* 133 (No.1), 228–240. doi:10.1175/mwr-2853.1

Poveda, G., Moncada, O., Waylen, P. R., and Rasmussen, R. (2019). "The pluviometric optimum on the Andes of Colombia," in *Poster2019 American geophysical union fall meeting, A24K-09.* (San Francisco, CA: American Geophysical Union), 9–13.

Poveda, G., Waylen, P. R., and Pulwarty, R. (2006). Modern climate variability in northern south america and southern mesoamerica. *Palaeogeogr. Palaeoclimatol. Palaeoecol.* 234, 3–27. doi:10.1016/j.palaeo.2005.10.031

Pulwarty, R. S., Barry, R. G., Hurst, C. M., Sellinger, K., and Mogollon, L. F. (1998). Precipitation in the venezuelan andes in the context of regional climate. *Meteorol. Atmos. Phys.* 67, 217–237.

Quinn, W. H., and Neal, V. T. (1983). Long-term variations in the southern oscillation, el Niño and Chilean subtropical rainfall. *Fish. Bull.* 81, 363–374.

Rabatel, A., Francou, B., Soruco, A., Gomez, J., Cáceres, B., Ceballos, J. L., et al. (2013). Current state of glaciers in the tropical Andes: a multi-century perspective on glacier evolution and climate change. *Cryosphere* [Epub ahead of print]. doi:10.5194/tc-7-81-2013

Rasmussen, K. L., and Houze Jr, R. A. (2011). Orogenic convection in subtropical South America as seen by the TRMM satellite. *Mon. Weather Rev.*, 139, 2399–2420. doi:10.1002/joc.4693

Rau, P., Bourrel, L., Labat, D., Melo, P., Dewitte, B., Frappart, F., et al. (2016). Regionalization of rainfall over the peruvian pacific slope and coast. *Int. J. Climatol.* 37 (1), 143–158. doi:10.1002/joc.4693

Rau, P., Bourrel, L., Labat, D., Frappart, F., Ruelland, D., Lavado, W., et al. (2017). Hydroclimatic change disparity of Peruvian Pacific drainage catchments. *Theor. Appl. Climatol.* 1–15. doi:10.1007/s00704-017-2263-x

Recalde-Coronel, G. C., Barnston, A. G., and Muñoz, A. G. (2014). Predictability of december–april rainfall in coastal and andean ecuador. *J. Appl. Meteor. Climatol.* 53, 1471–1493. doi:10.1175/JAMC-D-13-0133.1

Recalde-Coronel, G. C., Zaitchik, B., and Pan, W. K. (2020). Madden-Julian oscillation influence on sub-seasonal rainfall variability on the west of south america. *Clim. Dyn.* 54, 2167–2185. doi:10.1007/s00382-019-05107-2

Renwick, J. A., and Revell, M. J. (1999). Blocking over the south pacific and rossby wave propagation. *Mon. Weather Rev.* 127, 2233–2247.

Réveillet, M., Macdonell, S., Gascoin, S., Kinnard, C., Lhermitte, S., and Schaffer, N. (2019). Uncertainties in the spatial distribution of snow sublimation in the semi-arid andes of chile. *Cryosphere Discuss.* 1-34, 1–34. doi:10.5194/tc-2019-31

Rivera, J. A., Penalba, O. C., Villalba, R., and Araneo, D. C. (2017). Spatio-temporal patterns of the 2010–2015 extreme hydrological drought across the central andes, argentina. *Water* 9, 652. doi:10.3390/w9090652

Roche, M. A., Aliaga, A., Campos, J., Pena, J., Cortes, J., and Rocha, N. (1990). Hétéréogéneité des précipitations sur la cordillère des andes boliviennes. hydrology in mountainous regions. I–hydrological measurements; the water cycle. *IAHS* 193, 381–388.

Rollenbeck, R., and Bendix, J. (2011). Rainfall distribution in the Andes of southern Ecuador derived from blending weather radar data and meteorological field observations. *Atmos. Res.* 99 (2), 277–289. doi:10.1016/j.atmosres.2010.10.018

Romatschke, U., and Houze, R. A., Jr (2013). Characteristics of precipitating convective systems accounting for the summer rainfall of tropical and subtropical south america. *J. Hydrometeorol.* 14 (1), 25–46. doi:10.1175/JHM-D-12-060.1

Ronchail, J., and Gallaire, R. (2006). ENSO and rainfall along the zongo valley (Bolivia) from the Altiplano to the amazon basin. *Int. J. Climatol.* 26, 1223–1236. doi:10.1002/joc.1296

Rondanelli, R., Hatchett, B., Rutllant, J., Bozkurt, D., and Garreaud, R. (2019). Strongest MJO on record triggers extreme atacama rainfall and warmth in antarctica. *Geophys. Res. Lett.* 46, 3482–3491. doi:10.1029/2018gl081475

Rondanelli, R., Molina, A., and Falvey, M. (2015). The atacama surface solar maximum. *Bull. Am. Meteorol. Soc.* 96, 405–418. doi:10.1175/BAMS-D-13-00175.1

Rotunno, R., Klemp, J. B., and Weisman, M. L. (1988). A theory for strong, long-lived squall lines. *J. Atmos. Sci.* 45 (3), 463–485.

Rubin, M. J. (1955). An investigation of relationships between northern and southern hemispheres meteorological parameters. *Notes* 4, 122–126.

Ruiz-Vasquez, M., Arias, P. A., Martinez, J. A., and Espinoza, J. C. (2020). Effects of amazon basin deforestation on regional atmospheric circulation and water vapor transport towards tropical south america. *Clim. Dynam.* 54 (9), 4169–4189. doi:10.1007/s00382-020-05223-4

Rutllant, J., and Fuenzalida, H. (1991). Synoptic aspects of the central Chile rainfall variability associated with the southern oscillation. *Int. J. Climatol.* 11, 63–76.

Saavedra, M., Junquas, C., Espinoza, J. C., and Silva, Y. (2020). Impacts of topography and land use change on the air surface temperature and precipitation over the central peruvian andes. *Atmos. Res.* 234, 104711. doi:10.1016/j.atmosres.2019.104711

Saavedra, M., and Takahashi, K. (2017). Physical controls on frost events in the central andes of peru using *in situ* observations and energy flux models. *Agric. For. Meteorol.* 239, 58–70. doi:10.1016/j.agrformet.2017.02.019

Sakamoto, M., Ambrizzi, T., and Poveda, G. (2011). Moisture sources and life cycle of convective systems over western colombia. *Adv. Meteorol.* 11, 890759. doi:10.1155/2011/890759

Satgé, F., Espinoza, R., Pillco, Z. R., Roig, H., Timouk, F., Molina, J., et al. (2017). Role of climate variability and human activity on poopó lake droughts between 1990 and 2015 assessed using remote sensing data. *Rem. Sens.* 9, 1–17. doi:10.3390/rs9030218

Scaff, L., Rutllant, J. A., Rahn, D., Gascoin, S., and Rondanelli, R. (2017). Meteorological interpretation of orographic precipitation gradients along an andes west slope basin at 30° S (elqui valley, Chile). *J. Hydrometeorol.* 18 (3), 713–727.doi:10.1175/JHM-D-16-0073.1

Schoolmeester, T., Johansen, K. S., Alfthan, B., Baker, E., Hesping, M., and Verbist, K. (2018). The Andean glacier and water atlas–the impact of glacier retreat on water resources. UNESCO and GRID-arendal, 80.

Segura, H., Espinoza, J. C., Junquas, C., Lebel, T., Vuille, M., and Garreaud, R. (2020). Recent changes in the precipitation-driving processes over the southern tropical andes/western amazon. *Clim. Dynam.* 54 (5-6), 2613–2631. doi:10.1007/s00382-020-05132-6

Segura, H., Espinoza, J. C., Junquas, C., and Takahashi, K. (2016). Evidencing decadal and interdecadal hydroclimatic variability over the central andes. *Environ. Res. Lett.* 11, 094016. doi:10.1088/1748-9326/11/9/094016

Segura, H., Junquas, C., Espinoza, J. C., Vuille, M., Jauregui, Y. R., Rabatel, A., et al. (2019). New insights into the rainfall variability in the tropical andes on seasonal and interannual time scales. *Clim. Dynam.* 53 (1-2), 405–426. doi:10.1007/s00382-018-4590-8

Serna, L. M., Arias, P. A., and Vieira, S. C. (2018). Las corrientes superficiales de chorro del chocó y el caribe durante los eventos de El Niño y El Niño Modoki. revista de la acadamia colombiana de ciencias exactas. *Físicas y Naturales* 42 (165), 410–421. doi:10.18257/raccefyn.705

Shimizu, M. H., and Ambrizzi, T. (2016). MJO influence on ENSO effects in precipitation and temperature over south america. *Theor. Appl. Climatol.* 124, 291–301. doi:10.1007/s00704-015-1421-2

Shimizu, M. H., Ambrizzi, T., and Brant, L. (2016). Extreme precipitation events and their relationship with ENSO and MJO phases over northern south america. *Int. J. Climatol.* 37, 2977–2989. doi:10.1002/joc.4893

Sicart, J. E., Espinoza, J. C., Queno, L., and Medina, M. (2016). Radiative properties of clouds over a tropical bolivian glacier: seasonal variations and relationship with regional atmospheric circulation. *Int. J. Climatol.* 36 (8), 3116–3128. doi:10.1002/joc.4540

Sierra, J. P., Arias, P. A., Vieira, S. C., and Agudelo, J. (2018). How well do CMIP5 models simulate the low-level jet in western colombia?. *Clim. Dynam.* 51 (5-6), 2247–2265. doi:10.1007/s00382-017-4010-5

Silva, Y., Takahashi, K., and Chávez, R. (2008). Dry and wet rainy seasons in the Mantaro River basin (central Peruvian Andes). *Adv. Geosci.* 14, 261–264. doi:10.5194/adgeo-14-261-2008

Silvestri, G., and Vera, C. (2009). Nonstationary impacts of the southern annular mode on southern hemisphere climate. *J. Clim.* 22 (22), 6142–6148. doi:10.1175/2009jcli3036.1

Seiler, C., Hutjes, R. W. A., and Kabat, P. (2013). Climate variability and trends in Bolivia. *J. Appl. Meteorol. Climatol.* 52 (1), 130–146.

Solman, S. A., and Menéndez, C. G. (2002). ENSO-related variability of the southern hemisphere winter storm track over the eastern pacific–atlantic sector. *J. Atmos. Sci.* 59, 2128–2141. doi:10.1175/1520-0469(2002)059<2128:ervots>2.0.co;2

Sorí, R., Nieto, R., Drumond, A., Stojanovic, M., and Gimeno, L. (2019). On the connection between atmospheric moisture transport and dry conditions in rainfall climatological zones of the Niger river basin. *Water* 11, 622. doi:10.3390/w11030622

Soruco, A., Vincent, C., Rabatel, A., Francou, B., Thibert, E., Sicart, J. E., et al. (2015). Contribution of glacier runoff to water resources of La Paz City, Bolivia (16S). *Ann. Glaciol.* 56, 147–154. doi:10.3189/2015aog70a001

Staal, A. (2018). Forest-rainfall cascades buffer against drought across the amazon. *Nat. Clim. Change.* 8, 539–543. doi:10.1038/s41558-018-0177-y

Stuecker, M. F. (2018). Revisiting the Pacific Meridional mode. *Sci. Rep.* 8, 3216 doi:10.1038/s41598-018-21537-0

Sulca, J., Takahashi, K., Espinoza, J. C., Vuille, M., and Lavado, W. (2017). Impacts of different ENSO flavors and tropical Pacific convection variability (ITCZ, SPCZ) on austral summer rainfall in south america, with a focus on peru. *Int. J. Climatol.* 38 (1), 420–435. doi:10.1002/joc.5185

Sulca, J., Vuille, M., Silva, Y., and Takahashi, K. (2016). Teleconnections between the Peruvian central Andes and northeast Brazil during extreme rainfall events in austral summer. *J. Hydrometeorol.* 17, 151026144022007. doi:10.1175/JHM-D-15-0034.1

Sulca, J., Vuille, M., Roundy, P., Takahashi, K., Espinoza, J. C., Silva, Y., et al. (2018). Climatology of extreme cold events in the central Peruvian Andes during austral summer: origin, types, and teleconnections. *Q. J. R. Meteorol. Soc.* [Epub ahead of print]. doi:10.1002/qj.3398

Sun, X., Renard, B., Thyer, M., Westra, S., and Lang, M. (2015). A global analysis of the asymmetric effect of ENSO on extreme precipitation. *J. Hydrol.* 530, 51–65. doi:10.1016/j.jhydrol.2015.09.016

Takahashi, K., and Battisti, D. (2007). Processes controlling the mean tropical pacific precipitation pattern. Part II: the SPCZ and the southeast pacific dry zone. *J. Clim.* 20, 5696–5706.

Takahashi, K., and Martínez, A. G. (2019). The very strong coastal El Niño in 1925 in the far-eastern Pacific. *Clim. Dynam.* 52, 7389–7415. doi:10.1007/s00382-017-3702-1

Takahashi, K., Montecinos, A., Goubanova, K., and Dewitte, B. (2011). ENSO regimes: reinterpreting the canonical and Modoki el Niño. *Geophys. Res. Lett.* 38, L10704. doi:10.1029/2011GL047364

Tedeschi, R. G., Cavalcanti, I. F. A., and Grimm, A. M. (2013). Influences of two types of ENSO on South American precipitation. *Int. J. Climatol.* 33, 1382–1400. doi:10.1002/joc.3519

Torres-Batlló, J., Martí-Cardona, B., and Pillco-Zolá, R. (2020). Mapping evapotranspiration, vegetation and precipitation trends in the catchment of the shrinking lake poopó. *Rem. Sens.* 12, 73. doi:10.3390/rs12010073

Tovar Pacheco, J. A., Sayán Miranda, J. L., Verástegui, P. G., and Guzmán Martínez, A. (2006). Estado del conocimiento de la hidrogeología en perú. *Bol. Geol. Min.* 117 (1), 147–161.

Trachte, K., Rollenbeck, R., and Bendix, J. (2010a). Nocturnal convective cloud formation under clear-sky conditions at the eastern andes of south ecuador. *J. Geophys. Res.* 115, D24203. doi:10.1029/2010jd014146

Trachte, K., Nauss, T., and Bendix, J. (2010b). The impact of different terrain configurations on the formation and dynamics of katabatic flows: idealised case studies. *Bound Layer Meteorol.* 134, 307–325. doi:10.1007/s10546-009-9445-8

Trachte, K., and Bendix, J. (2012). Katabatic flows and their relation to the formation of convective clouds—idealized case studies. *J. Appl. Meteor. Climatol.* 51 (8), 1531–1546. doi:10.1175/JAMC-D-11-0184.1

UNESCO (2006). *Balance hídrico superficial del Perú a nivel multianual. Documentos Técnicos del PHI-LAC, No. 1.*

Programa Hidrológico Internacional (PHI) de la Oficina Regional de Ciencia para América Latina y el Caribe de la Organización de las Naciones Unidas para la Educación, la Ciencia y la Cultura (UNESCO), Montevideo- Uruguay.

Urrea, V., Ochoa, A., and Mesa, O. (2019). Seasonality of rainfall in Colombia. *Water Resour. Res.* 55, 4149–4162. doi:10.1029/2018WR023316

Vallejo-Bernal, S. M., Urrea, V., Bedoya-Soto, J. M., Posada, D., Olarte, A., Cárdenas-Posso, Y., et al. (2020). Ground validation of TRMM 3B43 precipitation data over colombia monthly and seasonal timescales. *Int. J. Climatol.* 1–24. doi:10.1002/joc.6640

Velásquez-Restrepo, M., and Poveda, G. (2019). Estimation of the water balance of the colombian pacific region. *Dyna.* 86 (208), 297–306. doi:10.15446/dyna.v86n208.73587

Vera, C. (2006). Toward a unified view of the american monsoon systems. *J. Clim.* 19, 4977–5000. doi:10.1175/jcli3896.1

Viale, M., Bianchi, E. L. J., Cara, L., and Ruiz. (2019). Contrasting climates at both sides of the Andes in Argentina and Chile. *Front. Environ. Sci.* doi:10.3389/fenvs.2019.00069

Viale, M., and Garreaud, R. (2015). Orographic effects of the subtropical and extratropical Andes on upwind precipitating clouds. *J. Geophys. Res. Atmos.* 120, 4962–4974. doi:10.1002/2014jd023014

Viale, M., Houze, R. A., Jr., and Rasmussen, K. L. (2013). Upstream orographic enhancement of a narrow coldfrontal rainband approaching the andes. *Mon. Weather Rev.* 141, 1708–1730. doi:10.1175/mwr-d-12-00138.1

Viale, M., and Nuñez, M. (2011). Climatology of winter orographic precipitation over the subtropical central andes and associated synoptic and regional characteristics. *J. Hydrometeorol.* 12 (4), 481–507. doi:10.1175/2010jhm1284.1

Vuille, M., Bradley, R., and Keimig, F. (1999). Climate variability in the andes of ecuador and its relation to tropical pacific and atlantic sea surface temperature anomalies. *J. Clim.* 13 (14), 2520–2535.

Vuille, M., Francou, B., Wagnon, P., Juen, I., Kaser, G., Mark, B. G., et al. (2008). Climate change and tropical andean glaciers: past, present and future. *Earth Sci. Rev.* 89 (3-4), 79–96. doi:10.1016/j.earscirev.2008.04.002

Vuille, M., Carey, M., Huggel, C., Buytaert, W., Rabatel, A., Jacobsen, D., et al. (2018). Rapid decline of snow and ice in the tropical andes–impacts, uncertainties and challenges ahead. *Earth. Rev.* 176, 195–213. doi:10.1016/j.earscirev.2017.09.019

Vuille, M., and Keimig, F. (2004). Interannual variability of summertime convective cloudiness and precipitation in the central andes derived from ISCCP-B3 data. *J. Clim.* 17, 3334–3348. doi:10.1175/1520-0442(2004)017<3334:ivoscc>2.0.co;2

Wang, H., and Fu, R. (2002). Cross-equatorial flow and seasonal cycle of precipitation over south america. *J. Clim.* 15, 1591–1608. doi:10.1175/1520-0442(2002)015<1591:cefasc>2.0.co;2

Zalazar, L., Ferri Hidalgo, L., Castro, M., Gargantini, H., Gimenez, M., Pitte, P., et al. (2017). Glaciares de argentina: resultados preliminares del inventario nacional de glaciares glaciers of argentina: preliminary results of the national inventory of glaciers. *Revista de Glaciares y Ecosistemas de Montañas* 2, 13–22. doi:10.36580/rgem.i2.13-22

Zemp, D. C., Schleussner, C.-F., Barbosa, H. M. J., van der Ent, R. J., Donges, J. F., Heinke, J., et al. (2014). On the importance of cascading moisture recycling in south america. *Atmos. Chem. Phys.* 14, 13337–13359. doi:10.5194/acp-14-13337-2014

Zemp, D. C., Schleussner, C. F., Barbosa, H. M., Hirota, M., Montade, V., Sampaio, G., et al. (2017). Self-amplified Amazon forest loss due to vegetation-atmosphere feedbacks. *Nat. Commun.* 8, 14681. doi:10.1038/ncomms14681

Ziegler, C. L., and Rasmussen, E. N. (1998). The initiation of moist convection at the dryline: forecasting issues from a case study perspective. *Weather Forecast.* 13, 1106–1131.

Zipser, E. J., Liu, C. T., Cecil, D. J., Nesbitt, S. W., and Yorty, D. P. (2006). Where are the most intense thunderstorms on Earth? *Bull. Am. Meteorol. Soc.* 87, 1057–1071. doi:10.1175/BAMS-87-8-1057

Conflict of Interest: The authors declare that the research was conducted in the absence of any commercial or financial relationships that could be construed as a potential conflict of interest.

Copyright © 2021 Arias, Garreaud, Poveda, Espinoza, Molina-Carpio, Masiokas, Viale, Scaff and van Oevelen. This is an open-access article distributed under the terms of the Creative Commons Attribution License (CC BY). The use, distribution or reproduction in other forums is permitted, provided the original author(s) and the copyright owner(s) are credited and that the original publication in this journal is cited, in accordance with accepted academic practice. No use, distribution or reproduction is permitted which does not comply with these terms.

Advantages of publishing in Frontiers

OPEN ACCESS
Articles are free to read for greatest visibility and readership

FAST PUBLICATION
Around 90 days from submission to decision

HIGH QUALITY PEER-REVIEW
Rigorous, collaborative, and constructive peer-review

TRANSPARENT PEER-REVIEW
Editors and reviewers acknowledged by name on published articles

Frontiers
Avenue du Tribunal-Fédéral 34
1005 Lausanne | Switzerland

Visit us: www.frontiersin.org
Contact us: frontiersin.org/about/contact

REPRODUCIBILITY OF RESEARCH
Support open data and methods to enhance research reproducibility

DIGITAL PUBLISHING
Articles designed for optimal readership across devices

FOLLOW US
@frontiersin

IMPACT METRICS
Advanced article metrics track visibility across digital media

EXTENSIVE PROMOTION
Marketing and promotion of impactful research

LOOP RESEARCH NETWORK
Our network increases your article's readership